uncatalogued

UNITED STATES DEPARTMENT OF THE INTERIOR

GEOLOGICAL SURVEY

PROCEEDINGS OF WORKSHOP XXVIII On the Borah Peak, Idaho, Earthquake

Volume A

Convened under Auspices of

NATIONAL EARTHQUAKE PREDICTION AND HAZARD PROGRAMS

3 - 6 October 1984

OPEN-FILE REPORT 85-290

This report (map) is preliminary and has not been reviewed for conformity with U.S.Geological Survey editorial standards (and stratigraphic nomenclature). Any use of trade names is for descriptive purposes only and does not imply endorsement by the U.S.G.S.

Menlo Park, California

1985

CONFERENCES TO DATE

Conference I	Abnormal Animal Behavior Prior to Earthquakes, I Not Open-Filed
Conference II	Experimental Studies of Rock Friction with Application to Earthquake Prediction Not Open-Filed
Conference III	Fault Mechanics and Its Relation to Earthquake Prediction Open-File No. 78-380
Conference IV	Use of Volunteers in the Earthquake Hazards Reduction Program Open-File No. 78-336
Conference V	Communicating Earthquake Hazard Reduction Information Open-File No. 78-933
Conference VI	Methodology for Identifying Seismic Gaps and Soon-to-Break Gaps Open-File No. 78-943
Conference VII	Stress and Strain Measurements Related to Earthquake Prediction Open-File No. 79-370
Conference VIII	Analysis of Actual Fault Zones in Bedrock Open-File No. 79-1239
Conference IX	Magnitude of Deviatoric Stresses in the Earth's Crust and Upper Mantle Open-File No. 80-625
Conference X	Earthquake Hazards Along the Wasatch and Sierra-Nevada Frontal Fault Zones Open-File No. 80-801
Conference XI	Abnormal Animal Behavior Prior to Earthquakes, II Open-File No. 80-453
Conference XII	Earthquake Prediction Information Open-File No. 80-843
Conference XIII	Evaluation of Regional Seismic Hazards and Risk Open-File No. 81-437
Workshop XIV	Earthquake Hazards of the Puget Sound Region, Washington Open-File No. 83-19
Workshop XV	Preparing for the Responding to a Damaging Earthquake in the Eastern United States Open-File No. 82-220
Workshop XVI	The Dynamic Characteristics of Faulting Inferred from Recording of Strong Ground Motion Open-File No. 82-591
Workshop XVII	Hydraulic Fracturing Stress Measurements Open-File No. 82-1075

Open-File Service Section
Branch of Distribution
U.S. Geological Survey
Box 25425, Federal Center
Denver, Colorado 80225

Continued on inside back page

UNITED STATES DEPARTMENT OF THE INTERIOR

GEOLOGICAL SURVEY

PROCEEDINGS OF

WORKSHOP XXVIII

On the Borah Peak, Idaho, Earthquake

Volume A

Convened under Auspices of

NATIONAL EARTHQUAKE PREDICTION AND HAZARDS PROGRAMS

3 - 6 October 1984

Editors and Convenors

Ross S. Stein
U.S. Geological Survey
Menlo Park, California 94025

Robert C. Bucknam
U.S. Geological Survey
Denver, Colorado 80225

Organizing Committee

Roy M. Breckenridge	Idaho Geological Survey
Anthony J. Crone	U.S. Geological Survey
Robert B. Smith	University of Utah
Spencer H. Wood	Boise State University

Administrators

Wanda H. Seiders and Kay E. Johnson
U.S. Geological Survey

OPEN-FILE REPORT 85-290

Compiled by
Muriel Jacobson

This report is preliminary and has not been reviewed for conformity with U.S. Geological Survey editorial standards and stratigraphic nomenclature. Any use of trade names is for descriptive purposes only and does not imply endorsement by the USGS.

MENLO PARK, CALIFORNIA
1985

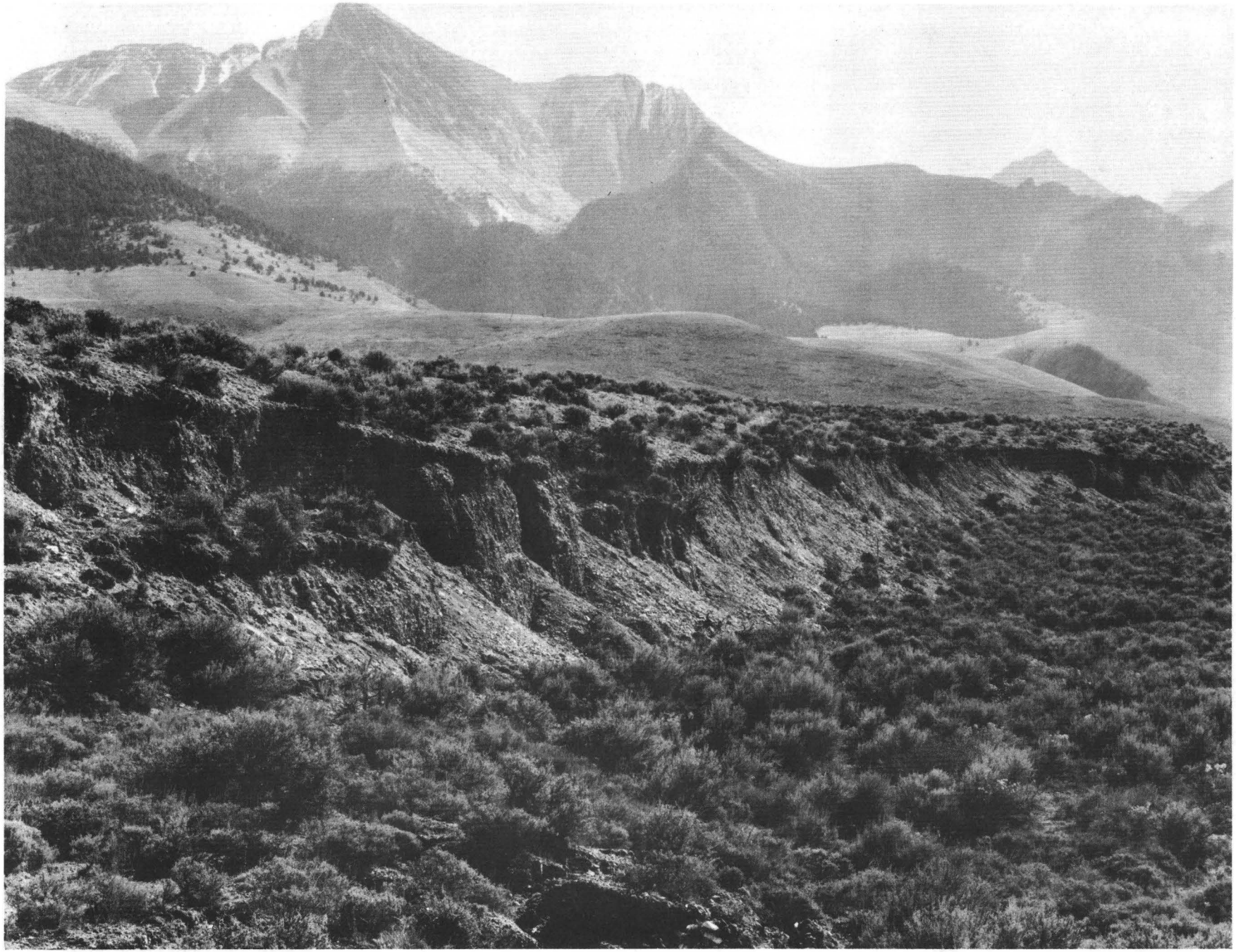

Frontispiece Caption

The 4.8-m-high scarp formed by the Borah Peak earthquake of 28 October 1983, at the place of maximum scarp height. Borah Peak is in the background. Photographed by Harold E. Malde, U.S. Geological Survey. [Denver U.S.G.S. photographic library reference number Malde 1493.]

Photographic Data:

Date of photo:	8 October 1984
Time:	12:12 pm, MDT
Location:	Borah Peak Quadrangle; 2075 ft N & 325 ft E of SW corner of Sec 28, T10N/R22E
Orientation:	S 58° E
Camera height:	201 cm above the ground

Field Guide and Map to Accompany the Research Papers

Volume B of this report contains a self-guided field excursion of the spectacular surface faulting features, landslides, and sand boils that formed during the 1983 Borah Peak, Idaho, earthquake. Three annotated topographic maps that are referred to in the guide as Plates 1-3 are located in the map flap of Volume B. The field guide is ancillary to the collection of research papers that are contained in this volume of the Report.

TABLE OF CONTENTS

Introduction and Acknowledgements:
Ross S. Stein and Robert C. Bucknam..... v

List of Participants..... ix

OVERVIEW

Quaternary Tectonic Setting of the 1983 Borah Peak Earthquake, Central Idaho
William E. Scott, Kenneth L. Pierce, and H.M. Hait, Jr..... 1

Variations in slip rates, migration, and grouping of slip events on faults in the Great Basin Province
Robert E. Wallace..... 17

Perspective from the Fairview Peak-Dixie Valley Earthquakes of 1954
George A. Thompson..... 27

SURFACE FAULTING

Characteristics of surface faulting accompanying the Borah Peak Earthquake, Central Idaho
Anthony J. Crone, Michael N. Machette, Manuel G. Bonilla, James J. Lienkaemper, Kenneth L. Pierce, William E. Scott and Robert C. Bucknam..... 43

Patterns of offset associated with the 1983 Borah Peak, Idaho, earthquake and previous events
Stephen L. Salyards..... 59

Measurement of vertical tectonic offset using longitudinal profiles of faulted geomorphic surfaces near Borah Peak, Idaho: A preliminary report
Kirk R. Vincent..... 76

Documentation for benchmark photographs showing some effects of the 1983 Borah Peak Earthquake with considerations for studies of scarp degradation
Michael N. Machette..... 97

Identifying active faults by aerial photography: A comparison of the Lost River fault before and after the Borah Peak Earthquake of October 28, 1983
Roy M. Breckenridge..... 110

Late Quaternary activity along the Lone Pine fault, Eastern California
Lester Lubetkin and Malcolm M. Clark..... 118

Comparison of the geomorphic and surficial fracturing effects of the 1983 Borah Peak, Idaho Earthquake with those of the 1959 Hebgen Lake, Montana Earthquake
William B. Hall and Peter E. Sablock..... 141

NEAR-SURFACE FAULT STRUCTURE

The 1983 Borah Peak Earthquake: A calibration event for quantifying earthquake recurrence and fault behavior on Great Basin normal faults
David P. Schwartz and Anthony J. Crone..... 153

Shallow seismic refraction studies across the Willow Creek fault rupture zone and the Chilly Buttes Sand Boils
J.R. Pelton, C.W. Meissner, C.J. Waag, and S.H. Wood..... 161

Subsurface radar imagery of near-surface fractures associated with the Borah Peak Earthquake, Idaho
Roger Bilham..... 182

Quaternary history of faulting on the Arco segment of the Lost River fault, Central Idaho
Kenneth L. Pierce..... 195

Quaternary faulting near Arco and Howe, Idaho
Harold E. Malde..... 207

[See also Skipp and Harding, pp. 666 - 669]

SEISMOLOGY

The 1983 Borah Peak, Idaho, Earthquake: Regional seismicity, kinematics of faulting, and tectonic mechanism
R.B. Smith, W.D. Richins, and D.I. Doser..... 236

Instrumental seismicity of Central Idaho
James W. Dewey..... 264

The 1983 Borah Peak, Idaho Earthquake: Relationship of aftershocks to the mainshock, surface faulting, and regional tectonics
W.D. Richins, R.B. Smith, C.J. Langer, J.E. Zollweg, J.J. King, and J.C. Pechmann..... 285

Characteristics of the aftershock sequence of the Borah Peak, Idaho, Earthquake determined from digital recordings of the events
John Boatwright..... 311

Later aftershocks of the 1983 Borah Peak, Earthquake and related activity in Central Idaho
J.E. Zollweg and W.D. Richins..... 345

The 1983 Borah Peak, Idaho and 1959 Hebgen Lake, Montana Earthquakes: Models for normal fault earthquakes in the Intermountain Seismic Belt
Diane I. Doser..... 368

Acceleration data from the 1983 Borah Peak, Idaho Earthquake recorded at the Idaho National Engineering Laboratory
Suzette M. Jackson..... 385

Isoseismal map and intensity distribution for the Borah Peak, Idaho, Earthquake of October 28, 1983
Carl W. Stover..... 401

Teleseismic estimates of the energy radiated by shallow earthquakes
John Boatwright and George L. Choy..... 409

An eyewitness observation of oscillatory fault motion accompanying an M_L5.5 aftershock of the Borah Peak Earthquake
Frances M. Boler..... 449

[See also Barrientos et al., pp. 495 - 497]

GEODESY

The 1983 Borah Peak, Idaho, Earthquake: Geodetic evidence for deep rupture on a planar fault
Ross S. Stein and Sergio E. Barrientos..... 459

Inversion for moment as a function of depth from geodetic observations and long period body waves of the 1983 Borah Peak, Idaho Earthquake
Sergio E. Barrientos, Steven N. Ward, Jaime R. Gonzalez-Ruiz, and Ross S. Stein..... 485

Vertical movements associated with the 1959 M=7.1 Hebgen Lake Montana Earthquake
Robert Reilinger..... 519

Dislocation Models for the 1954 Earthquake Sequence in Nevada
Richard A. Snay, Michael W. Cline, and Edward L. Timmerman.. 531

HYDROLOGY

Hydrologic changes following the Idaho Borah Peak Earthquake
R.L. Whitehead..... 556

Regional increase in groundwater discharge after the 1983 Idaho earthquake: Coseismic strain release, tectonic and natural hydraulic fracturing
Spencer H. Wood..... 573

Groundwater eruptions and sediment boil formation in the Chilly Buttes Area, Mt. Borah, Idaho Earthquake
Charles J. Waag..... 593

Hydrothermal Changes in the Upper Geyser Basin, Yellowstone National Park, after the 1983 Borah Peak, Idaho, Earthquake
Roderick A. Hutchinson..... 612

Liquefaction generated by the 1983 Borah Peak, Idaho, Earthquake
T.L. Youd, E.L. Harp, D.K. Keefer, and R.C. Wilson..... 625

Magnetic and soil gas measurements along the surface rupture of the Borah Peak Earthquake of October 28, 1983
F. Scherbaum, C. Roecken, R.H. Ware, and M. Wyss..... 645

[See also, Pelton et al., pp. 170 - 173, and Stein and Barrientos pp. 468 - 469]

REGIONAL GEOLOGY AND GEOPHYSICS

Preliminary Report on geology of Borah Peak area, Idaho, including interpretation of seismic and gravity data
Betty Skipp and Samuel T. Harding..... 657

P-wave travel times and crustal structure of SW Montana from aftershocks of the October 28, 1983 Borah Peak, Idaho, Earthquake
Michael C. Stickney..... 672

Regional gravity and magnetic anomalies in the Borah Peak region of Idaho
Don R. Mabey..... 680

[See also Smith et al., pp. 237 - 240, and Dewey, pp. 264 - 284]

INTRODUCTION AND ACKNOWLEDGMENTS

A large earthquake leaves clues of its nature that can be interpreted only by a diverse group of scientists. We cannot hope to form a coherent picture of the Borah Peak shock, a rare Great Basin event, without listening to each other and reflecting on the historical and geological record of its antecedents. At a workshop held less than a year after the Borah Peak mainshock we shared our observations, exchanged ideas, and revisited the spectacular landforms at the earthquake site. In the forty reports of this volume we present our findings, a wealth of preliminary, but interdisciplinary research.

Within weeks of the Borah Peak earthquake the snow began to fall in Thousand Springs Valley, hampering essential field activities. Many local ranchers opened their homes to us, and representatives of county, state, and federal agencies gave enormous help. Chief among these people, we would like to thank William Savage from Challis National Forest for his constant aid. We would also like to express our debt to the Reverend Harry E. Boughey, who dedicated the workshop to the memory of the children who died tragically in Challis on 28 October 1983, Tara Leaton and Travis Franck, with this invocation:

> The earthquake came like a rushing mighty wind. In a few seconds much damage was done to buildings and homes, causing the tragic death of two young children on their way to school. Fear and uncertainty suddenly grips the minds, hearts, and will of all the people. And the question arises, where is the answer? We live in a world of uncertainties. Being a preacher, I have to say there is a God Who cares about His Earth and His people; because of Him we live and move and have our being.
>
> You are gathered as a group of scientists to seek ways to find out how or why these things happen. We mourn the loss of the two children. Their families will never forget the tragedy of this happening. What shall we say? We live in deeds, not years, in thoughts, not breath, in feelings, not in figures on a dial, and he lives most who thinks most and acts the best. In your effort to discover the origin of these natural disasters, you have a great task ahead of you. Toil on and in thy toil rejoice. May the Lord bless you and keep you and be gracious to you, as you seek an answer to the unsolved problems within and through the Universe.

The Borah Peak earthquake provided a stunning validation of the study of Holocene and late Pleistocene fault scarps to assess the location and magnitude of future large earthquakes. The 35-km-long surface rupture that was formed by the 1983 earthquake mimicked the Holocene fault scarp with astounding precision. The scarp had been excavated and examined a decade before the 1983 earthquake, and was found to have been created by one or two prehistoric slip events cut into a 12,000- to 14,000-yr-old surface. When exhumed in 1984, the old and new earthquakes were seen to have left nearly identical patterns of near-surface faulting. Not only did the prehistoric and 1983 event share an average surface slip of about 2 m, but even more striking, the two events display a similar variation of surface slip from one end of the fault to the other. When combined, the two earthquakes yield an average slip rate of about 0.3 mm/yr during the past 14,000 yr. This Holocene slip rate and record of earthquakes are in remarkable accord with the 4-7 M.yr.-old slip rate of 0.2-0.4 mm/yr estimated from the total structural relief on the fault. At this rate events equal in size to the 1983 shock would repeat every 5,000 to 10,000 yr. The scarp is better developed at Borah Peak than anywhere else along the 150-km-long Lost River Range front. While it is not yet clear if surface slip mirrors the seismic slip at depth, it is indisputable that Holocene scarps provide an unsurpassed tool to identify likely sites for earthquakes. In contrast, microseismicity proved no oracle: although Borah Peak lies within the diffuse Intermountain seismic belt, no shock with $M \geq 3.5$ had occurred near the epicentral region during the past two decades of monitoring.

It is now manifest that reliable estimates of the maximum magnitude of earthquakes along particular fault sections can be made. While this capability falls short of earthquake prediction, it is nevertheless vital to earthquake preparedness and to the design of effective building codes. The fault slip expected during future earthquakes can be estimated from the Holocene-late Pleistocene fault scarps, and the length of the expected fault rupture can be gaged by the length of continuous fault segments. The Borah Peak fault segment meets both of these criteria: The southern end of the 1983 rupture corresponds to a 50° bend in the Lost River fault, and the northern end of the fault splays into two branches with markedly diminished prehistoric and 1983-event scarp heights. The rather uniform fault depth (about 15 km) and dip (45°-60°) of the large historical Great Basin earthquakes means that the fault width (the down-dip dimension) of $M \geq 7$ events tends to cluster around 20 km. Thus the fault slip, length, and width can be judged for assessment of the maximum seismic moment and hence magnitude of future events. Forecasting the time of earthquakes with recurrence periods measured in thousands to tens of thousands of years is a much more tenacious problem, particularly given the dearth of documented preseismic ground deformation or precursory seismicity for Great Basin events.

A vast outpouring of water followed the Borah Peak earthquake for several months, amounting to an excess of nearly one cubic kilometer. About 30 giant sandblows formed or were revitalized near the

mainshock epicenter in isoseismal intensity zone VII. Major changes in spring and stream flow occurred throughout the region that sustained shaking of intensity VI, up to 150 km from the epicenter. Even Old Faithful responded to the shock, lengthening its eruption interval from 69 to 77 minutes. The Yellowstone National Park geysers that changed their eruption durations and intervals lie 250 km from the earthquake, in intensity zone V. The postseismic effusion is still largely a mystery. It is known that the flow did not issue from seismic depths, however, for neither the temperature nor the chemistry of the water differed much from the past. Either water was liberated from fractured rock and sediments during the passage of the seismic waves, which produce large but transient cycles of contraction and extension alternating over periods of seconds, or the water issued where the much smaller permanent strains were compressive, as when a sponge is squeezed. It seems hard to create such a torrent, however, in a region where the predicted permanent strain changes are just a few parts per million, and where changes in the gradients of streams are equally small.

Large Historical Great Basin Earthquakes

Date	Location	Moment Magnitude **M**	Reference
9 January 1872	Inyo, CA	7.8	(1)
2 October 1915	Pleasant Valley, NV	7.2	(2)
10 December 1932	Cedar Mountain, NV	7.0	(3)
16 December 1954	Fairview Peak, NV	7.2	(3)
19 August 1959	Hebgen Lake, MT	7.3	(3)
28 October 1983	Borah Peak, ID	7.0	(3,4)

With the Borah Peak earthquake, we now have a small but valuable inventory of large ($\mathbf{M} \geq 7$) Great Basin shocks to compare. During the past century the inter-event time for these earthquakes of a few decades has made synthesis an exercise in patience, but it is now emerging that all of the well-studied Great Basin events occurred on planar high-angle normal faults extending to about 15 km depth. This is an astonishing record in the face of numerous geologic and seismic reflection interpretations that favor old thrust sheets, reborn as normal faults, to be the principal sites for accommodation of Great Basin extension. Rather, seismic and geodetic evidence for listric and detachment faulting is notably absent. While it is difficult to reconcile these disparate views of continental rifting, it is clear that the Borah Peak event did not reactivate the Mesozoic White Knob thrust sheet that intersects the Lost River fault near the mainshock. Instead, the Lost River fault cuts cleanly through the crust in the plane of near-maximum shear stress predicted by Mohr-Coulomb failure.

So either the historical earthquakes are not representative, or slip on detachments occurs largely by creep, or many of the sub-horizontal reflectors are not in fact faults.

In 1883 the brilliant geologist G. K. Gilbert wrote an article for the Salt Lake Tribune, entitled "A theory of earthquakes of the Great Basin," which began:

> There are many geologists who are very wise, but even they do not understand the forces which produce mountains. And yet it must be admitted, not only that mountains have been made, but that some mountains are still rising (5).

One hundred years later Borah has proved to be among those mountains still rising; during the earthquake the Lost River Range was lifted 0.2-0.3 m along the scarp relative to distant points, and down-tilted away from the fault. The downthrown side of the fault subsided as much as 1.2 m, and was also tilted down toward the fault. The similarity between the earthquake deformation and the cumulative deformation preserved by the geology is striking, and tends to confirm Gilbert's suggestion that basin-range topography is built by repeat of slip events on the range-bounding normal faults.

Looking ahead from Borah Peak, the historically unbroken and heavily populated Wasatch frontal fault looms large. The 1983 shock attests to the vital role played by continuing studies of the Wasatch fault scarp morphology, slip history and segmentation begun by G. K. Gilbert. Augmented by seismic and geodetic monitoring programs and forewarned by the havoc an extra cubic kilometer of water could wreak in an urban setting, we press on.

References: (1) T.C. Hanks and H. Kanamori, **J. Geophys. Res., 84**, 2348, 1979; (2) R.E. Wallace, **U.S. Geol. Surv. Prof. Pap. 1274-A**, 1984; (3) D.I. Doser, this volume; (4) R.S. Stein and S.E. Barrientos, this volume; (5) G.K. Gilbert, **Am. Jour. Sci.-3rd Ser., 27**, 49, 1884.

Participants at the Borah Peak Workshop

Sergio Barrientos
C. F. Richter Laboratory
University of California, Santa Cruz
Santa Cruz, California 95064

Roger Bilham
University of Colorado
Boulder, Colorado 80309

Mike Blackford
Palmer Observatory
POB Y,
Palmer, Arkansas 99645

Jack Boatwright
U.S. Geological Survey
345 Middlefield Road, MS 977
Menlo Park, California 94025

Fran Boler
CIRES
Campus Box 449
Boulder, Colorado 80309

M. G. Bonilla
U.S. Geological Survey
345 Middlefield Road, MS 977
Menlo Park, California 94025

Roy Breckenridge
Idaho Geological Survey
Room 332, Morrill Hall
University of Idaho Campus
Moscow, Idaho 83843

Robert C. Bucknam
U.S. Geological Survey
Denver Federal Center, MS 966
Denver, Colorado 80225

Mr. Chen
University of Utah
Salt Lake City, Utah 84108

Malcolm Clark
U.S. Geological Survey
345 Middlefield Road, MS 977
Menlo Park, California 94025

A. J. Crone
U.S. Geological Survey
Denver Federal Center, MS 966
Denver, Colorado 80225

Jim Dewey
U.S. Geological Survey
Denver Federal Center, MS 967
Denver, Colorado 80225

Diane Doser
University of Utah
Salt Lake City, Utah 84112

W. B. Hall
Department of Geology
University of Idaho
Moscow, Idaho 83843

Tom Hanks
U.S.Geological Survey
435 Middlefield Road, MS 977
Menlo Park, California 94025

Roderick Hutchinson
Old Faithful, P.O. Box 2207
Yellowstone National Park
Wyoming 82190

Suzette Jackson
EG&G Geosiences
ILF P.O. Box 1625
Idaho Falls, Idaho 83401

Dr. J.J. King
EG&G Geosciences
IFL P.O.Box 1625
Idaho Falls, Idaho 83401

Charles Langer
U.S. Geological Survey
Denver Federal Center, MS 966
Denver, Colorado 80225

Ms. Leu
University of Utah
Salt Lake City, Utah 84108

Jim Lienkaemper
U.S. Geological Survey
345 Middlefield Road, MS 977
Menlo Park, California 94025

Paul Karl Link
Idaho State University
Department of Geology
Pocatello, Idaho 83209-0009

Don Mabey
Utah Geologic & Mineral Survey
606 Blackhawk Way
Salt Lake City, Utah 84108

Michael N. Machette
U.S. Geological Survey
Denver Federal Center, MS 913
Denver, Colorado 80225

Harold E. Malde
U.S. Geological Survey
Denver Federal Center, MS 913
Denver, Colorado 80225

Gary Maltz
College of Mines & Geology
University of Idaho
Moscow, Idaho 83843

Mr. Clark Meek
Bureau of Disaster Services
State of Idaho
650 W. State Street
Boise, Idaho 83702

Tom Ore
Department of Geology
Idaho State University
Pocatello, Idaho 83209

James Pechmann
University of Utah
Salt Lake City, Utah 84108

Jack Pelton
Department of Geology & Geophysics
Boise State University
Boise, Idaho 83725

John Pfluke
U.S. Geological Survey
345 Middlefield Road, MS 977
Menlo Park, California 94025

Kenneth L. Pierce
U.S. Geological Survey
Denver Federal Center, MS 913
Denver, Colorado 80225

Rob Reilinger
AF Geophysics Lab/LWH
Hanscom AFB
Massachusetts 01731

Williams D. Richins
Department of Geology & Geophysics
University of Utah
Salt Lake City, Utah 84112

Albert M. Rogers
U.S. Geological Survey
Denver Federal Center, MS 966
Denver, Colorado 80225

William P. Rogers
Colorado Geological Survey
1313 Sherman Street, Room 715
Denver, Colorado 80225

Michael Rymer
U.S. Geological Survey
345 Middlefield Road, MS 977
Menlo Park, California 94025

P. Sablock
Department of Geology
University of Idaho
Moscow, Idaho 83843

Stephen Salyards
California Institute of Technology
Pasadena, California 91125

William Savage
Challis National Forest
P.O. Box 404
Challis, Idaho 83226

David Schwartz
Woodward-Clyde Consultants
1 Walnut Creek Ctr.
100 Pringle Avenue
Walnut Creek, California 94596

William E. Scott
U.S. Geological Survey
Denver Federal Center, MS 903
Denver, Colorado 80225

Robert V. Sharp
U.S. Geological Survey
345 Middlefield Road, MS 977
Menlo Park, California 94025

Betty Skipp
U.S. Geological Survey
Denver Federal Center, MS 913
Denver, Colorado 80225

Robert B. Smith
Department of Geology & Geophysics
University of Utah
Salt Lake City, Utah 84112

Richard Snay
NGS, N/CG113
Rockville, Maryland 20852

Kenneth Sprenke
Department of Geology
University of Idaho
Moscow, Idaho 83843

Donald Steeples
Kansas Geological Survey
1930 Avenue A
Campus West
Lawrence, Kansas 66044

Ross Stein
U.S. Geological Survey
345 Middlefield Road, MS 977
Menlo Park, California 94025

Mike Stickney
Montana Bureau of Mines & Geology
Butte, Montana 59701

Carl Strand
1436 S. Bentley, #6
Los Angeles, California 90025

George Thompson
Department of Geophysics
Stanford University
Stanford, California 94305

Kirk Vincent
Department of Geology & Geophysics
U.C. Berkeley
Berkeley, California 94720

Charles J. Waag
Department of Geology & Geophysics
Boise State University
1910 University Drive
Boise, Idaho 83725

Bob Wallace
U.S. Geological Survey
345 Middlefield Road, MS 977
Menlo Park, California 94025

Dick Whitehead
USGS - WRD
230 Collins Road
Boise, Idaho 83702

Raymond C. Wilson
U.S. Geological Survey
435 Middlefield Road, MS 998
Menlo Park, California 94025

Dr. Wojcik
University of Kansas
Lawrence, Kansas 66044

Spencer Wood
Department of Geology
Boise State University
Boise, Idaho 83725

T. Les Youd
U.S. Geological Survey
345 Middlefield Road, MS 977
Menlo Park, California 94025

James Zollweg
Department of Geology
University of Washington
Seattle, Washington 98105

QUATERNARY TECTONIC SETTING OF THE 1983 BORAH PEAK EARTHQUAKE, CENTRAL IDAHO

William E. Scott, Kenneth L. Pierce, and M. H. Hait, Jr.
U.S. Geological Survey
Denver Federal Center, Denver, CO 80225

Abstract

The 1983 Borah Peak earthquake was accompanied by extensive surface faulting along a part of the Lost River fault that has abundant evidence of latest Quaternary (last 15,000 yr) offset. This fault and two similar range-front normal faults along the Lemhi Range and Beaverhead Mountains lie in an area of basin-and-range structure in central Idaho that is part of a semicircular belt of latest Quaternary surface faulting that extends from the Wasatch fault, through the Yellowstone area, to the Lost River fault. The central segments of the Lost River, Lemhi, and Beaverhead faults have been active more recently, and probably more active throughout Quaternary time, than the southern and northern segments. The 1983 surface faulting occurred in an area of high structural relief along a part of the Lost River fault that has ruptured in latest Quaternary time, which suggests that comparable areas along other range fronts in the area should be regarded as likely sites of future surface faulting. Other perspectives of fault behavior suggest additional possible sites, and all segments of the range-front faults are regarded as capable of surface faulting.

Introduction

The Borah Peak earthquake (Ms=7.3) of October 28, 1983, occurred in an area of basin-and-range structure (Reynolds, 1979) in central Idaho that contains widespread evidence of latest Quaternary (last 15,000 yr) faulting but has had little historic seismicity (Figs. 1, 2, and 3; Smith and Sbar, 1974). A 34-km-long zone of surface faulting along the north-central part of the western front of the Lost River Range accompanied the earthquake; both field evidence and focal mechanism indicate that the fault movement was normal-sinistral on a southwest-dipping plane (Crone and Machette, 1984).

This report briefly describes the neotectonic setting of the Borah Peak area, summarizes our knowledge of the distribution and ages of Quaternary faulting there, and discusses possible sites of future surface faulting.

Regional Neotectonic Setting

Figure 1 shows the location of the surface faulting associated with the 1983 earthquake in relation to other areas of historic surface faulting and to major late Cenozoic normal faults in the northeastern part of the Basin and Range province. This part of the Basin and Range can be subdivided into domains based on (1) amount of latest Quaternary surface faulting, (2) high rates of Quaternary faulting as shown by geologic studies or inferred by high structural relief along imposing range fronts, and (3) structural setting

(Fig. 2). Domains 2-5 represent several structural settings and contain few and widely distributed faults that have moved in latest Quaternary time. In contrast, domain 1 contains many faults that have moved in latest Quaternary time and most of these have evidence of a high rate of Quaternary faulting. In addition, two of the three historic surface-faulting events in the northeastern Basin and Range occurred in domain 1.

Domain 1 includes the Wasatch fault (1a; Fig. 2), which has slip rates that locally exceed 1 m/1000 yr (Swan and others, 1980) and has accomodated much of the east-west regional extension between the Great Basin and stable interior in latest Quaternary time, and the following active neotectonic elements that form a semicircular belt (1b) north of the Wasatch fault. These are (a) a set of right-stepping faults that extend from Cache Valley, Utah, to Star Valley, Wyoming; (b) the Teton fault; (c) faults in the Yellowstone area; (d) the Deep Creek, Madison, Centennial, and Red Rock faults in Montana; and (e) the Beaverhead, Lemhi, and Lost River faults in Idaho.

This neotectonic belt of major Quaternary faults has a remarkable spatial relation to the Yellowstone-Snake River Plain axis (Y-SRP axis; Fig. 2). The northern part of the most active portion (stippled on Fig. 2) of this belt lies generally from several tens to 100 km beyond the margin of the eastern Snake River Plain, whereas the southern part lies from 100 to 200 km from the Plain margin in the west and merges to within 100 km of the Plain margin in the Teton area. Both parts join within the Yellowstone area.

Major silicic volcanism started about 15 my ago on the Y-SRP axis in southwest Idaho, migrated northeastward along the axis at an average rate of about 3.5 cm/yr, and presently is centered in the Yellowstone area (Armstrong and others, 1975; Christiansen and McKee, 1978). This volcanism was accompanied by crustal heating and uplift; subsequent cooling is reflected in the decrease in elevation southwestward along the Y-SRP axis (Brott and others, 1978; Smith, and others, 1985). The passage of this thermal activity along the axis also produced an outwardly migrating thermal front with a geometry analogous to the wake of a moving boat.

The belt encompassing the major Quaternary faults of the northeastern Basin and Range (Fig. 2) also has a wake-like pattern about the Y-SRP axis and converges with the axis at Yellowstone suggesting the pattern of neotectonic activity may relate to the thermal front migrating outward from the Y-SRP axis. If this association between the thermal front and the active neotectonic belt is valid, it provides a testable late Cenozoic tectonic history for areas within the belt. That is, the passage of the thermal front produces first high rates of faulting as the crust is heated and thinned, followed by decelerating rates of deformation or relative quiescence as heating ceases and cooling occurs.

For range-front faults between the Snake River Plain and the belt of major Quaternary faulting (Fig. 2), tectonic histories that reflect a high rate of faulting followed by a decelerating rate appear to confirm the above prediction, especially on the south side of the Plain where numerous basins and ranges attest to active late Cenozoic faulting, but where there is little evidence of Quaternary faulting. For example, the Cotterel and Jim Sage Mountains are adjacent to the western part of the eastern Snake River Plain and consist of volcanics and sediments emplaced in a topographic low about 10 my ago, at about the time silicic volcanism was centered along the adjacent part of the Y-SRP axis (Armstrong and others, 1975; Williams and others, 1982). Subsequently the basin was extended greatly along an east-dipping, low-angle detachment and the ranges were uplifted to produce about 1 km of structural relief on the 10-my-old volcanics. High rates of deformation

between 10 and 5 my ago contrast with low rates during the last 5 my (Covington, 1983, Fig. 5; H. R. Covington, written commun., 1984) and low rates of Quaternary deformation (Williams and others, 1982; K. L. Pierce, unpublished data, 1984). Further northeast along the south margin of the eastern Snake River Plain, the Blackfoot Mountains were uplifted at high rates (0.8 m/1000 yr) between 5.9 and 4.7 my ago to attain most of their present relief (Allmendinger, 1982). At about this time, major silicic volcanism was centered along the adjacent part of the Y-SRP axis (Armstrong and others, 1975). In contrast, there is no evidence of significant Quaternary surface faulting along the main range-front fault on the west side of the Blackfoot Mountains.

We do not intend to suggest that the cause of Basin and Range deformation marginal to the eastern Plain is solely the result of thermal activity associated with the Y-SRP axis, but rather that a thermal front may have localized faulting in a wake-like belt that propagated outward through the northeastern Basin and Range from the Y-SRP axis.

The Lost River, Lemhi, and Beaverhead faults define an area of similar structural pattern and neotectonic activity at the northwestern end of the latest Quaternary belt of surface faulting that is the focus of the rest of this discussion.

The present topographic relief of the Lost River, Lemhi, and Beaverhead ranges is the result of late Cenozoic faulting (Baldwin, 1951; Ruppel, 1982). Most of this faulting may have occurred during the last 4-7 m.y. based on (1) the presence of fluvial-gravel clasts that must have been transported from west of this area and that now underlie 6.6-m.y.-old volcanic rocks in the Lemhi Range (x on Fig. 3) and (2) uplift-induced east dips of basalts that overlie 4-m.y.-old ash-flow tuffs near the southern ends of the ranges (Fig. 3; M. H. Hait, Jr., unpub. data; dates from McBroome and others, 1981). Ruppel (1982) suggests that the Lemhi Range and Beaverhead Mountains are block uplifts of mostly Miocene age, and that the fault scarps on the southwest sides of the ranges reflect eastward tilting in late Pliocene to Holocene time. In contrast, Hait (1984) finds evidence for considerable extension during middle Cenozoic time. We favor an interpretation that the three ranges are parts of normal-fault-bounded blocks that range from structurally flat-topped (Ruppel, 1982) to eastward-tilted. Faulting during Quaternary time appears largely related to eastward tilting because: (1) fault scarps that cut Quaternary deposits occur mainly on the west sides of the ranges, (2) some parts of the ranges are assymetric with steep west sides and gentler sloping east sides, and (3) upper Tertiary tuffs and basalts in and between the southern parts of the ranges have easterly dips (Fig. 3).

Quaternary Surface Faulting in the Lost River-Beaverhead Area

Quaternary surface faulting has broken most of the Lost River, Lemhi, and Beaverhead range-front faults. Similar geometric and temporal patterns of breakage and structural relief are repeated along each fault (Fig. 3).

The mapped patterns of the faults are strikingly similar. All three generally hug the western range fronts, change trend by as much as 90°, and, in places, diverge from range fronts and strike across basins. Quaternary offset on the faults is dominantly normal slip, but lateral components can be recognized locally by *en echelon* patterns of faults (Fig. 3).

Structural relief along the three faults, as estimated from topographic and geophysical data, is generally greater along central segments, which are

partly coincident with an arch north of and parallel to the Snake River Plain (see discussion in Ruppel, 1982), than along distal segments (Fig. 3). These relations suggest that the central segments have higher long-term rates of faulting, which is consistent with estimates of short-term slip rates for various segments. In the Borah Peak area, which has about 2.7 km of structural relief, the 15,000-yr-old surface of the Willow Creek fan (Pierce and Scott, 1982) is offset 3.5-4.5 m, including the 1.5-2-m offset of 1983 (Crone and Machette, 1984). The mean slip rate there is about 0.3 m/1000 yr. Similar relations along the central segments of the Lemhi and Beaverhead faults suggest they have similar rates. In contrast, the Arco segment of the Lost River fault, which has about one-half the structural relief of the Borah Peak area, has a maximum mean slip rate of 0.1 m/1000 yr (see discussion of Arco segment; Pierce, 1985); the southern segment of the Lemhi fault probably has a similar rate.

In addition to having greater structural relief, the central segments of the faults have moved more recently than the distal segments. The ages of latest faulting shown on Figure 3 are based on the stratigraphic relationship of fault scarps to surficial deposits whose ages are estimated by stratigraphic, geomorphic, and soil-development evidence (Malde, 1971; Hait and Scott, 1978; Pierce and Scott, 1982; Scott, 1982). The latest Quaternary scarps are typically 2-5 m high and displace alluvial and glacial deposits of Pinedale age (as young as 12,000-15,000 yr). The late Pleistocene and older scarps are as high as 20 m. These do not displace latest Quaternary deposits, but do offset surficial deposits that are locally as young as 30,000 yr, but that are commonly more like deposits dated about 160,000 yr (see discussion of Arco segment; Pierce, 1985).

A consistent pattern of ages of fault scarps on the western fronts of the ranges is evident on Figure 3. Late Pleistocene or older scarps occur along the southern sections of the range fronts within about 25 km of the Snake River Plain; scarps along the central and north-central sections of the ranges are latest Quaternary; and the absence of scarps along the northernmost range fronts suggests that in these areas the last surface-faulting event is older than late Pleistocene.

Lost River Fault and 1983 Surafce Faulting

Reconnaissance and detailed mapping of the Lost River fault defines 6 or 7 fault segments that are characterized by different geomorphic expression, structural relief, and ages of last movement that follow the pattern discussed above (Fig. 3).

Fault scarps along the 20-km-long Arco segment do not displace latest Quaternary deposits, but do offset extensively preserved older fan surfaces by as much as 20 m. In the area of a trench across the fault (Malde, 1971, 1985), several stratigraphic datums allow estimates of the slip rate of this segment (Pierce, 1985). A surface estimated to be about 160,000 yr old based on uranium-series ages of layered carbonate coats on clasts in soils is offset about 19 m or possibly more and a volcanic ash estimated to be about 70,000-110,000 yr old is offset about 8 m. Because of burial and limited exposure, the existence of back rotation or graben formation can not be evaluated, so the slip rate of 0.07-0.1 m/1000 yr estimated from these datums is regarded as a maximum.

Near the northern end of the Arco segment, the youngest faulting offsets fan gravels about 3 m (Pierce, 1985). The inner part of a carbonate coat on a

clast from the soil in the faulted gravel has uranium-series dates of 23,000±4,000 and 30,000±5,000 yr (John Rosholt, written commun., 1979). Carbonate coats from the faulted gravel and slightly younger unfaulted gravel are about twice as thick as coats from a nearby surface estimated to be about 15,000 yr old (Pierce and Scott, 1982). Based on these U-series dates, carbonate-coat thicknesses, and the morphology of the scarp, the youngest faulting on the Arco segment occurred about 30,000 yr ago.

South of the Arco segment, a zone of discontinuous scarps as high as 10 m that displace surficial deposits and lavas of late and middle Pleistocene age extends 12 km onto the Snake River Plain (Kuntz, 1978). The exact age relationship of these scarps to the scarps along the Arco segment is not known, but both sets of scarps displace deposits of similar age.

North of the Arco segment, the Pass Creek segment, which forms a marked dogleg in the range front, extends 30 km to just south of Lower Cedar Creek. Fault scarps are preserved only locally along this segment. The range front maintains a steep faceted profile as in adjacent segments, has high structural relief, and is doubtless bounded by a fault. Surficial deposits older than about 30,000 yr are not well exposed along most of this segment, so the general lack of scarps is difficult to interpret, but faulting may not have occurred in the last 30,000-50,000 yr.

The 22-km-long Mackay segment extends from Lower Cedar Creek, east of Mackay, to the prominent bend in the range front at Elkhorn Creek. Fault scarps of latest Quaternary age occur throughout the entire segment, and generally are preserved even on steep (30°) slopes at the base of the range front. A trench across the fault scarp at the mouth of Lower Cedar Creek in a pre-Pinedale fan deposit records several surface-faulting events, the last of which occurred after the deposition of a pod of Mazama ash (6800 ^{14}C yr old; Hait and Scott, 1978). A date of 4,320±130 ^{14}C yr B.P. (W-4427) from organic matter buried by colluvium derived from the free face formed during the last surface-faulting event indicates that this event probably occurred about 4,000 yr ago. The Mackay segment has less structural relief than the Thousand Springs segment to the north, suggesting that the Mackay segment has a lower long-term slip rate. However, the lack of evidence of pedimentation of the front, the position of the latest Quaternary scarp on steep faceted spurs, and the burial of the head of extensively exposed middle Pleistocene and older alluvial-fan deposits by younger fan deposits suggest that this segment has been very active in late Quaternary time.

The Thousand Springs segment, which extends from Elkhorn Creek north to the Willow Creek hills, was the site of the greatest amount surface rupturing during the 1983 Borah Peak earthquake (Crone and Machette, 1984). This segment has the greatest structural relief (2.7 km; Fig. 3) measured along the Lost River fault, and therefore probably has the highest long-term slip rate. Pre-1983 fault scarps of latest Quaternary age are best preserved at sites where the scarp lies a short distance out from the steep mountain front, such as at Cedar, Rock, and Willow Creeks. Trenches across the scarp at the mouth of Willow Creek (Hait and Scott, 1978; D. P. Schwartz and A. J. Crone, personal communication, 1984) where the scarp offsets an alluvial surface estimated to be about 15,000 yr old (Pierce and Scott, 1982) and a reconstruction of geomorphic surfaces across the fault (Vincent, 1985) indicate that one pre-1983 surface-faulting event occurred along the central part of this segment in latest Quaternary time. That event occurred in late Holocene time based on the following soil-development evidence (Hait and Scott, 1978). The soil formed in the alluvium of the hanging wall where it is buried by fault-scarp colluvium is almost as well developed as soils formed in

the same alluvial surface above the scarp. This indicates that most of the 15,000-yr-interval since the stabilization of the fan surface and initiation of soil development had passed prior to the pre-1983 event.

Near Willow Creek, many features of the 1983 break (Crone and Machette, 1984, fig. 4) closely mimic features of the pre-1983 scarp. The offset of the Willow Creek fan accompanying the 1983 earthquake was 1.5-2 m, compared to the pre-1983 offset of 2-2.5 m. Other features include a right-stepping pattern of short faults, a broad complex graben with a conspicuous horst, and minor thrust features west of the graben.

The segment of the 1983 break that diverges from the Lost River fault and strikes west into the Willow Creek hills in part occurs on remnants of older scarps marked by conspicuous benches and changes in slope, but also displaces surfaces having no apparent evidence of late Pleistocene offset. The higher structural position of the Willow Creek hills compared to the basins to the north and south suggests recurrent uplift of the hills during the late Cenozoic. Elsewhere this similar pattern of a fault splay crossing a basin occurs at Middle Ridge (Fig. 3).

The Warm Springs segment extends for 15 km north of the Willow Creek hills as a conspicuous fault scarp of latest Quaternary age as high as 5 m. The scarp ends at Devils Canyon, which is also the northern end of ground cracking associated with the 1983 earthquake. Along this segment the 1983 ground breakage generally lies on the mid-slope of the older fault scarp, and ranges from 1-m scarps to small, discontinuous cracks. As is the case for the Mackay segment, the structural relief along the Warm Springs segment is not as great as that of the Thousand Springs segment; however, the character of the range front and the position of the young scarps suggest that the Warm Springs segment has had late Quaternary slip rates similar to those of the other two segments.

The northernmost segment of the Lost River fault extends from Devils Canyon to the end of the Lost River Range near Challis, has low structural relief, and shows no evidence of late Quaternary faulting.

Likely Sites of Future Faulting in the Lost River-Beaverhead Area

In view of our understanding of the 1983 Borah Peak earthquake and its Quaternary tectonic setting, what are likely sites in the area for future extensive surface faulting accompanying large earthquakes? Widespread evidence of late Quaternary surface faulting and the morphology of the range fronts suggest that future ruptures could occur along any part of the Lost River, Lemhi, or Beaverhead faults. Prediction of specific sites of future surface faulting requires an understanding of several conditions at depth including patterns and rates of strain accumulation, physical properties of the rocks, and linkages between the range-front faults. Unfortunately, we know little about these. Nevertheless, one can view the history of surface faulting and the geomorphic and structural features of the area and the 1983 break from the following perspectives to gain insight as to which of the segments are more likely to rupture than others. The site of the next event is difficult to predict with confidence based on these perspectives, but they are useful for identifying potential sites for the next 10 or so surface ruptures in the area.

Sites comparable to 1983 break: The 1983 surface faulting occurred along a segment with both high structural relief, which indicates high long-term

slip rates, and latest Quaternary offset. Consequently, similar segments can be viewed as likely sites for future surface faulting. The part of the Lost River fault that broke in 1983 and the central segments of the Lemhi and Beaverhead faults have these characteristics (Fig. 4A) and therefore are likely sites.

Movement triggered along faults linked at depth with the 1983 break: If the Lost River, Lemhi, and Beaverhead faults are linked to a single west-dipping detachment at depth, then the 1983 slip along the central segment of the Lost River fault might trigger movements along one or several of the central segments of the faults to the northeast (Fig. 4A) that would lie higher on the assumed detachment plane. This is analogous to the displacement of blocks in a landslide, in which the movement of a block that provides a buttress for blocks higher on the failure plane would trigger movement of some of those blocks.

Segments adjacent to the ends of the main 1983 break: The Mackay and Warm Springs segments have less structural relief than the Thousand Springs segment, which accounted for the main part of the 1983 surface rupture; however, the similar height and morphology of the range along these segments and the position of latest Quaternary fault scarps on the lower slopes of the steep faceted spurs of the range front suggest that all three segments have had comparable activity in late Quaternary time. Therefore, future surface-faulting events along the adjacent segments seem likely if these sections of range front are to keep pace with slip along the Thousand Springs segment (Fig. 4B).

Unfortunately, we don't know the age relations of the last events on the Mackay and Warm Springs segments and the pre-1983 event on the Thousand Springs segment. Based on the ^{14}C date from the Lower Cedar Creek trench, the soil-development evidence at the Willow Creek trench, and stratigraphic and geomorphic relations along the Warm Springs segment, any sequence of events is permissable. Knowledge of this sequence is critical to predictions of sites of future surface faulting based on fault history. For instance, if the pre-1983 event on the Thousand Springs segment were significantly older than the last events on the Mackay and Warm Springs segments, then the 1983 event could be viewed as a gap-filling event. Of more concern, if the pre-1983 event on the Thousand Springs segment preceded closely the last events on the Warm Springs and Mackay segments, then surface faulting along both of these segments adjacent to the 1983 rupture would be considered highly likely.

Surface-faulting gap: A seismic gap is a fault segment that has not ruptured in historic time and that lies between historic fault scarps; such a gap is thought to be a likely site for future rupture (Wallace and Whitney, 1984). By analogy, a fault segment that lies between ones having evidence of more recent, but prehistoric, breakage can be called a surface-faulting gap, and be considered a likely site for future faulting. The Pass Creek segment of the Lost River fault has no evidence of late Pleistocene or Holocene movement; however, it lies in an area having high structural relief and an imposing range front (Fig. 4C), which suggests that it probably has a long-term rate of faulting similar to that of adjacent segments that have ruptured in late Pleistocene or Holocene time. A few segments of the Lemhi and Beaverhead faults also fall in this category.

Other possible gaps are shown in Figure 4C by the dashed bold lines along latest Quaternary faults; however, so little is known about the age relations

between individual segments of these latest Quaternary faults that surface-faulting gaps can not be defined with certainty.

Constant strain accumulation and characteristic offset: Schwartz and Coppersmith (1984) propose that a given fault segment ruptures when a certain strain threshold is reached and results in a characteristic surface offset. If we assume that slip rates estimated from geologic relations reflect mean strain rates on a segment, then an offset is likely when the product of the slip rate and the time since the last surface-faulting event approaches the characteristic offset. The Arco segment has an estimated maximum long-term slip rate of about 0.1 m/1000 yr and has not ruptured in the past 30,000 yr, which suggests a potential strain accumulation of as much as 3 m (Pierce, 1985). As the surface offset accompanying the 1983 earthquake and prehistoric offsets estimated from trench studies are less than this, movement on the Arco segment can be considered overdue (Fig. 4D). The potential strain accumulation on other fault segments is not as well known; however, limited geomorphic information on the southern segment of the Lemhi fault suggests that surface-faulting events may have a similarly long (10^4 yr) recurrence interval. The time since the last surface-faulting event on this segment is >15,000 yr, which implies a potential strain accumulation of >1.5 m by using the slip rate for the Arco segment.

Grouping of events: Surface faulting along segments may not occur at uniform rates, but rather as intervals of activity along one segment or a belt of several segments separated by periods of diminished or no activity during which surface faulting is concentrated in another area (e.g., Wallace and Whitney, 1984; Wallace, 1985). If such grouping in space and time occurs in the Lost River-Beaverhead area, some of the preceding perspectives may simply be manifestations of it. For instance, grouping provides an explanation for surface-faulting gaps; the gaps are segments that are in a relatively inactive interval. Likewise, the occurrence of latest Quaternary offsets on the central segments of the faults may be a function of grouping. In addition, non-uniform rates of surface-faulting for a given segment would negate the assumption of uniform strain accumulation for the characteristic offset perspective. The demonstration of grouping is a poorly understood but key component in understanding the kinematics of late Cenozoic deformation in the Lost River-Beaverhead area (as well as other sites in the Basin and Range), and thereby predicting the most likely sites of future faulting.

Acknowledgments

We thank S. S. Oriel for encouraging and supporting our research during the late 1970's on Quaternary faulting in the Borah Peak region, as part of the U.S. Geological Survey's Snake River Plain Project. We appreciate the constructive reviews of the manuscript provided by A. J. Crone, S. S. Oriel, M. W. Reynolds, and E. T. Ruppel

References

Allmendinger, R. W., 1982, Sequence of late Cenozoic deformation in the Blackfoot Mountains, southeastern Idaho, in, Bonnichsen, Bill, and Breckenridge, R. M., eds., Cenozoic Geology of Idaho: Idaho Bureau of

Mines and Geology Bulletin 26, p. 505-516.
Arabasz, W. J., and Smith, R. B., 1979, Introduction: What you've always wanted to know about earthquakes in Utah, in, Smith, R. B., Arabasz, W. J., and Richins, W. D., eds., Earthquake studies in Utah 1850-1978: Publication of the University of Utah Seismograph Stations, Salt Lake City, p. 1-31.
Armstrong, R. L., Leeman, W. P., and Malde, H. E., 1975, K-Ar dating, Quaternary and Neogene volcanic rocks of the Snake River Plain, Idaho: American Journal of Science, v. 275, no. 3, p. 225-251.
Baldwin, E. M., 1951, Faulting in the Lost River Range area of Idaho: American Journal of Science, v. 249, p. 884-902.
Brott, C. A., Blackwell, D. D., and Mitchell, J. C., 1978, Tectonic implications of the heat flow of the western Snake River Plain, Idaho: Geological Society of America Bulletin, v. 89, p. 1697-1707.
Christiansen, R. L., and McKee, E. H., 1978, Late Cenozoic volcanic and tectonic evolution ot the Great Basin and Columbia intermontane regions, in, Smith, R. B., and Eaton, G. P., eds., Cenozoic tectonics and geophysics of the western Cordillera: Geological Society of America Memoir 152, p. 283-312.
Covington, H. R., 1983, Structural evolution of the Raft River basin, Idaho, in Miller, D. M., Todd, V. R., and Howard, K. A., eds., Tectonic and stratigraphic studies in the eastern Great Basin: Geological Society of America Memoir 157, p. 229-237.
Crone, A. J., and Machette, M. N., 1984, Surface breakage caused by the Borah Peak earthquake, central Idaho: Geology, v. 12, no. 11, p. 664-667.
Crosthwaite, E. G., Thomas, C. A., and Dyer, K. L., 1970, Water resources in the Big Lost River basin, south-central Idaho: U.S. Geological Survey Open-File Report, 109 p.
Hait, M. H., Jr., 1984, Detachment tectonics north of the Snake River Plain, east-central Idaho and southwest Montana: Geological Society of America Abstracts with Programs, v. 16, no. 6, p. 527.
Hait, M. H., Jr., and Scott, W. E., 1978, Holocene faulting, Lost River Range, Idaho (abs.): Geological Society of America Abstracts with Program, v. 10, no. 5, p. 217.
Howard, K. A., and others, 1978, Preliminary map of young faults in the United States as a guide to possible fault activity: U.S. Geological Survey Miscellaneous Field Studies Map MF-916, scale 1:5,000,000.
Kuntz, M. A., 1978, Geologic map of the Arco-Big Southern Butte area, Butte, Blaine, and Bingham Counties, Idaho: U.S. Geological Survey Open-File Report 78-302, scale 1:48,000.
Mabey, D. R., Peterson, D. L., and Wilson, C. W., 1974, Preliminary gravity map of southern Idaho: U.S. Geological Survey Open-File Report 74-78, scale 1:500,000.
Malde, H. E., 1971, Geologic investigation of faulting near the National Reactor Testing Station, Idaho, with a section on microearthquake studies by Pitt, A. M., and Eaton, J. P.: U.S. Geological Survey Open-File Report, 167 p.
Malde, H. E., 1985, Geologic investigation of faulting near Arco, Idaho, in Workshop XXVIII on the Borah Peak Earthquake: U.S. Geological Survey Open-File Report, in press.
McBroome, L. A., Doherty, D. J., and Embree, G. F., 1981, Correlation of major Pliocene and Miocene ash-flow sheets, eastern Snake River Plain, Idaho, in Tucker, T. E., ed., Guidebook to southwestern Montana: Montana Geological Society 1981 Field Conference and Symposium, p. 323-330.

Nakata, J. K., Wentworth, C. M., and Machette, M. N., 1982, Quaternary fault map of the Basin and Range and Rio Grande Rift Provinces, western United States: U.S. Geological Survey Open-File Report 82-579, scale 1:2,500,000.

O'Neill, J. M., and Lopez, D. A., 1985, Character and regional significance of Great Falls tectonic zone of east-central Idaho and west-central Montana: American Association of Petroleum Geologists Bulletin, in press.

Pierce, K. L., 1985, Neotectonic history of the Arco segment of the Lost River fault, Idaho, in Workshop XXVIII on the Borah Peak Earthquake: U.S.Geological Survey Open-File Report, in press.

Pierce, K. L., and Scott, W. E., 1982, Pleistocene episodes of alluvial-gravel deposition, southeastern Idaho, in Bonnichsen, Bill and Breckenridge, R. M., eds., Cenozoic Geology of Idaho: Idaho Bureau of Mines and Geology Bulletin 26, p. 685-702.

Reynolds, M. W., 1979, Character and extent of basin-range faulting, western Montana and east-central Idaho: Rocky Mountain Association of Geologists and Utah Geological Association 1979 Basin and Range Symposium, p. 185-193.

Ruppel, E. T., 1982, Cenozoic block uplifts in east-central Idaho and southwest Montana: U.S. Geological Survey Professional Paper 1224, 24 p.

Schwartz, D. P., and Coppersmith, K. J., 1984, Fault behavior and characteristic earthquakes: Examples from the Wasatch and San Andreas fault zones: Journal of Geophysical Research, v. 89, p. 5681-5698.

Scott, W. E., 1982, Surficial geologic map of the eastern Snake River Plain and adjacent areas, 111° to 115° west, Idaho and Wyoming: U.S. Geological Survey Miscellaneous Investigations Series Map I-1372, scale 1:250,000,

Smith, R. B., and Sbar, M. L., 1974, Contemporary tectonics and seismicity of the western United States with emphasis on the Intermountain seismic belt: Geological Society of America Bulletin, v. 85, p. 1205-1218.

Smith, R. B., Richins, W. D., Doser, D. I., Eddington, P. K., Leu, L. L., and Chen, G, 1985, The Borah Peak earthquake: Seismicity, faulting kinematics, and tectonic mechanism, in Workshop XXVIII on the Borah Peak Earthquake: U.S. Geological Survey Open-File Report, in press.

Swan, F. H., III, Schwartz, D. P., and Cluff, Lloyd, 1980, Recurrence of moderate to large magnitude earthquakes produced by surface faulting on the Wasatch fault zone, Utah: Bulletin Seismological Society of America, v. 70, no. 5, p. 1431-1462.

Vincent, K. R., 1985, Measurement of vertical tectonic offset using longitudinal profiles of faulted geomorphic surfaces near Borah Peak, Idaho: A preliminary report, in, Workshop XXVIII on the Borah Peak Earthquake: U.S. Geological Survey Open-File Report, in press.

Wallace, R. E., 1985, Variations in slip rates, migration, and grouping of slip events on faults in the Great Basin Province, in, Workshop XXVIII on the Borah Peak Earthquake: U.S.Geological Survey Open-File Report, in press.

Wallace, R. E., and Whitney, R. A., 1984, Late Quaternary history of the Stillwater seismic gap, Nevada: Bulletin Seismological Society of America, v. 74, no. 1, p. 301-314.

Williams, P. L., Covington, H. R., and Pierce, K. L., 1982, Cenozoic stratigraphy and tectonic evolution of the Raft River basin, Idaho, in, Bonnichsen, Bill, and Breckenridge, R. M., eds, Cenozoic Geology of Idaho: Idaho Bureau of Mines and Geology Bulletin 26, p. 491-504.

Figure Captions

Figure 1. Neotectonic setting of the 1983 Borah Peak earthquake in the northeastern Basin-and-Range Province showing major, late Cenozoic normal-slip faults (modified from Howard and others, 1978; Nakata and others, 1982). Those with latest Quaternary movement that lie at the base of high, steep range fronts are shown by a bold line; those with historic rupture are hachured. Light-shaded areas include zones of earthquake epicenters between 1850 and 1974 (from Arabasz and Smith, 1979) that define the Intermountain Seismic Belt (ISB) and Idaho Seismic Zone (ISZ) of Smith and Sbar (1974). * indicates epicenter of 1983 Borah Peak earthquake.

Figure 2. Neotectonic domains (see text) of the same area as Figure 1, including latest Quaternary faults from Figure 1. Large arrows show trajectory of thermal activity along the Yellowstone-Snake River Plain (Y-SRP) axis. JC = Jim Sage and Coterell Mountains; BFM = Blackfoot Mountains.

(1) Wasatch (1a)-Yellowstone-Lost River (1b) belt of latest Quaternary surface faulting. Area of greatest activity is stippled.

(2) Southwestern Montana. Many late Cenozoic faults, but only a few, widely distributed range-bounding faults with evidence of latest Quaternary surface faulting. Recent studies (e.g., O'Neill and Lopez, 1985) indicate that some additional latest Quaternary surface faults occur in this area, but the widely distributed pattern is maintained.

(3) Idaho batholith. Relatively rigid block broken locally by Quaternary faults.

(4) Eastern Snake River Plain. Little evidence of late Quaternary faulting except for rifts associated with basaltic volcanism.

(5) Northeastern Basin and Range west of (1). Many late Cenozoic faults, but only widely distributed evidence of latest Quaternary surface faulting.

Figure 3. Major frontal faults in the Lost River-Beaverhead area. 1983 break from Crone and Machette (1984). Estimates of minimum structural relief in kilometers 2.7 from sum of thickness of basin fill (Crosthwaite and others, 1970; Ruppel, 1982) and altitude of range, and, at north end of Lost River fault, from minimum offset of Challis Volcanics. Thick basin fills (stippled) interpreted from gravity lows with >15 mgal of closure (Mabey and others, 1974). Direction of dip of upper Tertiary volcanics are shown by strike-and-dip symbol. X = gravel transported from west of area that underlies 6.6-my-old basalt (see text). Segments that have evidence of a left- or right-lateral component of slip in pre-1983 events are shown by L and R, respectively. DC = Devils Canyon; WSV = Warm Springs valley; WCH = Willow Creek hills; TSV = Thousand Springs Valley; WC = Willow Creek; BP = Borah Peak; EC = Elkhorn Creek; LCC = Lower Cedar Creek.

Figure 4. Likely sites of future surface faulting in the Lost River-Beaverhead area based on several perspectives (see text). 1983 surface fault shown by hachures. Identified sites are shown by bold line; others identified with less certainty are shown by dashed bold line. Areas of thick basin fills (dark stipple) are taken from Figure 3. Upland areas are in light stipple; basins in white.

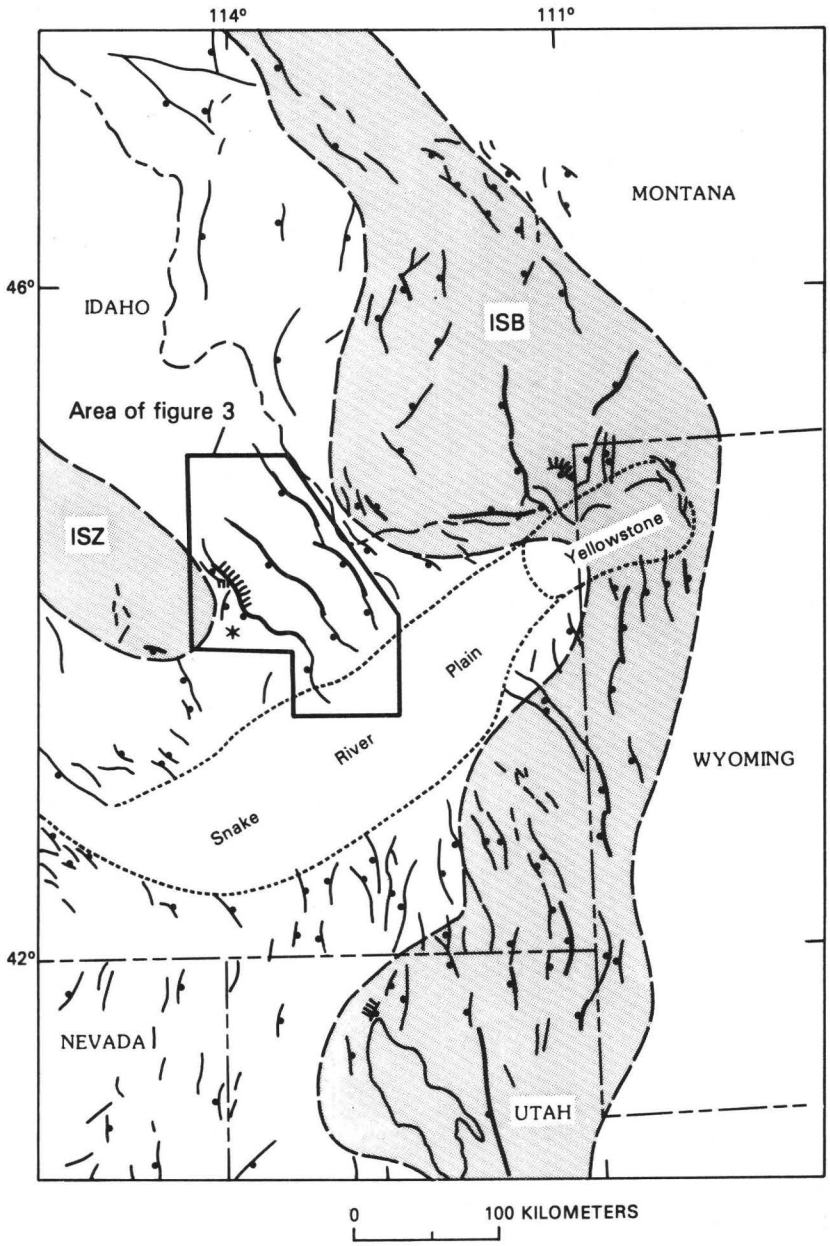
114°
111°
MONTANA
46°
IDAHO
ISB
Area of figure 3
ISZ
Yellowstone
Plain
River
Snake
WYOMING
42°
NEVADA
UTAH
0
100 KILOMETERS

FIGURE 1

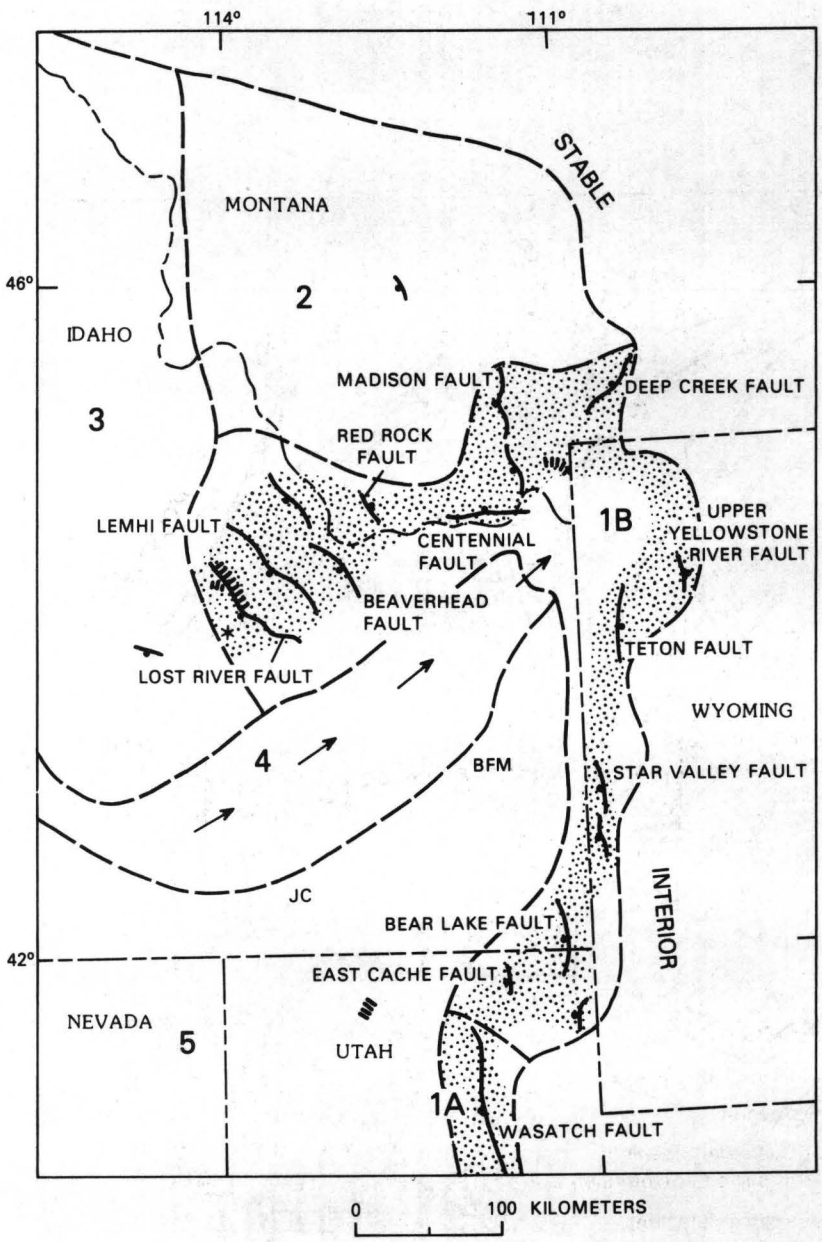
114°
111°
46°
42°
STABLE
MONTANA
IDAHO
NEVADA
UTAH
WYOMING
2
3
4
5
1A
1B
MADISON FAULT
DEEP CREEK FAULT
RED ROCK FAULT
LEMHI FAULT
CENTENNIAL FAULT
BEAVERHEAD FAULT
LOST RIVER FAULT
UPPER YELLOWSTONE RIVER FAULT
TETON FAULT
STAR VALLEY FAULT
BFM
JC
INTERIOR
BEAR LAKE FAULT
EAST CACHE FAULT
WASATCH FAULT
0
100 KILOMETERS

FIGURE 2

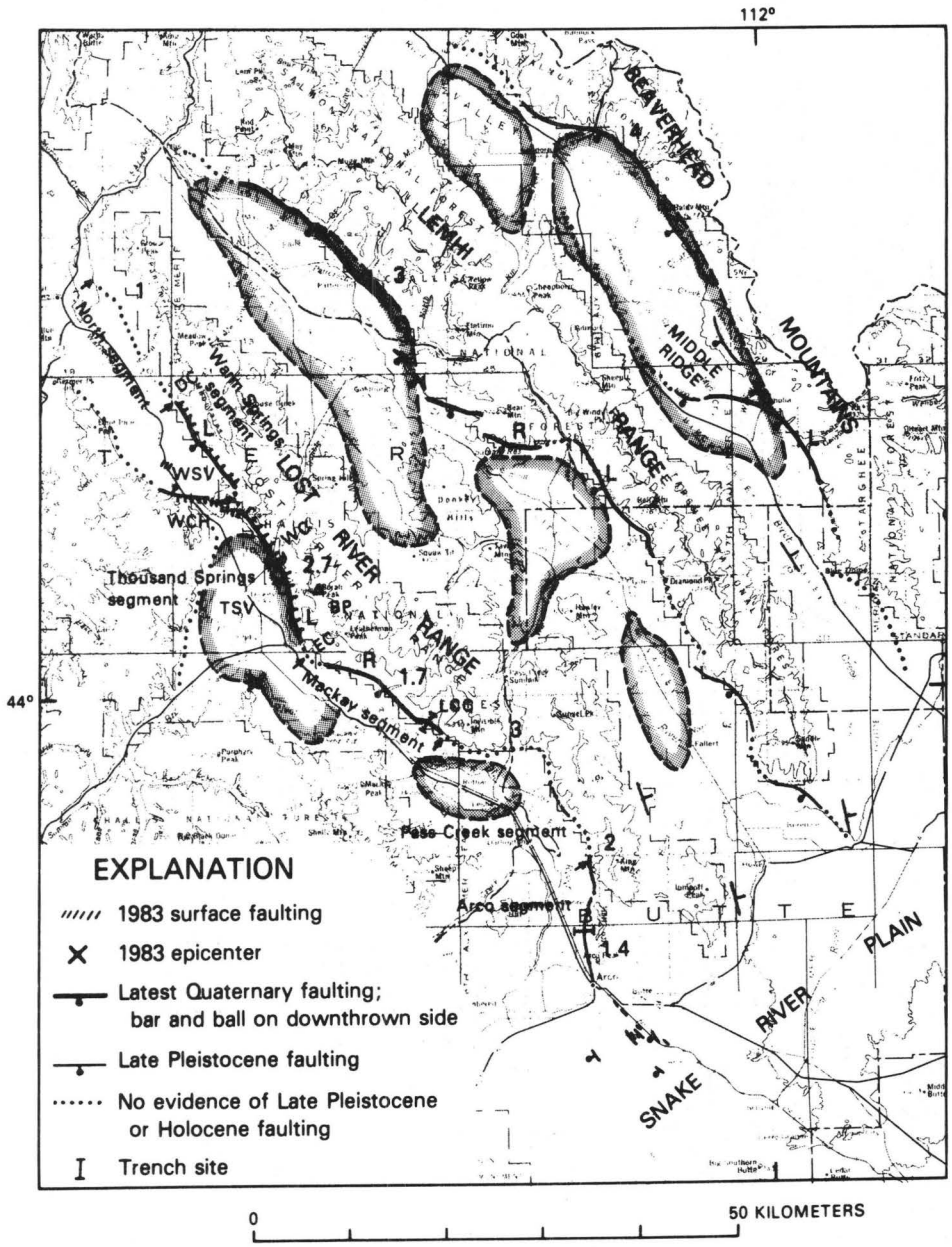
112°
44°
BEAVERHEAD
MOUNTAINS
LEMHI
MIDDLE
RIDGE
RANGE
LOST
RIVER
RANGE
Warm Springs segment
North segment
WSV
WCP
Thousand Springs segment
TSV
2.7
1.7
Arco segment
1.4
Pass Creek segment
SNAKE
RIVER
PLAIN
EXPLANATION
1983 surface faulting
1983 epicenter
Latest Quaternary faulting; bar and ball on downthrown side
Late Pleistocene faulting
No evidence of Late Pleistocene or Holocene faulting
Trench site
0
50 KILOMETERS

FIGURE 3

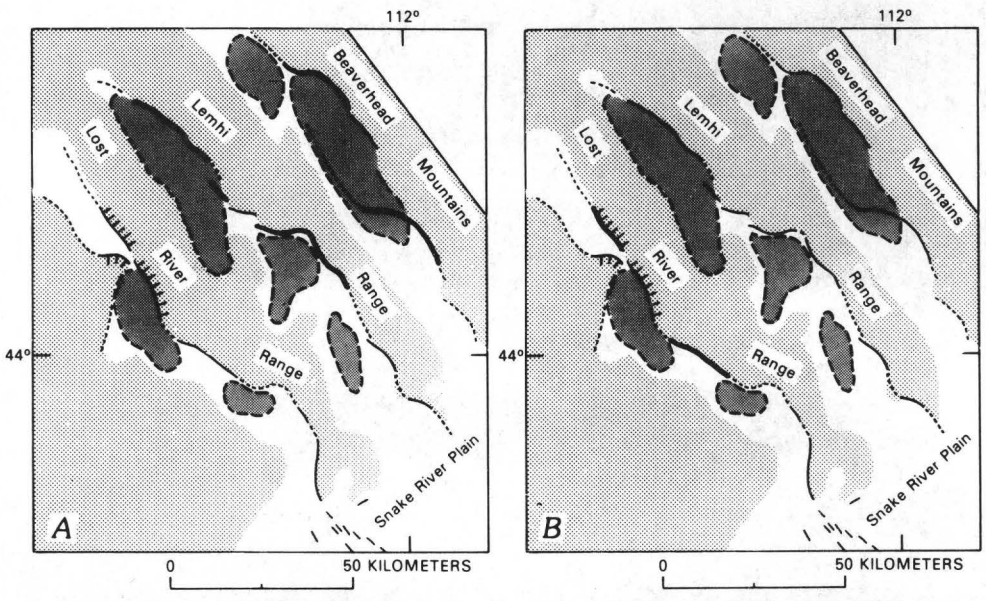
112°
Beaverhead
Mountains
Lemhi
Lost
River
Range
Range
44°
Snake River Plain
A
0
50 KILOMETERS
Sites comparable to 1983 break and movement triggered along faults linked at depth to the 1983 break
112°
Beaverhead
Mountains
Lemhi
Lost
River
Range
Range
44°
Snake River Plain
B
0
50 KILOMETERS
Segments adjacent to the ends of the main 1983 break
112°
Beaverhead
Mountains
Lemhi
Lost
River
Range
Range
44°
Snake River Plain
C
0
50 KILOMETERS
Surface-faulting gaps
112°
Beaverhead
Mountains
Lemhi
Lost
River
Range
Range
44°
>1.5m
?
3m
Snake River Plain
D
0
50 KILOMETERS
Constant strain accumulation and characteristic offset

FIGURE 4

VARIATIONS IN SLIP RATES, MIGRATION, AND GROUPING OF SLIP EVENTS ON FAULTS IN THE GREAT BASIN PROVINCE

Robert E. Wallace
U.S. Geological Survey
Menlo Park, California 94025

Abstract

Nonuniformity of slip rate on seismogenic faults, both in time and space, probably represents the norm in the Great Basin province. Variations through time of slip rate on faults are exemplified by the change in tilt rates of the East Range and Cortez Mountains, Nevada. Temporal grouping of faulting events is represented on the Lost River fault, Idaho, where several events occurred along the Thousand Springs segment of the fault while segments previously active in late Quaternary time remained quiescent. Migration and extension of slip along the strike of a fault apparently occurred on the northwest flank of the Humboldt Range, Nevada. Long-term migration or shifting of slip back and forth from one fault to another along subparallel range-front faults is shown by the history of displacement along the faults that generated the 1954 earthquakes in Dixie Valley, Nevada.

Introduction

Slip rates on seismogenic faults in the Great Basin province, western United States, have not been uniform. Variations exist on many time scales ranging from less than a thousand years to several million years. Variations involve both temporal and spatial grouping of large slip events and migration of slip both along individual faults and regionally.

In general, the average recurrence interval for large-scale displacements (those measured in meters of displacement along fault traces several kilometers long) on individual faults or segments of faults have been several thousands of years to more than a hundred thousand years. Slip rates are of the order of 0.01-0.5 mm/yr on the average, but for a few hundred or a few thousand years the slip rate may be an order of magnitude greater or smaller depending on some of the factors described below. Only a few examples are presented to illustrate several types of variations in slip rate.

Long-term changes in slip rate

Two ranges in north central Nevada, the East Range and Cortez Mountains, are members of a set of southeast or east-tilted ranges that are bounded on their western flanks by active faults. Both range blocks contain a core of rocks of Paleozoic and Mesozoic age and are capped by basaltic or andesitic lava flows of ages between 10 and 14 my. The flows on each range dip between 8 and 10 degrees southeastward forming crude dip slopes on their east or south-east flanks. The west or northwest flanks of both ranges are fault generated and an active fault lies at the base of each.

Despite these similarities, the fault-generated range fronts of each are geomorphically very different. The profile of the East Range (Fig. 1B) displays a pediment a km or two wide at the front of the range, and a map of the range front shows an irregular, sinuous form characterized by embayments and projecting spurs. Faceted spurs are absent, and the steepest part of the range is near its crest.

In contrast, on the fault-generated, northwest flank of the Cortez Mountains, the fault trace, on some segments represented by young scarps of Holocene age, lies at the immediate base of a series of faceted spurs. No pediment is present between the range-front fault and the geomorphic range front (fig. 1C).

These differences in range-front geomorphology are interpreted as follows: During the approximately ten million years required for each range block to tilt approximately 10 degrees southeastward, the rate of tilt of the range block, and thus the slip rate on the frontal fault on the East Range, was more rapid in the earlier part of the ten-million year interval and slower in the latter part. On the other hand, the Cortez Mountain block must have tilted more slowly in the early part of the range-tilting interval and more rapidly in the latter part (see fig. 1A). The formation of both ranges has involved about the same amount of tilt, but at different rates during the life time of range development.

Long-term changes in fault slip rate are also reflected in nonuniform distribution of seismic activity throughout the Great Basin province. Localization of seismic activity in belts and subprovinces for periods of centuries to thousands of years has been described by Bucknam (1980) and by Wallace (1981), and will not be reviewed here.

Migration of fault displacement

Slip rate on individual range-bounding faults can be changed markedly by the migration of fault activity. In the extensional domain of the Great Basin province, fault slip near a range front may shift inward or outward from the main range boundary to subparallel faults, displacement may extend along strike, or new branches may form to smooth irregularities in previous fault patterns. Change in stress orientation may induce new faults to form or to reactivate long-dormant faults.

Two examples of migration of slip on range-bounding faults are chosen from northcentral Nevada.

In Dixie Valley, Nevada, surface faulting occurred in 1954 producing spectacular fault scarps several meters high along the range-front fault at the immediate eastern base of the Stillwater Range. Such geomorphic evidence as faceted spurs hundreds of meters high, wine glass-shaped drainage basins and a sharp break in slope at the base of the range front attest to repeated displacement on the range-front fault over millions of years. Apparently, however, no major displacement occurred along that fault throughout at least Holocene time, inasmuch as there are no pronounced bevels or other remnants of young fault scarps older than 1954 along or near the 1954 scarps (Wallace and Whitney, 1984, Slemmons, 1957). A few kilometers east of the main range front, however, several

displacement events occurred on a subparallel fault that offset the piedmont slope by 15-18 meters in Holocene and late Quaternary time (Bell and others, 1984) and up to half a meter displacement took place in 1954 (fig. 2). The moderate degree of erosion of the scarp along this parallel fault suggests that the fault was principally active in late Quaternary time during the period when the main range-front fault remained quiescent. The history of fault displacement along the range front, thus, included eastward (outward from the range) migration of displacement for a period of more than ten thousand years, then activity renewed on the main range front fault in 1954. Shifting of displacement from one fault to another presents a problem in determining the slip rate for any individual fault.

Faulting at the north end of the Humboldt Range, Nevada, appears to display a shift in displacement from a part of the main range front fault to a branch fault which, furthermore, is interpreted to have formed and elongated to the northeast late in the history of faulting.

The range-bounding fault along most of the west flank of the Humboldt Range trends generally north, but near the north end of the range the trend changes sharply to the east-northeast, and a four-kilometer segment even trends nearly east. From the bend in the range front, a fault branches and extends northeastward for about 8 km (fig. 3). Displacement on the range-bounding fault over approximately 10 million years accounts for relief of between 1200 and 1800 m between the crest of the range and surrounding valleys. Relief across the branching fault, however, is relatively small, about 100 m near the range, and decreasing to nothing at its northeast end. A raised pediment or terrace lies between the branching fault and the main range front.

The branching fault is interpreted to have formed principally in late Quaternary time. The degree of dissection of the scarp and pediment or terrace bounded by the fault suggests such an age. Also, if a meter or two is assumed as the characteristic amount of displacement per faulting event and faulting events occur at intervals of a few thousand years, 100 meters of fault-scarp height could have been created in less than 250,000 years.

During late Quaternary time the main range-front fault northeast of its junction with the branching fault appears to have been inactive, inasmuch as little or no evidence of young fault scarps are displayed there. Southwest of the junction of the two faults, however, young faults are present.

The size, age and distribution of the youngest fault scarps along the branching fault suggest that the fault elongated to the northeast through late Quaternary time. The youngest fault scarp, a meter or two high, crosses the high beach line of glacial Lake Lahontan near Imlay, Nevada, and to the northeast of the beach line gravels of the floor of the lake are displaced. The age of this displacement, thus, is clearly post high stand of the lake or within about the past 12,000 years. The youngest scarp also extends southwest of the beach line of the lake and forms a subtle bevel at the base of a compound fault scarp that increases in height to the southwest. The presence of a scarp of more-or-less uniform

height extending along both the base of a high, older scarp as well as into newly broken materials suggests growth along strike. An alternate interpretation suggests a hinge-like configuration of displacement, that is, greater displacement along the higher parts of the scarp and lesser displacement along the lower parts of the scarp. Although the latter interpretation cannot be ruled out, and is not mutually exclusive from the interpretation of elongation along strike, elongation along strike is preferred and warrants consideration elsewhere in the Great Basin province.

Temporal grouping of displacement events along segments of range-front faults

Along many range front faults repeated displacement, as shown by young fault scarps, appears to have occurred along a single segment of the fault while adjacent segments of the range-front fault have remained quiescent. Range blocks, however, commonly are tilted or uplifted by approximately equal amounts along their entire lengths. The overall tilting or uplift of a range, therefore, must be accomplished by first one segment then another having a series of displacements events followed by a period of quiescence. Slip rates during an active period along a segment of fault, thus, would be considerably greater than the long-term average represented by the overall uplift rate of the range; likewise during the long quiescent periods the slip rates would be lower than the overall uplift rate or even zero.

This temporal grouping phenomenon is exemplified by faulting along the west flank of the Lost River Range, Idaho (fig. 4). In October, 1983, an earthquake of M 7.3 was accompanied by surface displacement on about a 34-km long segment of the range-bounding fault along the west flank of the Lost River Range (Crone and Machette, 1984). In the previous approximately 15,000 years, displacement had occurred at least 3 times (Hait, T., pers. commun., 1983) along this same segment of range-front fault, while at the same time the Arco segment of the range-front fault, farther south, was quiescent. Analysis of geomorphic and stratigraphic data, some obtained from exploratory trenches across the Arco segment, show that no displacement had occurred there in at least thirty thousand years (Pierce, K. L., 1985). Similar evidence of temporal grouping can be found along the East, Humboldt and Stillwater Ranges in northcentral Nevada.

If temporal grouping, indeed, is common, as preliminary analysis suggests, care must be exercised in interpreting slip rates and in expressing the recurrence intervals of large earthquakes in the Great Basin. Temporal grouping of displacement events separated by long quiescent periods is illustrated diagrammatically in figure 5. Given such a model, the waiting time until the next event cannot be derived simply by subtracting the elapsed time since the last event from the average recurrence interval.

Discussion and summary

Nonuniformity or variations of slip rates, both in time and space, may represent the norm in the Great Basin province. Considering that extension generally characterizes the 800 km-wide province and that the brittle crust, as represented by the depth of earthquakes, is less than 20

km thick in most places, it would be surprising if slip on individual faults, were uniform for long periods of time, or if local areas did not become active while others were quiescent. Irregularities in crustal thickness, heat flow, and volcanism, reorientation of regional stress systems, and the complex prefractured nature of the Great Basin prior to the initiation of Basin and Range structure represents a tectonic setting conducive to considerable irregularity rather than simple uniformity of slip rates.

Variations in slip rate on faults can be demonstrated at regional and subprovince scales, on the scale of groups of ranges and within single range and basin blocks. The variations take the form of migration of activity across subprovinces or along belts (Wallace, 1981), inward or outward from, or along an individual range-front fault. Temporal grouping of displacements may occur within subprovinces or belts, or on segments of individual faults.

References

Bell, J. W., Slemmons, D. B., and Wallace, R. E., 1984, Reno to Dixie Valley-Fairview Peak earthquake areas, road log: in Lintz, Joseph, Jr., ed., Western Region Excursions, v.4: Reno, Nevada, Dept. Geological Sciences, Mackay School of Mines, p. 425-472.

Bucknam, R. C., 1980, Patterns of late Quaternary faulting in western Utah and an application in earthquake hazard evaluation, in Proceedings of Conferences X, Earthquake hazards along the Wasatch and Sierra-Nevada frontal fault zones: U.S. Geological Survey Open-File Report 80-801, p. 299-314.

Chrone, A. J. and Machette, M. N., 1984, Surface faulting accompanying the Borah Peak earthquake, central Idaho: Geology, v. 12, p. 664-667.

Pierce, K. L., 1985, Neotectonic history of the Arco segment of the Lost River fault, Idaho: Proceeding volume, Conference on the Borah Peak, Idaho earthquake of October 28, 1983: U.S. Geological Survey Open-file Report (this volume, in press).

Slemmons, D. B., 1957, Geologic effects of the Dixie Valley-Fairview Peak, Nevada, earthquakes of December 16, 1954: Bulletin of the Seismological Society of America, v. 47, p. 353-386.

Wallace, R. E., 1979, Map of young fault scarps related to earthquakes in northcentral Nevada: U.S. Geological Survey Open-File Report 79-1554, 2 sheets.

Wallace, R. E., 1981, Active faults, paleoseismology and earthquake hazards in the western United States: in Simpson, David W., and Richards Paul G., eds., Earthquake Prediction -- An International Review, Maurice Ewing Series 4: American Geophysical Union, p. 209-216.

Wallace, R. E., and Whitney, R. A., 1984, Late Quaternary history of the Stillwater Seismic Gap, Nevada: Bulletin of the Seismological Society of America, v. 74, p. 301-314.

Figure Captions

Fig. 1 (A) Graph showing variation in tilt rates of East Range and Cortez Mountains, Nevada. (B) Profile of East Range. (C) Profile of Cortez Mountains. The differences in profiles of the fault-generated range fronts result from different rates of tilting of the two range blocks during the earlier and later periods in their lifetime of range-block tilting.

Fig. 2 Map of fault scarps along the east flank of the Stillwater Range, Nevada. Displacement occurred in 1954 principally on the main range-front fault, but none had occurred there previously in Holocene time. In contrast, along the fault that breaks the piedmont slope a kilometer or two east of the range front, displacement occurred in 1954 and previously in Holocene time as well as several times in late Quaternary before Holocene time, while the range-front fault remained quiescent.

Fig. 3 Map of faults at the north end of the Humboldt Range, Nevada. During late Quaternary time displacement migrated from the rangefront fault to a branch fault which then elongated northeastward with time.

Fig. 4 Cartoon showing repetition of 3 or 4 displacement events along the Thousand Springs segment of the Lost River fault, Lost River Range, Idaho, during about the past 15 thousand years. During the same time the Arco segment remained quiescent.

Fig. 5 Diagrammatic graphs of two types of fault-displacement time histories. (A) Temporal grouping of slip events separated by quiescent periods. (B) More regular recurrence of slip events. Dashed lines show average displacement rate. I suggest that A rather than B represents more nearly the characteristic time history of individual faults and fault segments in the Great Basin province.

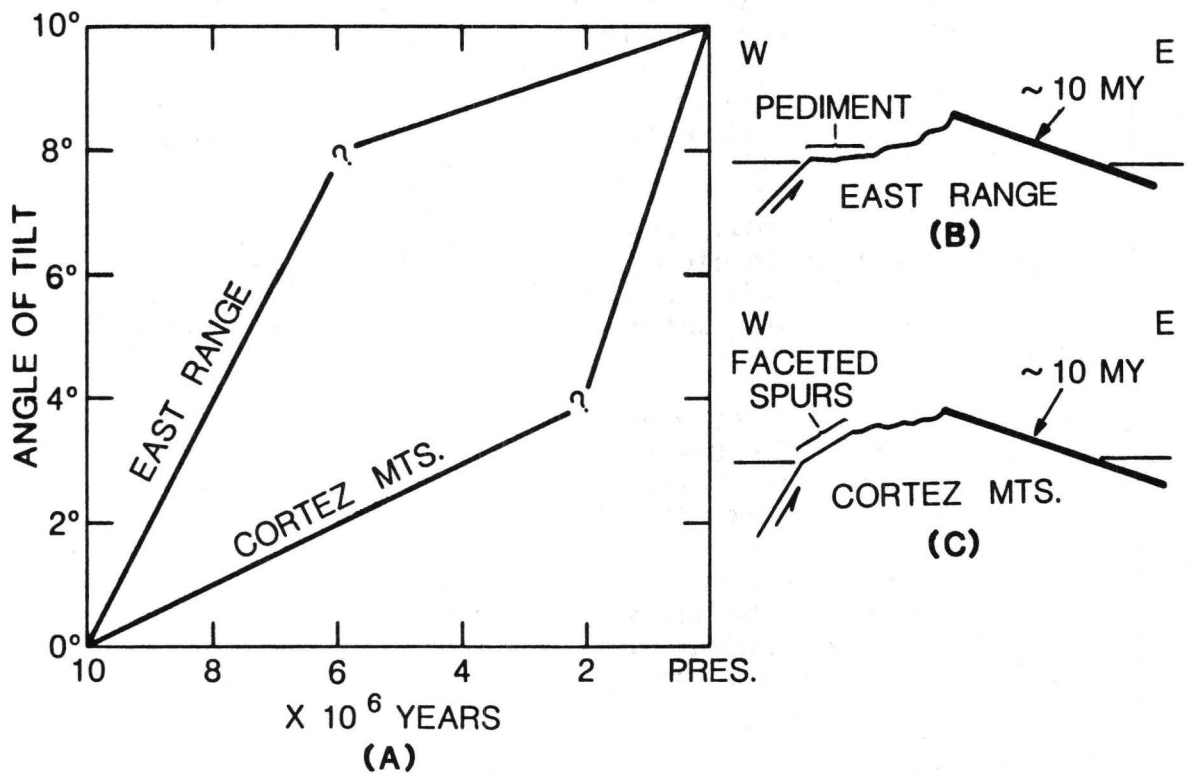
10°
8°
6°
4°
2°
0°
ANGLE OF TILT
EAST RANGE
CORTEZ MTS.
?
?
10
8
6
4
2
PRES.
X 10 6 YEARS
(A)
W
E
PEDIMENT
~ 10 MY
EAST RANGE
(B)
W
E
FACETED
SPURS
~ 10 MY
CORTEZ MTS.
(C)

Figure 1

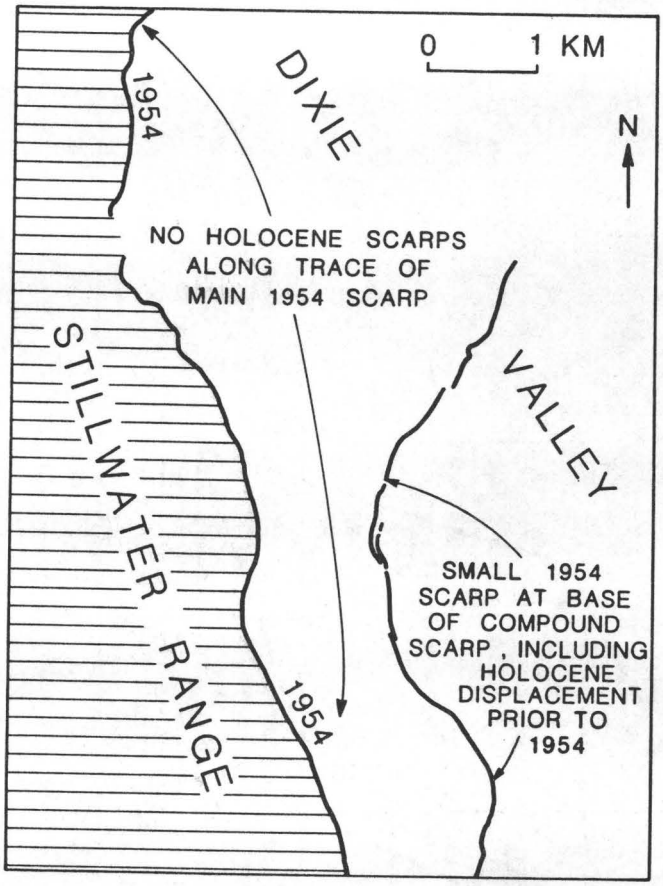

Figure 2

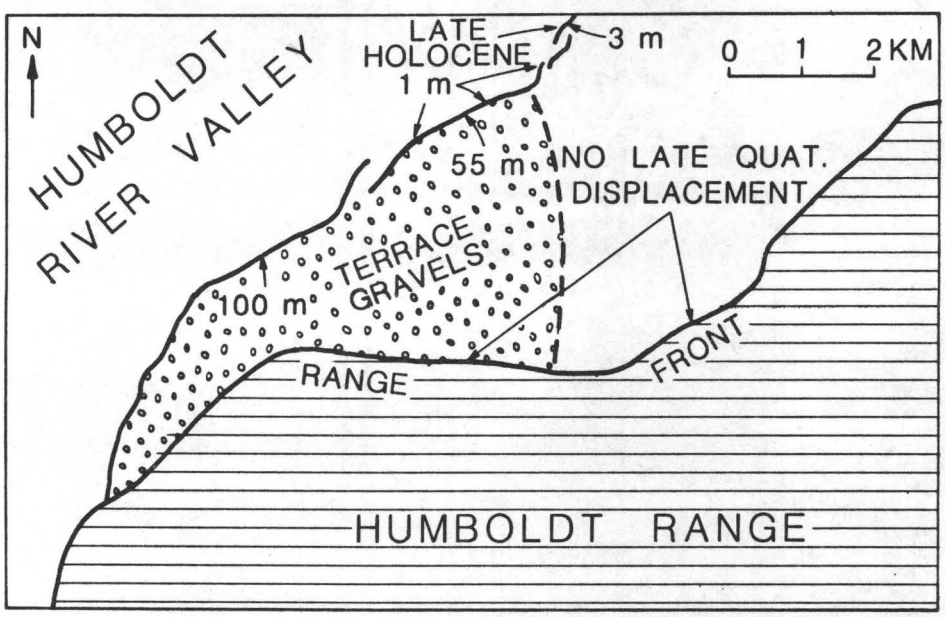

Figure 3

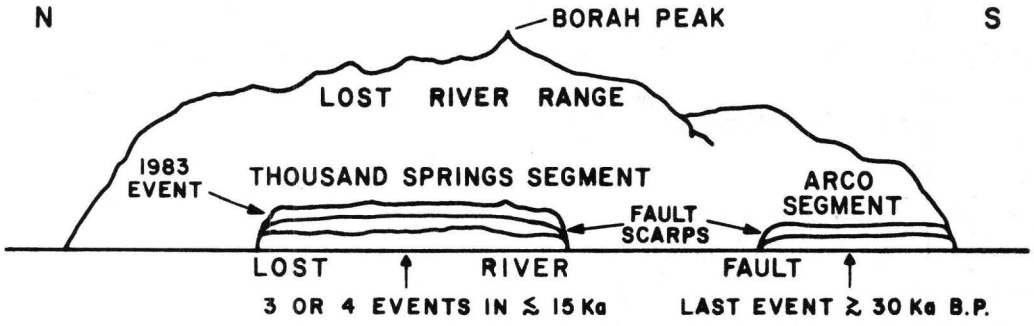
N
BORAH PEAK
S
LOST RIVER RANGE
1983
EVENT
THOUSAND SPRINGS SEGMENT
ARCO
SEGMENT
FAULT
SCARPS
LOST
RIVER
FAULT
3 OR 4 EVENTS IN ≲ 15 Ka
LAST EVENT ≳ 30 Ka B.P.

Figure 4

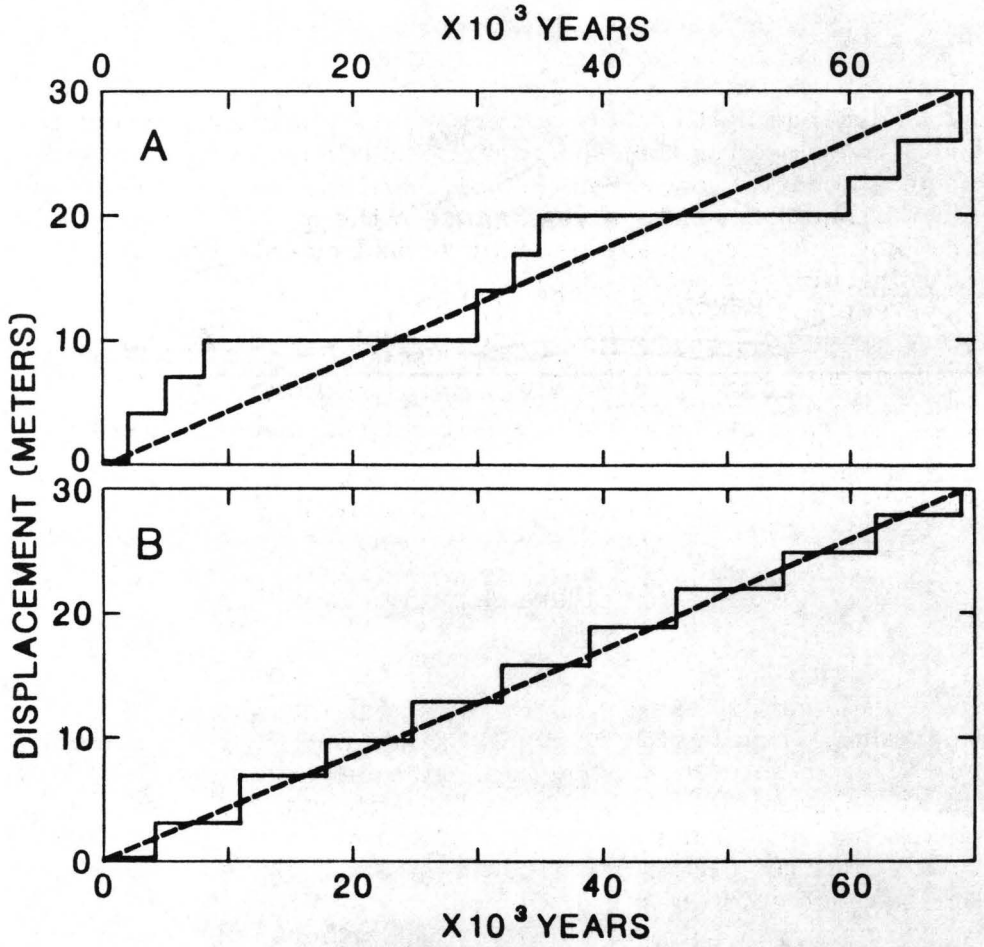
X10 3 YEARS
0
20
40
60
30
20
10
0
A
B
DISPLACEMENT (METERS)
X10 3 YEARS

Figure 5

PERSPECTIVE FROM THE FAIRVIEW PEAK - DIXIE VALLEY EARTHQUAKES OF 1954

George A. Thompson
Dept. of Geophysics
Stanford University
Stanford, CA 94305

ABSTRACT

Large Basin and Range earthquakes accompanied by surface faulting are rare events, and it is even rarer that such earthquakes have been "captured" with timely seismic, geodetic, and geologic observations. The 1954 Fairview Peak-Dixie Valley earthquakes were unprecedented in the quality and extent of the studies. Pre- and post-earthquake geodetic measurements are especially noteworthy, and refraction and reflection seismic exploration have contributed importantly. This early body of information takes on new meaning as a basis for comparison with the 1983 Borah Peak earthquake and perhaps as a general model for large Basin and Range earthquakes. The 1954 and 1983 events are similar in many ways, including: (1) magnitudes about 7, (2) hypocentral depths about 15 km, (3) dips of faults about 60° from outcrop to hypocentral depth, consistent with focal mechanisms and geodetic strain, (4) no evidence of listric faulting, and (5) geologic evidence of repeated Holocene faulting.

INTRODUCTION

Two western Nevada earthquakes -- the Fairview Peak followed 4 m and 20 s later by the Dixie Valley -- constituted a scientific gold mine. These 1954 earthquakes are comparable in several respects to the Borah Peak earthquake: the dip of the faults, the hypocentral depth, the magnitudes, and the character of the surface breaks. The 1954 faults cut a first-order triangulation net that was surveyed before and after the earthquakes. Seismic, geodetic and geologic data were testable against each other in rare detail and they generally agreed nicely. The fault breaks extended over a distance of 100 km. Earthquakes of magnitude 6.6 and 6.8 (Richter, 1958) in July and August of 1954 preceded the December 16 Fairview Peak-Dixie Valley shocks of magnitude 7.1 and 6.8 (Fig. 1). The July-August earthquakes broke ground for about 35 km in a zone about 30 km west of the FP-DV zone.

Retriangulation was underway at the time of the August earthquake, and a member of the survey party vividly described his experience in the Stillwater Range near Job Peak (Whitten, 1957): "I was approximately two miles from the summit.... when the earthquake started. It came in a series of three violent quakes, about 15 seconds apart, each lasting for approximately 15 to 20 seconds, and each series was stronger than the one before. These three quakes could not be defined as tremors, but were rapid, hard vibrations. During all of the series I could hear rocks pounding and sliding together. It sounded like it

was directly below me. The last vibration of the third series was by far the hardest and loudest. The slipping of the rocks ended with a loud bang. It felt and sounded as if the earth had lurched and caught..... One reason I remained seated was that I did not believe I could stand, so violent was the quake."

The 1954 faults are part of the prominent zone of historic breaks (118th-meridian seismic zone, Fig. 2) extending from Owens Valley (1872) to Pleasant Valley (1915). Ground breakage is recorded in 1872, 1903, 1915, 1932, 1934, and 1954. A prominent spatial gap between the 1915 and 1954 faults displays evidence of intense pre-historic activity.

A high level of prehistoric activity on the seismic zone is also demonstrated by the fact that Dixie Valley has been tectonically maintained as the regional topographic low point - 500 feet lower than Carson Sink. Dixie Valley had its own late Pleistocene lake which stood at a lower level and was not connected with Lake Lahontan.

THE SEISMIC DATA

The Fairview Peak earthquake was recorded worldwide, and the focal mechanism, replotted from Romney's 1957 data, is shown in Figure 3. The preferred fault plane (N11°W, 62°E) differs in strike by about 20° from the surface break but agrees with dips measured at the surface. An alternative solution for the focal mechanism by Wickens and Hodgson (1967) gave the fault plane as N4°W, 54° E, closer in strike to the geologic trend (about N9°E). Romney's slip direction, shown by the cross in Figure 3, agrees well with geodetic displacement vectors. A simple dislocation model of the geodetic data (Savage and Hastie, 1969) shows a best-fit plane (N9°E, 57°E) that matches well with surface faults. Snay et al. (1985) have calculated much more elaborate models of the geodetic data. Offset topographic features on the Fairview Peak fault show clearly a right-lateral component about equal to the dip-slip component, in agreement with the focal mechanism and geodetic measurements. All data for the Fairview Peak fault thus converge to define an oblique-normal, right-lateral fault zone. The zone dips about 60° from the surface to a depth of about 15 km, where it presumably enters a more ductile part of the crust.

No focal mechanism was obtainable for the Dixie Valley earthquake because the seismograms were contaminated by the earlier Fairview Peak shock. Romney (1957) obtained hypocentral depths of 15 km for the Fairview Peak and a less certain 40 km for the Dixie Valley earthquake. Okaya recently reexamined the evidence and concluded that both earthquakes originated at about the same depth, 15 km (Okaya and Thompson, 1985). Microearthquakes in the region also cluster at depths of 10 to 15 km (Fig. 4).

In contrast to Fairview Peak the surface breaks of the Dixie Valley earthquake indicate nearly pure dip slip. As previously noted, no focal mechanism is available, and the faults extend outside the triangulation net. It is noteworthy that the Dixie Valley shock nucleated near the north end of the zone (epicenter, Fig. 1), farthest from the Fairview Peak faults. The physical mechanism for the 4-minute delay between shocks remains an intriguing question. It is tempting to speculate that pore-pressure changes may be responsible, for the hydrologic regime was strongly disturbed after the Dixie Valley earthquake.

Cloud's (1957) isoseismal map shows that attenuation on bedrock was generally more rapid to the west. Damage at several reservoirs and tanks as far away as Sacramento was caused by surging.

THE GEODETIC DATA

Coseismic displacement vectors are shown in Figure 5. Points about 60 km east and west of the FP-DV faults did not appear to be displaced relative to each other and were assumed fixed. It appears that blocks on opposite sides of the fault contracted elastically in a NW-SE direction and broke apart obliquely at the fault zone. The pull-apart created a potential void that explains the lowering of the valley. This is a classic illustration of elastic rebound in which slow accumulation of extensional strain is relieved by coseismic contraction and oblique normal faulting. The obliqueness of the faulting is simply a function of the strike of the break relative to the extension direction.

As the total fault offsets are measured in kilometers (topographic relief plus depth of valley fill) the 1954 displacements are only the last of hundreds or thousands of displacements. The elastic strains and displacements by themselves would produce a regional lowering of the land surface, which instead has remained high (about 1.5 km). A concurrent, broad regional uplift is thus required.

Savage and Church (1974) found that leveling in 1967 implies continued (partly aseismic?) slip on the Fairview Peak fault zone beginning at least 6 months after the earthquake. The inferred postearthquake slip is about 5 percent of the displacement observed at the time of the earthquake. Recent strain rates across the 118th-meridian seismic zone are shown in Figure 6 (Savage, 1983). The average east-west strain rate of 0.06 μ strain/year translates to a spreading rate of about 2.5 mm/yr across the network breadth of 40 km. As Savage points out, this is higher than the geologically estimated rate of about 1 mm/yr in Dixie Valley (Thompson and Burke, 1974).

GEOLOGICAL AND GEOPHYSICAL EXPLORATION

The average extension direction for Dixie Valley during the last few million years as recorded by fault grooves in bedrock is N55° W-S55°E (Thompson and Burke, 1973). Although the fault varies in strike by more than 90°, the groove directions remain more nearly constant. Hence the various fault segments, depending on their orientation have undergone left- or right-oblique normal motion (Fig. 7). The constancy of the extension direction over large areas has introduced a beautiful simplification to the complexity of Basin and Range spreading (Zoback and Zoback, 1980).

The rate of spreading in Dixie Valley can be estimated from offset of the highest shoreline ("bathtub ring") of the late Pleistocene lake that occupied the valley 12,000 years ago. The 9 m of vertical offset documented by Thompson and Burke (1973) translates to 10 m of extension if the faults are assumed to dip 60°. This is slightly less than 1 mm/yr.

Total horizontal extension was estimated from the refraction seismic section of the valley (top part of Figure 8). The bottom part of Figure 8 shows the minimum (4 km) width of a hypothetical dike that would be required to fill the void created by extension. Okaya recently estimated the rate of extension based on basalt about 8 m.y. old which caps the Stillwater Range and which was also detected in a seismic reflection section (Fig. 9) in Dixie Valley (Okaya and Thompson, 1985). The extension rate over this time period is about 0.4 mm/yr.

CONCLUSIONS

Various lines of evidence in remarkable harmony with each other, indicate that the FP-DV region undergoes continuous extension in a WNW direction, punctuated episodically by rupture and elastic contraction in that direction. Coseismic contraction allows the basin blocks to drop. The regional high elevation is an independent product of slow, perhaps continuous, uplift, whereas basin blocks drop relatively at the time of earthquakes. As a result the bedrock surface of many basins is far below sea level but the average elevation of the land is about 1 1/2 km above sea level.

In the FP-DV region the seismogenic upper crust is about 15 km thick, and faults appear to be planar, maintaining a dip of 50-60° to that depth. There is no evidence for any subhorizontal detachments or listric normal faults that bottom out at depths of only about 5 km. Perhaps the FP-DV zone is part of a more fundamental break in the crust, with a higher strain rate and deeper extent. Although one would expect the temperature at 15 km in a conductive model to be at least 400°C (Lachenbruch et al., 1976) and the rocks to be deforming ductilely, seismic evidence indicates that this is not the case. Hypocenters at 15 km attest to brittle deformation at this depth and suggest that the conductive model may be too simplistic. Deep hydrothermal circulation in active fault zones may produce an abrupt transition below to self-sealing, ductile rocks with high pore pressure. Seismic reflection profiles typically show abundant subhorizontal reflectors below a depth of about 10 to 15 km in the Basin and Range province.

Finally, not all data are in agreement and many intriquing questions remain. Savage (1983) points out that the current extension rate based on trilateration networks (about 2.5 mm/yr) is several times the estimated long-term rate. Similarly the estimated recurrence period of 600-800 years on the Fairview Peak zone is much shorter than regional geologic estimates. Moreover, the VLBI measurements (Savage, 1983) have not indicated any significant extension at all across the Basin and Range province.

ACKNOWLEDGMENTS

The writer's long fascination with the mysteries of the Dixie Valley region has benefitted from discussions with too many students and colleagues to enumerate here. Jill McCarthy's suggestions improved the manuscript substantially.

REFERENCES CITED

Cloud, W.K., (1957) Intensity distribution and strong-motion seismograph results, Nevada earthquakes of December 16, 1954, Bull. Seismol. Soc. Am., 47, 327-334.

Lachenbruch, A.H., J.H. Sass, R.J. Munroe and T.H. Moses Jr. (1976) Geothermal setting and simple heat conduction models for the Long Valley caldera, J. Geophys. Res., 81, 769-791.

Meister, L.J., R.O. Burford, G.A. Thompson and R.L. Kovach (1968) Surface strain changes and strain energy release in the Dixie Valley-Fairview Peak area, Nevada, J. Geophys. Res., 73, 5981-5994.

Okaya, D.A. and G.A. Thompson (1985) Geometry of extensional faulting: Dixie Valley, Nevada, Tectonics, in press.

Richter, C.F. (1958) Elementary Seismology, W.H. Freeman and Co., San Francisco, 768 pp.

Romney, C. (1957) Seismic waves from the Dixie Valley-Fairview Peak earthquakes, Bull. Seismol. Soc. Am., 47, 301-319.

Savage, J.C. (1983) Strain accumulation in western United States, Ann. Rev. Earth Planet. Sci., 11, 11-43.

Savage, J.C. and J.P. Church (1974) Evidence for postearthquake slip in the Fairview Peak, Dixie Valley, and Rainbow Mountain fault areas of Nevada, Bull. Seismol. Soc. Am., 64, 687-698.

Savage, J.C. and L.M. Hastie (1969) A dislocation model for the Fairview Peak, Nevada, earthquake, Bull. Seismol. Soc. Am., 59, 1937-1948.

Snay, R.A., M.W. Cline and E.L. Timmerman (1985) Dislocation models for the 1954 earthquake sequence in Nevada, U.S.G.S. Open file Report, in press.

Stauder, W. and A. Ryall (1967) Spatial distribution and source mechanism of microearthquakes in central Nevada, Bull. Seismol. Soc. Am., 57, 1917-1345.

Thompson, G.A. and D.B. Burke (1973) Rate and direction of spreading in Dixie Valley, Basin and Range province, Nevada, Geol. Soc. Amer. Bull., 84, 627-632.

Thompson, G.A. and D.B. Burke (1974) Regional geophysics of the Basin and Range province, Ann. Rev. Earth Planet. Sci., 2, 213-238.

Thompson, G.A., L.J. Meister, A.T. Herring, T.E. Smith, D.B. Burke, R.L. Kovach, R.O. Burford, I.A. Salehi and M.D. Wood (1967) Geophysical study of Basin-Range structure, Dixie Valley region, Nevada, Air Force Cambridge Research Laboratories, AFCRL-66-848.

Whitten, C.A. (1957) Geodetic measurements in the Dixie Valley Area, Bull. Seism. Soc. Am., 47, 321-325.

Wickens, A.J. and J.A. Hodgson (1967) Computer re-evaluation of earthquake mechanism solutions 1922-1962, Pub. Dom. Obs., Ottawa, 33, 1-500.

Zoback, M.L., R.E. Anderson and G.A. Thompson (1981) Cainozoic evolution of the state of stress and style of tectonism of the Basin and Range province of the western United States, Phil. Trans. R. Soc. Lond. A, 300, 407-434.

Zoback, M.L. and Zoback, M. 1980) State of stress in the Conterminous United States, J. Geophys. Res., 85, 6113-6156.

ILLUSTRATIONS

Figure 1. The 1954 faults and epicenters.

Figure 2. Historic breaks, including the 118th-meridian seismic zone (1872-1915) and the Borah Peak earthquake (1983). Adapted from Thompson and Burke, 1974.

Figure 3. Focal mechanism (Romney, 1957) and geodetic displacement vectors (Whitten, 1957) for the Fairview Peak earthquake (star marks the epicenter). From Zoback et al., 1981.

Figure 4. Depth distribution of earthquakes in northern part of Fairview Peak zone.

Figure 5. Displacement vectors 1954-1955.

Figure 6. Strain along the 118th-meridian seismic zone.

Figure 7. Dip slip and oblique slip on crooked normal fault.

Figure 8. Top part of section shows structure of central part of Dixie Valley. The increments of extension are based on seismic refraction data. Bottom part shows hypothetical composite dike of width equal to the extension.

Figure 9. Migrated seismic reflection section, west side of northern Dixie Valley. A, basin deposits; B, alluvial fan deposits; C, volcanics; D, Mesozoic bedrock; Dm, migrated fault reflection. From Okaya and Thompson, 1985.

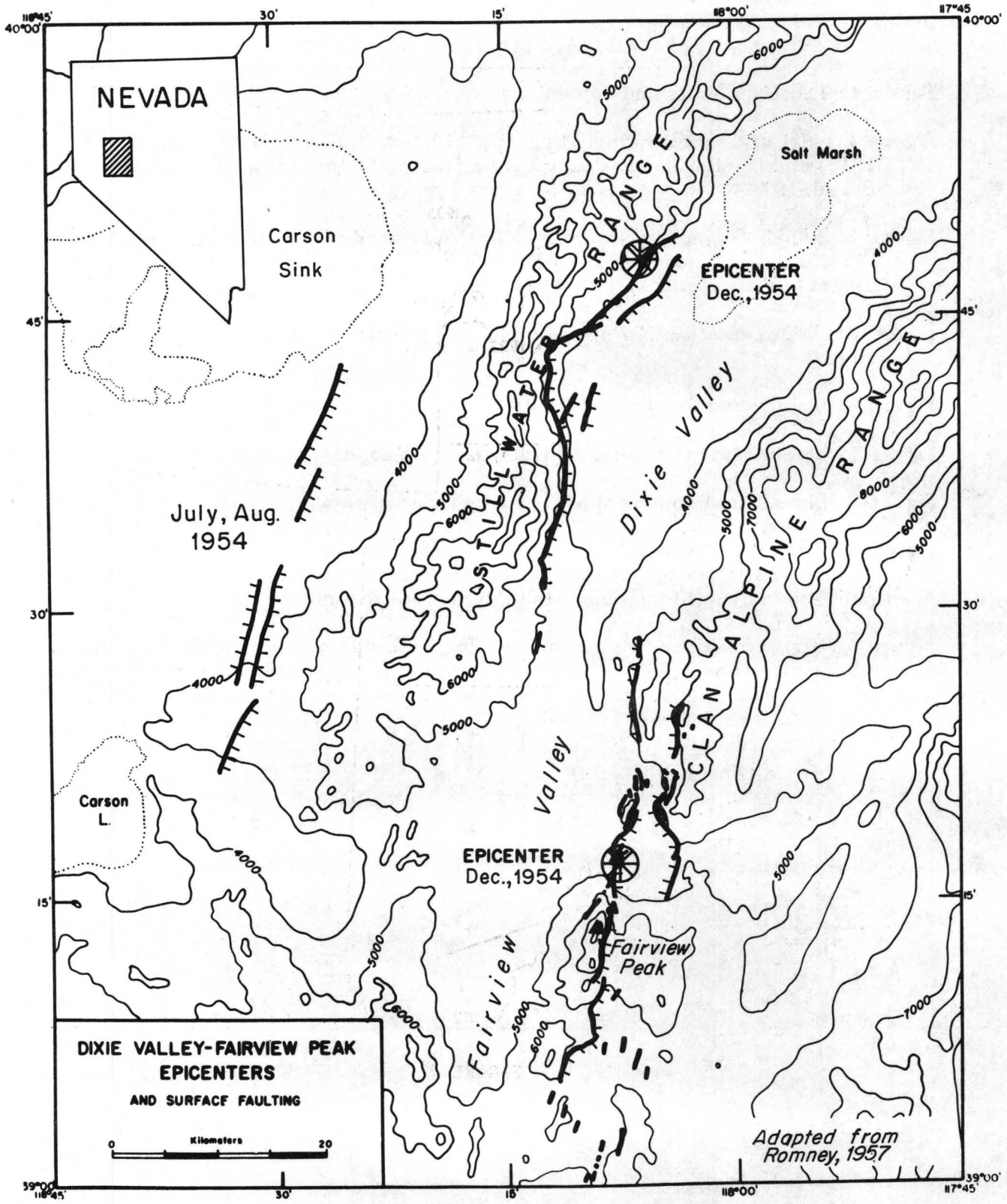
NEVADA
Carson Sink
Carson L.
July, Aug. 1954
EPICENTER Dec., 1954
EPICENTER Dec., 1954
Salt Marsh
STILLWATER RANGE
Dixie Valley
CLAN ALPINE RANGE
Fairview Valley
Fairview Peak
DIXIE VALLEY-FAIRVIEW PEAK EPICENTERS AND SURFACE FAULTING
0 Kilometers 20
Adapted from Romney, 1957
118°45'
30'
15'
118°00'
117°45'
40°00'
45'
30'
15'
39°00'

Figure 1

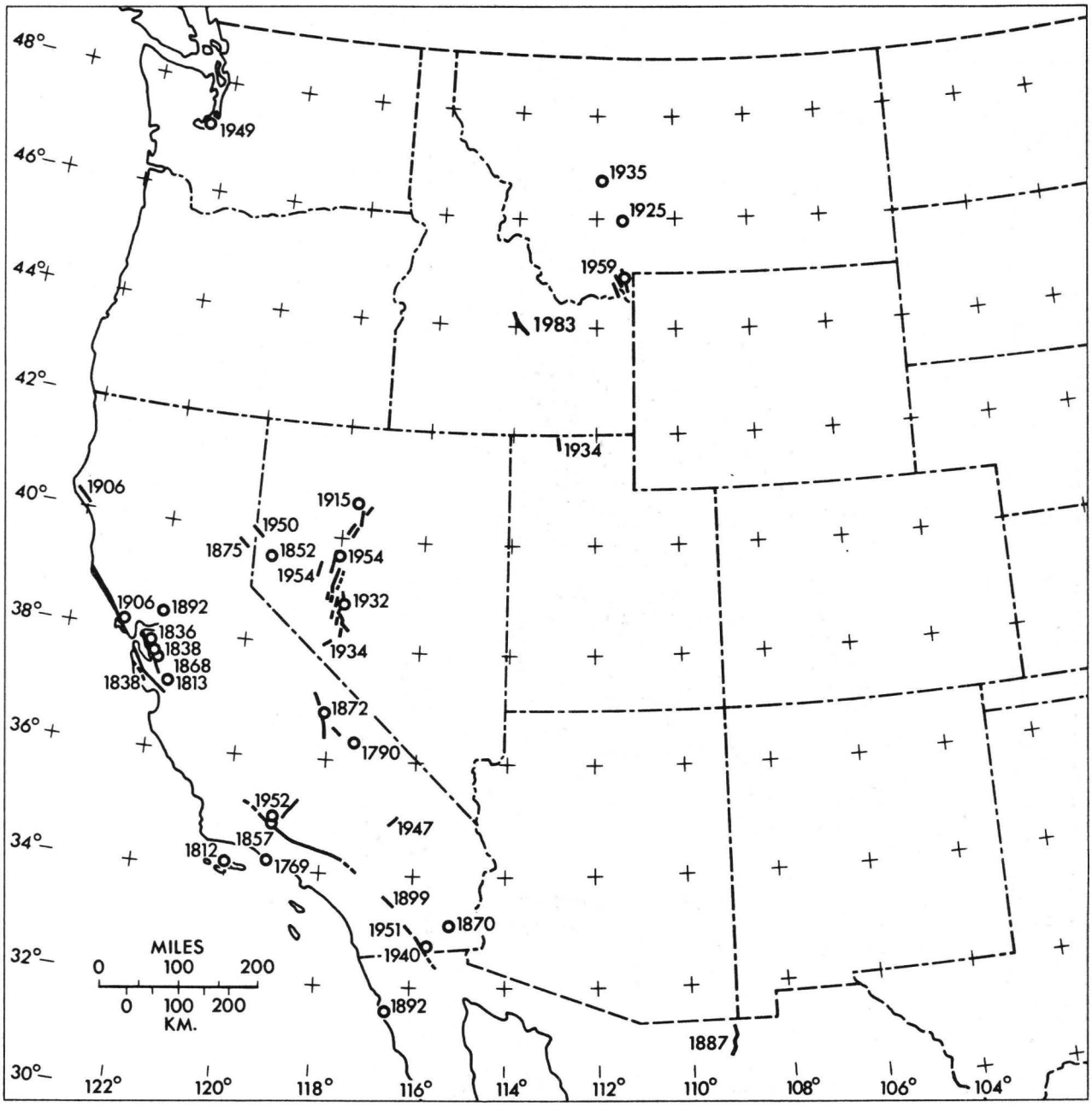
48°
46°
44°
42°
40°
38°
36°
34°
32°
30°
122°
120°
118°
116°
114°
112°
110°
108°
106°
104°
1949
1935
1925
1959
1983
1934
1906
1915
1950
1875
1852
1954
1954
1932
1906
1892
1836
1838
1868
1838
1813
1934
1872
1790
1952
1947
1857
1812
1769
1899
1951
1870
1940
1892
1887
MILES
0 100 200
0 100 200
KM.

FIGURE 2

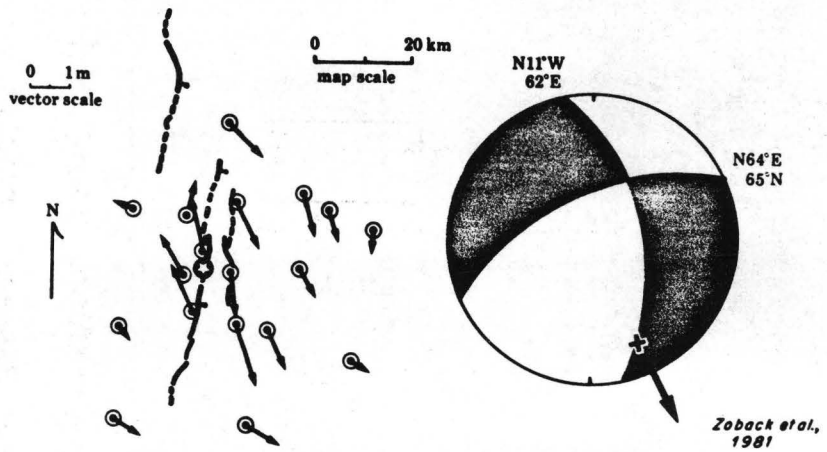

Figure 3. Focal mechanism (Romney, 1957) and geodetic displacement vectors (Whitten, 1957) for the Fairview Peak earthquake. Star marks the epicenter.

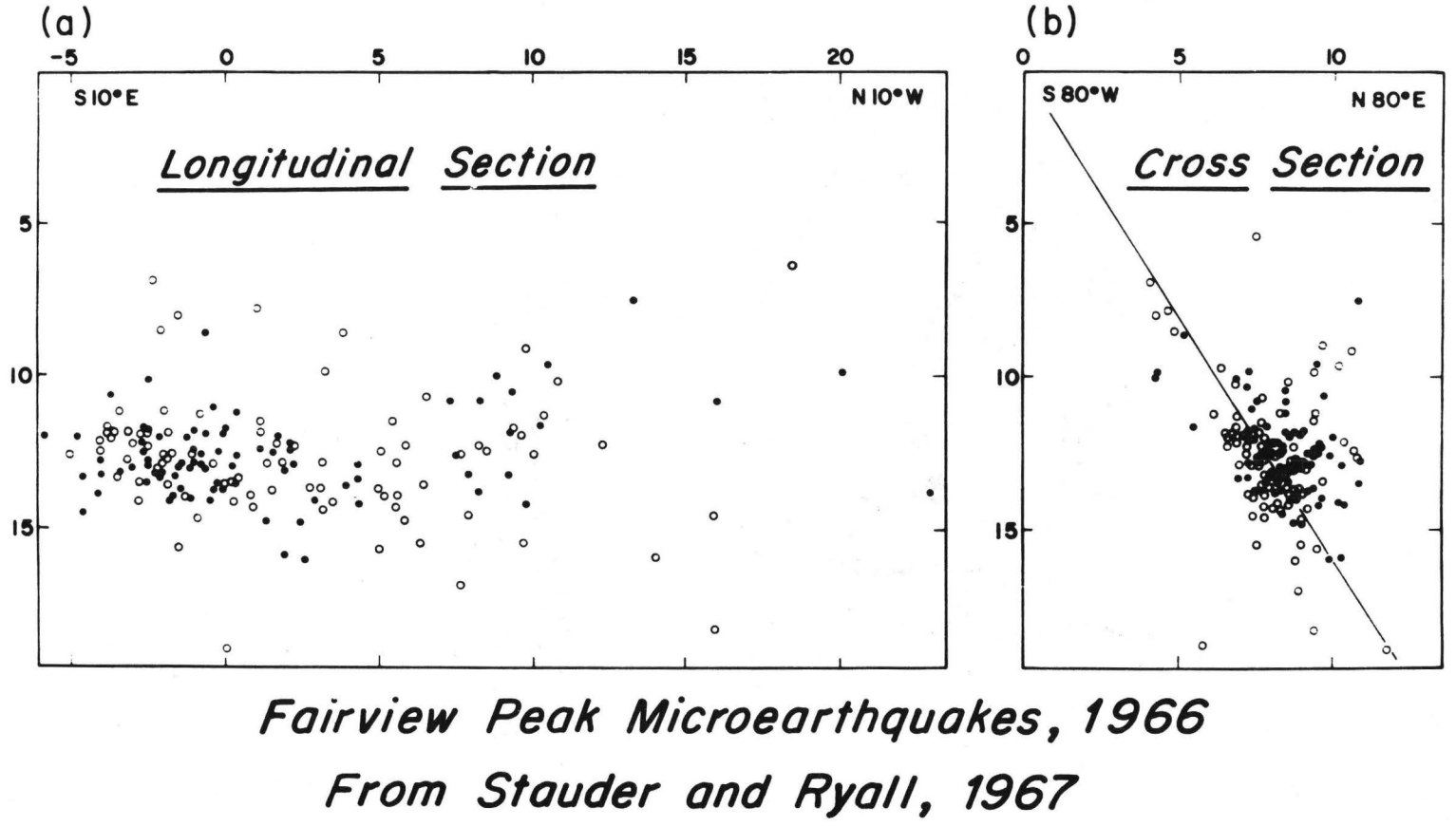

Figure 4. Depth distribution of earthquakes in northern part of Fairview Peak zone.

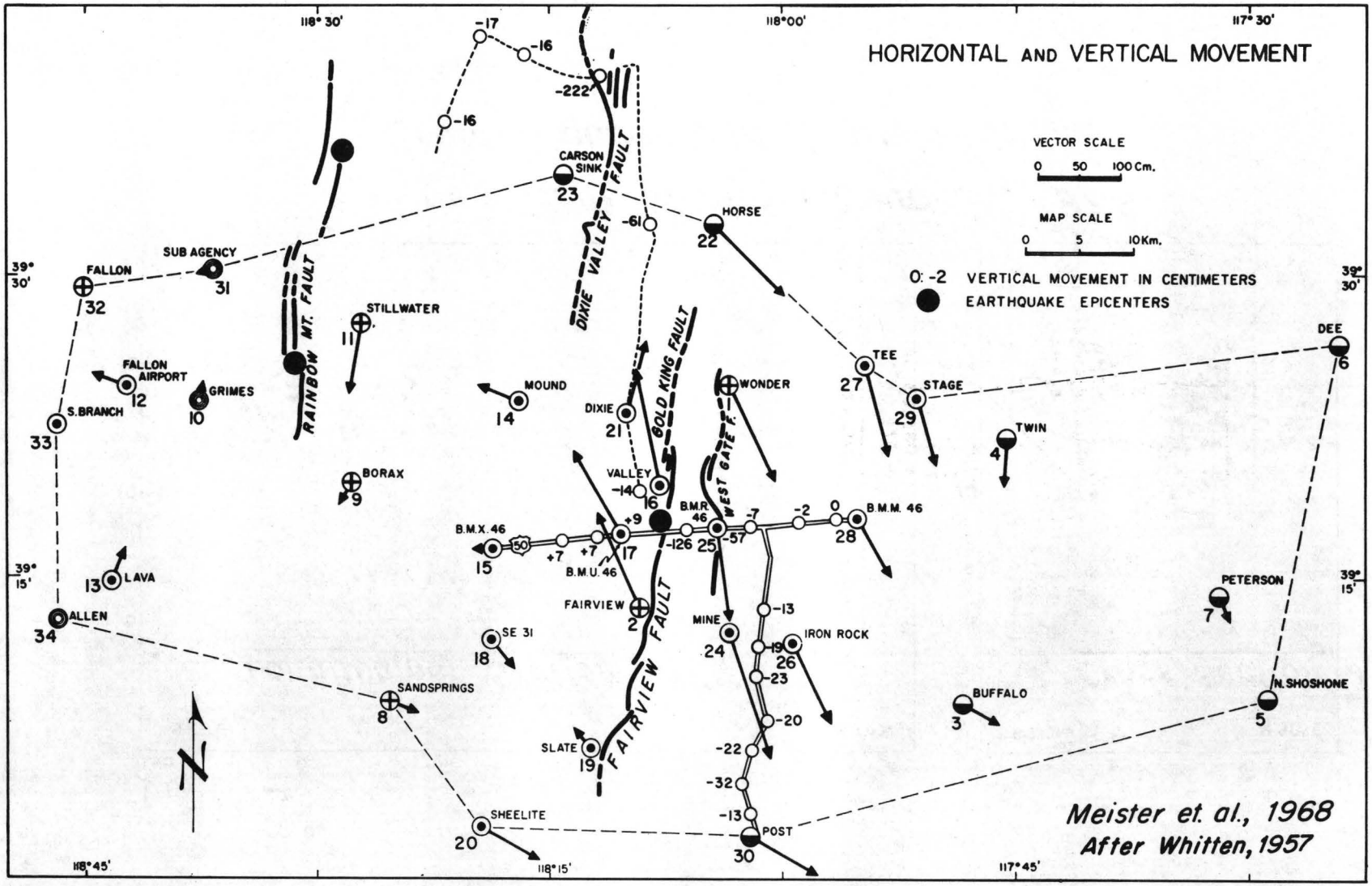

Figure 5. Displacement vectors 1954-1955.

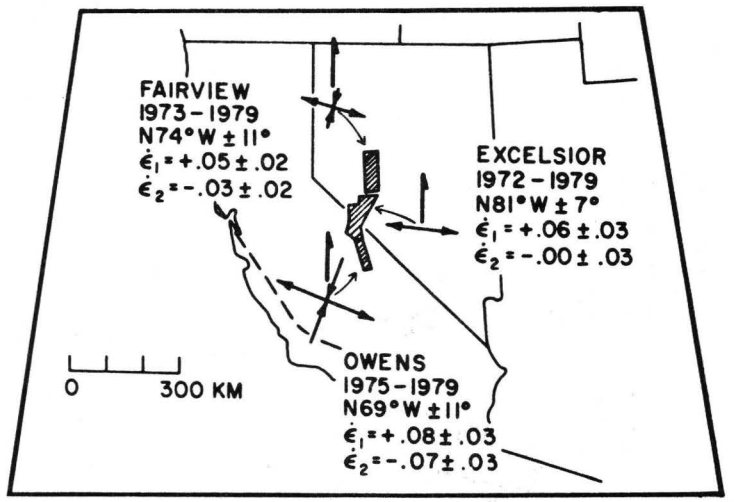

DETAIL OF TRILATERATION NETWORKS, From Savage, 1983

Figure 6 Strain along the 118th-meridian seismic zone.

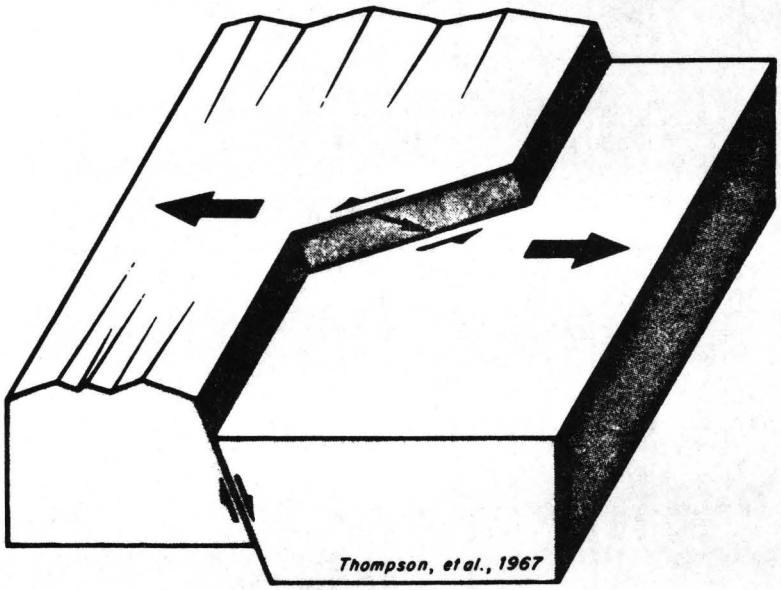

Dip slip and oblique slip on crooked normal fault

Figure 7.

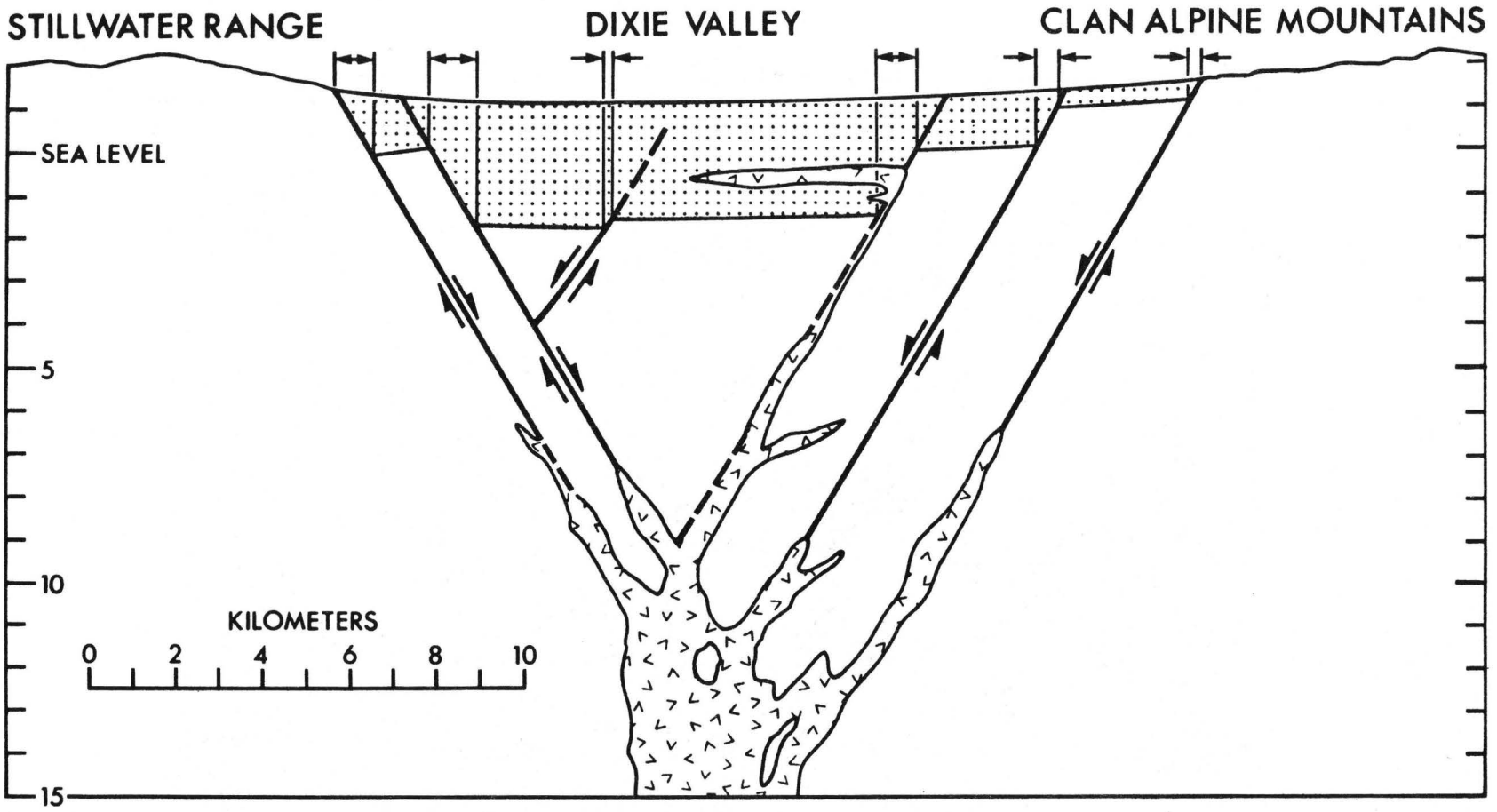
STILLWATER RANGE
DIXIE VALLEY
CLAN ALPINE MOUNTAINS
SEA LEVEL
5
10
15
KILOMETERS
0 2 4 6 8 10

FIGURE 8

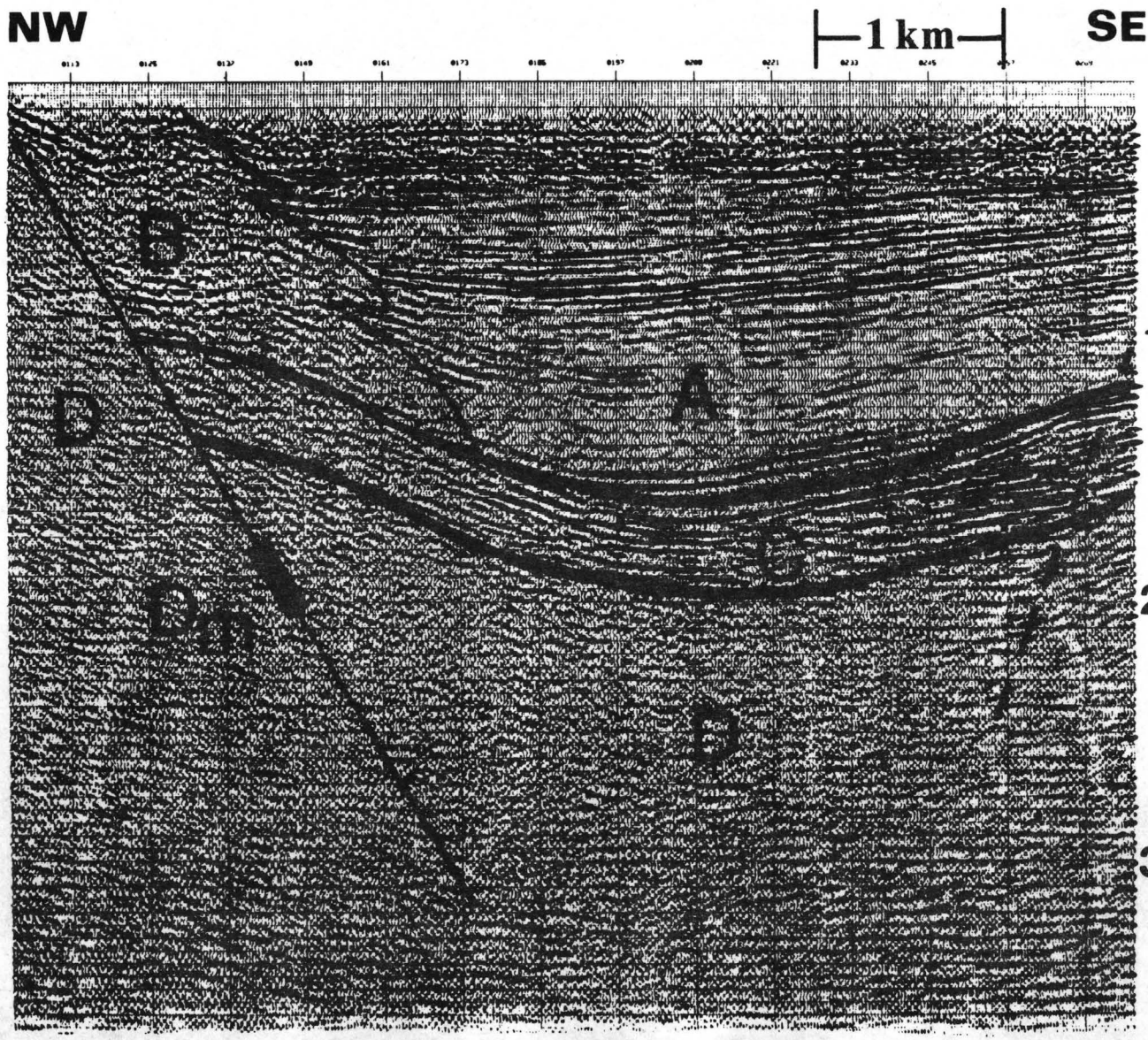

FIGURE 9

CHARACTERISTICS OF SURFACE FAULTING ACCOMPANYING THE BORAH PEAK EARTHQUAKE, CENTRAL IDAHO

by

Anthony J. Crone,[1] Michael N. Machette,[1]
Manuel G. Bonilla,[2] James J. Lienkaemper,[2]
Kenneth L. Pierce,[1] William E. Scott,[1] and Robert C. Bucknam[1]

[1] U.S. Geological Survey, Box 25046 DFC, Denver, Colorado 80225
[2] U.S. Geological Survey, 345 Middlefield Road, Menlo Park, California 94025

ABSTRACT

The zone of surface ruptures that formed during the M_s 7.3 Borah Peak earthquake on October 28, 1983 has a total length of about 36±3 km. The maximum throw measured along the new fault scarps is 2.7 m near the western base of Borah Peak. The rake of slickensides in colluvium show that the near-surface displacement averaged 17 cm sinistral slip for 100 cm of dip slip.

The largest amount of throw, most complex ruptures, and best evidence of sinistral slip occur along the 19.4-km-long southern section of surface faulting which coincides with part of the Lost River fault. Surface faulting along this section, extending from Elkhorn Creek northwestward to the west flank of Dickey Peak, is characterized by extensive ground breakage up to 100 m wide, several en echelon scarps with synthetic and antithetic displacements, and individual scarps up to about 5 m high.

From the west flank of Dickey Peak, a 14.2-km-long western section of ruptures crosses the alluvial valley of Arentson Gulch and a series of bedrock hills, and extends out into Antelope Flat. The throw along this section is generally less than 0.5 m but locally is as much as 1.6 m. The new ruptures are poorly developed across the crest and north flank of the bedrock hills; here they are primarily an alignment of downhill-facing arcuate scars, perhaps incipient landslides, that may overlie a deeper zone of tectonic movement.

The northern section, also along the Lost River fault, is at least 8.2 km long and has a maximum throw of about 1 m. Ground rupture patterns are simple compared to the patterns along the southern section. The northern and southern sections are separated by a 4.8-km-long gap in 1983 surface faulting; this gap contains upper Pleistocene fault scarps.

Morphologic variations in the Borah Peak scarps demonstrate how the distribution of fault strands, sediment sorting and water content influence the morphology of new scarps. Synthetic displacement on closely-spaced, strands locally created a stair-step series of scarps that will appear morphologically older in the near future. Scarps in matrix-rich gravels maintain prominent free faces; the same scarps in matrix-poor gravels rapidly lost most of their free faces and raveled to slopes of 30°–37°. Fine-grained, water saturated sediment near springs deformed plastically into monoclines.

Three separate sections of surface faulting, each with different characteristics, and the gap in surface faulting reflect the complex interaction of faults that ruptured during the earthquake. The rupture probably propagated northward from the epicenter and encountered a barrier on the fault plane near the gap that either deflected the primary rupture away from the Lost River fault or halted the primary rupture and initiated a secondary rupture.

INTRODUCTION

At 8:06 a.m. (MDT) on October 28, 1983, a M_s 7.3 earthquake struck east-central Idaho, causing two deaths in the town of Challis, and an estimated $12.5 million damage in the sparsely-populated surrounding area (Federal Emergency Management Agency, 1983, oral commun.). A northwest-trending zone of surface faulting about 36 km long formed during the earthquake (fig. 1). Most of the new fault scarps are along the surface trace of the Lost River fault (the western boundary of the Lost River Range), but a prominent west-trending splay diverges from the range-front fault at the base of Dickey Peak and cuts through the bedrock hills near Willow Creek Summit that separate Thousand Springs Valley on the south from Warm Spring Valley to the north (fig. 2). This report describes the distribution and general characteristics of the surface faulting associated with the earthquake.

The Lost River Range and adjacent ranges to the northeast form typical basin-range topography north of the Snake River Plain and east of the Idaho Batholith. The ranges are composed of complexly folded and faulted Paleozoic and Precambrian sedimentary rocks that were thrust west to east in the Mesozoic (Ross, 1947; Ruppel, 1978; Skipp and Harding, 1985). Cenozoic normal faults bound one or both flanks of the ranges (Baldwin, 1951; Skipp and Hait, 1977; Ruppel, 1982).

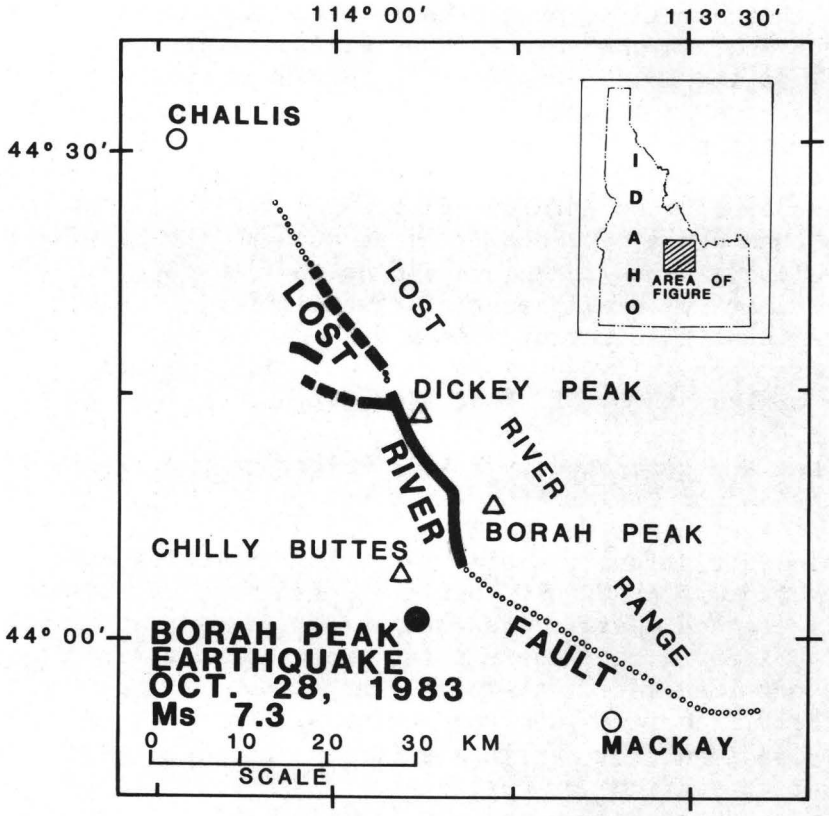

Figure 1. Location of Borah Peak earthquake. Heavy line shows zone of surface ruptures associated with earthquake; dashed where discontinuous. Dotted line is unruptured part of the Lost River fault. Area of Figure 2 is shaded. Solid dot is earthquake epicenter.

Movement on the range-bounding normal faults postdates the Challis Volcanics, mostly of Eocene age (Skipp and Hait, 1977), and may have started in Oligocene or Miocene time. However, much of the present topography probably results from late Pliocene and Pleistocene displacements (Baldwin, 1951; M. H. Hait, Jr., 1984, written commun.). The net displacement across many of these normal faults is uncertain but, along parts of the west side of the Lost River Range, it may be as much as 6.1 km (Skipp and Hait, 1977). The net Cenozoic displacement across the Lost River fault near Thousand Springs Valley is at least 2.5 km based on the present 1.9 km of topographic relief between Borah Peak, the highest point in Idaho, and the floor of the valley, plus an estimated 0.6-0.9 km of valley fill (Crosthwaite and others, 1970).

The Borah Peak earthquake occurred in a region of relatively low seismicity west of the most active part of the Intermountian Seismic Belt (Smith and Sbar, 1974). Relocation of instrumentally recorded earthquakes in central Idaho for the 20 years preceding the Borah Peak earthquake shows that the area within 10 km of the 1983 epicenter has been aseismic at a sensitivity of M $\geq$3.5 (Dewey, 1985). However, abundant Holocene and upper Pleistocene scarps along the Lost River fault (Hait and Scott, 1978; Nakata and others, 1982) attest to large magnitude prehistoric earthquakes.

CHARACTERISTICS OF SURFACE FAULTING

The surface faulting (fig. 2) associated with the earthquake formed a 36-km-long, Y-shaped zone of ruptures that are divided into: 1) a 19.4-km-long southern section that coincides with the surface trace of the Lost River fault (Baldwin, 1951) from just south of Elkhorn Creek to east of Arentson Gulch, 2) a 14.6-km-long western section that extends from east of Arentson Gulch, west-northwest toward Antelope Flat, and 3) a northern section (also along the surface trace of the Lost River fault) at least 8.2-km-long, that extends from 2 km north of Sheep Creek to just south of McGowan Creek. North of McGowan Creek, cracks with little or no displacement are locally present for another 5 km, to about 75 m south of Devil Canyon. If the last 5 km of cracks are included, the total rupture length is more than 39 km.

The northern and southern sections are separated by a 4.8-km-long gap in new surface faulting along the Lost River fault, centered on Sheep Creek, that is adjacent to the bedrock hills separating Thousand Springs Valley and Warm Spring Valley. The 1983 earthquake failed to generate surface faulting in this gap but obvious upper Pleistocene fault scarps show that ground breakage has occurred here in past earthquakes. At the south end of the gap, the western section of surface faulting diverges from the range-front fault. These relationships suggest that the portion of the Lost River fault at the gap responded differently to accumulated strain and to the propagating rupture than did the part of the fault along Thousand Springs Valley.

Slickenside data and displaced cultural features show that, during the earthquake, primarily normal slip with subordinate amounts of sinistral (left-lateral) slip occurred on a northwest-trending segment of the Lost River fault. Nodal planes from the focal mechanism based on teleseismic data are N22°W 59°SW, and N76°W 45°NE (fig. 3). The N22°W nodal plane is preferred based on the similar northwest strike and southwest dip of the new scarps, and the trend of the Lost River fault. The focal mechanism for this plane indicates a sinistral-slip component that is 73 percent of the dip-slip component versus 17 percent from field measurements. These data suggest that much of the sinistral-slip component did not propagate to the surface.

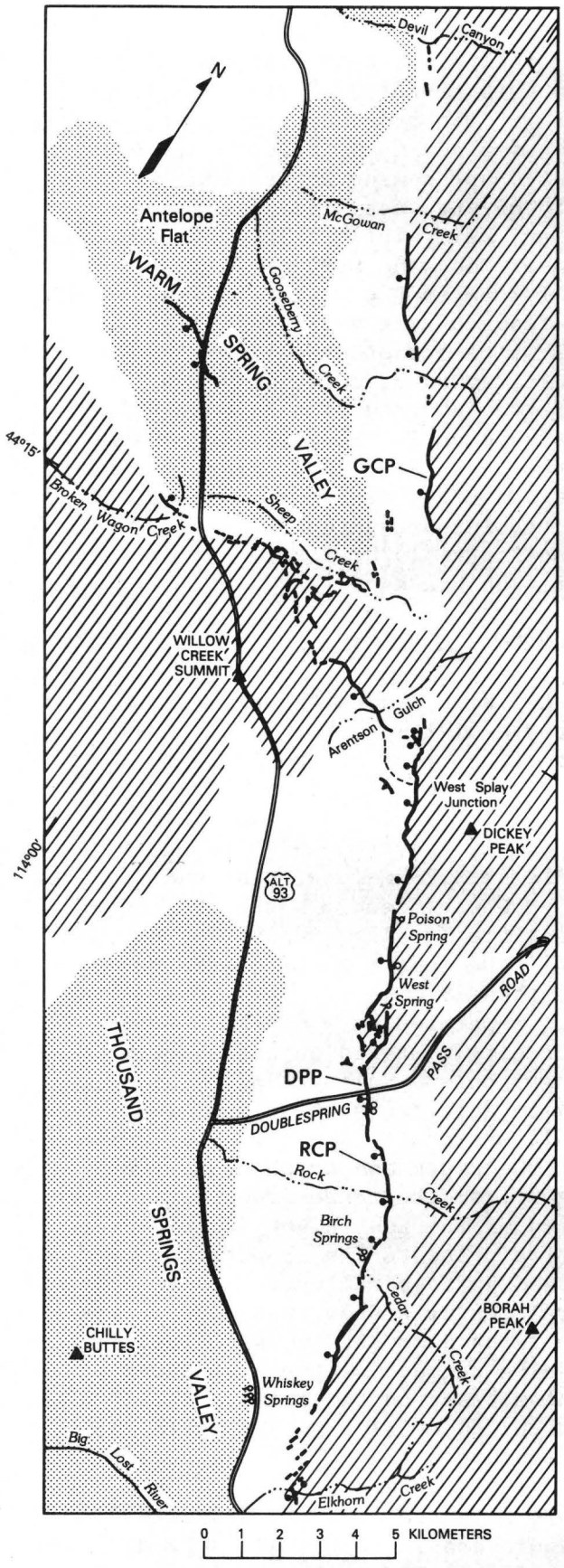

Figure 2. Generalized map of fault scarps and ground ruptures associated with Borah Peak earthquake. Heavy solid lines are prominent scarps, bar and ball are on downthrown side; dashed lines are poorly defined scarps or cracks. Stipple pattern indicates valley bottoms; hachure pattern indicates mountainous part of Lost River Range and bedrock hills near Willow Creek Summit. RCP, DPP, and GCP are locations of Rock Creek, Doublespring Pass and Gooseberry Creek profiles discussed in the text and shown in Figures 5 and 7. See Crone (1985) for detailed maps of scarps.

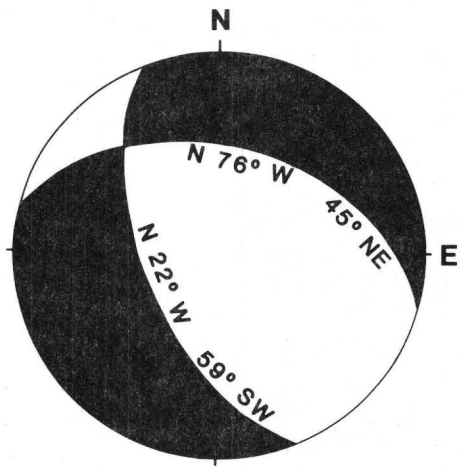

Figure 3. Focal mechanism for Borah Peak earthquake (lower hemisphere projection). Shaded areas are compressional first motions; unshaded areas are dilational first motions. Preferred nodal plane strikes N22°W and dips 59°SW. (Data and focal mechanism provided by C. Langer and R. Needham, February 22, 1984).

It was difficult to obtain reliable measurements of the lateral component across the entire width of the deformed zone, thus we have characterized the near-surface displacements on the fault by measurments of throw (vertical component of slip). Our measurments of throw represent the total offset of the prefault ground surface and compensate for the effects of antithetic faults, local warping and backrotation, and complex ground breakage adjacent to the fault. The best measurements were from previously unfaulted Holocene deposits such as stream alluvium and the colluvium that mantles the hillslopes.

Southern Section

The southern section is the main area of surface faulting; it has the largest amount of throw, clear evidence of sinistral slip, the highest scarps, and the most complex ruptures. In this section, the throw is less than 50 cm along the southernmost 3 km, but northward, increases to more than 1.0 m. From this point to just south of West Spring (fig. 4), a distance of about 10 km, the throw is commonly more than 1 m and locally more than 2 m. The maximum throw along the entire fault, 2.55-2.70 m, occurs just south of Rock Creek at the western base of Borah Peak. Just south of West Spring, the surface faults enter a 1.5-km-wide shattered block of bedrock and form a complex pattern of widely spaced east- and west-facing scarps. North of West Spring, the throw generally is about 1.0 m all the way to the gap at Sheep Creek.

Our best measurements of net slip are from the southern section of the fault. Here, near the base of the free face of some large scarps, clasts dragged along the fault plane formed grooves and corrugations on weakly polished gouge surfaces. The rake of these grooves indicate a sinistral component that averages about 17 percent of the dip-slip component (i.e. 17 cm of left slip per 100 cm of dip slip) along fault planes having near surface dips of 60°-80°. The upper part of the free face of the large scarps is

commonly vertical to overhanging owing to increased coherency of the colluvium from soil development and plant roots (Wallace, 1977).

Displaced cultural features also show a sinistral slip component. The most striking example was at Rock Creek where a concrete irrigation ditch with a strike 37° oblique to the scarp had a vertical displacement of 2.90 m and a geometrically corrected lateral displacement of 0.43 m. A fence line located about 30 m north of Rock Creek and the old Doublespring Pass road both show obvious left-lateral displacements (Crone, 1985).

The complexity and amount of displacement on individual scarps along this section varies considerably. In many places, en echelon scarps show both synthetic and antithetic displacements. The most extensive breakage is along the 8-km-long zone between West Spring and Cedar Creek (fig. 2). The violent shaking, combined with differential movement on individual faults along this zone, shattered the ground surface into randomly tilted blocks several meters in width (fig. 5). The ground breakage is up to 100 m wide and commonly has four to eight en echelon scarps that may be as much as 1-2 m high (fig. 6). Along strike, these scarps typically diminish in height until the ground surface is simply warped; farther along strike the warping decreases to zero. As the displacement on one scarp decreases, a corresponding increase usually occurs on an en echelon scarp. In plan view, the en echelon scarps and cracks commonly form a right-stepping pattern that is characteristic of sinistral movement. The largest scarps commonly bound the upthrown block and are highest where adjacent antithetic faults form grabens. The largest individual scarp we found- nearly 5 m high -is 0.3 km northwest of the Doublespring Pass road.

Between Cedar Creek and the shattered block of bedrock near West Spring, the coincidence of most of the new surface faulting with preexisting scarps is striking, not only along the main fault, but also along major graben-bounding faults. At a major unnamed drainage midway between Cedar Creek and Rock Creek, a broad graben formed by pre-1983 surface faulting has diverted the westward-flowing intermittent stream northwestward along the graben. The 1983 surface faulting reactivated the main fault and antithetic faults in this area, redefining the topographic depression of the graben into which the stream will remain confined.

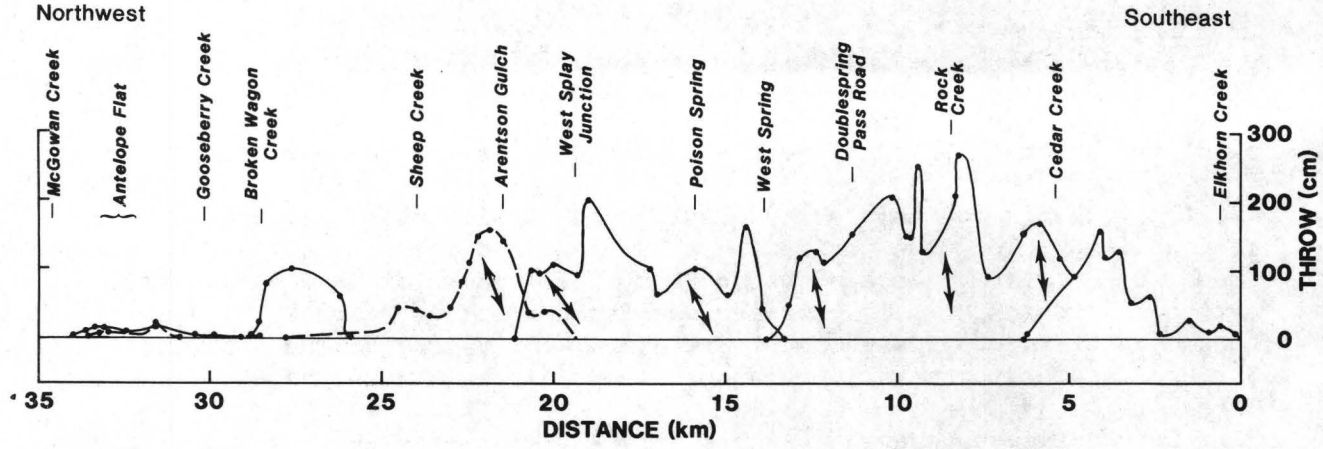

Figure 4. Amount of throw on surface faults associated with Borah Peak earthquake. Solid line is throw along range-bounding fault, queried where uncertain; dashed line is throw along western section (measurements shown by solid circles). Arrows show net-slip direction from rake of slickensides or displaced cultural features. Vertical exaggeration is 2000X.

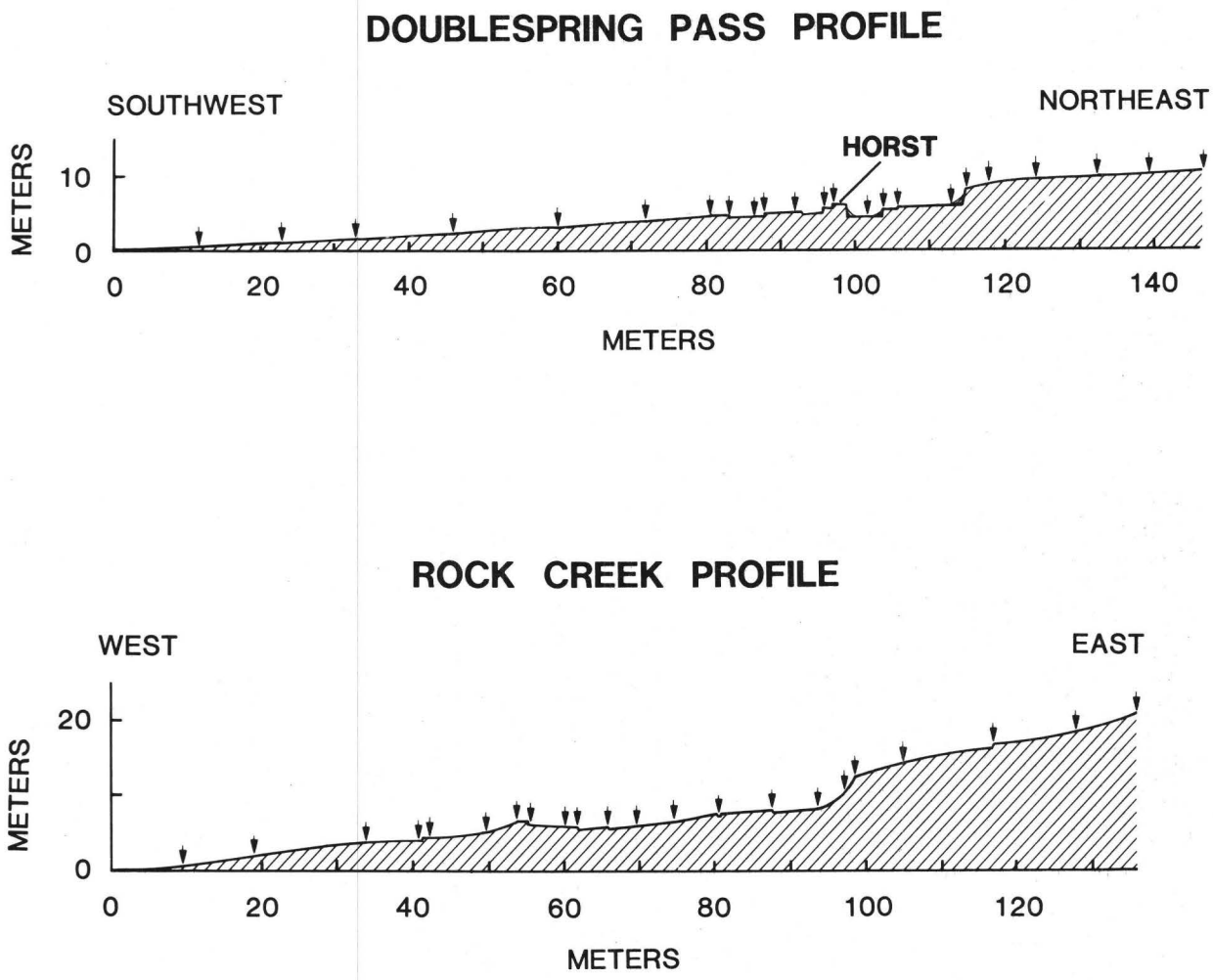

Figure 5. Topographic profiles showing complexity of ground breakage from the Borah Peak earthquake at Doublespring Pass road and Rock Creek. Profile locations shown on Figure 2. Arrows show locations of measurements for the profiles. No vertical exaggeration. Horst labeled on the Doublespring Pass profile is also shown on Figure 6.

Another example of new ruptures following preexisting scarps is just north of the Doublespring Pass road at the site of the trenches described by Hait and Scott (1978) and Crone (1985). The pre-earthquake trench and pre-1983 aerial photographs show a well-defined horst block within the graben adjacent to and west of the main fault scarp. During the Borah Peak earthquake the faults bounding the horst were reactivated, renewing the topographic expression of the block (figs. 5 and 6). Preliminary data from a post-earthquake trench, excavated at the same site as the pre-earthquake trench, indicate that even faults with a few tens of centimeters of displacement were reactivated in 1983 (see Crone, 1985).

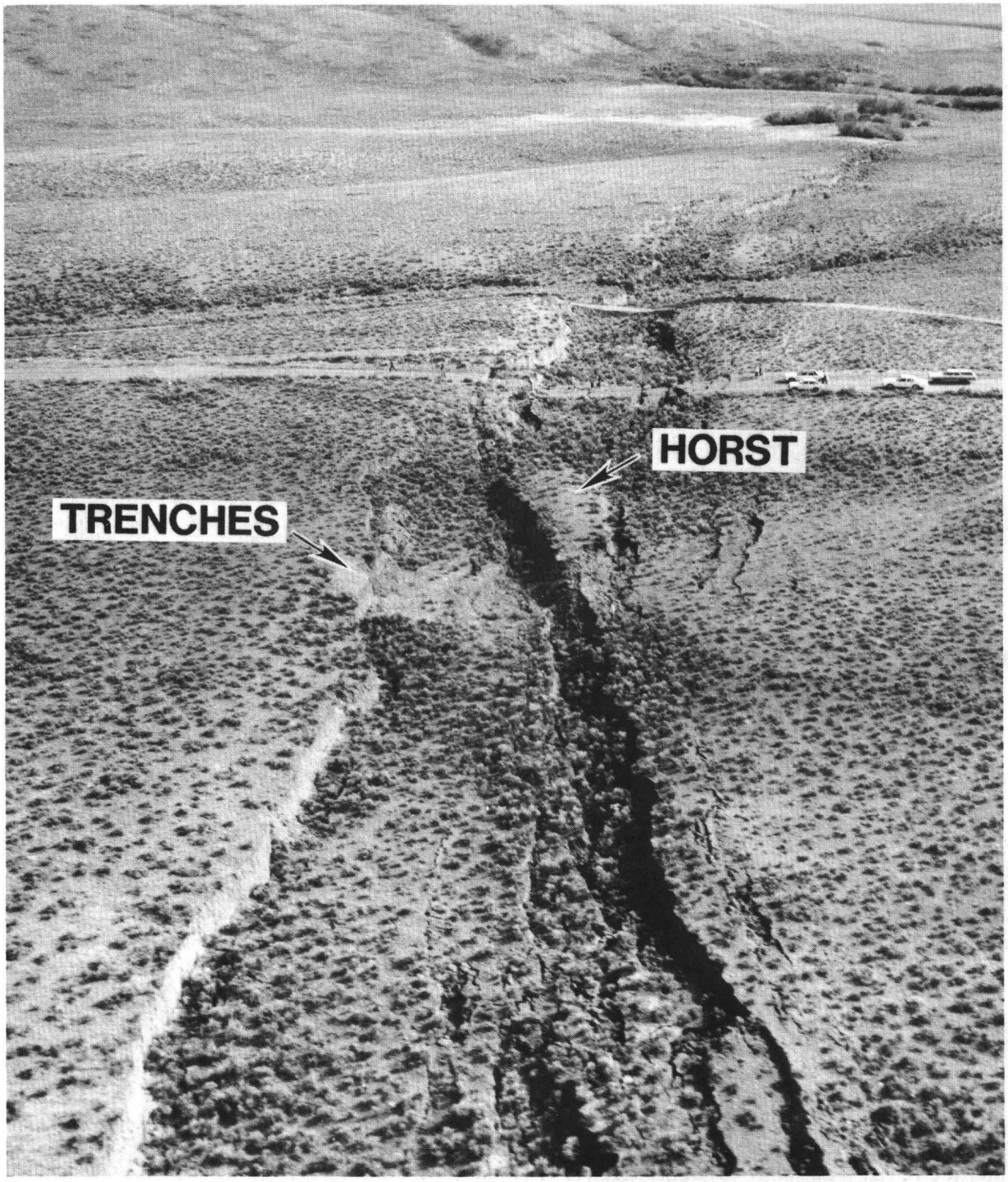

Figure 6. Oblique aerial photograph showing 25- to 50-m-wide zone of complex surface ruptures associated with Borah Peak earthquake. Site of exploratory trenches described by Hait and Scott (1978) and by Crone (1985) is shown. Horst is discussed in the text and shown on Figure 5. View to southeast; Doublespring Pass road is in middle distance, and Rock Creek Canyon is in far distance. Photograph by R. E. Wallace, Nov. 3, 1983.

The net throw along the southern section is consistently down-to-the-valley except for two groups of uphill-facing scarps at the south end, on the hillslopes north of Elkhorn Creek (Crone, 1985). Individual uphill-facing scarps are commonly a few tens to slightly more than 100 m long and are distributed over distances of several hundred meters along the hillslopes. They have a maximum throw of 71 cm and show no evidence of lateral slip. The sense of movement on the scarps has produced local benches in the hillslopes up to a few tens of meters wide.

These hillslopes are one of the few places where newly formed cracks extend into and through bedrock outcrops. The outcrops, primarily on the upper half of the hillslopes, consist of gray to white, jointed and fractured quartzite. The fresh cracks in the outcrops indicate that some of the fracturing is related to modern processes.

The origin of the uphill-facing scarps is unclear; they may be true tectonic features related to fault dislocation at depth, or they may be gravity-induced features not directly related to deep fault movements. The morphology of the hillslope near these scarps and the anomalous outcrops of shattered bedrock immediately downslope favor the gravity-induced origin but this interpretation cannot be undisputably proven. If tectonic features, the restricted distribution of the scarps and their sense of displacement (opposite to the displacement of virtually all of the other scarps associated with the earthquake) implies an unusual and complex local stress field. If the scarps are gravity-induced, the violent shaking during the earthquake probably initiated downslope creep and deep-seated lateral spreading of the entire hillslope (Radbruch-Hall and others, 1976; Bovis, 1982). Seismic shaking has been proposed as the triggering mechanism for the formation of similar uphill-facing scarps and ridge trenches in New Zealand (Beck, 1968) and in the Carpathian Mountains (Jahn, 1964).

Western Section

The western section of faulting extends from the west splay junction (fig. 2) through the alluvial valley at Arentson Gulch, across a series of rounded bedrock hills, and out into Antelope Flat. The throw along the western section is commonly less than 0.5 m, except for a 3-km-long scarp at Arentson Gulch that has as much as 1.6 m of throw. Two hunters watched the scarp form across the Arentson Gulch road (Pelton and others, 1984); here, where the scarp is essentially perpendicular to the road, it has a throw of 1.4 m and a sinistral slip of about 0.6 m.

Westward from the junction point, scarps (with up to 85 cm of displacement) and cracks are concentrated along two separate strands that merge 0.4 km southeast of Arentson Gulch. On these strands there is evidence of local dextral and reverse movement. Westward from Arentson Gulch, a single well-defined scarp extends to the crest of the low bedrock hills. Across the crest and to the north flank of these hills, scarps are poorly developed; new ruptures are an aligned series of northwesterly-trending, downhill-facing, arcuate scars which may represent incipient landslides. The alignment of these scars along the northwesterly projection of the well-defined scarps at Arentson Gulch and at the crest of the bedrock hills suggests that they may overlie a deeper zone of tectonic movement. However, displacement on this deeper zone was insufficient to produce distinct, continuous fault scarps. Along the north flank of the hills and just west of Broken Wagon Creek, the deformation is limited to small displacement, down-to-the-north cracks. Much of the vertical displacement on these cracks may result from differential compaction in the alluvium and may not reflect tectonic slip. An isolated

series of 5- to 20-cm-high, down-to-the-south scarps and cracks on Antelope Flat define the western end of this section.

Northern Section

Surface faulting along the northern section is expressed as a segment of scarps along the Lost River fault that extend northward for about 3 km from the north end of the gap near Sheep Creek. Generally, the 1983 surface faulting is superimposed on preexisting scarps. The maximum throw here is about 1 m (fig. 4) and the rupture pattern is relatively simple compared to the pattern of ruptures along the southern section (fig. 7). Most of the displacement is commonly concentrated on a single scarp and rarely is the zone of ground breakage more than 10 m wide. Northward, the displacement on these scarps decreases rapidly to zero about 1 km south of Gooseberry Creek.

Near Gooseberry Creek, pre-1983 aerial photographs show a complex, 0.5-km-wide graben that extends about 2.2 km northwestward from the termination of the newly formed ruptures. The graben contains as many as four antithetic and two synthetic scarps. The scarps are probably Holocene or upper Pleistocene in age based on their morphology. All of the larger scarps in the graben were traversed on foot at least once and the largest new displacements observed were throws of 5 cm on an antithetic scarp and 3 cm on a synthetic scarp. Any fault displacements at depth were probably distributed among several fault strands in the graben system.

North of the north end of the graben, the throw along the range-front fault increases rapidly to a maximum of 17 cm and then decreases gradually until it can no longer be recognized in a talus slope about 0.6 km south of McGowan Creek. A sinistral slip component is generally present in this area; the only two accurate measurements show a lateral slip of 25 to 40 percent of

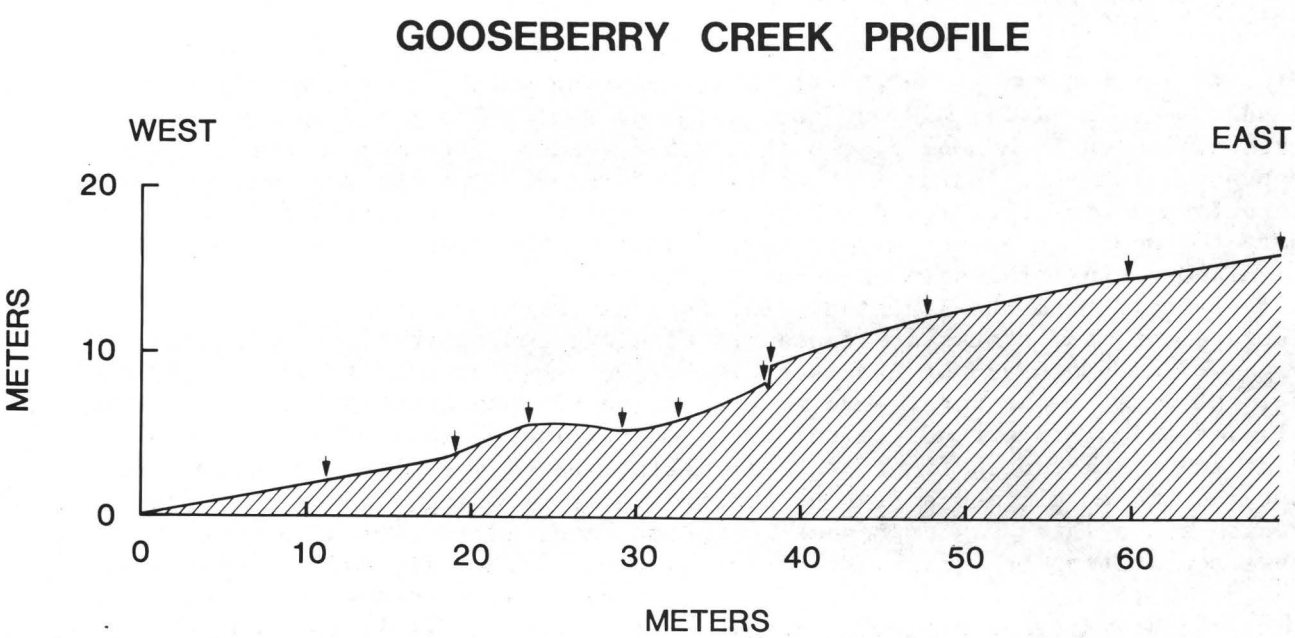

Figure 7. Topographic profile showing ground breakage from the Borah Peak earthquake near Gooseberry Creek. Location of the profile shown in figure 2. Arrows show locations of measurements for the profile. No vertical exaggeration. The bulge between meters 20 and 30 is not tectonic.

the throw. At the mouth of McGowan Creek Canyon, there are no new ruptures on the older scarp along the Lost River fault. A careful search of the old scarps to the north revealed no new ruptures until small cracks were found in the vicinity of Devil Canyon. Here, the ruptures are discontinuous cracks, generally without measureable displacement, however, locally there is up to 4 cm of throw. The ruptures near Devil Canyon occur along the bedrock-alluvium contact interpreted from a lineament on the aerial photographs, and locally there are subdued scarps along this contact.

COMPARISON OF RUPTURE DIMENSIONS TO RUPTURES FROM OTHER EARTHQUAKES

Based on empirical correlations, the surface rupture length associated with the Borah Peak earthquake is somewhat less than expected for a M_s 7.3 earthquake, but the surface displacement is within the expected range of empirically determined values. Determining a specific value for the total length of the 1983 surface faulting is complicated by ambiguities at the terminations of the fault.

Near the northern end of the surface faulting, the tectonic rupture surely extends to about 0.6 km southeast of McGowan Creek because ruptures in this area have both sinistral slip and dip slip components. Farther north, discontinuous fractures extend another 1.3 km to the south slope of Devil Canyon. It is not clear if these fractures are tectonic or merely the result of shaking. The fact that they follow a straight, pre-earthquake lineament locally coincident with subdued old scarps, and that vertical displacement is locally 4 cm on moderate slopes suggests but does not prove a tectonic origin.

At the southern end of surface faulting near Elkhorn Creek, the tectonic ruptures merge with an incipient landslide in the NE $\frac{1}{4}$, Sec. 35, T. 9N, R. 22E., making the extent of the ruptures uncertain. However, fractures in the SE $\frac{1}{4}$ of the same section produce a larger uncertainity because here, a nearly continuous, 0.2-km-long zone of fractures crosses a broad spur and nearly reaches the adjacent drainage to the southeast. Another fracture about 30 m long crosses a small spur farther southeast, making the whole zone 0.3 km long. The open fractures mainly indicate extension but in places the southwest side is downdropped as much as 5 cm. and minor left- or right-lateral displacements are present locally. This zone of fractures may be tectonic or the result of incipient downslope movement.

Thus, the minimum length of surface faulting along the Lost River fault extends at least from a point 0.6 km southeast of McGowan Creek to 0.2 km southeast of Elkhorn Creek, a distance of 33.3 km. The maximum length may extend from the south slope of Devil Canyon to a point 1.6 km southeast of Elkhorn Creek, a distance of 39.5 km. Allowing for these extremes, the surface rupture length is about 36±3 km. For a M_s 7.3 earthquake, empirical magnitude-length correlations for all types of faults in western North America yield an expected surface rupture length of 49 km and, 56 km for all types of faults throughout the world (Bonilla and others, 1984).

Empirical correlations of magnitude vs. maximum surface displacement indicate a M_s 7.3 earthquake should produce an expected displacement of 3.9 m using data for normal faults, and 2.2 m using data for all types of faults in western North America (Bonilla and others, 1984). The observed maximum displacement of about 2.7 m is lower than expected for normal faults but larger than expected for all types of faults in western North America.

MORPHOLOGY OF THE SCARPS

Scarp morphologic data, quantified as plots of scarp height versus maximum slope angle, has been applied frequently in recent years as a means of establishing relative age relationships and estimating the general age of scarps associated with normal faults (Bucknam and Anderson, 1979; Machette, 1982; Hanks and others, 1984; Mayer, 1984). An important assumption in applying these techniques is that the newly formed scarp is a relatively simple rupture that produces an abrupt step in the topography with a morphology similar to that described by Wallace (1977). Only when the step has raveled to the angle of repose do the time dependent processes used to yield age estimates begin to operate (Nash, 1980; Colman and Watson, 1983). Morphologic variations that occur locally in the Borah Peak scarps demonstrate how the distribution of fault strands, and sediment sorting and interstitial water content influence tha morphology of the new scarps. These variations emphasize the need for careful site selection when collecting scarp morphology data; poor site selection can substantially reduce the quality of the data set and thus the reliability of inferences based on the data.

About 300 m north of the Doublespring Pass road, approximately 2 m of net displacement is distributed on several synthetic strands of the fault to form a stair-step group of scarps (fig. 8). Directly to the north, these strands merge into a single scarp having a similar net displacement. As the stair-step scarps erode, they will coalesce into a broad integrated scarp having a more gentle slope than the adjacent simple scarp. Thus, in the near future the integrated scarp will seem anomalously degraded and therefore, apparently older than the adjacent simple scarp.

The grain size distribution of the faulted materials has a major influence on the morphology of the newly formed scarps (see Wallace, 1980). This influence is apparent near Rock Creek where the scarps formed in colluvium composed of subangular, poorly sorted gravel with a silty to clayey matrix are nearly vertical to overhanging and have prominent free faces. A few tens of meters away, the same scarps are formed in stream alluvium composed of rounded, well-sorted coarse sand and pebble-cobble gravel. Within one day after the earthquake, these scarps had lost most of their free faces and had raveled to slopes at angles of repose of 30°-37°.

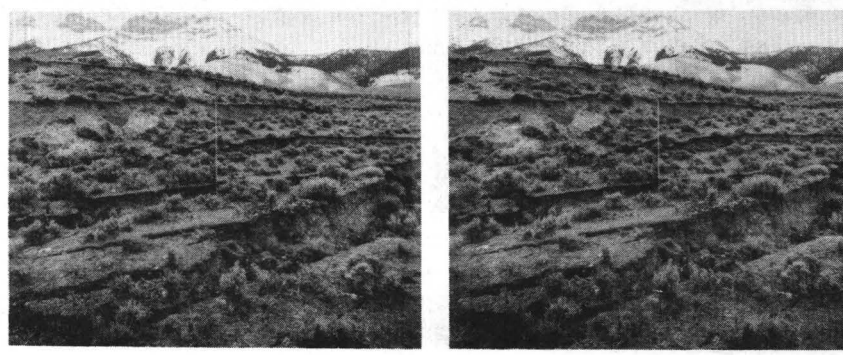

Figure 8. Stereo-pair of stair-step fault scarps located about 300 m north of Doublespring Pass Road. Stadia rod is 2.5 m long. Photographs by M. N. Machette, Nov. 8, 1983.

Another morphologic variation occurs locally where the newly formed scarps cut fine-grained, water-saturated sediments near springs. At two spring locations, an unnamed spring 0.9 km northwest of West Spring, and unnamed springs about 0.8 km southeast of Doublespring Pass road (fig. 2), the net displacement across the fault zone is more than 1 m. The scarps formed in poorly-sorted gravelly colluvium and alluvium adjacent to the springs have sharp, well-defined free faces, but where the scarps extend into the fine-grained, water-saturated sediment near the springs, the ground surface is locally warped into a broad monocline, with no free face and with a comparatively low slope angle. Near the crest of the monocline, tension cracks with little or no vertical displacement may form in the area of maximum flexure. In places, the water-saturated sediments deformed plastically whereas the unsaturated gravelly colluvium consistently ruptured in a more brittle fashion. In a few hundred years, the monoclines will appear to be more degraded and morphologically older than the scarps formed in the colluvium.

CONCLUSIONS

The formation of three separate sections of scarps, each with different characteristics, and the gap in the new surface faulting along the Lost River fault northeast the bedrock hills (fig. 2) provide some insight into the complex interaction of the faults that ruptured during the earthquake. Geologic mapping (Mapel and others, 1965) shows that the cumulative Cenozoic throw on the Lost River fault is considerably less at the bedrock hills than it is at the margin of Warm Springs Valley. Similarly, there is probably less throw on the Lost River fault at the bedrock hills than at the margin of Thousand Springs Valley to the south, although this cannot be confirmed from available mapping. Less Cenozoic throw and the gap in 1983 surface faulting on the Lost River fault at the hills both suggest that this part of the fault responds differently to strain than do the basin-bounding parts of the fault. This behavior suggests that there is a major segment boundary on the Lost River fault near the bedrock hills, similar to the segment boundaries proposed by Schwartz and Coppersmith (1984) for the Wasatch fault zone in Utah.

The 1983 rupture propagated northward along the Lost River fault from an epicenter near Chilly Buttes (fig. 1) in Thousands Springs Valley (fig. 2; Smith and others, 1984). We speculate that, at the junction point (fig 2), a barrier on the fault plane either halted the primary rupture along the Lost River fault and immediately triggered a secondary rupture on the western section, or diverted the primary rupture away from the Lost River fault and onto the western section in the bedrock hills. Along the western section, the height of the scarps and the continuity of the surface ruptures diminish rapidly, suggesting that the displacement at depth also decreases. In fact, it is uncertain if the surface ruptures along the entire western section truly represent a continuous, through-going subsurface structure. The scarps along the Lost River fault, north of the gap, may be only indirectly related to the initial rupture that propagated from the hypocenter and to the rupture on the western secton. If this interpretation of the rupture propagation is correct, then perhaps segment boundaries may halt or deflect propagating ruptures during large earthquakes in the Intermountain Seismic Belt. However, as demonstrated by the scarps along the northern section, secondary surface faulting might develop on adjacent segments of the main fault.

REFERENCES CITED

Baldwin, E. W., 1951, Faulting in the Lost River Range area of Idaho: American Journal of Science, v. 249, p. 884-902.

Beck, A. C., 1968, Gravity faulting as a mechanism of topographic adjustment: New Zealand Journal of Geology and Geophysics, v. 11, p. 191-199.

Bonilla, M. G., Mark, R. K., and Lienkaemper, J. J., 1984, Statisical relations among earthquake magnitude, surface rupture length, and surface fault displacement: Seismological Society of America Bulletin, v. 74, p. 2379-2411.

Bovis, M. J., 1982, Uphill-facing (antislope) scarps in the Coast Mountains, southwest British Columbia: Geological Society of America Bulletin, v. 93, p. 804-812.

Bucknam, R. C., and Anderson, R. E., 1979, Estimation of fault-scarp ages from a scarp-height-slope-angle relationship: Geology, v. 7, p. 11-14.

Colman, S. M., and Watson, Ken, 1983, Ages estimated from a diffusion equation model for scarp degradation: Science, v. 221, p. 263-265.

Crone A. J., 1985, Fault scarps, landslides and other features associated with the Borah Peak, Idaho earthquake of October 28, 1983-- A field trip guide, in R. S. Stein and R. C. Bucknam, eds, Proceedings of Conference XXVIII-- The Borah Peak earthquake: U.S. Geological Survey Open-File Report, in press.

Crosthwaite, E. G., Thomas, C. A., and Dyer, K. L., 1970, Water resources in the Big Lost River Basin, south-central Idaho: U.S. Geological Survey Open-File Report, 109 p.

Dewey, J. W., 1985, A reanalysis of the instrumental seismicity of central Idaho on the basis of locally-recorded aftershocks to the 1983 Borah Peak earthquake, in R. S. Stein and R. C. Bucknam, eds, Proceedings of Conference XXVIII-- The Borah Peak earthquake: U.S. Geological Survey Open-File Report, in press.

Hait, M. H., Jr., and Scott, W. E., 1978, Holocene faulting, Lost River Range, Idaho: Geological Society of America Abstracts with Program, v. 10, no. 5, p. 217.

Hanks, T. C., Bucknam, R. C., Lajoie, K. R., and Wallace, R. E., 1984, Modification of wave-cut and fault-controlled landforms: Journal of Geophysical Research, v. 89, no. B7, p. 5771-5790.

Jahn, A., 1964, Slopes morphological features resulting from gravitation: Zeitschrift fur Geomorphologie, Supplement Band 5, p. 59-72.

Machette, M. N., 1982, Quaternary and Pliocene faults in the La Jencia and southern parts of the Albuquerque-Belen basins, New Mexico--Evidence of fault history from fault-scarp morphology and Quaternary geology, in Grambling, J. A., and Wells, S. G., eds., Albuquerque Country II: New Mexico Geological Society Guidebook, 33rd Field Conference, 1982, p. 161-169.

Mapel, W. J., Read, W. H., and Smith, R. K., 1965, Geologic map and sections of the Doublespring quadrangle, Custer and Lemhi Counties, Idaho: U.S. Geological Survey Geologic Quadrangle Map GQ-464, scale 1:62,500.

Mayer, Larry, 1984, Dating Quaternary fault scarps formed in alluvium using morphologic parameters: Quaternary Research, v. 22, p. 300-313.

Nakata, J. K., Wentworth, C. M., and Machette, M. N., 1982, Quaternary fault map of the Basin and Range and Rio Grande rift provinces, western United States: U.S. Geological Survey Open-File Report 82-579, scale 1:2,500,000.

Nash, D. B., 1980, Morphologic dating of degraded normal fault scarps: Journal of Geology, v. 88, p. 353-360.

Pelton, J. R., Meissner, C. W., and Smith, K. D., 1984, Eyewitness account of normal surface faulting: Seismological Society of America Bulletin, v. 74, p. 1083-1089.

Radbruch-Hall, D. H., Varnes, D. J., and Savage, W. Z., 1976, Gravitational spreading of steep-sided ridges ("Sackung") in western United States: International Association of Engineering Geologists, Bulletin No. 14, p. 23-35.

Ross, C. P., 1947, Geology of the Borah Peak quadrangle, Idaho: Geological Society of America Bulletin, v. 58, p. 1085-1160.

Ruppel, E. T., 1978, Medicine Lodge thrust system, east-central Idaho and southwest Montana: U.S. Geological Survey Professional Paper 1031, 23 p.

_____, 1982, Cenozoic block uplifts in east-central Idaho and southwest Montana: U.S. Geological Survey Professional Paper 1224, 24 p.

Schwartz, D. P., and Coppersmith, K. J., 1984, Fault behavior and characteristic earthquakes-- Examples from the Wasatch and San Andreas fault zones: Journal of Geophysical Research, v. 89, no. B7, p. 5681-5698.

Skipp, Betty, and Hait, M. H., Jr., 1977, Allochthons along the northeast margin of the Snake River Plain, Idaho: Wyoming Geological Association, 29th Annual Field Conference Guidebook, p. 499-515.

Skipp, B. A., and Harding, S. T., 1985, Preliminary report on geology of the Borah Peak area, Idaho, including interpretation of seismic and gravity data, in R. S. Stein and R. C. Bucknam, eds., Proceedings of Conference XXVIII-- The Borah Peak earthquake: U.S. Geological Survey Open-File Report, in press.

Smith R. B., Richins, W. D., Doser, D. I., Pechmann, J. C., and Langer, C., 1984, The 1983 M_s 7.3 Borah Peak, Idaho, earthquake-- A model for active crustal extension: Geological Society of America Abstracts with Programs, v. 16, no. 6, p. 661.

Smith, R. B., and Sbar, M. L., 1974, Contemporary tectonics and seismicity of the western United States with emphasis on the Intermountain Seismic Belt: Geological Society of America Bulletin, v. 85, p. 1205-1218.

Wallace, R. E., 1977, Profiles and ages of young fault scarps, north-central Nevada: Geological Society of America Bulletin, v. 88, p. 1267-1281.

_____,1980, Degradation of the Hebgen Lake fault scarps of 1959: Geology, v. 8, p. 225-229.

ACKNOWLEDGMENTS

M. M. Clark, S. K. Plymell, M. J. Rymer, R. V. Sharp, and B. A. Skipp helped map the surface ruptures and kindly provided their data. We thank F. A. McKeown, J. R. Pelton, R. E. Wallace, and S. H. Wood additional information and R. E. Anderson, M. M. Clark, A. R. Nelson, B. A. Skipp and M. L. Zoback for their comprehensive reviews and comments. K. A. Monger's careful preparation of the figures is greatly appreciated.

Patterns of offset associated with the 1983 Borah Peak, Idaho, earthquake and previous events

Stephen L. Salyards

Seismological Laboratory
California Institute of Technology
Pasadena, California 91125

Abstract

The Borah Peak, Idaho, earthquake of October 28, 1983 was associated with 34 km of surface breakage along the Lost River Fault and associated faults. Most of this breakage was along a preexisting fault scarp. I made twenty-eight profiles across the fault along 26 km of the recent break and examined them for evidence of older rupture. The pattern of offset seen in the total height of the scarps produced in previous events is very similar to the pattern of offset in the October 1983 event. In most cases, the places where the fault cuts moraines or older terraces are the places where the total scarp offset is usually much greater than the amount of recent offset at that location. Some of the profiles showed bevels, so assuming that each bevel on a scarp is associated with a discrete slip event, I calculated the bevel heights to determine the offset that formed the bevel. This method is dependent on normal erosion of the bevels and properly identifying the bevels on the old scarp. The results show that where bevels are present the offset in the recent event is similar to the offset in previous events. Also, for multiple fault traces, the behavior of each individual trace in the 1983 event was similar to its behavior in earlier faulting episodes. Other measures of the previous offsets on the fault are the terraces cut by Willow Creek and bands of lichen growth found on rock exposed in the footwall. The youngest alluvial fan surfaces (Pinedale age?) show only one offset previous to 1983. Using fault scarp morphology, and "typical" values for the erosion of scarps in the Basin-Range province, the most recent offset before 1983 would be 5600 yr. b.p. All these measurements show a similarity between the magnitude of the 1983 offset and that of previous offsets supporting the idea of a characteristic earthquake on the Lost River Fault.

I. Introduction

The Borah Peak earthquake of October 28, 1983 (M_s 7.3) was associated with 34 km of surface breakage in central Idaho. The fault trace commonly has higher angle slopes immediately above it, that were cut by the recent breakage. Observation suggests that these older scarps are more pronounced where the recent offset is greater. The purpose of this study is to quantify these observations and determine if the pattern of offset in the recent event is similar to the pattern of previous events. To do this I primarily used scarp-profile data from which different sections on the scarp that have developed from offsets in different events may be recognized. Some other less commonly occurring indicators of offset, stream terraces and lichen bands, are also used.

This study is mainly concerned with the height of offsets along 26 km of the 34 km of rupture. It does not deal at length with the timing of the offsets. During previous episodes of slip sections of the fault may have ruptured at the same time or at different times.

The scarp formed in the earthquake of October 28, 1983 will herein be referred to as the scarp from the "recent" event, and the degraded scarp above it will be referred to as being the result of "previous" events. A portion of the degraded scarp which has a relatively constant slope is referred to as a "bevel".

II. Data collection and analysis

The scarp profile used for this analysis were measured by the method of Wallace (1977), using a 183 cm (6 foot) rod. Twenty-eight profiles across portions of the faults that ruptured were measured (locations shown in figure 1). These include profiles across the Lost River fault, the Arentson Gulch fault (fault names as used by Wallace, 1984), and another short branch fault northwest of the Arentson Gulch fault. The profiles cover the length of the surface breakage, with the exception of the breakage on the Lost River fault north of Arentson Gulch. At all the locations where the fault was profiled, the surface material was unconsolidated sediments and reasonably homogeneous along the profile.

For the ideal evolution of the scarp of a normal fault in homogeneous material, if the fault breaks at the same point as it did in the previous event the break will fall in the middle of the old scarp (Nash, 1980). Because of this, the piece of scarp on the upthrown side will only be half of the total offsets that formed it. To obtain the total scarp offset, as used by Hanks et al. (1984), the upper and lower original slopes (far-field slopes) are projected to the recent breakage (ideally the middle of the previous scarp) (figure 2a). If the recent breakage was obviously displaced from the previous scarp, the middle of the previous scarp was used.

For a composite scarp composed of bevels from multiple offset events a given bevel will result from half the height of the free-face from that event. So, half-height of the free-face from a previous event was estimated by extrapolating the slope above the bevel of interest to the fault plane and measuring the vertical height of the bevel (figure 2b). If the slope above

the bevel has remained constant, this would be exactly half the height of the offset, as would be the case if the "lay-back" of the upper slope has been rotation about point A in figure 2b. Although neither of these cases may be exactly true, this still appears to be a good estimate of the offset with a minimal number of assumptions.

The strategy for choosing bevels was to find lengths of the profile that had similar slopes (generally within a 3 degree range), but that varied from the slopes above and below it. The existence of a bevel might be recognized, but typically its beginning and end were rounded to match the surrounding slopes. The largest source of error in this analysis is the accurate identification of bevels above the recent scarp. Further error in the measurements would be induced by nonideal erosion, or rotation and breakage of the surface from later fault movement.

Two other measures of previous offset are also used, although they cover only a small section of the Lost River fault. First, measurements were made of the stream terraces cut by Willow Creek where it crosses the fault, and second, where rock is exposed on the hanging wall of the fault the regions of differing lichen growth were measured. These two sets of information should give accurate measures of the offset on the fault at these points.

III. Results of scarp profiling

The results of the analysis of the scarp profiles are shown in three different forms. Figure 3 shows the total offset of the upper previous scarp relative to the offset from the recent event. The results of analyzing the bevels on composite scarps are shown in a relative offset plot (figure 4) with the measured offsets of the events next to each other and a cumulative offset plot (figure 5) that shows the summed offsets that could be measured. In all plots the scarp heights from the October, 1983 event have been halved to match the previous scarp offsets, since the upper previous scarps are half-heights of the offset that formed them.

Figure 3 shows that there is good agreement between the recent offset and the total offset of the scarps. The general trend is for increasing offset toward the midpoint of the break, and most of the peaks and troughs are matched in form. A few of the peaks show very close matches. The work of Schwartz et al. (1985) and Vincent (1985) constrain locations 14 to 17 to only one previous offset and in figure 3 the agreement here between the recent and previous offsets is good. Schwartz et al. (1985) put a trench across the fault between locations 16 and 17 and showed that the 1983 event was only the second to cut the alluvial fan at that location (the profile at location 16 is shown in figure 6). Locations 14 to 17 are all on this fan surface which Vincent (1985) has suggested is Pinedale age because it is the youngest fan surface in the area. Good age control is not currently available.

Generally the points that show the greatest discrepancy between the recent offset and total offset of the scarps are on the oldest materials. Locations 7 through 11 are on the moraines at Cedar Creek, and location 28 is on a piece of Donkey Fanglomerate cut by the Arentson Gulch Fault north of Willow Creek Summit. All these locations show large offsets of remnant surfaces of which location 28 is the only one where this is the offset

plotted. The total offsets at locations 7 to 11 are larger than at location 28. They have offsets greater than 10 meters, and the values that are plotted are on smaller scarps superimposed on these features. These were used because they show a good scarp form (the error-function form of Hanks et al., 1984) and are the youngest features representing the most recent activity.

Figures 4 and 5 show individual bevel heights where I observed bevels. There were few locations where bevels were observed and even fewer where they were not debatable. One of the better places is location 11 where I identified one distince bevel and two more questionable ones (figure 7). Only the height of the distinct bevel is plotted in figures 4 and 5. The recent offset at location 11 is about half of what the bevels would have predicted. This profile is on the older, outer arm of the North side of the Cedar Creek moraine and its large cumulative offset reflects this. I identified 3 bevels here but the assumption of one bevel per event may be wrong and the bevels may represent multiple events. At locations 19, 21 and 28, where bevels were also seen, at each location at least one bevel is similar in height to the recent offset. At location 21 there are three distinct bevels, two of which have values very close to the amount of recent offset. At some locations, like location 22, bevels may not have been well enough developed to recognize them. Location 22 shows a large difference between previous scarp height and the recent offset. Another point of interest is location 20. In the recent event this location showed 5 cm of mountain-side-down motion and no valley-side-down scarps could be identified there. The offset of the hillslope shows that the trend of the upper original slope is 7.05 m below the trend of the lower original slope indicating reverse motion in previous events. This is assuming that it began as a continuous, constant slope.

Using the strategy for choosing bevels, it was not always possible to identify distinct bevels within the scarp. An example of this is the scarp at location 11 between Birch Springs and Cedar Creek that was discussed above (figure 7). Here three possible bevels were chosen: the slope of the fan surface is about 7 degrees, and the bevels are 11, 16, and 25 degrees. As can be seen in figure 7b, the bevel at 11 degrees is ideal with 3 segments all having slopes within one degree of 11 degrees. The last two bevels are debatable, but they were chosen for the similar slopes of the segments and the difference from the slopes of the other bevels. Because they are so debatable they are not plotted on figures 4 and 5. This profile shows another problem, that of multiple breaks. The method of calculating the bevel heights assumes that there was only one surface break. If previous events had ruptured with multiple, closely spaced breaks, as it did in 1983, a scarp will develop that has a shallower slope than if there was only one break.

Locations 5, 12, and 13 all have three traces with roughly the same recent offset on each. In figures 3, 4 and 5 each trace is plotted separately. In the case of location 5, the one large scarp shows that one trace was dominant in the previous event. However, the scarps here are not of ideal shape and the recent breakage missed the midpoints of the previous scarps, so a complex rupture pattern may have also occurred here in the past. Locations 12 and 13 show one of the traces with more offset than the other two, and the bevels indicate that this trace had more offset in the previous events. A second type of multiple trace is the antithetic fault on the graben formed in the event. This is best developed at location 16 (figure 6). The half-height of the recent offset is 74 cm, while the scarp

shows a previous offset of 138 cm. This difference of a factor of 2 may be due to a true difference in the offset amounts or may reflect the graben influencing the erosion of the scarp. In the neighboring trench, dug across the fault by Schwartz, the antithetic fault is seen to have very similar offsets in the recent event and the previous event. An example of where the recent offset did not follow the previous multiple offset is location 10. Here there was one trace with a half-height of 1.07 m which lies between the two scarps with half-offsets of 0.20 m and 0.26 m. These measurements suggest that multiple fault traces on the Lost River fault have generally behaved similarly in the recent event and the previous event although there are exceptions.

A scarp offset-scarp slope plot of these scarps is shown in figure 8. Hanks et al. (1984) showed that for a scarp that evolves according to the "diffusion equation model" from a free-face, that is, a vertical slope, its scarp will be an error function with the scarp offset and maximum scarp angle related by $\tan \theta_s = \frac{a}{(\pi kt)^{\frac{1}{2}}} + b$ where "θ_s" is the maximum scarp angle, "a" is the half height of the scarp, "k" is the "diffusion constant" incorporating the erosion processes, the material being eroded and the climate; "t" is the age of the scarp, and "b" the tangent of the slope angle of the surface the scarp was formed on. By rearranging to $\tan \theta_s - b = \frac{a}{(\pi kt)^{\frac{1}{2}}}$ it can be seen that by plotting "$\tan \theta_s - b$" versus "a" scarps with the same kt will fall on a straight line through the origin. I will refer to $\tan \theta_s - b$ as the "reduced scarp angle". In figure 8, where the data are plotted, lines of various values of kt are included.

The data do not fall on a straight line but some trends are apparent. Most scarps have $1 < kt < 10$, but there is scatter in the points. A set of scarps on alluvial fans have a good linear trend at about $kt = 6.2\ m^2$. These scarps are all on alluvial fan material between Rock Creek and Willow Creek, or the alluvial fan material at Arentson Gulch. So for this material there is good agreement. The fact that they lie on two different faults suggests that these faults both moved in the last event. Also, the fans appear to be the same age and the scarps do not show multiple bevels, suggesting only one previous, post-fan event.

Two trends are visible in the scarps on the older features. In the case of locations 8 and 10, multiple previous scarps were found developed on the moraines which showed greater amounts of offset. Each of these lies on a good line: $kt = 2.7\ m^2$ for location 8 and $kt = 1.1\ m^2$ for location 10. The second trend is for locations 11 and 28. These two locations are also on older material, but they have developed as a larger, composite scarp. They fall on a line with a $kt = 23.3\ m^2$. Although many lines could be drawn that would include several data points it is significant that these described show some internal consistency.

These values of "kt" can be used to calculate the age of the scarp if the values of "k" for this area are known. Hanks et al. (1984) showed that for alluvial fans in the Basin-Range province a "typical" value was $1.1\ m^2/ka$. For the scarps on similar alluvial fans here, a value of $kt = 6.2\ m^2$ was found giving an age of the scarps of 5600 yrs. The climate in this area may be

moister than for the scarps studied by Hanks et al. (1984) which would increase the value of "k" and decrease the age of the scarps. But a value of $k = 1.1\ m^2/ka$ would be a lower limit making 5600 yrs. an upper limit on the age of the last event.

IV. Other indicators of offset

Another measure of the amount of offset is the two terraces that Willow Creek has cut into the alluvial surface (cross-section in figure 9). Vincent (1985) demonstrated by correlating terraces across the fault, that the upper terrace is not tectonic in origin, but that the lower terrace is. The offset between the terraces is about 2.2 metres, similar to the recent 2.05 metre offset across the fault zone at this point.

A second indicator of offset on the fault is patterns of lichen growth on rocks that are exposed in the footwall. When the fault moves in an event, a new band of fresh rock is exposed and lichen growth can begin. The result of periodic movements will be bands of lichen of similar growth stages with the bands showing increasing age upward. Two sites were found that showed these lichen patterns, site L1 immediately south of Rock Creek on dolostone, and site L2 between Rock Creek and Willow Creek on a conglomerate (locations in figure 1). At the first site the recent offset was 11 cm, and the one visible band is about 14 cm wide. At the second site the recent offset is 30 cm, and the vertical widths of the lichen bands above it are 35 cm, and 40 cm in order upward. Although the alluvial fans in this area have only been offset once this location is on rock at the base of the hill slope and could have preserved multiple events. At both of these sites there are multiple surface breaks formed during the recent event, and so there is no control across the whole fault, but it suggests the amount of motion on these traces is similar for the past three events.

V. Conclusions

From scarp profiles, terrace offsets, and lichen bands it appears that, at the sites studied, the pattern of offset on the Lost River fault is similar from one event to the next. The scarps show the same general pattern of offset along the fault. Where multiple traces of the fault exist, the dominant trace in the recent event was usually dominant in the first previous event. Antithetic faulting of a graben also shows similar behavior as the previous event. These data lend credence to Schwartz and Coppersmith's (1984) concept of a characteristic earthquake, that is, that these faults show the same pattern of offset in the most recent two events. There are suggestions that these faults all broke at the same time the last time that they moved which, based on scarp morphology, was less than 5600 yrs. ago.

These results are based on only the one or two previous events and may not represent the long-term behavior of the fault. But as an indicator of long-term offset patterns, it is interesting, through not conclusive, that the largest offset in this event lies at the base of Borah Peak, the highest point in the Lost River Range. This fact suggests recurring larger offsets here.

Acknowledgments

I thank Michael Gardosh for assistance collecting the data and thank Heidi Houston for helping with both collection and the initial processing of the data. I thank Kerry Sieh and Chris Sanders for helpful discussions and for reviewing this paper. I also thank Clarence Allen and Ray Weldon for their helpful reviews of early revisions of this paper, and thank Tom Hanks for a helpful, critical review of the final version.

This work was supported by the Earthquake Research Affiliates of the California Institute of Technology. Contribution number 4136, Division of Geological and Planetary Sciences, California Institute of Technology, Pasadena, California 91125.

References

Hanks, T.C., Bucknam, R. C., Lajoie, K. R., and Wallace, R. E., 1984, Modification of wave-cut and faulting controlled landforms: Jour. of Geophys. Res., v. 89, p 5771-5790.

Nash, David B., 1980, Morphologic dating of degraded normal fault scarps: Jour. of Geol., v. 88, p. 353-360.

Schwartz, D. P. and Coppersmith, K. J., 1984, Fault behavior and characteristic earthquakes: examples from the Wasatch and San Andreas faults: Jour. of Geophys. Res., v. 89, p 5681-5698.

Schwartz, D. P., Page, W. D., and Taylor, C. L., 1985, Significance of the 1983 Borch Peak earthquake for the evaluation of fault behavior and earthquake recurrence in the Great Basin in Workshop XXVIII on the Borah Peak Earthquake: U.S.G.S. Open-File Report, in press.

Vincent, K. R., 1985, Measurement of vertical tectonic offset using longitudinal profiles of faulted geomorphic surfaces near Borah Peak, Idaho: A Preliminary Report, in Workshop XXVIII on the Borah Peak Earthquake: U.S.G.S. Open-File report, in press.

Wallace, Robert E., 1977, Profiles and ages of young fault scarps, north-central Nevada: Geol. Soc. of Amer. Bull., v. 88, p 1267-1281.

Wallace, Robert E., 1984, Eyewitness account of surface faulting during the earthquake of 28 October 1983 Borah Peak, Idaho: Bull. of the Seis. Soc. of Amer., v. 74, p 1091-1094.

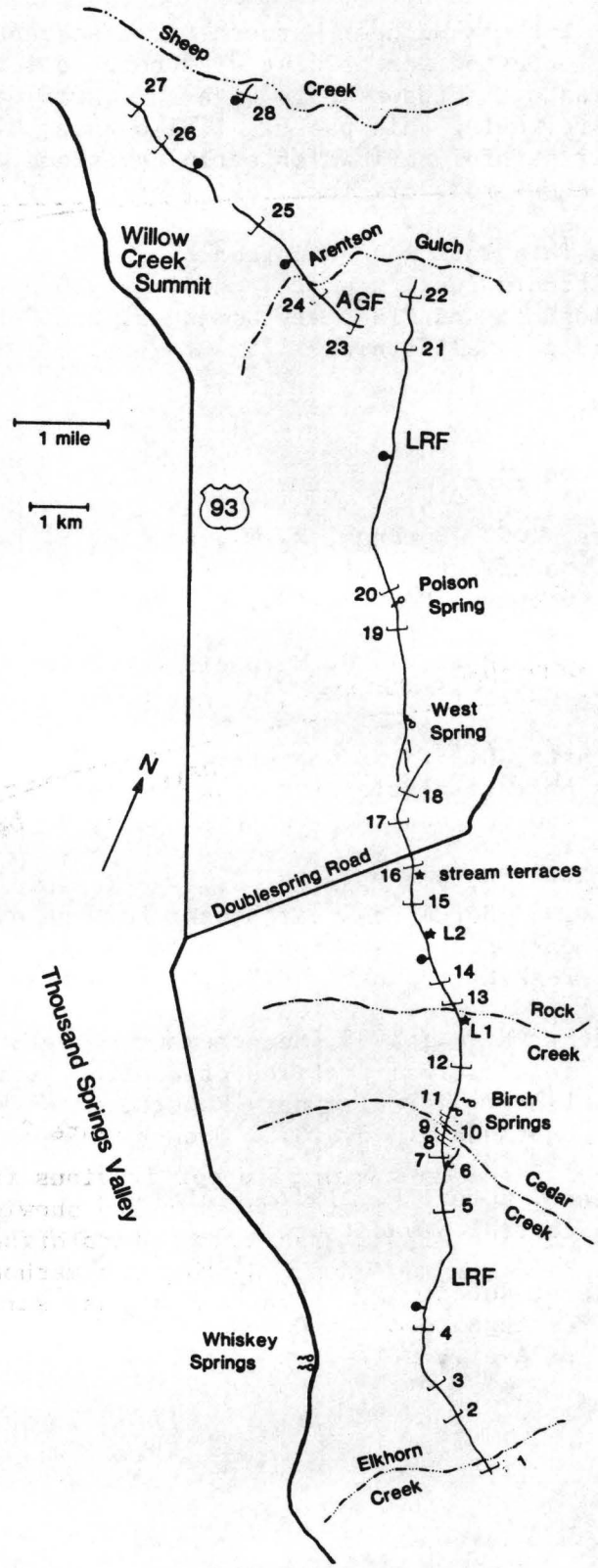

Figure 1
Map of the location of measurements. Numbered cross lines are profiles across the fault. Starred points are the locations of other types of measurements. The map shows surface breakage associated with the 1983 Borah Peak, Idaho, earthquake. LRF- Lost River fault, AGF- Arentson Gulch Fault

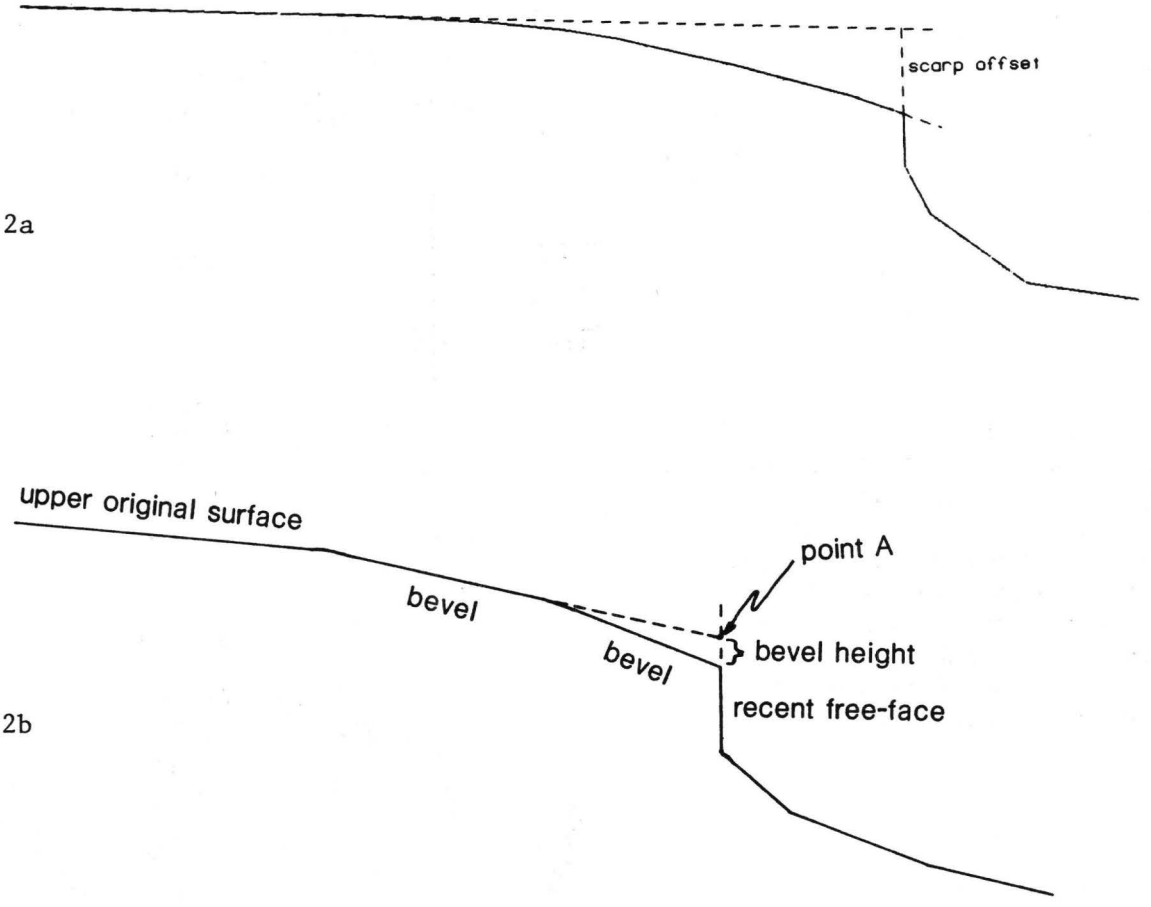

Figure 2

Two types of upper previous fault scarps. Figure 2a is a simple fault scarp showing the method of measuring the previous total scarp offset. Figure 2b is a composite fault scarp showing the method of measuring the bevel height. "Upper origional surface" and "recent free-face" apply to 2a also.

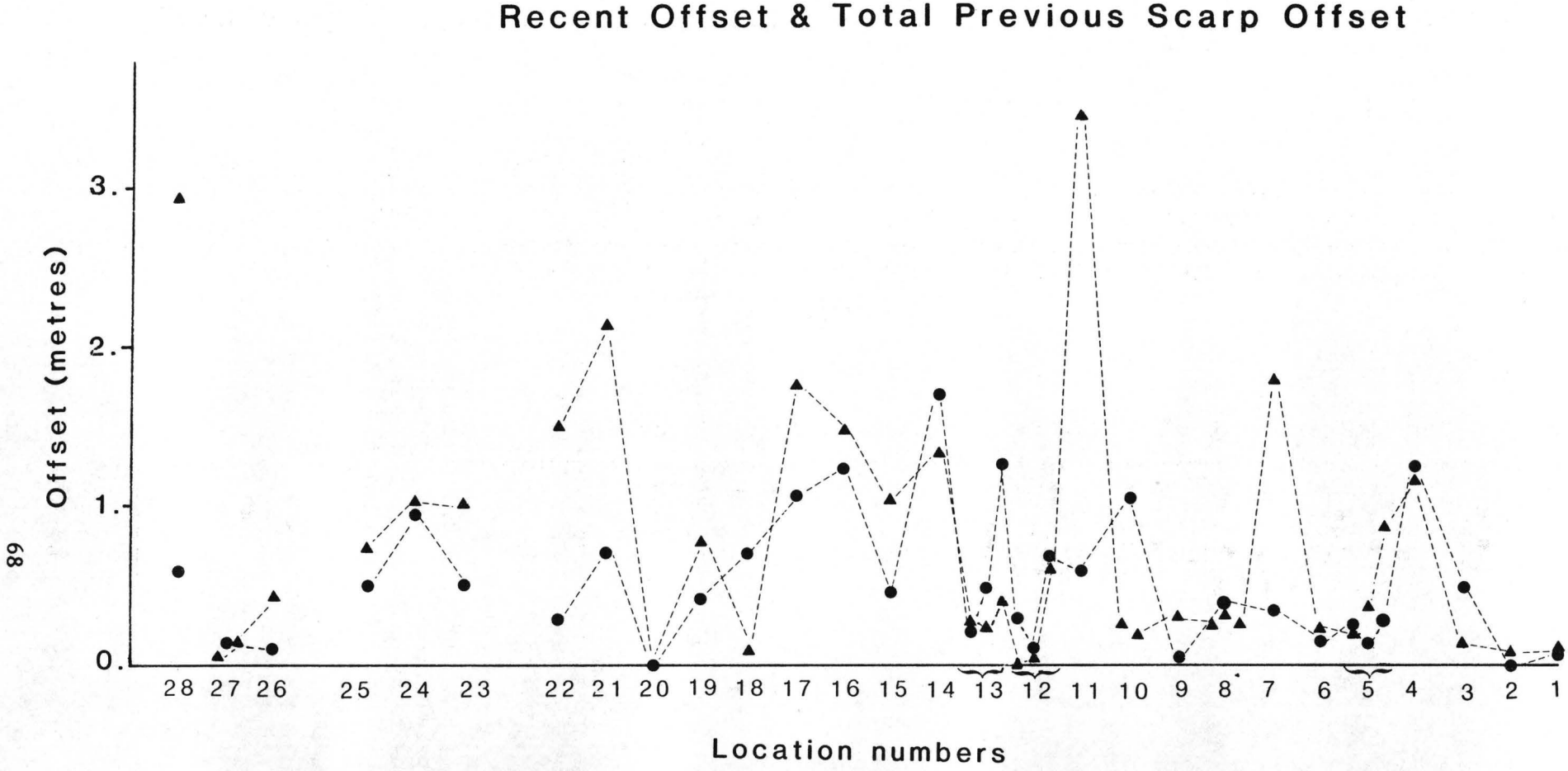

Figure 3

Plot of recent offset and total previous offset for all locations profiled. Circles are amount of recent offset, triangles are the total previous scarp offset.

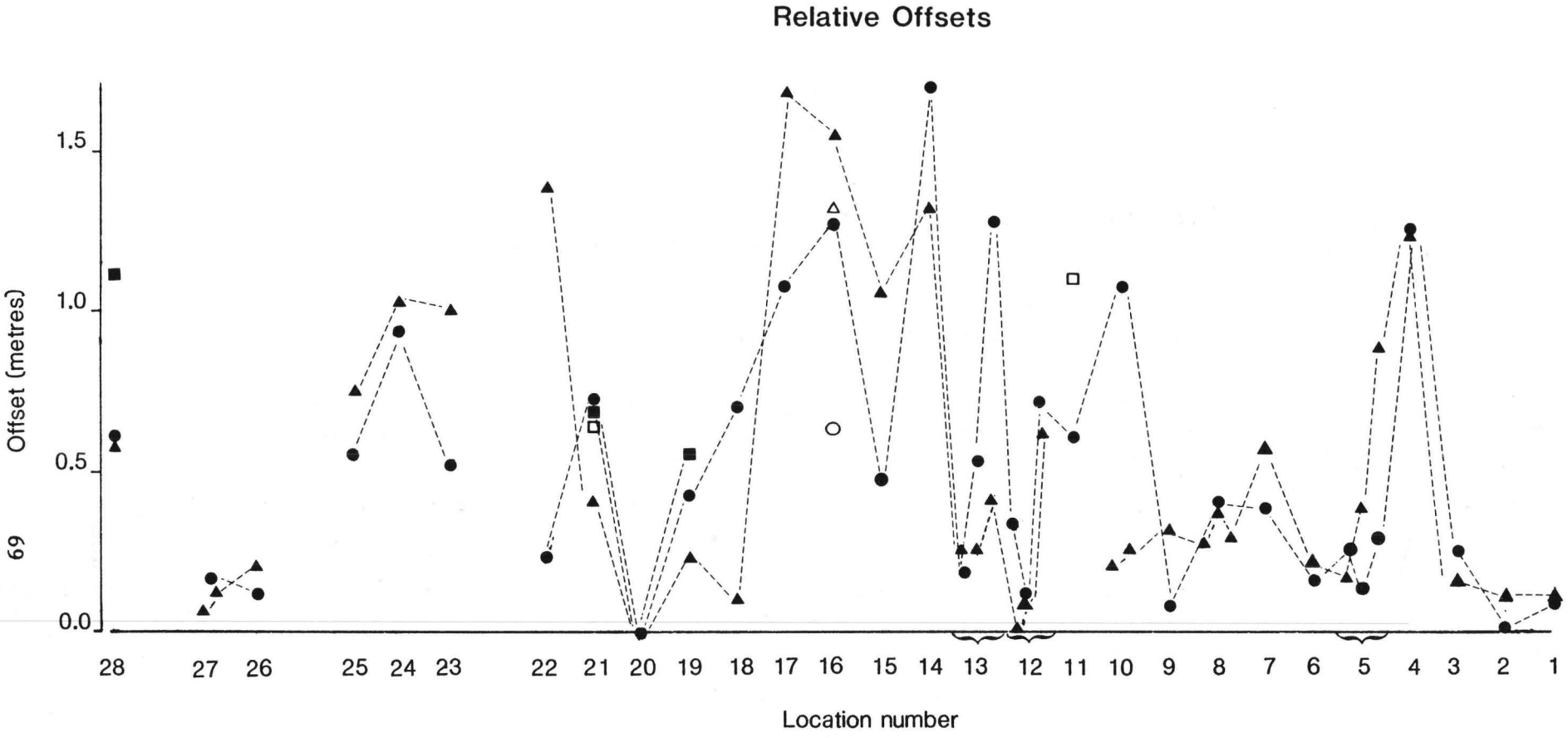

Figure 4

Plot showing the offsets calculated from individual bevels. Circles are the recent offset, triangles are the lowest bevel (or total scarp offset if only one bevel is present), squares are the second bevel upward, and open squares are the third bevel. Open circle and triangle for antithetic fault.

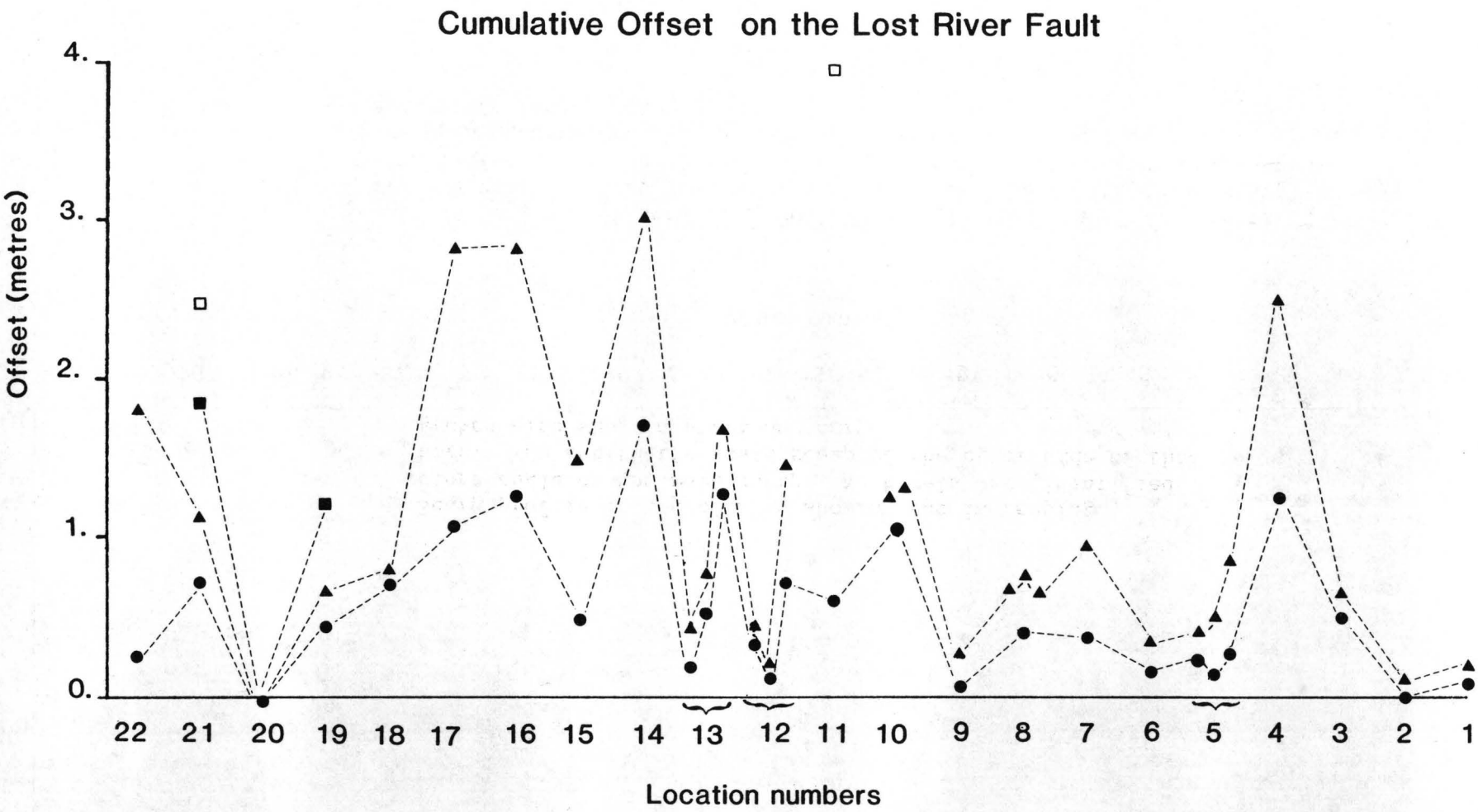

Figure 5

Height of bevels added to the recent offset for the Lost River fault. Circles are the recent offset, triangles are the first bevel, squares are the second bevel, and open squares are the third bevel.

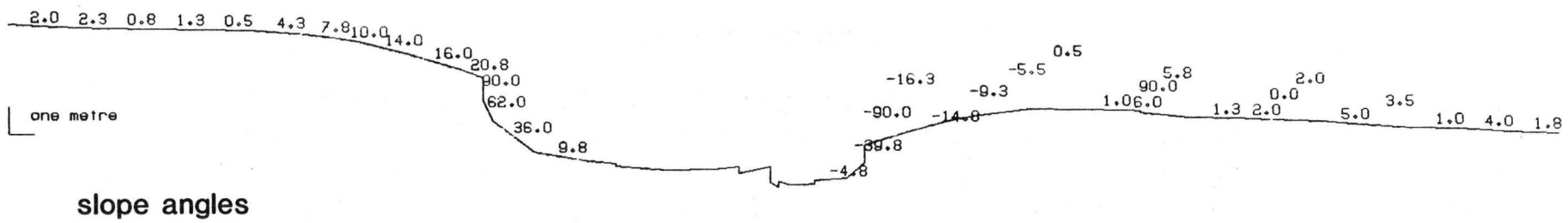

Figure 6

Scarp profile at location 16 showing the increasing slope angle of the main scarp. No bevels were identified here. The antithetic fault scarp on the other side of the graben also shows a previous scarp.

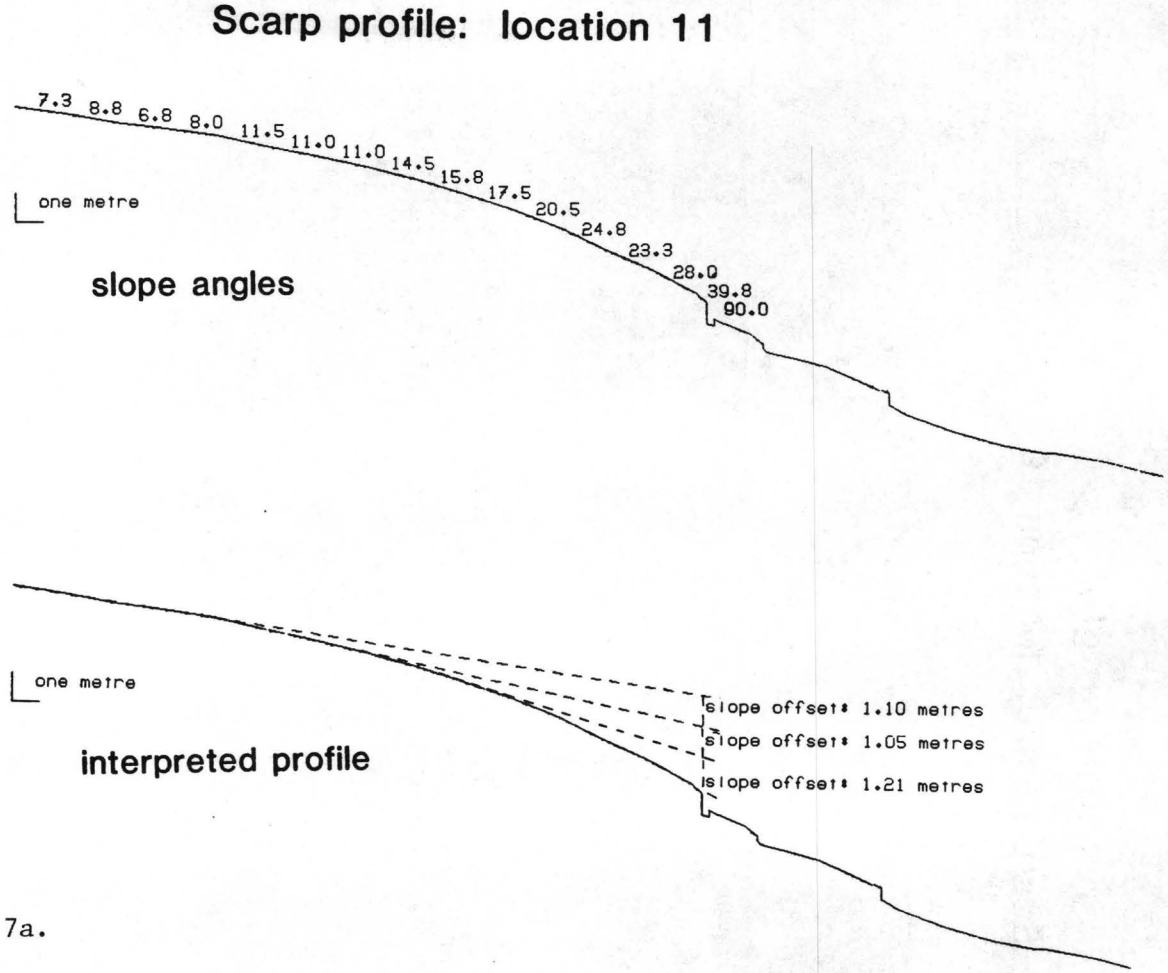

7a.

Figure 7

Scarp profile at location 11, and the interpretation of the three bevels. Figure 7b is a slope angle plot of the profile showing slope angles for consecutive segments of the profile above the free-face (segment 16). bevels are marked by braces.

Location 11

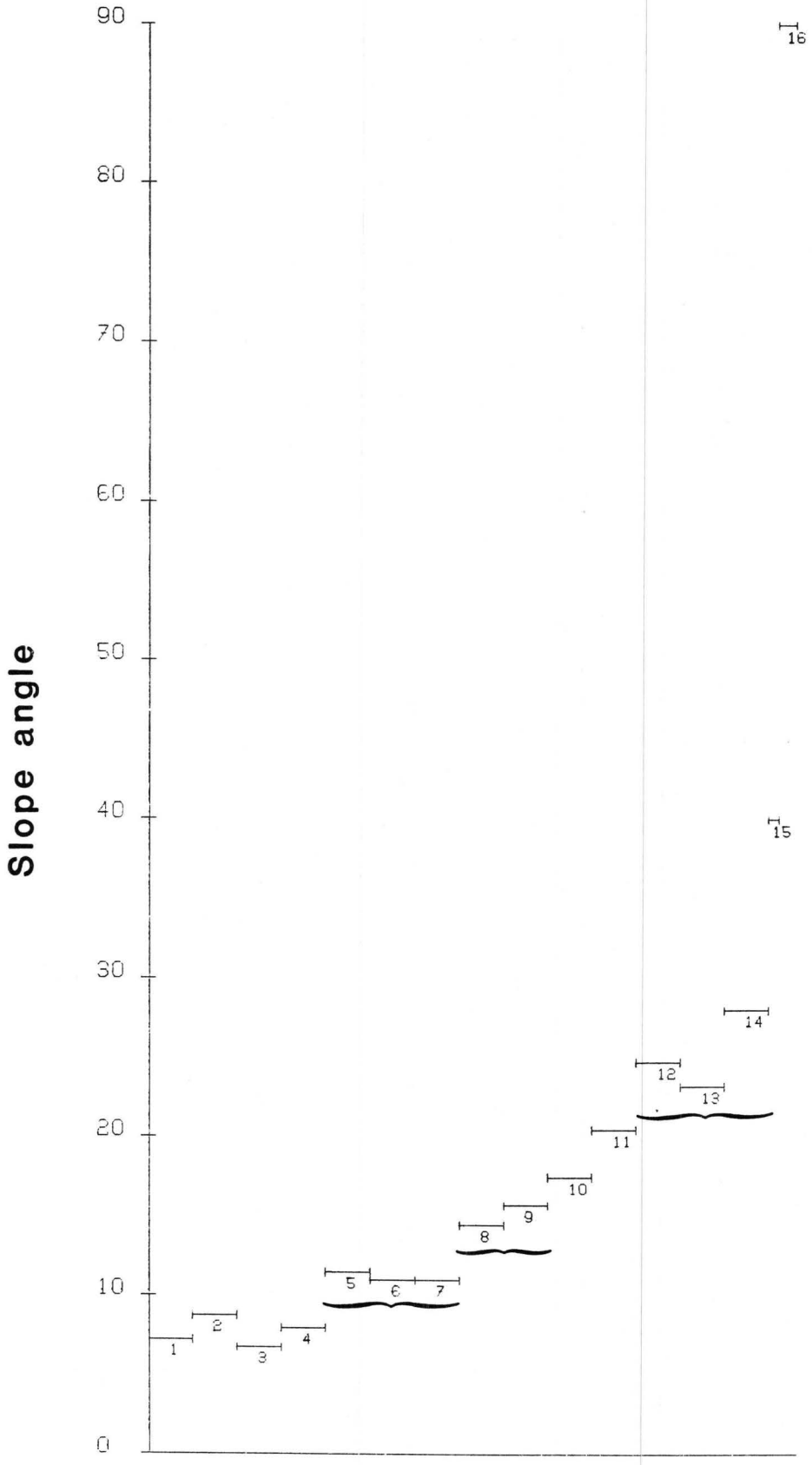

Figure 7b

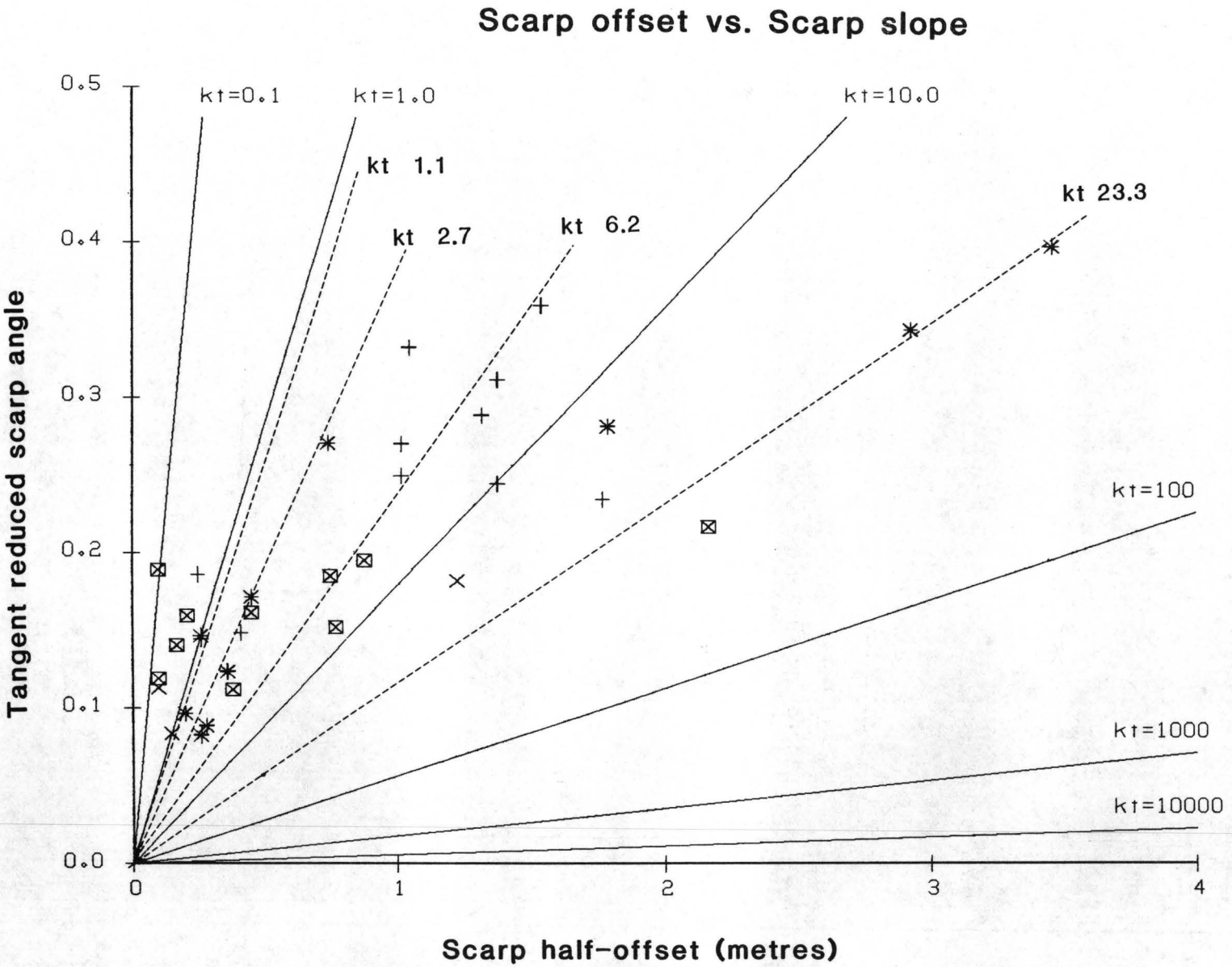

Figure 8

Plot of the scarp half-offset against the tangent of the "reduced maximum scarp angle". Crosses are low angle alluvial fans (slopes less than 15 degrees), X's are high angle alluvial fans (slopes about 20 degrees), squares are colluvial surfaces, and asterisks are moraine or other older surfaces cut by the scarps.

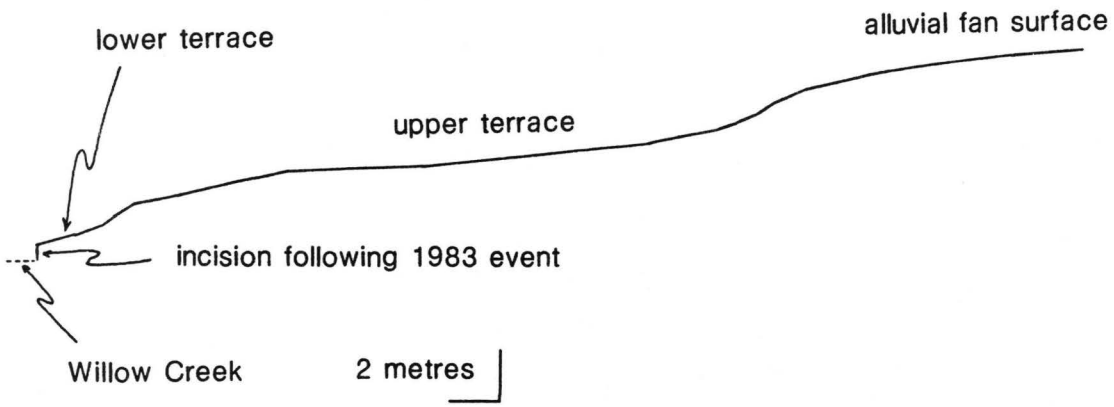

Figure 9

Profile across the stream-cut terraces at Willow creek.

MEASUREMENT OF VERTICAL TECTONIC OFFSET USING LONGITUDINAL PROFILES OF FAULTED GEOMORPHIC SURFACES NEAR BORAH PEAK, IDAHO: A PRELIMINARY REPORT

Kirk R. Vincent
U.S. Geological Survey and
Department of Geology and Geophysics
University of California, Room 301 ESB
Berkeley, California 94720

ABSTRACT

Along the segment of maximum vertical offset, ground surface rupture created during the Oct. 1983 Borah Peak earthquake (M_S = 7.3) truncated late Pleistocene alluvial fan remnants, Holocene fluvial terraces and stream floodplains roughly along contour. Longitudinal profiles were surveyed on these landforms using level, rod and chain. Survey traverses followed the path of flow responsible for the landform, a length of 600 to 900 m, and were centered on the faulted zone. Profile segments proved remarkably straight and well constrained on both sides of surface faulting, suggesting a straight pre-earthquake profile at the site of rupture. Both straight profile segments were projected into the faulted zone and the vertical profile-offset was taken as the best measure of near-field vertical tectonic slip. However, at each location the upthrown and downthrown profile segments were not parallel, but rather consistently less steep on the downthrown side. The downstream diminishing gradient is either relict of an original concave-up fluvial profile, or it is a record of some form of tectonic differential tilt of the hanging and footwall blocks. This limits the precision of the profile-offset technique to something less than ±.4 m vertical slip. Commonly on the alluvial and fluvial landforms a main scarp forms the edge of the upthrown block. Faulting and deformation extend 100 to 200 m onto the downthrown block, with the surface either sagged and faulted into a graben, or bulged up with minor thrusting toward the basin. Faulting was most intense within 30 to 50 m of the main scarp, and diminished basinward into a block of alluvium almost void of surface faulting. These blocks of alluvium (70 to 100 m wide) are tilted or sagged toward the main scarp, or tilted or bulged away from the main scarp. If measured from only within the obviously faulted zone, vertical slip could be over/or underestimated more than 1 m because of the presence of the subtly deformed blocks of alluvium. Offset stratigraphy in an excavation across the main scarp indicates older surfaces had been faulted once previously.

At profile locations the 1983 rupture is within (or at the edge of) the old fault zone with similar and additive deformation. During the Borah Peak earthquake the modern Willow Creek floodplain was vertically offset 2.4 m. The floodplain, and a late Holocene terrace, at Rock Creek were offset about 1.9 m. The latest Pleistocene alluvial fan remnants at Willow and Rock Creeks show cumulative profile-offsets of 4.3 and 4.4 m respectively. The early to middle Holocene terrace at Willow Creek also experienced more than 4 m of vertical slip. These data indicate that the

previous earthquake occurred during middle (to late?) Holocene. In addition, both events seem to have resulted in about the same near surface vertical tectonic slip in this area--slightly more than 2 m.

INTRODUCTION

The Oct. 28, 1983 Borah Peak Earthquake (M_s - 7.3) ruptured the ground surface along a 30 km segment of the Lost River Fault between Mackay and Challis, Idaho. The fault trace is located at the base of the steep mountain front on the west side of the Lost River Range. Near Borah Peak (Figure 1) the normal fault truncates alluvium at the mouths of both Willow Creek and Rock Creek valleys. The fault trace is roughly perpendicular to the flow directions of the two streams as well as adjacent Holocene fluvial terraces and late Pleistocene alluvial fan remnants. On these stream-related landforms, the 1983 fault trace is at a zone of surface rupture from previous Quaternary faulting. Holocene vertical offset of two meters had been measured in a trench excavation of the large incised alluvial fan near Willow Creek, by Hait and Scott (1978).

LANDFORMS WEST OF BORAH PEAK, IDAHO

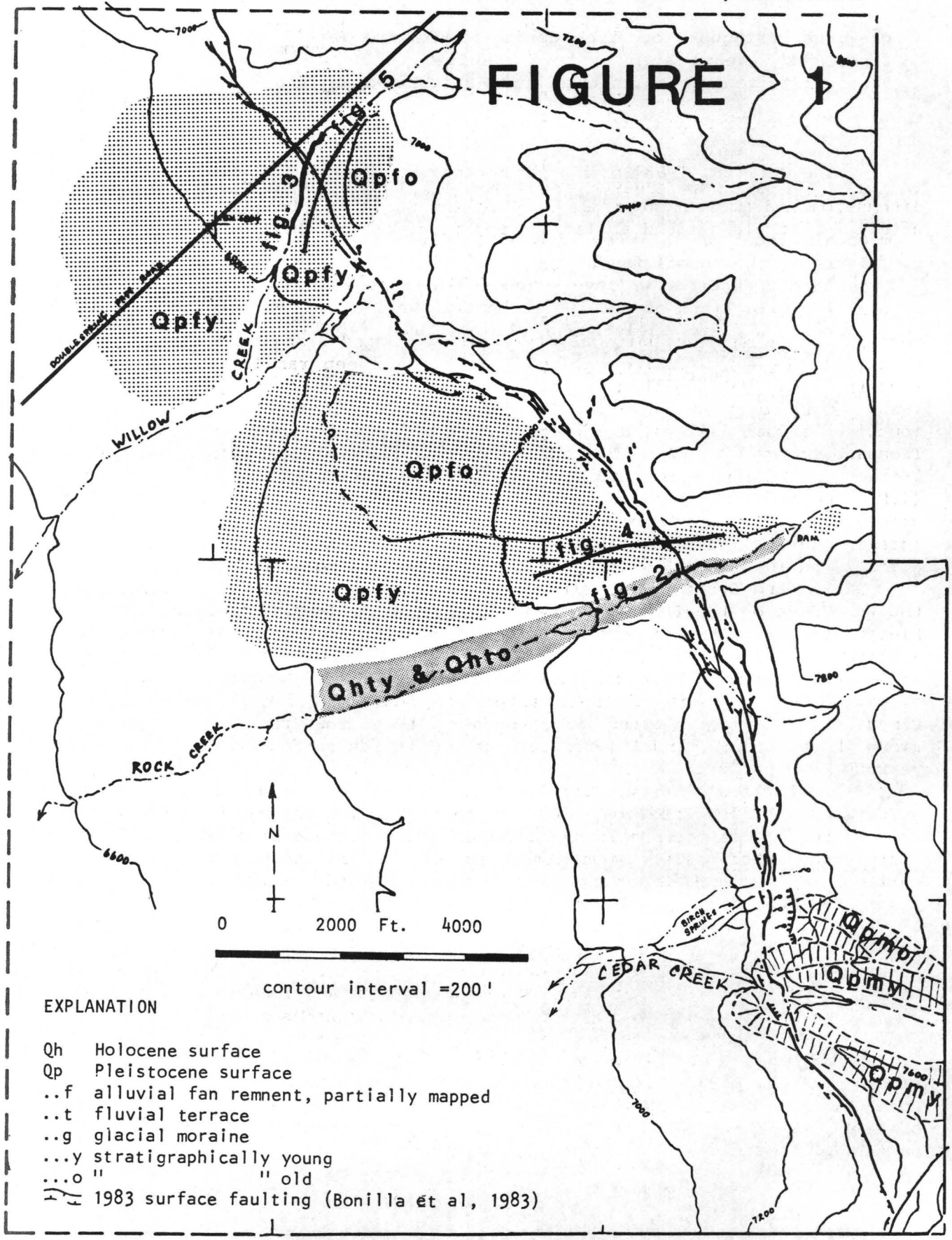

This occurrence presented the opportunity to survey longitudinal profiles of fluvial and alluvial surfaces cut by a normal fault. Modern floodplain profile-offsets might reflect 1983 coseismic vertical tectonic offset and terrace profile-offsets might provide magnitude as well as time constraints for previous faulting. Work by Swan, and others (1980) has demonstrated the utility of profiling alluvial fans and lacustrine terraces offset by Holocene normal faulting.

Spencer H. Wood suggested this project and donated enthusiastic discussion and manuscript review. Caroline Wurts and Bob VanKirk deserve credit for tireless field assistance and discovery of charcoal samples.

GEOMORPHIC SETTING

The Lost River Range in Idaho is similar to other Basin and Range terrain of the western United States. These rugged elongate mountains are flanked by alluvial filled valleys and have a steep range-front on their western side. The region near the center of the range, just west of Borah Peak, is illustrated on Figure 1. Emerging from the range-front, at the mouths of stream valleys, are large alluvial fans which coalesce toward the Thousand Springs Valley. The apex of these alluvial fans are now deeply incised by Willow Creek and Rock Creek, and have been mapped by Scott (1982) as originating from glacial outwash. Each fan seems to have one prominent surface (Qpfy) with a higher older fan surface (Qpfo) preserved locally (Figure 1). At the apex of the Cedar Creek alluvial fan a young glacial end moraine (Qpgy) cuts across an older end moraine (Qpgo).

Pierce and Scott (1982) studied alluvial fans and glacial moraines on the west side of the Lost River Range as part of a larger investigation of Pleistocene episodes of gravel deposition. The thickness of carbonate coatings on the bottoms of limestone clasts found within the soil was used as a dating tool. They conclude the gravel of the "youngest extensive alluvial fan" at each of their sites was deposited during the time of Pinedale glaciation or latest Pleistocene. The Willow Creek fan (Qpfy) was among those studied, and I infer the age of the fan surface is about 14,000 years B.P.

Fluvial terraces also exist within several meters above the modern streams. At Willow Creek only one low terrace (Qht) can be observed along the channel. This terrace is named Rabbit Brush Terrace because this plant (Chrysothannus naseosus) grows almost exclusively on the abandoned fluvial surface. Along Rock Creek two low terraces are widespread with several other small terraces only locally preserved at different levels. The older of the two pervasive terraces, labeled (Qhto), is complicated by localized inset and onset surfaces making it unrealistic to profile. The lowest terrace (Qhty) or Big Sage Terrace is clearly defined by: dense growth of Mountain Big Sagebrush (Artemisia tridentata) thin and locally nonexistent organic soil cover, and by bar and distributary channel surface topography. The Big Sage Terrace appears to be the predominantly erosional product of late Holocene braided streams with larger effective discharge than the modern Rock Creek. It has no counterpart at Willow Creek. The meandering Rock Creek is incised into this terrace about 1.2 m. The relative heights of these alluvial and fluvial surfaces above the stream's floodplain are summarized in Table 1.

TABLE 1

APPROXIMATE RELATIVE HEIGHT OF FLUVIAL AND ALLUVIAL SURFACES
ABOVE FLOODPLAIN
For two Drainages West of Borah Peak, Idaho - Meters

ROCK CREEK	u;d	WILLOW CREEK	u;d
Qpfo FAN SURFACE	Pe;18	Qpfo FAN SURFACE	8;np
minor surface			
Qpfy FAN SURFACE	10;12	Qpfy FAN SURFACE	3.7;2.1
minor surface			
LOW TERRACES			
minor surface	np?		
Qhto	1.8 to 2.7;2.7	RABBIT BRUSH TERRACE	2.7; 0 to 1.2
BIG SAGE TERRACE	1.2; 1.2		
FLOODPLAIN	0	FLOODPLAIN	0

u - upslope of fault
d - downslope of fault
np - not present, buried or eroded away
Pe - present but eroded

METHODS

PROFILING METHODS IN GENERAL

Six longitudinal profiles were surveyed, on floodplains or terraces adjacent to Rock Creek or Willow Creek, following the path of discharge responsible for the landform. The profiles ranged 900 to 600 m in length and were made using a quality self-leveling level, twenty-five foot expandable rod and a steel chain. At turning points, a stable rod-rest was located or constructed, and the position on the rod for all three hairs was read to .001 foot in an effort to minimize error. At ground surface points the rod was read to the nearest .1 foot. Turning point shots were typically less than 45 m long. Slope distance was reduced to horizontal where significant. Elevation closure was 6.8 cm/km for the 1150 m long Willow Creek Loop, and 9.6 cm/km for the 2210 m Rock Creek Loop. If closure errors were due only to a single turning point blunder it would probably be less than 10 cm. If the error accumulated gradually over less than one-fourth of the loop, along only the profile of a downfaulted surface for example, that segment's gradient would be distorted less than .0005.

During each survey traverse, elevations and tape distances were measured for points on the ground surface and positions of geomorphic features or surficial properties were noted. In particular the locations of scarps and cracks in the soil along with their magnitude and sense of motion was recorded. In addition the condition of the ground was observed and described if indicative of surficial degradation since the time the surface was formed and abandoned. The level and chain data was reduced and plotted with appropriate symbols on Figures 2, 3, 4, and 5. Data for uneroded surfaces were plotted as points. Straight lines were fit by eye

to these points. Clearly, alternative lines can be drawn, with slightly modified gradients, and still pass close to the data. The channel bed, and obviously eroded ground, are shown as lines sketched through survey values. Faults and significant ground cracks created during the 1983 earthquake are drawn on the profiles. All fault locations and motion arrows shown in the figures were documented. However, fault dips are speculative and probably exaggerated if other than vertical. Notice the elevation scale for all profiles is exaggerated 10 times the horizontal.

An additional caution should be mentioned concerning the projection of two surface profiles onto the same vertical "plain." As in Figures 3 and 5 each profile has a unique length scale due to the degree of flow path sinuosity, and is "unfolded" onto the figure page. Projecting two profiles (such as a floodplain and fan) together onto the same figure will result in distortion of both elevation and gradient. Two fan profiles can be reliably projected together if they diverge radially from a point about which contours are concentric. Fan profiles must be projected radially along contour.

ALLUVIAL FAN TRAVERSES

The profile traverses were chosen to follow the line of true or maximum gradient and are therefore curved on the map. Alluvial fan terrace profiles traversed straight down what appeared to be locally planar ground, and were arced in segments within subdued distributary flow paths. The fans are vegetated by sparse grass and sage brush (0.5 m high) that is both scattered and clumped on slightly elevated (20 cm) patches of patterned ground. A day of surveying progressed up to 900 m down the fan surface. The lay of the land was not obstructed from view during surveying. However terrace and distributary features are subtle and topographic map and air photos aid in the decisions of traverse location. Deviation of survey traverse from the flow path down an alluvial fan will result in an apparent concave upcurve of the profile (either abrupt or smooth) where the traverse cuts obliquely across contours.

WILLOW CREEK TRAVERSE

Floodplain profiles follow the meandering course of the stream approximating the hydraulic-grade line. Willow Creek is perennial--August 1984 it was flowing at 5 cfs. The channel is 1 m wide, 0.3 m deep, and contains pebbles and gravel less than 0.1 m in diameter. The Willow Creek floodplain is narrow (0.5 to 7 m), but is recognized by an obvious, and often flat, surface covered by a lawn of grass and clover. The clover is restricted to the flat floodplain down to the water's edge, while grass extends from the channel up to an abrupt line less than .5 m above bankfull stage. Stream erosion by Willow Creek since the earthquake has scoured a trench shaped gully upstream of the scarp. However the former flood plain is intact; and downstream of the main scarp the floodplain is covered only locally by a fresh veneer of pebbles and fine gravel. Wild rose and berry bushes grow scattered along the stream usually about 1 m in height, and not more than 2 m. Hence, the view is largely unobstructed.

The traverse on this surface consisted of straight segments, usually less than 70 m long, connected end to end. The tape traverse did not leave the floodplain and was always within 3 m of the channel. The rod was placed on the grassy floodplain within 1 m of the stream or at an obvious flat. The channel bed was also surveyed. Slope distance was obtained by

projecting from the tape to the rod, such that the projection was perpendicular to the traverse segment. Rod locations on the Rabbit Brush Terrace were also projected to the tape during the same survey. This traverse progressed 400 m per day.

A sketch map of the channel and traverse was made during surveying to clarify the notes and aid interpretation. If the sinuous path of bankfull or flood discharge is not followed carefully, a distortion of horizontal scale will result. For instance if a significant meander reach is "cut off" the profile will appear to have an abrupt downshift without a change in gradient.

The Rabbit Brush Terrace was surveyed with the Willow Creek floodplain. This partially eroded surface is found on both sides of the stream covered by sage brush and rabbit brush. Rabbit brush grows almost exclusively on this terrace. The surface is seen at a height above the floodplain of 0.2 to 2.5 m depending on distance from the fault. It is locally missing from one side of the stream or the other but usually is a 5 to 15 m wide terrace. Where the terrace has a large surface area it is flat and inclined in the direction of gross stream flow--down the fan. However, at most locations it is inclined toward the channel as well. The upper limit of the terrace is marked by a break-in-slope where it meets the steeper face eroded into the higher alluvial fan. The absence of rabbit brush is also an indicator of the upper terrace limit. Toward the stream the surface is eroded or truncated by lateral erosion of the incised pre-earthquake channel. During the survey the rod was placed at both the upper and lower breaks-in-slope. Longitudinal position was projected to floodplain traverse. Because of the lack of a continuous flat terrace surface, elevations were not projected to a traverse less sinuous than that of the floodplain.

ROCK CREEK TRAVERSE

Rock Creek is larger and in other ways significantly different from Willow Creek. Rock Creek is 2.5 to 4 m wide, .15 m deep and has a bed of cobbles up to 0.4 m in diameter. The channel is overgrown by cottonwood, aspen, and mountain mahogany downstream. This perennial has been seasonally diverted for irrigation on the distal end of the fan since the turn of the century. The diversion dam is located on the map 500 m upstream of the fault and has significantly altered the downstream dry season moisture regime. For example, during late July and August of 1984 the channel downstream of the dam was dry but at the dam it was flowing 25 cfs. Peak discharges annually pass over the dam and are probably little affected by diversion. The entire length of the traverse is below this dam.

The active channel of Rock Creek is incised into a low terrace and does not have a flat continuous floodplain. However other identifiable features of the modern channel bank can be recognized along the waterway. Two types of features were surveyed in the field--lowest moss or succulent plant growing on the bank, and small flat unvegetated bars of sand or pebbles. These features may not actually be at the elevation of the conceptual floodplain but they should be parallel to it. Presumably discharges dominating construction and maintenance of the channel would scour away vegetation growing too low on the bank, as well as transport and deposit sand and pebbles into bars. These horizons were observed right to the fault on the upstream side. The pre-earthquake channel bed on the upstream side was also well preserved despite post-earthquake incision of a

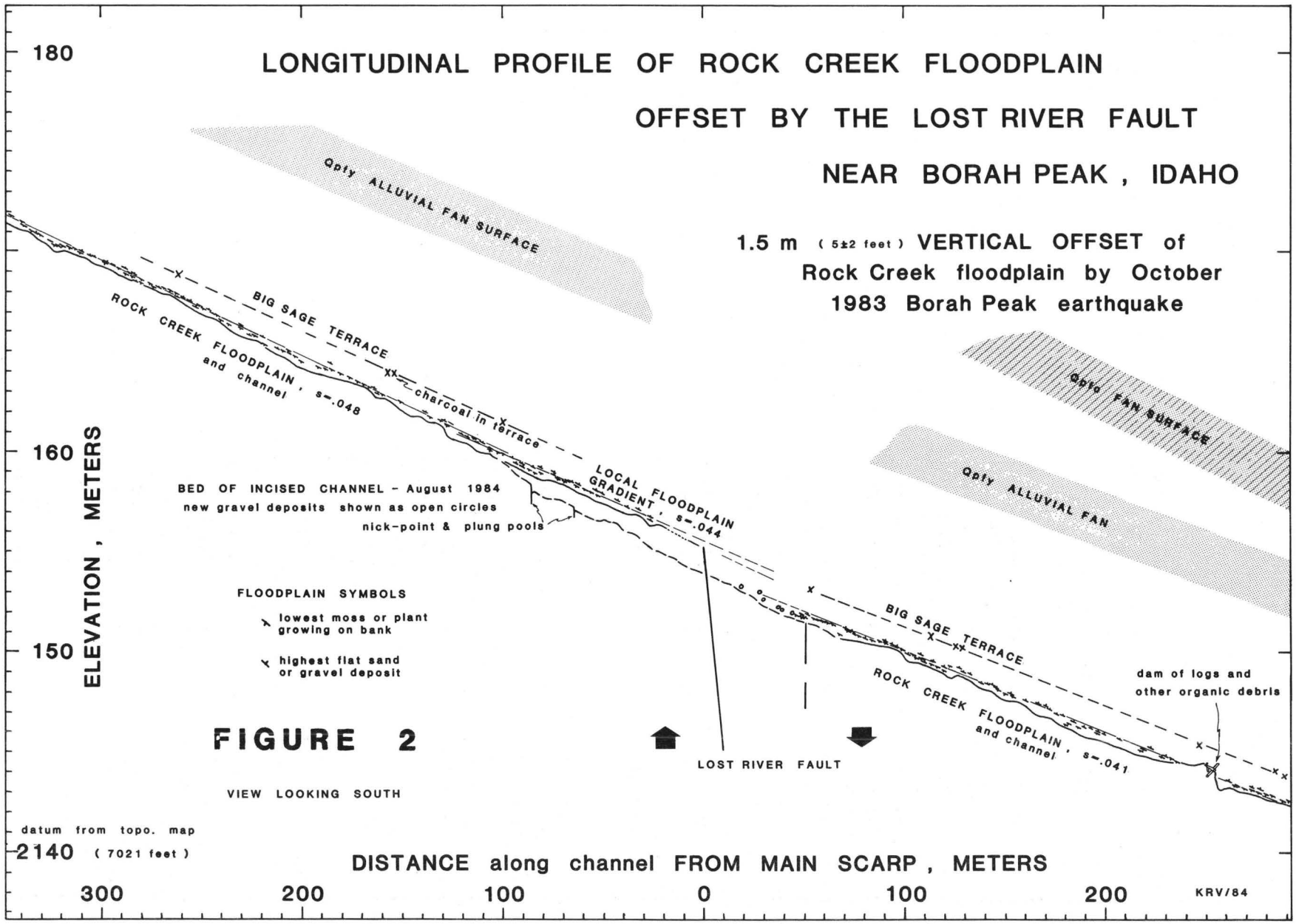
LONGITUDINAL PROFILE OF ROCK CREEK FLOODPLAIN
OFFSET BY THE LOST RIVER FAULT
NEAR BORAH PEAK , IDAHO
1.5 m (5±2 feet) VERTICAL OFFSET of Rock Creek floodplain by October 1983 Borah Peak earthquake
Qpty ALLUVIAL FAN SURFACE
BIG SAGE TERRACE
charcoal in terrace
ROCK CREEK FLOODPLAIN , s=.048
and channel
LOCAL FLOODPLAIN GRADIENT , s=.044
BED OF INCISED CHANNEL - August 1984
new gravel deposits shown as open circles
nick-point & plung pools
Qpfo FAN SURFACE
Qpty ALLUVIAL FAN
FLOODPLAIN SYMBOLS
lowest moss or plant growing on bank
highest flat sand or gravel deposit
BIG SAGE TERRACE
ROCK CREEK FLOODPLAIN , s=.041
and channel
dam of logs and other organic debris
LOST RIVER FAULT
FIGURE 2
VIEW LOOKING SOUTH
ELEVATION , METERS
180
160
150
datum from topo. map
2140 (7021 feet)
DISTANCE along channel FROM MAIN SCARP , METERS
300
200
100
0
100
200
KRV/84

trench 1 to 2 m wide. On the downstream side these horizons were found, seemingly unaltered by faulting or by runoff during the previous season, starting a distance of less than 50 m from the main scarp.

The traverse along Rock Creek was always within the channel and turned with the major meanders every 10 to 25 m. In addition to the two horizons and channel or trench bed mentioned above, other features were surveyed as well. Along the stream bank, the rod was placed on flat bars covered by leaf-litter and supporting shrubs more than a meter in height. Shots were also made to the beds of relatively young distributary or braided channels which probably flood only during extreme runoff events. The profile of each of these features is continuous and basically parallel to other horizons, but so limited in number of data points that it is not presented in this report. Also surveyed where practical, was the surface of the Big Sage Terrace situated more than a meter above bankfull stage. Fortunately the channel was dry from irrigation diversion during surveying, but the rough bed of large rocks and overhanging limbs made for fatiguing work. This traverse progressed a long the channel 230 m per day. Individual profiles were made across the fault on other surfaces near Rock Creek but are not illustrated here: the Big Sage Terrace, and an irrigation ditch constructed circa. 1910 but long since abandoned.

RESULTS

ROCK CREEK

Figure 2 shows the surveyed longitudinal profile of the modern Rock Creek floodplain. More precisely, two features of the bank found along the

TABLE 2
VERTICAL OFFSET OF FLUVIAL AND ALLUVIAL SURFACES BY THE LOST RIVER FAULT NEAR BORAH PEAK, IDAHO

ROCK CREEK			WILLOW CREEK
	Cumulative Offset	Number of Events	Cumulative Offset	
Qpfo SURFACE. . . . . ?	2+?	10 to 14.6m*. . .	Qpfo SURFACE
Qpfy SURFACE. . . . . 4.4m ± .5m	2	4.3m ± .3.	Qpfy SURFACE
Qhto . . . . . 2?	2	4.6m ± .6m	RABBIT BRUSH TERRACE
BIG SAGE TERRACE. . . 2.1m	1		
FLOODPLAIN . . . . . 1.5m ± .6m	1	2.4m ± .3.	FLOODPLAIN
DITCH (ca. 1910) . . 1.8m	1		

*If buried on down-thrown side rather than eroded away.

channel length were surveyed. Elevation of the lowest moss or other plant growing on the bank is plotted as a short line with tick mark down. The highest occurrence on the bank of small fresh sand or fine gravel bars is plotted as line with tick up. Typically the moss-plant horizon plots .17 m below the flat sand bars. Straight profile segments were drawn by eye through the combined set of values. Over a distance of 650 meters no measurement deviates more than 0.3 m from a profile segment, and most are within 0.15 m of the line. This suggests that such horizons reliably depict a stream profile of uniform gradient.

Two profile segments were drawn above the fault. One line was drawn for all data from 0 to 400 m and has a gradient of .048. A second line was drawn to represent the local floodplain gradient just up from the fault. This profile segment spans 110 m and 6 major bends in the channel with gradient of .044. No faults or cracks were observed in soil adjacent to this reach. A segment with gradient of .041 was drawn through data in the downstream reach. Projection and comparison of both the local floodplain segment on the upside and the profile for the downside, to the center of the 1983 fault zone yields a profile-offset of 1.5 ± 0.6 m (5 ± 2 ft). projection to the main scarp itself would produce a slightly larger profile-offset of 1.7 m. Use of the segment spanning all data upslope of the fault yields a profile-offset of 1 to 1.2 m.

Also shown on Figure 2 are a number of elevation values taken for the Big Sage Terrace where visible from the channel. This terrace seems consistently 1 to 1.3 m above the floodplain on both sides of the fault. A separate survey traversed on the low terrace surface. The profile from that survey is not reproduced in this report but shows a vertical offset of 2.1 m. The surface of the Big Sage Terrace has probably been faulted only during the 1983 earthquake.

WILLOW CREEK

Figure 3 shows the Willow Creek floodplain in three basic segments, over the meandering 700 m profile. Elevation values for the grassy, often flat, floodplain do not deviate anywhere more than 0.2 m from the sketched segments. The 300 meter upstream segment has a gradient of .035. The 350 m downstream segment slopes .034. Projection of these two lines yields 2.4 m (8 ± 1 ft) of vertical offset of the Willow Creek floodplain. Within the 100-m-wide zone of faulted and cracked soil the floodplain profile is inclined more steeply at .045. The undulatory pre-earthquake channel thalweg is .1 to .45 m below the floodplain. By late May 1984, the original channel bed had been incised to a knickpoint 43 m upstream from the main scarp. The incision created by snowmelt runoff was not obviously changed by summer storm runoff or baseflow. This newly incised trench shaped channel had up to 1 m high vertical banks and was the width of the original channel about 1 m. A comparatively small volume of gravel from the entrenchment is deposited immediately downstream of the fault. Most of the fresh deposits cease 20 m below the main scarp. However, minor deposits are located 120 m down from the scarp on a dirt road where it crosses Willow Creek. At this location a portion of the water in Willow Creek floods down the road and over the floodplain even at baseflow. The runoff flows back into the channel 70 m downstream. Insignificant deposition and erosion has occurred along this diversion created during the 1983 earthquake. Elsewhere the floodplain has not been buried and appears to be undisturbed other than by surface faulting.

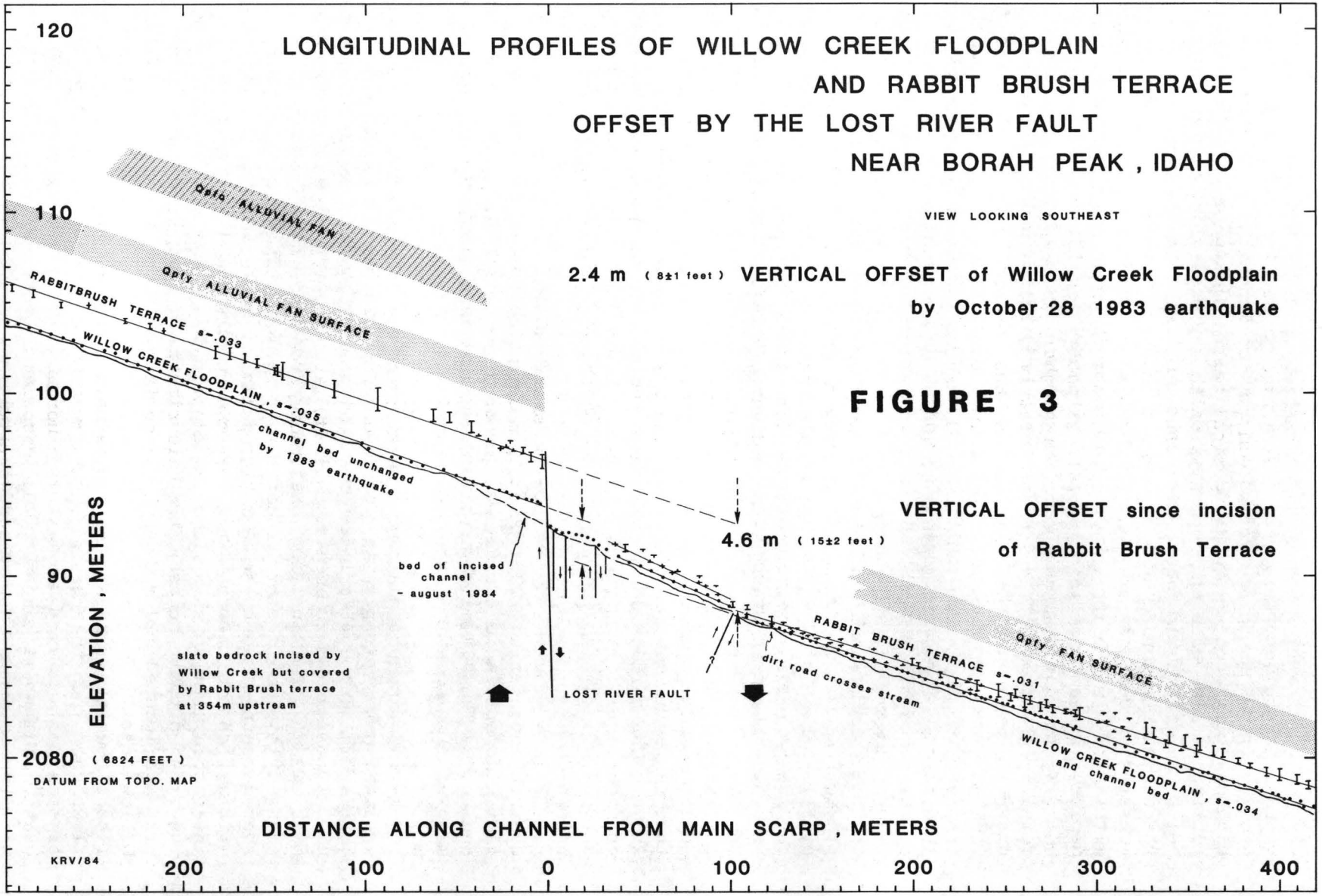
LONGITUDINAL PROFILES OF WILLOW CREEK FLOODPLAIN
AND RABBIT BRUSH TERRACE
OFFSET BY THE LOST RIVER FAULT
NEAR BORAH PEAK , IDAHO
VIEW LOOKING SOUTHEAST
2.4 m (8±1 feet) VERTICAL OFFSET of Willow Creek Floodplain
by October 28 1983 earthquake
FIGURE 3
VERTICAL OFFSET since incision
of Rabbit Brush Terrace
4.6 m (15±2 feet)
Qpfq ALLUVIAL FAN
Qpfy ALLUVIAL FAN SURFACE
RABBITBRUSH TERRACE s=.033
WILLOW CREEK FLOODPLAIN , s=.035
channel bed unchanged
by 1983 earthquake
bed of incised
channel
- august 1984
slate bedrock incised by
Willow Creek but covered
by Rabbit Brush terrace
at 354m upstream
LOST RIVER FAULT
RABBIT BRUSH TERRACE s=.031
dirt road crosses stream
Qpfy FAN SURFACE
WILLOW CREEK FLOODPLAIN , s=.034
and channel bed
ELEVATION , METERS
120
110
100
90
2080 (6824 FEET)
DATUM FROM TOPO. MAP
DISTANCE ALONG CHANNEL FROM MAIN SCARP , METERS
200
100
0
100
200
300
400
KRV/84

A profile of the Rabbit Brush Terrace along Willow Creek is also shown on Figure 3. The upper break-in-slope, and the lowest uneroded point on the terrace, are connected as vertical bars. The terrace is situated 2 to 2.5 m above the floodplain upslope of the fault. The sketched line has a gradient of .033. Downslope from the fault zone the terrace diverges from the floodplain. Near the western limit of 1983 surface breakage the terrace is hardly more than .3 m above the floodplain. Downstream of surface faulting it is at least 1 m above the floodplain, and the line sketched on the figure slopes .031. Although the illustrated lines through the terrace data can be drawn with slightly different slopes, the Rabbit Brush Terrace profile-segments are clearly offset on the order of 4.6 m (15 ± 2 ft). This low terrace surface was faulted in 1983, and probably previous to 1983 as well. Within the zone of cracked soil the terrace is about .5 m above the floodplain and inclined (possibly by surface deformation) to a slope of .047.

ALLUVIAL FANS

Figure 4 diagrams a surveyed longitudinal profile of the Rock Creek "Pinedale-Age" alluvial fan. Surveyed ground elevations are shown as points defining a slightly undulating surface with wavelengths of approximately 120 m. The straight line drawn through the 400 m reach of data above the fault zone has a gradient of .054. A line (.047) was placed over values starting at 230 m downslope from the main scarp, to 450 m down from the scarp. Projection of these two profile segments over the fault zone yields a vertical profile-offset of 4.4 m (14.5 ± 1.5 ft). No elevation value deviates more than .35 m from these straight line segments. Within the zone of obvious surface faults and soil cracks the alluvial gravel is downfaulted into a graben. A similar graben, although erosion modified, existed here before the earthquake and was presumably formed during Holocene faulting. On the west side of the fault zone the fan profile is straight and cut by few small cracks showing down to the east offset of less than 6 cm. The 110 m long straight segment meets the next segment down slope with a change in gradient of .037 - .047 = -.01. This change in gradient may represent cumulative back tilting or sagging of a block of alluvium into the fault graben.

Figure 5 depicts most of the along-gradient profile on the prominent alluvial fan Qpfy at Willow Creek. The "Pinedale Age" terrace has a gradient of .041 for the upfaulted segment, and .037 for the segment starting at 110 m down from the main scarp. These two segments show a vertical offset of 4.3 m (14 ± 1 ft) at the fault zone. The data, and straight line fit, are similar to those from the same surface at Rock Creek with two exceptions.

At a distance of 290 m downslope from the scarp the traverse entered the head of a subdued distributary channel on the alluvial fan. In this case the profile segment projects .35 m above, but roughly parallel to the distributary, which suggests the distributary is slightly incised but has a gradient similar to the upslope fan surface.

On Figure 5 the majority of surface offset occurred along two normal faults in the alluvium. West of the main scarp many open cracks separating elongate blocks of alluvium .3 to 1 m wide were observed. With one exception the cracks were vertical; with normal offset .01 to 0.1 m, open .03 to 0.3 m, and 0.3 to 2 m deep. The scarp faces appeared fresh 10 months after the earthquake. On Figure 5 the apparent width is 72 m for this zone of

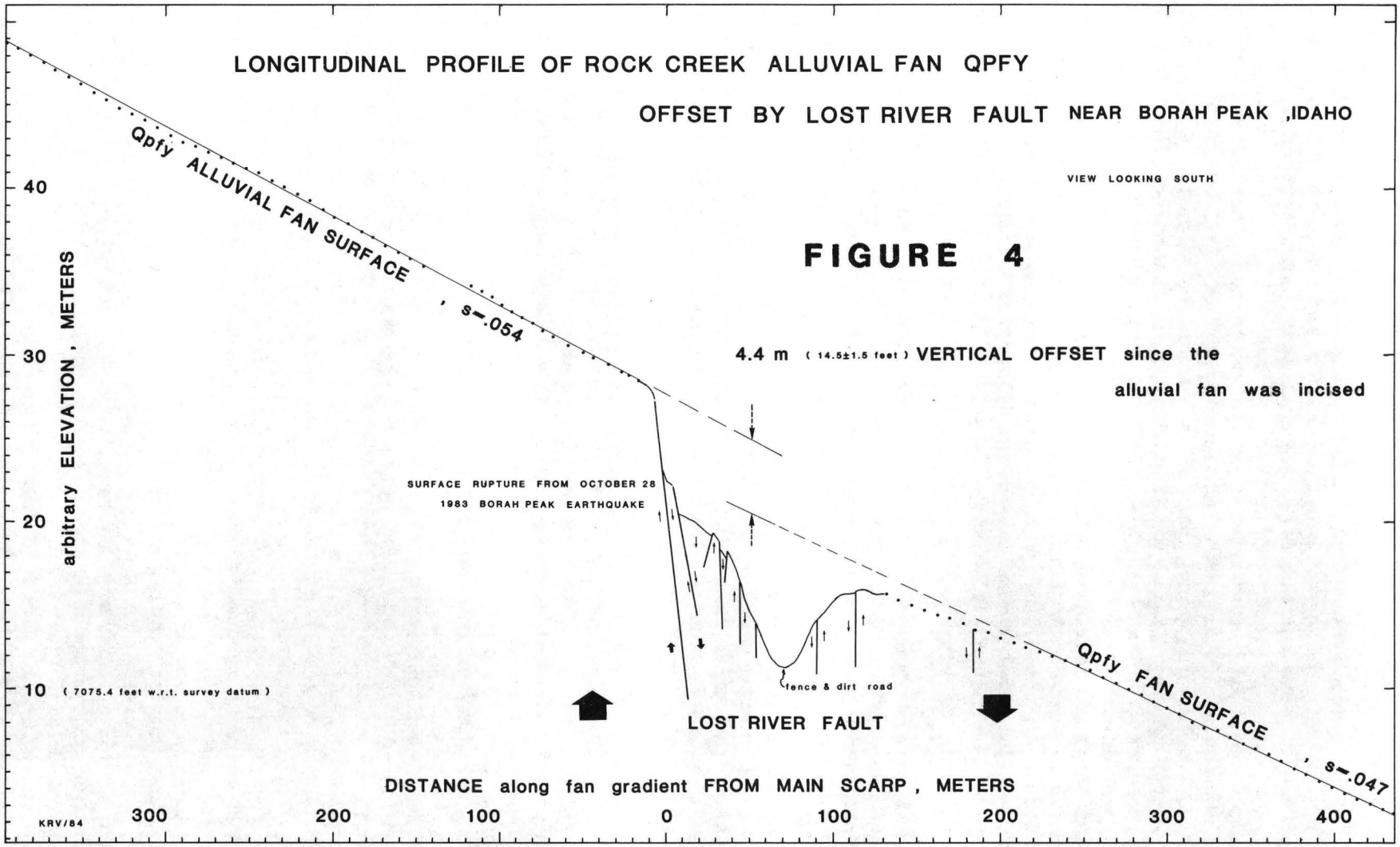
LONGITUDINAL PROFILE OF ROCK CREEK ALLUVIAL FAN QPFY
OFFSET BY LOST RIVER FAULT NEAR BORAH PEAK ,IDAHO
VIEW LOOKING SOUTH
FIGURE 4
Qpfy ALLUVIAL FAN SURFACE , s=.054
4.4 m (14.5±1.5 feet) VERTICAL OFFSET since the alluvial fan was incised
SURFACE RUPTURE FROM OCTOBER 28 1983 BORAH PEAK EARTHQUAKE
fence & dirt road
Qpfy FAN SURFACE , s=.047
LOST RIVER FAULT
arbitrary ELEVATION , METERS
40
30
20
10
(7075.4 feet w.r.t. survey datum)
DISTANCE along fan gradient FROM MAIN SCARP , METERS
300
200
100
0
100
200
300
400
KRV/84

surface faulting, but true width was 54 m. This discrepancy is due to oblique intersection of the traverse with the fault trend. One fault did not have a normal sense of motion. The feature was observed as a tiny scarp 3 to 9 centimeters high. It was followed on the ground a distance of 145 m parallel to the rupture zone. The scarp was traced to within several meters of the Willow Creek channel and is shown on Figure 3. Nowhere along its length was there an open crack. At one location a 13 cm stone was seen tilted, out of its socket in the soil, over this small scarp. From a single location the scarp was seen to go downhill in both directions acute to contours and appears to have high angle thrust displacement. On both Figures 3 and 5 the thrust angle may be exaggerated but the sense of motion can be observed in the field.

West of the main scarp (Figure 5) alluvium was faulted into two main blocks, and has a dome shaped surface. In the center a block 25 m wide was downdropped. To the west a block of alluvium 18 m wide was apparently thrust up at least 0.2 m relative to its surroundings. West of the cracked zone the fan surface is inclined steeply over a distance of 50 m. This style of surface rupture is in contrast to the style illustrated on Figure 4 where the faulted segment of the Rock Creek fan profile shows downfaulting from both sides toward a graben axis. On this profile the surface experienced the major normal faulting, but on a lesser scale the surface within the fault zone bulged upward and was overthrust slightly to the west. The bulge shape of the surface may not be entirely due to the Oct. 28, 1983 event. It may have been previously bulged during a Holocene event.

Figure 5 also shows the surveyed profile of the Qpfo fan terrace. This profile is intended to show the relative elevation of the two alluvial fan terraces at the upthrown edge of the fault. The two profiles were projected together and errors may have resulted due to differing conical surfaces of the different-aged fans. Extension of the line placed on the uneroded Qpfo surface is 14.6 m above the downthrown "Pinedale Age" Qpfy terrace. The high terrace traverse crossed a knob which was possibly only slightly eroded. The knob shown on Figure 5 was separated from the planar surface by a clearly eroded slope and shallow swale. The projected height of this knob is 10 m above the Qpfy surface at the east edge of the fault. No remnant of the Qpfo terrace is obvious on the downthrown side of the fault near Willow Creek.

DISCUSSION

INTERPRETATION OF FAULTED GEOMORPHIC SURFACES

Landforms constructed and maintained by streamflow are unique, compared to all other subaerial geomorphic surfaces, because they inherently tend to possess a predictable profile shape, if looked at in the appropriate vertical "plane". Where not deformed by surface faulting, the profiles presented in this paper are in fact nearly straight over distances of several hundred meters. Consequently fluvial longitudinal profiles have great potential for providing the essential, but otherwise rare, knowledge of the ground-surface shape previous to deformation by normal faulting. Scientists studying Cenozoic normal-faulting should look for the opportunity to use the techniques outlined in this paper, and give consideration to the following: Surfaces of the same age must be identified on both sides of the fault. Examining physiographic relationships and ground

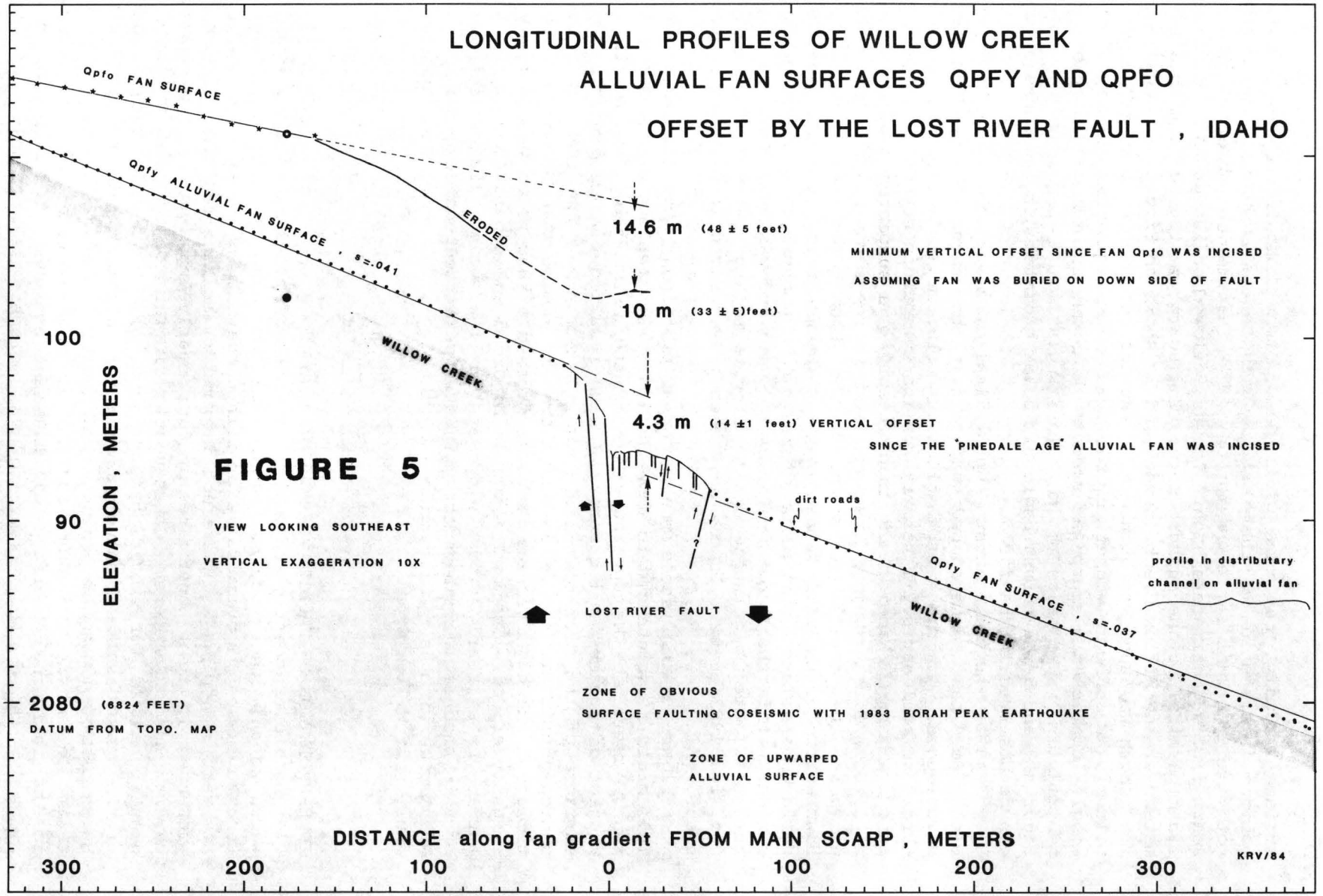

FIGURE 5

VIEW LOOKING SOUTHEAST

VERTICAL EXAGGERATION 10X

90

surface texture both in the field and on areal photographs is the first step, but this should be followed by the study of soil properties on both sides of the fault. The use of soil-development properties, such as carbonate coatings (Pierce and Scott 1982), also allows relative or even absolute dating. Errors made during surveying, as discussed above, can be minimized. In addition, if the profile of a fluvial or an alluvial surface was not straight or smoothly curved before faulting (over a distance of hundreds of meters), post-faulting measurement of profile-offset will be in error. This is not a significant problem however, on the profiles illustrated here.

An active floodplain profile-offset provides a measure of local vertical movement at the fault during a historical event, but faulted floodplains are rare. A terrace profile-offset serves as an indication of local cumulative vertical movement, since the time the terrace surface was abandoned by processes responsible for its form (in other words, the time since the active geomorphic surface was incised to become a terrace). An offset terrace is recognized, in the field at a suspected Quaternary scarp, by a significant abrupt decrease in the height-of-terrace above floodplain (or above a younger terrace) while walking from the upthrown side to the downthrown side of the faulted zone. The age of any surface is useful as the boundary between two time periods. The physical situation provides knowledge of presence or absence of strain accumulation or faulting during the two time periods.

A terrace preserved only on the upthrown side of a fault is of limited use. A straight line can be projected down the gradient of such an ancient alluvial fan, or fluvial terrace, to the fault zone. This assumes the form of the old feature before it was eroded or faulted away. At the upthrown edge of the fault a height above a younger horizon can be measured. If it is assumed the older surface is buried under the younger horizon on the downthrown side, this height represents a minimum vertical offset within a specific time bracket: the time bracket between incision of the old surface and incision of the young horizon. If the old-surface's profile is projected across the fault zone to above the downthrown block, a different meaning is ascribed to the relative height of such a projection above a younger surface. The height of an old upthrown surface above a young downthrown surface is the minimum local vertical offset during the time span--from the present time to the time of incision of the old surface. However, if the old surface is not buried in the basin, this exercise is of no value and is probably misleading.

1983 VERTICAL OFFSET

The pre-earthquake Rock Creek floodplain (Figure 2) was vertically offset 1.5 (± .6) m during the October 28, 1983 Borah Peak earthquake. This excludes the profile segment within the zone of surface rupture. This measure is thought to represent the relative offset of alluvium resting on bedrock and not deformed as part of the fault zone. Although not published, profiles were surveyed of the lowest terrace along Rock Creek and an old abandoned ditch built on the terrace. The Big Sage terrace shows an offset of 2.1 (± .6) m with no indication of previous faulting. The ditch (ca. 1910) showed a bed-offset of 1.8 (± ?) m. The plus-minus values presented here are the author's subjective statement of confidence for each survey (Table 2). A reasonable estimate of 1983 vertical offset in the Rock Creek area might be 1.9 m.

The Willow Creek floodplain was vertically offset 2.4 (± .3) m during the 1983 earthquake. This value is larger than any estimate for the Rock Creek area 2.6 km to the south. Surface rupture diminishes further south and is not mapped just beyond Elkhorn Creek (Bonilla et al., 1984). From the most southerly surface fractures, Rock Creek is 77% of the total distance to Willow Creek. Perhaps only coincidentally, Rock Creek seems to have experienced 79% of the total vertical offset at Willow Creek.

Crone and Machette (1984) estimate slip along the length of surface rupture by careful reconstruction of scarps and faulted cultural artifacts. They document about 2.2 and 2.7 m vertical slip at Rock Creek which are larger than the value of 1.9 m derived from profile-offsets. The faulted zone at Rock Creek (Figure 4) is deformed into a graben, and the presence of a large (100 m wide) block of alluvium tilted without much surface rupture might lead to an overestimate of slip using scarp reconstruction. At Willow Creek they measured 1.6 m of slip which is smaller than the profile-offset of 2.4 m. The faulted zone at Willow Creek (Figure 3) contains a block or wedge of alluvium tilted and thrust up toward the basin. This deformation devoid of significant surface faulting, might lead to underestimation of vertical slip using scarp reconstruction. D. Schwartz (personal communication, 1984) documented two stratigraphic offset events in a trench excavated across the main scarp and intensely faulted zone. The trench was also located on the Willow Creek alluvial fan, and the stratigraphic offsets of 1.5 and 3.5 are both smaller than comparable profile-offset values determined in this study. Apparently tectonic dislocation at the surface is taken up over a relatively wide zone (100 to 200 m) by mechanisms other than shear of gravel alluvium with normal sense of motion. The significance of these rotated blocks of alluvium was not obvious to me in the field without the aid of long surveyed profiles reported in this study.

COMPARISON TO GEODETIC RELEVELING

A line of benchmarks established in 1933 and in 1948 was releveled following the earthquake by the National Geodetic Survey. Figure 6 is a preliminary profile of relative elevation change furnished by R. Stein (Written communication, 1984). The profile follows the Doublespring Pass Road ("May-Patterson Road") along Willow Creek near the area of floodplain and terrace profiles (Figures 3 and 5). The pattern of change in benchmark elevation values, is thought to represent the vertical surface expression of the release of elastically strained bedrock beneath the alluvium during faulting. The benchmark closest to the fault is about 0.55 km down the alluvial fan from the fault rupture. The Willow Creek floodplain profile spans 700 m across the fault and could provide an additional datum from which the very-near-field deformation can be interpreted to augment the picture derived from benchmark releveling. Data in the present study indicate 2.4 ± 0.3 m offset of the modern pre-earthquake floodplain during the 1983 earthquake. This "length" of vertical slip is "hung" from the lip of the upthrown block on Figure 6. If assumptions are valid, an additional (2.4 m - 1.6 m) 0.8 ± .3 m of coseismic slip could be added to Figure 8 in order to reconcile the floodplain profiling with geodetic data. This suggests that near-field coseismic vertical slip and tilting into the fault may be even greater than shown on the releveling profile. Figure 6 depicts coseismic land-surface tilt of (.036 m over 1.2 km) about 30 micro-radians, or essentially 30 mm/km, on the upthrown block more than one-half kilometer

from the fault. The downthrown block appears tilted (.16 m over .92 km) about 174 micro-radians more than one-half kilometer from the fault. The upthrown side experienced only 17% as much tilt as experienced by the downthrown block. Considering now the offset floodplain datum, coseismic tilt on the hanging wall block next to the fault might be on the order of .8 m (or at the least .5 m) over a distance of .55 km. This is tilt of 1450 micro-radians (or at least 900 micro-radians). Broad coseismic tilt of 100 to 500 micro-radians, over a distance of 6 to 12 km, is common in the hanging wall block of other normal-faults in the Basin and Range province (Wood, 1984). The apparent tilt calculated above using longitudinal profiles is substantially larger than near-field coseismic tilt measured previously by geodetic leveling. Another question regarding tilt is evaluated below using measured change in gradient of geomorphic surfaces over the Lost River Fault.

On each of the five surveyed profiles in this report, the downthrown

FIGURE 6

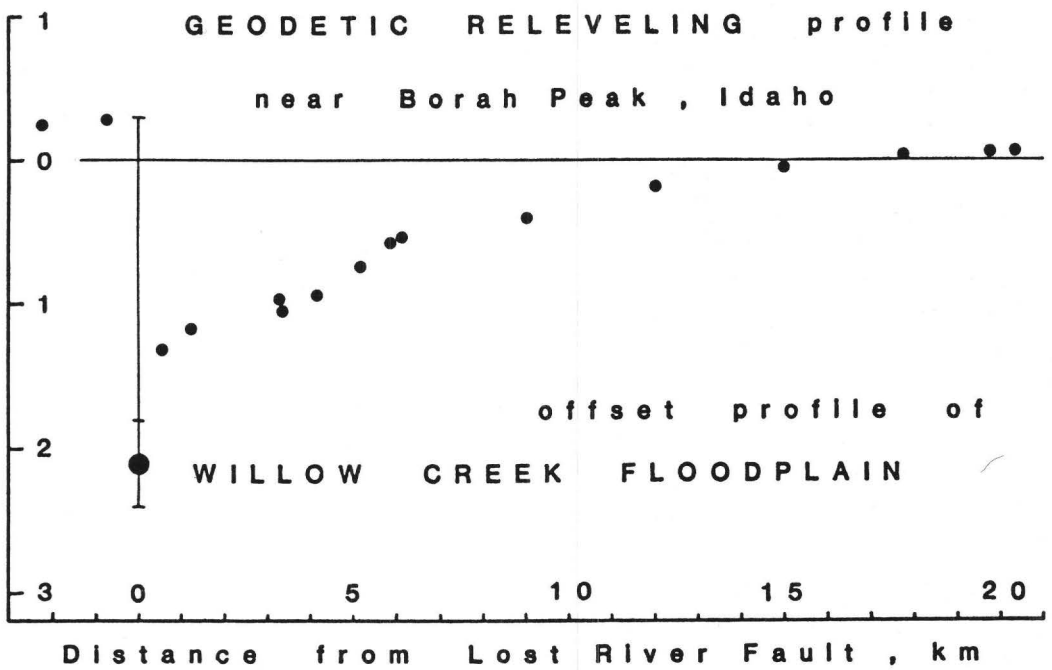

Figure 6. Vertical geodetic releveling (USCGS) on the Willow Creek alluvial fan crossing 1983 rupture of Lost River fault (modified from draft of Stein and Barrientos, this volume). Near field vertical tectonic slip from surveyed floodplain profile-offset is shown "hung" from lip of upthrown block.

straight segment is less steep than the upthrown straight segment as can be seen in Table 3 this change in gradient ranges from .001 to .007. "Gradient" is the dimensionless ratio: rise over run. Although perhaps only coincidental, these values are not the result of surveying errors (see above). Could these landforms record some type of permanent differential tilt in the vicinity of surface rupture? The profile of the (Qpfy) alluvial fan remnant near Willow Creek on Figure 5 is the only example worth discussing. This is because at this site there is no indication the fan profile could have been concave-up when the landform was incised. In other words, it probably did not originally decrease in gradient downstream across what is now the faulted zone. In looking down the two unfaulted segments on Figure 5 it is obvious that if a line other than straight is drawn through the data of either segment--it would have to be convex-up. The Qpfy surface shows a change in profile gradient of .004 and was faulted twice during the Holocene. Perhaps .004 is a cumulative of two episodes of permanent tilt each on the order of .002 gradient change. Theoretically the change in gradient of profile segments would represent the difference: tilt on the upthrown side minus tilt on the downthrown side of the fault. Using the differential tilt factor calculated above from geodetic data, minimum tilt of the hanging wall block near the fault would be on the order of (.002 x .83) - .0017 change in gradient, or 1700 micro-radians per event.

In conclusion, this study demonstrates the near-field coseismic deformation can be detected and measured by using the along gradient profile of faulted geomorphic surfaces. In addition, it appears an elastic deformation model of the 1983 deformation should honor a steep near-field coseismic tilt, perhaps greater than 1200 micro-radians, in the hanging wall block within the .5 km next to the Lost River Fault.

TABLE 3
CHANGE IN PROFILE GRADIENT ACROSS THE LOST RIVER FAULT
For Fluvial and Alluvial Surfaces Near Borah Peak, Idaho

	Number of Offsets	Upstream of Fault	Downstream of Fault	Change in Gradient
WILLOW CREEK:				
FLOODPLAIN	1	.035	.034	.001
RABBIT BRUSH TERRACE	2	.033	.031	.002
Qpfy FAN TERRACE	2	.041	.037	.004
ROCK CREEK:				
FLOODPLAIN	1	.048 to .044	.041	.007 to .003
Qpfy FAN TERRACE	2	.054	.047	.007

NEOTECTONIC HISTORY

The 1983 earthquake faulted young and modern geomorphic surfaces west of Borah Peak The Willow Creek floodplain experienced close to 2.4 m vertical tectonic slip. 2.7 km to the south east, the Rock Creek floodplain and a late Holocene terrace were offset 1.9 ± .4 m during the

earthquake. The range plus or minus .4 m encompasses three profile-offset values made under non-ideal conditions. The late Holocene Big Sage terrace was not faulted previously, and datable organic carbon was obtained from what appears to be a prehistoric Indian fire pit located just beneath the terrace surface. A carbon-14 age for this material will imply the minimum time since previous faulting. The latest Pleistocene alluvial fan surfaces have cumulative offsets of 4.4 m at Rock Creek and 4.3 m at Willow Creek. Evidence for two stratigraphic offset events (including the 1983 earthquake) was observed in a trench excavated across the main scarp on the Willow Creek fan (D. Schwartz, personal communication, 1984). I infer from Pierce and Scott (1982) the age of this latest Pleistocene fan surface to be about 14,000 years. These numbers allow calculation of a maximum average relative neotectonic uplift rate for two surface-faulting events of 0.3 mm/year. The early to middle Holocene Rabbit Brush Terrace at Willow Creek was also faulted twice (including the 1983 event), a total of 4.6 m. In conjunction with the once faulted late Holocene terrace, it appears the previous faulting event occurred during middle to late Holocene.

REFERENCES CITED

Bonilla, R.C., Bucknam, R.C., Clark, M.M., Crone, A.J., Lienkaemper, J.J., Machette, M.M., Pierce, K.L., Plymell, S.K., Rymer, M.J., Scott, W.E., Sharp, R.V., and Skipp, B.A., 1984, Preliminary map of surface faulting associated with the 1983 Borah Peak, Idaho earthquake: U.S. Geological Survey Open-File Report.

Crone, A.J., and Machette, M.N., 1984, Surface faulting accompanying the Borah Peak earthquake, central Idaho: Geology, v. 12, p. 664-667.

Hait, M.H., Jr., and Scott, W.E., 1978, Holocene faulting, Lost River Range, Idaho: Geological Society of America, Abstracts with Programs, v. 10, no. 5, p. 217.

Pierce, K.L., and Scott, W.E., 1982, Pleistocene episodes of alluvial-gravel deposition, southeastern Idaho, in Bill Bonnichsen and R.M. Breckenridge, editors, Cenozoic Geology of Idaho: Idaho Bureau of Mines and Geology Bulletin 26.

Ross, C.P., 1947, Geology of the Borah Peak quadrangle, Idaho: Geological Society of America Bulletin, v. 58, p. 1085-1160.

Scott, W.E., 1982, Surficial geologic map of the eastern Snake River Plain and adjacent areas, 111° to 115° W., Idaho and Wyoming: U.S. Geological Survey Miscellaneous Geologic Investigations Map MI-1373.

Stein, R.S., and Barrientos, S.E., (this volume).

Swan, F.H., III, Schwartz, D.P., and Cluff, L.S., 1980, Recurrence of moderate to large magnitude earthquakes produced by surface faulting on the Wasatch fault zone, Utah: Bulletin of the Seismological Society of America, v. 70, no. 5, p. 1431-1462.

Wood, S.H., 1984, Contemporary vertical tectonics along the Wasatch Fault Zone measured by repeated geodetic leveling: in Evaluation of Regional and Urban Earthquake Hazards and Risk in Utah, U.S. Geological Survey open-file report (in press), 22 p.

Documentation for benchmark photographs showing some effects of the 1983 Borah Peak Earthquake with considerations for studies of scarp degradation

Michael N. Machette
U.S. Geological Survey
Denver, Colorado

Abstract

During a geologic study of surface faulting associated with the October 28, 1983 Borah Peak Earthquake of central Idaho, I established monumented benchmark stations for systemmatic rephotography of selected deformational features. Photographs were made from these stations in November 1983 to show some of the intricate details of the new fault scarps, grabens, and an associated landslide. In October 1984, about one year later, this record was augmented by repeating most of the 1983 photographs and taking additional ones from new stations. This paper provides a descriptive account of the location, subject, and details of the high-quality photographs now on file with the U.S. Geological Survey Photo Library in Denver. The photographs are a valuable data base for future studies of deformational features associated with the 1983 earthquake and the subsequent degradation of these features with time.

Photographic monitoring of fault-scarp degradation

Fault scarps such as those produced during the 1983 Borah Peak earthquake are a common recorder of large magnitude earthquakes. When fresh, a fault scarp is usually near vertical, but may quickly collapse to form a slope of 33°-35°. Further erosion wears down the scarp, eventually producing a subtle rounded slope. Recent studies of the morphology and degradation of fault scarps (Wallace, 1977; Bucknam and Anderson, 1979; Nash, 1980; Machette and McGimsey, 1983) have enhanced our ability to estimate the age and recurrence intervals of prehistoric faulting. Thus, understanding the degradation of fault scarps is a fundamental part of modern earthquake studies.

In the early phase of scarp degradation, the free face is removed and the scarp erodes to the angle of repose of the faulted material, mainly by gravitational collapse (Wallace, 1977). For small scarps, the angle of repose may be reached in as little as a hundred years, a time scale that is appropriate for monitoring by photography. Later phases of scarp degradation proceed more slowly, owing to erosion mainly by slope wash and colluviation. However, the rates and processes of degradation are still poorly understood because there have been few quantitative studies of the morphology and erosion of historic fault scarps. Moreover, these studies require a long-term commitment and are often given low scientific priority. However, much lost data on scarp degradation can be recovered by relocating the sites from which photographs of historic fault scarps were made and rephotographing the same scenes. For example, the Photo Library of the U.S. Geological Survey has about 250,000 photographs made during the past 100 years, and some of these photographs contain useful views of historic fault scarps.

Repeat photography from terrestrial benchmark stations

The changes in morphology of new fault scarps that occur over intervals of months to years are difficult, if not impossible, to monitor except by repeat photography. Malde elaborated on this aspect of repeat photography in his 1973 paper. "Terrestrial photographs have many obvious advantages over other methods of recording changes in landscapes, although standard methods of surveying (including aerial photographs) can never be replaced. The camera sees all the intricate qualities of the terrain that may otherwise escape notice: the staining of outcrops, the cracking of soil, small rills made by runoff on bare ground, the growth of plants, the impact of man's use, and countless other features that are virtually impossible to map and describe by other means. These aspects, moveover, are recorded by the camera impartially and completely, without the bias of observing only selected features that are expected to change."

Repeat photography is a technique of landscape study in which a scene depicted in an earlier photograph is "rephotographed," generally after months or years, in a manner that duplicates the original scene as precisely as possible (Lambert, 1984). The time between photographs is usually dictated by the rate at which features are changing; for example, Malde (1973) repeated photographs of an arroyo after a month to document erosional changes caused by flooding. Rephotographing provides a permanent record of changes that occur between photographs. A further advantage is that changes are measurable on the photographs, thus providing a quantitative data base for analytical studies of landscape modification. Rephotographing can be accomplished quickly by establishing permanent benchmark stations (Malde, 1973).

Repeat photography of fault scarps

The bibliography of repeat photography by Rodgers, Malde, and Turner (1984) reveals but a few attempts to repeat photographs of fault scarps. Foremost among these are the efforts of R.E. Wallace (1977, 1980a, 1980b). During the past 30 years, Wallace has rephotographed fault scarps formed during the following earthquakes: 1915 Pleasant Valley, Nevada (photographs in 1957 and 1974); 1954 Fairview Peak, Nevada (photograph of Steinbrugge in 1954, repeat photographs in 1957 and 1974); 1959 Hebgen Lake, Montana (photographs in 1958 and 1978); as well as a prehistoric fault scarp on the Wasatch fault zone near Little Cottonwood Canyon, Utah (1979 repeat of Gilbert's 1901 photograph). Scarps of the famous 1906 San Francisco, California earthquake have been rephotographed recently in the Point Reyes area (Thatcher, 1974; Anonymous, 1981), but because of man's influence, photographs of these scarps have more of a historic than a geologic significance.

It appears that Morisawa (1975) was the first to rephotograph a recently formed fault scarp over short intervals of time. A side-by-side comparison of her photographs of the 1959 Hebgen fault scarp of Montana taken near the Cabin Creek campground one month, two years, and four years after the earthquake document the rapid collapse of the scarp's free face and the recovery of vegetation on the scarp. Unfortunately, Morisawa's sites were not permanently marked and the photographs are not closely matched; thus, her photographs cannot be used to make detailed comparisons or measurements of scarp degradation. However, using photographs of John Stacy (in Witkind, 1964), Wallace (1980a) relocated and photographed four sites along the Hebgen fault scarp and documented its degradation since 1959.

These examples show that repeat photography is a useful technique for studying scarp degradation, but that a systematic approach of repeat photography from benchmark stations has not been used. Many historic fault scarps in the United States (Ryall and others, 1966), and some fluvial scarps of known age that could serve as standards for degradation rates, should be photographed from permanently marked sites for future study. In addition of the historic fault scarps mentioned above, scarps associated with the 1857 Fort Tejon, 1872 Owens Valley, and 1940 Imperial earthquakes (California), the 1932 Cedar Mountain and 1954 Rainbow Mountain earthquakes (Nevada), and the 1934 Hansel Valley, Utah earthquake are likely candidates for repeat photography from benchmark stations.

Most investigations of surface faulting rely heavily on vertical aerial photography to document ground rupturing. Low-altitude, low-sun-angle aerial photographs at an approximate scale of 1:6,000 were flown the day after the Borah Peak earthquake. These photographs proved invaluable for mapping intricate patterns of ground breakage (Crone and Machette, 1984; Crone 1985). However, small features such as en echelon tears, thrusts in the soil, tensional gaps, and complex antithetic faults in grabens still are poorly documented. Because the earthquake occurred in late fall, Crone and Machette did not have time to map adequately many of the delicate deformational features that were obliterated the next year. Thus, the Borah Peak study has shown that high-quality, ground-based photography employed immediately after the earthquake is essential for documenting small deformational features.

Technique and equipment for repeat photography

Successful repeat photography relies basically on good photography and careful record keeping. Repeat photographs of fault scarps should have (1) a known location, time, and scale, (2) good clarity and definition, and (3) good image stablity. Malde (1973) and Harrison (1974) discuss methods for establishing or relocating stations for repeat photography, and Lambert's (1984) newsletter is a good primer on techniques of repeat photography.

The following equipment was used for most of the photographs made in this study:

1) Hasselblad 500 CM[1] camera (70 mm film) with lenses (wide view, 50 mm focal length; normal view, 80 mm; narrow view, 250 mm), and a calibrated light meter;
2) A sturdy tripod and a plumb bob for marking the position of the diaphram of the camera lens on the ground;
3) A scale for the photographs such as a ranging pole or expandable stadia rod (1.5 to 6.5 m long) with metric divisions; and
4) Kodak Panatomic-X and Agfapan 25 films (high resolution fine-grain films having a stable base).

H. E. Malde established several new benchmark stations during October, 1984. His photographs (from sites designated 84M; fig. 1, tables 2 and 4) were made using 4- by 5-inch and 8- by 10-inch view cameras and black and white film. In addition, Malde also made exposures on 4- by 5-inch Ektachrome 64 color transparency film at most of his benchmark stations.

---

1 Use of trade or brand names in this report is for descriptive purposes only and does not constitute endorsement by the U.S. Geological Survey.

The stations are marked by one-meter long sections of 1/2-inch diameter rebar (steel reinforcing rod), of which all but 10 to 15 cm is driven into the ground. Rebar is preferred because it is easy to drive into the ground but cannot be pulled out easily, and is readily available, inexpensive, and durable. Malde and I used plastic survey markers driven onto the top of the rebar to identify the photo stations. Stations 83MM5 and 83MM6 (table 1) are marked by 30-inch-long, copper-clad survey rods rather than by rebar.

Description of benchmark stations and photographs

The current photographic record includes both close-up views of fault scarp and graben features and long-distance views where fault scarps are well displayed along the front of the Lost River Range (Crone and Machette, 1984). Several photographs showing different scenes were made at most stations, thus forming a relatively large catalog of photographs from a limited number of stations. Depending on the subject, either single images or stereopairs using about 15 cm of separation in camera position were made at each benchmark station. Panoramas were made from several stations.

Tables 1 and 2 show information for the 1983 and 1984 benchmark stations (respectively) that include station number, area, subject, and locality (section, township and range, quadrangle, and altitude). Data for photographs taken in 1983 and 1984 (tables 3 and 4, respectively) include station number, film roll and exposure number; type of view, camera and lens; orientation of view; time (Mountain Standard Time) and date of exposure; and size of, type of, and distance to scale. Specific information for each site and photograph are on file with the negatives at the U.S. Geological Survey Photo Library in Denver. (Prints from these negatives may be obtained by writing to the Photo Librarian, U.S. Geological Survey Photo Library, MS 914, P.O. Box 25046, Federal Center, Denver, Colorado 80225. Information may also be obtained by phone (303-236-1010) on workdays from 7:30 AM to 4 PM.)

An experiment in repeat photography for studies of scarp degradation

Repeat photography is a promising technique for the study of degradation of modern fault scarps. This technique could be used to document collapse of the free face of a scarp and the accumulation of the colluvial wedge at the base of a scarp, and to map the retreat of knick points in streams that flow across a scarp. One could even monitor the obliteration of small features such as tension cracks, the formation of rills, and the revegetation of the scarp. Using high-quality benchmark photographs and a photogrammetric plotter, one could make topographic maps of the face of a scarp and estimate volumes of material that have collapsed or eroded from a scarp.

During October 1984, H. E. Malde, R. C. Bucknam, and M. N. Machette established an experimental site for photogrammetric modelling of scarp degradation. We set up two pairs of camera stations (84M123 and 84M124, 84M125 and 84M126; fig. 1) from which we made wide-baseline stereo images of a set of small fault scarps. The purposes of this experiment are two fold. First, identical images were made using four cameras having different formats to determine the differences in degree of resolution of fault related features. We used the following combination of cameras, lenses, and films: 1) an Olympus 35 mm camera, 50 mm lens, and Kodak Technical Pan roll film; 2) a Hasselblad 70 mm camera, 80 mm lens, and Agfapan 25 roll film; 3) a Sinar 4- by 5-inch view camera, 150 mm lens, and Ilford FP-4 sheet film); and 4) a Sinar 8- by 10-inch view camera, a 300 mm lens, and Tri-X sheet film. (The focal lengths listed here are nominal lengths and do not reflect the actual focal length of the lens when focused at finite distances.)

The second purpose of the experiment is to determine the analytical precision that we can expect in measurements made from the photographs. We placed four permanent markers (1/2-inch diameter rebar with plastic caps) in the ground 1-2 m above the fault scarp and measured the distance and direction from each marker (points A-D, table on fig. 1) to the two camera setups. From these measurements we then calculated the distance from the diaphram of the camera lens to each of the markers (see table 5). The stereopairs will be setup in a Kern PG-2 photogrammetric plotter, just as traditional aerial photographs are used for topographic mapping. From the stereoimages, we will measure the distance to and between each marker and plot the position and size of fault-related features relative to these markers. This phase of the experiment will allow us to determine the accuracy of measurements made from the stereoimages and to evalute determinations of scarp degradation using established methods of repeat photography suitable for rapid, post-earthquake field studies.

At the present time we have not evaluated the analytical precision of the photogrammetric experiment. However, our experiments with different camera-lens-film combinations have been completed and show interesting results. As one would expect, the 8- by 10-inch photographs made with the two view cameras have the best resolution, but photographs made with the 70 mm and 35 mm cameras are suprisingly good. The 70 mm camera gives a square format negative that is more suitable for photogrammetry than the rectangular format negative of the view cameras and the 35 mm camera. The photographs made from 35 mm negatives on Kodak Technical Pan film are sharp and comparable to those made from 70 mm negatives in all cases except those of extreme enlargement. Thus, for most repeat photography the 35 mm Technical Pan film would be quite adequate, especially if one considers the advantages of the 35 mm camera system, such as affordablity, light weight, small size, and ease of changing lenses.

A wide variety of data is needed to calibrate rates of degradation analyzed from repeat photographs of historic fault scarps. For example, various physical properties control the rate and style of degradation of young fault scarps. These properties probably include texture, density, and cohesion of the faulted materials; type of clay minerals; degree of soil development and type and density of root mat; orientation of the scarp relative to wind direction (which might control drifts of snow, sand, or loess); and position of the scarp relative to the water table. As part of this experiment, R. C. Bucknam sampled the materials exposed in the scarp at the experimental site in order to measure their physical properties.

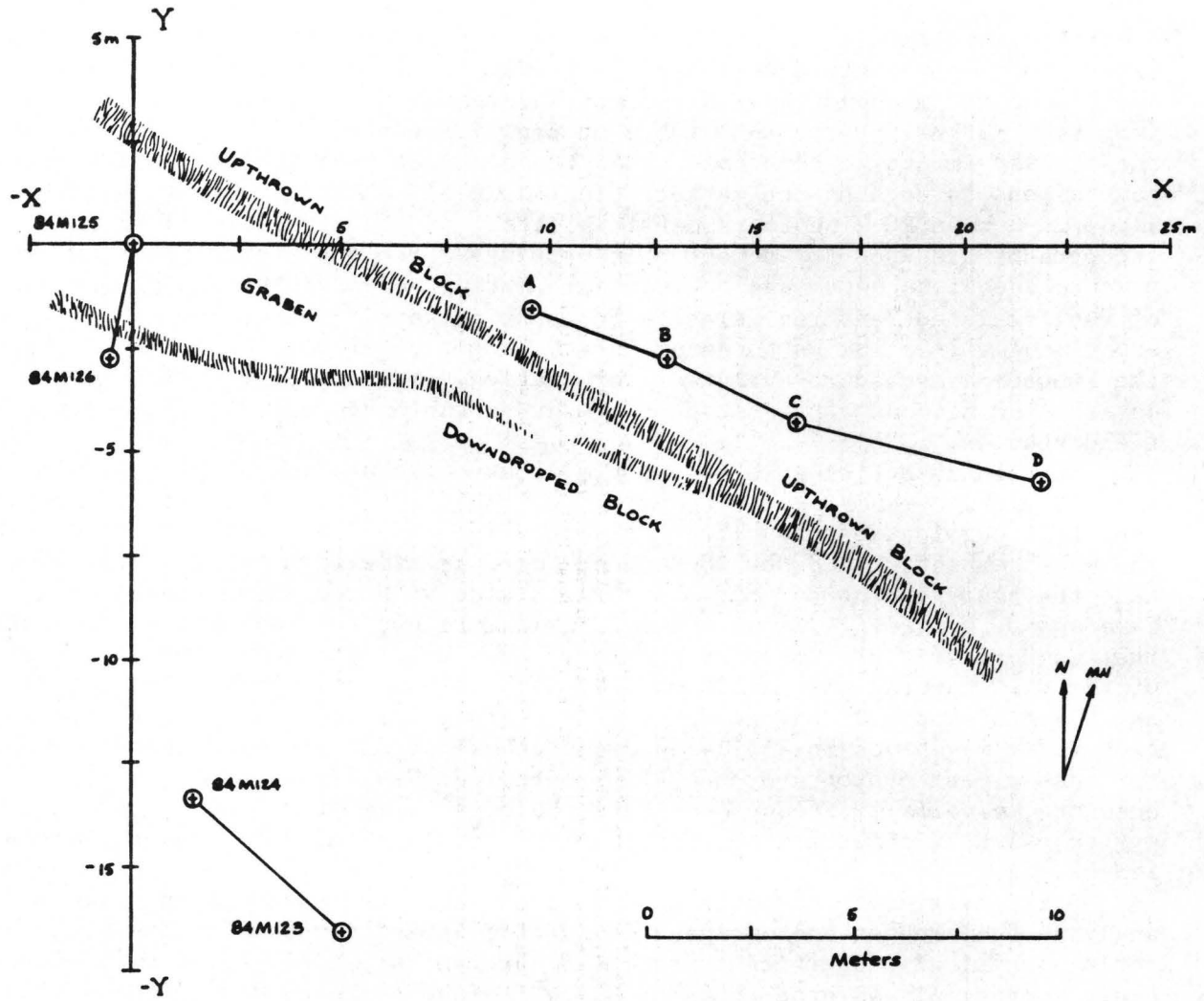

MARKER PINS (x, y, z)	CAMERA STATIONS (x, y, z)			
	84M123 (5.15, -16.45, 1.60)	84M124 (1.52, -13.30, 0.95)	84M125 (0.0, 0.0, 0.0)	84M126 (-0.53, -2.75, 0.37)
A (9.55, -1.55, 2.82)	15.72, N. 16° E.	14.43, N. 34° E.	10.12, S. 81° E.	10.47, N. 83° E.
B (12.85, -2.65, 3.56)	16.07, N. 29° E.	15.76, N. 46.5° E.	13.63, S. 78° E.	13.76, East.
C (15.95, -4.25, 4.28)	16.59, N. 41° E.	17.39, N. 47.5° E.	17.06, S. 75.5° E.	17.00, S. 85° E.
D (21.90, -5.55, 6.09)	20.45, N. 57° E.	22.40, N. 59° E.	23.41, S. 75° E.	23.32, S. 83° E.

Figure 1. Map showing location of camera stations and marker pins. Location of fault scarps shown by hachure pattern. Table shows inclined distances (in meters) and directions between camera stations and marker pins. Location of stations and pins relative to station 84M125 are given by x (east), y (north), and z (vertical) coordinates.

Table 1.--Benchmark stations for 1983 photographic study of the Borah Peak, Idaho earthquake

Station [1]	Area, description of scene, and location of benchmark station
83MM1	Birch Springs area. Three views of complex fault scarps northeast of road on north side of Birch Springs. 170 m N., 780 m E., SW cor. sec. 3, T. 9 N., R. 22 E., Borah Peak quadrangle, altitude 7280 ft (2220 m). Downthrown block, 30 m S. and 8 m E. of sharp south bend in new road.
83MM2-4	Landslide scar and debris flow at Birch Springs. Pre-existing landslide was reactivated and enlarged headward by the earthquake shaking. Borah Peak quadrangle. 83MM2: 85 m N., 790 m W., SE cor. sec. 3, T. 9 S., R. 22 E., altitude 7320 ft (2232 m). Southward view of landslide. 5 m S. of crest of WNW-trending ridge. 83MM3: 175 m S., 730 m W., NE cor. sec. 10, T. 10 S., R. 22 E., altitude 7380 ft (2250 m). Northward view of head of landslide. 83MM4: 100 m S., 875 m W., NE cor. sec. 10, T. 9 N., R. 22 E., altitude 7260 ft (2213 m). On downdropped fault block, 30 m W. of fault, between southern two of three spring-fed streams. Debris flow over 1983 fault scarp.
83MM5	Arentson Gulch area. Views of fault scarp in loose, coarse-grained alluvium. Station is 5 m SE. of eye-witness report of scarp formation (Pelton and others, 1984). 690 m S., 55 m E., NW cor. sec. 36, T. 11 N., R. 21 E., Dickey Peak quadrangle, altitude 7320 ft (2232 m). On downdropped fault block, 28 m S. 20° E. of center of road where displaced by fault. Used copper-clad station marker set by A. J. Crone.
83MM6	Valley of Scratching Post Spring. Views of fault scarp in loose, fan alluvium of Arentson Gulch (east side) and in compact, fine-grained valley alluvium (west side). Shows contrasting scarp morphology in different texture of material. 2610 m S., 250 W., NE cor. sec. 35, T. 11 N., R. 21 E., Dickey Peak quadrangle, altitude 7205 ft (2297 m). On downdropped fault block, 12.5 m SW. of scarp and 15 m E. of edge of pond. Most of scarp obliterated in 1984.
83MM7	Terrace on north side of Rock Creek. Distant views of scarp along faceted spurs between Rock Creek and Birch Springs. Along National Forest Service boundary, 117 m S., NW cor. sec. 3, T. 9 N., R. 22 E., Borah Peak quadrangle, altitude 7040 ft (2146 m).
83MM8	First drainage north of Rock Creek. Medium-distance views of new scarp superposed on pre-existing fault scarp. Shows two levels of tectonic terraces on upthrown block. 425 m N., 215 m E., SW cor. sec. 34, T. 10 N., R. 22 E., Borah Peak quadrangle, altitude 7070 ft (2155 m). 45 m W. of scarp where fault cuts stream channel.
83MM9	First drainage north of Rock Creek. Close-up, oblique views of new fault scarp and distant view of scarp between Bull Creek and Rock Creek. 465 m N., 245 m E., SW cor. sec. 34, T. 10 N., R. 22 E., Borah Peak quadrangle, altitude 7095 ft (2163 m). 15.4 m N. 70° W. of scarp where fault displaces stream channel.
83MM10	Hill 7443, west of Scratching Post Spring. Views of scarp near locality of second eye-witness report (Wallace, 1984) and a distant view of scarp near base of snow-covered Dickey Peak. Crest of hill 7443, 770 m N., 565 m E., SW cor. sec. 35, T. 11 N., R. 21 E., Dickey Peak quadrangle, altitude 7443 ft (2269 m).
83MM11	Doublespring Pass Road. Fault scarps about 320 m NW of road. View southeast along 30-m-wide zone of deformation, road in middle distance. 655 m N., 215 m E., SW cor. sec. 28, T. 10 N., R. 22 E., Borah Peak quadrangle, altitude 6890 ft (2100 m). On upthown block of fault, just south of sharp bend in fault.
83MM12	Doublespring Pass Road. Complex fault scarps about 220 m NW of road. Views of horsts and grabens in 30-m-wide zone of deformation. 510 m N., 215 m E., SW cor. sec. 28, T. 10 N., R. 22 E., Borah Peak quadrangle, altitude 6875 ft (2096 m). On crest of horst at W. edge of prominent graben.
83MM13	Doublespring Pass Road, near Forest Service boundary. Distant views of fault scarp along foothills at base of Lost River Range between Willow Creek and Cedar Creek. 70 m S., 10 m E., NW cor. sec. 32, T. 10 N., R. 22 E., Borah Peak quadrangle, altitude 6800 ft (2073 m). Near wooden Forest Service boundary marker, 71 m S. 8° E. of BM 6804.
83MM14	Cedar Creek. Near road along edge of terrace, north side of Cedar Creek. Views of the 1983 scarps that cross Pinedale lateral moraines of Cedar Creek. 165 m S., 90 m E., NW cor. sec. 10, T. 9 N., R. 22 E., Borah Peak quadrangle, altitude 7040 ft (2146 m). Just west of cut for road that leads down to small dam for diversion canal.

1 Symbol denotes year (1983), photographers initials (MM, Machette), and site number.

Table 2.--Benchmark stations for 1984 photographic study of the 1983 Borah Peak, Idaho earthquake

Station [1]	Area, description of scene, and location of benchmark station
84MM1	North of Doublespring Pass Road. New view of fault scarps about 220 m N. of road. Complex horst and graben in 30-m-wide zone of deformation. Same site as 83MM12.
84MM2	North of Doublespring Pass Road. Repeat of 83MM12A.
84MM3-5	North of Birch Springs. Repeats of 83MM1A, 83MM1B, and 83MM1C, respectively.
84MM6	Arentson Gulch Road. Repeat of 83MM5A.
84MM7	Scratching Post Spring. New view of fault scarp in loose, fan alluvium of Arentson Gulch and in compact, fine-grained alluvium of valley of Scratching Post Spring. Shows contrasting scarp morphology in different materials. View more northerly than shown in 83MM6D, which has been disturbed. Same site as 83MM6.
84MM8	Scratching Post Spring. Repeat of 83MM6C.
84MM9	Scratching Post Spring. New view of fault scarp between areas shown in 83MM6A/83MM6B and 83MM7. Scarp shown in 83MM7A and 83MM7B has been obliterated where it crosses the valley bottom. Same site as 83MM6.
84MM10	New site, west flank of Dickey Peak. View of en echelon fault scarps in avalanche scree deposits. On ridge crest, W of toe of deposit. 745 m N., 145 m W., SE cor. sec. 7, T. 10 N., R. 22 E., Dickey Peak quadrangle, altitude 7900 ft (2408 m).
84MM11-13	Rock Creek. New close-up views of large fault scarp, first drainage north of Rock Creek (concave to the south). Same site as 83MM9.
84MM14,15,17	Birch Springs. Repeats of 83MM2, 83MM3, and 83MM4, respectively.
84MM16	Birch Springs. New close-up view of scarp along head of landslide. Same site as 83MM3.
84M123-126	New site, south of Rock Creek. Site of experiment to determine precision of measurements of fault scarp degradation from oblique stereophotographs. Photographs made from two paired camera setups using four different formats of camera. 290 m S., 410 m E., NW cor. sec. 3, T. 9 N., R 22 E., Borah Peak quadrangle, altitude 7280 ft (2220 m).
84M127	New site, north of Doublespring Pass Road. Complex stair-stepped scarps about 40 m W. of 83MM11, along west side of dirt road at base of scarp. 520 m N., 150 m E., SW cor. sec. 28, T. 10 N., R. 22 E., Borah Peak quadrangle, altitude 6875 (2096 m).
84M128	New site north of Doublespring Pass Road. Shows fault scarp at maximum height and offset. 630 m N., 100 m E., SW cor. sec. 28, T. 10 N., R. 22 E., Borah Peak quadrangle, altitude about 6870 ft (2095 m).
84M129	New site north of Birch Springs. Shows scarp at foot of faceted bedrock spur about 300 m N. of Birch Springs. 320 m N., 725 m. E., SW cor. sec. 3, T. 9 N., R. 22 E., Borah Peak quadrangle, altitude 7240 ft (2207 m).
84M130	New site at Birch Springs. Shows debris-flow material that was deposited across the scarp just minutes after the earthquake. 45 m N., 685 m E., SW cor. sec. 3, T. 9 N., R. 22 E., Borah Peak quadrangle, altitude 7200 ft (2195 m).
84M131	New site on west flank of Dickey Peak (same subject as 84MM10). Shows two en echelon fault scarps in avalanche scree deposits. On south edge of ridge crest, north of valley. 695 m S., 120 m W., NE cor. sec. 7, T. 10 N., R. 22 E., Dickey Peak quadrangle, altitude 8060 ft (2457 m).
84M132	New site, first drainage north of Rock Creek. Shows graben in foreground and main scarp in middle distance. 500 m N., 210 m E., SW cor. sec. 34, T. 10 N., R. 22 E., Borah Peak quadrangle, altitude 7080 ft (2158 m). 50 m N. of 83MM9.
84M133	New site, first drainage north of Rock Creek. Shows antithetic fault in foreground and main fault in middle distance. 440 m N., 245 m E., SW cor. sec 34, T. 10 N., R 22 E., Borah Peak quadrangle, altitude 7090 ft (2161 m).
84M134	New site along Doublespring Pass Road. Repeats photograph (35 mm Kodachrome transparency) of K. L. Pierce on May 3, 1979. The pre-1983 scarp was displaced by movement along the Lost River fault during the 1983 Borah Peak earthquake. 205 m N., 200 m E., SW cor. sec. 28, T. 10 N., R. 22 E., Borah Peak quadrangle, altitude 6840 ft (2085 m).
84M135	New site just north of Rock Creek. Shows fault scarp in relatively fine-grained terrace alluvium. 60 m S., 410 m E., NW cor. sec. 3, T. 9 N., R. 22 E., Borah Peak quadrangle, altitude 7080 ft (2158 m).
84M136	New site just north of Rock Creek. Shows fault scarp in relatively fine-grained terrace alluvium. 30 m S., 375 m E., NW cor. sec. 3, T. 9 N., R. 22 E., Borah Peak quadrangle, altitude 7080 ft (2158 m).
84M137	New site north of Rock Creek. Shows left-lateral offset of fence. 20 m N., 500 m E., SW cor. sec. 34, T. 10 N., R. 22 E., Borah Peak quadrangle, altitude 7100 ft (2165 m).
84M138	New site just above fault scarp at Arentson Gulch. Long view to southeast of 1983 rupture superposed on midslope of older fault scarp, which is marked by a relatively barren slope. 650 m S., 100 m E., NW cor. sec. 36, T. 11 N., R. 21 E., Dickey Peak quadrangle, altitude 7330 ft (2235 m).

1 Symbol denotes year (1984), photographers initials (MM, Machette; M, Malde), and site number.

Table 3.—Data for 1983 photography, Borah Peak, Idaho, earthquake

[All 1983 photographs were made by Machette using 70-mm black and white film. Abbreviations for type of view: S, single; Sp, stereopair; Pan, panorama; r-v, right-view; c-v, center-view; and l-v, left-view. N.d., not determined.]

Station [1]	U.S.G.S. number for negative [2]	Type of view and camera/lens size (mm)	Orientation of view	Time (MST) and date	Scale: size type and distance from station	Remarks
PHOTOGRAPHS FROM BENCHMARK STATIONS:						
83MM1A-----	2	Sp and r-v Pan, 70/50.	S. 73° E.	15:15, 3 Nov. 83	1.5 m stadia rod, 32 m----	En echelon scarps in alluvium.
83MM1B-----	3	Sp and c-v Pan, 70/50.	N. 51° E.	16:00, 3 Nov. 83	1.5 m stadia rod, 21 m----	Do.
83MM1C-----	4	Sp and l-v Pan, 70/50.	N. 20° E.	16:15, 3 Nov. 83	1.5 m stadia rod, 47.5 m--	Right-stepping scarps at base of hills.
83MM1C-----	5	Sp and l-v Pan, 70/50.	N. 20° E.	16:20, 3 Nov. 83	1.5 m stadia rod, 47.5 m--	Repeat of photos MM-4.
83MM2------	34	Sp, 70/50----------	S. 3° W.	12:40, 9 Nov. 83	None----------	Landslide scar from ridge crest.
83MM3------	33	--Do----------	N. 13° E.	12:15, 9 Nov. 83	3.5 m stadia rod----------	Close-up, landslide scar and rotated blocks.
83MM4------	32	--Do----------	S. 66° E.	11:20, 9 Nov. 83	2.4 m stadia rod----------	Landslide (debris flow) over 1983 fault scarp.
83MM5A-----	6	Sp, 70/80----------	S. 88° E.	13:10, 4 Nov. 83	2.8 m stadia rod----------	Near site of eye-witness report (Pelton and others, 1984).
83MM5B-----	7	S, 70/80----------	S. 74° E.	14:00, 4 Nov. 83	2.8 m stadia rod----------	100 m E. of scarp that crosses road along Arentson Gulch.
83MM6A-----	16	Sp, 70/80----------	N. 41° W.	11:05, 8 Nov. 83	--Do----------	Scarp in Scratching Post Spring Valley.
83MM6B-----	17	Sp, 70/50----------	N. 41° W.	11:15, 8 Nov. 83	2.5 m stadia rod, 25 m----	Do.
83MM6C-----	18	--Do----------	N. 87° E.	11:40, 8 Nov. 83	2.5 m stadia rod, 20 m----	Scarp in fan of Arentson Gulch.
83MM6D-----	19	--Do----------	N. 57° E.	11:45. 8 Nov. 83	--Do----------	Do.
83MM7A-----	8	Sp, 70/80----------	S. 51° E.	11:15, 7 Nov. 83	None----------	Scarps on colluvial slope on bedrock.
83MM7B-----	9	Sp, 70/50----------	S. 57° E.	11:55, 7 Nov. 83	None----------	Do.
83MM8A-----	10	--Do----------	S. 70° E.	13:30, 7 Nov. 83	2.6 m stadia rod----------	New break on old scarp, two tectonic terraces.
83MM8B-----	13	Sp, 70/80----------	S. 65° E.	15:45, 7 Nov. 83	None----------	Scarps on slope north of Rock Creek.
83MM8C-----	14	S, 70/50----------	S. 65° E.	16:00, 7 Nov. 83	2.6 m stadia rod----------	Tectonic terraces, uplifted fault block.
83MM8D-----	15	--Do----------	Southeast	16:05, 7 Nov. 83	None----------	Scarps north of Rock Creek.
83MM9A-----	11	Sp, 70/80----------	N. 16° W.	15:20, 7 Nov. 83	2.6 m stadia rod----------	Large scarp in colluvium, view to north.
83MM9B-----	12	Sp, 70/80----------	S. 64° E.	15:35, 7 Nov. 83	2.6 m stadia rod----------	Large scarp in colluvium, view to south.
83MM10A----	20	S and l-v Pan, 70/50-	North----	12:30, 8 Nov. 83	None----------	Scarp at site of eye-witness report (Wallace, 1984).
83MM10B----	21	S and r-v Pan, 70/50-	N. 52° E.	12:35, 8 Nov. 83	--Do----------	Do.
83MM10C----	22	S, 70/250----------	S. 85° E.	12:45, 8 Nov. 83	--Do----------	Scarp at west base of Dickey Peak.
83MM11-----	23	Sp, 70/80----------	S. 51° E.	14:45, 8 Nov. 83	2.0 m stadia rod----------	Scarp and wide, complex graben.
83MM12A----	24	Sp, 70/50----------	S. 75° E.	15:05, 8 Nov. 83	3.2 m stadia rod----------	Complex system of stair-stepped scarps.
83MM12B----	25	S, 70/50----------	S. 59° E.	15:15, 8 Nov. 83	2.9 m stadia rod----------	Do.
83MM12C----	26	Sp, 70/50----------	N. 36° W.	15:40, 8 Nov. 83	None----------	Do.
83MM13-----	27	Sp, 70/80----------	S. 55° E.	16:10, 8 Nov. 83	--Do----------	Scarp at Rock Creek, Borah Peak in rear.
83MM13-----	28	S, 70/80----------	--Do-----	16:30, 8 Nov. 83	--Do----------	Do.
83MM13-----	29 to 31	S, 70/50----------	S. 55°-60° E.	16:35-16:45, 8 Nov. 1983.	--Do----------	Various exposures and types of filters.
83MM14-----	37	Sp, 70/50----------	Southeast	13:30, 9 Nov. 83	--Do----------	Scarp across moraine of Cedar Creek.
PHOTOGRAPHS FROM UNMARKED STATIONS:						
----------	35	S, 70/80----------	S. 15° E.	13:00, 9 Nov. 83	--Do----------	Close-up of landslide. Near 83MM2.
----------	36	--Do----------	S. 10° E.	13:05, 9 Nov. 83	--Do----------	Do.
----------	38 to 43	S, 70/50----------	N.d.-----	Afternoon, 9 Nov. 1983.	2.8 m stadia rod----------	Snapshots of scarps next to Doublespring Pass Road.
----------	44, 45	S, 70/50----------	Northeast	--Do----------	2.9 m stadia rod----------	Snapshots of complex scarps, 40 m W. of site 83MM11.
----------	46	--Do----------	Southeast	--Do----------	--Do----------	Do.
----------	47	Sp, 70/50----------	N.d.-----	--Do----------	2.8 m stadia rod----------	Hand-held snapshots from 2.5 m above ground, 40 m W. of site 83MM11.

1 Symbol denotes year (1983), photographers intials (MM, Machette) site number, and separate views from each station (letter).
2 Numbers of photo negative(s) archieved under Machette and Malde respective files at U.S. Geological Survey Photo Library.

Table 4.--Data for 1984 photography, Borah Peak, Idaho, earthquake

[Abbreviations for type of view: S, single; Sp, stereopair; Pan, panorama; r-v, right-view; c-v, center-view; and l-v, left-view.]

Benchmark station [1]	U.S.G.S. number for negative [2]	Type of view and camera/lens size (mm) [3]	Orientation of view	Time (MST) and date	Scale: size, type, and distance from station	Remarks
PHOTOGRAPHS FROM NEW BENCHMARK STATIONS:						
84MM1--------	55	Sp, 70/80-----	N. 66° E.	11:28-11:38, 8 Oct. 84	2.3 m stada rod, 7.4 m.--	Same site as 83MM12.
	56	Sp, 70/50-----	N. 66° E.	11:30-11:39, 8 Oct. 84	--Do----------	Do.
84MM7--------	66	Sp, 70/80-----	N. 61° E.	10:01-10:04, 9 Oct. 84	Ranging pole, 0.5 m marks	Same site as 83MM6.
84MM9--------	68	Sp, 70/80-----	N. 21° E.	10:48-10:57, 9 Oct. 84	None----------	Same site as 83MM6.
84MM10-------	69	Sp, 70/50-----	N. 52° E.	13:13-13:18, 9 Oct. 84	None----------	New site.
84MM12-------	74	S, 70/80------	S. 4° W.	11:32, 10 Oct. 84-----	None----------	Similar to photos MM-24.
84MM13-------	72	Sp, 70/80-----	N. 75° E.	16:46-16:50, 9 Oct. 84	Ranging pole, 0.5 m marks	New view from site 83MM9.
84MM16-------	76	Sp, 70/80-----	Northeast	12:24, 10 Oct. 94-----	2.4 m stadia rod, 11 m---	Same site as 83MM3, close up view.
84M123A, 124A	692ct, 693ct	Sp, 4 x 5/150-	N. 31° E.	12:11-12:17, 7 Oct. 84	Ranging pole, 0.5 m marks	Experimental site for photogrammetry.
84M123B, 123B	1408, 1411	--Do----------	--Do-----	12:12-12:18, 7 Oct. 84	--Do----------	Same views as 84M123A and 83MM124A.
84M123C, 124C	1409, 1412	Sp, 8 x 10/287	--Do-----	12:54-13:04, 7 Oct. 84	--Do----------	Do.
84M123D, 124D	1410, 1413	Sp, 70/80-----	--Do-----	13:20-13:26, 7 Oct. 84	--Do----------	Do.
84M125A, 126A	694ct, 695ct	Sp, 4 x 5/150-	S. 79° E.	14:54-15:01, 7 Oct. 84	--Do----------	Experimental site for photogrammetry.
84M125B, 126B	1414, 1418	--Do----------	--Do-----	14:55-15:02, 7 Oct. 84	--Do----------	Same views as 83M125A and 126A.
84M125C, 126C	1415, 1419	Sp, 8 x 10/287	--Do-----	15:25-15:33, 7 Oct. 84	--Do----------	Do.
84M125D, 126D	1416, 1420	Sp, 70/80-----	--Do-----	14:54-15:01, 7 Oct. 84	--Do----------	Do.
84M125E, 125E	1417, 1421	Sp, 35/50-----	--Do-----	15:52-16:06, 7 Oct. 84	--Do----------	Do.
84M127A------	696ct	Sp, 4 x 5/90--	N. 64° E.	11:16, 8 Oct. 84------	--Do----------	New site. Like photos MM-47.
84M127B------	1422	--Do----------	--Do-----	11:18, 8 Oct. 84------	--Do----------	Do.
84M128A------	697ct	Sp, 4 x 5/210-	S. 58° E.	12:11, 8 Oct. 84------	--Do----------	New site. Largest scarp.
84M128B------	1423	--Do----------	--Do-----	12:12, 8 Oct. 84------	--Do----------	Do.
84M129A------	698ct	Sp, 4 x 5/150-	S. 43° E.	14:00, 8 Oct. 84------	--Do----------	New site.
84M129B------	1424	--Do----------	--Do-----	14:01, 8 Oct. 84------	--Do----------	Do.
84M130A------	699ct	Sp, 4 x 5/210-	S. 58° E.	15:40, 8 Oct. 84------	--Do----------	New site. Similar to photo MM-32.
84M130B------	1425	--Do----------	--Do-----	15:42, 8 Oct. 84------	--Do----------	Do.
84M131A------	700ct	Sp, 4 x 5/150-	S. 50° E.	12:28, 9 Oct. 84------	--Do----------	New site. Same subject as MM-69.
84M131B------	1426	--Do----------	--Do-----	12:32, 9 Oct. 84------	--Do----------	Do.
84M131B------	1427	--Do----------	--Do-----	12:40, 9 Oct. 84------	--Do----------	Repeat of 1426.
84M132A------	701ct	Sp, 4 x 5/150-	S. 63° E.	16:07, 9 Oct. 84------	--Do----------	New site. Near site 83MM10.
84M132B------	1428	--Do----------	--Do-----	16:11, 9 Oct. 84------	--Do----------	Do.
84M133A------	702ct	Sp, 4 x 5/150-	N. 46° E.	16:56, 9 Oct. 84------	--Do----------	New site. Near site 83MM10.
84M133B------	1429	--Do----------	--Do-----	16:57, 9 Oct. 84------	--Do----------	Do.
84M134A------	703ct	Sp, 4 x 5/150-	N. 39° E.	10:10, 10 Oct. 84-----	--Do----------	New site. Matches Pierce's slide.
84M134B------	1430	--Do----------	--Do-----	10:12, 10 Oct. 84-----	--Do----------	Do.
84M135A------	704ct	Sp, 4 x 5/150-	N. 8° E.	11:35, 10 Oct. 84-----	--Do----------	New site. Near profile of Crone's.
84M135B------	1431	--Do----------	--Do-----	11:36, 10 Oct. 84-----	--Do----------	Do.
84M136A------	705ct	Sp, 4 x 5/150-	N. 54° E.	12:42, 10 Oct. 84-----	--Do----------	Do.
84M136B------	1432	--Do----------	--Do-----	12:43, 10 Oct. 84-----	--Do----------	Do.
84M137A------	706ct	Sp, 4 x 5/300-	S. 42° E.	13:32, 10 Oct. 84-----	--Do----------	New site. Lateral offset of fence.
84M137B------	1433	--Do----------	--Do-----	13:33, 10 Oct. 84-----	--Do----------	Do.
84M138A------	707ct	Sp, 4 x 5/300-	S. 72° E.	15:46, 10 Oct. 84-----	--Do----------	New site. Similar to MM-22.
84M138B------	1434	--Do----------	--Do-----	15:47, 10 Oct. 84-----	--Do----------	Do.

1 Symbol denotes year (1984), photographers initials (MM, Machette; M, Malde) site number; letter indicates separate views from station (Machette) or different film types (Malde). Machette's film: 70 mm black and white (84MM). Malde's film: A, 4 x 5-inch Ektachrome 64 color transparency sheet film; B, 4 x 5-inch Ilford FP-4 black-and-white sheet film; C, 8 x 10-inch Kodak Tri-X black-and-white sheet film; D, 70 mm Agfapan 25 black-and-white roll film; and E, 35 mm Kodak Technical Pan black-and-white roll film.

2 Numbers of photo negative(s) archieved under Machette and Malde respective files at U.S. Geological Survey Photo Library.

3 Camera and lens sizes in mm, except 4 x 5 and 8 x 10 cameras which are in inches.

Table 4.—Continued

[Abbreviations for type of view: S, single; Sp, stereopair; Pan, panorama; r-v, right-view; c-v, center-view; and l-v, left-view.]

Station [1]	U.S.G.S. number for negative [2]	Type of view and camera/lens size (mm) [3]	Orientation of view	Time (MST) and date	Scale: size, type, and distance from station	Remarks
REPEAT PHOTOGRAPHS:						
84MM2--------	57	Sp, 70/50----	S. 75° E.	12:02-12:10, 8 Oct. 84	Stadia rod, 6.3 m-------	Matches photos MM-24.
	58	Sp, 70/80----	--Do-----	12:05-12:15, 8 Oct. 84	--Do----------	
84MM3--------	59	Sp, 70/50----	S. 73° E.	14:05-14:13, 8 Oct. 84	2.7 m stadia, 24.5 m-----	Matches photos mM-2.
	60	Sp, 70/80----	--Do-----	14:07-14:15, 8 Oct. 84	--Do----------	
84MM4--------	61	Sp, 70/50----	N. 51° E.	14:32-14:41, 8 Oct. 84	2.7 m stadia, 20.5 m-----	Matches photos MM-3.
	62	Sp, 70/80----	--Do-----	14:34-14:45, 8 Oct. 84	--Do----------	
84MM5--------	63	Sp, 70/50----	N. 20° E.	15:05-15:09, 8 Oct. 84	2.7 m stadia rod, 27.3 m-	Matches photos MM-4.
	64	Sp, 70/80----	--Do-----	15:07-15:10, 8 Oct. 84	--Do----------	
84MM6--------	65	--Do---------	S. 88° E.	10:00-10:04, 9 Oct. 84	Ranging pole, 0.5 m marks	Matches photos MM-6.
84MM8--------	67	Sp, 70/50----	N. 87° E.	10:47-10:55, 9 Oct. 84	--Do----------	Matches photos MM-18.
84MM11-------	70	Sp, 70/80----	N. 16° W.	15:55-15:57, 9 Oct. 84	--Do----------	Matches photos MM-11.
84MM12-------	71	--Do---------	S. 47° E.	16:35-16:36, 9 Oct. 84	None(?)----------	Similar to photos MM-12.
84MM14-------	73	Sp, 70/50----	S. 3° W.	11:23-11:25, 10 Oct. 84	None----------	Matches photos MM-34.
84MM15-------	75	--Do---------	N. 10° E.	12:15-12:18, 10 Oct. 84	2.5 m stadia rod---------	Matches photos MM-33.
84MM17-------	77	--Do---------	S. 65° E.	13:15-13:16, 10 Oct. 84	2.9 m stadia rod---------	Matches photos MM-32.
PHOTOGRAPHS FROM UNMARKED STATIONS:						
----------	78	Sp, 70/80----	North----	13:32-13:35, 10 Oct. 84	None----------	Scarps north of road to Birch Spring.
----------	79	S, 70/80-----	--Do-----	14:00, 10 Oct. 84------	--Do----------	Do.

1 Symbol denotes year (1984), photographer (MM, Machette; M, Malde) site number; letter indicates separate views from station (Machette) or different film types (Malde). Machette's film: 70 mm black and white (84MM). Malde's film: A, 4 x 5-inch Ektachrome 64 color transparency sheet film; B, 4 x 5-inch Ilford FP-4 black-and-white sheet film; C, 8 x 10-inch Kodak Tri-X black-and-white sheet film; D, 70 mm Agfapan 25 black-and-white roll film; and E, 35 mm Kodak Technical Pan black-and-white roll film.

2 Numbers of photo negative(s) archieved under Machette and Malde respective files at U.S. Geological Survey Photo Library.

3 Camera and lens sizes in mm, except 4 x 5 and 8 x 10 cameras which are in inches.

Table 5. Data for experiment in measuring distances using photogrammetric plotter and oblique stereopair photographs

[All distances in meters; n.a., not applicable.]

INCLINED (R) AND HORIZONTAL (R′) DISTANCE BETWEEN MARKER PIN (A-D) AND CAMERA STATION

Camera stations	A		B		C		D	
	R	R′	R	R′	R	R′	R	R′
84M123	15.72	15.65	16.07	15.85	16.59	16.35	20.45	19.95
84M124	14.43	14.30	15.76	15.55	17.39	17.10	22.40	21.80
84M125	10.12	9.71	13.63	13.16	17.06	16.50	23.41	22.60
84M126	10.47	10.20	13.76	13.40	17.00	16.55	23.32	22.60

HEIGHT OF CAMERA LENS (AND BASE MARKER) FOR DIFFERENT CAMERA STATIONS

Camera station and height of base	35 mm	70 mm	4 x 5 inch	8 x 10 inch
84M123 (1.60)	N.a.	2.690	2.895	2.905
84M124 (0.95)	n.a.	2.200	2.405	2.415
84M125 (0.00)	1.500	1.520	1.725	1.735
84M126 (0.37)	1.460	1.480	1.685	1.695

DISTANCE BETWEEN DIAPHRAM OF CAMERA LENS AND MARKER PIN (A-D)

Camera station to marker pin	35 mm [1]	70 mm [2]	4 x 5 inch [3]	8 x 10 inch [4]
84M123 to A	n.a.	20.28	20.20	20.14
to B	n.a.	16.47	16.41	16.35
to C	n.a.	15.91	15.86	15.80
to D	n.a.	15.69	15.65	15.59
84M124 to A	n.a.	22.18	22.11	22.05
to B	n.a.	17.27	17.20	17.14
to C	n.a.	15.65	15.59	15.53
to D	n.a.	14.35	14.31	14.25
84M125 to A	23.10	23.10	23.03	22.97
to B	16.77	16.77	16.70	16.66
to C	13.35	13.35	13.28	13.22
to D	9.84	9.84	9.77	9.71
84M126 to A	23.10	23.10	23.02	22.96
to B	16.82	16.82	16.75	16.69
to C	13.60	13.60	13.53	13.47
to D	10.33	10.33	10.33	10.21

1 Diaphram of lens is 4 cm behind camera marker along line of view.
2 Diaphram of lens is 4 cm behind camera marker along line of view.
3 Diaphram of lens is directly above camera marker along line of view.
4 Diaphram of lens is 6 cm in front of camera marker along line of view.

References

Anonymous, 1981, Earthquake trail at Point Reyes National Seashore [California]: U.S. Geological Survey Earthquake Information Bulletin, v. 13, no. 2, p. 52-61.

Bucknam, R. C., and Anderson, R. E., 1979, Estimation of fault-scarp ages from a scarp height-slope angle relationship: Geology, v. 9, p. 11-14.

Crone, A. J., 1985, Fault scarps, landslides, and other features associated with the Borah Peak, Idaho earthquake of October 28, 1983 (with a section on the Doublespring Pass road trench by M. H., Hait, Jr.), in R. S. Stein and R. C. Bucknam, eds., Proceedings of Conference XXVIII--The Borah Peak Earthquake: U.S. Geological Survey Open-File Report (this volume).

Crone, A. J., and Machette, M. N., Surface faulting accompanying the Borah Peak earthquake, central Idaho: Geology, v. 12, no. 11, p. 664-667.

Harrison, A. E., 1974, Reoccupying unmarked camera stations for geologic observations: Geology, v. 2, p. 469-471.

Lambert, P. W., editor, 1984, Materials and techniques [for repeat photography]: Repeat Photography Newsletter, v. 1, no. 1, p. 4-6. (Available from Department of Geosciences, West Texas State University, Canyon, Texas, 79016.)

Machette, M. N., and McGimsey, R. G., 1983, Map of Quaternary and Pliocene faults in the Socorro and western part of the Fort Sumner 1° x 2° quadrangles, central New Mexico: U.S. Geological Survey Miscellaneous Field Studies Map MF-1465-A with pamphlet, scale 1:250,000.

Malde, H. E., 1973, Geologic bench marks by terrestrial photography: U.S. Geological Survey Journal of Research, v. 1, p. 193-206.

Morisawa, Marie, 1975, Tectonics and geomorphic models, in W. N. Melham and R. C. Flemal, eds., Theories of landform development: Binghamton, New York, State University of New York, Publications in Geomorphology, no. 6, p. 199-216.

Nash, D. B., 1980, Morphologic dating of degraded normal fault scarps: Journal of Geology, v. 88, p. 353-360.

Pelton, J. R., Meissner, C. W., and Smith, K. D., 1984, Eyewitness account of normal surface faulting: Bulletin of the Seismological Society of America, v. 74, p. 1083-1089.

Rodgers, G. F., Malde, H. E., and Turner, R. M., 1984, Bibliography of repeat photography for evaluation of landscape change; compiled and annotated, with an introduction: Salt Lake City, University of Utah Press, 179 p.

Ryall, Alan, Slemmons, D. B., and Gedney, Larry, 1966, Seismicity, tectonism, and surface faulting in western United States during historic time: Bulletin of the Seismological Society of America, v. 56, p. 1105-1135.

Thatcher, Wayne, 1974, Strain release mechanism of the 1906 San Francisco earthquake: Science, v. 184, no. 4143, p. 1283-1285 and cover photo.

Wallace, R. E., 1977, Profiles and ages of young fault scarps, north-central Nevada: Geological Society of America Bulletin, v. 88, p. 1267-1281.

_____1980a, Degradation of the Hebgen Lake fault scarps of 1959: Geology, v. 8, p. 225-229.

_____1980b, G. K. Gilbert's studies of faults, scarps, and earthquakes, in E. L. Yochelson, ed., The scientific ideas of G. K. Gilbert: Geological Society of America Special Paper 183, p. 35-44.

_____1984, Eyewitness account of surface faulting during earthquake of 28 October, 1983, Borah Peak, Idaho: Bulletin of the Seismological Society of America, v. 74, p. 1091-1094.

Witkind, I. J., 1964, Reactivated faults north of Hebgen Lake [Montana]: U.S. Geological Survey Professional Paper 435-G, p. 37-50.

Identifying Active Faults by Aerial Photography: A Comparison of the Lost River Fault Before and After the Borah Peak Earthquake of October 28, 1983

by

Roy M. Breckenridge
Idaho Geological Survey
Moscow, Idaho 83843

ABSTRACT

Aerial photography is a valuable and effective tool in identifying active basin and range faults where geologic mapping and seismic research are unavailable. The Lost River fault is an excellent example for comparing studies of scarp recognition and fault interpretation. The pre-1983 Borah Peak earthquake scarp can be readily identified and mapped using satellite imagery or aerial photographs. Many of the surface faulting characteristics noted in post-earthquake investigations such as splays, grabens, segmented scarps, evidence for recurrent faulting, and associated landslides are evident on the pre-earthquake photographs.

INTRODUCTION

This paper describes the observable features of the Lost River fault by using aerial photographs taken before the October 28, 1983, Borah Peak earthquake and compares them with the subsequent surface rupture. Comparative studies like this eventually can provide information for hazard assessment and disaster mitigation by delineating other active faults. This is especially true for Idaho where the tectonic setting is complex, and little work has been done on potentially active faults. Furthermore, the seismicity of the state has not been thoroughly studied and only a preliminary list of earthquakes exists (Breckenridge and others, 1984).

Several studies (Greensfelder, 1976; Howard, 1978) have discussed active faulting in Idaho, but these were based mostly on a fault inventory by Witkind (1972). Seismic studies have regionally addressed the Intermountain Seismic Belt and some specific local areas, yet earthquake potential for most of Idaho, including the Idaho Seismic Zone (Smith and Sbar, 1974), remains unknown. In an attempt to assess geologic hazards in Idaho, the Northwest Regional Commission funded a Landsat Application Study by the Idaho Geological Survey.

PREVIOUS WORK

Ross (1947) described the general geology of the region and the structural geology of the Lost River Range. He mentioned a fault on the west side of the range, but did not map one. Instead, he emphasized a

set of northeast-southwest trending faults. Baldwin (1951) identified a major fault along the Lost River Range front and called it the Lost River fault. This fault was also mapped to the north by Mapel and others (1965). The fault was noted by Witkind (1972) on his 1:500,000-scale map of active faults, and was designated as late Quaternary (Wisconsin) in age for most of its trace. Scott (1982) mapped three segments of the fault at apexes of alluvial fans of Cedar, Lower Cedar, and Willow creeks. Scott's map shows the fault cutting Pinedale and pre-Pinedale deposits at Willow Creek and Cedar Creek but not disturbing Holocene alluvial fans or colluvium. Hait and Scott (1978) presented evidence of Holocene displacement at Willow Creek, as well as apparent recurrent movement on the fault. Othberg and Breckenridge (1981) demonstrated the capability of high-resolution return beam vidicon (RBV) satellite imagery to identify potentially active faults, including the Lost River fault.

PROCEDURE

After the October 28, 1983, event, the pre-earthquake photography of the area was reassessed. Interpretation of the satellite imagery proved accurate at a scale of 1:500,000 in the area of the new scarp, and even showed the branch at Willow Creek summit (Figure 1). In the satellite study, the Lost River fault was classified as part Holocene and part Pleistocene in age. The length of the potentially active fault was judged from the satellite imagery to be about 47 kilometers. However, Holocene faulting south of Leatherman Peak was not mapped. Recognition of scarplets or other associated small-scale fault-related features would have been precluded by the scale of the imagery.

The present analysis used more detailed high-resolution color-infrared U-2 photography. Transparencies from NASA flight 73-172, flown 5 October 1973, were viewed stereoscopically on an interpretive light table. Photographic coverage was available along the Lost River front from Upper Cedar Creek on the south to Lime Creek on the north. Standard photogeologic techniques for fault recognition (Othberg and Breckenridge, 1981) were employed, and fault morphology characteristics (Bull and McFadden, 1977) were also examined. For comparison, a series of color oblique photographs flown the day after the big earthquake was studied, in addition to the information collected in the field by a team of University of Idaho geologists a week after the event. Fault rupture data from Crone and others (1984) was also used for comparison with the photography. Additional information was shared by observations of other geologists in the area and by newspaper accounts.

RESULTS

The trace of the pre-earthquake scarp is easily recognized on the photography, and many of the charactersitics of the 1983 event are apparent in previous faulting. Obviously, this interpretation was enhanced by the knowledge of the latest earthquake, yet the comparison demonstrates the reliability of careful observation. Although the faulting had been previously mapped and shown to be late Pleistocene and

Holocene in certain areas, much more information about the fault could have been determined from the photography before the earthquake.

Nearly the entire trace of the 1983 event was manifested by previous rupture (Figure 2). The fault system can be traced continuously, yet separate segments of the scarp appear differently due to variations in factors such as rock type, erosional texture, vegetation, slope, and ground-water and soil development. Most segments could be readily recognized from characteristics directly resulting from older faulting.

Terms for the parts of a scarp profile have been discussed by Wallace (1977, 1984). Most segments of the fault are probably discernible due to the reflectance of the unvegetated break in slope. In some places of large displacement, the actual scarp crest and free face may be visible, but most of the scarp seems to be recognized from the debris slope and wash slope. In areas with more than one fault trace pattern, complex ruptures formed en echelon scarplets, stair-step scarps, or grabens. Graben formation is suggested by topographic depressions and the resulting drainage and vegetation changes. The grabens seem to be confined to the areas of thicker alluvial cover. The mechanism that forms grabens in alluvial materials over dip-slip faults has been demonstrated by Lade and Cole (1984), and apparently is common in basin and range faulting. Evidence on the aerial photography for recurrent faulting is indicated by the offset of landforms and morphologic differences in separate fault segments. Scarp height and slope angle vary with the type of surface rupture and affect the prominence of the trace. The transection of segments also seems to indicate recurrent activity on different parts of the fault.

The McCaleb section of the fault, south of the latest rupture, is interpreted as very "fresh" from Upper Cedar Creek to north of Jones Creek. The difference in lithology and complementary strike of outcrops from Lone Cedar Creek to north of Elkhorn Creek made that portion distinguishable, but not distinctly attributable to scarp formation. The Elkhorn Creek-Cedar Creek-Rock Creek-Willow Creek section is distinct and can be recognized to transect glacial deposits, fan alluvium, and colluvium at the mountain front. The segment from Willow Creek across the summit to Sheep Creek is topographically more subdued, and the branching of scarplets is recognizable. A number of smaller scarps are visible in this section, but it was not determined whether they represent faulting or slope movements. From Gooseberry Creek to Devil Canyon the scarp has a fresher appearance. From the pre-earthquake photography, the part of the fault that ruptured in the October 28 event appears to be between two geomorphically "fresher" scarps.

Alluvial fans and colluvial aprons form at the margin of the front, in part owing to the active tectonics of the area. Pierce and Scott (1982) have pointed out relationships of alluvial fan deposition and climatic changes in southeastern Idaho. These landforms also seem to have the best chance for recording the tectonic history of this area. Fan remnants of Scott's (1982) "Fan Alluvium 4" seem to be truncated by a tectonic feature near Upper Cedar Creek. On the Jones Creek alluvial fan, the drainage pattern changes from confluent to diffluent, perhaps indicating a response to slope change.

Recognition of associated earthquake features such as landslides, sand boils, and liquefaction phenomena was also attempted. Springs and old landslides are generally common along the length of the old fault trace. Most of the features are small, but recognizable by the infrared response to vegetation. The Birch Creek landslide has had previous movement and was the largest mass movement noted. No sand boil activity was readily noted--perhaps due to the scale--although some of these features had reportedly existed previous to the October 28 event and had been filled with debris. On a larger scale, the Big Lost River has a suspect position at the east margin of the valley, indicating active subsidence at or near the mountain front. The location of "drowned" channels at Thousand Springs and the modification of the distal ends of all the fans on the Lost River front by the Big Lost River indicates tilting of the basin block toward the range front.

Procedures for photo interpretation of young faults have been discussed by a number of authors and are not reviewed here. For the most part, the criteria used could be checked with another source of photography, a topographic map, or ground information. Familiarity with the area is particularly valuable. The main sources of misinterpretations are considered to be the following: (1) bedrock stratigraphy parallel to mountain front; (2) irrigation canals and ditches; (3) artifacts from sagebrush spraying; (4) vegetation differences in grazing caused by fence lines; (5) tracks from 4-wheel drive vehicles, seismic exploration lines, and drill holes; and (6) photographic artifacts (a bubble on the emulsion was inadvertantly classed as a sand boil).

CONCLUSIONS

The Lost River fault can be readily identified from satellite and aerial photography dated prior to the October 28, 1983, earthquake, although some interpretations obviously benefit from knowledge of this event. Researchers have generally been conservative in assigning young faults to a category of capable movement, partly due to the lack of seismic information and age-dating criteria. Aerial photographs of basin and range areas should be analyzed for more information on faulting history. Although photogeologic techniques are commonly known, they have not been widely used. Yet, they are inexpensive and can augment seismic information that is both expensive to fund and difficult to acquire in the unpopulated parts of the basin and range.

REFERENCES

Baldwin, E.M., 1951, Faulting in the Lost River Range area of Idaho: American Journal of Science, v. 249, p. 884-902.

Breckenridge, R.M., K.F. Sprenke, and B.A. Stryhas, 1984, List of Idaho earthquakes, 1872-1983: Idaho Bureau of Mines and Geology Technical Report 84-1, 41 p.

Bull, W.B. and L.D. McFadden, 1977, Tectonic geomorphology north and south of the Garlock fault, California, in D.O. Doehring, editor, Geomorphology in Ahrid Regions: Proceedings, Eighth Annual Geomorphology Symposium, State University of New York at Binghamton, p. 115-138.

Crone, A.J., M.N. Machette, M.G. Bonilla, J.J. Lienkaemper, R.C. Bucknam, K.L. Pierce and W.E. Scott, 1985, Characteristics of Surface Faulting Accompanying the Borah Peak Earthquake, central Idaho, in Workshop XXVIII on the Borah Peak earthquake: U.S. Geological Survey Open-File Report, in press.

Greensfelder, R.W., 1976, Maximum probable earthquake acceleration on bedrock in the State of Idaho: Idaho Department of Transportation, Division of Highways, Research Project No. 79, 69 p.

Hait, M.H. and W.E. Scott, 1978, Holocene faulting, Lost River Range, Idaho [abstract]: Geological Society of America Abstracts with Programs, v. 10, p. 217.

Howard, K.A., 1978, Preliminary map of young faults in the United States as a guide to possible fault activity: U.S. Geological Survey Map MF 916, 2 sheets.

Lade, P.V. and D.A. Cole, Jr., 1984, Ground rupture zones in alluvium over dip-slip faults: Proceedings 21st Engineering Geology and Soils Engineering Symposium, University of Idaho, Moscow, p. 29-44.

Mapel, W.J., W.H. Read, and R.K. Smith, 1965, Geologic map and sections of the Doublespring quadrangle, Custer and Lemhi Counties, Idaho: U.S. Geological Survey Geologic Quadrangle Map GQ-464, scale 1:24,000.

Othberg, K.L. and R.M. Breckenridge, 1981, Interpreting geologic hazards in Idaho from remotely sensed imagery: Idaho Bureau of Mines and Geology Technical Report 81-6, 65 p.

Pierce, K.L. and W.E. Scott, 1982, Pleistocene episodes of alluvial-gravel deposition, southeastern Idaho, in Bill Bonnichsen and R.M. Breckenridge, editors, Cenozoic Geology of Idaho, Idaho Bureau of Mines and Geology Bulletin 26, p. 685-702.

Ross, C.P., 1947, Geology of the Borah Peak quadrangle, Idaho: Geological Society of America Bulletin, v. 58, no. 12, p. 1087-1125.

Scott, W.E., 1982, Surficial geologic map of the eastern Snake River Plain and adjacent areas, 111° to 115° W., Idaho and Wyoming: U.S. Geological Survey Miscellaneous Geologic Investigations Map MI-1373, scale 1:250,000.

Smith, R.B. and M.L. Sbar, 1974, Contemporary tectonics and seismicity of the western United States with emphasis on the Intermountain Seismic Belt: Geological Society of America Bulletin, v. 85, p. 1205-1218.

Wallace, R.E., 1977, Profiles and ages of young fault scarps, north-central Nevada: Geological Society of America Bulletin, v. 88, no. 9, p. 1267-1281.

--------, 1984, Fault scarps formed during the earthquakes of October 2, 1915, in Pleasant Valley, Nevada, and some tectonic implications: U.S. Geological Survey Professional Paper 1274-A, 33 p.

Witkind, I.J., 1972, Preliminary map showing known and suspected active faults in Idaho: U.S. Geological Survey Open-File Report 75-278, 71 p., 1 plate scale 1:500,000.

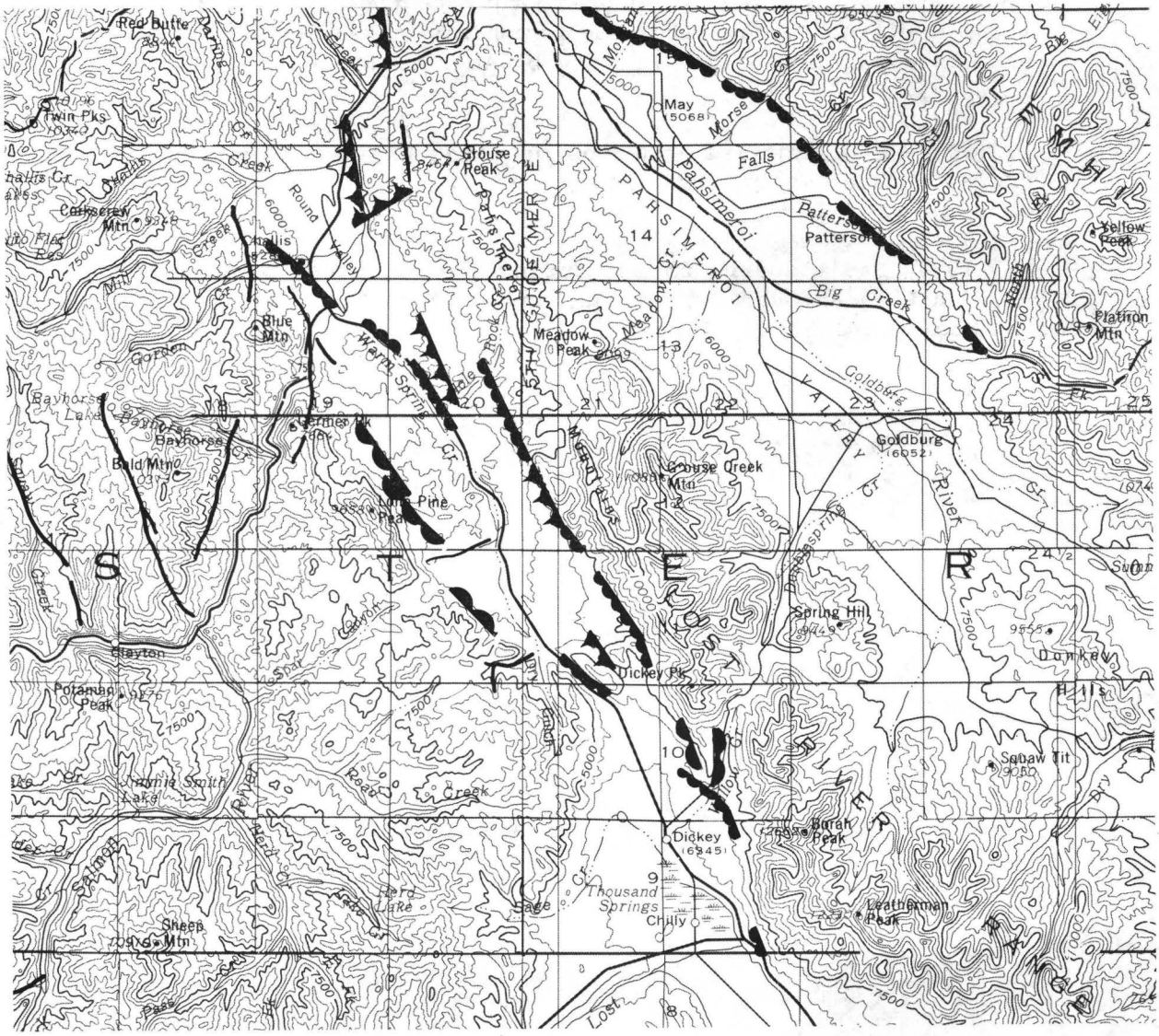

Figure 1. Map of the Lost River fault area showing faults mapped from satellite imagery (from Othberg and Breckenridge, 1981, Plate 1). Explanation: ▲▲▲▲ Scarp. Best potential for actual trace of young fault; fresh and undissected; possible Holocene fault scarp. ▬▬▬▬ Low Sinuosity Mountain Front or Escarpment. Good potential for actual trace of young fault; may be dissected and somewhat eroded, but foot of front/escarpment is virtually straight and unbroken; location of possible late Quaternary faulting. ▬▬▬▬ Moderate Sinuosity Mountain Front or Escarpment. Least potential for actual trace of young fault; easily identified, but has been embayed and pedimented so that a relatively sinuous boundary exists; location of possible early Quaternary or late Tertiary faulting.

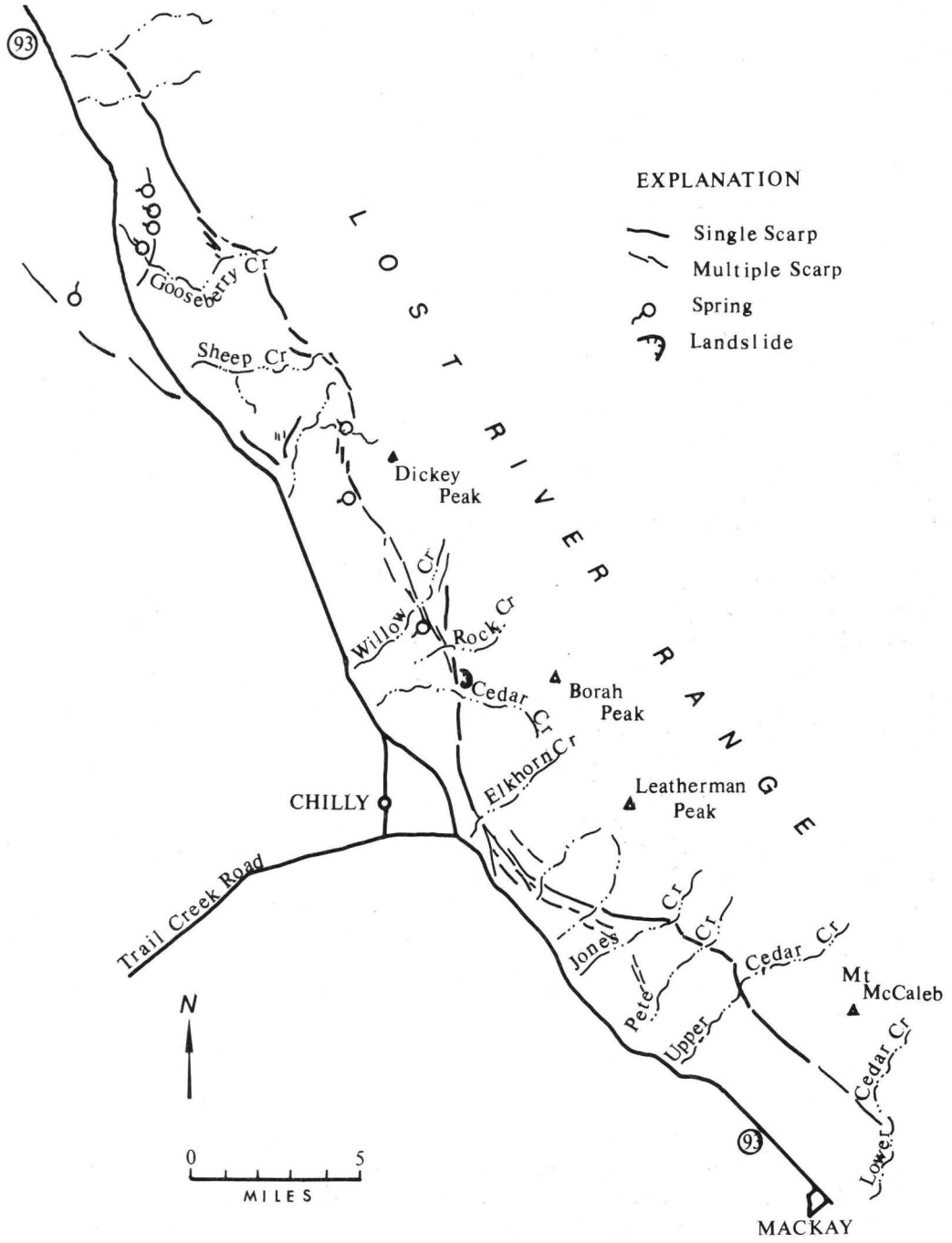

Figure 2. Generalized map of pre-1983 Lost River fault scarp interpreted from NASA photography (Flight 73-172, 5 October 1973). See map in Crone and others, 1985, for fault that ruptured in the October 28, 1983, Borah Peak earthquake.

LATE QUATERNARY ACTIVITY ALONG THE LONE PINE FAULT, EASTERN CALIFORNIA

LESTER LUBETKIN

U.S. Forest Service, Eldorado National Forest, Placerville, Calif. 95630

MALCOLM M. CLARK

U.S. Geological Survey, Menlo Park, Calif. 94025

ABSTRACT

The Lone Pine fault is a north-trending secondary break in the Owens Valley fault zone, 1.4 km west of Lone Pine, Calif. This fault forms a prominent east-facing scarp across an abandoned fan of the Tioga (latest Pleistocene) glaciation, and was the site of significant displacement during the 1872 Owens Valley earthquake. Knowledge of the character and amount of slip at this site in 1872 may be of value in assessing earthquake potential in this region and in other parts of the Great Basin.

Dip slip along this scarp from the 1872 earthquake was 1 to 2 m. A young debris flow that crosses the scarp has been offset 6 to 7 m right laterally and 1 to 1.5 m vertically, apparently in 1872. Average total dip slip of this fan surface is about 5.5 m. About three 1872-size earthquakes could have produced the scarp. This number of events is also indicated by desert varnish patterns on boulders in the fault scarp and by scarp morphology. An average recurrence interval for three such events is 3,300 to 10,500 yrs. This estimate is based on the age of the fan surface, which is bracketed by a 21,000 year-old shoreline of Lake Owens, and by the time of abandonment of the fan, about 10,000 years ago. This average recurrence interval, combined with the total 1872 offset of the debris flow, gives an average late Quaternary slip rate of 0.6-2 mm/yr for the Lone Pine fault. The average recurrence interval applies to the Lone Pine fault only, rather than to the Owens Valley fault zone as a whole. Other fault scarps near Lone Pine suggest that earthquakes occur in this region more frequently than every 3,300 to 10,500 years.

INTRODUCTION

The great earthquake of March 26, 1872 in Owens Valley was one of the three largest historic shocks in California. The earthquake produced extensive surface ruptures along the Owens Valley fault zone and caused strong ground shaking throughout a vast region (Oakeshott and others, 1972). Yet surprisingly little has been published about the extensive surface ruptures of 1872 and almost nothing about previous late Quaternary faulting in this region. Although several geologists reported important characteristics of the surface rupture during the 35 years after the earthquake (Whitney, 1872, 1888; Gilbert, 1884; Hobbs, 1910), and more recent investigations verified reported 1872 right slip of about 4 m (Bateman, 1961; Bonilla, 1968), no investigations

studied displacement from earlier earthquakes, a crucial element in seismic hazard assessment. Indeed, the prominent 6.5 m-high scarp of the Lone Pine fault that is the subject of this report was widely and incorrectly identified as the result solely of displacement in 1872 (for example, Gilbert, 1884; Hobbs, 1910). Knowledge of the character and amount of slip in 1872 and during earlier earthquakes may be of value in assessing slip rates and recurrence intervals for faults along the eastern front of the Sierra Nevada and elsewhere in the Great Basin, particularly those with oblique-normal slip, as at Borah Peak in 1983.

This study focuses on late Quaternary activity along the Lone Pine fault, a major strand of the Owens Valley fault zone of eastern California (fig. 1). We investigated a prominent scarp of this fault where it crosses an abandoned fan of Lone Pine Creek. At this place the scarp preserves some of the clearest evidence in the Owens Valley fault zone of 1872 and earlier displacement. From fault scarp morphology, weathering, and sediments we have estimated the amount of displacement that occurred along the Lone Pine fault during the 1872 earthquake, and have attempted to characterize both slip rates and recurrence of large earthquakes along this fault during late Quaternary time. This report is based on Lubetkin (1980) and unpublished field investigations by Clark. We concentrate here on the dip-slip component of displacement; detailed study of the strike-slip component is in progress.

The Owens Valley fault zone near Lone Pine consists of a main trace, several prominent secondary traces, and many branch and smaller secondary traces (fig. 1). The main fault trace extends across the western part of Lone Pine and forms the east side of Diaz Lake. Prominent secondary traces lie as much as 1.4 km west of the main trace at Lone Pine and extend southward discontinuously to Diaz Lake. Lubetkin (1980) informally named the most westerly of these prominent secondary faults the Lone Pine fault.

Scarps of the Lone Pine fault across the surface of the abandoned fan of Lone Pine Creek (fig. 2) locally reach 6.5 m high. The fan surface is inactive except for ongoing encroachment of locally derived colluvium along the western and northwestern margins and infrequent debris flows from the flanking hills along one of the relict channels on the fan surface.

1872 FAULT SLIP

We have estimated offset in 1872 of the abandoned outwash fan from three sources. One source is detailed scarp profiles and weathering features of the scarp. Another is a backhoe trench that exposed the fault and strata of the fan. The third source is detailed mapping of a recent debris flow offset by the Lone Pine fault. The offset debris flow provides the total slip for one site, whereas the trench and profiles yield dip slip only, but at many places along the scarp.

Profiles and Weathering Features of the Fault Scarp

We estimate a dip slip component of 1.2 to 2.0 m along the Lone Pine fault in 1872, using both surface profiles measured across the fault scarp in 1978

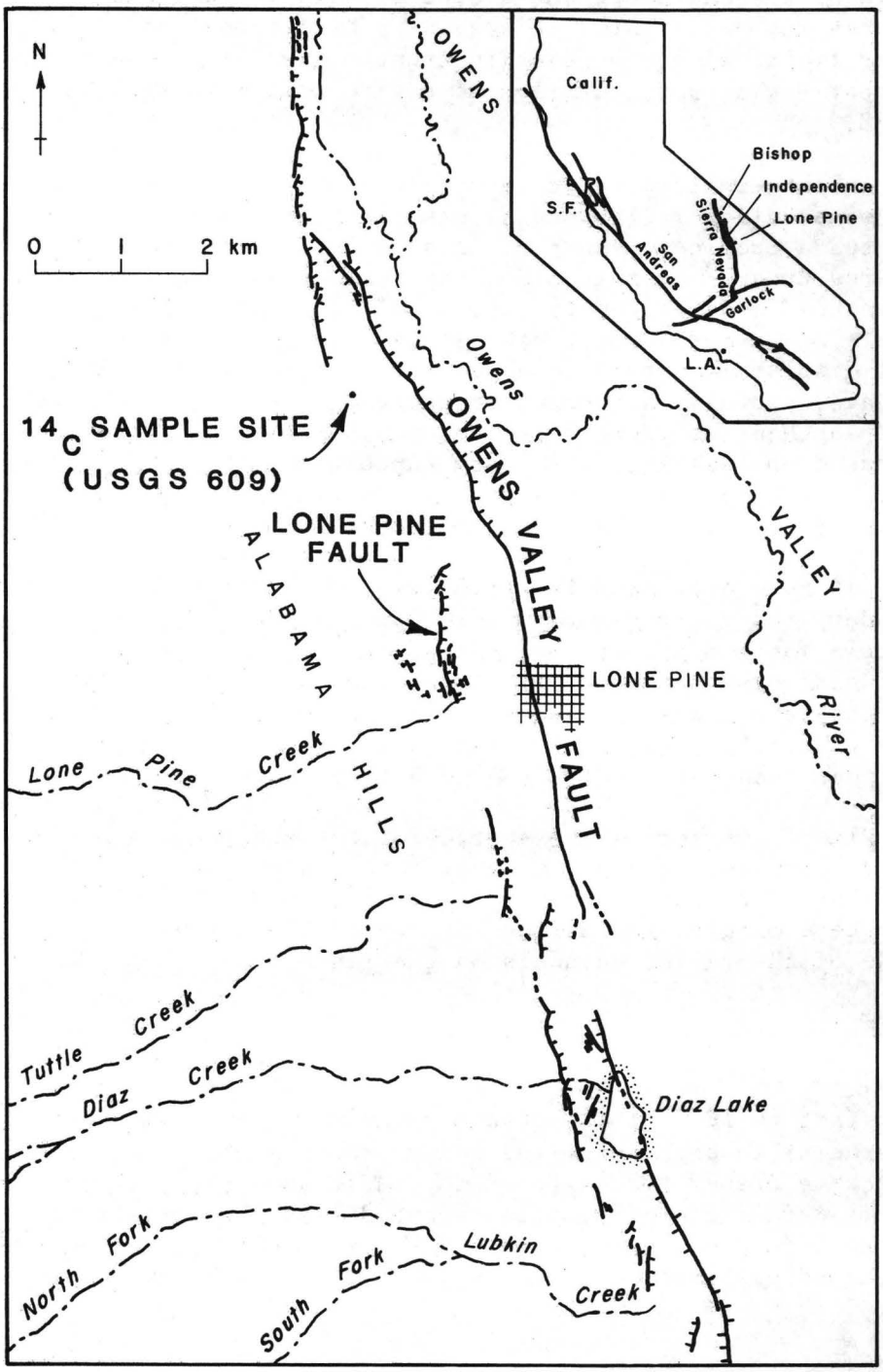

Figure 1 Map showing location of Owens Valley fault zone and Lone Pine fault, eastern California. Hachures on downthrown side of scarps.

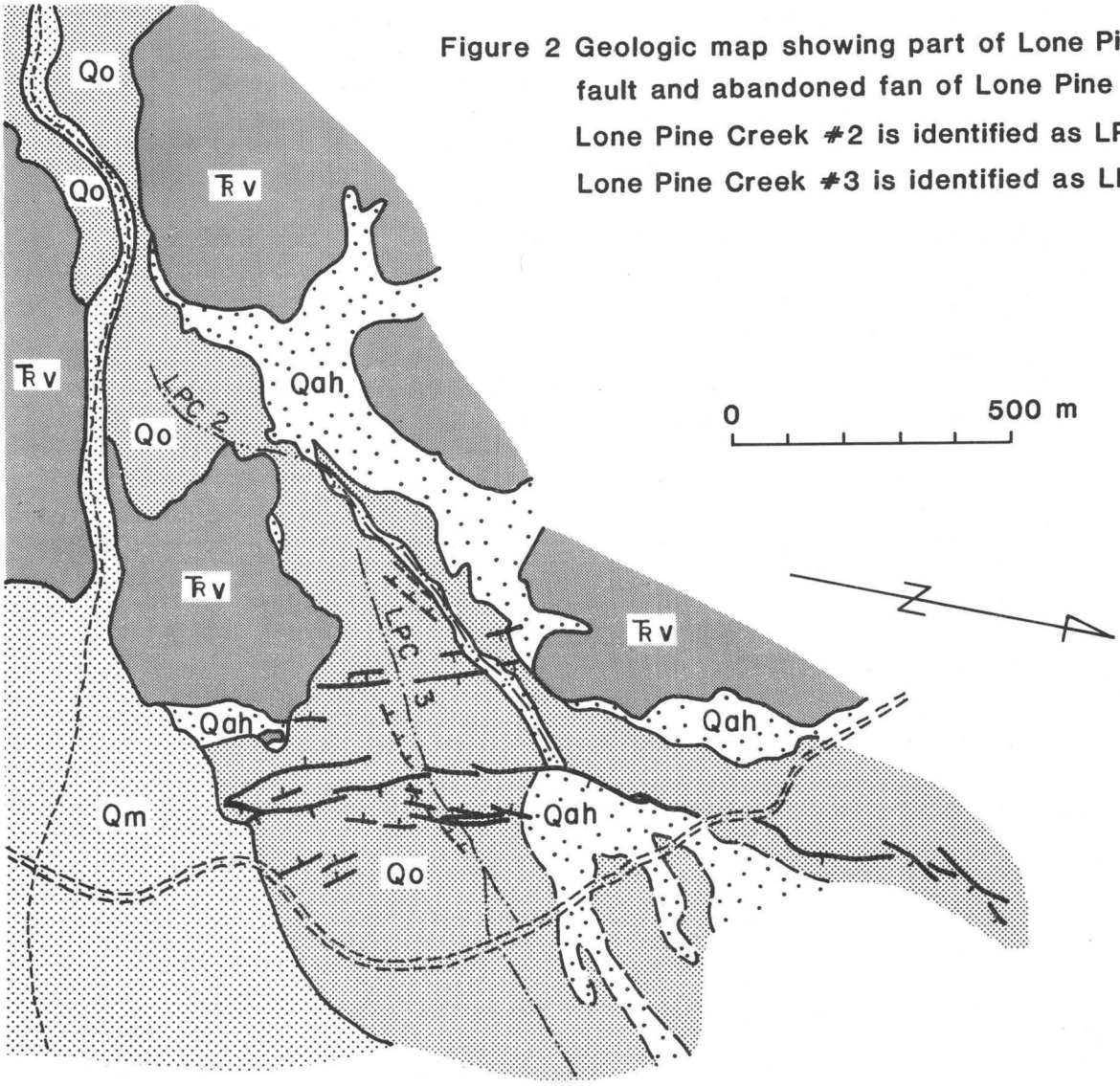

Figure 2 Geologic map showing part of Lone Pine fault and abandoned fan of Lone Pine Creek. Lone Pine Creek #2 is identified as LPC 2 and Lone Pine Creek #3 is identified as LPC 3.

Qm — Holocene alluvium, predominantly sierran debris

Qah — Holocene colluvium/alluvium derived from Alabama Hills

Qo — Tioga(?) glacial outwash, sierran debris

Tr v — Triassic metavolcanic bedrock

contact, dashed where approximate

fault, hachure on downthrown side

terrace, symbol marks crest of channel bank, hachures on terrace side

position of abondoned channel

Whitney Portal Road

Los Angeles Aqueduct

and reconstructed 1872 post-earthquake profiles (Lubetkin, 1980). The 1872 profiles came from detailed examination of features within the Lone Pine fault scarp and comparison of these features to their appearance in 1907 photographs.[1] The mean dip slip component for all profiles is 1.6±0.4 m. Our estimates of 1872 dip slip are less than the associated total scarp heights by factors of 1.5 to 4.

In profile, the Lone Pine fault scarp has an upper convex portion, a steep mid-slope, and a lower concave portion (fig. 3). The scarp is compound, the result of more than one slip event. The steep midslope is the erosionally modified scarp from the most recent slip event, whereas the upper convex portion is the modified scarp remnant of one or more older slip events. The lower concave portion is a sedimentary apron that conceals the original fault scarp and consists of colluvium and wash deposits from the upper part of the scarp.

The fault scarp is the modified surface expression of a fault at depth. The originally exposed fault surface is no longer completely preserved, hence the position and dip of the fault plane cannot be directly measured without subsurface exploration. Examination of natural and artificial cuts across the Owens Valley fault zone in the Lone Pine area show that the fault planes commonly have a steep dip (70° to 90°) and trend parallel to the scarp of the Lone Pine fault. Erosional retreat of one meter or more is common for the youngest fault scarps.

Figure 4 shows profiles of the present ground surface at 8 sites, prepared by a method similar to that used by Wallace (1977) and Bucknam and Anderson (1979). From these profiles, 1872 post-earthquake surface profiles are reconstructed by identification of features of the present fault scarp that record, or are remnants of, the 1872 pre-earthquake scarp. These features include the upper convex slope, the wash-controlled slope, exposed desert varnish rings, caliche coatings on clasts, and weathering of cobbles and boulders. The exposed varnish rings show the actual position of an earlier ground surface (Smith, 1979), whereas caliche coatings and disintegrated clasts, which develop near, but below the surface (Birkeland, 1974), commonly indicate only a lower limit for position of the earlier surface. The reconstructed 1872 profiles closely approximate the scarp just after the earthquake, before erosional or depositional modification.

Detailed comparisons between 1907 and 1978 conditions at various places along the fault scarp show that the upper convex slope has experienced little degradation or aggradation, except for some narrow rills that have cut into the scarp. In contrast, material eroded from the midslope buries the lower portion of the scarp. Figure 5 shows these relationships with photographs of the same site taken in 1907 and 1978. The photographs show no more than a few centimeters of change in the ground surface. The upper convex slope therefore can be treated as a surface that has been essentially stable for at least 71 years.

1 Taken by Willard D. Johnson during a study of the effects of the 1872 earthquake. The photos are in the Denver library of the U.S. Geological Survey. Johnson's work was reported by Hobbs (1910).

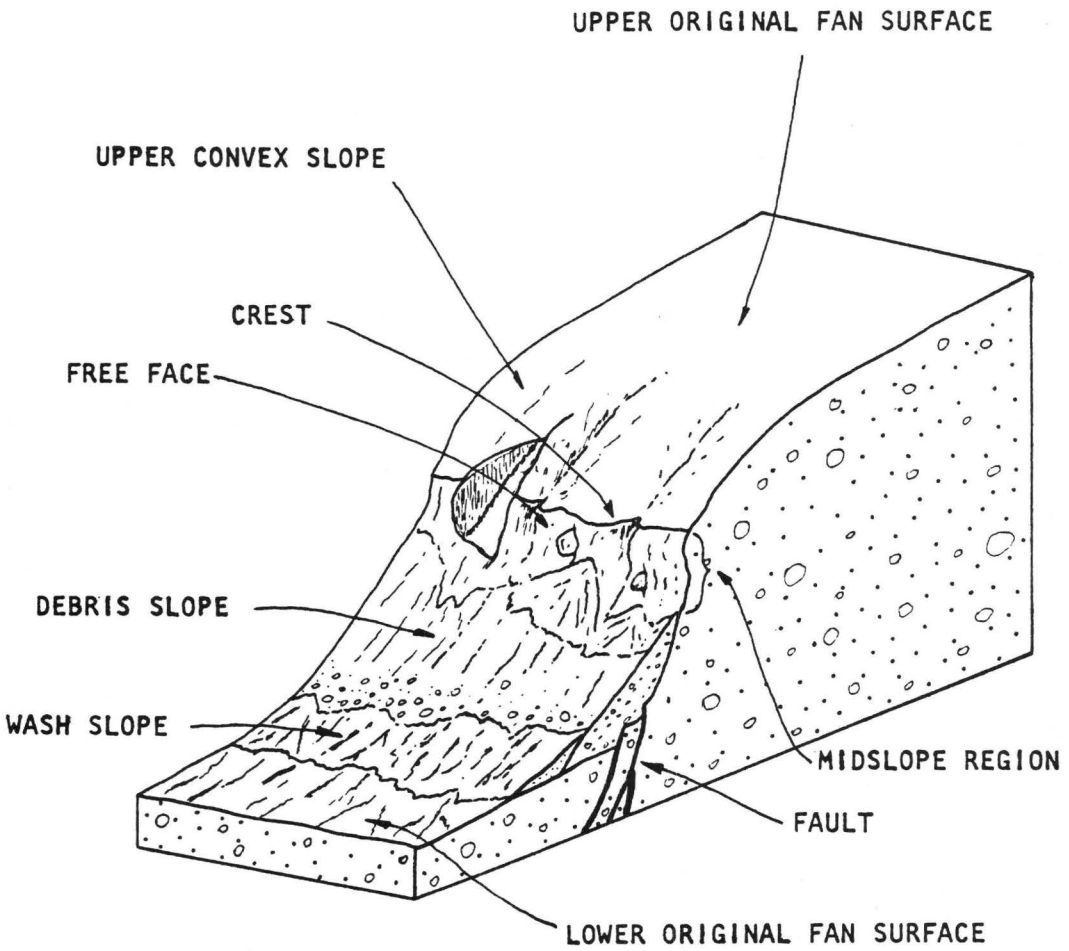

Figure 3 Idealized scarp profile showing units described in text. Modified from Wallace (1977), terminology from Wallace (1977), Young (1972), and Cooke and Warren (1973).

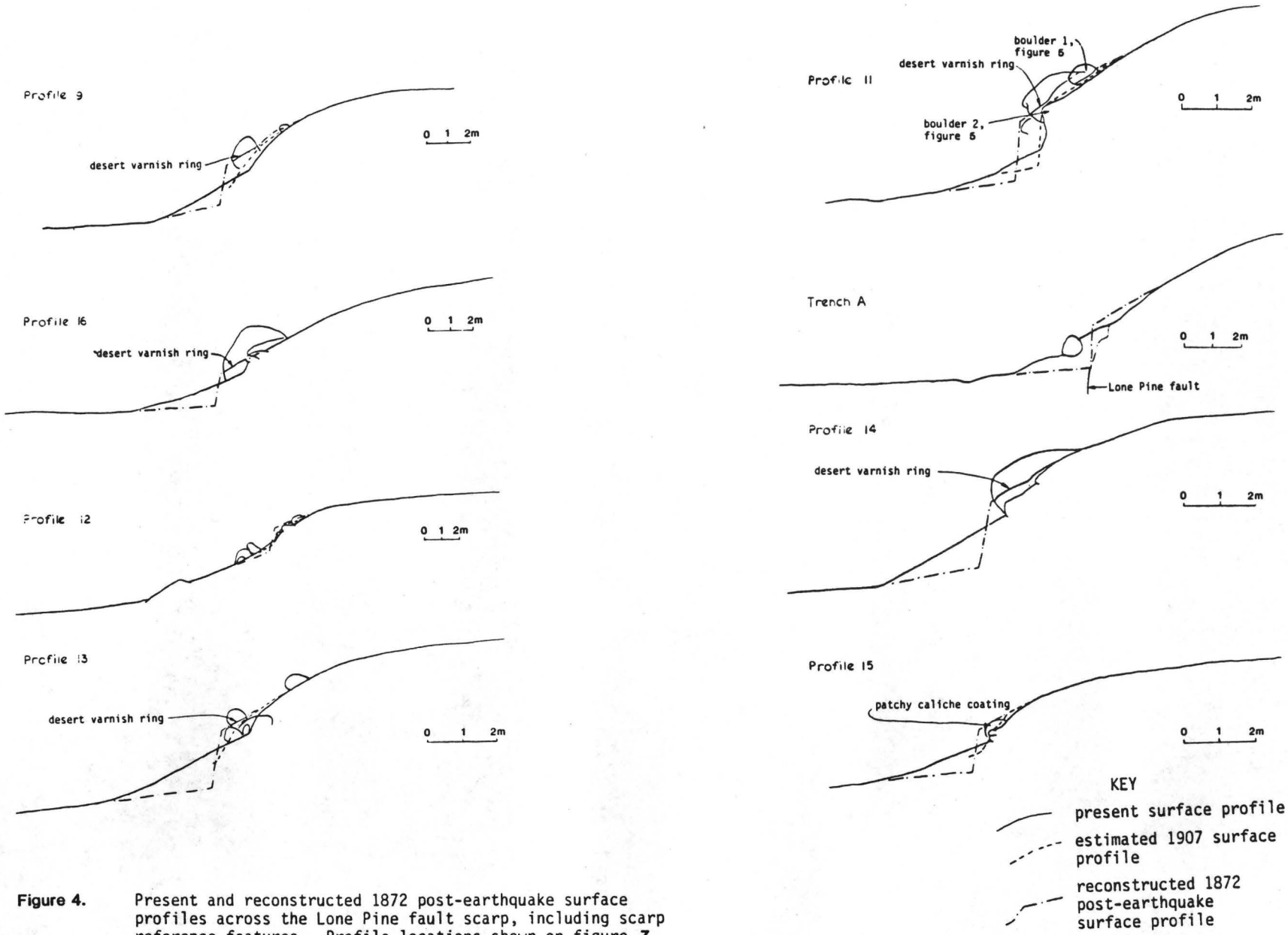

Figure 4. Present and reconstructed 1872 post-earthquake surface profiles across the Lone Pine fault scarp, including scarp reference features. Profile locations shown on figure 7.

Desert varnish rings provide evidence that the ground surface around the boulders must have been stable for a period of time at least as great as that required for development of such coatings, probably on the order of hundreds of years (R. M. Potter, oral commun., 1978). Projection of the exposed rings on boulders toward the fault scarp converges with the lower part of the upper convex slope (fig. 4). That is, the former ground surface recorded by the rings of desert varnish coincides with the portion of the scarp that has been nearly stable during the last 71 years. This stability strongly suggests that the upper convex slope and its downward projection to a surface represented by the varnish rings closely mark the true ground surface profile before and immediately after the most recent faulting in 1872. This postulated surface is also evidenced by cobbles and boulders exposed in the scarp that show caliche coatings or slight disintegration. These clasts lie below the postulated ground surface before the 1872 earthquake.

The lower portion of each reconstructed profile includes the lower original fan surface plus the wash slope and its projection into the fault. Several 1907 photographs show only a small debris slope and an older(?) wash slope (for example, fig. 5A). A large debris slope now covers the older wash slope. If all of the debris derived from erosion of the upper portions of the scarp is not removed from the base of the scarp, then a wash slope will result from reworking of material from the debris slope.

The position of the 1872 rupture surface in the fault scarp can be approximated from the position of boulders in the midslope of the scarp, together with observed fault-plane dips and estimated amounts of scarp retreat throughout the study area. Profiles were constructed by the method shown in figure 6, using both 70 and 90 degrees for the dip of the fault plane in order to bracket the estimated amount of dip slip. Figure 7 shows estimated 1872 and total dip slip for these profiles and measurements.

We consider the most recent slip event recognizable in the reconstructed profiles to be that associated with the 1872 earthquake, based on the reports of ground rupture along faults of the Owens Valley fault zone, the lack of post-1872 faulting, and on the extensive occurrence of the steep midslope within the scarp. In the brief pre-1872 historic record, the only earthquake likely to have been large enough to produce surface rupture was an event described by elderly Paiute Indians as having occurred around 1790 (about 80 years before the 1872 earthquake). This earlier earthquake is very poorly documented, and no surface displacement was reported (Townley and Allen, 1939).

Subsurface Exposure

A backhoe trench excavated across the Lone Pine fault scarp during this study exposed the eroded and buried portion of the fault scarp and a small filled-in graben at the base of the scarp (fig. 8). The trench was excavated to identify the position of the fault relative to the scarp, and to document the amount of scarp retreat at this site. A detailed log of the trench wall is in Lubetkin (1980). Undisturbed fan deposits exposed in the lower part of the trench consist of lightly cemented gravelly silty sand, with abundant boulders. An aggradational wedge of debris eroded from the fault scarp

Figure 5 1907 and 1978 photos of Lone Pine scarp at location of profile 11 (fig. 4), showing changes with time. Boulders are numbered for reference. Little or no change occurs above line A–A'. Individual cobbles 150 to 200 mm in diameter are recognizable in identical positions.

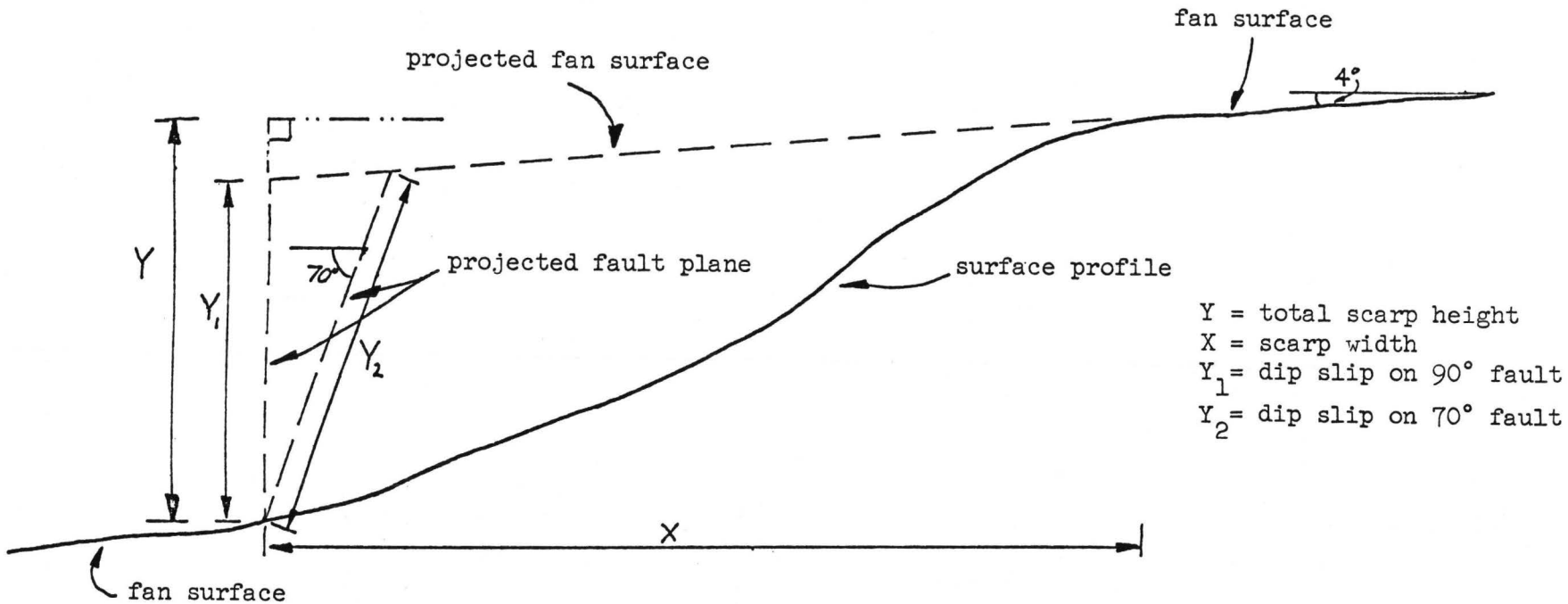

Figure 6 Method used to estimate dip slip. Scarp height, Y, and width, X, were measured graphically from fault scarp profiles, or were measured with plane table and alidade. Y_1, dip slip for assumed vertical fault, Y_2, dip slip for fault with assumed 70 dip.

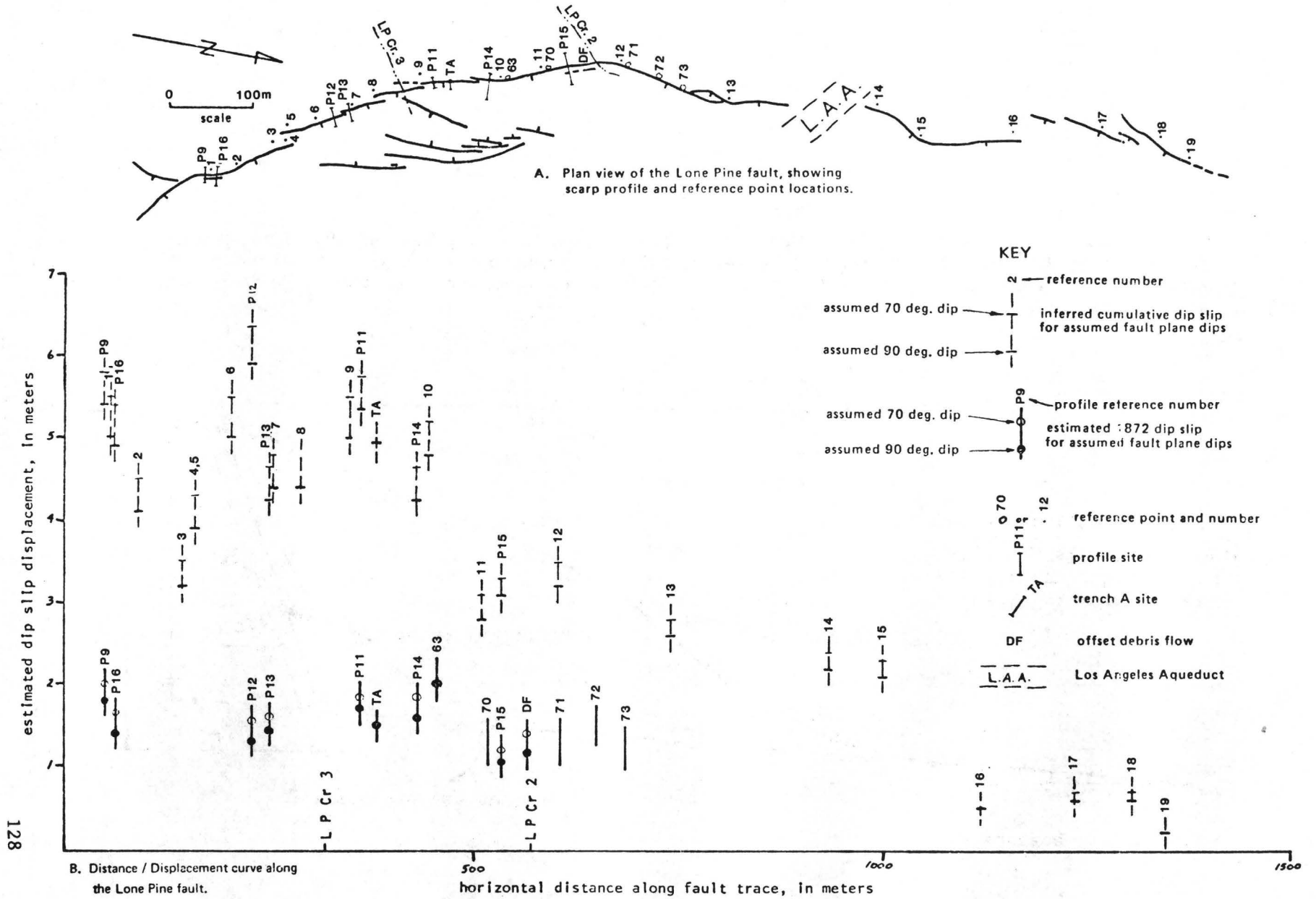

Figure 7 A. Map of Lone Pine fault, showing locations of profiles, trench A, and reference points.
B. Variation of displacement with location for Lone Pine fault, showing estimated 1872 dip slip and total dip slip.

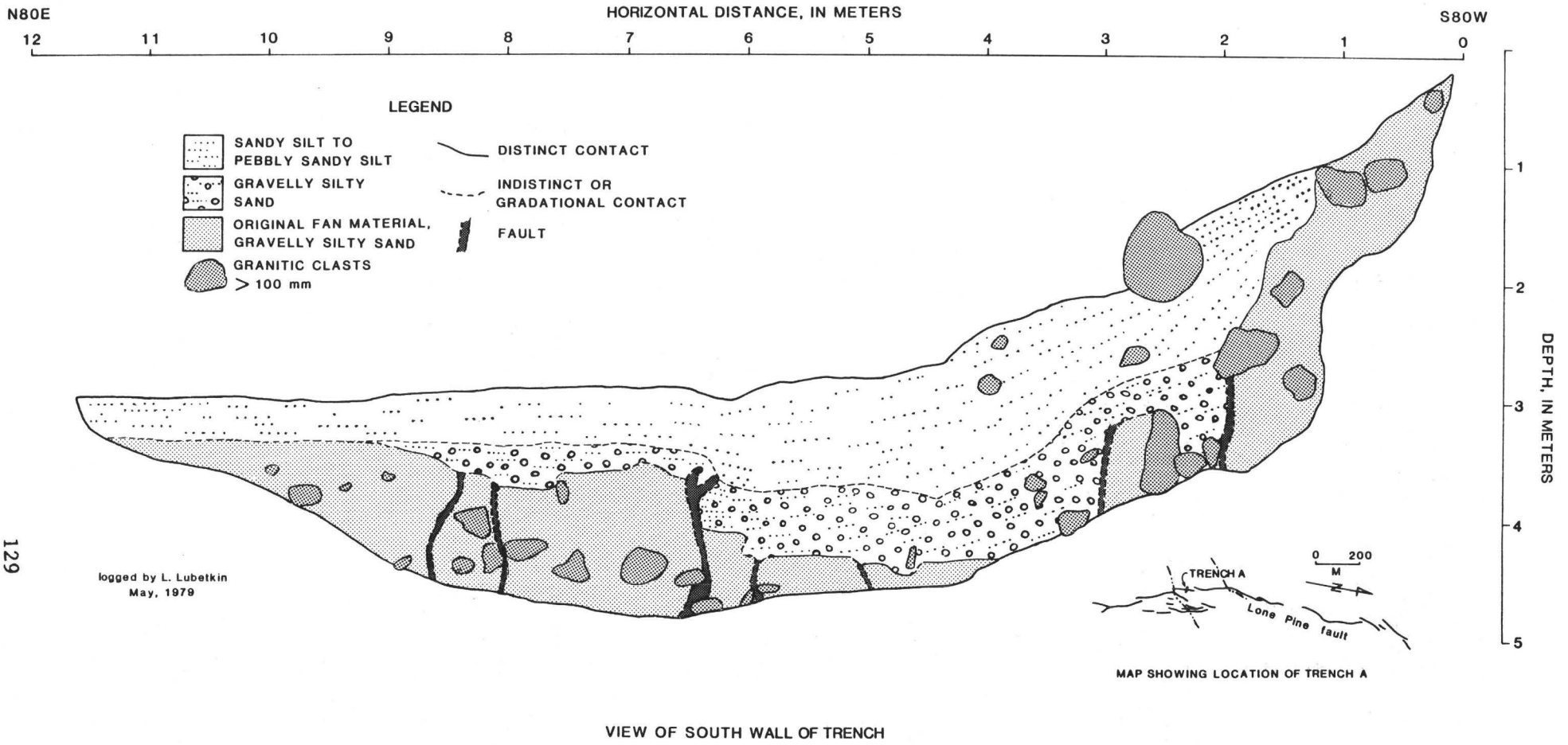

Figure 8 Interpretive log of exploratory trench A, Lone Pine Fault. Location shown on fig. 7.

overlies the fan materials. This wedge ranges from uncemented gravelly silty sand to sandy silt with only small amounts of gravel. The wedge generally becomes progressively finer-grained both upward and away from the fault scarp and lacks sedimentary structure except for local faint bedding. This aggradational wedge comprises two subunits; gravelly silty sand overlain by pebbly sandy silt. The contact between the two subunits is gradational over 100 to 150 mm.

The contact between fan deposits and the overlying two aggradational units is an unconformity over much of its exposed length, except near the west end of the trench. The westernmost 2 m of the trench wall (between stations 0 and 2, fig. 8) exposes fan material nearly to the ground surface. The upper 2/3 of the contact between these fan deposits (to the west) and the aggradational silt (to the east) is the eroded and buried lower part of the fault scarp of 1872 (an unconformity). The lower 1/3 (below 2 m) is a fault contact that juxtaposes in-situ fan material against aggradational sand. This fault is the main Lone Pine fault, which trends approximately north-south and has a near-vertical dip. The point at which this contact changes from a fault to an unconformity is complicated by the presence of a large boulder. The gradational contact separating the sand from the overlying silt ends westward against this boulder. The sand presumably predates the 1872 earthquake, whereas the overlying silt postdates 1872 and is the product of scarp erosion and retreat. About 0.8 m of recession of the 1872 scarp is recorded by this unconformable contact.

Offset Debris Flow

A debris flow complex that fills much of the northern relict channel of the fan (Lone Pine Creek #2, fig. 2) has been offset by the Lone Pine fault. This complex consists of many individual tongue-like masses of debris derived from the Alabama Hills. One of the most recent debris flows has been offset right-laterally 5.9 to 6.9 m and vertically 1.0 to 1.6 m, east side down (unit "1", fig. 9) where it crosses the Lone Pine fault. Net oblique offset of this debris flow is 6 to 7 m.

The common debris flow components, such as coarse-grained lateral deposits and fine-grained medial channel deposits (Johnson, 1965; Jahns, 1949), are obvious and have sharp boundaries. The outer margin of the lateral deposit is still distinct and shows little evidence of subsequent reworking, but its outer flank is not as steep as on most fresh debris flows of similar coarseness. The scarcity of matrix at the surface suggests some deflation of the lateral deposits.

We measured the total fault offset of this youngest debris flow along its southern margin, because the margins of a debris flow tend to be straighter than deposits of the later, less viscous fluid in the sinuous, irregular medial channel.

The narrow graben at the base of the east-facing fault scarp conceals the immediate continuation of the medial channel and the southern margin, so that the exact offset cannot be readily measured. However, the apparent offset of the medial channel is greater than that of the outer margin of the southern lateral deposit (fig. 9).

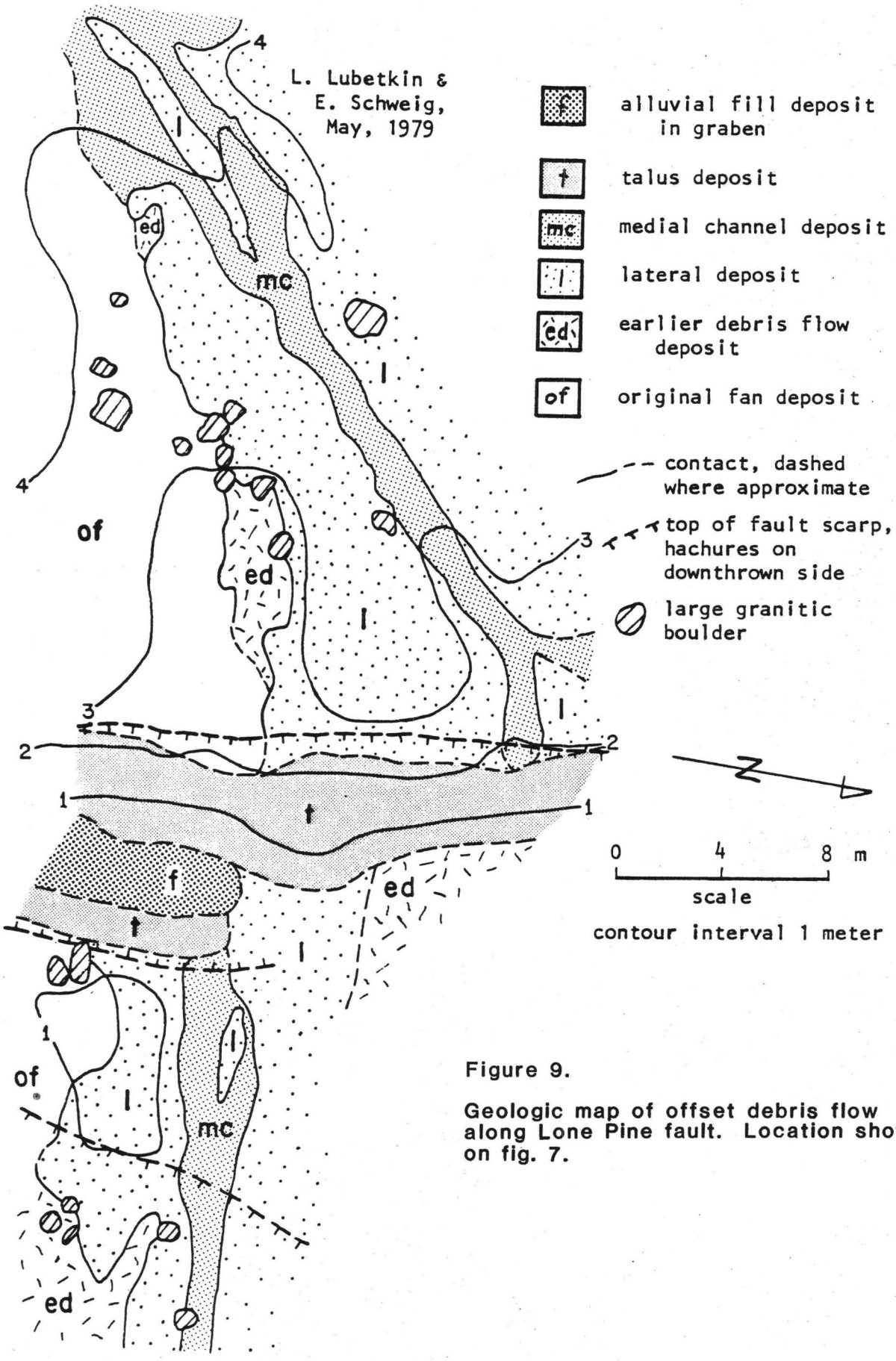

Figure 9.

Geologic map of offset debris flow along Lone Pine fault. Location shown on fig. 7.

This young debris flow probably has been offset only by the 1872 event. The dip-slip component of offset of the debris flow, 1 to 1.6 m, is consistent with the 1872 component of dip slip nearby along the 3-4 m high scarp (fig. 7). Furthermore, if it had been affected by two slip events, a pre-1872 earthquake had to occur after the debris flow was deposited. However, the debris flow appears to be relatively young, because so much of the primary form (distinct units and sharp contacts) is still preserved. In contrast, the pre-1872 portion of the fault scarp immediately south of the debris flow shows more erosion than we would expect in such a short time interval. The pre-1872 portion of the scarp to the south has a surface slope of 30 to 38 degrees and has developed several rills and gullies, suggesting that it is many times older than the 100 years since the 1872 earthquake. Thus, the total displacement of the debris flow may be the true offset during the 1872 event at this site. Evidence of horizontal displacement in earlier events has evidently been eroded by the ephemeral creek of Lone Pine Creek #2 as it has migrated laterally within its channel.

Horizontal offset of the older relict channel 220 m to the south (Lone Pine Creek #3, fig. 2) is obscured by deposition east of the fault. The margins of this channel suggest horizontal offset of 10-15 m, presumably the result of one or more pre-1872 earthquakes. This older channel is the subject of continuing investigations.

LATE QUATERNARY RECURRENCE INTERVAL AND SLIP RATE

Consideration of total scarp height, dip slip in 1872, and coatings on boulders exposed in the scarp across the Lone Pine fan suggests that slip during 3 earthquakes created the scarp. Total scarp height of 6.5 m along the Lone Pine fault generally decreases northward (fig. 7). We estimate total dip slip from total scarp height (fig. 6) for comparison with the 1872 dip-slip component. If the 1872 earthquake is a characteristic event for this fault during late Quaternary time, this comparison suggests that a total of three slip events would produce the present fault scarp. This conclusion is supported by the position of coatings on a 3 x 5 m boulder exposed in the scarp between profiles 12 and 13 (fig. 4). This boulder records at least three slip events (fig. 10).

In addition, the large boulder shown in profile 11 (fig. 4) suggests that the latest large event before 1872 produced at least as much vertical offset as did the 1872 event. The desert varnish coating on this boulder above the ring appears fairly uniform, suggesting that the boulder was completely buried before the latest pre-1872 event. If the upper scarp surface does approach some stable form as seen in the historic record, then that surface must have been above the boulder before the earlier event. Otherwise, a darker zone of varnish would likely be present over that part of the boulder exposed for a longer time. Profile reconstruction at this site suggests a minimum value for vertical offset accompanying a pre-1872 event of about 1 m (fig. 4).

Our estimate of the number of earthquakes recorded in the scarp assumes that all surface displacement results from sudden coseismic slip with possibly some afterslip, rather than long-term creep. We also assume that this fault experiences recurrent great earthquakes, rather than many small to moderate

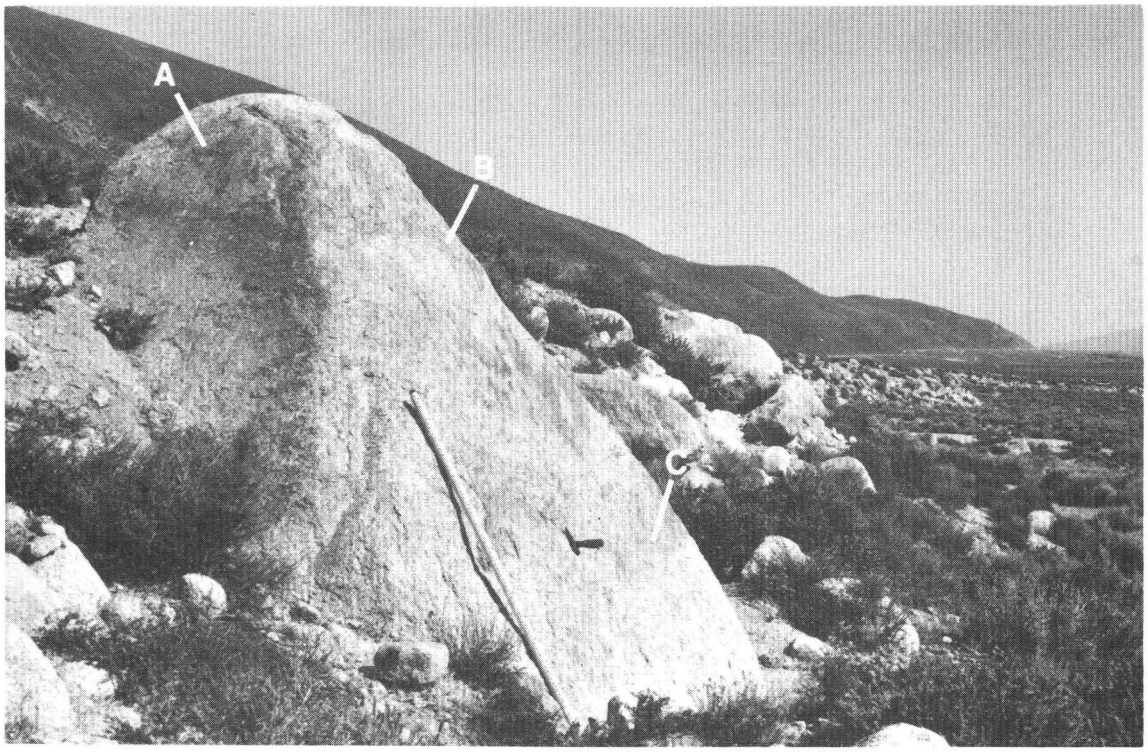

Figure 10 1978 photo of boulder in scarp between profiles 12 and 13 (fig. 4) that records 3 slip events. Line A separates areas of different intensity of weathering, and coincides with the projection of the original upper fan surface. This horizon suggests that the part of this boulder above line A lay above the ground surface before scarp development. Two rings of desert varnish, B and C, apparently record later stable positions of the ground surface, each following prehistoric faulting.

earthquakes accompanied by small surface slip. During the past 100 years, the Owens Valley fault zone has had a low level of seismicity. Only two earthquakes of magnitude 5.0 to 5.9 have occurred in Owens Valley between Owens Lake and Bishop from 1900 through 1984. During the same period, in contrast, the area between Bishop and Long Valley has experienced 12 earthquakes of magnitude >5.0 (Real and others, 1978; R. S. Cockerham, written commun., 1984).

Strain gauges spanning the Lone Pine fault and associated faults east of it have documented no significant fault creep since measurements began in 1968 (R. D. Nason, 1978, oral commun.). Photographic evidence indicates a lack of creep along this fault during the past 71 years. Post-1872 cultural features have not been offset along the main Owens Valley fault trace, which also indicates a lack of historic fault creep.

The postulated 1872-type earthquakes recorded by the scarp permit calculations of average late Quaternary recurrence intervals and slip rates, although we have not dated individual events. The maximum age of the fault scarp is limited by the maximum age of the fan surface, which in turn is limited by a date of 21,000±130 years for a high-stand of former Lake Owens (see discussion below). Climatic evidence and relative age methods suggest that the minimum age of the fan surface is about 10,000 years.

Three slip events during the past 10,000 to 21,000 years give an average recurrence interval along the Lone Pine fault of 3,300 to 10,500 years. The 3,300-yr interval assumes that the fan surface was deposited 10,000 years ago, just after an earthquake. The two pre-1872 events then occurred 6,700 and 3,300 years ago. The 10,500-yr interval assumes the fan was deposited 21,000 years ago just before an earthquake. The two pre-1872 events then occurred 21,000 and 10,500 years ago. These intervals obviously assume uniform recurrence, which may not be correct. Nonetheless, the scarp morphology suggests that the calculated values are significant. The maximum slope for the youngest pre-1872 scarp ranges from 30 to 38 degrees, and is distinctly less than the maximum slope angle for the 1872 portion of the scarp. The time required to modify the scarp formed in the pre-1872 rupture event to its 1872 shape is the true interval between those two events. The interval between those slip events appears to be much longer than the 112 years since the 1872 earthquake, based on the differences in maximum slope angles and the evidence of low erosion rates on gentler slopes. The actual erosion rate, and its variations with time and slope, are unknown, hence this time interval cannot be measured accurately.

The estimate of average recurrence interval for 1872-type earthquakes in turn leads to an estimate of late Quaternary slip rate for the Lone Pine fault. The postulated 1872 oblique slip of 6 to 7 m at Lone Pine Creek #2 has an average recurrence between 3,300 and 10,500 yrs. The resulting slip rates range from 0.6 to 2 mm/yr. Alternatively, if the horizontal offset at Lone Pine Creek #2 accumulated in either 2 or possibly 3 events, then the slip rates would be smaller by factors of 2 and 3, respectively.

DATING OF THE ABANDONED FAN SURFACE

Shorelines of Pleistocene Lake Owens are older than the abandoned outwash fan. Gravelly beach deposits with some tufa coatings and low wave-cut cliffs of this lake are preserved along short reaches of the eastern flank of the Alabama Hills at a maximum elevation of 1,144 m. These shoreline features record a temporary high-stand of Lake Owens. The old shoreline does not cut the surface of the abandoned fan, nor does geomorphic or sedimentary evidence indicate that the fan was built into a lake at this high-water stand. The abandoned fan surface therefore postdates the high-stand of the lake.

Lithoid tufa from the beach gravels yielded a ^{14}C age of 21,000±130 years B.P. (USGS 609, fig. 1). We took this sample from near the stratigraphic top of the shoreline deposit. It gives an approximate age for the high-stand of the lake and a maximum age for the fan surface.

^{14}C dates from tufa can be in error because of contamination by later atmospheric carbon or the presence of older carbon in the lake water. However the date is consistent with the record from down-stream Lake Searles and from Pleistocene lakes of the Great Basin. High-stands of Lake Searles from roughly 24,000 to 17,000 ^{14}C years ago required overflow from Lake Owens (Smith, 1976, 1983; Smith and Street-Perrott, 1983). In addition, Lakes Lahontan and Bonneville, to the north and northeast, had high-stands 18,000 and 17,500 years B.P., respectively (Morrison and Frye, 1965; Benson, 1978). If younger carbon has entered the tufa, the shoreline could possibly represent an older, early Wisconsin lake, but in the absence of additional information, we provisionally accept 21,000 years as the maximum age of the surface of the abandoned Lone Pine fan.

Relative age techniques provide a minimum age for the Lone Pine fan surface. The amount of sculpting and degree of weathering of granitic boulders, differences in soil oxidation color, and fan surface morphology indicate a latest Pleistocene age for the surface of the abandoned Lone Pine fan. In addition, these criteria for relative dating demonstrate that the abandoned fan surface is younger than the surface of the alluvial fans west of the Alabama Hills.

Boulders larger than 0.5 m exposed on the surface of the abandoned fan show approximately 5 to 30 mm of weathering relief (fig. 11). This relief is expressed by protruding mafic inclusions and dikes, large feldspar phenocrysts, and by a slight bell-like configuration at the base of boulders (indicating greater weathering and erosion above ground). Boulders of similar granitic lithology located on the surface of fans west of the Alabama Hills show greater weathering relief of 30 to 150 mm (fig. 11) and a more exaggerated bell shape. In contrast, those on the modern Lone Pine fan, east of the Alabama Hills and south of the abandoned fan, show less than 5 mm of weathering relief; inclusions and dikes commonly are flush with the surrounding boulder surfaces.

Granular disintegration of buried granitic boulders also indicates that the alluvial fans west of Alabama Hills are older than the abandoned fan of Lone Pine Creek. The fans west of Alabama Hills have a greater percentage of disintegrated or partially disintegrated granitic clasts, a relationship that

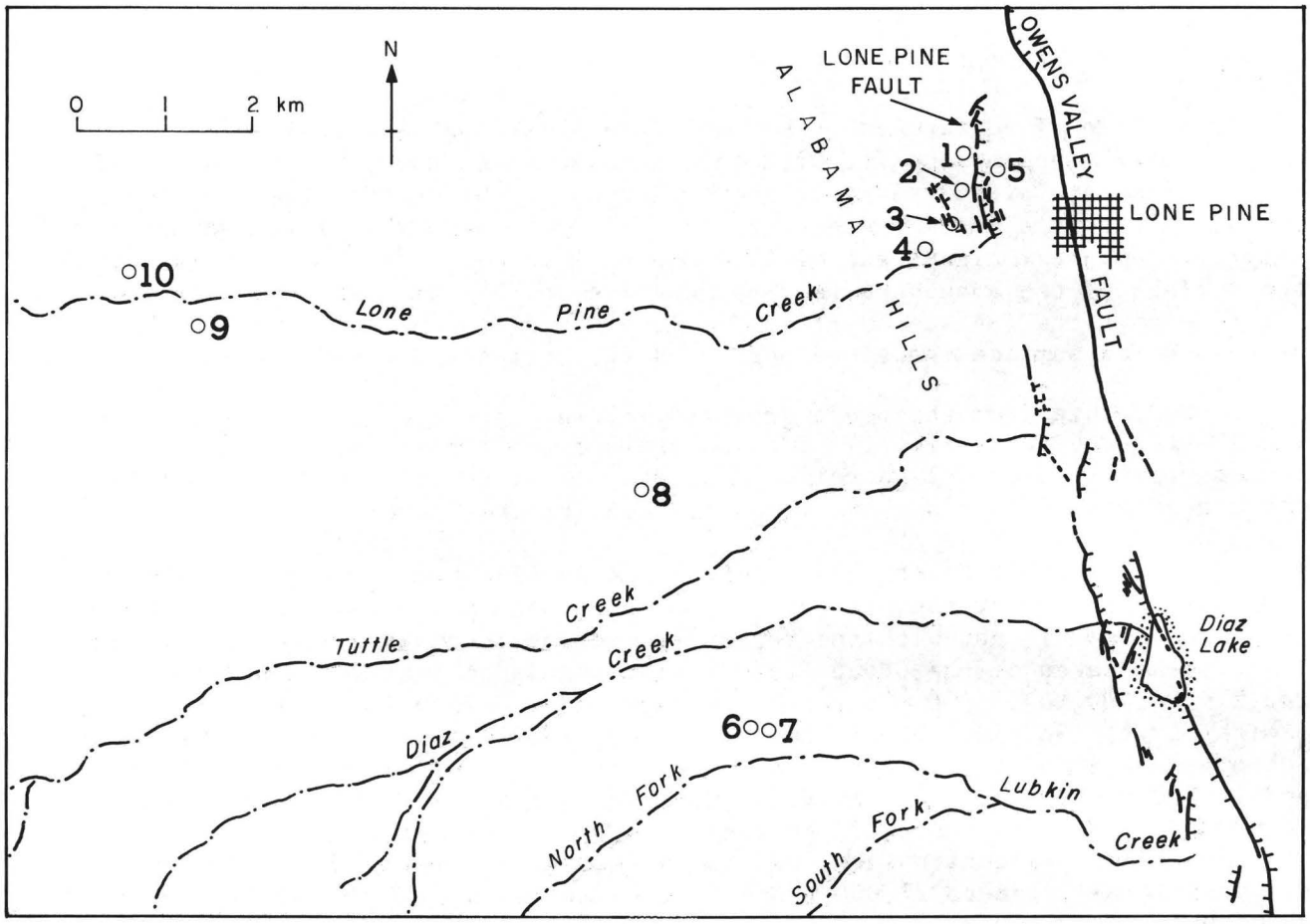

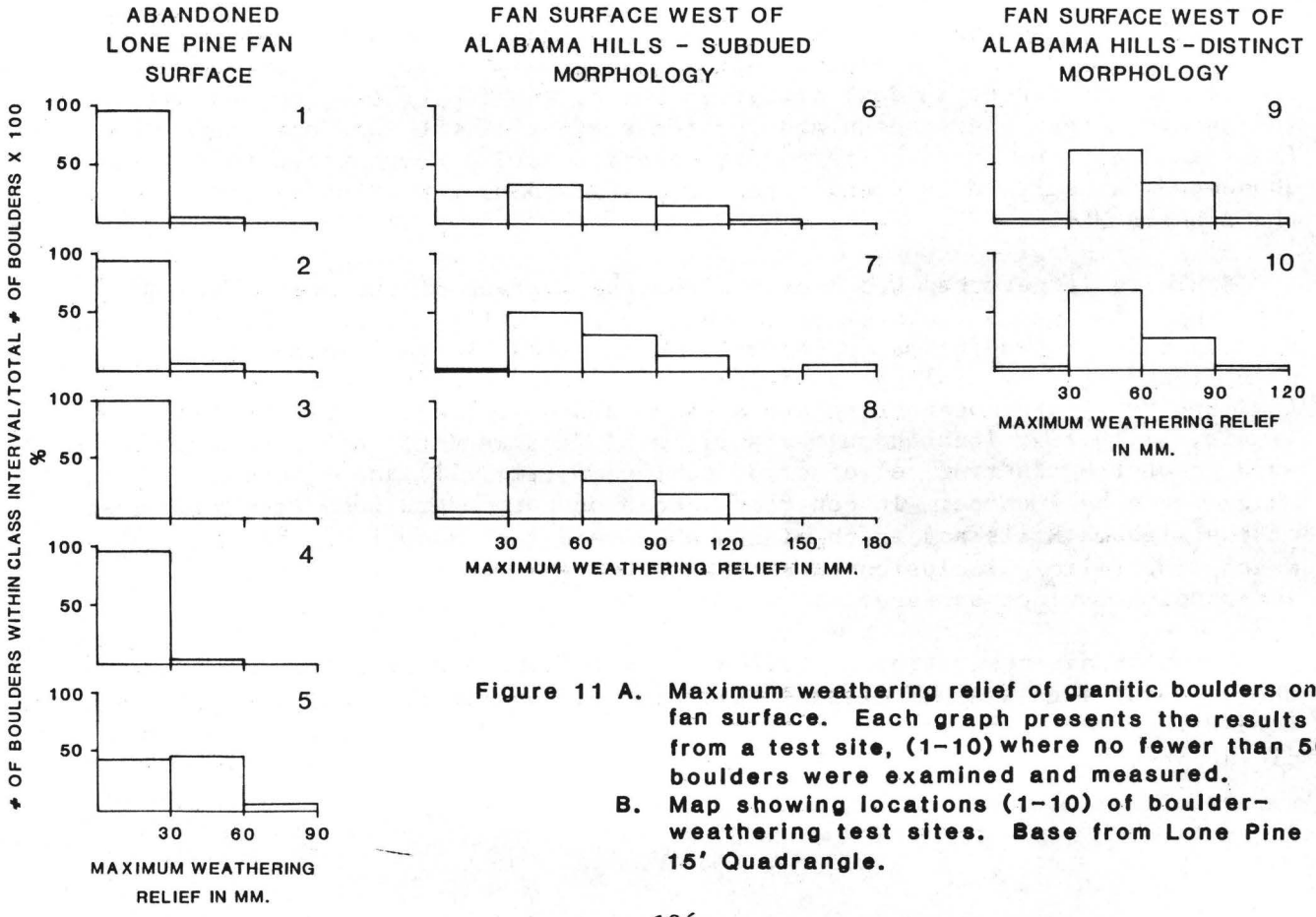

Figure 11 A. Maximum weathering relief of granitic boulders on fan surface. Each graph presents the results from a test site, (1–10) where no fewer than 50 boulders were examined and measured.

B. Map showing locations (1–10) of boulder-weathering test sites. Base from Lone Pine 15' Quadrangle.

separates glacial deposits of different ages (Birman, 1964; Burke and Birkeland, 1979). From 5 to 50 percent of the granitic clasts at six locations in the fan deposits west of the Alabama Hills are at least slightly disintegrated, whereas fewer than 5 percent of the subsurface granitic clasts of the abandoned fan in soil pits are slightly disintegrated.

We consider the fans west of the Alabama Hills to be contemporary with moraines of the Tahoe glaciation (ca 50,000-150,000 B.P.) of the eastern Sierra Nevada from similarity of weathering. This is in agreement with the conclusions of Knopf (1918) and Richardson (1975). The criteria of relative age, as mentioned above, are internally consistent and indicate that the abandoned Lone Pine fan is distinctly younger than the fans west of the Alabama Hills. We consider the abandoned fan to be contemporary with the younger, Tioga, glaciation, which ended about 10,000 years ago (Burke and Birkeland, 1979), from similarity to weathering of deposits of that glaciation along the eastern slope of the Sierra Nevada. Because production of large amounts of outwash would continue to the end of the Tioga glaciation, and because the modern fan of Lone Pine Creek south of the abandoned fan is relatively small, we believe the surface of the abandoned fan may be as young as 10,000 years.

Thus the tufa-dated shoreline, the regional record of Pleistocene lakes, and relative weathering strongly indicate that the faulted surface of the abandoned fan of Lone Pine Creek is between 10,000 and 21,000 years old, more likely closer to 10,000 years.

RELATIONSHIP OF THE LONE PINE FAULT TO THE OWENS VALLEY FAULT ZONE

Because the Lone Pine fault is only one of several strands within the Owens Valley fault zone, the late Quaternary average recurrence interval for major seismic events and the nature of slip for the Lone Pine fault cannot be assumed to define activity over the entire fault zone. Information on relationships among the various faults in the zone, and on changes in these relationships with time, are necessary for a more complete analysis.

The Lone Pine fault shows a large vertical component of recent displacement in the region where the main Owens Valley trace does not, based on topographic expression. However, the Owens Valley fault forms a large east-facing scarp northward beyond the north end of the adjacent Lone Pine fault. It thus appears that the Lone Pine fault accommodates vertical displacement present along the Owens Valley fault farther north. This relationship does not necessarily indicate that the two faults have ruptured concurrently, but only that the strain relief along them has been compatible.

Several fault scarps cross the surface of the abandoned Lone Pine fan subparallel to that of the Lone Pine fault (fig. 2). These scarps, some east-facing and some west-facing, range in height from 0.5 to 4 m. The west-facing scarps east of the Lone Pine fault have resulted, at least in part, from rupture in 1872, according to accounts of early investigators and the morphology of the fault scarps. The faults west of the Lone Pine fault apparently did not rupture in 1872. This is shown by the uniform gradients of Lone Pine Creeks 2 and 3 where they cross the faults, and by the lack of

well-preserved free faces similar to those along the Lone Pine fault scarp. The maximum slope angle of these scarps commonly is greater than that of the upper convex western portion of the Lone Pine fault scarp, suggesting that these faults ruptured between 1872 and the latest pre-1872 event along the Lone Pine fault. This may indicate that the frequency of occurrence of large earthquakes and associated ground rupture in the area is greater than that estimated solely from relationships along the main Lone Pine fault scarp.

We do not know if the Lone Pine fault characteristically ruptures at the same time as the Owens Valley fault, as it did in 1872. If it does, recurrence on the Lone Pine fault applies also to the Owens Valley fault. If not, regional hazard might be greater than indicated for the Lone Pine fault alone. In either case, slip rates for the Lone Pine fault apply only to it, and add to slip rates for the Owens Valley fault in hazard assessments.

REFERENCES CITED

Bateman, P. C., 1961, W. D. Johnson and the strike-slip component of fault movement in the Owens Valley, California earthquake of 1872: Bulletin of the Seismological Society of America v. 51, p. 483-493.

Benson, L. V., 1978, Fluctuation in the level of pluvial Lake Lahontan during the last 40,000 years: Quaternary Research, v. 9, p. 300-318.

Birkeland, P. W., 1974, Pedology, weathering and geomorphological research: Oxford University Press, New York, 285 p.

Birman, J. H., 1964, Glacial geology across the crest of the Sierra Nevada, California: Geological Society of America Special Paper 75, 80 p.

Bonilla, M. G., 1968, Evidence for right-lateral movement on the Owens Valley, California, fault zone during the earthquake of 1872, and possible subsequent fault creep: Proceedings of the Conference on Geological Problems of the San Andreas Fault System, Stanford University Publications in the Geological Sciences, v. 11, p. 4-5.

Bucknam, R. C. and Anderson, R. E., 1979, Estimation of fault-scarp ages from a scarp-height-slope-angle relationship: Geology, v. 7, p. 11-14.

Burke, R. M. and Birkeland, P. W., 1979, Reevaluation of multiparameter relative dating techniques and their application to the glacial sequence along the eastern escarpment of the Sierra Nevada, California: Quaternary Research, v. 11, p. 21-51.

Cooke, R. U. and Warren, A., 1973, Geomorphology in deserts: University of California Press, Berkeley, 374 p.

Gilbert, G. K., 1884, A theory of the earthquakes of the Great Basin, with a practical application: American Journal of Science, 3rd Series, v. 27, p. 49-53.

Hobbs, W. H., 1910, The earthquake of 1872 in the Owens Valley, California: Beiträge zur Geophysik, v. 10, p. 352-385.

Jahns, R. H., 1949, Desert floods: Engineering and Science Monthly, v. 12, no. 8, p. 10-15.

Johnson, A. M., 1965, A model for debris flow: unpublished Ph.D. thesis, The Pennsylvania State University, University Park, Pennsylvania, 248 p.

Knopf, A., 1918, A geologic reconnaissance of the Inyo Range and the eastern slope of the southern Sierra Nevada, California: U.S. Geological Survey Professional Paper 110, 130 p.

Lubetkin, L. K. C., 1980, Late Quaternary activity along the Lone Pine fault, Owens Valley fault zone, California: Unpublished M.S. thesis, Stanford Univ., Calif., 85 p.

Morrison, R. B., and Frye, J. C., 1965, Correlation of the middle and late Quaternary successions of the Lake Lahontan, Lake Bonneville, Rocky Mountain (Wasatch Range), Southern Great Plains, and Eastern Midwest areas: Nevada Bur. Mines Rept. 9, 45 p.

Oakeshott, G. B., Greensfelder, R. W., Kahle, J. E., 1972, 1872-1972 ... one hundred years later: California Geology, v. 25, p. 55-61.

Real, C. R., Toppozada, T. R., and Parke, D. L., 1978, Earthquake epicenter map of California, 1900 through 1974: California Division of Mines and Geology, Map Sheet 39.

Richardson, L. K., 1975, Geology of the Alabama Hills, California: unpublished M.S. thesis, University of Nevada, Reno, Nevada.

Smith, G. I., 1976, Paleoclimatic Record in the Upper Quaternary sediments of Searles Lake, California: Paleolimnology of Lake Biwa and the Japanese Pleistocene, v. 4, p. 577-603.

---1983, Core KM-3, a surface-to-bedrock record of late Cenozoic sedimentation in Searles Valley, California: U.S. Geological Survey Professional Paper 1256, 23 p.

Smith, G. I., and Street-Perrott, F. A., 1983, Pluvial lakes of the Western United States, chap. 10 of Wright, H. E., Jr., ed., Late-Quaternary environments of the United States: Minneapolis, University of Minnesota Press, v. 1, p. 190-212.

Smith, R. S. U., 1979, Holocene offset and seismicity along the Panamint Valley fault zone, western Basin and Range Province, California: Tectonophysics, v. 52, p. 411-415.

Townley, S. D., Allen, M. W., 1939: Descriptive catalogue of earthquakes of the Pacific Coast of the United States 1769-1928: Bulletin of the Seismological Society of America, v. 29, p. 1-297.

Wallace, R. E., 1977, Profiles and ages of young fault scarps, north-central Nevada: Geological Society of America Bulletin, v. 88, p. 1267-1281.

Whitney, J. D., 1872, The Owens Valley Earthquake: Overland Monthly, v. 9, p. 130-140, 266-278.

---1888, The Owens Valley Earthquake, in Goodyear, W. A., Inyo County, California Division of Mines, 8th Annual Report of the State Mineralogist, p. 224-309. (Reprinted from the Overland Monthly, 1872).

Young, Anthony, 1972, Slopes: Oliver and Boyd, Edinburgh, 288 p.

COMPARISON OF THE GEOMORPHIC AND SURFICIAL FRACTURING EFFECTS OF THE 1983 BORAH PEAK, IDAHO EARTHQUAKE WITH THOSE OF THE 1959 HEBGEN LAKE, MONTANA EARTHQUAKE

by

William B. Hall and Peter E. Sablock

University of Idaho, Moscow, Idaho

ABSTRACT

The assigned 7.3 MS magnitude of the 1983 Borah Peak earthquake implies a significantly larger energy release than that of the 1959 Hebgen Lake earthquake, rated at 7.1 MS. However, personal recollection suggested that the surficial geologic effects produced by the Hebgen Lake event were much more extensive than those reported for the Borah Peak shock. Therefore, a systematic comparison of the surficial geologic effects produced by both events was undertaken to determine the validity or significance of such a discrepancy. Comparisons indicate that the Hebgen Lake earthquake did indeed cause significantly greater geologic effects than did the Borah Peak earthquake in seven of the eight categories assessed. Therefore, the apparent discrepancy between magnitudes and effects is real.

Two possible reasons for such a discrepancy are: 1) The total energy release during the first 24 hours was greater for the Hebgen Lake earthquake than for the same time span of the Borah Peak event, and 2) Both moment calculations and the seismograms indicate that the Hebgen Lake event was a release of greater energy than the Borah Peak event; thus at least one of the assigned magnitudes for the two events is erroneous.

INTRODUCTION

Preliminary reports and brief on-site observations of faulting and other geologic surface effects associated with the Borah Peak earthquake of October, 1983, indicated a surprisingly limited array of geologic and physiographic changes for a shock of magnitude 7.3, especially when contrasted with the observed and well documented widespread effects produced by the 1959 Hebgen Lake earthquake, which was rated at only 7.1. Because magnitude can empirically be related to maximum intensity (Richter, 1958), the apparent disparity between observed surficial geologic effects of the Borah Peak and Hebgen Lake earthquakes and their assigned Richter magnitude values has prompted a review of the field effects of both events to see if the calculated magnitude ratings can be used as relative indicators of actual geologic changes produced.

The 7.3 magnitude of the Borah Peak event suggests an energy release far greater than the Hebgen Lake event, rated at 7.1. However, personal recall of the visible geologic effects produced by the Hebgen Lake quake, when compared to the observed and reported effects of the Borah Peak quake, suggest that the Hebgen Lake earthquake was geologically much more significant, and perhaps may have in fact released more energy, despite the ratings assigned.

Stover (1984, p.1) has made the interesting observation that, in a comparison of surface wave magnitude averages for distances greater than 30 degrees, the Hebgen Lake event would be rated at 7.5MS, and the Borah Peak event at 7.3MS. Those magnitude ratings would seem more consistent with the field observations and the data we have reviewed.

TECTONIC SETTING

The two earthquakes occurred in the same general section of the Intermountain Seismic Belt, and originated at approximately the same depth, of 15 to 16 km. However, the Lost River Range, and flanking valleys in south-central Idaho are typical of classic Basin and Range structure, whereas the Madison Range in southwestern Montana is in part atypical for Basin and Range structure, with major west-northwest trending structures (Hall, 1961). Moreover, regional fault plane solutions are interpreted (Smith and others, 1985, p. 9) as indicating a distinct change in stress field between the Lost River Range and the Hebgen Lake region. Both ranges are bounded on the west by steeply inclined normal (?) faults, probably of Miocene age. Both show obvious piedmont fault scarps along their western flanks, although the scarps of the Madison Range are much longer and higher than those along the Lost River Range. In addition, near the southern end of the Madison Range there are at least two major and separated piedmont scarps of obviously different ages (based upon relationship to alluvial fan sequences).

In the case of the Lost River Range, the rocks adjacent to the western bounding fault are largely deformed Paleozoic sedimentary strata. In the Madison Range the rocks abutting the bounding fault are largely deformed metamorphic and igneous rocks of Precambrian age, with only minor patches of Paleozoic strata remaining from the cover.

In both cases, the earthquakes here studied are believed to have activated previously developed fault surfaces. However, there is an important difference between the events in regard to the types of faults reactivated. In the case of the Borah Peak event, the new trace very closely follows the older piedmont fault scarp along the west flank of the range that was easily seen on the ground and from airphotos prior to the 1983 earthquake. But in the case of the Hebgen Lake event, only about 5 km of the western boundary piedmont fault was reactivated (actually along the west edge of the Henrys Lake Range, south of the Madison River). The major 1959 faults were renewed movements on much older Laramide age faults that are internal to the range. The traces of those faults prior to the 1959 event were so subtle, if present at all, that they had not been identified in a geomorphic sense, although their approximate locations were known on the basis of geologic and structural mapping (Hall, 1961, Plate I). Figure 1 shows the locations of the various fault scarp sets produced during the Hebgen Lake earthquake. The original fractures of both the Hebgen Ridge Fault and the Red Canyon/Kirkwood Ridge Fault are essentially Laramide displacements developed in a strongly compressional stress system, and their trends are integral to the structures of the region. The late Cenozoic western boundary fault completely transects the Laramide and older structures, and developed in a tensional stress regime. It must be recognized that the structures of the Hebgen Lake area are sufficiently complex that the timing and sequence of Laramide faulting is not yet well understood, and that the "ancestral" faults may themselves have been "normal" in displacement, even though part of the overall compressional package. They do not easily fit the antithetic fault model of a reverse-fault master structure. See Witkind (1969, p. 67- 72) for a more thorough discussion of possible structural models for the Hebgen Lake and Kirkwood Ridge structures. This much is clear: the 1983 Borah Peak earthquake reactivated the Cenozoic tensional range-bounding fault of the Lost River Range, whereas the 1959 Hebgen Lake earthquake reactivated long-dormant Laramide compressional system faults within the range block, and generated little response along the range-bounding tensional Cenozoic fractures. It is on this basis that we propose the mechanisms fundamental to the two earthquakes are not identical.

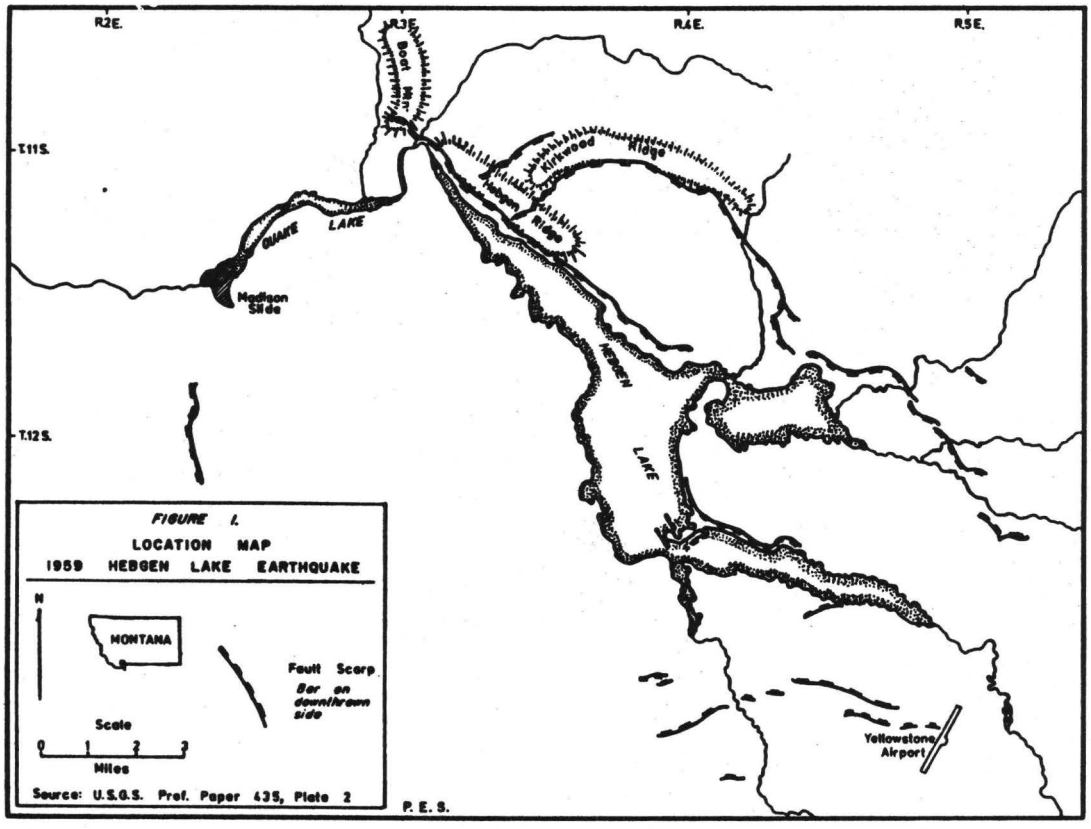

FIELD EFFECTS ASSESSED

The following criteria were selected to compare surface effects of the two events, even though we recognize that some of the data could not be gathered in the same fashion after a separation interval of more than 24 years:

1. total felt area
2. length of surface fault ruptures
3. number of documented sites of bedrock offset
4. maximum reported fault displacement (surface)
5. number, types and sizes of landslides triggered
6. number of sand spout sites
7. aggregate length of paved roads destroyed by ground motion
8. major physiographic changes produced.

For this study no comparison has been made of the types or numbers of structural failures in buildings, although such damage was far greater from the Hebgen Lake event than the Borah Peak. Nor does this paper deal with the various changes in hydrologic conditions and behavior, which are discussed by Waag (1985), and Youd and others (1985). Isoseismal maps and intensity distributions have been discussed by Stover (1984).

FELT AREAS

The Borah Peak earthquake was felt over an area of approximately 670,000 sq. km. The Hebgen Lake earthquake of August 1959 was felt over an area of approximately 870,000 sq. kilometers (Stover, 1984, p. 1,2). Thus the felt area of the Hebgen event was about 30 percent greater than that of the Borah Peak event.

LENGTH OF SURFACE FAULT ZONES

For this criterion we have recorded the length of each known fault zone as determined by new escarpments, without attention to zones of multiple scarps in the same system. There is some disagreement between reports on the Borah Peak event as to the length of the new faults produced. Crone and Machette (1985, p. 664) have suggested 34 km of faulting as a reasonable composite figure for the Borah Peak event, arrived at by assuming that the Northwest Branch Fault (Arentson Gulch Fault of some workers) approximately equals the gap in the Lost River Fault trace between Sec. 36 and Sec. 14, T. 11 N., R. 21 E.

Taylor and others (1984, p. 12) report 42 km of surface faulting on the Lost River Fault, and 8 km on the Arentson Gulch Fault, for a combined total of 50 km of surface faults.

Our measurements were made on the maps of Crone and others (1985) for the Borah Peak event, and on the U.S. Geological Survey's 1964 (Plate 2) map for the Hebgen Lake event. See Figure 1 for a simplified fault location map of the Hebgen Lake area. All measurements were made in the same fashion, and both chord and arc distances recorded.

Stover measured the total fault distance from the map by Witkind and others (1962) for the Hebgen Lake event as about 27 km. Using the 1964 map by the U.S. Geological Survey (1964, Plate 2), the five distinct fault zones total 52.8 km, using the chord distance method described by Bonilla (personal communication, Oct. 4, 1984), and used to calculate the Borah Peak lengths. That figure is 55.3 % greater than the 34 km total for Borah. Using an arc-distance measurement (See Table 1) for the 2 fault branches at Borah yields a total of 41.9 km, which compares to the arc distance total at Hebgen of 61.3 km, some 46.3 % greater than at Borah Peak.

Table 1. Arc Distance Fault Trace Lengths

Lost River Fault	31.0 km
Arentson Gulch Fault	10.9 km
Total	41.9 km
Hebgen Fault	17.0 km
West Fork-Kirkwood-Red Canyon Fault	24.68 km
West Yellowstone Flats faults	11.25 km
Henrys Lake Range Fault	3.25 km
Madison Arm faults	5.13 km
Total	61.31 km

NUMBER OF DOCUMENTED SITES OF BEDROCK FAULTING

Until further observations are reported, only one site in the Borah Peak area has been mentioned where a fault "probably cuts bedrock". That was in the Rock Creek portion of the fault trace. In several places the Lost River Fault trace climbs up and over foothill shoulders which appear to be rock cored, and we believe the geomorphic evidence is strong that the fault cuts bedrock along such reaches, but bedrock offset has not been directly observed.

For the Hebgen Lake fault traces, there are at least three known and photographed sites which show a scarp cutting through bedrock, with rock exposed on both sides of the fracture. Two of these are on the southwestern extension of Boat Mountain, in Sec. 15, T. 11 S., R. 3 E., Gallatin County, Montana. They are along subsidiary faults, roughly parallel to, and on either side of, the

obvious main scarp of the Hebgen Fault, near its westernmost end. The subsidiary faults are not shown on the 1964 U.S. Geological Survey map, and may not have been seen by investigators following the main scarp over the ridge top. The third site is along the western end of Kirkwood Ridge, Sec 19, T. 11 S., R. 4 E. , where one branch of the Red Canyon Fault climbs up and across the bedrock (Quadrant Quartzite) cliff. There are other locations along the Red Canyon Fault where we have photographed portions of the scarp that are sheer faces from three to six meters high of nearly vertical Madison Limestone bedrock, but where the downdropped block is beneath a rubble cover. Because the colluvium just above the scarp is only a few centimeters deep, it is unlikely that the rubble on the lower side of the trace was more than a meter or so deep, and thus bedrock would be present there also. This would suggest bedrock faulting, although we have not yet examined these sites on the ground. Witkind did not mention any of the specific sites discussed above, and commented that "No clearly cut and offset exposures of bedrock were found. Where the fault scarp abuts bedrock, the bedrock has parted along the fault trace, but the breaking seems to be along preexisting joint surfaces or bedding planes, and the general impression is that the rocks have fallen apart rather than been torn apart." (1964, p. 40).

MAXIMUM REPORTED FAULT DISPLACEMENT

The largest surface displacement we have observed along the Borah Peak Fault is 2.0 meters, at Rock Creek, in Sec. 34, T. 10 N., R. 22 E., Custer Co., Idaho. The maximum throw measured by Crone and Machette is 2.55-2.7 meters,

Table 2. Scarp Height Measurements from the Hebgen Lake Area*

Hebgen Lake Fault		Red Canyon Kirkwood Fault	
scarp height/net height		scarp height/net height	(in feet)
2/ -**	20/18	3/ 2	19/14
4/ 2	18/16	3/ 2	19/15
2/ 1	10/ -	2/ 2	15/ -
5/ 2	10/ -	2/ 2	15/12
4/ 3	9/ 8	8/ 7	15/13
7/ 5	13/11	8/ 7	10/ 8
2/ -	7/ 5	10/ 7	6/ 5
5/ 4	9/ 9	12/ 9	3/ 1
8/ 6		15/12	5/ 2
8/ 5		10/ 8	14/10
1/ 1		15/10	9/ 7
9/ 7		12/ 9	10/ 9
12/ 9		15/ -	5/ 3
6/ 4		6/ -	6/ 6
3/ 2		16/ -	2/ 2
6/ 3		18/14	.3/.3
13/10		19/15	
Totals: /131 ft		/213.3 ft	
6.55 ft avg of 20 net figures		7.36 ft avg of 29 net figures	

* Values are those shown on U.S. Geol. Survey's Hebgen map (1964, Pl. 2.)
** - indicates no net figures furnished

near Rock Creek in the Birch Springs section of the Lost River Fault (1985, p. 665). Taylor and others mention several places in the Birch Springs area of the Lost River Fault where the maximum "net vertical tectonic displacement across the fault zone" is 2.4 meters (1984, p. 13).

For the Hebgen Lake area, Witkind (1964, p. 39-42) reports several places where the maximum scarp height reached about 20 feet (6 meters) on both the Hebgen and Red Canyon Faults. That should also represent the vertical component of displacement, since the heights are assumed to have been measured vertically. Figures on the Hebgen map show both raw scarp height, and net vertical offset on the two main faults at many spots. Based on 20 measurements (see Table 2) along the 17.0 km arc length of the Hebgen Ridge Fault, the average vertical displacement was 6.6 feet (2.0 meters). Based on 29 measurements, the average vertical displacement over the 24.7 km arc length of the Red Canyon/Kirkwood Ridge Fault was 7.4 feet (2.3 meters). The sample sites are rather uniformly positioned all along the lengths of the faults, and can be checked on their map (U.S. Geol. Survey, 1964, Plate 2). If all 49 measurements are combined for the two faults, they average 2.14 meters over the combined arc length of 41.7 km for the Hebgen Ridge and Red Canyon faults. Thus, the average vertical displacement on those two systems is about 3 times the 0.8 meter average over the 31.0 km arc length of the Lost River Fault.

NUMBER, SIZES AND TYPES OF LANDSLIDES TRIGGERED

Although Stover (1984, p. 3) mentioned "numerous landslides and rockfalls" associated with the Borah Peak event, and Taylor and others (1984, p. 11,12) mention a "large landslide" at Birch Springs, and another at Whiskey Springs, the actual sizes are not given, and they are neither classified as to type, nor described. A comprehensive summary of the Borah Peak triggered landslides has been presented by Keefer and others (1985), and nearly all of the features cited were rock falls, or ground cracks and failures in little geologic significance. The one real exception was the Birch Springs slump-debris flow, with an estimated volume of 100,000 cu m (Keefer and others, 1985, p. 21-25). Some mention was made also of the need to clear roads of rockfall debris, but it was noted that such effects were minimal.

In contrast, the Hebgen Lake earthquake triggered one major catastrophic rockslide, created two new earthflows, reactivated three older earthflows, and produced 24 medium-sized slump blocks, in addition to many hundreds of rockfalls.

The Madison Canyon Rockslide dammed the Madison River, resulted in the loss of 26 lives, and involved 37 million cubic yards of bedrock (Hadley, 1964, p. 108).

The new earthflows are not mentioned in any reports we have examined, but were photographed by Mrs. S.W. Nile in late August, 1959. They are both rather small in comparison to many others in the same region (Hall, 1960b), only a few hundred meters long. They formed on the lower slopes of the western flank of the Madison Range, between the Madison Canyon and Deadman Creek, in Secs. 27 & 34, T. 11 S., R. 2 E., Madison County.

One reactivated earthflow occurred on a south-facing steep slope of Kirkwood Creek valley, and is about 1/2 mile long by about 1/10 mile wide (Hadley, 1964, p. 124). Two much larger and older earthflows were reactivated by the quake, and their frontal sections jostled forward, resulting in numerous transverse tension fissures as much as 4 meters deep and 1 meter wide at the top. One of these is pictured in the Hebgen Lake earthquake area guidebook (Hall, 1960, p. 203), and has its terminus along

the north shore of Hebgen Lake in Secs. 7 & 8, T. 12 S., R. 5 E. The other modestly reactivated earthflow is located on the steep west-facing slopes below Lava Butte in Yellowstone Park's northwestern corner, some 30 miles from the epicentral area. A small debris slide(?) came down upon the southwestern abutment of Hebgen Dam, but over-dam seiches of the lake swept most of the debris away.

Slump blocks along the north shore of Hebgen Lake carried sections of the highway into the lake. They varied from 50,000 to 110,000 cu. yards in volume. Another 20 slumps involving bedrock were large enough to be mapped by Woodard (1960) at a scale of 1:62,500.

Rockfalls were so numerous (many hundreds) and occurred over such a large area that no attempt was made to record them all. They occurred from the vicinity of Terrace Mountain in Yellowstone Park, 31 km northeast of the epicenter, to cliff Lake campground, some 35 km west of the epicenter, where two people were killed by a large boulder which rolled across their tent. The roads through Yellowstone Park were closed mainly because of rockfall hazards along the roads and in campgrounds, and the great damage to the highways from fallen rocks and bounding boulders.

It is thus evident that the mass gravity effects of the Hebgen Lake event far surpass in scale, variety, number, area, and damage, those of the Borah Peak event.

NUMBER OF SAND SPOUT SITES

Included in this category are the hydro-geomorphic features variously referred to as sand spouts, sand boils, sand springs, sand fountains, earthquake fountains, cold water geysers, and fissure springs. The Borah Peak shock reactivated one site of sand spouts just south of Chilly Buttes, about 10 km NNW of the epicenter and 7 km from the trace of the Lost River Fault. The several springs at this location are shallow conical depressions, the largest about 4-6 meters across (Taylor and others, 1984, p. 10).

In the Hebgen area I visited two separate sites of sand spouts in the week following the main shock. The springs were quietly seeping minor amounts of water at the time, but not pulsing. There was abundant evidence of very vigorous prior spouting or fountaining discharge, the area about each opening being covered with fresh mounds and ridges of sand. The eastern site was just north of the highway in the SW 1/4, Sec. 8, T. 12 S., R. 5 E.; about 1 km south of the trace of the Hebgen Fault and 6.4 km from the USCGS epicenter. The western site was just west of the junction of the Beaver Creek road with the highway, in the W 1/2 of Sec. 21, T. 11 S., R. 3 E., about 23 km from the USCGS epicenter. Most of this site is now flooded as a result of the combined effects of the tectonic subsidence from the quake and the post-quake relative rise in water table. Both of these locations were shown on the U.S. Geological Survey map (1964, Plate 2), and have been described in some detail by Swenson (1964), along with several other sites. The Hebgen event produced at least four main sand spout sites on land. In addition, F. W. Woodard reported "many small to large sublake sand spouts" beneath the surface of Hebgen Lake in the vicinity of the SW 1/4 of Sec. 14, T. 12 S., R. 4 E. (Swenson, 1964, p. 164). Although most of the spring openings showed an oval or rounded shallow conical form, they were nearly all aligned along visible fractures in the soil. Woodard plotted 42 sand spouts on his map (1960). The largest spout crater recorded was 61 meters across (compared to a maximum of about 20 meters at Chilly Buttes). From the field evidence we have seen, and the minimal literature on the topic from the Hebgen event, we conclude that the sand spring activity was perhaps similar for the two events, and may even have been more spectacular in the Borah area, because the largest springs in the Hebgen area were beneath the waters of Hebgen Lake.

AGGREGATE LENGTH OF PAVED ROADS DESTROYED

The epicentral regions of both the Borak Peak and Hebgen areas are similar in having a single paved highway aligned along the length of the principal (structurally controlled) valley, and another paved road joining that at about 60 degrees. The Borah Peak event destroyed no significant stretches of paved highway, but did result in several areas of settling which required minor repair. No highways became impassable. The Lost River fault escarpment system did offset several gravelled roads and smaller tracks.

The Hebgen event caused many kilometers of highways to become impassable, and a great proportion of those had to be completely replaced, rather than repaired. Hundreds of minor transverse and longitudinal fissures developed from segmentation of the road during ground motion on those sections of highway built on sandy outwash of the West Yellowstone Flats, rendering those roads impassable. Such damage is well shown in the photographs accompanying magazine and newspaper articles from that time, for example in Ball (1960, p.1). A major rockslide and consequent flooding destroyed Highway 287 from the mouth of Beaver Creek to the edge of Missouri Flats, a distance of 6.4 km. That highway was rendered impassable for the next 21 km east to its junction with Highway 191, owing to transverse minor consolidation scarps and slumps carrying the roadbed into Hebgen Lake. Ground motion segmentation also closed about 29 km of the roads around West Yellowstone. A conservative estimate would place the total length of paved highway destruction in the immediate epicentral area at more than 56 km, with several known shorter sections outside the immediate area rendered impassable by rockfall damage or settling of bridge-ramp fills. For a total distance of about 11 km the former right-of-way of Highway 287 along Hebgen Lake and the Madison Canyon was not even available, and a new alignment had to be created.

We see then, that the road damage from the Borah Peak shock was so slight that no stretches of the paved highway, even close to the faults, were destroyed, whereas many kilometers of paved roadway were rendered impassable in the Hebgen event.

MAJOR PHYSIOGRAPHIC CHANGES PRODUCED

This topic treats geomorphic effects other than the fault escarpments and mass gravity features discussed above. No major physiographic changes have yet been attributed to the Borah Peak earthquake, although the results of regional resurveying and levelling may indicate such changes.

The Hebgen Lake earthquake produced a new lake (Quake Lake) behind the Madison Canyon rockslide, and altered the shoreline and shape of existing Hebgen Lake itself as a result of consolidation and basin tilting. Regional resurveying and levelling has shown major tilting and subsidence of the Henrys Lake block just to the southwest of the Hebgen Fault, along with some elevation of the Madison Range block to the north. These effects have been discussed in detail by Myers and Hamilton (1964), and depicted by contours on the U.S. Geological Survey map (1964, Plate 2). The largest downtilted block, here termed the Henrys Lake Range Block, has a surface area of about 440 square kilometers. It was tilted down toward the northeast against the Hebgen Fault, with maximum depression of about 6 meters along the northeast shore of the narrow northwestern arm of Hebgen Lake, over a distance of about 6.4 km. The smaller Red Canyon Block (37.6 square km) was tilted down to the north against the arcuate trend of Kirkwood Ridge. Maximum depression along part of the northern margin was about 5 meters.

CONCLUSIONS

On the basis of these comparisons of surface effects from the Borah Peak earthquake with the Hebgen Lake earthquake, we conclude that the Hebgen event was significantly more important in terms of geologic effects in all seven of the categories considered. This suggests that the energy released to produce so much more substantial an array of effects may have been greater for the Hebgen event than for the Borah Peak event, despite the implication of the reverse by certain magnitude calculations based upon the seismic records.

If that is true, the question naturally arises as to how so much more energy could have been released in the Hebgen Lake case, and avoid detection by the instrumental networks. The late S. W. Nile, physicist and collaborator in seismology for Montana and Idaho, U. S. Coast and Geodetic Suvey, provided one answer. In September, 1959, he prepared a map of the region which showed the Hebgen Lake epicenters active during the first 48 hours, and pointed out that all had become active in the first night of the quake, and that all were magnitude 6 or greater during the first 24 hour period following the main event (Nile, 1960, p. 24). These preliminary magnitude observations were later confirmed by Steinbrugge and Cloud (1962, p. 182), and only one magnitude revised downward to 5.5-5.75.

This suggests that the total 24-hour energy package may easily have been much greater in the case of the Hebgen Lake event than for the Borah Peak event. Finally, a review of the seismograms of the two earthquakes as recorded on the same Wood-Anderson instruments have been reviewed, and the Hebgen Lake earthquake, although farther from the station, shows traces with a much greater amplitude than those from the Borah Peak earthquake. This has been confirmed by D.I. Doser (1984, personal communication). It seems possible that either the Hebgen Lake event was under-rated, or the Borah Peak event over-rated, in error. At the present time geophysicists have already informally changed the magnitude rating assigned to the Hebgen Lake earthquake, based upon re-examination of the seismic records, and calculations of the seismic moments of the main shock and aftershocks (Doser, loc cit), and the revised ratings have already been used in recent literature (Stover, 1984, p. 1; Smith and others, 1985, p. 2,3).

REFERENCES

Baldwin, E.M., 1951, Faulting In The Lost River Range of Idaho: American Journal of Science, vol. 249, p. 884-902.

Ball, R.M., 1960, The Madison Earthquake And Its Effects: in, Campau, D.E., and Anisgard, H.W., eds.: 11th Annual Field Conf. Guidebook, Billings Geological Society, p. 71-77.

----------, 1960?, The Madison Earthquake And Its Effects: undated report, no publisher listed, 13 p.

Crone, A.J., Machette, M.N., Bonilla, M.G., and others, 1985, Characteristics of Surface Faulting Accompanying the Borah Peak Earthquake, Central Idaho: in Workshop XXVIII on the Borah Peak Earthquake: U.S.G.S. Open-File Report, in press.

Crone, A.J., and Machette, M.N., 1985, Surface Faulting Accompanying the Borah Peak Earthquake, Central Idaho: in, Geology, vol. 12, no. 11, p. 664-667.

Doser, D.I., 1985, The 1983 Borah Peak, Idaho and 1959 Hebgen Lake, Montana Earthquakes: Models for Normal Fault Earthquakes in the Intermountain Seismic Belt: in Workshop XXVIII on the Borah Peak Earthquake: U.S.G.S. Open-File Report, in press.

----------, 1984, Source Parameters and Faulting Processes of the 1959 Hebgen Lake, Montana Earthquake Sequence: in press.

Hadley, J.B., 1960, The Madison Landslide: in, Campau, D.E., and Anisgard, H.W., eds.: 11th Annual Field Conf. Guidebook, Billings Geological Society, p. 45-48.

----------, 1964, Landslides and Related Phenomena Accompanying the Hebgen Lake Earthquake of August 17, 1959: U. S. Geol. Survey Prof. Paper 435-K, p. 107-138.

Hait, M.H., Jr., and Scott, W.E., 1978, Holocene Faulting, Lost River Range, Idaho: Geological Society of America, Abstracts with Programs, vol. 10, no. 5, p. 217.

Hall, W.B., 1960, Mass-Gravity Movements in the Madison and Gallatin Ranges, Southwestern Montana: in, Campau, D.E., and Anisgard, H.W., eds.: 11th Annual Field Conf. Guidebook, Billings Geological Society, p. 200-206.

----------, 1961, Geology of Part of the Upper Gallatin Valley of Southwestern Montana: Unpublished Ph. D. Dissertation, Univ. of Wyoming, 239 p.

Keefer, D.K., and others, 1985, Landslides in the Borah Peak, Idaho Earthquake of 1983: in Workshop XXVIII on the Borah Peak Earthquake: U.S.G.S. Open-File Report, in press.

Myers, W.B., and Hamilton, Warren, 1964, Deformation Accompanying the Hebgen Lake Earthquake of August 17, 1959: U.S. Geol. Survey Prof. Paper 435-I p. 55-98.

Nile, S.W., 1960, The Hebgen Lake Earthquakes: in, Campau, D.E. and Anisgard, H.W., eds.: 11th Ann. Field Conf. Guidebook, Billings Geol. Soc., p. 24-30.

Reagor, Glen, and Baldwin, F.W., 1984, Intensity Survey of the Borah Peak, Idaho, Earthquake of October 28, 1983: U.S.G.S. Open-File Report 84-166, 67 p.

Reilinger, Robert, 1985, Vertical Movements Associated with the 1959, M=7.1 Hebgen Lake Montana Earthquake: in Workshop XXVIII on the Borah Peak Earthquake: U.S.G.S. Open-File Report, in press.

Richter, C.F., 1935, An Instrumental Earthquake Magnitude Scale: Seismological Soc. of America Bull., vol. 21, p. 1-32.

Ruppel, E.T., 1964, Strike-slip Faulting and Broken Basin-Ranges in East-Central Idaho and Adjacent Montana: U.S. Geol. Survey Prof. Paper 501-C, p. 14-18.

Ryall, A.S., 1962, The Hebgen Lake, Montana, Earthquake of August 17, 1959: P Waves: Seismological Soc. of America Bull., vol. 52, no. 2, p. 235-271.

Scott, W.E., Pierce, K.L., and Hait, M.H., 1985, Quaternary Tectonic Setting of the 1983 Borah Peak Earthquake, Central Idaho: in Workshop XXVIII on the Borah Peak Earthquake: U.S.G.S. Open-File Report, in press.

Smith, R.B., Richins, W.D., Doser, D.I., Eddington, P.K., Leu, L.L., and Chen, G., 1985, The Borah Peak Earthquake: Seismicity, Faulting Kinematics, and Tectonic Mechanism: in Workshop XXVIII on the Borah Peak Earthquake: U.S.G.S. Open-File Report, in press.

Stein, R.S., and Barrientos, S.E., 1985, The 1983 Borah Peak, Idaho, Earthquake: Geodetic Evidence for Deep Rupture on a Planar Fault: in Workshop XXVIII on the Borah Peak Earthquake: U.S.G.S. Open-File Report, in press.

Steinbrugge, K.V., and Cloud, W.K., 1962, Epicentral Intensities and Damage in the Hebgen Lake, Montana, Earthquake of August 17, 1959: Seismological Soc. of America Bull., vol. 52, no. 2, p. 181-234.

Stover, C.W., 1984, Preliminary Isoseismal Map and Intensity Distribution for the Borah Peak, Idaho, Earthquake of October 28, 1983: U.S. Geol. Survey Open-File Rept. 84-297, 6 p.

Swenson, F.A., 1964, Ground-Water Phenomena Associated With the Hebgen Lake Earthquake: U.S. Geol. Survey Prof. Paper 435-N, p. 159-165.

Taylor, C.L., Cline, K.M., Page, W.D., and Schwartz, D.P., 1984, Surface Faulting and Other Phenomena Associated With the October 28, 1983, Borah Peak Earthquake, Idaho: in, Earthquake Engineering Research Institute (EERI) 1984 Reconnaissance Report on Borah Peak, Idaho, Earthquake, in press.

Tocher, Don, 1962, The Hebgen Lake, Montana, Earthquake of August 17, 1959, MST: Seismological Soc. of America Bull. V. 52, No. 2, p. 153-162.

U.S. Geological Survey, 1964, The Hebgen Lake, Montana, Earthquake of August 17, 1959: U.S. Geol. Survey Prof. Paper 435, 242 p.

Vincent, K.R., 1985, Measurement of Vertical Tectonic Offset using Longitudinal Profiles of Geomorphic Surfaces near Borah Peak, Idaho: a Preliminary Report: in Workshop XXVIII on the Borah Peak Earthquake: U.S.G.S. Open-File Report, in press.

Waag, C.J., 1985, Groundwater Eruptions and Sediment Boil Formation in the Chilly Buttes Area, Mt. Borah, Idaho Earthquake: in Workshop XXVIII on the Borah Peak Earthquake: U.S.G.S. Open-File Report, in press.

Witkind, I.J., 1960, The Hebgen Lake, Montana, Earthquake of August 17, 1959, in Campau, D.E., and Anisgard, H.W., eds.: 11th Annual Field Conf. Guidebook, Billings Geological Society, p. 31-44.

----------, 1964, Reactivated Faults North of Hebgen Lake: U.S. Geol. Survey Prof. Paper 435-G, p. 37-50.

----------, 1969, Geology of the Tepee Creek Quadrangle, Montana-Wyoming: U.S. Geol. Survey Prof. Paper 609, 101 p.

Witkind, I.J., Myers, W.B., Hadley, J.B., Hamilton, Warren, and Fraser, G.D., 1962, Geologic Features of the Earthquake at Hebgen Lake, Montana, August 17, 1959: Seismological Soc. of America Bull., vol. 52, no. 2, p. 163-180.

Wood, H.O., and Neumann, F., 1931, Modified Mercalli Intensity Scale of 1931: Seismological Soc. of America Bull., vol. 21, p. 38-54.

Woodard, F.W., 1960, Red Canyon Fault, Hebgen Lake, Montana, Earthquake August 17, 1959: in, Campau, D.E.,and others, eds.: 11th Ann. Field Conf. Guidebook, Billing Geol. Soc., p. 49-55.

----------, 1960, Some Causes and Effects of Earthquakes in the Hebgen Lake, Montana, Area: in, Campau, D.E. and others, eds.: 11th Ann. Field Conf. Guidebook, Billings Geol. Soc., Plate I.

Youd, T.L., Harp, E.L., Keefer, D.K., and Wilson, R.C., 1985, Liquefaction Generated by the 1983 Borah Peak, Idaho, Earthquake: in Workshop XXVIII on the Borah Peak Earthquake: U.S.G.S. Open-File Report, in press.

The 1983 Borah Peak Earthquake: A Calibration Event for Quantifying Earthquake Recurrence and Fault Behavior on Great Basin Normal Faults

David P. Schwartz
Woodward-Clyde Consultants
One Walnut Creek Center
100 Pringle Avenue
Walnut Creek, California 94596

Anthony J. Crone
U.S. Geological Survey
Box 25046 Federal Center
Denver, Colorado 80225-0046

ABSTRACT

Exploratory trenching across the Lost River fault and 1983 surface displacements at Doublespring Pass Road shows that 1) only one surface faulting event occurred along this fault between the time of formation of the surface of a Pinedale age outwash fan (approximately 15,000 years ago) and the 1983 earthquake, 2) fault displacement for the pre-1983 and 1983 events is nearly identical, and 3) the analysis of scarp-derived colluvial deposits provides an accurate basis for quantifying recurrence of surface faulting earthquakes on normal-slip faults. The similarity in the slip distribution between the 1983 and pre-1983 events along the length of the surface rupture suggests that the 1983 event is a characteristic earthquake for this segment of the Lost River fault. The relationship between the timing of individual past surface faulting events and bedrock structure of the Lost River Range has the potential to provide important insights into processes of fault zone segmentation.

INTRODUCTION

The 1983 Borah Peak earthquake on the Lost River fault is an important earthquake for evaluating fault behavior, earthquake recurrence, and the earthquake generation process in the Great Basin. This event may be a realistic approximation of the magnitude and surface displacement that would occur during an earthquake on the Wasatch fault zone, and its effects deserve extremely careful attention. Fault scarp formation and degradation, and slip distribution, from the 1983 event provide a basis for calibrating observations and interpretations of earthquake recurrence and past displacement per event that have been made for other Great Basin normal faults from trench exposures and morphometric scarp analysis. In addition, the detailed study of scarps and recurrence along the entire Lost River Range front has the potential to provide important insights into processes of fault segmentation, barriers and asperities, and mechanisms of strain accumulation and release in intraplate environments. In the following sections we discuss these aspects of the Borah Peak earthquake as well as the preliminary results and interpretations of an

ongoing trenching study across the 1983 surface rupture at Doublespring Pass Road.

NUMBER EVENTS AND DISPLACEMENT PER EVENT ON NORMAL FAULTS

During the past eight years trenching studies on normal faults in the eastern Great Basin, for example the Wasatch (Swan and others, 1980; Schwartz and Coppersmith, 1984) and Drum Mountains (Crone, 1983) faults, have been undertaken to develop information on fault-specific earthquake recurrence and the amount of displacement that occurred during past surface faulting earthquakes. These studies have used the occurrence of scarp-derived colluvial units adjacent to the main fault as the basis for estimating the number of past events and the displacement per event. In trenches the colluvial stratigraphic sequence is commonly seen as stacked units or wedges that grade away from the main fault. The number of colluvial wedges is a basis for determining the number of events. The thickness of the wedge provides a minimum value of the height of the free face that was produced during the event.

In 1976 a trench was excavated across a fault scarp that was developed in a Pinedale age outwash fan at Doublespring Pass Road just north of Willow Creek (Hait and Scott, 1978). Relationships in this trench suggested that only one major surface faulting event had occurred since formation of the fan surface approximately 15,000 years ago. As part of the evaluation of the 1983 earthquake, we excavated a parallel trench (Figure 1) to re-expose these pre-1983 relationships and observe the changes that occurred in 1983. A preliminary log of the 1984 trench is shown on Figure 2. Within this trench, correlative stratigraphic marker horizons occur on both sides of the main fault and can be traced across the graben. Because of this, the complete post-fan faulting history is exposed, and measurement of pre-1983 displacements can be made and compared with 1983 displacements (Table 1). Mapping and analysis of the stratigraphic and structural relationships in the trench indicate the following sequence of events:

1. Pre-1983 surface faulting. The fan surface was displaced and a series of graben and a horst were produced across a 40m-wide zone west of the main scarp. The amount of displacement on individual faults formed during this event is the same across the base of a pedogenic carbonate horizon (Ck) that was near the surface of the fan and lithologic contacts at the base of the trench (for example, the top of a distinctive silty gravel).

2. Deposition of scarp-derived colluvium. This occurred at and west of the main fault (meters 5 through 10) and in graben (meters 15 through 19; 24 through 27). Fissure infills also developed (meters 24 and 39). These deposits are shown by the grey stippled pattern.

3. Continued colluviation and the development of an organic A-horizon (slanted pattern) at the pre-1983 ground surface.

4. 1983 surface faulting. All pre-1983 faults were reactivated, one new trace (G) developed, and the existing colluvial wedge at the main fault was back tilted to the east.

5. Deposition of scarp-derived colluvium. Post-faulting colluvial de-

posits (cross-hatched pattern) bury fault scarp free faces and are prominantly developed at the main fault (meter 5) and in a graben (meters 15 and 19).

Important conclusions that can be drawn from the new Doublespring Pass trench are:

1. Only one pre-1983 surface faulting earthquake occurred along the Lost River fault between the time of formation of the surface of the Pinedale age outwash fan and the 1983 event.

2. Surface displacement that occurred in 1983 closely mimicked displacement from the prior event in both style and amount. All individual pre-1983 faults were reactivated, including small graben and the well-defined horst. Displacement across the main fault was similar for both events as was displacement on many of the synthetic and antithetic faults. A comparison of 1983 and pre-1983 displacements is given in Table 1.

3. The development of scarp-derived colluvial deposits from successive earthquakes, the relationship between colluvium and fault scarp free faces, and other structural and stratigraphic relationships frequently used to quantify recurrence, can be clearly observed and support the techniques that have been developed to evaluate recurrence and the interpretations that have been made on other normal faults. In this regard, the 1983 earthquake is a major calibration event for evaluating earthquake recurrence on normal faults.

EARTHQUAKE RECURRENCE MODELS

The 1983 Borah Peak earthquake provides important data to test and evaluate earthquake recurrence models for Great Basin normal faults. Crone and Machette (1984) have shown the distribution of displacement along the length of the 1983 surface rupture. Although precise measurements of pre-1983 displacements have not been systematically made, our mapping suggests that scarp heights from 1983 were extremely similar to heights developed during the one pre-1983 event; small 1983 scarps are associated with small pre-1983 scarps and large 1983 scarps are associated with large pre-1983 scarps. The pattern of faulting is also remarkably consistent. At Elkhorn Creek, for example, a 25 cm high scarplet from 1983 is associated with a similar-height, degraded, pre-1983 scarp. Near Arentson Gulch individual en enchelon scarps formed in 1983 have the same heights (approximately 1 m) as the pre-1983 en echelon scarps. The trench excavated across the 1983 surface rupture at Doublespring Pass Road indicates that the displacement across the main fault is 174 to 198 cm for the 1983 event and 126 to 150 cm for the pre-1983 event. Therefore, it appears that the distribution of slip along the length of the fault in 1983 essentially duplicated the slip distribution of the pre-1983 faulting event.

Schwartz and Coppersmith (1984) proposed the characteristic earthquake model. This model of earthquake recurrence suggests that the occurrence of earthquakes on individual faults and fault segments does not follow a log linear frequency magnitude relationship of the form (log N=a-bM); rather, faults tend to generate essentially same size earthquakes having a relatively

narrow range of magnitudes near the maximum. To a large degree the characteristc earthquake is based on the observation of repeated similar-displacement events at a specific point along a fault. Much of the data come from the Wasatch fault, which has not had a historical surface faulting earthquake. Estimates of individual paleodisplacements were based on the colluvial stratigraphy observed in trenches, and on other geomorphic features such as the heights of tectonic terraces and amounts of individual stream offsets. For the Lost River fault the slip distribution for the 1983 event has been well-defined. Reconnaissance mapping and trench measurements show that point-specific displacement is essentially the same for the past two events and that small displacement events do not appear to have occurred. These observations support the characteristic earthquake as one model of earthquake recurrence and imply that the 1983 earthquake was a characteristic event for this segment of the range front fault zone that bounds the Lost River Range.

FAULT ZONE SEGMENTATION

Investigations of long range front faults in the eastern Great Basin, such as the 370 km long Wasatch fault zone, suggest that they are segmented and that individual segments might persist through several seismic cycles (Schwartz and Coppersmith, 1984). Segment boundaries proposed for the Wasatch fault zone are defined by differences in the timing of events and the age of scarps based on trenching and scarp morphology data, and are associated with the occurrence of salients and re-entrants in the range, changes in trend of the range, and major cross structures.

Implicit in segmentation modeling is the idea that each segment defines a distinct rupture segment during a surface faulting earthquake. If this is the case, segmentation has important implications for assessing seismic hazards. A discrete segment, bounded by structures that decouple it from adjacent segments, implies a fixed fault length. This provides one important parameter for constraining the maximum earthquake on a fault. A fixed scale is also consistent with the observed occurrence of similar-displacement events and the characteristic earthquake model, both of which imply similar seismic moments for successive earthquakes. In addition, information on differences in the timing of individual events, differences in the elapsed time since the most recent event, and differences in mean recurrence on different segments can be used to more realistically evaluate the most likely location and timing of the next large magnitude earthquake, especially on long fault zones.

The Lost River Range extends for approximately 140 km, from Arco to Challis, and only ruptured for 34 km (Crone and Machette, 1984) in 1983. Scott and others (1985), based on detailed and reconnaissance mapping, have suggested that the Lost River fault may be composed of five or six segments characterized by different geomorphic expression, structural relief, and timing of most recent displacement. At Elkhorn Creek, near the southern end of the rupture zone, a 25 cm high scarp formed in 1983 is coincident with a degraded scarp of approximately the same height that defines the pre-1983 event at this location. South of Elkhorn Creek, the strike of the range charges sharply and a set of higher fault scarps, along which there was no slip in 1983, can be traced southward. These preliminary observations suggest the possibility of a segment boundary south of Elkhorn Creek. Another major eastward step in the range occurs at Elbow Canyon. Crone and Machette (1984) also suggest that a segment boundary may occur near the bedrock hills at the northern end of the

1983 rupture zone. Detailed study of the scarps south of Elkhorn Creek and of the bedrock geology and structure at proposed boundary zones has the potential for providing important insight into processes of fault segmentation and rupture dynamics.

SUMMARY

The surface rupture from the 1983 Borah Peak earthquake, and the other scarps that occur along the front of the Lost River Range, provide an important laboratory for evaluating seismogenic normal faulting. Continuing studies should be directed towards developing tighter constraints on: the timing of individual past events, the elapsed time since the most recent event at different locations along the zone, and segmentation of range front faulting. Results from these studies have the potential for having major impacts on our understanding of the earthquake process and the assessment of seismic hazards in the Great Basin.

REFERENCES

Crone, A. J., 1983, Amount of displacement and estimated age of Holocene surface faulting event, eastern Great Basin, Millard County, Utah: Utah Geological and Mineral Survey Special Studies 62, p. 49-55.

Crone, A. J., and Machette, M. N., 1984, Surface faulting accompanying the Borah Peak earthquake, central Idaho: Geology, v. 12, p. 664-667.

Hait, M. J., Jr., and Scott, W. E., 1978, Holocene faulting, Lost River range Idaho: Geological Society of America, Abstracts with Programs, v. 10, No. 5, p. 217.

Schwartz, D. P. and Coppersmith, K. J., 1984, Fault behavior and characteristic earthquakes: examples from the Wasatch and San Andreas fault zones: Journal of Geophysical Research, v. 89, p. 5681-5698.

Swan, F.H., III, Schwartz, D. P., and Cluff, L.S., 1980, Recurrence of moderate to large magnitude earthquakes produced by surface faulting on the Wasatch fault, Utah: Bulletin of the Seismological Society of America, v.70, p. 1431-1462.

Scott, W .E., Pierce, K. L., and Hait, M. H., 1985, Quaternary tectonic setting of the 1983 Borah Peak earthquake: U.S.G.S. Open-File Report, in press.

ACKNOWLEDGMENTS

We thank M. H. Hait, Jr. for providing unpublished data on the 1976 trench. Kathryn Hanson and M. H. Hait, Jr. aided us in mapping the 1984 trench. F. H. Swan, III and Kevin J. Coppersmith provided instructive comments on the manuscript. Trenching was done under a U.S. Geological Survey contract to Woodward-Clyde Consultants.

Fault Letter	1983 Offset (cm)	Pre-1983 Offset(cm)	Comments
A	174-198	126-150	Main fault. Includes displacement across reverse fault to southeast of the main fault zone.
B	18	90	Synthetic displacement.
C	94-108	--	Synthetic displacement. Datum to measure pre-1983 displacement not exposed.
D	156-168	42-54+?	Pre-1983 displacement may be minimum value. Northeast boundary of horst.
B-D	72	38	Net displacement between northeast block of fault B and southwest block of fault D.
E	80	0	No pre-1983 displacement. Zone of shearing within the horst.
F	36	76+?	Southwest boundary fault of horst. Pre-1983 is very poorly known.
G	52	--	Southwest boundary fault of horst. Datum to measure pre-1983 displacement not exposed.
H	16	--	Antithetic displacement. Datum to measure pre-1983 displacement not exposed.
F-H	72	44-48	Net displacement between northeast block of fault F and southwest block of fault H.
I	6	24	Small antithetic fault.
F-I	48-68	0-28	Net displacement between northeast block of fault F and southwest block of fault I.
J	44	46+?	Synthetic displacement.
K	8	44+?	Antithetic displacement
L	14	20	Antithetic displacement.
M	10	10+	Pre-1983 displacement is minimum value.

Table 1. Comparison of 1983 and pre-1983 displacements of faults exposed in the trench. Fault letter refers to faults labeled in Figure 2. Top of distinctive silty gravel is datum used to determine pre-1983 displacements. Measurements are queried where uncertain; labeled with (+) where value is likely to be a minimum.

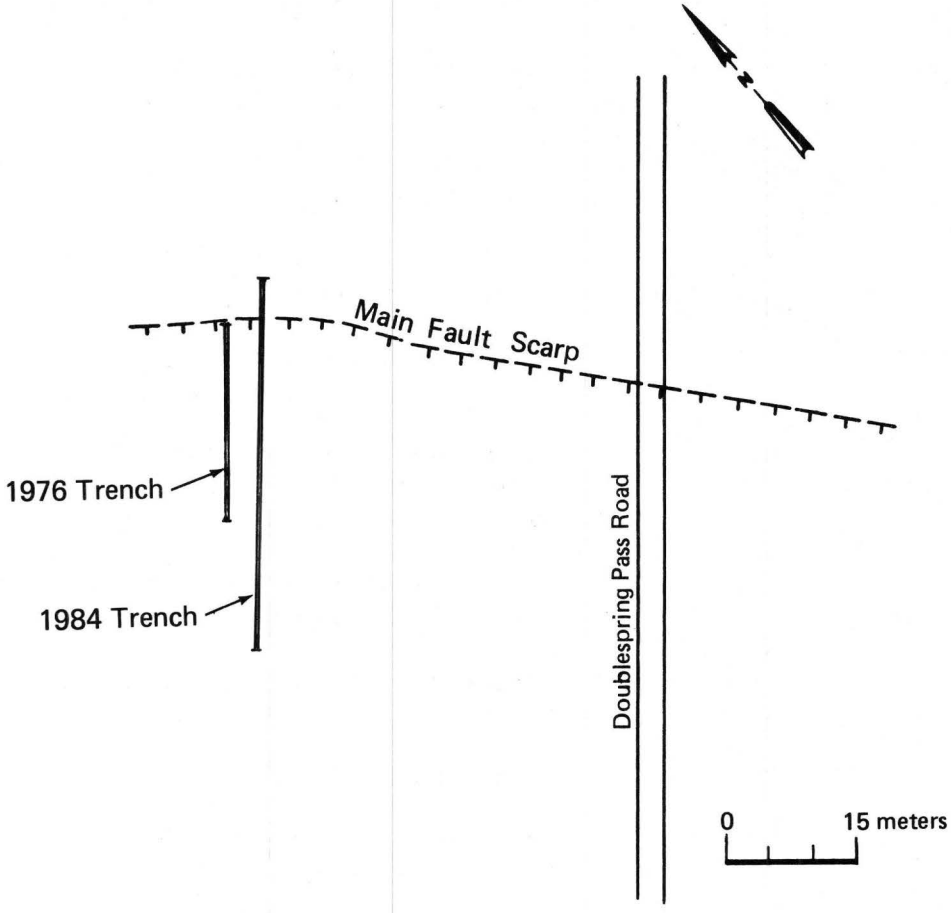

Figure 1. SKETCH MAP SHOWING LOCATION OF 1984 TRENCH AT DOUBLESPRING PASS ROAD.

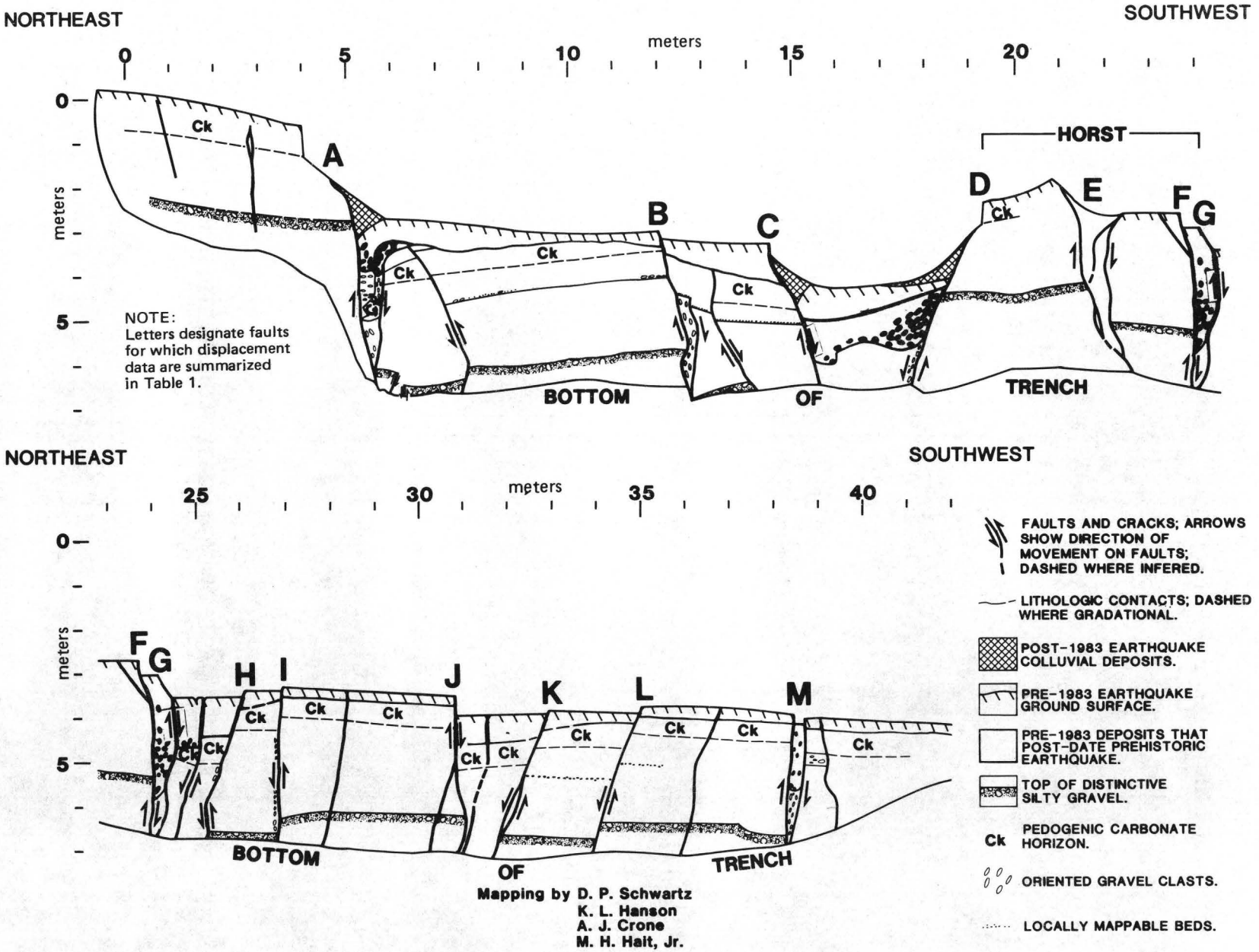

Figure 2. PRELIMINARY TRENCH LOG ACROSS 1983 SURFACE RUPTURE AT DOUBLESPRING PASS ROAD.

SHALLOW SEISMIC REFRACTION STUDIES ACROSS THE WILLOW CREEK FAULT RUPTURE ZONE AND THE CHILLY BUTTES SAND BOILS

J. R. Pelton
C. W. Meissner
C. J. Waag
S. H. Wood
Department of Geology and Geophysics
Boise State University
Boise, Idaho 83725

ABSTRACT

Seismic refraction data indicate the thickness of surficial unconsolidated material in the vicinity of the Willow Creek fault rupture zone and the Chilly Buttes sand boils.

Willow Creek: The thickness of unconsolidated material is approximately 13 m beneath a point located on the upthrown side 10 m northwest of Doublesprings Pass road and 140 m northeast of the main scarp where it crosses Doublesprings Pass road. From this point the thickness gradually increases to the southwest along Doublesprings Pass road and is in the range 27-35 m beneath the main scarp. No definitive conclusion can be made from the refraction data concerning the thickness of unconsolidated material on the downthrown side. Semiconsolidated sediment or sedimentary rock with a compressional wave velocity of 2950 m/s underlies the unconsolidated material on the upthrown side. The upper surface of the layer of semiconsolidated sediment or sedimentary rock dips 8-18 degrees to the southwest beneath the upthrown side; no definitive conclusion can be made from the refraction data concerning the continuity of this surface across the fault rupture zone.

Chilly Buttes: The thickness of unconsolidated material beneath the southern portion of the zone of Chilly Buttes sand boils increases from west to east as follows: west edge of zone, 30-40 m; center of zone, 35-50 m; east edge of zone, 40-60 m. The Brazer limestone (Ross, 1947) with a compressional wave velocity of 3780 m/s underlies the unconsolidated material beneath the sand boil zone. The upper surface of the limestone dips 3-10 degrees to the east.

INTRODUCTION

The nature of surface features caused by faulting or seismic motion in unconsolidated material is probably controlled to some extent by the thickness of the unconsolidated material. Two surface features associated with the Borah Peak, Idaho earthquake of 28 October 1983 are the fault rupture zone observed along the southwest side of the Lost River

Range and the sand boils which developed in Thousand Springs Valley. The fault rupture zone in the vicinity of Willow Creek and the sand boils near Chilly Buttes occur in unconsolidated Quaternary alluvium of unknown thickness. In this report, we present the results of preliminary seismic refraction studies done to place constraints on the thickness of surficial unconsolidated material in the vicinity of the Willow Creek fault rupture zone and the Chilly Buttes sand boils.

FIELD WORK AND DATA REDUCTION

Equipment: The instrumentation consisted of a truck-mounted twelve-channel analog SIE seismic refraction system: RA-44 recording amplifier, R-6 oscillographic recorder, and PCB-12B capacitor blaster. The smallest marked interval on the oscillographic record is 0.01 sec, but time can be interpolated to 0.001 sec (1 msec). A cable with 10 m takeouts was used at Willow Creek; at Chilly Buttes, a different cable with 30 m takeouts was used. Geophones were Dresser 10 htz transducers deployed singly at each station. The energy source for every shot was Kinestick (1/3 lb. approximately equivalent to 1/2 lb. 60% dynamite) detonated with Atlas Rockmaster 0/Instant blasting caps.

Willow Creek: Thirty-five stations at 10 m intervals were laid out along the northwest side of Doublesprings Pass road (approximately 10 m northwest of the road centerline) on the alluvial fan spreading from the mouth of the Willow Creek drainage (Figure 1a). The line had the following properties: (1) it was oriented perpendicular to the fault rupture zone, (2) it was centered on the fault rupture zone, (3) it ran parallel to the direction of topographic slope on the fan, and (4) it had a total length of 340 m. Station 1 on the southwest end and station 35 on the northeast end were the shotpoints. It was necessary to fire each shotpoint 3 times to reach an offset of 340 m with the twelve-channel recording system and 10 m station spacing. Single-station overlap of successive spreads was used to provide travel-time checks for each shot. Some shots were redone because of equipment malfunction or a need to increase the charge. Shot depths below the ground surface ranged from 0.9 to 1.5 m.

The datum was chosen to be the surface of the alluvial fan on the upthrown side of the profile, and the extension of this surface on the downthrown side (Figure 4). Static corrections were computed that would vertically displace the shots and stations to this datum. All static corrections were made assuming vertical incidence and a velocity of 825 m/s which was established for the near surface by shooting a short (24 m) velocity spread (Figure 2). The vertical incidence assumption was spot-checked against a more elaborate static correction method which takes into account non-vertical incidence; the two methods when carried to the nearest millisecond never disagreed by more than 1 msec, and usu-

ally agreed. Any distortion in the 10 m station interval caused by vertically displacing the stations to the datum was judged negligible (less than 0.5 m in the most extreme case).

The quality of first arrivals was quite good, with nearly all first arrivals classified as impulsive. A conservative statement of the timing precision of each first arrival is plus or minus 2 msec. The use of later arrivals was precluded by the strength of the first arrivals which dominated the records. The field work was carried out on December 2, 1983.

Chilly Buttes: Thirteen stations at 30 m intervals were laid out in a straight line along the north edge of an east-west dirt road terminating at the east edge of Chilly Buttes (Figure 1b). The orientation of the line was roughly perpendicular to the trend of the zone of sand boils, and was centered on this zone near its southern end. The total length of the line was 360 m. Station 1 on the west end and station 13 on the east end were the shotpoints. The west shotpoint was fired three times with increasing charges to achieve first-arrival data of adequate quality; the east shotpoint was fired once. Shot depths below the ground surface for the west and east shotpoints were approximately 0.8 and 1.0 m, respectively.

The datum was chosen to be the elevation of station 1 (the western shotpoint). All other stations were on nearly flat ground 3 m below the datum. Static corrections were made in the manner described for the Willow Creek line, using 825 m/s as the near-surface velocity. No short velocity spreads were shot for the Chilly Buttes line, and the 825 m/s velocity is simply borrowed from experience gained at Willow Creek. The ideal velocity to use for the static corrections would be the average velocity down to 3 meters beneath station 1, but this is unknown, and conceivably could be higher than 825 m/s because bedrock outcrops nearby. In fact, we had difficulty putting down the west shothole because of what appeared to be bedrock just below the surface. On the other hand, static corrections carried out with 825 m/s do not cause a significant discrepancy between the reciprocal times (travel times from 1 to 13 and 13 to 1; computed either on the ground surface or on the datum), and there is no inconsistency between the trend of the datum-corrected travel-time curve from 13 to 1 and the datum-corrected reciprocal time from 13 to 1. We therefore adopted the 825 m/s velocity for lack of a better alternative.

The first-arrival data for the Chilly Buttes line are not as good as the Willow Creek data. A conservative statement of the timing precision of the first arrivals is plus or minus 2 msec up to 150 m from the shot points, and then plus or minus 4 msec from 150 m to 360 m; impulsive first arrivals were observed at the shorter distances but they became increasingly emergent at longer distances. In addition, the time break for the eastern shot was poorly recorded and we were unable to repeat the shot. However, in spite of these difficulties, the datum-corrected

travel-time curves do define several distinct segments, and as mentioned before, there is no significant discrepancy between reciprocal times. Like the Willow Creek line, only first arrivals were judged to be useful. The field work was carried out on December 2, 1983.

INTERPRETATION

Eaton and Watkins (1970) published a table of observed minimum and maximum compressional velocities for different layers in the alluvial fill of intermontane basins in California and Arizona. The data are meant to indicate what one might encounter in an intermontane basin in the western United States. Layers are given in order of increasing depth but thicknesses are left unspecified. The minimum and maximum velocities of the first three layers and their lithologies are as follows:

1. V0 340-1490 m/s (unsaturated alluvium)

2. V1 1460-2260 m/s (saturated alluvium)

3. V2 1710-3290 m/s (semiconsolidated sediment; possibly sedimentary rock if the velocity is above 3000 m/s)

In the discussion below, reference will frequently be made to these velocity ranges and lithologies.

Willow Creek

The forward and reverse datum-corrected travel-time data for Willow Creek can be grouped into five distinct segments labeled A through E (Figure 3). The most critical aspect of the interpretation is the correlation of segments A, B, and C on the southwest to northeast profile with segments D and E on the northeast to southwest profile. By correlation, we mean identifying those segments which represent the direct wave arrivals, and those segments which represent head wave arrivals from the same interface. The initial interpretation deals with this question of correlation, and then a quantitative interpretation is made using the reciprocal method described by Hawkins (1961). We assume throughout that there are no low-velocity layers.

Initial Interpretation: Segments A and D with apparent velocities 730 m/s and 910 m/s, respectively, are interpreted to be the direct wave arrivals. An interpretation of significant lateral velocity change in the upper layer based on the different apparent velocities of A and D is probably not warranted because the 180 m/s velocity difference could be

reduced to insignificance by a slight change in interpreted slopes which would still be consistent with the data. The apparent velocities of A and D are comparable to the apparent velocity of 825 m/s indicated by the 24 m velocity spread (Figure 2). A velocity of 825 m/s is midway in the range of velocities for the layer of unsaturated alluvium given by Eaton and Watkins (1970), and the geology map by Ross (1947) indicates that the surface material in the vicinity of the refraction profile is Quaternary alluvium. On this basis an upper layer of unsaturated alluvium with velocity 825 m/s is interpreted to extend across the entire length of the profile.

A perplexing problem is the non-zero intercept (10-14 msec) indicated for A and D in Figure 3; a non-zero intercept of comparable magnitude is also seen in the 24 m velocity spread (Figure 2). The standard explanation for a non-zero intercept is the presence of a thin low velocity upper layer of soil which would produce first arrivals only close to the source. However, this explanation is not appropriate for the Willow Creek line because the upper 25 cm of ground was frozen during the field work, and thus would not be expected to be a layer of low velocity. The true explanation may be a combination of several factors such as an unexpected time delay between the recorded time break and the detonation of the blasting cap, or an extremely low velocity around the shot caused by loose fill in the shothole. It is also possible that the shots for the Willow Creek line, which were below the frozen layer, generated head waves in the frozen layer which were the first arrivals out to offsets of 30-40 m with 825 m/s apparent velocities. In this situation the non-zero intercept would be the result of low velocity (substantially lower than 825 m/s) along that part of the travel path from the shot to the frozen layer, and 825 m/s would have to be regarded as an overestimate of the velocity of the unsaturated alluvium.

Independent tests suggest that the Atlas Rockmaster O/Instant blasting caps may have a few msec of delay relative to more expensive zero-delay caps designed specifically for seismic work (Paul Donaldson, Boise State University, personal communication). In addition, the PCB-12B blaster uses a spring-loaded plunger that closes a bar switch on two contacts; one contact leads to the blasting cap and the other leads to the oscillographic recorder where the time break is written. Relative delays could be caused by a warp in the bar switch or different RC rise times in the cap and recorder lines, but we would expect such delays to be less than 1 msec.

The extremely low apparent velocity of 150 m/s between 0 and 2 m on the 24 m velocity spread of Figure 2 is even less than the velocity of a compressional wave in air (approximately 330 m/s). This result is not surprising if one considers that the material between the blasting cap source (at 0 m and 0.4 m below the ground surface) and the geophone (at 2 m) was mostly loose fill and ground disturbed by repeated blasting at the northeast shotpoint. Thus the bulk and shear moduli of the material, although undoubtedly greater than the bulk modulus of air, are

probably small, while the density of the material is probably 1000 times greater than the density of air. The result could easily be an extremely low compressional wave velocity, even less than that for air. Similar comments apply to the low apparent velocities observed for the 0-10 m and 340-330 m intervals on the Willow Creek line.

Segment E has a well-defined apparent velocity of 2205 m/s in the 300-150 m interval and represents a head wave generated by the northeast shot and propagating to the southwest. Although significant irregularities exist in the 150-0 m interval, there is no obvious and sustained shift to a higher apparent velocity which would indicate possible crossover to a deeper refractor. Therefore, E in the 300-0 m interval is interpreted to represent a head wave traveling along a single refracting interface that extends beneath the entire length of the profile. We shall call this refracting interface the main refractor. The occurrence of D followed by E suggests that unless thin "hidden" layers are present, the head wave traveling from northeast to southwest along the main refractor initially follows the lower boundary of the 825 m/s layer (i.e., the lower boundary of the unsaturated alluvium). However, we keep open the possibility that this head wave does not necessarily follow the lower boundary of the unsaturated alluvium for the entire length of the profile. More specifically, in the second of two possible interpretations of the Willow Creek data we will find it necessary to allow for an intermediate layer of saturated alluvium between the unsaturated alluvium and the main refractor, and this intermediate layer will pinch out against the main refractor on the upthrown side.

There is no obvious indication that the main refractor is downfaulted on the southwest side of the fault rupture zone. Significant downfaulting would displace E on the downthrown side upwards (greater travel time) relative to the straight-line trend established on the upthrown side. However, downward displacement of E (less travel time) is actually observed; an explanation for this is given in the quantitative interpretation section. Segment E does provide a subtle indication that the main refractor may be downfaulted; note the trend to lower apparent velocities in the 110-0 m interval. This suggests a change in dip of the main refractor and/or a decrease in head wave velocity as the wave propagates to the southwest on the downthrown side. Two important points should be made here: (1) if the main refractor dips to the southwest, an increase in southwesterly dip is consistent with lower apparent velocities, and given the limited resolution of the data, an increase in southwesterly dip could represent downward step faulting; (2) a decrease in the velocity of head wave propagation to the southwest suggests a lateral change in the geologic materials beneath the main refractor, with the lower velocity materials occurring on the downthrown side of the fault. Thus the main refractor may not be a continuous geologic horizon, and it may overly different geologic materials on either side of the fault.

Another interpretation for segment E is suggested by the slightly hyperbolic shape of E in the 150-0 m interval. This hyperbolic shape

may indicate a diffraction, possibly from a discontinuity in the main refractor beneath the fault rupture zone. However, analysis shows that the travel time at the greatest offset from the hypothesized point of discontinuity would require an average velocity of at least 2000 m/s, or more than twice the 825 m/s velocity established for the unsaturated alluvium. Thus we rule out the possibility of a diffraction causing the somewhat hyperbolic shape of E in the 150-0 m interval.

Segment B with apparent velocity 1275 m/s represents a head wave generated by the southwest shot and propagating to the northeast, probably along the lower boundary of the 825 m/s layer. The apparent velocity suggests that saturated alluvium is the underlying material; in other words, B probably represents a head wave propagating to the northeast along the water table. Segment C with apparent velocity 4285 m/s also represents a head wave generated by the southwest shot and propagating to the northeast. It is reasonable to assume that this head wave propagates along the main refractor, and this means that C and E represent head waves from the same interface and are therefore correlated.

The interpretation can now be seen to involve two possibilities: either B and C both correlate with E, or only C correlates with E and B does not. If both B and C correlate with E, then the main refractor is properly reversed in the 40-310 m interval, and we have the following implications which correspond to Figure 4a: (1) on the upthrown side, the main refractor dips to the southwest with a true velocity between 2205 m/s and 4285 m/s; (2) on the downthrown side, the main refractor dips to the northeast with a true velocity between 1275 m/s and 2205 m/s; (3) the main refractor coincides with the lower boundary of the 825 m/s layer beneath the entire profile (given that there are no thin "hidden" layers). Referring to the data of Eaton and Watkins (1970), we would conclude that the layer of unsaturated alluvium overlies saturated alluvium on the downthrown side, whereas it overlies semiconsolidated sediment or sedimentary rock on the upthrown side. If C correlates with E but B does not, then the main refractor is properly reversed only in the 130-310 m interval, and we have the following alternate implications which correspond to Figure 4b: (1) on the upthrown side, the main refractor dips to the southwest with a true velocity between 2205 m/s and 4285 m/s; (2) on the downthrown side, the main refractor probably dips to the southwest under a layer of saturated alluvium, but the lack of correlated data prevents us from making interpretations there with the degree of certainty achieved on the upthrown side; (3) the main refractor probably coincides with the lower boundary of the 825 m/s layer only on the northeast side of the profile. In this second possible interpretation the apparent velocities still suggest that unsaturated alluvium overlies saturated alluvium on the downthrown side and semiconsolidated sediment or sedimentary rock on the upthrown side. The only real difference is the lateral extent of the layer of saturated alluvium. The first interpretation requires the layer of saturated alluvium to end at the fault rupture zone, whereas in the second interpretation the layer of saturated alluvium is expected to pinch out on

the upthrown side against semiconsolidated sediment or sedimentary rock at a location determined by the dip of the water table. Thus application of the reciprocal method to obtain quantitative results should not reveal a great deal of difference between the two possible interpretations for the upthrown side.

Quantitative Interpretation: The arguments given above are the basis for a quantitative interpretation using the reciprocal method as described by Hawkins (1961). This method provides the depth to a given refractor beneath each receiver in the interval over which the refractor is properly reversed. The results for the case in which B and C are correlated with E are illustrated in Figure 4a; results for the case in which C correlates with E but B does not are shown in Figure 4b. Solid lines indicate refracting interfaces for which depth computations were made with the reciprocal method; short dashed lines indicate extrapolation of the refracting interfaces in a manner consistent with the solid lines.

If both B and C are indeed correlative with E, and there are no thin "hidden" layers present, then segments B,C, and E represent arrivals from head waves traveling along the lower boundary of the 825 m/s layer over the entire length of the profile. A sufficient condition for this to occur would be a substantial vertical offset of the 2950 m/s layer beneath the fault rupture zone (this offset is indicated by the dotted line at position X in Figure 4a). If there is in fact no vertical offset at X, or it is not sufficiently large, or if the vertical offset occurs southwest of position X, then the 2950 m/s layer effectively continues across the fault rupture zone beneath the saturated alluvium. In this case correlation of B with E in the 40-150 m interval may be incorrect because data from segment E in that interval could represent head wave propagation along the interface between the saturated alluvium and the 2950 m/s layer, whereas data from segment B most likely represents head wave propagation along the water table.

If C correlates with E but B does not, and we interpret B to represent the head wave propagating along the water table, then the position of the water table is uncertain because segment B is not reversed. In this situation, the correct interpretation would depend on the true velocity of the saturated alluvium. The behavior of groundwater flow within alluvial fans would suggest a water table that parallels the ground surface (Kirk Vincent, UC Berkeley, personal communication). If we assume that the water table extends parallel to the seismic datum (the unfaulted ground surface), then the 1275 m/s apparent velocity of segment B is the true velocity of the saturated alluvium, and we easily compute a water table depth of 20 m below the datum (see Figure 4b where the long dashed line represents the water table constrained by the B intercept and the 1275 m/s true velocity). Application of the reciprocal method to segments C and E then gives an interpretation for the upthrown side that is not significantly different from that of Figure 4a (compare Figures 4a and 4b). Since the refracting interface associated with E

(i.e., the main refractor) has been interpreted to extend beneath the entire profile, an extrapolation of the 2950 m/s refractor beneath the downthrown side is indicated in Figure 4b. We have shown this extrapolation to be continuous because there is no obvious evidence in the data for vertical offset of the main refractor. Continuity of the 2950 m/s refractor over the length of our profile would imply either the main refractor is geologically so young that vertical offsets detectable with the seismic refraction method have not been developed, or the main Lost River fault is located further to the southwest than our profile.

The geology map by Ross (1947) suggests that the Mississippian Brazer limestone may underly the alluvium on the upthrown side of the profile. However, 2950 m/s is 830 m/s lower than the velocity estimated for the Brazer limestone with the Chilly Buttes refraction line (see discussion below). Other candidates for the 2950 m/s layer would be the Mississippian Milligen formation which underlies the Brazer limestone and is mostly carbonaceous shale with some limestone, and the Tertiary Donkey fanglomerate which mantles the slopes just east of the refraction profile and is more thoroughly consolidated than the Quaternary alluvium (Ross, 1947).

There is some evidence to support extension of the 2950 m/s refractor under the saturated alluvium to the downthrown side as required by the interpretation of Figure 4b. Consider the head wave generated by the northeast shotpoint along the main refractor. In Figure 4b, the indicated extension of the refractor would suggest that the head wave energy reaching the surface in the 200-0 m interval would encounter increased velocity in that portion of the upward ray path through the saturated alluvium. This is consistent with the offset of segment E data from the 2205 m/s apparent velocity line; the offset is in the direction of less time as required by the higher velocity. However, the model of Figure 4b suggests that we should observe the offsets beginning at 200 m and that the offsets should increase to the southwest, but this is not the case. The actual situation could be complicated by factors which would act opposite to the higher velocity along the upward travel path. These might include step faulting (down to the southwest) of the main refractor, or increasing dip of the main refractor to the southwest. In addition, near surface velocity variations could play a role. A seismic test to determine the extent of the 2950 m/s refractor beneath the downthrown side would be to displace the southwest shot to the southwest. If the crossover from B to C also shifts west, then the 2950 m/s refractor extends beneath the saturated alluvium on the downthrown side. Another possibility would be to shoot a line parrallel to the fault rupture zone on the downthrown side.

Our preferred model is that of Figure 4b which has the following features: (1) a water table which essentially parrallels the ground surface, (2) a layer of semiconsolidated sediment or sedimentary rock with an upper surface dipping to the southwest and extending in a continuous manner beneath the entire length of the profile, and (3) a layer of sat-

urated alluvium which pinches out on the upthrown side of the fault rupture zone against the layer of semiconsolidated sediment or sedimentary rock. We feel that the eastward dip of the water table in Figure 4a is suspicious although it may reflect a distortion in groundwater flow at the fault rupture zone caused by an anomaly in porosity and permeability. It is perhaps best to regard the two interpretations of Figure 4 as providing reasonable bounds on the thickness of unconsolidated material beneath the upthrown side. Our data do not provide the means to interpret a thickness for the unconsolidated material on the downthrown side, nor can we establish with certainty the position of the water table or the continuity of the layer of semiconsolidated sediment or sedimentary rock.

Chilly Buttes

The forward and reverse datum-corrected travel-time data for Chilly Buttes can be grouped into three distinct segments labeled A, B, and C (Figure 5). We first make an initial interpretation in which these segments are correlated, then a quantitative interpretation is made using the reciprocal method. We assume throughout that there are no low-velocity layers.

Initial Interpretation: Ross (1947) shows that the surface material surrounding Chilly Buttes is Quaternary alluvium. Our data are not sufficient to determine the velocity of the unsaturated alluvium because the 30 m station spacing was too great for detection of direct waves as first arrivals, and we were unable to shoot a short velocity spread in the vicinity of the profile. Therefore, in the quantitative interpretation we consider both the 825 m/s figure established for the Willow Creek profile, and an estimate based on the intercept time for the water-table refractor and a knowledge of the depth and dip of the water table.

Segment A with apparent velocity 2560 m/s represents a head wave propagating from west to east. Notice that A shows no clear trend to a higher apparent velocity which might mean crossover to a deeper refractor, and first arrivals consistently plot along A from 60 m out to the end of the profile. These observations indicate that A represents a single refracting interface which extends beneath the entire length of the profile. A geologic map by Ross (1947) shows that the Brazer limestone underlies Chilly Buttes, and it is likely that we had the west shot resting nearly on the limestone bedrock. From the west shotpoint we would expect that the limestone dips to the west under the alluvial cover, assuming that the limestone is not sharply downfaulted to great depth at the edge of Chilly Buttes. The occurrence of A suggests that in fact the limestone is not sharply downfaulted to great depth, and we interpret A to represent the head wave propagating along the top of the

limestone, at least initially, and probably over the entire length of the profile. The 2560 m/s apparent velocity is lower than expected for limestone, but this is explained by the anticipated dip of the limestone to the east. Although there is some scatter in the data defining A, there does not appear to be a fundamental change in dip or refractor velocity, unless there are simultaneous changes in dip and refractor velocity that compensate. The non-zero intercept of A (35 msec) suggests that the limestone is offset downward to a limited extent at the west shotpoint, or that a lower velocity weathered layer exists at the top of the limestone.

Segment B with apparent velocity 1860 m/s represents a head wave propagating from east to west, probably along the water table. Segment C with apparent velocity 6000 m/s also represents a head wave propagating from east to west. It is reasonable to assume that this head wave propagates along the limestone refractor, and this means A and C are correlated. The correlation of B with A involves the same difficulties encountered during correlation of B with E on the Willow Creek profile. If B does correlate with A, then the refractor represented by A dips east from the west shotpoint with velocity between 2560 m/s and 6000 m/s, and dips west from the east shotpoint with velocity between 1860 m/s and 2560 m/s. If B does not correlate with A, then the data still imply that the refractor associated with A dips east from the west shotpoint with velocity between 2560 m/s and 6000 m/s, but the lack of correlated data on the east side of the profile prevents us from making interpretations there with the degree of certainty achieved on the west side. In the quantitative results to follow, both possibilities are considered: (1) both B and C correlate with A, and (2) C correlates with A, but B does not.

Quantitative Interpretation: If we assume a velocity for the unsaturated alluvium of 825 m/s and require that B and C correlate with A over the 60-330 m interval, then application of the reciprocal method results in the interpretation shown in Figure 6a. The solid lines indicate refracting interfaces for which depth computations were made with the reciprocal method; the dashed lines represent extrapolations that are consistent with the solid lines; the dashed-dotted line is an extrapolation of the 3780 m/s refractor towards the west shotpoint and is a qualitative assessment based on the occurrence of outcropping limestone and the non-zero intercept of segment A. The 3780 m/s refractor can be reasonably identified as the limestone, but the identity of the 2370 m/s refractor is uncertain. Because 2370 m/s is somewhat high for the Eaton and Watkins (1970) range for saturated alluvium, we prefer the westward dipping refractor be interpreted as semiconsolidated sediment. A downward vertical offset (not small) of the 3780 m/s refractor is consistent with the assumption that B correlates with A (this offset is indicated in Figure 6a by the dotted line at X). Continuation of the 3780 m/s refractor beneath the 2370 m/s refractor without downward offset is probably not consistent with the correlation of A and B for reasons similar to those discussed in the Willow Creek interpretation. We do not

have a sound explanation for the opposing dips of the two refractors, and we are troubled by the lack of a head wave arrival from the water table if we correlate B with A. Furthermore, it seems unlikely that a simultaneous change in dip and refractor velocity would exactly compensate to preserve the straight line trend of segment A. All things considered, Figure 6a is not our favored interpretation of the Chilly Buttes refraction data but we include it for completeness.

If B does not correlate with A, then it most likely represents the head wave along the water table. Water well data and the depth of the deepest sand boil which was dry on the day of the refraction work places constraints on the water table depth beneath the profile: 4.6 to 10.8 m from the surface. The well data also suggest that the water table parallels the surface (before the earthquake, and presumably after). Given this information, the intercept time for B yields unsaturated alluvium velocities of 370 m/s and 645 m/s for 4.6 m and 10.8 m depth, respectively. These estimates and the reciprocal method applied to the west side of the profile result in the interpretations shown in Figure 6b for 370 m/s and Figure 6c for 645 m/s. As before, the solid lines indicate interfaces for which depth computations were made with the reciprocal method. The long dashed lines show the positions of the water table that correspond to the different unsaturated alluvium velocities. The short dashed lines show extrapolations of the limestone refractor beneath the zone of sand boils. We consider the extrapolations of the limestone refractor beneath the zone of sand boils to be acceptable because there is no clear and sustained deviation in the apparent velocity of A which would suggest a change in dip. The abrupt change in dip of the limestone interface at 120 m in Figures 6b and 6c is based on a single data point and probably has no significance. However, this change in dip coincides with the expected location of a fracture with possible vertical offset in the Brazer limestone along which the zone of sand boils seems to have developed (Figure 1b).

The three possible interpretations of the Chilly Buttes refraction data consistently indicate that the Brazer limestone dips to the east at the west edge of the sand boil zone (see the 60-120 m interval in Figures 6a, 6b, and 6c). The depth of the limestone beneath the 120 m point on the ground surface is 20 m in Figure 6a and 30 m in Figures 6b and 6c (the 120 m point is just outside the sand boil zone); the true depth at the 120 m point should fall within this 20-30 m range unless we have made gross errors in estimating the velocities of the unsaturated and saturated alluvium. Our preferred models are given in Figures 6b and 6c, but unfortunately the limestone refractor in these models is not properly reversed across the zone of sand boils so that we cannot make a definitive statement regarding the depth of the limestone there. However, for reasons explained above, we consider the extrapolation of the limestone refractor to the east in Figures 6b and 6c to be reasonable. Thus preliminary estimates of the depth ranges to the limestone at the west and east edges of the sand boil zone are 30-40 m and 40-60 m, respectively (see Figures 6b and 6c).

CONCLUSIONS

The objective of this study was to place constraints on the thickness of surficial unconsolidated material in the vicinity of the Willow Creek fault rupture zone and the Chilly Buttes sand boils. We have the following conclusions which pertain to that objective:

Willow Creek: The two interpretations shown in Figure 4 can be considered together to give a range for the thickness of the unconsolidated material on the upthrown side of the Willow Creek fault rupture zone. The thickness of unconsolidated material is about 13 m beneath a point 10 m northwest of Doublesprings Pass road and 140 m northeast of the main scarp where it crosses Doublesprings Pass road. This thickness gradually increases to the southwest and is in the range 27-35 m beneath the main scarp. No definitive conclusion can be made from the refraction data concerning the thickness of unconsolidated material on the downthrown side. Semiconsolidated sediment or sedimentary rock with a compressional wave velocity of 2950 m/s underlies the unconsolidated material on the upthrown side. The upper surface of the layer of semiconsolidated sediment or sedimentary rock dips 8-18 degrees to the southwest beneath the upthrown side; no definitive conclusion can be made from the refraction data concerning the continuity of this surface across the fault rupture zone.

Chilly Buttes: The two preferred interpretations shown in Figures 6b and 6c can be considered together to give a range for the thickness of unconsolidated material beneath the zone of Chilly Buttes sand boils where that zone crosses the refraction profile: west edge of zone, 30-40 m; center of zone, 35-50 m; east edge of zone, 40-60 m. The Brazer limestone (Ross, 1947) with a compressional wave velocity of 3780 m/s underlies the unconsolidated material; the upper surface of the limestone dips 3-10 degrees to the east.

Finally, we emphasize that these are preliminary conclusions based on reconnaissance refraction work. We hope to test them with additional refraction work that can be tied to shallow drill holes.

ACKNOWLEDGMENTS

This study was supported by National Science Foundation Grant No. CEE-840-3585.

REFERENCES

Eaton, G. P., and J. S. Watkins, 1970, The use of seismic refraction and gravity methods in hydrogeological investigations, in Mining and Groundwater Geophysics/1967, edited by L. W. Morley, Economic Geology Report No. 26, Geological Survey of Canada, 722 pages.

Hawkins, L. V., 1961, The reciprocal method of routine shallow seismic refraction investigations, Geophysics, 26, pages 806-819.

Ross, C. P., 1947, Geology of the Borah Peak quadrangle, Idaho, Bulletin Geol. Soc. Amer., 58, pages 1085-1160.

FIGURE CAPTIONS

Figure 1. (a) Map showing location of Willow Creek refraction line. Black squares are shot points, connecting straight line is refraction line. Heavy line with northwest strike is main scarp of fault rupture zone. Contour interval 40 feet. Roads and topographic features from USGS 7.5' Borah Peak quadrangle, 1967, T10N, R22E, Section 28. (b) Map showing location of Chilly Buttes refraction line. Black squares are shot points, connecting straight line is refraction line. Black dots are sand boils and/or sinkholes. Black dots with tails are muddy water eruptions from the margins of Chilly Buttes. Crooked line is a fracture in the Brazer limestone, dashed where inferred. Countour interval 100 feet. Roads and topographic features from USGS 7.5' Chilly Buttes quadrangle, 1967, T9N, R22E, Section 30.

Figure 2. Travel-time data for short velocity spread shot at northeast end of Willow Creek refraction line. Source was an Atlas Rockmaster O/Instant blasting cap buried 0.4 m beneath the ground surface. Symbol size represents estimate of timing precision (plus/minus 1 msec).

Figure 3. Datum-corrected travel-time data for Willow Creek refraction line. Symbol frz shows location of fault rupture zone; letters A, B, C, D, E represent interpreted direct wave arrivals or head wave arrivals with indicated apparent velocities. Circles are used for forward travel times and squares are used for reverse travel times; symbol size represents timing precision (plus/minus 2 msec).

Figure 4. Two possible interpretations of the Willow Creek refraction data. Symbol frz shows location of fault rupture zone; MS with vertical bar shows location of main scarp; WT means water table. Stations shown by small black squares on ground surface. Numbers in meters shown below ground surface (e.g., 13 m) indicate thickness of unconsolidated mate-

rial at different locations. Different line types and symbol X explained in text. Horizontal and vertical scales equal.

Figure 5. Datum-corrected travel-time data for Chilly Buttes refraction line. Extent of sand boil zone indicated along horizontal axis. Letters A, B, C represent interpreted head wave arrivals with indicated apparent velocities. Circles are used for forward travel times and squares are used for reverse travel times; symbol size represents timing precision (small symbols = plus/minus 2 msec, large symbols = plus/minus 4 msec).

Figure 6. Three possible interpretations of the Chilly Buttes refraction data. Extent of sand boil zone indicated along ground surface. Symbol LS means limestone; WT means water table. Stations shown by black squares on ground surface. Datum is elevation of station 1 at 0 m. Numbers in meters shown below ground surface (e.g., 20 m) indicate thickness of unconsolidated material at different locations. Different line types and symbol X explained in text. Horizontal and vertical scales equal.

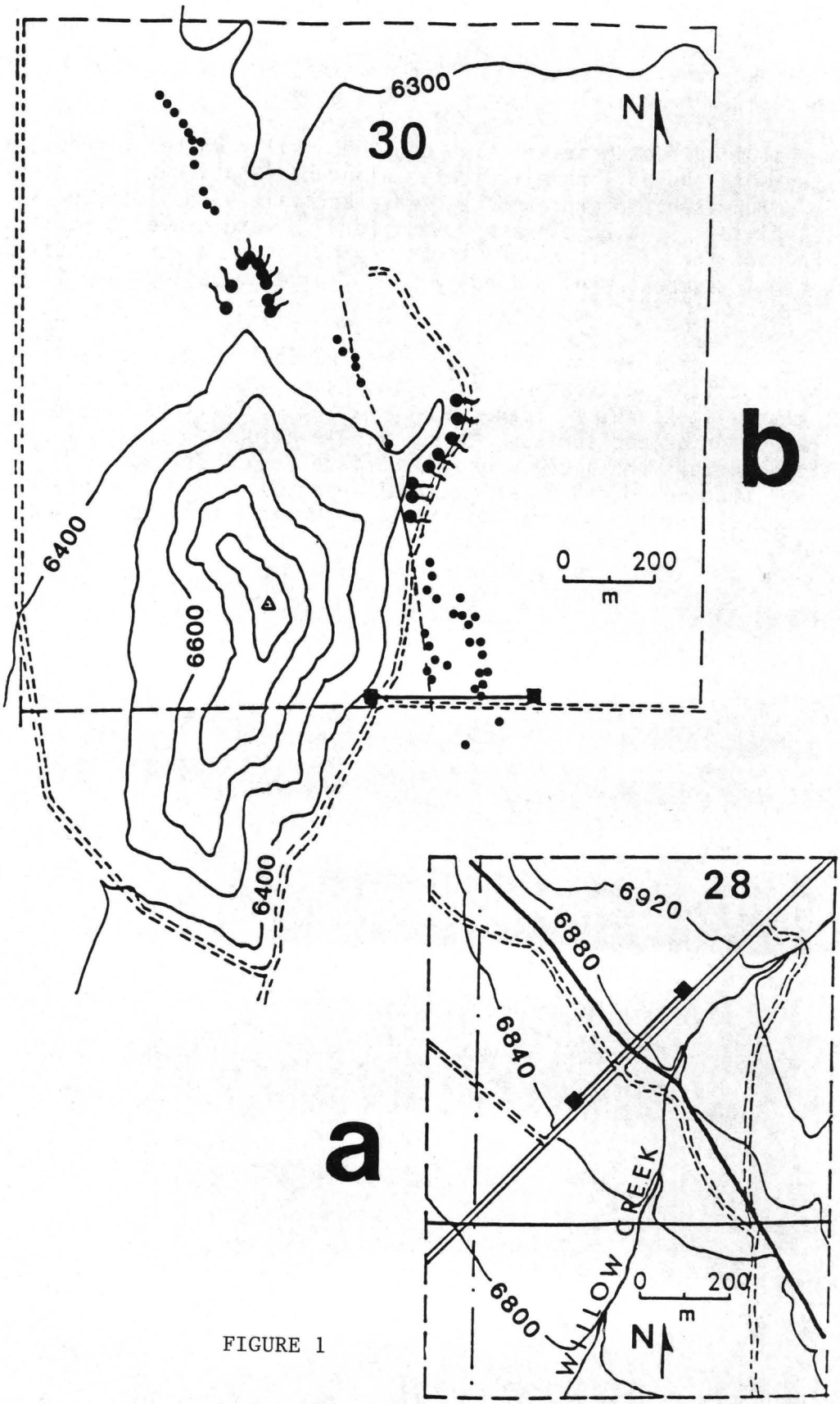
6300
30
N
b
6400
6600
0 200
m
6400
28
6920
6880
6840
a
WILLOW CREEK
6800
0 200
m
N

FIGURE 1

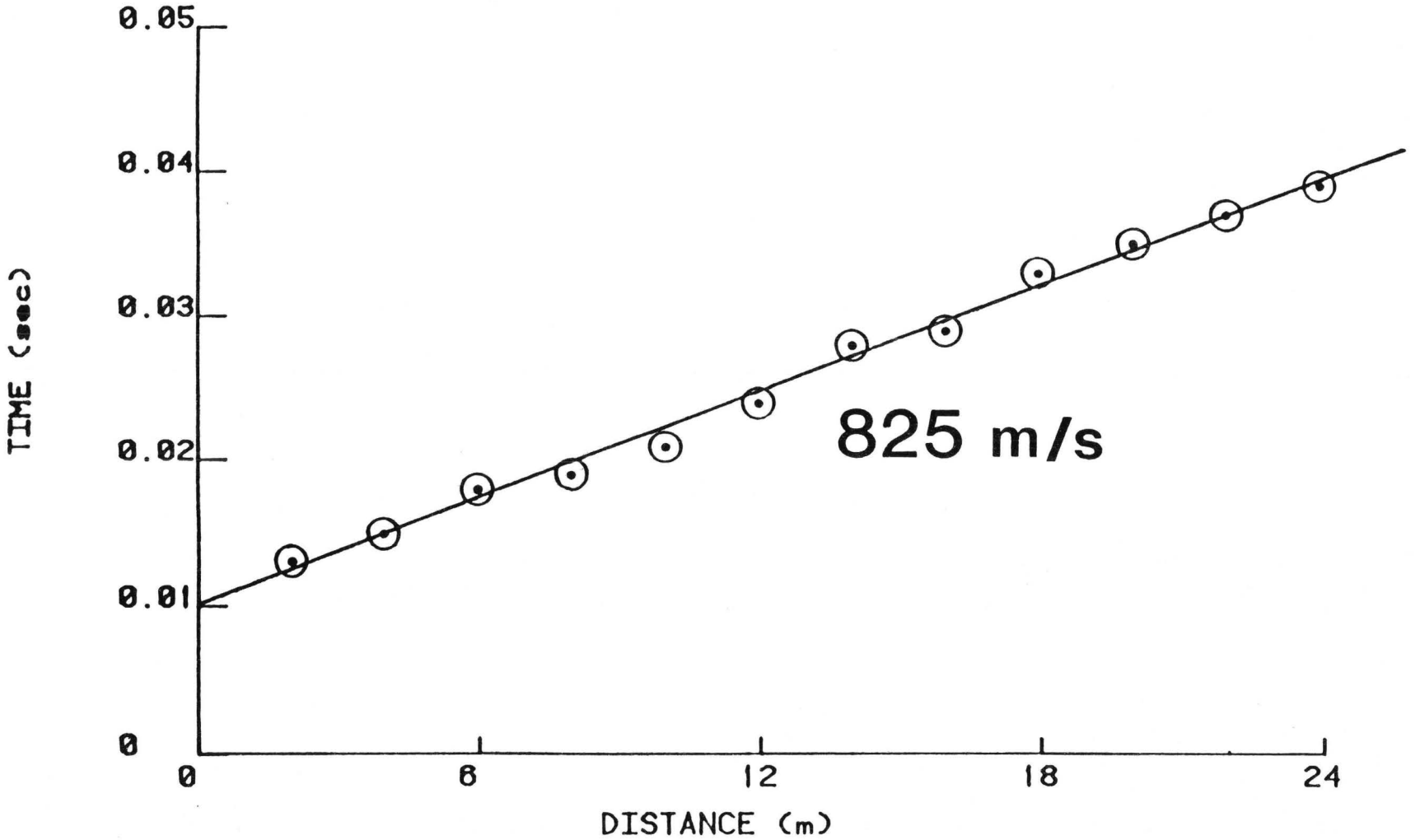

FIGURE 2

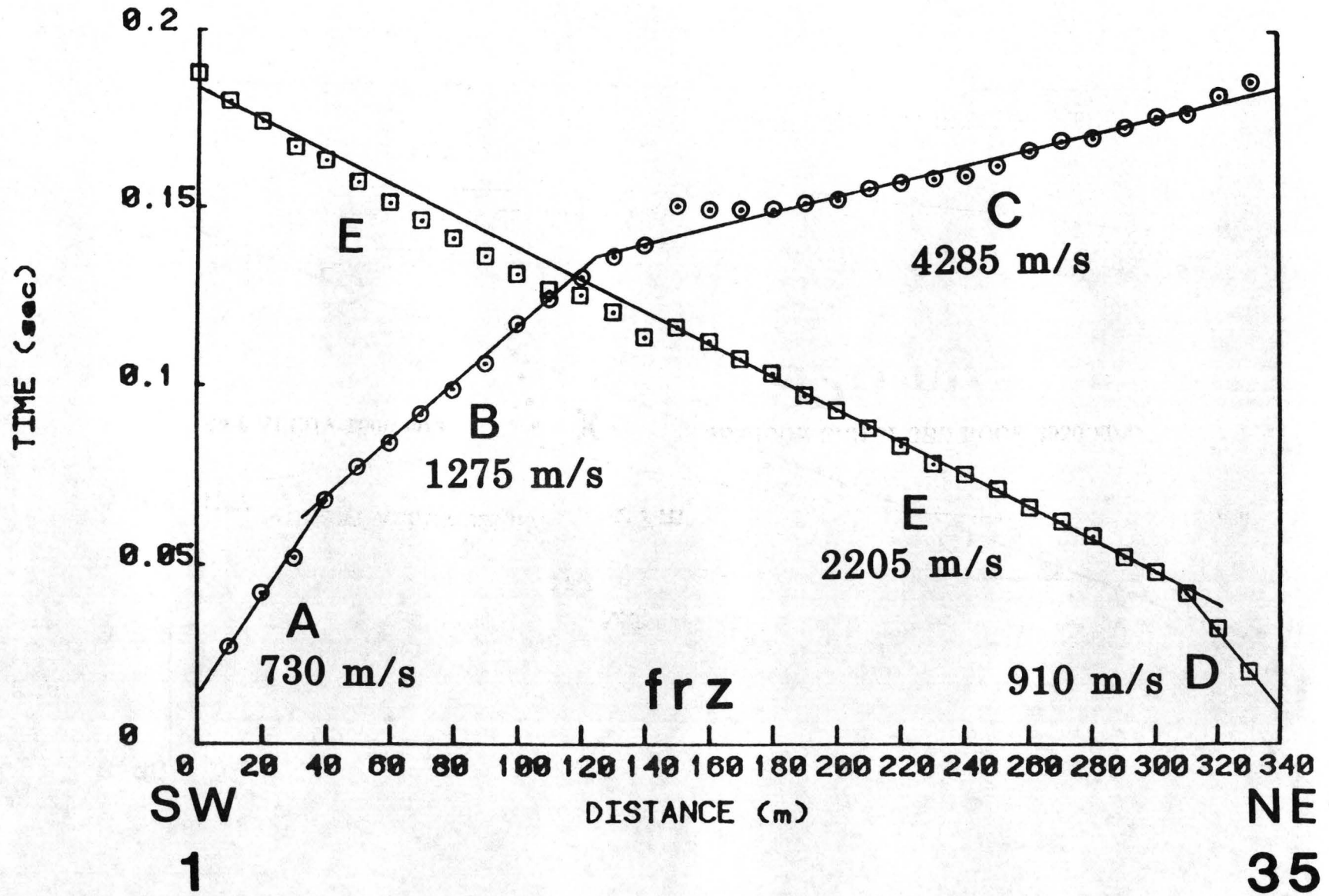
0.2
0.15
0.1
0.05
0
TIME (sec)
E
C
4285 m/s
B
1275 m/s
E
2205 m/s
A
730 m/s
frz
910 m/s
D
0 20 40 60 80 100 120 140 160 180 200 220 240 260 280 300 320 340
SW
DISTANCE (m)
NE
1
35

FIGURE 3

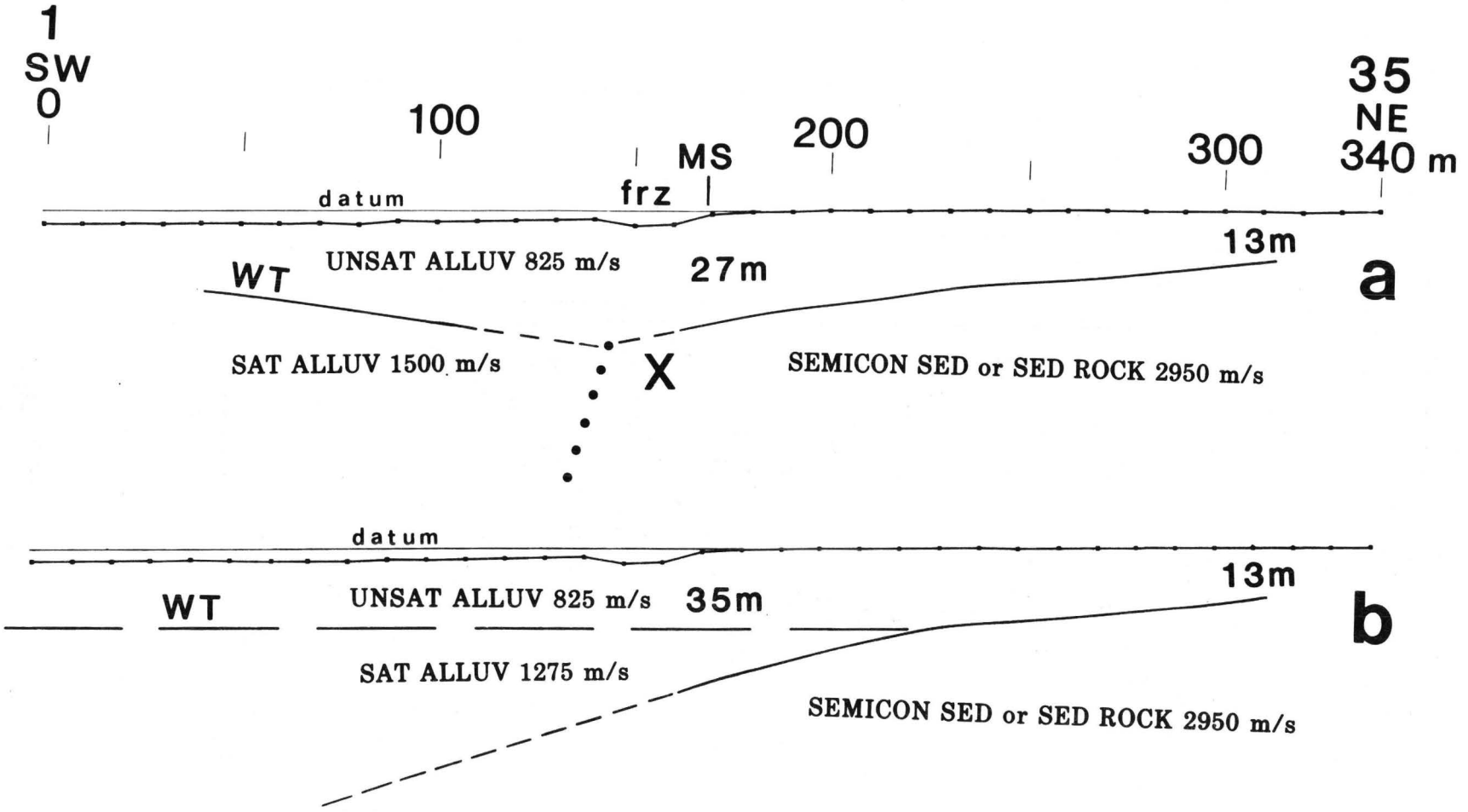
1
SW
0
100
MS
200
300
35
NE
340 m
datum
frz
13m
a
WT
UNSAT ALLUV 825 m/s
27m
SAT ALLUV 1500 m/s
X
SEMICON SED or SED ROCK 2950 m/s
datum
13m
b
WT
UNSAT ALLUV 825 m/s
35m
SAT ALLUV 1275 m/s
SEMICON SED or SED ROCK 2950 m/s

FIGURE 4

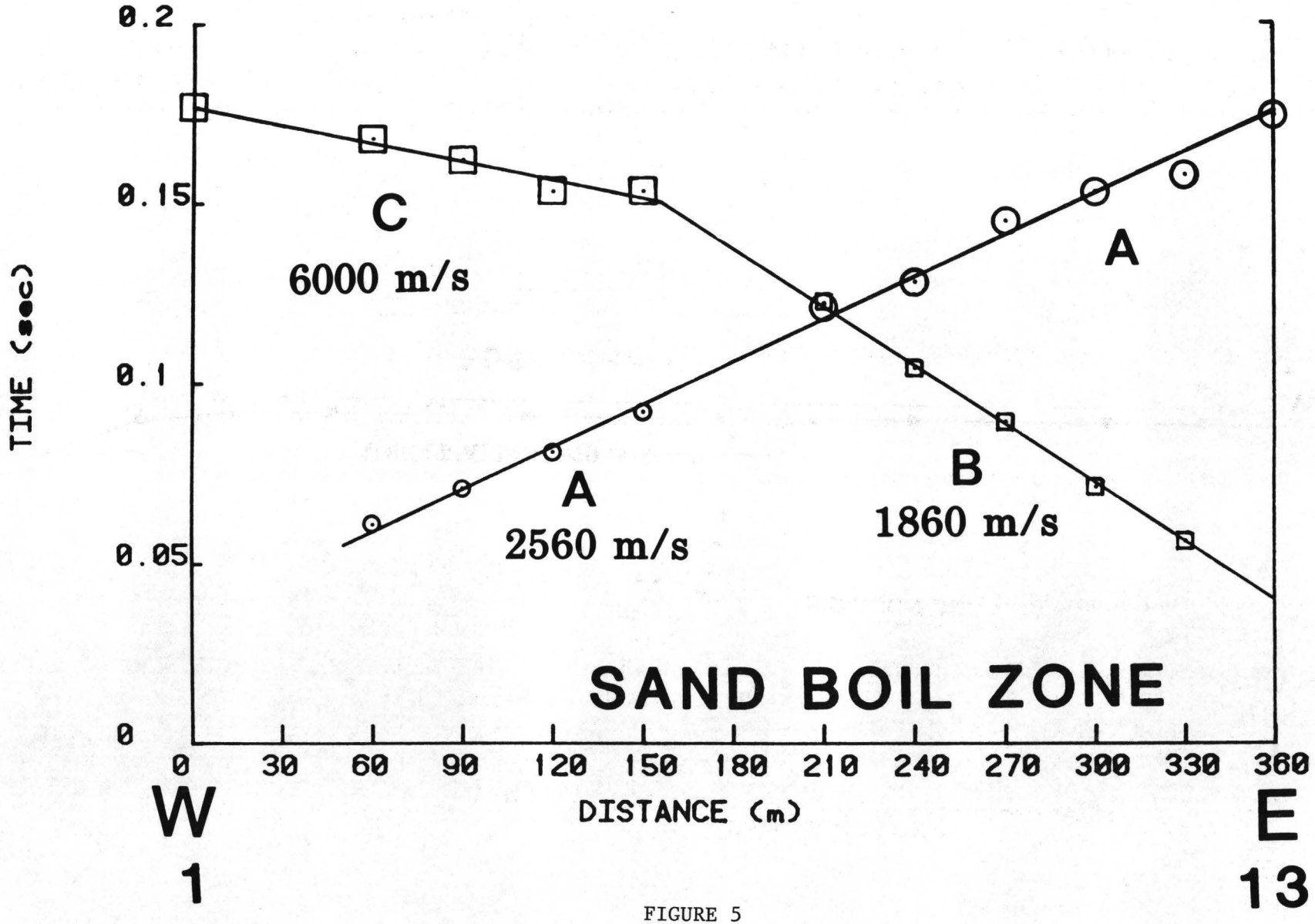
0.2
0.15
0.1
0.05
0
TIME (sec)
C
6000 m/s
A
2560 m/s
A
B
1860 m/s
SAND BOIL ZONE
0
30
60
90
120
150
180
210
240
270
300
330
360
DISTANCE (m)
W
1
E
13

FIGURE 5

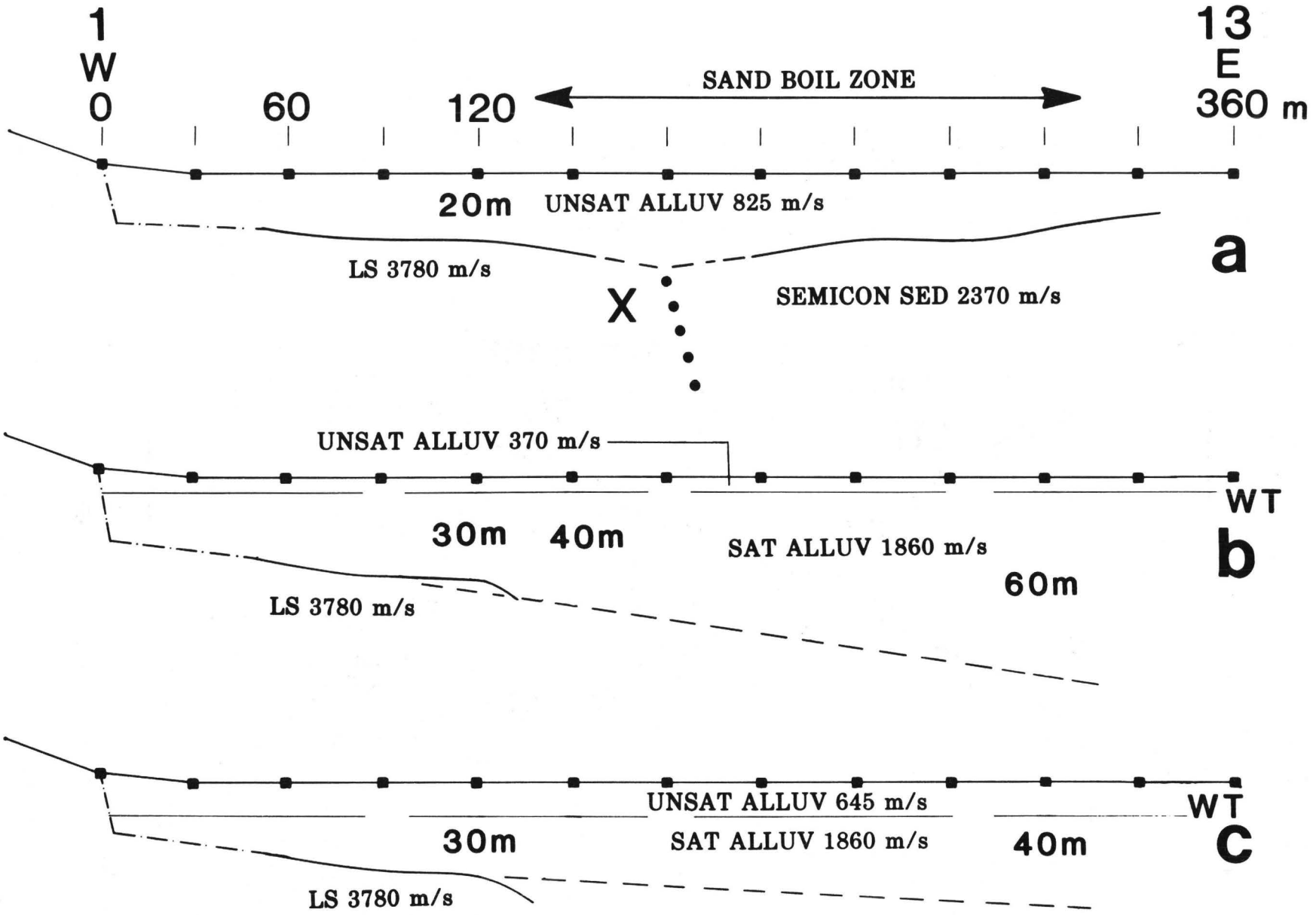
1
W
0
60
120
SAND BOIL ZONE
13
E
360 m
20m
UNSAT ALLUV 825 m/s
LS 3780 m/s
X
SEMICON SED 2370 m/s
a
UNSAT ALLUV 370 m/s
WT
30m
40m
SAT ALLUV 1860 m/s
60m
b
LS 3780 m/s
UNSAT ALLUV 645 m/s
WT
30m
SAT ALLUV 1860 m/s
40m
c
LS 3780 m/s

FIGURE 6

SUBSURFACE RADAR IMAGERY OF NEAR-SURFACE FRACTURES ASSOCIATED WITH THE BORAH PEAK EARTHQUAKE, IDAHO.

Roger Bilham*

Lamont Doherty Geological Observatory
Palisades, NY 10964

Abstract

Subsurface fault features associated with the Borah Peak earthquake (Oct. 28, 1983) and former earthquakes that have occurred at the base of the Lost River Range, Idaho, have been investigated using an impulse radar system. At Cedar Creek it was possible to map part of the floor of a graben formed during a previous event and at Lone Cedar Creek, more than 6 km southeast of fractures associated with the 1983 event, a similar paleoseismic graben has been tentatively identified.

The successful identification of paleoseismic features at 1-4 m depths associated with the Lost River Range fractures is attributed to the development of a radar reflective soil at the base of the fault-scarp before its subsequent burial by scarp-derived material. A near-absence of dielectric layering within coarse alluvial fans is found to be more typical of faulted range-fronts in Nevada, Utah and parts of California. It is concluded that impulse radar profiling may provide useful subsurface structural information in locations where contrasting sedimentation is likely to yield stratigraphy of value in subsequent trench excavations, but that the corollary may not be true, i.e. lithologic structure in near-surface sediments may be invisible to radar.

Introduction The Borah Peak earthquake of October 28, 1983, ruptured one of the three or more segments that serially form the Lost River Fault, a 130-km-long, NW-trending fault between Challis and Arco, Idaho (Baldwin, 1951; Crone et al., 1985). Estimates of the frequency, magnitude and spatial extent of former events on segments of the Lost River Fault have important consequences in estimating future seismic hazard in the region, and may provide insights for evaluating fault behavior elsewhere in the Great Basin (Schwartz et al., 1985). A potential method for accessing former earthquake recurrence rates is the excavation of near-surface fault features in a search for paleoseismic offsets and datable material entombed at the time of fault movement (Hait and Scott, 1978; Swan et al., 1980; Malde, 1980; Schwartz and Coppersmith, 1984; Schwartz et al., 1985). It is clear that considerably additional trenching in each of the Lost River segments will be necessary if the Quaternary record of fault movement in the region is to be reconstructed.

Trenching is time consuming and can be unrewarding if a chronological sequence of events cannot be established. It would be of great value, therefore, to be able to locate and examine the detailed structure of potential trenching sites prior to excavation. Few geophysical techniques have the desired resolution and penetration in unconsolidated materials to make this possible; however, a potential technique is the use of pulsed electromagnetic waves in the microwave region, i.e. radar. Subsurface radar profiling is inexpensive and fast and is capable of producing subsurface imagery with decimeter resolution in the field. The penetration depth of current radar systems is potentially suited to the mapping of features at depths of more than 60 m (Annan, 1983) although typical maximum ranges in soils and unconsolidated materials are more than an order of magnitude less using the equipment available to this study. A 6-m-depth range, however, enables subsurface features from three faulting episodes to be investigated, given suitable reflectors and less than 2 m of vertical displacement for each event. In addition to seeking a record of former fault movements on the Lost River Fault, the investigations of the Borah Peak fractures provide an opportunity to obtain radar imagery from freshly fractured soils presumably

*current address: Cooperative Institute for Research in Environmental Sciences, Campus Box 449, University of Colorado, Boulder, CO 80309.

similar to those buried by erosional processes following previous earthquakes.

Experimental details. Impulse radar systems operating in the frequency range 20 MHz-2 GHz have been available for more than a decade (e.g. Robin, 1975; Olhoeft, 1979; Ulriksen, 1982; Annan, 1983). The systems have typically found use in locating buried pipes and cables at shallow depths, or for measuring depth to water table or the thickness of ice or permafrost. The apparatus usually consists of a transceiver that may be towed across the ground by hand or behind a vehicle (Figure 2). Radar echoes from the subsurface are stacked sequentially on a chart recorder with arrival time (the product of depth and electromagnetic velocity) and echo amplitude (proportional to image darkness) displayed vertically, and distance-traversed displayed horizontally. Since information within the radar echo is contained in the first 10-200 ns of the radar return, a duration which is too short to be plotted directly be a graphic recorder, each scan of the chart (approximately 40 ms) is formed by the successive sampling of several hundred radar echoes. The duration of the transmitted pulse is designed to be as short as possible to provide high resolution. An ideal gaussian-shaped impulse is seldom attained and more usually a pulse with 10-30% negative overshoot preceding and following the maximum positive pulse is transmitted, the total duration of which is marginally longer than the period of a single cycle of the wave corresponding to the center frequency of the antenna selected. The pulse length of the transmitted signal from the 300-MHz antenna is approximately 30 cm in air, 10-15 cm in dry granite, silt or sand, and 3-6 cm in water-saturated sands and soils.

Figure 3 provides a graphic representation of electromagnetic properties associated with various soil types summarized in Table 1. The reflection coefficient associated with the interface between any two materials shown in Figure 3 is proportional to their separation along the velocity axis. Hence strong reflections may be obtained from planar surfaces separating dry and wet soil, clay and dry sand, soil and rock, water and clay, etc. Weak reflections are obtained from dry-sand/granite interfaces or silt/clay interfaces. A characteristic of all impulse radar systems in contact with the ground is that signals arriving in the few nanoseconds after the transmitted pulse leaves the antenna contain little subsurface information since the arrivals seen by the receiving antenna consist of a mixture of direct wave and a strong surface reflection. In subsurface radar profiles shown later the effect can be seen as a zone of unvarying imagery from the surface down to a depth proportional to the antenna impulse-length in air (30-120 cm).

Table 1. Electromagnetic properties of common subsurface materials at 100 MHz (Annan, 1983)

Material	Dielectric Constant	Conductivity mS/m	Velocity m/ns	Attenuation mS/m
Air	1	0	0.3	0
Water	80	0.01	0.033	0.1
Sea Water	80	3000	0.01	1000
Dry Sand	3-5	0.01	0.15	0.01
Wet Sand	20-30	0.1-1	0.06	0.3
Clay	5-7	2-1000	0.06	15
Granite	4-6	0.01-1	0.13	0.07
Limestone	4-8	0.5-2	0.12	0.7
Shale	5-15	1-100	0.09	5
Silt	5-30	1-100	0.07	6

Three different radar antennas were used with nominal impulse center frequencies of 300 MHz, 120 MHz and 80 MHz corresponding to pulse durations of 3 ns, 5 ns and 8 ns, respectively. The peak output power used in the survey was approximately 40W. A beam divergence of approximately 90° about a horizontal axis results in confusing imagery for all but flat, horizontal reflectors or line reflectors. The spatial resolution is further degraded if fast transverse rates are attempted due to the averaging involved in acquiring each recorder scan. Most of the lines were

towed by hand at 1-3 cm/s but a few were measured at up to 20 cm/s using the 80 MHz antenna mounted 30 cm above the ground and 1.5 m behind a vehicle. The location of fractures is usually possible (given horizontal reflectors) to within 10 cm at depths of less than 1 m and to within 1 m at depths up to 3 m. Surface vegetation more than 30 cm high can be detected by the 80 MHz antenna and to a lesser extent by the 120 MHz antenna, due to their radiation patterns not being limited to the downward direction. For this reason profiles beneath trees and heavy undergrowth, or near conductors such as wire fences or overhead cables using these two antennas were often found to be too noisy to be of value. The 300 MHz and 120 MHz antennas must be in good contact with the ground in order to suppress pulse ringing which otherwise obscures early arrivals. This presented difficulties in profiling over rocky ground or surfaces covered with this vegetation (e.g. sagebrush). The best locations for traverses near the Borah Peak fractures were found to be cattle paths and jeep trails.

The depth of penetration of the radar pulse is severely reduced by the presence of conductive materials near the surface. In low-loss materials such as dry conglomerates and dry sands, reflections from 20 m can sometimes be detected. More typically, few reflections from below 3 m were obtained in any of the areas examined. This may partly be due to the rarity of dielectric layering in the subsurface in these locations and partly due to the absorption of electromagnetic energy by near-surface moisture. No processing of the imagery presented in Figures 4-6 has been attempted. Gain ranging is applied at the time of data acquisition and some of the data have had signals with common arrival times along the traverse removed by a background removal process built into the radar control system.

Data. Field data from surveys conducted in late July 1984 are presented in Figures 4-6. The vertical scale is exaggerated relative to the horizontal scale by more than a factor of five. Many such profiles were obtained over a five-day period but only the most readily interpretable images are presented. These consist of profiles where subsurface structure possible related to fault activity is outlined by reflections from one or more layers in the upper 4 m. The interpretation of profiles is complicated by the imperfect waveform and extended duration of the transmitted beam, by the depth-dependent attenuation of high frequencies in the received reflections and by differences in gain from profile to profile. Two characteristics are common to all profiles: the upper fraction of a meter near the surface is featureless (see previous section) and reflections from the deeper parts of a profile are weak and are close to the noise level in the system due to attenuation by lossy materials in the ground. Thus the data of primary interest are to be found at 1-3 m depths. The topography of each profile has not been added to the imagery (all the images represent two-way travel times from the surface) but has an important contribution to the interpretation of the data due to the $> 5{:}1$ vertical exaggeration. Figure 5 was obtained on horizontal ground but the other profiles are from rough undulating terrain. Horizontal reflectors appear as anticlines in Figure 6 where they are imaged beneath a surface hollow and as dipping horizons beneath an alluvial fan in Figure 7.

1983 Surface Break: The large amplitude of the main scarp made it possible to obtain measurements across it only at Willow Creek and Cedar Creek where tracks had been forged for vehicular traffic (Figure 1). At Willow Creek no deep subsurface reflectors could be found to estimate the amplitude of former movements of the fault. At the Doublespring Pass Road at Willow Creek a diversion road had been constructed to bridge the 1.5-m deep, 20-m wide graben. It was possible to take advantage of this artificial surface to estimate penetration depth and approximate subsurface velocities. Figure 4 shows imagery obtained at 300 MHz and 120 MHz with the approximate profile of surface fissures sketched. The fill material has a velocity of approximately 7 cm/ns which is close to the velocity that would be predicted from its moist constituents; sand, silt and gravel. The foot of the main scarp and secondary fractures within the artificially-filled graben can be identified at depths of 1-2 m but the dielectric contrast between the original ground surface and the fill material is insufficient to provide good imagery. It would appear that recently disturbed surface material acquires a dielectric constant close to that of its undisturbed counterpart within a year. A subsurface electromagnetic velocity of 7 cm/ns has been assumed in estimating depths in Figures 4-6.

The 120-MHz and 300-MHz images in Figure 4 demonstrate the difference in resolution attending the selection of antenna center frequency. In the 120-MHz image the reflection from the foot of the new scarp is lost since it is too close to the surface.

Secondary features: Figure 5 illustrates imagery obtained across cracks within the 10-m wide graben that interrupts the Cedar Creek track. The main scarp is more than 3 m high at this location and forms the northeast margin to the traverses shown in Figure 5. Ground cracks varied in width from 2-20 mm within the graben and were open at least to depths greater than 30 cm. The irregularity of the surface contributed to the obvious fragmentation in the radar imagery. Where cracks had no opening or offset or were filled with fine, loose material they were invisible to radar. At this location a pronounced local development of sagebrush (*Artemesia tridentata*) up to 2 m high indicates that favorable growth conditions existed within the graben prior to the Borah Peak event. The graben has presumably existed far longer than the 50 years indicated by growth rings in the sagebrush since some soil development is evident with above average moisture supporting various types of grass. It was anticipated that the traverse might reveal ancient soil layers at depth offset by former events. At two locations it was possible to discern a horizon that increased in depth from the present surface toward the main scarp and toward the antithetic scarp bounding the southeastern edge of the graben. The maximum detected depth of this horizon is approximately 2 m close to the fault and it is possible that it is the image of an historic sub-horizontal surface layer covered by slope-wash material from the former scarp, that is, the base of the colluvial wedge. In Figure 5 the layer appears as an anticline since the data are displayed as depth from the present graben surface.

Paleoseismic features southeast of Borah Peak: A reconnaissance of promising trench sites was undertaken at Lone Cedar Creek in an attempt to locate former paleoseismic features. Part of the profile (Figure 6) revealed disturbed subsurface reflections corresponding the what appears to be a similar graben development to that found at Cedar Creek 13 Km to the northeast. The closest 1984 fractures extend only as far as Elkorn Creek and are poorly developed (Crone, 1985) and the mapped location of the Lost River Fault lies several Km to the East. The radar profile crosses a lineation extending southeast from the 1983 surface break on infra-red imagery of the region (Breckenridge, 1985). After crossing the fan the lineation defines the southwestern edge of a faceted spur. Creek erosion has exposed fault gouge at the western corner of the spur. The graben in the fan deposits may be as much as 60 m wide and 2 m deep shadowing to the southwest. The imagery is confused and the identification of a simple graben must be considered tentative, however, the principal subsurface features coincide with surface evidence suggesting recent fault activity: a vestigial scarp marked by a perceptible change of slope along the vehicle track and by a line of disturbed dolomite boulders along the hillside.

A distinct weathering characteristic of these boulders is that solution of the buried face forms a jagged pitted surface whereas the surface exposed to the weather is smooth. Historic rotation of the boulders may be recognized by the development of desert varnish on the formerly buried surface. The 1983 earthquake rotated and overturned many large, half-buried boulders lying above fault fractures. Boulders close to the fractures remained undisturbed. A possible method to date the time of most recent activation of this branch of the fault may be to compare varnish development (Dorn, 1984) on the buried and exposed parts of the rotated boulders. A second profile 100 m to the northwest of the track on a small alluvial fan failed to detect subsurface evidence for faulting. The absence of reflections at this location may be due to a higher depositional rate that may have inhibited the development of a buried radar reflector.

Discussion: The mapping of subsurface features using radar methods requires the existence of stratigraphic marker horizons with adequate dielectric contrast to provide velocity discontinuities capable of generating radar reflections. However, the coarse alluvial fans characterizing range fronts in much of Idaho, Nevada, Utah and parts of California have been found to be generally deficient in dielectric variability in the upper 10 m. The debris slopes of fault scarps in these locations consist of materials deposited close to their point of origin with little permanent change to their dielectric properties. The Borah Peak features are visible to radar presumably due to the existence in some locations of a soil with dielectric properties different from those of the

fanglomerate materials from which the later fill material is derived. If the Cedar Creek exposure is typical of this form of stratigraphic development the graben should host datable organic growth buried by the advancing debris wash from the main scarp (Figure 7). That is, the detection of radar reflective layers may signify the presence of soil layers, datable material or other marker horizons that might provide the basic stratigraphic framework for subsequent trench investigations. The converse is clearly invalid. A useful trenching site may contain stratigraphic information invisible to radar.

Normal faulting and strike-slip faulting pose somewhat different problems to radar investigations. Unless a high sedimentation rate is present, several strike-slip earthquakes of large throw may be accessible to radar imagery of limited penetration depth (Bilham et al., 1983) whereas it is possible that one or two large normal faulting events with little or no sedimentary influx may bury dielectric reflectors to the point of invisibility.

Interpretable imagery was obtained from sections at all three of the investigated locations crossing the Lost River Fault. Under what circumstances will radar profiling fail to yield useful results and can we anticipate more revealing imagery in future studies? The transmission power and resolution of the radar system imposes certain fundamental restrictions on the visibility of subsurface features even when adequate dielectric layering may be present. Paleoseismic scarps larger than the 1983 scarp may have lowered all but the most recent buried colluvial wedge to a depth invisible to the present radar profiling system (> 3 m). Paleoseismic scarps less than 30 cm high at depths greater than 1.5 m may not be visible to the current profiling system without digital processing to enhance late arriving radar returns stripped of their high-frequency components by attenuation in shallower layers. Certain provinces have been found to be undesirable for radar investigations: steep slopes, areas covered by coarse, unsorted deposits, salt-encrusted soils (when damp), rocky, bushy or forested terrain, areas close to pipelines, cables and scattered metallic debris. In general, most potential trench sites along the Lost River Fault are suited to radar profiling, but ironically, the surface break of the 1983 event has made the study of previous events in its vicinity difficult since it has generated major topographic impediments that prevent profiling across the entire fault zone, and major lateral dielectric discontinuities in the form of near-surface cracking that distort subsurface imagery.

The radar system used in the investigation does not represent the most advanced systems currently available. Considerable progress in improving depth penetration and resolution has occurred recently through the use of impulse antennas with less beam divergence and higher power and through the use of digital processing of the subsurface imagery. The imagery presented in this article would be considerably enhanced through the application of some of these techniques.

Conclusions: Subsurface imagery of fractures and graben-like features associated with faulting were obtained using an impulse radar profiling system at three locations at the foot of the Lost River Range. Surface cracks along the 1983 Borah Peak earthquake surface-break were found to be visible on radar imagery 9 months after the earthquake but where these has been filled they were invisible to radar. Subsurface fractures were visible where these had offset buried reflectors by more than a few cm. No reflectors below 4 m were detected presumably due to the absorptive properties of near-surface layers. At Cedar Creek a colluvial wedge from a previous period of faulting may be recognized and at Lone Cedar reek more than 6 Km southwest of the 1983 fractures a buried fault graben has been tentatively identified. The latter lies off the mapped location of the Lost River Fault and may be a splay fault associated with the change of trend defining the southwestern limit of the Borah Peak event.

The detection of a colluvial wedge is attributed to the development of a basal soil with a mineral or moisture content different from the local fan materials. Conditions favorable to the development of a soil or other form of dielectrically differentiated sedimentary unit at the base of a fault scarp may not be common in arid parts of the Basin and Range province.

Impulse radar profiling enables an insight to be gained of the near-surface structure of potential trenching sites but there exist interpretive ambiguities that can only be resolved by excavation. The preliminary investigations indicate that radar profiling is likely to assist

Quaternary geologists concerned with characterizing trench sites on segments of the Lost River Range Fault and similar faults in the region.

Acknowledgments: The radar investigations have been made possible by USGS contract 21926 and by Lamont Doherty Institutional Funds. Thanks are due to Bob Smith and Bob Buchnam for maps and enthusiastic discussions. The paper has been reviewed critically by Terry Engelder, John Beavan, Leonardo Seeber and Max Wyss. The author is indebted to GSSI for preparing some of the some of the equipment used for the study. The profiles were measured with the assistance of Krysia Bilham, Grigory Bilham and Christopher Bilham. The article was completed at the Cooperative Institute for Research in Environmental Sciences, University of Colorado, Boulder with partial funding from the National Geophysical Data Service. Lamont Doherty Geological Observatory publication number 3704.

References

Annan, A.A., 1983, General state-or-the-art review of ground probing radar, *Earth Physics Branch Open File Number, 83-14*, pp 89, Energy Mines and Resources, Canada.

Baldwin, E.M., 1951, Faulting in the Lost River Range, *Am. J. Sci., 249*, 994-902.

Bilham, R., W. Black and P. Williams, 1983, Subsurface radar imagery of the San Andreas Fault, *EOS Trans. Am. Geophys. Union, 64*, 313.

Breckenridge, R.M., 1985, Aerial photography interpretation of active faults using the Lost River Fault as an example, in Workshop XXVIII on the Borah Peak earthquake: *USGS Open File Report*, in press.

Crone, A.J., 1985, Fault scarps, landslides and other features associated with the Borah Peak, Idaho, earthquake of October 28, 1983, a field trip guide, in Workshop XXVIII on the Borah Peak earthquake: *USGS Open File Report*, in press.

Crone, A.J., M.N. Machette M.G. Bonilla, J.J. Lienkaemper, R.C. Buchnam, K.L. Pierce and W.E. Scott, 1985, Characteristics of surface faulting accompanying the Borah Peak earthquake, in Workshop XXVIII on the Borah Peak earthquake: *USGS Open File Report*, in press.

Dorn, R.I., 1984, Cause and implications of rock varnish microchemical laminations, *Nature, Land*, 310, 767-770.

Hait, M.J. and W.E. Scott, 1978, Holocene faulting, Lost River Range, Idaho, *Geol. Soc. Amer.*, Abst. with Programs, *10*, 5, 217.

Malde, H.E., 1985, Geologic investigation of faulting near Arco, Idaho, in Workshop XXVIII on the Borah Peak earthquake: *USGS Open File Report*, in press.

Olhoeft, G.R., 1979, Impulse radar studies in near surface geological structure, *Lunar Planet. Sci., 10*, 943-945.

Robin, G. de Q., 1975, Radio echo sounding: glaciological interpretations and applications, *J. Glac., 15*, 49-64.

Schwartz, D.P. and K.J. Coppersmith, 1984, Fault behavior and characteristic earthquakes: examples from the Wasatch and San Andreas faults, *J. Geophys. Res., 89*, 5681-5698.

Schwartz, D.P., W.D. Page and C.L. Taylor, 1985, Significance of the Borah Peak earthquake for the evaluation of fault behavior and earthquake recurrence in the Great Basin, in Workshop XXVIII on the Borah Peak earthquake: *USGS Open File Report*, in press.

Swan, F.H., D.P. Schwartz and L.S. Cluff, 1980, Recurrence of moderate to large earthquakes produced by surface faulting on the Wasatch Fault, Utah, *Bull. Seism. Soc. Amer., 70*, 1431-1462.

Ulriksen, C.P.F., 1982, *Application of Impulse Radar to Civil Engineering,* Ph.D. thesis, Lund Technical University, Sweden.

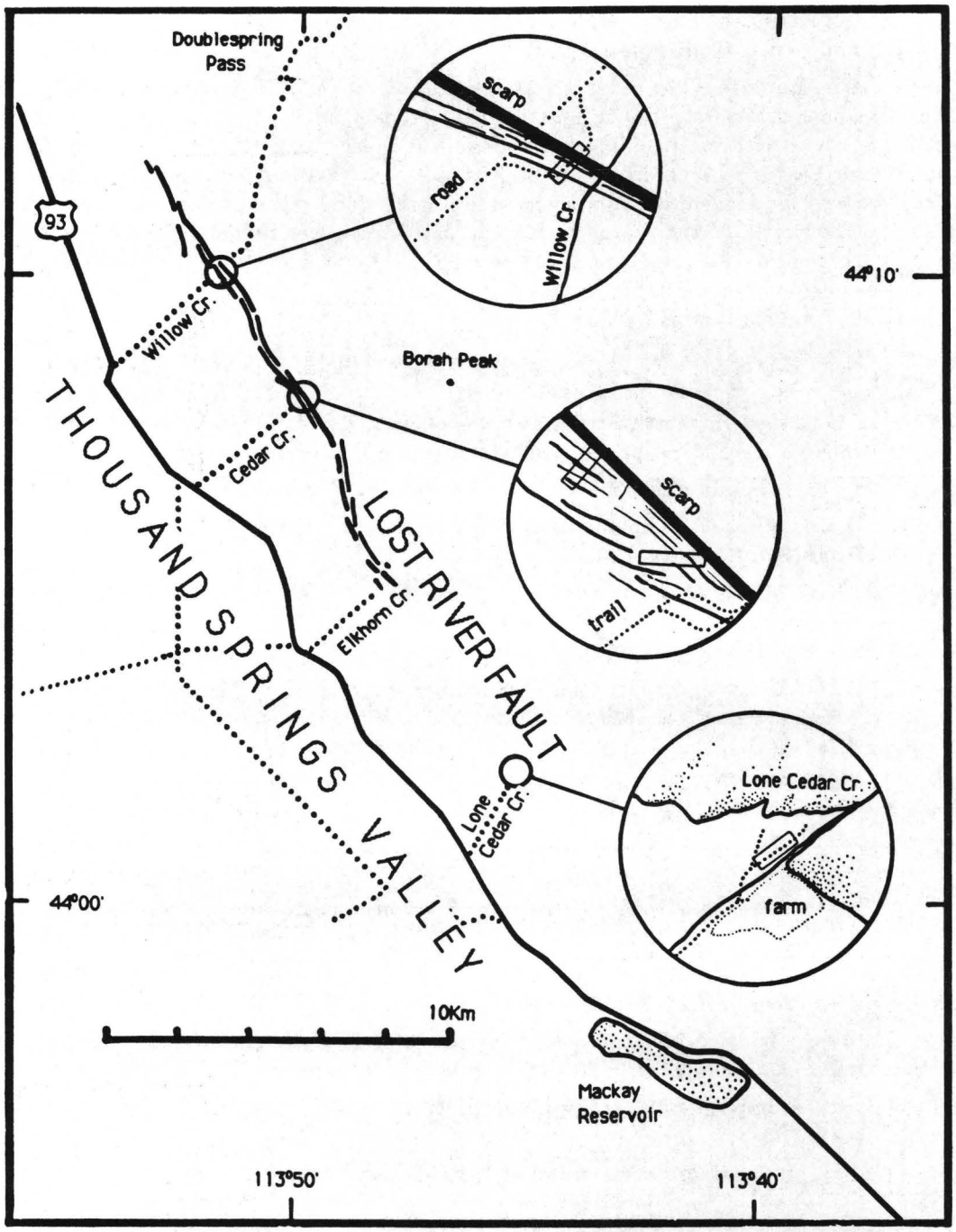

Figure 1. Lost River Range, Idaho, showing approximate location of 1983 ground breakage and location of radar profiles (rectangles) described in text. Traverse details in inset circles are sketched to different scales -- diameters are approximately 200 m, 100 m and 1 Km from top to bottom, respectively. The central part only of the 500-m Lone Cedar Creek traverse is shown in Figure 6.

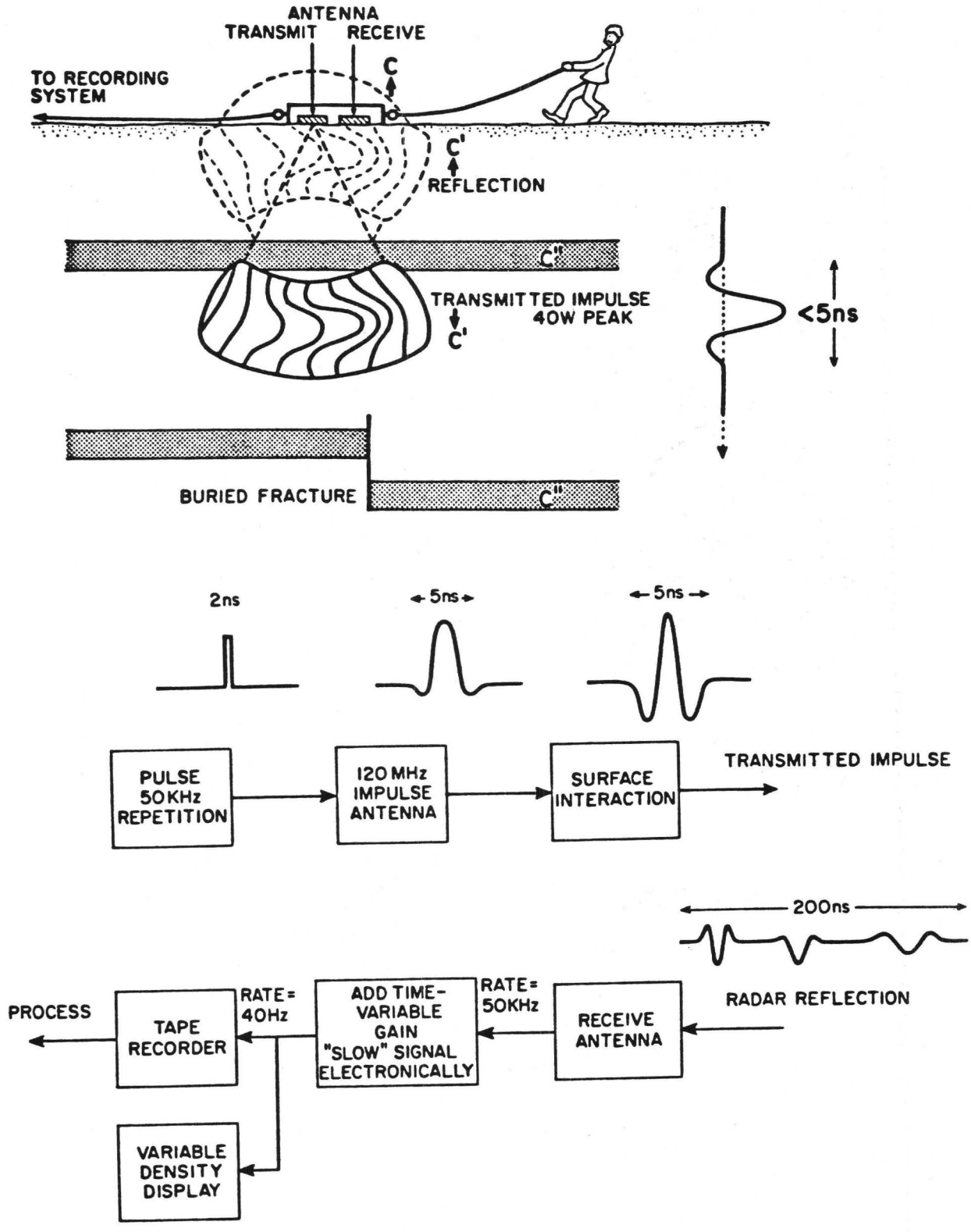

Figure 2. Field operation and schematic details of the G.S.S.I. subsurface radar profiling system used in the survey. The peak impulse power was approximately 40W for the traverses illustrated in later figures.

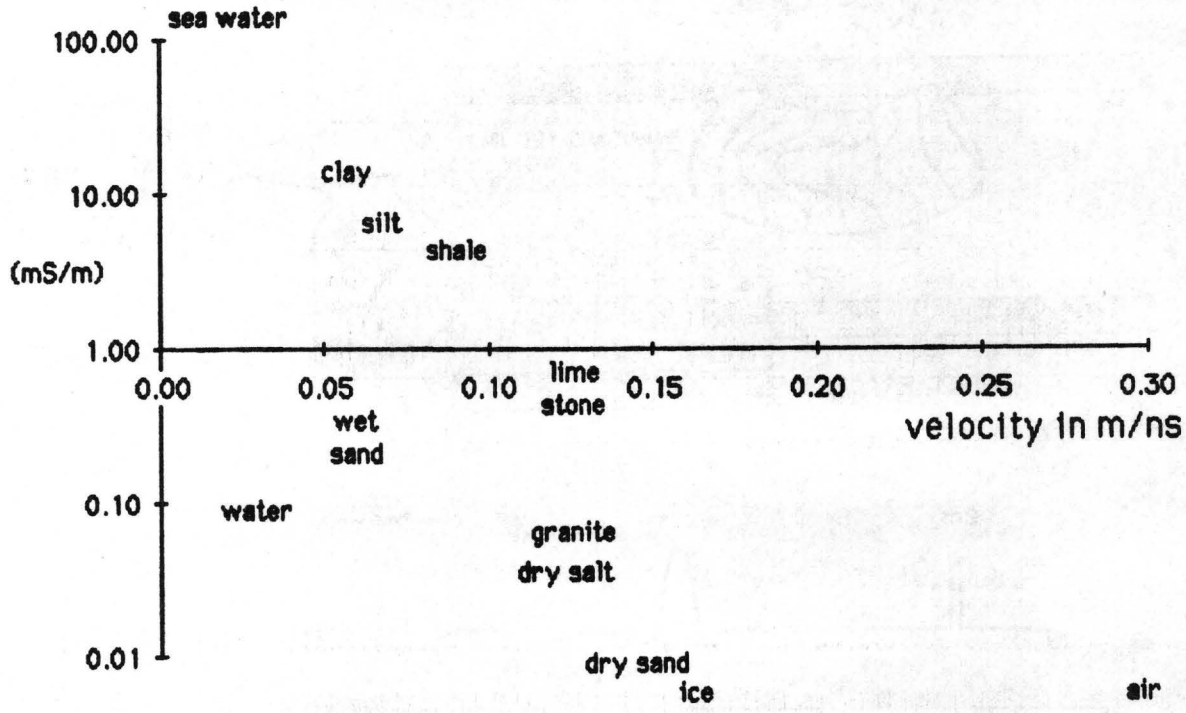

Figure 3. Electromagnetic attenuation and velocity characteristics for common subsurface materials (from Annan, 1983). For horizontal interfaces between materials the strength of the radar return signal is approximately proportional to the ratio in electromagnetic velocities. Penetration is poor in clay-like materials.

WILLOW CREEK, DOUBLESPRING PASS ROAD

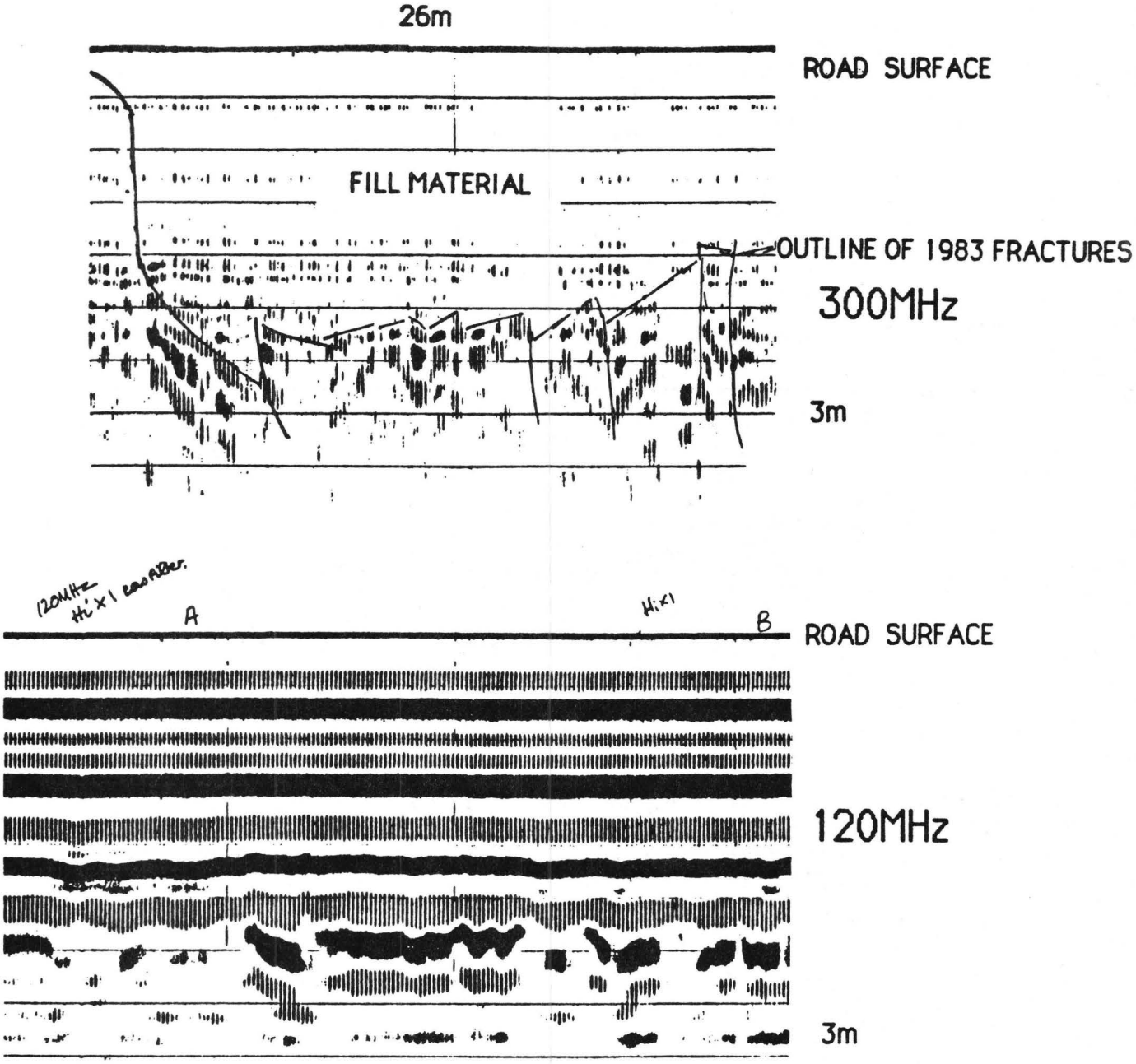

Figure 4. Upper figure shows a 25-m-long, 300-MHz traverse across the Borah Peak fault where it passes beneath the Doublespring Pass Road at Willow Creek. The outline of the main fault and secondary fractures within the slump graben adjoining the scarp have been interpolated from their exposed location on either side of the road fill material. The horizontal lines correspond to 10-ns round-trip travel time increments (approximately 50-cm depth intervals). Lower figure is the same traverse at 120 MHz but with a 20% greater horizontal scale.

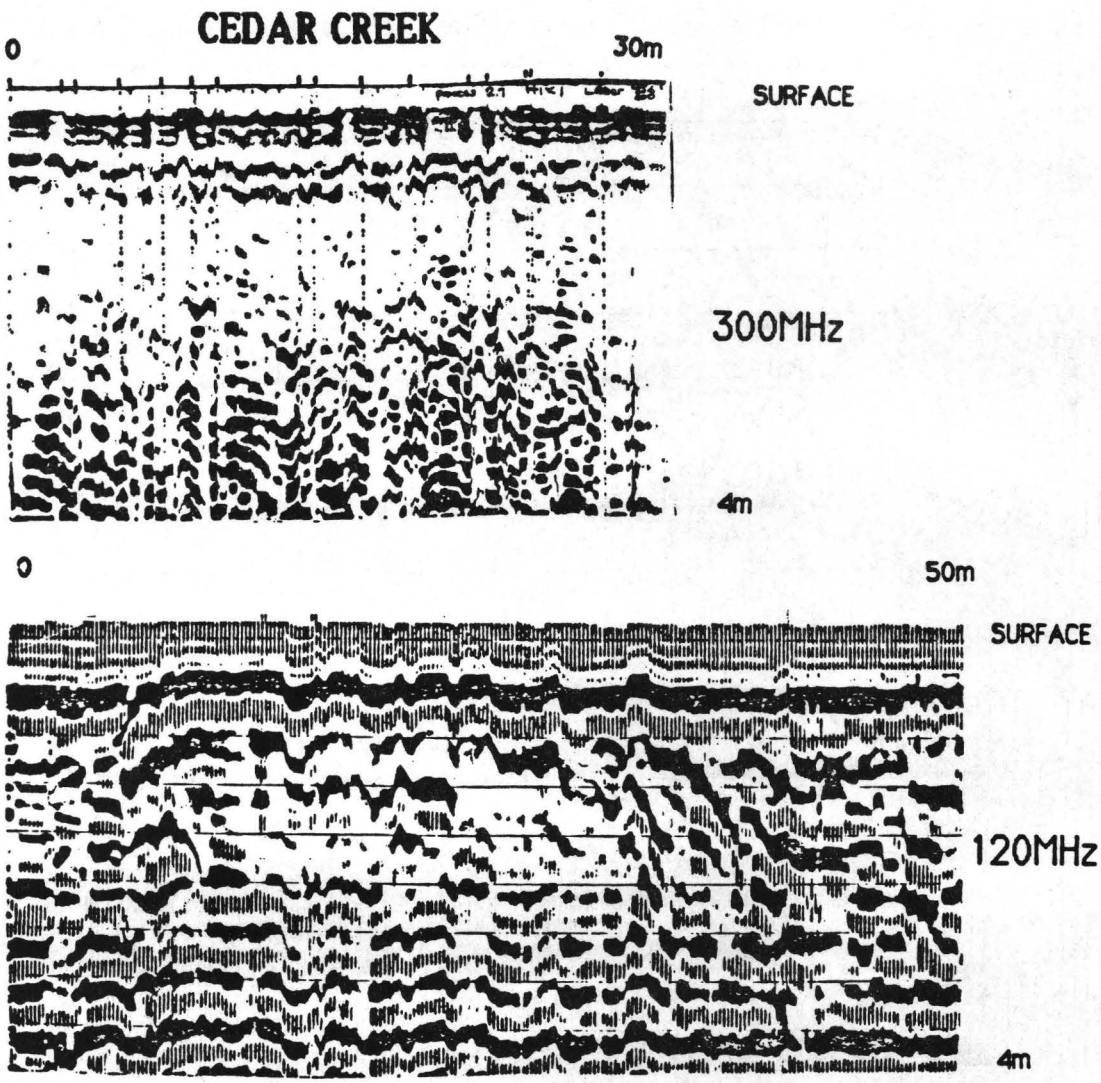

Figure 5. Upper figure shows a 30-m-long, 200-MHz profile across fractures within the graben across the Cedar Creek trail. The location of 16 fissures and fractures are indicated by tick marks. Lower figure is a 50-m-long, 120-MHz image obtained from an East-West diagonal profile across the graben floor. Buried fractures interrupt a horizon that approaches 1 m of the surface near the left center of the profile. The curve of this horizon is artificial since it is approximately the inverse of the topography at this point. The radar reflector is believed to be the base of a fault-induced colluvial wedge.

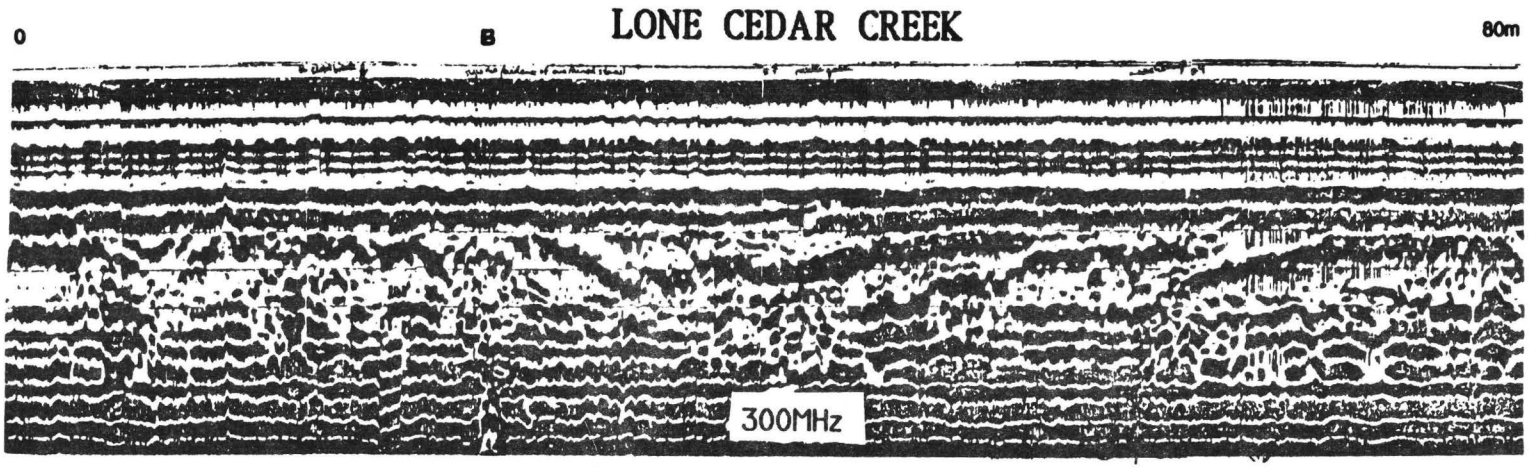

Figure 6. An 80-m-long, 300-MHz profile. Part of a 500-m traverse along the Lone Cedar Creek jeep trail showing complex reflections to roughly 4-m depth in the vicinity of surface evidence for paleoseismic activity. The surface topography at this location dips gently down from left to right along an alluvial fan. Several horizons that apparently dip gently to the left (NE) are approximately horizontal layers. The uppermost of these layers dips steeply up to the left towards a disturbed zone, suggesting the existence of a buried colluvial wedge. Overturned surface boulders (B) suggest the presence of a former scarp above the disturbed zone. Further disturbed ground appears to the left of the feature and is associated with a gentle change of surface slope.

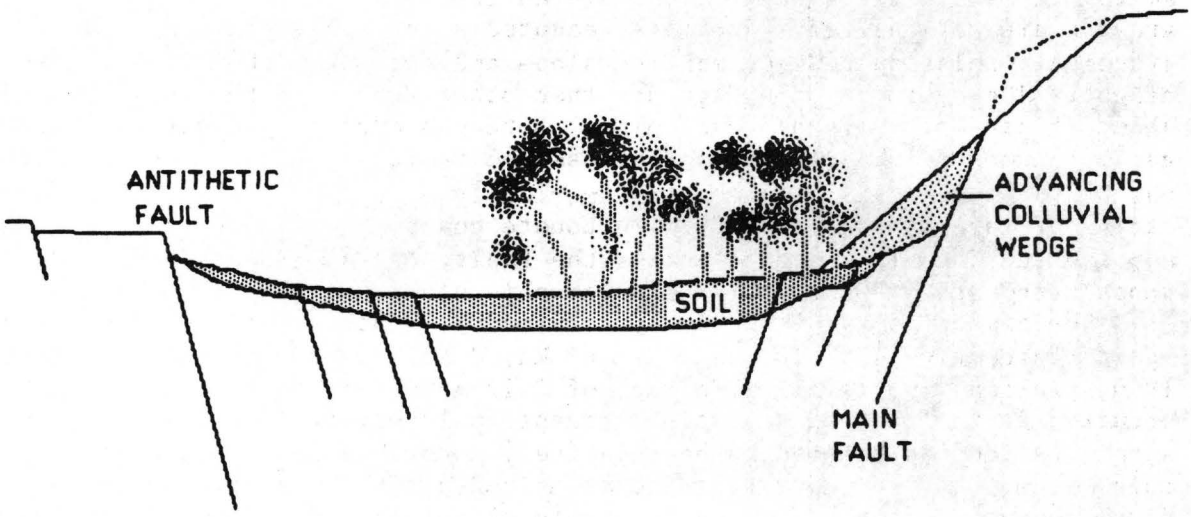

Figure 7. Development of a radar-reflective soil prior to burial by spoil from the free face of a fault scarp (e.g., Swan et al., 1980). At Cedar Creek the graben hosts a pronounced development of sagebrush.

QUATERNARY HISTORY OF FAULTING ON THE ARCO SEGMENT OF THE LOST RIVER FAULT, CENTRAL IDAHO

By Kenneth L. Pierce
U.S. Geological Survey

ABSTRACT

The Arco segment forms the southern 15-20 km of the Lost River range-front fault. Quaternary faulting on this segment is manifest by prominent scarps in middle Pleistocene alluvial-fan gravels. Latest Pleistocene fan gravels are not faulted. Profiles measured along the fault scarp show a systematic relation between maximum slope and the logarithm of the scarp height. The scarp is more degraded than other scarps in the region dated as about 15 ka (ka, thousand years old). Both the surface geology and the geology exposed in a deep trench across the fault scarp are used to determine the history of faulting, which is numerically dated by $^{230}Th/^{234}U$-isochron dating of layers from stratified carbonate coats, by fission-track dating of ash exposed deep in a trench across the fault, by rates of carbonate coat deposition, and by Quaternary stratigraphic studies in the region.

The history of faulting is constrained by 7 points on a plot of offset against age (fig. 4). In the past 160 ka, displacement has totaled about 19 m, yielding an overall slip rate of 0.12 m/ka. No fault displacement has occurred in the past 30 ka, which suggest fault movement is well overdue if strain buildup is assumed to be relatively constant. Some evidence suggests this assumption is incorrect and that episodes with multliple fault displacements are separated by intervals of quiescence; in this case the next offset on this segment could occur either soon or not for tens of thousands of years.

INTRODUCTION

The Borah Peak earthquake of October 28, 1983 occurred on the Thousands Springs segment of the Lost River fault (fig. 1). The Arco segment is the southern segment of this fault, and is about 50 km south of where surface faulting occurred during the Borah Peak earthquake (fig. 1). The Arco segment is about 15-20 km long and extends from near Arco to a few kilometers north of King Canyon (fig. 1). The topographic relief of the Lost River Range along the Arco segment is only about half that where surface faulting occurred during the Borah Peak earthquake.

In an evaluation of faulting near the National Reactor Testing Station, Malde (1971 and 1985 (this volume)) described the Arco fault scarp, including a detailed sketch of a 10-m-deep trench across the fault scarp. This report builds on the work of Malde with the objective of quantifying the fault history by defining the fault displacement through time. Towards this end, new numerical-age information was gained by measurement of the thickness of carbonate coats on stones in alluvial-fan gravels, $^{230}Th/^{234}U$ isochron dating of layers from these coats, fission-track dating of a volcanic ash, regional Quaternary stratigraphic studies, and profiling of the fault scarp.

SCARP MORPHOLOGY

The Arco segment of the Lost River fault (fig. 1) is defined by prominent but discontinuous scarps (Malde, 1985) in middle Pleistocene alluvial-fan deposits. Younger alluvium partially buries the lower part of the fault scarp and thus diminishes the heights of the scarp, excepting for some low scarps east of the main fault. Scarp heights based on measurement of 27 scarp

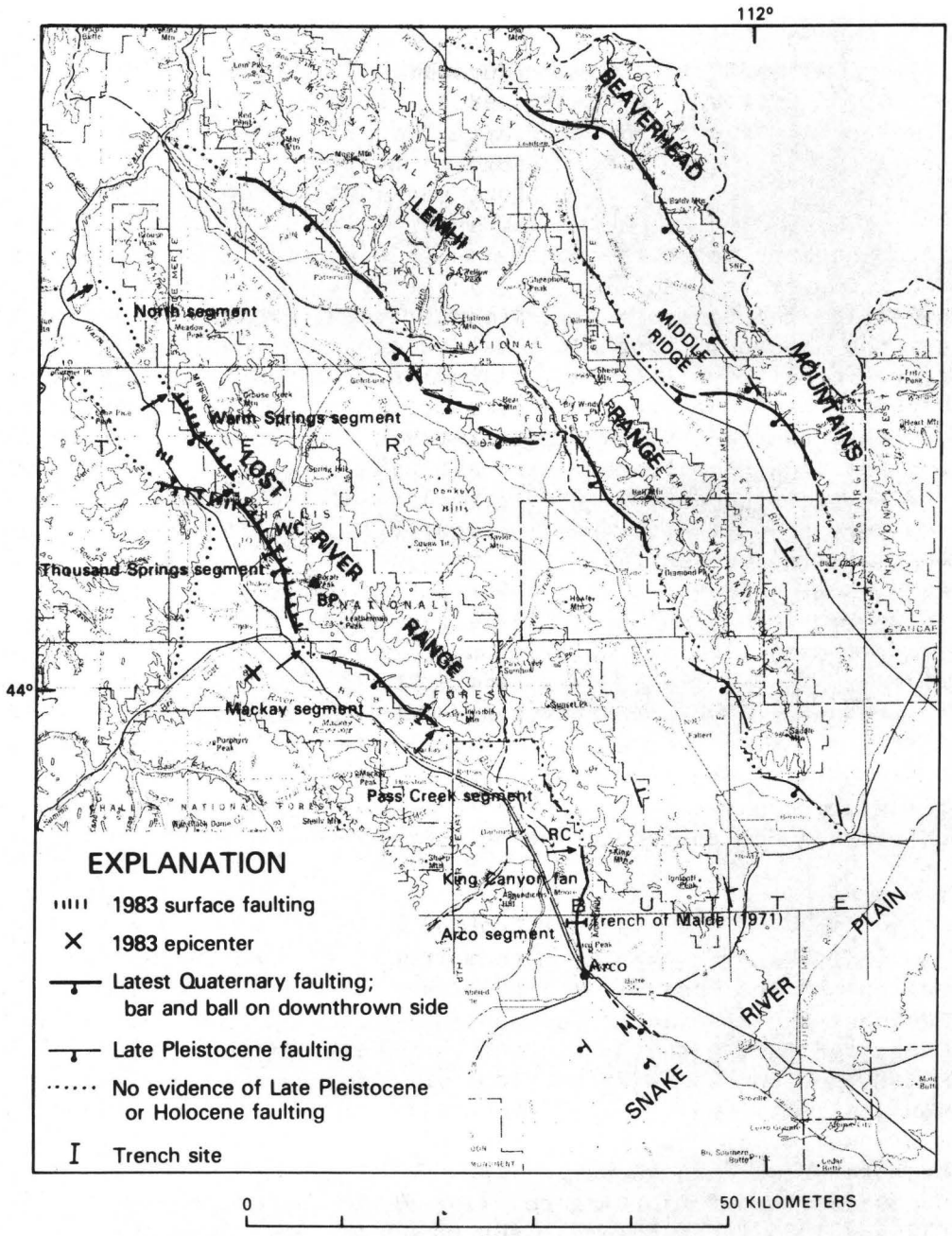

Figure 1. Map showing location of the Arco segment of the Lost River fault and other Quaternary faults in the Lost River-Beaverhead area. See Scott and others (1985, this volume) for discussion of regional setting, and for distinction of the named segments of the Lost River fault. Arrows indicate boundaries between segments of the Lost River fault. RC, Ramshorn Canyon, WC, Willow Creek, BP, Borah Peak.

profiles range from 2 to 25 m (fig. 2). The higher scarps result from multiple movements because offsets greater than 2 m are unlikely, especially considering the scarps that formed during the Borah Peak earthquake averaged only 0.8 m high (Crone and others, 1985). The maximum scarp angle generally spans more than half the scarp height. The scarp generally shows no oversteepened sections surviving from the last movement on the fault, although with very oblique morning light, a steeper slope is visible on the scarp at the position of the fault trace just south of the trench (fig. 1).

Comparison of the maximum scarp angle with the logarithm of scarp height shows that 80 percent of the variation in maximum scarp slope can be explained by scarp height (fig. 2). This correlation seems high, particularly because the scarps profiled are the product of many individual movements, and they are buried to differing degrees by younger alluvium. The data from the Arco segment plots clearly below those for either the Lake Bonneville shoreline scarps (Bucknam and Anderson, 1979), and the west-facing, late-glacial terrace scarps on nearby alluvial fans (Pierce and Colman, in preparation), which are both about 15 ka (Scott and others, 1983; Pierce and Scott, 1982). Studies of scarp morphology show that, all factors other than time being equal, if two scarps have similar heights but different maximum slope angles, the scarp with the lower maximum slope is older. The fault scarp displacing the King Canyon alluvial fan ("K" on fig. 2) result only from the youngest faulting event(s?). This scarp is more degraded than 15 ka scarps in similar materials under similar climates (fig. 2), thus suggesting the last movement on the Arco segment is older than 15 ka.

QUATERNARY STRATIGRAPHY RELEVANT TO FAULTING

The Quateranry history of the Arco segment is based mostly on displaced alluvial-fan deposits. The Quaternary stratigraphy and correlation of these deposits is based on: (1) geologic sequence within deposits from a given drainage basin and between deposits of adjacent drainage basins, (2) degree of preservation of the original surface morphology on the alluvial fans, (3) soil development, and particularly (4) thickness of laminated calcium carbonate coats from the undersides of limestone clasts collected from a depth in the soil where coats are the thickest.

These fan deposits are subdivided into younger (Qfy), middle (Qfm), and older (Qfo) units (table 1). The youngest time of widespread alluvial fan deposition occurred in late Pleistocene time, and little accumulation has occurred in Holocene time except along drainageways in the mountains and at the fan heads (Pierce and Scott, 1982). The late Pleistocene episode of fan depositon, and presumably the earlier episodes, is related to the colder climates of the Pleistocene apparently when winter precipitation was more effectively stored as snow and released in concentrated seasonal runoff during snowmelt (Pierce and Scott, 1982).

The oldest alluvial-fan deposit (unit Qfo_1) is exposed on the upthrown side of the fault. Carbonate coats commonly are between 7 and 10 mm thick (table 1). Soils have stage III (locally stage IV) carbonate morphology one-half meter or more thick. Unit Qfo_1 forms a flat-topped alluvial deposit that extends for several hundred meters from the fault scarp back into the range, where it fills old valleys to depths of more than 10 m. The fault scarp along the Arco segment is formed mostly by Qfo_1.

At the site of the trench excavated across the fault scarp (fig. 1; Malde, 1971 and 1985), alluvium of the next oldest unit, Qfo_2, was deposited on the downthrown side of the fault, presumably in response to stream grade

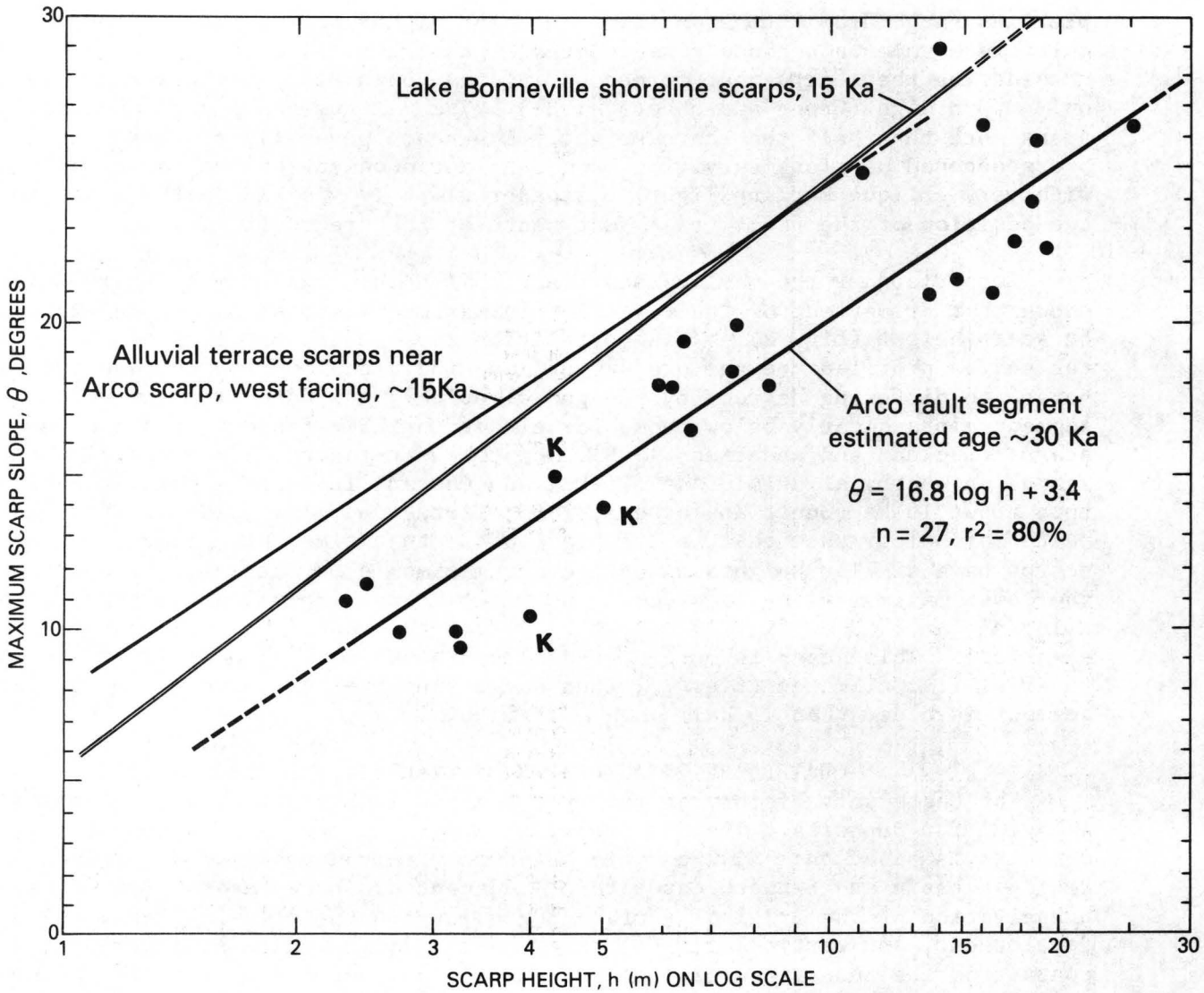

Figure 2. Scarp morphology of the Arco segment of the Lost River fault. Regression line for the maximum slope against the log of scarp height has a coefficient of determination of 80 percent. K, scarp displacing unit Qfm_1 on King Canyon fan. This plot, and especially the scarps marked "K" suggest the scarp of the Arco segment is older than two other scarps which are dated about 15 ka (see text).

TABLE 1. Thickness of carbonate coats from soils on alluvial fans along the Arco segment and on deposits to the north of the Arco segment. Each mean and standard deviation is based on 25 or more coats measured at a site. For a few sites discussed in the text, averages of several means given in bold type beneath short line. Vertically aligned "#", time of youngest faulting, King Canyon fan.

LOCATION	STRATIGRAPHIC UNIT AND ESTIMATED AGE						
	Holocene 0–10 ka	Qfy 15 ka	Qfm_2 25 ka	Qfm_1 30 ka	$Qfo_{3?}$?	Qfo_2 80 ka	Qfo_1 160 ka
DEPOSITS ALONG THE ARCO SEGMENT							
King Canyon fan		0.9 ± 0.3 1.1 ± 0.4 1.0 ± 0.2 **1.0**	1.7 ± 0.5 # 1.6 ± 0.4 # 1.5 ± 0.5 # **1.6**	1.5 ± 0.7 2.0 ± 0.6 2.1 ± 0.7 2.2 ± 1.0 2.3 ± 1.0 **2.0**		Qfo (undivided) 6.9 ± 2.6 6.2 ± 2.1	
Anderson Canyon fan		0.8 ± 0.3					
Section 35 fan (area of fault trench, of Malde, 1971).	0.3 ± 0.3	0.9 ± 0.4 0.8 ± 0.8	1.7 ± 0.7 1.5 ± 0.5 1.2 ± 0.6		3.3 ± 1.3 2.3 ± 1.1 3.2 ± 1.5 4.3 ± 2.1	5.0 ± 2.4 5.1 ± 1.4 5.4 ± 1.5 **5.2**	10.1 ± 5.4
Section 11 fan	0.4 ± 0.3		1.4 ± 0.7 1.7 ± 0.9				7.7 ± 1.6 5.4 ± 2.9 4.8 ± 2.8
Section 2 fan							7.3 ± 2.1
DEPOSITS NORTH OF THE ARCO SEGMENT							
Ramshorn Canyon fan (Pierce and Colman, in preparation)		1.2 ± 0.4 1.3 ± 0.5 1.1 ± 0.4 1.3 ± 0.4 1.0 ± 0.3 1.0 ± 0.2		2.6 ± 1.5 2.0 ± 0.5			
Willow Creek (see Scott and others, 1985)							
Pinedale-age fan		1.3 ± 0.2					
Pinedale-age outwash		1.0 ± 0.4					
Pinedale-age end moraine		1.4 ± 0.4					

changes in response to faulting. A few tens of meters south of the trench, carbonate coats from unit Qfo_2 average 5 mm thick (table 1), and occur above a calcic soil-horizon 1/4 m thick with stage IV carbonate morphology. Loess exposed near the bottom of the trench beneath gravels of unit Qfo_2 contains two volcanic ashes. The upper ash has a chemical composition similar to ashes from the Yellowstone area (G. A. Izett, pers. commun., 1982), which indicates an age no younger than 70 ka, the age of the youngest erruptions from Yellowstone (Christiansen and Blank, 1972). N. D. Naeser (written commun., 1981) obtained a fission-track age of 76 ± 34 ka on glass shards of the upper ash. This age might only be a minimum one, for fission-tracks can anneal in glass, particularly for samples more than a million years old. But both the cold climate and young age of the ash may make the effect of annealing neglible compared to the large 34 ka uncertainty in the age determination.

At the King Canyon fan, units Qfm_1 and Qfm_2 bracket the youngest displacement on the Arco segment. Unit Qfm_1 is offset 2-3 m and has carbonate coats that average 2.0 mm thick, whereas unit Qfm_2 is unfaulted and has coats that average 1.6 mm thick (table 1).

Unit Qfy lies across the trace of the fault in many places, but is not faulted along the Arco segment. These gravels have carbonate coats about 1.0 mm thick (table 1) and a calcic soil horizon about 1/4 m thick having stage I-II carbonate morphology. Aerial photographs show well-preserved braided channel morphology on the surface of unit Qfy (Pierce and Scott, 1982, fig. 7). Based on regional studies, the surfaces of these alluvial fans are considered to be of late Pleistocene age, estimated to be about 15 ka (Pierce and Scott, 1982).

$^{230}Th/^{234}U$-ISOCHRON DATING OF THE CARBONATE COATS

In addition to using the thickness of carbonate coats as an age indicator, layers from the carbonate coats were separated and $^{230}Th/^{234}U$-isochron dated. The carbonate coats are layered forming a miniature stratigraphic sequence that increases in age from the outer to the inner part of the coat, a relation that is analogous to a stalagmite formation. Carbonate coats were removed from stones and 2-3 layers from a given locality dated by John Rosholt (written commun., 1980; table 2).

When deposited as a chemical precipitate, $CaCO_3$ will have a very low ration of thorium to uranimun, but some contaminating thorium is likely to be present in any detrital material such as clay or silt incorporated in the coat. The dating (table 2) involves an isochron technique described by Szabo and Rosholt (1982) which is similar to that used by Ku and others (1979) and employs separate isotopic analyses of the soluble and insoluble phases in order to correct for contaminant thorium in the insoluble phase. For the dated samples, this correction was small, decreasing the age by no more than 30 percent of the apparent age based solely on the $^{230}Th/^{234}U$ ratio of the soluble phase.

Plots of the Th/U ages versus coat thickness can be used to estimate the time when deposition of the coat started and thus the time of stabilization of the fan surfaces (table 2). Such a plot from the thickness and age data in Table 2 defines an age of 160 ± 35 ka for stabilization of the surface of unit Qfo_1 from a site at the upper end of the trench (fig. 1).

Carbonate coats from faulted unit Qfm_1 at King Canyon yielded older ages for the outer coat than for the inner coat (table 2), which is incompatible with their sequence of deposition. Also, the ages of the outer coats from unit Qfm_1 (98 and 42 ka) are much older than the dates for the stratigraphic-

Table 2. $^{230}Th/^{234}U$ isochron ages of stratigraphic layers separated from carbonate coats in soils on deposits adjacent to the Arco fault segment. Age determinations by J. N. Rosholt (written commun., 1980).

LOCATION, STRATIGRAPHIC UNIT (FIELD NUMBER), AND COAT LAYER, (THICKNESS AND SAMPLE LETTER)	$^{230}Th/^{234}U$ ISOCHRON AGE (ka, 1000 YRS)	RATE OF CARBONATE COAT DEPOSITION (mm/10ka)***
Section 11 fan, Qfo_1 (P75-64)		
Outer (4.3 mm, c, inc. pendants)	17 ± 3	
Middle (4.2 mm, b)	67 ± 12	
Inner (3.6 mm, a)	133 ± 33	
Estimated initial age	160 ± 35	0.63
King Canyon fan, Qfo (P7922B1)		
Pendants (2.8 mm, not dated)	-----	
Outer (2.2 mm, r)	24 ± 4 *	
Middle (1.5 mm, s)	31 ± 6	
Inner (1.85 mm, u)	92 ± 20	
Estimated intial age	105 ± 30 **	0.62
King Canyon fan, Qfm_1 (P7922F)		
Pendants (0.8 mm, not dated)	-----	
Outer (1.2 mm, o)	98 ± 25 *	
Inner (0.8 mm, p)	30 ± 5	
Estimated initial age	40 ± 10 **	0.50
King Canyon fan, Qfm_1 (P7922E1)		
Pendants (1.3 mm, not dated)	-----	
Outer (1.3 mm, y)	42 ± 8 *	
Inner (1.2 mm, x)	23 ± 4	
Estimated initial age	30 ± 5 **	0.67
	Average =	0.60 mm/10ka

* Age considered to be too great, most likely due to leaching of uranium.

** Estimated age based on age of inner coat and constant rate of carbonate coat deposition.

*** Based on estimated age and average thickness of carbonate coats measured on local stratigraphic unit

ally correlative outer coat from the Section 11 fan, as well as for the estimated 15-ka age for the equivalent thickness of coats on glacial outwash of the last glaciation. The old age for these outer coats probably results from leaching of uranium late in the history of the sample. For the King Canyon deposits, stones with carbonate coats from unit Qfm_1 were collected from natural fluvial scarps cut into these fans and those from Qfo were collected from the surface. Leaching was currently taking place at both these locations. The inner layers of all the coats yielded ages that appear reasonable, probably because they are less affected by recent leaching because the inner layers are denser than the outer layers and they are buffered by the outer layers.

PRELIMINARY HISTORY OF THE ARCO SEGMENT

The Quaternary stratigraphy and associated dating information permit the following reconstruction of the history of faulting along the Arco segment from the present to about 160 ka. The Arco fault scarps do not cut unit Qfy, which on some fans in the Lost River Valley can be traced to Pinedale glacial moraines (table 1; Pierce and Scott, 1982). Dating of glacial deposits in the region (Porter and others, 1983) and correlation of unit Qfy with other fan deposits which can be related to the 15 ka Bonneville shoreline indicate the surface of unit Qfy is also about 15 ka (Pierce and Scott, 1982). Along the Lost River fault about 60 km north of the Arco segment, the surface of unit Qfy on the Willow Creek fan was offset about 2 m prior to 1983 faulting (Hait and Scott, 1978; Vincent, 1985).

Based on faulted and unfaulted deposits at the King Canyon fan (fig. 1), the most recent displacement on the Arco segment occurred about 30 ka. Unit Qfm_1 is faulted 2-3 m and has carbonate coats 2 mm thick (table 1). Unit Qfm_2 is not faulted and has coats 1.6 mm thick. Dates on the inner parts of carbonate coats from unit Qfm_1 suggest an age of 30 ka and 40 ka for the start of coat deposition (table 2), as does the overall rate of carbonate coat buildup of about 0.6 mm/10ka. In addition, these coats are twice as thick as the 1 mm coats on unit Qfy, suggesting an age twice the estimated 15 ka age of unit Qfy, or also about 30 ka.

At and near the trench (fig. 1), the surface of unit Qfo_1 is offset 19-20 m (fig. 3D), or possibly more. About 50 m south of the trench on the downthrown side of the fault, a combined backhoe and auger excavation successively penetrated the following: 1) gravelly fault-scarp colluvium, 2) eolian sand, and 3) gravelly soil with carbonate coats at a depth of 5.2 m. Assuming the gravelly soil is the top of downfaulted unit Qfo_1, the total offset in the past 160 ka is 18 m. These coats may be from a soil developed on the top of downfaulted unit Qfo_1. Excavation in the bottom of the trench exposed a pebbly silt colluvium overlain by loess that contains two volcanic ashes (fig 3D). The pebbly silt and loess have an observed thickness of 3 m. Two soils within the colluvium each have carbonate coats that average 1.0 mm thick, each implying as much time in their deposition as the 15 thousand years for the coats on unit Qfy. The dips of these buried scarp colluviums in relation to the fault plane suggest the top of unit Qfo_1 is less than 2 meters below the base of the trench. If so, unit Qfo_1 has been offset 19-20 m (fig. 3D), an amount that is consistent with the 18 m of offset determined 50 m to the south.

At the time of deposition of the upper volcanic ash, unit Qfo_1 was displaced at least a little more than the thickness of the colluvium on the lower half of the scarp, or a minimum of 4 m (fig. 3B). A estimate of the maximum displacement of unit Qfo_1 can be based on the decrease in slope of the

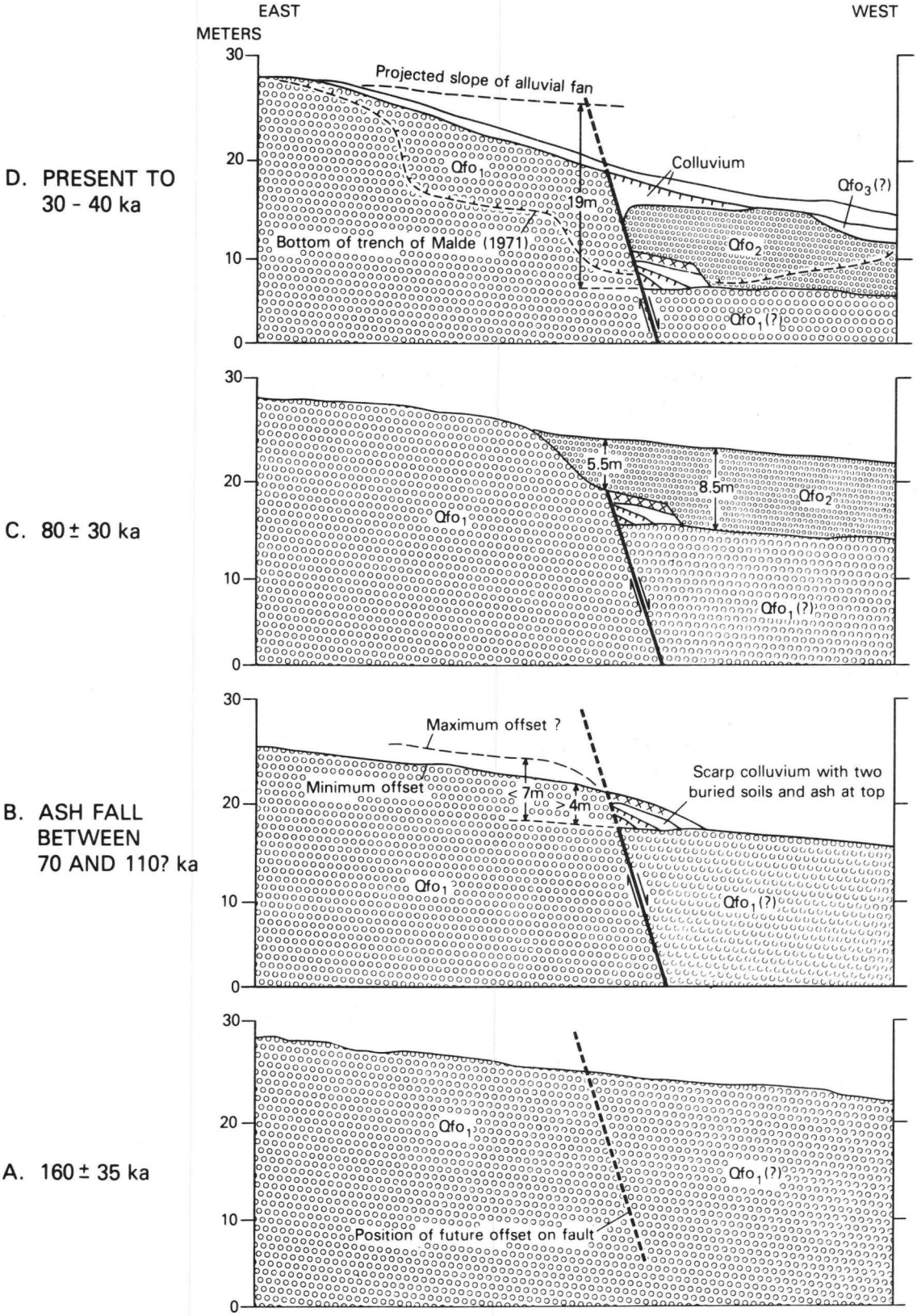

Figure 3. Schematic cross sections showing progressive displacement during the past 160 ka on the Arco segment. Cross sections modified from trench diagram of Malde (1971) combined with dating and other information described in the text.

colluvial deposits that grade upward into the loess containing the volcanic ashes (fig. 3B). At the time of ash deposition, offset of unit Qfo_1 was was probably no more than 7 m, for bedding is nearly horizontal in this deposit which was deposited immediately downslope from the fault. If the scarp were higher than that shown shown by the curved dashed line in Figure 3B, which represents a 7 m offset of unit Qfo_1, the slope of bedding in these scarp deposits would not be so gentle (Fig. 3B).

An estimate of the offset at a time intermediate between 30 ka and the time of ash deposition can be determined by from unit Qfo_2, which has 5-mm thick carbonate coats (table 1). Based on a rate of coat deposition of 0.6 mm/10 ka (table 2), unit Qfo_2 has an estimated age of 80 ± about 30 ka. On the upthrown side of the fault, Qfo_2 did not aggrade higher than and thus bury Qfo_1 (fig. 3C). Thus by the time Qfo_2 was deposited, at least 8.5 m of displacement had occurred to accomodate the thickness of Qfo_2 on the downthrown side of the fault (fig. 3C). After deposition, unit Qfo_2 was itself displaced. Assuming unit Qfo_2 extended eastward across the fault as shown in Figure 3C, the amount of truncation of unit Qfo_2 by the fault (fig. 3D) requires at least 5.5 m of displacement of unit Qfo_2.

For the Arco segment of the Lost River fault, seven constraints can be applied to the history of age versus displacement (fig. 4, shaded rectangles and solid boxes). For the overall history during the past 160 ka, the apparent slip rate averaged about 0.12 m/ka. Between about 160 and 30 ka, the rate was higher- about 0.15 m/ka. The detailed history of individual displacements is not known, and a variety of pathways through the 7 constraints shown on figure 4 are possible. Offsets of 2 m are arbitrarly assumed for the purposes of illustration (fig. 4). During the Borah Peak earthquake, offsets as great as 2.7 m occurred, but average offset was 0.8 m (Crone and others, 1985).

One pattern of offset versus age assumes buildup of strain is constant and faulting occurs at intervals directly related to the amount of displacement so the resulting stairstep pattern has a slope similar to the overall slip rate (fig. 4, solid line). If strain accumulation is assumed to be constant, about 4 m of strain has accumulated since the last movement on the fault about 30 ka ago. Based on typical offsets of about 1 m during the Borah Peak Earthquake (Crone and others, 1985), this amount of strain is four times that expected to be released in a single faulting event. Assuming a model with constant accumulation of strain, renewed surface faulting should have occurred about 10-20 thousand years ago.

A second pattern of offset versus age assumes grouping in time of multiple displacements separated by intervals of quiescence (fig. 4, dashed line). R. E. Wallace (1984) suggests displacement on a given fault in the Great Basin Province may be spaced quite unevenly in time with intervals of multiple movements separated by intervals of quiescence. A history showing such temporal grouping of activity is shown by the dashed line on Figure 4. This line better fits the apparent constraints provided by the quiescence for the past 30 ka as well as the age of the volcanic ash, assuming annealing is not an important problem. Thus, if temporal grouping of activity on the Arco segment is valid, prediction of future activity is quite uncertain, for the quiescence of the past 30 ka may either continue for many thousands of years, or may soon be broken by a new episode of activity.

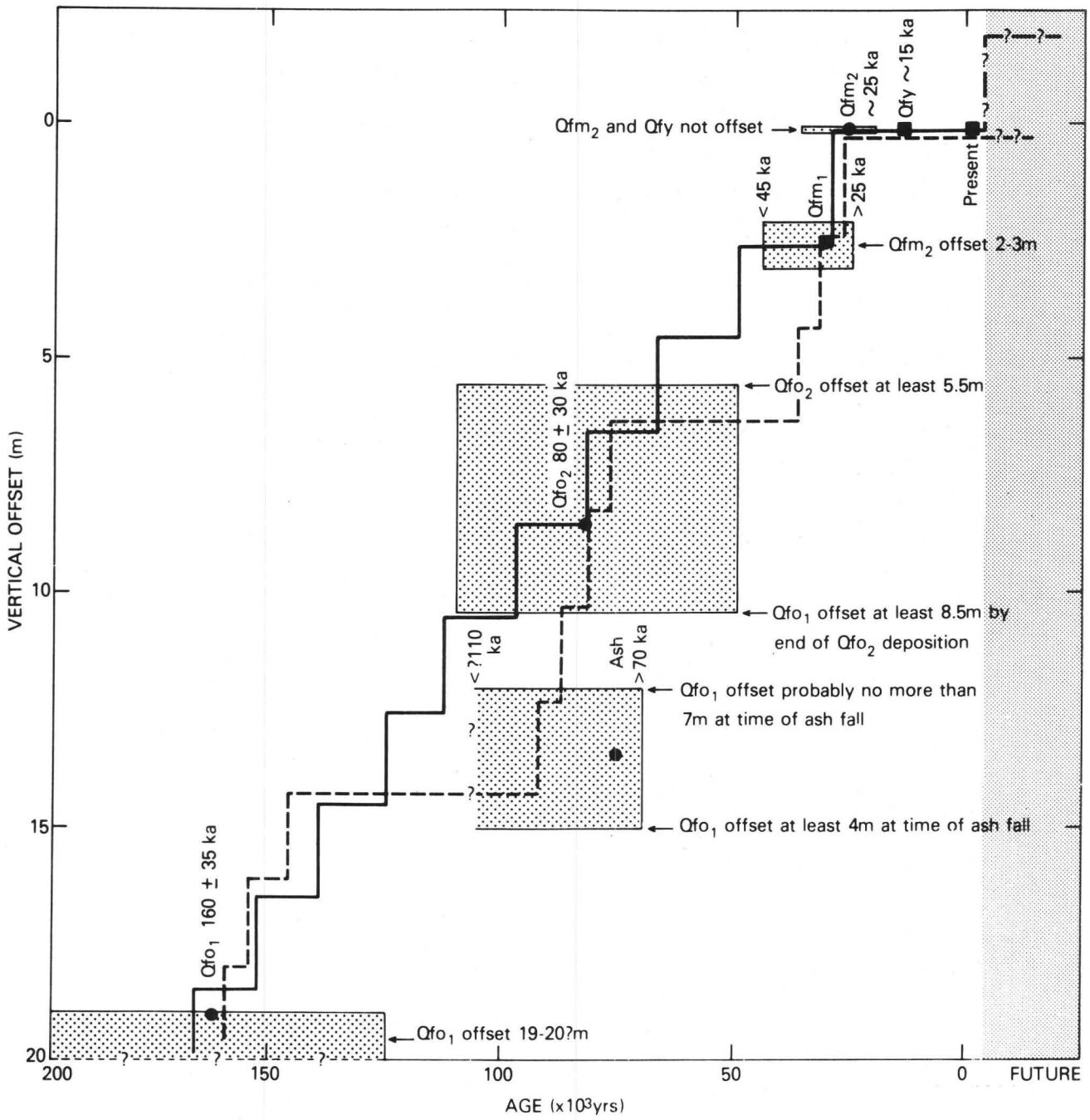

Figure 4. Apparent constraints in history of faulting along the Arco segment of the Lost River fault and two contrasting patterns of offset versus age that fit these constraints. Solid line is constant strain accumulation model, which implies that another displacement is long overdue. Dashed line is model of clustering of offsets in time separated by intervals of quiescence, which is compatible with either continued quiescence, or with renewed offset. To simplify this illustration, individual offsets are arbitrarily assumed to be 2 m.

REFERENCES CITED

Bucknam, R. C., and Anderson, R. E., 1979, Estimation of fault-scarp ages from a scarp-height--slope-angle relationship: Geology, v. 7, p. 11-14.

Crone, A. J., Machette, M. N., Bonilla, M. G., Lienkaemper, J. J., Bucknam, R. C., Pierce, K. L., and Scott, W. E., 1985, Characteristics of surface faulting accompanying the Borah Peak earthquake, central Idaho, in R. S. Stein and R. C. Bucknam., eds, Proceedings of Conference XXVIII-The Borah Peak Earthquake: U.S. Geological Survey Open-File Report, this volume.

Hait, M. M. Jr., and Scott, W. E., 1978, Holocene faulting, Lost River Range, Idaho: Geological Society of America Abstracts with Programs, v. 10, p. 217.

Ku, T. L., Bull, W. B., Freeman, S. T., and Knauss, K. G., 1979, Th^{230}-U^{234} dating of pedogenic carbonates in gravelly desert soils of Vidal Valley, southeastern California: Geological Society of America Bulletin, Part I, v. 90, p. 1063-1073.

Malde, H. E., 1971, Geologic investigation of faulting near the National Reactor Testing Station, Idaho, with a section on microearthquake studies by A. M. Pitt and J. P. Eaton: U.S. Geological Survey Open-File Report, 167 p.

Malde, H. E., 1985, Quaternary faulting near Arco and Howe, Idaho, in R. S. Stein and R. C. Bucknam eds., Proceedings of Conference XXVIII-The Borah Peak Earthquake: U.S. Geological Survey Open-File Report, this volume.

Pierce, K. L., and Scott, W. E., 1982, Pleistocene episodes of alluvial-gravel deposition, southeastern Idaho, in Bill Bonnichsen and R. M. Breckenridge, eds., Cenozoic Geology of Idaho: Idaho Bureau of Mines and Geology Bulletin 26, p. 685-702.

Pierce, K. L., and Colman, S. M., in preparation, Effect of height and orientation (microclimate) on geomorphic degradation rates and processes, late-glacial terrace scarps in central Idaho: manuscript with Branch approval, U.S. Geological Survey.

Porter, S. C., Pierce, K. L., and Hamilton, T. D., 1983, Late Wisconsin mountain glaciation in the western United States, in S. C. Porter, ed., The Late Pleistocene, v. 1, in H. E. Wright, Jr., ed., Late Quaternary Environments of the United States: Minneapolis, University of Minnesota Press, p. 71-111.

Scott, W. E., McCoy, W. D., Shroba, R. R., and Ruben, Meyer, 1983, Reinterpretation of the exposed record of the last two lake cycles of Lake Bonneville, western United States: Quaternary Research, v. 20, p. 261-285.

Scott, W. E., Pierce, K. L., and Hait, M. H., Jr., 1985, Quaternary tectonic setting of the 1983 Borah Peak Earthquake, central Idaho, in R. S. Stein and R. C. Bucknam, eds., Proceedings of Conference XXVIII-The Borah Peak Earthquake: U.S. Geological Survey Open-File Report, this volume.

Szabo, B. J., and Rosholt, J. N., 1982, Surface continental sediments, in M. Ivanovich and R. S. Harmon, eds., Uranium Series Disequilibrium: Applications to Environmental Problems, Oxford, Clarendon Press, p. 246-267.

Vincent, K. R., 1985, Measurement of vertical tectonic offset using longitudinal profiles of faulted geomorphic surfaces near Borah Peak, Idaho- a preliminary report, in R. S. Stein and R. C. Bucknam, eds., Proceedings of Conference XXVIII-The Borah Peak Earthquake: U.S. Geological Survey Open-File Report, this volume.

Wallace, R. E., 1984, Patterns and timing of late Quaternary faulting in the Great Basin Province and relation to some regional tectonic features: Journal of Geophysical Research, v. 89, No. B7, p. 5763-5769.

Quaternary Faulting near Arco and Howe, Idaho

Harold E. Malde
U.S. Geological Survey
Denver, CO 80225

ABSTRACT

Well-defined high-angle faults were exposed in 1969 by trenching across scarps in alluvial fans along mountain ranges north of Arco and Howe, Idaho.

The Arco scarp coincides with a zone of closely spaced faults in alluvial fans along the western foot of the Lost River Range. From Arco, the scarp extends northward about 16 km (10 miles), where it merges into an unstudied scarp in bedrock. At a trench across the scarp 10 km (6 miles) north of Arco, multiple movements in the fault zone have resulted in aggregate vertical displacement of at least 12 m (40 ft). Measured offsets of stratigraphic units exposed in the trench indicate at least two times of vertical movement on individual faults. One episode of movement caused a minimum offset of 4.6-6.1 m (15-20 ft), and another offset was more than 3 m (10 ft).

The Howe scarp coincides with a zone of closely spaced faults in alluvial fans along the western foot of the Lemhi Range. A southern segment of the scarp trends northwest along the southern part of the range a distance of 15 km (9 miles), and a northern segment trends north at least another 6 km (4 miles). These segments are separated by a bedrock ridge 3 km (2 miles) wide in which the scarp is indistinct. At a trench across the scarp about 11 km (7 miles) north of Howe, multiple movements in the fault zone have resulted in aggregate vertical displacement of at least 15 m (50 ft). Measured offsets of stratigraphic units exposed in the trench indicate five or more times of vertical movement on individual faults, ranging from 0.3 m (1 ft) to more than 3 m (10 ft).

Faulting at both the Arco and Howe scarps disrupts strong caliche soils that are considered to be about 30,000 years old. On the other hand, both scarps have gaps occupied by unbroken alluvial fans that are probably younger than 15,000 years old.

INTRODUCTION

This report describes the geology exposed in two trenches excavated in 1969 across fault scarps in alluvial fans a few miles north of Arco and Howe, Idaho. The descriptions are taken almost verbatim from my 1971 U.S. Geological Survey Open-File Report (Malde, 1971) but have been revised in light of new information on the ages of the alluvial fans. The trenches show that both the Arco and Howe scarps were offset more than 3 m (10 ft) about 30,000 years ago, but the scarps have probably not been displaced in the last 15,000 years. The geologic features seen in the trenches, particularly in the trench north of Arco, are of current interest because of their proximity to the surface ruptures associated with the 1983 Borah Peak Earthquake. Accordingly, this revised description of Quaternary faulting near Arco and Howe has been prepared as a contribution to the Redbook on the Borah Peak Earthquake.

Background of Study

The work reported here stems from a concern in 1967 by the Division of Reactor Development and Technology, U.S. Atomic Energy Commission, about the potential for faulting and strong earthquakes near the National Reactor Testing Station (NRTS)--now named the Idaho National Engineering Laboratory (INEL). At the request of the Division, M. G. Bonilla and G. H. Chase of the U.S. Geological Survey made a reconnaissance from October 23 through November 4, 1967, and found various sites near the INEL in which several kinds of geologic features indicated possible faults. Two of the sites were scarps in alluvial fans along the western flank of the Lost River Range north of Arco and along the foot of the Lemhi Range north of Howe. Bonilla and Chase, in a 1968 written communication to the Commission, attributed these scarps to geologically young faulting.

Bonilla and Chase recommended additional geologic study to test their conclusion that geologically young faulting has occurred near the INEL, and that the potential for strong seismic effects at the INEL is greater than previously supposed. The Division of Reactor Development and Technology thereupon authorized the U.S. Geological Survey to make further geologic and seismologic studies. My resulting investigation of the Arco and Howe scarps lasted from September 1968 to August 1969.

Between the time of my study and this report, other investigations have been made of the local and regional geology, and I have used the results of these studies to better estimate the ages of the latest times of Quaternary faulting. One of these studies was further investigation by K. L. Pierce, U.S. Geological Survey, of the age of the Arco scarp, which is reported elsewhere in this volume.

Fieldwork

In the geologic study for this report prior knowledge of the regional geology was applied, especially information about landforms, soils, and erosion by which young geologic events are dated. The Arco and Howe scarps were examined on foot to study their geomorphic features and to determine the distribution, nature, and ages of the associated sedimentary deposits and soils. The scarps were then trenched at two sites to expose faults and the geologic details of the subsurface stratigraphy and structure. Particular attention was given at the trenchs to the amounts of displacement on recognizable faults and to features that indicate the probable ages of times of fault movements.

Acknowledgments

This investigation was done as part of a research program by the U.S. Geological Survey on geologic, seismologic, and hydrologic factors that pertain to the design of nuclear facilities and the selection of their sites. At the time of the fieldwork this program was sponsored by the U.S. Atomic Energy Commission (AEC), Division of Reactor Development and Technology, under W. G. Belter, Chief of the Environmental and Sanitary Engineering Branch. The Idaho Operations Office of the AEC, under W. L. Ginkel, Manager, provided heavy equipment and operators for the trenching.

The geologic work was facilitated in many ways by personnel at the INEL. Cooperative assistance was also received from G. L. Voelt, AEC, and J. T. Barraclough, USGS, and their associates. At various times I benefitted from

consultation in the field with members of the U.S. Geological Survey, including E. H. Baltz, J. T. Barraclough, M. G. Bonilla, E. G. Crosthwaite, A. H. Harder, J. B. Robinson, R. Schneider, S. Subitsky, and H. H. Waldron. Also, my understanding of soils developed on the surficial deposits was improved by advice in the field from J. O. Harwood, Soil Conservation Service.

ARCO SCARP

General Features

The Arco scarp is a subdued step about 8 m (25 ft) high that interrupts the slope of alluvial fans where the Lost River Range faces the Big Lost River Valley north of Arco (fig. 1). The angle of slope along the Arco scarp is commonly between 18° and 27°, in contrast with slopes of about 5° on the adjoining fans. This contrast in slope, together with a general straightness, makes the scarp conspicuous both at ground level and from the air. The scarp follows the outline of the mountain range within a few tens of meters of outcropping bedrock from Arco northward a distance of 16 km (10 miles), where it merges into bedrock and becomes indistinct. As discussed below, excavation across the Arco scarp 10 km (6 miles) north of Arco reveals that the scarp coincides with a narrow zone of high-angle faults. Former vertical displacements on these faults evidently produced abrupt topographic relief, now softened in contour by erosion and deposition of colluvium but still recognizable as the Arco scarp.

Alluvial fans above and below the Arco scarp have subtle differences in soils, vegetation, and erosional aspects that further emphasize the scarp. Coupled with topography, these differences show that the scarp is not continuous but is instead a series of segments about 150-300 m (500-1,000 ft) long interrupted by scarp-free gaps commonly 30-90 m (100-300 ft) wide. The higher alluvial fans east of the scarp are dissected by gullies 3 m (10 ft) or more deep and are covered by drought-resistant vegetation (chiefly black sagebrush, shadscale, and horsebrush) that is rooted in caliche soil. At the toe of the scarp are alluvial fans with inconspicuous shallow gullies about half a meter deep. These low fans generally support plants less tolerant of drought, which grow in soil not conspicuously cemented with caliche. The low fans spread outward from gaps that interrupt the continuity of the Arco scarp. That is, the Arco scarp is expressed by an abrupt rise to higher, apparently older, alluvial fans, and it is interrupted by gaps occupied by lower, apparently younger, alluvial fans. The ages of these respective fans thus pertain to the age of the Arco scarp and its time of formation by faulting. The problem of dating the fans and the scarp is discussed at the end of this section.

Faulting at site A-2

A particularly straight segment of the Arco scarp (site A-2 near the center of sec. 35, T. 5 N., R. 26 E.; see fig. 1) was selected for trenching, partly because some of the required earth moving had been previously accomplished by erosion along a perpendicular stream, and partly because this site is about midway along the length of the scarp. Presumably, site A-2 is representative of geologic relations that would be found elsewhere along the scarp. Figure 2 is a vertical aerial photograph of the area of site A-2, and Figure 3 shows its appearance at ground level. The Arco scarp at site A-2 is about 60 m (200 ft) west of the nearest bedrock outcrops at the foot of the mountain range.

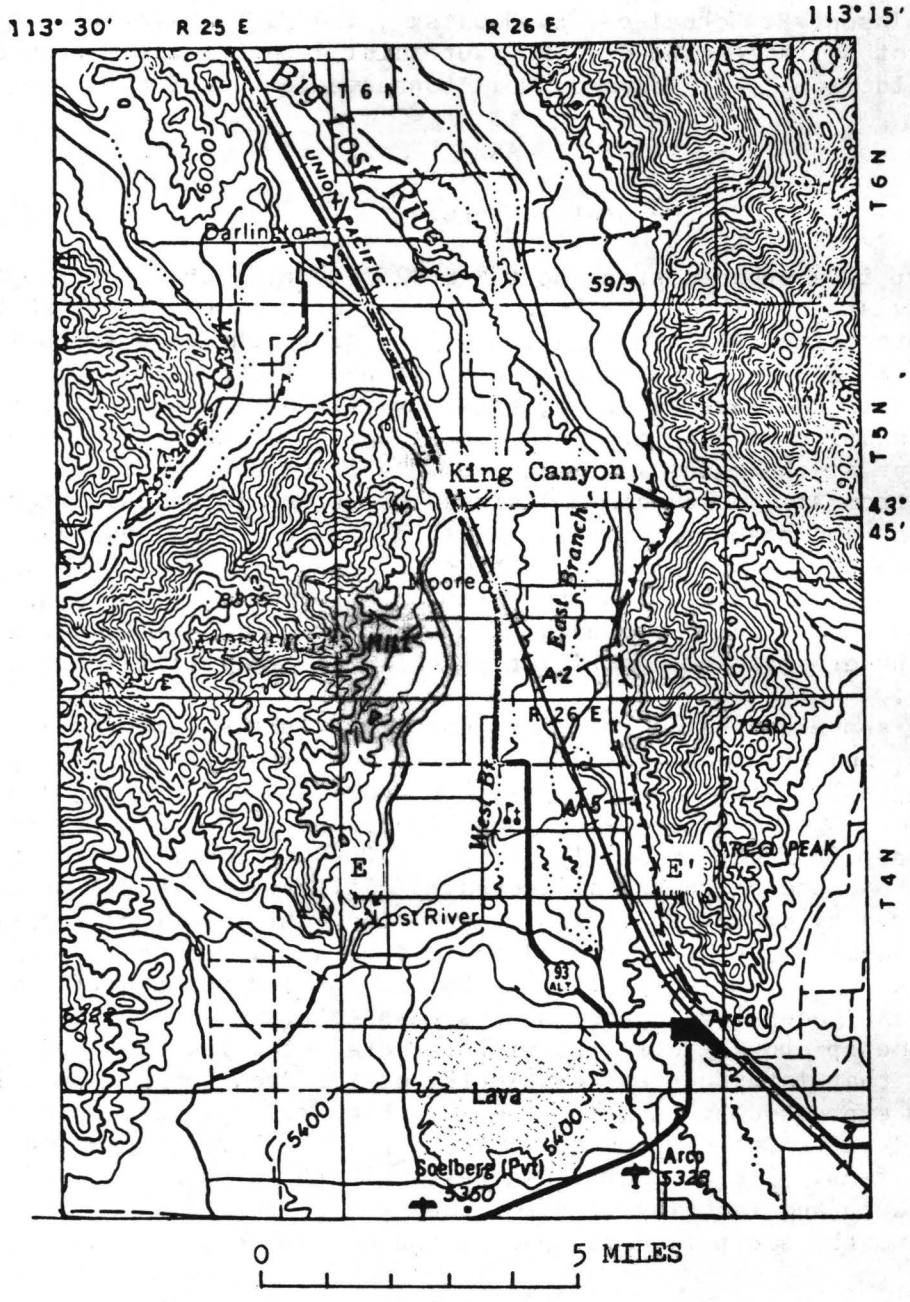

Figure 1.--Map of the Arco scarp north of Arco, Idaho, showing the location of geologic cross-section E-E′ and site A-2 discussed in the text. Intermittent gaps in the scarp line are places where the continuity of the scarp is interrupted by alluvial fans younger than the scarp.

Figure 2.--Vertical view of the Arco scarp in sec. 35, T. 5 N., R. 26 E., showing the location of site A-2 on the south side of a stream perpendicular to the scarp. (Enlarged from U.S. Department of Agriculture aerial photograph CPP-3W-185 taken July 16, 1959.)

Figure 3.--View north-northeast toward the Arco scarp in sec. 35, T. 5 N., R. 26 E. The scarp is a step 9 m (30 ft) high in the general gradient of the adjacent alluvial fans, but the topographic relief from the head to the toe is about 15 m (50 ft). Site A-2 is near the left-hand side of this photograph, where the bulldozer can be seen.

With a large backhoe and bulldozer, a trench 8-11 m (25-35 ft) deep and more than 52 m (170 ft) long was excavated across the Arco scarp at site A-2. A cross-section of the geologic features thereby exposed is shown in figure 4. As in other geologic sketches, attempts to represent all the variable aspects of the lithology and bedding would be needlessly confusing, and the section therefore emphasizes only distinctive lithologic units, large or small, that can be readily recognized and traced.

The cross-section shows bedded gravel on the west and east disrupted by a zone of high-angle faults located two-thirds the distance down the scarp face. For convenience of discussion, the principal fault planes (which are at most about 5 cm wide) are designated by letters. Between planes A and B, the material is structureless gravel, which was evidently churned by movement during one or more times of faulting. This interval is here called the fault zone. The bedded gravel between planes B and C matches the sequence of beds on the east and thus demonstrates about 0.6 m (2 ft) of vertical displacement on fault C, the western side having moved relatively down. Also, the beds between planes B and C have an exaggerated westward dip, about 12°, which indicates drag by downward relative movement to the west. The excavated trench gives only a two-dimensional view of these faults and does not permit measurement of possible strike-slip movements--that is, offsets parallel to the trend of the scarp.

The fan gravel east of the faults is arranged in fairly regular thick beds that alternate between brown layers of limestone pebble to boulder gravel and open-textured gray layers of angular limestone pebbles. The brown layers have a matrix of sand and silt, which is represented on the sketch by a stipple pattern. The upper 4.6 m (15 ft)--that is, the gravel above the highest bedding plane drawn between survey marks 15 and 21--is less conspicuously stratified but includes brown and gray layers of angular pebbles, rounded cobbles, and sand. These gravel beds dip westward at 5°. The fan gravel west of the fault zone extends upward to a conformable contact 3.7 m (12 ft) below survey mark 9 and 2 m (7 ft) below survey mark 5. (Above this contact are deposits of eolian sand and colluvium that will be discussed shortly.) This fan gravel lacks the alternating bedding found east of the fault zone and is dominated by gravel of different character, namely gray lenticular layers of angular pebbles and cobbles that lack abundant interstitial sand and silt. The bedding planes dip systematically westward at 2°. The change in dip from 5° on the east to 2° on the west is apparently due to backward rotation during faulting.

Aggregate Displacement at Site A-2

The sketch illustrates an obvious fact, determined by close scrutiny during the week after the trench was first excavated (April 23-29, 1969), that no beds west of the fault zone match beds on the east. However, because the upper 4.6 m (15 ft) of gravel east of survey mark 15 is more than 6 m (20 ft) from the fault zone, and because gravel in alluvial fans typically changes character in short distances, a possible match between this gravel and the lowest exposed deposits on the west cannot be categorically ruled out. Thus, by projecting the bedding plane at the base of the upper 4.6 m (15 ft) of gravel westward, and by then measuring down to the base of the exposed beds west of the fault zone, a minimum vertical offset of at least 12 m (40 ft) is indicated. Virtually all this displacement was in the fault zone bounded by planes A and B.

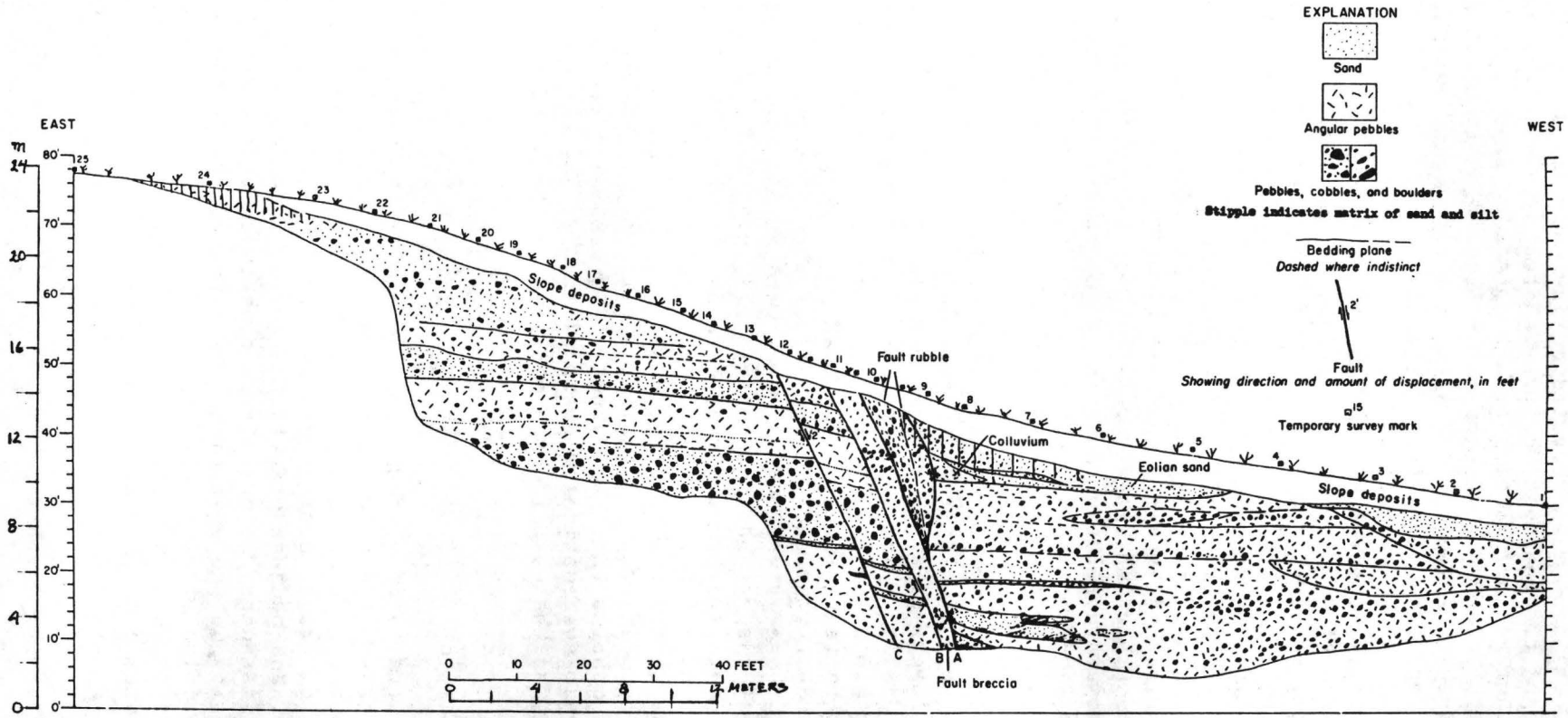

Figure 4.--Cross-section of unconsolidated fan gravel disrupted by high-angle faults exposed in a trench across the Arco scarp at site A-2, 10 km (6 miles) north of Arco (NE 1/4 SE 1/4 NW 1/4 sec. 35, T. 5 N., R. 26 E.).

Evidence of Multiple Movement

Study of details near the fault zone indicates that the aggregate displacement, whatever its magnitude, was accomplished during two or more times of movement. These details also demonstrate that each of the offsets exceeded 3 m (10 ft). The features to be described are between survey marks 8 and 11 on Figure 4.

Immediately west of plane A, at survey mark 10, a wedge of loose gray fault rubble is composed of angular pebbles and some cobbles. Virtually all the tabular pieces in this rubble lie on edge more or less parallel with the fault plane. From a present width of 1.5 m (5 ft) at the top, the wedge pinches out downward against the fault plane at a depth of 7.6 m (25 ft). Adjacent to this wedge on the west is more fault rubble, also gray and loose, but easily distinguished by its random distribution of stones. At survey mark 9, at a depth of 3.7 m (12 ft), the fault rubble is abutted perpendicularly by the contact between fan gravel and overlying colluvium. Still farther west, below the present surface deposits, the colluvium merges with eolian sand that also rests on the fan gravel. The origin of these features is interpreted in the diagrams of Figure 5.

As shown on Figure 5A, deposition of colluvium on fan gravel west of the fault zone was probably a consequence of at least one episode of faulting, because an exposed fault scarp in the gravel was the most likely source for the colluvium. A lack of soil on the fan gravel where it is buried by the colluvium indicates that this faulting occurred while deposition of gravel by a stream debouching from the mountains was still in progress. After faulting, during buildup of the colluvium, stream deposition along the mountain front stopped in this immediate area, perhaps because of topographic changes brought by faulting, and eolian sand on the downthrown surface mingled with colluvium near the fault scarp. If the inclined bedding in the colluvium is projected upslope to plane A, given a preserved thickness of 3 m (10 ft), the indicated scarp height (fault displacement) could have been as much as 4.6-6.1 m (15-20 ft).

The perpendicular intersection of loose fault rubble with the horizontal boundary between fan gravel and colluvium at survey mark 9 demonstrates fault movement between the rubble and the adjacent deposits (fig. 5B). The fault rubble is so loose that it could not have survived intact as a vertical face against which the colluvium might have been deposited. (Indeed, this rubble began to crumble into the trench as soon at it was exposed by the excavating equipment.) In short, the steeply dipping contact of rubble against colluvium appears to be a fault. If so, because of the preserved thickness of the colluvium, displacement on the fault was at least 3 m (10 ft). It seems probable that the rubble was produced by this movement.

The colluvium and the immediately adjacent fault rubble near survey mark 9 contain in the upper part conspicuous soft caliche to a depth of about a meter (3-4 ft), as shown in a zone of light-colored streaks at the upper right of Figure 6. In the colluvium, the caliche forms a network of veins, some of them conforming with inclined bedding planes, while others are more or less vertical. In the rubble, the caliche occupies much of the space around the stones but does not hold them tightly. The caliche clearly represents the carbonate horizon of a calcareous soil. It is recognizable westward nearly as far as survey mark 6 but ends abruptly on the east, apparently against the wedge of rubble at survey mark 10. The relations suggest that the caliche ends abruptly because of further faulting between the rubble wedge and soil-covered deposits on the west (fig. 5B).

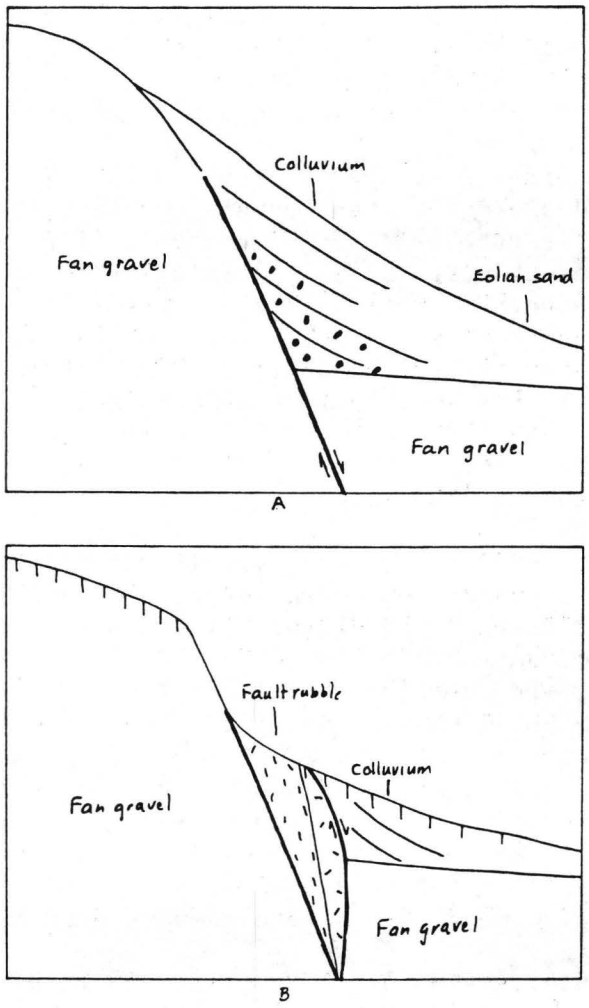

Figure 5.--Suggested fault movements at the Arco scarp.

A. Movement in the fault zone dropped the fan gravel relatively downward on the west. Colluvium derived from the higher fault block was then deposited against the exposed fault face and mingled westward with eolian sand on the fan surface.

B. Further movement produced a gap occupied by fault rubble, and the old colluvium was displaced downward against this rubble. A caliche soil on the colluvium was possibly displaced by still later movement in the fault rubble.

Figure 6.--Upper part of the trench wall of site A-2 at survey mark 9, showing fan gravel and overlying colluvium on the west (right) against fault rubble. Marks on the vertical tape are 0.3 m (1 ft) apart.

In summary, initial vertical displacement of at least 4.6-6.1 m (15-20 ft) in a narrow zone of faulting and subsequent displacement of more than 3 m (10 ft) are indicated by the geologic features at site A-2. Still later displacement of indeterminate amount is suggested by the abrupt vertical boundary of a relic soil. Displacement of about 2 feet on a parallel fault 2 m (7 ft) east (fault C on fig. 4) is associated with exaggerated dip in the intervening beds, which expresses drag during movements in the fault zone. These displacements, together with other possible displacements not yet determined, represent at least 12 m (40 ft) of vertical offset at the Arco scarp.

Age of Faulting

Regional relations

All the alluvial fans that border this reach of the Big Lost River are younger than basalt of the Snake River Plain southeast of Arco. This age relation derives from the circumstance that the Big Lost River is incised in a gorge 15-23 m (50-75 ft) deep and 10 km (6 miles) long in the lava plain shortly after leaving Arco. At an earlier time, before the river became incised, it must have flowed at a higher grade at Arco on valley deposits that have since been removed by erosion (or carried downward on faults) probably during cutting of the gorge. Alluvial fans at the edge of the valley would have then been considerably higher than the present fans. The former presence of higher alluvial fans is suggested by inclined bedrock facets on mountain spurs, which are graded to a level above the existing fans (fig. 7). The present alluvial fans, in contrast, are graded to levels more or less close to the valley floor and must date from the closing stages of river entrenchment to the present depth. The limiting date for the start of this entrenchment is the age of basalt incised by the Big Lost River on the Snake River Plain. This basalt is part of the Snake River Group of late Pleistocene age that occupies most of the eastern Snake River Plain (Walker, 1964; Malde, 1965). The age of the basalt can be estimated by comparing its weathering with that of other lavas of established age in the region.

The lava incised by the Big Lost River has well-preserved features of initial surface relief and is incompletely covered by a thin mantle of surficial deposits (Scott, 1982). Based on the degree of weathering, amount of surficial cover, and magnetic polarity, this basalt is part of an assemblage of lava flows estimated to be from 15,000 to 200,000 years old (Kuntz and others, 1984). Thus, the alluvial fans near Arco that are displaced by faulting along the Arco scarp date near the end of an episode of valley entrenchment that probably began no more than 200,000 years ago.

Geophysical evidence

Despite the geologic youth of the Arco scarp, faulting has been in progress for a long time between a relatively subsiding crustal block represented by the Big Lost River Valley and relatively rising blocks represented by the adjoining mountains. Such faulting has been determined from regional geophysical studies by D. R. Mabey and his associates, U. S. Geological Survey, including observations along a section across the Big Lost River Valley north of Arco (section E-E′, fig. 1). The geophysical observations indicate that a fault with 460 m (1,500 ft) of aggregate displacement between valley deposits and adjacent bedrock of the Lost River Range coincides approximately with the Arco scarp (fig. 8). Other related faults in this section displace Tertiary

Figure 7.--Faceted bedrock spurs graded to a level above existing alluvial fans along the western flank of the Lost River Range, 14 km (9 miles) north of Arco, Idaho.

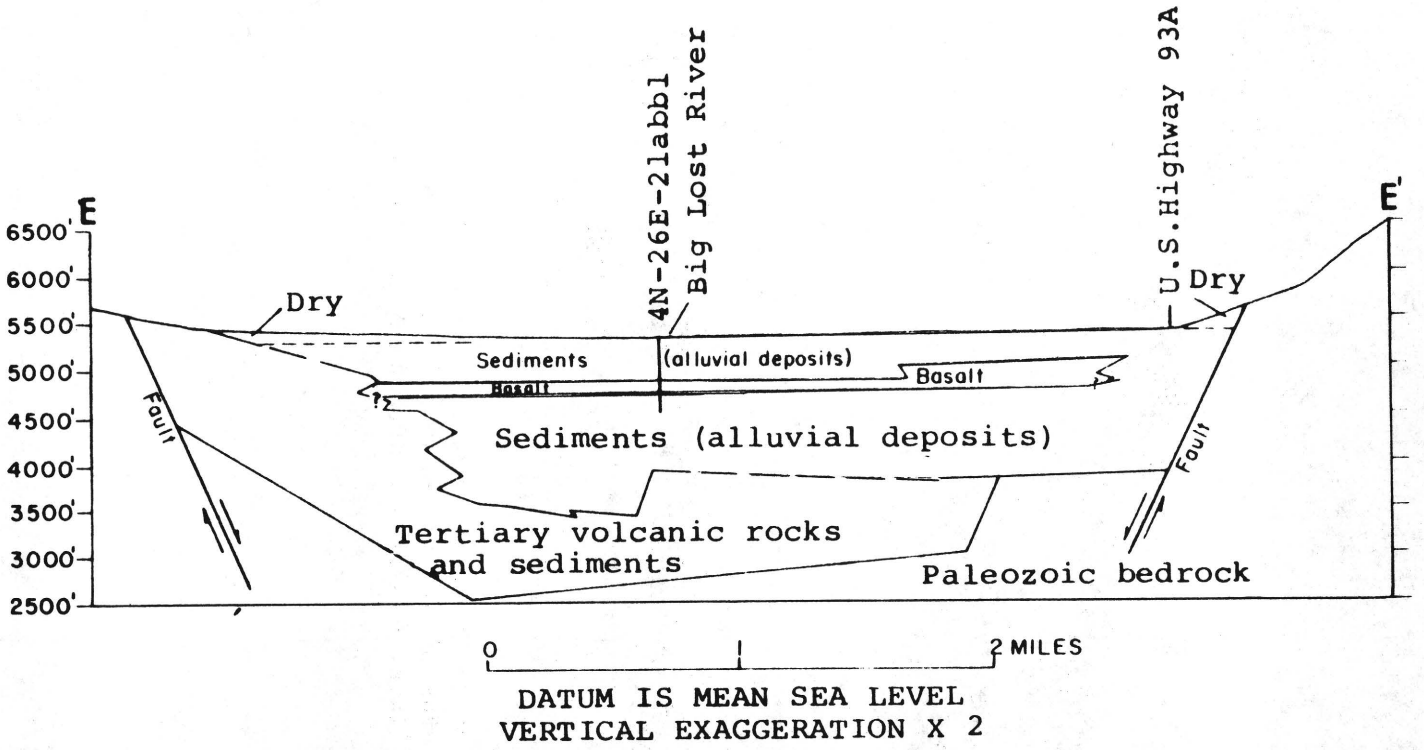

Figure 8.--Generalized geologic cross-section 3 km (2 miles) north of Arco, Idaho, compiled by D. R. Mabey and others, U.S. Geological Survey, from gravity, seismic-refraction, and resistivity surveys completed in 1968. (From Crosthwaite and others, 1970, Figure 15.)

volcanic rocks. Clearly, therefore, the Arco scarp expresses only the latest fault movements that began long ago.

Inferences from landforms

Landforms in the area of the Arco scarp provide some evidence about the geologic age of tectonic movements.

One aspect of the landscape, which suggests that the area near the Arco scarp is currently subsiding, presumably by movement on a fault, is the route of the Big Lost River. The river hugs the east side of the valley and is eroding the extremities of the alluvial fans. On the opposite side, the alluvial fans merge imperceptibly with the valley floor. A possible explanation for the path taken by the river is that subsidence is gradually tilting the valley floor eastward at a rate fast enough to prevent diversion of the river by the westward spread of fan gravel. If so, the existing condition of approximate equilibrium between river erosion and fan building implies that subsidence by faulting is currently active.

On the other hand, a traverse along the Arco scarp shows that none of the young alluvial fans that occupy gaps where the scarp has been breached by streams are themselves visibly offset by faults. Evidently, faulting is not currently active. Building of the young fans surely occurs slowly and intermittently when sheets of debris are brought down every decade or so by sporadic runoff from storms. Thus, the surfaces of the young fans are mostly several hundred years old. Meanwhile, while the young fans have been building without noticable interruption by faulting, the Arco scarp has been slowly eroding to its present subdued slope. Such relations suggest that the last faulting along the scarp is at least several hundred years old, possibly several thousand years old.

Geomorphic study since the time of my work on the Arco scarp indicates that no movement on the scarp has occurred in the last 15,000 years. First, the maximum slope of the Arco scarp, when compared with nearby late-glacial scarps of similar height and with shoreline scarps formed by Pleistocene Lake Bonneville in Utah, indicates that the Arco scarp is older than 15,000 years (Pierce, 1985). Second, some of the unbroken young fans, which have surfaces braided with well-preserved channels, are related to Pinedale glacial moraines and, hence, are about 15,000 years old (Pierce and Scott, 1982).

Soils at site A-2

The alluvial fan at the head of the Arco scarp at site A-2 has a strong caliche soil. Pierce (1985) finds that carbonate coatings on individual stones in the soil profile are as thick as 10 mm. Further, Pierce reports that the carbonate began to form on the stones about 160 thousand years ago, as determined by John Rosholt of the U.S. Geological Survey, using a uranium-series isochron method to date stratigraphic layers in the carbonate coatings.

The deposits at the foot of the Arco scarp also have a well-developed caliche soil. For this soil, Pierce (1984) finds that the carbonate coatings average 5 mm thick. This thickness, assuming that carbonate was added at a rate of 0.6 mm per 10,000 years, indicates to Pierce that the soil is about 80,000 years old.

Finally, Pierce (1985) has found a place on the Arco scarp (King Canyon) where the fault displacement is 2-3 m. Here, carbonate coatings 2 mm thick that have formed since the last time of faulting suggest an age of about 30,000 years. Such an age is supported by uranium-series dates for the inner

parts of carbonate coatings in two samples. In contrast, Pierce finds that carbonate coatings on a younger terrace not offset by faulting are only 1.6 mm thick. Carbonate coatings of similar thickness are also found on gravel of the unbroken young fans that interrupt the continuity of the Arco scarp.

HOWE SCARP

General Features

The Howe scarp is an step of variable height along the upper reach of alluvial fans that descend westward from the Lemhi Range to the Little Lost River north of Howe (fig. 9). Like the Arco scarp, the maximum slope along the Howe scarp is commonly between 20° and 25°, whereas slopes on the adjoining fans are no steeper than 8°. The scarp is therefore conspicuous as a more or less linear break in slope. The Howe scarp follows the irregular outline of the Lemhi Range, although the distance from outcropping bedrock widens on the south to about 0.8 km (1/2 mile). The Howe scarp has two parts, a northern segment 6 km (4 miles) long centered on North Creek, and a southern segment 14 km (9 miles) long centered approximately on Black Canyon (sec. 3, T. 6 N., R. 29 E., also known locally as West Canyon). Although scarplike features are found in a hilly area of bedrock between these segments, the two parts of the Howe scarp could have formed at different times. As discussed below, excavation midway along the length of the southern segment shows that this part of the Howe scarp coincides with several closely spaced high-angle faults that moved at different times. The northern segment of the Howe scarp, which has similar surface characteristics, also almost surely formed because of faulting.

Because the Howe scarp is interrupted at many places by gaps occupied by young alluvial deposits, neither of the two principal segments is entirely continuous. Moreover, the height and length of individual parts of the scarp are irregular, especially in contrast with the general uniformity of the Arco scarp. The scarp height varies from a faintly recognizable step in the SE 1/4 sec. 3, T. 6 N., R. 29 E., to more than 12 m (40 ft) in several places. Substantially continuous stretches of the Howe scarp range from 90 m (300 ft) to more than 0.8 km (1/2 mile) long. The scarp-free gaps are commonly from 90 m (300 ft) to more than 150 m (500 ft) wide, and one gap north of Berenice is 2.4 km (1 1/2 miles) across. Such differences in height and length along the Howe scarp are partly the result of local differences in the interplay of erosion and deposition, which in time tend to subdue or conceal former topography, but the variable height and length may also reflect different ages of alluvial fans that have been displaced by faulting. Interpretations of the height and length are given below in the section on landforms.

As at the Arco scarp, differences in soils, vegetation, and dissection by gullies are also found in alluvial fans above and below the Howe scarp. In similar ways these differences indicate that the Howe scarp forms a general boundary between older fans cut by the scarp and younger fans that interrupt its continuity and that spread outward at the scarp toe. Times of faulting along the Howe scarp, as discussed at the close of this section, therefore can be appraised from the ages of these alluvial fans.

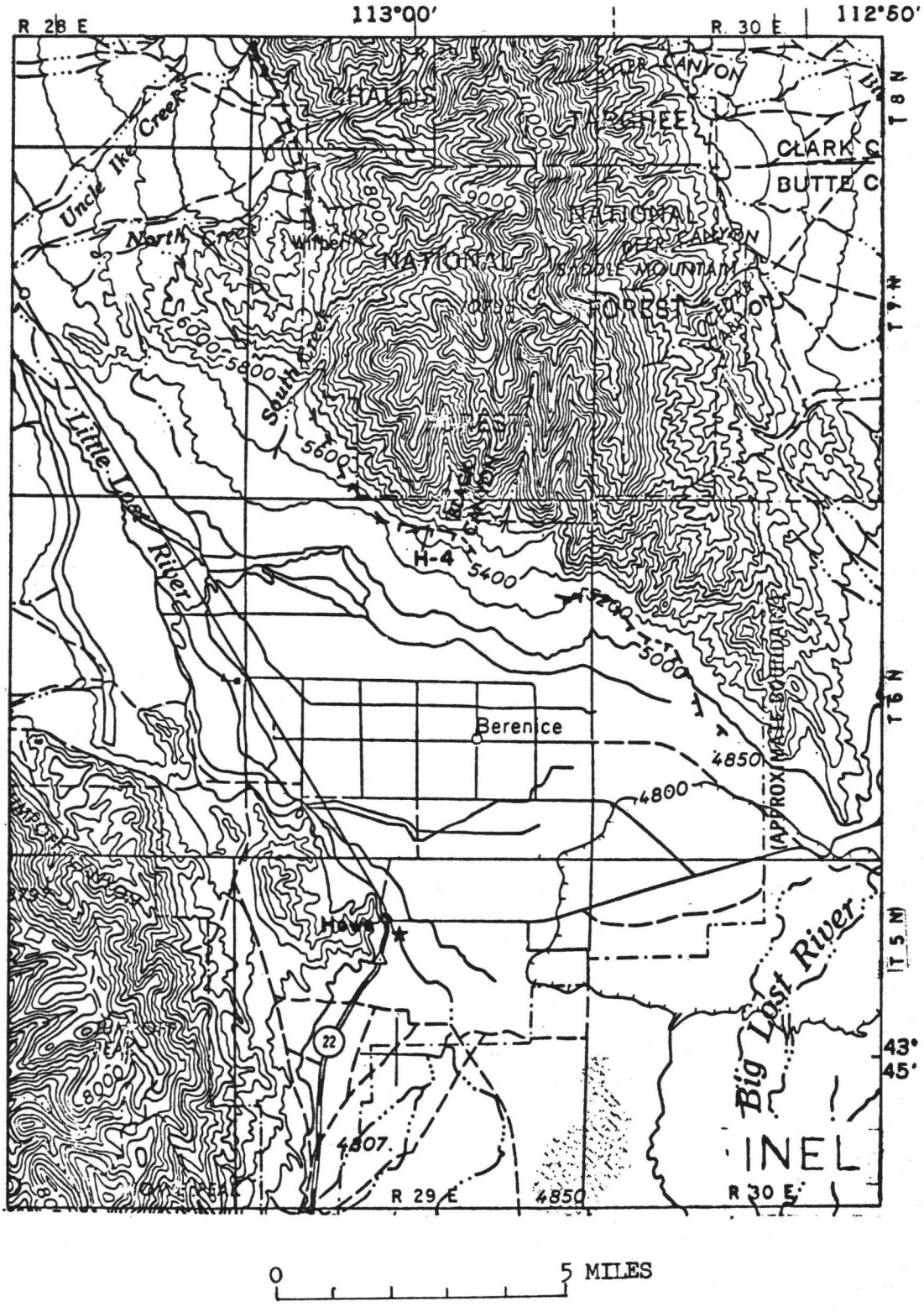

Figure 9.--Map of the Howe scarp in alluvial fans north of Howe, Idaho, showing the location of site H-4 discussed in the text. A gap in the scarp between North Creek and South Creek is occupied by a bedrock ridge. The wide gap north of Berenice is formed by a broad alluvial fan younger than the scarp. Shorter gaps elsewhere along the trend of the scarp are also filled by young fans.

Faulting at Site H-4

Selection of the site

A clearly defined stretch of the Howe scarp at the front of a high alluvial fan midway along the Black Canyon segment about 11 km (7 miles) north of Howe was selected for detailed study (site H-4 near the center of sec. 3, T. 6 N., R. 29 E.; fig. 9). Site H-4 was chosen partly because a backhoe could be maneuvered to a digging position at the head of the scarp, and partly because the variable height of the scarp in the area is representative of the appearance of the Howe scarp at most places along its length. Figure 10 is a vertical aerial photograph of the area of site H-4, and Figure 11 is a view from ground level. The Howe scarp at site H-4 is 150 m (500 ft) from the nearest bedrock outcrops at the foot of the Lemhi Range. Bedrock in this part of the Lemhi Range consists of quartzite and limestone formations that strike north, perpendicular to the local trend of the Howe scarp (Beutner, 1968). The fan gravel at site H-4, however, is composed almost entirely of quartzite.

A secondary factor in selecting site H-4 for excavation was the presence of a flattened bench that extends 90 m (300 ft) south from the toe of the scarp to the head of a lower alluvial fan. This bench perhaps conceals a grabben--that is, a trough between opposing high-angle faults--and I anticipated that a trench at the scarp could be continued across the bench to investigate its internal features. As matters turned out, the excavating equipment was needed for other work when excavation of the scarp itself was completed, and no observations have yet been made in the bench at the scarp toe.

A trench 8-9 m (25-30 ft) deep and 120 m (400 ft) long was excavated at site H-4 perpendicular to the Howe scarp. Beds of fan gravel interrupted by high-angle faults in the middle of the scarp face were thereby exposed (fig. 12). As in the sketch made at Arco site A-2, the cross-section drawn at site H-4 emphasizes distinctive beds that can be reliably traced, especially beds that are useful for measuring displacements on the faults. Where the direction of fault movement can be determined at site H-4, fault blocks toward the scarp toe moved relatively down, and it seems likely that this sense of movement applies also to the faults of indeterminate displacement.

The scarp at site H-4 is a step 14 m (45 ft) high, if allowance is made for the local slope above and below. This measurement of height is called the surface offset (Buckman and Anderson, 1979). More typically, the offset at the Howe scarp is only 5-6 m (15-20 ft). The greater height at site H-4 might suggest that displacement on faults is uncommonly large at this place and is therefore misleading in predicting displacement at sites where the surface offset is small. However, several factors make the offset at any locality an untrustworthy indicator of fault displacement, even though the offset undoubtedly measures the minimum aggregate displacement. For example, erosion above the scarp, deposition of colluvium at the toe, and overlap by adjacent younger fan deposits are all factors that tend to reduce the surface offset and obscure the evidence of fault displacement. Thus, in the absence of detailed study at several sites along the Howe scarp, it would be groundless to assume that the offset at site H-4 is misleading evidence of locally excessive fault displacement. Displacements of similar magnitude might be found by excavating on the Howe scarp where geologic processes have reduced the surface offset. For instance, 180 m (600 ft) east of site H-4, the scarp decreases in height and disappears for a short stretch by reason of overlap by younger fan deposits, but it is unlikely that the faults which account for the scarp could similarly decreased abruptly in displacement; faults are ordinarily several

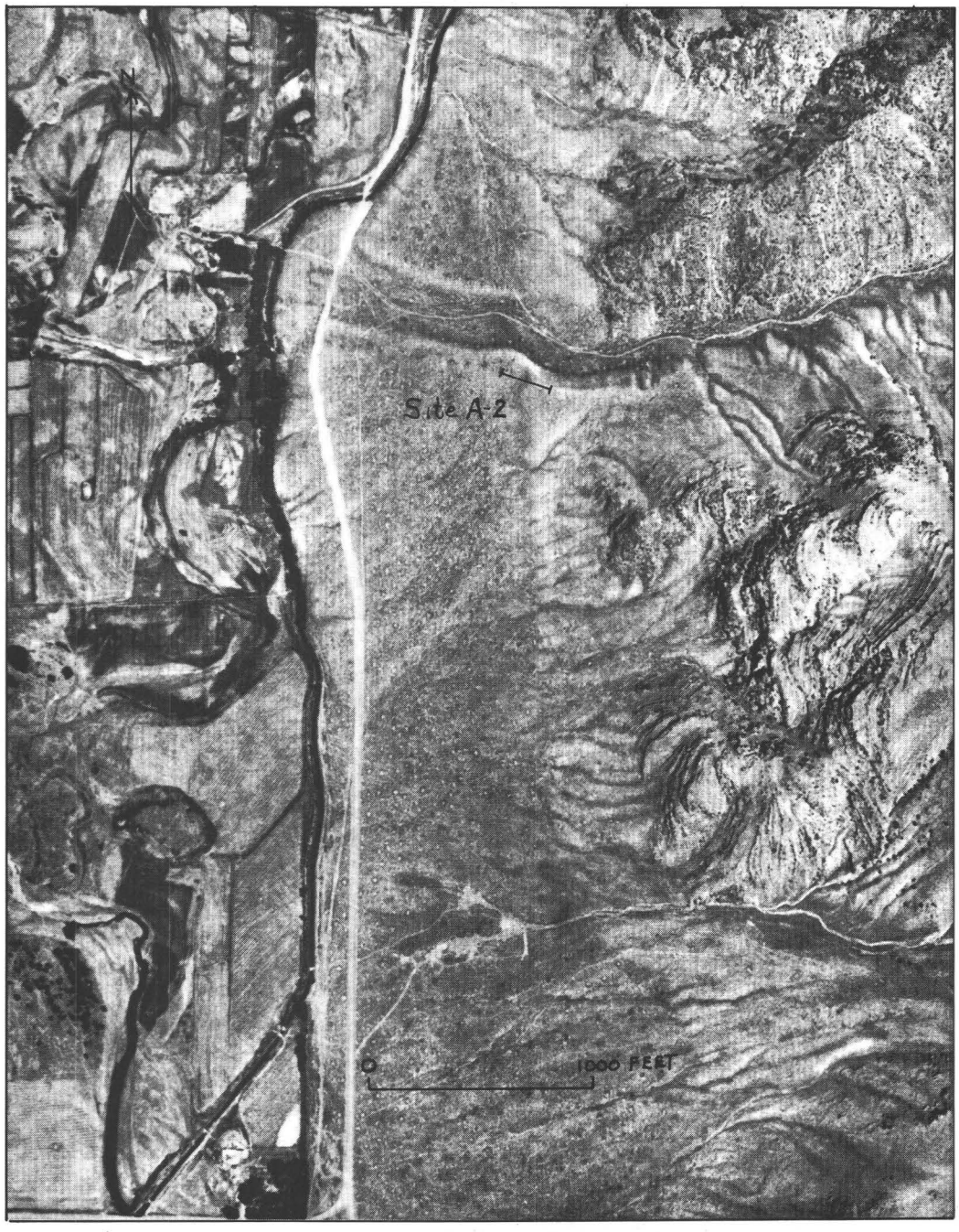

Figure 10.--Vertical view of the Howe scarp in sec. 3, T. 6 N., R. 29 E., showing the location of site H-4 in an alluvial fan. The stream debouching from Black Canyon on the left (west) has built an alluvial fan younger than the Howe scarp. (Enlarged from U.S. Department of Agriculture aerial photograph CVP-11W-47 taken August 23, 1959.)

Figure 11.--View northeast toward the Howe scarp in SE 1/4 sec. 3, T. 6 N., R. 29 E. from a distance of 2 km (1 1/4 miles). Segments of the scarp at the right and left are separated by a gap occupied by an alluvial fan younger than the scarp. Site H-4 is in the middle of the left-hand segment.

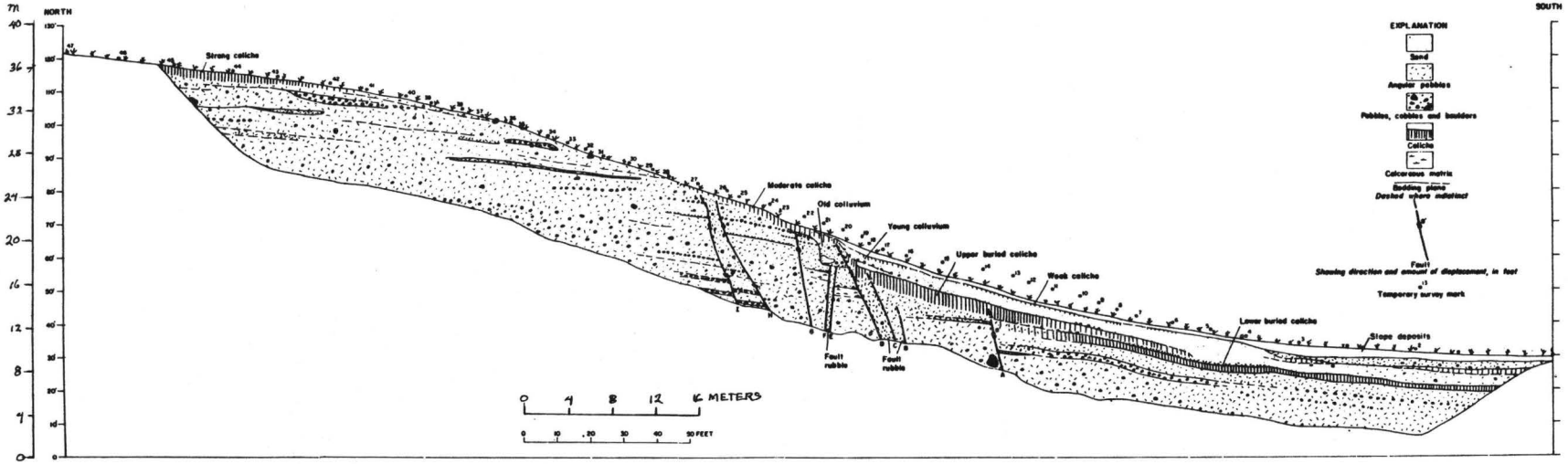

Figure 12.--Cross-section of unconsolidated fan gravel and buried caliche soils disrupted by high-angle faults exposed in a trench perpendicular to the Howe scarp at site H-4, 11 km (7 miles) north of Howe, Idaho (NW 1/4 NW 1/4 SE 1/4 sec. 3, T. 6 N., R. 29 E.).

thousand times longer than their displacement. I therefore conclude that site H-4 is likely to be as typical as any other site that could be selected for detailed study along the Howe scarp.

Geologic relations of the faults

For convenience of discussion, the fault planes recognized at site H-4 are designated by letters. Several of these faults displace coherent sequences of bedded gravel and are well-defined planes generally no wider than a single pebble in cross section. Some of the identified faults, however, are better described as zones of fault rubble--for instance, the fault zone bounded by planes E and F. At such a zone of fault rubble the initial faulting was probably by simultaneous displacement at both boundaries, thus producing the rubble, but later movement may have occurred in lesser amount anywhere within the fault zone. The straightness of the fault planes at site H-4 suggest that the dominant component of movement on these faults was vertical, but indeterminate components of strike-slip movement cannot be ruled out. Because of the complexities caused by multiple movements on the numerous faults at site H-4, the various geologic features will first be described from the toe to the head. The significance of these features in estimating aggregate displacement, times of movement, and the age of faulting is interpreted in subsequent sections.

At the toe of the scarp at site H-4 a mantle of slope deposits (pebbly sand) 0.6-1 m (2-3 ft) thick buries colluvium and eolian deposits that include remnants of a weak caliche soil, 1.2 m (4 ft) below the surface (see the units identified on fig. 12). This soil continues intermittently upslope to survey mark 19. At a depth 2.7 m (9 ft) below survey mark 3, the colluvium rests abruptly on a compact layer of strong caliche (lower buried caliche on fig. 12), which represents a soil that originally formed on the old ground surface directly on gravel of the alluvial fan. This gravel, which is a thick-bedded unit of angular pebbles and some layers of angular cobbles, has no other signs of buried soils. The gravel beds dip about 7° south. The buried caliche on the gravel is easily traceable upslope conformably to bedding. Near survey mark 6, the caliche is overlapped by another strong caliche soil of similar appearance (upper buried caliche on fig. 12), and both soils then continue together upslope. Between these soils is a thin layer of sand, pebbles, and cobbles. Below the caliche soils, at a depth of 4.3 m (14 ft) between survey marks 5 and 13, a distinctive layer of open-textured cobble gravel is partly impregnated with carbonate material that was precipitated from ground water.

The first break encountered in continuity of the fan gravel, fault A, offsets a readily identified graded bed of angular pebbles a vertical distance of 2.4 m (8 ft). In approaching fault A the lower buried caliche becomes somewhat less conspicuous, but it is nonetheless clearly bounded by the fault. The upper buried caliche continues across fault A, and the fault appears to be faintly expressed in the deposits in which the caliche has formed. Farther upslope, beginning at survey mark 15, the upper buried caliche becomes distinctly platy and forms a hardpan.

Fault B is visible at the trench floor. It places bedded gravel on the south against fault rubble, but the amount and direction of offset are indeterminate. Although fault B is clearly defined in the lower part of the trench, it does not disrupt the upper buried caliche at the top of the gravel.

Planes C and D define a fault zone 1.5 m (5 ft) wide in which tabular pebbles in the lower part are mostly arranged on edge more or less parallel to the boundaries of the zone. The dip of the fault zone, 64°, matches the dip

of the faults at Arco site A-2. Plane C, like the upper reach of fault A, is vaguely discernible in the upper buried caliche, but it does not displace the caliche. Plane D, however, clearly terminates the upslope extent of strong caliche, evidently by relative downward displacement of the block on the south. This direction of movement is indicated by a triangular wedge of the upper buried caliche immediately south of the upper part of plane D. The wedge appears to be a piece of the upper buried caliche that lodged against plane D when the block on the south moved downward. The upper reach of plane D, 0.6 m (2 ft) below the surface, also coincides with the downslope end of a moderate caliche soil. This soil is less well developed than the buried caliche soils south of the fault zone bounded by planes A and D but is nonetheless thicker, more calcareous, and more persistent than the weak caliche near the surface downslope. The terminus of the moderate caliche also coincides with a cross-cutting contact of young colluvium (pebbles and sand) on the triangular wedge of upper buried caliche at survey mark 20, and evidence for the abrupt end of the moderate caliche is ambiguous. The young colluvium at survey mark 20 thickens downslope beneath a thin mantle of slope deposits, and it locally has a weak caliche soil in its upper part.

A careful search immediately after site H-4 was excavated (June 19-22, 1969) failed to identify any bed north of plane D that matches a bed on the south. The total displacement on plane D is therefore indeterminate. Deposits adjacent to plane D on the north at survey mark 21 represent two kinds of material: bedded gravel overlain unconformably by old colluvium. Both the gravel and the old colluvium are sharply cut by plane D. Thus, one offset on plane D appears to have been more than 3 m (10 ft), which is the preserved thickness of the old colluvium. The old colluvium in turn covers the eroded upper reach of a zone of fault rubble bounded by planes E and F. This rubble zone is nearly 0.6 m (2 ft) wide, even though the vertical displacement in the zone is only 1.2 m (4 ft), as measured by the offset of a sequence of several distinctive beds. The rubble bounded by planes E and F is a zone of reverse faulting, in which the rubble zone passes above the block that moved relatively down. Hence, the exaggerated width of the rubble was perhaps caused by extension related to this reverse movement.

Fault G expresses 0.3 m (1 ft) of vertical offset, as shown by displacement of a distinctive pair of gravel layers near the top of the section, namely a graded pebble layer overlain by a layer of angular cobbles. Fault G is exceptionally well-defined and straight, being only a few centimeters (an inch or two) wide. Fault G is truncated at the top by a thin surficial layer in which the moderate caliche soil noted at plane D is formed.

Beginning close to fault G, a conspicuous bed of open-textured angular pebbles 3 m (10 ft) below survey mark 23 persists upslope beyond faults H and I. Displacement of this layer, together with one of the gravel layers above, demonstrates 1.2 m (4 ft) of vertical offset in a disrupted zone between the upper reach of faults H and I. At greater depth, gravel between these faults is preserved in a bedded sequence, and matching beds indicate 0.3 m (1 ft) of vertical offset on fault H and 0.9 m (3 ft) of offset on fault I. Fault H dips noticably less steeply than the other faults. Fault I makes a comparatively irregular trace in the trench wall, which may be a result of variable resistance to movement in adjacent gravel beds of contrasting texture. Like the other fault planes, faults H and I do not reach the present ground surface. They are recognizable, however, half a meter (1 1/2 ft) below the surface, where they are truncated by the moderate caliche.

The fan gravel upslope from fault I is exposed along the trench to the head of the Howe scarp. No other faults are visible. It is noteworthy that the fan gravel, in common with gravel elsewhere along the trench, is conspicuously silty. H. H. Waldron, during a field conference on June 18, 1969, suggested that the silt may have been carried to the site by southwesterly winds while the gravel fan was accumulating. The gravel bedding is lenticular, but several beds can be traced far enough to define a consistent southward of dip of 7°, which is virtually identical to the dip of beds south of the fault zone. Thus, movement on the faults did not differentially rotate the beds above and below the scarp.

Finally, upslope from survey mark 42, a strong caliche hardpan at the surface closely resembles the two buried caliche soils that extend downslope from planes A and D, respectively. This strong caliche conforms with the surface of the alluvial fan above the scarp but is being eroded by gradual headward retreat of the scarp.

Aggregate Displacement at Site H-4

The total vertical offset of the various faults of known displacement at site H-4 amounts to 5.2 m (17 ft): 2.4 m (8 ft) at fault A; 1.2 m (4 ft) in the zone bounded by planes E and F; 0.3 m (1 ft) at fault G; and 1.2 m (4 ft) at faults H and I. To this can be added at least 3 m (10 ft) of vertical offset on plane D, which placed the upper buried caliche against the old colluvium. A minimum measurable offset of 8.2 m (27 ft) is thereby obtained. The aggregate vertical displacement, however, cannot be less than the surface offset--14 m (45 ft)--if movement on all the scarps was relatively down toward the scarp toe. Further, the amount of surface offset should be augmented by the depth to the lower buried caliche on fan gravel at the scarp toe, and this addition yields an aggregate displacement of more than 15 m (50 ft). Finally, as at Arco site A-2, an indeterminate amount of the original fan gravel above the scarp has surely been lost by erosion, making the total offset even greater. The unknown displacement is surely represented by movement shared between planes B, C, and D.

Fault Sequence at Site H-4

The details of faulting visible in the trench at site H-4 require several times of movement to account for the arrangement of the various blocks of gravel and fault rubble. Despite an appearance of complexity, the geology provides clear evidence of relative movement between several neighboring faults and thereby establishes partial sequences of multiple displacement. The relative times of movement on other faults that are farther apart, although less certain, can be interpreted from a knowledge of geologic processes. By deciphering the partial sequences of faulting, and by considering overlap of geologic events identified in these sequences, a composite record of faulting at site H-4 can be deduced. This composite sequence, as summarized below, includes at least five times of faulting.

Three sequences of features related to faulting at site H-4 are listed in table 1. The first two sequences are derived from the exposed deposits, and the third sequence is deduced from indirect evidence. The features listed in the table are partly described in the preceeding pages, and their geologic relations are further elaborated in the discussion that follows.

Table 1.--Sequence of geologic features related to faulting at site H-4

Feature	Relation to other nearby feature
	Sequence 1
Weak caliche	Formed on young colluvium
Young colluvium	Derived from scarp at fault D
Fault plane D	Displaced upper buried caliche
Buried scarp	Truncates faults A, B, and C
Fault plane A	Displaced lower buried caliche
Lower buried caliche	Formed on fan gravel
	Sequence 2
Fault plane D	Displaced old colluvium
Old colluvium	Deposited on faults E and F
	Sequence 3
Fault planes B and C	Locally changed old colluvium to fault rubble
Old colluvium	Derived from scarps at faults G, H, and I

The relative ages of the features enumerated in the first sequence are conveniently discussed in ascending order. The lower buried caliche on fan gravel marks the surface of the alluvial fan that was cut by displacement on fault A. Sometime before, during, or after movement on fault A, displacements occurred on faults B and C. Thereafter, erosion of the elevated fan gravel north of fault A (and probably some deposition of colluvium south of fault A) formed a subdued scarp virtually identical in slope with the present Howe scarp. A stable scarp with this slope is marked by the upper buried caliche. The upper buried caliche was in turn cut by movement on plane D. Young colluvium on the upper buried caliche apparently incorporated debris partly derived from the scarp that was created by displacment on plane D. The formation of a weak caliche soil near the present surface completed this sequence.

Evidence for the second sequence is found at survey mark 21, where old colluvium that is cut by plane D rests on the truncated edge of the fault zone bounded by planes E and F.

The third sequence represents one hypothesis that explains certain relations among deposits, which are otherwise hard to understand. These relations hinge on the origin of the old colluvium and its involvement in faulting. The old colluvium consists of mixed debris of small and large sizes unconformable on the fan gravel. The only probable source for this debris was a fault scarp upslope, and the old colluvium is accordingly considered to be younger than faults G, H, and I. Relatively early movement on these faults is also suggested by a general lack of colluvial debris downslope from their scarps (except the small amount preserved as the old colluvium) and by the further absence of the scarps themselves. In short, topographic steps that were created by displacements on faults G, H, and I have been obliterated by gradual slope retreat. The other part of the third sequence concerns the geology downslope from plane D, where the old colluvium is unrecognizable. If the old colluvium had been dropped down by displacement on plane D, the colluvium would be expected to appear somewhere below the upper buried caliche--for instance, 4.6 m (15 ft) below survey mark 17. The absence of identifiable old colluvium in this part of the profile could be a consequence of movement on planes B and C. Such movement could have converted the colluvium into fault rubble, thus permitting subequent movement on plane D to place rubble against the old colluvium. If so, faults B and C are younger than the old colluvium.

These three sequences, when combined, allow some latitude in assembling a composite record of faulting. One combined sequence of faulting is suggested in table 2.

Table 2.--Suggested sequence of faulting at site H-4
(Features listed in order of increasing age)

Feature	Vertical offset of faults
Weak caliche.....	------
Young colluvium.....	------
Fault plane D.....	More than 3 m (10 ft)
Upper buried caliche.....	------
Buried scarp.....	------
Fault planes B and C.....	Not determined
Old colluvium.....	------
Fault planes G, H, and I.....	1.5 m (5 ft)
Fault planes E and F.....	1.2 m (4 ft)
Fault plane A.....	2.4 m (8 ft)
Lower buried caliche.....	------
Fan gravel.....	------

The composite sequence in table 2 is subject to several uncertainties, in addition to the unprovable premises about the origin and fate of the old colluvium. An obvious weak link is the relative age of fault A, which could be younger than faults B and C--or of any intermmediate age. However, movement on either fault B or fault C prior to movement on fault A probably would have produced colluvial debris not identifiable in the profile. By this argument, displacement on fault A appears to have been an early event. Another uncertainty is the number of movements on plane D, which is associated with a wide zone of fault rubble. Early displacement on plane D, combined with movement on plane C, may account for a considerable part of the observed scarp height at site H-4. Still another problematical aspect of the fault sequence is that several of the faults could have moved either simultaneously or individually.

Notwithstanding the uncertainties of the fault sequence at site H-4, several times of faulting are evident. The field relations suggest at least five times of movement. Together, these displacements resulted in more than 8 m (27 ft) of measurable vertical offset and a total vertical displacement of at least 15 m (50 ft), as indicated by the surface offset.

Age of Faulting

Regional relations

The alluvial fans that spread outward from mountain canyons at the foot of the Lemhi Range near Howe grade almost imperceptibly into alluvium carried by the Little Lost River. That is, the fans are comparatively young features of the landscape. Traced headward, the fans form an intricate group of deposits, which are expressed as surfaces that differ in height and degree of dissection. The topographic relief between neighboring fans is seldom more than 9 m (30 feet). From such differences, sequences of fan building can be generally deciphered in local areas. Although some active (modern) fans are in the process of covering stable (relic) fans, the spread of fan gravel toward the valley mostly has been accompanied by headward erosion, leaving parts of older fans as erosional remnants near the mountain front. It is the higher, apparently older, alluvial fans that are marked by the Howe scarp. Such fans are perched well above the principal streams at canyon mouths. The Howe scarp therefore resembles the position of the Arco scarp in the regional landscape, and other topographic aspects of alluvial fans near Howe and Arco are also similar. Probably the fans of both areas embrace approximately the same range in age.

The alluvium near Howe grades southward over basalt of the Snake River Plain at the Lost River sinks and grades in places into lake beds (Scott, 1982). Well records show that a few thin alluvial and lacustrine deposits are also interbedded with the basalt (Walker, 1964). Evidently, the fan gravel is mostly (or entirely) younger than the basalt. This basalt is part of the lava estimated to be from 15,000 to 200,000 years old, as previously explained (Kuntz and others, 1984). From these relations the Howe scarp expresses faulting in deposits probably no more than 200,000 years old.

Inferences from landforms

One of the geologically interesting aspects of the Howe scarp is its variability in height in short distances. At such places a traverse along the scarp generally shows that changes in scarp height correspond with fairly

abrupt boundaries between adjacent alluvial fans. An instructive example is the stretch of the Howe scarp that extends 0.8 km (1/2 mile) east of site H-4. From a surface offset of 14 m (45 ft) in fan gravel contiguous to Black Canyon at site H-4, the scarp abruptly diminishes to a faintly discernible trace on the surface of a neighboring fan derived from Middle Canyon.

If it were possible to determine differences in age between adjacent alluvial fans, the differences in height could be equated with differences in aggregate displacements during different lengths of time. An equation of this kind might be theoretically sound, but such an equation is still impractical because the ages of fans cut by the Howe scarp are not yet accurately known. A chronological scheme for the alluvial fans near Howe requires detailed study at various places along the mountain front, but such a study is beyond the scope of this investigation.

Nonetheless, from a traverse along the length of the Howe scarp, many examples can be found in which differences in surface offsets on adjoining fans appear to be partly a function of differences in age. The higher scarps, for instance, occur only at fans that are the older local units. Also, fans that are not broken by the Howe scarp are clearly young features of the landscape. Many of these young fans spill from canyon mouths entrenched below the high fans, such as the young fan at East Canyon (sec. 12, T. 6 N., R. 29 E.). Like the young fans near Arco, the unbroken fans probably were deposited in the last 15,000 years, and the latest faulting on the Howe scarp is correspondingly older.

Exceptionally low scarps at fans that are relatively old, however, are not hard to find. For example, the fan of Middle Canyon (sec. 2, T. 6 N., R. 29 E.), which is marked only by a faint scarp, is incised along Middle Canyon Creek by a valley 10 m (33 ft) deep and 120 m (400 ft) wide. The downcutting shows that the Middle Canyon fan is older than nearby fans that are less dissected. One inference is that the scarp in the fan of Middle Canyon is partly buried by a younger alluvial fan. Another inference is that intermittent movements expressed by differences in scarp height may have occurred throughout the length of the Howe scarp. If so, the landforms in alluvial fans near Howe reinforce the evidence of intermittent movement found at site H-4. In any case, none of the landforms visibly involved in faulting include the young alluvial fans of the last 15,000 years.

REFERENCES

Beutner, E. C., 1968, Structure and tectonics of the southern Lemhi Range, Idaho: Pennsylvania State Univ., Ph. D. Dissertation, 181 p.

Bucknam, R. C., and Anderson, R. E., 1979, Estimation of fault-scarp ages from a scarp-height-slope-angle relationship: Geology, v. 7, p. 11-14.

Crosthwaite, E. G., Thomas, C. A., and Dyer, K. L., 1970, Water resources in the Big Lost River basin, south-central Idaho: U.S. Geol. Survey Open-File Rept.

Kuntz, M. A., Skipp, Betty, Scott, W. E., and Page, W. R., 1984, Preliminary geologic map of the Idaho National Engineering Laboratory and adjoining areas, Idaho: U.S. Geol. Survey Open-File Rept. 84-281, 23 p.

Malde, H. E., 1965, The Snake River Plain, in Wright, H. E., Jr., and Frey, D. G., eds., The Quaternary of the United States: Princeton, New Jersey, Princeton Univ. Press, p. 255-263.

Malde, H. E., 1971, Geologic investigation of faulting near the National Reactor Testing Station, Idaho, with a section on microearthquake studies by A. M. Pitt and J. P. Eaton: U.S. Geol. Survey Open-File Rept., 167 p.

Pierce, K. L., 1985, Neotectonic history of the Arco segment of the Lost River fault, Idaho, in Workshop XXVIII on the Borah Peak Earthquake: U. S. Geological Survey Open-File Report, in press.

Pierce, K. L., and Scott, W. E., 1982, Pleistocene episodes of alluvial-gravel deposition, southeastern Idaho, in Bonnichsen, Bill, and Breckenridge, R. M., eds., Cenozoic geology of Idaho: Idaho Bureau of Mines and Geology Bull. 26, p. 685-702.

Scott, W. E., 1982, Surficial geologic map of the eastern Snake River Plain and adjacent areas, 111° to 115° W., Idaho and Wyoming: U.S. Geol. Survey Map I-1372.

Walker, E. H., 1964, Subsurface geology of the National Reactor Testing Station, Idaho: U.S. Geol. Survey Bull. 1133-E, p. E1-E22.

THE 1983 BORAH PEAK, IDAHO, EARTHQUAKE: REGIONAL SEISMICITY, KINEMATICS OF FAULTING, AND TECTONIC MECHANISM

By

R.B. Smith, W.D. Richins, D.I. Doser
Department of Geology & Geophysics
University of Utah
Salt Lake City, UT 84112-1183

ABSTRACT

The M_s 7.3, 1983 Borah Peak, Idaho, earthquake occurred in an extensional tectonic regime characterized by northwest-trending Late Cenozoic range-bounding normal faults. This Late Cenozoic extensional style is superimposed on northeast verging Laramide thrusting. Regional seismicity suggests that the Borah Peak earthquake occurred on the margin of an earthquake zone in east-central Idaho that may be the NW margin of a broad 'V-shaped' pattern of regional seismicity paralleling the Yellowstone-Snake River Plain volcanic track. To the west, NE-trending seismicity in central Idaho is nearly orthogonal to that of the Borah Peak sequence suggesting a distinct change in stress field. Space-time patterns of fault plane solutions for the initial 3.5 weeks of the aftershock sequence show dominant NE-SW extension on NW-trending normal faults with varying amounts of strike-slip components. Normal faulting dominates at depth, from 4 km to the depth of the main shock at 16 km. A cluster of earthquakes with E-trending nodal planes, 20 km north of the main shock, may indicate a throughgoing basement structure and perhaps the north end of the main fault break. Strain-rates from cumulative seismic moments give a 1.4 m displacement for the main shock and an additional 0.1-0.2 m slip from the 3 week aftershock sequence. A seismic reflection profile orthogonal to the aftershock sequence begins within 2 km of the fault scarp but does not show a definitive fault plane image. The profile shows that the valley is underlain by a complex zone of folds and faults but is not similar to the Basin-Range valleys to the south that have deeper unconsolidated sediments in simple asymmetric basins. Using a brittle/quasi-plastic constituitive law for a quartz rheology, the Borah Peak main shock appears to have nucleated near the maxima in shear stress. This and other evidence suggests that the earthquake nucleated on a 50° SW dipping fault near the brittle/ductile transition and on a unilateral planar rupture that propagated northward and upward to the surface. Similar geometries of main shock faulting, nucleation depth, and fault dip have been determined for the M_s 7.5, 1959 Hebgen Lake, Montana and the M 7.1, 1954 Dixie Valley, Nevada earthquakes. These and the information from the Borah Peak earthquake provide a hypothetical model that can be applied to earthquake hazard evaluation of other large normal faults.

INTRODUCTION

In the past few years there has been renewed interest in earthquakes of the intraplate western United States principally because of the occurrence of several large normal faulting events in the last 3 decades and the recognition of earthquake risks associated with major population centers. Earthquake studies have been accelerated using new techniques and data such as: 1) derivation of strain rates from the seismic moment tensor; 2) detailed earthquake studies from microearthquake and regional network studies; 3) models of geodetic data for long-term crustal deformation; and (4) the elucidation of detailed upper-crustal structure and seismic imaging of active fault zones using the seismic reflection/refraction methods. Recent studies of the M_s 7.5, 1959 Hebgen Lake, Montana, earthquake (Doser, 1984a; Doser and Smith, 1985), the M 7.1, 1954, Dixie Valley, Nevada, earthquake (Okaya and Thompson, 1985), and the M_s 7.3, 1983 Borah Peak earthquake (Richins, et. al., 1984, 1985; Doser, 1984b, 1985) have provided important insights into the processes of normal faulting. New studies of normal-fault nucleation have focused on the importance of strain rates, the influence of brittle/quasi-plastic rheologies on the nucleation process, the relationship of faulting to pre-existing structures, and the geometry and style of normal faulting (Smith and Bruhn, 1984). These studies, taken in the context of regional strain fields inferred from focal mechanisms, in situ stress and Quaternary slip-rate data further serve to quantify the driving mechanism for intraplate extension.

REGIONAL TECTONICS OF 1983 BORAH PEAK EARTHQUAKE

The October 18, 1983, M_s 7.3, m_b=6.9 (NEIS determinations) Borah Peak earthquake was located in a northward extension of the Basin-Range and in an area geologically considered to have the potential for large magnitude earthquakes because of the occurrence of extensional late Quaternary faulting (Figure 1). It was not preceded by detectable foreshock activity (Richins et al., 1985; Dewey, 1985) nor was it associated with regional seismic trends that might be expected to coincide with the large Quaternary faults on the southwest flank of the Lost River Range (Figure 1).

A regional tectonic map (Figure 1) compiled for the central Idaho region depicts the distribution of Laramide thrust structures, Quaternary normal faults, the Challis volcanics, and the Snake River Plain volcanics. These features are thought to be the principal structures that relate to earthquake nucleation in this area. Of particular importance is the distribution of large northwest-trending normal fault zones that extend up to 160 km in length from the edge of the Snake River Plain northwestward to the Challis area. These tectonic features have all combined to deform and attenuate the lithosphere and together influence the earthquake potential of the region.

Little detailed data on the crustal structure in the vicinity of Borah Peak is available. Inferences on total crustal thickness by Smith (1978) suggest plausible thicknesses of 40-45 km, whereas Sheriff and Stickney (1984) infer a 32 km-thick crust. Modeling of regional travel-times by Richins et. al. (1984, 1985) and regional refraction/gravity profiling by Braile et. al. (1982), and Sparling et. al. (1982) are consistent with a 35-45 km crust necessary to match the observed P-wave travel times. These models suggest

that the crustal structure of the Borah Peak earthquake may be transitional between that of the tectonically active Basin-Range crust, 25-30 km thick, and that of the stable Rocky Mountains, 40-45 km thick.

Of related importance to earthquake nucleation in the central Idaho area is the possible influence of Laramide crustal structures on normal faulting, i.e., thrust faulting and folding and its influence on localization of later extensional faults. Skipp and Hait (1977), Mohl and Artzis (1984) and Skipp (1985) suggest a complex zone of northeast-directed, low- to moderate-angle dipping thrusts underlain by a regional detachment. Whether the thrusts have been reactivated to form low-angle normal faults is an important question. Some of the normal faults occur in close spatial association with the pre-existing thrusts and suggest a causative relation (Figure 1).

Although not completely documented, the major Quaternary normal faults of the Lost River Range appear to be segmented into discrete zones of continuous displacement (Scott et. al., 1985). The segments appear are bounded by lateral terminations such as pre-existing transverse structures, termination of thrust planes, and variations in topography. On the basis of these features and the shape and size of the surface break of the Borah Peak earthquake, the Lost River fault may have four major segments: 1) from Arco to Mackay, 2) from Mackay to the south end of the 1983 Borah Peak earthquake epicenter, 3) the segment that broke during the 1983 Borah Peak earthquake, and 4) the northwest segment from the 1983 Break to Challis.

An examination of the Bouguer gravity map of Idaho (Bankey and Kleinkopf, 1984) shows large anomalies associated with the alluvial filled valleys of east-central Idaho. In particular they show a notable increase in magnitude from the Lost River Range northeast toward the Beaverhead Mountains. This increase suggests a significant deepening of the valleys resulting from greater Late Cenozoic displacement in a northeasterly direction i.e. in the same direction as the propagation of the Snake River Plain silicic volcanics. This trend may represent a tectonic response to the passage of the Yellowstone hotspot. The range-front valleys farther north may be likely sites of future large earthquakes.

Seismicity

Regional Seismicity--The general pattern of historic earthquakes throughout the central Idaho-central Intermountain seismic belt is shown in Figure 2 (a compilation of the USGS-NEIS, University of Utah, and NOAA data for earthquakes from about 1932 through 1981). Also plotted is the location and extent of the Yellowstone-Snake River Plain silicic volcanic province.

The principal occurrence of earthquakes along the central part of the Intermountain seismic belt extends from the northern Wasatch Front, northeasterly through southwestern Idaho, western Wyoming and terminates in the area of intense activity at the Yellowstone Plateau. During historic time, two M7+ and eight M6+ earthquakes have occurred in this region (Figure 2) and demonstrate that it is indeed an area of importance with respect to earthquake risk.

A notable 'V-shaped' pattern of epicenters (Figure 2) paralleling the boundaries of the NE-trending track of the Yellowstone-Snake River Plain volcanic province suggest a causal relationship. Conceivably the earthquakes along the central part of the Intermountain seismic belt and the central Idaho zone may occur in a trailing "wave" following the passage of the lithospheric Yellowstone hot spot to its currently active location beneath the Yellowstone caldera.

Microearthquake Seismicity--Central Idaho has long been known for its broad distribution of earthquakes and earthquake swarms across a region extending from Stanley Basin to Challis. In Figure 3 epicenters from several detailed microearthquake surveys, including field recording of the 1983 Borah Peak sequence have been plotted. The University of Utah carried out a series of four microearthquake surveys in central Idaho during the summers of 1972, 1976, 1977, and 1978. These investigations focused on the possible relationship between pronounced swarm activity and extensive hot springs. These surveys operated 6 to 12 portable seismographs with station spacings ranging from 10 to 20 km.

Several notable clusters of earthquakes were mapped in these studies (Figure 3): 1) a diffuse but extensive zone of activity extending east from Stanley Basin ; 2) dense clusters of activity west of Challis that trend east to northeast; and 3) a restricted zone of microearthquake activity 40 km north of Challis.

Recent studies by Fisher et. al. (1983) define the boundary of a caldera complex associated with the Challis volcanics that generally coincides with the seismicity west of Challis. The east- to northeast-trend of epicenters suggests a possible association of caldera boundary faults similar to that of the Yellowstone caldera.

The 1983 Borah Peak sequence shows a northwest trend extending from Mackey to Challis, nearly orthogonal to the trend of the seismicity pattern associated with the Twin Peaks caldera. This rapid change in trend of seismicity may be related to a change in tectonic trend.

August 22-September 30, 1984 sequence--Following an aftershock of M_L 5.8 south of Challis on 22 August, 1984, the University of Utah deployed portable seismograph stations in conjunction with the Idaho National Engineering Laboratory and the U.S. Geological Survey-Denver. Instruments were deployed at approximate 5 km spacings across the valley and in adjacent ranges. In this survey, a cluster of activity was mapped that extended from the area of intense aftershocks west of the north end of the 1983 Borah Peak fault northward 20 km (Figure 3). This aftershock sequence is notable because it is near the northwest segment of the Lost River fault zone that might be expected to break adjacent to the Borah Peak segment. The occurrence of the M_L 5.8 event and its several M4+ aftershocks are considered important in analyzing the possibility of triggering of this northerly segment.

The NW-trending Borah Peak earthquake sequence appears to trend orthogonal to the earthquakes of the central Idaho (Figure 3) or it may be continuous with the zone that extends from the activity west of Challis SE for more than

200 km. Nonetheless the pattern of detailed microearthquakes and aftershocks shows swarm-like activity in the vicinity of the central Idaho hot springs district and a linear zone of activity along the range-bounding faults of the Lost River Range. Whether the linear trends of the Lost River seismicity reflect a major lithospheric discontinuity or simple block tectonic readjustment from pre-existing structures is not known.

Fault Plane Solutions

Regional Pattern--The distribution of fault plane solutions for the central Intermountain seismic belt and central Idaho are shown on Figure 4 (data taken principally from a compilation by Smith and Lindh, 1978). The importance of the fault plane solutions, on a regional scale, is the predominance of normal-faulting mechanisms generally on moderate-dipping nodal planes. In central Idaho, north to northeast directed T-axes characterize the regional trend. The general conclusion from Figure 4 is that a distinct 90° rotation of T-axes from east-west in southern Utah to north-south at Yellowstone, occurs over a distance of approximately 200 km implying a distinct change in the stress field. The central Idaho region is intermediate with north- to northeast-trending T-axes.

In general, the east-west T-axes in northern Utah are orthogonal to the main Quaternary fault scarps as expected. The north-south trending T-axes in the Hebgen Lake region are also orthogonal to the main Quaternary faulting indicating primary north-south extension, but they are parallel to the Madison fault, a major north-south normal fault zone. The north-northeast trending axes reflect a transitional pattern in central Idaho suggesting principal motion on northwest-trending normal faults even as far west as the central Idaho.

1983, Borah Peak Earthquake Sequence--The fault plane solution for the main shock of the Borah Peak sequence (Doser, 1985) shows normal faulting along a moderate, 50° SW dipping nodal plane. A compilation of 39 fault plane solutions was made for the three-week aftershock period for events that were well recorded across the region, particularly on the University of Utah network. These solutions were from events that generally had magnitudes greater than 3.5 and are thought to be representative of the principal strain release. However, several magnitude 4+ earthquakes in the initial 4-6 hour period are not included because they were within the coda's of continuous aftershocks and their phases are not discernible. Details of individual fault plane solutions are not given here because of space limitations. They will be included in appendices of a future publication.

During the initial 24 hours following the main shock (Figures 5 and 6), predominant normal faulting with northwest-trending nodal planes extended along the main portion of the aftershock zone. As noted by Richins et. al. (1985) the entire fault plane associated with surface displacement apparently fractured during the main shock with predominant dip-slip release during the first several hours.

Approximately 12 hours following the main shock, a normal fault mechanism with east-west trending nodal planes occurred near the Willow Creek Summit

marking a change in the pattern of NE extension. The second 24-hour period of activity showed a complexity of mechanisms, including events with strike-slip components in the northern Thousand Springs Valley and a variety of normal faulting earthquakes south of the Willow Creek Summit with nodal planes ranging from north-south to northwest to east-west.

Detailed mapping of the Thousand Springs Valley and adjacent Lost River Range by Skipp (1985) has revealed an east-west trending basement fault that transects the Lost River fault near the cluster of east-west trending normal fault solutions at the south end of the surface faulting (clustered around solution #18, Figure 5). This basement structure may represent a boundary or asperity, as most aftershocks were restricted to the north of this fault and the normal faulting inferred from the fault plane solution could reflect subsidiary motion on the main fault. The 20 km gap between the aftershock, #18, and the main shock thus may represent the main break that continued north to produce the main fault scarp.

The long-term southeast to northwest progression of M4.5+ earthquakes (Richins et al., 1985) supports the concept for a progressive strain release following the main shock. A preliminary fault plane solution (Zollweg and Richins, 1985) for the August 22, 1984 aftershock shows a normal fault with northwest trending nodal planes that dips at moderate angles parallel to the trend of the Lost River fault. The data are insufficient to define whether the aftershocks occurred along the northwest segment of the Lost River fault or along subsidiary sub-basin faults. These aftershocks occur 10-15 km north of the main Borah Peak aftershock area and suggests the continuation of the aftershock zone northward.

A plot of the fault plane solutions from Figure 5 with depth (Figure 6) does not show a major change in nodal-plane attitudes between the surface and 10 km. However spatial clustering near the south end of the aftershock zone, for events at depths greater than 10 km, marks an inferred termination with substantial normal-fault strain release. This observation emphasizes the implication for normal faulting along a moderate-dipping planar fault zone.

To depict the space-time distribution of fault mechanisms, a plot of fault plane solutions for the three week period of the main shock and its aftershocks is shown in Figure 7. Focal mechanism sizes are scaled to magnitude. Figure 7 shows the dominance of NE- to N-directed crustal extension associated with the predominant normal fault mechanisms, particularly in the first 72-hours of the aftershock sequence. A notable quiescence from 31 October to 1 November, days 3 to 5, was followed by predominant N- to NE-directed crustal extension associated with smaller aftershocks.

Complexities in the rupture pattern are depicted by the appearance of several events with strike-slip components particularly in the knot of seismicity south and west of the Willow Creek Summit. Here several of the larger aftershocks, M4+, show distinct components of lateral slip mixed with north-south normal faulting.

The general space-time distribution (Figure 7) of earthquakes thus depicts a northwest-trending, southwest dipping focal zone associated with the

main shock and the M4+ aftershocks. The predominant energy release of the Borah Peak earthquake and its aftershocks is that of northeast crustal extension. However there is a notable absence of earthquakes in the area of maximum surface fault displacement and at the ends of the surface fault, as well as any surface faulting near the main shock.

A hypothetical model for the nucleation process might be one in which the main shock initially ruptured upward and northwest, breaking the surface only to the north. The splay of surface faulting to the northwest of Willow Creek Summit resulting as a consequence of the NW fault propagation. This pattern has the same appearance as that of the M7.5, 1959 Hebgen Lake earthquake (Doser, 1984) where the main shock occurred at the east end of the main zone of surface rupture and a similarly shaped splay extended westward from the main fault.

Cumulative Displacements From Seismic Moments

The cumulative fault plane displacements of the main shock and first three and a half weeks of aftershocks of the Borah Peak earthquake sequence were computed by summing the seismic moments by the method described by Doser and Smith (1982). For these calculations, seismic moments were determined for the M_s 7.3 main shock and about 400 aftershocks, $2.0<M_L<5.8$, including three events of $5.0<M_L<5.8$ that occurred within 48 hours of the main shock. The magnitudes were converted to seismic moment by the relationship, $\log M_o = 1.1 M_L + 18.4$, that was derived for normal faulting earthquakes in Utah by Doser and Smith (1982). The 80 km-long Borah Peak aftershock zone, was subdivided into eight volumes (Figure 8): 10 km-long (parallel to the NW aftershock trend), 10 km-wide (the width of the aftershock zone), and 15 km-deep, the maximum depth of aftershocks. The main shock, with a focal depth of 16 km (Doser, 1984b, 1985) was included.

The seismic moments were then summed for each volume for the period 28 October to 20 November, 1983. Fault plane solutions for the larger events (Figure 7) were used to constrain the directions of the moment tensor that was diagonalized to give the principal axes of the moment rate tensor similar to the method. Moment rates were converted to volumetric strain rates that were then converted to the vertical and horizontal displacements for each volume (Figure 8).

Figure 8 shows a plot of the vertical and horizontal components calculated from the seismic moments and the surface fault displacement that accompanied the Borah Peak main shock. Note that the surface fault displacement was primarily normal slip with a 17% left-lateral component and occurred on a near-vertical fault in unconsolidated sediments (Crone and Machette, 1984). For the three-week aftershock period, the seismic strain release produced nearly equal components of vertical and horizontal displacement commensurate with the 50° SW dip inferred from the main shock fault plane solution (Figure 5).

Using the moment tensor calculation, the main shock produced about 1 m of vertical and horizontal slip respectively (Figure 8), but no surface displacement occurred within 10 km of the epicenter. The aftershocks contributed a

much smaller displacement, up to 3 cm, on the subsurface portion of the fault zone (Figure 8). Note that while the method to calculate the displacement from the moment tensor placed all of the main shock displacement along the 10 km segment containing the main shock hypocenter, the 1 m displacement should probably be distributed northwest along the aftershock zone. This effect has not yet been modeled.

In Figure 8 the directions of the cumulative horizontal displacements from the moment tensor calculations (in each volume) are shown by the directions of the arrows (oriented to north vertically on the figure). These data show that the Borah Peak earthquake was primarily associated with nearly equal, 1 m horizontal and vertical, displacements associated with northeast-southwest crustal extension along the moderately southwest-dipping normal fault. The nearly equal horizontal and vertical components of afterslip are also commensurate with the main shock crustal deformation. Taken together, the main shock and aftershock slip totals 1.5 m, with 1.4 m associated with the main shock. The main shock displacement compares with 1.56 m vertical offset the surface fault measured across the fault from releveling by Stein and Barrientos (1984), but is less than the mean 2.2 m net fault slip modeled from the complete leveling set. This suggests that the seismically derived moment, $M_o^S = 2.9 \times 10^{26}$ dyne-cm, should be less than that derived geodetically of $M_o^G = 3.2 \times 10^{26}$ dyne-cm from Stein and Barrientos (1984). The 1.5 m total slip compares to 2.7 m of fault displacement (maximum) measured on the surface scarp (Crone and Machette, 1984), where the surface displacement is amplified because of compaction, dewatering of sediments, etc. The displacement suggests a dip-slip, finite strain release of 5.2×10^{-5} associated with the 21 km-wide fault.

The sum of the scaler moments was 2.86×10^{26} dyne-cm for the main shock and all aftershocks of $M>2.0$ for the first 3.5 weeks. Subtracting the main shock moment gave 1.72×10^{25} dyne-cm. Thus the aftershocks contributed only 6% to the total seismic moment.

Seismic Reflection Profile, Thousand Springs Valley (Plate A)

The central Idaho region has been the focus of renewed oil exploration because of the potential of hydrocarbon deposits associated with the NW extension of the Cordilleran overthrust belt. Industry proprietary data summarized by Mohl and Artzis (1984; unpublished report) have discussed the general geology of the Thousand Springs area including the interpretation of a Vibroseis reflection profile that was recorded in 1982 across the Thousand Springs Valley, from near the southern end of the 1982 surface rupture. The reflection profile produced data to about 9 km depth. (See Plate A)

The reflection profile shows complex intrabasin structure with a thin alluvial cover underlain by complexly folded and faulted Paleozoic sediments. The northeast end of the profile was approximately 2 km from the southwest exposure of the recent 1983 Borah Peak surface faulting. While there is no notable fault plane reflection, northeast stratal tilt of shallow Quaternary sediments suggests the presence of a fault that has accommodated Quaternary deformation. Complexities that may also be interpreted include both southwest

Plate A

VIBROSEIS REFLECTION PROFILE OF SOUTHERN THOUSAND SPRINGS VALLEY, IDAHO, COURTESY OF NANCE PETROLEUM CO.

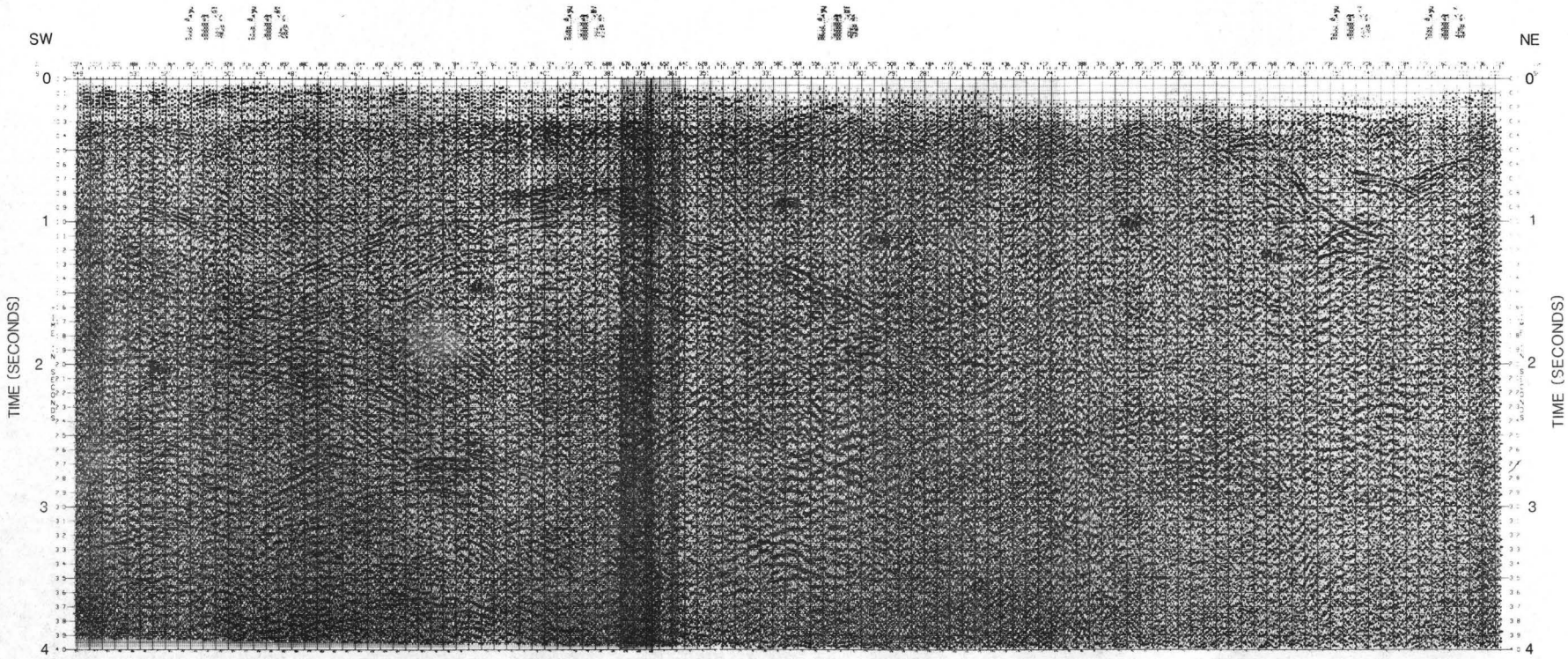

Profile from the vicinity of Elkhorn Creek 25 km southwest parallel to Big Lost River to Trail Creek Road, VP: 134m Group Interval: 67m

dipping normal faulting and NW trending thrust faulting. The reflection data suggests that the structure of the basin is more complex than generally seen on the seismic profiles of the eastern Basin-Range (Smith and Bruhn, 1984) where stratal tilts of Tertiary sediments are generally uninterrupted by large interbasin faults.

Mohl and Artzis (1984, unpublished report) interpret a basal detachment at approximately 3 km that underlies the entire Thousand Springs Valley and accommodates much of the crustal shortening. A plot of hypocenters, projected along the reflection profile suggests a through-going approximately 45-50° zone of earthquakes that extends through the Paleozoic sediments and through the interpreted detachment, well into the crystalline Precambrian basement and intermediate crust.

Borah Peak Fault Kinematics

The Borah Peak earthquake and its aftershock sequence have been monitored by a dense network of portable seismograph stations (Richins et. al., 1984, 1985) that allowed the determination of hypocenters with a precision of 1 km or less. Figure 9 shows a generalized cross-section across the Lost River fault zone where hypocenters within 10 km of a northeast profile across the southern end of the aftershock zone and the main shock have been plotted. Also shown is a vertical cross section of the fault plane solution of the main shock (Doser, 1984b) at its calculated focal depth of 16 km $\pm$ 4 km. The aftershocks show a distinct 50° southwest dipping zone with aftershocks beginning at 4 km depth and extending to approximately 12 km in depth. The aftershock zone may be 2-4 km wide, but it's geometry, consideration of possible hypocenter errors, suggests a finite-width, planar fault zone. Note the correspondence of the projection of the westward dipping nodal plane of the main shock through the aftershocks to the Lost River fault scarp at the surface.

The hypothetical shear-stress distribution with depth, calculated as a function of brittle and quasi-plastic rheologies, has been considered important in normal-faulting nucleation (Sibson, 1982; Smith and Bruhn, 1984). These studies show that for extensional stress regimes the maximum shear stress resistance occurs at the transition between brittle and quasi-plastic creep, a depth that corresponds to the approximate 80-percentile of background and aftershock seismicity (Sibson, 1982; Smith and Bruhn, 1984). We further hypothesize that large-moment earthquakes occur near the depth of the peak shear stress resistance or slightly deeper in a zone where the shear stress is changing at its greatest rate.

For the Borah Peak model (Figure 9) a shear-stress versus depth curve for a quartz rheology is plotted for a strain rate of 10^{-14} s^{-1} and a regional heat flow of 90 mWm^{-2}. It is clear from this figure that about 90% of the plotted aftershocks in the cross section occurred above the modeled shear stress maximum and that the main shock nucleated in a region of the hypothesized transition from brittle to plastic flow. Note that the rheological model is based upon a hypothetical calculation and could be in error by $\pm$5 km.

In a recent examination of large extensional-type earthquakes of the

western U.S. (Figure 10), Smith and Richins (1984) noted that the M_s 7.5, 1959 Hebgen Lake, Montana; M_s 7.3, 1983 Borah Peak, Idaho; and the M7.1, 1954 Dixie Valley, Nevada, earthquakes nucleated at midcrustal depths of approximately 15 km along normal faults dipping 40° to 65°. In these cases the principal distribution of aftershocks and later seismicity occurred above the depth of main shock nucleation (Figure 10). If the geometries for these large extensional earthquakes can be generalized to other areas of normal faulting, such as the Wasatch Front, they can provide a conceptual model within which seismic earthquake risk can be considered.

Regional Tectonic Mechanisms

The mechanism for regional extension of the central Idaho region is best considered by integrating other geological and geophysical information. An important problem regarding the three large range-front faults in east-central Idaho (Figure 1) is the possible association of the normal faults with pre-existing, large scale overthrusts. Also, the passage, at about 8 million years ago, of the Yellowstone hot spot on the Snake River Plain on a track to the northeast may also have influenced the thermal and hence the mechanical structure of the lithosphere of this region. To examine the latter idea, the regional seismicity (Figure 2) can be viewed as a map of the regional strain-release field associated with passage of an instantaneous thermal event. In Figure 2 the epicenters from the central ISB, appear as the trailing edges of a lithospheric disturbance pointed in the direction of the now active Yellowstone hot spot. In unpublished calculations by R. B. Smith and L. W. Braile radially averaged topographic profiles for the Yellowstone region show a large lithospheric bulge, approximately 400 km in diameter, centered on the Yellowstone Plateau, well beyond the 100 km uplift of the Yellowstone caldera. This suggests that the Yellowstone hot spot has had a more profound effect on the lithosphere producing 300-400 wide thermal tumescence followed by thermal contraction.

Digital, colored topographic maps (not reproduced here) of the eastern Snake River Plain-Yellowstone system show a distinct increase in elevation from the Boise area (from 1.25 km) northeastward along the track of the hot spot to its present location at Yellowstone (2.5 km). Numerical fitting of topography along the Snake River Plain suggests a dependence on age, $z = 3.07 - 0.52 \sqrt{t}$; where t is equal to the age in millions of years since inception of silicic volcanism. This systematic decrease of topography with increasing age fits a systematic model for a continuous crustal volume increase following an instantaneous passage of thermal transient similar to that modeled by Brott et al. (1981). The implied 300-400 width of the current Yellowstone lithospheric anomaly, when traced backward along the Snake River Plain, extends to distances of 50-100 km northwest and northeast of the geologic boundary of the Snake River Plain (Figure 2). Rather interestingly this distance corresponds to the general boundary of seismicity in the Borah Peak region.

Further elaboration of this concept is seen by plotting the terminations of ages/trends of normal faulting of the Snake River Plain region (Figure 11). In this depiction normal faults with Holocene displacement are located 50-100 km beyond the mapped Snake River Plain boundary. Perhaps cooling and concomitant subsidence of the pre-existing Basin-Range structures has released stored

strain energy and developed a more brittle lithosphere. Nonetheless, it is clear that there is a spatial correlation between the boundaries of seismicity, the location of Holocene faulting, the development (in the case of the three large range front valleys in east-central Idaho) of a distinct bifurcation in regional drainage patterns, and a topographic anomaly--all along a boundary near the epicenter of the 1983, Borah Peak earthquake (Figures 2 and 11).

Modeling by Furlong (1979) and Brott et. al. (1981) suggest thermal-mechanical models in which the passage of a lithospheric fracture or a hot spot, respectively, significantly distorts the regional stress field. Brott et al. (1981) model the decrease in topography following thermal tumescence and the inferred stress re-orientations are consistent with a broad lithospheric subsidence extending 100 km or more beyond the Snake River Plain volcanics. While these models are hypothetical they imply that variable lithospheric stress fields may have a more important influence on the potential of large earthquakes than heretofore considered.

Lessons and Implications From the 1983 Borah Peak Earthquake

Our investigations of the Borah Peak earthquake, in conjunction with studies of similar large normal faulting earthquakes in the western U.S., provide new information relevant to earthquake hazard evaluation in the Basin-Range. Important paradigms and new questions are evident from these results and include:

1) In the past thirty years, the three largest earthquakes in the western U.S. have occurred in an extensional environment on moderate dipping normal faults at mid-crustal depths (M 7.1, 1954, Fairview Peak, Nevada; M_s7.5, 1959 Hebgen Lake, Montana; M_s7.3, 1983, Borah Peak, Idaho). What are the earthquake hazard implications for large-earthquake occurrence on 45°-60° dipping normal faults that nucleate at depths of 15 km? Can their location and stress state be mapped prior to large event?

2) The Quaternary history of the Lost River fault is similar to that of the Wasatch fault. For example, detailed mapping and trenching suggest that the Wasatch fault can be subdivided into independent segments several of which have ruptured in Holocene time (Schwartz and Coppersmith, 1984; Smith and Bruhn, 1984). For the Lost River fault zone, several segments seem apparent. The segment that ruptured in the 1983 Borah Peak earthquake has broken at least once during Holocene time (Hait, 1978), while the adjacent segments appeared to be active in Quaternary time (Scott et al., 1985). Perhaps individual segments may be active for a discrete period, say thousands to tens of thousands of years, while adjacent segments remain seismically inactive. If this is a reasonable model, Will the "likely" locations of future large earthquake be associated with segments of large normal faults with demonstrated Holocene displacement? Will adjacent segments remain quiescent, thus reducing their risk?

3) Should a fault with evidence of Late Pleistocene slip adjacent to a segment with Holocene slip segment be considered a seismic "gap", i.e., Will the gaps "fill-in" and hence should they be considered the "likely" locations of future large earthquakes?

4) Doser (1984a) noted a spatial correlation between the location of the Hebgen Lake and Red Canyon normal faults and nearby Laramide thrusts for the 1959 Hebgen Lake earthquake. Thus, an important question to be answered is, Has Basin-Range type extension been accommodated or partly controlled by pre-existing zones of weakness inherited from Laramide structures? To date, data are insufficient to conclude this as a working model, but the spatial correlation of normal faulting and regional thrusts suggest a need for further investigation.

Acknowledgments

We gratefully thank our colleagues at the University of Utah Seismograph Stations for their help and efforts during the arduous work following the Borah Peak earthquake: J. Pechmann, G. J. Chen, L. L. Leu, H. M. Benz, T. J. Owens, W. J. Arabasz, J. Peinado, J. Saffer, K. Wooten, and D. J. Williams. P. K. Eddington was particularly helpful in the seismic moment calculations. We also thank our colleagues C. Langer and R. S. Stein from the U.S. Geological Survey who helped in the field work and provided ancillary data, and our colleagues: J. Zollweg, the University of Washington; M. Stickney, the Montana Bureau of Mines and Geology; S. Jackson, INEL; J. Pelton, Boise State University; and J. P. Bailey, Nance Petroleum. W. J. Arabasz and R. S. Stein provided critical reviews of the manuscript. This work was supported by the U.S. Geological Survey Grant Nos. 14-08-0001-21856 and 14-08-0001-21857, and by the National Science Foundation Grant No. EAR-8400470.

References

Bankey, V. L., and M. D. Kleinkopf, 1984. Idaho--A new Bouguer gravity and derivative map using Fourier analysis: EOS, Trans. Amer. Geophys. Union, 65, 1084.

Brott, C. A., D. D. Blackwell, and J. P. Ziagos, 1981. Thermal and tectonic implications of heat flow in the eastern Snake River Plain, Idaho, Jour. Geophys. Res., 86, 11,209-11,734.

Braile, L. W., R. B. Smith, J. Ansorge, M. R. Baker, M. A. Sparlin, C. Prodehl, M. M. Schilly, J. H. Healy, St. Mueller, and K. H. Olsen, 1982, The Yellowstone-Snake River Plain seismic profiling experiment: Crustal structure of the eastern Snake River Plain, J. Geophys. Res., 87, 2597-2609.

Crone, A. J., and M. N. Machette, 1984, Surface faulting accompanying the Borah Peak earthquake, central Idaho, Geology, 12, 664-667.

Dewey, J. W., 1985, A reanalysis of the instrumental seismicity of central Idaho on the basis of locally-recorded aftershocks to the 1983 Borah Peak earthquake, in Workshop XXVIII on the Borah Peak Earthquake: U.S. Geological Survey Open-File Report, (this volume).

Doser, D. I., 1984a, Source parameters and faulting processes of the August 1959 Hebgen Lake, Montana earthquake sequence, Ph.D Thesis, University of Utah, Salt Lake City, 152 p.

Doser, D. I., 1984b, The 1959 Hebgen Lake, MT and the 1983 Borah Peak, ID earthquakes: Examples of large normal events in the Intermountain Region, Earthquake Notes, 55, 14.

Doser, D. I., 1985, The 1983 Borah Peak, Idaho and 1959 Hebgen Lake, Montana Earthquakes: Models for normal fault earthquakes in the Intermountain seismic belt, in Workshop XXVIII on the Borah Peak Earthquake: U.S. Geological Survey Open-File Report, (this volume)

Doser, D. I., and R. B. Smith, 1982, Seismic moment rates in the Utah region, Bull. Seism. Soc. Am., 72, 525-551.

Doser, D. I., and R. B. Smith, 1985, Source parameters of the October 18, 1983, Borah Peak, Idaho earthquake from body wave analysis, J. Geophys. Res., in press.

Fisher, F. S., D. H. McIntyre and R. M. Johnson, 1983, Geologic map of the Challis 1° x 2° quadrangle, Idaho: Geol. Survey Open File Report 83-523.

Furlong, K. P., 1979, An analytic stress model applied to the Snake River Plain (Northern Basin and Range province, U.S.A.), Tectonophysics, 58, T11-T15.

Hait, M. H., Jr., 1978, Holocene faulting Lost River Range, Idaho, Program, Rocky Mtn. Section, Geol. Soc. America, Ann Meeting, p. 217.

Mapel, W. J., W. H. Read, and R. K. Smith, 1965, Geologic map and sections of the Doublesprings Quadrangle, Custer and Lemhi Counties, Idaho; USGS Map Investigations Series.

Mohl, K. L., and A. Artzis, 1984, Thousand Springs Project, unpublished report, Nance Petroleum, Billings, Montana.

Okaya, D. A., and G. Thompson, 1985, Geometry of Cenozoic extensional faulting; Dixie Valley, Nevada, Tectonics, (in press).

Richins,W. D., R. B. Smith, J. J. King, C. J. Langer, C. W. Meissner, J. C. Pechmann, W. J. Arabasz, J. E. Zollweg, 1984, The 1983 Borah Peak, Idaho, earthquake: A progress report on the relationship of aftershocks to the main shock, surface faulting, and regional tectonics, Earthquake Notes, 55, 29.

Richins, W. D., R. B. Smith, C. J. Langer, J. E. Zollweg, J. J. King, and J. C. Pechmann, 1985, The 1983 Borah Peak, Idaho, Earthquake: Relationship of aftershocks to the main shock, surface faulting, and regional tectonics, in Workshop XXVIII on the Borah Peak Earthquake: U.S. Geological Survey Open-File Report, (this volume).

Rupel, E. T., 1982, Cenozoic block uplifts in east-central Idaho and northwest Montana, Geol. Surv. Prof. Paper 1224.

Schwartz, D. P., and K. J. Coppersmith, 1984, Fault behavior and characteristic earthquakes: examples from the Wasatch and San Andreas fault zone, J. Geophys. Res., 89, 5681-5698.

Scott, W. E., 1982, Surficial geologic map of the eastern Snake River Plain and adjacent areas, 111° to 115°W, Idaho and Wyoming Geological Survey, Map I-1372.

Scott, W. E., K. L. Pierce and M. H. Hait, Jr., 1985, Quaternary tectonic setting of the 1983 Borah Peak earthquake, Central Idaho, in Workshop XXVIII on the Borah Peak Earthquakes: i U.S. Geological Survey Open-File Report, (this volume).

Sheriff, S. D., and M. C. Stickney, 1984, Crustal structure of southwestern Montana and east-central Idaho: Results of a reversed seismic refraction line, Geophys. Res. Letters, 11, 299-302.

Sibson, R. H., 1982, Fault zone models, heat flow, and the depth distribution of earthquakes in the continental crust of the United States, Bull. Seism. Soc. Am., 72, 151-164.

Skipp, B., 1985, Structure and stratigraphy of the area of the 1983 Borah Peak, Idaho, earthquake, in Workshop XXVIII on the Borah Peak Earthquake: U.S. Geological Survey Open-File Report, (this volume).

Skipp, B., and M. H. Hait, Jr., 1977, Allochthons along the northeast margin of the Snake River Plain, Idaho, 29th Ann. Field Conf., Wyoming, Geol. Assoc., 499-515.

Smith, R. B., 1978, Seismicity, crustal structure, and intraplate tectonics of the interior of the Western Cordillera, Geol. Soc. Am., Memoir 152, R. B. Smith and G. Eaton, editors, 111-144.

Smith, R. B. and Sbar, 1974, Contemporary tectonics and seismicity of the western United States with emphasis on the Intermountain seismic belt, Bull. Seism. Soc. Am., 85, 1205-1218.

Smith, R. B., and A. Lindh, 1978, A compilation of fault plane solutions of the Western United States, in Cenozoic Tectonics and Regional Geophysics of the Western Cordillera, editors, R. B. Smith and G. P. Eaton, Geol. Soc. America Memoir 152, 107-110.

Smith, R. B., and R. L. Bruhn, 1984, Intraplate extensional tectonics of the western U.S. Cordillera: Inferences on structural style from seismic reflection data, regional tectonics, and thermal-mechanical models of brittle-ductile deformation, J. Geophys. Res., 89, 5733-5762.

Smith, R. B. and W. D. Richins, 1985, Seismicity and earthquake hazards of Utah and the Wasatch Front: Paradigm and Paradox (abs.), in Workshop XXVII on "Evaluation of Regional and Urban Earthquake Hazards and Risk in Utah," U.S. Geological Survey Open-File Report, in press.

Sparlin, M. A., L. W. Braile, and R. B. Smith, 1982, Crustal structure of the Eastern Snake River Plain determined from ray trace modeling of seismic refraction data, J. Geophys. Res., 87, 2619-2633.

Stein, R. S. and S. E. Barrientos, 1985, The 1984 Borah Peak, Idaho, earthquake: geodetic evidence for deep rupture on a planar fault, in Workshop XXVIII on the 1983 Borah Peak Earthquake, U.S. Geological Survey Open-File Report, (this volume).

Witkind, I. J., 1975a, Preliminary map showing known and suspected active faults in Idaho, U.S. Geol. Sur. Open-File Report 75-278.

Witkind, I. J., 1975b, Preliminary map showing known and suspected active faults in Wyoming, U.S. Geol. Sur. Open-File Report 75-279.

Witkind, I. J., 1975c, Preliminary map showing known and suspected active faults in Montana, U.S. Geol. Sur. Open-File Report 75-285.

Zollweg, J. E., and W. D. Richins, 1985. Later aftershocks of the 1983 Borah Peak, Idaho, Earthquake and related activity in the central Idaho seismic zone, in Workshop XXVIII on the Borah Peak Earthquake: U.S. Geological Survey Open-File Report, (this volume).

Figure Captions

1. Regional tectonic map of central Idaho (data from Fisher et. al., 1983; R. Bruhn and D. Gallagher, 1984, personal comm.; Rupel, 1982; Mapel et. al., 1965; Scott, 1982; Witkind, 1975a,b,c; Crone and Machette, 1984). Normal faults shown by light lines; heavy line corresponds to surface fault accompanying 1983 Borah Peak earthquake.

2. Seismicity of central Idaho and central Intermountain seismic belt. Star indicates location of 1983 Borah Peak earthquake. Solid line marks boundary of Yellowstone-Snake River Plain volcanic province. Dashed line corresponds to plausible edge of lithospheric, thermal subsidence shoulder.

3. Epicenters of University of Utah 1972, 1976, 1977, 1978, and 1983 Borah Peak earthquake surveys on a regional tectonic map.

4. Fault plane solutions of the central Idaho and central Intermountain seismic belt (modified from Smith and Lindh, 1978). Lower-hemisphere, compressional quadrant is dark.

5. Fault plane solutions of the Borah Peak earthquake sequence, 28 October-19 November, 1983 and event of August 22, 1984. Lower-hemisphere, compressional quadrant is dark.

6. Fault plane solutions of the Borah Peak earthquake sequence as a function of focal depth: a) surface to 5 km, b) 5 to 10 km, and c) greater than 10 km. Zero-time line corresponds to initiation of detailed search for precursory activity.

7. Space-time distribution Borah Peak earthquake fault plane solutions for period, 28 October-19 November, 1983. Arrows indicate direction of T-axes.

8. Comparison of measured surface-fault displacement (throw) with seismic-moment derived vertical and horizontal displacements for main shock and aftershocks, 28 October to 20 November 1984. Surface faulting from Crone and Machette (1984). Vectors are averaged directions of T-axes for each source volume.

9. Borah Peak earthquake model: crustal P-velocity model, NE-SW cross-section of main shock-aftershock hypocenters and hypothetical shear stress vs. depth profile.

10. Fault plane geometries and focal depth histograms for large Basin-Range earthquakes: 1) M7.1, 1954 Dixie Valley, Nevada (Okaya and Thompson, 1984); 2) M7.5, 1959 Hebgen Lake, Montana (Doser, 1984a); and 3) M7.3, 1983 Borah Peak, Idaho (Richins et. al., 1984, 1985; Doser, 1984a,b).

11. Distribution of Late Tertiary normal faulting and outline of Yellowstone-Snake River Plain lithospheric thermal subsidence shoulder. Star indicates location of 1983 Borah Peak earthquake. Heavy lines = faults with Holocene-Late Quaternary displacement, light lines = faults with Quaternary-Late Tertiary displacement.

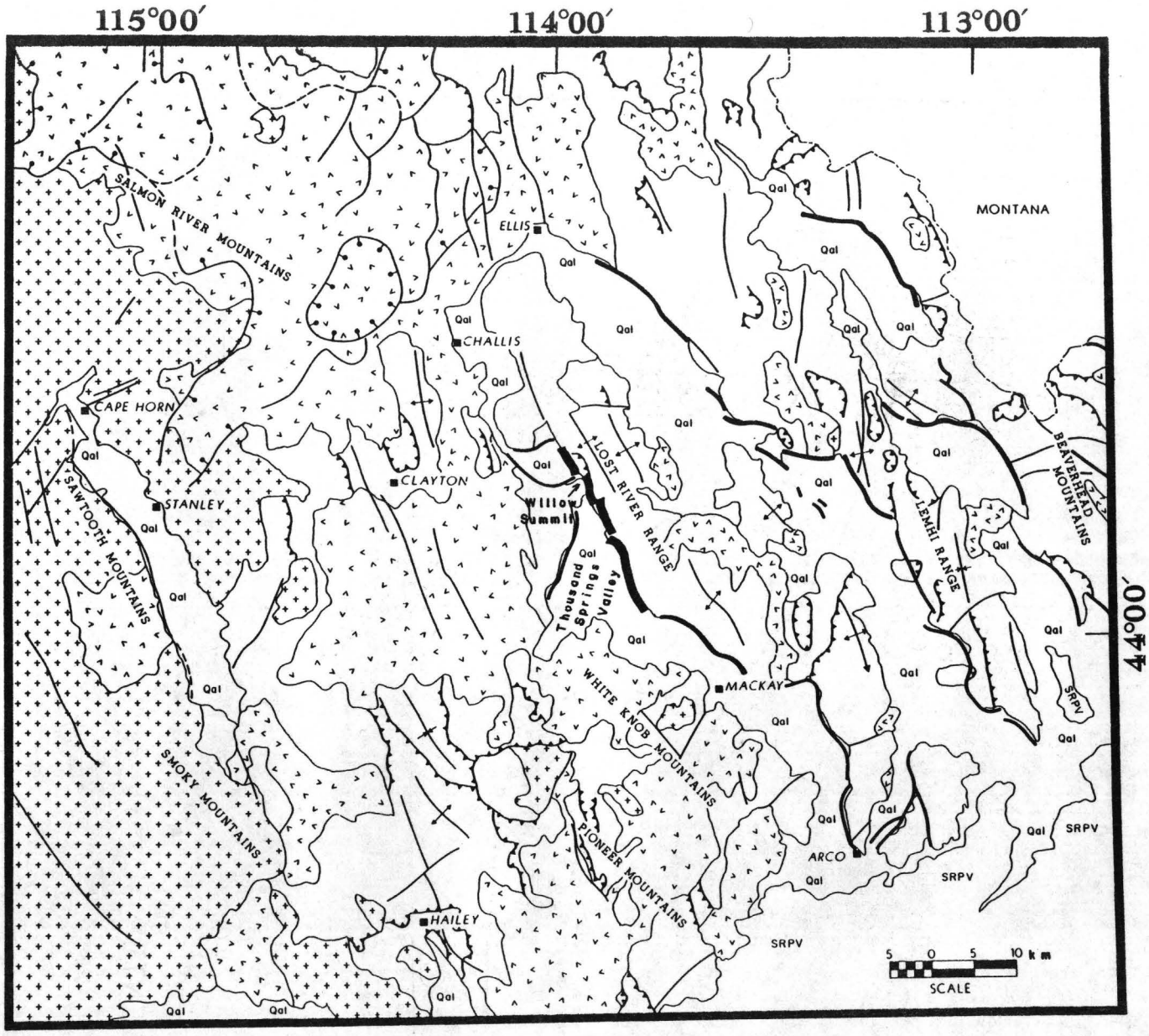
115°00′
114°00′
113°00′
44°00′
MONTANA
SALMON RIVER MOUNTAINS
ELLIS
CHALLIS
CAPE HORN
STANLEY
CLAYTON
SAWTOOTH MOUNTAINS
Willow Summit
LOST RIVER RANGE
Thousand Springs Valley
BEAVERHEAD MOUNTAINS
LEMHI RANGE
MACKAY
WHITE KNOB MOUNTAINS
SMOKY MOUNTAINS
PIONEER MOUNTAINS
ARCO
HAILEY
Qal
SRPV
5 0 5 10 km
SCALE

Figure 1

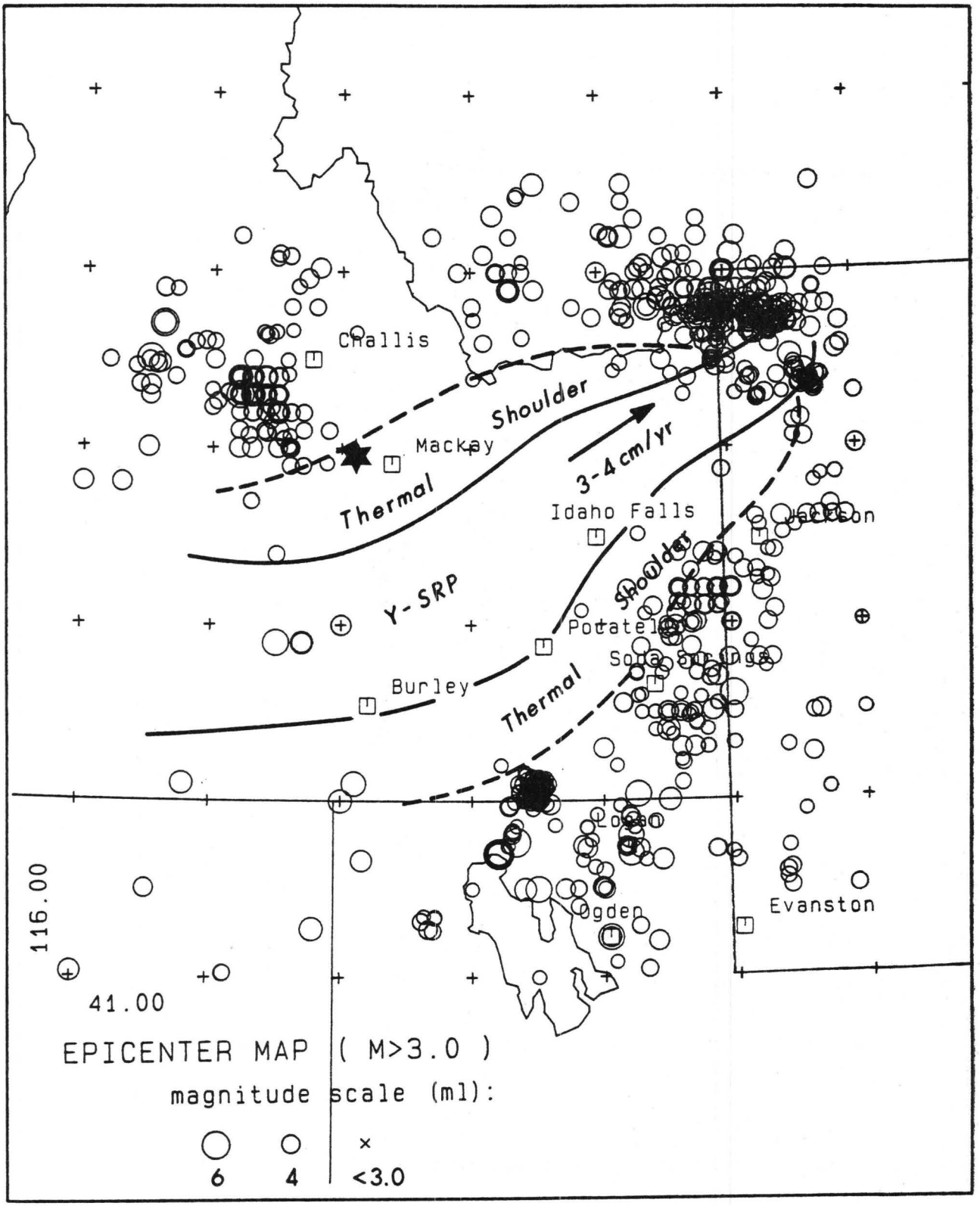
Challis
Mackay
Shoulder
Thermal
3-4 cm/yr
Idaho Falls
Jackson
Y-SRP
Shoulder
Burley
Thermal
Logan
Ogden
Evanston
116.00
41.00
EPICENTER MAP (M>3.0)
magnitude scale (ml):
6
4
<3.0

Figure 2

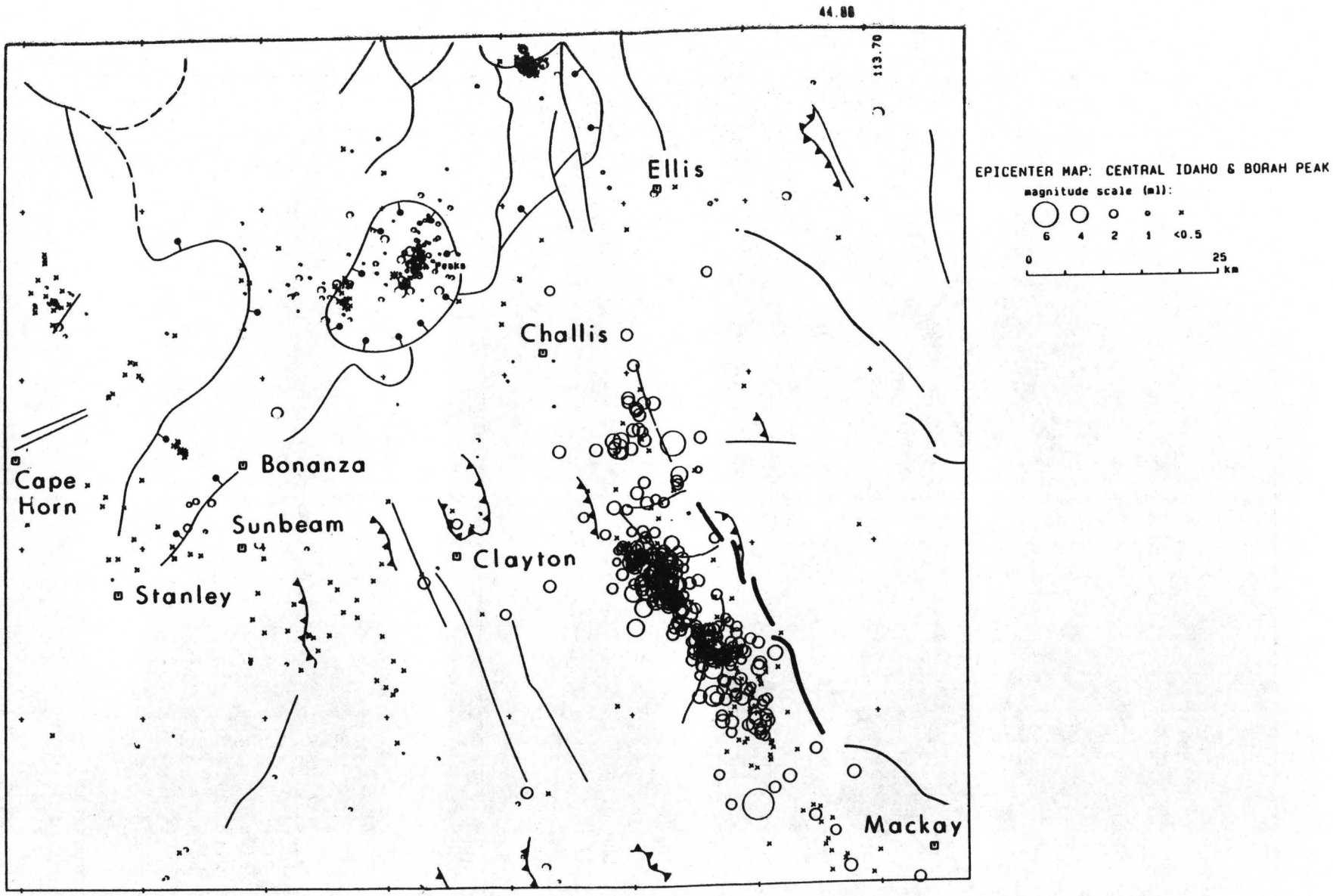
44.00
113.70
Ellis
Challis
Bonanza
Cape
Horn
Sunbeam
Clayton
Stanley
Mackay
EPICENTER MAP: CENTRAL IDAHO & BORAH PEAK
magnitude scale (ml):
6 4 2 1 <0.5
0
25
km

Figure 3

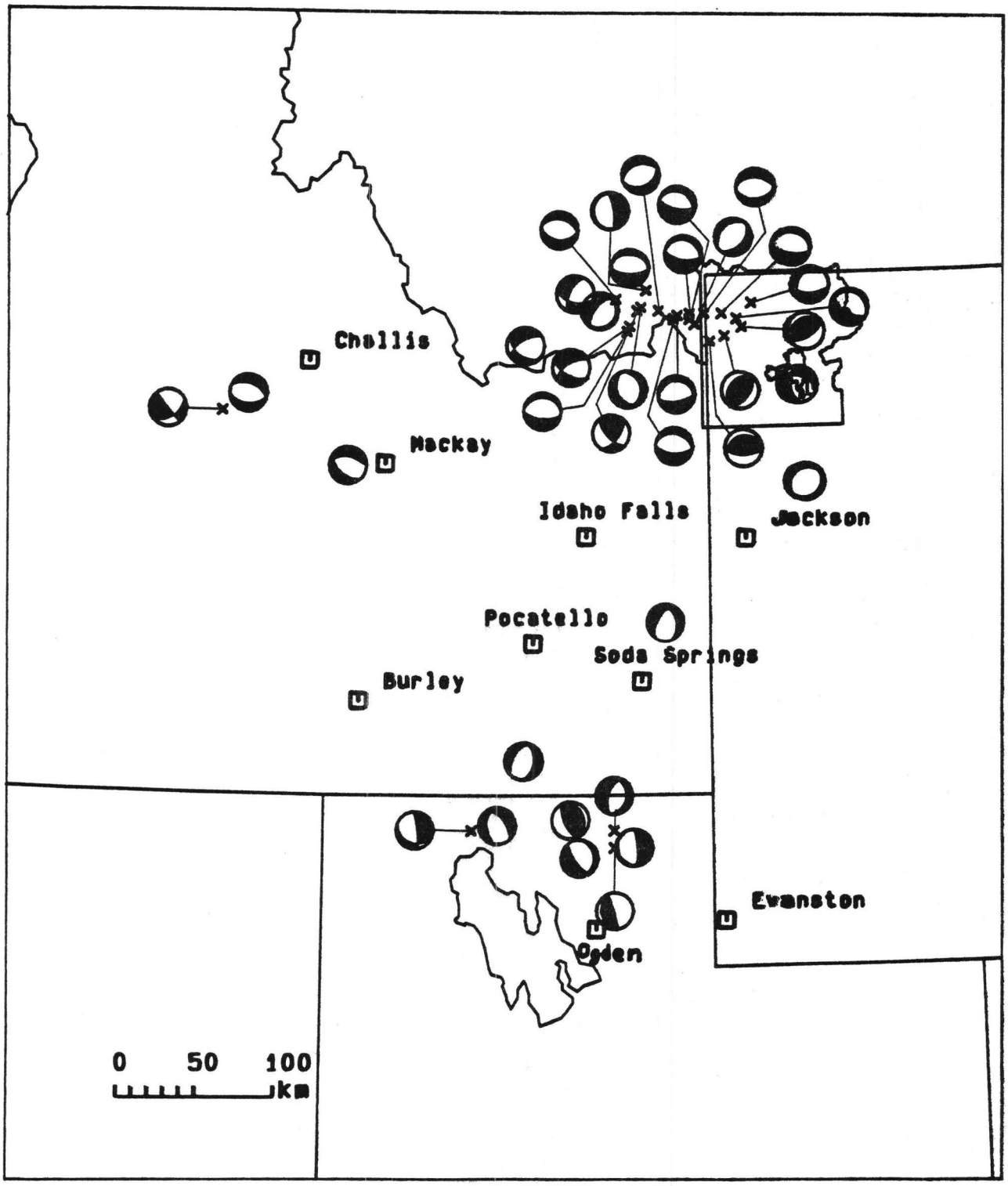
Challis
Mackay
Idaho Falls
Jackson
Pocatello
Soda Springs
Burley
Evanston
Ogden
0 50 100
km

FIGURE 4

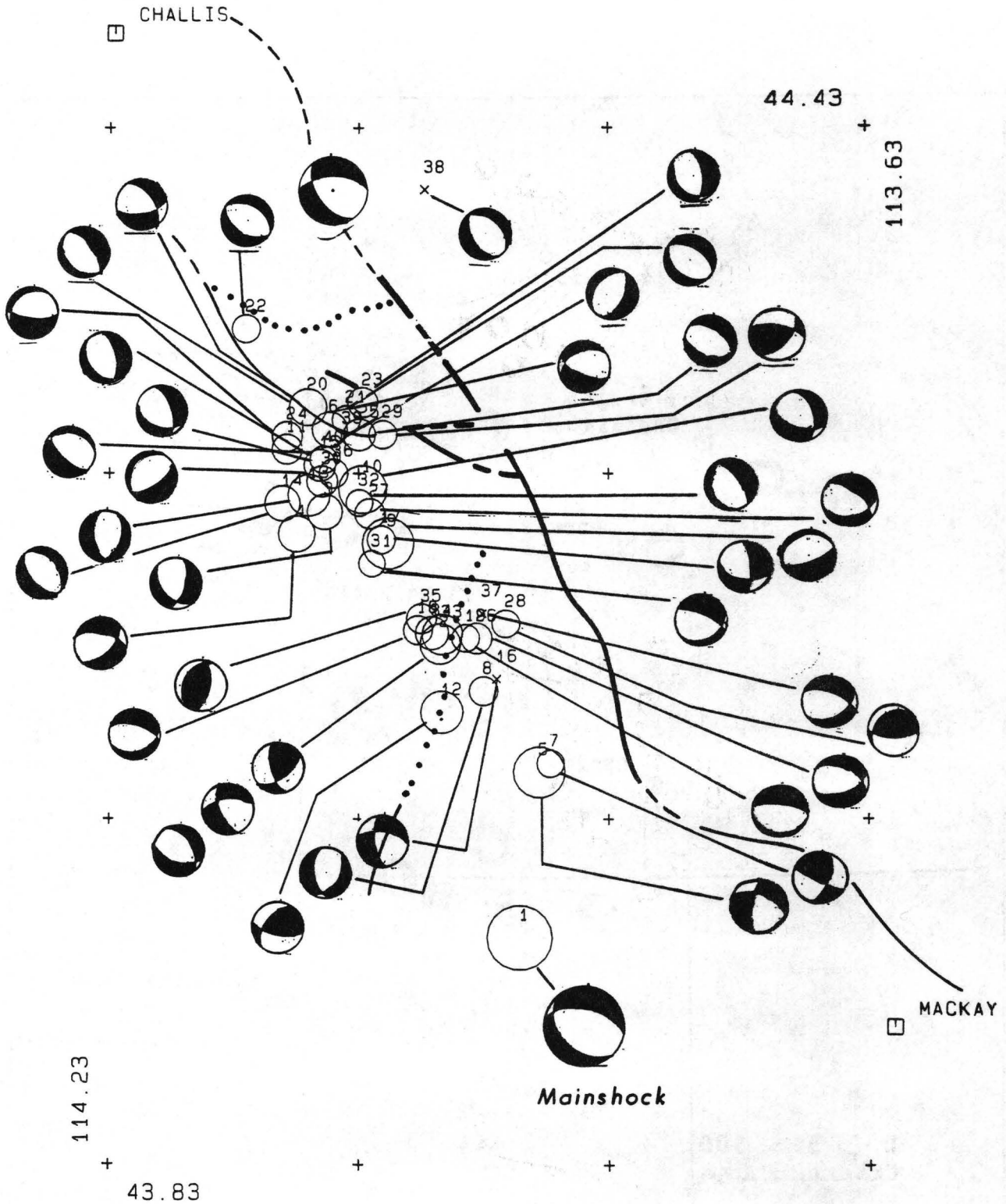

BORAH PEAK FAULT PLANE SOLUTIONS (Oct.28-Nov.19, '83)

magnitude scale (ml):

6 4 <3 0

FIGURE 5

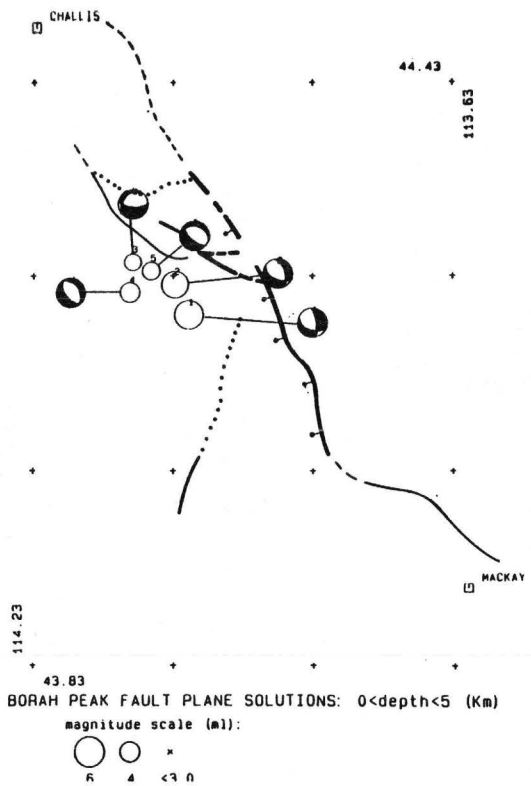
CHALLIS
44.43
113.63
MACKAY
114.23
43.83
BORAH PEAK FAULT PLANE SOLUTIONS: 0<depth<5 (Km)
magnitude scale (ml):
6 4 <3.0

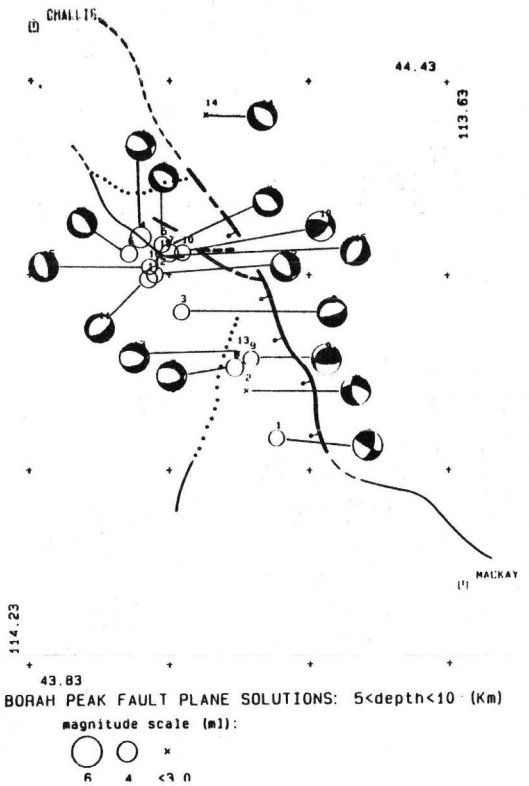
CHALLIS
44.43
113.63
MACKAY
114.23
43.83
BORAH PEAK FAULT PLANE SOLUTIONS: 5<depth<10 (Km)
magnitude scale (ml):
6 4 <3.0

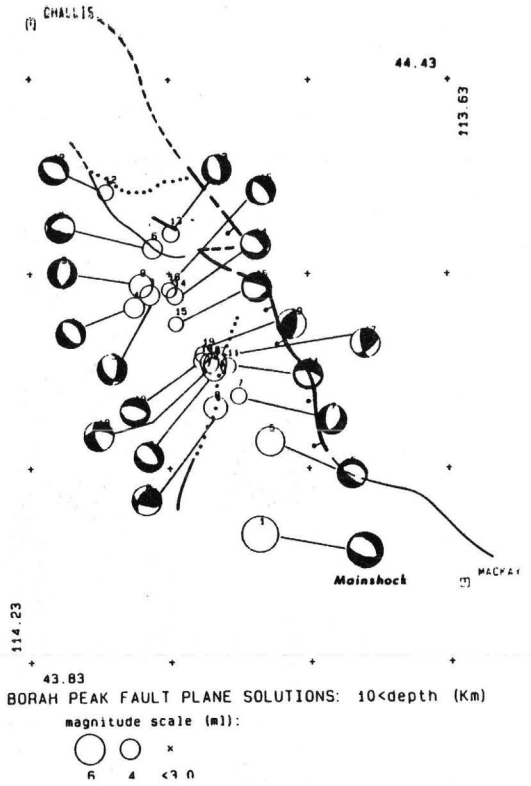
CHALLIS
44.43
113.63
Mainshock
MACKAY
114.23
43.83
BORAH PEAK FAULT PLANE SOLUTIONS: 10<depth (Km)
magnitude scale (ml):
6 4 <3.0

FIGURE 6

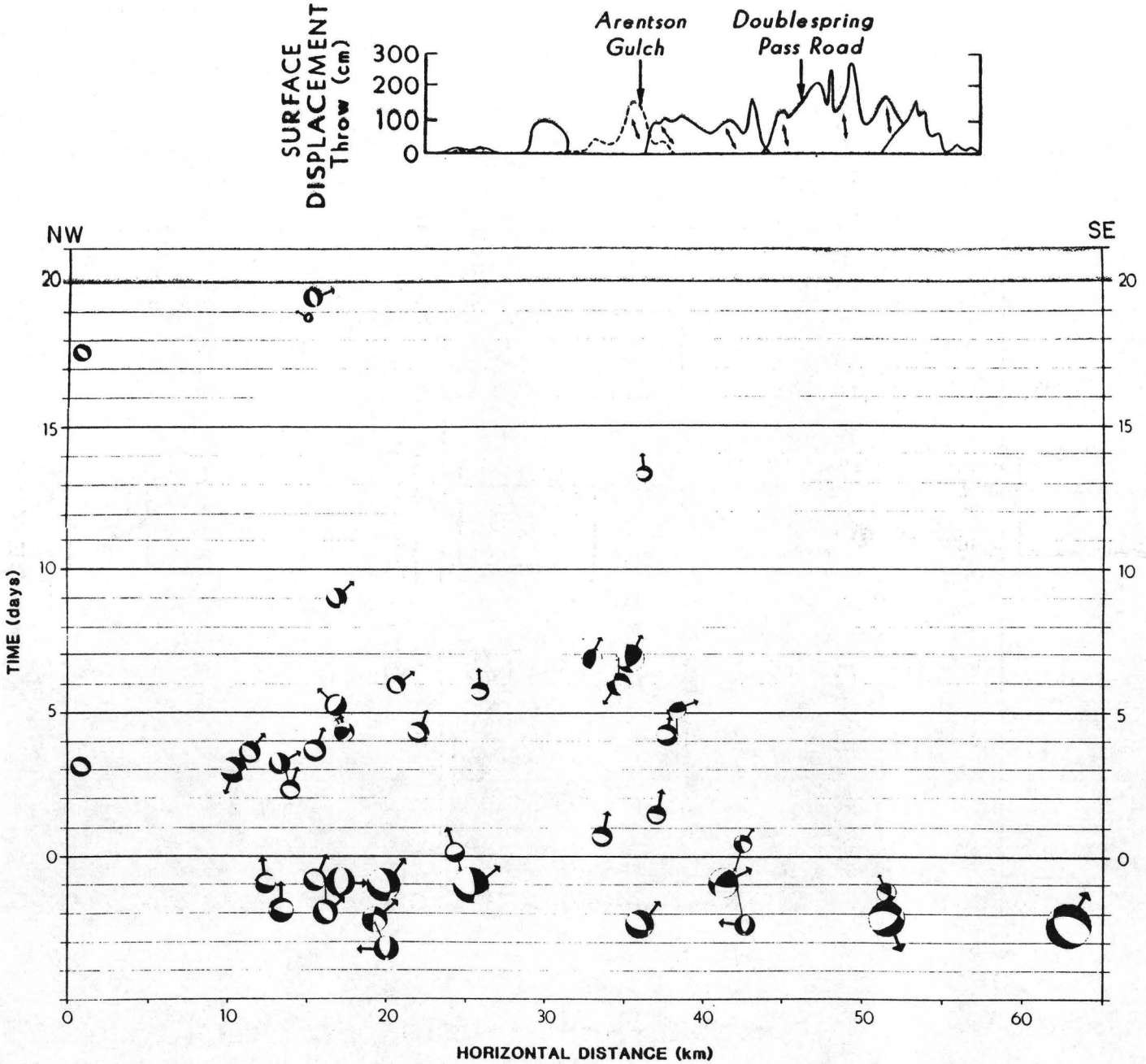
SURFACE DISPLACEMENT Throw (cm)
300
200
100
0
Arentson Gulch
Doublespring Pass Road
NW
SE
20
15
10
5
0
TIME (days)
0
10
20
30
40
50
60
HORIZONTAL DISTANCE (km)

FIGURE 7

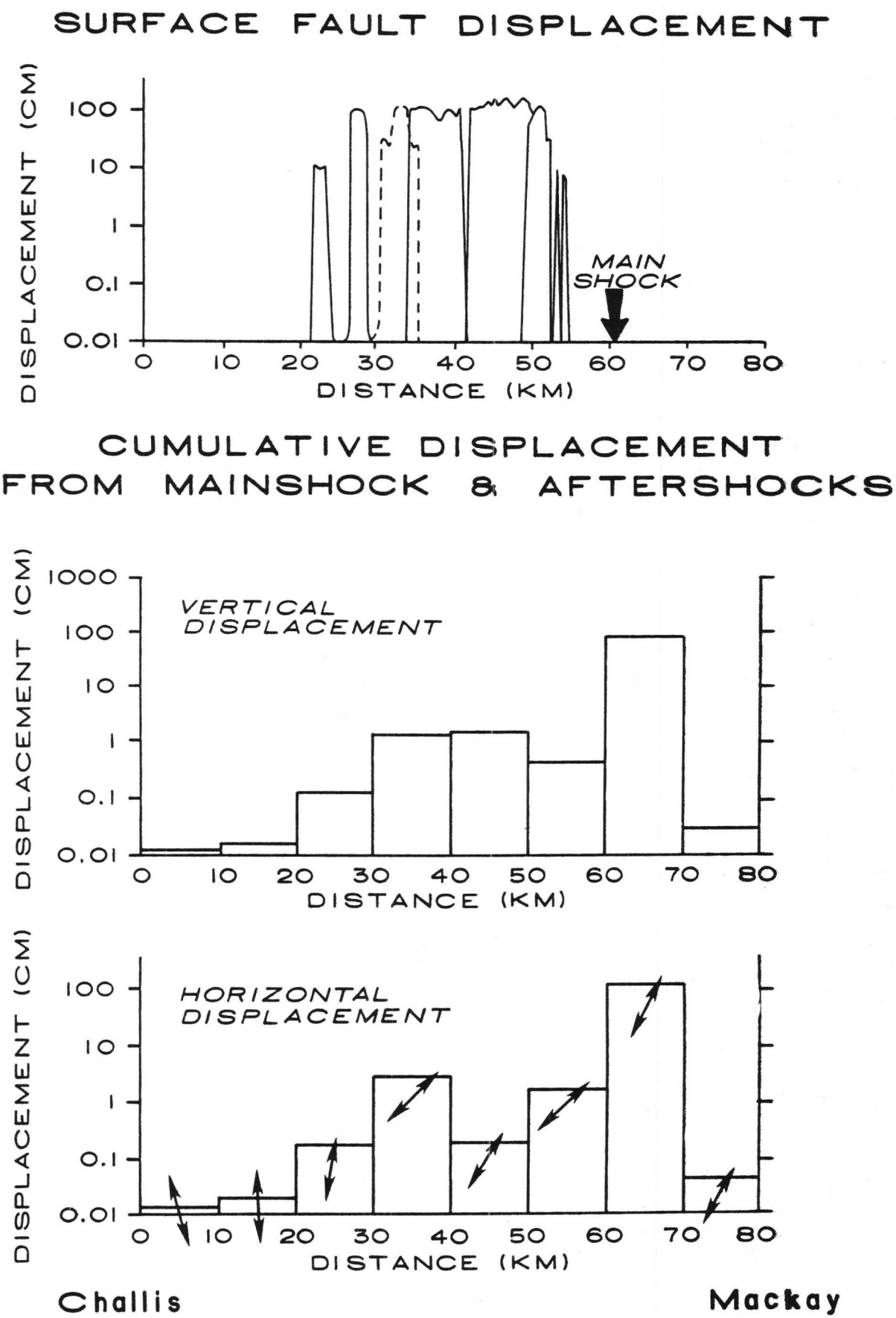
SURFACE FAULT DISPLACEMENT
DISPLACEMENT (CM)
100
10
1
0.1
0.01
0
10
20
30
40
50
60
70
80
DISTANCE (KM)
MAIN SHOCK
CUMULATIVE DISPLACEMENT
FROM MAINSHOCK & AFTERSHOCKS
DISPLACEMENT (CM)
1000
100
10
1
0.1
0.01
VERTICAL DISPLACEMENT
DISTANCE (KM)
HORIZONTAL DISPLACEMENT
Challis
Mackay

FIGURE 8

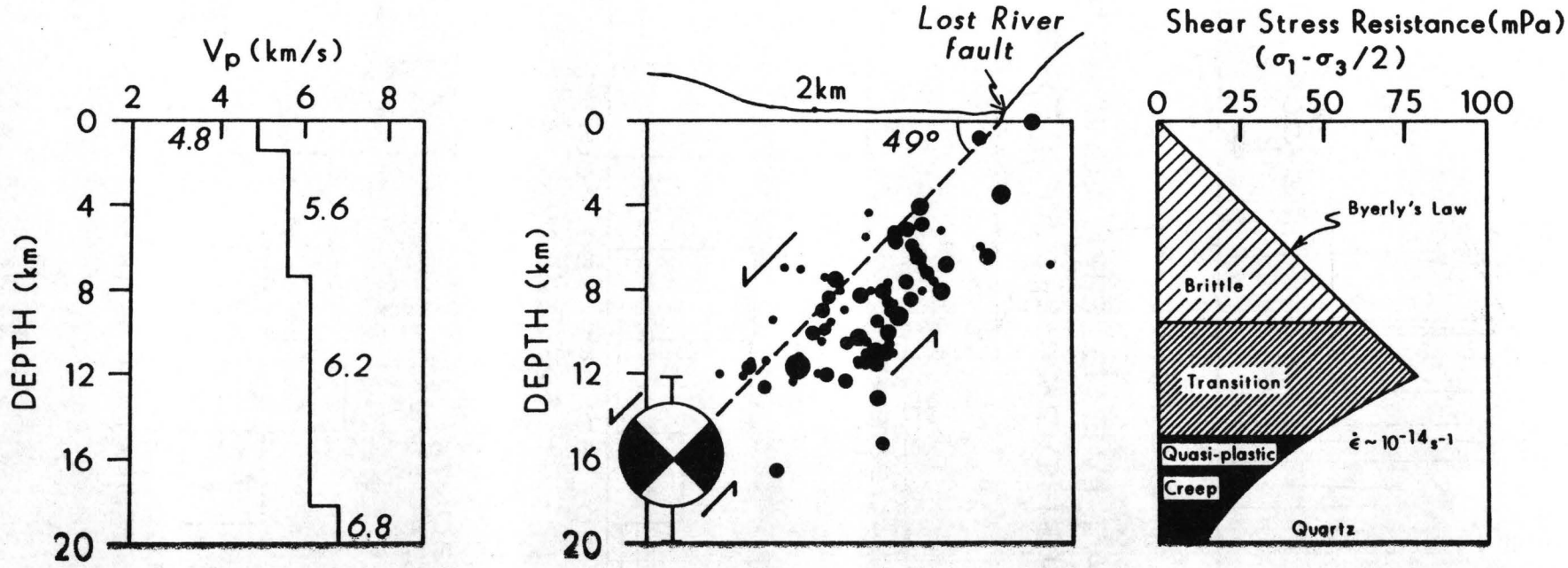
Vp (km/s)
2
4
6
8
0
4
8
12
16
20
DEPTH (km)
4.8
5.6
6.2
6.8
Lost River
fault
2km
49°
Shear Stress Resistance(mPa)
(σ1-σ3/2)
0
25
50
75
100
Byerly's Law
Brittle
Transition
Quasi-plastic
Creep
Quartz
ε̇ ~ 10-14s-1

Figure 9

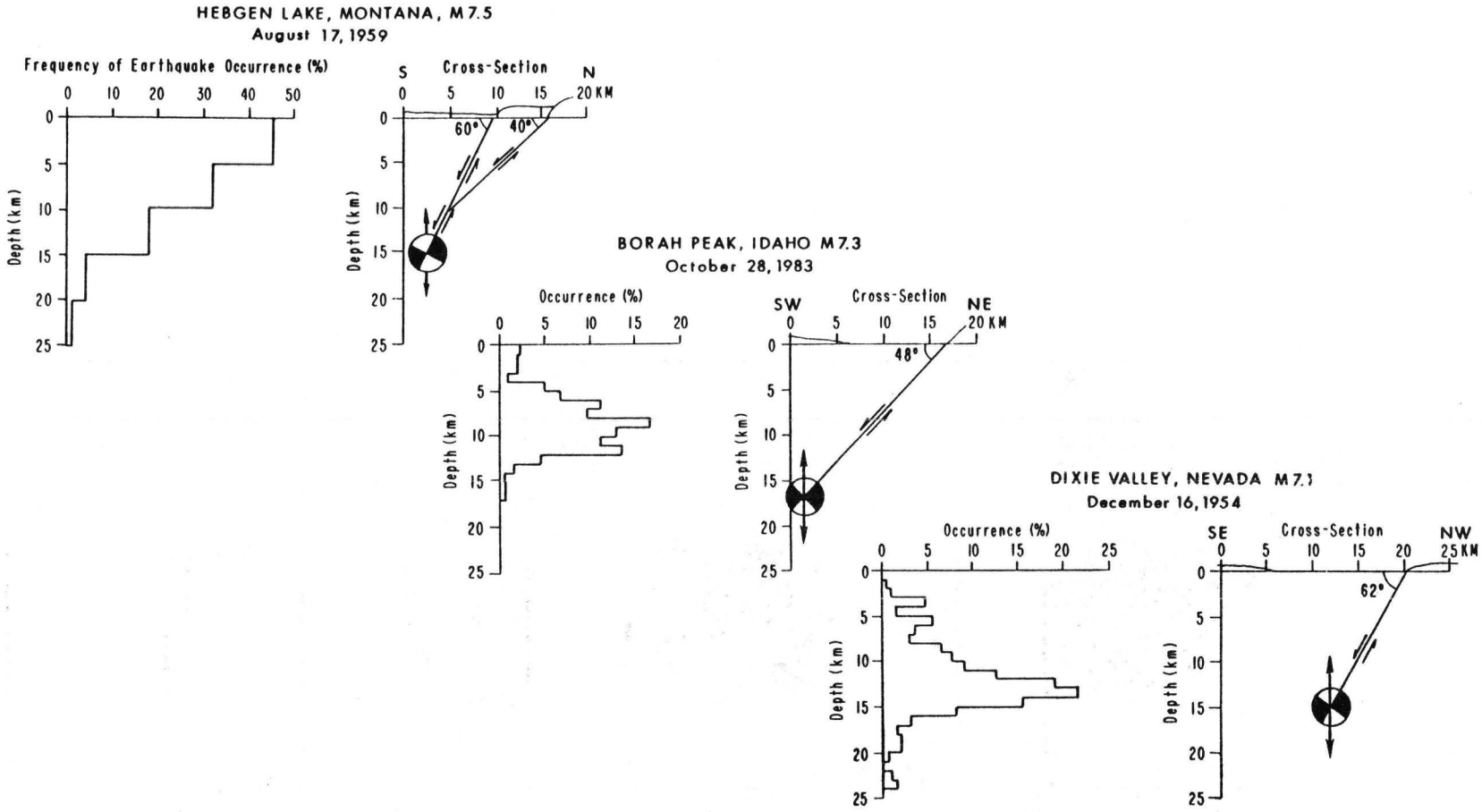
HEBGEN LAKE, MONTANA, M7.5
August 17, 1959
Frequency of Earthquake Occurrence (%)
0 10 20 30 40 50
Depth (km)
0 5 10 15 20 25
S Cross-Section N
0 5 10 15 20 KM
60°
40°
BORAH PEAK, IDAHO M7.3
October 28, 1983
Occurrence (%)
0 5 10 15 20
SW Cross-Section NE
0 5 10 15 20 KM
48°
DIXIE VALLEY, NEVADA M7.1
December 16, 1954
Occurrence (%)
0 5 10 15 20 25
SE Cross-Section NW
0 5 10 15 20 25 KM
62°

Figure 10

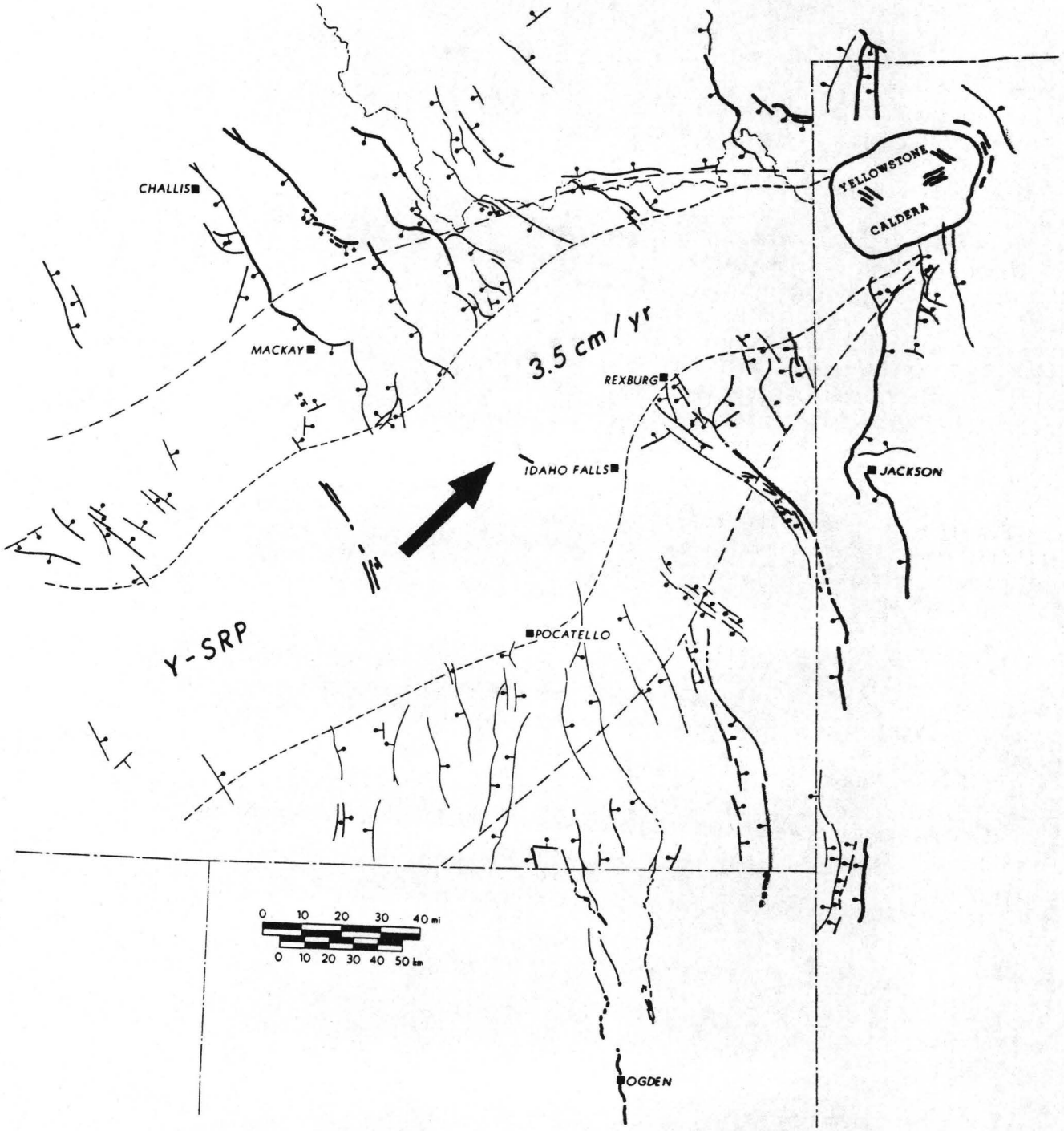
CHALLIS
MACKAY
REXBURG
IDAHO FALLS
POCATELLO
OGDEN
JACKSON
YELLOWSTONE
CALDERA
3.5 cm / yr
Y-SRP
0 10 20 30 40 mi
0 10 20 30 40 50 km

Figure 11

Instrumental Seismicity of Central Idaho

James W. Dewey
U. S. Geological Survey
Denver, Colorado, 80225

Abstract

Hypocenters of regionally recorded earthquakes that occurred in central Idaho from 1944 through March, 1984, have been recomputed with travel-times calibrated by locally recorded aftershocks of the Borah Peak, Idaho, earthquake of 1983. The effect of the relocation is to define more sharply the sizes and relative positions of seismic source zones in central Idaho and to move epicenters systematically south, often by more than ten kilometers, from their previously catalogued positions. The distribution of epicenters of the Borah Peak main shock and early aftershocks suggest that the fault segment that ruptured in the main shock was approximately a parallelogram with one pair of sides parallel to the zone of surface fault scarps associated with the earthquake and with the other pair of sides parallel to the slip vector of the earthquake. Such a main-shock rupture shape would be expected on geometrical grounds if the 1983 rupture zone were terminated on the north and south by intersection with adjacent segments of the Lost River fault that have the same slip vector as the 1983 rupture. Epicenters of earthquakes occurring before 1983 define a seismic zone, the White Cloud Peaks zone, that is approximately parallel to the Lost River fault and situated about 30 km west of the Borah Peak aftershock zone. The relocated epicenters may also be interpreted as defining a north-northeast trending seismic zone near Seafoam and a north-northeast trending seismic zone that is situated north and west of Challis, here called the Twin Peaks-Myers Cove zone. The Seafoam zone includes the epicenter of the largest instrumentally recorded central Idaho earthquake prior to the Borah Peak earthquake, the magnitude 6.1 shock of July 12, 1944. The region within 25 km of the epicenter of the Borah Peak main shock was quiescent for at least two decades before the main shock for magnitudes of 3.5 and greater.

Introduction

Following the Borah Peak earthquake of 1983.10.28 (dates of earthquakes are abbreviated as year.month.day) research groups from the U.S. Geological Survey and several universities installed portable seismographs in the meizoseismal region and recorded strong aftershocks that were also recorded teleseismically (Boatwright, 1985; Richins and others, 1985). I have used arrival times from the locally and teleseismically recorded aftershocks to calibrate the location of the hypocenters of the Borah Peak mainshock and of other earthquakes from central Idaho and vicinity (fig. 1) that were instrumentally recorded to epicentral distances of at least five degrees. The earliest such shock occurred in 1944, and the period covered by this study ends in March, 1984. Prior to the local registration of the 1983 aftershocks, absolute positions of most central Idaho earthquakes would have had to be considered uncertain by ten or twenty kilometers, because of lateral variations of seismic wave velocity in the earth's mantle beneath the western United States (Herrin and Taggart, 1982).

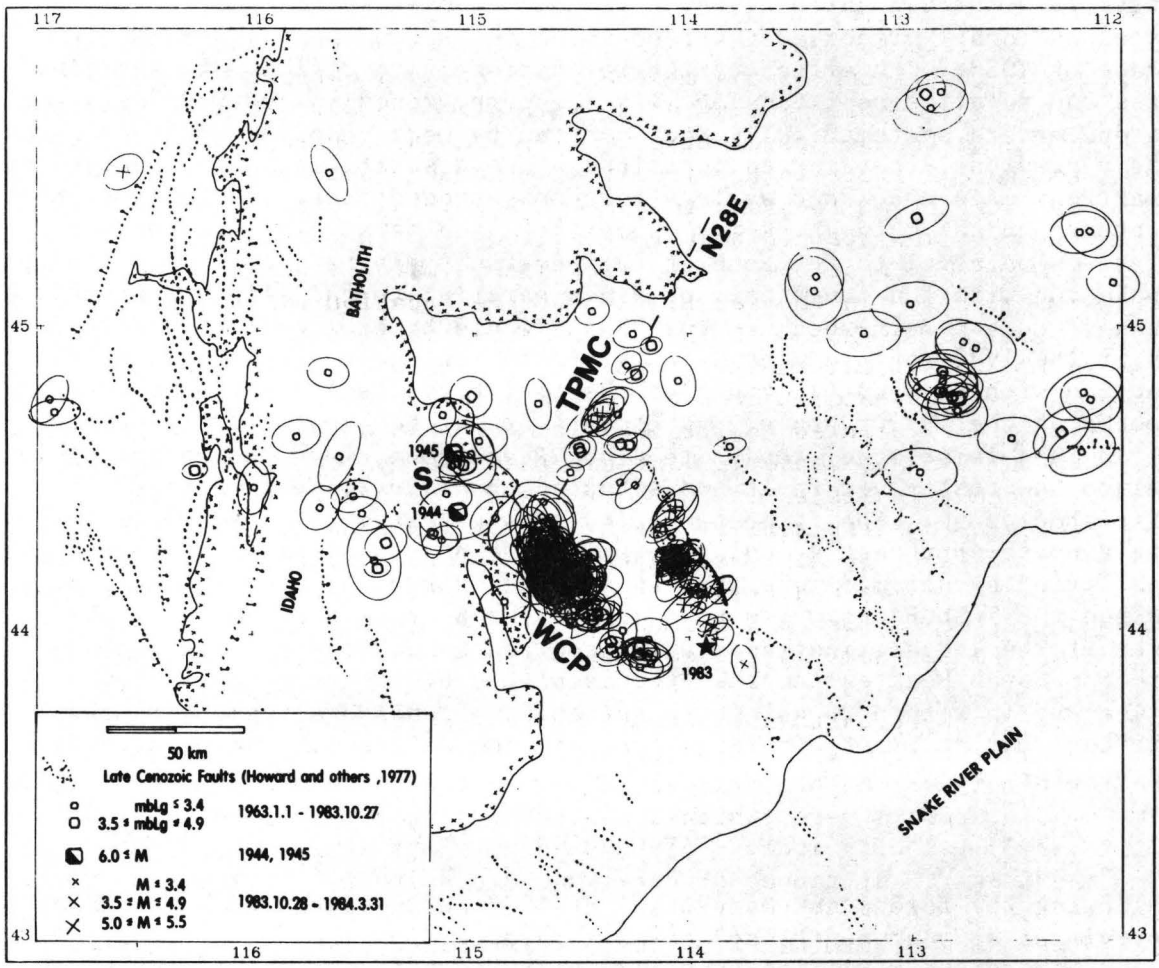

Figure 1. The most reliably located epicenters (those with 90% confidence-ellipse semi-axes shorter than 15 km) for the period 1944-1984.3.31. WCP = White Cloud Peaks zone. S = Seafoam zone. TPMC = Twin Peaks - Myers Cove zone. The line striking N28E is parallel to the horizontal projection of the slip vector of the Borah Peak main shock.

Methods of relocating hypocenters and recomputing magnitudes

I used as the general location method a two-step procedure based on the method of joint epicenter determination. The general method is described by Dewey (1983); in detail, the earthquakes were divided up into four groups on the basis of their previous epicentral positions and their dates of occurrence, and each group was treated slightly differently. The four groups, and the ways in which they were analyzed, are discussed in subsequent paragraphs in this section.

For all four groups, the first step of the location procedure consisted of processing up to fifteen of the most widely recorded earthquakes in each group by the method of joint epicenter determination (JED). The JED provided station adjustments to the travel-time tables, and the JED estimated variances of the observations for use in constructing weighting functions. Focal depths were fixed at this stage, in order to prevent the joint computation of location parameters and station adjustments from becoming unstable in the event that a focal depth of one of the earthquakes were computed to be negative (Dewey,1983). In the second step of the location procedure, I used a single-event location method with the JED-computed station adjustments and variances to locate all earthquakes (not just the 15 used in the JED computation), and I computed both focal depth and epicenter. If the free-depth hypocenter was computed to lie above the earth's surface or if the free-depth computation did not converge, I recomputed the epicenter with depth fixed. The hypocenters listed in Table 1 were determined in the second step. In addition to first arriving P-waves from stations located out to epicentral distances of 86 degrees, later phases (pP,Pg,S,Lg) were used in the location process. P-wave and S-wave travel-time tables were constructed from velocity model T7 of Burdick and Helmberger (1978); Pg and Lg velocities were taken to be 6.0 km/sec and 3.5 km/sec respectively (Sheriff and Stickney, 1984).

The first group of earthquakes comprised shocks of the 1983 Borah Peak sequence. Rather than use a calibration event (Dewey, 1979) to constrain the JED computation, I assumed that travel-times to local stations out to distances of 0.6 degrees were unbiased and as predicted by the Burdick and Helmberger (1978) velocity model. Station adjustments were computed for stations at epicentral distances of more than 0.6 degrees. In the JED computation, focal depths of Borah Peak aftershocks occurring after October 29 were fixed to values determined from locally-recorded data by HYPO71 using a local velocity model similar to that used by Richins and others (1985) (S. Plymell, personal communication). Focal depths of several large aftershocks occurring on October 28 and 29 were fixed in the JED computation to depths implied by pP-wave arrival times at the teleseismic station PMR (all station abbreviations are as given by Poppe and others, 1978).

Earthquakes occurring in the study area west of longitude 113.5W from 1963 through October 27, 1983 were treated as the second group in the location procedure. There were 24 stations that recorded many of the second group of earthquakes and that also recorded the 1983 Borah Peak earthquakes. In the JED computation for the second group of earthquakes, adjustments at these stations were fixed to the values computed for the Borah Peak sequence. These 24 stations then became "calibration stations" with respect to which station adjustments were computed for 76 other stations that recorded many of the

second group of earthquakes but that did not record the Borah Peak aftershock sequence. In this fashion, the locations of the pre-1983 earthquakes were calibrated with respect to the Borah Peak sequence. There may be an uncertainty of several kilometers in the position of the second group of earthquakes with respect to the Borah Peak group, due to departures from the assumption that station adjustments for the 24 calibration stations are constant for all source regions in central Idaho.

For the purpose of computing station adjustments, the focal depths of the second group of earthquakes were fixed at 10 km in the JED computation. In the event that the assumed 10 km focal depth were systematically too large or too shallow, the focal depths of hypocenters computed by the single-event location program and listed in Table 1 would also be systematically too deep or too shallow (Dewey, 1983). To obtain independent estimates of focal depth, I tried computing focal depths, rather than fixing them, at the same time that I was computing the station adjustments: instead of using joint epicenter determination to compute the station adjustments, I used joint hypocenter determination. The median of depths thus computed was 10 km, the deepest focal depth computed was 18 km, and the shallowest was computed to lie above the surface. The precision of the focal depth computation is low for most of the hypocenters computed in the joint hypocenter determination of the group 2 events, but the results of the joint hypocenter determination give support to my choice of 10 km as the depth to which events are fixed in the joint epicenter computation of station adjustments.

Instrumentally recorded earthquakes occurring in the study region west of longitude 113.5W from 1944 through 1962 constituted the third group of shocks. Half of the stations used for the third group had been used in the first or second groups; these stations were used as calibration stations for the third group, with their station adjustments taken to be those computed for group one or group two. Focal depths for earthquakes in this group were fixed to 10 km throughout the location procedure.

The fourth group of earthquakes consisted of shocks located east of longitude 113.5W. The epicenters of these easternmost earthquakes may be biased by 5 or 10 km; such an error would be in addition to the possible errors accounted for by the 90 percent confidence ellipses associated with the epicenters. The possibility of source bias must be considered because the epicenters are halfway between the Borah Peak source and the source of the Yellowstone Park earthquake of 1975.6.30, the location of which is also known to high accuracy as a result of aftershock studies (Pitt and others, 1979). Station adjustments computed for Yellowstone Park earthquakes differ from station adjustments computed for Borah Peak earthquakes, probably due to the rapid variations of upper mantle velocities in the Yellowstone region. The epicenter of 1965.1.6 computed on the basis of station adjustments calibrated by the Yellowstone Park earthquake is 8 km west of the epicenter computed on the basis of station adjustments calibrated by the Borah Peak earthquake. The epicenters for the region east of 113.5W were computed with respect to 1965.1.6 as a calibration event, with the epicenter of this shock fixed to a position midway between the epicenters computed with the Borah Peak and the Yellowstone Park station adjustments. Focal depths were fixed to 10 km in the JED computation of the station adjustments. As with group 2, the final hypocenters computed by the single-event program will be systematically too deep or too shallow in proportion to the amount by which the 10 km focal depth assumed in the JED computation is deeper or shallower than the mean depth of the earthquakes.

The arrival times obtained within 0.6 degrees of the Borah Peak aftershocks are those recorded by temporary seismographs installed in the meizoseismal region by the U.S. Geological Survey, University of Utah, Boise State University, and the Idaho National Engineering Laboratory (Boatwright, 1985; Richins and others, 1985). Arrival times at more distant stations are mostly those reported in international seismological bulletins such as the bulletins of the International Seismological Centre, the bulletins of the Bureau Central International Seismologique, and the Earthquake Data Reports of the U.S. Geological Survey. For earthquakes occurring in 1963-1982, I supplemented the previously published arrival time data with data I read from nearby stations of the World Wide Standardized Seismograph Network (WWSSN) and the Canadian national network.

Magnitudes of earthquakes occuring prior to the Borah Peak mainshock are mb(Lg) magnitudes (Nuttli, 1973) computed from amplitudes measured on stations of the World Wide Standardized Seismograph Network and stations of the Canadian national network. Because of lateral variations in attenuation of Lg waves propagating from central Idaho, different values of the anelastic attenuation parameter (here called g*) were used for Lg waves recorded at different stations. Values of g* were interpolated from contour maps of Espinosa (1981) and Singh and Herrmann(1983) and then adjusted slightly in order that magnitudes from different stations agree with each other for most earthquakes. For MSO,PNT, and SES (Poppe and others, 1978), g* was taken as .07/deg.; for EDM, .2/deg.; for BOZ and DUG, .3/deg; and for GOL, .4/deg. I found it necessary to use two different values of g* for Lg waves recorded at LON, in order to avoid systematic inconsistencies between mb(Lg) computed for LON and mb(Lg) computed for other stations. For earthquakes west of 113.5W, I used g* = .4 at LON. For earthquakes east of 113.5W, I used g* = .2 at LON. Magnitudes of almost all earthquakes in Table 1 are based on amplitude measurements from at least two stations.

Hypocenters of the larger earthquakes relocated in this study are given in Table 1, together with the semi-lengths (in km), trends (degrees clockwise from N), and plunges of the axes of the 90 percent confidence ellipsoids associated with the hypocenters.

Changes in the absolute and relative locations of central Idaho earthquakes resulting from this study.

Figure 2 shows the consequences of relocating the most widely recorded members of a group of earthquakes that occurred in central Idaho, west of the Borah Peak aftershock zone, in 1963-1973. The effect of the relocation was to move the shocks systematically to the south and to show that the earthquakes occurred in a narrower source region than would have been inferred from the previously accepted epicenters of the shocks. The southward shift in the recomputed epicenters with respect to the previous epicenters is probably due to removing the bias that results from upper mantle velocities to the south of Idaho being slower than upper mantle velocities to the north of Idaho (Herrin and Taggart, 1962). The reduction in scatter of the epicenters is due partly to correcting for lateral variations in velocity and partly to the improvement of the quantity and quality of the data used to locate the shocks.

The difference between my hypocenters and those routinely computed by the U.S. Geological Survey are generally smaller for the Borah Peak sequence than for the earthquakes shown in figure 2. My main shock epicenter is 10 km south

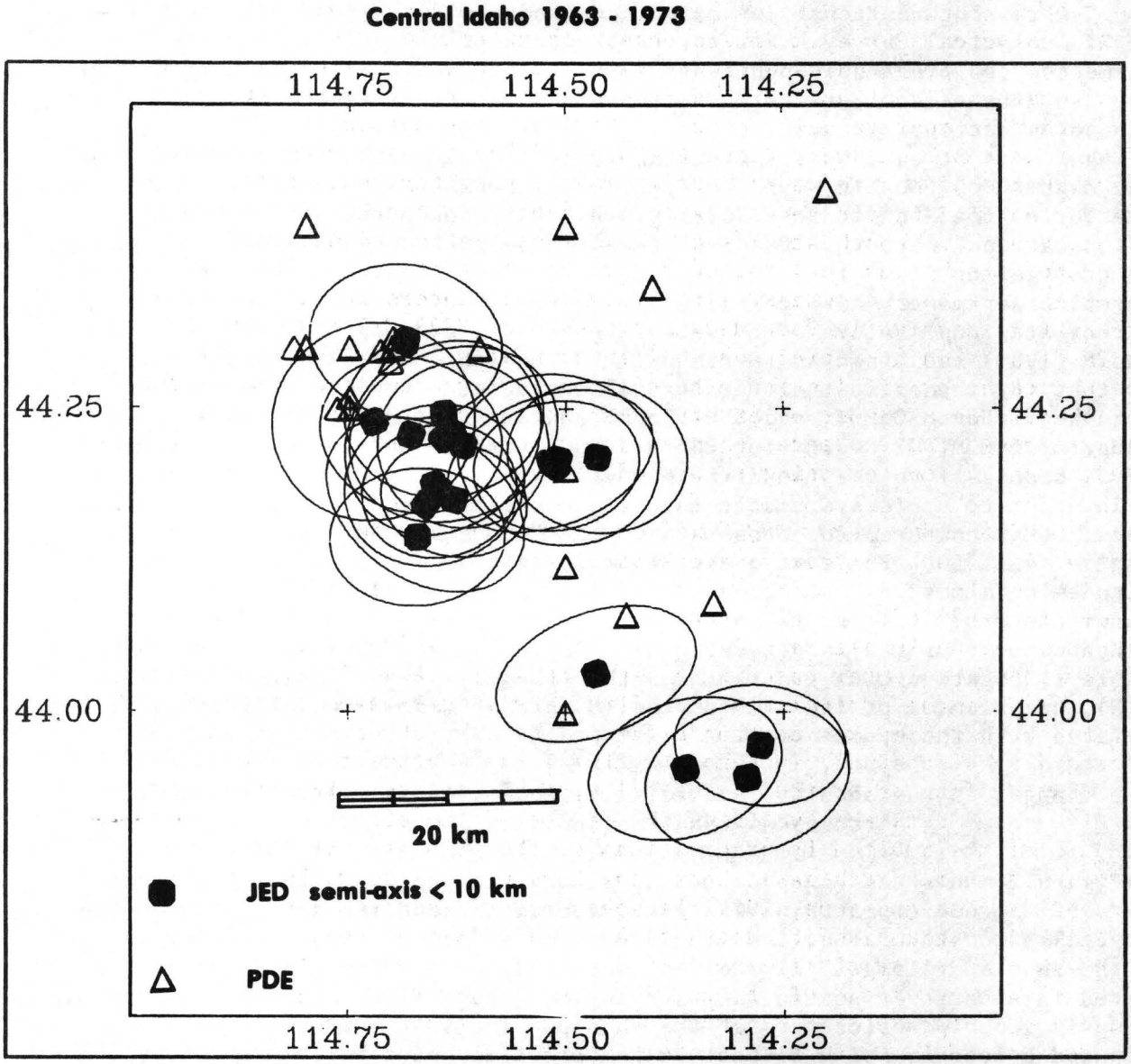

Figure 2. Comparison of epicenters determined in this study (JED) with the corresponding routinely determined epicenters(PDE), for the White Cloud Peaks zone. Earthquakes plotted are those that occurred in 1963-1973 and whose relocated epicenters are estimated to be precise to within 10 km.

of the routine USGS main shock epicenter. Most of the revised epicenters of aftershocks are south of the corresponding routine USGS epicenters, by distances of less than 10 km. The lower bias in the routine USGS locations of the 1983 shocks, compared to that for the 1963-1973 shocks, is probably due to a larger number of seismographic stations in 1983 that were within several degrees of the epicenters.

Richins and others (1985) have also determined epicenters of the Borah Peak main shock and aftershocks using station adjustments that were calibrated by locally recorded Borah Peak aftershocks. In principle, the epicenters resulting from the two studies would be expected to differ slightly. We used different location algorithms, arrival times from quite different sets of stations, and different velocity models. However, our epicenters for the Borah Peak main shock are very close (within 1.5 km) to each other. Most other earthquakes of the sequence likewise have epicenters determined by our two studies that lie within several kilometers of each other, and it would appear that the use in both studies of calibrated station adjustments outweighs the differences in location algorithms and data sets. The most notable exceptions to the general similarity of epicenters in our two studies are for the teleseismically recorded aftershocks of 2329 GMT and 2339 GMT on October 29, for which our epicenters differ by nearly 7 km. The set of epicenters located by Richins and others(1985) is more complete than my own, because it includes a number of aftershocks that were not reported from stations at epicentral distances of more than 5 degrees and hence did not meet this study's criterion for being relocated.

Focal depth of the Borah Peak main shock computed from P-wave arrival times

The focal depth of the main shock hypocenter (i.e. the depth at which fault rupture began) is estimated to be 14 km, with the 90 percent confidence ellipsoid on the hypocenter spanning a depth range of about 5 km. This depth is determined from the arrival times of first-arriving P-waves that have been adjusted by the JED-computed station adjustments. The JED-computed station adjustments are constrained, in turn, by fixing the depths of post-October 29 aftershocks to values determined by HYP071 with a local velocity model and local arrival-time data and by fixing the depths of the aftershocks of October 28 and 29 to depths implied by observations of the pP phase for these events. For the Borah Peak main shock, the P-wave raypaths would have had take-off angles (Pho and Behe, 1972) between about 18 degrees (for a station at an epicentral distance of 86 degrees) and from 60 to 90 degrees (for a station at an epicentral distance of .68 degrees); this range of take-off angles and the low variance of the arrival-times after they have been corrected by the JHD-computed station adjustments account for the rather small depth range spanned by the confidence ellipsoid.

Why the southward displacement of the 1983 main shock epicenter with respect to the surface fault scarps may be due to oblique slippage on a single planar fault

The position of the Borah Peak main shock epicenter with respect to the southern end of the zone of associated, surface, fault scarps is not in the direction of dip on the fault plane (azimuth S110W, henceforth called

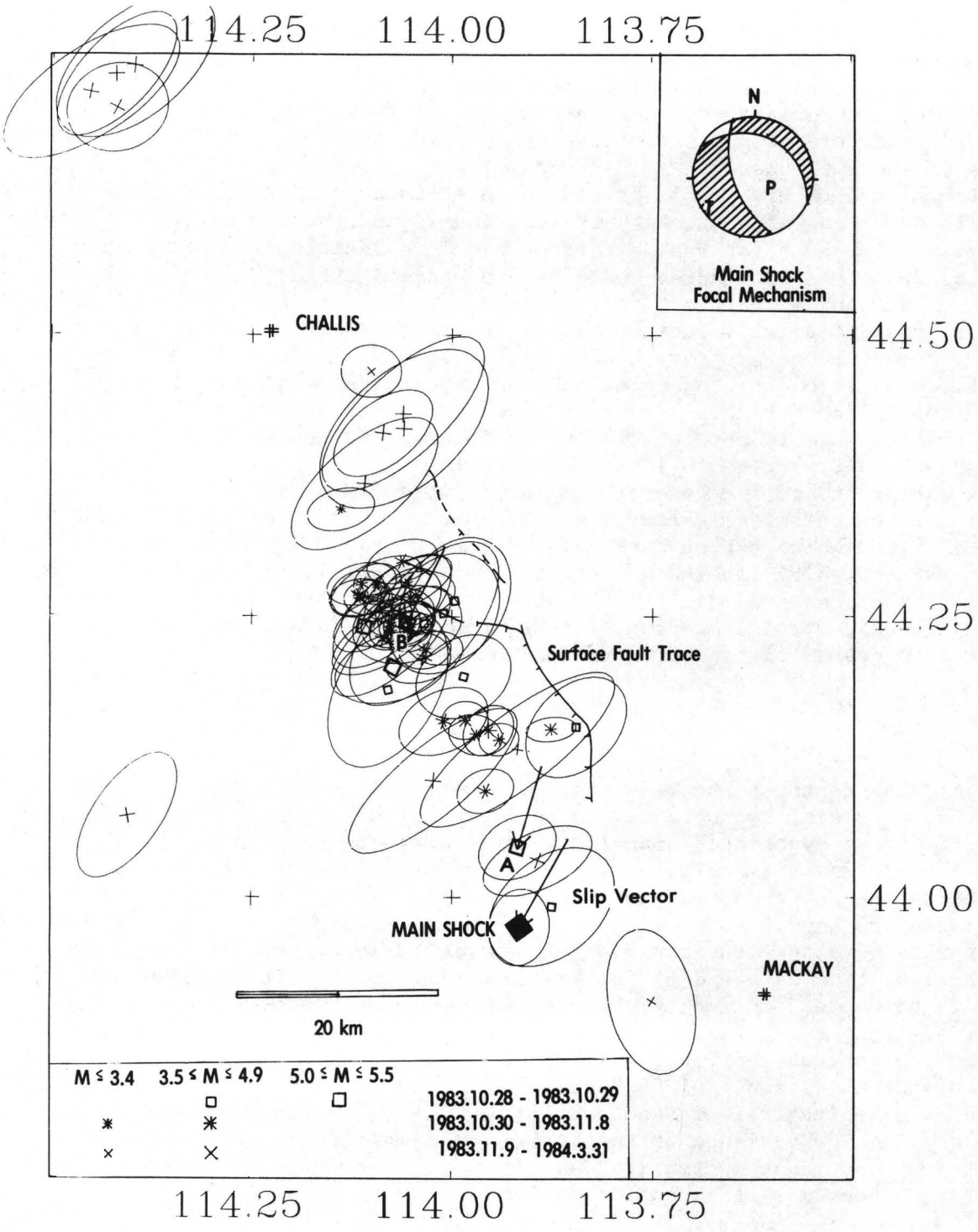

Figure 3. Regionally and teleseismically recorded earthquakes from the Borah Peak sequence, 1983.10.28 - 1984.3.31. Focal mechanism (strike = 160 deg.,dip = 63 deg., slip = -68 deg.) and slip vector of the main shock were determined by the method of Sipkin (1982) (U.S. Geological Survey, 1984). Slip vectors for the aftershocks of 28 October, 1951 UTC (event A) and 29 October, 2329 UTC (event B) are determined by the method of Dziewonski and others (1981) (U. S. Geological Survey, 1984). Surface fault trace from Crone and others (1985).

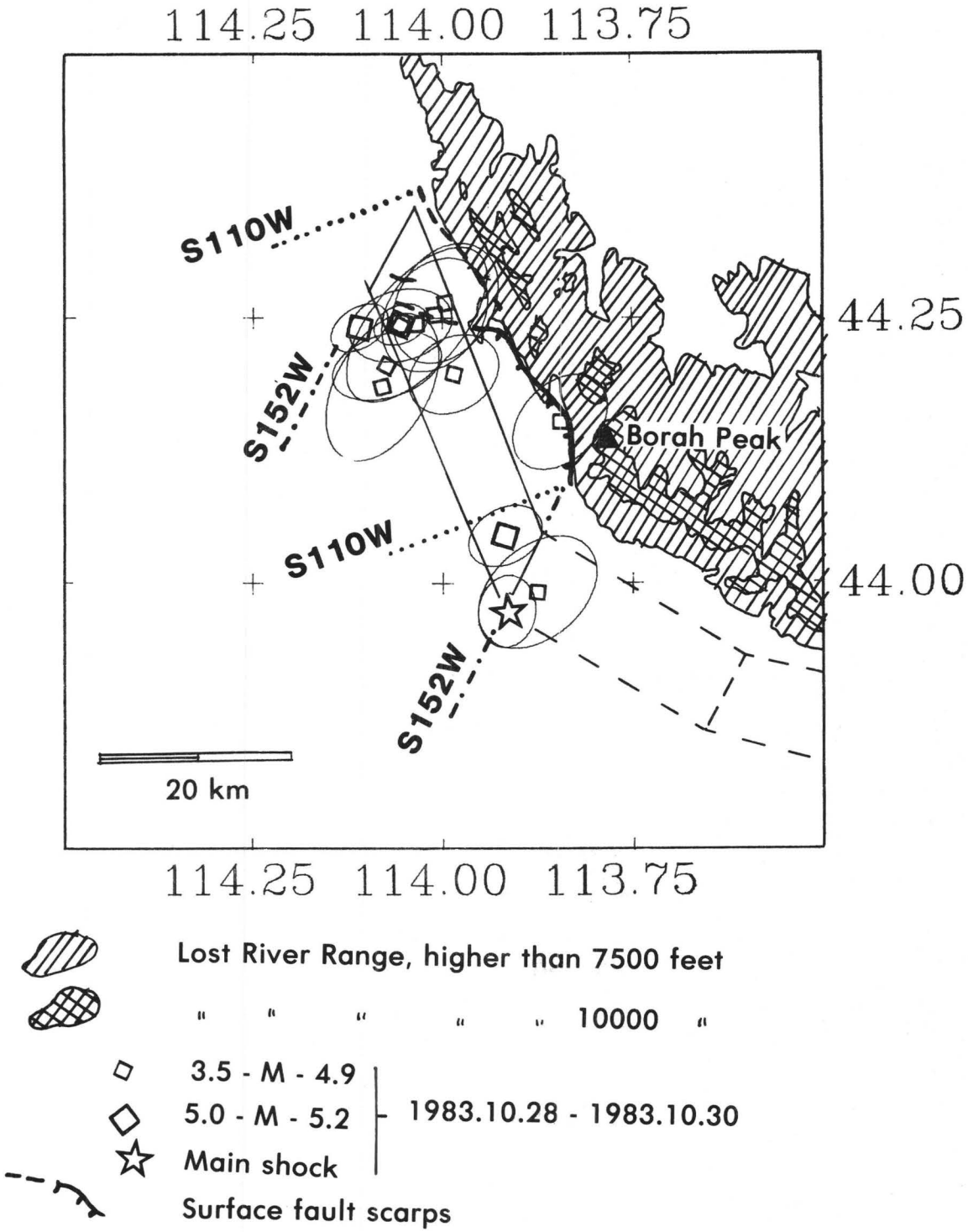

Figure 4. Map view of an idealized main-shock rupture plane that has two sides parallel to the zone of surface fault-scarp and two sides parallel to the slip vector of the Borah Peak earthquake. S110W is the azimuth of dip on the fault plane; S152W is the azimuth of slip. Dashed lines to the southeast of the main-shock rupture show how neighboring segments of the Lost River fault would appear if they were parallel to the local trend of the mountain front and if they had the same slip vector as the Borah Peak rupture.

"downdip"), but is instead well south of the downdip projection of the surface fault scarps (fig. 4). Furthermore, the entire zone of teleseismically recorded aftershocks occurring in the period 1983.10.28 - 1983.10.30 (henceforth called "early aftershocks") is located south of the downdip projection of the surface fault scarps. On the assumption that the positions of the mainshock and early aftershock hypocenters approximately outline the shape of the mainshock fault rupture, the above cited observations might be interpreted as evidence that the Borah Peak earthquake involved multiple rupture planes at depth that are grossly misrepresented by the fault scarps observed at the ground surface.

However, other data suggest that the Borah Peak earthquake resulted from slippage that was concentrated on a single, approximately planar, fault. The geodetic deformation associated with the earthquake is well-modeled by slippage on a single planar fault (Stein and Barrientos, 1985). Seismograms of body-waves imply a simple source-time function at long periods (Doser, 1985). The largest aftershock to the Borah Peak earthquake was two magnitude units smaller than the main shock (Table 1), suggesting that the main-shock rupture was not so geometrically complicated that it had to be accomodated by large motions on subsidiary faults. It is the purpose of this section to explain how the relative positions of the surface fault scarps and the early aftershock zone, rather than implying a severely contorted or segmented rupture zone at depth, might instead be a logical consequence of oblique slippage on a single planar surface.

Faulting during the Borah Peak earthquake was not purely dip-slip but contained a component of strike-slip motion (e.g. Crone and others, 1985; Doser, 1985) Although the principal zone of aftershocks is not downdip of the surface fault trace, it is located in a direction that is approximately downslip (azimuth S152W) of the surface fault traces (fig.3). Map projections of slip vectors plotted in figure 3 are for the main shock, and the aftershocks of 1951 UTC, October 28, and 2329 UTC, October 29. The projections plotted in figure 3 are the surface projections of rays extending from the hypocenter upslip to where they intersect with the ground surface. The fact that the rays all intersect at points several kilometers on the southwest side of the surface fault traces could be due to some combination of small errors (several kilometers) in the hypocenters, small errors (10 degrees) in the orientation of the focal mechanisms, and slight non-planarity of the fault between the hypocenters and the free surface.

There is a set of conditions that would require that the main-shock rupture plane be a parallelogram which has one pair of sides parallel to the surface trace of the Lost River fault and the other pair of sides parallel to the main-shock slip vector. The conditions may plausibly have been approximately satisfied in the case of the Borah Peak earthquake, so that the shape of the rupture would be approximately that of the parallelogram expected under ideal conditions. The ideal parallelogram is shown in figure 4 and would be expected on geometrical grounds if: 1, the entire Lost River fault zone were composed of a number of planar segments with different orientations, 2, the Borah Peak earthquake involved complete rupture of one of the segments, and 3, the Borah Peak segment were terminated on the north and south by intersection with adjacent segments of the Lost River fault that have the same slip vector as the Borah Peak segment. Condition 1 has been postulated for the Lost River fault on geomorphological evidence (Scott and others, 1985). Condition 2 is equivalent to the hypothesis of Schwartz and

others (1985) that the Borah Peak earthquake was a characteristic earthquake (Schwartz and Coppersmith, 1984) for the section of the Lost River fault west of Borah Peak. Condition 3 enables slippage to occur in the future on all segments of the Lost River fault without slippage on one segment truncating an adjacent segment and thereby locking it (Jackson and McKenzie, 1983). Equivalently, condition 3 would permit displacement on all segments without requiring the occurrence of subsidiary faulting in the hanging wall or footwall of the Lost River fault (King and Yielding, 1984). Condition 3 determines the shape of the fault surface; from elementary geometry, two non-parallel planes containing a common line (the slip vector in this case) will intersect at that line.

Seismic trends and association of epicenters with previously mapped faults

North-northwest trending seismic zones.

The 1983 Borah Peak earthquake occurred on the north-northwest trending Lost River fault. The system of Cenozoic normal faults of which the Lost River fault is a member extends to the northeast to the region of seismicity centered near 44.8N, 112.8W (fig. 1). Several of the north-northwest trending Cenozoic faults in this system were essentially aseismic during the period of study. Since the Lost River fault was also aseismic along most of its length during the two decades prior to the main shock (see section below entitled "Characteristics of regional seismicity in the two decades preceding the Borah Peak earthquake"), the lack of earthquake activity on other Cenozoic faults is no assurance that those faults will continue to remain quiescent.

The 70-km-long zone of epicenters that is approximately parallel to the Borah Peak aftershock zone, but displaced from it by 30 to 40 km to the southwest (fig.1), is not associated with any major mapped Cenozoic fault of which I am aware. I will refer to this zone as the White Cloud Peaks zone. Seismicity in the White Cloud Peaks zone during 1963-1983 occurred in episodes that were localized in both space and time; the whole zone was not uniformly active in any single year (fig. 5). Focal depths for most earthquakes in the zone are not well determined; the more reliably determined focal depths are similar to the upper-crustal depths of the Borah Peak sequence (see also discussion in the section above entitled "Methods of relocating hypocenters and recomputing magnitudes"). P-wave first motions observed by Smith and Sbar(1974) for the shock of 1963.9.11, 0208 UTC, mblg = 4.8, imply predominately normal faulting with nodal planes striking due east or southeast (fig. 5).

Possible north-northeast trending seismic zones.

The earthquakes of July 12, 1944, M(PAS) = 6.1, and February 14, 1945, M(PAS) = 6.0, were the largest instrumentally recorded earthquakes in Central Idaho prior to the Borah Peak earthquake of 1983. The epicenters of these shocks, together with epicenters of small shocks occurring in 1963-1983, may be viewed as defining a NNE-trending zone, here called the Seafoam zone, that extends from 44.35N, 115.15W to 44.80N, 115.00W (figure 6). There were rather detailed reports of intensity for the 1944 earthquake (Bodle, 1944) that

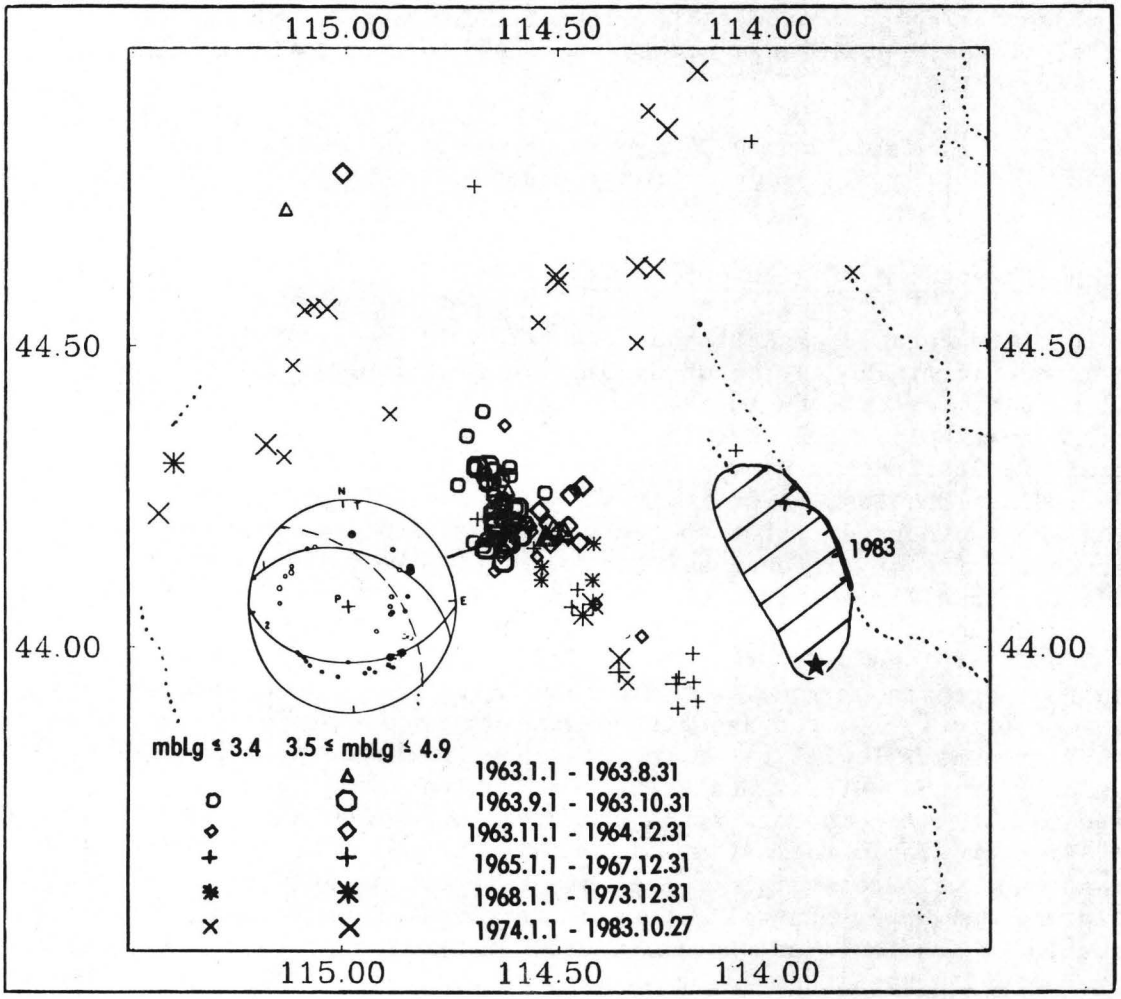

Figure 5. Temporal and spatial clustering of earthquakes in central Idaho. Only events with 90% confidence-ellipse semi-axes shorter than 15 km are plotted. The focal mechanism solution is that of Smith and Sbar (1974) (solid lines) for the earthquake of 1963.9.11, to which I have added another possible orientation of the north-dipping plane (dashed line).

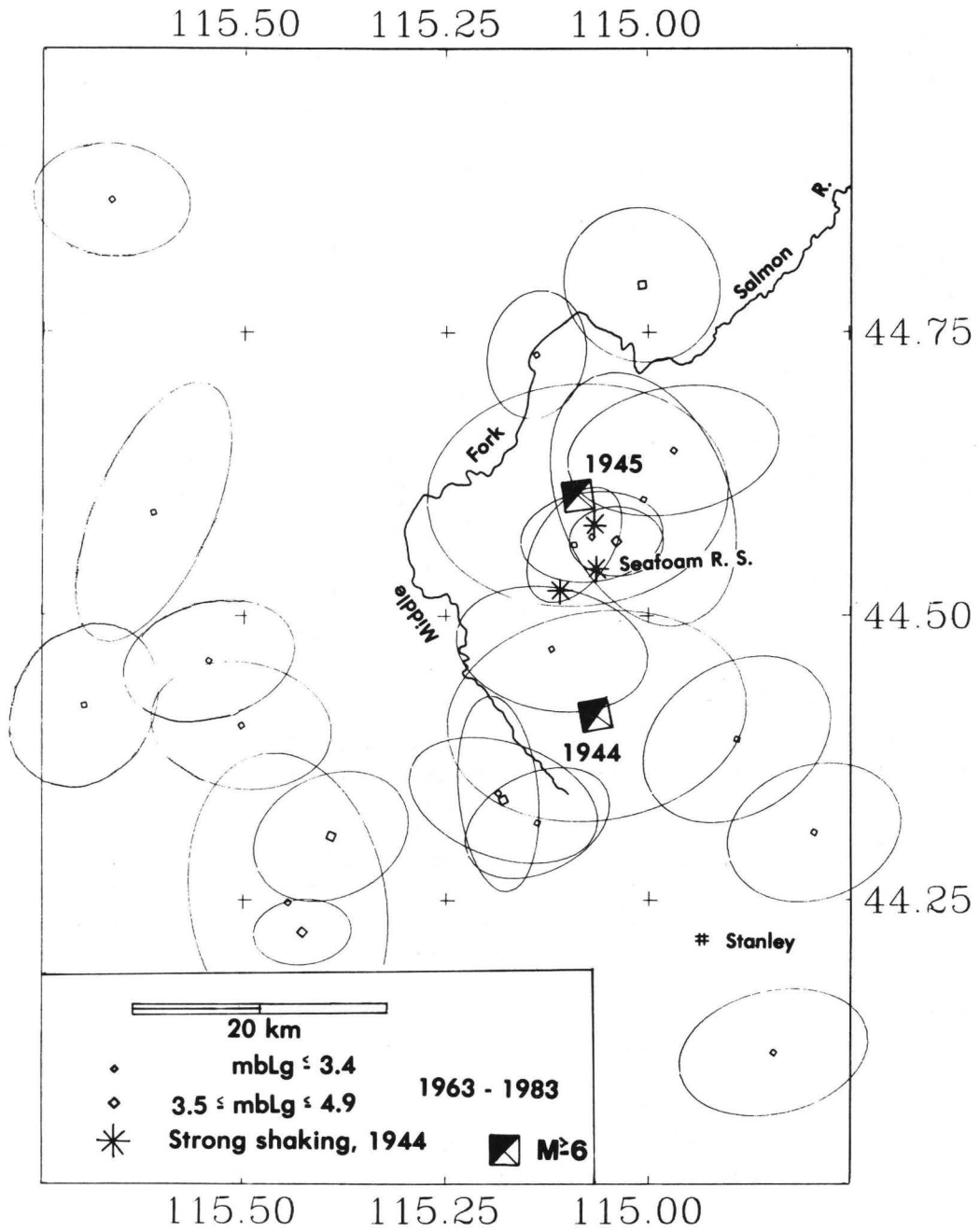

Figure 6. Seismicity in the Seafoam zone. Regions of strong shaking are sites of intensity VII in the earthquake of 1944.7.12 (Bodle, 1946).

indicate that the meizoseismal area of the earthquake lay in the region between the epicenters of the 1944 and 1945 shocks. These intensity data, and the relative positions and dates of the earthquakes, suggest that the 1944 earthquake ruptured toward the epicenter of the 1945 earthquake and that the 1945 earthquake occurred near the northern extremity of the 1944 fault as a delayed aftershock.

The epicenters of the 1944 and 1945 earthquakes were difficult to locate. In various attempts at locating the shocks with slightly different starting assumptions, I had their positions varying from the plotted positions (fig. 6) to positions that were west of the plotted positions by as much as 40 km. As the epicenters and origin times changed, they were always consistent with about 80 percent of the data and inconsistent with another 20 percent. The 90 percent confidence ellipses, which are constructed from the linearized equations of condition that are used in hypocenter determination algorithms (Flinn, 1965), grossly underestimate the size of the area in which the 1944 and 1945 epicenters could be moved, as a pair, without significantly increasing the variance of the residuals. The epicenters shown in figure 6 are those that are most consistent with the intensity data for the 1944 earthquake, and they are slightly more consistent with the arrival-time data than solutions further to the west. They are therefore preferred.

Another NNE-trending seismic zone in central Idaho may be interpreted from epicenters extending from 44.55N, 114.55W, to 45.00N, 114.15W (fig. 1). The zone is here called the Twin Peaks - Myers Cove zone, after geographic landmarks with which Smith and others (1985) associated two microearthquake sources in the zone. The strike of the Twin Peaks - Myers Cove zone is nearly parallel to the horizontal projection of the slip vector of the Borah Peak earthquake (fig. 1). One might speculate that the zone is a region of transcurrent faulting between the extensional terrane to the southeast, in which the Borah Peak earthquake occurred, and the relatively undeformed region to the west-northwest. On the other hand, the seismicity of the Twin Peaks section of the zone is spatially associated with a caldera (Smith and others, 1985), and Zollweg and Richins (1985) interpret first motions for the earthquake of 1984.3.24 in the Twin Peaks - Myers Cove zone as indicating normal faulting similar to that of the Borah Peak earthquake. These last results suggest that the Twin Peaks - Myers Cove seismic zone does not mark a single through-going fault.

Characteristics of regional seismicity in the two decades preceding the Borah Peak earthquake

A plot of magnitude versus cumulative frequency (fig.7) suggests that the set of regionally and teleseismically recorded shocks that I have relocated is nearly complete above magnitude 3.5 for the period from 1963 until the Borah Peak earthquake. All shocks of magnitude 3.5 and above that I have relocated for the period from 1963 through September 1983 have epicentral confidence ellipses smaller than 15 km and are therefore plotted in figure 1.

No regionally recorded earthquakes of magnitude 3.5 or larger were located within 25 km of the Borah Peak main shock in the period from January 1963 until the occurrence of the main shock. None of the incomplete sample of shocks smaller than magnitude 3.5 had minimum variance epicenters within 15 km of the Borah Peak main shock, although one such earthquake has a confidence ellipse on the epicentral coordinates that extends to the epicenter of the

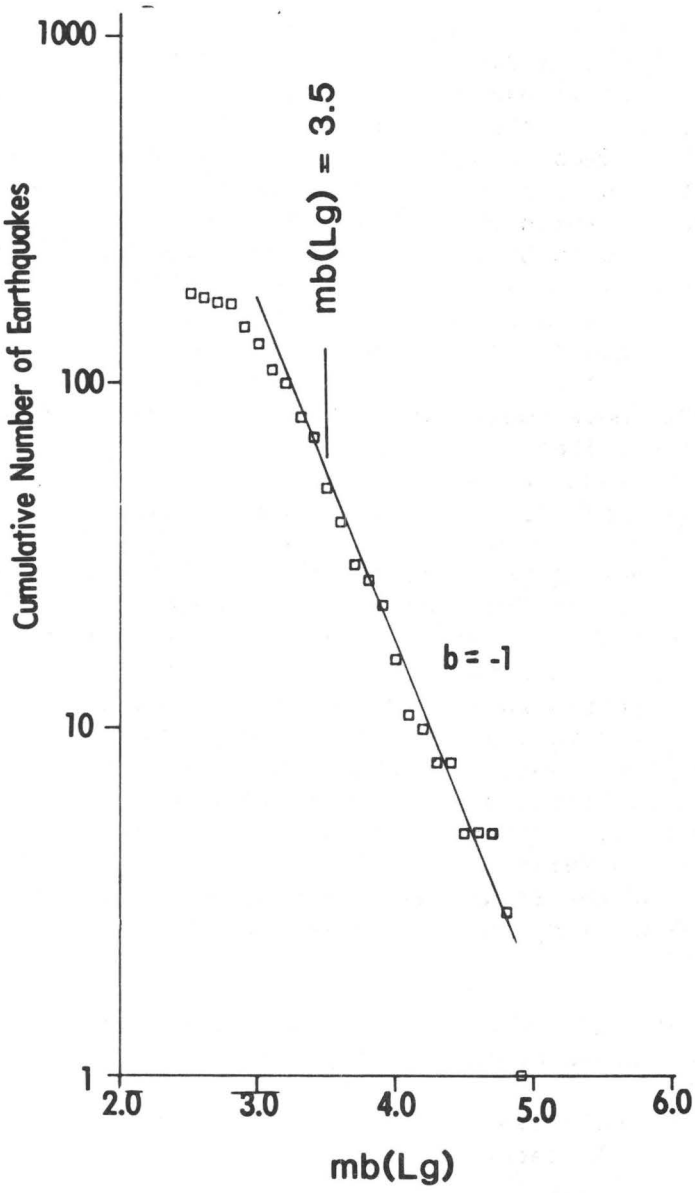

Figure 7. Magnitude(mb(Lg))-frequency relation for central Idaho excluding earthquakes east of longitude 113.5W for the period 1963-1983.10.27. Line with slope b = -1 has been fit through the data by inspection.

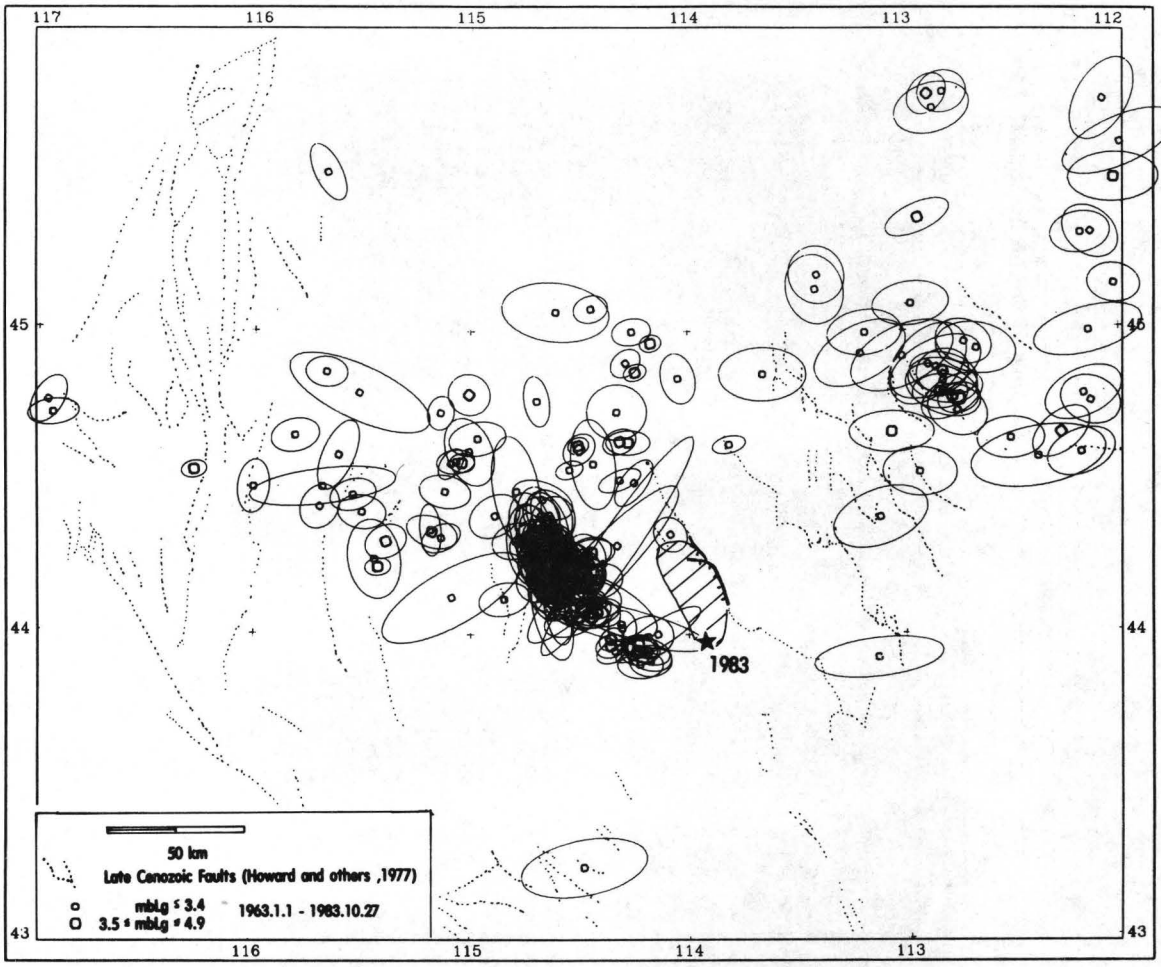

Figure 8. All regionally recorded epicenters that could be located with a precision of 50 km or better for the period 1963-1983.10.27.

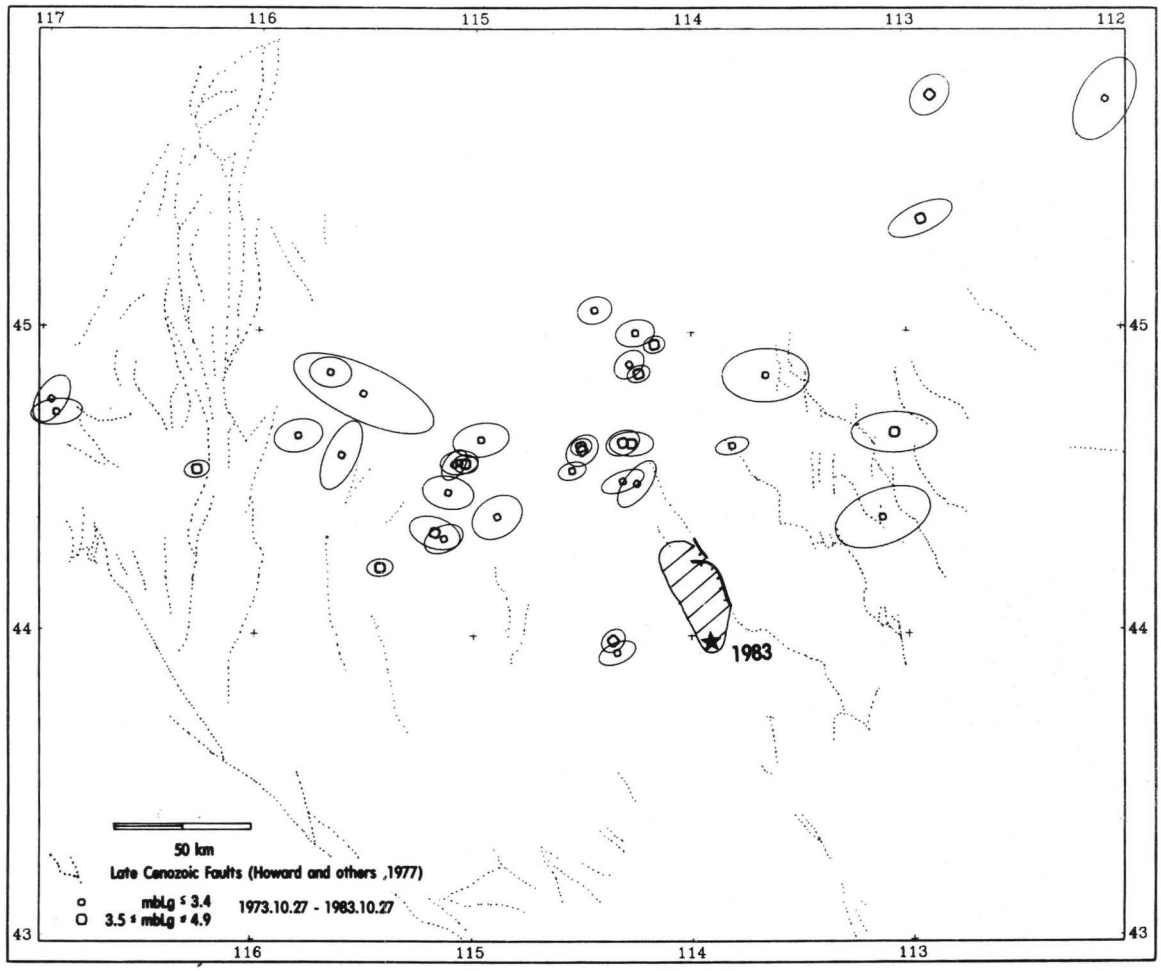

Figure 9. All regionally recorded epicenters that could be located with a precision of 50 km or better for the period 1973.10.27-1983.10.27.

main shock (figure 8). Other studies show that the vicinity of the Borah Peak hypocenter was aseismic down to magnitudes below 3.5 during sizeable periods before the main shock. King and Doyle(1982) found no shocks of magnitude 2 or greater within about 15 km of the Borah Peak epicenter for the period from October 1972 to June 1982; they found one shock of magnitude between 1 and 2 in the vicinity of the future main shock epicenter. Richins and others (1985) found no foreshocks of magnitude 2 or greater within 50 km of the surface rupture in the 2 months before the main shock.

Large Cenozoic normal faults occur at many locations in the Cordillera of the western United States, and many of these faults have been quiescent during the several decades for which instrumental seismicity data are available. With the occurrence of the Borah Peak earthquake on the Lost River fault, we have an example of a large normal fault that remained inaudible to regional seismographic stations right up to the occurrence of a major earthquake. By implication, other large normal faults may produce major earthquakes without first entering a period of increased small to moderate earthquake activity.

Epicenters of earthquakes in the two decades preceding the Borah Peak main shock did define the White Cloud Peaks zone of seismicity that was roughly parallel to the Borah Peak aftershock zone but offset from it by 30 to 40 km(figs. 1 and 8). The trend of the White Cloud Peaks zone suggests that it may have been caused by stresses of the same orientation as the stresses producing the Borah Peak earthquake; the P-wave first-motions reported by Smith and Sbar (1974) for one of the earthquakes are consistent with this possibility (fig.5). Most activity in the White Cloud Peaks zone occurred more than 10 years before the Borah Peak earthquake (figure 9) and the most intense activity occurred twenty years prior to the Borah Peak earthquake (fig. 5). The long time-interval between the occurrence of intense activity in the White Cloud Peaks zone and the occurrence of the Borah Peak earthquake notwithstanding, hypotheses of long-term precursory seismicity patterns in other parts of the world (Reyners, 1981) suggest that we not reject out-of-hand the possibility that the White Cloud Peaks seismicity was in some sense precursory to the Borah Peak earthquake.

Acknowledgments

I thank Susan Plymell and Jack Boatwright, USGS, and Bill Richins, University of Utah, for providing me with the locally recorded arrival times of Borah Peak aftershocks that were the basis for calibrating the absolute positions of the Central Idaho earthquakes. Thorough reviews by Walt Arabasz and Jim Taggart were most helpful.

References

Boatwright, John, 1985, Characteristics of the aftershock sequence of the Borah Peak, Idaho, earthquake determined from digital recordings of the events, in Workshop XXVIII on the Borah Peak Earthquake: USGS Open-File Report, in press.

Bodle, R.R.,1946, United States Earthquakes 1944, U.S. Coast and Geodetic Survey Serial No. 682, U. S. Department of Commerce, 43p.

Burdick, L.J., and Helmberger, D.V.,1978, Upper mantle P velocity structure of the western United States: Jour. Geophys. Res., v. 83, p. 1699-1712.

Crone, A.J., Machette, M.N., Bonilla, M.G., Lienkaemper, J.J., Bucknam, R.C., Pierce, K.L., and Scott, W.E., 1985, Characteristics of surface faulting accompanying the Borah Peak earthquake, Central Idaho, in Workshop XXVIII on the Borah Peak Earthquake: USGS Open-File Report, in press.

Dewey, J.W., 1979, A consumer's guide to the instrumental determination of hypocenters, in Hatheway, A.W., and McClure, C.R., Jr., eds., Geology in the siting of nuclear power plants: Geological Society of America Reviews in Engineering Geology, v. IV, p.109-117.

Dewey, J.W. ,1983, Relocation of instrumentally recorded pre-1974 earthquakes from the South Carolina region: in Gohn, G.S., ed., Studies related to the Charleston, South Carolina, earthquake of 1886--tectonics and seismicity: U.S. Geological Survey Professional Paper 1313, Q1 - Q9.

Doser, D.I., 1985, The 1983 Borah Peak, Idaho, and the 1959 Hebgen Lake, Montana earthquakes: models for normal fault earthquakes in the Intermountain Seismic Belt, in Workshop XXVIII on the Borah Peak Earthquake: USGS Open-File Report, in press.

Dziewonski, A.M., Chou, T.A., and Woodhouse, J.H., 1981, Determination of earthquake source parameters from waveform data for studies of global and regional seismicity: Jour. Geophys. Res., 86, p. 2825-2852.

Espinosa , A.E., 1981, Seismic wave attenuation studies in conterminous United States, in Summaries of Technical Reports, vol XII, Open File Rep. 81-833, U.S. Geol. Survey, Menlo Park, Calif., 1981.

Evernden, J.R., 1969, Precision of epicenters obtained by small numbers of world-wide stations: Bull. Seism. Soc. Am., 59, p.1365-1398.

Flinn, E.A., 1965, Confidence regions and error determinations for seismic event location: Reviews of Geophysics, 3, p.157-185.

Herrin, Eugene, and Taggart, James, 1962, Regional variations in Pn velocity and their effect on the location of epicenters, Bull. Seism. Soc. Am., 52, p. 1037-1046.

Howard, K.A., and others, 1978, Preliminary map of young faults in the United States as a guide to possible fault activity: U. S. Geological Survey Miscellaneous Field Studies Map MF-916, scale 1:5,000,000.

Jackson, J., and McKenzie, D., 1983, The geometrical evolution of normal fault systems: J. Struct. Geol., 5, p.471-482.

King, Geoffrey, and Yielding, Graham, 1984, The evolution of a thrust fault system: processes of rupture initiation, propagation and termination in the 1980 El Asnam (Algeria) earthquake: Geophys. J. R. astr. Soc., v.77. p. 915-933.

King, J.J., and Doyle, T.E., 1982, Earthquake catalog for the eastern Snake River Plain region Idaho (43.0 deg. - 44.5 deg. N, 111.5 deg. - 114.0 deg. W) October 1972 - June 1982, Informal report EGG-PHYS-6145, prepared for the U.S. Department of Energy under DOE contract no. DE-AC07-76ID01570, 45 pp.

Nuttli. O.W.,1973, Seismic wave attenuation and magnitude relations for eastern North America: Jour. Geophys. Res., 78, p.876 - 885.

Pho, Hoang-Trong, and Behe, L., 1972, Extended distances and angles of incidence of P Waves, Bull. Seism. Soc. Am., 62, p. 885 - 902.

Pitt, A.M., Weaver, C.S., and Spence, William, 1979, The Yellowstone Park earthquake of June 30, 1975: Bull. Seism. Soc. Am., 69, p. 187 - 205.
Poppe, B.P., Naab, D.A., and Derr, J.S., 1978, Seismographic station codes and characteristics: U.S. Geological Survey Circular 791, 171 pp.
Reyners, Martin, 1981, Long- and intermediate-term seismic precursors to earthquakes -- state of the art: in Simpson and Richards (eds), Earthquake Prediction, An International Review, American Geophysical Union, p. 1 - 19.
Richins, W.D., Smith, R.B., Langer, C.J., Zollweg, J.E., King, J.J., and Pechmann, J.C., 1985, The Borah Peak, Idaho, earthquake: relationship of aftershocks to the main shock, surface faulting, and regional tectonics, in Workshop XXVIII on the Borah Peak Earthquake: USGS Open-File Report, in press.
Schwartz, D.P., and Coppersmith, K.J., 1984, Fault behavior and characteristic earthquakes: examples from the Watsatch and San Andreas faults: Jour. Geophys. Res., v.89, p. 5681-5698.
Schwartz, D.P., Page, W.D., and Taylor, C.L., 1985, Significance of the 1983 Borah Peak earthquake for the evaluation of fault behavior and earthquake recurrence in the Great Basin, in Workshop XXVIII on the Borah Peak Earthquake: USGS Open-File Report, in press.
Scott, W.E., Pierce, K.L., Hait, M.H., 1985, Quaternary tectonic setting of the 1983 Borah Peak earthquake, central Idaho, in Workshop XXVIII on the Borah Peak Earthquake: USGS Open-File Report, in press.
Sheriff, S.D., and Stickney, M.C., 1984, Crustal structure of southwestern Montana and east-central Idaho: results of a reversed refraction line: Geophysics Research Letters, 11, p.299-302.
Singh, Sudarshan, and Herrmann, R.B., 1983, Regionalization of crustal coda Q in the continental United States: Jour. Geophys. Res., v.88, p. 527-538.
Sipkin, S.A., 1982, Estimation of earthquake source parameters by the inversion of waveform data: synthetic seismograms: Physics of the Earth and Planetary Interiors, 30, p. 242-259.
Smith, R.B., and Sbar, M.L., 1974, Contemporary tectonics and seismicity of the western United States with emphasis on the Intermountain seismic belt: Geol. Soc. Am. Bull. , 85, p.1205-1218.
Smith, R.B., Richins, W.D., Doser, D.I., Eddington, P.K., Leu, L.L., and Chen, G., 1985, The Borah Peak earthquake: seismicity, faulting, kinematics, and tectonic mechanism, in Workshop XXVIII on the Borah Peak Earthquake: USGS Open-File Report, in press.
Stein, R.S., and Barrientos, S.E., 1985, The Borah Peak, Idaho,earthquake: geodetic evidence for deep rupture on a planar fault, in Workshop XXVIII on the Borah Peak Earthquake: USGS Open-File Report, in press.
U.S. Geological Survey, 1984, Preliminary Determination of Epicenters, Monthly Listing, October 1983, 20 pp.
Zollweg, J.E., and Richins, W.D., 1985, Later aftershocks of the Borah Peak, Idaho, earthquake and related activity in the Central Idaho Seismic Zone, in Workshop XXVIII on the Borah Peak Earthquake: USGS Open-File Report, in press.

Table 1. Catalog of central Idaho earthquakes of M = 6.0 or larger, 1944-1962, and with m = 4.0 or larger, 1963-March, 1984. Asterisk by depth indicates that depth was fixed in computation. Lg denotes mb(Lg) magnitude.

DATE	TIME	LAT (N)	LONG (E)	DEPTH	MAG	90% CONFIDENCE ELLIPSOID	SEMI-LENGTH	TREND	PLUNGE
1944.07.12	193020.7	44.412	-115.063	10.0*	6.1 PAS	MAJOR AXIS	14.8	81.1	0.0
						MINOR AXIS	10.2	171.1	0.0
						**********	0.0	0.0	0.0
1945.02.14	3 111.3	44.607	-115.087	10.0*	6.0 PAS	MAJOR AXIS	14.8	85.8	0.0
						MINOR AXIS	10.9	175.8	0.0
						**********	0.0	0.0	0.0
1963.01.06	18 743.5	44.654	-112.274	9.3	4.3 Lg	MAJOR AXIS	24.2	40.9	62.6
						INTER AXIS	10.6	-100.7	22.2
						MINOR AXIS	7.3	162.8	15.4
1963.01.27	152443.8	44.190	-114.528	11.4	4.8 Lg	MAJOR AXIS	12.2	169.0	65.0
						INTER AXIS	8.1	-98.5	1.2
						MINOR AXIS	4.5	-7.9	25.0
1963.02.01	163856.1	44.197	-114.486	8.1	4.4 Lg	MAJOR AXIS	53.8	104.2	87.7
						INTER AXIS	11.1	-1.1	0.6
						MINOR AXIS	8.2	-91.1	2.3
1963.09.11	2 843.7	44.177	-114.615	8.1	4.8 Lg	MAJOR AXIS	10.3	121.4	70.2
						INTER AXIS	5.2	-87.2	17.6
						MINOR AXIS	3.9	5.7	8.9
1963.09.12	62348.9	44.181	-114.621	9.2	4.7 Lg	MAJOR AXIS	12.9	129.5	75.0
						INTER AXIS	5.8	-105.5	8.7
						MINOR AXIS	4.5	-13.6	12.1
1963.09.14	1558 1.6	44.147	-114.629	12.1	4.4 Lg	MAJOR AXIS	11.4	156.1	72.4
						INTER AXIS	6.0	-93.3	6.4
						MINOR AXIS	4.1	-1.4	16.3
1963.10.16	153629.1	44.279	-114.666	4.4	4.0 Lg	MAJOR AXIS	25.0	54.7	78.7
						INTER AXIS	6.9	-63.3	5.4
						MINOR AXIS	6.4	-154.3	10.0
1964.01.06	1935 7.9	44.272	-114.443	10.0*	4.2 Lg	MAJOR AXIS	8.3	83.5	0.0
						MINOR AXIS	4.9	173.5	0.0
						**********	0.0	0.0	0.0
1964.01.09	31056.4	44.257	-114.472	24.4	4.0 Lg	MAJOR AXIS	29.5	93.7	82.8
						INTER AXIS	10.0	-15.6	2.4
						MINOR AXIS	7.7	-105.8	6.8
1964.02.08	622 7.5	44.206	-114.477	16.7	4.1 Lg	MAJOR AXIS	23.4	74.6	76.0
						INTER AXIS	7.0	-60.1	10.0
						MINOR AXIS	6.3	-151.8	9.8
1965.01.06	2 120.7	44.772	-112.746	10.0*	5.0 Lg	MAJOR AXIS	7.7	77.3	0.0
						MINOR AXIS	5.5	167.3	0.0
						**********	0.0	0.0	0.0
1967.12.23	163414.0	43.943	-114.229	23.4	4.0 Lg	MAJOR AXIS	25.7	109.3	86.0
						INTER AXIS	7.6	-97.0	3.6
						MINOR AXIS	5.5	-6.9	1.8
1969.04.26	104153.1	44.058	-114.444	18.2	4.9 Lg	MAJOR AXIS	11.9	-65.4	84.8
						INTER AXIS	7.4	66.9	3.5
						MINOR AXIS	4.3	157.2	3.9
1969.05.05	7 910.0	44.076	-114.420	16.1	4.0 Lg	MAJOR AXIS	17.6	164.5	82.3
						INTER AXIS	9.9	-103.7	0.2
						MINOR AXIS	4.9	-13.7	7.7
1970.12.05	25415.2	44.306	-115.392	14.2	4.0 Lg	MAJOR AXIS	29.4	31.7	85.2
						INTER AXIS	9.0	-111.4	3.8
						MINOR AXIS	6.7	158.4	2.9
1976. 7.26	104528.2	44.962	-114.171	11.1	4.2 Lg	MAJOR AXIS	15.8	-134.9	84.7
						INTER AXIS	4.5	84.6	4.1
						MINOR AXIS	3.6	-5.7	3.4
1977.11.27	92555.6	44.537	-116.276	8.9	4.4 Lg	MAJOR AXIS	10.8	-128.1	87.9
						INTER AXIS	5.4	78.6	1.9
						MINOR AXIS	3.6	-11.4	1.0
1978.10.29	134645.6	44.866	-114.243	11.9	4.7 Lg	MAJOR AXIS	21.9	83.5	88.2
						INTER AXIS	4.9	-110.7	1.8
						MINOR AXIS	3.5	-20.7	0.5
1983.10.28	14 6 6.5	43.974	-113.916	14.0	7.3 MS	MAJOR AXIS	5.5	147.3	67.3
						INTER AXIS	3.6	26.0	12.3
						MINOR AXIS	2.6	-68.2	18.8
1983.10.28	195125.0	44.045	-113.918	13.1	5.2 MS	MAJOR AXIS	5.5	83.3	59.1
						INTER AXIS	3.7	-142.1	22.8
						MINOR AXIS	2.6	-43.4	19.7
1983.10.29	232911.8	44.244	-114.055	9.6	5.0 MS	MAJOR AXIS	3.1	77.8	23.7
						INTER AXIS	2.4	-176.9	30.9
						MINOR AXIS	1.0	-42.8	49.2
1983.10.29	2339 5.4	44.241	-114.109	10.7	5.0 MS	MAJOR AXIS	3.3	60.4	9.1
						INTER AXIS	2.5	156.5	33.4
						MINOR AXIS	1.0	-42.9	55.0
1983.10.30	12451.3	44.095	-113.958	12.6	4.3 mb	MAJOR AXIS	3.0	70.5	13.4
						INTER AXIS	2.1	162.3	7.3
						MINOR AXIS	1.3	-79.9	74.7
1983.11.06	21 448.6	44.149	-113.954	11.3	4.3 mb	MAJOR AXIS	2.8	-135.3	0.2
						INTER AXIS	2.2	134.7	8.9
						MINOR AXIS	1.7	-43.8	81.1
1983.12.12	45536.5	44.413	-114.086	6.6	4.5 mb	MAJOR AXIS	7.0	81.4	65.9
						INTER AXIS	5.5	-136.9	19.3
						MINOR AXIS	2.7	-42.0	13.8
1983.12.27	122129.3	44.255	-114.074	9.0	4.4 mb	MAJOR AXIS	7.9	53.1	35.3
						INTER AXIS	6.3	-154.7	51.3
						MINOR AXIS	2.9	-46.9	13.8
1984.01.24	21 758.1	44.072	-114.403	10.0*	4.5 mb	MAJOR AXIS	7.2	-145.4	0.0
						MINOR AXIS	3.3	124.6	0.0
						**********	0.0	0.0	0.0
1984.03.24	0 747.5	44.774	-114.359	5.4	4.2 mb	MAJOR AXIS	12.2	156.0	82.6
						INTER AXIS	8.4	55.1	1.4
						MINOR AXIS	4.4	-35.0	7.2

THE 1983 BORAH PEAK, IDAHO EARTHQUAKE: RELATIONSHIP OF AFTERSHOCKS TO THE MAIN SHOCK, SURFACE FAULTING, AND REGIONAL TECTONICS

by

W. D. Richins, R. B. Smith
Department of Geology & Geophysics,
University of Utah, Salt Lake City, UT 84112-1183

C. J. Langer
U.S. Geological Survey,
Denver, CO 80225

J. E. Zollweg
Geophysics Program
University of Washington, Seattle, WA 98195

J. J. King
EG&G Inc., Idaho Falls, ID 83415

J. C. Pechmann
Department of Geology & Geophysics,
University of Utah, Salt Lake City, UT 84112-1183

Abstract

The October 28, 1983 Borah Peak, Idaho earthquake (M_s = 7.3) occurred in an area of low historic seismicity within east-central Idaho along a segment of the Lost River fault active during the Holocene. A dense network of portable short period seismographs (up to 45 stations, station spacings of 2 to 10 km) was installed beginning several hours after the main shock and operated for 22 days. In addition to records from the portable instrumentation, data from permanent seismograph stations operating in Idaho, Utah, Montana, Oregon, Washington, and Wyoming, provide a good regional data base. No foreshock activity above magnitude 2.0 (M_L) was detected for the two month period preceding the main shock. The distribution of 421 aftershocks of $M_L > 2$ defines an epicentral pattern, 75 km x 15 km, trending north-northwest parallel to the surface rupture but displaced laterally southwest by 5 to 10 km. The epicenter of the main shock is $\sim$14 km south-southwest of the end of surface faulting. This relationship suggests unilateral rupture propagating to the northwest. Aftershocks extend to depths of approximately 16 km and in the southeastern portion of the aftershock pattern define a zone, dipping approximately 45° SW, that intersects the surface near the fault scarp. The entire aftershock zone as

observed during the first 3.5 weeks was active shortly after the main shock occurred. Fault plane solutions indicate predominantly normal faulting with varying components of strike slip.

Introduction

The October 28, 1983 Borah Peak, Idaho earthquake occurred along a segment of the Lost River fault, a major normal fault in central Idaho exhibiting Quaternary surface rupturing events. The magnitude 7.3 (M_s, NEIS determination) main shock was accompanied by approximately 36 km of surface faulting with maximum vertical displacements of 2.7 m (Crone et al., 1985) and resulted in 2 deaths and approximately $12.5 million damage (Stover, 1984). A dense network (station spacings of 2 to 10 km) of portable short-period seismographs was installed beginning approximately seven hours after the main shock to provide aftershock coverage. In addition to records from the portable instrumentation, data from permanent seismographs in Idaho, Utah, Montana, Oregon, Washington, and Wyoming provide a good regional data base.

Figure 1 shows the location of the Borah Peak, Idaho earthquake in relation to the Intermountain seismic belt (ISB) which trends generally north-south through western Montana, Yellowstone Park, southeast Idaho, and central Utah. The Borah Peak, Idaho earthquake occurred west of one of the most active parts of the ISB in an area of very low historical seismicity, and east of an active portion of central Idaho near Stanley (see also Dewey, 1985). The epicentral zone is east of the Idaho Batholith and northwest of the Snake River Plain, in an area of northwest-trending Cenozoic faulting with Basin and Range type structure. Faults with Quaternary and Holocene displacement (Hait, M. A., Jr., 1984, personal communication; Witkind, 1975) in the vicinity of the 1983 earthquake are shown in Figure 2.

Mapping of the surface faulting accompanying the Borah Peak, Idaho earthquake was done primarily by U.S. Geological Survey geologists (see Figure 2). Crone et al., (1985) measured maximum vertical displacements (throw) of 2.7 m with an average of 0.8 m. They also measured a component of left-lateral fault slip averaging 17% of the dip-slip component. A trench across the Lost River fault was excavated prior to the 1983 earthquake by Hait and Scott (1978) who conclude that at least one and possibly multiple Holocene surface rupturing events have occurred near Willow Creek (Double Springs Pass Road).

Velocity Models

Refraction profiles in the vicinity of Lost River Valley (Figure 2) provided local velocity structure of the crust and upper mantle. Profile 7 is an unreversed profile shot in 1978 as part of the Yellowstone-Snake River Plain project (Sparlin et al., 1982; and unpublished University of Utah data) with station spacings of 3 to 5 km. The northwest portion of profile 7 extends into Lost River Valley, northwest of Mackay, Idaho to within 15 km of the location of the main shock. Data to the southeast in profile 7 extend into the eastern Snake River Plain and were used as a

constraint on velocity at mid-crustal depths.

Profile 5 is a detailed, reversed profile shot in 1980 (Elbring, 1984; and unpublished University of Utah data) with station spacings of approximately 1 km. This profile is located 35 km northeast of Lost River Valley. The velocity model derived from profile 5 (Elbring, 1984) was used as a starting model for interpreting profile 7.

Sheriff and Stickney (1984) recorded a 250 km long reversed profile using quarry blasts near Challis, Idaho and Butte, Montana (Figure 2, profile A). Station spacings were approximately 25 km. Results from this profile were used to model the velocity of the upper mantle.

Figure 3a shows a record section for profile 7 with a reducing velocity of 6 km/sec. Theoretical travel time curves for our interpreted velocity model in Figure 3b are also shown on the record section. In general, the velocity structure for the top 18 km of crust was determined from profile 7. The velocity structure for the crust below 18 km was taken from a model for the area northwest of the Snake River Plain (Sparlin et al., 1982). The velocity of the uppermost mantle, 8.0 km/sec, was taken from Sheriff and Stickney (1984). We placed the Moho (crust-mantle boundary) at a depth of 40 km in our model. With this Moho depth, our model and the model of Sheriff and Stickney both give similar arrival times for refracted waves from the Moho, even though the crust in Sheriff and Stickney's model is only 33 km thick. The reason for this is that the crust in Sheriff and Stickney's model has a uniform velocity of 5.9 km/sec whereas our model has significantly higher velocities than this throughout the lower crust. The velocity model shown in Figure 3b was used for all subsequent earthquake data processing for the Borah Peak, Idaho earthquake sequence. The surface datum is 2000 m.

Search for Foreshock Activity

Analog and digital records from the Idaho National Engineering Laboratory network in southeastern Idaho (Δ = 70 to 210 km, 5 stations) and analog records from the Boise State University network in southwestern Idaho (Δ = 155 to 245 km, 3 stations) were examined in detail for the two month period prior to the main shock in order to identify and locate any foreshock activity. No foreshocks within 50 km of the surface rupture above the estimated detection threshold of magnitude 2.0 (M_L) were detected during this two month period. Dewey (1985), in an examination of regionally recorded earthquakes in central Idaho, reports that no earthquakes above magnitude 3.5 have occurred within 25 km of the 1983 main shock epicenter since at least 1963.

Calibration of Regional Network

Arrival time data from 23 regional stations (Δ <650 km) were collected for the main shock, the first 24 hours of aftershocks ($M_L \geq 2.5$), and six well-located master events. Data from four local stations (Δ <50 km) were available for some of the later events during the first 24 hours as well as the master events. The master events (see Figure 8) were aftershocks

located with the portable network with magnitudes of 3.5-4.5 (M_L), 20-25 local recording stations, maximum azimuthal gaps of approximately 80°, and at least one station within 4 km of the epicenter. All earthquake locations for this study were computed using the program HYPOINVERSE (Klein, 1978). Data from the 27 calibrated stations were not used in locating the master events. Average P-wave delays for each regional station determined from travel time residuals (observed travel time minus calculated) for the master events are shown in Figure 4. Positive delays indicate P-wave arrival times at specific stations that are late with respect to the velocity model. These delays are interpreted to be due, in part, to lateral velocity variations in the crust, particularly for raypaths across the Snake River Plain.

Reduced travel time plots for a sample master event are shown in Figure 5. Figure 5a illustrates the excellent fit of the P-arrival data for the local portable network to the velocity model. Figure 5b is the expanded travel time plot out to 650 km. Large average delays of up to +2.60 sec are indicated for some regional stations (Δ = 120 to 650 km).

Figure 6 is a reduced travel time plot for the main shock located using the station delays applied to data from the regional network and a fixed focal depth of 16 km (Doser, 1984). After the delays were applied, the regional station data shows a good fit to the velocity model with P-wave residuals less than $\pm$1.1 sec.

Location of Main Shock and Early Aftershocks

Figure 7 shows the distribution of earthquake activity during the first 24 hours after the main shock. A total of 48 earthquakes ($M_L \geq 2.5$) were locatable during this period. Records for most regional stations were saturated during the first hour following the main shock preventing complete detection of events with magnitudes less than 4.0 (M_L) during the one hour period. The 48 earthquakes were located using the calibrated regional network and data, where available, from four calibrated local stations installed within the aftershock zone during the first 24 hours (see Figure 4). The focal depth of the main shock was fixed at 16 km. The focal depths of the 47 aftershocks were fixed at 10 km. The largest aftershock (M_L = 5.8) during this period occurred approximately six hours after the main shock. Location and magnitude data are listed in Table 1.

Allowing for as much as 5 to 10 km of error in the location of the main shock, it is clear that the epicenter is south of the surface faulting suggesting unilateral rupture propagating to the northwest. Epicenters of the main shock and early aftershocks define a 10 to 15 km wide zone trending north-northwest parallel to the surface rupture. The northeast boundary of the aftershock zone is located approximately 3 to 5 km southwest of the surface break. The main shock epicenter and all but three of the aftershocks located during the first 24 hours lie within a parallelogram whose northeast edge is nearly coincident with the surface break (dashed lines, Figure 7). This suggests that this parallelogram may represent the surface projection of the primary fault rupture.

Local Network Configuration and Magnitude Determination

To examine aftershock activity in detail, a local network of portable seismographs was established surrounding the surface rupture within several hours after the main shock. At least 75 sites were occupied during the period October 28 to November 19, 1983 (Figure 8). Approximately 70% of these stations were operational at any one time. The instruments were installed in a cooperative effort by the University of Utah, U.S. Geological Survey, Boise State University, Idaho National Engineering Laboratory, University of Washington, and the Montana Bureau of Mines and Geology.

An attempt was made to locate all events with magnitudes of 2.5 (M_L) and greater using data from the local network (Δ <100 km) during the period October 29, 1983 at 17:00 UTC to November 19, 1983 at 14:00. Preliminary magnitudes were determined using Wood-Anderson data from the Salt Lake City (SLC) and Dugway (DUG), Utah stations for earthquakes above M_L 3.6. Magnitudes for smaller events were estimated using total signal durations on stations HPI and/or TMI of the Idaho National Engineering Laboratory network. Location and magnitude data for the largest shocks are listed in Table 1.

Distribution of Aftershocks

The distribution of 374 aftershocks located using the local network (Figure 9) shows an aftershock zone covering an area of approximately 75 km x 15 km trending north-northwest parallel to the surface rupture but displaced laterally southwest by 5 to 10 km. Intense clustering is evident near the western splay of the surface rupture. The two largest aftershocks of the sample period with magnitudes (M_L) 5.8 and 5.4 were located within this cluster (Figure 9). Few aftershocks were located within 5 to 10 km of the main shock. The aftershock zone extends about 15 km beyond the northwest end of the surface break and 25 km beyond the southeast end of the break. However, the intensity of the aftershock activity is notably higher along the central 30 to 35 km long portion of the aftershock zone immediately adjacent to the surface rupture.

Figure 10 shows vertical cross sections taken perpendicular to the strike of the aftershock zone and surface rupture. The depth shown for the main shock, 16 $\pm$ 4 km, was determined by Doser (1984) from body-wave teleseismic waveform modeling. Cross section A-A' crosses the western splay of the surface rupture and shows a complex distribution of foci with depth. Cross sections B-B' and C-C' show a concentration of aftershock hypocenters within a tabular zone dipping to the southwest. The projection of a plane extending downward at $\sim 45^{\circ}$ dip from the surface break (heavy lines on cross sections) passes close to the upper edge of the envelope of hypocenters and through the main shock hypocenter. This constitutes evidence that the Borah Peak earthquake occurred along a fault plane with an average dip of $\sim 45^{\circ}$ to the southwest from the surface fault, in agreement with the geodetic data (Stein and Barrientos, 1985).

The space-time distribution for all aftershocks located in this study is shown in Figure 11a, a plot of earthquake distribution along the strike

of the aftershock zone versus time. Note the absence of any detectable foreshock activity during the four days prior to the main shock shown in Figure 11a. Figure 11b shows the location and amount of surface displacement (vertical throw) as determined by Crone et al., (1985). The depth distribution along the strike of the aftershock zone is shown in Figure 11c. The majority of the aftershocks occur at depths between 4 and 12 km.

Virtually the entire aftershock zone became active shortly after the main shock (Figure 11a). Note that earthquakes during the first hour following the main shock were not locatable due to saturated records at the regional stations. The northwestern portion of the aftershock zone (see Figure 11a) exhibited an increase in activity beginning about mid-day on November 7, 1983. The lack of earlier activity in this area may be the result of limited station coverage. An intense cluster of activity began in this area in early December, 1983 (see Zollweg and Richins, 1985). Limited activity is evident in Figure 11 for the southeastern portion of the aftershock zone. Although Figure 11 shows some time and spacial clustering of aftershock activity, there is no clear evidence for migration during the 3.5 weeks following the main shock. However, the events over magnitude 5.0 show a systematic progression from southeast to northwest (Figure 12). Included in this figure is the August 22, 1984 aftershock (M_L=5.8) located with the calibrated regional network (Zollweg and Richins, 1985). As noted previously, few aftershocks occurred in the immediate vicinity (5 to 10 km) of the main shock, which suggests that the rupture initiated with a clean fault break near the location of the main shock.

Focal Mechanisms

Single-event, lower-hemisphere focal mechanisms for seven arbitrarily selected aftershocks are shown in Figures 13 and 14. The magnitudes (M_L) for these events vary from 2.8 to 3.8 with depths ranging from 7 to 12 km. The map locations of these mechanisms are shown in Figure 15.

The main shock mechanism (Figure 15; from Doser, 1984) shows predominantly normal faulting along a preferred fault plane dipping 45° to 53° SW with a significant component of left-lateral motion. The strike of the preferred fault plane is consistant with the strike of the surface rupture. Focal mechanisms 3, 5, 6 and 7 (Figures 13 and 14) also show predominantly normal faulting with a preferred fault plane striking NNW to NW, in good agreement with the strike and dip of observed surface faulting. Focal mechanism 4 (Figure 13) shows normal faulting on more nearly E-W striking planes. Focal mechanisms 1 and 2 (Figure 13), coincidentally for the two deepest earthquakes selected, have nearly pure strike slip solutions on N-S or W to WNW trending planes. Focal mechanisms 1, 2 and 4 suggest that some aftershock activity occurred on subsidiary structures at depth and cannot be directly associated with the main rupture plane.

Conclusions

The Borah Peak, Idaho earthquake occurred along a segment of a major normal fault zone with evidence of Holocene displacement. No foreshock activity above magnitude 2 was detected for at least two months prior to

the main shock. The main shock and aftershocks were located within an areal zone 75 km in length and 10-15 km in width offset laterally by 5 to 10 km from the surface rupture. The entire aftershock zone as observed during the first 3.5 weeks appears to have become active shortly after the main shock occurred. The location of the main shock 15 km southwest of the southeast end of the surface rupture suggests unilateral rupture propagation to the northwest. Cross sections of aftershock hypocenters along the central and southern portions of the surface rupture and the location of the main shock hypocenter relative to the surface break both indicate a moderately-dipping ($\sim 45^{\circ}$) fault plane. Fault plane solutions indicate predominately normal faulting with varying components of strike slip.

Acknowledgments

A large number of individuals assisted in field data acquisition including D. M. Anderson, W. J. Arabasz, T. T. Barnhard, H. M. Benz, J. Boatwright, H. B. Boschetto, R. L. Dart, D. I. Doser, D. Halloran, S. T. Harding, R. F. Henrisey, S. M. Jackson, C. Jonientz-Trisler, E. McPherson, C. W. Meissner, K. A. Monger, D. Mullen, G. Newman, J. F. Peinado, S. K. Plymell, M. C. Stickney, D. T. Whipp, and J. K. Whipp. Data analysis and processing were accomplished with the help of M. J. Adams, J. Boatwright, G. J. Chen, G. M. Hathaway, L. L. Leu, P. J. Oehmich, S. Plymell, L. L. Sells, M. C. Stickney, and D. J. Williams. Regional seismographic data were made available by various institutions including Boise State University, Idaho National Engineering Laboratory, Montana Bureau of Mines and Geology, Ricks College, University of Utah, and University of Washington. W. J. Arabasz and J. R. Pelton critically reviewed the manuscript. Support for the work at the University of Utah was provided by the U.S. Geological Survey, Contract No. 14-08-001-21857 (for field aftershock recording and data analysis) and Contract No. 14-08-0001-21856 (for supplementary research).

REFERENCES

Arabasz, W. J., and R. B. Smith, 1981. Earthquake prediction in the Intermountain seismic belt--An intraplate extensional regime, in Earthquake Prediction, An International Review, ed. D. W. Simpson and P. G. Richards, American Geophysical Union, Maurice Ewing Series 4, 248-258.

Crone, A. J., M. N. Machette, M. G. Bonilla, J. J. Lienkaemper, R. C. Bucknam, K. L. Pierce, and W. E. Scott, 1985. Characteristics of Surface Faulting Accompanying the Borah Peak Earthquake, Central Idaho, in Workshop XXVIII on the Borah Peak Earthquake: U.S. Geological Survey Open-File Report, in press.

Dewey, J. W., 1985. A reanalysis of the instrumental seismicity of central Idaho on the basis of locally-recorded aftershocks to the 1983 Borah Peak Earthquake, in Workshop XXVIII on the Borah Peak Earthquake: U.S. Geological Survey Open-File Report, in press.

Doser, D. I., 1984. The 1959 Hebgen Lake, MT and the 1983 Borah Peak, ID earthquakes: Examples of large normal fault events in the Intermountain region, (abstract): Earthquake Notes, 55, (1), 14.

Elbring, G., 1984. A method for inversion of two-dimensional seismic refraction data with applications to the Snake River Plain region of Idaho, Unpublished Ph.D. Thesis, Purdue University.

Hait, M. A., Jr., and W. E. Scott, 1978. Holocene faulting, Lost River Range, Idaho, (abstract), Geol. Soc. America, Abstract with Programs, 10, 217.

Klein, F. W., 1978. Hypocenter location program HYPOINVERSE, U.S. Geol. Surv. Open-File Rep. 78-694.

Sheriff, S. D., and M. C. Stickney, 1984. Crustal structure of southwestern Montana and east-central Idaho: Results of a reversed seismic refraction line, Geophys. Res. Letters, 11, 299-302.

Smith, R. B., 1978. Seismicity, crustal structure, and intraplate tectonics of the Western Cordilera, in Cenozoic Tectonics and Regional Geophysics of the Western Cordilera, R. B. Smith and G. P. Eaton, editors, Memoir 152, Geol. Soc. Am., 111-144.

Sparlin, M. A., L. W. Braile, and R. B. Smith, 1982. Crustal structure of the Eastern Snake River Plain determined from ray trace modeling of seismic refraction data, J. Geophys. Res., 87, 2619-2633.

Stein, R. S. and S. E. Barrientos, 1985. The 1983 Borah Peak, Idaho earthquake: geodetic evidence for deep rupture on a planar fault, in Workshop XXVIII on the Borah Peak Earthquake: U.S. Geological Survey Open-File Report, in press.

Stover, C. W., 1984. Preliminary isoseismal map and intensity distribution for the Borah Peak, Idaho, earthquake of October 28, 1983, U.S. Geological Survey Open-File Report 84-297, 6 p.

Witkind, I. J., 1975. Preliminary map showing known and suspected active faults in Idaho, U.S. Geol. Sur. Open-File Report 75-278.

Zollweg, J. E., and W. D. Richins, 1985. Later aftershocks of the 1983 Borah Peak, Idaho earthquake and related activity in central Idaho, in Workshop XXVIII on the Borah Peak Earthquake: U.S. Geological Survey Open-File Report, in press.

TABLE 1

Borah Peak, Idaho Earthquakes: Oct 28 - Nov 19, 1983
(magnitude 4.0 and larger)

yr	date	origin time (UTC)	lat-n	long-w	depth (km)	magnitude
83	1028	1406 6.79	43-58.07	113-53.94	16.0#	7.3 (MS, from NEIS)
83	1028	1416†				4.1 (ML, U of Wash)
83	1028	1419†				4.7 (ML, U of Wash)
83	1028	1425†				4.1 (ML)
83	1028	1500†				4.0 (ML, U of Wash)
83	1028	1514 7.71	44- 7.61	113-58.08	10.0*	4.6 (ML)
83	1028	1554 31.67	44-12.39	114- 3.46	10.0*	4.0 (ML)
83	1028	1720 24.25	44-10.56	114- 5.49	10.0*	4.0 (ML)
83	1028	1831 52.49	44-11.91	114- 4.68	10.0*	4.1 (ML)
83	1028	1951 25.07	44- 3.74	113-53.71	10.0*	5.8 (ML)
83	1029	237 3.73	44-15.32	114- 3.30	10.0*	4.0 (ML)
83	1029	2329 12.53	44-11.59	114- .62	10.0*	5.8 (ML)
83	1029	2339 6.25	44-13.45	114- 1.83	4.7	5.4 (ML)
83	1030	124 51.55	44- 5.73	113-58.03	11.6	4.8 (ML)
83	1030	159 1.55	44-13.25	114- 4.42	16.1	4.7 (ML)
83	1030	254 39.93	44-12.97	114- 5.69	4.6	4.0 (ML)
83	1102	2343 55.00	44-16.30	114- 4.47	7.3	4.2 (ML)
83	1106	2104 48.75	44- 8.43	113-58.02	10.5	4.6 (ML)

number of earthquakes = 18

† not locatable due to saturated records
# depth determined using body wave modeling (Doser,1984)
* restricted depth

FIGURE CAPTIONS

Figure 1. Map of the Intermountain seismic belt (Arabasz and Smith, 1981; see also Smith, 1978) showing earthquake epicenters for the period 1950-1976 (small dots). Historic earthquakes with magnitudes above 6.0 are indicated by large dots and are labeled with the date and magnitude.

Figure 2. Map of the area surrounding the 1983 Borah Peak, Idaho earthquake showing: 1) location of surface rupture (from Crone et al., 1985); 2) faults with Quaternary and Holocene displacement from Hait, M. A. Jr (1984, personal communication) and Witkind (1975), dotted lines indicate buried faults, dashed lines indicate inferred or discontinuous faults; 3) location of three seismic refraction lines, blast sites indicated by asterisks (see text).

Figure 3. a) Record section for profile 7 of Figure 2 with travel time curves calculated from the model in Figure 3b; b) P-wave velocity model used for analysis of the Borah Peak, Idaho earthquake sequence, location of blast site indicated by asterisk. Surface datum is 2000 m.

Figure 4. Map of P-wave station delays used to locate the larger events during the first 24 hours of the Borah Peak earthquake sequence. Delays noted in seconds, stations indicated by solid triangles. The four stations located within the aftershock zone are portable stations installed within 24 hours after the main shock (delays <0.37 sec). Data from these four stations were available for some aftershocks during the first 24 hours.

Figure 5. Travel time plots (P-arrival times plotted with +) for a sample master earthquake used to determine regional station delays in Figure 4. The solid lines represent theoretical travel times based on the velocity model in Figure 3b. a) 0-50 km, reduced using 6.0 km/sec; b) 0-650 km, reduced using 8.0 km/sec.

Figure 6. Travel time plot of P-arrival times used for location of the main shock of the Borah Peak, Idaho earthquake sequence. Station delays were applied. Reducing velocity is 8.0 km/sec. The solid lines represent theoretical travel times based on the velocity model in Figure 3b.

Figure 7. Epicentral map of the first 24 hours of the Borah Peak, Idaho earthquake sequence. The dashed lines define a parallelogram within which all but three of the aftershocks are located.

Figure 8. Map of the local temporary seismic network (October 28-November 19, 1983) surrounding the area of the Borah Peak, Idaho, earthquake sequence. The location of six calibration events are shown as numbered solid circles.

Figure 9. Epicentral map of the Borah Peak, Idaho earthquake sequence for October 29 at 17:00 UTC to November 19 at 14:00 UTC, 1983.

Figure 10. Depth cross sections of earthquakes in the Borah Peak, Idaho earthquake sequence. The projection of surface faulting is indicated as 45° solid lines projecting downward from the surface. The locations of the cross sections are indicated in the key map. Projection limits are ± 7 km.

Figure 11. a) Space-time plot of the Borah Peak, Idaho earthquake sequence along the strike of the aftershock zone and surface rupture, b) surface displacement from Crone et al., (1985), and c) depth cross section along the strike of the aftershock zone and surface rupture. Because the depths of aftershocks located using the regional network were fixed to 10 km, there is a concentration of hypocenters at this depth.

Figure 12. Epicentral map of the five largest events of the Borah Peak, Idaho sequence for the time period October 28, 1983 to August 22, 1984.

Figure 13. Single event, lower hemisphere focal mechanisms from the Borah Peak, Idaho earthquake sequence. C's indicate compressional first motions. D's indicate dilatational first motions. P and T indicate compression and tension axes, respectively. Z is the focal depth.

Figure 14. Single-event, lower-hemisphere focal mechanisms from the Borah Peak, Idaho earthquake sequence. Notation as in Figure 13.

Figure 15. Epicenters of the Borah Peak, Idaho earthquake sequence and selected lower-hemisphere single-event focal mechanisms for October 28-November 19, 1983. Shaded quadrants are compressional. The location of surface rupture is from Crone et al., (1985). The main shock focal mechanism is from Doser (1984).

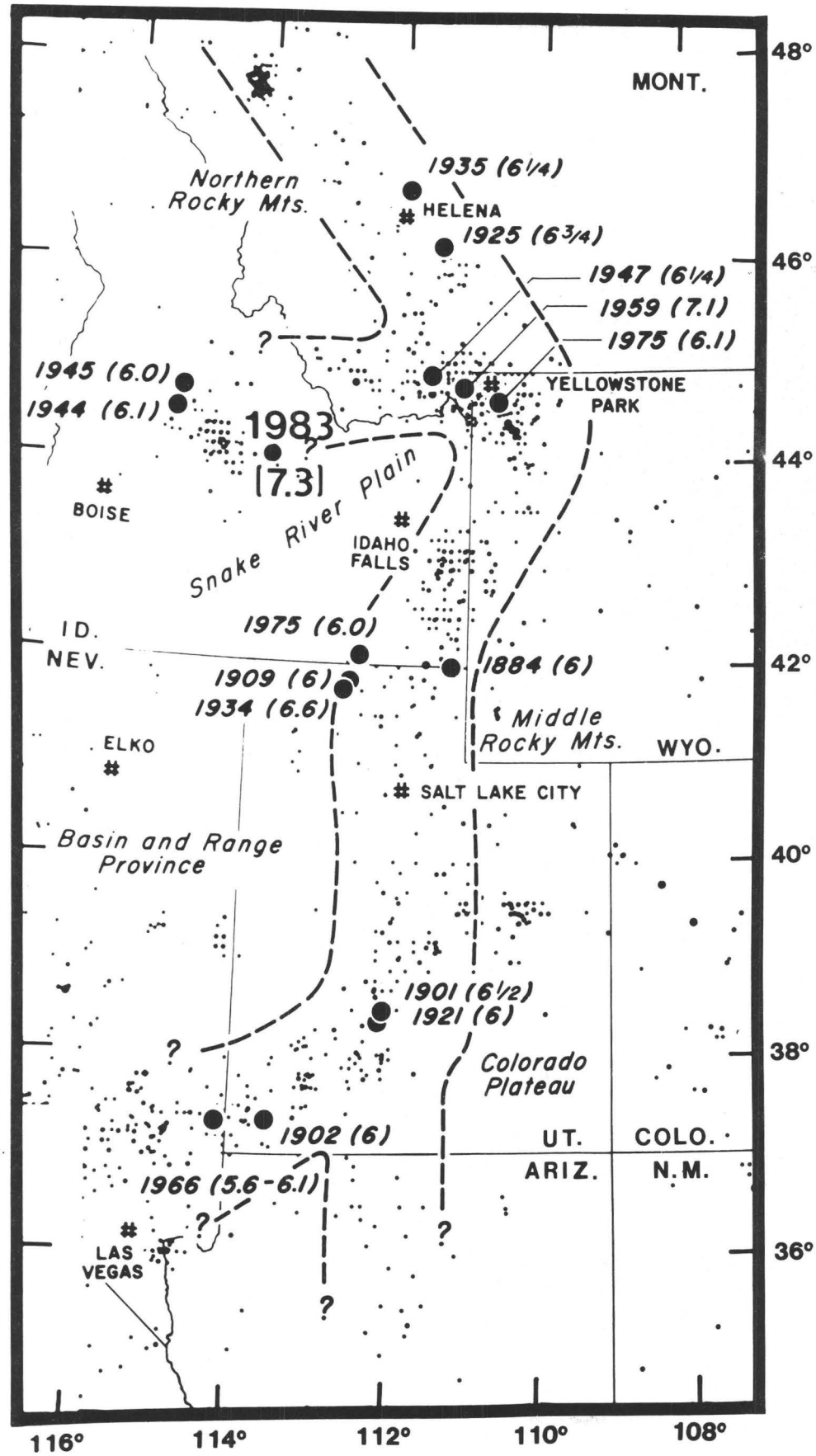
MONT.
48°
Northern Rocky Mts.
1935 (6¼)
HELENA
1925 (6¾)
46°
1947 (6¼)
1959 (7.1)
1975 (6.1)
1945 (6.0)
1944 (6.1)
YELLOWSTONE PARK
1983
(7.3)
44°
BOISE
Snake River Plain
IDAHO FALLS
ID.
NEV.
1975 (6.0)
1884 (6)
42°
1909 (6)
1934 (6.6)
Middle Rocky Mts.
WYO.
ELKO
SALT LAKE CITY
Basin and Range Province
40°
1901 (6½)
1921 (6)
38°
Colorado Plateau
1902 (6)
UT.
COLO.
ARIZ.
N.M.
1966 (5.6-6.1)
LAS VEGAS
36°
116°
114°
112°
110°
108°

FIGURE 1

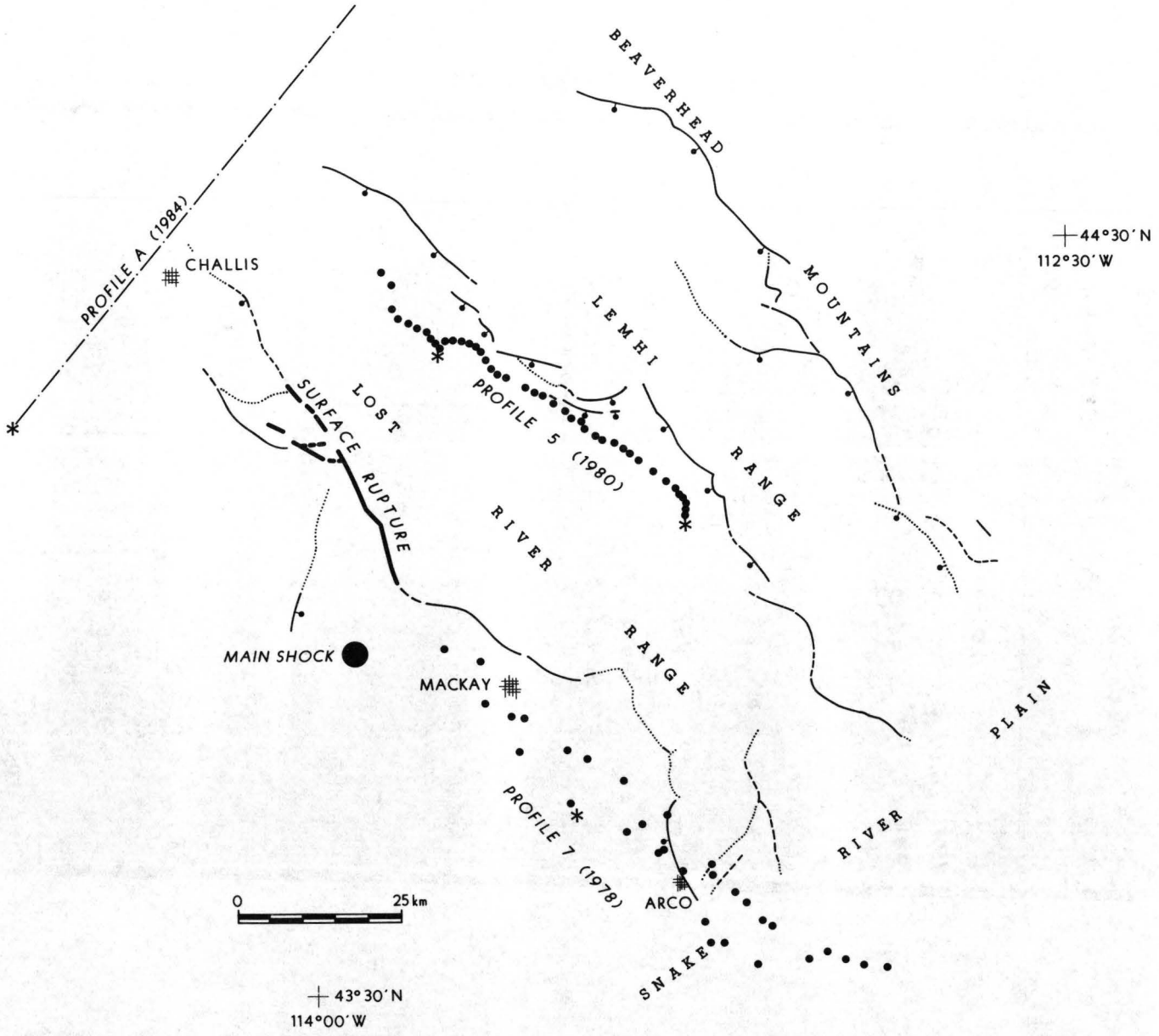
BEAVERHEAD
MOUNTAINS
44°30′N
112°30′W
PROFILE A (1984)
CHALLIS
LEMHI
RANGE
LOST
RIVER
RANGE
SURFACE RUPTURE
PROFILE 5 (1980)
MAIN SHOCK
MACKAY
RANGE
PLAIN
PROFILE 7 (1978)
ARCO
RIVER
SNAKE
0
25 km
43°30′N
114°00′W

FIGURE 2

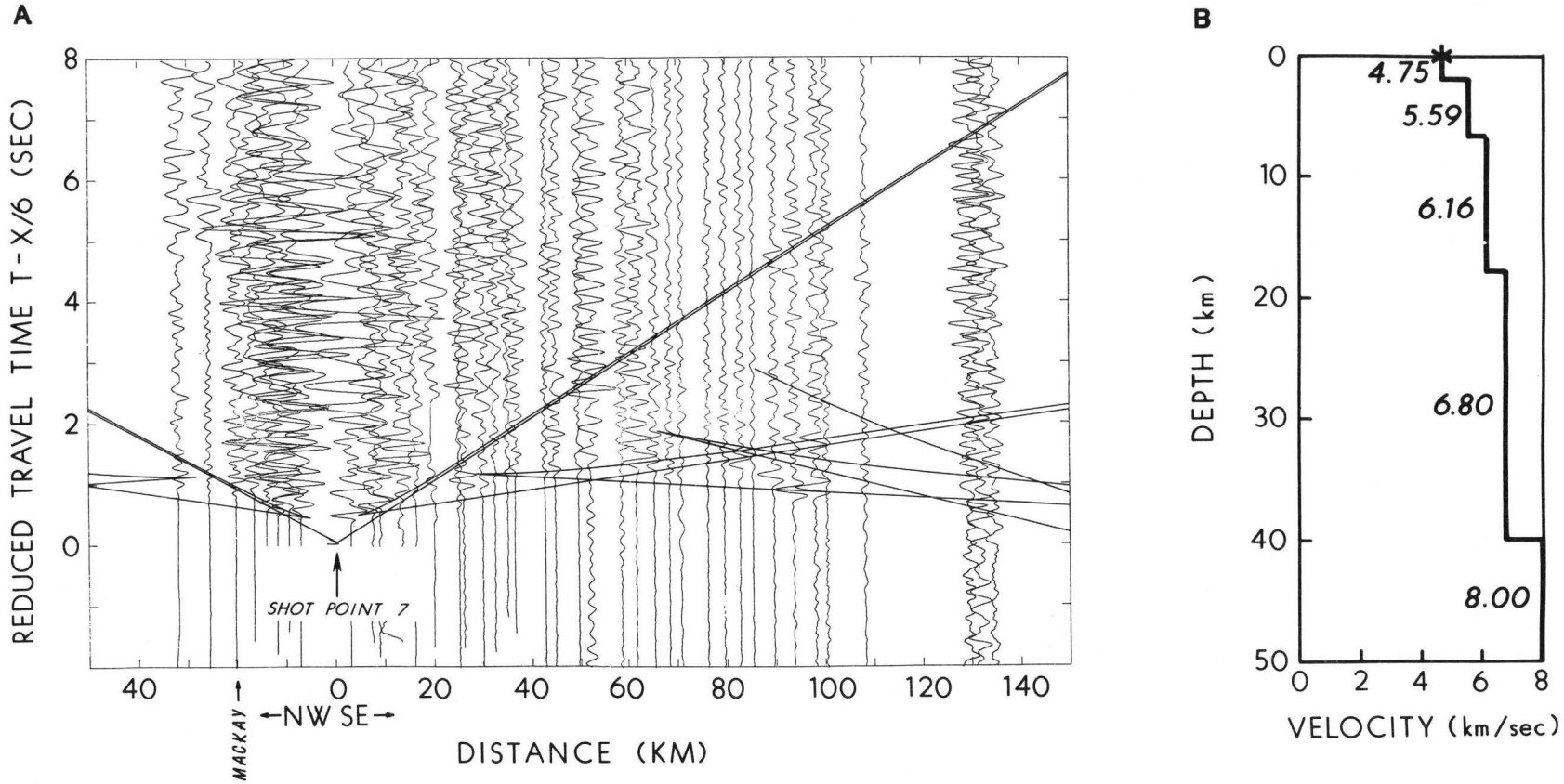
A
REDUCED TRAVEL TIME T-X/6 (SEC)
8
6
4
2
0
SHOT POINT 7
40
0
20
40
60
80
100
120
140
MACKAY
NW SE
DISTANCE (KM)
B
DEPTH (km)
0
10
20
30
40
50
4.75
5.59
6.16
6.80
8.00
0
2
4
6
8
VELOCITY (km/sec)

FIGURE 3

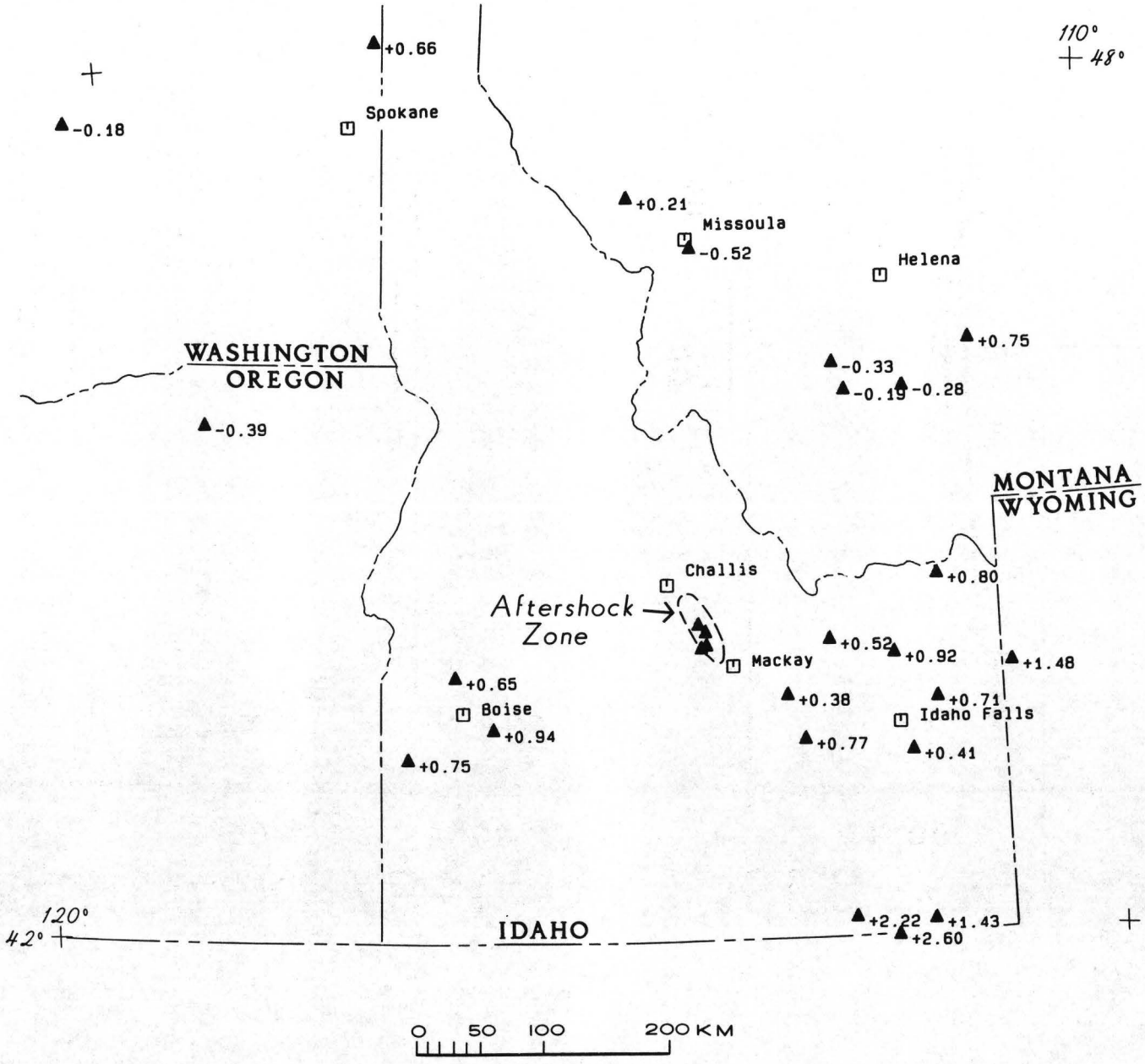
110°
48°
+0.66
Spokane
-0.18
+0.21
Missoula
-0.52
Helena
+0.75
-0.33
-0.19
-0.28
WASHINGTON
OREGON
-0.39
MONTANA
WYOMING
Challis
Aftershock
Zone
+0.80
+0.52
+0.92
Mackay
+1.48
+0.65
Boise
+0.94
+0.38
+0.71
Idaho Falls
+0.77
+0.41
+0.75
120°
42°
IDAHO
+2.22
+1.43
+2.60
0 50 100 200 KM

FIGURE 4

SAMPLE MASTER EVENT

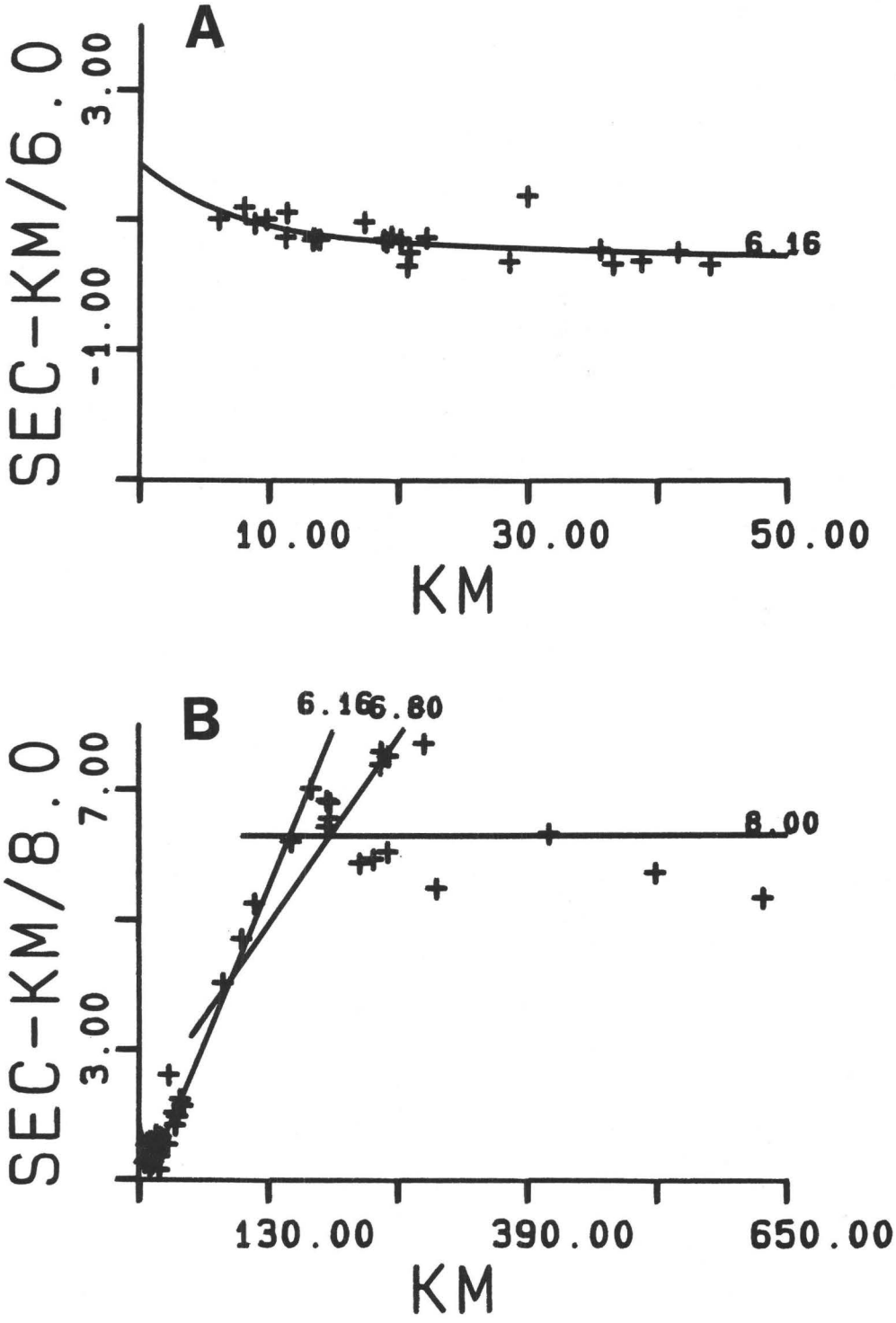

FIGURE 5

MAIN SHOCK USING STATION DELAYS

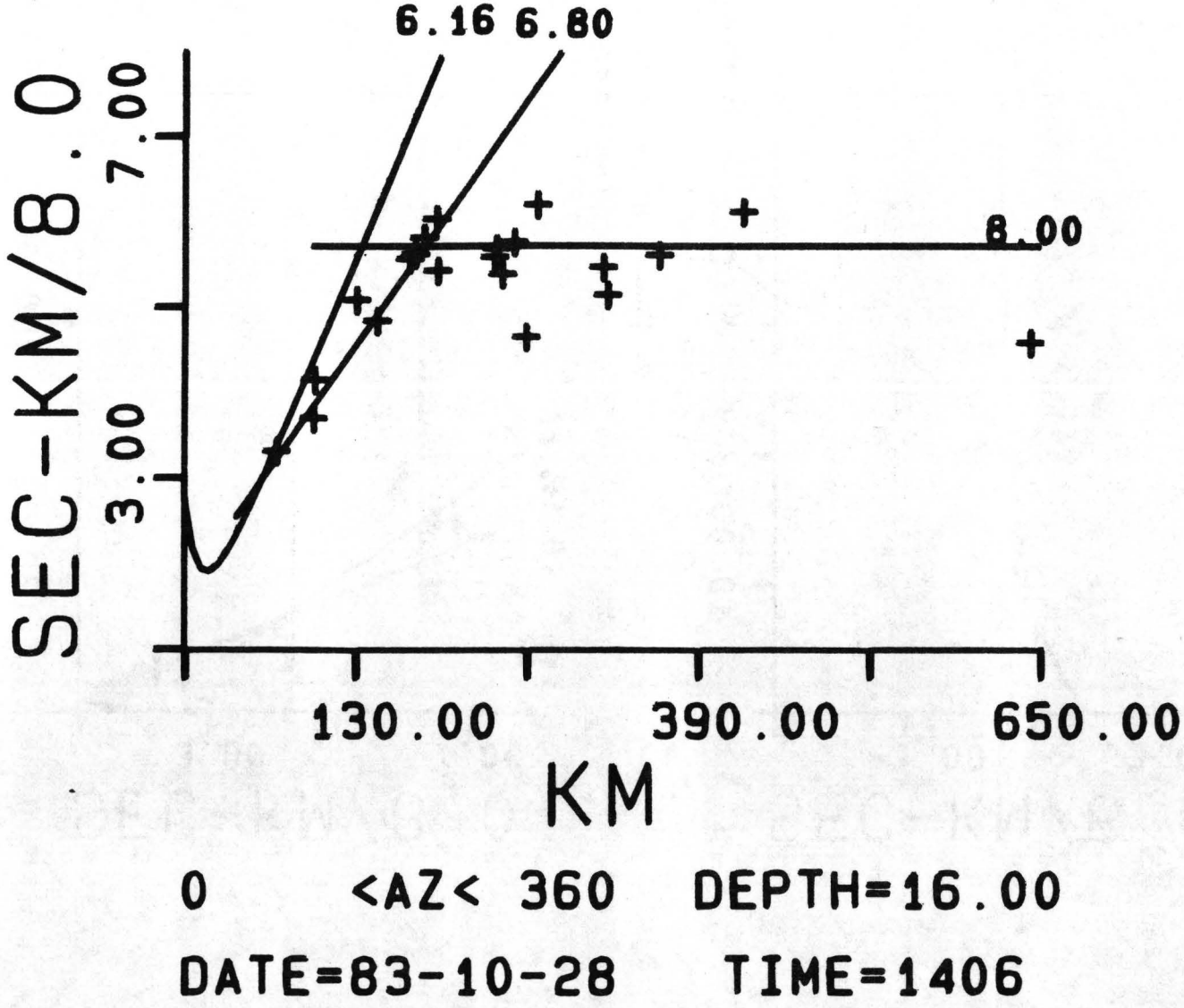

FIGURE 6

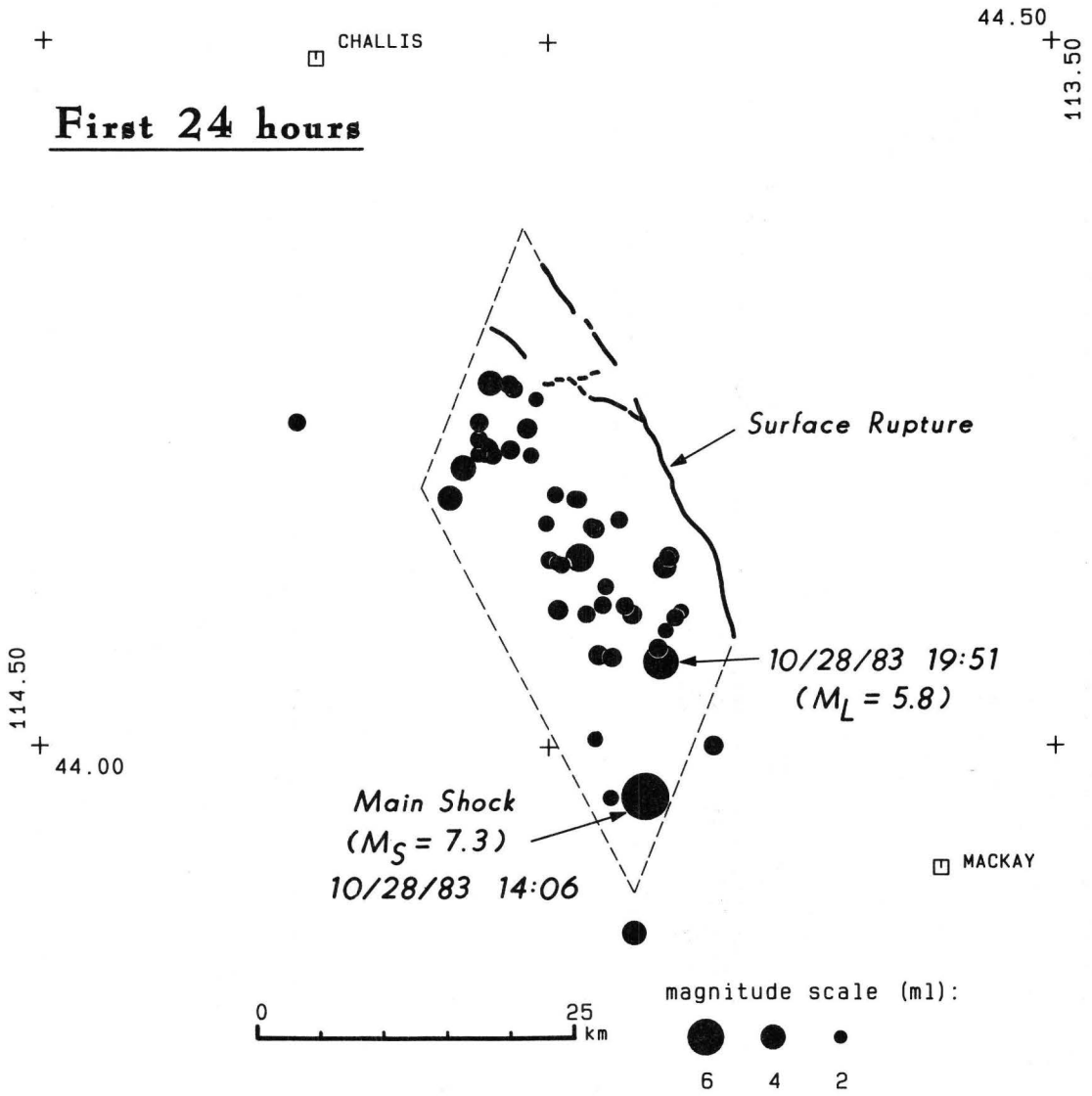
CHALLIS
44.50
113.50
First 24 hours
Surface Rupture
10/28/83 19:51
(ML = 5.8)
114.50
44.00
Main Shock
(MS = 7.3)
10/28/83 14:06
MACKAY
0
25
km
magnitude scale (ml):
6
4
2

FIGURE 7

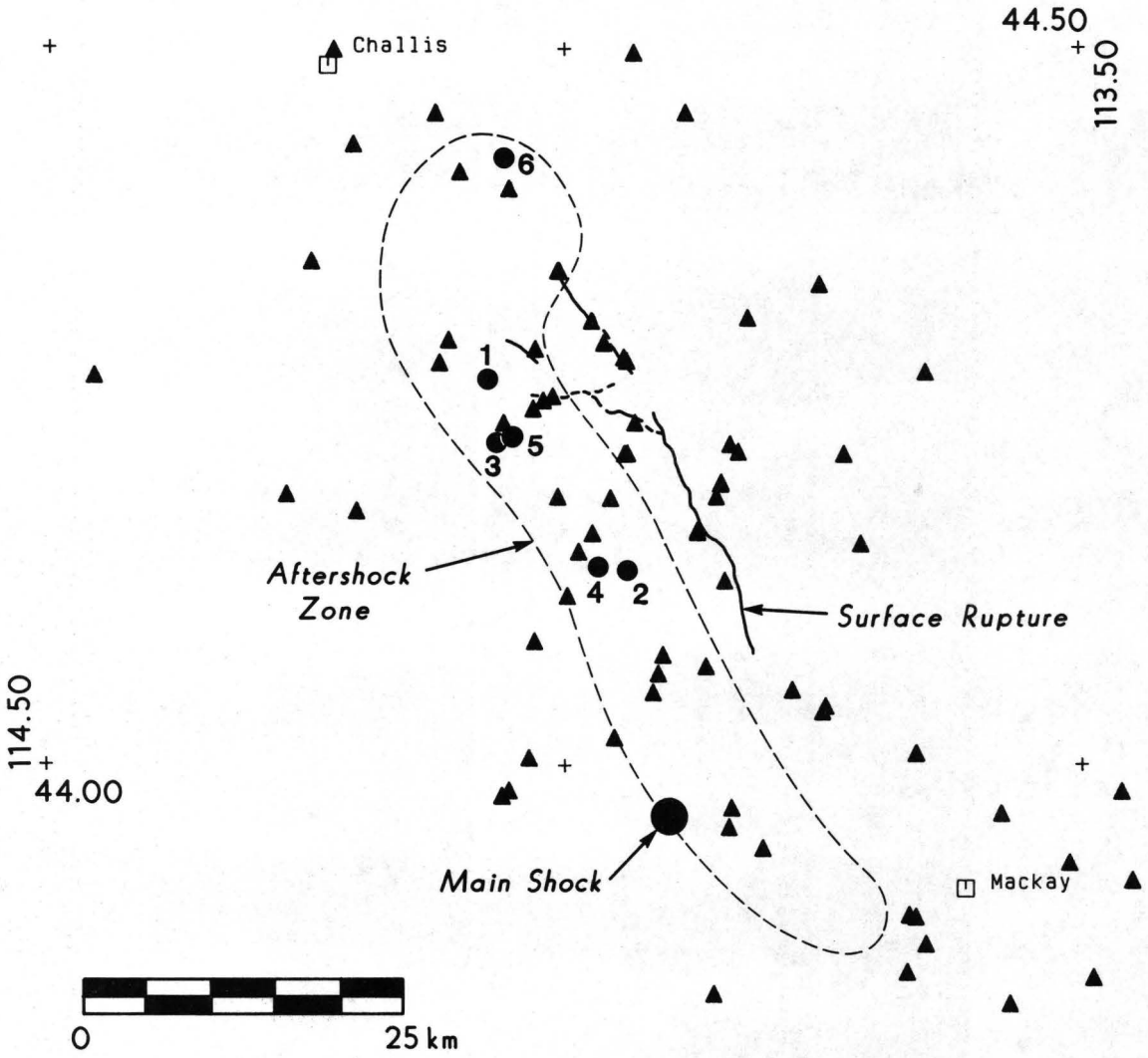
Challis
44.50
113.50
6
1
5
3
4
2
Aftershock Zone
Surface Rupture
114.50
44.00
Main Shock
Mackay
0
25 km

FIGURE 8

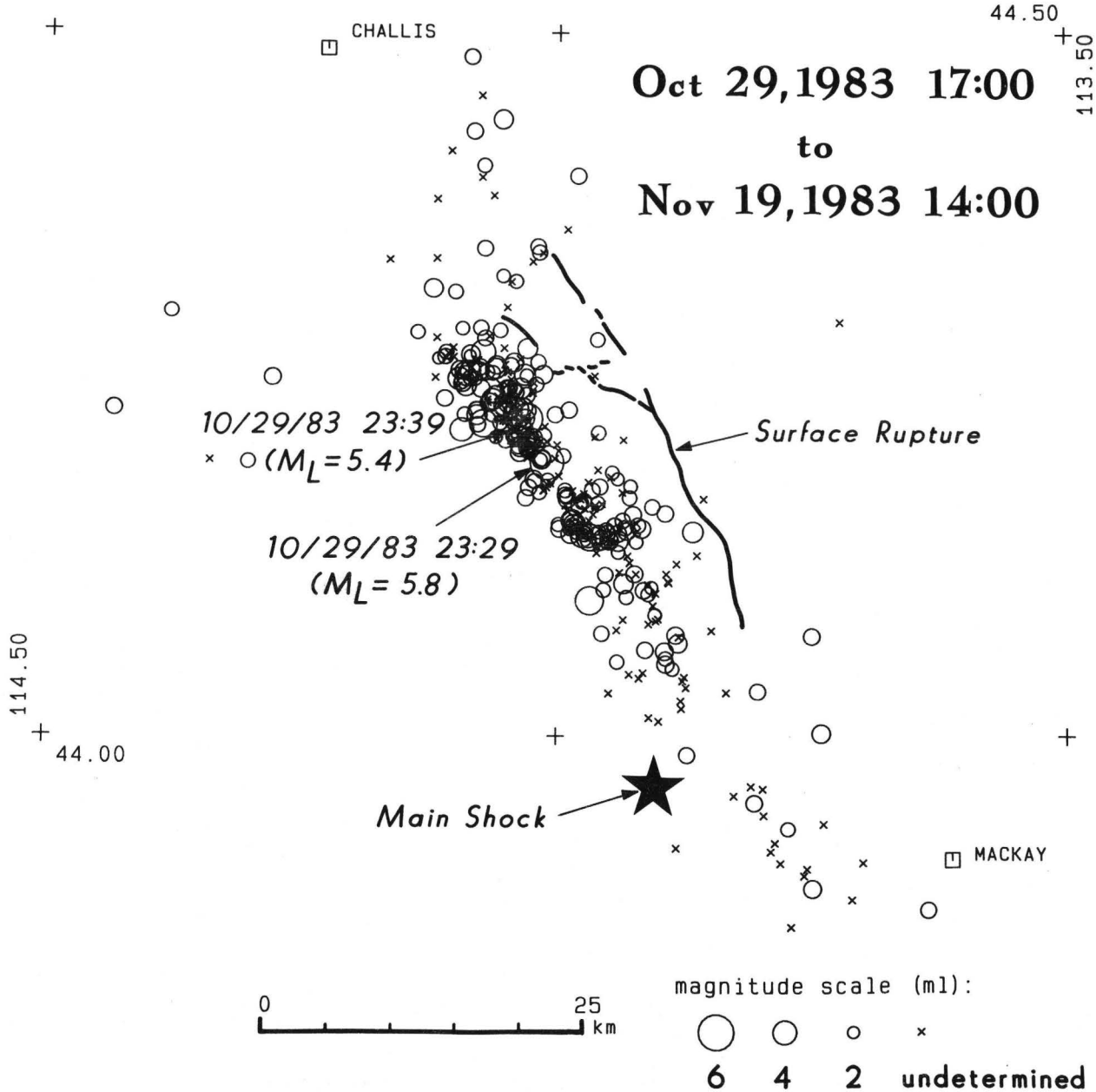
CHALLIS
44.50
113.50
Oct 29,1983 17:00
to
Nov 19,1983 14:00
10/29/83 23:39
(M_L=5.4)
10/29/83 23:29
(M_L= 5.8)
Surface Rupture
114.50
44.00
Main Shock
MACKAY
0
25
km
magnitude scale (ml):
6 4 2 undetermined

FIGURE 9

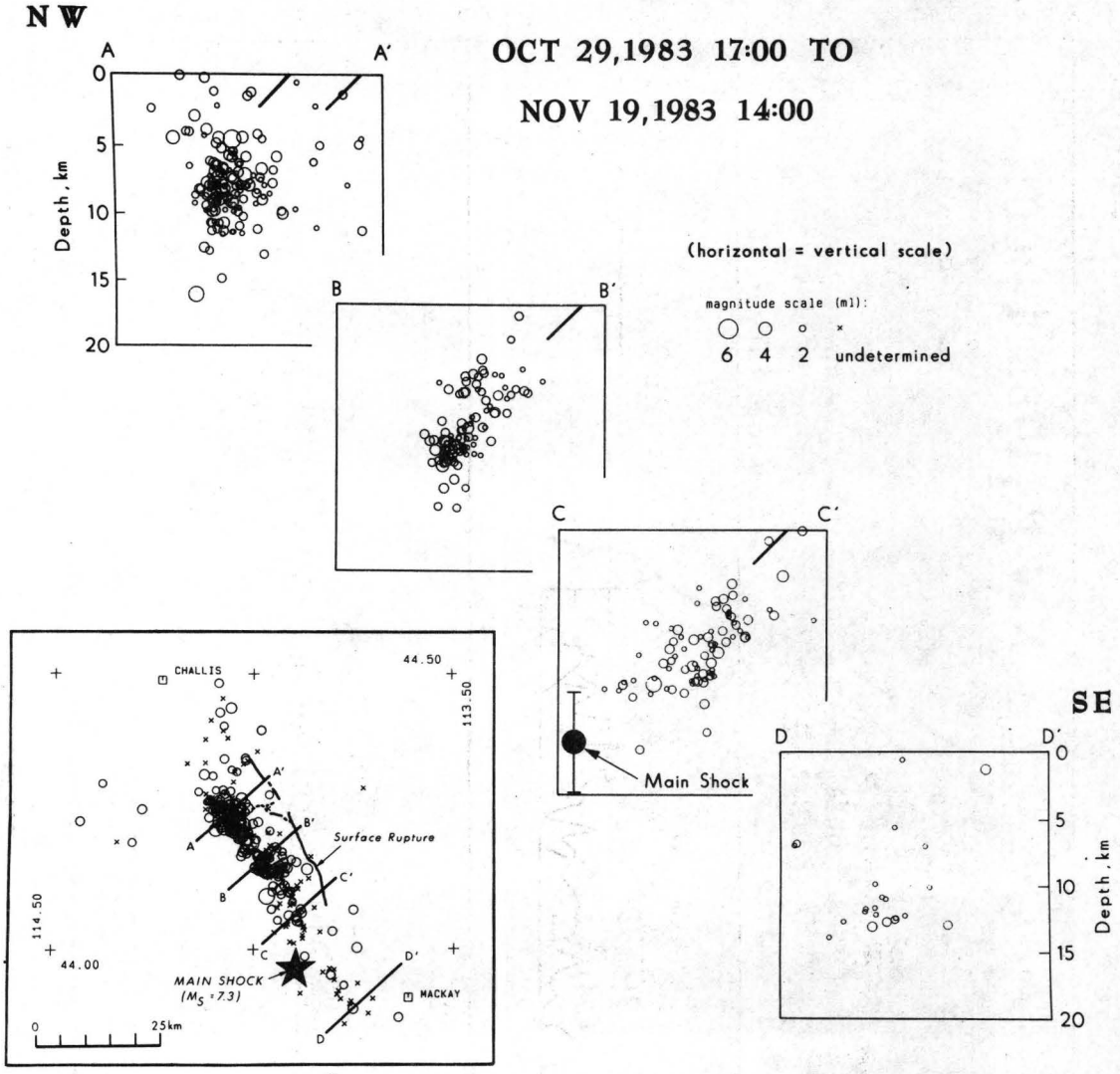
NW
A
A'
0
5
10
15
20
Depth, km
OCT 29,1983 17:00 TO
NOV 19,1983 14:00
(horizontal = vertical scale)
magnitude scale (ml):
6 4 2 undetermined
B
B'
C
C'
Main Shock
SE
D
D'
0
5
10
15
20
Depth, km
CHALLIS
44.50
113.50
114.50
44.00
Surface Rupture
MAIN SHOCK
(M_S = 7.3)
MACKAY
0
25km

FIGURE 10

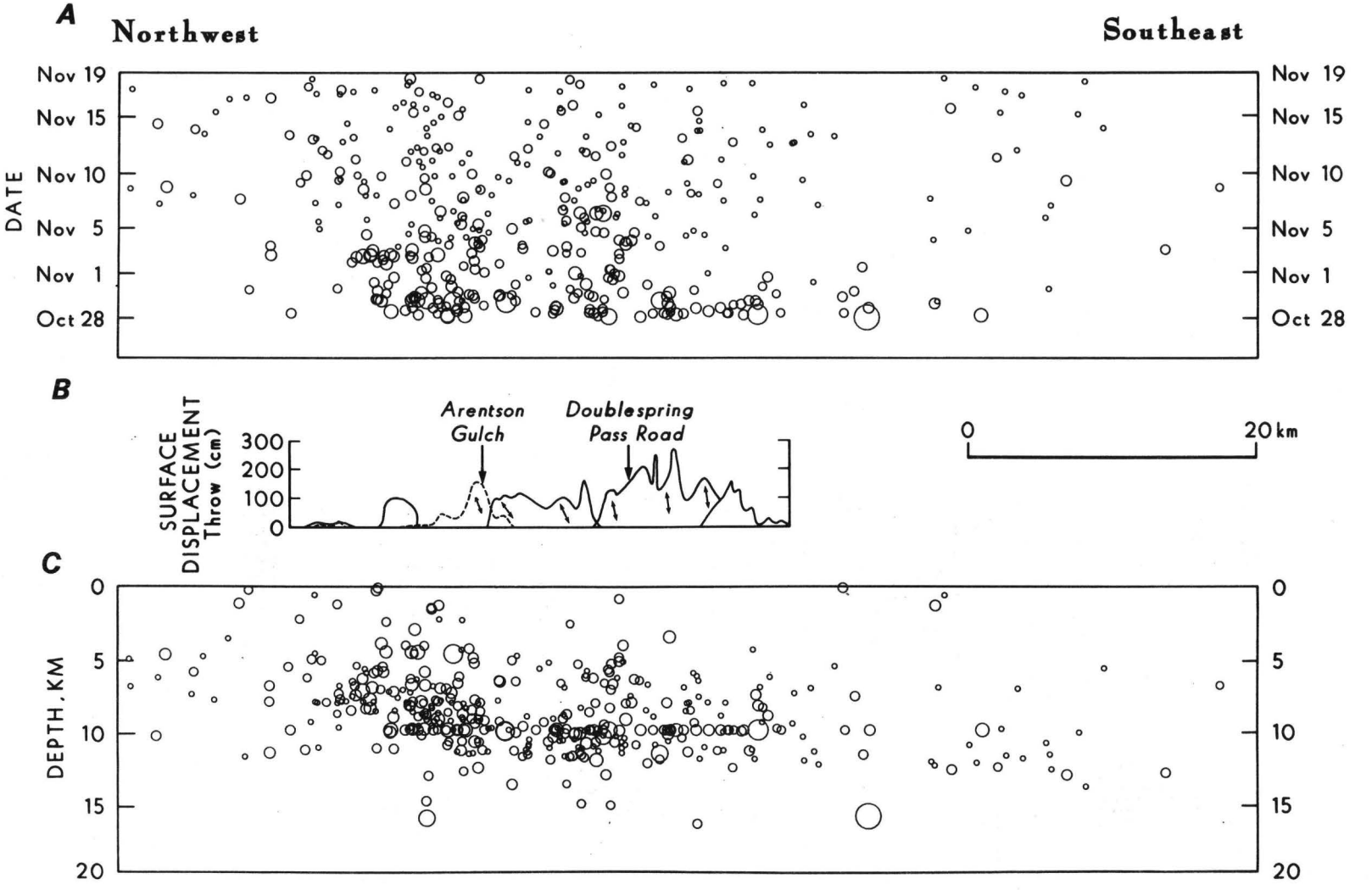
A
Northwest
Southeast
DATE
Nov 19
Nov 15
Nov 10
Nov 5
Nov 1
Oct 28
B
SURFACE DISPLACEMENT Throw (cm)
300
200
100
0
Arentson Gulch
Doublespring Pass Road
0
20 km
C
DEPTH, KM
0
5
10
15
20

FIGURE 11

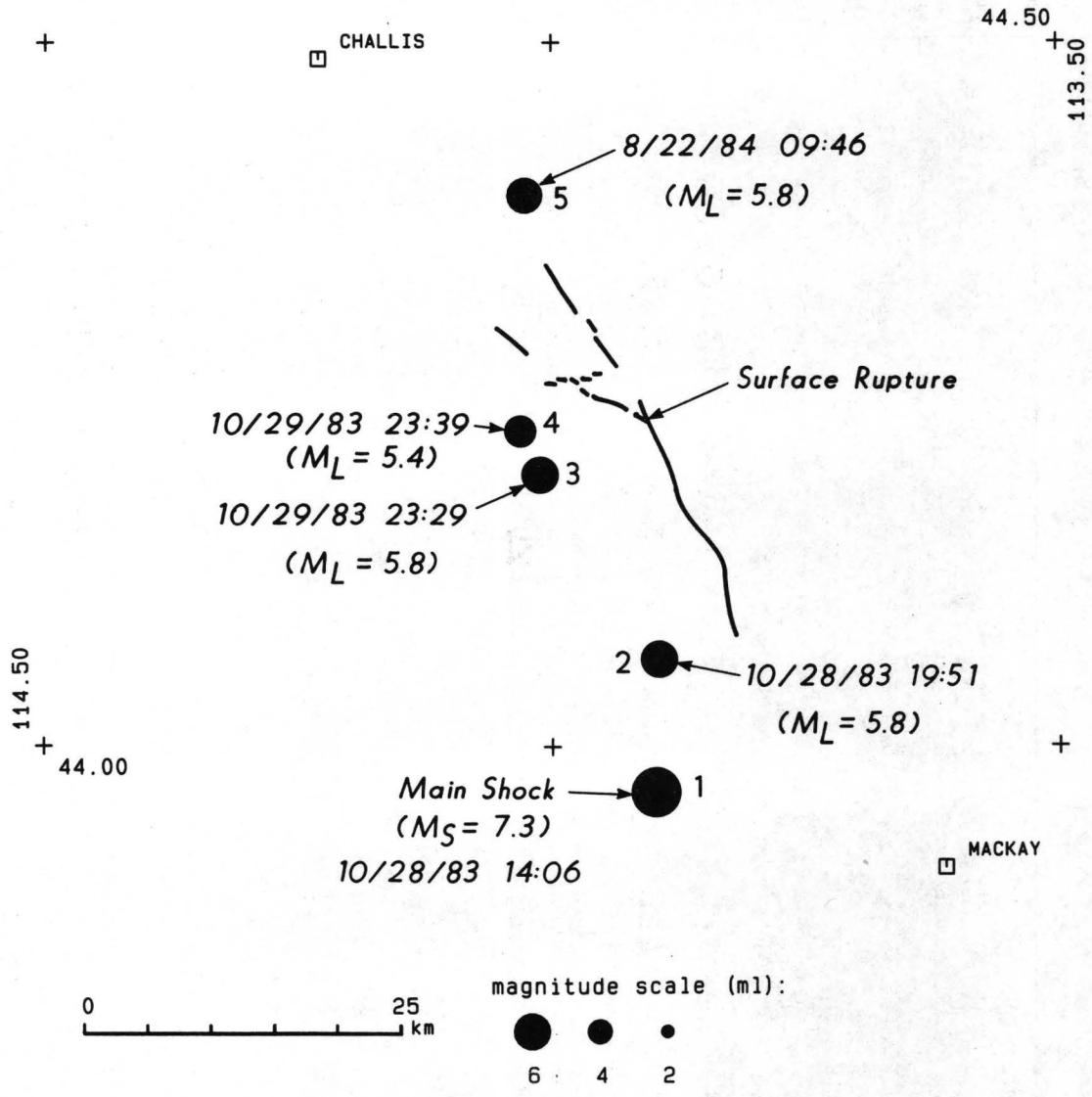
CHALLIS
44.50
113.50
8/22/84 09:46
(M_L = 5.8)
5
Surface Rupture
10/29/83 23:39
(M_L = 5.4)
4
3
10/29/83 23:29
(M_L = 5.8)
2
10/28/83 19:51
(M_L = 5.8)
114.50
44.00
Main Shock
(M_S = 7.3)
10/28/83 14:06
1
MACKAY
0
25
km
magnitude scale (ml):
6
4
2

FIGURE 12

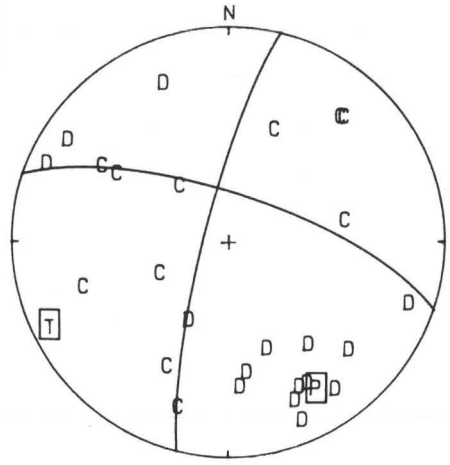

Nov 11, 1983 22:50

M_L = 2.8 Z = 12 km

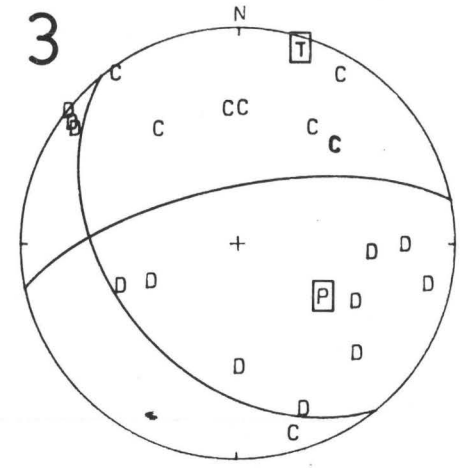

Nov 4 1983 05:00

M_L = 3.5 Z = 9 km

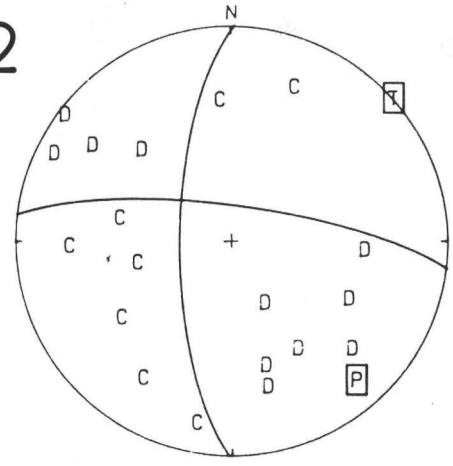

Nov 6, 1983 21:11

M_L = 3.8 Z = 12 km

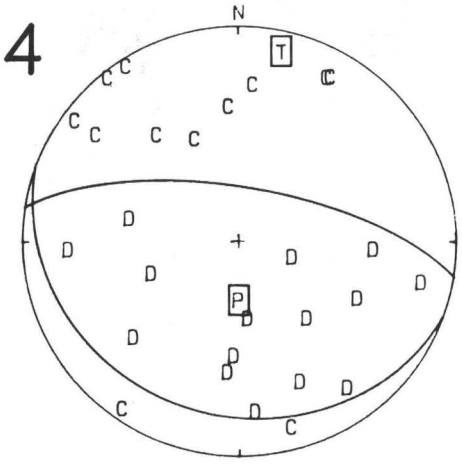

Nov 1, 1983 10:30

M_L = 3.1 Z = 10 km

FIGURE 13

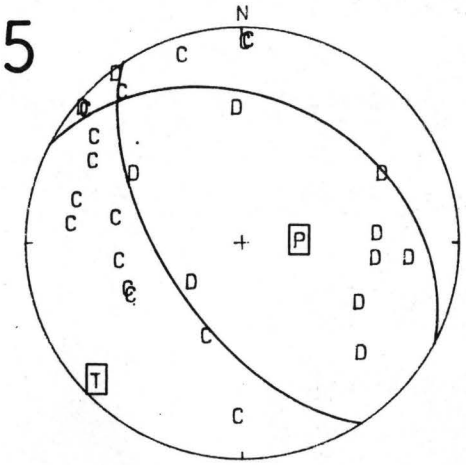

Nov 5,1983 05:37

M_L = 3.5 Z = 10 km

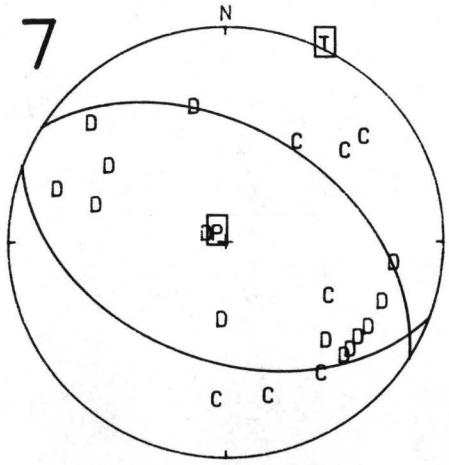

Nov 3,1983 15:47

M_L = 3.6 Z = 7 km

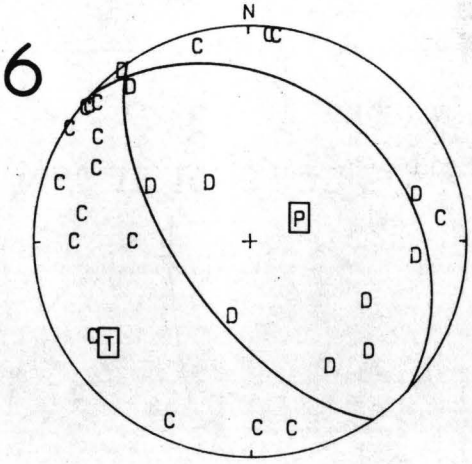

Nov 8 1983 06:46

M_L = 3.2 Z = 9 km

FIGURE 14

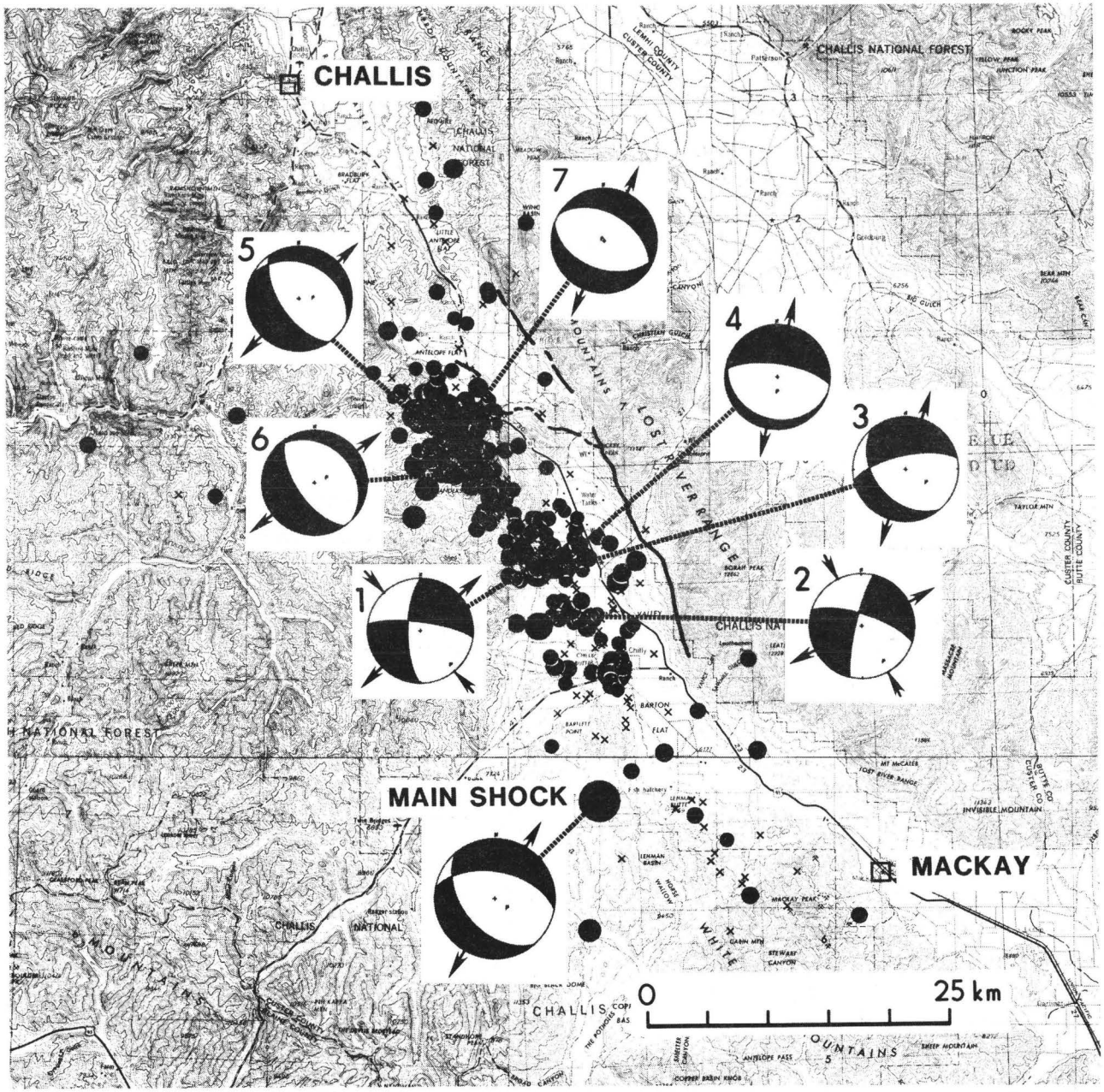
CHALLIS
CHALLIS NATIONAL FOREST
7
5
4
3
6
1
2
MAIN SHOCK
MACKAY
0
25 km

FIGURE 15

Characteristics of the Aftershock Sequence of the Borah Peak, Idaho, Earthquake Determined from Digital Recordings of the Events

John Boatwright

U.S. Geological Survey
345 Middlefield Road
Menlo Park, CA 94025

Abstract

The U.S. Geological Survey, Menlo Park, deployed and maintained a network of twelve digital instruments over the two weeks following the October 28, 1983, Borah Peak, Idaho, earthquake. The network recorded 45 events with $\underline{M} > 3.0$, and 6 events with $\underline{M} > 4.0$. The epicenters are located in a narrow band which parellels the trace of the surface faulting up to the Willow Creek summit; the depths of the events range from 5 to 16 km. In the south, the distribution of hypocenters delineate a plane which dips to the southwest at 50°; to the north, the hypocenters dip steeply to the east. Composite focal mechanisms for three groups of events show normal faulting mechanisms; the mechanism of the aftershocks in the north appear rotated in both strike and dip from the aftershock in the south. The seismic moments of the aftershocks increase with increasing hypocentral depth below 12 km. The rms dynamic stress drops of the events do not show any systematic variation with depth, however. Most of the events with large stress drops are clustered in the northwest limb of the aftershock distribution; the average stress drop of the southern events is 31±16 bars, while the average stress drop of the events in the northwest limb is 77±52 bars. This clustering of events with large stress drops appears to mark a stress concentration, possibly associated with the arrest of the mainshock rupture propagation by a fracture barrier at depth.

Introduction

The Borah Peak earthquake of October 28, 1983, (M_s = 7.3, m_b = 6.9), was the largest recorded earthquake to occur in Idaho and the largest intermountain event to occur since the 1957 Hegben Lake earthquake and the 1954 Fairview Peak-Dixie Valley earthquake sequence. The earthquake generated a 35 km long scarp with 1-2 meters of vertical offset in the Lost River Range, north of the Snake River Plain, and was strongly felt (Modified Mercalli Intensity VI) over an area of 55,000 km^2 (Stover, 1984). Within 36 hours of the mainshock, the U.S. Geological Survey, Menlo Park, deployed a network of 12 digital recorders in the epicentral area. This network was maintained for two weeks, recording forty-five events with moment magnitudes greater than 3.0 (seismic moments greater than $3x10^{20}$ dyne-cm) and six events with moment magnitudes greater than 4.0 (seismic moments greater than 10^{22} dyne-cm).

This paper presents a complete analysis of the digital recordings. The events are located by complementing the P- and S-wave arrival times recorded at the digital stations with the P-wave arrival times recorded on MEQ-800 instruments deployed by the University of Utah and the U.S. Geological Survey, Golden (Richins et al., 1985). Composite mechanisms are determined for three groups of the aftershocks. The seismic moments and rms dynamic stress drops of the events are calculated by analyzing the displacement and acceleration spectra of the recorded body-waves. The analysis of Anderson and Hough (1984) is also applied to the acceleration spectra, in an attempt to determine an attenuation structure for the region. The seismic energy radiated by the aftershocks is then calculated from the energy flux in the recorded body-waves, after correcting the energy flux for the body-wave attenuation.

The Discussion Section combines the locations, mechanisms, and source parameters of the aftershocks together to infer characteristics of both the faulting environment and the rupture process of the mainshock. This effort is more descriptive than scientific; many of these characteristics can not be uniquely determined. For example, the locations and occurrence times of the aftershocks can be used to describe the initial extent and the subsequent evolution of the stress field produced by the stress release in the mainshock. Unfortunately, this seismic description is necessarily incomplete; it cannot provide any information about the aseismic response of the fault occurring through ductile flow or fault creep. The source parameters of the aftershocks,

specifically the seismic moment and stress drop, can be used to gauge the interaction of the stress field with the faulting environment. However, inferences about the fault strength should only be derived from averages over large subsets of the events, or correlations with depth or position along the fault. Variations between source parameters associated with specific events simply reflect the irregularities in the evolving stress field. Particular care must be exercised in using the aftershock stress drops to estimate the mainshock stress drop, as the variation of stress drop with both seismic moment and position along the fault must be considered in this extrapolation.

Locations and Mechanisms

Locations for the aftershocks were calculated using the P-wave velocity structure determined by Richins et al. (1984) and compiled in Table 1. The S-wave velocity structure was estimated from a Wadati diagram analysis of the P- and S-waves that were recorded digitally; the average α/β for all the recordings was 1.75±.04. Arrival times from the MEQ-800 networks operated by both the U.S. Geological Survey, Denver, and the University of Utah were also used to locate the earthquakes, although the strongest weights were given to the arrival times measured on the digital instruments. The epicentral locations are plotted in Figure 1 and listed in Table 2. The uncertainties of the better recorded events average about 1.1 km in hypocentral depth and .8 km in epicentral location. The symbol sizes are determined from the moment magnitudes of the events, defined as

$$\underline{M} = \frac{2}{3} \log M_o - 10.66 \qquad (1)$$

(Hanks and Kanamori, 1978). The method used to estimate the seismic moments is described in a later section of the paper.

The aftershock epicenters exhibit a strong lineation which approximately parellels the trace of the surface faulting. There are almost no aftershocks near the epicenter of the mainshock, shown in Figure 1 as a star approximately 12 km from the southern end of the surface faulting (Richins et al., 1985). In general, the larger aftershocks are clustered near the northwest end of the fault break, although there is one large event (0124, $\underline{M}$ = 4.4) in the southern half of the aftershock distribution.

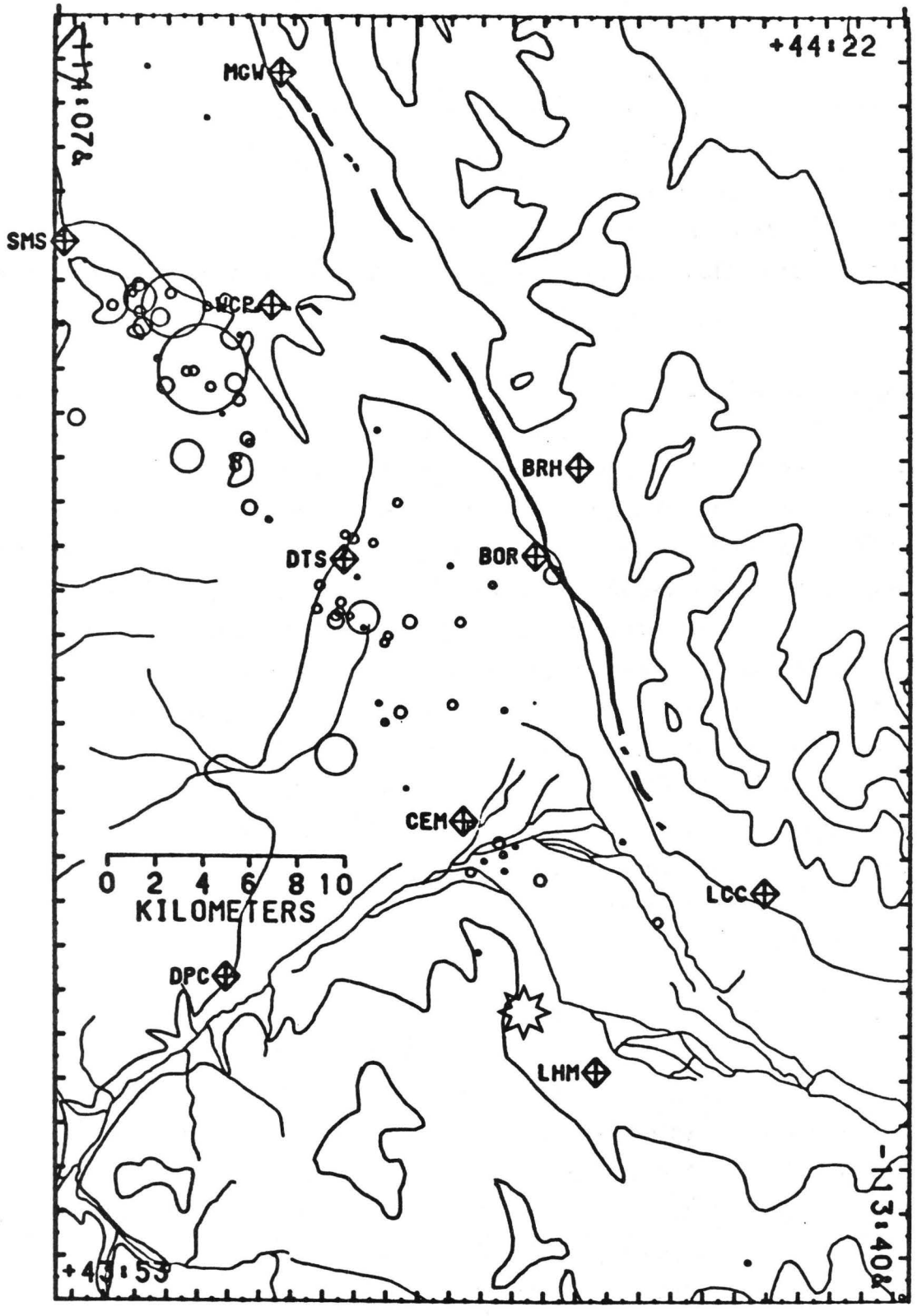
+44:22
+44:07
MCW
SMS
MCP
BRH
DTS
BOR
CEM
LCC
DPC
LHM
0 2 4 6 8 10
KILOMETERS
-113:40
+43:53

Figure 1. Map of the epicentral area, showing the major fault breaks, the digital station distribution, the epicenter of the mainshock, the 7000', 9000' and 1100' contours, and the Lost River and Mackay Reservoir. The epicentral locations of the aftershocks recorded on the digital network are denoted as circles. The largest symbol represents the $\underline{M}$ = 5.1 2329 event, while the smallest symbol corresponds to a $\underline{M}$ = 2.2 event. The radii of the circles is equal to the source radius of the events, estimated from the seismic moment and the assumption of a constant static stress drop of 30 bars. The lines marked A-A', B-B', and C-C' show the locations of the three cross-sections plotted in Figure 2.

Figure 2 shows the spatial distribution of the aftershocks, as projected onto three cross-sections. The long cross-section (A-A') runs parallel to the strike of the surface faulting. The cluster of events around 10 km depth in the middle of the plot corresponds to the 2104 ($\underline{M}$ = 4.2) event and its aftershocks. The 0159 ($\underline{M}$ = 4.2) event, located at nearly 16 km depth, was the deepest aftershock recorded.

The cross-section normal to the strike of the fault (B-B') of the southern events shows a distribution of hypocenters which dips at 45° to south-west from the surface trace, exactly as expected for a normal faulting event. No events occurred at depths shallower than 5 km. The surface faulting suggests that the rupture is approximately continuous down to 5 km; the lack of aftershocks indicates that the fault zone is weak in this depth range. One relatively shallow event (1749, $\underline{M}$ = 3.7) appears to have occurred to the east of the Lost River Fault, in the uplifted block of the Lost River Range.

The cross-section normal to the strike of the fault of the northern events (C-C') shows a markedly different distribution of hypocenters. Rather than dipping to the south-west similar to the distribution in the southern cross-section, the events appear to dip steeply to the northeast; unfortunately, the distribution is too diffuse to determine an unambiguous lineation. The nearly vertical distribution shown in this cross-section produces the lineation of the northern epicenters apparent in Figure 1; the lineation also appears to be correlated with an extension of the surface trace of an east-dipping normal fault which forms the western boundary of Antelope Flat. The fault trace runs along the 7000' contour drawn in the upper left hand corner of Figure 1, passing east of station SMS.

To investigate the difference between the northern and southern aftershocks more thoroughly, composite focal mechanisms were determined for three sets of events. These composite mechanisms are plotted in Figure 3. The mechanism for the southern events plotted in Figure 3a was obtained only after excluding the arrivals from the 2104 event and its aftershocks. Whether the data fully constrain the mechanism shown here is problematic, but the west dipping nodal plane is parallel to the strike of the fault and exhibits approximately the dip of the hypocenters in the southern cross-section of Figure 2b. The confusion of polarities in the southern quandrant is interpreted as the result of a variable amount of left-lateral slip.

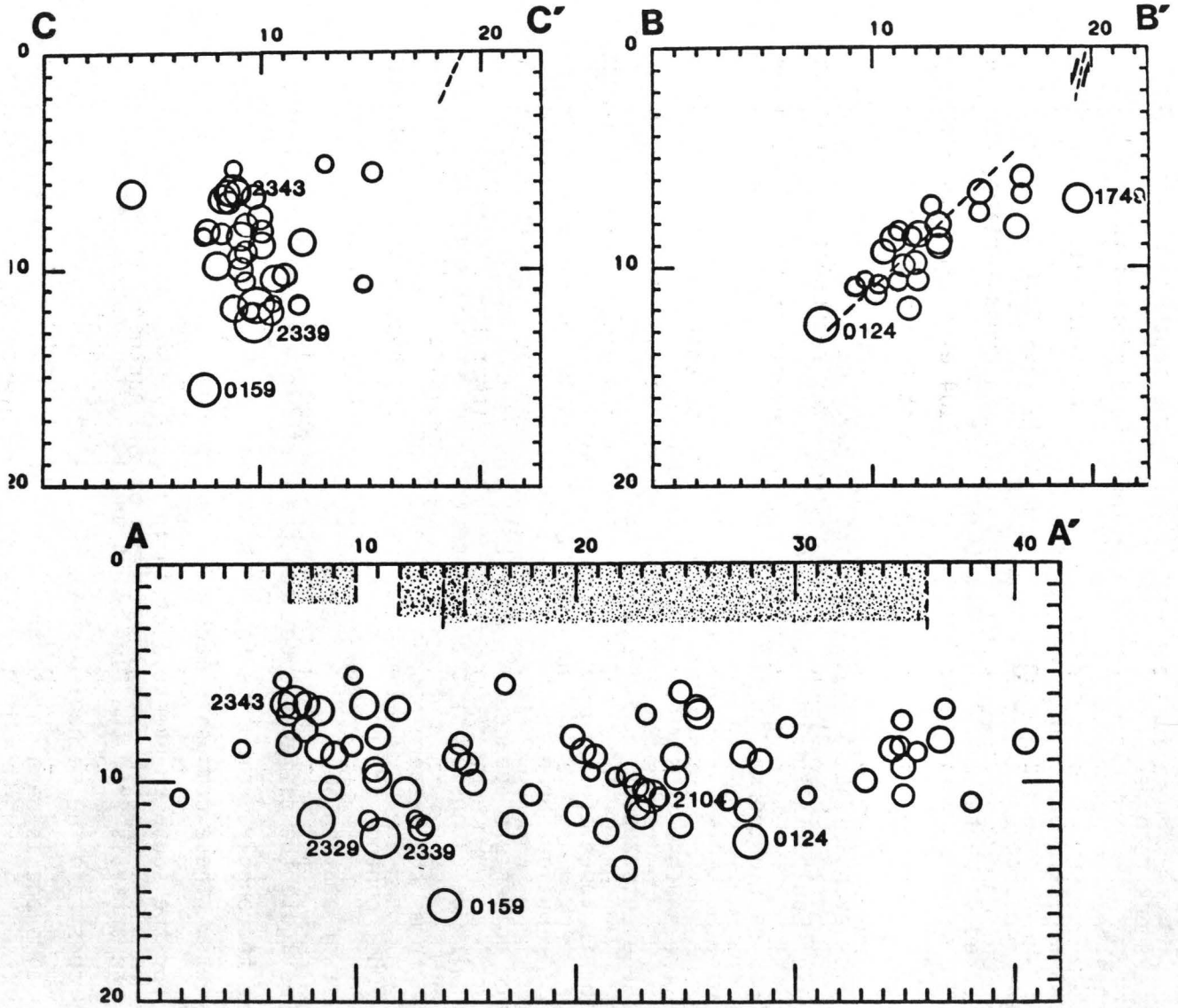

Figure 2. Cross-sections of the aftershock distribution, whose projections are drawn in Figure 1. The profile A-A' runs parellel to the strike of the fault breaks, indicated by the stippled areas at the top of the cross-section. B-B' shows a cross-section of the events in the southern half of the distribution and the location of the fault scarp, while C-C' shows the northern half. The size of the symbols is proportional to the moment magnitude of the events, but the proportionality is slightly different than in Figure 1.

The composite mechanism for the northern events plotted in Figure 3c is less well determined than the mechanism for the southern events. The dip of the west-dipping nodal plane is poorly constrained, owing to the station distribution. Note that the strike of this plane is rotated to the west by 15° or 20° from that of the southern events. The dashed line is the fault plane deduced from the locations and mechanism of the southern events. Comparison with the northern cross-section of hypocenters plotted in Figure 2b suggests that the east-dipping nodal plane in this mechanism may be the fault plane. The dip of this nodal plane is substantially less than the apparent dip of the distribution of hypocenters in the northern cross-section, however.

Figure 3b shows a composite mechanism for the 2104 event and its aftershocks. The mechanism of the 2104 event is different from the composite mechanism of the southern events but similar to that of the northern events, suggesting that the 2104 event and its aftershocks may represent the southernmost extension of the faulting associated with the events in the northern part of the aftershock distribution.

In summary, the locations and mechanisms indicate that the faulting in the southern part of the aftershock distribution is relatively simple. The hypocentral locations appear to define a fault plane which dips to the south-west at 50° from the surface trace. The composite mechanism for these aftershocks exhibits a nodal plane which has a similar strike and dip. The hypocenter for the mainshock is significantly further south than either the aftershock distribution or the surface faulting, however. The faulting in the northern part of the aftershock sequence is relatively complex. The hypocentral locations dip very steeply to the east; the northernmost events are located below the surface trace of a normal fault which bounds Antelope Flat to the west. We note that the surface faulting in the northern part of the aftershock zone shows a substantial offset on the Lost River Fault with a strong splay (the Arensen Gulch segment) to the west (Crone and Machette, 1984). This surface faulting geometry, in particular the offsets on the northen continuation of the Lost River Fault, is not evident in the aftershock distribution, and may be surficial features. The composite mechanism for the northern events has a different strike and dip than that of the southern events, but is incompatible with the nearly vertical distribution of hypocenters. To accomodate both the composite mechanism and the vertical distribution requires a set of en echelon fault segments which dip to the north-east at 55°-70°.

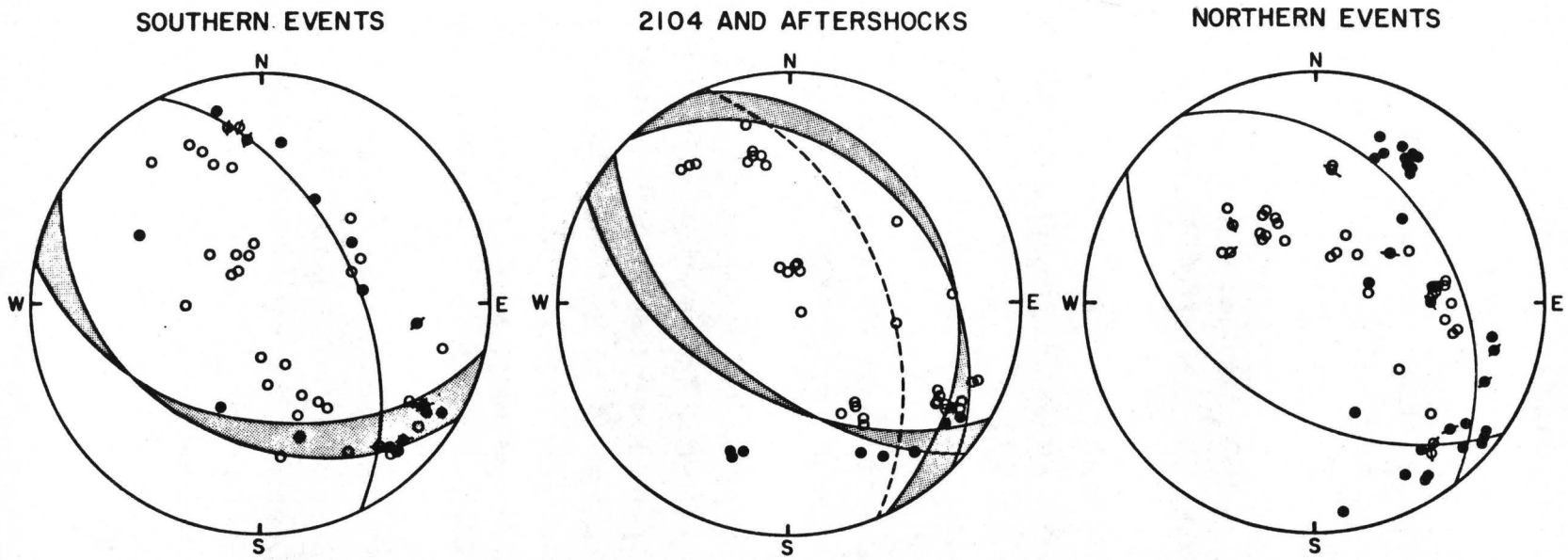

Figure 3. Upper hemisphere projections of the composite focal mechanisms for three sets of aftershocks: on the left, the southern events without 2104 and its aftershocks, in the middle, 2104 and its aftershocks, and on the right, the northern events. The dashed line on the composite mechanism of the 2104 event and its aftershocks shows the fault plane obtained from the composite mechanism for the southern events.

Spectral Analysis

All events larger than $\underline{M}$ = 3.0 recorded in the two-week deployment of the digital instruments were analyzed to determine the source parameters of seismic moment, radiated energy, source radius, and dynamic stress drop. Every P-wave recorded on the vertical component and S-wave recorded on a horizontal component was used in the analysis. An example of the spectral analysis performed on each phase is shown in Figure 4. A short sample containing the body-wave arrival is tapered with a 10 percent cosine bell. The Fourier transform of the tapered sample is corrected for the response of the velocity sensor. The integral of the square of the ground velocity, I_c, is computed using Parseval's theorem. The long-period level, $\bar{u}_c$, and the corner frequencies, ν_c, are estimated from the displacement amplitude spectrum, as shown in Figure 4b. The acceleration amplitude spectrum is then fit by the function $\bar{a}e^{-\omega t^*/2}$ for the angular frequencies, $\omega > 2\pi\nu_c$, as shown in Figure 4c. This fitting procedure assumes that the acceleration spectrum is essentially flat or "white" above the corner frequency and that the spectral falloff is due to the attenuation suffered in the body-wave propagation (Anderson and Hough, 1984). Displacement spectra which exhibit an intermediate falloff over an extended frequency band above the corner frequency are fit only for the frequencies where they fall off as ω^{-2} or greater. The spectral fits were graded into three categories (good, fair, and poor) using a subjective assessment of the quality of the fit. Stations which exhibit strong site resonances were poorly fit by this spectral model, in general.

Seismic Moment

The seismic moments of the aftershocks were calculated from the estimates of the long-period levels of the displacement spectra of the recorded body-waves, $\bar{u}_c$, using the formula

$$M_0 = 4\pi[\rho(s)\rho(x)c(x)]^{\frac{1}{2}}\, c^{\frac{5}{2}}(s)\, \frac{R}{F^c}\, \bar{u}_c \qquad (2)$$

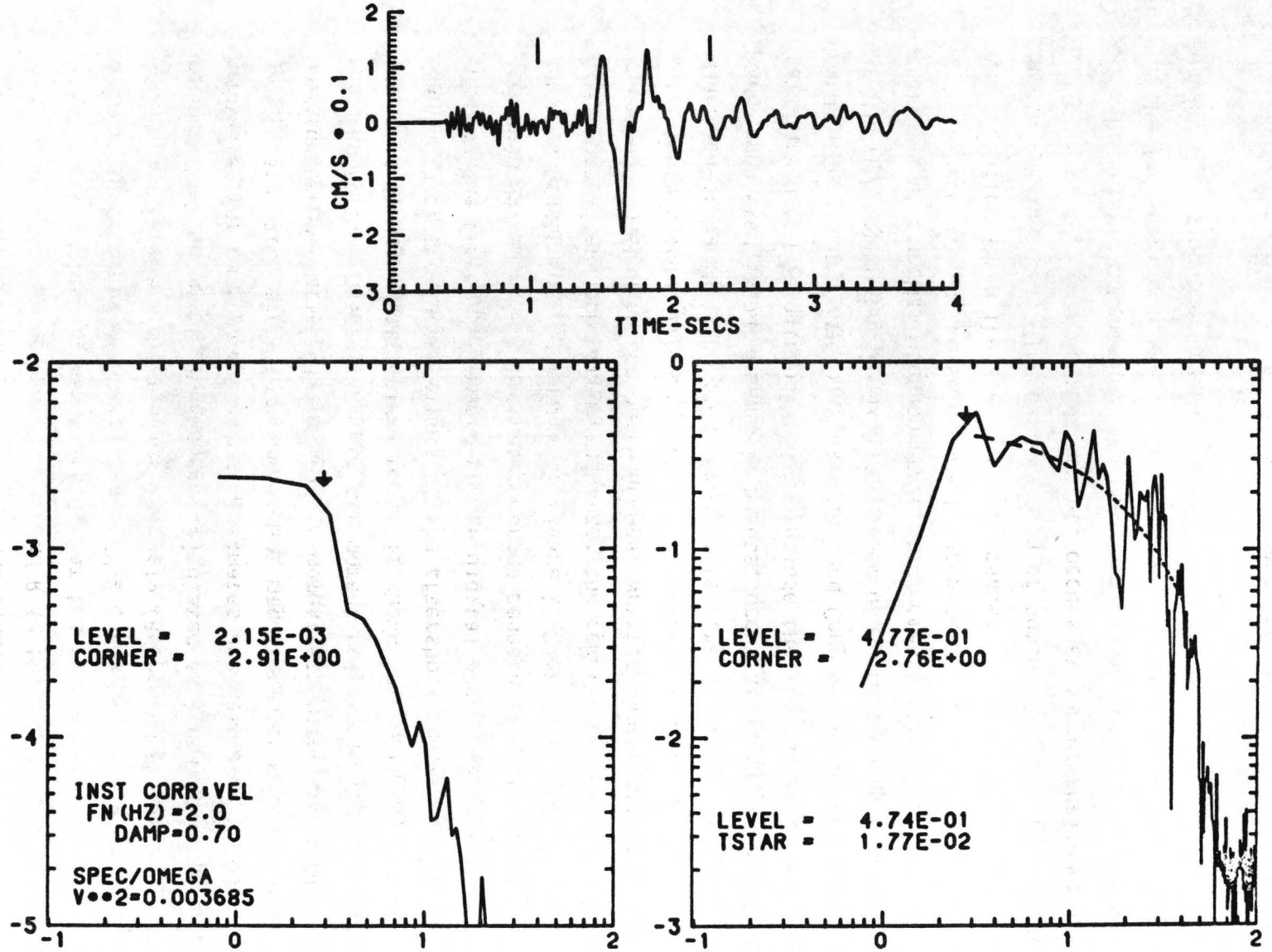

Figure 4. Example of the spectral analysis performed on each recorded phase. The sample chosen for the spectral analysis is delimited by the vertical bars above the seismogram. The long period level and corner frequency are picked on the displacement spectrum (on the left), while the acceleration spectrum is fit by the dashed curve at the frequencies above the corner frequency to estimate the high-frequency spectral level and t*. This fit was graded as good.

where $\rho(s)$, $c(s)$ and $\rho(x)$, $c(x)$ are the density and wave velocity at the source and receiver, respectively, and R is the geometrical spreading factor, which incorporates the amplification at the free-surface (Aki and Richards, 1980). The mean radiation patterns $F^P = .44$ and $F^S = .42$ were used for the P- and S-wave analyses, respectively (Boore and Boatwright, 1984). The seismic moments of the events are calculated as the arithmetic averages of the estimates for each phase. These estimates are compiled in Table 3 for the 58 events analyzed, along with the moment magnitudes computed from eq. (1). The average uncertainties of the seismic moment estimates are about 30 per cent.

The spatial distribution of the moment release in the aftershock sequence recorded by the digital instruments is shown in Figure 1. The clustering to the north of the larger events of the aftershock sequence is somewhat exaggerated by the temporal sampling of the digital array. Before the digital array was deployed, a $M_L = 5.8$ event occurred beneath station CEM among the southernmost cluster of epicenters in Figure 1 (Richins et al., 1985). In contrast, the large aftershocks occurring after the removal of the digital instruments have been located to the north (Dewey, written communication, 1984).

Figure 5 shows the distribution of moment release in the aftershocks as a function of depth. The plot demonstrates the surprising result that most of the large events, but few small events, occur at depths greater than 10 km. This trend can be extrapolated to include the initial rupture event of the mainshock, as analyzed by Boatwright and Choy (1984), which occurred at ≈15 km depth with approximately 6×10^{25} dyne-cm of seismic moment. The 85 per cent quantile of the distribution of seismic moments is plotted as a function of depth. The average seismic moment increases by a factor of five from 11 km to 15 km, below which there are no earthquakes. The behavior at shallow depths is markedly different. The distribution of moment does not vary above 10 km, and no aftershock, regardless of moment, occurs at depths shallower than 5 km.

Radiated Energy

Before calculating the seismic energy radiated by the aftershocks, it is necessary to determine the attenuation structure. The estimates of t*, calculated in the fits to the acceleration amplitude spectra, were inverted to determine the P- and S-wave attenuation in the three uppermost layers and

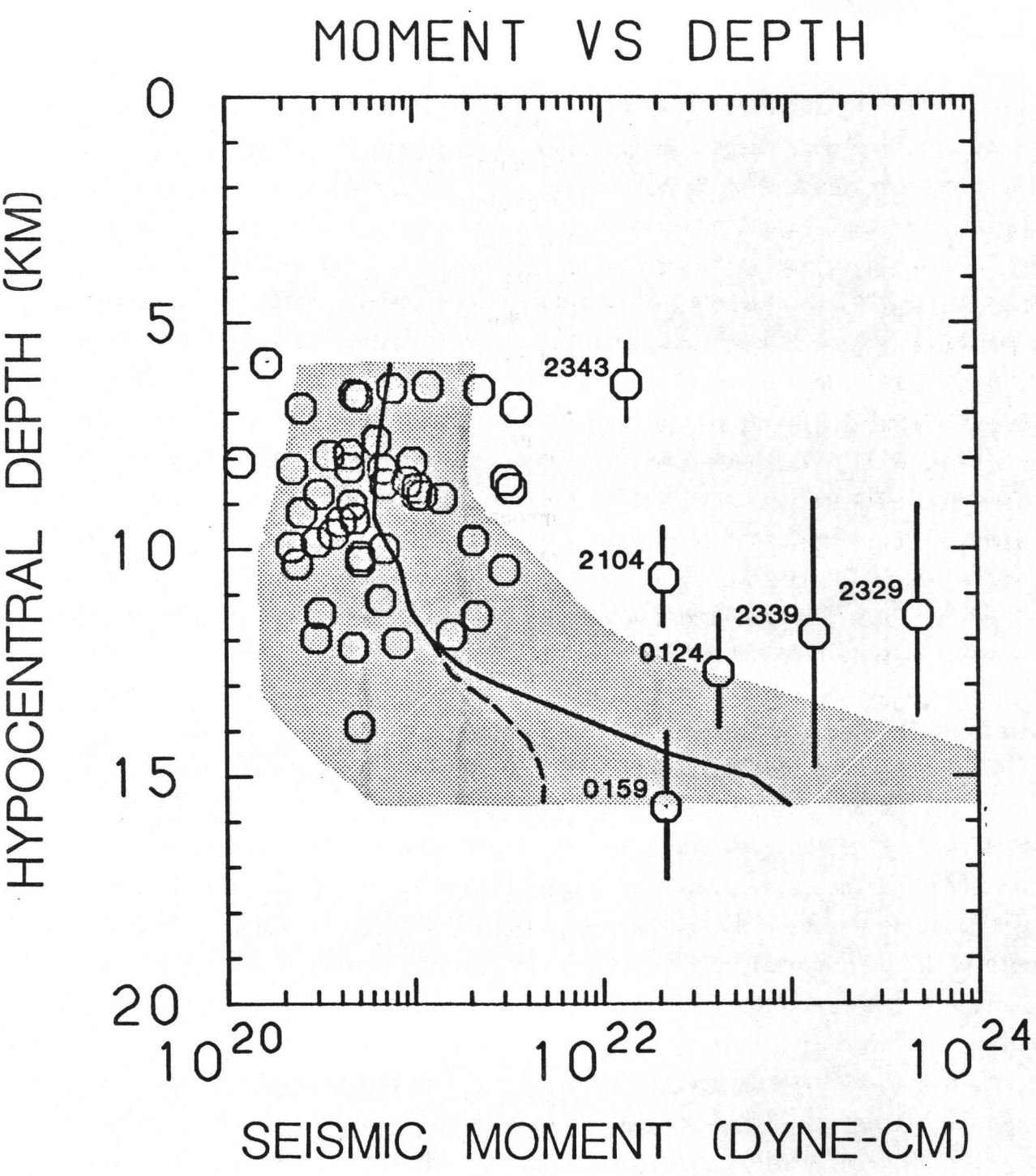

Figure 5. Seismic moments of the aftershocks plotted against hypocentral depths. The error bars plotted for the larger aftershocks show the relative uncertainty in their depth estimates. The dark line is the average seismic moment, potted as a function of depth. The stippled region shows the 85 per cent quantile for the distribution of moments. The dashed line is the average seismic moment obtained by including the initial event of the mainshock. The depth interval over which the seismic moments are averaged is four km.

station residuals for each wave-type. Unfortunately, the scatter in the t* estimates made the inversion unstable. Following the observational results of Anderson and Hough (1984), a simple attenuation structure was chosen which satisfied the data and concentrated the attenuation in the uppermost layer. Because the attenuation appeared to be due mostly to scattering, rather than anelastic absorption, the P- and S-wave Q's were constrained to be as similar as possible (Richards and Menke, 1983). The attenuation structure is listed in Table 1. The t* estimates determined from the "good" fits are shown in Figure 6, along with the attenuation as a function of travel time predicted for events with hypocentral depths of 6 and 12 km, respectively. While the P-wave measurements appear to be fit by the assumed attenuation structure, the S-wave measurements comprise a cloud surrounding the curves for the predicted t_c^*'s. The station residuals for each wave type are listed in Table 4.

Estimates of the energy radiated in each wave-type are determined from the corrected measurements of the integral of the square of the ground velocity in a single component of motion, I_c^*, and the relations,

$$E_s^p = 4\pi\rho(x)\alpha(x)R^2 I_p^* \ , \tag{3a}$$

$$E_s^s = 8\pi\rho(x)\beta(x)R^2 I_s^* \ , \tag{3b}$$

derived by Boatwright and Fletcher (1984). The integrals of the square of the ground velocity, I_c, were corrected for the body-wave attenuation as

$$I_c^* = I_c e^{2\pi\nu_c t_c^*} \tag{4}$$

(Boatwright and Fletcher, 1984), where ν_c is the corner frequency and t_c^* is predicted from the source-receiver geometry and the attenuation structure. The total radiated energy was determined from the energy radiated in the P- and S-waves by assuming that the partition of energy is given by $E_s^s/E_s^p = q = 13.5$. The P and S-wave energies radiated by the 26 best recorded events in the sequence returned an estimate of $q = 14.7 \pm 2.2$. The cumulative distribution of the 26 estimates is plotted in Figure 7; it has been fit with a curve showing the distribution function of a lognormal distribution with the appropriate mean and standard deviation. The estimates of the radiated energy determined by combining the P and S-wave estimates are compiled in Table 3 for all events.

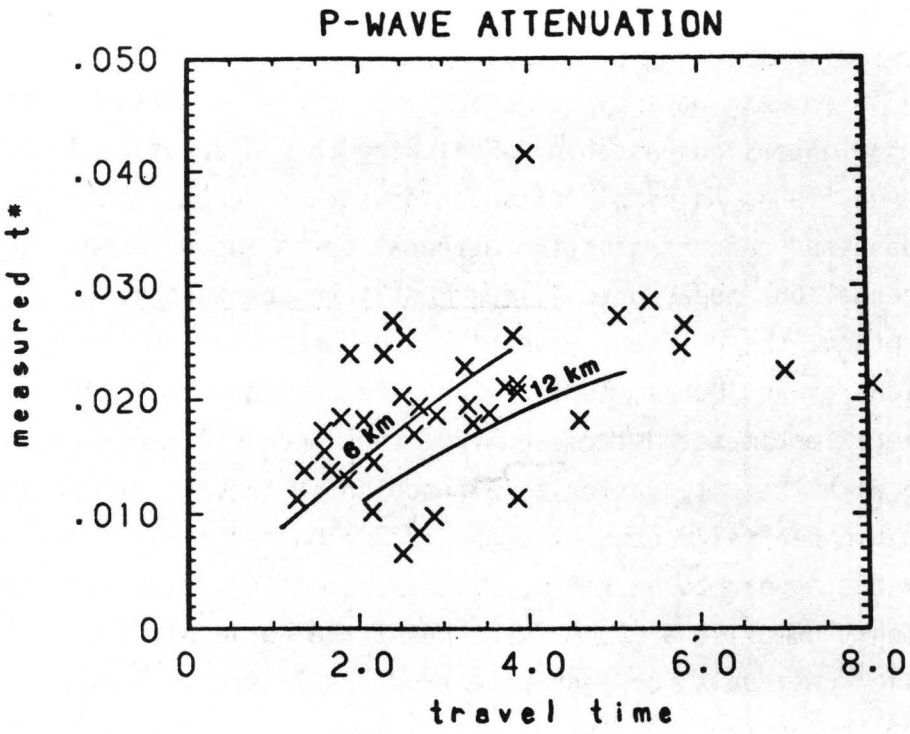

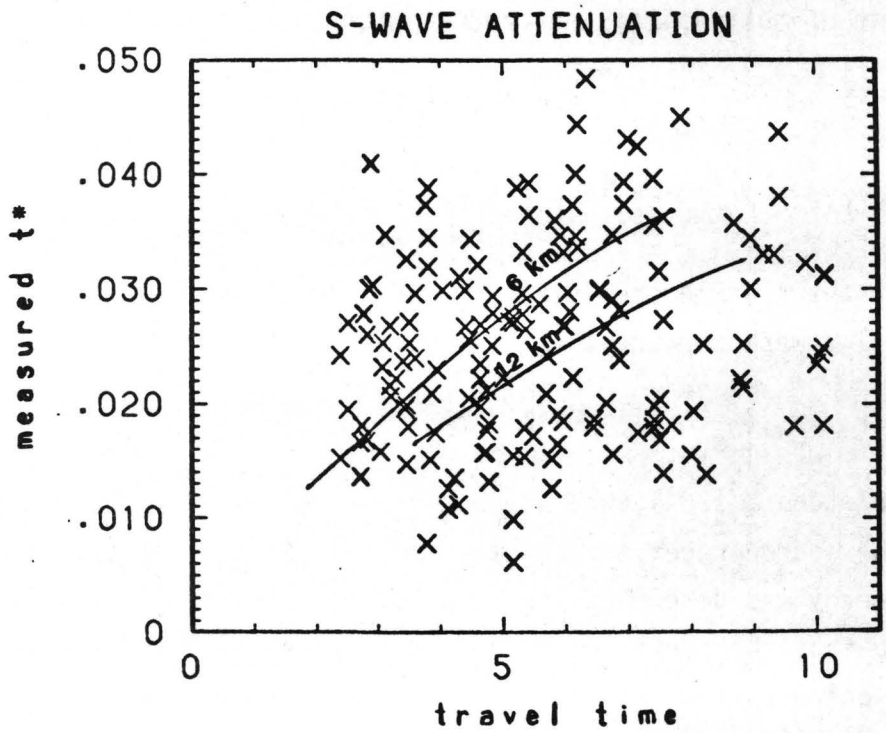

Figure 6. Estimates of t* plotted against travel time for both P and S-waves; only the estimates from the "good" fits are shown. The scatter is a realistic measure of the uncertainty of the technique. The smooth curves show the prediction of t_c^* as a function of travel time from the attenuation model listed in Table 1 and used to correct the integrals of the square of the velocity for attenuation in equation (4).

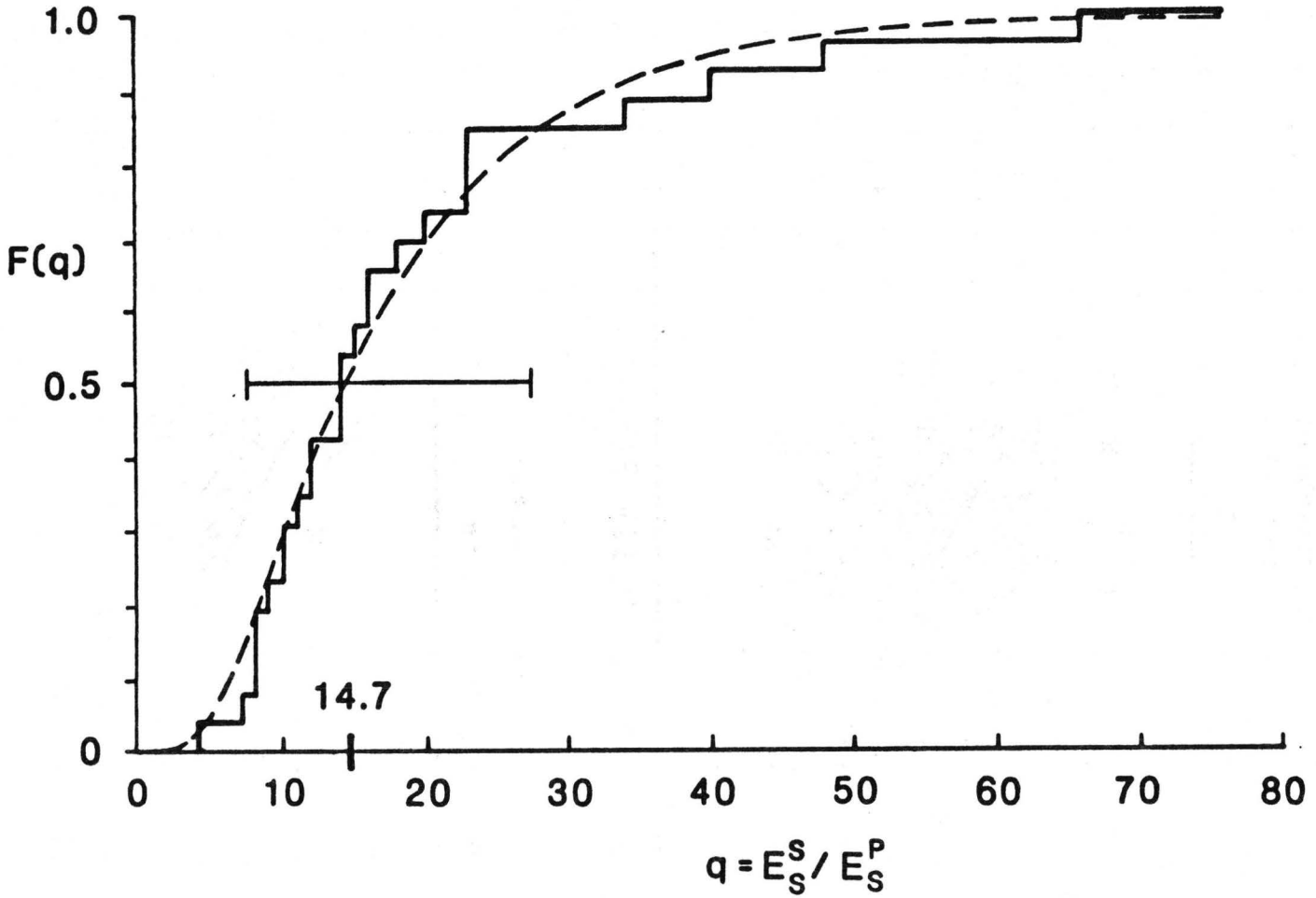

Figure 7. Cumulative distribution function for the 26 estimates of the partition of radiated energy, $q = E_s^S/E_s^P$, obtained from the 26 best recorded events. The smooth line shows a log-normal distribution function with a mean of 14.7 and the standard deviation of .23 log units.

The seismic energies radiated by the aftershocks are plotted against their seismic moments in Figure 8. The two diagonal lines through the estimates represent a constant apparent stress of 10 and 50 bars. The radiated energies of the aftershocks increase with increasing seismic moment at a rate which is slightly greater than linear; this dependence implies that the larger events tend to have higher values of apparent stress.

Dynamic Stress Drops

Brune's (1970, 1971) relation between corner frequency and source radius

$$a = \frac{2.34\beta}{2\pi\nu_\beta} \tag{5a}$$

was used to estimate the source radius from estimates of the S-wave corner frequency; the relation

$$a = \frac{2.03\alpha}{2\pi\nu_\alpha} \tag{5b}$$

was used for P-wave corner frequencies. Equation (5b) assumes that the corner frequency shift is equal to 1.5, slightly less than the ratio α/β assumed by Hanks and Wyss (1974), but more in line with the tehoretical results from rupture models studies by Madariaga (1976) and Boatwright (1980). The estimates of the source radius derived from each spectra were averaged arithmetically; the averages are compiled in Table 3.

The dynamic stress drops of the events have been calculated following the analysis proposed by Boatwright (1982), which uses the estimates of the source radius and the high-frequency acceleration spectral level. Modifying equation (15) of Boatwright (1982) for a heterogeneous velocity structure gives

$$\Delta\sigma = \frac{[\rho(s)\rho(x)\beta(s)\beta(x)]^{\frac{1}{2}}}{(\frac{\Delta V}{\beta(s)})\ A^{\frac{1}{2}}} (\frac{R}{R^c})\ \bar{a} \tag{6}$$

where Δv is the peak rupture velocity, assumed to be $.85\beta(s)$, $A = \pi a^2$ is the rupture area, and $R^s = .25$ or $R^p = .065$ are the high-frequency radiation patterns appropriate for an S-wave recorded on a horizontal component or a

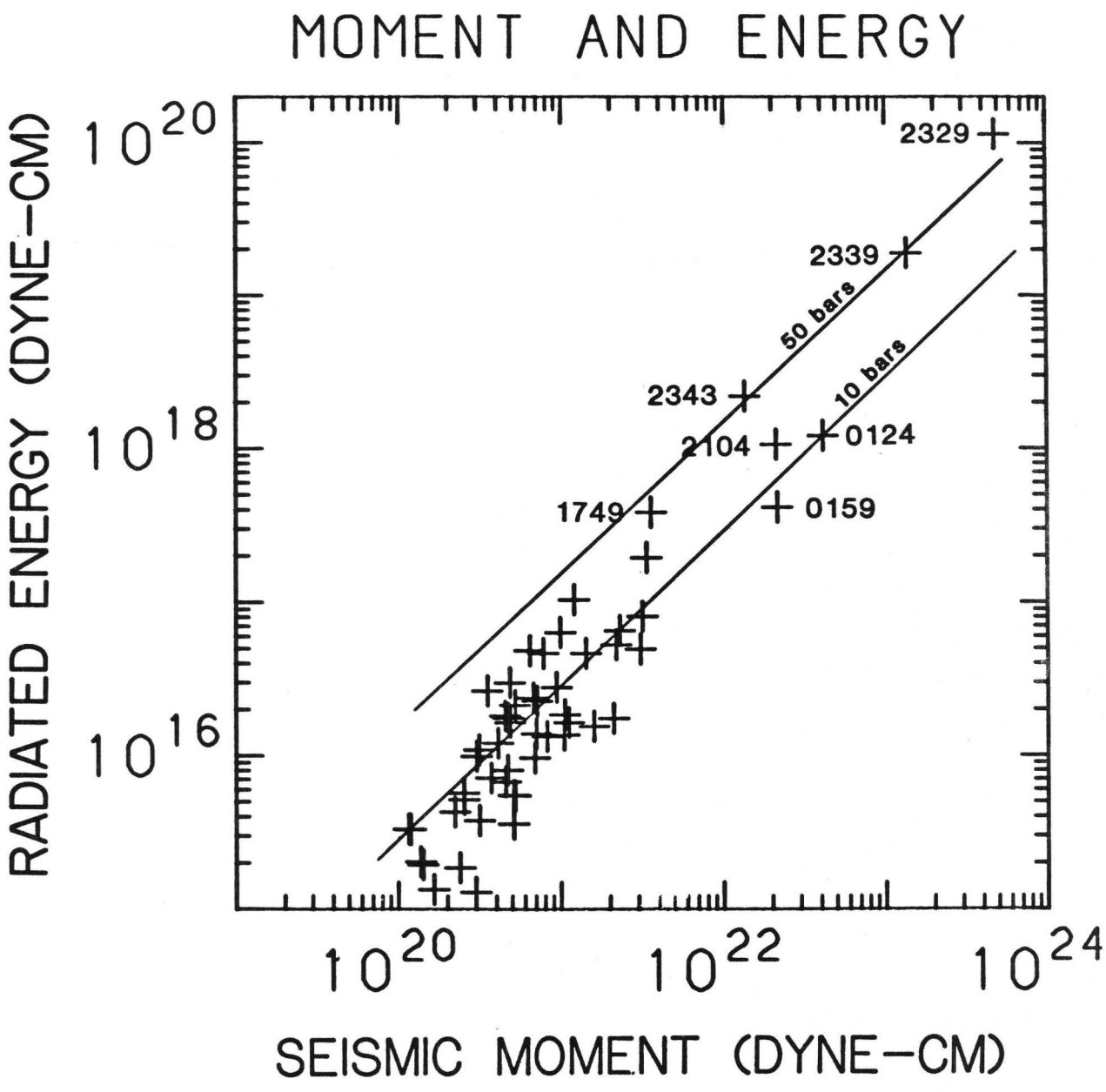

Figure 8. Radiated energy plotted against seismic moment for the aftershocks. The two diagonal lines represent lines of constant apparent stress equal to 10 and 50 bars.

P-wave recorded on a vertical component, respectively. The rms dynamic stress drops are about 35 percent larger than the static stress drops obtained from the seismic moments, source radii and Brune's (1970) relation. Body-wave spectra which exhibit intermediate falloffs above the corner frequency show the largest discrepancy, as predicted by Brune's (1970) discussion of events in which the stress release is "incomplete".

The dynamic stress drops are plotted as a function of seismic moment in Figure 9. Over a range of seismic moment from 3×10^{21} to 10^{23} dyne-cm, the dynamic stress drops are approximately independent of the moment, ranging from 10 to 100 bars with an average of 40 to 45 bars. The stress drops of the two largest events (2329 and 2339) are significantly greater the stress drops of the other events. Below 3×10^{21} dyne-cm, the stress drops begin to falloff as function of seismic moment. In this range the estimates of stress drop are assumed to be unreliable because the correction for body-wave attenuation made in the analysis is not an automatic correction.

The dynamic stress drops of the events with $\underline{M} > 3.0$ are plotted as a function of depth in Figure 10. In contrast to the marked dependence of seismic moment on depth evident in Figure 5, the stress drops show no apparent depth dependence. Over the range in depth from 6 km to 12 km, the normal stress on the fault plane, and therefore the strength and stress drop, should increase by a factor of two (Byerlee, 1978). This increase is not evident in the distribution of the stress drops as a function of depth.

To consider the variation of stress drop along strike, the epicenters of the events with $\underline{M} > 3.0$ have been plotted in Figure 10 with three different shadings to indicate the stress drop. The open symbols have stress drops less than 40 bars, the lightly shaded symbols have stress drops from 40 to 80 bars, and the heavily shaded symbols have stress drops greater than 80 bars. The dependence of the symbol size on the seismic moment has been halved from that used in Figure 1. Of the plotted sample of 45 events, 4 events (8 per cent) are heavily shaded, while 16 events (33 per cent) are lightly shaded. The events with moderate stress drops appear to be distributed randomly, while the events with large stress drops are clustered at the northwest limb of the aftershock distribution. Of the eleven events located north of 44°14'N, 3 have small stress drops, 4 have moderate stress drops, and 4 have large stress drops. The average stress drop of this group of aftershocks is 77±53 bars,

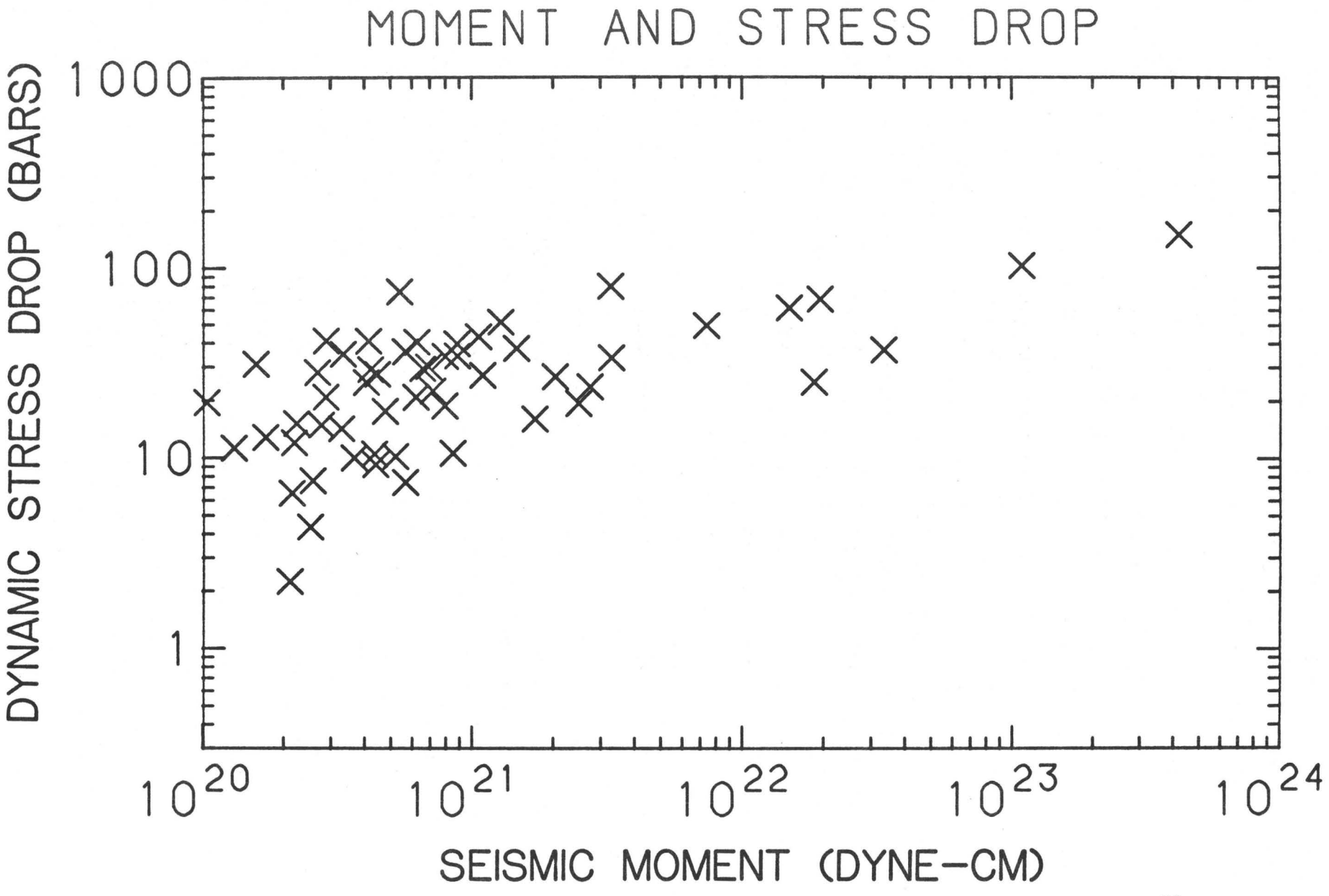

Figure 9. Dynamic stress drop plotted against seismic moment for the aftershocks. Below 3×10^{21} dyne-cm, the dynamic stress drops are assumed to be unreliable, as the attenuation prohibits obtaining unbiased estimates of the corner frequency or the high-frequency spectral level.

twice the average stress drop, 30±15 bars, for the rest of the events. The clustering of large stress drops indicates that the northwest limb of the aftershock distribution is more strongly loaded than the rest of the aftershock zone.

Discussion

We will discuss in detail three characteristics of the aftershock sequence: the variation along strike of the aftershock distribution and mechanisms, the variation of the seismic moments with hypocentral depth, and the variation of the dynamic stress drops with location and seismic moment. These characteristics will then be combined with the teleseismic analyses of the mainshock performed by Boatwright and Choy (1985) and Barrientos et al. (1985) to speculate on the dynamics of the mainshock rupture process.

The epicentral distribution of the aftershocks parellels the surface faulting, running north-northwest for 33 km from south of Chilly Buttes to the Willow Creek summit. In the southern half of the aftershock area, the hypocenters delineate a fault plane which dips to the west at 45°-50°; the composite focal mechanism for this group of events has a normal faulting mechanism, a west dipping nodal plane, and some left-lateral slip, consistent with the geologic measurements of the surface faulting. Richins et al. (1985) locate the epicenter of the mainshock to the south of the surface faulting and almost all of the aftershocks which occurred in the first two weeks. If this location is correct, the lack of nearby aftershocks implies that the stress release in the initial rupture event was complete, in the sense that there were no residual stress concentrations. This inference coincides with teleseismic analysis of the mainshock of Boatwright and Choy (1985). The initial pulse of the teleseismic waveforms appears to be simple; it has a duration of ~4 sec, which corresponds to a source radius of 10 km.

In the northern half of the aftershock area, the character of the aftershocks changes signficantly; their hypocenters dip very steeply to the east and their composite focal mechanism, although still a normal faulting mechanism, is different in strike and dip from the mechanism of the southern events. In cross-section, the northern aftershocks appear uncorrelated with the surface faulting, which continues to the northwest along the Lost River

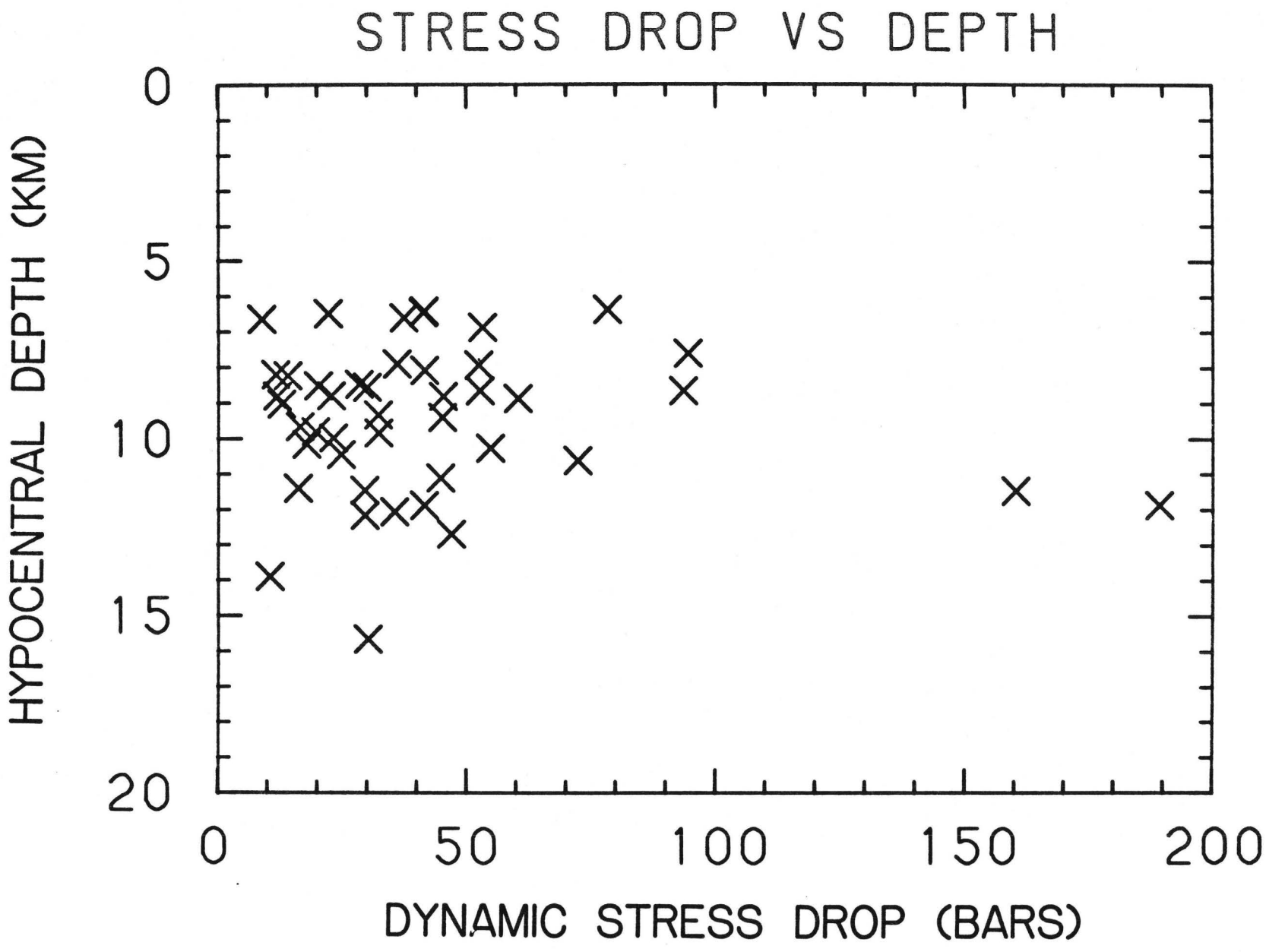

Figure 10. Dynamic stress drop plotted against hypocentral depth for the aftershocks with moments greater than 3×10^{21} dyne-cm. The source parameters for the eleven events which occurred in the northwest limb of the aftershock distribution are circled.

Fault until it reaches Arentson Gulch, where it splays towards the west. Sections of the Lost River Fault as far as 15 km north of the splay are also offset. The lack of aftershock activity at depth on these fault segments implies that the surface displacements are not reliable indicators of the slip at depth. The aftershocks appear to occur on a set of east dipping fault segments rather than on the west dipping Lost River Fault. If the aftershocks are indicative of the slip at depth in the mainshock rupture, the westward splay at Arentson Gulch may represent a tear fault driven by the difference between the faulting at depth and at the surface.

This interpretation is conditioned by the depth distribution of the aftershocks. There are no aftershocks at depths shallower than 5 km; thus we have no direct information about the slip geometry at these depths. In the southern part of the aftershock zone, however, where the aftershock distribution correlates with the surface faulting, the absence of aftershocks indicates that the Lost River Fault is relatively weak or compliant at shallow depths.

In contrast to the compliant behavior at shallow depths, the aftershocks at depths below 12 km exhibit an unexpected depth dependence: the average seismic moment increases with increasing depth. Figure 8 shows that the stress drops of the aftershocks do not decrease systematically with depth: thus the increase of the average seismic moment implies that the average or minimum source radius increases with depth. To analyze this possibility, consider the critical crack length for rupture propagation as an estimate of the minimum source radius. In slip-weakening models, the critical crack length

$$L_c \propto \frac{(\sigma_u - \sigma_f)\, d_o}{\Delta\sigma^2} \qquad (7)$$

depends on the yield stress, σ_u, the frictional stress, σ_f, the stress drop, $\Delta\sigma$, and the slip weakening displacement, d_o (Andrews, 1976). Sibson (1982) suggests that the bottom of the seismogenic zone is fixed by the transition between brittle and ductile modes of deformation; in these zones, he shows that the yield stress decreases with increasing depth. Equation (7) then implies that the slip weakening displacement increases with depth below 12 km. Physically, the increase of the critical crack length means that small stress concentrations are less likely to be relieved seismically, so that there are fewer small events in the transition zone.

Large stress concentrations in the transition zone are still able to accelerate into earthquakes. The initial rupture event in the mainshock appears to have nucleated at 16 km and ruptured to at least 22 km depth (Boatwright and Choy, 1985); similarly, the centroid of the long-period teleseismic model of Barrientos et al. (1985) is fixed at 15 km depth. These results indicate that the mainshock ruptured entirely through the seismogenic thickness of the crust, and that a substantial component of aseismic slip may be included in the post-seismic response.

The stress drops of the aftershocks appear to depend more on the locations of the events than their seismic moments. For events with $\underline{M} > 3.0$, the aftershocks to the south have an average stress drop of 31±16 bars while the aftershocks in the northwest limb have an average stress drop of 77±52 bars. This difference suggests that the northwest limb of the aftershock distribution represents a stress concentration, possibly where a fracture barrier stopped the rupture in the mainshock. The strong loading of this barrier (and large stress drops of the aftershocks) are interpreted as resulting from the redistribution of stress in the mainshock: specifically, the stress concentration at the edge of the region of stress release.

The fracture barrier interpretation suggests that the events in this limb of the aftershock distribution should be excluded from the extrapolation of the aftershock stress drops to estimate the mainshock stress drop. If these eleven aftershocks are excluded, the resulting average of 31 bars coincides exactly with the teleseismic estimate of 28±8 bars determined by Boatwright and Choy (1985) for the dynamic stress drop of the initial rupture event. We note that this apparent correlation may be fortuitious, however. Teleseismic estimates of stress drop are generally lower than near field estimates. Moreover, we note that we have excluded the two largest events (2329, $\underline{M} = 5.1$ and 2339, $\underline{M} = 4.8$) with the largest stress drops from the aftershock distribution. The largest aftershock remaining in the distribution has a seismic moment that is less than a thousandth of the seismic moment of the mainshock. The estimate of the stress drop of the mainshock is clearly speculative.

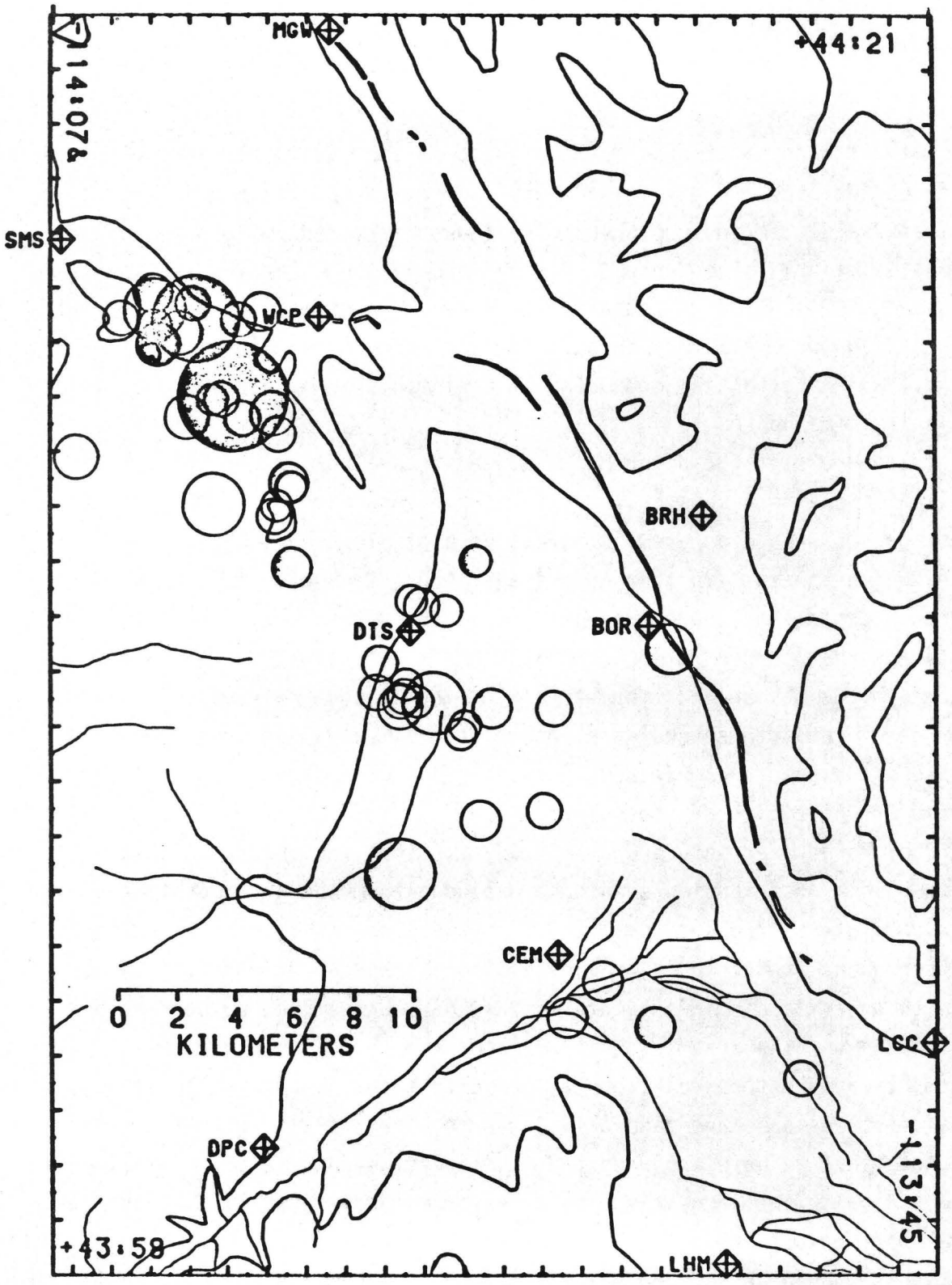

Figure 11. Epicenters of the aftershocks with moments greater than 3×10^{21} dyne-cm, plotted to show the distribution of stress release in the aftershocks. The symbols without shading represent events with stress drops less than 40 bars, the symbols with light shading represent events with stress drops between 40 and 80 bars, and the symbols with heavy shading represent events with stress drops greater than 80 bars.

Conclusions

In general, the aftershock locations and composite mechanisms determined in this paper correlate well with the surface faulting in the mainshock. The correlation is better in the southern part of the aftershock area than in the northern part, where the surface faulting splays and diffuses onto a number of fault segments. Many of these fault segments appear to have no aftershocks at depth associated with them; the surface offsets on these segments are assumed to be secondary, or surficial, features.

The distribution of the aftershocks as a function of depth is the most unusual result of the analysis. The seismogenic zone is relatively narrow; the hypocenters of the aftershocks range from 5 to 15 km in depth. The seismic moments of the events deeper than 12 km appear to increase with increasing depth, possibly indicating the transition from brittle to ductile deformation. The strong variation of the stress drops from event to event masks any systematic variation of stress drop at these depths, however.

For events with $\underline{M} > 3.0$, the stress drops of the aftershocks vary more strongly with location than with seismic moment. The northwest limb of the aftershock sequence has the strongest stress drops: the average stress drop in this cluster (77±52 bars) is more than twice the average stress drop of the rest of the events (31±16). This cluster of aftershocks is interpreted as representing a stress concentration; possibly, it is the manifestation of a fracture barrier that stopped the rupture in the mainshock. The average stress drop of the aftershocks to the south, in the rupture area of the mainshock, is relatively small for crustal earthquakes; together, the narrow seismogenic zone and small stress drops suggest that the Lost River Fault is weak.

Acknowledgements

I am indebted to Gene Sembera and Chuck Mueller for their hard work in the field, deploying and troubleshooting the instruments, to Ed Cranswick and Linda Haar for their help analyzing the recordings, locating the events, and plotting the figures, and to Carol Sullivan for her eleventh hour typing of the manuscript. The paper was reviewed by Joe Fletcher and Art McGarr.

Table 1

layer	depth (km)	α (km/sec)	β (km/sec)	ρ (gm/cm^3)	Q_α	Q_β
1	0.0	4.75	2.70	2.2	50	50
2	1.0	5.60	3.20	2.5	200	300
3	7.0	6.15	3.55	2.7	500	500
4	18.0	6.80	3.95	2.8	-	-
5	32.0	7.85	4.55	3.0	-	-

Table 2

DATE	ORIGIN TIME	LAT N	LON W	DEPTH	RMS	ERH	ERZ	GAP
83-10-29	1624 14.54	44 3.77	133 54.36	9.95	.05	2.82	1.25	119
83-10-29	1737 40.72	44 2.54	113 52.14	8.09	.05	3.32	2.41	166
83-10-29	1923 24.30	44 2.71	113 54.36	9.32	.04	2.72	0.96	160
83-10-29	2113 59.53	44 6.30	113 56.58	8.74	.09	1.76	1.10	197
83-10-29	2329 11.81	44 14.00	114 2.88	12.54	.13	2.72	2.43	312
83-10-29	2339 5.41	44 15.42	114 3.83	11.72	.03	3.46	2.95	324
83-10-30	116 39.40	44 3.37	113 53.47	8.52	.08	1.48	1.02	162
83-10-30	120 1.41	44 3.30	113 52.94	7.21	.10	3.49	2.72	155
83-10-30	124 51.30	44 5.33	113 58.62	12.69	.09	2.23	1.22	233
83-10-30	159 2.01	44 12.03	114 3.37	15.60	.04	2.75	1.64	296
83-10-30	254 39.65	44 12.89	114 6.88	6.49	.07	2.66	2.49	252
83-10-30	345 19.29	44 20.01	113 49.56	2.43	.16	1.75	10.25	238
83-10-30	8 5 23.59	44 14.77	114 1.71	11.74	.09	4.66	2.88	222
83-10-30	1225 52.64	44 6.48	113 54.95	9.07	.09	1.03	0.93	136
83-10-30	1638 7.17	44 2.74	113 53.29	8.64	.08	2.15	1.04	181
83-10-30	1749 19.88	44 9.42	113 51.73	6.91	.07	1.14	0.74	175
83-10-30	23 2 34.54	44 1.59	113 48.44	8.18	.08	0.69	1.30	113
83-10-30	2356 26.05	44 15.28	114 4.88	6.46	.08	0.82	0.66	167
83-10-31	1 4 33.77	44 6.36	113 53.30	7.52	.06	1.82	1.61	138
83-10-31	7 2 1.62	43 53.89	113 45.60	13.49	.07	1.31	1.91	199
83-10-31	841 48.99	44 2.96	113 53.95	8.38	.08	1.92	0.93	181
83-10-31	1033 26.28	44 11.02	113 56.70	7.93	.07	1.63	1.25	126
83-10-31	1055 37.32	44 6.50	113 57.27	10.83	.10	2.12	1.37	183
83-10-31	1515 16.27	44 12.65	113 57.35	5.55	.10	1.63	0.97	108
83-10-31	2227 45.97	44 0.90	113 54.13	10.93	.13	1.29	2.68	116
83-11-1	027 47.58	44 9.61	113 55.03	6.91	.09	1.19	0.48	173
83-11-1	1 5 28.21	44 13.95	114 3.17	7.95	.11	0.78	1.63	84
83-11-1	5 2 46.62	44 3.11	113 53.33	10.62	.12	0.97	3.10	98
83-11-1	1030 33.63	44 8.02	113 56.98	9.82	.10	0.77	1.11	78
83-11-1	1234 24.89	44 8.20	113 57.76	10.69	.08	0.85	1.02	103
83-11-1	1350 25.05	44 9.15	113 59.14	12.22	.06	0.81	1.57	86
83-11-2	2224 4.60	44 13.94	114 3.40	9.42	.06	0.99	1.34	134
83-11-2	2342 1.86	44 15.89	114 4.92	6.45	.04	0.70	0.96	92
83-11-2	2343 55.14	44 15.60	114 4.88	6.37	.10	0.66	0.63	131
83-11-3	018 48.40	44 15.55	114 2.16	8.76	.05	1.37	3.23	137
83-11-3	122 15.70	44 15.70	114 3.91	7.59	.07	1.07	2.01	156
83-11-3	150 20.34	44 14.95	114 4.80	6.75	.10	0.85	0.64	157
83-11-3	259 19.12	44 13.69	114 1.86	10.45	.06	1.45	1.48	120
83-11-3	415 16.37	44 15.16	114 4.25	8.47	.08	1.17	1.97	154
83-11-3	17 0 14.03	43 53.09	113 40.73	8.18	.03	1.66	2.11	186
83-11-3	2026 53.80	44 9.89	113 58.34	9.53	.08	0.79	1.84	76
83-11-3	22 9 24.54	44 6.07	113 57.07	11.29	.07	0.90	0.77	81
83-11-3	2337 8.67	44 20.82	114 4.68	7.51	.08	0.96	1.30	168
83-11-4	0 2 25.50	44 10.62	114 0.76	10.56	.06	0.60	0.78	81
83-11-4	5 0 14.83	44 8.34	113 56.30	8.83	.11	0.61	0.92	75
83-11-4	7 8 19.21	44 12.43	114 1.45	8.88	.10	0.77	0.86	84
83-11-4	9 4 12.87	44 8.34	113 54.70	6.60	.10	0.94	0.55	87
83-11-4	1343 1.06	44 12.01	114 1.76	9.18	.06	0.84	1.08	85
83-11-4	1730 44.28	44 15.39	114 1.18	5.10	.10	0.75	0.96	111
83-11-4	2259 37.73	44 4.59	113 56.41	10.61	.05	0.71	0.90	80
83-11-4	2329 49.29	44 15.43	114 5.75	8.25	.10	0.76	1.15	100
83-11-4	2336 45.37	44 14.23	114 4.32	8.34	.08	0.65	1.08	84
83-11-5	018 31.34	44 9.34	113 57.97	9.76	.08	0.68	1.22	76
83-11-5	151 49.13	44 7.87	113 57.09	11.96	.09	1.04	1.99	129
83-11-5	353 34.35	44 9.18	113 53.69	5.90	.09	0.62	0.93	92
83-11-5	422 8.99	44 8.46	113 58.19	10.33	.06	0.58	1.12	81
83-11-5	537 39.75	44 13.62	114 4.06	9.81	.09	0.82	1.26	82
83-11-5	813 39.42	44 12.34	114 1.38	8.24	.07	0.76	1.31	85
83-11-5	1041 35.95	44 19.66	114 2.79	10.70	.10	0.75	0.74	126
83-11-5	1736 25.32	44 10.89	114 1.37	11.89	.09	0.71	1.28	81
83-11-5	1743 54.75	44 8.62	113 59.23	13.91	.16	0.80	1.17	89

Table 2 (cont.)

DATE	ORIGIN TIME	LAT N	LON W	DEPTH	RMS	ERH	ERZ	GAP
83-11-5	2029 30.15	44 11.82	114 1.82	9.99	.08	1.46	1.28	142
83-11-5	2256 42.74	44 13.31	114 1.72	12.07	.08	0.67	1.07	81
83-11-5	23 1 29.05	44 13.46	114 1.75	11.68	.06	0.70	1.04	105
83-11-6	326 9.41	44 15.70	114 5.12	6.90	.01	1.21	1.62	214
83-11-6	644 15.89	44 10.29	113 58.34	11.41	.07	0.83	1.58	74
83-11-6	735 10.66	44 15.87	114 5.07	5.38	.08	0.56	0.64	79
83-11-6	1449 59.74	44 12.99	114 2.26	12.03	.09	0.99	1.58	105
83-11-6	21 4 48.73	44 8.43	113 57.77	10.63	.08	0.84	1.07	137
83-11-6	21 7 10.16	44 8.47	113 58.62	11.12	.06	1.01	1.46	127
83-11-6	2111 54.97	44 8.36	113 58.63	11.47	.07	0.88	1.17	126
83-11-6	2119 56.43	44 8.77	113 58.47	9.67	.04	1.31	1.04	150
83-11-6	2120 40.25	44 8.55	113 58.51	10.17	.08	0.88	1.59	150
83-11-6	2311 38.63	44 13.60	114 2.63	6.65	.03	1.56	1.17	166
83-11-7	933 31.20	44 10.20	113 58.08	8.56	.08	0.87	0.80	71
83-11-7	14 5 46.57	44 16.43	114 6.63	8.48	.07	0.90	0.95	101
83-11-7	1733 6.09	44 15.41	114 2.74	10.28	.09	0.84	0.62	90
83-11-8	643 2.52	44 10.11	113 57.46	8.80	.10	0.85	1.32	72

TABLE 3

Event	Depth (km)	M	Seismic Moment ($\times 10^{20}$ dyne-cm)	Source Radius (km)	Stress Drop (bars)	Radiated Energy ($\times 10^{15}$ dyne-cm)
1624	10.0±1.3	2.90	2.2±0.4	.21±.03	18± 8	4.3±3.1
1737	8.1±2.4	3.33	9.9±3.0	.26±.03	42±21	63.±54.
1923	9.3±1.0	3.12	4.9±0.7	.24±.02	32±18	16.±10.
2113	8.8±1.1	3.34	10.±2.7	.37±.06	12± 5	14.±6.5
2329	11.5±2.4	5.12	$(4.8\pm2.0)\times10^{3}$	1.02±.12	160±43	$(1.1\pm0.9)\times10^{5}$
2339	11.9±3.0	4.75	$(1.4\pm0.6)\times10^{3}$	.76±.07	189±116	$(1.9\pm0.9)\times10^{4}$
0116	8.5±1.0	3.31	9.4±2.6	.35±.04	20± 4	28.±13.
0124	12.7±1.2	4.41	$(4.1\pm1.4)\times10^{2}$	.59±.08	47±19	$(1.2\pm0.8)\times10^{3}$
0159	15.7±1.6	4.22	$(2.2\pm0.8)\times10^{2}$	.62±.05	30±10	$(4.2\pm1.6)\times10^{2}$
0254	6.5±2.5	3.57	23.±16.	.35±.04	22± 6	65.±30.
1225	9.0±0.9	3.11	4.7±1.0	.34±.05	13± 5	8.0±3.8
1749	6.9±0.7	3.70	36.±12.	.39±.05	53±23	$(3.8\pm2.3)\times10^{2}$
2302	8.2±1.3	3.11	4.6±0.7	.32±.02	12± 4	6.7±3.4
2356	6.5±0.7	3.26	7.8±1.7	.23±.02	41± 8	46.±12.
1033	7.9±1.3	3.03	3.5±1.3	.14±.02	53±13	26.±16.
0105	7.9±1.6	3.10	4.5±1.0	.24±.02	36±10	18.±11.
0502	10.6±3.1	2.77	1.4±0.2	.23±.03	28±16	2.0±1.7
1030	9.9±1.1	3.03	3.0±0.5	.20±.02	32±10	9.9±4.7
1350	12.2±1.6	3.12	4.7±1.0	.23±.03	30± 7	18.±13.
2224	9.4±1.3	3.07	4.1±0.8	.21±.03	45±24	12.±11.
2342	6.5±1.0	3.39	12.±2.9	.26±.02	42± 9	$(1.0\pm.75)\times10^{2}$
2343	6.4±0.7	4.17	$(1.8\pm.35)\times10^{2}$	.52±.02	77±15	$(1.4\pm.44)\times10^{3}$
0018	8.7±3.2	3.35	11.±2.3	.29±.03	53± 31	18.±5.4
0122	7.6±2.0	3.20	6.4±2.1	.22±.04	95± 51	48.±40.
0150	8.7±0.6	3.68	34.±3.8	.41±.04	94± 37	$(1.9\pm1.5)\times10^{2}$
0259	10.5±1.5	3.66	31.±8.3	.74±.06	25± 8	49.±20.
0415	8.5±2.0	3.67	32.±6.2	.53±.04	28± 7	81.±22.
1700	8.1±2.1	2.72	1.2±1.2	.19±.02	24±20	3.3±4.2
2209	11.3±1.8	2.76	1.4±0.2	.23±.02	12± 3	2.0±1.0

(CONTINUED)

TABLE 3 (CONTINUED)

Event	Depth (km)	M	Seismic Moment ($\times 10^{20}$ dyne-cm)	Source Radius (km)	Stress Drop (bars)	Radiated Energy ($\times 10^{15}$ dyne-cm)
0002	10.6±1.3	2.58	.73±.19	.19±.02	17± 8	.81±.78
0500	8.8±0.9	3.36	11.±2.9	.30±.03	45±13	16.±4.9
0708	8.9±0.9	3.43	14.±2.2	.32±.02	60±19	46.±19.
0904	6.6±0.6	3.12	4.8±1.9	.26±.03	38±25	30.±22.
1343	9.2±1.1	2.94	2.5±.90	.24±.03	18± 7	5.2±3.1
2329	8.3±1.2	3.22	6.9±2.5	.33±.03	14± 4	9.7±4.7
2336	8.3±1.1	2.71	1.2±.29	.18±.02	21± 5	3.2±1.1
0018	9.8±1.2	2.40	.40±.01	.25±.02	2± 1	.63±.20
0151	12.0±2.0	2.98	3.0±.58	.32±.02	5± 1	1.3±.44
0353	5.9±0.9	2.81	1.7±.29	.33±.04	5± 2	1.3±.44
0422	10.3±1.1	2.92	2.4±.53	.36±.04	7± 3	1.9±1.0
0537	9.8±1.3	3.55	21.±8.5	.54±.04	20± 8	17.±8.7
0813	8.2±1.3	2.90	2.2±.51	.43±.05	3± 1	67.±.34
1736	11.9±1.3	3.47	16.±3.3	.28±.02	42±12	15.±7.9
1743	13.9±1.2	3.14	5.1±1.1	.31±.02	11± 2	3.6±.75
2029	10.0±1.3	3.23	7.0±2.3	.27±.02	23± 6	14.±5.8
2256	12.1±1.1	3.27	8.2±2.0	.28±.01	36±11	13.±4.1
0326	6.9±1.6	2.93	2.5±.72	.23±.03	19± 6	5.7±1.9
0644	11.4±1.6	3.00	3.2±1.3	.25±.03	16± 4	3.8±3.0
2104	10.6±1.1	4.22	$(2.1\pm.36)\times 10^{2}$	.65±.04	72±16	$(1.1\pm.58)\times 10^{3}$
2107	11.1±1.5	3.22	6.7±1.5	.25±.02	45±12	24.±7.4
2111	11.5±1.2	3.56	22.±3.9	.45±.03	30± 8	53.±18.
2119	9.7±1.0	3.05	3.7±.90	.29±.02	17± 4	7.2±3.2
2120	10.2±1.6	3.14	5.2±1.0	.30±.03	18± 6	5.5±1.9
2811	6.7±1.2	3.14	5.1±1.3	.36±.03	9± 2	5.5±1.7
0933	8.6±0.8	3.23	7.1±1.5	.31±.02	30± 7	23.±13.
1733	10.3±0.6	3.14	5.2±1.7	.20±.02	55±18	21.±8.4
0643	8.8±1.3	3.00	3.1±1.2	.25±.02	23±13	11.±9.1

Table 4

station	Δt^*_α (sec)	Δt^*_β (sec)
DTS	-.0009	-.0001
WCP	+.0033	+.0041
SMS	+.0008	+.0030
MGW	+.0011	+.0006
DPC	+.0001	-.0004
BOR	+.0006	+.0017
UCC	-.0010	-.0012
LCC	-.0003	-.0018
CEM	+.0006	+.0035
BRH	+.0004	-.0001

Bibliography

Aki, K. and P.G. Richards (1980). Quantitative Seismology: Theory and Methods, W.H. Freeman and Company, San Francisco, Ca.

Andrews, D.J. (1976). Rupture velocity of plane strain shear cracks, J. Geophys. Res. 81, 3575-3582.

Anderson, J.G. and S.E. Hough (1984). A model for the shape of the fourier amplitude spectrum of acceleration at high frequencies, Bull. Seism. Soc. Am. 74, 1969-1994.

Barrientos, S., S.N. Ward, J.R. Gonzalez-Ruiz, and R.S. Stein (1985). Inversion for moment as a function of depth from geodectic observations and long period body waves of the 1983 Borah Peak, Idaho, earthquake, Proceedings of Conference XXXμ, The Borah Peak, Idaho, earthquake of October 28, 1983, U.S. Geological Survey Open-File Report 85-μμμ, in press.

Boatwright, J. (1980). A spectral theory for circular seismic sources; simple estimates of source dimension, dynamic stress drop and radiated seismic energy, Bull. Seism. Soc. Am., 70, 1-27.

Boatwright, J (1982). A dynamic model for far-field acceleration, Bull. Seism. Soc. Am. 72, 1049-1068.

Boatwright, J. and G.L. Choy (1985). Teleseismic estimates of the energy radiated by shallow earthquakes, submitted to J. Geophys. Res. 89.

Boatwright, J. and J.B. Fletcher (1984). The partition of radiated energy between P and S waves, Bull. Seism. Soc. Am. 74, 361-376, 1984.

Boore, D.M. and J. Boatwright (1984). Average body-wave coefficients, Bull. Seism. Soc. Am. 74, in press.

Brune, J.N. (1970). Tectonic stress and the spectra of seismic shear waves, J. Geophys. Res., 75, 4997-5009.

Brune, J.N. (1971). Correction, J. Geophys. Res., 76, 5002.

Byerlee, J.D. (1978). Friction of rocks, Pure Appl. Geophys. 116, 615-626.

Crone, A.J. and M. Machette (1984). Surface faulting accompanying the Borah Peakearthquake, central Idaho, Geology 12, 664-667.

Hanks, T.C. and H. Kanamori (1979). A moment magnitude scale, J. Geophys. Res. 84, B5, 2348-2350.

Hanks, T.C. and M. Wyss (1972). The use of body-wave spectra in the determination of seismic source parameters, Bull. Seism. Soc. Am., 62, 561-589.

Madariaga, R. (1976). Dynamics of an expanding circular fault, Bull. Seism. Soc. Am. 66, 639-666, 1976.

Richards, P.G. and W. Menke (1983). The apparent attenuation of a scattering medium, Bull. Seism. Soc. Am. 73, 1005-1021.

Richins, W.D., R.B. Smith, C.J. Langer, J.E. Zollweg, J.J. King, and J.C. Pechman (1984). The 1983 Borah Peak, Idaho, earthquake: relationship of aftershocks to the mainshock, surface faulting, and regional tectonics, Proceedings of Conference XXXμ, The Borah Peak, Idaho, earthquake of October 28, 1983, U.S. Geological Survey Open-File Report 85-μμμ, in press.

Sibson, R.H. (1982). Fault zone models, heat flow, and the depth distribution of earthquakes in the continental crust of the United States, Bull. Seism. Soc. Am. 72, 151-163.

Stover, C.W., Preliminary isoseismal map and intensity distribution for the Borah Peak, Idaho, earthquake of October 28, 1983, U.S. Geol. Surv. Open-File Report 84-297, 6 p., 1984.

LATER AFTERSHOCKS OF THE 1983 BORAH PEAK, IDAHO, EARTHQUAKE AND RELATED ACTIVITY IN CENTRAL IDAHO

J. E. Zollweg
Geophysics Program AK-50
University of Washington
Seattle, WA 98195

W. D. Richins
Department of Geology and Geophysics
University of Utah
Salt Lake City, UT 84112-1183

Abstract

106 earthquakes that occurred in central Idaho between 19 November 1983 and 23 August 1984 were located using data recorded at regional stations. Epicenters for the first 3.5 weeks of the 28 October 1983 Borah Peak earthquake aftershock sequence (which were chiefly derived from data recorded on local portable stations) and those for the later aftershocks through 23 August 1984 suggest the existence of a NNW-trending seismic zone at least 120 km long, beginning in the southeast near the epicenter of the Borah Peak earthquake and continuing to the Twin Peaks region northwest of Challis. Comparison of the later epicenters with activity patterns observed in the first 23 days of the Borah Peak sequence indicates that most of the recent activity occurred within the previously defined aftershock zone. However, a 15 x 10 km area at the northwest end of the aftershock region that produced few events prior to December 1983 has since exhibited intense activity, including a magnitude 5.8 (M_L) earthquake on 22 August 1984. A focal mechanism for the 22 August earthquake indicates normal faulting with a large component of left-lateral motion similar to the main shock. The southern half of the aftershock zone has remained relatively inactive during this time period. Cumulative seismic moment for aftershocks occurring south of latitude 44.3° N between 19 November 1983 and 1 July 1984 is about two orders of magnitude smaller than the cumulative afterslip moment estimated from geodetic data, suggesting aseismic creep is the dominant mechanism for afterslip in much of the 1983 rupture zone.

Extensive migration of the endpoints of the aftershock zone has occurred, particularly to the northwest where migration of 30 to 60 km has occurred. Two intense swarms occurred in early 1984 near Twin Peaks, 50 to 60 km northwest of the northwest end of the aftershock zone established in the first few days of the Borah Peak sequence. The largest swarm event had a magnitude of 4.7 and a focal mechanism similar to that of the Borah Peak earthquake. Because of the alignment of these swarms with the Borah Peak aftershock zone and the similarity of focal mechanisms, this activity may be occurring on a through-going fault system.

Introduction

Numerous earthquakes have occurred in central Idaho since the M_S 7.3 Borah Peak earthquake of 28 October 1983. A dense network of portable seismographs provided detailed information on aftershocks occurring through mid-day on 19 November 1983 (Richins *et al.*, 1985). While a few portable stations remained in operation as late as 25 November 1983, no permanent stations were installed to provide continuing local coverage of the aftershock zone. Events between 19 November 1983 and 23 August 1984 have therefore been monitored by permanent regional networks, supplemented by sporadic operation of some telemetered stations in and around the aftershock zone itself. While the same level of detail and resolution provided by the portable network cannot be achieved with the regional stations, the data suffice to document the continuing evolution of the aftershock zone and the occurrence of earthquakes in adjacent areas.

In this study, we examine the spatial and temporal characteristics of over 100 of the larger (magnitude 3.2 or greater) earthquakes that occurred after most temporary stations were removed on 19 November 1983, through the early stages of an aftershock sequence that followed a large (M_L 5.8) event near Challis on 22 August 1984. We report additional focal mechanism solutions, mainly from events near the northern limits of early aftershock activity, that support the existence of a linear trend of seismicity over 100 km long that is evident from epicenter plots. Finally, we compare geodetic observations of afterslip on the portion of the Lost River Fault that broke in 1983 with instrumentally derived estimates of cumulative seismic moment and infer that aseismic creep accounts for nearly all of the afterslip observed in the southeastern part of the 1983 rupture.

Data Collection and Analysis

Regional networks of telemetered seismograph stations provided most of the information used in this study. Data were used from stations maintained by the Idaho National Engineering Laboratory, the Montana Bureau of Mines and Geology, the University of Montana, the University of Washington, the University of Utah, Ricks College, the U. S. Geological Survey's Newport Observatory, and Boise State University (see Figure 1). A local network of telemetered stations in or near the aftershock zone was installed by the U. S. Geological Survey in November 1983, but effective recording of waveform data did not begin until mid-December. Figure 2 shows the surface rupture area in more detail and includes the locations of the five USGS telemetered stations recorded at the University of Utah. Unfortunately, these stations could not be maintained in stable operation and information from most is not continuous. Station JECI performed best with nearly continuous records of good quality being available between late December 1983 and late March 1984. Other stations were less reliable, with the result that no more than four local stations recorded any of the shocks, and most were recorded by only one or two (if any). The operational history of the USGS stations is bracketed by 15 December 1983 and 15 April 1984; over 90% of our epicentral solutions during that period used data from at least one local station. Except when data from the local stations were available, the distance to the first recording station was generally 70 to 150 km. As may be seen from Figure 1, azimuthal coverage was generally good with redundant stations in all directions. In late March 1984, the three stations

within 50 km of Boise, Idaho, were closed. Since these stations furnished critical azimuthal control, epicenters computed for most earthquakes that occurred after 25 March 1984 are of relatively poorer quality, especially since the local USGS stations ceased operation at about the same time.

P-wave arrival times at distances less than 650 km were used to locate epicenters. Most arrivals were read from analog records. Timing accuracy varies with the size of the earthquake and the quality of the arrival but is rarely better than 0.1 second. S-waves were not used, nor were P-waves with estimated reading errors greater than 0.7 second. All events were located using a version of HYPOINVERSE (Klein, 1978) that was modified to include calculation of elevation delays to a reference datum, here taken to be 2000 m above mean sea level. Focal depths are given with reference to that datum.

The velocity model used was that developed by Richins et al. (1985) and is given in Table 1. Velocities in the upper 18 km are based on reversed and unreversed refraction profiles shot within 75 km of the epicenter of the Borah Peak earthquake, as recorded on stations within 200 km of that epicenter (Sparlin et al., 1982; Elbring, 1984; and unpublished University of Utah data). Mid-crustal velocity structure was taken from studies of the nearby Eastern Snake River Plain (Braile et al., 1982) of which the experiment reported by Sparlin et al. was a part. The upper-mantle velocity reported by Sheriff and Stickney (1984) was utilized, but the Moho was placed at a depth of 40 km by Richins et al. Sheriff and Stickney's reversed profile was 250 km long.

Elevation delays were computed assuming the same P-wave velocity above the datum as in the first layer given in Table 1. Station-dependent P-wave delays for the regional network were determined by Richins et al. (1985) from several well-recorded Borah Peak aftershocks that were located using data from portable stations alone. These delays were also used for all epicenter computations in this study and are shown adjacent to the station symbols in Figure 1. Many of these delays exceed 0.5 second, and some exceed 2.0 seconds. While large, such delays are adequately explained from interpretations of refraction profiles shot in and around the Eastern Snake River Plain. In particular, the large delays used at the three stations in the southeastern corner of Idaho can mainly be accounted for by velocity variations in the upper 8 km of the crust beneath those stations (see Sparlin et al., 1982).

Delays have not been determined for the USGS telemetered stations, owing to the lack of a suitable calibration event during the time they operated. Therefore, delays for the local stations were assumed to be zero. For events within the Borah Peak aftershock region proper, distances to the local telemetered stations are generally 60 km or less, and it is unlikely that delays along such paths would exceed 0.5 second due to lateral inhomogeneities. In the calibration of the regional network, Richins et al. (1985) found that two permanent stations that generally were between 60 and 120 km from aftershocks had delays less than 0.6 second.

Magnitudes were computed from a local scale that relates signal duration (defined as P-onset time to the first time the S and surface wave group drops below the background noise level for at least twice the predominant signal period, on a standard 1-Hz vertical seismograph) at two stations in eastern Washington to M_L. It is provisional but does seem reliable for magnitudes of 3.6 and above that can be checked against Wood-Anderson data recorded in Utah, Montana, and Washington. For smaller events the scale gives results that are about one-half unit larger than the routine

University of Utah duration magnitudes.

Boatright (1985) determined seismic moments from locally-recorded digital records for 46 Borah Peak aftershocks that were also recorded on the eastern Washington stations. Figure 3 shows that a linear relation exists between the common logarithms of Boatright's seismic moments (M_o) and M_L as estimated from durations at the eastern Washington stations:

$$\log M_o = 17.02 + 1.14\ M_L$$

This relation is valid for M_L between 3.0 and 5.8 and was used to estimate cumulative aftershock moments.

Location Results: 19 November 1983 - 23 August 1984

136 central Idaho earthquakes with magnitude 3.2 or larger were identified in the time interval between 14:00 UTC on 19 November 1983 and 13:23 UTC on 23 August 1984. 98 of these and 8 smaller earthquakes are considered well-enough located to merit discussion. While we believe about 40% of our locations are accurate within 3 km, uncertainties of 5 to 10 km are more typical and about 10% may be in error by as much as 15 km. All identified events with magnitude 3.6 or greater between 19 November 1983 14:00 UTC and 22 August 1984 09:46 UTC have been located. Half of the unlocated shocks with magnitude 3.2 or greater were secondary aftershocks of a strong earthquake on 22 August 1984. Hypocentral information on the 12 earthquakes between 19 November 1983 and 23 August 1984 having magnitudes of 4.0 or greater is given in Table 2.

Figure 4a shows the locations and focal mechanisms obtained in this study. In addition, the location for the 28 October 1983 Borah Peak main shock (Richins et al., 1985) and the focal mechanism for it obtained by Doser (1984) are plotted. Two earthquakes in August 1984 were located 20 to 30 km west of the map area. The most striking feature of the 104 events shown in Figure 4a is the spatial clustering within a northwest-trending zone about 100 km long and 10 to 20 km wide. This zone accounts for all but three of the epicenters within the map area. Two of the remaining earthquakes, including one of magnitude 4.4, occurred in the White Knob Mountains to the southwest of the linear zone. Dewey (1985) demonstrated a high average rate of activity at the magnitude 3.5 level in the White Knobs, particularly prior to 1974. The remaining epicenter, to the east of the linear trend, is that of a well-located magnitude 3.5 event north of Borah Peak.

A linear region of aftershock activity about 40 km in length roughly parallels the principal trace of the 1983 surface rupture along the Lost River Fault and makes up the southeasternmost portion of the northwest-trending zone of Figure 4a. This segment is generally less than 10 km wide and is offset to the southwest of the surface rupture by 8 - 15 km. It extends only a few kilometers south of the 1983 faulting. No events were located as far south as the main shock epicenter. Richins et al. (1985) found that hypocenters in the southern part of the aftershock zone were clustered about a plane dipping about 45° SW that extended to a depth of about 16 km and intersected the surface near the fault scarp. Our depth control is generally inadequate and over 80% of our hypocenters were restrained to 10 km. The remainder fall in the range of 6 to 14 km but are too few in number to permit any geometric interpretation.

The activity paralleling the 1983 rangefront faulting ends abruptly naer latitude 44.3° N, at a point southwest of the terminus of the main 1983 rupture. The general northwest trend of the seismicity in Figure 4a is then offset to the northeast by 10 to 15 km. Figure 4a shows a number of epicenters along the line of offset, including several that we consider among our most accurate (estimated uncertainties less than 3 km). The high-quality locations alone are sufficient to outline the offset, but are too few to illuminate its nature. The offset may be the expression of activity along a near-vertical northeast-striking fault or more simply may be a narrow zone of activity extending downdip on a fault surface dipping to the southwest. Other interpretations are also possible, given the lack of a larger number of good quality hypocenters.

The offset terminates in a 15 x 10 km region of intense seismicity that seems to have a poorly defined north to northwesterly trend. This feature initially developed in mid-December 1983, with two of the larger aftershocks (magnitudes 4.6 and 4.2) occurring within it only three days apart. The M_L 5.8 earthquake of 22 August 1984 occurred at almost the same location as these two mid-December earthquakes. It was the largest Borah Peak aftershock to occur more than 1.5 days after the 28 October 1983 main shock, and was one of the three largest aftershocks recorded (all three were of the same magnitude as determined from Wood-Anderson seismographs). Since we have located only two aftershocks of the 22 August 1984 event, most of the epicenters clustered around it in Figure 4a are those of earthquakes occurring between December 1983 and mid-August 1984. No increase in activity in this area immediately prior to the 22 August 1984 event was evident in our data set.

We have located no earthquakes between the region of the 22 August 1984 event and the vicinity of Challis. The four earthquakes less than 20 km west-northwest of Challis all occurred after 28 January 1984; at least three of them are located within an estimated accuracy of 5 to 10 km. We therefore cannot judge whether these four events represent tightly clustered activity or if they really are spread out between Challis and Twin Peaks. The concentration of epicenters near Twin Peaks in the northwest corner of the map area occurred as two discrete swarms, one between 29 January and 8 February 1984 (11 located events, magnitudes 3.2 - 3.8 M_L), and the other between 21 March and 13 April 1984 (22 located events, magnitudes 3.2 - 4.7 M_L). The latter swarm was particularly vigorous and included four earthquakes of magnitude 4 or greater; the largest had a magnitude of about 4.7 and occurred on 24 March 1984. Hundreds of events were recorded on local stations during each of the swarms. Fisher *et al.* (1983) have mapped a large Eocene caldera complex around Twin Peaks. Microearthquake surveys conducted in the 1970's by the University of Utah recorded large numbers of events from a small source area within the caldera (Smith *et al.*, 1985). Stickney (1984) also located some earthquakes in 1982 near Twin Peaks, although the precision of his locations was not as high as in the microearthquake surveys. The 1984 swarms are located near the northern edge of the caldera. Because of the history of activity near Twin Peaks prior to 1983, the relationship of the 1984 earthquakes to the development of the Borah Peak aftershock zone is tenuous. The temporal coincidence and vigor of the 1984 swarms may nevertheless indicate that they play some role in the readjustment process.

Fault Plane Solutions

Because of the low density and spottiness of focal sphere coverage by the regional network, fault plane solutions have been determined for only three of the earthquakes in this study. Equal-area, lower-hemisphere projections of these solutions are shown in Figure 4a, along with the focal mechanism for the 28 October 1983 main shock determined by Doser (1984). A more detailed solution, with individual observations, is shown in Figure 5 for the M_L 5.8 earthquake of 22 August 1984. Our solution relies heavily upon low-amplitude first motions recorded at regional stations to the northwest of the epicenter. While these first motions were weak, only those that seemed fairly clear were used in determination of the nodal planes (the data plotted in the northwest quadrant in Figure 5 represent only 20% of the stations in that range of azimuth whose seismograms we examined). Fewer stations recorded the earthquakes of 27 December 1983 (M_L 4.5, northern Borah Peak aftershock zone) and 24 March 1984 (M_L 4.7, Twin Peaks), but first motions were generally of higher quality than those for the 22 August 1984 event. In addition, both were recorded by local stations and the Boise State University stations, markedly improving focal sphere coverage.

The three fault-plane solutions we have determined all show predominantly normal faulting with near-horizontal T-axes trending NE-SW (Figure 4a and Table 3). The focal mechanisms of the 24 March 1984 and 22 August 1984 earthquakes closely resemble Doser's (1984) solution for the Borah Peak earthquake. The majority of the fault plane solutions presented by Richins et al. (1985) and Smith et al. (1985) have a northwest-striking nodal plane that agrees with the strike of observed surface faulting and, if projected updip, intersects the surface near the fault scarp. Both Richins et al. and Smith et al. point out that all mechanisms cannot be explained by a single fault. Our interpretation of the nodal planes for the 22 August 1984 event is complicated by its epicenter near the offset of the northwest-striking zone of activity of Figure 4a. While the northwest-striking nodal plane would appear to be more consistent with other activity, we cannot at this time completely rule out the possibility that the east-west striking nodal plane that dips generally north is the fault plane. Aftershocks of the 22 August 1984 earthquake were recorded on portable stations by investigators from the U. S. Geological Survey and the University of Utah, and a preliminary examination of several of the larger events indicates a spatial pattern that may be too complex to be attributed to a single northwest-striking fault plane (Smith et al., 1985). Nevertheless, we can infer from our mechanisms that earthquakes around the north end of the Borah Peak aftershock zone and at Twin Peaks are occurring under essentially the same stress field as that responsible for the 1983 surface rupture in the Borah Peak earthquake, although the 1983 faulting did not extend as far to the northwest as the epicenters of the 22 August 1984 and 24 March 1984 earthquakes.

Comparison with Earlier Aftershock Activity

Figure 4b shows the epicenters located by Richins et al. (1985), principally using data from the portable stations operated between 28 October and 19 November 1983. In general, activity after 19 November 1983 south of the latitude of Challis (Figure 4a) occurs within the aftershock zone defined by Richins et al. There are substantial differences, however, in

the patterns of activity within the aftershock zone observed after 1 December 1983. The most prominent of these differences occur at the ends of the aftershock zone.

None of the aftershocks located after 19 November 1983 occurred in the southeastern 20 km of the aftershock zone. This area was characterized by low levels of activity during the first 3.5 weeks of the sequence, including the time immediately after the main shock of 28 October 1983. Because of the proximity to the main shock epicenter, it is unusual that so little aftershock activity has occurred in this region.

Activity in the northwestern portion of the aftershock zone has been more vigorous. Prior to 20 November 1983, intense clustering of aftershocks was observed about 10 km west of a major bifurcation of the surface fault trace. The northern edge of this cluster occurred near the point where the western segment of the fault trace terminated, and only minor activity was observed to the north (Figure 4b). Figure 4a shows that considerable activity still occurs in this cluster, but that many shocks occurring after 20 November 1983 have been located in a region extending to the north of the terminus of the western fault trace. This is the region already discussed as being north of an offset in the generally linear pattern of epicenters in Figure 4a. Since it was the locus of the two largest aftershocks observed in this study (M_L 5.8 and 4.6) as well as at least 25% of the identified aftershocks with magnitudes of 3.2 or greater, development of this small region of activity represents a major change in the pattern of energy release observed prior to 20 November 1983.

A plot was prepared of the logarithm of elapsed time after 27 October 1983, versus distance along a line striking 150° from a point near Twin Peaks. This line, whose strike is indicated by points A and A' on Figure 4a and begins at point A, is approximately parallel to the observed average strike of the surface fault break. Epicenters of all located events along the linear trend of Figures 4a and 4b were projected onto the line to determine their relative positions. On this plot (Figure 6), several space-time relationships stand out clearly. The first observation we make is that Borah Peak aftershock activity migrated both to the northwest and the southeast of a 55-km-long initial aftershock zone. In the southeast migration was gradual, beginning about 5 days after the main shock and involving a distance of about 10 km. Of particular interest is the fact that southeastward migration terminated less than two weeks after the main shock, and the southeasternmost 30 to 35 km of the aftershock zone has had no located events since 1 December 1983.

Northwestward migration seems to have begun suddenly about 10 days after the main shock, and continued until the time the portable stations were removed on 19 November 1983. The lack of earlier activity in this area could possibly have been the result of limited station coverage, but larger events should have been noticed and located had they occurred. The December 1983 activity occurred directly adjacent to the northern boundary of the initial aftershock region. Migration to the north and northwest is at least 30 km in extent; if the Challis and Twin Peaks activity is directly related to the aftershock zone it could be up to 60 km. The distance from Twin Peaks to the southeasternmost Borah Peak aftershocks is 120 km. A final observation is that the entire active region seems to be migrating northwest with time.

Discussion

The epicentral and focal mechanism data shown in Figures 4a and 4b suggest that a seismic zone extends from Mackay to the Twin Peaks region. From our data, it is debatable whether this zone consists of a single throughgoing fault, with complications such as sudden bends and changes in strike, or whether it is made up of a number of closely spaced faults having differing strikes (and, presumably, different dips). To answer such questions it will be necessary to improve the correlation of earthquake hypocenters with mapped surface faults. Bond (1978) draws the Lost River Fault as diverging into parallel traces and curving somewhat to the north near the point where the northeast limb of the 1983 rupture dies out; Rember and Bennett (1979) show a number of mapped faults in the immediate Challis area. Because of the complex pattern of mapped faults at the surface a high level of hypocentral resolution, in particular good depth control, is required if earthquakes are to be correlated with specific faults. Nevertheless, we believe the spatial pattern of epicenters and the close correspondence of focal mechanisms suggest a single fault zone is responsible for most of the observed activity. A single, continuous fault surface may not extend the entire length of the trend, but there clearly exists a long, relatively narrow region of earthquake activity occurring under a fairly uniform stress regime. Perhaps the Lost River Fault continues beneath a surface veneer of Eocene Challis Volcanics deposits to the vicinity of the Twin Peaks caldera. Smith et al. (1985) describe microearthquake activity in the Twin Peaks area as striking east to northeast. With our comparatively poor spatial resolution on Twin Peaks epicenters, no trends are apparent in our locations for the 1984 swarms. However, the focal mechanism for the 24 March 1984 Twin Peaks earthquake (M_L 4.7) is suggestive of continuation of the northwest-striking zone at least that far.

The distance from the southeasternmost extent of the Borah Peak aftershocks near Mackay to the Twin Peaks activity of 1984 is approximately 120 km. The southeastward extension of the Lost River Fault from Mackay is presently inactive down to the regional network detection threshold at about M_L 2.5. Still, there is evidence of Holocene or late Pleistocene displacement along most of the Lost River Fault southeast of the 1983 rupture (Malde, 1971; Scott et al., 1985), and Scott et al. caution that all segments of the rangefront faults are regarded as capable of renewed surface faulting. Such renewed activity would probably increase the length of the trend we have observed in the 1983-4 data by up to 50 to 75 km, the distance from the southernmost activity observed in the Borah Peak sequence to the mapped end of the Lost River Fault near where it intersects the Snake River Plain. The length of the inactive segments of the Lost River Fault southeast of Mackay is about equal to the initial aftershock zone length of the Borah Peak earthquake, suggesting the magnitude of the Borah Peak event (7.3 M_S) as a rough upper limit for any event that might occur between Mackay and the Snake River Plain.

The surprisingly low level of aftershock activity in the vicinity of the main shock epicenter is a characteristic the Borah Peak sequence shares with at least two other aftershock sequences of earthquakes of comparable magnitude: the St. Elias, Alaska, earthquake of 28 February 1979 (M_S 7.1; Stephens et al., 1980) and the Imperial Valley, California, earthquake of 15 October 1979 (M_S 6.9; Johnson and Hutton, 1982). These earthquakes were interplate events with chiefly thrust and strike-slip displacement, respectively, implying that such aftershock sequences are a property of certain

types of fault irrespective of mode of dominant slip or occurrence in an intraplate or interplate environment. Stephens et al. attributed the lack of aftershocks near the main shock to a relatively smooth rupture surface in the vicinity of the main shock hypocenter. For the Borah Peak earthquake, there is additional evidence that this may be the case.

Geodetic elevation change data for the Borah Peak earthquake are of particularly high quality and an additional survey was run in June-July 1984 to determine elevation changes due to afterslip in the period after 23 November 1983 (Stein and Barrientos, 1985). Their survey was run near Borah Peak and the endpoints are shown as points B and B' in Figure 4a. They estimated that afterslip in the period 24 November 1983 - June 1984 added 50 $\pm$ 15 mm to the coseismic slip. Stein and Barrientos estimate a cumulative moment for the afterslip of 0.5 to 1.0 x 10^{25} dyne-cm, more than an order of magnitude less than that obtained for the coseismic slip.

If aftershocks were mainly responsible for the postseismic slip, the cumulative seismic moment estimated from aftershocks should roughly agree with that estimated from geodetic data. Levelling data along profile BB' is virtually insensitive to small displacements occurring as far away as the northern ends of the surface rupture. We therefore summed moments only for those aftershocks occurring south of 44.3° N between 23 November 1983 and 1 July 1984 (the exact choice of cut-off dates has little effect on the result). We estimate the cumulative seismic moment for these earthquakes to be approximately 0.5 x 10^{23} dyne-cm. The two-orders-of-magnitude discrepancy between the cumulative aftershock seismic moment and the geodetic moment indicates that the afterslip process is mainly proceeding by means of aseismic creep, at least in the southeastern portion of the rupture zone. This inference, combined with the overall lack of aftershocks in the region of the main shock epicenter, gives further support to the idea that the fault surface in the southeastern part of the 1983 aftershock zone is relatively smooth and uncomplicated, having few barriers or asperities to inhibit displacement or concentrate stress.

Conclusions

Central Idaho earthquakes occurring up to 267 days after the 28 October 1983 Borah Peak earthquake suggest a 120-km-long, north-northwest trending region of seismicity exists between Mackay, Idaho and the Twin Peaks region northwest of Challis. At least part of this trend is directly related to the Lost River Fault, part of which ruptured in the Borah Peak earthquake. A large proportion of the trend in the southeast is defined by aftershocks of the Borah Peak earthquake recorded within 3.5 weeks of its occurrence, but much of the northwest part is defined by earthquakes occurring after 1 December 1983. Focal mechanism data indicate the seismicity occurs under a fairly uniform stress field dominated by near-horizontal extension in the northeast-southwest direction. This result is in good general agreement with studies of early aftershocks and with observations of the 1983 fault break.

Comparison of activity 23 to 267 days after the Borah Peak earthquake with that occurring within the first 23 days indicates that migration of 30 to 60 km may have occurred on the northwest end of the aftershock zone. The locus of most aftershock activity has also shifted to the northwest, leaving 30 to 35 km of the southeastern aftershock region (including the area of the main shock epicenter) virtually devoid of located earthquakes

since 5 weeks after the Borah Peak earthquake. Geodetic observations of afterslip on the Lost River Fault are about 100 times too large to be explained by aftershocks and suggest aseismic creep is an important process in the southeastern part of the 1983 rupture zone. This inference, together with the low level of observed aftershock activity in the southeastern part of the 1983 aftershock zone, indicates a smooth and uncomplicated rupture plane exists in the region of the epicenter of the Borah Peak earthquake.

Acknowledgements

We are particularly indebted to those individuals who provided us with readings or original seismograms from the regional seismograph stations. These were M. Stickney (Montana Bureau of Mines and Geology), S. Jackson (EG and G Idaho, Inc.), and J. Pelton (Boise State University). W. Ellsworth arranged for installation and operation of the USGS telemetered stations. R. Halliday, R. Horner, and A. Johnston provided copies of regional and teleseismic stations' seismograms for the 22 August 1984 earthquake. C. Jonientz-Trisler and J. Pechmann assisted with some data reduction, and conversations with R. B. Smith were useful in defining some aspects of the pre-1983 seismicity. A. Johnston and C. Weaver critically reviewed the manuscript and suggested many improvements. Data collection and analysis at the University of Utah were supported by USGS Contract Nos. 14-08-001-21856 and 14-08-0001-21857.

REFERENCES

Boatright, J., 1985, Characteristics of the aftershock sequence of the Borah Peak, Idaho, earthquake determined from digital recordings of the events, in Workshop XXVIII on the Borah Peak Earthquake, U. S. Geological Survey Open-File Report, in press.

Bond, J. G., 1978, compiler, Geologic Map of Idaho, Idaho Bureau of Mines and Geology, 1 sheet.

Braile, L. W., R. B. Smith, J. Ansorge, M. R. Baker, C. Prodehl, M. M. Schilly, J. H. Healy, St. Mueller, and K. H. Olsen, 1982, The Yellowstone-Snake River Plain seismic profiling experiment: Crustal structure of the eastern Snake River Plain, Journal of Geophysical Research, 87, 2597-2610.

Dewey, J. W., 1985, A reanalysis of the instrumental seismicity of central Idaho on the basis of locally-recorded aftershocks to the 1983 Borah Peak earthquake, in Workshop XXVIII on the Borah Peak Earthquake, U. S. Geological Survey Open-File Report, in press.

Doser, D. I., 1984, The 1959 Hebgen Lake, MT and the 1983 Borah Peak, ID earthquakes: Examples of large normal fault events in the intermountain region (abstract), Earthquake Notes, 55, 14.

Elbring, G., 1984, A method for inversion of two-dimensional seismic refraction data with applications to the Snake River Plain region of Idaho, unpublished Ph. D. thesis, Purdue University.

Fisher, F. S., D. H. McIntyre, and R. M. Johnson, 1983, Geologic map of the Challis 1° x 2° quadrangle, Idaho, U. S. Geological Survey Open-File Report 83-523.

Johnson, C. E., and L. K. Hutton, 1982, Aftershocks and pre-earthquake seismicity, the Imperial Valley, California Earthquake, October 15, 1979, U. S. Geological Survey Professional Paper 1254, 59-76.

Klein, F. W., 1978, Hypocenter location program HYPOINVERSE, U. S. Geological Survey Open-File Report 78-694.

Malde, H. E., 1971, Geologic investigation of faulting near the National Reactor Test Station, Idaho, with a section on microearthquake studies by Pitt, A. M., and Eaton, J. P., U. S. Geological Survey Open-File Report.

Rember, W. C., and E. H. Bennett, 1979, Geologic Map of the Challis Quadrangle, Idaho, Idaho Bureau of Mines and Geology, 1 sheet.

Richins, W. D., R. B. Smith, C. J. Langer, J. E. Zollweg, J. J. King, and J. C. Pechmann, 1985, The 1983 Borah Peak, Idaho earthquake: Relationship of aftershocks to the main shock, surface faulting, and regional tectonics, in Workshop XXVIII on the Borah Peak Earthquake, U. S. Geological Survey Open-File Report, in press.

Scott, W. E., K. L. Pierce, and M. H. Hait, Jr., 1985, Quaternary tectonic setting of the 1983 Borah Peak earthquake, central Idaho, in Workshop XXVIII on the Borah Peak Earthquake, U. S. Geological Survey Open-File Report, in press.

Sheriff, S. D., and M. C. Stickney, 1984, Crustal structure of southwestern Montana and east-central Idaho: Results of a reversed seismic refraction line, Geophysics Research Letters, 11, 299-302.

Smith, R. B., W. D. Richins, and D. I. Doser, 1985, The 1983 Borah Peak, Idaho earthquake: Regional seismicity, faulting kinematics, and tectonic mechanism, in Workshop XXVIII on the Borah Peak Earthquake, U. S. Geological Survey Open-File Report, in press.

Sparlin, M. A., L. W. Braile, and R. B. Smith, 1982, Crustal structure of the eastern Snake River Plain determined from ray trace modeling of seismic refraction data, Journal of Geophysical Research, 87, 2619 - 2633.

Stein, R. S., and S. E. Barrientos, 1985, The 1983 Borah Peak, Idaho, earthquake: Geodetic evidence for deep rupture on a planar fault, in Workshop XXVIII on the Borah Peak Earthquake, U. S. Geological Survey Open-File Report, in press.

Stephens, C. D., J. C. Lahr, K. A. Fogelman, and R. B. Horner, 1980, The St. Elias, Alaska earthquake of February 28, 1979: Regional recording of aftershocks and short-term, pre-earthquake seismicity, Bulletin of the Seismological Society of America, 70, 1607-1633.

Stickney, M. C., 1982, Montana seismicity 1982, Montana Bureau of Mines and Geology Open-File Report 149, 11 pp.

TABLE 1

Velocity model used to locate Borah Peak, Idaho events

Depth to top of layer, km	P-velocity in layer, km/sec
0.0	4.75
1.64	5.59
6.95	6.16
18.0	6.80
40.0	8.00

TABLE 2

Borah Peak, Idaho Earthquakes: 19 November 1983 - 23 August 1984 #

(magnitude 4.0 and larger)

yr	date	origin time (UTC)	lat-n	long-w	depth (km)	magnitude**
83	1211	1958 18.8	44-15.55	114- 5.63	10.0*	4.1 (M_L)
83	1212	0455 36.7	44-23.32	114- 6.07	10.0*	4.6 (M_L)
83	1215	0613 35.3	44-23.63	114- 6.23	10.0*	4.3 (M_L)
83	1227	1221 29.5	44-14.10	114- 4.15	9.6	4.5 (M_L)
83	1228	0816 53.8	44-13.97	114- 4.53	10.7	4.0 (M_L)
84	0124	2107 57.9	44- 1.47	114-25.97	10.0*	4.4 (M_L)
84	0302	0029 45.5	44-19.54	114- 6.28	7.2	4.3 (M_L)
84	0324	0007 47.9	44-42.06	114-26.52	10.0*	4.7 (M_L)
84	0324	2103 16.5	44-42.41	114-27.29	10.0*	4.1 (M_L)
84	0401	0539 28.3	44-43.09	114-24.70	10.0*	4.1 (M_L)
84	0411	1551 56.6	44-44.22	114-24.29	10.0*	4.2 (M_L)
84	0822	0946 30.1	44-22.63	114- 4.90	10.0*	5.8 (M_L)
84	0822	1334 21.7	44 24.84	114- 6.61	10.0*	4.1 (M_L)
84	0823	1321 53.4	44 25.12	114- 5.98	10.0*	4.1 (M_L)

* restricted depth

** M_L for 22 August 1984 0946 UTC from Wood-Anderson seismographs; remainder are estimated as discussed in text.

\# may not be complete for aftershocks of 22 August 1984 0946 UTC

TABLE 3

Parameters of Fault Plane Solutions

date					nodal plane 1		nodal plane 2		P-axis		T-axis	
yr	mo	da	hr	mn	strike	dip	strike	dip	azimuth	plunge	azimuth	plunge
1983	1227		12:21		N70W	60SW	N33W	35NE	N21W	68	S35W	12
1984	0324		00:07		N28W	50SW	N74W	50NE	S51E	66	N40E	0
1984	0822		09:46		N27W	50SW	N83W	57NE	S49E	58	N36E	7

Figure Captions

Figure 1. Map showing aftershock zone of the 28 October 1983 Borah Peak, Idaho earthquake and the regional seismograph stations (triangles) used to locate aftershocks reported in this paper. Average P-wave delays (in seconds) obtained from aftershocks located only using data from portable stations are shown adjacent to each station's location. Stations in the immediate area of the aftershock zone are shown in Figure 2.

Figure 2. Map of epicentral region of the 28 October 1983 Borah Peak earthquake and its surface fault traces, showing locations of local telemetry stations installed by the U. S. Geological Survey.

Figure 3. Plot of magnitude M_L estimated from coda lengths at eastern Washington stations, versus the common logarithm of the seismic moment M_O (estimated by Boatright, 1985) for 46 Borah Peak aftershocks.

Figure 4a. Map showing distribution of central Idaho earthquakes recorded between 20 November 1983 and 23 August 1984. Lower hemisphere, equal-area stereographic projections of fault plane solutions are shown for earthquakes of (1) 24 March 1984, M_L 4.7; (2) 22 August 1984, M_L 5.8; (3) 27 December 1983, M_L 4.5; and (4) the Borah Peak main shock of 28 October 1983 (as determined by Doser, 1984). Compressional quadrants are shaded. Points A and A' mark the line of projection of Figure 6; points B and B' are the endpoints of the geodetic elevation change surveys (Stein and Barrientos, 1985).

Figure 4b. Map of the same area as Figure 4a, but showing Borah Peak aftershocks located in the first 23 days of the aftershock sequence (Richins *et al.*, 1985).

Figure 5. Lower hemisphere, equal-area stereographic projection of first motions recorded for the 22 August 1984 earthquake (M_L 5.8). C and D represent good-quality compressions and dilatations, respectively, while poorer-quality compressions and dilatations are indicated by + and -, respectively. The solid lines indicate the preferred fault plane solution.

Figure 6. Plot of distance along strike of line AA' of Figure 4a (distance in km from 44.75° N, 114.5° W, along a line striking 150°), versus the logarithm of elapsed time in days after 27 October 1983 00 UTC, showing all located Borah Peak aftershocks. Regional activity has been removed. The latest events on this plot occurred on 23 August 1984.

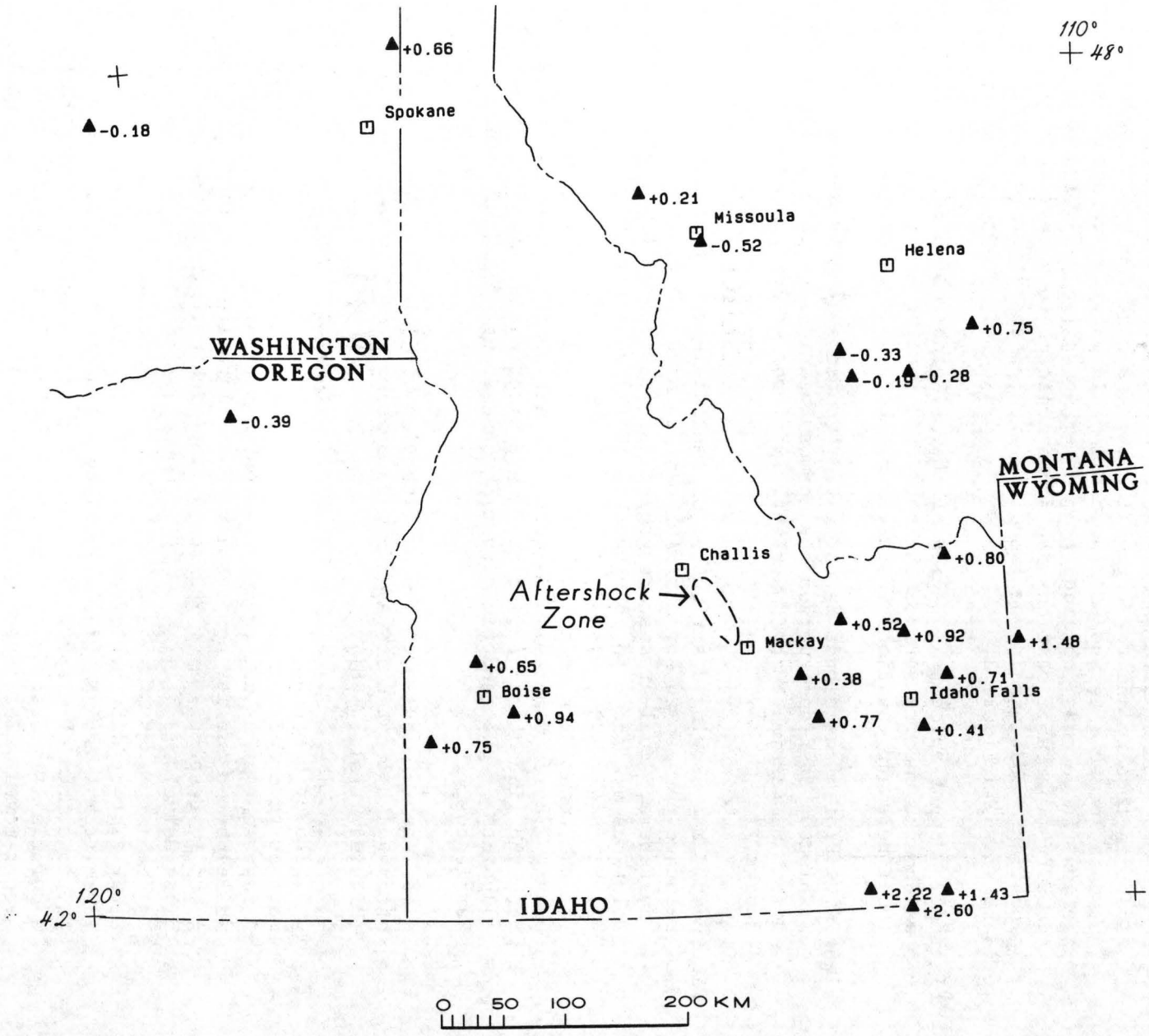
110°
48°
+0.66
Spokane
-0.18
+0.21
Missoula
-0.52
Helena
+0.75
-0.33
-0.19
-0.28
WASHINGTON
OREGON
-0.39
MONTANA
WYOMING
Challis
+0.80
Aftershock
Zone
+0.52
+0.92
+1.48
Mackay
+0.65
+0.38
+0.71
Boise
Idaho Falls
+0.94
+0.77
+0.41
+0.75
120°
42°
IDAHO
+2.22
+1.43
+2.60
0 50 100 200 KM

FIGURE 1

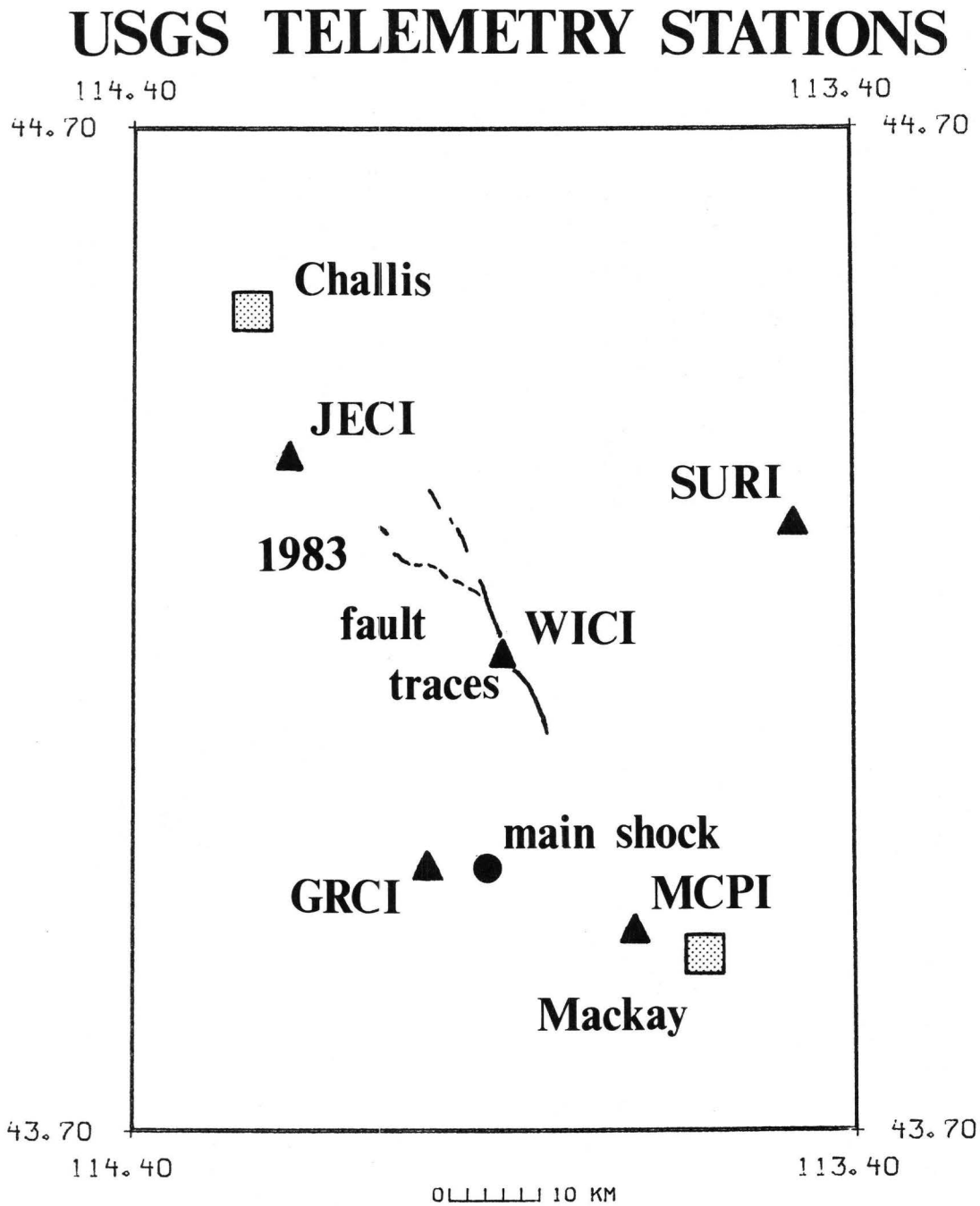
USGS TELEMETRY STATIONS
114.40
113.40
44.70
44.70
Challis
JECI
SURI
1983
fault
traces
WICI
main shock
GRCI
MCPI
Mackay
43.70
43.70
114.40
113.40
0
10 KM

FIGURE 2

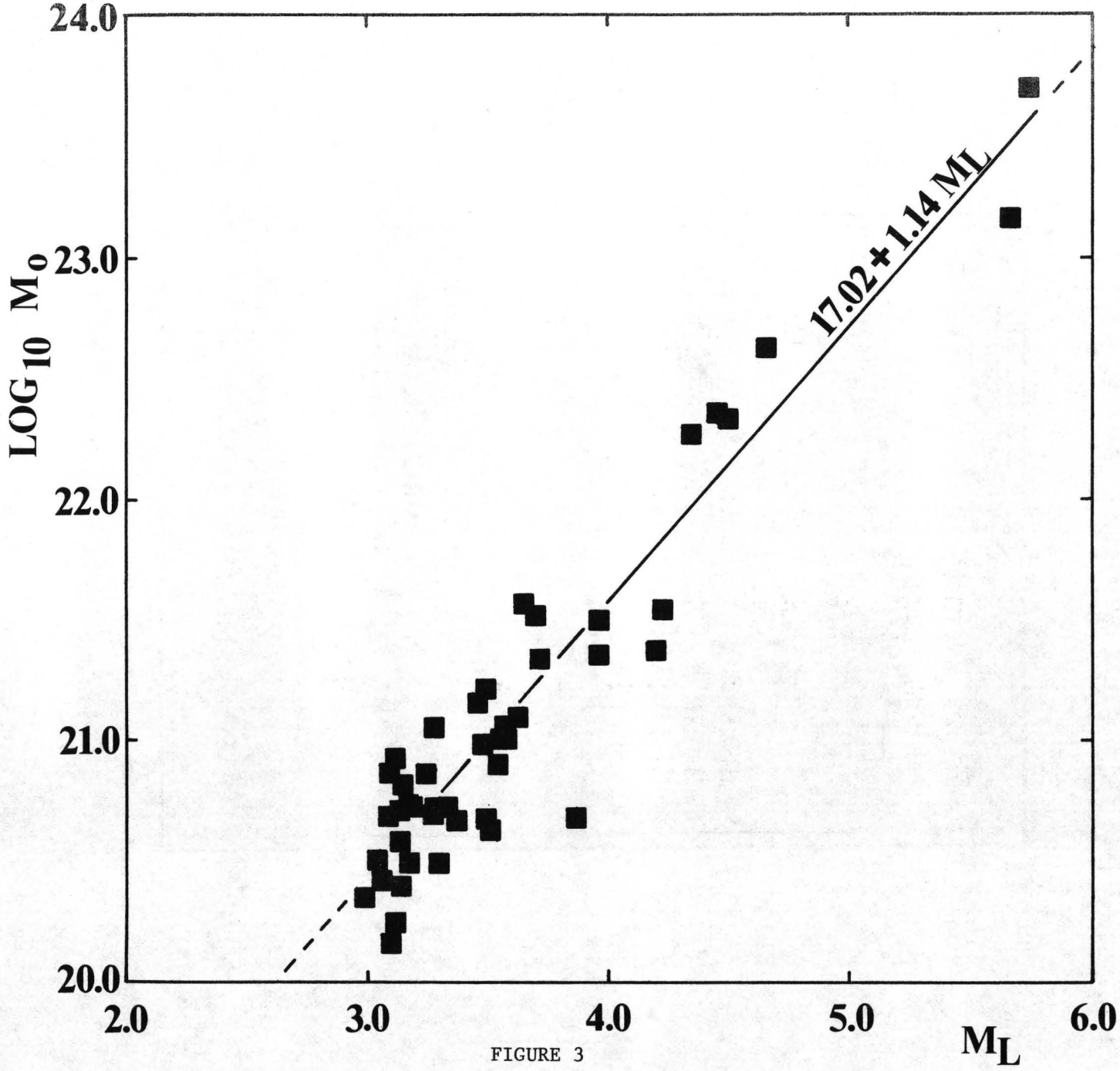

FIGURE 3

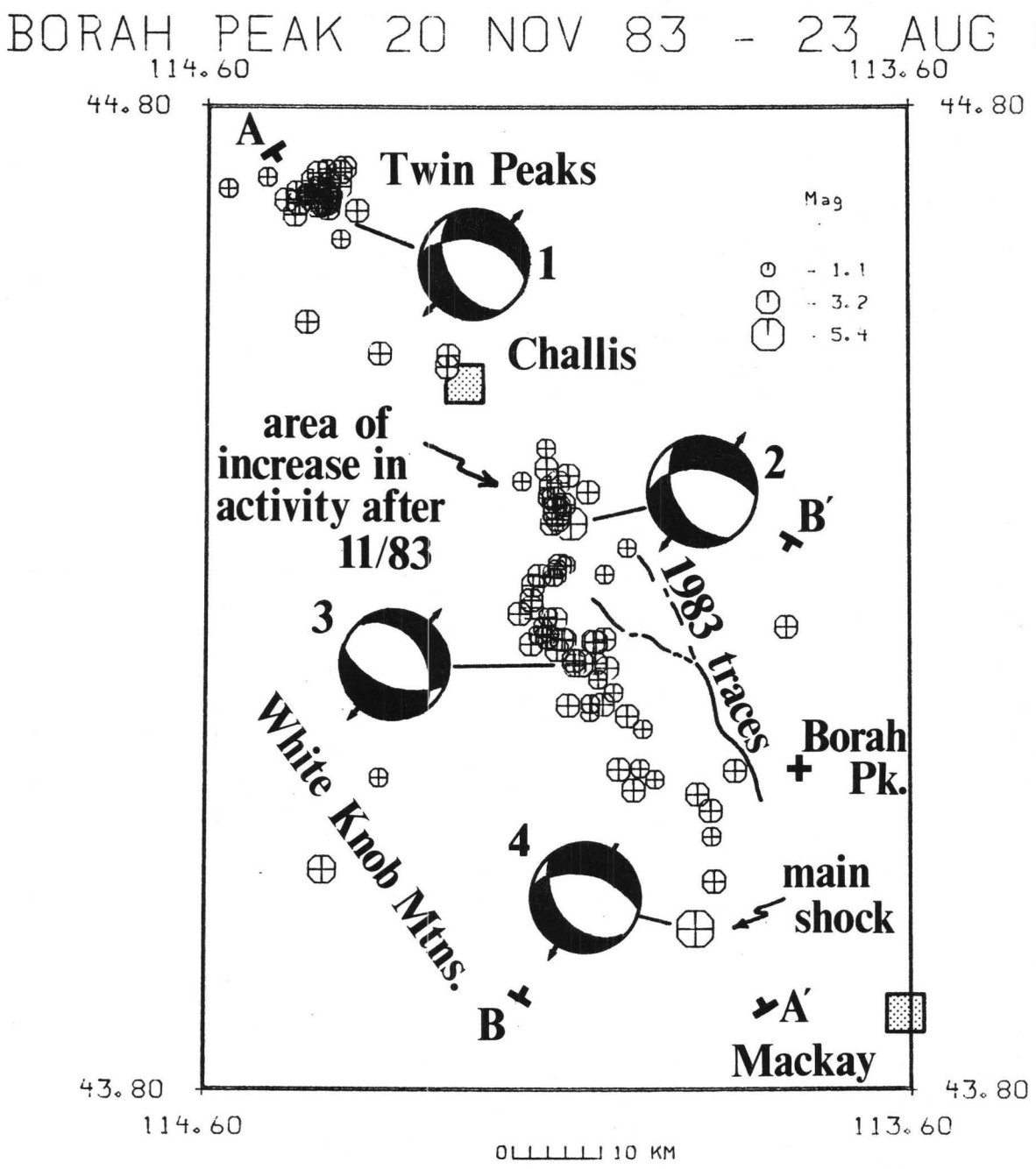
BORAH PEAK 20 NOV 83 - 23 AUG 84
114.60
113.60
44.80
44.80
A
Twin Peaks
1
Mag
- 1.1
- 3.2
- 5.4
Challis
area of increase in activity after 11/83
2
B'
1983 traces
3
White Knob Mtns.
Borah Pk.
4
main shock
B
A'
Mackay
43.80
43.80
114.60
113.60
0 10 KM

FIGURE 4a

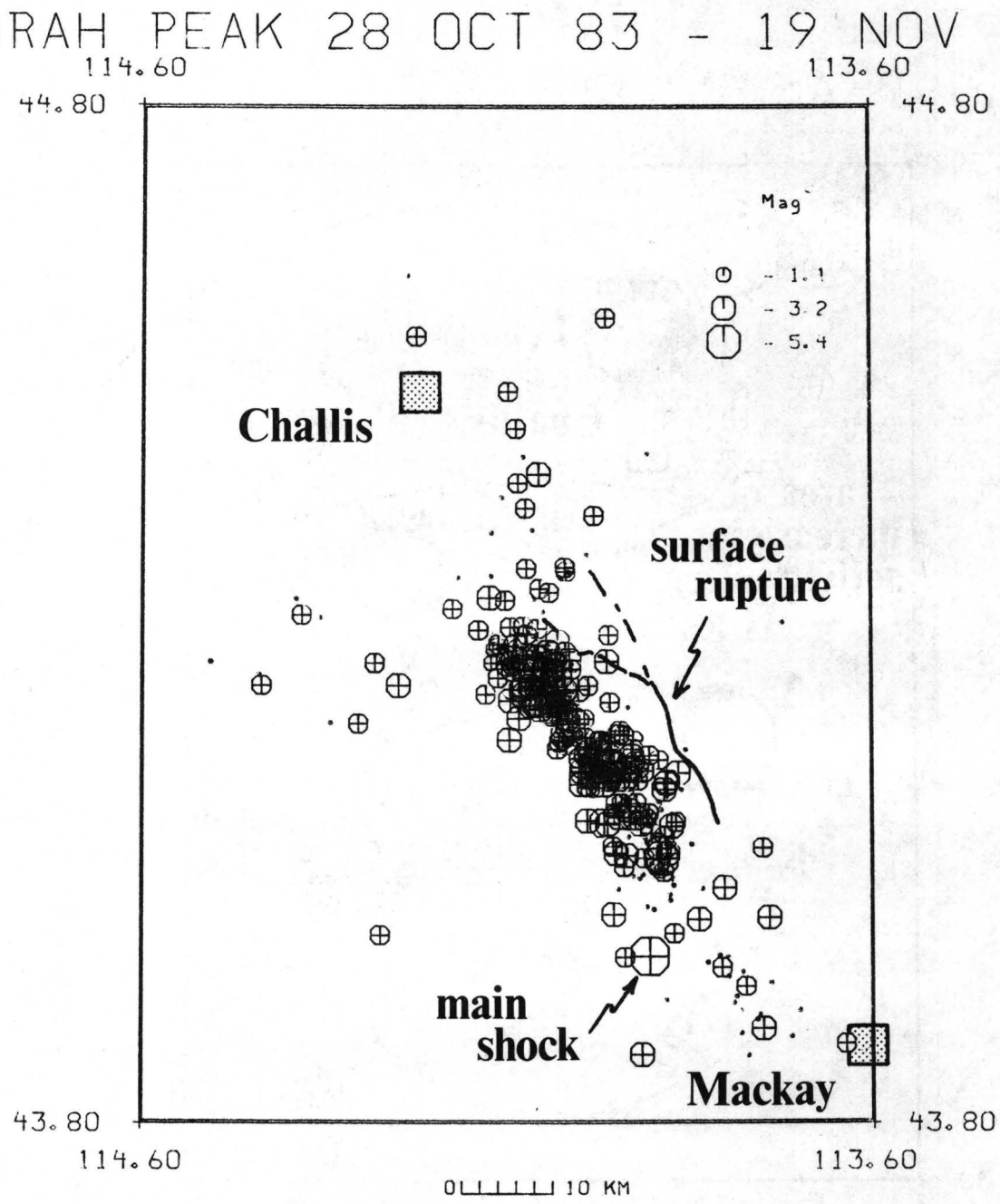
BORAH PEAK 28 OCT 83 - 19 NOV 83
114.60
113.60
44.80
44.80
Mag
- 1.1
- 3.2
- 5.4
Challis
surface
rupture
main
shock
Mackay
43.80
43.80
114.60
113.60
0 10 KM

FIGURE 4b

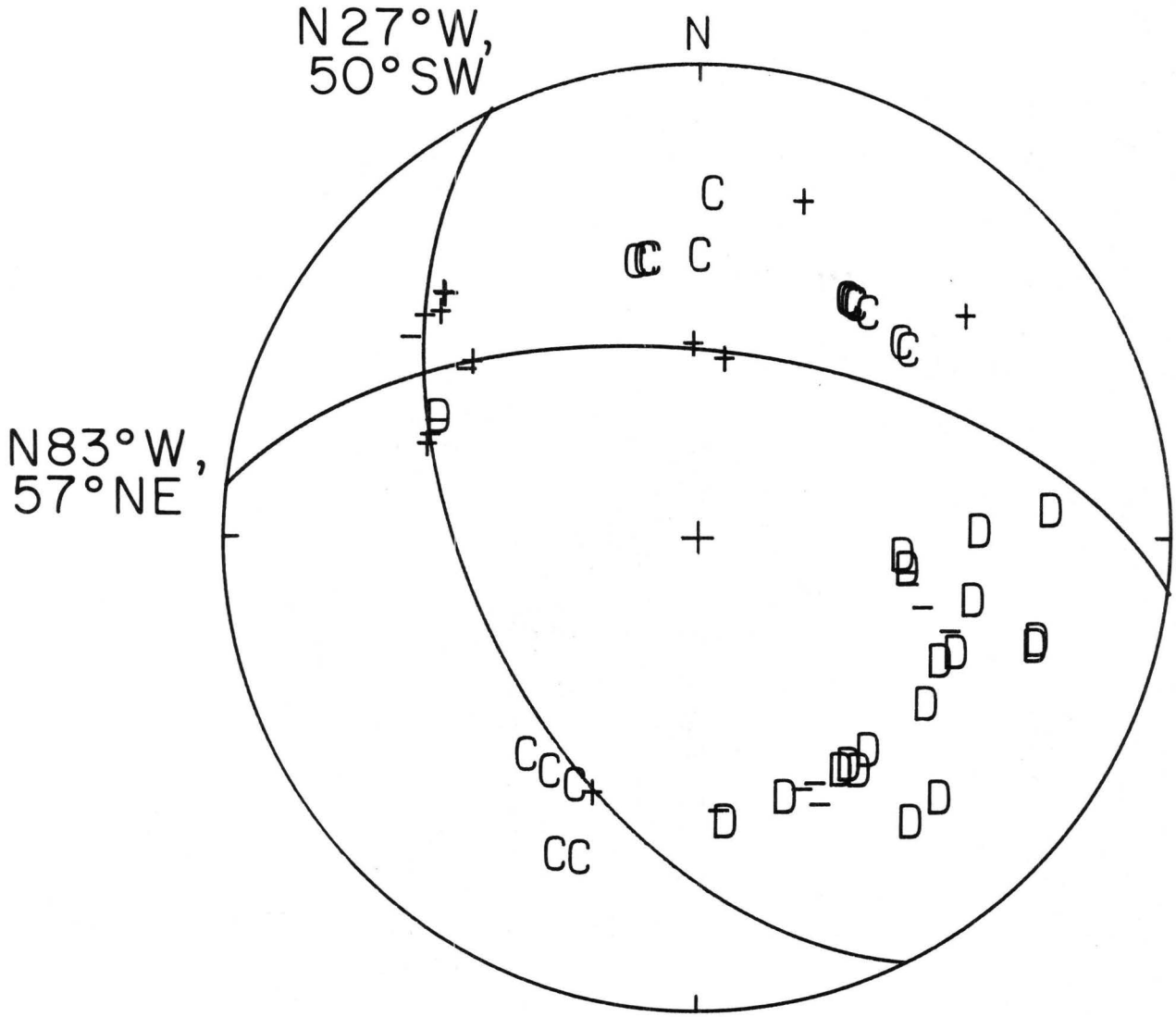

Aug 22, 1984 09: 46 Mag 5.8
Borah Peak, Idaho

FIGURE 5

Borah Peak Aftershocks
Log10(days)
0.00
1.00
2.00
3.00
0.0
30.0
60.0
90.0
120.0
150.0
Distance (km)
Mag
- 0.0
- 2.0
- 4.0
- 6.0
00h 27 Oct.83
Portable stations removed

FIGURE 6

The 1983 Borah Peak, Idaho and 1959 Hebgen Lake, Montana Earthquakes: Models for Normal Fault Earthquakes in the Intermountain Seismic Belt

By Diane I Doser*
Department of Geology and Geophysics
University of Utah
Salt Lake City, Utah 84112

Abstract

Data obtained from studies of the Borah Peak and Hebgen Lake earthquake sequences are compared with information on other normal fault earthquakes in the Intermountain seismic belt to determine what kinds of similarities exist between these sequences. The comparisons suggest that the earthquakes can be divided into two groups, moderate ($6 \leq M \leq 6\ 3/4$) and large ($7 \leq M \leq 7\ 1/2$) earthquakes, on the basis of fault length, surface displacement, focal depth, geologic setting, and other parameters. Two generalized models of normal fault earthquakes are developed from these observations. The models are compared to normal fault earthquakes that have occurred in the central Nevada seismic belt, and the agreement between the models and the earthquakes suggests that the models are valid for earthquakes in the Basin-Range region. Fault displacement along the Wasatch fault zone during past earthquakes, as inferred from geologic information is similar to the observed surface displacement in the Borah Peak earthquake implying that the Borah Peak earthquake may be a good model for earthquakes expected along the Wasatch fault. The Hebgen Lake earthquake serves well as a model for the maximum expected event in the Intermountain seismic belt.

Introduction

The October 28, 1983 (M_s=7.3) Borah Peak, Idaho, and August 19, 1959 (M_s=7.5) Hebgen Lake earthquakes are the largest normal fault earthquakes to have occurred in the Intermountain seismic belt (ISB) in historic time. The seismicity and tectonics of the Hebgen Lake region appear to be related to the Yellowstone volcano-tectonic system, 20 km to the southeast; while the Borah Peak earthquake occurred 50 km northwest of the eastern Snake River Plain (Figure 1) in a region of Basin-Range type block faulting. In spite of differences in tectonic setting, these earthquakes share many similarities. The similarities are examined by comparing surface geology, fault geometry, historical seismicity, pre-historic slip along faults, and static and dynamic source parameters obtained from aftershock distributions, waveform modeling, and maps of surface faulting. In addition, the

*Now at: Seismological Laboratory, California Inst. of Tech., Pasadena, CA 91125

mainshocks of these earthquake and their aftershock sequences are compared with other moderate to large normal fault earthquakes in the ISB. These observations suggest that earthquakes in the ISB can be grouped into two classes, moderate $6 \leq M \leq 6\ 3/4$, and large, $7 \leq M \leq 7\ 1/2$ earthquakes based on similarities in geologic and seismic parameters. Models are developed that describe an "average" earthquake for each class, and then are compared with moderate and large normal fault earthquakes that have occurred in historic time in the central Nevada seismic belt.

Regional Geology and Seismicity

Block faulting in the southwestern Montana-central Idaho region began during mid to late Tertiary (Witkind et al., 1964; Ruppel, 1982), contemporaneous with the development of the Basin-Range to the southwest. The entire region was gradually elevated, and high angle normal faults developed that were guided in part by pre-existing Laramide structures generally trending north to northwest (Witkind et al., 1964) (Figure 1).

Pleistocene and Holocene faulting in the Hebgen Lake area has occurred along north- to northwest-trending faults that are orthogonal to the northeastward propagation direction of the Snake River Plain-Yellowstone volcano-tectonic system (Armstrong et al., 1975). In addition, faulting has occurred along the younger east-west trending faults (e.g. the Centennial fault) that appear to be related to the uplift of the Yellowstone Plateau and subsidence of the Snake River Plain (Figure 1), rather than following the trend of Laramide structures. Surface rupture during the Hebgen Lake sequence occurred along a 24 km long portion of a 45 km-long fault zone that extends from the northwest end of Hebgen Lake southeastward to within 10 km of the 600,000 year old Yellowstone caldera boundary (Figure 1). A close association between two major segments of observed surface faulting, the Red Canyon and Hebgen faults, and pre-existing Laramide thrust faults suggests that normal faulting may have paralleled or occurred along the older thrusts (Doser, 1985).

Pleistocene and Holocene faulting in the Borah Peak area has occurred along the northwest trending Lost River fault whose splays locally may change strike by as much as 90° (Scott et al., 1985). This system and two similar faults to the northeast bound the southwestern sides of high mountain ranges. The Quaternary faulting in the region (Figure 1) was accompanied by uplift of northeast trending arches that parallel the northern edge of the Snake River Plain (Ruppel, 1982), suggesting that regional extension has been related to the development of the arches. Surface rupture in the Borah Peak sequence occurred along a 34 km long north-central portion of the 140 km-long Lost River fault (Figure 1). Present information on the relationship of the surface scarps of the Borah Peak earthquake to Laramide structures is not sufficient to determine whether or not compressional structures were reactivated or facilitated the slip along the Lost River fault. These fault properties suggest that normal faults initially developed in both areas under similar geologic conditions; but that Pleistocene and Holocene movement along these faults may be controlled by somewhat different tectonic processes.

Historically the Hebgen Lake area has been the most seismically active region in the ISB. Seven earthquakes with $M \geq 6.0$ have occurred in the area since 1947. In contrast, no earthquakes with intensity greater than V have occurred in the Borah Peak region in historic time (Coffman et al., 1982). Differences in rates of seismicity between these regions are also reflected in paleoseismic slip rates along major faults in the regions. Myers and Hamilton (1964) observed 24 to 30 m of post-Pinedale (15,000 to 30,000 years B.P.) displacement along the Red Canyon-Hebgen fault system, and Nash (1981) has estimated that the latest pre-1959 earthquake occurred along the fault system 3250±850 years B.P. from morphologic dating techniques. These values give estimated slip rates of 0.8 to 2.5 mm/yr. Slip rate estimates for other major faults in the region range from 0.4 to 0.7 mm/yr for the Madison fault (Mathieson, 1983) and 0.5 to 1.0 mm/yr for the Centennial fault, inferred from the geologic information of Myers and Hamilton (1964).

The mean Quaternary slip rate for the segment of the Lost River fault that ruptured in 1983 is 0.3 mm/yr and maximum slip rates along other segments of the fault vary from 0.07 to 0.1 mm/yr (Scott et al., 1985). These estimates are clearly less than those along faults in the Hebgen Lake region.

Summary of Seismological Studies

Studies of the Hebgen Lake earthquake sequence by Ryall (1962), Dewey et al. (1973), and Doser (1985) discuss seismicity patterns, source parameters of the mainshock and aftershocks, and the area's relationship to tectonic processes in the Yellowstone system. Important observations concerning the mainshock include: 1) The mainshock was a double event (Ryall, 1962; Doser, 1985). 2) The locations of the subevent epicenters with respect to the observed surface faulting and the length of rupture obtained from waveform modeling (Doser, 1985) suggest that the rupture was unilateral (Figure 2). 3) Rupture occurred along a fault plane dipping 45° to 60° south with pure dip-slip motion (Ryall, 1962; Dewey et al., 1973; Smith and Sbar, 1974; Doser, 1985). The strike of the fault plane was somewhat discordant with the strike of the surface faulting. 4) No foreshocks were observed (Murphy and Brazee, 1964). 5) Analysis of long-period teleseismic data imply that the Hebgen Lake sequence began as a moderate sized earthquake with $M_W 6.0$ at a depth of 10±2 km that triggered a larger ($M_W 7.0$) earthquake 5 seconds later at a depth of 15±3 km near the base of the seismogenic zone (Doser, 1985). Poor seismographic coverage at local and regional distances during the entire earthquake sequence does not allow for detailed studies of aftershocks with $M_L < 4.0$ that would help to resolve the fault geometry at depth and delineate any asperities associated with the rupture process. Important source parameters of the mainshock obtained from geologic and seismologic information are summarized in Table 1.

Aftershocks of the Hebgen Lake sequence exhibited normal, strike-slip, and reverse mechanisms (Figure 2); many were not consistent with the observed surface faulting or the focal mechanism of the mainshock (Doser, 1985). This suggests local variations in the stress field associated with the complex geology and tectonics of the region. Four aftershocks had

$M_L \geq 6.0$, of which two had an M_L of 6.5. The zone of aftershocks with $M \geq 4.0$ (Figure 2) extended 40 km to the east and west of the mainshock (Dewey et al., 1973).

Seismicity and source parameters for the 1983 Borah Peak sequence are discussed by Richins et al. (1984) and Doser and Smith (1985). Notable observations for this earthquake are: 1) No subevents or rupture complexities were observed in long-period data for the mainshock (Doser and Smith, 1985). 2) The location of the epicenter 14 km to the southeast of the observed surface faulting (Figure 2), the aftershock distribution, and source parameter values also suggest unilateral rupture propagation (Smith et al., 1984; Doser and Smith, 1985). 3) Moment tensor and fault plane solutions suggest that rupture occurred along a fault plane dipping 45° to 53°, with a small component (15-20%) of left lateral strike-slip motion (Doser and Smith, 1985). The strike of the seismically determined fault plane is consistent with the strike of the surface faulting, and at the surface the component of left-lateral strike-slip motion was measured to be about 17% of the dip-slip component (Crone et al., 1985). 4) No foreshocks were observed (W. D. Richins, oral comm., 1984). 5) The focal depth for the mainshock was estimated at 16 ± 4 km (Doser and Smith, 1985), a depth that may be near the base of the seismogenic zone in the region, since few aftershocks had depths exceeding 16 km (Richins, et al., 1984). Additional parameters obtained from geologic and seismologic information are listed in Table 1.

Focal mechanisms of aftershocks in the Borah Peak sequence also showed a variety of orientations, but most were consistent with the orientation of the main fault or subsidiary splays striking west-northwest (Figure 2). The largest aftershock magnitudes were $M_L = 5.8$, and only three had $M_L \geq 5.0$. All aftershocks with $M_L \geq 4.0$ were located northwest of the mainshock in a zone 35 km long.

Comparisons of source parameters (see Table 1) suggest that although the Hebgen Lake earthquake had a seismic moment nearly four times as large as that of Borah Peak, the earthquakes occurred along faults with similar dimensions. The unilateral rupture lengths determined from seismological data for both earthquakes were not comparable to the total lengths of the surface scarps, but were comparable to the length of scarps with displacements over 0.5 m. This suggests that the total length of surface faulting may not be a good indicator of subsurface rupture length. The major differences between the earthquakes appear to be in the amount of slip along the fault plane and in the complexity of the rupture process.

The large magnitude aftershocks of the Hebgen Lake sequence may be related, in part, to the size of the mainshock, but they also may be related to the tectonic complexity of the region. Redistribution of stress in a region of diversely trending faults may require more movement along separate faults than in a region where faults have more uniform orientations.

Comparisons with Other Earthquakes in the ISB

Although the Hebgen Lake and Borah Peak earthquakes are the best studied large normal fault earthquakes in the ISB, inferences from limited data can be made for other normal fault earthquakes in the region. Since we are interested in what may happen during large earthquakes expected to occur along faults that exhibit Quaternary or Holocene displacement, emphasis should be placed on earthquakes in the ISB that have produced surface breakage or measurable geodetic uplift and/or subsidence.

The minimum magnitude required to produce surface breakage in the region appears to be in the range of $6.0 \leq M_L \leq 6.5$. This value is based on the observation that none of the following earthquakes had identified surface faulting: Pocatello Valley, Idaho, M_L=6.0, (Bucknam, 1976); Yellowstone Park, Wyoming, M_L=6.1, (Pitt et al., 1979), and Virginia City, Montana, M=6 1/4, (Qamar and Stickney, 1983). Co-seismic subsidence of Pocatello Valley of 13 cm (Bucknam, 1976) was observed for the 1975 Pocatello Valley earthquake. A subsidence of 12 cm between 1960 and 1975 was probably associated with the Yellowstone Park earthquake of 1975 (Pitt et al., 1979).

The 1925, M=6 3/4, Clarkston, Montana earthquake also had no observed surface displacement, although some surface cracks were seen in the region with local subsidence of 0.6 m near the cracks (Pardee, 1926). There is some question about the focal mechanism for this earthquake. The preferred focal mechanism of Dewey et al., (1973) and Smith and Sbar (1974) for this earthquake showed strike-slip motion, but the probable causative fault, the Clarkston fault, shows predominantly dip-slip motion (Pardee, 1926). Focal mechanisms of aftershocks of an earthquake of m_b=4.8 in the region in 1977 showed dip-slip motion associated with the fault (Qamar and Hawley, 1979).

In contrast, the 1934 Hansel Valley Utah earthquake with M=6.6 had observed fault displacement along a northerly trend on the west side of an alluvial filled valley. A maximum vertical displacement of 0.5 m was measured along a discontinuous scarp that had a total length of ©10 km.

Source parameters for earthquakes in the ISB with associated surface breakage or deformation measured by leveling are listed in Table 2. These data show that the earthquakes have remarkably similar fault lengths of 10 to 15 km, although there is up to a factor of 10 difference in their seismic moments.

The degree of foreshock and aftershock activity varied considerably among the moderate sized earthquakes in the ISB for which there is significant information. Foreshocks (e.g. earthquakes occurring within 24 hours of the mainshock) were observed in association with the earthquakes in Pocatello Valley (Arabasz et al., 1981), Clarkston (Pardee, 1926), and Yellowstone Park (Pitt et al., 1979), however no foreshocks were associated with the Hansel Valley earthquake (Shenon, 1934). The Hansel Valley and Clarkston sequences had aftershocks within one magnitude unit of the mainshock. It is interesting to note that only 50 km separated the Hansel Valley and the Pocatello Valley epicenters; thus, differences in foreshock

and aftershock patterns cannot be explained by major differences in tectonic setting.

None of these moderate earthquakes occurred along major range bounding fault systems exceeding 40 km in total length. Therefore, one cannot rule out the possibility that "blind" earthquakes with $6<M<6\ 3/4$ may occur in parts of the ISB where there is little evidence for major Holocene or Pleistocene faulting.

Geologic information on normal faults in the ISB helps to supplement the limited historic data used in developing a hypothetical model for large normal fault earthquakes. The most detailed geologic study to date has been along the Wasatch fault. Analyses of trenches across the Wasatch fault have shown that earthquakes with Quaternary and Holocene displacement produced an average of 2 m of slip, with a range of values from 1.6 to 3.7 m (Schwartz and Coppersmith, 1984). No events with displacements between 0.5 and 1.5 m have been recognized although events with displacements $\geq$0.5 m should be detectable (Schwartz and Coppersmith, 1984).

The Borah Peak earthquake, with a maximum displacement of 2.7 m and an average displacement of 1.0 m, would thus be in the magnitude range of a postulated event expected to occur along the Wasatch fault in the future. It is also possible that earthquakes similar to that of the Pocatello Valley or Yellowstone Park events, with no surface rupture and geodetic measured displacements of <15 cm, could have occurred along the fault, since this amount of displacement may not be detectable in the geologic record. The Hebgen Lake earthquake with a maximum vertical displacement of 6.7 m (Myers and Hamilton, 1964) would represent an earthquake larger than that expected along the Wasatch fault. In fact, no greater single event displacement has been observed in the limited geologic and historic data; suggesting that the 1959, M7.5 Hebgen Lake earthquake may represent the maximum expected earthquake for the region.

Discussion

Studies of moderate to large normal fault earthquakes in the ISB suggest that they can be divided into two magnitude groups, with a separate model for each group. A model for moderate sized earthquakes with $6\leq M\leq 6\ 3/4$ would predict a fault length of 10 to 15 km, surface or geodetically detectable displacements of 0.1 to 0.5 m, faulting along faults not necessarily associated with major fault systems, and a good possibility of foreshocks. A model for large earthquakes, $7\leq M\leq 7\ 1/2$, would predict a fault rupture length of 20 to 30 km, an average surface displacement of 1 to 4 m displacement along major fault systems showing repeated movements in Quaternary-Holocene times, and unilateral rupture nucleating at a depth that is at or near the base of the seismogenic zone. The fault rupture length would roughly correspond to the length of the surface scarp that has a throw of $\geq$0.5 m. Thus, the total length of surface faulting could be longer than 30 km.

In order to test the accuracy of these hypothetical models, the models are compared with moderate and large earthquakes from the central Nevada seismic belt (Table 3). This area is similar in seismicity and tectonic history to the ISB.

Earthquakes in Nevada in the magnitude range 6 to 6 3/4 agree well with the model for moderate sized earthquakes. Surface faulting lengths were 14 km or less, with maximum surface displacements of 0.15 to 0.4 m. Earthquakes between $6\ 3/4 \leq M < 7$ appeared to fit the model for large earthquakes better than the model for moderate earthquakes, with fault lengths where displacement exceeded 0.5 m of 10 and 22 km, maximum surface displacements of 0.8 and 2.1 m, and faulting along major Quaternary fault systems. Earthquakes with $M \geq 7$ had fault lengths of 28 to 60 km. Maximum vertical displacements for $M \geq 7$ earthquakes ranged from 0.6 to 4.6 m and horizontal displacements from 1.0 to 3.7 m. These values are not inconsistent with displacements observed at Hebgen Lake and Borah Peak.

The most notable misfit between the $7 \leq M < 7\ 1/2$ model and the Nevada earthquakes was the 1932 Cedar Mountain earthquake. The earthquake produced a zone of fissures 60 km long and 6 to 14 km wide, however no fissure exceeded 6 km in length (Gianella and Callagham, 1934). This makes an assessment of the fault length difficult. The July 1954 Rainbow Mountain earthquake also did not fit the ISB model because the event occurred along a major fault system. The Rainbow Mountain earthquake was followed by a M=6.8 event in August 1954. Foreshocks were observed for the Excelsior Mountain, Pleasant Valley, and Cedar Mountain earthquakes.

There are several suggestions of unilateral rupture in the Nevada earthquake sequences, in agreement with the $7 \leq M < 7\ 1/2$ model. In the Rainbow Mountain sequence, seismicity and surface faulting migrated northeastward from July through August 1954. The epicenters for both the Fairview Peak and Dixie Valley earthquakes were located near the northern end of their surface ruptures, suggesting unilateral rupture toward the southwest.

Little information on focal depths and their relationship to the depth of the base of the seismogenic zone is available for the Nevada events. The 15 km focal depth estimated from pP-P arrivals (Romney, 1957) for the Fairview Peak earthquake agrees well with the observed maximum depth of 16 km for microearthquakes in the region (Stauder and Ryall, 1966). A 40 km focal depth was estimated by Romney (1957) for the Dixie Valley earthquake, a value that places the earthquake far below the base of the seismogenic zone in this region. A recent study by Okaya and Thompson (1984) suggests that Romney may have misidentified the P and pP phases, and that the Dixie Valley earthquake also occurred at a depth of 15 km.

Conclusions

Observations from normal fault earthquakes of the ISB have been used to develop hypothetical models for moderate, $6 \leq M \leq 6\ 3/4$, and large, $7 \leq M \leq 7\ 1/2$, earthquakes that could occur in other parts of this intraplate region. The models agree well with observations from moderate to large earthquakes in the central Nevada seismic belt, suggesting that the important features of normal fault earthquakes occurring in the Intermountain region are reasonable well described by these models. Comparisons of the Borah Peak and Hebgen Lake earthquakes to models inferred from geologic information on the Wasatch fault indicate that the Borah Peak earthquake is a good model for earthquakes expected along this fault. The Hebgen Lake earthquake serves best as a model for the maximum expected earthquake in the Intermountain seismic belt.

Acknowledgments

This work was supported by the U.S. Geological Survey Earthquake Hazards Reduction Program, contract to the University of Utah, No. 14-08-0001-21856. I would like to thank M. R. Baker, H. Kanamori, J. C. Pechmann, R. B. Smith and S. G. Wesnousky for helpful comments.

References

Arabasz, W. J., W. D. Richins, and C. J. Langer (1981). The Pocatello Valley (Idaho-Utah border) earthquake sequence of March to April 1975, Bull. Seism. Soc. Amer., 71, 803-826.

Armstrong, R. L., W. D. Leeman, and H. E. Maulde (1975). K-Ar dating, Quaternary and Neogene volcanic rocks of the Snake River Plain, Idaho, Am. J. Sci., 275, 225-251.

Bache, T. C., D. G. Lambert, and T. G. Barker (1980). A source model for the March 28, 1975 Pocatello Valley earthquake from time-domain modeling of teleseismic P-waves, Bull. Seism. Soc. Amer., 70, 405-418.

Battis, J. C., and K. Hill (1977). Analysis of seismicity and tectonics of the central and western United States, Interim Scientific Report No. 1, AFCSR Contract No. F44620-76-C-0063, Texas Instruments, Incorporated, Dallas, Texas.

Bucknam, R. C. (1976). Leveling data from the epicentral area of the March 27, 1975, earthquake in Pocatello Valley, Idaho, U.S. Geol. Survey Open-File Rept. 76-52, 6 pp.

Callagham, E., and V. P. Gianella (1935). The earthquake of January 30, 1934 at Excelsior Mountains, Nevada, Bull. Seism. Soc. Amer., 25, 161-168.

Coffmann, J. L., C. A. von Hake, and C. W. Stover (1982). Earthquake History of the United States, NOAA Publication 41-1, U.S. Dept. of Commer., Boulder, Colo.

Crone, A. J., M. N. Machette, M. G. Bonilla, J. L. Lienkaemper, R. C. Bucknam, K. L. Pierce and W. E. Scott (1985). Surface faulting accompanying the Borah Peak earthquake, central Idaho, Workshop XXVIII on the Borah Peak earthquake: U.S.G.S. Open-File Rept., in press.

Dewey, J. W., W. H. Dillinger, J. Taggart, and S. T. Algermissen (1973). A technique for seismic zoning: Analysis of earthquake locations and mechanisms in northern Utah, Wyoming, Idaho, and Montana, NOAA Tech. Rept. ERL 267-ESL30, p 28-48, U.S. Dept. of Commer., Boulder, Colo.

Doser, D. I. (1985). Source parameters and faulting processes of the 1959 Hebgen Lake, Montana earthquake sequence, submitted to J. Geophys. Res.

Doser, D. I., and R. B. Smith (1985). Source parameters of the October 28, 1983 Borah Peak, Idaho earthquake from body wave analysis, submitted to Bull. Seism. Soc. Amer.

Doser, D. I., and R. B. Smith (1982). Seismic moment rates in the Utah region, Bull. Seism. Soc. Amer., 72, 525-551.

Gianella, V. P., and E. Callagham (1934). The Cedar Mountain, Nevada earthquake of December 10, 1932, Bull. Seism. Soc. Amer., 24, 345-384.

Jones, J. C. (1915). The Pleasant Valley, Nevada earthquake of October 2, 1915, Bull. Seism. Soc. Amer., 5, 109-205.

Mathieson, E. L. (1983). Post-Pinedale displacement rate on the Madison Range fault along its 1959 rupture trace, Madison County, Montana, (abstract), Geol. Soc. Amer. Abstr. Prog., 15, 376.

Murphy, L. M., and R. J. Brazee (1964). Seismological investigations of the Hebgen Lake earthquake, U.S. Geol. Surv. Prof. Paper, 435, 13-18.

Myers, W. F., and W. Hamilton (1964). Deformation accompanying the Hebgen Lake earthquake of August 17, 1959, U. S. Geol. Surv. Prof. Paper, 435, 37-98.

Nash, D. B. (1981). Fault scarp morphology: Indicator of paleoseismic chronology, U.S. Geol. Surv. Final Tech. Report, Contract number 14-08-0001-19109, 132 p.

Okaya, D. A., and G. A. Thompson (1984). Geometry of extensional faulting in Dixie Valley, Nevada, Tectonics, in press.

Pardee, J. T. (1926). The Montana earthquake of June 27, 1925, U.S. Geol. Surv. Prof. Paper 147-B, 17 p.

Pitt, A. M., C. S. Weaver, and W. Spence (1979). The Yellowstone Park earthquake of June 30, 1975, Bull. Seism. Soc. Amer., 69, 187-205.

Qamar, A. I., and B. W. Hawley (1979). Recent earthquake activity near Three Forks basin, Montana, Bull. Seism. Soc. Amer., 69, 1917-1930.

Qamar, A. I., and M. C. Stickney (1983). Montana earthquakes 1869-1979, Historical seismicity and earthquake hazard, Montana Bureau of Mines and Geology Memoir, 51, 1-53.

Richins, W. D., R. B. Smith, J. J. King, C. J. Langer, C. W. Meissner, J. C. Pechmann, W. J. Arabasz, and J. E. Zollweg (1984). The 1983 Borah Peak, Idaho, earthquake: A progress report on the relationship of aftershocks to the mainshock, surface faulting, and regional tectonics (abstract), Earthquake Notes, 55, 129.

Romney, C. (1957). Seismic waves from the Dixie Valley-Fairview Peak earthquakes, Bull. Seism. Soc. Amer., 47, 301-319.

Ruppel, E. T. (1982). Cenozoic block uplift in the southwest Montana and east-central Idaho, U.S. Geol. Surv. Prof. Paper 1224, 24 p.

Ryall, A., (1962). The Hebgen Lake, Montana, earthquake of August 17, 1959, P-waves, Bull. Seism. Soc. Amer., 52, 235-271.

Scott, W. E., K. L. Pierce, and M. H. Hait, Jr., (1985). Quaternary tectonic setting of the 1983 Borah Peak earthquake, central Idaho, Workshop XXVIII on the Borah Peak Earthquake: U.S.G.S. Open-File Report, in press.

Schwartz, D. P., and K. J. Coppersmith (1984). Fault behavior and characteristic earthquakes: Examples from the Wasatch and San Andreas faults, J. Geophys. Res., 89, 5681-5698.

Shenon, P. J. (1934). Hansel Valley earthquake, March 12, 1934, unpublished report, U.S. Geol. Surv.

Slemmons, D. B. (1957). The Dixie Valley-Fairview Peak, Nevada, earthquakes of December 16, 1954 - Geological effects, Bull. Seism. Soc. Amer., 47, 353-376.

Smith, R. B., and R. L. Christiansen (1980). Yellowstone Park as a window on the earth's interior, Scien. Am., 242, 104-117.

Smith, R. B., W. D. Richins, D. I. Doser, J. C. Pechmann, and C. J. Langer (1984). The 1983, M_S=7.3 Borah Peak, Idaho, earthquake: A model for active crustal extension, (abstract), Geol. Soc. Amer. Abs Abstr. With Prog., 661.

Smith, R. B., and M. L. Sbar (1974). Contemporary tectonics and seismicity of the western United States with emphasis on the Intermountain seismic belt, Geol. Soc. Amer. Bull., 85, 1205-1218.

Stauder, W., and A. Ryall (1967). Spatial distribution and source mechanism of microearthquakes in central Nevada, Bull. Seism. Soc. Amer., 57, 1317-1345.

Tocher, D. (1956). Movement on the Rainbow Mountain fault, Bull. Seism. Soc. Amer., 46, 10-14.

U.S. Geological Survey (1972). Geologic map of Yellowstone National Park, Misc. Geol. Invest. Map I-711.

Walter, H. G., (1934). Hansel Valley, Utah earthquake, The Compass of Sigma Gamma Epsilon, 14, 178-181.

Witkind, I. J. (1964). Reactivated faults north of Hebgen Lake, U.S. Geol. Surv. Prof. Paper 435, 37-50.

Table 1--Source Parameters of the Hebgen Lake and Borah Peak Earthquakes*

Parameter	Hebgen Lake	Borah Peak
Magnitude (M_S)	7.5	7.3
Moment (S)**	1.0×10^{27} dyne-cm	2.9×10^{26} dyne-cm
Unilateral rupture length (S)	28 km	21 km
Length of surface scarp (G)+	27 km	22 km
Average surface displacement (G)	4 m	1 m
Average displacement (S)	8 m	2 m
Focal depth (S)	15±3 km	16±4 km
Fault dip (S)	45-60°	45-53°
Stress drop (S)	115 bars	24 bars

*values from Doser (1985) and Doser and Smith (1985). Seismologically determined parameters for Hebgen Lake represent the sum of the parameters of the two subevents.

**(S)=seismologically determined

(G)=geologically determined

+length of segments along which displacement exceed 0.5 m

Table 2--Source Parameters of ISB Earthquakes with Observed Geodetic or Geologic Displacements

Event	Maximum Surface Displacement (m)	Fault Length (km)	Focal Depth (km)	Moment (dyne-cm)	Reference
Clarkston	0.6	16?	--	--	5
Hansel Valley	0.5	10	--	7.7×10^{25}	4,7
Pocatello Valley	0.13	10-15	5-9	1.5×10^{25}	1,2
Yellowstone	0.12	10	6	7.5×10^{24}	3,6

1-Arabasz et al. (1981)

2-Bache et al. (1980)

3-Battis and Hill (1977)

4-Doser and Smith (1982)

5-Pardee (1926)

6-Pitt et al. (1979)

7-Shenon (1934)

Table 3--Moderate to Large Normal Fault Earthquakes in the Central Nevada Seismic Belt

Event	M	Scarp Length (km)	Surface Displacement+ (m)	Reference
Pleasant Valley (1915)	7 3/4	35	4.6	Jones (1915)
Cedar Mountain (1932)	7.3	60*	0.6 vert. 1.0 hor.	Gianella and Callagham (1934)
Excelsior Mountains (1934)	6.5	1.4**	0.15	Callagham and Gianella (1935)
Rainbow Mountain July (1954)	6.6	14	0.4	Tocher (1956)
Rainbow Mountain August (1954)	6.8	10**	0.8	Tocher (1956)
Dixie Valley (1954)	6.8	22**	2.1	Slemmons (1957)
Fairview Peak (1954)	7.1	28**	3.7 vert. 3.7 hor.	Slemmons (1957)

* total length of fracture zone, individual fissures up to 6 km in length

** length of segment along which displacement exceeded 0.5 m

+ vertical displacement unless denoted

Figure Captions

Figure 1.

Map showing location of major Quaternary faults and other tectonic features of southwest Montana and central Idaho. Fault locations in central Idaho are from Ruppel (1982) and Scott *et al.* (1984). Fault locations and caldera boundary in the Yellowstone-southwestern Montana area are from Smith and Christiansen (1980) and the U.S. Geol. Survey (1972). Holocene arches are from Ruppel (1982).

Figure 2.

Surface faulting, mainshock and aftershock distributions, and focal mechanisms for the Hebgen Lake and Borah Peak earthquake sequences. Focal mechanisms are from Doser (1984), Doser and Smith (1984) and unpublished data. The focal mechanisms are lower hemisphere projections where white quadrants indicate dilatation; dark quadrants compression. Surface faulting is from Crone and Machette (1984) and Witkind (1964). Error bars for the Hebgen Lake earthquakes indicate probable bias in locations (Doser, 1984). Error bars for the Borah Peak earthquakes reflect mislocation errors for individual events (Richins, 1984, written communication).

QUATERNARY FAULTS IN THE SOUTHWEST-MONTANA CENTRAL-IDAHO REGION

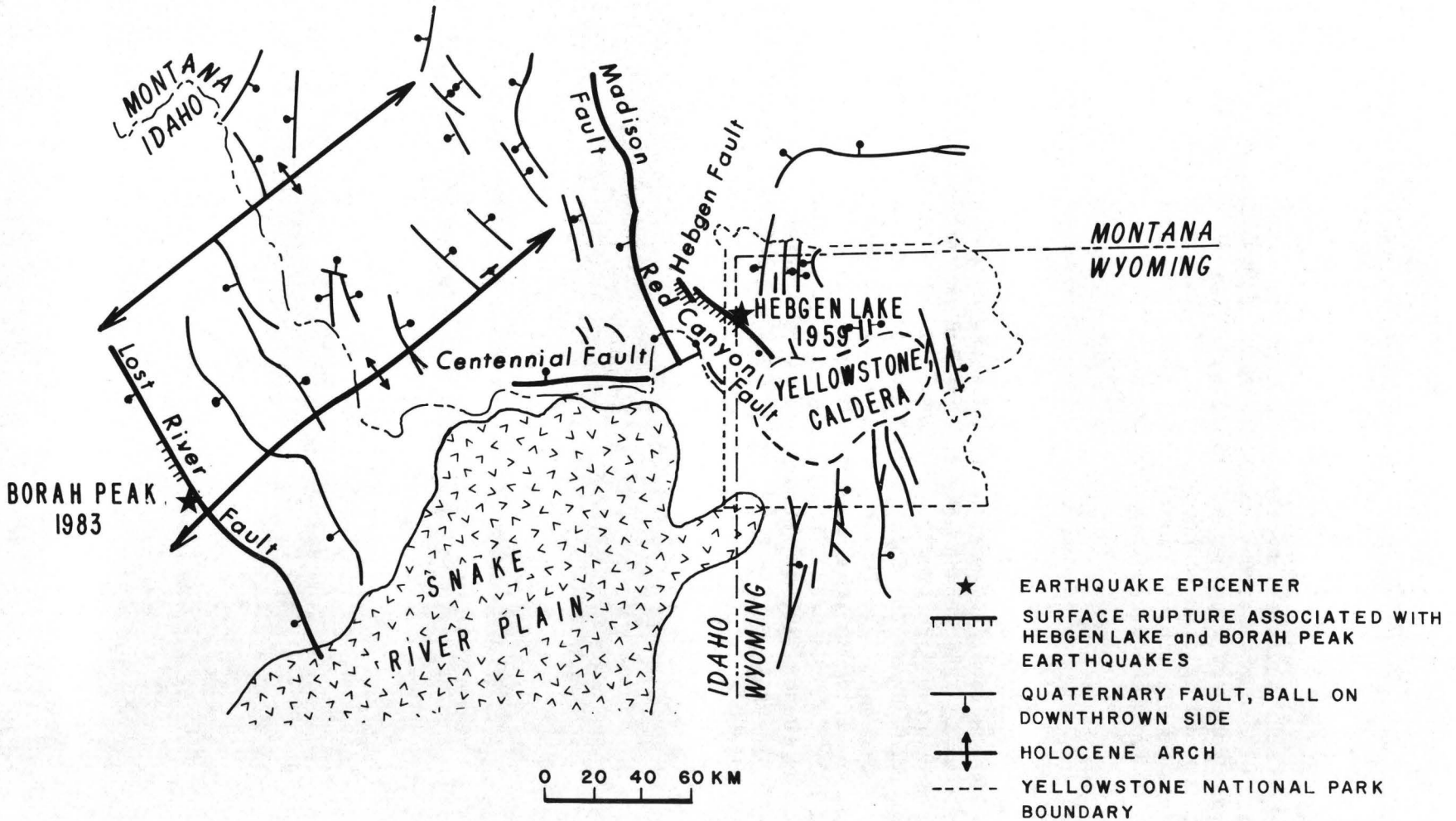

Figure 1

SURFACE FAULTING AND AFTERSHOCK DISTRIBUTION

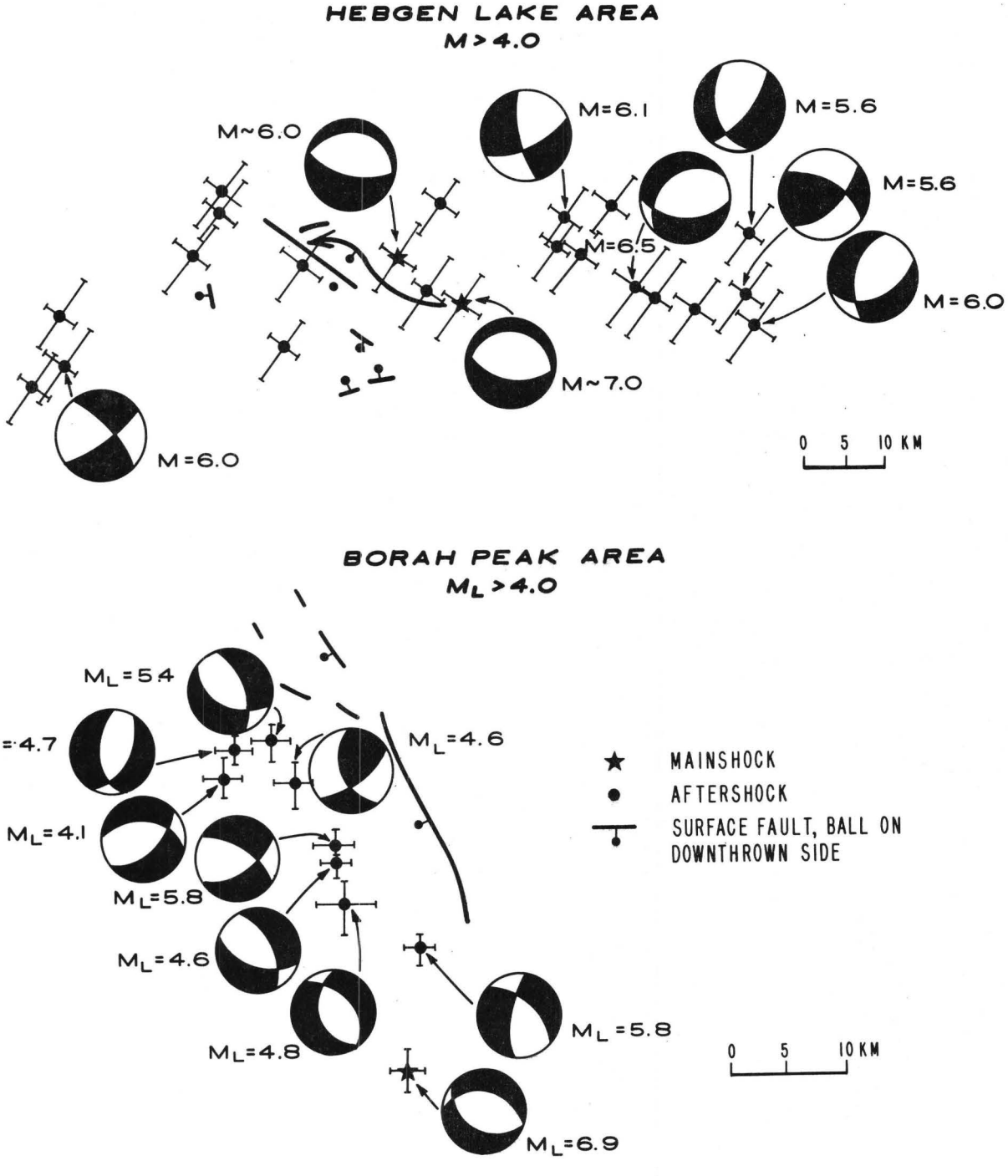

Figure 2

ACCELERATION DATA FROM THE 1983 BORAH PEAK, IDAHO EARTHQUAKE RECORDED AT THE IDAHO NATIONAL ENGINEERING LABORATORY

Suzette M. Jackson
EG&G Idaho, Inc.
Earth & Life Sciences Branch
P. O. Box 1625
Idaho Falls, ID 83415

ABSTRACT

The Idaho National Engineering Laboratory (INEL) is located approximately 80 km southeast of the epicenter for the 1983 M_S = 7.3 Borah Peak, Idaho Earthquake. Thirteen strong-motion accelerographs located at various facilities around the INEL site recorded ground motion from the Borah Peak earthquake. The strong-motion records were digitized and processed resulting in corrected acceleration, velocity, and displacement time-histories along with response and Fourier spectra. Peak horizontal accelerations range from 0.022 g to 0.078 g for free field accelerographs and accelerographs located in basements. Values of 0.037 g - 0.187 g were recorded at accelerographs located within structures above the basement. Peak vertical accelerations range 0.016 g (ground level) to 0.059 g (top of structures). The peak horizontal accelerations recorded at the free field sites are consistent with the 4-6% g estimated for the area of the INEL on a map of peak horizontal accelerations in rock with a 90% probability of not being exceeded in 50 years. The peak horizontal accelerations are compared to attenuation curves for predicted accelerations as a function of distance and moment magnitude. The peak horizontal accelerations are consistent with the predicted accelerations for the 84 percentile, but exceed what is predicted for the 50 percentile at distances of 89 - 110 km and moment magnitude of 6.9.

INTRODUCTION

The Idaho National Engineering Laboratory (INEL) is located on the southwest region of the Eastern Snake River Plain. The Lost River, Lemhi and Beaverhead Mountain ranges lie to the northwest of the INEL site and trend northwest-southeast. The INEL is approximately 80 km southeast of the 1983 M_S = 7.3 Borah Peak, Idaho earthquake. The INEL operates five seismograph stations located near and around the site and, at the time of the earthquake, sixteen strong-motion accelerographs (currently 20 SMAs) located at various facilities on the site. The seismograph station network was installed in 1972 to monitor microearthquake activity within the site boundaries. The strong-motion network was started in 1973 to measure ground motion in the event of a large earthquake near the INEL site. Thirteen of the sixteen strong-motion accelerographs recorded the Borah Peak earthquake.

INSTRUMENTATION

The location of the strong-motion accelerographs and seismograph stations are shown in Figure 1. Each facility has at least two strong motion accelerographs with the exception of the Old Fire Station No. 2 (OFS#2) and the Idaho Laboratory Facility (ILF-1) located in Idaho Falls, which both have one accelerograph.

Thirteen of the accelerographs are model RFT-250 Teledyne Geotech, and three are model RFT-350 Terra Technology. The RFT-250 has a sensitivity of 1.85 cm/0.5 g and the RFT-350, 1.85 cm/1.0 g. The RFT-250 and RFT-350 accelerographs have a natural frequency of 16-21 hz and are damped 60% of critical. The three component traces are recorded on 70 mm film with at least one time trace. The accelerograph records ground motion for about 7 seconds after the last trigger occurs. Several of the accelerographs are interconnected so that when one is triggered they all turn on. The interconnected accelerographs are also noted in Figure 1. The accelerographs are serviced quarterly and tilt-test calibrations were performed prior to the earthquake.

Accelerograph locations and description of the facilities and subsurface geology are listed in Table 1 for accelerographs that recorded ground motion. Seven of the accelerographs are located within the basement of structures. At PBF-620, there are accelerographs in the upper and lower basements below ground level referred to as first and second basement, respectively. Two accelerographs are at free field sites and both sit on concrete pads. The accelerograph at CPP-610 is situated on a pad connected to the structure surrounding it, while the accelerograph at TAN-719 is bolted to a pad that is not connected to the structure surrounding it. Four accelerographs are located above ground level within structures. Two accelerographs, CPP-601-1 and TAN-650-4, are located on the first and fourth floors, respectively. The other two sit at the top of structures, PBF-620-C on top of a crane beam (2 stories) and TAN-650-D at the top of a 10-story containment vessel. All sixteen accelerographs, with the exception of the ground level accelerographs, are within structures that are directly founded in basalt or have supports embedded in basalt. However, it is noted that the CPP-601 structure has the southern end embedded in basalt and the northern end in firm soil.

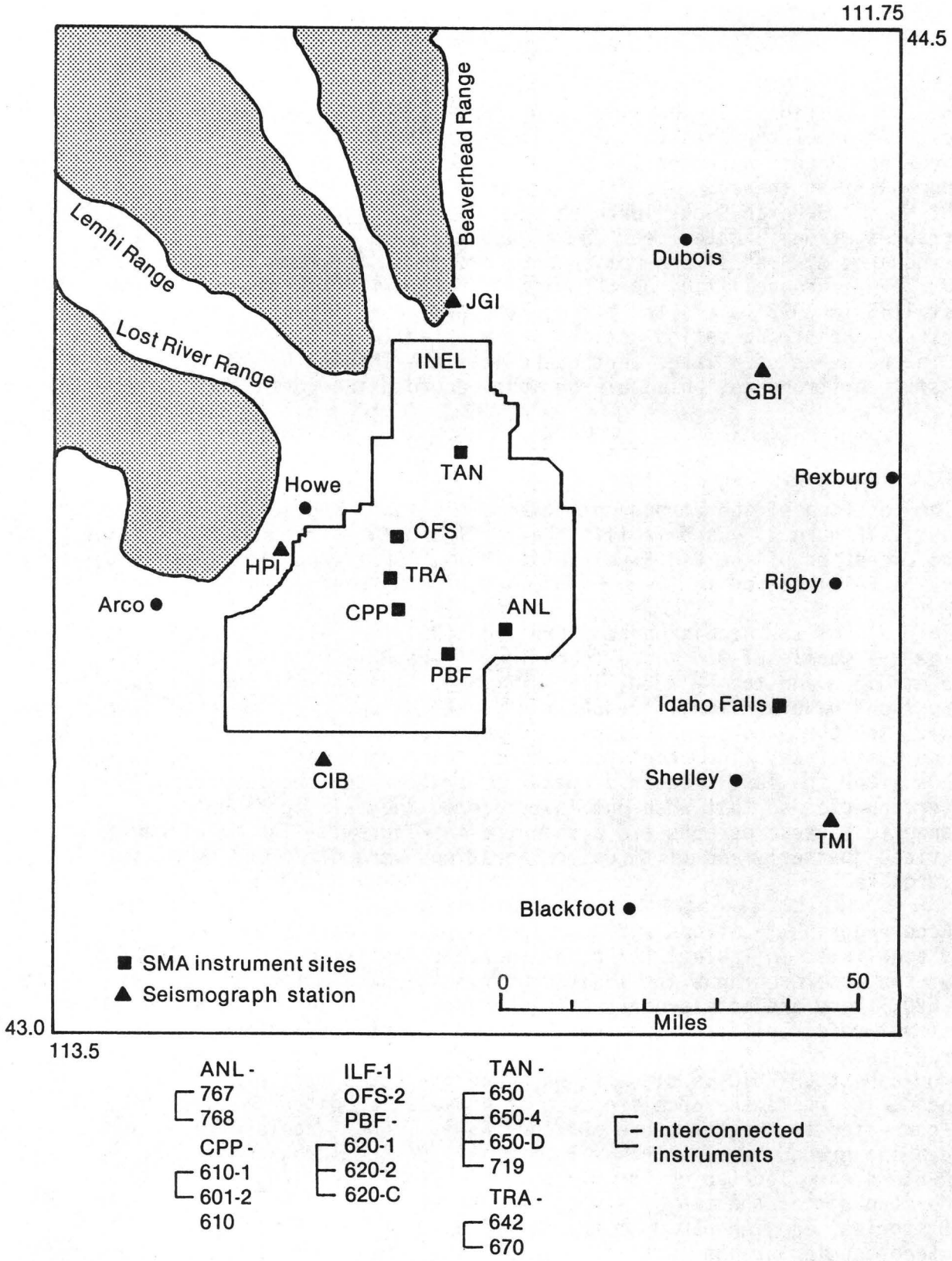

ANL -
767
768
CPP -
610-1
601-2
610

ILF-1
OFS-2
PBF -
620-1
620-2
620-C

TAN -
650
650-4
650-D
719
TRA -
642
670

Interconnected instruments

Figure 1. Map of Idaho National Engineering Laboratory site showing: 1) location of strong-motion accelerographs with notation of instrument inter-connections; 2) location of seismograph stations.

TABLE 1. DESCRIPTION OF INSTRUMENT LOCATIONS, FACILITIES AND SUBSURFACE GEOLOGY

FACILITY	INSTRUMENT LOCATION	STRUCTURE[a]	SUBSURFACE GEOLOGY[b]
TRA-670	Basement	4-story building supported by piers embedded in basalt	45-74 feet of sand and gravels with silty sand lenses overlaying basalt
TRA-642	Basement	4-story building supported by columns of various lengths embedded in basalt	45-74 feet of sand and gravels with silty sand lenses overlaying basalt
CPP-601-1 CPP-601-2	First Floor Basement	2-story building supported by footings that vary in lengths up to 20 feet in firm soil at the north end to 50 feet in basalt at the south end.	30-50 feet of sand and gravel with clay overlaying basalt
CPP-610	Ground level	1-story building supported by a 9-inch thick slab about 6 feet below the surface	30 feet of sand and gravel with clay overlaying basalt
TAN-650-4	Fourth Floor	4-story building supported by piers of 10-16 feet in length that are embedded in basalt	55 feet of lake and playa sediments overlaying basalt
TAN-650-D	Dome Top	10-story containment vessel tied into basalt with reinforced concrete columns	55 feet of lake and playa sediments overlaying basalt
TAN-719	Ground Level	Small shelter enclosing a 3 x 3 foot, 6-inch thick concrete pad	55 feet of lake and playa sediments overlaying basalt
PBF-620-1 PBF-620-2 PBF-620-C	First (upper) Basement Second (lower) Basement First floor high-bay bridge crane beam	2-story building founded directly in basalt	4-8 feet of silty sand overlaying basalt
ANL-767	Basement	6-story building founded on basalt	13-20 feet of sandy silt overlaying basalt (strata of lava cinders)

TABLE 1. DESCRIPTION OF INSTRUMENT LOCATIONS, FACILITIES AND SUBSURFACE GEOLOGY (cont.)

FACILITY	INSTRUMENT LOCATION	STRUCTURE[a]	SUBSURFACE GEOLOGY[b]
ANL-768	Basement	4-story building supported by piers 2 feet thick that terminate in spread footings 1 foot thick within the basalt	6-7.5 feet of silty sand overlaying basalt

[a] Personal communication, J. J. King, 1984; Gorman, V. W. and Guenzler, R. C., 1983.

[b] Personal communication, J. J. King and B. Lewis, 1984.

The sediment thickness over bedrock (basalt) varies at each of the facility areas. The least amount of sediment cover, 4-8 feet is at PBF. The TRA facility area has the greatest amount of sediment cover, 45-74 feet. The other facility areas have sediment cover that range between the TRA and PBF areas. Most of the sediments are sand and gravels. In some areas, the sand and gravels are mixed with clay and in other areas, with silt lenses. The sediments underlying the TAN facilities are lake and playa sediments (Refer to Table 1).

DATA

Thirteen of the sixteen accelerographs recorded the Borah Peak Earthquake. Two failed to operate properly; one, located at the basement of TAN-650, did not produce a record because the light bulb did not switch on to expose the film, and the other, OFS-2 (free field), did not start up because cold air temperature affected the normal performance of the accelerograph (personal communication, J. J. King, 1984). The third accelerograph, ILF-1, located at the Idaho Laboratory Facility in Idaho Falls (160 km from the earthquake), was not triggered.

The records were collected within three days following the Borah Peak earthquake. The accelerographs recorded ground motion for 30 - 40 seconds. The uncorrected acceleration records were sent to Structural and Earthquake Engineering Consultants of Arcadia, California for processing (personal communication, J. J. King, 1984). First, the records were digitized, then corrected for digitizing errors, instrument transducer response, and long period errors. The corrected accelerations were integrated once to produce the corrected velocity time-history and integrated twice to create the corrected displacement time-history. The acceleration (cm/sec/sec), velocity (cm/sec), and displacement (cm) were plotted against time in seconds. Figure 2 shows the corrected acceleration (cm/sec/sec) versus time (seconds) for the longitudinal components of TRA-642 (basement), TAN-719 (free field), and ANL-767 (basement). The peak acceleration (cm/sec/sec) is noted by a star and listed below each trace. The envelopes of peak amplitudes for the acceleration traces are similar. The selected traces are representative of the other accelerogram components recorded during the earthquake.

The corrected acceleration components were then processed to produce the response and Fourier spectra for single-degree-of-freedom-systems. The systems were chosen to have a period range of 0.4s - 14s and damping values of 0, 2, 5, 10 and 20 percent of critical. The results were plotted on a tripartite logarithmic graph. The pseudo-acceleration (PSA), pseudo-velocity (PSV), relative displacement (SD), and Fourier spectra (FS) for the transverse component of TRA-642 (basement) and the longitudinal components of PBF-620 (basement), CPP-610 (free field) and TAN-719 (free field) are shown in Figure 3, A, B, C, and D, respectively. The peak amplitudes of the response and Fourier spectra for the two basement located accelerographs (Figure 3, A and B) are approximately 2-3 hz. For the spectra of the two free field accelerographs (Figure 3, C and D), the peak amplitudes range 2-8 hz. The peak amplitudes of the response and Fourier spectra occur in the 2-10 hz frequency range for all of the other accelerogram components.

The corrected peak accelerations for each accelerograph are listed in Table 2 along with the distance from the epicenter of the Borah Peak earthquake to the accelerograph locations. The largest peak horizontal

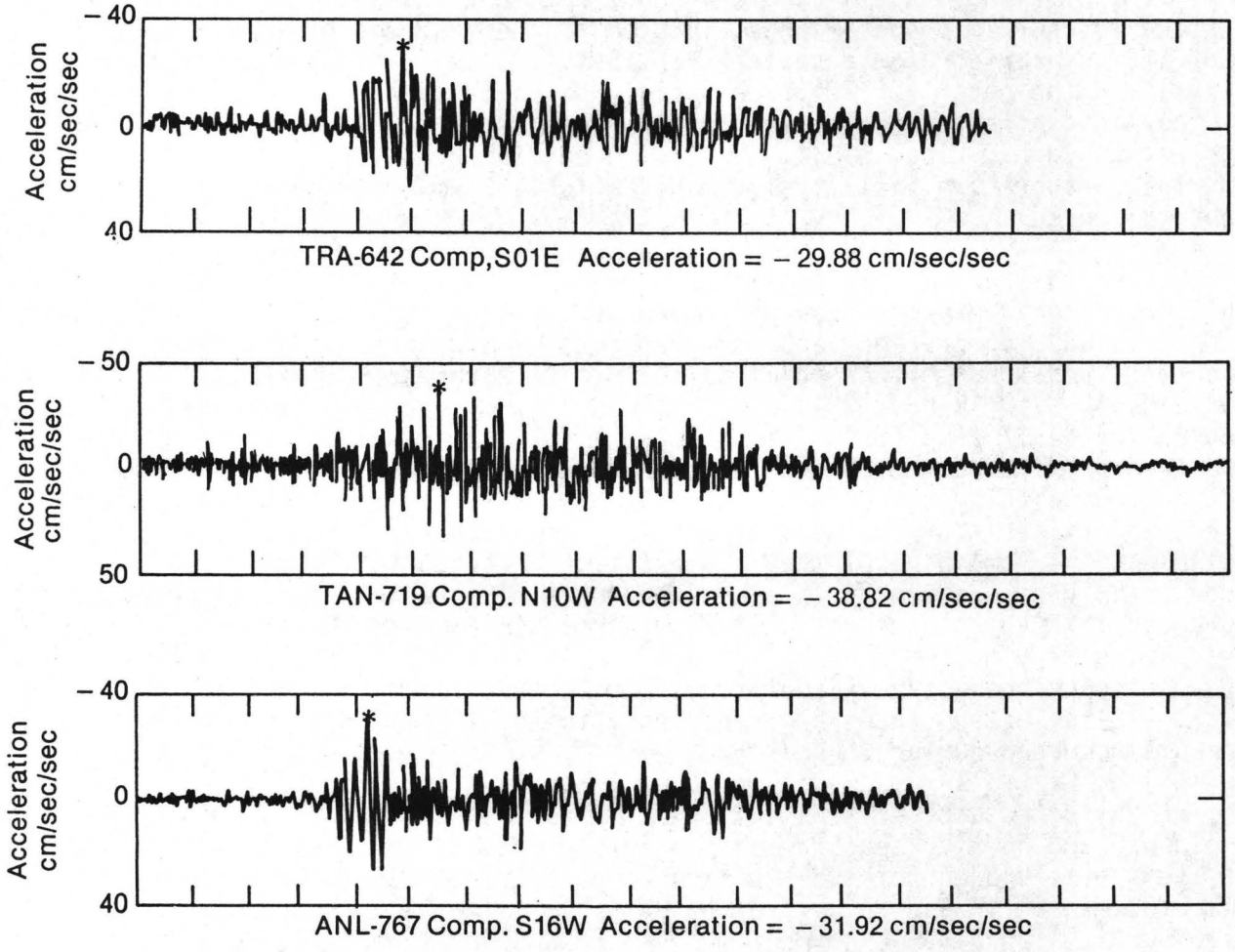

Figure 2. Plot of corrected acceleration (cm/sec/sec) versus time (seconds) for the longitudinal components of TRA-642, TAN-719, and ANL-767. Peak accelerations are listed below each trace. The star (*) designates maximum amplitude.

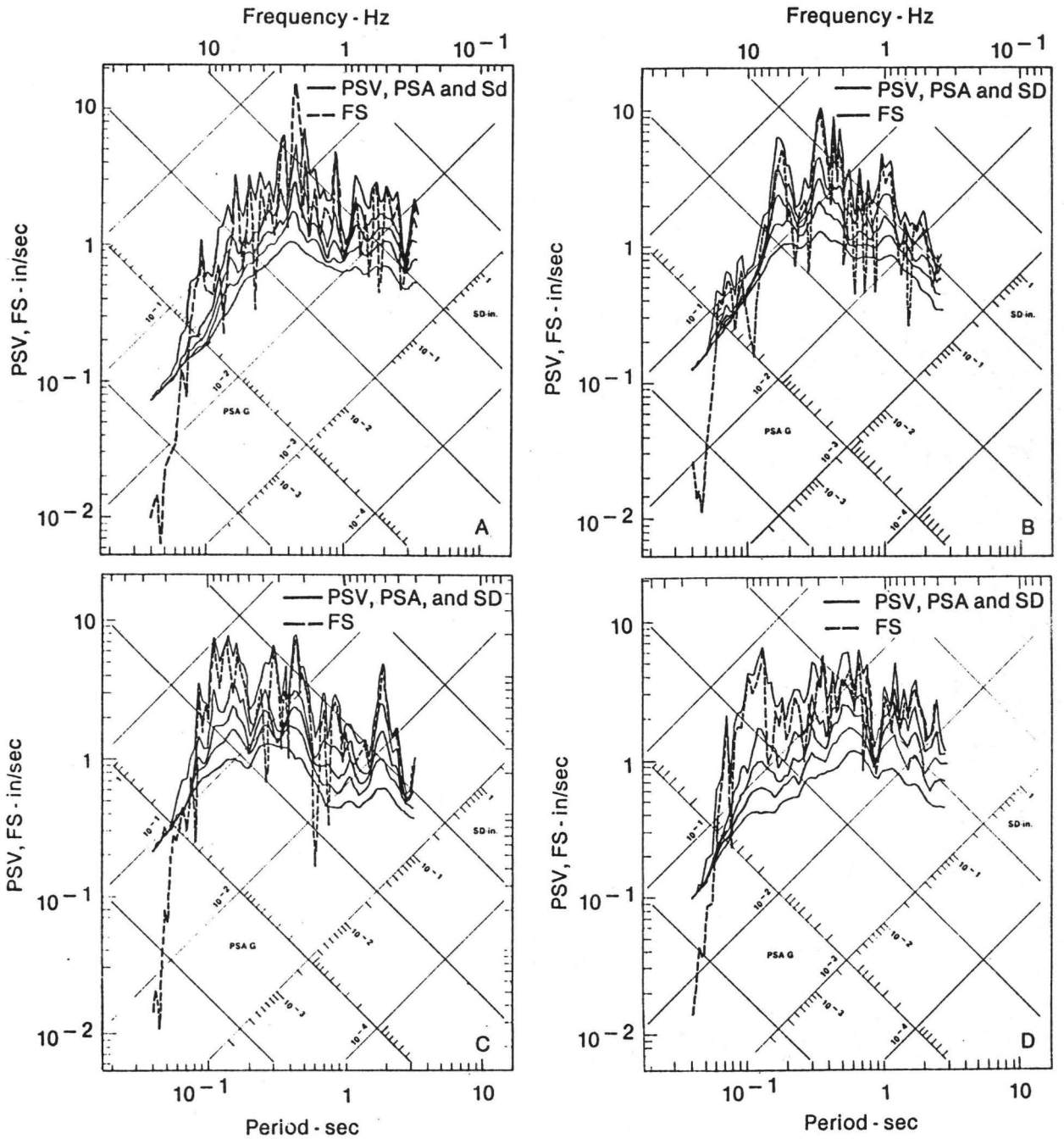

Figure 3. Plot of pseudo-acceleration (PSA), pseudo velocity (PSV), relative displacement (SD) and Fourier spectra (FS) for: 3A) transverse component of TRA-642 (basement); 3B) longitudinal component of PBF-620-2 (basement); 3C) longitudinal component of CPP-610 (free field); and 3D) longitudinal component of TAN-719 (free field). The response and Fourier spectra are plotted for damping values of 0, 2, 5, 10 and 20 percent of critical.

TABLE 2. CORRECTED PEAK ACCELERATION IN TERMS OF "g" FROM THE BORAH PEAK EARTHQUAKE[a]

FACILITY	LONGITUDINAL	VERTICAL	TRANSVERSE	DISTANCE (km)[b]	LOCATION
TRA-670	0.022	0.019	0.023	89	Basement
TRA-642	0.030	0.018	0.029	90	Basement
CPP-601-2	0.038	0.038	0.044	92	2nd Basement
CPP-601-1	0.043	0.033	0.065	92	1st Floor
CPP-610	0.078	0.035	0.058	93	Free Field
TAN-719	0.040	0.016	0.050	94	Free Field
TAN-650-4	0.037	0.021	0.090	94	4th Floor
TAN-650-D	0.097	0.028	0.137	94	Dome Top
PBF-620-2	0.050	0.032	0.051	97	2nd Basement[c]
PBF-620-1	0.057	0.033	0.050	97	1st Basement[c]
PBF-620-C	0.114	0.059	0.187	97	Crane Beam
ANL-767	0.033	0.031	0.032	110	Basement
ANL-768	0.038	0.028	0.048	110	Basement

[a] Processed by Structural and Earthquake Engineering Consultants of Arcadia, CA under direction of Drs. M. D. Trifunac and V. W. Lee.

[b] Distance calculated by short distance method calculation from Richter. Distance measured from epicenter, National Earthquake Information Service location 44.06° N, 113.86° W.

[c] First basement refers to upper basement and second basement refers to lower basement.

acceleration, 0.187 g and vertical acceleration, 0.059 g were recorded at PBF-620-C (crane beam). Another acceleration in excess of 0.1 g (0.137 g) was recorded on the transverse component at TAN-650-D (dome top). The lowest peak horizontal acceleration, 0.022 g, and the lowest peak vertical acceleration, 0.016 g, were recorded at TRA-670 (basement) and TAN-719 (free field), respectively. Higher accelerations were recorded at the free field accelerograph CPP-610 than at the free field accelerograph TAN-719. The largest peak horizontal acceleration for basement accelerographs was recorded at the first basement of PBF-620, PBF-620-1 and the accelerograph in the second basement, PBF-620-2, recorded the largest peak vertical acceleration.

SITE AND BUILDING EFFECTS

The accelerations recorded at the basements and free field sites may have been influenced by the size of the structure that houses the accelerograph and/or the sediment to bedrock thickness, but it appears that this effect is not significant. The variation of accelerations is small for the accelerographs located in basements and at free field sites when considering the distance of the accelerographs from the earthquake epicenter. Figure 4 is a map showing the facilities relative to the epicenter with notation displaying the longitudinal, vertical and transverse components (in that order) of the corrected accelerations for each of the basement and free field accelerographs at the facilities.

The accelerographs are 89-110 km southeast of the epicenter and are in line with the Lost River Range Fault. It is expected that the accelerographs closest to the earthquake would record the largest horizontal accelerations. However, the accelerations recorded at the TRA facilities, which are the closest to the epicenter (90 km), are the lowest (Figure 4). Recall, horizontal accelerations recorded at PBF (97 km from the epicenter) were the largest for basement accelerographs. PBF is a 2-story building founded in basalt with at most 8 feet of sediment thickness to basalt in the area. In comparison, the TRA facilities are 4-story structures supported by columns embedded in basalt with a sediment thickness in the area of 45-74 feet.

According to Boore et al., 1980, smaller accelerations are recorded at large structures. The difference in structure size between TRA and PBF may partially account for the smaller accelerations recorded at the TRA facilities than at PBF. Another example of smaller peak horizontal accelerations recorded at a large structure versus a smaller structure, is a comparison between the peak horizontal accelerations recorded at ANL-768 and ANL-767. ANL-768 is a 4-story structure and its basement accelerograph recorded slightly higher peak horizontal accelerations (Figure 4) than the basement accelerograph at ANL-767, a 6-story structure. However, a comparison between the peak horizontal accelerations recorded at TRA facilities and ANL-768 (all 4-story structures) show the peak horizontal accelerations at ANL-768 higher by 1.5% g. ANL-768 is 21 km further from the earthquake epicenter than the TRA facilities.

Another consideration for the differences in peak horizontal acceleration is the soil-structure interaction (Boore et al., 1980). The sediment to bedrock thickness differs between ANL-768 and the TRA facilities. The sediment to bedrock thickness in the area of ANL-768 is 6-7.5 feet, while

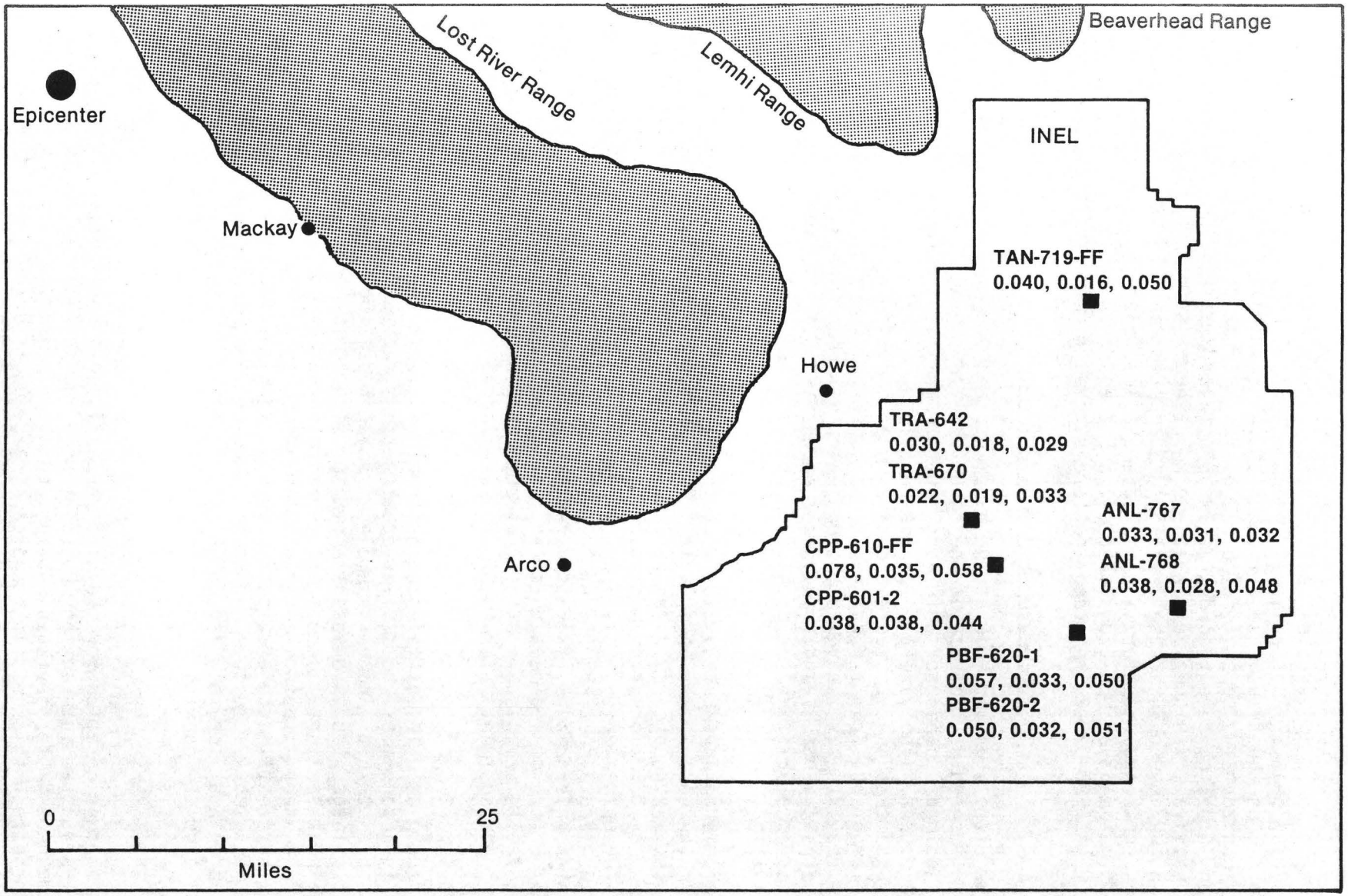

Figure 4. Map of Idaho National Engineering Laboratory facilities relative to the earthquake epicenter. Includes horizontal and vertical accelerations for basement and free field accelerograph locations. The accelerations in "g" are listed as follows: longitudinal, vertical, and transverse.

at the TRA facilities, the sediment to bedrock thickness is 45-75 feet. As mentioned above, the sediment to bedrock thickness of PBF is much less than at the TRA facilities. Hence, the previously noted differences in accelerations measured at these facilities may reflect an influence from the type of structure that houses the accelerograph and/or the thickness of sediments to bedrock. These differences in acceleration, however, are small when compared with the distance between the location of the accelerographs and the earthquake epicenter. There is a variation of peak horizontal accelerations for accelerographs located in basements and at free field sites centered about 5.0% g (2.2% to 7.8% g) with a distance separation of 21 km (89-110 km). This is a small variation in acceleration for a 21 km distance separation at greater than 89 km from the earthquake epicenter which indicates the effect from the size of the structure that houses the accelerographs and/or the thickness of sediments to bedrock are not that significant.

DISCUSSION

The peak horizontal accelerations recorded at the INEL from the Borah Peak earthquake compare well with a map of estimated probabilistic horizontal accelerations and with attenuation curves for predicted horizontal accelerations as a function of distance and moment magnitude. Since the site and building effects are not that significant, the peak horizontal accelerations recorded at both the basements and free field sites were taken into consideration for the comparisons.

The peak horizontal accelerations recorded at the free field accelerographs and accelerographs located in basements are consistent with what is estimated for this area of Idaho when examining a preliminary map of horizontal accelerations in rock with a 90% probability of not being exceeded in 50 years developed by Algermissen et al., 1982. An excerpt of their map, which includes the state of Idaho, is shown in Figure 5. The map shows 4-6% g is estimated for the area of the INEL (shown as a solid circle in Figure 5). The average peak horizontal acceleration recorded at the INEL (mentioned previously) is about 5.0% g. However, one peak horizontal acceleration (7.8% g), recorded on the longitudinal component of the free field site at CPP-610, did exceed 6% which is estimated on the map for the INEL area.

Figure 6 shows attenuation curves for the 50 and 84 percentile developed by Joyner and Boore, 1981. The predicted accelerations are shown for attenuation curves of moment magnitude, 5.5 to 7.5. The attenuation curves were constructed using strong-motion recordings from earthquakes that occurred in the western North American region. The analysis also used strong-motion records with distances of 100 km and greater from the earthquake. Joyner and Boore calculated the moment magnitude using the relation of Hanks and Kanamori (1979),

$$M = 2/3 \log M_0 - 10.7$$

where M_0 is the seismic moment in dyne cm. A moment magnitude of 6.9 was estimated for the Borah Peak earthquake. This estimate was calculated using a geodetic moment of 2.7×10^{26} dyne cm for the seismic moment determined by Barrientos et al., 1985. The moment obtained by Barrientos et al. is in good agreement with the seismic moment, 2.9×10^{26} dyne cm (M = 6.9), determined by Doser, 1985. However, a value of 1.85×10^{26} dyne cm was also obtained by Barrientos et al. from body wave modeling. This results in a moment magnitude of 6.8.

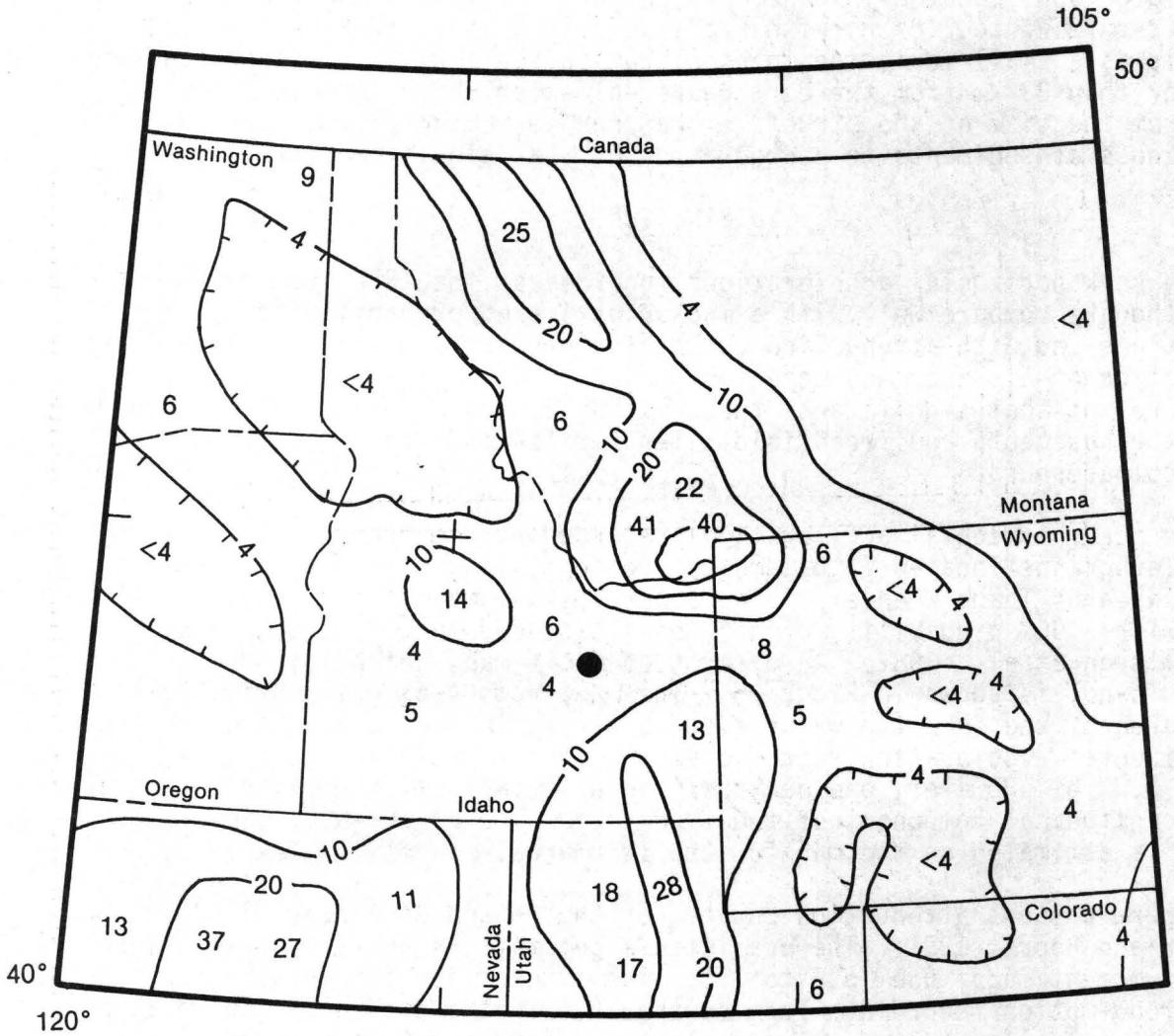

Figure 5. Preliminary map of horizontal accelerations in rock with a 90% probability of not being exceeded in 50 years (Algermissen, et al., 1982). Map shows estimated horizontal accelerations for the state of Idaho and surrounding area. The approximate location of the INEL is shown as a solid circle.

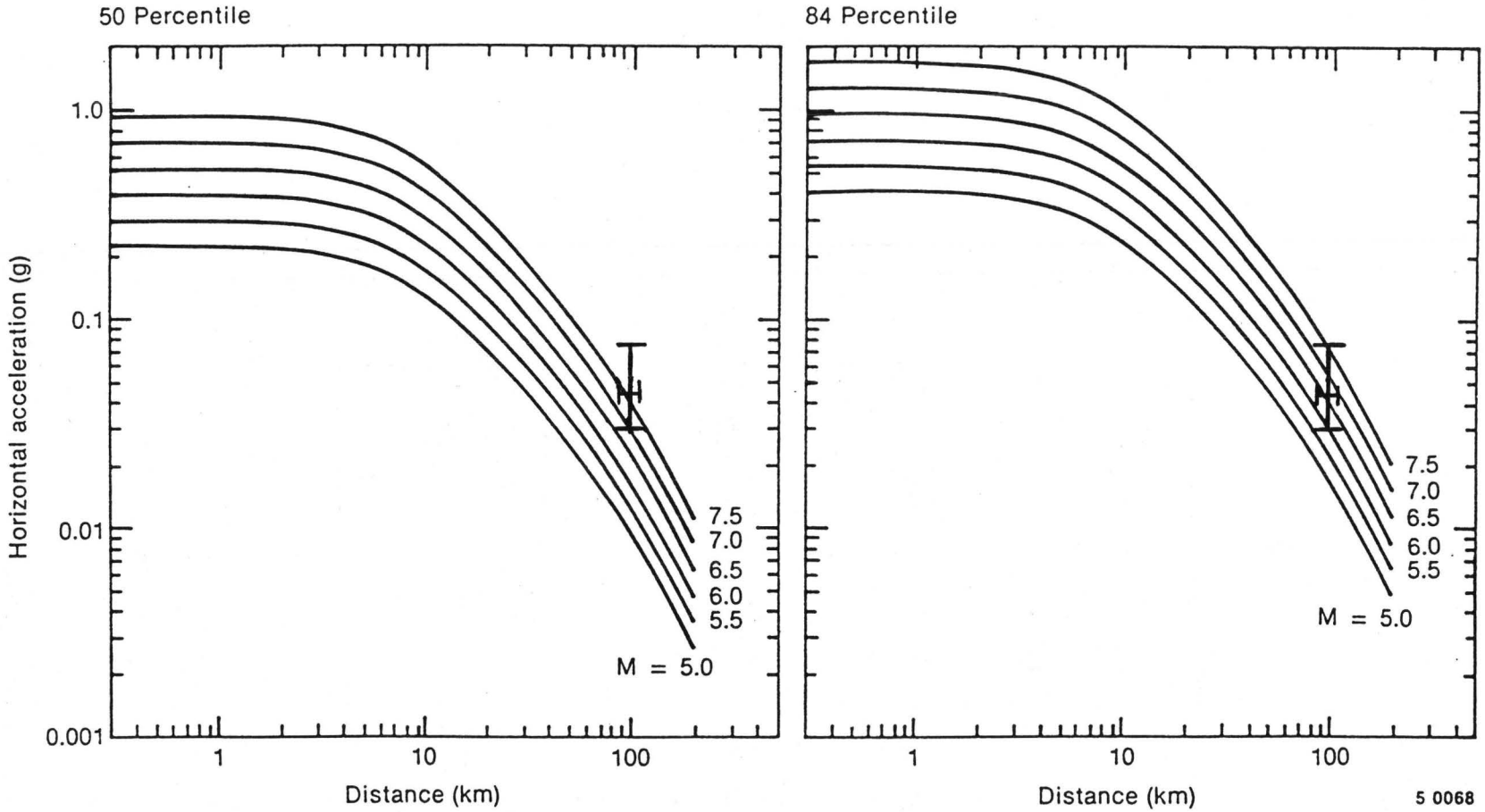

Figure 6. Attenuation curves for predicted horizontal accelerations as a function of distance and moment magnitude for the 50 and 84 percentiles (Joyner and Boore, 1981). The error bar represents the largest of the peak horizontal accelerations recorded at free field accelerographs and accelerographs located in basements.

The largest of the peak horizontal accelerations recorded at the free field accelerographs and accelerographs located in basements are plotted as a function of epicentral distance (shown as the error bar) in Figure 6. Although Joyner and Boore used the distance between the surface projection of fault rupture and the accelerograph location to construct the attenuation curves, the peak horizontal accelerations recorded at the INEL were plotted as a function of epicentral distance. The difference is small between the distance to the accelerographs at the INEL from either the epicenter or point of surface rupture for the Borah Peak earthquake and is not discernible on the graphs in Figure 6.

The error bar of the peak horizontal accelerations is greater than what is predicted for the moment magnitude 7.0 attenuation curve on the graph of the 50 percentile, shown on the left in Figure 6. The attenuation curves for the 50 percentile indicate that there is a 50% probability that the predicted horizontal accelerations will exceed the actual horizontal accelerations (Joyner and Boore, 1981). The horizontal accelerations recorded from the Borah Peak earthquake at a distance of 89-110 km exceed the horizontal accelerations predicted by the attenuation curves for this distance and a moment magnitude of 6.9. However, for the graph featuring the 84 percentile (shown on the right of Figure 6), the error bar of the peak horizontal accelerations extends below and above the predicted accelerations along the moment magnitude 7.0 curve. The attenuations curves for the 84 percentile indicate that there is an 84% probability that the predicted horizontal accelerations will exceed the actual horizontal accelerations. The horizontal accelerations recorded at 89-110 km are similar to what is predicted for this distance and a moment magnitude of 6.9 by the attenuation curves on the graph of the 84 percentile.

From this comparison with the attenuation curves, it can be concluded that the horizontal accelerations recorded at the INEL from the Borah Peak earthquake are consistent with the horizontal accelerations recorded for the earthquakes used in the analysis of these curves. This conclusion, however, does not suggest that these attenuation curves can be used to predict peak horizontal accelerations for future earthquakes in the area of the INEL. It only suggests that the peak horizontal accelerations recorded at the INEL from the Borah Peak earthquake are not anomalous when compared with the horizontal accelerations recorded for the earthquakes used in the analysis of these curves.

SUMMARY

Thirteen strong-motion accelerographs at the INEL recorded ground acceleration during the 1983 Borah Peak, Idaho earthquake. They recorded ground motion for 30-40 seconds. The accelerogram components were processed producing acceleration, velocity and relative displacement time-histories along with response and Fourier spectra. There is a similarity between the envelope of peak amplitudes for the corrected acceleration traces and the response and Fourier spectra have maximum amplitudes in the 2-10 hz frequency range.

The peak horizontal accelerations for accelerographs located in basements and at free field sites range 2.2% g to 7.8% g which results in an average of 5.0% g. The distance of the accelerographs from the earthquake epicenter is 89-110 km. When considering this distance and the small variation in

peak horizontal accelerations, there does not appear to be a significant effect on the peak horizontal accelerations recorded during the Borah Peak earthquake from the size of the structure that houses the accelerographs and/or the thickness of sediment to bedrock.

The peak horizontal accelerations recorded at the INEL are consistent with a map of estimated probabilistic peak horizontal accelerations in the area of the INEL. The map shows 4-6% g is estimated in the area of the INEL and the average of the peak horizontal accelerations is about 5% g. A comparison of peak horizontal accelerations to attenuation curves for predicted accelerations as a function of distance and moment magnitude agree well for the predicted accelerations on the graph of the 84 percentile at a distance of 89-110 km and moment magnitude of 6.9, but are above the predicted accelerations of the 7.0 magnitude attenuation curve for the 50 percentile at this same distance and moment magnitude. It is concluded that the peak horizontal accelerations recorded at the INEL during the Borah Peak earthquake are similar to the peak horizontal accelerations recorded for earthquakes used in the analysis of the attenuation curves.

ACKNOWLEDGEMENTS

The Author thanks John King and Jack Boatwright for their suggestions and helpful comments. Also, thanks to Tiffany Cox for typing of the paper.

REFERENCES

Algermissen, S. T., D. M. Perkins, P. C. Thenhaus, S. L. Hanson, and B. L. Bender, 1982, Probablistic Estimates Maximum Acceleration and Velocity in Rock in the Contiguous United States, U. S. Geological Survey Open File Report 82-1033, p. 99.

Barrientos, S., S. N. Ward, J. R. Gonzaliey-Ruiz and R. S. Stein, 1985, Inversion for moment as a function of depth from geodetic observations and long period body waves of the 1983 Borah Peak, Idaho Earthquake, in Workshop XXVIII on the Borah Peak Earthquake: U.S.G.S. Open File Report, in press.

Boore, D. M., W. B. Joyner, A. A. Oliver, III, and R. A. Page, 1980, Peak Acceleration, Velocity, and Displacement from Strong-Motion Records, Bull. Seism. Soc. Am. 70, 305-321.

Doser, D. I., 1985, The 1983 Borah Peak, Idaho and 1959 Hebgen Lake, Montana Earthquakes: Models for Normal Fault Earthquakes in the Intermountain Seismic Belt, in Workshop XXVIII on the Borah Peak Earthquake: U.S.G.S Open File Report, in press.

Gorman, V. W. and R. C. Guenzler, 1983. The 1983 Borah Peak Earthquake and INEL Structural Performance, EG&G Report #EGG-EA-6501, 56-58.

Joyner, W. B. and D. M. Boore, 1981, Peak Horizontal Acceleration and Velocity from Strong-Motion Records Including Records from the 1979 Imperial Valley, California, Earthquake, Bull. Seism. Soc. Am. 71, 2011-2038.

Richter, C. F., 1958, Elementary Seismology, W. H. Freeman and Company, San Francisco, 701-705.

Isoseismal map and intensity distribution for the Borah Peak, Idaho, earthquake of October 28, 1983

By Carl W. Stover[1]

ABSTRACT

The Borah Peak, Idaho earthquake of October 28, 1983 caused 2 deaths in Challis and injured one person in Mackay. The most severe damage occurred in Mackay and Challis where 11 businesses and 239 homes were damaged. Maximum Modified Mercalli intensity of VII was rated for both Challis and Mackay based on damage due to vibrational effects. This event is comparable to the 1959 Hebgen Lake, Montana earthquake which was assigned an intensity X based on geologic effects and VII - VIII on vibrational effects. The Borah Peak event was felt over 670,000 km^2 of the United States plus a large area of western Canada.

INTRODUCTION

The earthquake of October 28, 1983 in the Borah Peak, Idaho area was felt over a contiguous area of approximately 670,000 km^2 of the United States. It was felt in all or parts of seven western states: Idaho, Montana, Nevada, Oregon, Utah, Washington, and Wyoming. A single felt report from North Dakota was also received. According to press reports, the quake was also felt in many western Canada communities. The hypocenter was located by the U.S. Geological Survey at 44.058° N., 113.857° W., fixed depth of 10 km, origin time 14h06m06.6s UTC. The magnitude was computed at 6.2mb and 7.3MS. It caused the death of two children in Challis and injured one woman in Mackay. The Idaho Bureau of Disaster Services estimated the damage attributed to this earthquake at $12.5 million as of March 1, 1984.

The Borah Peak earthquake, maximum intensity VII, is the largest magnitude event in recorded history to occur within the state of Idaho. The largest magnitude previous to 1983 was the 1944 Seafoam earthquake, magnitude 6.1, located at 44.5° N., 115.5° W. Since many of the earlier earthquakes had no computed magnitudes, relative sizes can be based on the maximum intensities which have been published for most large events. Five earthquakes in Idaho have been documented with a maximum intensity VII and one with an intensity of VIII. The earliest of these was an intensity VII in 1884; the latest was the intensity VIII in 1975. These two earthquakes, in 1884 and 1975, and one in 1962 occurred in southeastern Idaho near the Utah border. The other three intensity VII events occurred in 1905, 1916, and 1944 and were located near Shoshone, Boise, and Seafoam respectively. None of these six quakes are located near the epicenter of the Borah Peak earthquake. The two closest ones are the 1905 Shoshone and 1944 Seafoam events which have published epicenters

that are located at distances of 136 and 138 km. The Borah Peak earthquake is located about 40 to 50 km east of the central Idaho seismic zone in an area that has almost no record of seismic activity.

The Borah Peak earthquake can be compared with the 1959 Hebgen Lake, Montana earthquake. The Hebgen Lake event was rated at a maximum intensity of X based on surface faulting; however, the maximum intensity based on vibrational motion was VII or VIII (Steinbrugge and Cloud, 1962). The Borah Peak earthquake was rated a maximum intensity of VII for vibrational effects (fig. 1). Surface faulting was not used as a basis of rating intensity even though faulting occurred over a distance of 43 km (Crone and Machette, 1984). If faulting had been a criteria for rating intensities the maximum intensity would probably be rated about the same as the Hebgen Lake earthquake. The magnitudes can be compared by averaging the magnitudes for the Hebgen Lake earthquake that were reported in the Bureau Central International de Seismologie, Bulletin Mensuel (BCIS), Strasbourg, France, at distances greater than 30 degrees and assuming they are surface wave (MS) magnitudes. The average for 8 magnitudes at distances of 67° to 125° was 7.5. Thus the Hebgen Lake event had a slightly larger surface wave magnitude of 7.5 compared to 7.3 for Borah Peak.

Isoseismal Map

Figure 1 shows the areal distribution of intensities in the United States for the Borah Peak earthquake. The press reported the quake as also being extensively felt in Canada as far north as Dawson Creek, British Columbia and in multi-story buildings in such widely separated cities as Vancouver, British Columbia; Edmonton, Alberta; and Regina and Saskatoon, Saskatchewan. A final version of the isoseismal map, including the felt data from Canada, will be published in 1985 in a U.S. Geological Survey Bulletin titled Publication "United States Earthquakes, 1983".

The isoseismal map was compiled from data obtained in a questionnaire canvass of postmasters and police departments (within 200 km of the epicenter), supplemented by a damage survey (Reagor and Baldwin, 1984) and by information from numerous press reports. Intensities were rated using the Modified Mercalli Intensity Scale of 1931 (Wood and Neumann, 1931).

The isoseismal defining the limit of perceptibility in figure 1 is drawn to enclose all contiguous localities that felt the earthquake. Two anamolous areas south of Portland, Oregon and Seattle, Washington outline a small region of numerous felt reports. A few isolated felt reports from communities in Nevada, Oregon, and Washington were rated at intensity III but they are not enclosed within an isoseismal and are not shown on the map.

The comparison of the isoseismal maps (figs. 1 and 2) for the Borah Peak and Hebgen Lake earthquakes shows a distinct difference in shape and orientation. This difference may be explained by the extent and direction of the associated faulting. The fault scarps and surface ruptures resulting from the

Borah Peak earthquakes trended in a northwesterly direction from the epicenter for a distance of 34 km (Crone and Machette, 1984), while the Hebgen Lake earthquake caused multiple surface ruptures that extended both to the southeast and northwest from the epicenter for a total distance of about 27 km (measured from fig. 1 by Witkind and others, 1962). The focal mechanisms for these shocks show a strike of N 28° W with a dip of 60° SW for Borah Peak (Crone and Machette, 1984), and a strike of N 80° W with a dip of 54° SW for Hebgen Lake (Ryall, 1962; Dewey and others, 1973). The focal mechanism for the Hebgen Lake earthquake is not consistent with the fault scarps which strike in a northwesterly direction, but it is believed to be associated with a deeper east-west structure in alignment with the 80-kilometer-long aftershock zone (Dewey and others, 1973). The shape of the isoseismal maps seems to correlate with the faulting and the direction of rupture since the major axis of both isoseismal maps are compatable with the strike of their respective focal mechanisms. This correlation would also explain the difference in the size of the felt area within the United States, about 870,000 km^2 for Hebgen Lake versus 670,000 km^2 for Borah Peak, for earthquakes of nearly equal magnitude, 7.5 and 7.3, as the nearly east-west faulting in the Hebgen Lake earthquake would cause shaking over a larger region of the United States.

Damage and Geologic Effects

The most severe damage occurred at Mackay and Challis, Idaho where the Governor's office has listed 11 businesses and 39 homes with major damage and 200 homes with minor to moderate damage. Both Mackay and Challis were rated at intensity VII. Most of the businesses located on Main Street of Mackey were damaged to some degree, eight of them were condemned as irreparable by building inspectors. Damaged buildings were of a masonry type of construction of brick, concrete block, or stone. The type of damage was mostly severe cracking or partial collapse of exterior walls, some cracking of interior walls, and some separation of walls at corners. One person was injured on Main Street by debris from a collapsing wall. About 90 percent of the chimneys in the residential area of Mackay were damaged to some extent; either they collapsed, were twisted, or were so severely cracked they had to be torn down. Large amounts of merchandise were thrown off store shelves and most glass containers were broken. Mackay High School suffered much the same type of damage as the masonry buildings along Main Street.

Challis had less damage to buildings than Mackay; however, two childern were killed when an upper part of the front wall of an old rock-exterior building, built in 1879, collapsed onto them. The Challis High School was the only other building to suffer major damage. Stone facing fell from the top of a wall, a chimney and exterior brick walls were cracked, the stone entrance was separated from the building, and interior walls were cracked. Some chimneys in both the residential and business districts were damaged but not as extensively as in Mackey. Reagor and Baldwin (1984) have published detailed descriptions from other communities in the epicentral area.

The most common damage and effects reported from the communities located within the intensity VI isoseismal (fig. 1) were: Cracked exterior brick or cinderblock walls, cracked foundations, cracked chimneys or bricks fallen from chimneys, many small objects overturned or fell, trees and bushes shaken moderately to strongly, and standing automobile or trucks rocked moderately. No damage was reported at any of the 30 dams located within 250 miles of the epicenter operated by the U.S. Bureau of Reclamation.

The Borah Peak earthquake had a large impact on the physiography of the region because of the amount of surface faulting, numerous landslides and rockfalls, water fountains, and changes in the flow of water from springs. The 34-kilometer-long discontinuous surface faulting had a throw that ranged from 50 cm to 2.7m and ground breakage over a width of as much as 100m (Crone and Machette, 1984). Landslides and rockfalls were common on the steep slopes of the Lost River Mountains. Highways in many areas had to be cleared of boulders that had rolled down the slopes. Some homes in Challis located at the base of large bluffs were damaged by falling boulders (Reagor and Baldwin, 1984).

The quake caused water fountains in at least two locations: Near Chilly Buttes and at the upper end of Mackay Reservoir (Reagor and Baldwin, 1984). The fountains lasted only a short time leaving many holes of various sizes and depths. The flow of water from springs was also affected. A spring near Mackay Reservoir increased its flow by more than 25 percent, another at Ingram Ranch near Challis became temporarily dry but flow returned in 13 days, and two others near Ketchum, Geyser Hot Springs and Easley Hot Springs, began flowing at a higher than normal rate. The flooding of the Clayton Silver Mine with more than 100 feet of water was attributed to this earthquake.

REFERENCES CITED

Crone, A. J., and Machette, M. N., 1984, Surface faulting accompanying the Borah Peak earthquake, central Idaho: Geology, v. 12 ,p. 664-667.

Dewey, J. W., Dillinger, W. H., Taggert, James, and Algermissen, S. T., 1973, A technique for seismic zoning: Analysis of earthquake locations and mechanisms in northern Utah, Wyoming, Idaho, and Montana: in Contributions to Seismic Zoning, National Oceanic and Atmospheric Administration Technical Report ERL 267-ESL 30, p. 29-48.

Eppley, R. A., and Cloud, W. K., 1961, United States earthquakes 1959: U.S. Coast and Geodetic Survey, 115 p.

Reagor, Glen, and Baldwin, F. W., 1984, Intensity survey of the Borah Peak, Idaho, earthquake of October 28, 1983: U.S. Geological Survey Open-File report 84-166, 67 p.

Ryall, Alan, 1962, The Hebgen Lake, Montana, earthquake of August 18, 1959: P waves: Seismological Society of America Bulletin, v. 52, no. 2, p. 235-271.

Steinbrugge, K. V., and Cloud, W. K., 1962, Epicentral intensities and damage in the Hebgen Lake, Montana, earthquake of August 17, 1959: Seismological Society of America Bulletin, v. 52, no. 2, p. 181-234.

Witkind, I. J., Myers, W. B., Hadley, J. B., Hamilton, Warren, and Fraser, G. D., 1962, Geologic features of the earthquake at Hebgen Lake, Montana, August 17, 1959: Seismological Society of America Bulletin, v. 52, no. 2, p. 163-180.

Wood, H. O., and Neumann, Frank, 1931, Modified Mercalli Intensity Scale of 1931: Seismological Society of America Bulletin v. 21, no. 4, p. 277-283.

FIGURE 1.--Isoseismal map for the Borah Peak, Idaho, earthquake of 28 October, 1983 UTC.

FIGURE 2.--Isoseismal map for the Hebgen Lake, Montana, earthquake of 18 August 1959 UTC (Eppley and Cloud, 1959).

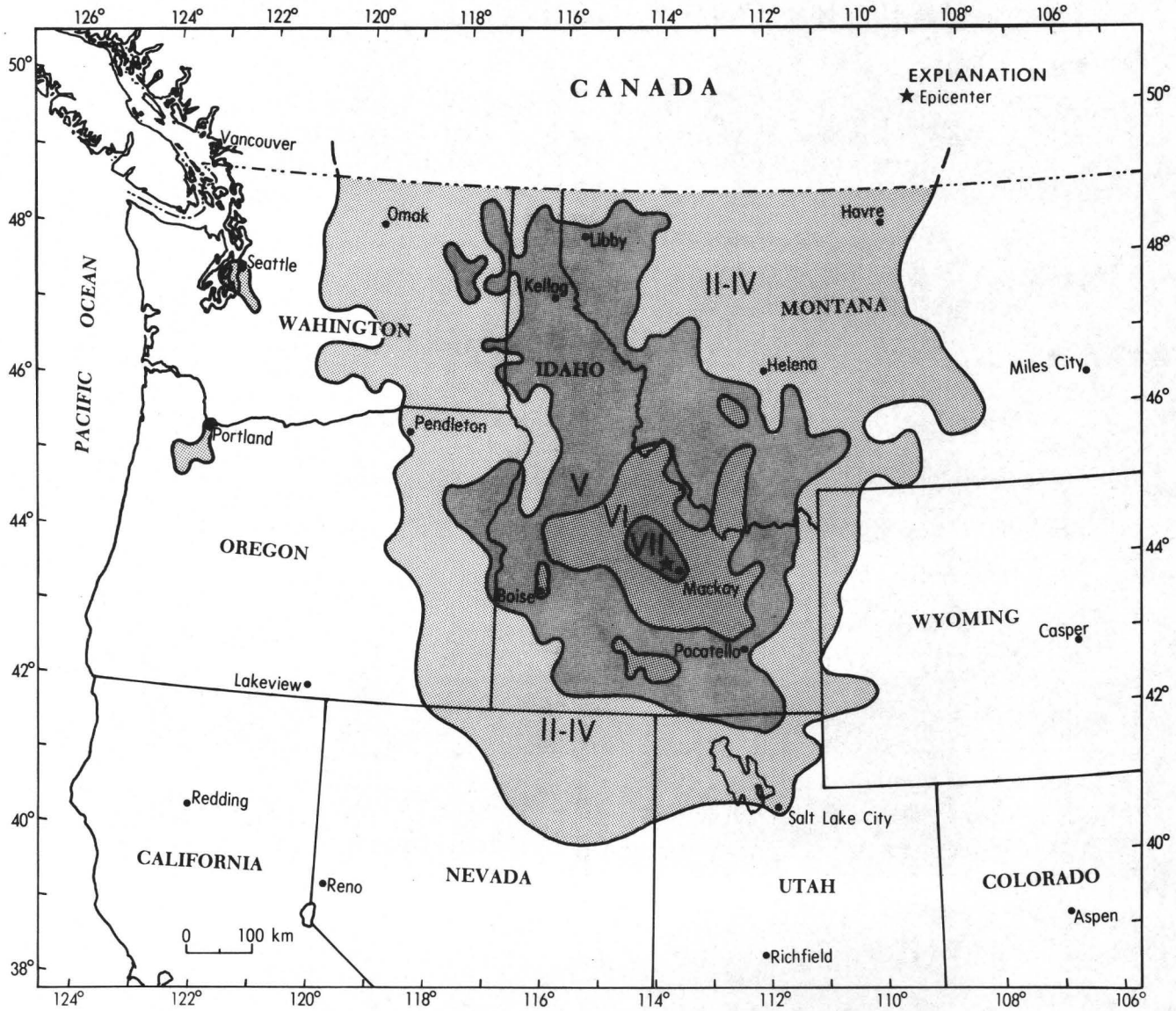
126°
124°
122°
120°
118°
116°
114°
112°
110°
108°
106°
50°
48°
46°
44°
42°
40°
38°
CANADA
EXPLANATION
★ Epicenter
Vancouver
Omak
Libby
Havre
Seattle
Kellog
II-IV
MONTANA
WAHINGTON
IDAHO
Helena
Miles City
PACIFIC OCEAN
Portland
Pendleton
V
VI
VII
OREGON
Boise
Mackay
WYOMING
Casper
Pocatello
Lakeview
II-IV
Redding
Salt Lake City
CALIFORNIA
NEVADA
Reno
UTAH
COLORADO
Aspen
0 100 km
Richfield

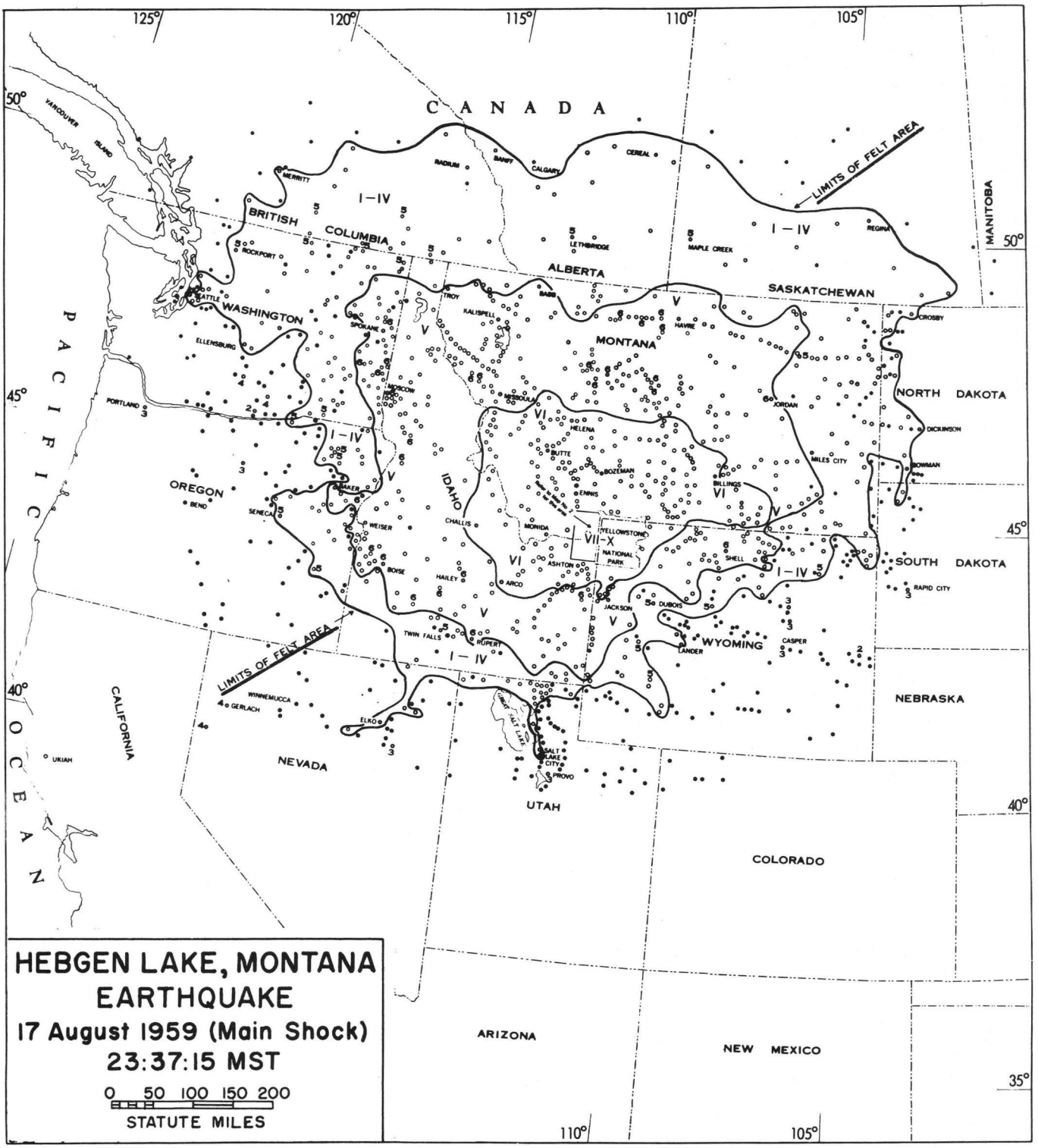
HEBGEN LAKE, MONTANA
EARTHQUAKE
17 August 1959 (Main Shock)
23:37:15 MST
0 50 100 150 200
STATUTE MILES
LIMITS OF FELT AREA
LIMITS OF FELT AREA
I – IV
V
VI
VII–X
CANADA
BRITISH COLUMBIA
ALBERTA
SASKATCHEWAN
MANITOBA
WASHINGTON
OREGON
CALIFORNIA
NEVADA
IDAHO
MONTANA
WYOMING
UTAH
COLORADO
ARIZONA
NEW MEXICO
NORTH DAKOTA
SOUTH DAKOTA
NEBRASKA
PACIFIC OCEAN
YELLOWSTONE NATIONAL PARK
125°
120°
115°
110°
105°
50°
45°
40°
35°

TELESEISMIC ESTIMATES OF THE ENERGY RADIATED BY SHALLOW EARTHQUAKES

John Boatwright
U. S. Geological Survey
345 Middlefield Road, MS/977
Menlo Park, CA 94025
(408) 323-8111, X2485

George L. Choy
Box 25046, MS/967
Denver Federal Center
Denver, CO 80225
(303) 236-1506

ABSTRACT

The energy flux contained in the P-wave groups $(P + pP + sP)$ or the S-wave groups $(S + pS + sS)$ radiated by a shallow earthquake is estimated assuming that the energy flux in the direct and depth phases adds incoherently. By defining generalized radiation patterns which incorporate this neutral interference, the wave groups may be analyzed as though they were comprised of a single phase. Measurements of the energy flux in the wave groups are corrected in the frequency domain for both the body-wave attenuation and the frequency band of the recording. The corrected measurements are then used to estimate the seismic energy radiated by the earthquake.

This analysis is applied to digital recordings of the teleseismic wave groups radiated by the May 2, 1983, Coalinga, California, earthquake and the October 28, 1983, Borah Peak, Idaho, earthquake. For the Coalinga earthquake, an estimate of $E_s = (1.5 \pm .40) \times 10^{21}$ dyne-cm was determined from six P-wave groups, while the SH wave group recorded at station COL returned an estimate of $E_s = 1.39 \times 10^{21}$ dyne-cm. For the Borah Peak earthquake, an estimate of $E_s = (3.07 \pm .44) \times 10^{21}$ dyne-cm was determined from seven P-wave groups. The distribution of the isoseismals for the Borah Peak earthquake suggest that the energy radiated by this event was focussed to the northwest, in the direction of rupture propagation. Correcting the teleseismic estimate for this focussing gives $E_s = (4.20 \pm .60) \times 10^{21}$ dyne-cm. Combining these estimates of the radiated energy with broad-band estimates of the seismic moment yields estimates of the apparent stress of 17 and 8 bars for the Coalinga and the Borah Peak earthquakes, respectively.

INTRODUCTION

In describing the overall size of an earthquake, the seismic moment is more important than the radiated seismic energy. By combining the seismic moment tensor with the hypocentral location and depth, seismologists obtain a concise description of the seismic change of state at the focus of the earthquake. This information is crucial to the tectonic interpretation of earthquakes, and has contributed greatly to our understanding of earthquake mechanics. In describing the potential for earthquake damage to man-made structures, however, the radiated seismic energy is more important than the seismic moment. The radiated seismic energy comprises an estimate of the total wave energy radiated by the earthquake. The energy density is strongly peaked at the corner frequency of the earthquake. For large shallow earthquakes, the energy density is peaked within the frequency band of greatest interest to seismic engineers; *i.e.*, from 0.1 to 10 Hz.

Unfortunately, the observational consideration of the radiated energy has been inhibited by the lack of reliable estimates. Where the seismic moment can be estimated from surface faulting or long-period recordings, broad-band seismic recordings of the earthquake are needed to estimate the radiated energy. Moreover, estimates of the radiated energy require analyzing a range of frequencies above and below the corner frequency, rather than a single frequency below the corner frequency, as required for estimates of the seismic moment.

Since the review by Bath (1967) of the early techniques and estimates of the radiated energy, seismological models of both the seismic source and the propagation of seismic energy have improved significantly. Wu (1968) and Chandra (1972) used double-couple radiation patterns to estimate the energy radiated by a few deep earthquakes from the arrivals recorded on long-period WWSSN instruments. Their estimates were hampered by the lack of high-frequency data and corrections for the attenuation of seismic energy suffered in the teleseismic propagation. Choy and Boatwright (1981), on the other hand, processed digitally recorded GDSN data to obtain broad-band body-wave time histories. By modelling these arrivals using quasi-dynamic sources, they were able to estimate the energy radiated by two deep events. Vassiliou and Kanamori (1982) modelled long-period WWSSN waveforms using triangular source pulses to estimate the energy radiated by deep events in the Tonga-Fiji Benioff zone. In these last two studies, the corrections for the body-wave attenuation were determined by considering the energy lost from the synthetic waveforms. In this paper, the energy loss is estimated directly from the data by correcting the recorded spectra for the frequency-dependent attenuation suffered in propagation.

Most large earthquakes which cause significant damage are shallow. Previous estimates of the energy radiated by shallow events have been made indirectly, usually by multiplying the seismic moment by half the assumed stress drop (Hanks and Kanamori, 1979). To estimate the energy radiated by shallow earthquakes directly, in contrast to deep earthquakes, it is necessary to account for the interference between the direct phase and the depth phases. In this analysis, we propose and test the assumption that this interference is neutral, that is, neither constructive or destructive. Under this assumption, the radiated energy can be estimated without modelling the velocity waveforms radiated by the earthquake. This advantage is considerable; the complexity of rupture is a consistent

feature of large earthquakes. Modelling the velocity waveforms radiated by a complex event is a difficult and time-consuming endeavor (see for example, Choy and Boatwright, 1981, or Archuleta, 1984). For large shallow earthquakes, such velocity modelling is beyond the present seismological capability.

The technique presented in this paper enables seismologists to directly measure the energy density, radiated teleseismically at frequencies at and above the corner frequency of shallow earthquakes. Because many damaging earthquakes are poorly recorded in the near-field, these measurements can be expected to significantly improve the general seismological description of large shallow earthquakes. Moreover, the comparison of the teleseismic measurements to measurements of the (near-field) strong ground motion will also improve the resolution of the rupture dynamics that may be obtained from either of these approaches alone.

THEORY

In the following analysis, a seismic event will be considered shallow if the delay time of the earliest depth phase is shorter than the duration of the velocity waveform of the direct phase. For such an event, the pulse shapes of the direct phase and the depth phases interfere. In general, the effect of this interference cannot be determined without modelling the velocity waveforms.

For a deep event, the energy radiated in the P- and S-waves can be estimated directly from measurements of the energy flux in the body-wave arrivals. Neglecting directivity, Boatwright and Fletcher (1984) derived the simple formulae

$$E_s^P = 4\pi < F^P >^2 \left(\frac{R^P}{F^P}\right)^2 \varepsilon_P^* \tag{1a}$$

$$E_s^S = 4\pi < F^S >^2 \left(\frac{R^S}{F^{Si}}\right)^2 \varepsilon_S^* i \tag{1b}$$

relating the total energy radiated in the body wave (E_s^P or E_s^S) to the energy flux contained in the P- or S-wave arrival. The energy flux of a plane wave is the product of the density, the wave velocity, and the integral of the square of the particle velocity (Bullen, 1965). The $*$ indicates that the measurement of the energy flux has been corrected for the body-wave attenuation due to either anelasticity or scattering. The attenuation correction represents an important problem for teleseismic estimates of the radiated energy; this correction will be discussed in detail in a later section. F^P and F^S are the radiation pattern coefficients, while $R^P \simeq R^S$ are the geometrical spreading factors. The sub/superscripts Si for the S-waves indicate that the energy flux measurement and the radiation pattern correction are specific to a single component of motion. $< F^P >^2 = 4/15$ and $< F^S >^2 = 2/5$ are the mean square radiation pattern coefficients (Aki and Richards, 1980).

Because the phases radiated by a shallow earthquake interfere, it is not possible to measure the energy flux in a single phase exactly. The teleseismic waveforms from shallow

events are usually modelled as a group of phases. For simplicity, we will use the notation gP, gSH, and gSV to describe the wave groups $P+pP+sP$, $SH+sSH$, and $SV+sSV+pS$, respectively. The relationship between the energy flux of the wave group and the energy flux of the phases in the wave group is conditioned by the interference of the phases. It is necessary to fix this relationship, however, to use the energy flux of the wave group to estimate the radiated energy.

In this analysis, we made the simplest assumption possible: that the energy flux of the wave group is equal to the sum of the energy flux of the phases comprising the wave group. This assumption is equivalent to assuming that the interference between the phases in the wave group is neither constructive or destructive. For the gP wave group, this assumption gives,

$$\varepsilon_{gP} = \varepsilon_P + \varepsilon_{pP} + \varepsilon_{sP} \quad , \tag{2a}$$

or, assuming that each phase suffers the same attenuation,

$$\varepsilon^*_{gP} = \varepsilon^*_P + \varepsilon^*_p P + \varepsilon^*_{sP} \quad . \tag{2b}$$

The extension of this assumption to the gSH and gSV wave groups is obvious.

Because this assumption is critical to the analysis, it is important to discuss it in further detail. The terms which equation (2) neglects are proportional to the cross-correlations of the phases of the wave groups, evaluated at lags equal to the delay between the two phases. Equation (2) is obviously appropriate for the limiting case of a deep event where the phases do not overlap in time; the cross-correlations are zero at these lags. As the average source depth decreases, the phases in the wave group begin to overlap. Equation (2) assumes that the effect of this overlap is small, that is, that the delay time is larger than the correlation time of the velocity waveforms. The correlation times of the velocity waveforms radiated in different directions will decrease as the complexity and directivity of the rupture process increase. The APPENDIX tests this approximation using synthetic waveforms from finite source models for three characteristic faulting geometries.

Exploiting equation (2) to obtain an estimate of the radiated energy from the energy flux in a wave group requires an estimate of the partition of energy between the P- and S-waves and some manipulations of equation (1). Inverting equation (1a) gives the energy flux in the direct wave as a function of the radiated energy:

$$\varepsilon^*_P = \frac{E^P_s}{4\pi < F^P >^2} \left(\frac{F^P}{R^P} \right)^2 \quad . \tag{3}$$

Similarly, the energy flux in the reflected pP phase is

$$\varepsilon^*_{pP} = \frac{E^P_s}{4\pi < F^P >^2} \left(\frac{\acute{P}\grave{P} F^{pP}}{R^P} \right)^2 \quad , \tag{4}$$

where $\acute{P}\grave{P}$ is the plane-wave reflection coefficient for the pP reflection at the free surface (Aki and Richards, 1980, p. 141). The analogous relation for the energy flux in the sP phase is somewhat more complicated because the wave arrives at the receiver as a P-wave rather than as an S-wave. Correcting the energy flux for the wave velocity at the receiver gives,

$$\left(\frac{\beta}{\alpha}\right) \varepsilon^*_{sP} = \frac{E^S_s}{4\pi < F^S >^2} \left(\frac{\acute{S}\grave{P}F^{sP}}{R^P}\right)^2 \quad . \tag{5}$$

$\acute{S}\grave{P}$ is the reflection coefficient for the sP reflection at the free surface; that is, the plane-wave reflection coefficient (Aki and Richards, 1980, p. 141) multiplied by a correction for the sphericity of the wavefronts near the source (Bache, written communication, 1975). The energy flux in the sP phase is a function of the S-wave energy and the mean square S-wave radiation pattern coefficient. Substituting the relations, $E^S_s = qE^P_s$, where q is the ratio of the S-wave energy to the P-wave energy, and $< F^S >^2 = 1.5 \ < F^P >^2$, gives

$$\varepsilon^*_{sP} = \frac{\frac{2\alpha}{3\beta} qE^P_s}{4\pi < F^P >^2} \left(\frac{\acute{S}\grave{P}F^{sP}}{R^P}\right)^2 \quad . \tag{6}$$

It is useful to compare the energy flux in the sP phase to the energy flux in the P phase. To make this comparison, we normalize the P and sP energy flux in equations (3) and (6) by their displacement pulse areas, which are proportional to $A^P = F^P$ and $A^{sP} = (\frac{\alpha}{\beta})^3 \acute{S}\grave{P}F^{sP}$, and divide equation (6) by equation (3):

$$\frac{\varepsilon^*_{sP}}{\varepsilon^*_P} = \frac{2}{3} \left(\frac{\beta}{\alpha}\right)^5 q \left(\frac{A^{sP}}{A^P}\right)^2 \quad . \tag{7}$$

Substituting equation (11) of Boatwright and Fletcher (1984),

$$\frac{< \psi_\beta >}{< \psi_\alpha >} = \frac{2}{3} \left(\frac{\beta}{\alpha}\right)^5 q \quad ,$$

where $< \psi_\alpha >$ and $< \psi_\beta >$ are the rms pulse energies of the P- and S-waves, respectively, reduces equation (7) to

$$\frac{\varepsilon^*_{sP}}{\varepsilon^*_P} = \frac{< \psi_\beta >}{< \psi_\alpha >} \left(\frac{A^{sP}}{A^P}\right)^2 \quad , \tag{8}$$

and confirms that equations (5) and (6) are consistent.

The results of Boatwright and Fletcher (1984) for the partition of energy between the S-waves and P-waves suggest that q may be as large as 25, although $12 < q < 16$ appears to be a more reasonable estimate. In a recent analysis of 26 digitally recorded aftershocks of the Borah Peak earthquake, Boatwright (1985) estimated $q = 14.7 \pm 2.2$. In this analysis, we will use the value $q = 13.5 \simeq \frac{3}{2} (\frac{\alpha}{\beta})^4$.

By combining equations (2), (3), (4) and (6), the P-wave energy can be written as a function of the energy flux in the gP wave group. Writing this relation as an analog to equation (1) gives

$$E_s^P = 4\pi < F^P >^2 \left(\frac{R^P}{F^{gP}}\right)^2 \varepsilon_{gP}^* \quad , \tag{9}$$

where

$$(F^{gP})^2 = (F^P)^2 + (\acute{P}\grave{P}F^{pP})^2 + \frac{2\alpha}{3\beta} q(\acute{S}\grave{P}F^{sP})^2 \tag{10}$$

is the "equivalent" radiation pattern coefficient for the gP wave group.

Examples of these equivalent radiation patterns are plotted in Figure 1 for the two characteristic faulting geometries: a high or low angle dip-slip fault and a vertical strike-slip fault. The takeoff angles for the rays range from 18° to 25° from the vertical. This range approximates the teleseismic "window"; that is, the cone of takeoff angles for which the teleseismic arrivals are not complicated by triplications or diffractions. The radiation patterns are plotted as functions of azimuth from the strike of the fault. Figure 1a indicates that F^{gP} is a weak function of azimuth and takeoff angle for dip-slip faults. The corresponding estimate of the radiated P-wave energy is relatively insensitive to variations in the focal mechanism of a dip-slip event. In contrast, however, Figure 1b shows that F^{gP} is a marked function of azimuth for strike-slip faults. The corresponding estimate of the radiated P-wave energy is sensitive to variations in the focal mechanisms of strike-slip earthquakes.

The manipulations of equations (3) through (7) can be readily applied to the analysis of the gSH and gSV wave groups. The result for the gSH wave group is particularly straightforward:

$$E_s^S = 4\pi < F^S >^2 \left(\frac{R^S}{F^{gSH}}\right)^2 \varepsilon_{gSH}^* \quad , \tag{11}$$

where

$$(F^{gSH})^2 = (F^{SH})^2 + (F^{sSH})^2 \quad . \tag{12}$$

The simplicity of equation (12) is the result of the identity $\acute{S}\grave{S} \equiv 1$ for the SH component of the sS reflection at the free surface.

For the gSV wave group, the energy flux in the pS phase can be calculated similarly to the energy flux in the sP phase. Writing the results in the same form as equations (9) and (10) gives

$$E_s^S = 4\pi < F^S >^2 \left(\frac{R^S}{F^{gSV}}\right)^2 \varepsilon_{gSV}^* \quad , \tag{13}$$

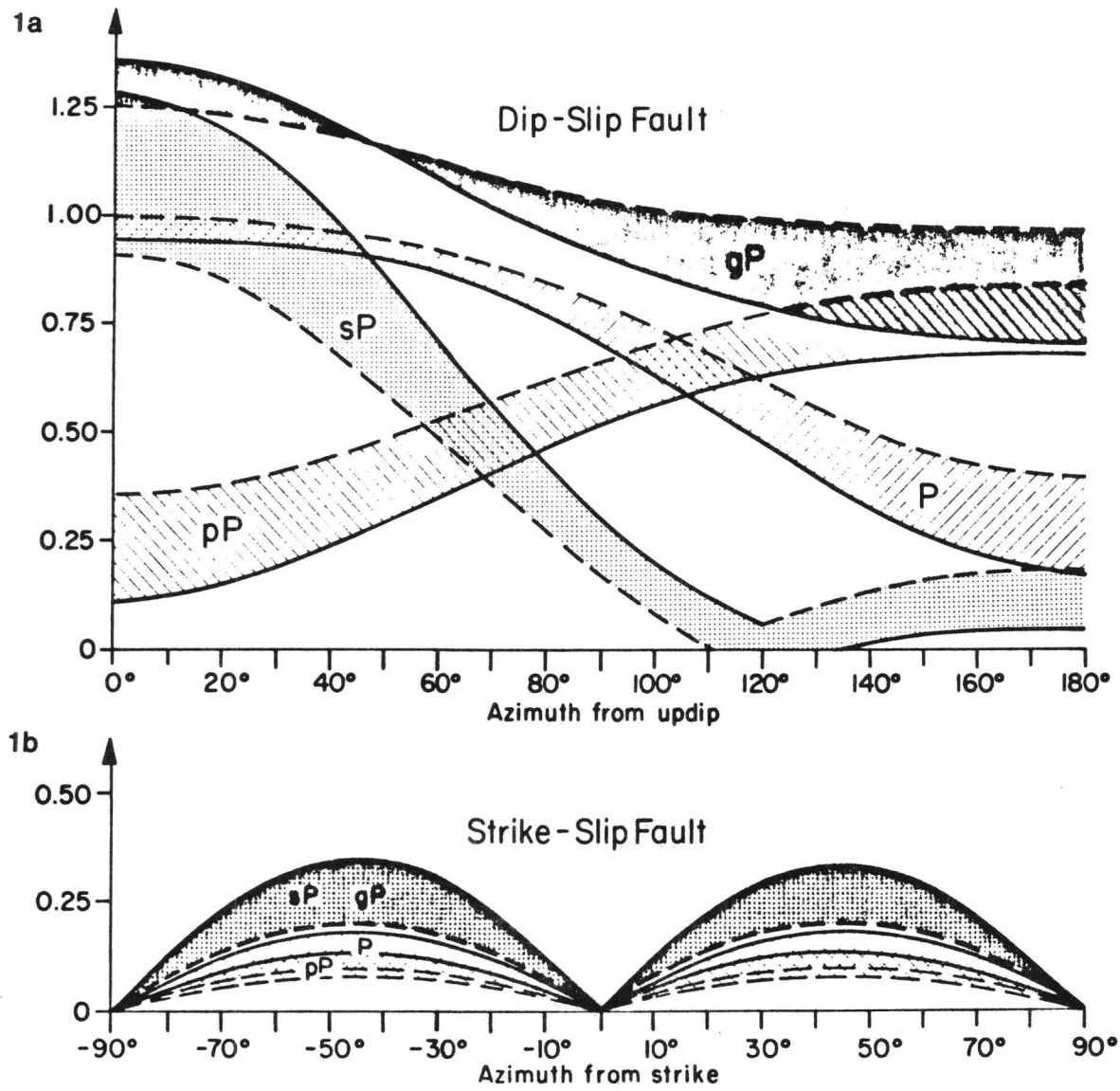

Figure 1a. Radiation patterns appropriate for a dip-slip fault: either a thrust fault dipping at 30° or a normal fault dipping at 60°. The shaded regions show the range of the radiation pattern coefficients for each phase, for takeoff angles between 17° and 28° (the teleseismic window). 1b. The radiation patterns for a vertical strike-slip fault. Note the factor of four decrease in overall amplitude for the strike-slip case.

where

$$\left(F^{gSV}\right)^2=\left(F^{SV}\right)^2+\left(\acute{S}\grave{S}F^{sSV}\right)^2+\frac{3\beta}{2\alpha q}\left(\acute{P}\grave{S}F^{pSV}\right)^2 \quad . \tag{14}$$

$\acute{S}\grave{S}$ and $\acute{P}\grave{S}$ are the reflection coefficients for the SV components of the sS and pS reflections at the free surface, respectively. The $\acute{P}\grave{S}$ reflection coefficient incorporates a correction for the sphericity of the wavefronts which is the inverse of the correction for the $\acute{S}\grave{P}$ reflection coefficient (Bache, written communication, 1975). The q^{-1} dependence, however, makes the contribution of the pS phase to the energy flux in the gSV wave group relatively small.

Estimates of the seismic energy determined from the energy radiated in either the P-waves or the S-waves alone require the formulae,

$$E_s=\left(1+q\right)E_s^P=\left(1+\frac{1}{q}\right)E_s^S \quad . \tag{15}$$

Estimates made from the gP wave groups depend linearly on the assumed value of q, in contrast to estimates made from the gSH or gSV wave groups. Because of the nature of body-wave attenuation in the earth, however, where S-waves suffer substantially more attenuation than P-waves, it is easier to use the gP wave groups to estimate the radiated seismic energy for dip-slip events.

THE COALINGA, CALIFORNIA, AND BORAH PEAK, IDAHO, EARTHQUAKES

We will use the analysis described in the last section to calculate the seismic energy radiated by the May 2, 1983, Coalinga, California, earthquake and the October 28, 1983, Borah Peak, Idaho, earthquake. Both these events have focal mechanisms which are predominantly dip-slip. Because of the difficulty of accurately preserving information at high frequencies using analog data, we use data that are digitally recorded by the Global Digital Seismograph Network (GDSN). Using the method of Harvey and Choy (1982), we obtain broad-band (.02–5 Hz) velocity waveforms by appropriately combining the deconvolved long- and short-period channels. For the Coalinga earthquake, we use six gP waveforms and one gSH waveform; the deconvolved broad-band velocity waveforms of the wave groups are plotted in Figure 2. The focal mechanism determined by Choy (1984) for the initial large sub-event of the rupture process is plotted in Figure 3a, along with the takeoff angles of the direct phases in the recorded wave groups. Choy (1984) estimated the hypocentral depth of the Coalinga event to be 9.5 km. Stein (1983) has interpreted the steeply-dipping nodal plane as the fault plane. In Figure 3b, the takeoff angles of the phases are plotted with respect to this fault plane. Including the depth phases substantially increases the sampling of the focal sphere.

The deconvolved broad-band velocity waveforms of the wave groups radiated by the Borah Peak earthquake are shown in Figure 4. For this earthquake, we used seven gP

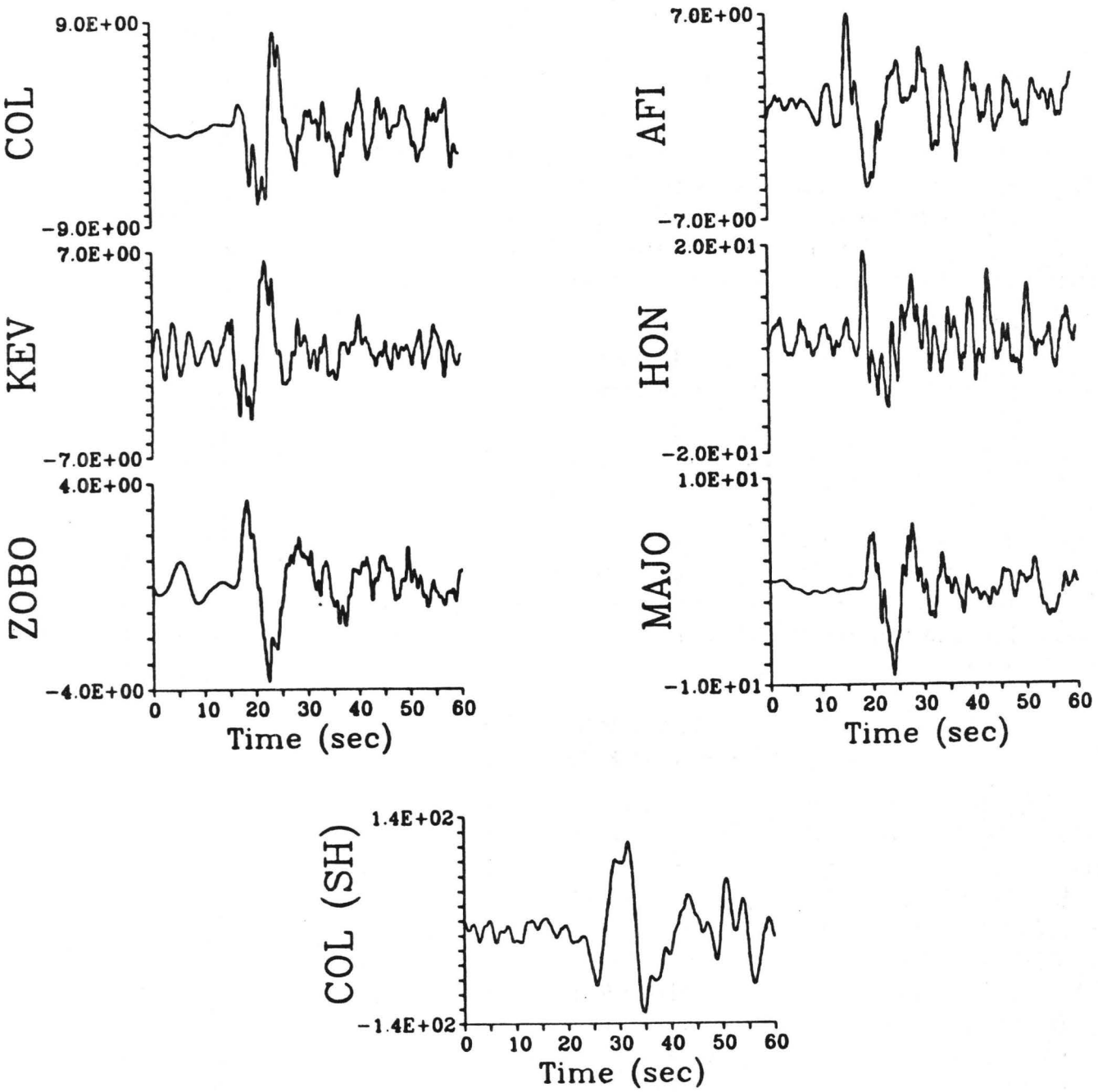

Figure 2. Deconvolved broad-band seismograms (ground velocity) from the Coalinga earthquake. The upper six traces are the *gP* arrivals recorded on the vertical component while the lowermost trace is the *gSH* arrival recorded on the tangential horizontal component at COL.

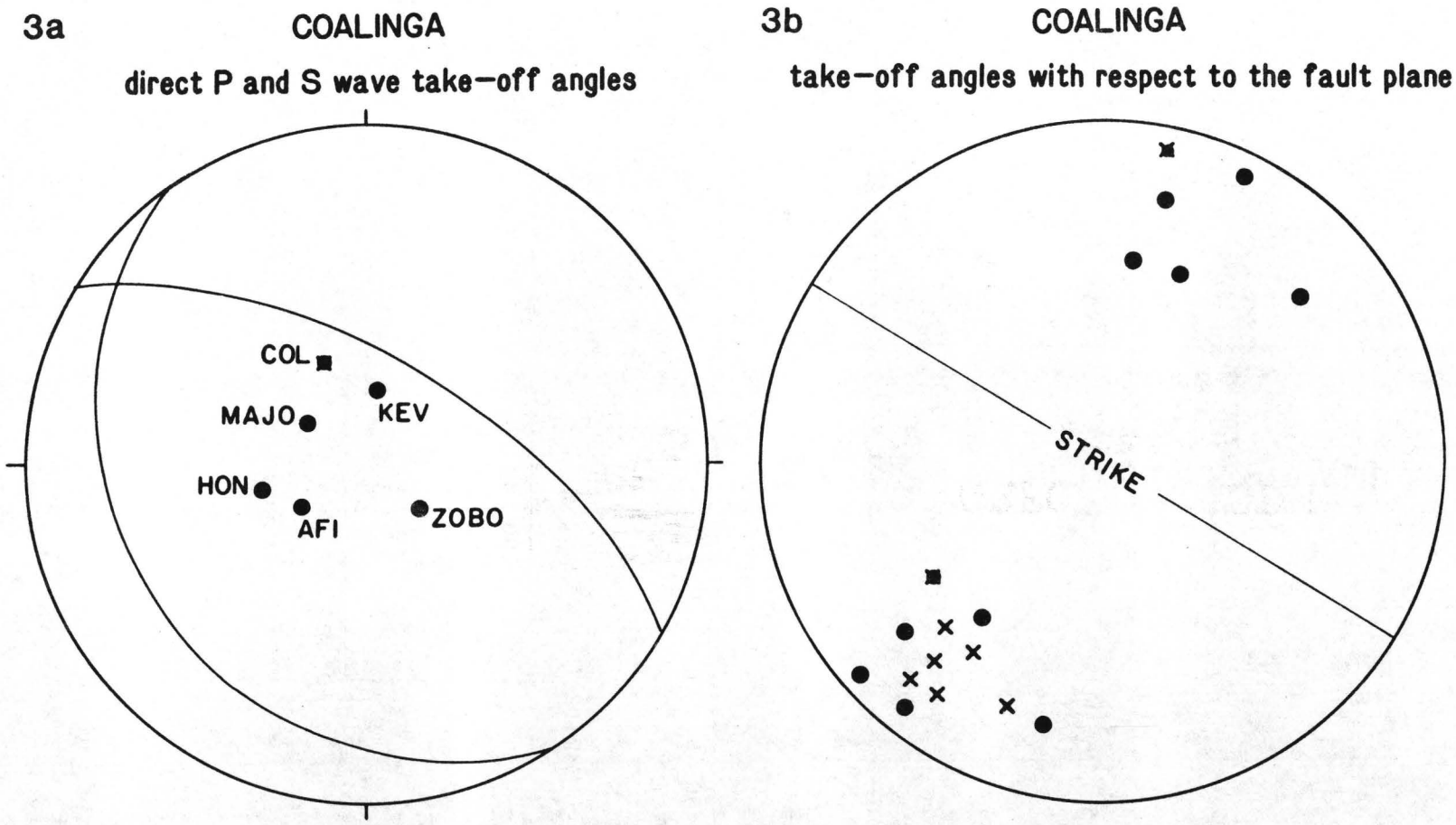

Figure 3a. Takeoff angles for the seven wave groups radiated by the Coalinga earthquake; the P-waves are plotted as solid circles while the S-waves are plotted as crosses. The P-wave nodal planes determined by Choy (1984) are also drawn. Stein (1983) has identified the nodal plane which dips steeply to the northeast as the fault plane. 3b. Takeoff angles for the phases comprising the wave groups, plotted relative to the fault plane. The direct phases (P and S) take off in the down-dip direction, while the depth phases (pP, sP, and sS) take off in the up-dip direction.

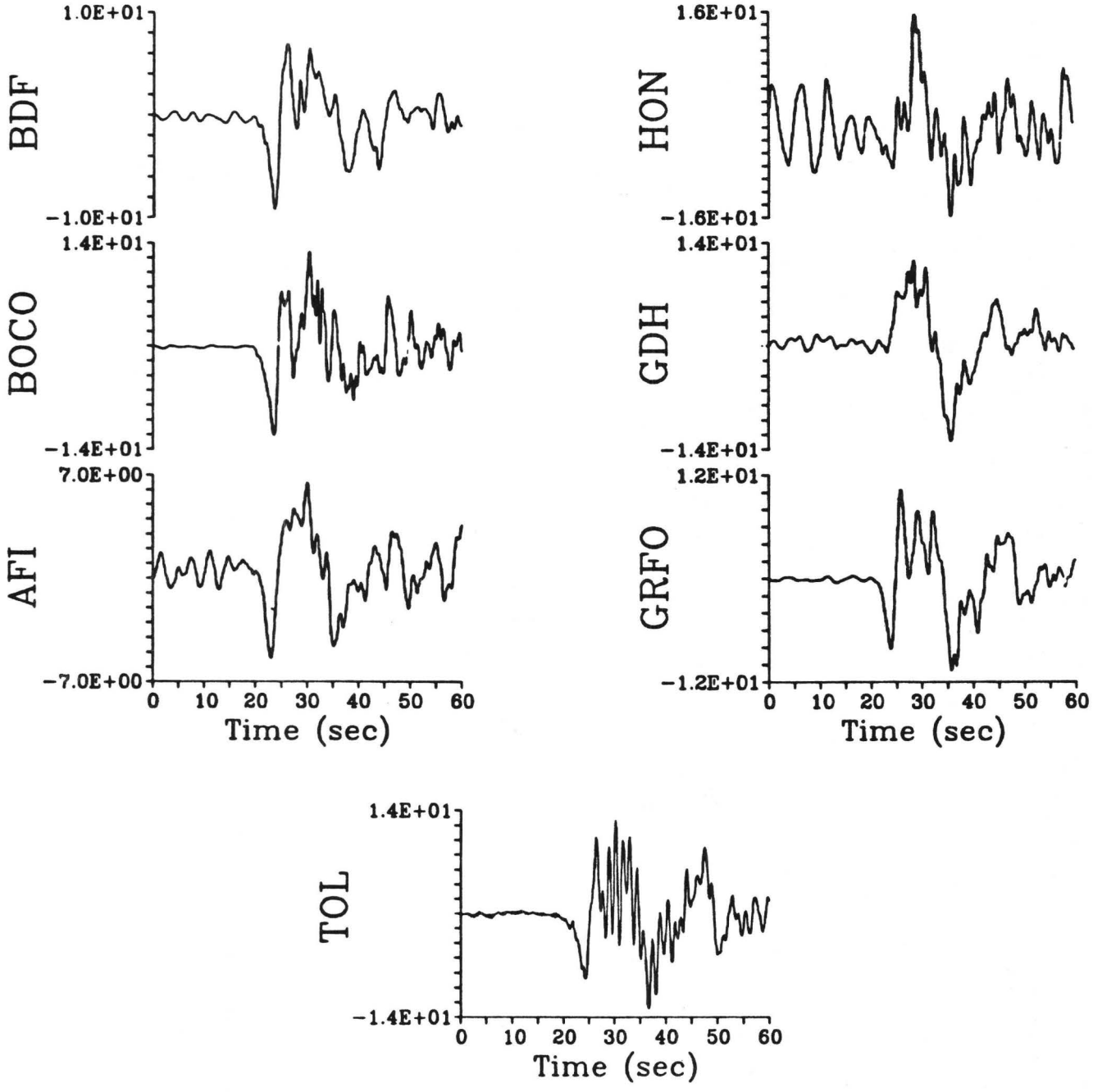

Figure 4. Deconvolved broadband seismograms (ground velocity) from the Borah Peak earthquake. Note the strong excitation of 1 Hz motion at TOL.

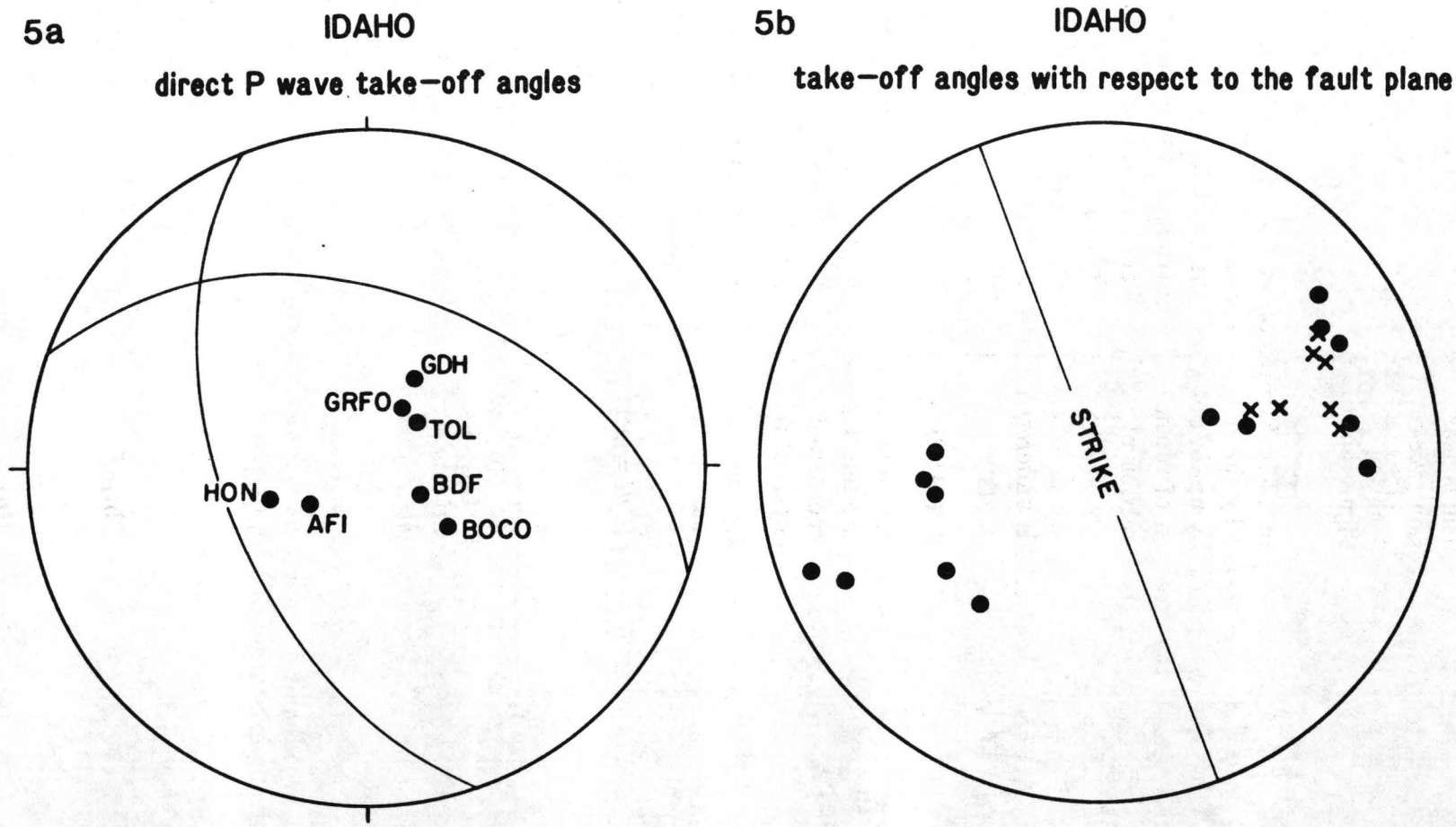

Figure 5a. Takeoff angles for the seven *gP* wave groups radiated by the Borah Peak earthquake. The P-wave nodal planes determined by Boatwright (1984b) are also drawn. The nodal plane which dips to the southwest can be identified as the fault plane, from the surface faulting. 3b. Takeoff angles for the phases comprising the wave groups, plotted relative to the fault plane.

waveforms. The composite mechanism determined by Boatwright (1985) for aftershocks in the epicentral area of the mainshock is shown in Figure 5a, along with the takeoff angles of the phases in the wave groups. This mechanism is nearly identical to the preliminary NEIS mechanism (Needham, written communication, 1984). The extended surface rupture on the east flank of Borah Peak with the west side down dropped indicates that the west-dipping nodal plane is the fault plane. In Figure 5b, the takeoff angles of the phases are plotted with respect to this fault plane.

The distributions of take-off angles plotted in Figures 3b and 5b demonstrate that the sampling of the focal sphere represented by the teleseismic window is relatively weak. For earthquakes which rupture predominately up- or down-dip, the depth or direct phases, respectively, adequately sample the direction of rupture. For earthquakes which rupture predominately along strike, however, the direction of rupture is poorly sampled. Because unilateral ruptures focus the radiated energy in the direction of rupture, the radiated energy determined from the teleseismic phases alone will underestimate the actual energy radiated by these events. The extent of this underestimate will increase with increasing directivity or average rupture velocity.

MEASUREMENT OF THE ENERGY FLUX

As discussed by Snoke *et al.* (1983) and Boatwright and Fletcher (1984) for near-field data, the noise characteristics and the attenuation correction are the most important factors affecting the measurement of the "corrected" energy flux. In this section, we consider how these factors condition the analysis of teleseismic data.

The energy flux in a plane wave is readily calculated from the product of the density, the wave velocity, and the integral of the square of the ground velocity,

$$\varepsilon_c = \rho c \int_0^\infty \dot{u}_c^2(t) dt = \rho c I_c \quad , \tag{16}$$

where the integration extends over the duration of the body-wave arrival. To correct this measurement for the attenuation suffered in the teleseismic propagation, Parseval's theorem should be used to replace the integral in equation (16) by an integral over angular frequency. The correction for the attenuation is determined using the function $t_c^*(\omega) = Q_c(\omega)/T_c$ in the integral over angular frequency:

$$\varepsilon_c^* = \frac{\rho c}{\pi} \int_0^\infty |\dot{u}_c(\omega)|^2 e^{\omega t_c^*(\omega)} d\omega = \rho c I_c^* \quad . \tag{17}$$

For this analysis, we will use the description of $t_c^*(\omega)$ determined by Der *et al.* (1981, 1982, unpublished observations). Their results are plotted in Figure 6, along with the approximation,

$$t_\alpha^*(\omega) = \begin{cases} .8 - .3 ln_{10} f & f < 1 \text{ Hz} \\ \\ .8 - .7 ln_{10} f & f > 1 \text{ Hz} \end{cases} \tag{18}$$

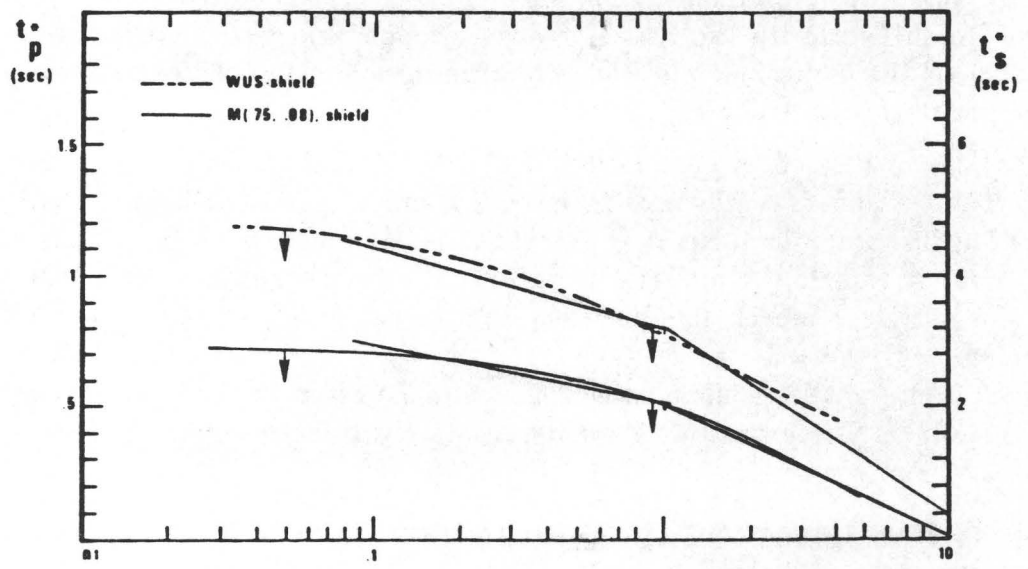

Figure 6. Attenuation as a function of frequency for teleseismic body waves, reprinted from Der *et al.* (1981, 1982). The dashed line is appropriate for the Western U.S.–Shield paths of the phases analyzed. The solid line made up of two straight line segments given by equation (18), is used to correct for the frequency-dependent attenuation.

used to correct the energy flux measurements for the attenuation suffered on the Western U.S.–Shield paths.

In transforming from equation (16) to equation (17), the square of the time history of the ground velocity is replaced by the power spectrum of the ground velocity. The range of integration in equation (17) extends to infinite frequency. Unfortunately, the power spectrum of the ground velocity can be reliably determined only for a restricted frequency band. Figure 7 shows a comparison of the recorded signal-to-noise as a function of frequency for three of the gP waveforms radiated by the Borah Peak earthquake and the gSH waveform radiated by the Coalinga earthquake. The noise samples are taken from the data shown in Figures 2 and 4 using 30-sec windows just before the body-wave arrivals. The gP spectra at stations BOCO and BDH are typical of stations with low noise; the signal falls to the noise level at 2–3 Hz. In contrast, the gP spectrum at HON and the gSH spectrum at COL fall to the noise level at .5 Hz. The numerical integration of the power spectrum of the ground velocity, corrected for attenuation following equations (17) and (18), must be truncated at a cutoff frequency lower than the frequency at which the signal falls to the noise level. We will write the result of the numerical integration as $N[I_c^*(\omega_c)]$.

To approximate the remainder of the integral in equation (17), it is necessary to compensate for the finite range of the numerical integration. The simplest approach is to estimate a "residual integral" for the corrected velocity power spectrum. If the cutoff frequency is greater than the corner frequency, the corrected velocity power spectrum can be approximated by the curve

$$|\dot{u}_c'(\omega)|^2 = |\dot{u}_c'(\omega_c)|^2 \left(\frac{\omega_c}{\omega}\right)^{2(\gamma-1)} \quad , \quad \omega > \omega_c \quad . \tag{19}$$

where ω_c is the cutoff frequency and γ is the falloff of the displacement spectrum above the corner frequency.

The residual integral can be determined by integrating equation (17) from ω_c to infinity using equation (19) as the integrand:

$$R\,[I_c^*(\omega)] = \frac{|\dot{u}_c'(\omega_c)|^2}{\pi} \int_{\omega_c}^{\infty} \left(\frac{\omega_c}{\omega}\right)^{2(\gamma-1)} d\omega = \frac{\omega_c |\dot{u}_c'(\omega_c)|^2}{\pi(2\gamma - 3)} \quad . \tag{20a}$$

To reduce the parameters of the corrected spectrum described in equation (19), the analyzed displacement spectra are assumed to falloff as $\gamma = 2$ above the corner frequency, following Brune (1970). This implies that the corrected acceleration spectra are approximately flat above the corner frequency. Writing the residual integral for $\gamma = 2$ gives

$$R\,[I_c^*(\omega_c)] = \frac{\omega_c}{\pi} |\dot{u}_c'(\omega_c)|^2 = \frac{|\ddot{u}_c'|^2}{\pi \omega_c} \tag{20b}$$

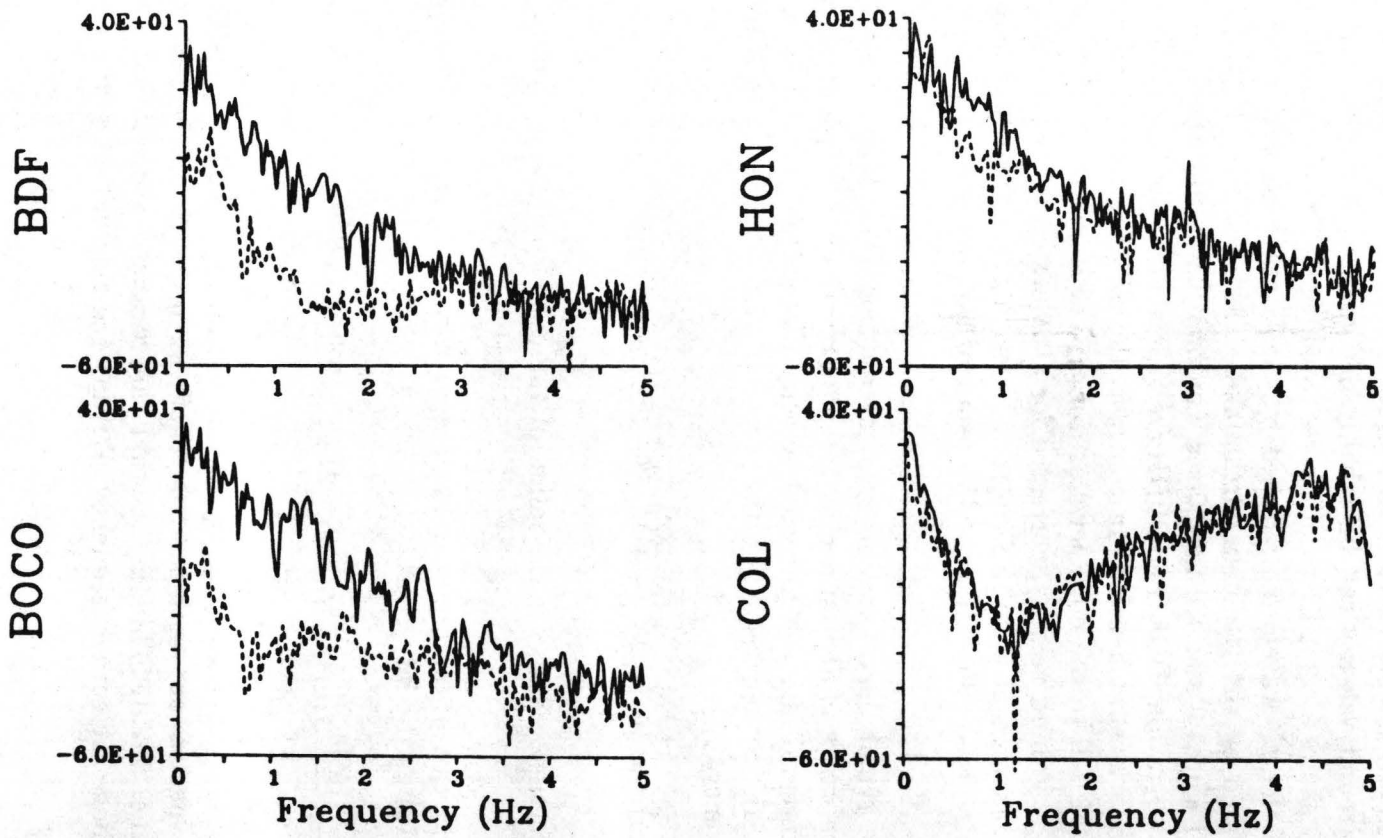

Figure 7. Signal-vs.-noise comparison for four of the waveforms analyzed, plotted as log power against linear frequency. The solid lines are the signal spectra while the dashed lines are the noise spectra, obtained from a 30-second sample before the arrival of the phase.

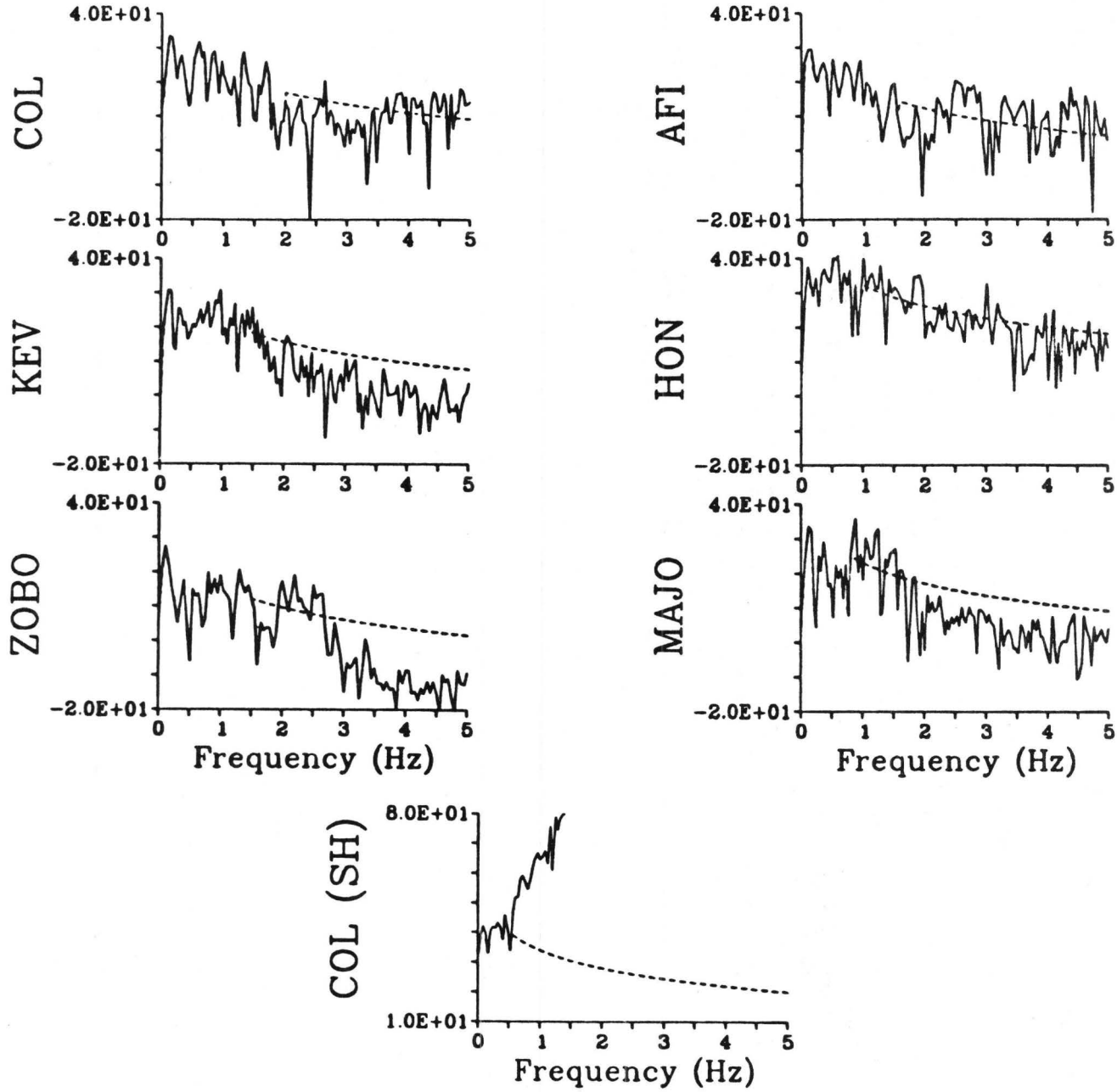

Figure 8. Corrected velocity spectra and spectral fits for equation (19) for the wave groups radiated by the Coalinga earthquake, plotted as log power against linear frequency. The residual integrals RI^* are calculated from these fits and equation (22). Note the spectral holes starting at 2–3 Hz in the spectra of the arrivals recorded at stations COL, KEV, ZOBO, and MAJO.

Calculating the residual integral thus requires fitting a corrected velocity spectrum with an ω^{-1} curve, $|\dot{u}'_c(\omega)|$, or a corrected acceleration spectrum with a flat line, $|\ddot{u}'_c|$, and choosing a cutoff frequency for the numerical integration. The residual integral is then calculated from the fit to either spectrum and the cutoff frequency. Adding the residual integral to the numerical integral, and multiplying by the density and wave velocity,

$$\varepsilon^*_c = \rho c N\left[I^*_c(\omega_c)\right] + \rho c R\left[I^*_c(\omega_c)\right] = \rho c I^*_c \quad , \tag{21}$$

gives the corrected energy flux.

In contrast to this hybrid estimate of the corrected energy flux, Wu (1968) and Chandra (1972) include no correction for the body-wave attenuation; the cutoff frequency of the integrals ($\approx$ 0.1 Hz) is less than the corner frequencies of the earthquakes, and they do not calculate residual integrals.

The corrected velocity spectra of the wave groups radiated by the Coalinga earthquake are plotted in Figure 8. The fits to these spectra used to calculate the residual integrals are plotted as dashed lines which begin at the cutoff frequency. Note that spectra for three of the stations (MAJO, KEV, and ZOBO) exhibit substantial holes beginning at about 2 Hz. In determining the fits to these spectra, these holes are assumed to result from an attenuating structure near the source, presumably underlying the San Andreas fault, rather than to be a characteristic of the source.

The results of the numerical integrations and the residual integrals are compiled in Table 1, together with the geometrical spreading factors and the equivalent radiation patterns for each arrival. The geometrical spreading factors have been divided by the free surface amplification at the receiver. The ratio of the integral of the square of the corrected ground velocity to the integral of the square of the uncorrected ground velocity, I^*_c/I_c, can be used to check the integration technique described in equations (17) through (21). For the gP phases shown in Table 1, this ratio ranges from 6 to 10 with a mean of 8. Figure 1 of Boatwright and Fletcher (1984) shows that this ratio is commensurate with a corner frequency of .28 Hz for a t^* of 1.0.

The corrected velocity spectra for gP wave groups radiated by the Borah Peak earthquake are plotted in Figure 9, along with the fits used to calculate the remainder functions. For the fits to the stations BOCO and TOL, low cutoff frequenccies were used so that apparently spurious peaks at high frequencies in the instrument behavior would not bias the measurements of the energy flux. The results of the integrations are compiled in Table 2. The ratios, I^*_c/I_c, range from 3 to 6 with a mean of 4 for these wave groups. This mean is commensurate with a corner frequency of .15 Hz, about twice the apparent corner frequency determined in a later section.

INVERSION FOR THE RADIATED ENERGY

Boatwright and Fletcher (1984) introduced the formula,

$$E^i_s = 4\pi < F^i >^2 \frac{\sum \varepsilon^*_c R^2}{\sum (F^c)^2} \quad , \tag{22}$$

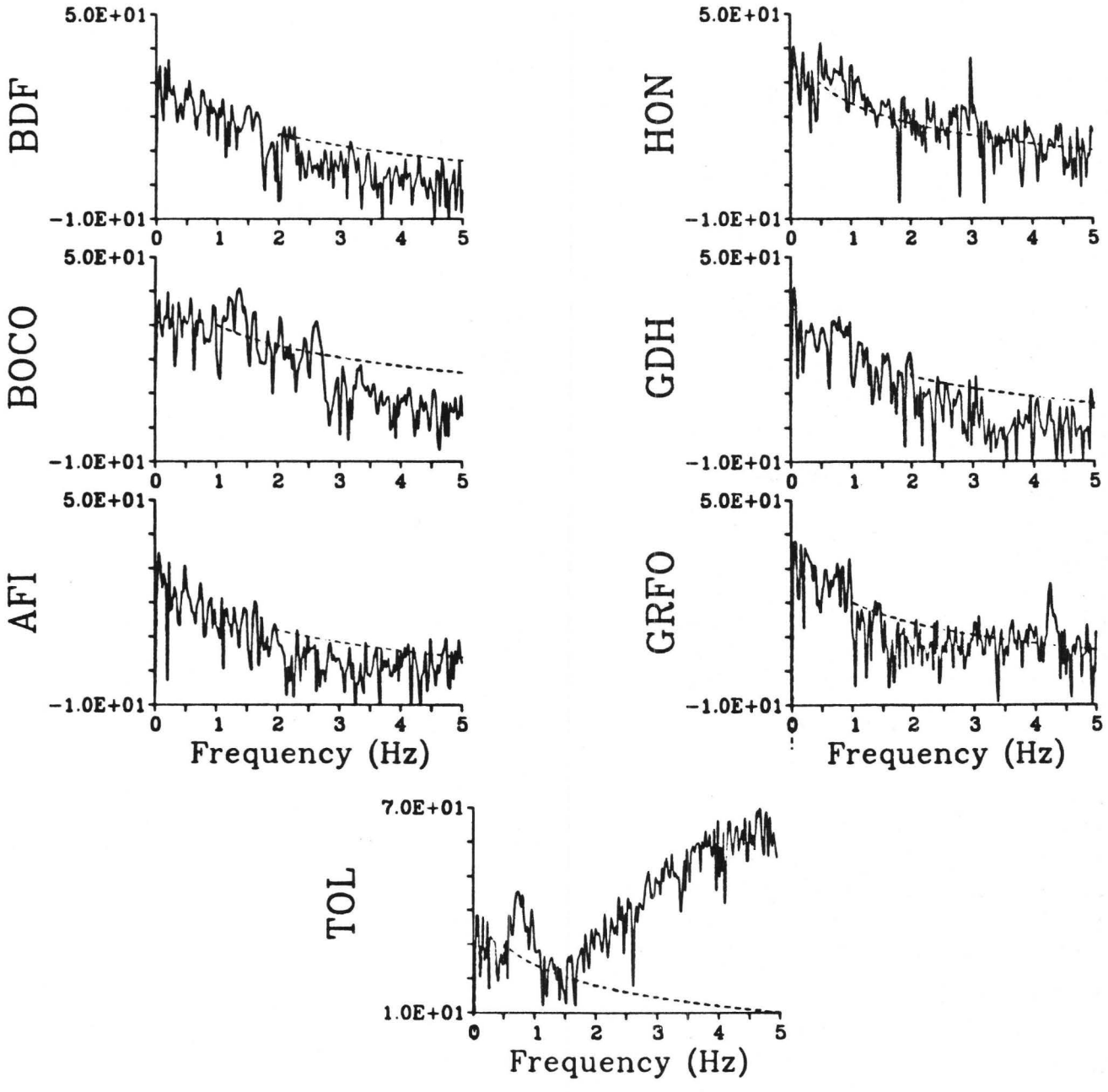

Figure 9. Corrected velocity spectra and spectral fits for the *gP* wave groups radiated by the Borah Peak earthquake, plotted as log power against linear frequency. The peaks at .8 Hz in the spectra of the arrivals recorded at stations HON and TOL, and at 1.5 Hz at BOCO are presumed to be spurious, and the fits for the residual integrals are used to excise these peaks.

TABLE 1

Station	Group	f_c Hz	I_c	$N[I_c^*]$ ($\times 10^{-6}$ cm^2/sec)	$R[I_c^*]$	I_c^*	F^g	R ($\times 10^9$ cm)	E_s ($\times 10^{20}$ dyne-cm)
COL	gP	2.0	2.17	13.21	2.01	15.22	.74	.73	12.5
AFI	gP	1.6	1.27	7.11	.80	7.91	1.13	1.06	5.9
MAJO	gP	1.0	1.95	8.24	6.12	14.36	.92	1.15	18.9
KEV	gP	1.5	1.19	8.35	1.89	10.24	.95	1.07	11.0
HON	gP	0.5	7.81	22.50	63.40	85.90	1.11	.75	34.5
ZOBO	gP	2.5	.92	8.00	1.19	9.20	.96	1.08	9.8
COL	gSH	0.5	9.42	126.10	100.00	226.10	.60	.64	13.9
				($\times 10^2$ cm^2/sec)				($\times 10^6$ cm)	($\times 10^{20}$ dyne-cm)
PVP 135°	S	10.0	10.9	16.1	1.8	46.8	.91	.76	15.8
PVP 45°	S	10.0	22.6	26.5	2.4				

TABLE 2

Station	Group	f_c Hz	I_c	$N[I_c^*]$ ($\times 10^{-6}$ cm^2/sec)	$R[I_c^*]$	I_c^*	F^g	R ($\times 10^9$ cm)	E_s ($\times 10^{20}$ dyne-cm)
AFI	gP	2.0	2.19	6.87	1.03	7.90	.85	1.19	13.1
BDF	gP	2.0	3.52	13.82	1.26	15.08	1.12	1.30	17.1
BOCO	gP	1.0	7.26	38.23	20.00	58.23	1.17	.90	29.1
GDH	gP	2.0	8.77	26.98	2.52	29.50	.74	.76	26.2
GRFO	gP	1.0	7.01	25.26	6.32	31.57	.87	1.14	45.7
HON	gP	0.5	10.29	22.84	10.00	32.85	.64	.81	44.4
TOL	gP	0.5	8.73	16.65	10.00	26.65	.92	1.16	35.8

to estimate the energy radiated in a particular wave-type (i = P or S) from the measurements of the energy flux in a set of arrivals, and the geometrical spreading factors and radiation pattern coefficients associated with these arrivals. They motivate this particular inversion by noting that equation (22) represents a discretely sampled analogue of the integral of the energy flux over the focal sphere. Because there is no correction for directivity in the analysis, the radiated energy will be underestimated if the direction of rupture is not sampled by the set of body waves analyzed.

The equations (9) through (14) are similar to equation (22); these formulae have the advantage of smoothing over any nodal arrivals of the phases comprising the wave groups. Owing to this smoothing, the arithmetic averages of the single station estimates of the radiated energy listed in Tables 1 and 2 are almost the same as the estimates determined from equation (22). For the Coalinga earthquake, the estimate of the radiated energy determined from the gP wave groups was $E_s = (1.5 \pm 0.4) \times 10^{21}$ dyne-cm, while the radiated energy estimated from the gSH wave group recorded at COL was $E_s = 1.4 \times 10^{21}$ dyne-cm.

Because the Coalinga earthquake was recorded in the near-field by a strong-motion instrument, the teleseismic estimate of the radiated energy can be checked directly. Figure 10 shows the horizontal components of the ground velocity of the S-wave arrivals at the Pleasant Valley Pumping Station (Maley *et al.*, 1983) above the respective velocity amplitude spectra, corrected for attenuation assuming $t_s^* = .07$ sec. The estimate of the attenuation was determined from the acceleration amplitude spectrum following the method of Anderson and Hough (1984); it is similar to the attenuation at nearby stations located on the alluvium (Mueller, personal communication, 1984). The components are combined into a single estimate in Table 1, using a cutoff frequency of 10 Hz to calculate I_c^*.

To determine the radiated energy following equations (21) and (1b) requires estimates of the density and shear wave velocity of the alluvium, in addition to the geometrical spreading factor and the radiation pattern coefficient. The Quaternary alluvium at the pumping station may be assumed to have a density of 2.0 gm/cm^3 and a shear wave velocity of .45 km/sec (Fumal, personal communication, 1984) in the upper 100-140 m. Eaton's (1983) focal mechanism and depth are nearly identical to Choy's (1984) results; Eaton's velocity model gives $F^s = .91$ and $R = 7.6$ km $\simeq$ the hypocentral distance divided by the free surface amplification. Combining equations (21), (1b) and (15) then returns an estimate of $E_s = 1.6 \times 10^{21}$ dyne-cm, which is slightly larger than the teleseismic average. While this comparison appears to verify the teleseismic estimate of the radiated energy, we note that it has been made using only one station, that the assumed site amplification is large, and that equations (1b) and (21) are derived for the far-field and may be inappropriate for a receiver which is located three source radii from the hypocenter.

The seismic energy radiated by the Borah Peak earthquake was estimated from the seven gP wave groups to be $E_s = (3.1 \pm 0.4) \times 10^{21}$ dyne-cm. Unfortunately, there were no near-field recordings of this earthquake, although 13 strong-motion instruments located

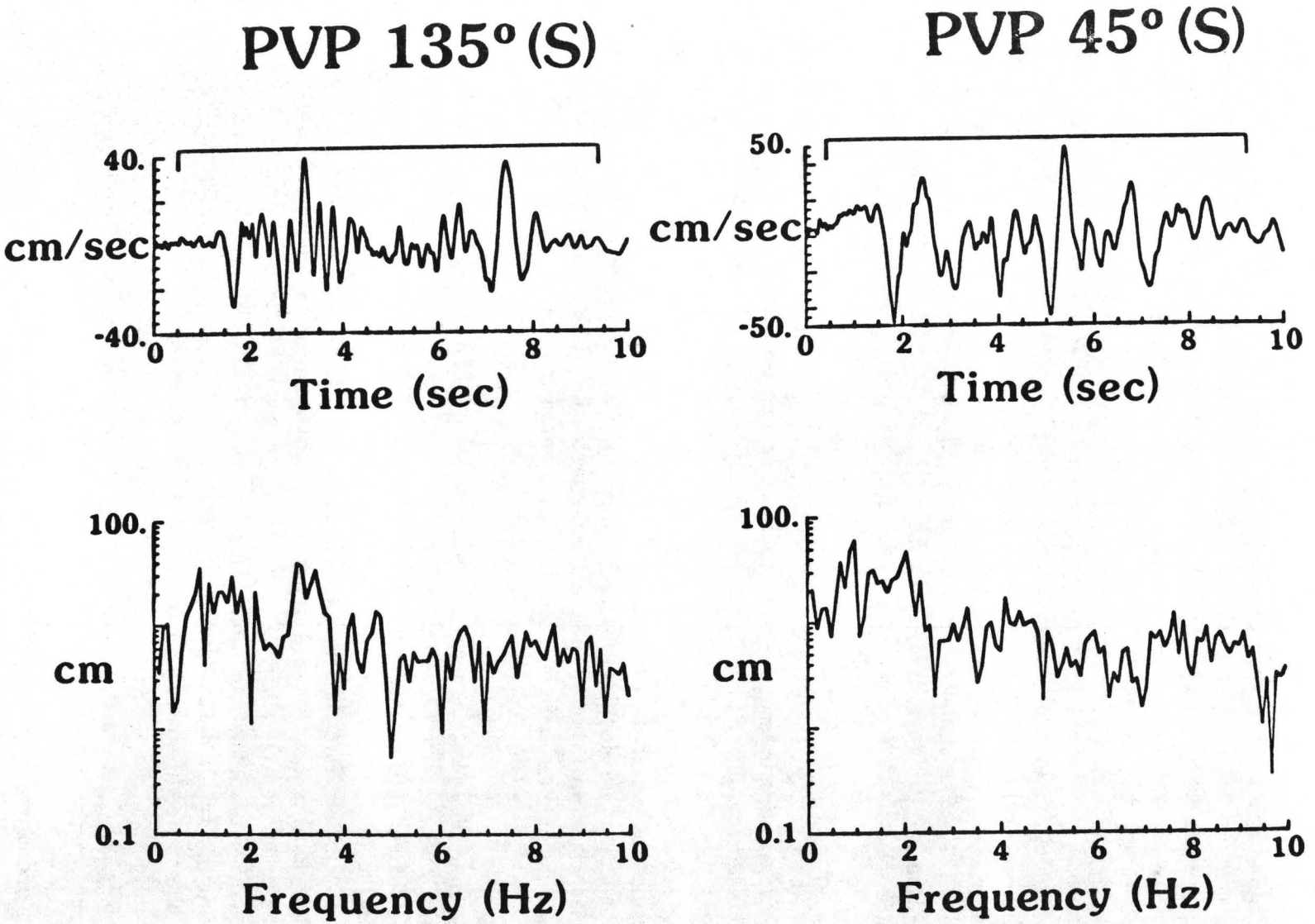

Figure 10. Horizontal components of the ground velocity recorded in the switchyard of the Pleasant Valley Pumping Station, 11 km to the northeast of the epicenter of the Coalinga earthquake, above the velocity amplitude spectra, plotted as log amplitude against linear frequency. The sample used for the velocity amplitude spectra is indicated by the bars over the time histories. The velocity amplitude spectra have been corrected for attenuation following equation (17), assuming $t^* = .07$ sec.

within the Idaho National Engineering Laboratory recorded the earthquake at an epicentral distance of 100 km (Jackson, 1985).

As discussed earlier, body waves which propagate to teleseismic distances have nearly vertical takeoff angles. For earthquakes which rupture along strike, averaging the energy flux in the teleseismic waveforms in equation (22) will underestimate the radiated energy. One method of checking for such an underestimate is to consider the distribution of the isoseismals. The isoseismals determined by Stover (1983, 1984) for the Coalinga and the Borah Peak earthquakes are plotted in Figure 11. The isoseismals which bound the areas of intensity V and VI for the Coalinga earthquake are approximately symmetric around the epicenter, suggesting that there was no strong focussing of energy in the event. In contrast, the isoseismals for the Borah Peak earthquake are distended to the northwest by a factor between 1.5 and 2.0; this distribution is compatible with the apparent rupture to the northwest in the event.

Following the analysis of Scholz *et al.* (1984), we assume that the limits of the isoseismal areas represent lines of equal energy flux, and that in the intermediate field of shallow earthquakes, this energy flux is carried by S-waves and higher mode surface waves excited by S-waves. To interpret the geometry of the isoseismal distributions, we assume that the energy flux attenuates as R^{-2}, that is, as body waves or Airy phases rather than as surface waves. The distension of the isoseismals to the northwest then represents an amplification between 2.2 and 4.0 relative to the energy flux radiated to the northeast/southwest or teleseismically. Assuming that this amplification occurs over a solid angle of $2\pi/3$ (*i.e.*, one sixth of the focal sphere) indicates that the teleseismic estimate of the radiated energy is low by 35 percent. Correcting the teleseismic estimate for this focussing yields $E_s = (4.2 \pm 0.6) \times 10^{21}$ dyne-cm.

ESTIMATES OF THE APPARENT STRESS

Fitting the broad-band teleseismic waveforms recorded by the GDSN, Choy (1984) determined a seismic moment of $(2.7 \pm 0.7) \times 10^{25}$ dyne-cm for the Coalinga earthquake. His estimate of the moment is smaller than the estimates made from surface waves [$(5.4 \pm 0.3) \times 10^{25}$, Kanamori, 1983] and long-period body waves recorded on the GDSN (5.7×10^{25}, centroid moment tensor solution, NEIS monthly listing; 4.7×10^{25}, Sipkin and Needham, 1984) and long-period body waves recorded on the WWSSN (4.3×10^{25}, Rial and Brown, 1983; 3.8×10^{25}, Hartzell and Heaton, 1983), but slightly larger than the estimate obtained from broad-band displacement seismograms recorded at Jamestown and Berkeley [$(2.3 \pm 1.2) \times 10^{25}$, Urhammer *et al.*, 1983]. These seven estimates of seismic moment clearly increase as a function of the period analyzed, from 2.6×10^{25} for the regional and teleseismic broad-band estimates at periods from 3–8 secs, to 4.0×10^{25} for the teleseismic estimates at periods from 12–16 secs, to 5.3×10^{25} for the teleseismic and surface wave estimates at periods from 20–25 secs.

Presuming that the increase of the seismic moment is a function of the dominant period of the data analyzed, but not the instrument or wave type, the frequency dependence of the seismic moment implies that the apparent stress,

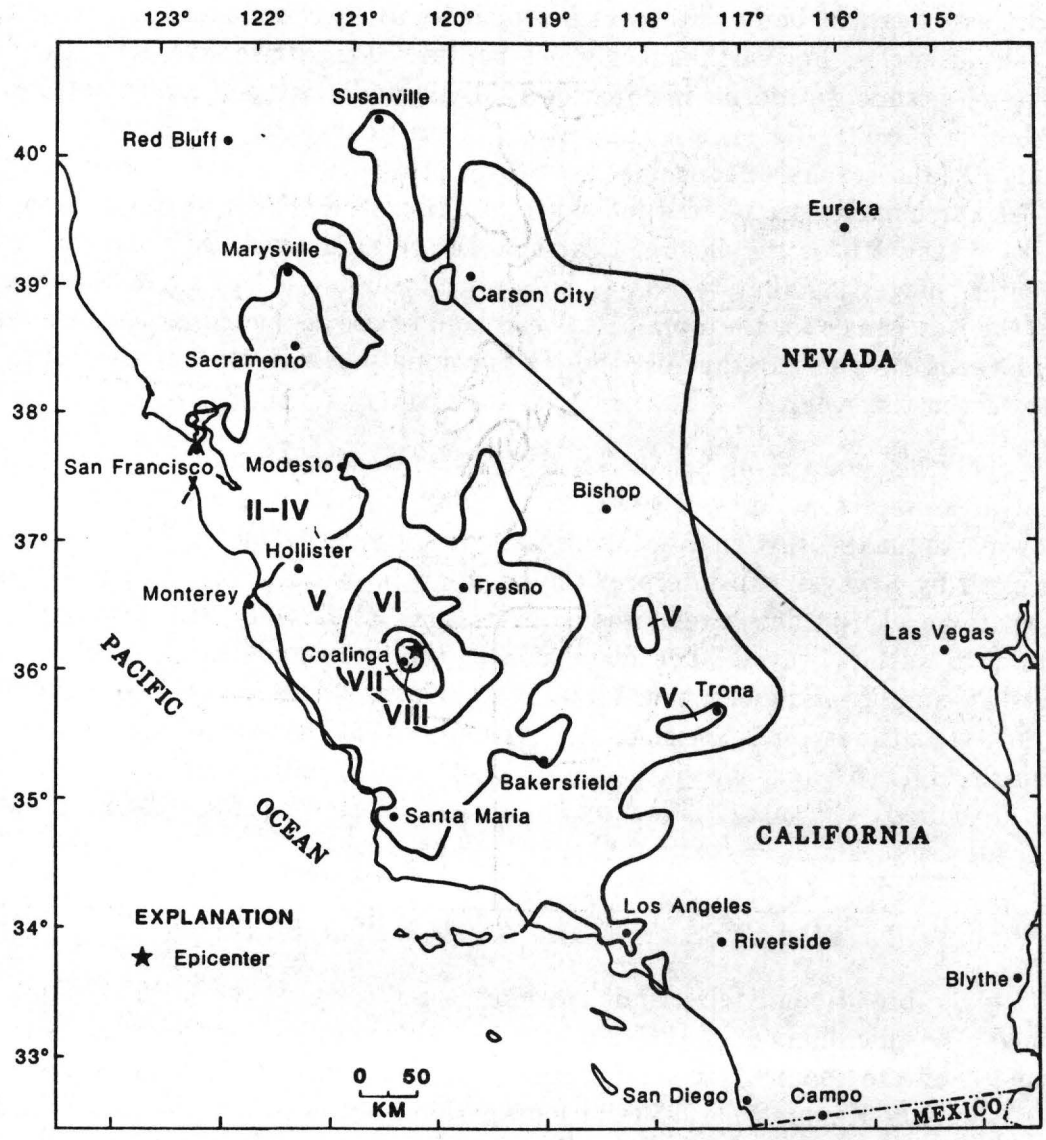

Figure 11a. Isoseismal map for the Coalinga earthquake, taken from Stover (1983).

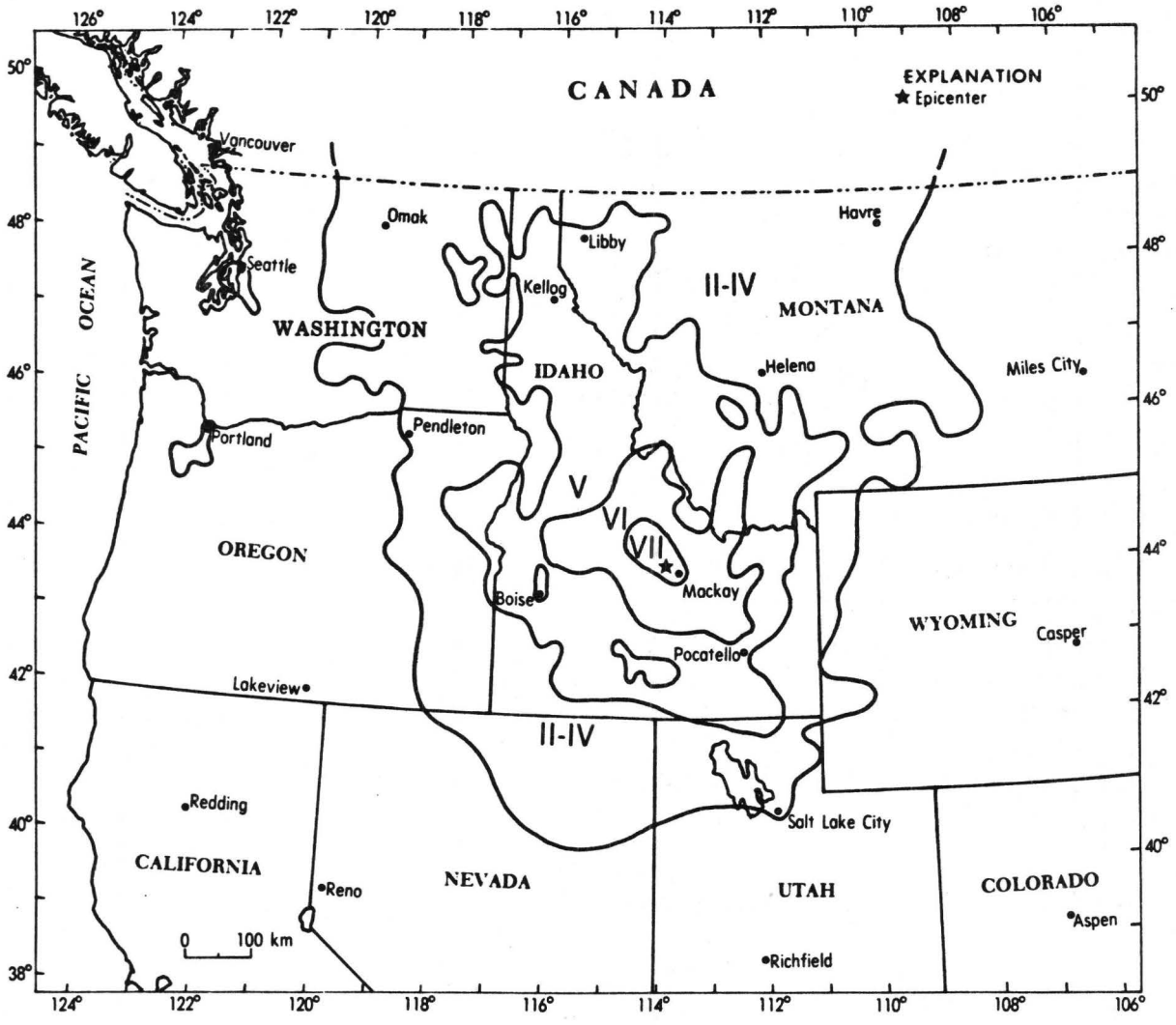

Figure 11b. Isoseismal map for the Borah Peak earthquake, taken from Stover (1984).

$$\tau_a = \mu \frac{E_s}{M_o} \quad , \tag{23}$$

also depends on the period used to estimate the seismic moment. To repress this frequency dependence, we use the moment determined from the broad-band analyses to calculate the apparent stress, that is, the moment evaluated at the corner period of the earthquake. This constraint insures that the apparent stress is linearly related to the *rms* dynamic stress drop (Boatwright, 1984). Using the broad-band estimate of the moment, $(2.7 \pm 0.7) \times 10^{25}$ dyne-cm, in equation (23) returns an estimate of 17 ± 6 bars for the apparent stress. Choy (1984) has estimated the static and dynamic stress drops of the primary rupture event of the mainshock to be 34 bars and 24–31 bars, respectively. The estimate of the dynamic stress drop is somewhat less than twice the apparent stress, the lower bound predicted by Madariaga's (1976) theoretical analysis.

To make similar comparisons for the Borah Peak earthquake, it is necessary to estimate both the dynamic stress drop and the seismic moment. The seismic moment for the event can be determined from the displacement spectra of the teleseismic *gP* arrivals, following the analysis of Hanks and Wyss (1972). These displacement spectra are plotted in Figure 12. Because the *P*, *pP*, and *sP* phases all contribute to the *gP* wave group, the generalized radiation pattern given in equation (10) is more appropriate than the direct P-wave radiation pattern used by Hanks and Wyss (1972). The low-frequency spectral amplitudes of the body waves are not affected by the corner frequency shift; therefore the ratio $q = 23.4$ appropriate for a point source (Boatwright and Fletcher, 1984) should be used to calculate the generalized radiation patterns. The seismic moment is then given by the relation,

$$M_o = 4\pi\rho\alpha^3 \frac{R}{F^{gP}} \bar{u} \quad . \tag{24}$$

The results of this analysis are compiled in Table 3; the average estimate of the seismic moment is $M_o = (1.7 \pm 0.3) \times 10^{26}$ dyne-cm, similar to the estimate of 1.7×10^{26} dyne-cm estimated from the long-period GDSN data by Sipkin (personal communication, 1984) and $(1.85 \pm 0.16) \times 10^{26}$ dyne-cm estimated from the long-period WWSSN body waves by Barrientos *et al.* (1985). Analyzing the same data as Barrientos *et al.* (1985), Doser (1985) estimated the moment as 2.9×10^{26} dyne-cm. We note that this is a long-period estimate, rather than a broad-band estimate, although the corner period of the Borah Peak earthquake ($\simeq$ 13 sec) is nearer to the 20-sec period range than that of the Coalinga earthquake. Combining this moment with the radiated energy estimate corrected for the horizontal focussing of energy gives $\tau_a = 7.9 \pm 1.5$ bars. This estimate of the apparent stress is less than half the dynamic stress drop of the initial rupture event.

The dynamic stress drop can be estimated directly from the waveforms plotted in Figure 4, using the relation

$$\tau_e = \frac{\rho R}{F^p} \left(\frac{\alpha}{v}\right)^3 \left(1 - \varsigma^2\right)^2 < \frac{\dot{u}}{t} > \tag{25}$$

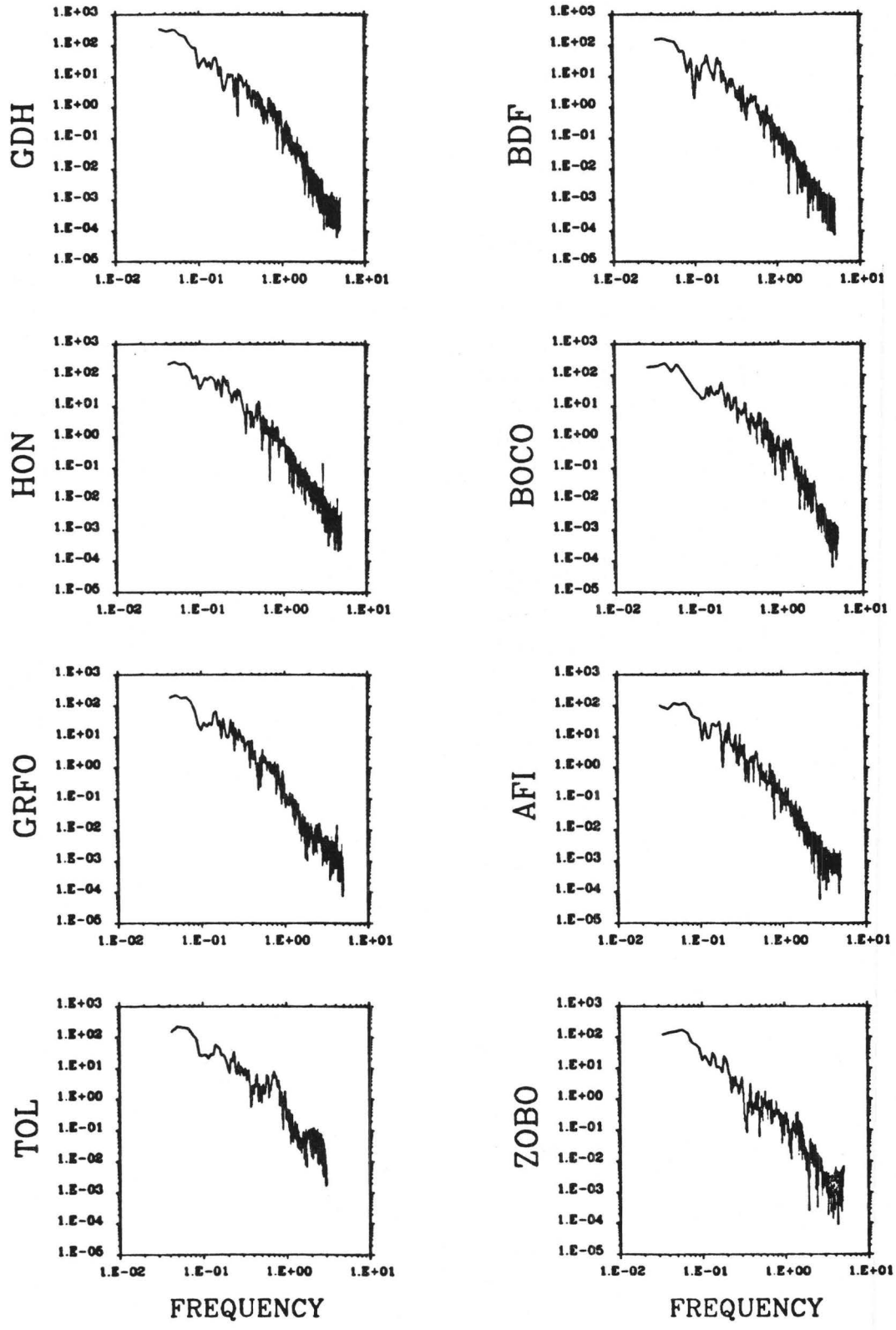

Figure 12. Displacement spectra for the *gP* wave groups radiated by the Borah Peak earthquake, plotted as log power against log frequency. The fits for the long-period asymptotes are shown as short horizontal lines. Station ZOBO has been used despite excessive high-frequency noise resulting from two apparent glitches in the recording.

TABLE 3

Station	$\bar{u}$ 10^2 μ-sec	F^{gP}	R 10^9 cm	M_o 10^{26} dyne-cm
AFI	1.1	.85	1.19	1.36
BDF	1.6	1.16	1.30	1.58
BOCO	2.0	1.24	.90	1.28
GDH	1.8	.83	.76	1.93
GRFO	1.8	.90	1.14	2.00
HON	2.3	.65	.81	2.52
TOL	1.8	.97	1.16	1.89
ZOBO	1.4	1.17	1.08	1.14

TABLE 4

Station	$\dot{u}$ μ/sec	τ sec	$\left\langle \frac{\dot{u}}{\tau - t^*/2} \right\rangle$ μ/sec^2	ζ	F^P	R 10^9 cm	Δσ bars
AFI	12	1.6	10.0	.41	.53	1.19	42
BDF	18	2.2	10.6	.33	.94	1.30	31
BOCO	24	2.6	11.4	.33	.99	.90	22
GDH	8	3.8	3.0	.30	.47	.76	11
GRFO	24	2.6	12.6	.31	.64	1.14	49
HON	14	4.1	4.0	.43	.30	.81	19
TOL	28	4.7	7.4	.30	.70	1.16	27
ZOBO	18	2.4	9.5	.33	.96	1.08	23

from Boatwright (1980). The measurements of the initial slope are corrected for attenuation by subtracting $t^*/2 = .5$ secs from the time interval, τ, used to measure the slope. The results are compiled in Table 4. Assuming an average rupture velocity of $v = .75\beta$ returns an estimate of $\tau_e = 28$ bars for the dynamic stress drop. Note that this stress drop corresponds only to the initial rupture event, which occurred on a buried segment of the fault 10 km to the south of the surface rupture. The initial rupture event appears to be marked by a gap in the aftershock distribution (Richins *et al.*, 1985).

The Borah Peak event appears to have ruptured to a depth of 20 km (Dozer, 1985); the lack of aftershock activity deeper than 15 km suggests that the earthquake ruptured through the seismogenic thickness of the plate. To calculate the static stress drop, Knopoff's (1958) formula for a 2D anti-plane fault should be used with the fault length rather than the fault width:

$$\Delta\sigma = \mu \frac{\Delta u_{\max}}{2a} \quad . \tag{26}$$

Crone and Machette (1984) give $\Delta u_{\max} = 2$ m as the peak displacement and $2a = 35$ km as the total length of faulting; equation (26) then gives the static stress drop as 17 bars, twice the estimate of the apparent stress. The difference between the static stress drop and the dynamic stress drop of the initial rupture event suggests that the initial rupture event had a stronger stress drop and triggered the subsequent weaker rupture to the north which was exposed in the surface faulting.

The difference in the apparent stress estimates for the Coalinga and the Borah Peak earthquake may result either from the difference in fault type or from the difference in the size of the events. As Byerlee (1978) has pointed out, the normal stress acting on the fault surface, and therefore the overall stress level of the faulting, are a maximum for thrust faults and a minimum for normal faults if the faulting is at the same depth. The Coalinga earthquake was either a high-angle reverse or a low-angle thrust faulting event; its hypocentral depth was about 10 km. In contrast, the Borah Peak earthquake was a large normal faulting event which had a substantial surface rupture and probably ruptured through the seismogenic thickness of the plate. Despite the slightly deeper faulting in the Borah Peak earthquake, the lower stress drops suggests that the crustal strength was weaker than at Coalinga.

DISCUSSION

The teleseismic estimates of the energy radiated by the Coalinga and the Borah Peak earthquakes are lower than the estimates predicted by either Gutenberg and Richter's (1956) relation between surface-wave magnitude and radiated energy, or the estimates predicted by Kanamori's (1977) or Hanks and Kanamori's (1979) relation between the long-period seismic moment and radiated energy. The discrepancy is particularly marked for the Borah Peak earthquake: the surface-wave magnitude of $M_s = 7.3$ gives $E_s = 5.6 \times 10^{22}$ dyne-cm, 13 times the teleseismic estimate of the radiated energy. The radiated energy

predicted by Kanamori's (1977) relation and the long-period seismic moments of the two events are 1.6 and 2.0 times the teleseismic estimates for the Coalinga and Borah Peak earthquakes, respectively.

There are two possible explanations for the disagreement between the teleseismic estimates of the radiated energy and the estimates predicted by the relation of Kanamori (1977). The disagreement could result either from a systematic underestimate of the attenuation in the body-wave propagation, or from the frequency dependence of the seismic moment. It is beyond the scope of this paper to test the teleseismic attenuation model of Der *et al.* (1982) in any detail. Although the differences between the teleseismic and the near-field spectra shown in Figures 8 and 10 suggest that the teleseismic model may underestimate the attenuation slightly, the constraints on the model derived by Der *et al.* (1981, 1982) insure that the underestimate is not severe. We note that increasing the assumed attenuation would increase the estimate of the energy radiated by the Coalinga earthquake significantly more than the estimate of the energy radiated by the Borah Peak earthquake.

Kanamori (1977) and Hanks and Kanamori (1979) derived their estimates of the radiated energy before the frequency dependence of seismic moment was discerned for a large shallow earthquake by Hartzell and Brune (1980). As discussed in the last section, this frequency dependence directly affects the relation between the seismic moment and the radiated energy. For the Coalinga earthquake, the long-period estimate of the moment was approximately twice the broad-band estimate: the overestimate from Kanamori's (1977) relation was a factor of 1.6. There is no similar broad-band estimate of the seismic moment of the Borah Peak earthquake; the spectral measurements shown in Figure 12 appear to be appropriate for the period around 20 sec.

Although Kanamori's (1977) relation between the seismic moment and the radiated energy of large events was derived without making direct estimates of the radiated energy of these events, the assumption of an approximately constant apparent stress appears appropriate for large shallow earthquakes. The results of this analysis suggest that the apparent stress of large shallow earthquakes ranges from 5 to 25 bars. Within this range, the apparent stress shows a systematic variation due to the faulting environment of the earthquake. The apparent stress of the Coalinga earthquake was twice as large as that of the Borah Peak earthquake, despite the deeper extent of the faulting in the Borah Peak event. This difference suggests that the apparent stress of great thrust earthquakes will be greater than 25 bars, because the depth of faulting in these events is significantly deeper than the faulting in the Coalinga earthquake. The weaker faulting environment and the relatively shallow extent of rupture in large strike-slip earthquakes in California, however, suggests that the apparent stress of these events will be about 10 bars.

For earthquakes which rupture through the seismogenic thickness of the plate, the frequency dependence of the seismic moment becomes significantly more pronounced (Silver and Jordan, 1983). The aseismic slip which accompanies these earthquakes can comprise a substantial fraction of the overall seismic moment, but it does not contribute to the radiated seismic energy. For earthquakes with a substantial amount of aseismic slip, Kanamori's (1977) relation overestimates the radiated seismic energy. Because great

earthquakes generally rupture through the seismogenic thickness of the plate boundary, the overestimate of the radiated energy predicted by Kanamori (1977) may be significant for these events.

CONCLUSIONS

The estimates of the radiated seismic energy determined in this analysis are well constrained, with uncertainties of 27 and 14 percent for the Coalinga and the Borah Peak earthquakes, respectively. The most likely sources of systematic error in the analysis result from the necessary assumption of an attenuation model and from the possible focussing of radiated energy in a horizontal direction not sampled by the teleseismic body waves. The areal distribution of the isoseismals of the Borah Peak earthquake indicates that the amplification of the energy flux radiated in the direction of rupture was a factor between 2.2 and 4.0; correcting the teleseismic estimate of the radiated energy increased the estimate by 35 percent.

There appears to be no adequate substitute for direct estimates of the energy radiated by large shallow earthquakes. While the approach of Scholz *et al.* (1984) suggests that intensity distributions may be used to provide crude estimates of the radiated energy, their analysis presently lacks any direct calibration. If geologic measurements are to be used to estimate the seismic moment, the results presented in this paper indicate that it is necessary to consider the tectonic environment, the depth of faulting, and the amount of aseismic slip to estimate the radiated energy from these moments. In the light of these difficulties, it appears more appropriate to directly estimate the radiated energy than to depend on simplistic relations between the seismic moment and the radiated energy.

APPENDIX

The assumption that the energy flux contained in the direct and depth phases is additive can be readily tested using the synthetic waveforms generated by a finite source model in a half-space. We consider all three characteristic faulting models: thrust, strike-slip, and normal faulting. Schematics of the faulting models are shown in Figure A1. The kinematic models described by Boatwright (1981) were used to generate the synthetics. The earthquakes are assumed to nucleate at depth and rupture towards the surface; the local stress drop is constant below 3 km depth; above 3 km, the local stress drop decreases linearly to zero. In the strike-slip case, the rupture proceeds along strike as well as updip, and the local stress drop decreases linearly below 12 km.

The teleseismic Pg velocity waveforms radiated by these earthquakes are shown in Figure A2, for five azimuths ± 80° from the strike of the fault plane of the events. For these smoothly rupturing models, the assumption that the energy flux in the particular phases is additive underestimates the total energy flux by about 20%. Introducing the notation,

$$\bar{F}^{pP} = \acute{P}\grave{P}F^{pP} \tag{A1}$$

$$\bar{F}^{sP} = \left[\frac{2}{3}\left(\frac{\beta}{\alpha}\right)^5\right]^{1/2} \acute{S}\grave{P}F^{sP} \tag{A2}$$

allows equation (10) to be rewritten as

$$\left(F^{gP}\right)^2 = \left(F^{P}\right)^2 + \left(\bar{F}^{sP}\right)^2 \quad . \tag{A3}$$

For these smooth ruptures in a half-space, the energy flux depends slightly on the coherence of the phases. A second-order approximation for the generalized radiation patterns that properly includes this coherence is given by

$$\left(F^{gP}\right)^2 = \left(F^{P}\right)^2 + \left(\bar{F}^{pP}\right)^2 + \left(\bar{F}^{sP}\right)^2 + \frac{2}{3}\left(\bar{F}^{pP}\bar{F}^{sP} - F^{P}\bar{F}^{pP} - F^{P}\bar{F}^{sP}\right) \quad . \tag{A4}$$

Note that the depth phases interfere constructively, and the direct phase and the depth phases interfere constructively, if the signs of the radiation pattern coefficients for the depth phases are the same, but opposite of that of the direct phase, which was the usual case for the synthetic models. This second-order approximation is appropriate only to the energy flux radiated by simple shallow ruptures. The coefficient of the second-order term in equation (A4) decreases as the rupture becomes more complex, as the hypocentral depth increases, or as the effects of the near-surface velocity structure distort the waveforms of the depth phases.

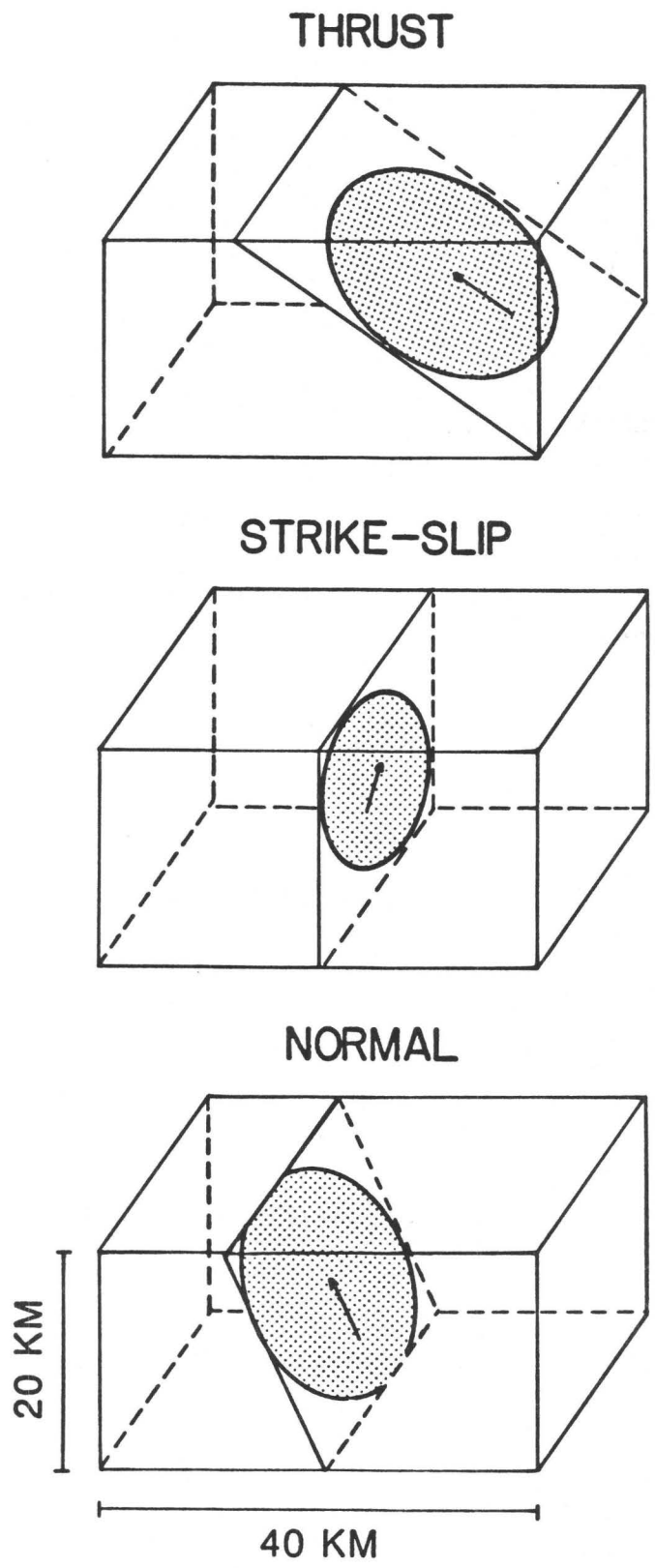

Figure A1. Schematic rupture diagrams for the finite rupture models used to test the additivity of the energy flux in the phases radiated by shallow earthquakes. The rose diagrams plotted above each schematic rupture indicate the set of azimuths for which the teleseismic waveforms are plotted in Figure A2.

For great thrust earthquakes, the duration of the rupture process and the average duration of slip at a point on the fault (*i.e.*, the rise time) may be greater than the delay time between the direct phase and the depth phases. For such an earthquake, the direct and depth phases will interfere destructively at the corner frequency of the earthquake; the technique presented in this paper then becomes inappropriate for estimating the radiated energy.

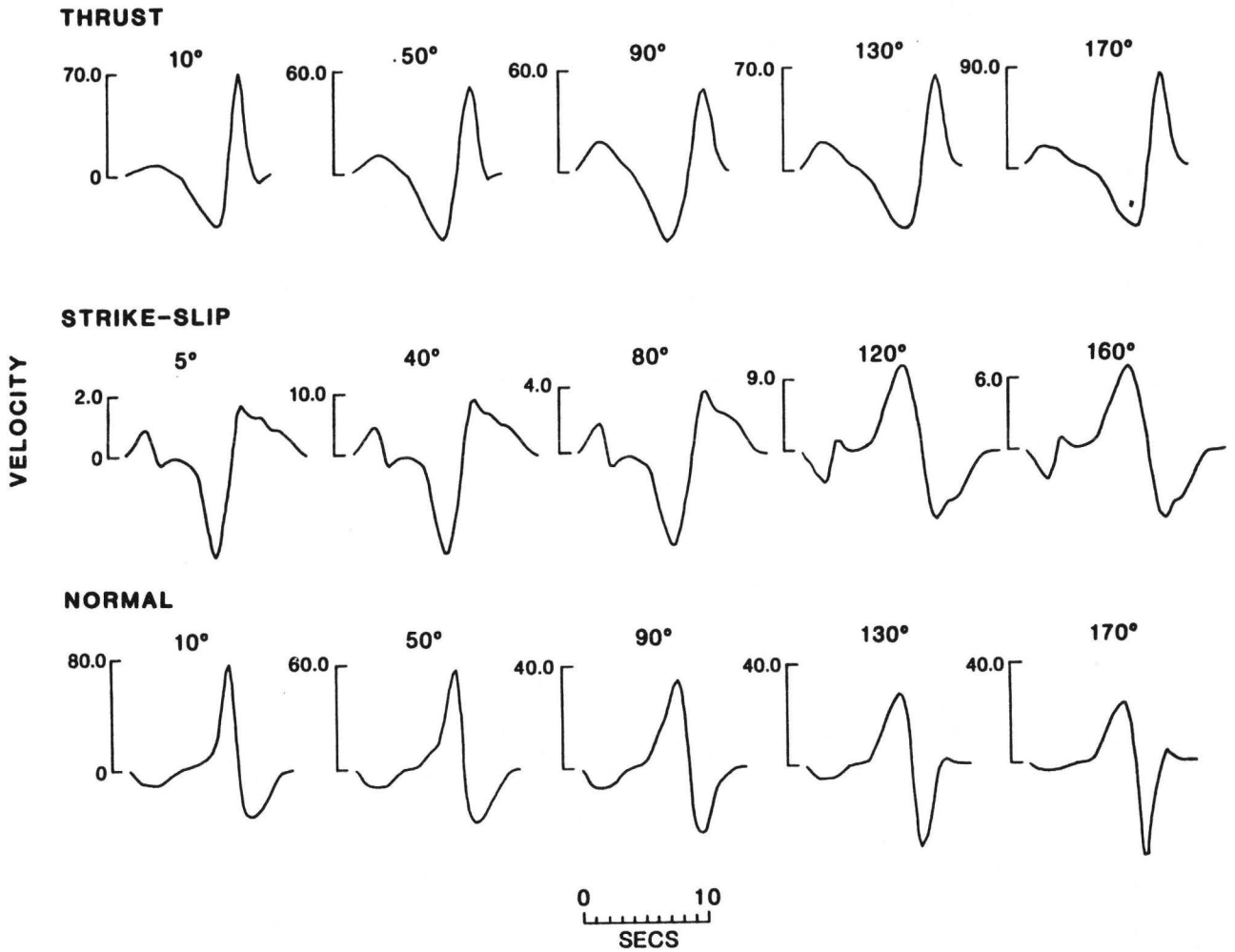

Figure A2. Broad-band velocity waveforms radiated by the rupture models plotted in Figure A1 radiated teleseismically at five azimuths from the direction of rupture (updip for the thrust and normal faults, along strike for the strike-slip fault) to the direction away from rupture.

BIBLIOGRAPHY

Aki, K. and P. G. Richards, *Quantitative Seismology: Theory and Methods*, W. H. Freeman and Company, San Francisco, CA, 1980.

Anderson, J. G. and S. E. Hough, A model for the shape of the fourier amplitude spectrum of acceleration at high frequencies, *Bull. Seismol. Soc. Am.* **74**, 1969–1994, 1984.

Archuleta, R. J., A faulting model for the 1979 Imperial Valley earthquake, *J. Geophys. Res.* **89**, 4559–4585, 1984.

Barrientos, S., S. N. Ward, J. R. Gonzales-Ruiz, and R. S. Stein, Inversion for moment as a function of depth from the geodetic observations and long-period body waves of the 1983 Borah Peak, Idaho, earthquake, *Proceedings of Conference XXX, The Borah Peak, Idaho, Earthquake of October 28, 1983, U. S. Geol. Surv. Open-File Rep.* **85 ???**, in press, 1985.

Bath, M., Earthquake energy and magnitude, *Phys. Chem. Earth* **1**, 115–165, 1967.

Boatwright, J., A spectral theory for circular seismic sources; simple estimates of source dimension, dynamic stress drop and radiated seismic energy, *Bull. Seismol. Soc. Am.* **70**, 1–27, 1980.

Boatwright, J., Quasi-dynamic models of simple earthquakes; application to an aftershock of the 1975 Oroville, California, earthquake, *Bull. Seismol. Soc. Am.* **71**, 69–94, 1981.

Boatwright, J., Seismic estimates of stress release, *J. Geophys. Res.* **89**, 6961–6968, 1984.

Boatwright, J., Characteristics of the aftershock sequence of the Borah Peak earthquake determined from digital recordings of the events, *Proceedings of Conference XXX, The Borah Peak, Idaho, Earthquake of October 28, 1983, U. S. Geol. Surv. Open-File Rep.* **85 ???**, in press, 1985.

Boatwright, J. and J. B. Fletcher, The partition of radiated energy between P and S waves, *Bull. Seismol. Soc. Am.* **74**, 361–376, 1984.

Brune, J. N., Tectonic stress and the spectra of seismic shear waves, *J. Geophys. Res.* **75**, 4997–5009, 1970.

Bullen, K. E., *An Introduction to the Theory of Seismology*, Cambridge University Press, Cambridge, 1965.

Byerlee, J. D., Friction of rocks, *Pure Appl Geophys.* **116**, 615–626, 1978.

Chandra, U., Analysis of body-wave spectra for earthquake energy determination, *Bull. Seismol. Soc. Am.* **60**, 539–563, 1970.

Choy, G. L., Source parameters of the Coalinga, California, earthquake of May 2, 1983, inferred from broadband body-waves, *Proceedings of Conference XXIX, The Coalinga, California, Earthquake of May 2, 1983, U. S. Geol. Surv. Open-File Rep.* **85 ???**, in press, 1984.

Choy, G. L. and J. Boatwright, The rupture characteristics of two deep earthquakes inferred from broadband GDSN data, *Bull. Seismol. Soc. Am.* **71**, 691–711, 1981.

Crone, A. J. and M. Machette, Surface faulting accompanying the Borah Peak earthquake, central Idaho, *Geology* **12**, in press, 1984.

Der, Z. A., T. W. McElfresh, and A. O'Donnell, Results of the SDCS (special data collection system) attenuation experiment, *Report No. VSC-TR-81-14*, Teledyne Geotech, Alexandria, Virginia, 1981.

Der, Z. A., T. W. McElfresh, and A. O'Donnell, An investigation of the regional variations and frequency dependence of anelastic attenuation in the United States in the 0.5–4 Hz band, *Geophys. J.* **69**, 67–100, 1982.

Doser, D. I., The 1983 Borah Peak, Idaho, and 1959 Hebgen Lake, Montana, earthquakes: models for normal fault earthquakes in the intermountain seismic belt, *Proceedings of Conference XXX, The Borah Peak, Idaho, Earthquake of October 28, 1983, U. S. Geol. Surv. Open-File Rep.* **85 ???**, in press, 1985.

Eaton, J. P., Seismic setting, location and focal mechanism of the May 2, 1983, Coalinga earthquake, *The Coalinga Earthquake Sequence Commencing May 2, 1983, U. S. Geol. Surv. Open-File Rep.* **83–511**, 20–26, 1983.

Gutenberg, B. and C. F. Richter, Earthquake magnitude, intensity, energy, and acceleration, *Bull. Seismol. Soc. Am.* **46**, 105–145, 1956.

Hanks, T. C. and H. Kanamori, A moment magnitude scale, *J. Geophys. Res.* **84**, B5 2348–2350, 1979.

Hanks, T. C. and M. Wyss, The use of body-wave spectra in the determination of seismic source parameters, *Bull. Seismol. Soc. Am.* **62**, 561–589, 1972.

Hartzell, S. H. and J. N. Brune, The Horse Canyon earthquake of August 2, 1975–Two stage stress-release process in a strike slip earthquake, *Bull. Seismol. Soc. Am.* **69**, 1161–1173, 1980.

Hartzell, S. H. and T. H. Heaton, Teleseismic mechanism of the May 2, 1983, Coalinga, California, earthquake from long-period P-waves, *The 1983 Coalinga, California Earthquakes, Special Publication* **66**, California Division of Mines and Geology, Sacramento, Ca, 1983.

Harvey, D. and G. L. Choy, Broadband deconvolution of GDSN data, *Geophys. J.* **69**, 659–668, 1982.

Jackson, S. M., Acceleration data from the 1983 Borah Peak, Idaho, earthquake recorded at the Idaho National Engineering Laboratory, *Proceedings of Conference XXX, The Borah Peak, Idaho, Earthquake of October 28, 1983, U. S. Geol. Surv. Open-File Rep.* **85 ???**, in press, 1985.

Kanamori, H., The energy release in great earthquakes, *J. Geophys. Res.* **82**, 2981–2987, 1977.

Kanamori, H., Mechanism of the 1983 Coalinga earthquake determined from long-period surface waves, *The 1983 Coalinga, California Earthquakes, Special Publication* **66**, California Division of Mines and Geology, Sacramento, CA, 1983.

Knopoff, L., Energy release in earthquakes, *Geophys. J. R. Astron. Soc.* **1**, 44–52, 1958.

Madariaga, R., Dynamics of an expanding circular fault, *Bull. Seismol. Soc. Am.* **66**, 639–666, 1976.

Maley, R., G. Brady, E. Etheridge, D. Johnson, P. Mork, and J. Switzer, Analog strong motion data and processed main event records obtained by the U. S. Geological Survey near Coalinga, California, *The Coalinga Earthquake Sequence Commencing May 2, 1983, U. S. Geol. Surv. Open-File Rep.* **83–511**, 1983.

Rial, J. E. and E. Brown, Waveform modelling of long-period P-waves from the Coalinga earthquake of May 2, 1983, *The 1983 Coalinga, California Earthquakes, Special Publication* **66**, California Division of Mines and Geology, Sacramento, CA, 1983.

Richins, W. D., R. B. Smith, C. J. Langer, J. E. Zollweg, J. J. King, and J. C. Pechmann, The 1983 Borah Peak, Idaho, earthquake: relationship of aftershocks to the main shock, surface faulting, and regional tectonics, *Proceedings of Conference XXX, The Borah Peak, Idaho, Earthquake of October 28, 1983, U. S. Geol. Surv. Open-File Rep.* **85 ???**, in press, 1985.

Scholz, C. H., C. A. Aviles, and S. G. Wesnousky, Stress-drop differences between large intra- and interplate earthquakes and their effect on intensity distributions, submitted to *J. Geophys. Res.* **89**, 1984.

Silver, P. and T. H. Jordan, Total moment spectra of fourteen large earthquakes, *J. Geophys. Res.* **88**, 3273–3293, 1983.

Sipkin and Needham, Kinematic source parameters of the 2 May 1983 Coalinga earthquake determined by time-dependent moment tensor inversion and an analysis of teleseismic first motions, *Proceedings of Conference XXIX, The Coalinga, California, Earthquake of May 2, 1983, U. S. Geol. Surv. Open-File Rep.* **85 ???**, in press, 1984.

Snoke, J. A., A. T. Linde and I. S. Sacks, Apparent stress: an estimate of the stress drop, *Bull. Seismol. Soc. Am.* **73**, 339–348, 1983.

Stein, R. S., Reverse slip on a buried fault during the 2 May 1983 Coalinga earthquake: evidence from geodetic elevation changes, *The 1983 Coalinga, California Earthquakes, Special Publication* **66**, California Division of Mines and Geology, Sacramento, CA, 1983.

Stover, C. W., Intensity distribution and isoseismal map, *The 1983 Coalinga, California Earthquakes, Special Publication* **66**, California Division of Mines and Geology, Sacramento, CA, 1983.

Stover, C. W., Preliminary isoseismal map and intensity distribution for the Borah Peak, Idaho, earthquake of October 28, 1983, *U. S. Geol. Surv. Open-File Rep.* **84–297**, 6 p., 1984.

Urhammer, R. A., R. B. Darragh, and B. A. Bolt, The 1983 Coalinga earthquake sequence: May 2 through August 1, *The 1983 Coalinga, California Earthquakes, Special Publication* **66**, California Division of Mines and Geology, Sacramento, Ca, 1983.

Vassiliou, M. S., and H. Kanamori, The energy release in earthquakes, *Bull. Seismol. Soc. Am.* **72**, 371–387, 1982.

Wu, F. T., Lower limit of the total energy of earthquakes and partitioning of energy among seismic waves, *Ph.D. Thesis*, California Institute of Technology.

AN EYEWITNESS OBSERVATION OF OSCILLATORY FAULT MOTION ACCOMPANYING AN M_L 5.5 AFTERSHOCK OF THE BORAH PEAK EARTHQUAKE

Frances M. Boler

Department of Geological Sciences and Cooperative Institute for Research in the Environmental Sciences, University of Colorado and NOAA, Boulder, Colorado, 80309.

Abstract

In this paper an eyewitness observation by the author of fault scarp motion during the 29 Oct 83 23:29 UT aftershock of the Borah Peak earthquake (28 Oct 83 14:06 UT M_S 7.3) is reported. During the passage of the wavetrain generated by the aftershock, oscillatory relative motion of the hanging wall and footwall sides of the fault scarp (formed during the main shock) was observed at a distance of 15 m from the fault scarp, 400 m southeast of the Doublespring Pass Road. The aftershock epicenter was 20 km northwest of the observation point. The motion was parallel to the fault scarp, dominantly or entirely horizontal (as was the felt ground motion), and consisted of 3 or more cycles of peak-to-peak amplitude 0.5 $\pm$ 0.1 m, and of period 2 $\pm$ 0.5 s. Two possible explanations for this observation are: (1) the wavetrain from the aftershock generated shear stresses high enough to exceed the frictional stress at the fault plane near the surface; or (2) the observation location was a region of localized amplification of wave motion, again causing shear stresses which exceeded the frictional stress at the fault scarp. For case (1), decoupling of the fault surface would have occurred to a depth of several hundred meters, assuming that the incoming wave was a fundamental mode Love wave in the alluvial layer of the observed amplitude and frequency. The observation has implications for the phenomenon of triggered slip and for seismic hazards evaluation.

INTRODUCTION

On October 29, 1983 23:29 UT, an M_L =5.5 aftershock of the Borah Peak earthquake occurred just as a field party from University of Colorado had finished deploying magnetometers and a soil gas sampling array (Scherbaum et al., 1985) near the Lost River fault. Figure 1 is a location map showing the 36-km long scarp which formed during the mainshock along the previously-mapped Lost River fault and the Arentson Gulch fault. The surface geology at the observation site is Quaternary alluvial valley fill, which reaches a thickness of 600-900 m in the center of the valley (Crosthwaite et al., 1970). A seismic reflection survey along the Doublespring Pass Road shows at least 450 m of alluvial fill overlying consolidated sediments on the downthrown side of the fault and 15-35 m of alluvial fill on the upthrown side (A. Crone, written commun., 1984). This alluvial thickness on the upthrown side of the fault is consistent with the thickness indicated by a refraction survey which crosses the fault at Doublespring Pass Road (Pelton et al., 1985).

Figure 2 is a sketch map of the observation position, 15 m west of the scarp and 400 m south of Doublespring Pass Road. The observation position was within a zone of complex faulting described by Crone et al. (1985) which occurred during the main shock.

At the observation site, the surface expression of faulting and deformation consisted of a 50 m wide zone bounded on the northeast by the main scarp, and on the southwest by a small thrust fault having about 10 cm of offset. Between these bounding faults, the ground surface was bowed upward as in compression, with tensile cracks occurring throughout (Figure 2). The existence of the southwest bounding thrust fault was unusual; along most of the fault length occurrence of an antithetic normal fault was more common (Crone et al., 1985). In the vicinity of the observation site the expression of the main scarp was complex. At point A in Figure 2, the scarp height was about 1.5 m, with a 1 - 1.5 m wide gap between the hanging wall and footwall; the gap formed a 1 m deep crevice which was filled with water. The source of the water is most likely a perched water table above a clay layer which exists on the upthrown side of the fault as seen in a trench dug across the fault scarp 100 m north of the observation location. The clay layer is absent at a trench at Doublespring Pass Road. At point B, just 15 m from point A, the scarp was broken into stairstep like segments, each scarp having a height of only a few tens of cm.

The aftershock occurred to the west of the Lost River fault and to the southwest of the Arentson Gulch fault, both of which sustained surface breaks during the mainshock. The distance from the aftershock epicenter (44 ° 11.58 ′ N, 114 ° 0.66 ′ W,D. Doser, written commun., 1984) to the observation site was 20 km, at an azimuth of N35W. The depth of the aftershock, 1.3 km, is not very well constrained (D. Doser, written commun., 1984). The aftershock focal mechanism and location are consistent with normal dip-slip motion on the Lost River fault.

THE OBSERVATION

In order to drive our vehicle across the fault scarp, our field party had filled in a segment of the scarp with dirt and branches at the point marked B in Figure 2. While I drove over the larger cracks, the other two members of our field party (F. Scherbaum and C. Roecken) stood on this filled-in section and directed. As the front wheels of the car crossed the easternmost and largest main crack of the fault, both Scherbaum and Roecken felt strong vertical accelerations, which they initially attributed to the weight of the car suddenly being transferred to the broken-up material on which they were standing. However, as I proceeded across the fault it became clear to Scherbaum and Roecken that they were experiencing the ground shaking accompanying an aftershock, and the vertical acceleration they had attributed to the car may have been the first arrival of such motion. Scherbaum looked at his watch and noted the time as 5:30 pm. I drove about 20 m beyond the fault. At a maximum speed of 5 mph, this took about 10 seconds. Immediately upon stopping the car I realized that we were experiencing an aftershock because the car was shaking. I jumped out of the car and ran three steps to the back of the vehicle, looking first at my companions to see if they knew what was happening, then looking at the ground at my feet, and finally looking at the scarp 15 m from where I stood. For all three of us the felt motion was horizontal. I felt no sensation of losing my balance or of dizziness. I stood in the same spot for the duration of the motion. As I looked at the section of the fault scarp nearest to me (at A in Figure 2), what I saw caused the following sequence of thoughts to pass through my mind: "Hey! the fault is moving. Hey! It's moving back. And back again! It's oscillating! A wave is passing... but ... the fault must be decoupled." I saw sagebrush and grasses on the downthrown side (here and throughout the paper, upthrown and downthrown refer to offsets which took place during the main shock) of the scarp translating horizontally with the ground (and without pendulum-like swaying) relative to the fault scarp immediately behind them. Objects such as pebbles and roots in the fault scarp served as reference points. I observed no swaying of vegetation on the upthrown surface. I estimated the amplitude as 0.5 m. The motion was in progress when I first looked at the

fault. I watched three turning points (reversals of sense of motion) before looking away from that segment of the fault toward my companions, who were standing within a meter of the easternmost crack of the scarp. I did not observe relative motion where they were standing; however, there was no scarp behind them to serve as a reference. They describe the motion where they were standing as horizontal, and having amplitudes of a few tens of cm. Looking in other directions away from the fault, I did not observe any oscillatory motion, leading me to conclude that the observation was not a global optical illusion. Looking back at the fault, I saw that it was still moving with the same character of motion as before. I looked along the fault to the north for 10-20 m, and saw that the motion was not restricted to the spot where I had first seen it. However, I did not see any more reversals of sense of motion, and everything stopped. Starting from when I stopped the car I estimate the duration of motion to have been about 10 seconds. The total duration of motion at the site was then about 20 seconds.

We left the scene immediately, unfortunately missing the next aftershock which occurred just 10 minutes later. I related what I had seen to Scherbaum and Roecken, who had not looked at the fault during the motion. Upon returning to our motel, I wrote a short note to myself about the aftershock, including the amplitude, period, and duration of the motion that I had seen. After returning to the University of Colorado and discussing the observation with colleagues there, I realized the uniqueness of the observation, and wrote a more complete description from memory.

In summary, I am reasonably certain of the following quantitative description of the observation. Ground motion at the observation site commenced at ~ 5:30 pm MDT. During the last 10 seconds of the total of 20 seconds or so of ground motion at the site, oscillatory relative motion of the two sides of the fault scarp was observed. The motion is best described as dominantly or entirely horizontal, having peak-to-peak amplitude of 0.4 to 0.6 m and a period of 1.5 - 2.5 s. The felt ground motion was also dominantly or entirely horizontal. The observed duration of the oscillatory motion was less than 10 seconds. I saw three turning points, looked away, looked back and saw one more; I estimate that I missed seeing two turning points during the time that I looked away. This implies at least three full cycles took place, and possibly more, since the motion was in progress when I first looked at the fault. The scarp motion stopped coincident with the cessation of felt ground motion. During the last half-cycle the apparent motion of the downthrown side was from southeast to northwest (right-lateral).

RELATED OBSERVATIONS OF THE AFTERSHOCK

A strong motion instrument had been deployed by J. Boatwright at a site 65-90 m west of the fault scarp, and 140 m north of Doublespring Pass Road, a total of ~ 520 m from the location of my observation. The instrument recorded a total of about 10 seconds of motion for the aftershock. The record shows horizontal motion parallel to the fault and having a period on the order of 1 - 2 seconds, with maximum displacement amplitude of 1 cm peak-to-peak. If the onset of motion at the instrument was coincident with the time that I drove over the scarp, then the motion indicated by the instrument would essentially have ended before my observation began. A small aftershock which preceded the 23:29 aftershock by a few seconds (D. Doser, oral commun., 1984) may explain this discrepancy in duration of motion. The onset of shaking at the observation site may have corresponded to the earlier aftershock, rather than the 23:29 event which triggered Boatwright's instrument.

A. Crone and R. Bucknam were near the fault scarp at Doublespring Pass Road, and W. Scott and K. Pierce were near the fault scarp in Arentson Gulch at the time of the aftershock. None of them noticed any unusual motion at the fault scarp, and they described the felt motion as having an amplitude of about 1 cm. The amplitude of

motion that I observed and felt, and that the others in my field party (Scherbaum and Roecken) reported feeling was 10 - 100 times greater than these other observations. This difference implies that the motion at the location of my observation was anomalously large.

INTERPRETATION OF THE OBSERVATION

The interpretation of the observation requires consideration of two possible situations: (1) the motion was caused by an incident wave from the aftershock, which alone generated shear stresses high enough to exceed the frictional stress holding the fault plane together at the surface and to some depth; or (2) the particular characteristics of the surface faulting at the site allowed amplification of the motion caused by the incident wavetrain. These two cases are considered below.

1. Dynamic stress on the fault plane from an incident wave.

I chose a Love wave as the most likely incident wave on the grounds that: (1) the observed motion was horizontal, (2) the motion was of large amplitude, and (3) it occurred at the end of the wavetrain. The alluvial basin fill in the Lost River Valley overlying consolidated sediments provides the velocity contrast to support Love waves. The observation of oscillatory fault motion implies that the two surfaces of the fault were decoupled to some degree, so that particle motion was discontinuous across the fault, at least at the surface, and to some undetermined depth. In an attempt to determine whether decoupling of the fault plane to significant depth is plausible, the shear stress generated by a propagating Love wave having the observed amplitude and frequency can be compared to the frictional stress holding together a fault plane of zero tensile strength. For the following calculation, shear velocities of 475 m/s in the alluvial layer, and 1700 m/s in the consolidated sediment bedrock are used. The alluvial layer is taken to be 900 m thick, and to have a density of 1900 kg/m^3. The velocities are estimated from P-wave velocities of 825 m/s for the alluvial layer and 2950 m/s for the bedrock given by Pelton et al. (1985), and the elastic properties of alluvium and sediments given in Clark (1966) and Birch (1942).

The equations for Love wave displacements are given in many texts (e.g. Aki and Richards, 1980). For the nth mode, the displacement in the y-direction as a function of propagation direction x, and depth z is

$$v_n = A e^{ik_n (x - c_n t)} \cos\left(\omega \left(\frac{1}{\beta_1^{\,2}} - \frac{1}{c_n^{\,2}}\right)^{\frac{1}{2}} z\right),$$

where n is the mode number, A is the amplitude, k_n is the horizontal wavenumber, ω is the angular frequency, β_1 is the shear velocity in the upper layer, and c_n is the phase velocity of the nth mode at the frequency ω. The corresponding shear stress is given by

$$\tau_{xy}^{n} = \mu \frac{\partial v_n}{\partial x} = ik_n \mu A e^{i(k_n x - \omega t)} \cos\left(\omega \left(\frac{1}{\beta_1^{\,2}} - \frac{1}{c_n^{\,2}}\right)^{\frac{1}{2}} z\right).$$

The equation for the cutoff frequency of the nth mode is given in Aki and Richards (1980) as:

$$\omega_{cutoff}^{n} = \frac{\dfrac{n \pi \beta_1}{H}}{\left(1 - \dfrac{\beta_1^{\,2}}{\beta_2^{\,2}}\right)^{\frac{1}{2}}},$$

where H is the upper layer thickness and β_2 is the shear velocity in the lower medium. This equation can be used to determine the highest possible mode. The n=2 mode has a

cutoff frequency of 0.55 Hz for the seismic velocity configuration quoted above. This frequency is within the range of the observation. In Figure 3, the maximum shear stress τ_{xy} in a cycle is plotted as a function of depth for the n = 0, 1, and 2 modes. The phase velocity of these modes at 0.55 Hz is 475 m/s (β_0) for n=0, 546 m/s for n=1, and 1700 m/s (β_2) for n=2.

Two lines, corresponding to the shear stress necessary for sliding against friction to occur (a) in the presence of lithostatic stress; and (b) in the presence of lithostatic stress modified by hydrostatic pore pressure, with a coefficient of friction of 0.7 (Paterson, 1978) for both, are also plotted in Figure 3. From this plot it is apparent that under the shear stress of a passing Love wave, the fault would be able to slide from the surface to a depth of 120 m without hydrostatic pressure, or 240 m with hydrostatic pressure, if the conditions and properties are similar to those assumed. If the effective coefficient of friction is lower than 0.7, the sliding region could extend correspondingly deeper. It should be noted here that for simplicity the x-direction above was taken as if the wave had normal incidence at the fault.

It is likely that an incident Love wave would be reflected at the fault plane in light of the greatly reduced thickness of alluvium on the upthrown side of the fault (described in the introduction). Although the abruptness of the thickness decrease for the alluvium has not been documented by the seismic studies to date, it is likely that the fault boundary is a sharp one, and that near vertical contact of alluvium with consolidated sedimentary rocks provides a significant contrast in shear velocity.

2. Site amplification.

The differences between my observation of motion at the fault scarp and those of other workers cited above strongly suggest that there was anomalous amplification of motion in the vicinity of my observation. The lateral extent of this amplification of motion is unknown. One cause of amplification may be reinforcing internal reflections of incident waves, such as a Love wave, in the local affected block. As noted above, one reflector may have been the fault plane itself. However, a second reflector in the vicinity is difficult to define.

As described in the introduction, the site had certain peculiar characteristics, including the southwest bounding thrust fault, the compressive bowing of the surface, and the presence of water in the fault zone gap (at A in Figure 2). These characteristics may have contributed to amplification of motion.

A hypothesis that may explain both the anomalous nature of the site and the amplification of shaking from the aftershock was suggested to me by Ray Wilson (written commun., 1985). Wilson suggests that the zone between the fault scarp and the small thrust may be a lateral spread landslide generated during the mainshock. Formation of such a lateral spread depends on the existence of a slide plane. The clay layer observed in the trench in the upthrown block, presumed to be present at several meters depth in the downthrown block, could provide the slide plane if it were saturated at the time of the main shock. Then, if this zone was also saturated during the aftershock, shaking from the aftershock could have reactivated the lateral spread, decoupling the block along the clay layer. The duration of the shaking at the site could be explained by an underdamped resonance of the block itself. This hypothesis is somewhat more satisfactory than the incident Love wave hypothesis since it accounts for many of the details of the observation.

DISCUSSION AND CONCLUSIONS

The large amplitudes of motion observed accompanying the dynamic shaking from the aftershock and the relative motion of the two sides of the fault scarp are important

for earthquake hazards assessments and for interpreting fault offsets observed for earthquakes in the historic or the geologic record. With regard to the second point, it is important to discover whether such dynamic shaking as I observed could result in permanent fault offsets. There may be some connection between the oscillations that I observed and the phenomenon of triggered slip. This phenomenon was hypothesized by Allen et al. (1972) when they reported that displacements of 10-25 mm occurred along 20-30 km segments of the Superstition Hills, San Andreas, and Imperial faults within four days of the 1968 Borrego Mountain earthquake. The Borrego Mountain earthquake took place on the Coyote Creek fault, 45-70 km from the other faults. Similar displacements were also observed on the Superstition Hills fault (Fuis, 1982), and on the San Andreas fault (Sieh, 1982) associated with the 1979 Imperial Valley earthquake which occurred on the Imperial Valley fault. In neither case were the remote faults part of the aftershock zones of the mainshock. Allen et al. (1972) hypothesized that dynamic shaking accompanying the main shock caused the displacements on the remote faults, and that the displacements released strain which had accumulated tectonically. In the case of the Borah Peak aftershock, the observed oscillatory motion of opposite sides of the fault was horizontal, while the tectonics there are normal faulting with dominantly vertical offsets. If the dynamic shaking there resulted in any permanent offset, it would be horizontal, and the offset would not be consistent with the tectonics. In cases of suspected triggered slip, it is important to know whether the magnitude and orientation of the offsets reflect the tectonics of the area or simply the dynamic shaking event itself.

With regard to earthquake hazards assessments, if the large observed displacements were caused by amplification, the hazards associated with an earthquake of a given magnitude would have to be re-evaluated in terms of the possibility for such amplification. Such a re-evaluation would require far more data on the phenomenon than is available from this particular observation.

ACKNOWLEDGEMENTS

The Department of Geological Sciences, University of Colorado provided travel funds for the field work for this research. Information related to the Borah Peak earthquake, the Oct. 29 aftershock, and the geology and surface expression of the fault at the observation location were kindly provided by: J. Boatwright, A. Crone, D. Doser, J. Pelton, S. Plymell, and W. Richins.

REFERENCES

Aki, K., and Richards, P.G., 1980, Quantitative Seismology (v. 1): W.B. San Francisco, Freeman and Co., p. 260-264.

Allen, C.R., Wyss, M., Brune, J.N., Grantz, A., and Wallace, R.E., 1972, Displacements on the Imperial, Superstition Hills, and San Andreas faults triggered by the Borrego Mountain earthquake of April 9, 1968: U.S. Geological Survey Professional Paper 787, p. 87-104.

Birch, F., 1942, Handbook of Physical Constants, Geological Society of America Special Paper 36.

Clark, S.P., 1966, Handbook of Physical Constants, Geological Society of America Memoir 97.

Crone, A., Machette, M., Bonilla, M.G., Lienkaemper, J.J., Bucknam, R. Pierce,K.L., and Scott, W., 1985, Characteristics of surface faulting accompanying the Borah Peak earthquake, central Idaho, in Workshop XXVIII on the Borah Peak Earthquake: U.S. Geological Survey Open-File Report, in press.

Crosthwaite, E.G., Thomas, C.A., and Dyer, K.L., 1970, Water resources in the Big Lost River basin, South-central Idaho: U.S. Geological Survey Open-File Report PR-WRD-3/17/70.

Fuis, G., 1982, Displacement on the Superstition Hills fault caused by the earthquake, in The Imperial Valley, California, Earthquake of October 15, 1979: U.S. Geological Survey Professional Paper 1254, p. 145-154.

Paterson, M.S.,1978, Experimental Rock Deformation - the Brittle Field: New York, Springer-Verlag.

Pelton, J., Meissner, C.W., Waag, C.J., and Wood, S.H., 1985, Shallow seismic refraction studies across the Willow Creek fault rupture zone and the Chilly Buttes sand boils, in Workshop XXVIII on the Borah Peak Earthquake: U.S. Geological Survey Open-File Report, in press.

Scherbaum, F., Roecken, C., Ware, R., and Wyss, M., 1985, Magnetic and soil gas measurements along the surface rupture of the Borah Peak earthquake of October 28, 1983, in Workshop XXVIII on the Borah Peak Earthquake: U.S. Geological Survey Open-File Report, in press.

Sieh, K., 1982, Slip along the San Andreas fault associated with the earthquake, in The Imperial Valley , California, Earthquake of October 15, 1979: U.S. Geological Survey Professional Paper 1254, p. 155-160.

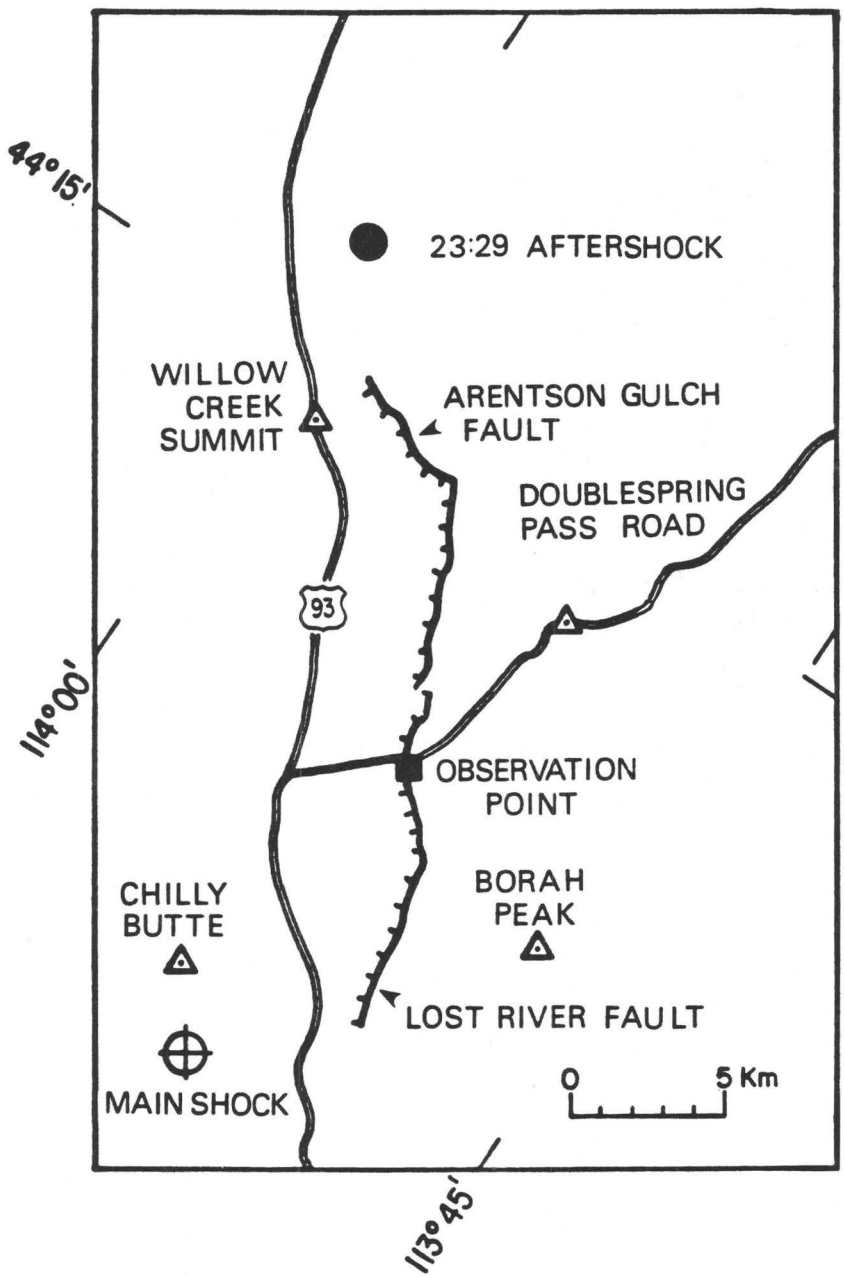

Figure 1. Location map for the Borah Peak earthquake surface rupture, the $M_L = 5.5$ aftershock, and the observation location.

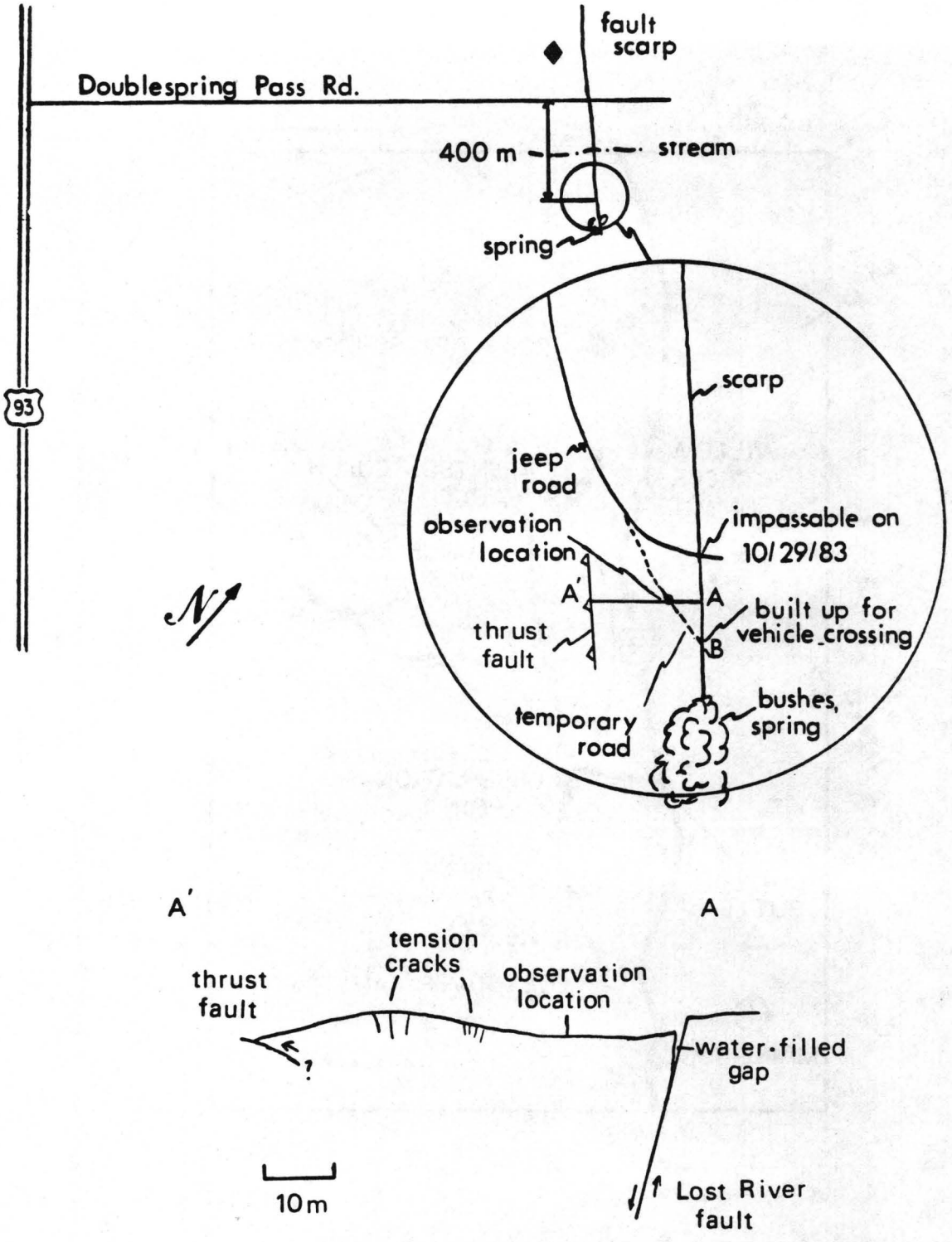

Figure 2. Sketch map and cross section of the observation location. "A" indicates the location of 1.5 m high scarp; "B" indicates the location of ~ 20 cm high individual cracks making up the scarp. The diamond shows the position of Boatwright's instrument.

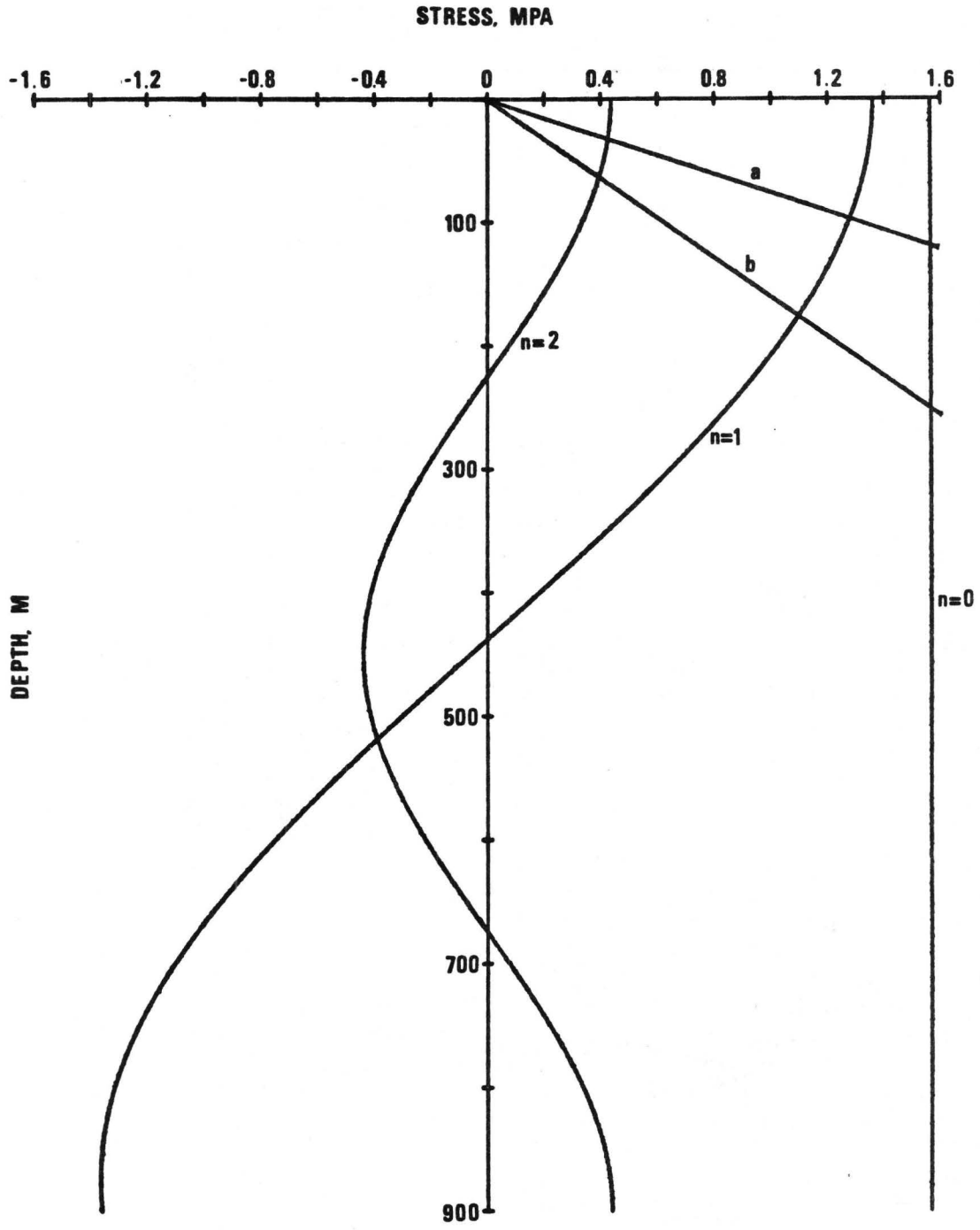

Figure 3. Love wave shear stress τ_{zy} and frictional stress resisting sliding as a function of depth. Numbered curves indicate the maximum shear stress τ_{zy} in a given cycle for the n=0, 1, and 2 modes. Line (a) indicates frictional stress on a fault plane of zero-strength in the presence of lithostatic stress and a coefficient of friction of 0.7. Line (b) is the same as line (a), but including hydrostatic pore pressure.

THE 1983 BORAH PEAK, IDAHO, EARTHQUAKE:

GEODETIC EVIDENCE FOR DEEP RUPTURE ON A PLANAR FAULT

Ross S. Stein

U.S. Geological Survey
Menlo Park, California 94025

Sergio E. Barrientos

C. F. Richter Laboratory
University of California
Santa Cruz, California 95046

Abstract. Geodetic elevation changes record the broad-scale surface deformation associated with the October 28, 1983, Borah Peak, Idaho, M_s=7.3 earthquake on the Lost River fault. During the coseismic period (1933-84), the crest of the Lost River Range rose 0.2 m, and adjacent Thousand Springs Valley subsided as much as 1.2 m. Observational uncertainties of the leveling data sum to less than 20 mm over the 70-km-long first-order leveling route. A planar fault extending from the surface to a depth of 13±3 km and dipping 45°±5° SW provides the best fit to the geodetic data. We find no evidence to support a hypothesis that the fault is listric or dips less steeply with depth, nor is slip on an upper-crustal detachment surface required by the deformation data. The mean coseismic slip on the fault is modeled to be 2.15±0.10 m; the estimated static-stress drop is 3±1 MPa. The geodetic moment of the Borah Peak event, $M_o = (3.3\pm1.1)\times10^{19}$ N m [$(3.3\pm1.1)\times10^{26}$ dyne cm], is similar to that of the 1954 Fairview Peak, Nevada, M_s=7.1 earthquake and is one-third that of the 1959 Hebgen Lake, Montana, M_s=7.5 event. These are the largest well-studied events in the Basin and Range province and the Intermountain seismic belt. Seismic and geodetic data from all three earthquakes are consistent with planar faults dipping 40°-50° and extending to a depth of 12-15 km, possibly within the brittle-ductile transition in the crust. From this evidence, listric and upper-crustal detachment faults would not appear to be the principal source of major shocks in the Great Basin.

INTRODUCTION

More than a century has passed since Joseph LeConte first advanced the hypothesis that earthquakes accompany permanent slip on faults. LeConte's insight crystallized from study of the 1872 Inyo, California, M~8 shock (Figure 1), one of the largest historical earthquakes in the Western United States. Writing in 1878, LeConte asserted that the earthquake resulted from slip on a steeply dipping normal fault bounding the Sierra Nevada from Owens

Valley, whose floor lies 3 km beneath the Sierran crest. LeConte was confronted with structures in the Basin and Range province of California quite similar to those at Borah Peak in the Intermountain seismic belt of Idaho, including a fault etched into the landscape at the foot of the State's highest peak. From these clues, LeConte grasped that the slip of a single shock is only a small increment in the total slip on the fault:

> "...we cannot estimate this [cumulative] slip as less than 15,000 feet. It is probably much more. It is almost certain that it was a slight re-adjustment of this slip which caused the Inyo earthquake of March 1872." (LeConte, 1878, p. 101)

Today, we still principally depend on large earthquakes and the permanent deformation they produce at the surface to investigate active faults and their earthquake potential.

Three large (M_s>7) normal shocks have struck in the Basin and Range province and the Intermountain seismic belt of the Western United States during the past half-century. From this modern earthquake sample and from geologic observations, we must assess seismic hazards along the major Wasatch Front and other active fault zones in the seven Western States shown in Figure 1. The damage that can be inflicted by large earthquakes in this region depends, first, on the proximity of the active faults to population centers and, second, on the subsurface geometry of these faults. We do not know whether active faults in the Great Basin and the Intermountain seismic belt commonly become listric (decrease in dip with depth to become flat lying) or dip steeply at depth. Resolution of this question is crucial because rupture of listric and detachments faults implies a shallower seismic source (4-10 km deep) farther from the fault trace than does rupture at the base of the crust (15-20 km deep) on high-angle planar faults. Deep seismic-reflection data from the Great Basin (e.g., Allmendinger et al., 1983; Crone and Harding, 1984; Smith and Bruhn, 1984) have been offered as support for the existence of shallow and listric normal faults rooted in subhorizontal detachments and shear zones in the upper crust, a geometry first proposed by Wernicke (1981). Steeply dipping structures can be poor reflectors, however, that make interpretation of many of the reflection profiles uncertain.

Analysis of the faults that have slipped in large earthquakes provides a direct test of the hypothesis of pervasive detachment surfaces. In this study, we use the geodetic record of the Borah Peak earthquake to distinguish between planar and listric fault rupture and to identify the maximum depth of coseismic fault slip. The results of geodetic modeling are incompatible with listric faulting or upper-crustal detachment. In addition, we compare the geodetic record for the Borah Peak earthquake with the record for the 1954 Fairview Peak, Nevada, and the 1959 Hebgen Lake, Montana, earthquakes to argue that low-angle detachments do not explain any of the large modern Great Basin and Intermountain-seismic belt earthquakes.

The precision and spatial coverage of the geodetic data for the Borah Peak earthquake surpass all records of vertical-elevation changes associated with large normal-faulting earthquakes. The 50-km-long leveling route that crosses the Lost River fault and the 16-km-long route that parallels the fault permit estimation of the fault geometry and slip independent of the seismic data and nearly independent of the surface geology. We compare the coseismic

model to the earthquake-source parameters measured at much shorter periods from seismic radiation, and we compare the coseismic deformation to the cumulative deformation preserved in the geologic structures.

GEODETIC DATA

The coseismic elevation changes were obtained by subtracting the relative heights of bench marks (BM's) surveyed after the earthquake in November 1983 and July 1984 from the heights of the same BM's surveyed before the earthquake in 1933 and 1948 (Figure 2a). Figure 3 (top) shows the profile of coseismic elevation change, projected onto an azimuth normal to the Lost River fault. We note that what we refer to as the "coseismic period" includes the 50 years preceding the earthquake and the 8 months after it. We assume that no artificial subsidence and no preearthquake deformation took place during this period. Tests of this assumption are discussed in the next section. The postseismic changes along a limited segment of the leveling route during 1-8 months after the main shock are shown separately in Figure 3 (middle). All leveling was conducted by the National Geodetic Survey (NGS); the 1983 and 1984 survey were carried out at the request of the U.S. Geological Survey.

In spirit leveling, height differences are measured between adjacent BM's by sighting a horizontal telescope on graduated rods. All data were corrected for level collimation (horizontal plumb of the level telescope), rod excess (calibration of rod graduations), rod thermal expansion (rod-length change as a function of temperature), and atmospheric refraction (bending of the line of sight through vertically stratified air). The observed rod temperatures were used for all surveys to compute rod expansion. For the 1933 and 1948 surveys, the thermal coefficient of expansion was assumed; for the 1983 and 1984 surveys, it was measured. The 1933 and 1948 surveys were corrected for refraction by using the REDUC4 program of Holdahl (1981), in which temperature gradients are modeled as a function of time and location, whereas the 1984 observations were corrected following Kukkamaki (1938), using observed temperature differences made at every instrument setup.

Survey errors. Potential sources of noise in the data include random and systematic surveying errors and nontectonic subsidence due to ground-water withdrawal. Estimated cumulative random error for the observed elevation changes nowhere exceeds 20 mm. Briefly, BM's are spaced 1-2 km apart (a pair of adjacent BM's is called a section). The elevation difference over each section can be obtained once or twice during a survey, by surveying forward and backward. If double-run, the section is rejected and rerun if the two levelings do not agree within the prescribed section tolerance. The mean difference for all (forward-backward) runnings must not differ significantly from zero, and the standard deviation of the difference, β, gives a good indication of the random error per section. The random error, σ, should propagate with the square root of the distance leveled: $\sigma = \alpha L^{1/2}$, where σ is in millimeters, α is a function of β, and L is the distance in kilometers (Bomford, 1971). In principle, if β is Gaussian distributed and the survey is double-run with BM's spaced 1 km apart, α should be about 1/3 of β. Because some of the 1984 survey was single-run using the procedure of Whalen and Balazs (1977), we set $\alpha = \beta$. Table 1 lists the values for α and β. Thus, the cumulative random error for the 70-km-long postearthquake survey is $1.38\ \text{mm}(L^{1/2}) = 12$ mm. For the 1933 survey, $\beta = 1.83$ mm, slightly larger than

that for 1983 or 1984. Because the 1948 leveling segment was single-run, β cannot be accurately assessed. We assume here that a value of $\alpha = 2.0$ mm provides a fair estimate for the combined 1933 and 1948 surveys; the cumulative error for the preearthquake leveling is then 17 mm. The random error for elevation change differenced from the preearthquake and postearthquake surveys becomes $(\alpha_1^2+\alpha_2^2)^{1/2} L^{1/2}$, were the subscript 1 denotes 1984 and the subscript 2 denotes 1933/48. The cumulative or maximum expected error is 20 mm, about the size of the dots in Figure 3, and only about 1-2% of the coseismic signal. Table 1 lists the leveling specifications.

We examined all surveys for elevation dependent error, using the method of Stein (1981), and found none. The procedure in which we seek correlation between geodetic tilt and topographic slope is briefly explained in Appendix 2. The method is limited to detection of errors greater than 20 ppm times the topographic height difference, permitting a maximum unresolved systematic error of 12 mm (20 ppm x 600 m) for either the coseismic or postseismic survey. Although tilt and slope can be related tectonically, McTigue and Stein (1984) showed that topographic amplification of stress produces elevation-dependent correlations of only a few parts per million. Because the end points of the coseismic survey lie at nearly the same elevation, these BM's are essentially unaffected by slope-dependent errors.

Subsidence Errors. Hydrologic data demonstrate that near-stasis of the water table during the coseismic period (1933-84) makes subsidence due to fluid withdrawal unlikely. A reconnaissance water-resource survey of the valley (Stearns et al., 1938, Plate 31) indicates that the water stood 3-6 m below the ground surface in 1930-37 in the vicinity of BM 6345 USGS (BM 22, Figure 2a). USGS observation well 9N22E-06CCA1, which was drilled about 150 m west of BM 22 (6345 USGS) in 1967, was observed in 1967/68, 1978, and 1983/84 (see Figure 2a). The water table stayed 5.4±0.9 m below the surface during 1967-84, indistinguishable from the 1930-37 level obtained by reconnaissance. USGS observation well 9N21E-14BBC1, located 4 km west of P15 (BM 23, Figure 2a), provides a continuous hydrograph during 1966-84. This well also shows a constant hydraulic head with only 1-m seasonal fluctuations (see record in Whitehead, 1985). The water table remained static because the alluvial aquifer beneath the leveling route has been recharged by canal diversions from the Big Lost River since 1931 (Crosthwaite et al., 1971).

The 1933 leveling (BM's 1-23) and the 1948 leveling (BM's 22-38) overlap one section at BM's 22-23 (6345 USGS - P15). We used the junction section to test for tilt during 1933-48. The 1933 and 1948 measurements of height difference over the junction section differ by only 1.56 mm, less than the expected random error for either survey. The absence of measurable tilt during this 15-year period in Thousand Springs Valley supplies a weak test of our assumption of negligible nonearthquake deformation or subsidence during the coseismic period.

To summarize, the cumulative uncertainty of BM displacements at each end of the leveling route is 20 mm; the uncertainty of points of greatest relief (km 30-km 40, Figure 3) is nearly the same, owing to smaller random error and a larger potential for slope-dependent error. The uncertainty in elevation change of adjacent BM's is less than 2 mm.

ANALYSIS

Coseismic Model. We seek the simplest dislocation that can explain the observed elevation changes, subject to surveying errors. Fault slip is approximated by uniform displacement on a rectangular surface embedded in an elastic half-space, using the expressions of Mansinha and Smylie (1971). We neglect changes in elastic moduli with depth and the stress singularities at the perimeter of the rectangular model fault plane.

Our strategy was, first, to model a fault of infinite length along strike, find the fault dip and width (downdip dimension) that gives the best fit to the data, and scale the elevation change to estimate the slip. We then model a fault with finite length, striking parallel to the surface rupture, using the two-dimensional results as a guide. By trial and error, we find the dip, width, and fault length that minimize the residuals in a least-squares sense. Faults with only pure dip slip were modeled because a lateral slip component of ±10° (up to 17% of the dip slip) cannot be discriminated, given the absence of BM's at the fault ends. We made no attempt to make the model fault consistent with the main-shock hypocenter, its fault-plane solution, or the locations of aftershocks. Although the distribution of BM's does not permit location of the north fault end, quite high sensitivity to the termination of slip at the south end of the fault allows the south fault end to be located to within about ±1 km. The geodetically determined coseismic elevation change across the fault at Double Springs Pass Road was 1.56 m on November 16, 1983 and 1.58 m by June 29, 1984, equivalent to the 1.52-m surface scarp throw measured at Double Springs Pass Road in October 29, 1983 by Crone and Machette (1984). The 1.5-km spacing of BM's across the fault (Z51 - T10N/22E, BM's 17-18, Figure 3) limits resolution of the slip distribution in the uppermost kilometer, and so we let the model fault cut the surface.

Model Fit. Elevation changes at 90% of the BM's are satisfied within expected random and systematic errors (20 mm) by the coseismic model (Figure 4). The parameters and uncertainties (representing a 5% increase in model residuals) of the coseismic model are: dip, 45°±5°; slip, 2.1±0.1 m; width, 18±2 km; and fault length, ≥21 km. Following Kanamori and Anderson (1975) for dip-slip faults, the static-stress drop for the coseismic model is 3.0±0.8 MPa (30±8 bars). From the displacement spectra of teleseismic P waves, Boatwright and Choy (1985) estimate a dynamic-stress drop of 2.8 MPa for the initial rupture event and a static-stress drop of 1.7 MPa bars for the entire fault. The leveling data constrain the fault to be at least 21 km long. Combination of this value with those for the fault slip and width yields a minimum geodetic moment, M_o, of 2.1×10^{19} N m (3×10^{26} dyne cm), under the assumption that the shear modulus is 3×10^4 MPa (3×10^5 bar). The 36-km-long 20-day aftershock zone (Figure 2b) provides an estimate of the maximum fault length and places an approximate upper bound on the geodetic moment of 4.5×10^{19} N m. Barrientos et al. (1985) find $M_o = (1.85 \pm 0.17) \times 10^{19}$ N m by modeling the P and SH waves from synthetic seismograms, Boatwright and Choy (1985) found $M_o = (1.7 \pm 0.2) \times 10^{19}$ N m, and Doser (1985a) obtained $M_o = 2.9 \times 10^{19}$ N m. Although the calculated geodetic moment may exceed most estimates of the seismic moment, these values do not differ significantly.

Critical features of the model fit are the decay of deformation on the upthrown block with distance from the fault (BM's 1-17, Figure 4), the

decreasing tilt of the downthrown block to the west (BM's 18-30), and the gentle rise or bulge 20-30 km west of the fault (BM's 31-39). The kinks in the model at BM's 22 and 26 result from the azimuth change of the leveling route, which is shown together with the contours of elevation change predicted for the model in Figure 2a. Three isolated BM's that showed elevation changes about 400 mm larger than adjacent BM's were eliminated from the model fitting as unstable. The misfitting BM closest to the fault trace on the downthrown block (BM 18, a section corner) was used in the modeling, although it does not meet the requirements for first-order survey marks and may have been unstable. Table 2 lists the model parameters.

Variation of slip along strike. A 16-km-long segment of the leveling route that is aligned parallel to the Lost River fault (BM's 21-27, Figure 2a) affords a comparison of surface slip and buried fault slip. The fault throw measured by Crone and Machette (1984) along this segment (from Poison Spring southward to Elkhorn Creek) is shown in Figure 5 (top) together with the subsidence on the downthrown block measured from releveling (middle). The string of BM's lie 4-5 km basinward from the fault trace; the locations of the BM's and surface break are shown on the accompanying map (Figure 5, bottom). Both the subsidence and the displacement on the surface rupture diminish toward the main shock epicenter. Slip must greatly diminish or terminate about 4-5 km northwest of the main shock, close to the south limit of surface rupture (the end of the model fault is situated at km-17 in Figure 5). Although this result may appear unusual, Archuletta (1984) found that slip associated with the strike-slip 1979 Imperial Valley, California, M_L=6.6 earthquake was a minimum 5 km north of the main shock and reached a maximum 30 km north of the epicenter. Barrientos et al. (1985) demonstrate that these BM's are most sensitive to slip within a depth interval of 2-7 km, and are insensitive to slip at the surface. Barrientos et al. (1985) also show that uniform slip of 2 m at this depth fits the observations significantly better than if the surface slip is imposed at depths of 2-7 km. Thus much of the ≈1-m-large variation of ground rupture is superficial and not intrinsic to the slip distribution at seismic depths.

Postseismic Model. The postseismic elevation changes (Figure 3, middle) can be fit to the coseismic fault model with slip of 50 ± 15 mm, roughly 2% of the coseismic slip, less than has been measured for other dip slip events during similar time periods. The fit is, however, poor on the upthrown block. The summed geodetic moment of the modeled afterslip at Borah Peak is ~5-10 x 10^{24} dyne-cm. Zollweg (1985) found that seismic moment release associated with aftershocks during the same period summed to about 7 x 10^{22} dyne-cm. Thus essentially all of the afterslip measured by releveling occurred as fault creep.

During nearly the same postseismic period (1-6 months after each earthquake) that the Borah Peak showed continued deformation, the 1971 M_s 6.4 San Fernando, CA, thrust earthquake showed about 3% of the coseismic slip (Savage and Church 1975), and the 1975 M_L 5.7 Oroville, CA, normal event slipped 22% of the coseismic magnitude (Savage et al., 1977). The 1954 Nevada quake slipped about 5% of the coseismic value 60-144 months after the event (Savage and Church 1974) and the 1959 Hebgen Lake earthquake showed about 200 mm of postseismic uplift 11 months to 24 years after the shock in a region of less than 50 mm coseismic uplift (Reilinger, 1985).

INTERPRETATION

Absolute Elevation Changes. Leveling across the Lost River Range and Thousand Springs Valley permits assignment of absolute elevation changes. Because the end points of the survey extend outside the region of observed or modeled coseismic deformation, they can be held as fixed. The end points (BM's 1 and 37, Figure 4) give the same elevation change within the measurement uncertainty (20 mm). Very broad wavelength tilts with magnitudes less than 1 ppm would go undetected, however, as would uniform vertical displacement over distances greater than 50 km.

Absolute uplift associated with the earthquake is 0.3 m (at BM 17); the crest of the Lost River Range in the vicinity of Borah Peak rose about 0.2 m (Figure 4). Absolute uplift of the ranges bounding a normal-faulting earthquake has never before been demonstrated because leveling was ambiguous or absent on the upthrown fault block. The maximum coseismic subsidence measured was 1.2 m at the east margin of Thousand Springs Valley. From the topographic relief, the geomorphic expression of the fault scarp, and the inferred thickness of the basin deposits, Scott et al. (1985) argue that 3 km of dip slip has accumulated over the past 4-7 m.y. on the Lost River fault, at a rate of 0.2-0.4 mm/yr. Unlike the coseismic displacement, however, the cumulative Pliocene displacement appears to be equally distributed between subsidence (1,500 m of valley fill) and uplift (1,500-2,000 m of topographic relief; see Figure 4, bottom). The discrepancy between the earthquake and geologic displacements may be due to the contribution of interseismic deformation.

The coseismic deformation exhibits a strong resemblance to the structure of other basins and ranges in south-central Idaho. The zones of coseismic subsidence and uplift are each about 15 km wide, similar to the width of Thousand Springs Valley and the Lost River Range (Figure 1). Both sides of the fault were tilted down to the east during the earthquake, a tilt consistent with the stratal dips of sedimentary rocks in the basin and the range (Figure 4). We interpret these fundamental similarities to indicate that the Borah Peak earthquake typifies the events which built the ranges.

Planar versus listric normal faulting. The leveling data can be simply explained by a planar rupture extending from the surface to a vertical depth of 13±3 km. Diminished slip at greater depths is possible because the model prescribes uniform slip everywhere on the fault. The fault model is consistent with analysis of the main-shock and aftershocks located by Richins et al. (1985), plotted in Figure 4. The surface deformation 15-30 km west of the fault depends almost exclusively on the dip of the deepest part of the fault situated beneath this region. The near-fault BM's on the upthrown block are sensitive to the fault dip in the upper 10 km; the good fit on the upthrown block provides persuasive evidence for a constant dip with depth. Compare the planar model (Figure 4) with the best fit for a listric normal fault (Figure 6) that passes through the main shock and aftershocks located by Richins et al. (1985). The fit to the listric model is poor on both the upthrown and downthrown blocks at large distances from the fault trace because the dip is too gentle and the fault is too shallow. No distribution of slip with depth on a listric fault can satisfy the observed data. Independent evidence for a planar geometry for the Lost River fault is supplied by a study of the 43 largest aftershocks by Smith et al. (1985), which showed no significant variation in dip of the nodal planes with depth.

Coseismic surface deformation steepens near the fault on both the upthrown and downthrown blocks (Figure 4); this is a dominant feature of the profiles of the data and the model. The pattern of increasing dip of strata toward the fault in the post-Tertiary structure (Figure 4, bottom) has been interpreted as caused by block rotation or void accommodation resulting from a listric fault geometry (Anderson et al., 1983). Increasing stratal dips toward the fault may, instead, be the product of elastic deformation associated with repeated earthquakes and thus be unrelated to block rotation.

Comparison of the Borah Peak, Fairview Peak, and Hebgen Lake Events. The fault dips estimated from geodetic elevation changes for the Fairview Peak, Nevada, M_s=7.1 (Savage and Hastie, 1969; Snay et al., 1985) and the Hebgen Lake, Montana, M_s=7.5 (Savage and Hastie, 1966; Doser, 1985b) events and for the Idaho shock average about 45°, less than the dips typical of faults at the surface (Meyers and Hamilton, 1964; Crone and Machette, 1984) but possibly greater than the subsurface dips inferred from seismic-reflection profiles (Wernicke, 1981; Allmendinger et al., 1983). Table 2 lists the geodetically determined fault parameters for these three events.

Neither the Nevada nor the Montana coseismic models was fitted to geodetic observations from the upthrown fault block, a circumstance that greatly hampers resolution of the fault geometry. The geodetic record for the Montana earthquake also lacks observations in the region 20-30 km from the fault on the downthrown block. The Nevada data are subject to systematic leveling-survey errors that have yet to be removed and that limit their utility (see Savage and Church, 1974, Figure 5). As can be seen in Figure 4, measurement of deformation at distances greater than the focal depth from the fault trace is critical to distinguish between planar and listric normal faulting and to establish absolute elevation changes. Although the 1954 and 1959 events may have occurred on listric faults, the evidence nevertheless favors a similar planar geometry for all three faults. The few well-studied shocks of M<7 also conform to this geometry: The 1954 M_s=6.8 earthquake on the Dixie Valley fault (Figure 1) also nucleated at a depth of 15 km on a fault dipping about 50°-60° (Okaya and Thompson, 1985; Snay et al., 1985). Arabasz et al. (1980) found a 13-14-km maximum depth of aftershocks associated with the 1975 Pocatello Valley, Idaho, M_s=6.0 earthquake (Figure 1).

Implications for Earthquake Prediction in the Great Basin. The deepest part or base of a seismic fault, which may lie within the brittle-ductile transition in the crust, is a plausible site for slippage before an earthquake. Detection of preseismic fault slip at a depth of 12-15 km is a much more challenging task than if premonitory slip were to take place on a detachment surface located at one-third that depth. To monitor slip at a depth of 12-15 km on a fault dipping 45°, geodetic surveys must extend from the fault trace for about 30 km on the downthrown block, and they must have sufficient precision to detect broad-wavelength deformation. A 4 by 4-km dislocation patch situated at the base of the fault would cause the ground to subside less than 20 mm per meter of fault slip. If the zone of preseismic slippage extended 35 km along strike (e.g., a 4 by 35-km strip beneath the entire Borah Peak rupture surface), then as much as 90 mm of subsidence per meter of buried slip would take place (Figure 7). The wavelength of the deformation would be about 25 km normal to the fault strike. The amplitude of the deformation decreases, and its wavelength increases, as the dip decreases from 90° to 0°, and so the gentler the fault dip, the more difficult would be the detection of

slip at a given depth. Occurrence of the peak elevation change (subsidence) within the basin would make discrimination of tectonic deformation from ground-water-related subsidence difficult. Leveling restricted to within 10 km of the fault trace will be insufficient to detect preseismic slip unless it takes place near the ground surface.

CONCLUSIONS

The best record of coseismic elevation change ever measured for a large normal faulting event in the United States is most compatible with a planar high-angle-fault rupture. Similarity of the fault dip (40°-50°) and the maximum depth of fault slip (12-15 km) for the Borah Peak, Hebgen Lake, Fairview Peak, and Dixie Valley events suggests that steeply dipping planar faults dominate in the Great Basin and the Intermountain seismic belt. These are the largest events since the 1915 Pleasant Valley, Nevada, M=7-3/4 shock (Doser, 1985a). The shared maximum depth of faulting lends evidence to the hypothesis of Sibson (1982) and Smith and Bruhn (1984) that this depth corresponds to the brittle-ductile transition in the crust. Despite widespread acceptance of listric faults and detachments as the principal faults in the Great Basin, the record of large earthquakes unequivocally points toward planar high-angle faults that cut through the entire seismic crust. If the Wasatch fault zone shares the geometry of the Hebgen Lake and Lost River faults, seismic-reflection profiles should be reexamined for deep planar bounding-fault structures, as Okaya and Thompson (1985) have done in Dixie Valley, Nevada.

Detection of premonitory elevation change and tilt caused by slip at the base of faults with geometries similar to that of the Lost River fault will be demanding and require precision-leveling deformation surveys that span the fault and the downthrown block for at least 30 km, or twice the probable depth of the fault.

ACKNOWLEDGMENTS

We are indebted to the lightning speed, skill, and tenacity of the NGS leveling crew headed by Curt Smith and guided by Bob Martine and Emery Balazs. Discussions with our colleagues at the Borah Peak Workshop and reviews by Mary Lou Zoback, Bob Smith, John Langbein, and Wayne Thatcher greatly improved our understanding.

APPENDIX

1. Volumetric strain changes and postseismic effusion. About one cubic kilometer of excess water flowed from streams and springs during the first 6 months after the Borah Peak earthquake (see Whitehead, 1985). We calculated the near-surface volumetric strain changes caused by the fault slip to investigate whether the flowage correlates with regions of postseismic compression. We found no convincing correlation.

The volumetric strain change, $\Delta V/V$, is equal to the sum of the principal strains ($\varepsilon_1 + \varepsilon_2 + \varepsilon_3$), where the 1, 2, and 3 axes are oriented north, east, and vertically downward, respectively. If Poisson's ratio is taken to be 1/4, then the condition of plane strain, that the normal stress acting on the free surface (σ_3) must equal zero, can be used to obtain the expression, $\varepsilon_3 = -(\varepsilon_1 + \varepsilon_2)/3$. Then $\Delta V/V = 2/3(\varepsilon_1 + \varepsilon_2)$ at the surface. This relation is a valid approximation within the uppermost few kilometers. The horizontal strains ε_1 and ε_2 are calculated using the coseismic dislocation model. $\Delta V/V$ is plotted in Figure 8, with sites of increased spring and stream flow reported by Whitehead (1985) and Wood (1985). The largest strains are compressive, and they are centered over the fault. However, 65% of the sites of effusion locate in regions with less than ± 2 ppm strain change. The remaining sites are equally distributed in zones of compression and dilatation. Most of the increased discharge issued from the Big Lost River Basin, located almost completely outside of the zone of significant static strain changes. The increased discharge of Big Lost River also cannot be explained by increased stream gradients: Comparison of Figure 8 with Figure 2a reveals that no significant tilt took place upstream of the gaging station.

The spectacular Chilly Buttes sediment boils (Waag, 1985) occurred in a region of near-maximum compression (about 40 ppm) as do the Elkhorn Creek and Birch Springs effusion sites. However, seven out of forty sink holes through which the water and sediments erupted predate the 1983 earthquake, and three of these may have erupted during the 1959 Hebgen Lake event, which is 250 km distant (Waag, 1985). If so, the correlation of 1983 sediment boils with coseismic compression should be discounted.

2. Elevation dependent errors. Inaccurate rod calibration corrections and in some cases unmodeled refraction error cause a dependence of elevation change on the elevation. In these cases, elevation change and elevation profiles tend to mimic or mirror each other, and thus disclose a systematic error unaccounted for by random-error estimates. If tilt and slope were correlated, this error could be identified and removed. Regression coefficients were calculated (see Figures 9-11), but the fact that none of these coefficients departs significantly from zero indicates no systematic errors larger than the limits of detection, or 20 ppm x the maximum topographic height difference. This comes to 12 mm (20 ppm x 600 m). Plots of tilt as a function of slope for the data are shown in Figures 9-11. The coseismic data have been segmented into the observations from the upthrown block and those from the downthrown block, because of the 1.56 m dislocation at the fault trace.

Table 1: Leveling Specifications

NGS line	Survey period	Segment (start BM - end BM)	Double- or single-run	Order of leveling	ReRuns (%)	Rejection tolerance (mm)	β (mm)
L24832	6-19-84 to 7-12-84	6345 USGS -E15	Single	1st	4.7	4.0	1.38
		L51-6345; E15-B15	Double	1st	6.8	4.0	
L24812	11-14-83 to 11-23-83	Y51-E15	Double	1st	1.2	4.0	1.09
L12785	8-18-48 to 8-23-48	L51-P15	Single	2nd	4.0	8.4	--
L951	10-4-33 to 11-24-33	6345 USGS - B15	Double	1st	4.8	4.0	1.83

Indices are explained in the text and in Federal Geodetic Control Committee (1980).

Table 2: Large Basin and Range and Intermountain Seismic-Belt Earthquakes

Event	Fault					Width of subsidence (km)	Geodetic moment[3] M_o (10^{19} N m)
	Dip slip (m)	Dip (°)	Length (km)	Width (km)	Depth (km)		
1983 M_s 7.3 Borah Peak	2.1±0.1	45±5	21-36	18±2	13±3	15-20	3.3±1.1
1959 M_s 7.5 Hebgen Lake[1]	8-10	45-60	30	15	15±3	20	10-14
1954 M_s 7.1 Fairview Peak[2]	2.8	38	50	8.5	5	5	5

[1]/From Savage and Hastie (1966) and Doser (1985a). [2]/From Savage and Hastie (1969); net slip is 4.0 m. [3]/The shear modulus assumed to be 3×10^4 MPa; 10^{19} MPa = 10^{26} dyne cm.

REFERENCES

Allmendinger, R.W., J.W. Sharp, D. Von Tish, L. Serpa, L. Brown, S. Kaufman, and J. Oliver, Cenozoic and Mesozoic structure of the eastern Basin and Range Province, Utah, from COCORP seismic-reflection data, Geology, 11, 532-536, 1983.

Anderson, R.E., M.L. Zoback, and G.A. Thompson, Implications of selected subsurface data on the structural form and evolution of some basins in the northern Basin and Range province, Nevada and Utah, Geol. Soc. Am. Bull., 94, 1055-1072, 1983.

Arabazs, W.J., R.B. Smith, and W.D. Richins, Earthquake studies along the Wasatch front, Utah: Network monitoring, seismicity, and seismic hazard, Seismol. Soc. Am. Bull., 70, 1479-1499, 1980.

Archuletta, R.J., A faulting model for the 1979 Imperial Valley Earthquake, J. Geophys. Res., 89, 4559-4585, 1984.

Barrientos, S., S.N. Ward, J.R. Gonzalez-Ruiz, and R.S. Stein, Inversion for moment as a function of depth from geodetic observations and long period body waves of the 1983 Borak Peak, ID earthquake, in Workshop XXVIII on the Borah Peak Earthquake: U.S. Geol. Surv. Open-File Rep., in press, 1985.

Boatwright, J., and G.L. Choy, Teleseismic estimates of the energy radiated by shallow earthquakes, in Workshop XXVIII on the Borah Peak Earthquake: U.S. Geol. Surv. Open-File Rep., in press, 1985.

Bomford, G., Geodesy, Oxford University Press, London, p.226-280, 1971.

Bond, J.G., Geologic Map of Idaho, Idaho Bur. Mines & Geol., Moscow, ID, 1978.

Crone, A.J., and S.T. Harding, Relationship of late Quaternary fault scarps to subjacent faults, eastern Great Basin, Utah, Geology, 12, 292-295, 1984.

Crone, A.J., and M.N. Machette, Surface faulting accompanying the Borah Peak earthquake, central Idaho, Geology, 12, 664-667, 1984.

Crosthwaite, E.G., C.A. Thomas, and K.L. Dyer, Considerations for water use and management in the Big Lost River Basin, Idaho, U.S. Geol. Surv. Open-File Rep., 15 pp., 1970.

Doser, D.I., The 1983 Borah Peak, Idaho, and 1959 Hebgen Lake, Montana, earthquakes: Models for normal fault earthquakes in the Intermountain seismic belt, in Workshop XXVIII on the Borah Peak earthquake: U.S. Geol. Surv. Open-File Rep., in press, 1985.

Doser, D.I., Source parameters and faulting processes of the 1959 Hebgen Lake, Montana earthquake sequence, submitted to J. Geophys. Res., 1985.

Federal Geodetic Control Committee, Specifications to support classification, standards of accuracy, and general specifications of geodetic control surveys, National Oceanic and Atmospheric Administration, Rockville, MD, 46 pp., 1980.

Holdahl, S.R., A model of temperature stratification for correction of leveling refraction, Bull. Geodesique, 55, 231-249, 1981.

Kanamori, H., and D.L. Anderson, Theoretical basis of some empirical relations in seismology, Bull. Seismol. Soc. Am., 65, 1073-1095, 1975.

Kukkamaki, T.J., Uber die nivellitische refraktion, Publ. 25, Finn. Geod. Inst., Helsinki, Finland, 1938.

LeConte, J., On the structure and origin of mountains, with special reference to recent objections to the "Contractional Theory", Am. Jour. Sci., 26(92), 95-112, 1878.

Mabey, D.R., Regional gravity and magnetic anomalies in the Borah Peak region of Idaho, in Workshop XXVIII on the Borah Peak earthquake: U.S. Geol. Surv. Open-File Rep., in press, 1985.

Mansinha, L., and D.E. Smylie, The displacement fields on inclined faults, Seismol. Soc. Am. Bull., 61, 1433-1440, 1971.

McTigue, D.F., and R.S. Stein, Topographic amplification of tectonic displacement: Implications for geodetic measurement of strain changes, J. Geophys. Res., 89, 1123-1131, 1984.

Meyers, W.B. and W. Hamilton, Deformation accompanying the Hebgen Lake earthquake of August 17, 1959, U.S. Geol. Surv. Prof. Pap. 435-I, 55-98, 1964.

Nakata, J.K., C.M. Wentworth, and M.N. Machette, Quaternary fault map of the Basin and Range and Rio Grande Rift provinces, Western United States, U.S. Geol. Surv. Open-File Rep. 82-579, 1982.

Okaya, D.A., and G.A. Thompson, Geometry of Cenozoic extensional faulting: Dixie Valley, Nevada, Tectonics, in press, 1985.

Richins, W.D., R.B. Smith, C.J. Langer, J.E. Zollweg, J.T. King, and J.C. Pechmann, The 1983 Borah Peak, Idaho, earthquake: relationship of aftershocks to the mainshock, surface faulting, and regional tectonics, in Workshop XXVIII on the Borah Peak earthquake, U.S. Geol. Surv. Open-File Rep., in press, 1985.

Reilinger, R., Vertical movements associated with the 1959, M=7.1 Hebgen Lake, Montana earthquake, in Workshop XXVIII on the Borah Peak earthquake, U.S. Geol. Surv. Open-File Rep., in press, 1985.

Savage, J.C., and L.M. Hastie, Surface deformation associated with dip-slip faulting, J. Geophys. Res., 71, 4897-4904, 1966.

Savage, J.C., and L.M. Hastie, A dislocation model for the Fairview Peak, Nevada, earthquake, Seismol. Soc. Am. Bull., 59, 1937-1948, 1969.

Savage, J.C., and J.P. Church, Evidence for postearthquake slip in the Fairview Peak, Dixie Valley, and Rainbow Mountain fault areas of Nevada, Seismol. Soc. Am. Bull., 64, 687-698, 1974.

Savage, J.C., and J.P. Church, Evidence for afterslip on the San Fernando fault: Seismol. Soc. Am. Bull., 65, 829-834, 1975.

Savage, J.C., M. Lisowski, W.H. Prescott, and J.P. Church, Geodetic measurements of deformation associated with the Oroville, California, earthquake, J. Geophys. Res., 82, 1667-1671, 1977.

Scott, W.E., K.L. Pierce, and M.H. Hart, Jr., Quaternary tectonic setting of the 1983 Borah Peak earthquake, Central Idaho, in Workshop XXVIII on the Borah Peak earthquake. U.S. Geol. Surv. Open-File Rep., in press, 1985.

Sibson, R.H., Fault zone models, heat flow, and the depth distribution of earthquakes in the continental crust of the United States, Bull. Seismol. Soc. Am., 72, 151-163, 1982.

Smith, R.B., and R.L. Bruhn, Intraplate extensional tectonics of the eastern Basin-Range: Inferences on structural style from seismic reflection data, regional tectonics, and thermal-mechanical models of brittle-ductile deformation, J. Geophys. Res., 89, 5733-5762, 1984.

Smith, R.B., W.D. Richins, D.I. Doser, R.K. Eddington, L.L. Leu, and G. Chen, The Borah Peak earthquake: Seismicity, faulting kinematics, and tectonic mechanism, in Workshop XXVIII on the Borah Peak Earthquake, U.S. Geol. Surv. Open-File Rep., in press, 1985.

Snay, R.A., M.W. Cline, and E.L. Timmerman, Dislocation model for the 1954 Nevada earthquakes: Preliminary Report, in Workshop XXVIII on the Borah Peak earthquake, U.S. Geol. Surv. Open-File Rep., in press, 1985.

Stearns, H.T., L. Crandall, and W. Steward, Geology and groundwater resources of the Snake River plain in southeastern Idaho, U.S. Geol. Surv. Water Supply Pap. 774, 260 pp., 1938.

Stein, R.S., Discrimination of tectonic displacement from slope-dependent errors in geodetic leveling from southern California, 1953-1979, in Simpson, D.W., and Richards, P.G., eds., Earthquake Prediction, An International Review: Maurice Ewing Ser., v. 4, AGU, Washington, D.C., 1981.

Waag, C.J., Groundwater eruptions and sediment boil formation in the Chilly Buttes area, Borah Peak, Idaho earthquake, in Workshop XXVIII on the Borah Peak earthquake: U.S. Geol. Surv. Open-File Rep., in press, 1985.

Wallace, R.E., Patterns and timing of late Quaternary faulting in the Great Basin Province and relation to some regional tectonic features, J. Geophys. Res., 89, 5763-5769, 1984.

Wernicke, B., Low-angle normal faults in the Basin and Range Province: nappe tectonics in an extending orogen, Nature, 291, 645-648, 1981.

Whalen, C.T., and E. Balazs, Test results of First-Order Class III leveling, NOAA Tech. Rep. NOS 68 NGS 4, Rockville, MD, 1977.

Wood, S.H., Regional increases in groundwater discharge caused by coseismic strain release, tectonic and hydraulic fracturing, in Workshop XXVIII on the Borah Peak Earthquake, U.S. Geol. Surv. Open-File Rep., in press, 1985.

Zollweg, J.E., and W.D. Richins, Later aftershocks on the 1983 Borah Peak, Idaho, earthquake and related activity in the central Idaho seismic zone, in Workshop XXVIII on the Borah Peak earthquake, U.S. Geol. Surv. Open-File Rep., in press, 1985.

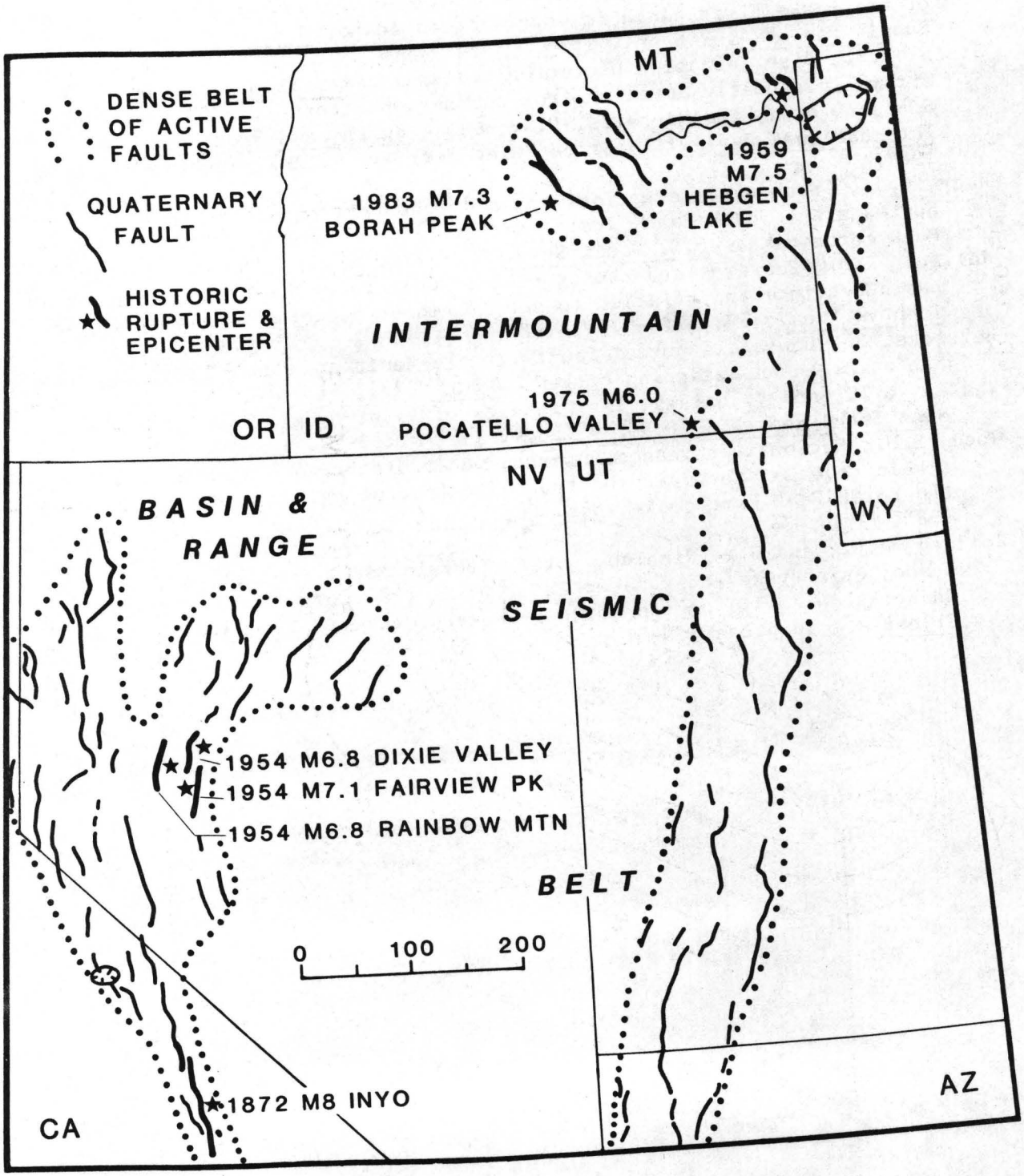

Figure 1. Sketch of Basin and Range province and Intermountain seismic belt of the Western United States, after Nakata et al. (1982), Wallace (1984), and Scott et al. (1985), showing locations of earthquakes discussed in text.

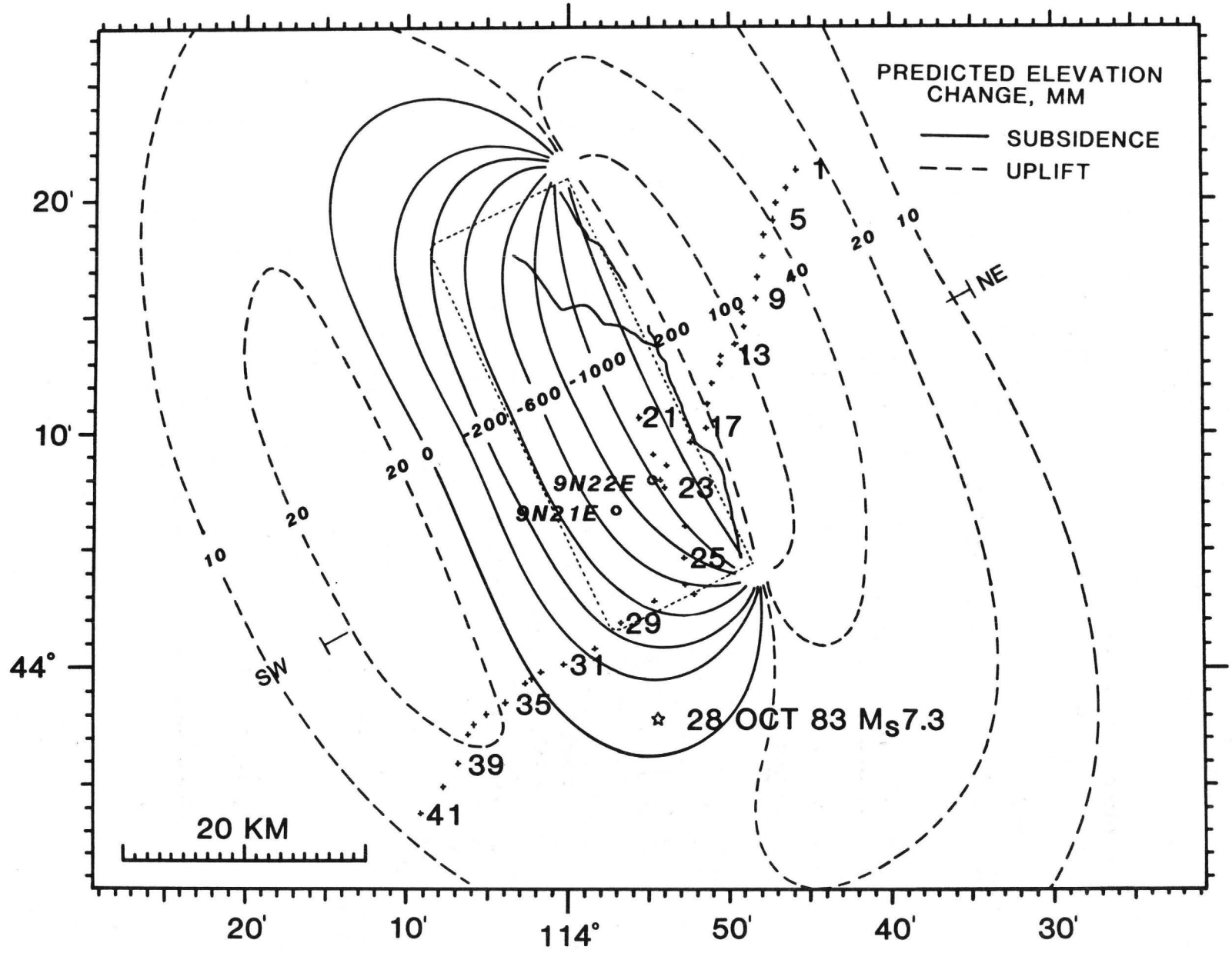

Figure 2a. Schematic map of Borah Peak earthquake site, showing locations of epicenter from Richins et al. (1985), surface rupture from Crone and Machette (1985), and BM's (crosses); contours of elevation change predicted by coseismic model; and line of projection for profiles in Figures 3, 4, and 6.

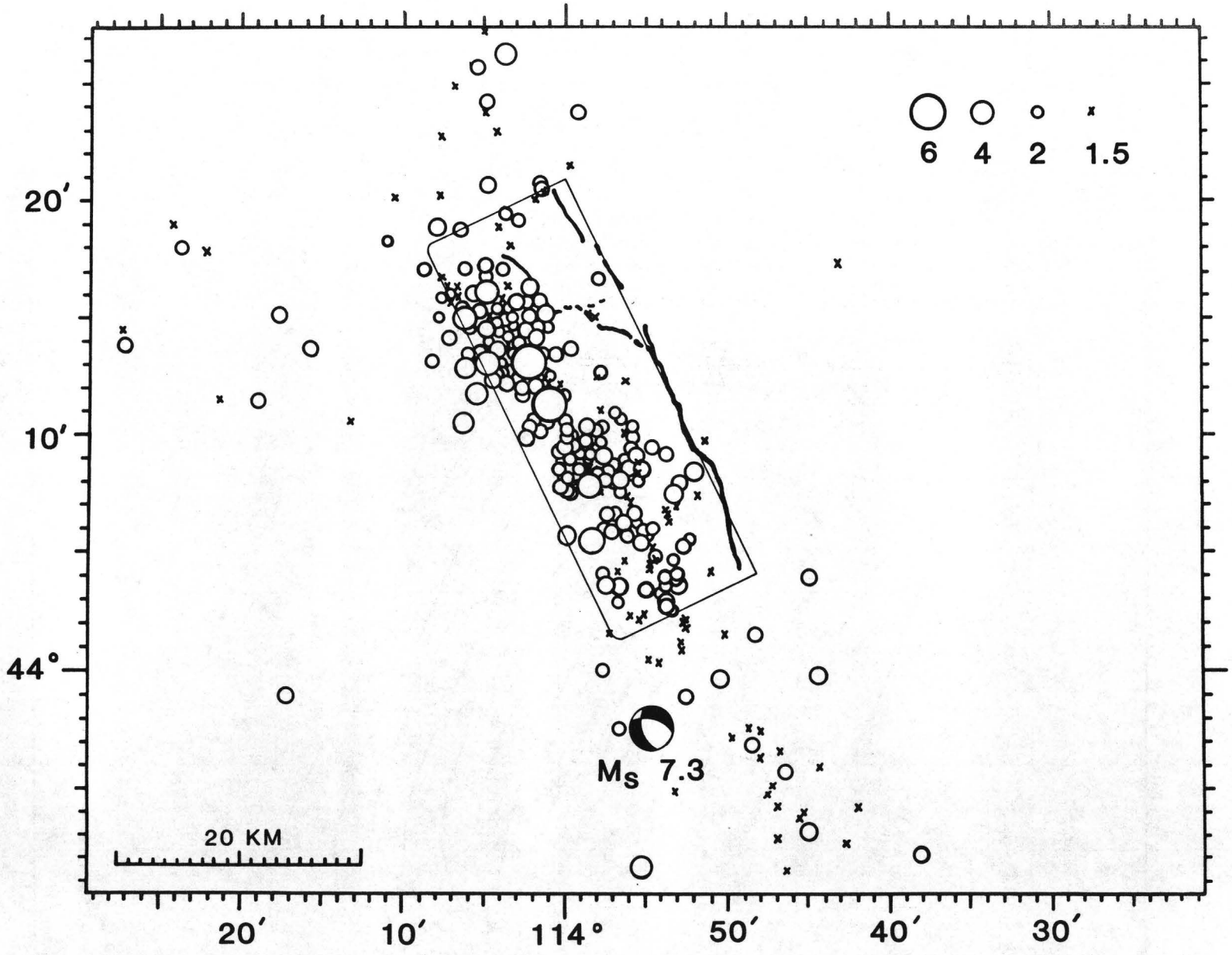

Figure 2b. Schematic map showing surface rupture and locations of the October 28, 1983, main shock and aftershocks from October 29 to November 19, 1983 (Richins et al., 1985), and coseismic fault model.

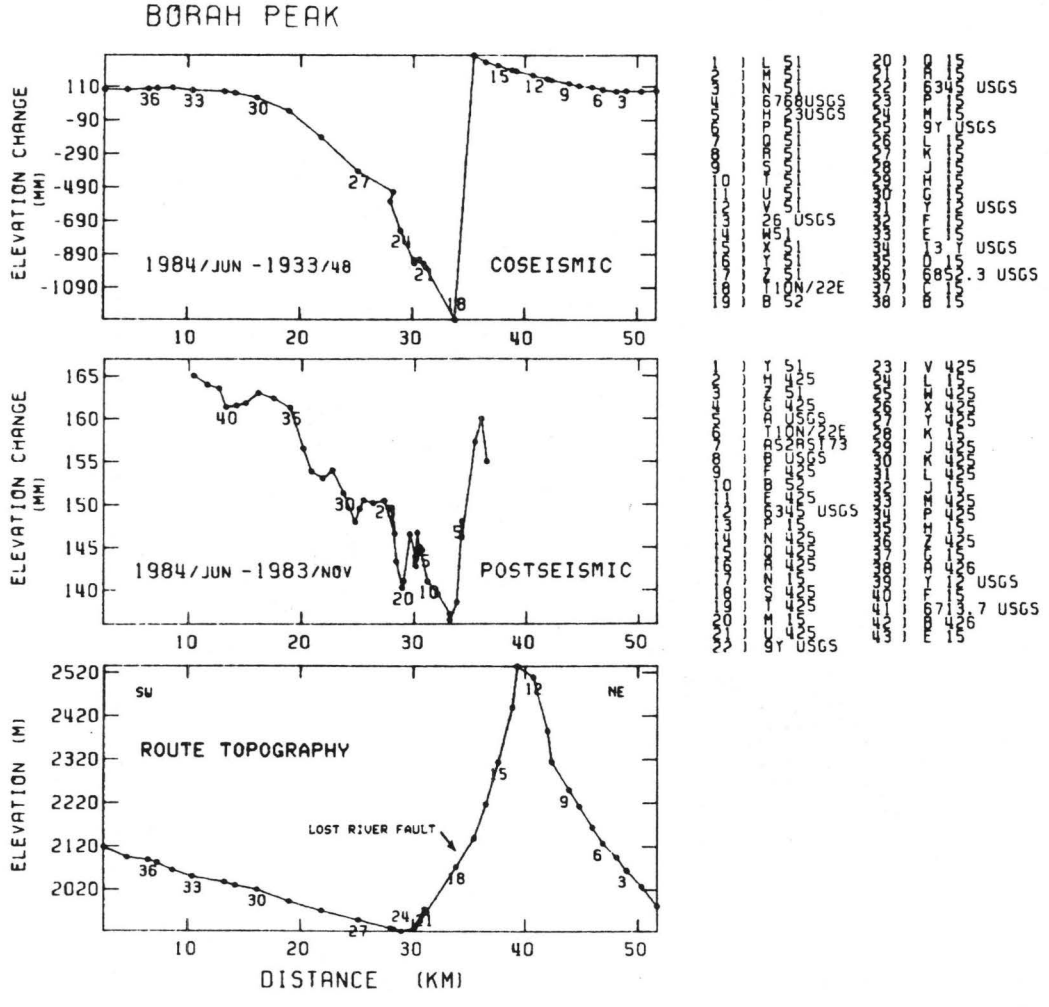

Figure 3. Profile of coseismic elevation change projected normal to the fault (top), the postseismic elevation changes measured 1-8 months after the main shock (middle), and the leveling route topography (bottom).

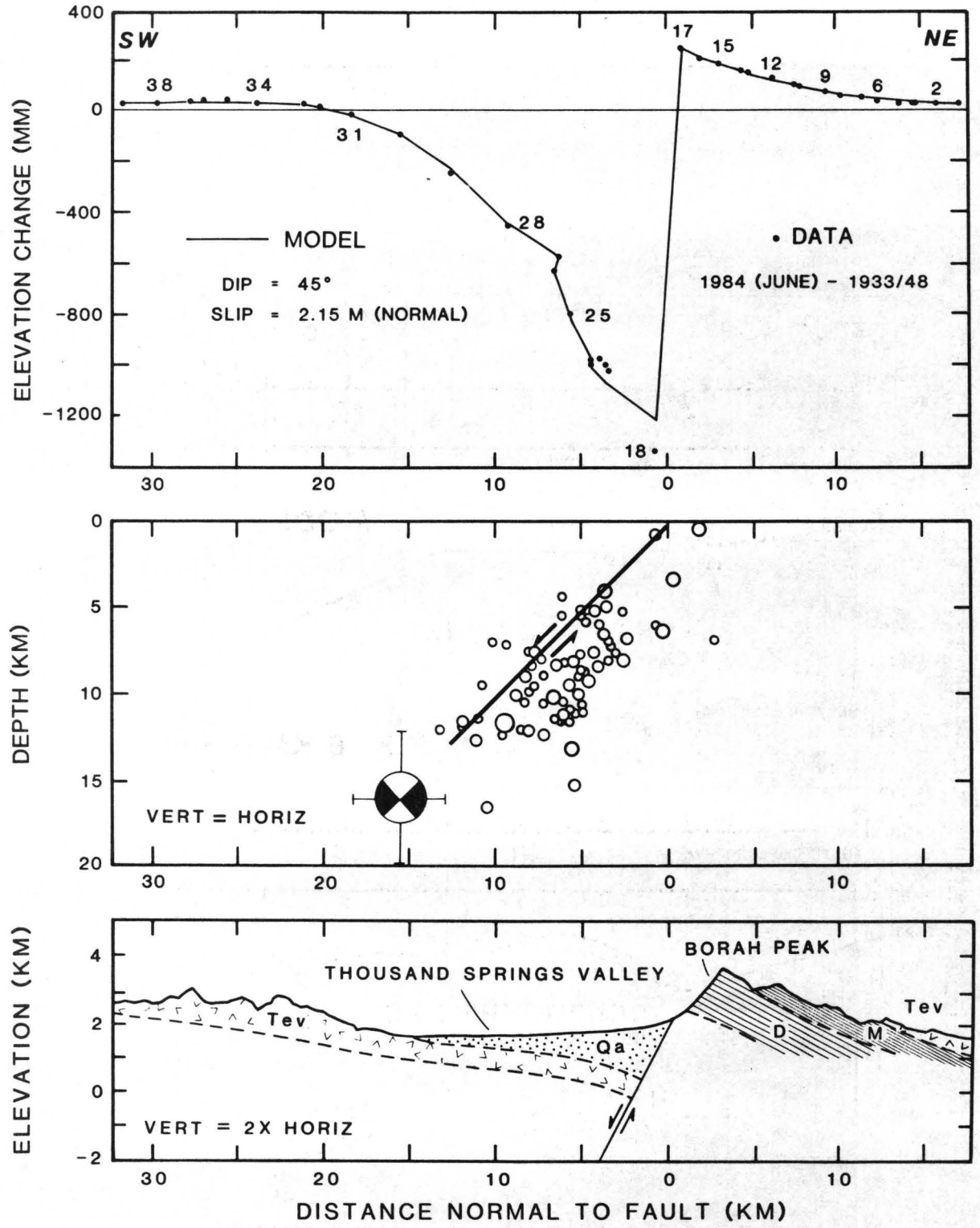

Figure 4. Top: Profile of observed coseismic elevation change for BM's in Fig 2a (dots), together with predicted changes (line) for coseismic model. "Kinks" in model profile result from changes in azimuth of leveling route shown in Figure 2a. Middle: Coseismic model, with main shock and aftershocks beneath leveling line from Richins et al. (1985). Bottom: Schematic geologic cross section from Bond (1978). Thickness of quaternary alluvium (Qa) is based on gravity modeling by Mabey (1985). Also shown are Tertiary volcanic deposits (Te_v) and Mississippian (M) and Devonian (D) carbonates.

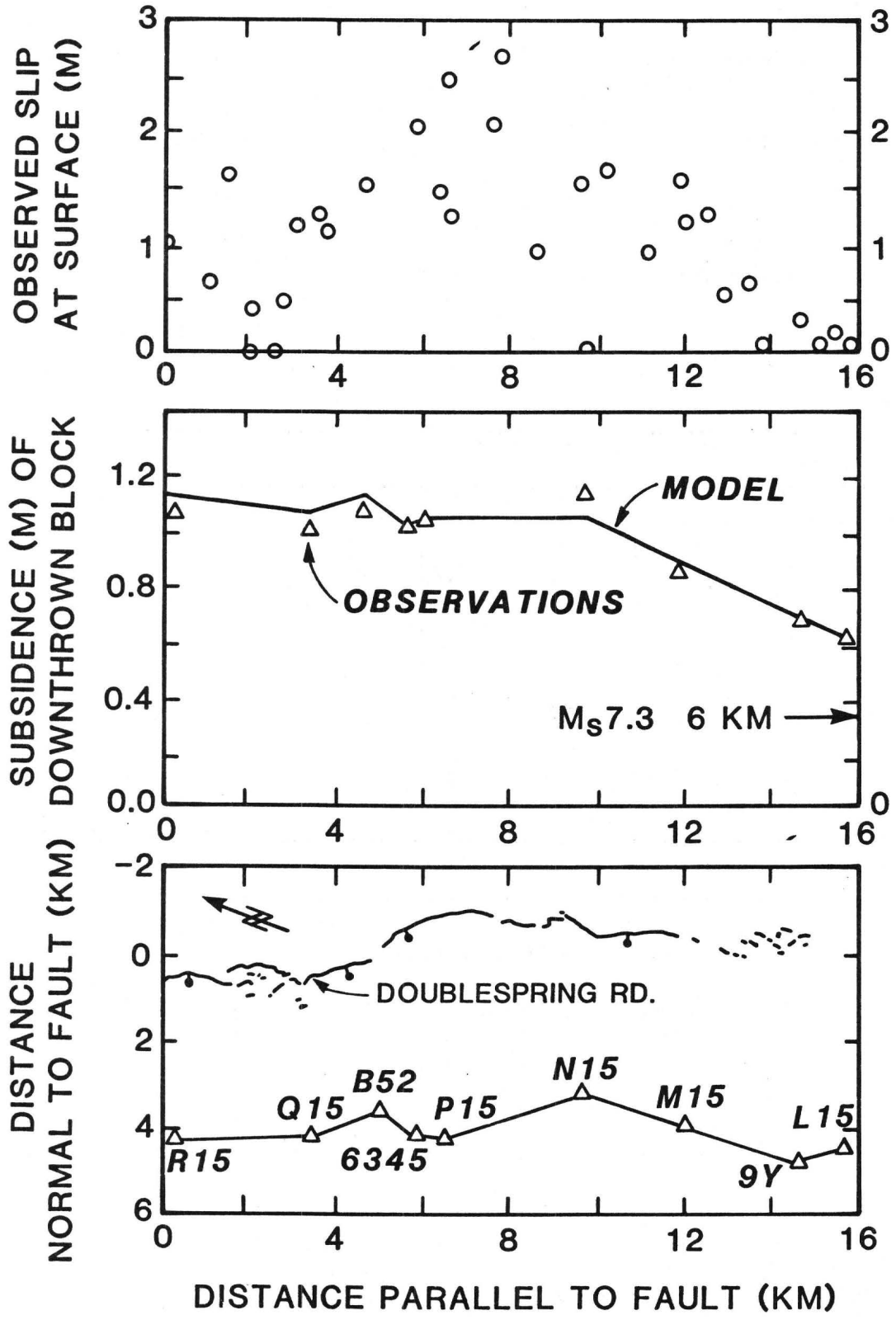

Figure 5. Variation of surface and buried slip along strike. Top: Fault throw from Crone and Machette (1984). Middle: Subsidence of downthrown block measured by releveling, located 4-6 km from fault trace. Bottom: Location map for fault and BM's.

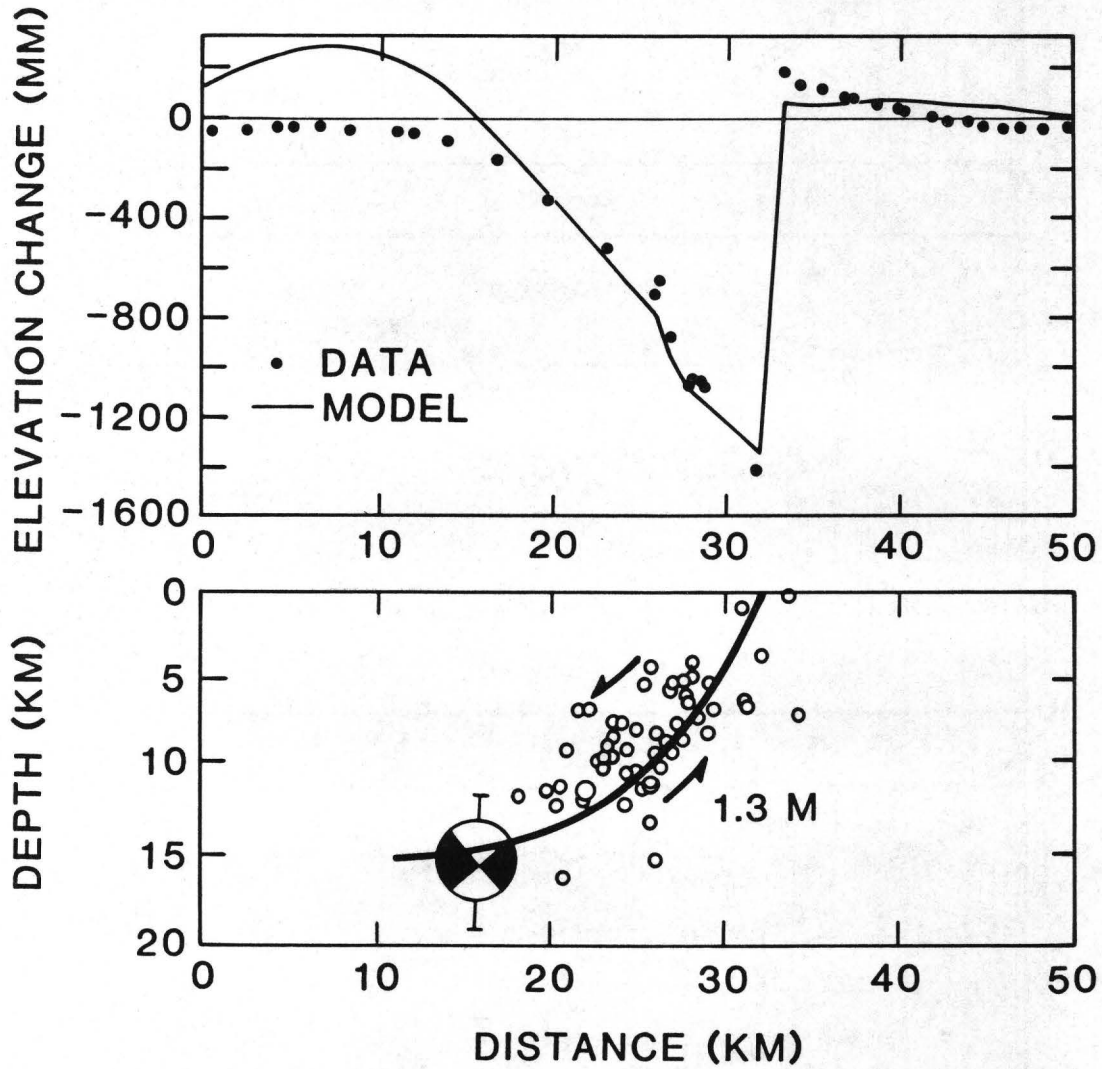

Figure 6. Best fit of coseismic deformation (dots) to a listric-fault model compatible with main shock and aftershock distribution of Richins et al. (1985). Zero datum has been raised to bring observations into best possible agreement with a listric-fault geometry.

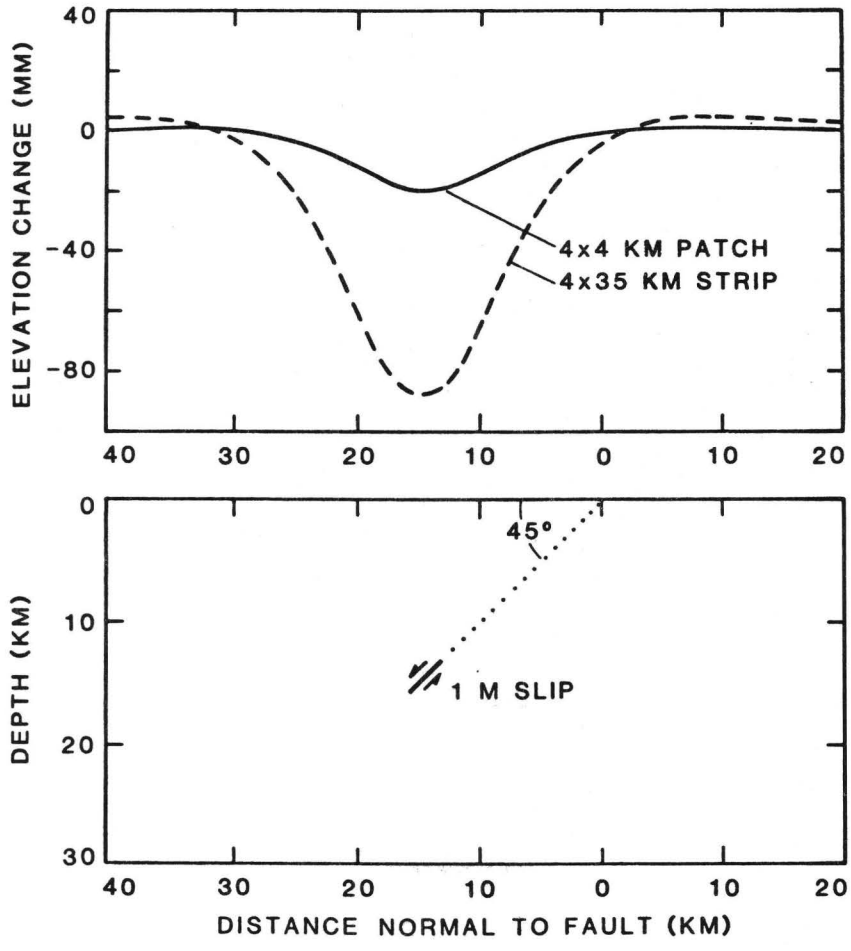

Figure 7. Surface deformation produced by hypothetical preseismic slippage at base of model fault, showing elevation change per meter of fault slip caused by a 4 by 4-km epicentral patch (line) and a 4-km-wide strip running the 35-km length of the coseismic fault (dashed).

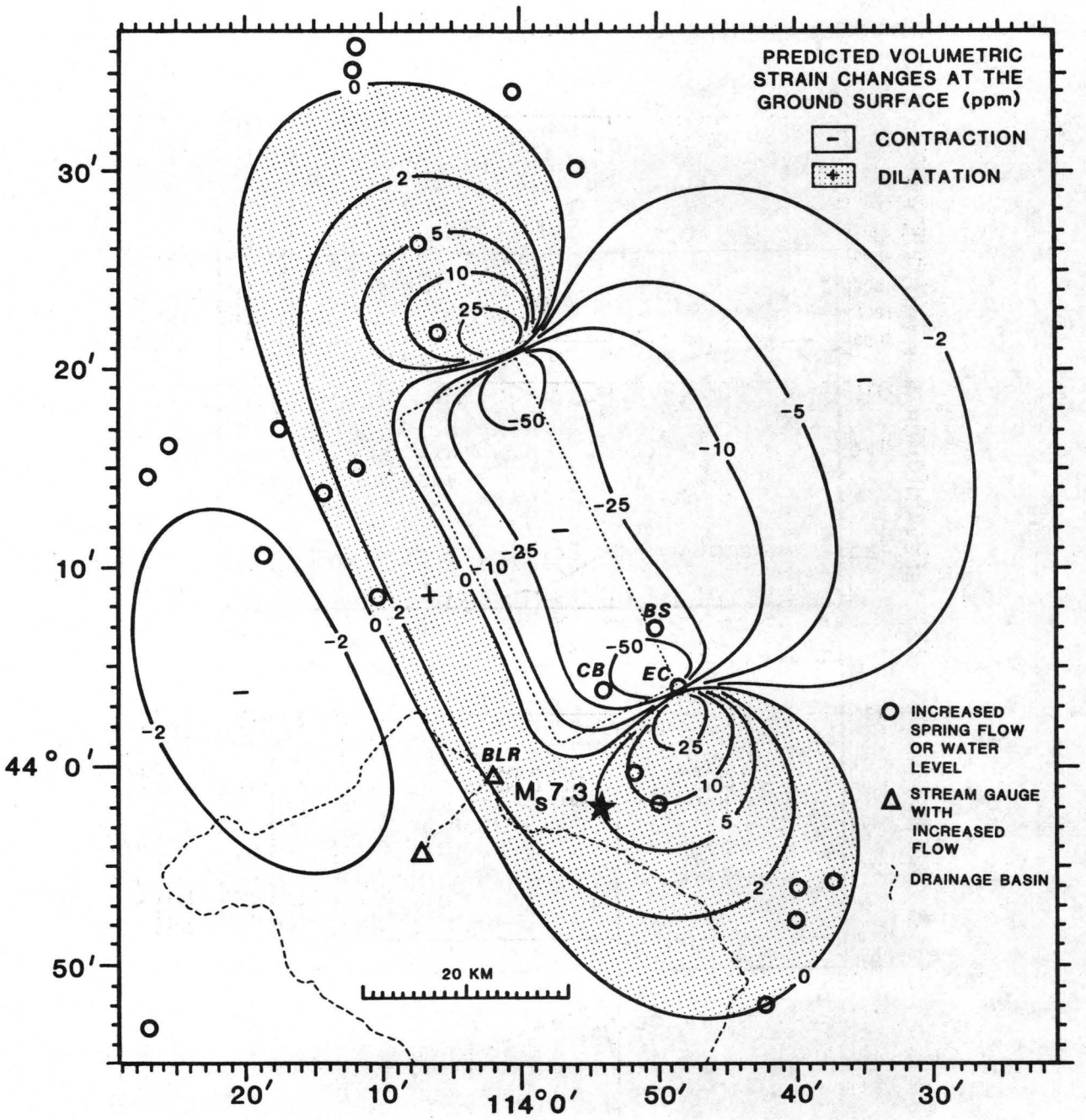

Figure 8. Near-surface volumetric strain changes calculated for the coseismic fault model. Sites of increased spring flow are shown as circles, and gages that record increased stream flow are shown as triangles. The Big Lost River (BLR) basin drained by the stream is dashed. CB is the site of the Chilly Buttes sediment boils, BS is the Birch Springs debris flow, and EC is the Elkhorn Canyon spring.

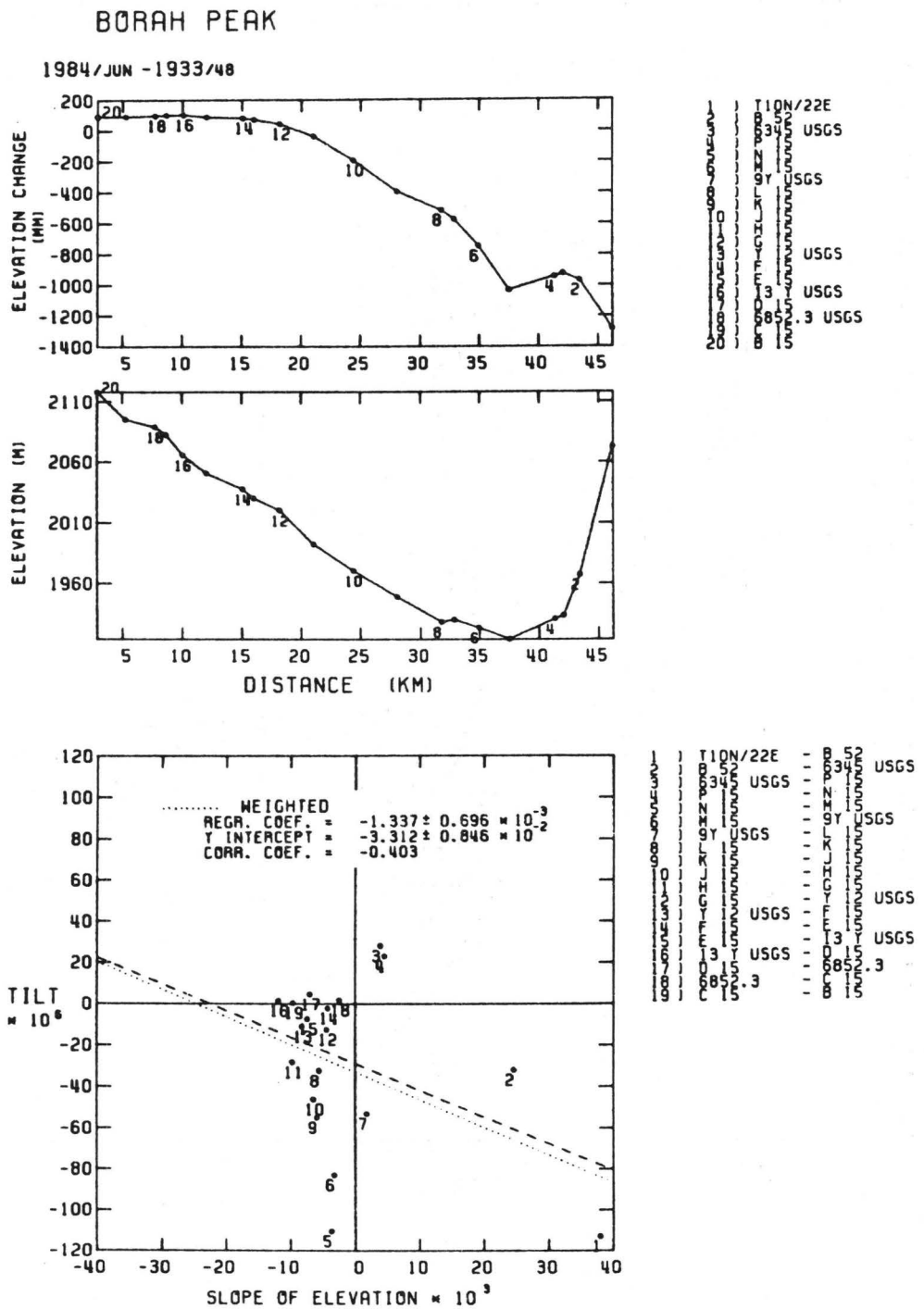

Figure 9. Profiles of coseismic elevation change (top) and route topography (middle) on the downthrown fault block. Geodetic tilt as a function of topographic slope is shown (bottom) following Stein (1981). The correlation coefficient (r = -0.403) is not significant at the 95% confidence level, indicative of negligible linear slope-dependent leveling error.

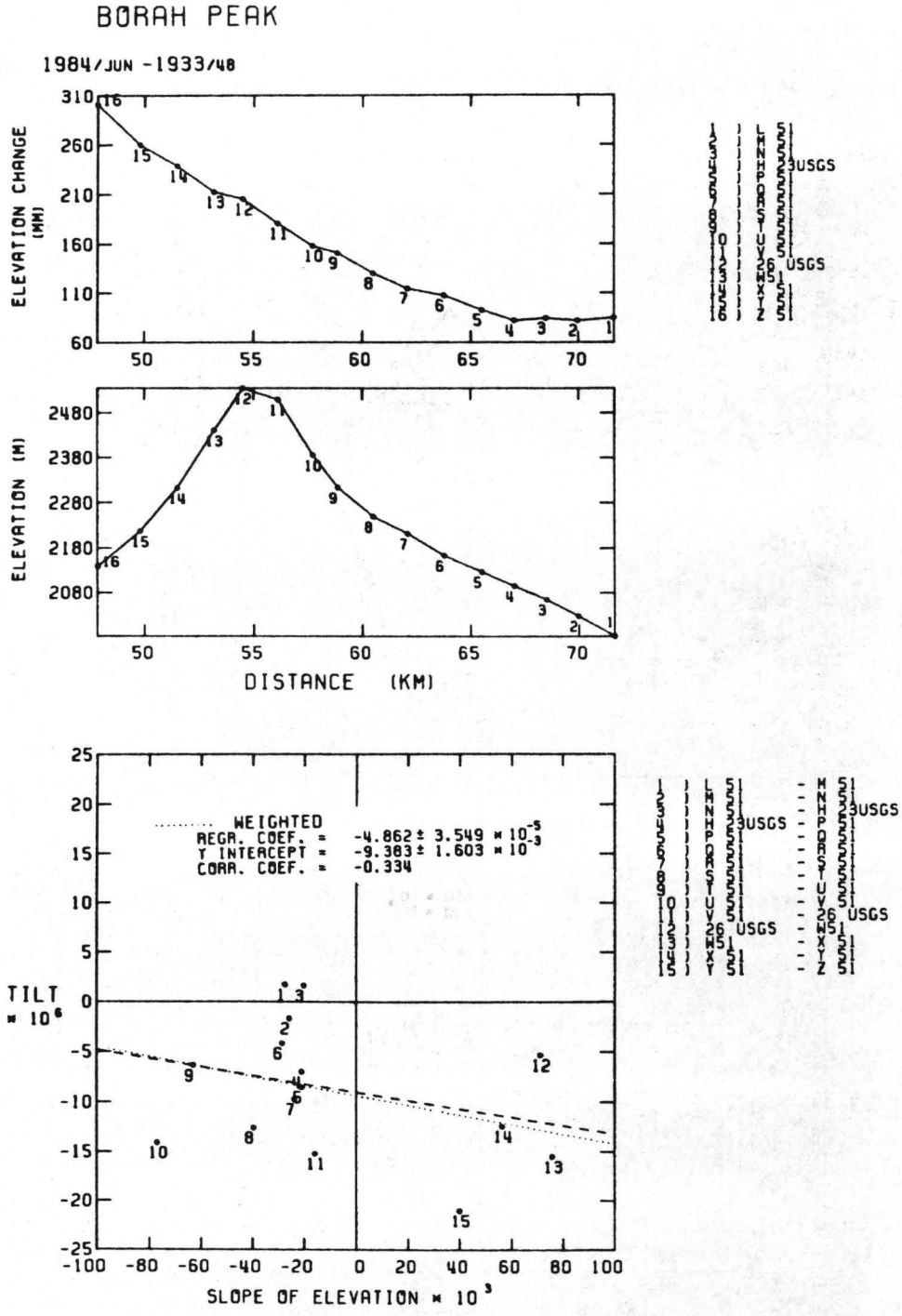

Figure 10. Profiles of coseismic elevation change and route topography on the upthrown block. The absence of a resemblance between elevation change and elevation (tilt and slope) is evident by inspection, and verified by the correlation coefficient (r = -0.334) which is not significant.

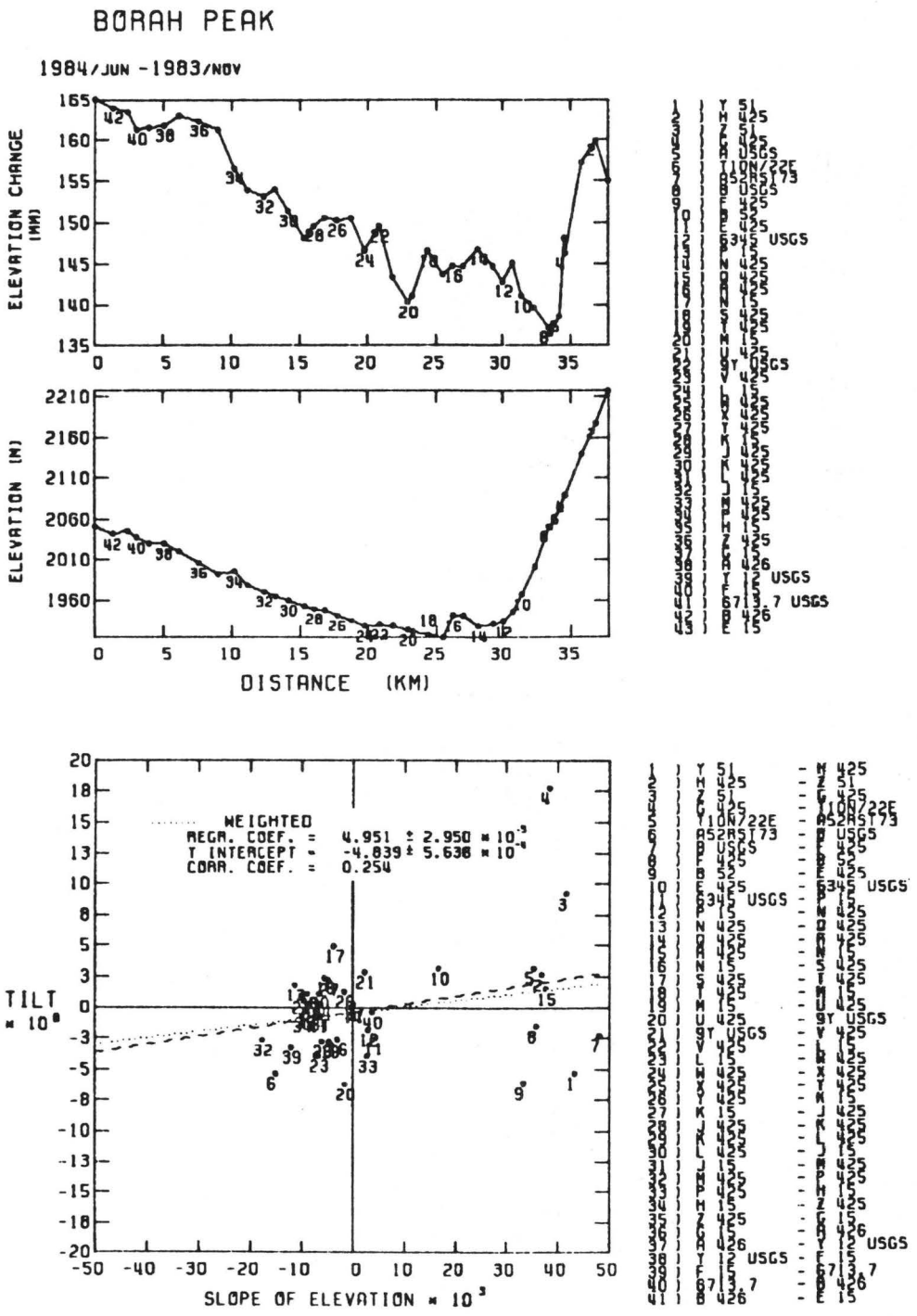

Figure 11. Profiles of postseismic elevation change and route topography. No statistically significant correlation is apparent between the tilt and slope, despite the gross resemblance of elevation change to topography.

INVERSION FOR MOMENT AS A FUNCTION OF DEPTH FROM GEODETIC OBSERVATIONS AND LONG PERIOD BODY WAVES OF THE 1983 BORAH PEAK, IDAHO EARTHQUAKE

Sergio E. Barrientos, Steven N. Ward, Jaime R. González-Ruiz, and
Ross S. Stein *

Charles F. Richter Seismological Laboratory
University of California
Santa Cruz, California 95064

* U. S. Gelogical Survey
345 Middlefield Road
Menlo Park, California 94025

ABSTRACT

We develop an inversion procedure for static vertical displacements associated with shallow faulting and apply the technique to model the Borah Peak Idaho earthquake ($M_S = 7.3$) of October 28, 1983. The data consist of elevation changes recorded on a 50 km long first order leveling line which crosses the fault at nearly a right angle. The inversion procedure finds the fault geometry, fault dimensions and the slip distribution with respect to depth or distance along strike which best reproduces the static offsets. The best fitting planar source is a fault which dips 49° southwest, has a width (down-dip dimension) of 21 km, a length (along strike) of 20 km, a strike-slip component (left-lateral) 25° away from a pure dip-slip displacement, and a total moment of 2.7 x 10^{19} Nm. Slip appears to be marginally greater in the depth range 8-14 km, where most aftershocks concentrate, and toward the southeast, where the main shock locates. Uniform slip models fit the observations better than models which extrapolate the observed surface slip to depth. This suggests that surface scarp height measurements are not good indicators of slip at depth. We investigated a broad class of curved faults by considering all members of a parabolic shape distribution. The best fitting model has a slight downward curvature, however, planar fault models also fall within the 5% contour of increased variance, so the downward curvature is probably not significant. Listric-like curvature of the fault is unacceptable. From calculated Sensitivity Kernels, we deduce that geodetic stations near the fault trace reveal information only about the shallowest elements of the fault. Measurements made further back from the fault trace reveal more information about deeper slip, however, the information is averaged over about 10 km of fault surface. The results obtained from the geodetic data inversion are found to be in good agreement with those returned from teleseismic waveform modeling of long period body waves. The geodetic moment is significantly larger than the seismic moment, suggesting that some of the fault slip took place at longer periods than those that can be detected by the body wave modeling.

INTRODUCTION

The 1983 Borah Peak earthquake (Ms=7.3) is the largest earthquake to occur in the Basin and Range Province of the western United States since the 1957 Hebgen Lake, Montana, event. To our fortune, geodetic leveling surveys of 1933 and 1948 passed virtually on top of the 1983 earthquake. A resurvey of these lines in 1984 provided the best record yet available of coseismic deformation associated with a large normal fault in the province.

Typically, coseismic deformation models assume a rectangular fault on which the strike-slip and dip-slip components of the dislocation are everywhere constant (Savage and Hastie 1966, 1969; Stein and Lisowski 1983). The restrictions of uniform slip and a planar rectangular fault however, are probably unrealistic. In our work, we have been able to remove these constraints and resolve the shape of faults and distribution of slip at depth as well as along strike. These data enable some important questions related to seismic hazard to be addressed:

- Is slip on the fault plane spatially uniform or variable ?
- Do variations of scarp heights measured at the fault trace reflect variations in slip at depth ?
- Does the dip of the rupture surface flatten with depth as suggested in listric fault models ?

DATA

Three leveling surveys of the Borah Peak, Idaho, region conducted in 1933, 1948 and 1984 enable the geodetic elevation changes associated with the earthquake of October 28, 1983 to be calculated. The northeastern elevations (points 1-21 in Figure 1) were measured in August 1948 with a single-run, second order leveling survey by the National Geodetic Survey. The southwestern portion of the 70 km long route was carried out in 1933 using first order, double-run standards which allowed much smaller error than the 1948 survey. The only common points of the two surveys are numbered 22 and 23 (Figure 1) and they correspond to bench marks P 15 and 6345

USGS respectively. In spite of the disparity of standards required for both levelings, the 1.58 mm elevation difference between the 1933 and 1948 runnings of the junction section is smaller than the expected random error for a first class leveling survey. The July 1984 leveling, which reoccupied the 1933 and 1948 stations, was conducted to first order single-run standards over the central portion of the survey, but was double-run over 15 km at the ends of the line. Figure 2 presents the changes in the 1984 elevations relative to the 1933/48 surveys. All of the data were corrected for level collimation, rod excess, rod thermal expansion, and atmospheric refraction. The uncertainty of the differences in elevation at the ends of the leveling route is 20 mm, and less than 2 mm for adjacent bench marks (Stein and Barrientos, 1985). Relative to the northeastern block, the maximum subsidence of the southwestern block is 1.6 m. The topography of the leveling route, plotted in Figure 2b, shows the gross correlation of the uplifted block with the higher elevations (Lost River Range) and the subsided block with the Thousand Springs Valley. Although systematic slope-dependent errors in the surveys might be suggested by this correlation, no such errors were uncovered in detailed analysis (Stein and Barrientos, 1985).

METHOD

Our method of constructing spatially finite faults uses a distribution of elemental point sources. At a point P(r,θ) on the free surface of a halfspace, the vertical displacement u which results from a static moment tensor buried at a depth h is

$$
\begin{aligned}
u(r,\theta) = m_0 \Bigg[& \frac{M_{xy}cos\theta + M_{yz}sin\theta}{4\pi\mu}\left(\frac{6h^2r}{R^5}\right) + \\
& \frac{M_{xy}sin2\theta}{4\pi\mu}\left\{\frac{\mu(R-h)^2(2+h/R)}{(\lambda+\mu)r^2R^2} - \frac{3hr^2}{R^5}\right\} + \\
& \frac{(M_{xx}-M_{yy})cos2\theta}{8\pi\mu}\left\{\frac{\mu(R-h)^2(2+h/R)}{(\lambda+\mu)r^2R^2} - \frac{3hr^2}{R^5}\right\} + \\
& \frac{(M_{xx}+M_{yy})}{8\pi\mu}\left\{\frac{h}{R^3}\left(-\frac{\lambda+2\mu}{\lambda+\mu} + \frac{3h^2}{R^2}\right)\right\} + \\
& \frac{M_{zz}}{4\pi\mu}\left\{\frac{\lambda h}{(\lambda+\mu)R^3} - \frac{3h^3}{R^5}\right\}\Bigg]
\end{aligned}
\tag{1}
$$

where $M_{ij}(i,j=1,3)$ are the components of the moment tensor, r is the horizontal distance between P and the point source, $R=\sqrt{r^2+h^2}$ and azimuth $\theta = tan^{-1}(y/x)$ where $x = rcos\theta$ and $y = rsin\theta$ (Comer, 1977). For a double couple, the trace and the determinant of the moment tensor **M** vanish. If the largest eigenvalue of **M** equals 1, then m_0 represents the scalar moment of the source. The components of **M** are assumed fault parameters and, if desired, they can be written in terms of the dip and slip angles of the dislocation (Ben-Menahem and Singh, 1981).

Vertical deformations at the surface of the halfspace due to four different point sources are shown in Figure 3. The left and right columns plot the displacement for dip-slip and strike-slip sources at 10 and 50 km focal depths. Note that a smaller amplitude and broader wavelength deformation is associated with the deeper sources. In comparing these schematic deformations with the observed static displacement (Figure 2a), we conclude that the Borah Peak earthquake faulting is both deep enough to generate a broad wavelength, and shallow enough to generate a discontinuity of displacement on the surface. Accordingly, the fault must be modeled as a finite source with possibly variable strength.

For the simplest of our finite source models, we generalize the scalar m_0 to $m(l)$, a function of the down-dip length l. By quantizing the continuous distribution $m(l)$ into equally spaced discrete sources along a line (Figure 4a), the theoretical vertical displacement, u, at the ith observation point can be written

$$u_i = \sum_{j=1}^{q} t_i(l_j) m(l_j) \tag{2}$$

where $t_i(l_j)$ is the displacement at the ith point due to a source at l_j (Figure 4b). Equation (2) states that the total displacement at the ith point is the sum of the displacements produced by the q sources, each weighted by moment $m(l_j)$. We parameterize $m(l_j)$ as a third degree polynomial in l_j

$$m(l_j) = \sum_{k=0}^{3} a_k l_j^k \tag{3}$$

By expressing $t_i(l_j)$ and l_j^k as matrices **T** and **L** the diplacement vector u can be written as

$$u = \mathbf{TL}a = \mathbf{B}a$$

where

$$T = \begin{vmatrix} t_1(l_1) & t_1(l_2) & t_1(l_3) & \dots & t_1(l_q) \\ t_2(l_1) & t_2(l_2) & t_2(l_3) & \dots & t_2(l_q) \\ t_3(l_1) & t_3(l_2) & t_3(l_3) & \dots & t_3(l_q) \\ \vdots & \vdots & \vdots & & \vdots \\ t_n(l_1) & t_n(l_2) & t_n(l_3) & \dots & t_n(l_q) \end{vmatrix}$$

and

$$L = \begin{vmatrix} 1 & l_1 & l_1^2 & l_1^3 \\ 1 & l_2 & l_2^2 & l_2^3 \\ 1 & l_3 & l_3^2 & l_3^3 \\ \vdots & \vdots & \vdots & \\ 1 & l_q & l_q^2 & l_q^3 \end{vmatrix}$$

The least squares solution for the vector of coefficients a is

$$a = (\mathbf{B}^t\mathbf{B})^{-1}\mathbf{B}^t u \tag{4}$$

By introducing (4) into (3) the moment distribution along the line source is obtained. Note that since the components of $\mathbf{M}$ are assumed, only the four moment distribution parameters a_k of equation (3) are subject to inversion.

LINE SOURCE

To illustrate this method, a line source model has been applied to the data of Figure 2a. By prescribing the dip , the fault length and the number of sources, the least squares scheme outlined above allowed us to determine the distribution of moment. Line source dips and lengths were searched at 1° (dip) and 0.1 km intervals (length) and the pair which minimized the residuals was selected as the best solution. Tests varying the number of sources were done, but similar results were found for sources numbering between 40 to 90. In this simple case, because we assumed that the data points lie perpendicular to the fault trace, the strike slip component of faulting is not recoverable. This can be seen in equation (1) where the strike-slip term M_{xy} vanishes for $\theta = 90°$. The best line source model has a down-dip fault length of 18.1 km and a

dip of 55° to the southwest, with larger moments concentrated in the deeper regions of the source (Figure 5). The sum of the individual moments of the 40 point sources is 1.0 x 10^{19} Nm. This is a minimum estimate, since in this model an arbitrary amount of strike slip moment can be added to the solution and not alter the fit.

PLANAR FAULT

Variation of Moment Down-Dip. To simulate a planar fault with both length (along strike) and width (the down-dip dimension), several parallel line sources were constructed. In this model, we assumed that the fault strikes parallel to the surface rupture and that the distribution of moment is constant at any given depth. As in the previous case, the fault dip and the fault width were varied within a prescribed range and the distribution of moment was found by minimizing misfit to the observed elevation changes. Three new parameters now enter into the procedure: the strike-slip component, the fault length and the southeast end point of the fault. The superposition of 20 line sources separated at 1 km intervals (Figure 6) produces the results shown in Figure 7. Relative to the single line source, the error in the fit has dropped by a factor of three. The dip of the fault is 49°, the width is 21 km, the length is 20 km, and the total moment is 2.7 x 10^{19} Nm. A small left lateral strike-slip component is indicated in this model which produces a slip angle 10° away from a pure normal displacement (Figure 6). The sensitivity of the variance to changes in each of the parameters involved in the inversion is shown in Figure 8. Fault dip, length and southeast terminus (y0) are well resolved with estimated precisions of ±2°, ±2 km and ±.2 km respectively. The high resolution of the position of the southeast terminus is mainly due to the distribution of bench marks. The fault width is determined to within ±5 km. The slip angle is less well resolved (±10°) because of the lack of survey stations toward the northwest and southeast. From the definition of scalar moment ($M_i = \mu s_i A_i$), we can associate with the ith source a certain area (A_i) and slip (s_i). For a half space rigidity of μ = 3.23 x 10^{10} Pa, the average slip on the fault is 2.0 m. A maximum fault slip of 2.5 m occurred at 10 km depth, where the greatest concentration of aftershocks also occurred (Richins *et al.* ,1985). Slip decreased toward shallower levels, and the 1.9 m surface slip underepresents the average fault slip by

5%. The 1.56 m of vertical slip at the surface agrees with the value measured by Crone and Machete (1984) at Double Springs Pass Road. Note that the main shock locates near the southwestern corner of the fault.

Variation of moment along strike. We have found that the down-dip moment (or equivalently, slip) distribution of the Borah Peak earthquake is surprisingly uniform, with less than a 5% variation in slip over 90% of the fault surface. Will the same uniformity be present if variations in slip along strike are allowed? Fairly strong variations in surface slip might be inferred from Crone and Machete's (1984) measurements of vertical scarp height (Top, Figure 9). In interpreting fault scarp heights, two questions always arise. First, do scarp measurements accurately reflect the surface slip of the fault or do they merely express local deformations such as soil failures or secondary mass movements? Second, even if scarp heights mirror surface dislocation patterns, can these surface slips be extrapolated to depth on the fault? We can address these questions by considering models which have uniform down-dip moment but non-uniform moment along strike. The analysis of moment variation along strike is similar to that used in the inversion for moment as a function of depth. The moment is represented as a third degree polynomial in distance along strike from the southeastern end of the fault because it the simplest way to test for varying slip along strike. The search for the minimum sum of residuals is then performed for different fault lengths, widths, positions of the southeastern end of the fault, and slip angles. The determined slip distribution along strike for faults of 20, 27 and 31 km length are shown in Figure 9b. Slip for each of the models is greatest at the southeast and slowly decreases toward the northwest. The best fit is found for a 20 km fault length. Note that it forces larger slips at the northwestern end of the fault, beyond bench marks that have been surveyed. If the fault length is increased to 31 km, variance increases by 60%. We conclude that variations in slip along strike exceeding 20% are not demanded by the data. Except for a 15° increase in the strike slip component, the rupture plane geometry found in this experiment is equivalent to that found in the case of variation of moment with depth, however, the relative misfit is reduced by 50% when variations along strike are permitted.

Comparison of slip at surface and at depth. Ideally, we would like to use the sur-

face slip and the bench mark vertical displacements to solve for slip everywhere on the fault. But we lack sufficient density of bench marks in the attempt of resolving complete slip functions with depth. However, we can compare surface slip to slip at some optimum depth where the bench mark sensitivity is best. The vertical surface deformation represents a weighted sum of contributions from all points on the fault. The weighting is complex and it is not immediatly clear at what depth and position on a fault a certain surface measurement is most sensitive. For example, there are locations where vertical surface measurements will yield a great deal about slip on a portion of the fault tens of kilometres away but yet tell virtually nothing about slip on a portion of the fault only a km or two distant. We consider this problem by calculating sensitivity kernels for surface displacement. Figure 10 shows the relative contributions to surface vertical displacement as a function of down-dip distance along a uniform slip fault 20 km long which dips 49°. Curve (a) is the sensitivity for a survey point located near the surface fault trace (See insert Figure 10). Plots (b) and (c) show the sensitivity for increasingly distant stations. These three kernels clearly have significantly different character. Sensitivity at point (a), for example, is strongly peaked at about 2 km depth and is virtually zero beyond 10 km depth. Thus, vertical geodetic measurements at (a) will contain much information about shallow slip on the fault but very little information about slip deeper than 10 km. As the observation point moves to (b) then (c), deeper and broader regions of the fault are sampled. Measurements at (c) are as much as twice as sensitive to slip below 13 km than measurements at (b) and about 100 times as sensitive as measurements at (a). Note that (b) shows the sensitivity of stations 27 to 21 whose subsidence is used as data in Figure 11. The main contribution to surface deformation at these bench marks originate at sources located between 3 and 8 km down-dip on the fault.

To examine the relevance of surface offset to slip at depth on the fault, we constructed three forward models. In one, the observed surface slip variation along strike was assumed to be the same as at depth, and in the second case, the maximum envelope of the observed slip variations along strike were extrapolated to depth on a 35 km long fault. The third model imposed uniform slip on a fault with the minimum 20 km length. The slip distributions along strike and the computed vertical displacement for stations 21 to 27 for these three forward models are shown in Figure 11. Both the observed and smoothed version of the observed slip models produce poorer fits than

the simple uniform slip model. From the inverse models of Figure 9, we conclude that strong variations in slip with strike in the southeasternmost 20 km are not demanded by the data. No firm coclusions can be reached about the northwestern fault slip. From the results of Figure 11, we can state that great variations in slip that are evident on the surface deformation are, in fact, excluded by the data. Thus, we conclude that scarp measurements provide only a rough indication of the slip at depth.

LISTRIC FAULTS

Several authors (e.g. Allmendinger *et al.* , 1983; Smith and Bruhn, 1984) have suggested that faults in the Basin and Range Province posses a degree of upward curvature and eventually become horizontal at a depth referred to as the level of detachment. To test this suggestion, we investigate a broad class of curved faults by considering all members of a parabolic shape distribution. With z positive downward and x positive toward the northeast, the cross sectional form of the fault models consist of all points x, z which satisfy $x = b_1 z + b_2 z^2$: b_1 and b_2 are unknown shape parameters which can be interpreted as the cotangent of the surface dip and the curvature of the fault. All planar models would be contained in the special case where $b_2 = 0$. Upward curving listric faults which dip to the southwest fall in the quarterspace $b_1 > 0, b_2 > 0$.

To keep these models reasonably simple we permitted down-dip variations in moment but limited other parameters to include : fault length, fault width, southeastern fault terminus and slip angle. A search of b_1, b_2 space, revealed gradients in variance which pointed very nearly to a single deep minimum from all points in the plane. We are confident that no other parabolic fault model exists which can fit the observations as well. Contours of equal variance versus b_1 and b_2 in the region near the absolute minimum are shown in Figure 12. The best fitting model has a surface dip of 45° and a slightly downward curvature (Top, Figure 13). A planar fault model dipping 49° falls within the 5 % contour of increased variance, so the downward curvature of the best fitting model is not significant. To obtain pronounced listric fault curvature, such as model (c) in the Figures 12 and 13, an unacceptably large (50%) increase must be tolerated.

BODY WAVE MODELING

In addition to static deformation models, we have applied waveform modeling to determine the source parameters and the rupture time history of the Borah Peak earthquake. The waveform data consist of long period P and SH waves as recorded at teleseismic distances (28 to 94 degrees) by the WWSSN. The method of analysis is that of generalized ray expansions and has been described in detail elsewhere [e.g. Langston and Helmberger, (1975); Helmberger, (1982)]. The method comprises the addition of direct (P and S) and surface reflected rays (pP, sP and sS) convolved with source time history, the Earth's attenuation, and the seismic instrument response. Instrument response from the WWSSN is well known and the Earth's attenuation effects can be accounted through Q(t) operator of Futterman (1962) using a constant ratio T/Q=1.0 s for P waves and 4.0 s for S waves. Here T is the total travel time and Q the frequency independent attenuation factor averaged along the ray. The far-field source time function is assumed to be three-parameter trapezoid as defined by Helmberger (1974). In this study we consider a point source embedded in a layer (V_p = 6.14 km/sec, V_s = 3.55 km/sec, ρ = 2.74 gr/cm^3 with a thickness of 20 km) over a half space. The procedure systematically varies fault strike, dip, slip and depth (within acceptable ranges consistent with observations from polarities of P-wave first motions) and the time function until the synthetic seismograms match the data. The fault geometry of the earthquake is reasonably well constrained by polarities of first motions of long-period records at WWSSN and Canadian stations (Figure 14). Vertical P-waveforms are generally very simple and consistent for all azimuths for which observations are available. A point source at a depth of 16 km and a teleseismic time function duration of 9 sec best reproduces the time separation between the different phases (P, pP and sP) as can be seen in Figure 14. The main trade-offs in depth determination are the assumed crustal source model and source time function. We estimate that source depth is constrained to within $\pm$ 4 km. The amplitude of the different phases is primarily source-geometry dependent. P-waves are not particularly sensitive to changes in strike and rake of up to 20° and dip up to 10° (Figure 15). To further constrain fault geometry we included a few observations of SH-waves obtained through a rotation of the horizontal components of selected seismograms. The final data set was selected by their waveform simplicity and spatial distribution. Results

from the SH waveform modeling are shown in Figure 16. SH-wave observations further constrain fault geometry to within $\pm 5°$ for the strike and dip, and $\pm 10°$ for the rake (Figure 17). Local geology suggests that southwesterly dipping plane is the fault plane. The final source parameters constrained by the P and SH modeling are : strike $= 166°$, dip $= 53°$, and slip angle $= -42°$. The Borah Peak earthquake represents normal faulting with a moderate left lateral strike-slip component. A seismic moment of $1.85 \pm 0.17 \times 10^{19}$ Nm is obtained by scaling the amplitudes of the data to the synthetic seismograms for both P and SH waves. This value agrees with that obtained by Boatwright and Choy (1985) of $1.7 \pm 0.2 \times 10^{19}$ Nm, but it is smaller than the 2.9×10^{19} Nm found by Doser and Smith (1984).

CONCLUSIONS

Using geodetically measured elevation changes, we have resolved the fault orientation, dimensions, shape and slip distribution of the 1983 Borah Peak earthquake. The deformation associated with elemental point dislocations is the keystone of the inversion technique. By summing the contributions of a large number of point sources, we can compute the static displacement field and recover the parameters from a wide class of fault models, including ones which are curved and contain non-uniform slip.

The planar fault model with variable down-dip slip which best reproduced the observed vertical displacement at the Earth surface had a 49° dip to the southwest, a fault width of 21 km, a of fault length of 20 km, a left-lateral strike slip component of 10° away from a pure dip-slip displacement, and a total moment of 2.7×10^{19} Nm. This fault model contained a non-uniform moment distribution with .5 m more of slip occurring at depth than at the surface. A still better fit was obtained by a planar fault which had uniform down-dip moment but variable moment along strike. The best model in this class had a slightly lower (20%) slip toward the northwest but otherwise retained source dimensions and an orientation very similar to the down-dip model. We conclude from this experiments that the Borah Peak Earthquake had a surprisingly uniform slip distribution.

To investigate the relevance of surface slip to slip on the fault at depth, we interpreted the variations of observed scarp heights along strike as variations in surface

fault slip and extrapolated these slip variations down-dip to the base of the fault. The subsidence that these models produced at bench marks close to the surface fault trace misfit the observations. We infer that scarp height measurements are very poor indicators of the deep slip pattern of the fault.

To test for listric-like curvature of the Borah Peak fault, we considered all possible faults of parabolic shape. The best fit was obtained for a model containing a very slight downward curvature. Planar models similar to those mentioned above however, fall within a 5% contour of increased variance, so improvements in fit due to a fault curvature are probably not significant. Listric fault models fall outside of the 50% level of increased variance and are inconsistent with the data.

The dip of the fault obtained from body wave modeling (53°) differs by four degrees from the best geodetic solution (49°). Slip angles determined by the two methods differ by 23°. The geodetic estimate of the moment is 30% greater than that found by the body wave analysis. This is consistent with some fault slip occurring at periods longer than those that can be detected by the body wave modeling. The body wave hypocenter corresponds approximately to the southwestern corner of the fault. Since body wave analysis reveals the focal mechanism of the nucleation phase of rupture and geodetic analysis reveals the mechanism of rupture in its final state, an increase in the dip slip component of faulting is indicated as the dislocation moved upwards and toward the northwest.

ACKNOWLEDGEMENTS

Portions of this work at the University of California, Santa Cruz have been supported by NSF Contract EAR82-19709 and USGS Contract 1408000 120546. We thank K. C. McNally for suggesting this study. We also thank John Boatwright and José Rial for reviewing this paper and offering constructive criticism.

REFERENCES

Allmendinger, R. W., J. W. Sharp, D. von Tish, L. Serpa, L. Brown, S. Kaufman, and J. Oliver, Cenozoic and Mesozoic structure of the Eastern Basin and Range Province, Utah, from COCORP seismic-reflection profile data, Geology, 11, 532-536, 1983.

Ben-Menahem, A., and S. J. Singh, Seismic Waves and Sources. Springer Verlag New York Inc, 1981.

Comer, R. P. Tsunami Generation by Earthquakes
Ph.D. Thesis, MIT, 1982.

Boatwright, J., and G. L. Choy, Teleseismic estimates of the energy radiated by shallow earthquakes, Workshop XXVIII on the Borah Peak Earthquake: U.S.G.S. Open-file Report, in press, 1985.

Crone, A. J., and Machete, M. N., Surface Faulting Accompanying the Borah Peak Earthquake, Central Idaho, Geology, 12, 664-667, 1984.

Doser, D. I., and R. B. Smith, Source parameters of the October 28, 1983 Borah Peak, Idaho earthquake from body wave analysis, in preparation, 1984.

Freund, L. B., and Barnett, D. M., A Two Dimensional Analysis of Surface Deformation Due to Dip-Slip Faulting, Bull. Seis. Soc. Am., 66, 667-675, 1976.

Futterman, W. I., Dispersive Body Waves, J. Geophys. Res., 67, 5279-5291, 1962.

Helmberger, D. V. Theory and Application of Synthetic Seismograms, Seismological Laboratory, California Institute of Technology, 1982.

Helmberger, D. V., Generalized Ray Theory for Shear Dislocations, Bull. Seism. Soc. Am., 64, 45-64, 1974.

Langston, C. A., and Helmberger, D. V., A procedure for modeling Shallow Dislocation Sources, Geophys. J. R. Astron. Soc., 42, 117-130, 1975.

Richins, W. D., Smith, R.B., Langer, C. J., Zollweg, J. E., King, J. T., and Pechmann, J. C.,The 1983 Borah Peak, Idaho Earthquake: relationship of aftershocks to mainshock, surface faulting, and regional tectonics, Workshop XXVIII on the Borah Peak Earthquake: U.S.G.S. Open-file Report, in press, 1985.

Savage, J. C., and Hastie, L. M., Surface Deformation Associated with Dip-Slip Faulting J. Geophys. Res., 71, 4897-4904, 1966.

Savage, J. C., and Hastie, L. M., A Dislocation Model for the Fairview Peak, Nevada, Earthquake Bull. Seis. Soc. Am., 59, 1937-1948, 1969.

Smith, R. B., and Bruhn, R. L., Intraplate Extensional Tectonics of the Eastern Basin-Range: Inferences on Structural Style from Seismic Reflection Data, Regional Tectonics, and Thermal-Mechanical Models of Brittle-Ductile Deformation, J. Geophys. Res, 89, 5733-5762, 1984.

Stein, R. S., and Barrientos, S., The 1983 Borah Peak, Idaho, Earthquake: Geodetic Evidence for Deep Rupture on a Planar Fault. Workshop XXVIII on the Borah Peak Earthquake: U.S.G.S. Open-file Report, in press, 1985.

Stein, R. S., and Lisowski, M., The 1979 Homestead Valley Earthquake Sequence, California: Control of Aftershocks and Postseismic Deformation J. Geophys. Res., 88, 6477-6490, 1983.

FIGURE CAPTIONS

Figure 1. Map view of the leveling routes showing stations (crosses) and the surface rupture (dark lines). Stations 1 through 22 were leveled in 1948, stations 21 through 41 were leveled in 1933, and all of the stations were releveled in 1984.

Figure 2. (a) Elevation changes projected on line L-L' of Figure 1. The reference level is arbitrary. (b) Relief along L-L'

Figure 3. Deformation of a half space due to a point source at 10 km (top) and 50 km focal depths (bottom). The left column is generated by a pure dip-slip point source. The right column is generated by a pure strike-slip point source. Vertical scale in top row is 25 times the scale of the bottom row. The area is 200 km by 200 km.

Figure 4. (a) Distribution of moment strength along the fault. (b) Deformation at the ith observation point as the sum of q sources on the fault plane (or line).

Figure 5. Comparison of observed and theoretical vertical displacement (top) and
downdip distribution of moment strength (bottom) for the best fitting line source.

Figure 6. Surface projection of the best fitting planar fault model and lower hemisphere representation of the focal mechanism.

Figure 7. Same as Figure 5 but for the planar source. The down-dip distribution of moment or equivalent slip is shown.

Figure 8. Sensitivity of the variance with respect to the parameters involved in the inversion. The dashed line, which corresponds to 5% increase of the variance above the minimum value, is used to estimate precision in the determination of the parameters.

Figure 9. (a) Observed variation of fault scarp height along strike. (b) Best fitting variation of slip along strike for three different fault lengths. The minimum residual is obtained for a fault length of 20 km. The 31 km fault increases the residual by 60%. Note that only a 20% variation of moment along strike is demanded by the data.

Figure 10. Relative contribution to surface vertical displacement as a function of the down-dip distance along a uniform slip fault 20 km long which dips 49°. These Sensitivity Kernels are calculated for points points $(a), (b)$ and (c) which correspond to the locations of stations 17, 21-27, and 30 of Figure 1.

Figure 11. (b) Theoretical and observed subsidence at stations 21 through 27 for three representations of slip on a fault 20 km width: (1) Extrapolation to depth of the scarp heights observed at the surface (solid line). (2) Extrapolation to depth of smoothed-observed slip at the surface (dashed line). (3) Uniform slip extrapolated to depth (dashed-dotted line).

Figure 12. Sensitivity of variance with respect to fault shape parameters b_1 (surface dip) and b_2 (curvature). Antilistric represents a fault which its dip steepens with depth. Contours connect points of equal variance: 5, 10, and 50% above the minimum value at (a).

Figure 13. Fault shapes for points $(a\text{-}e)$ depicted in Figure 11. The best solution [point (a)] represents a slightly downward curved fault, however, it does not fit significantly better than the best planar model. Models $(b), (c), (d)$ and (e) lie on the contour corresponding to a 50% increase in variance and are equally poor fits to the data.

Figure 14. Comparison of synthetic (top trace) and observed (bottom trace) long period P-waves. The preferred nodal plane is indicated by the arrows.

Figure 15. Variation of P waveforms for different source parameters. (a) Variation with azimuth. (b) Variation with dip. (c) Variations with rake. A source depth of 16 km and time function as depicted in Figure 14 are used.

Figure 16. Comparison of synthetic (top trace) and observed (bottom trace) long period SH-waves.

Figure 17. Variation of SH waveforms for different source parameters. (a) Variation with azimuth. (b) Variation with dip. (c) Variations with rake.

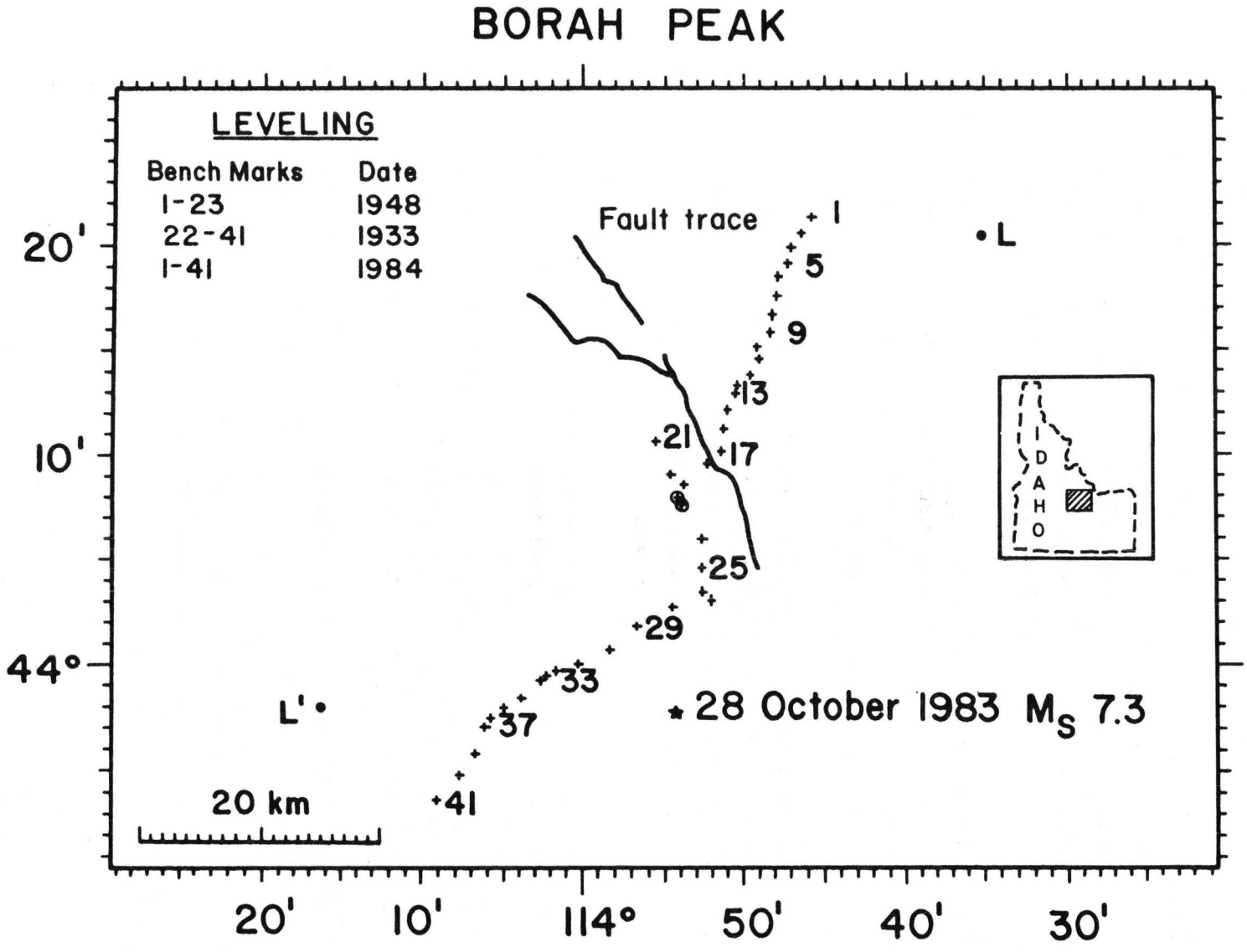
BORAH PEAK
LEVELING
Bench Marks
1-23
22-41
1-41
Date
1948
1933
1984
Fault trace
1
5
9
13
17
21
25
29
33
37
41
L
L'
28 October 1983 M_S 7.3
20 km
IDAHO
20'
10'
44°
20'
10'
114°
50'
40'
30'

FIG.1

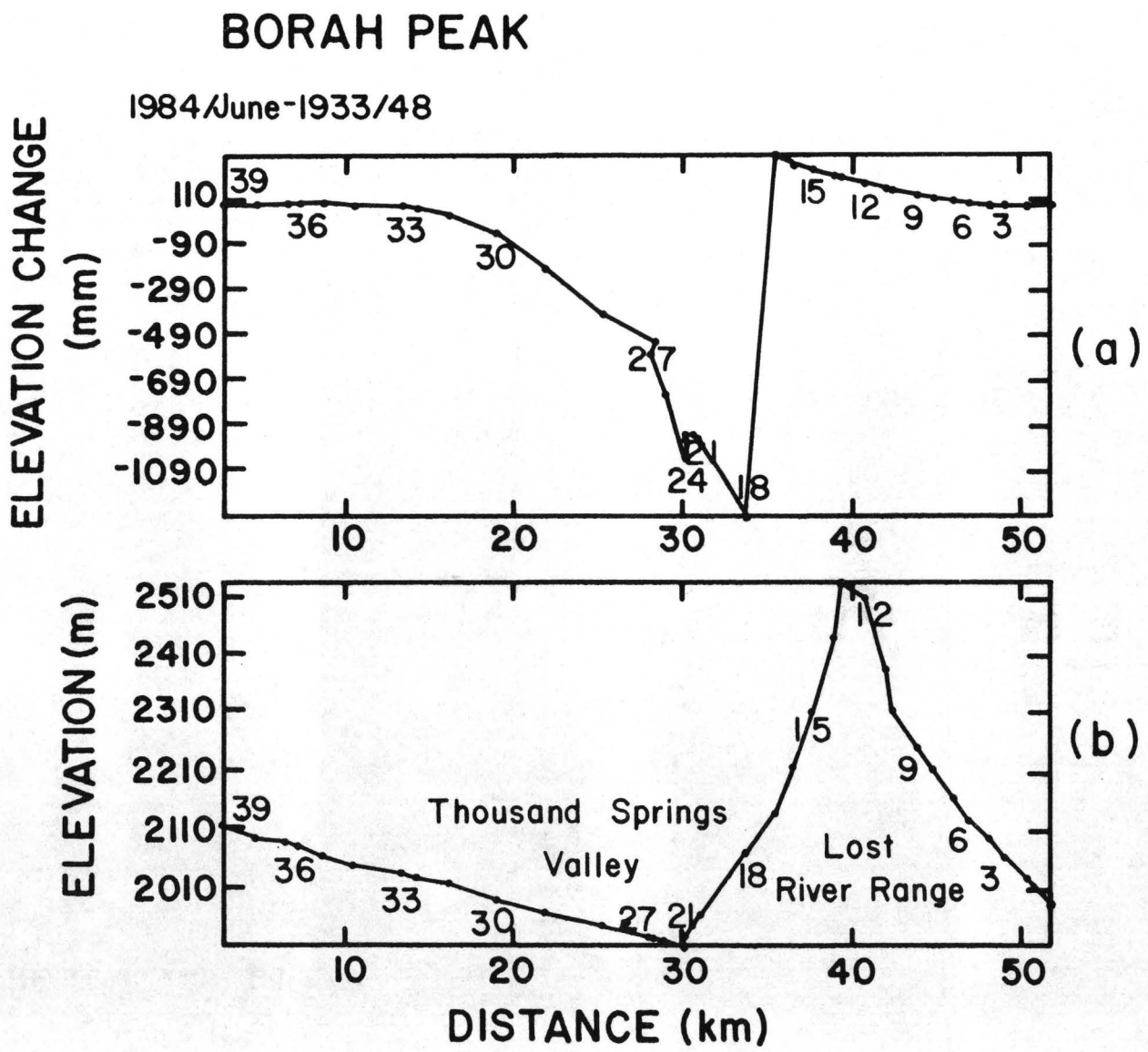
BORAH PEAK
1984/June-1933/48
ELEVATION CHANGE (mm)
110
-90
-290
-490
-690
-890
-1090
39
36
33
30
27
24
18
15
12
9
6
3
10
20
30
40
50
(a)
ELEVATION (m)
2510
2410
2310
2210
2110
2010
Thousand Springs Valley
Lost River Range
(b)
DISTANCE (km)

FIG. 2

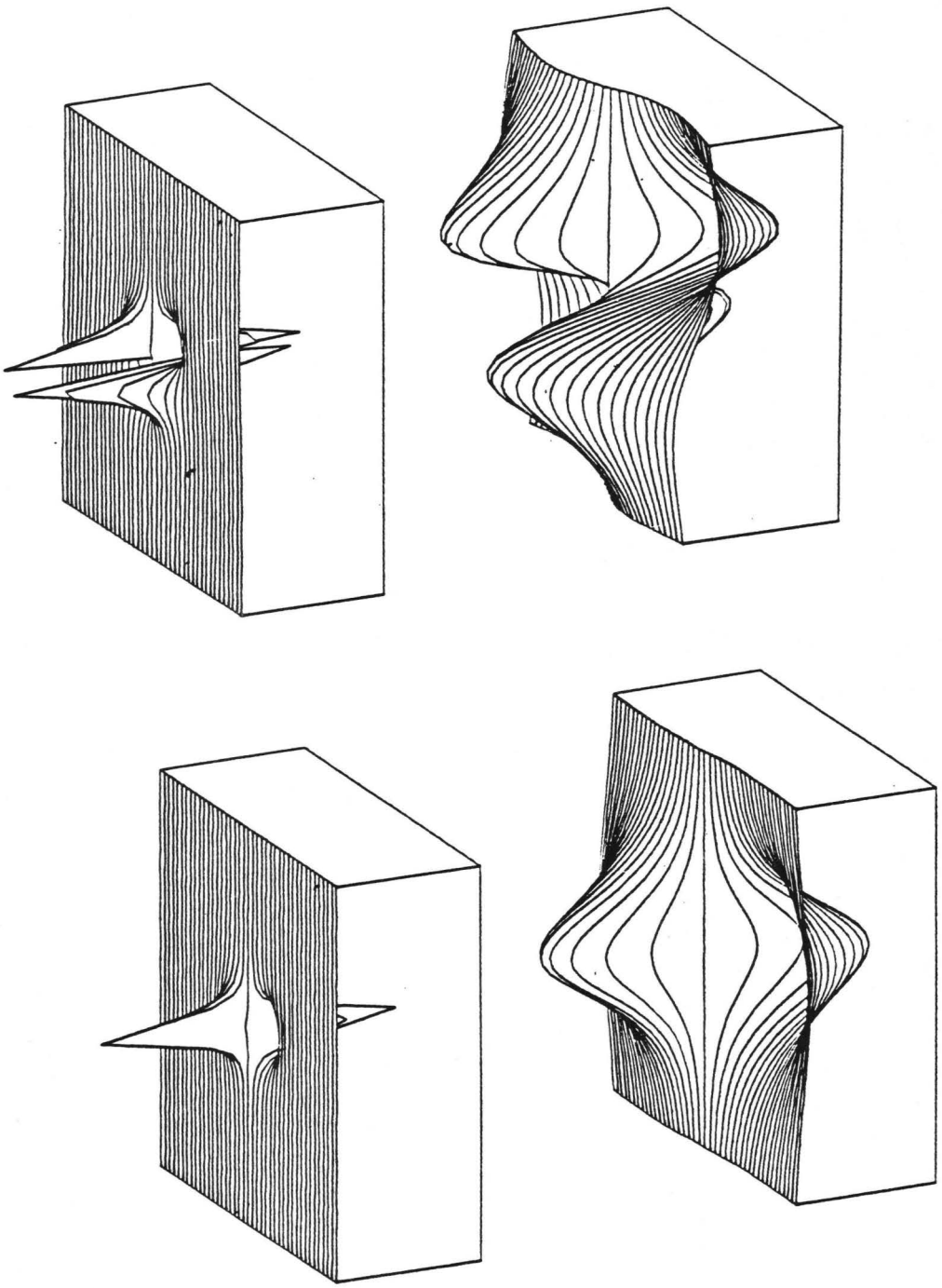

FIG. 3

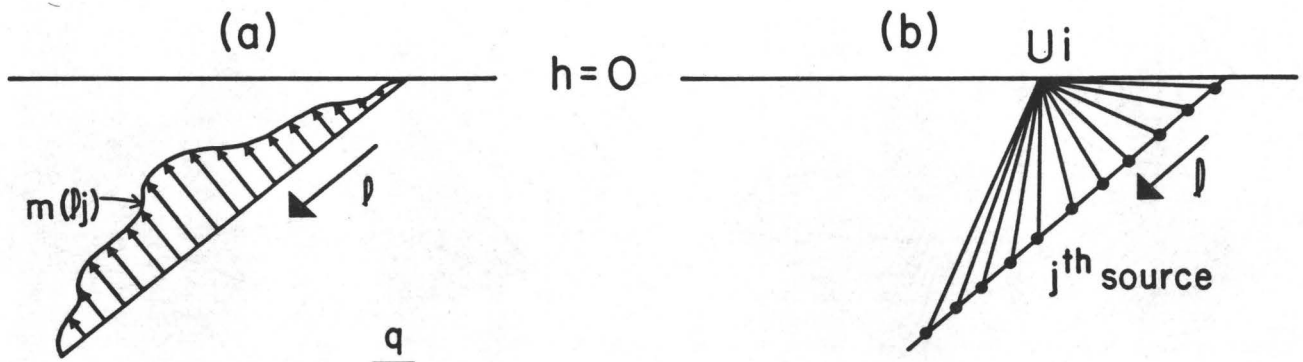

$$u_i = \sum_{j=1}^{q} t_i(\ell_j)\, m(\ell_j)$$

$t_i(\ell_j)$ = displacement at point i due to a source with moment m_j at ℓ_j

FIG. 4

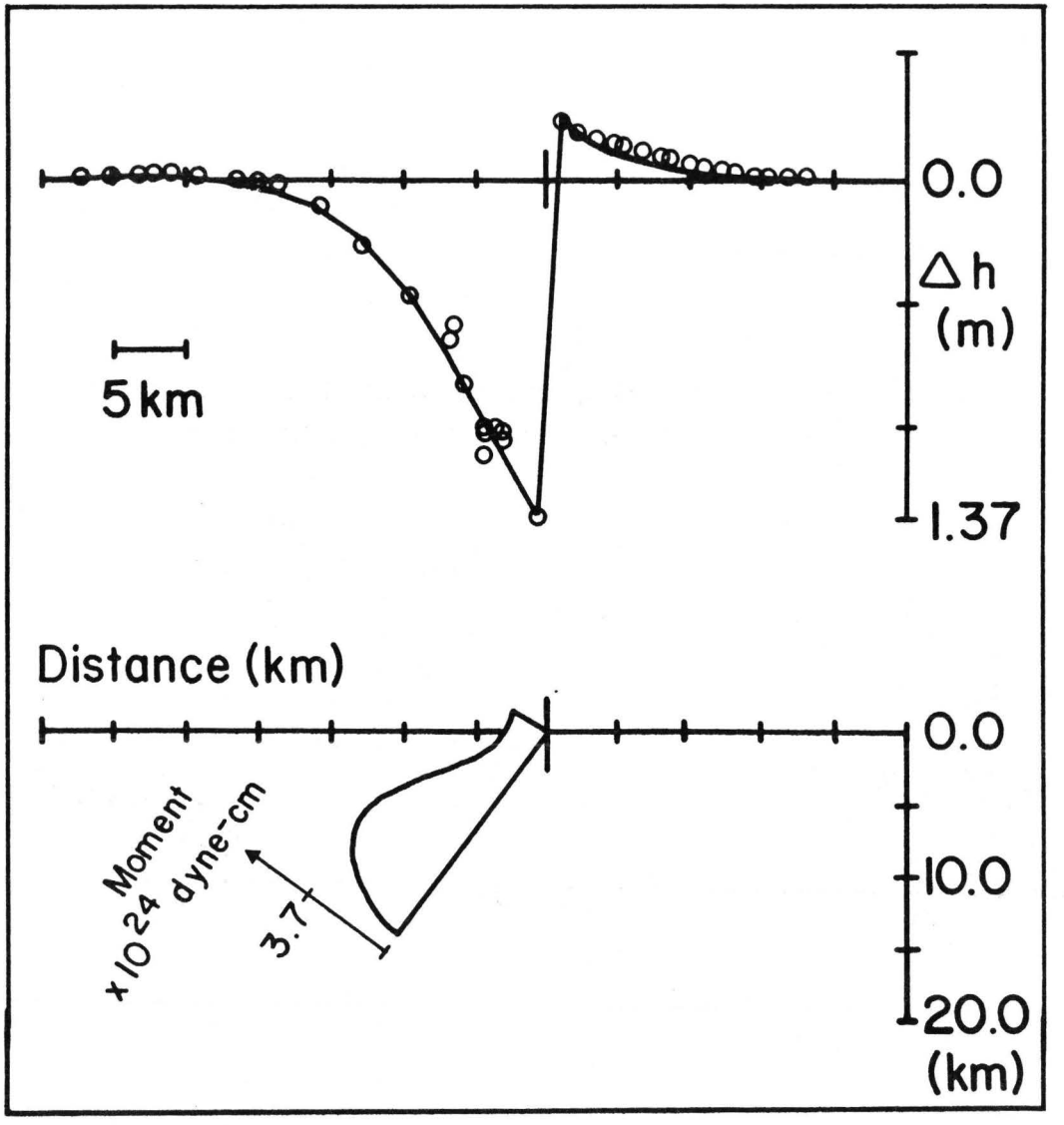
LINEAR MODEL
0.0
Δh
(m)
1.37
5km
Distance (km)
0.0
10.0
20.0
(km)
Moment
x1024 dyne-cm
3.7

FIG. 5

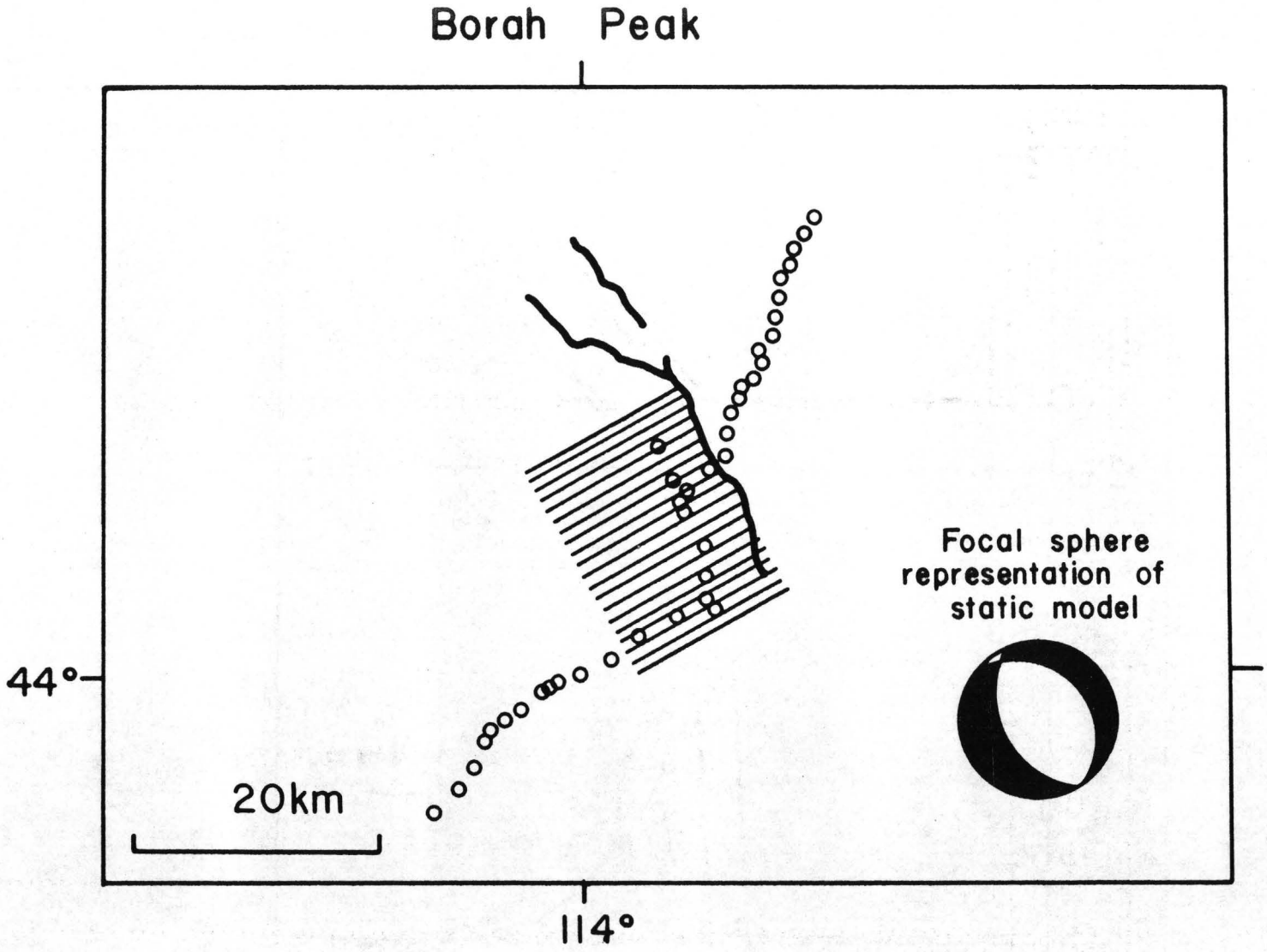
Borah Peak
44°
114°
20km
Focal sphere
representation of
static model

FIG. 6

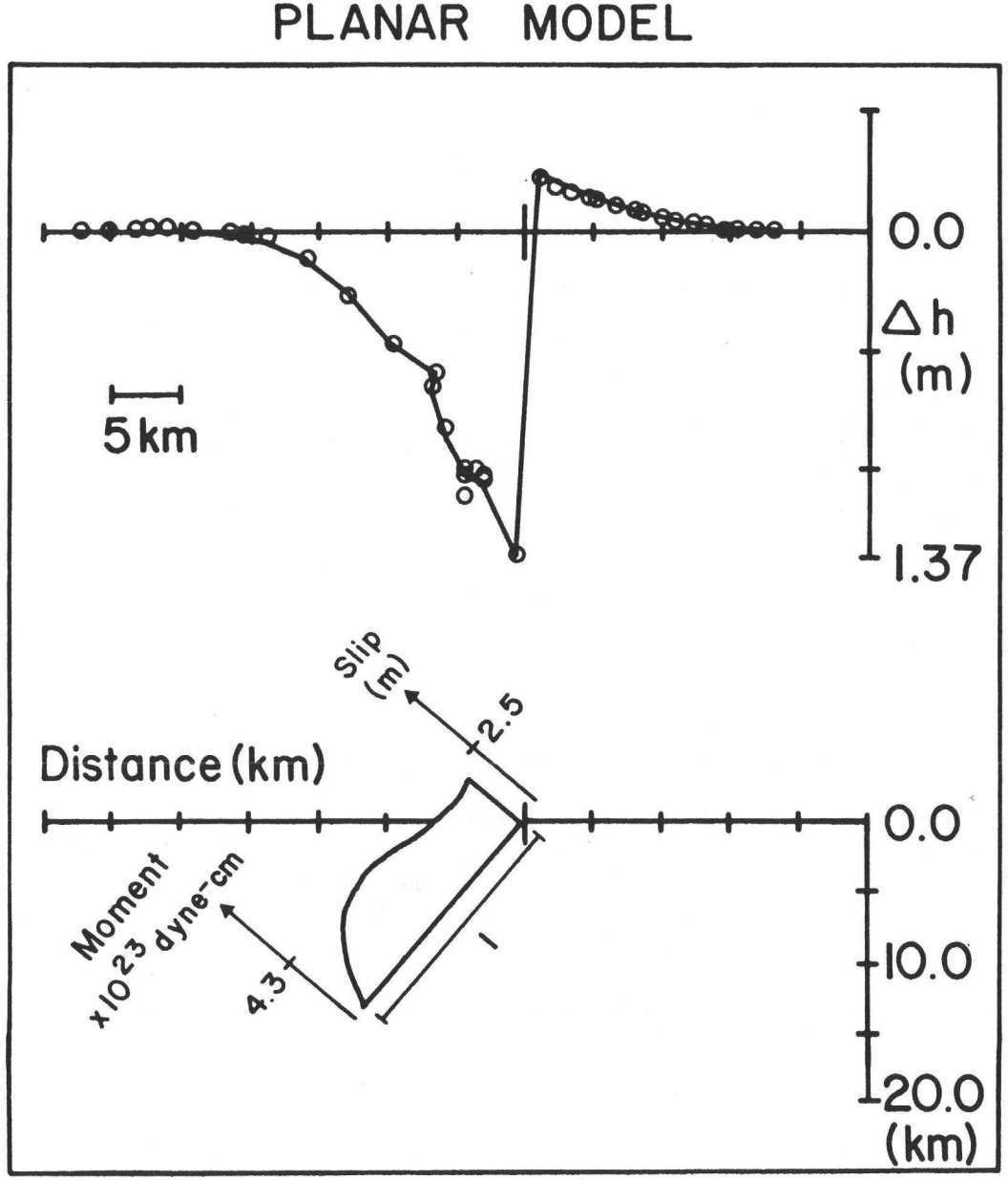
PLANAR MODEL
0.0
Δh
(m)
1.37
5km
Slip
(m)
2.5
Distance (km)
0.0
Moment
x1023 dyne-cm
4.3
l
10.0
20.0
(km)

FIG. 7

SENSITIVITY OF VARIANCE

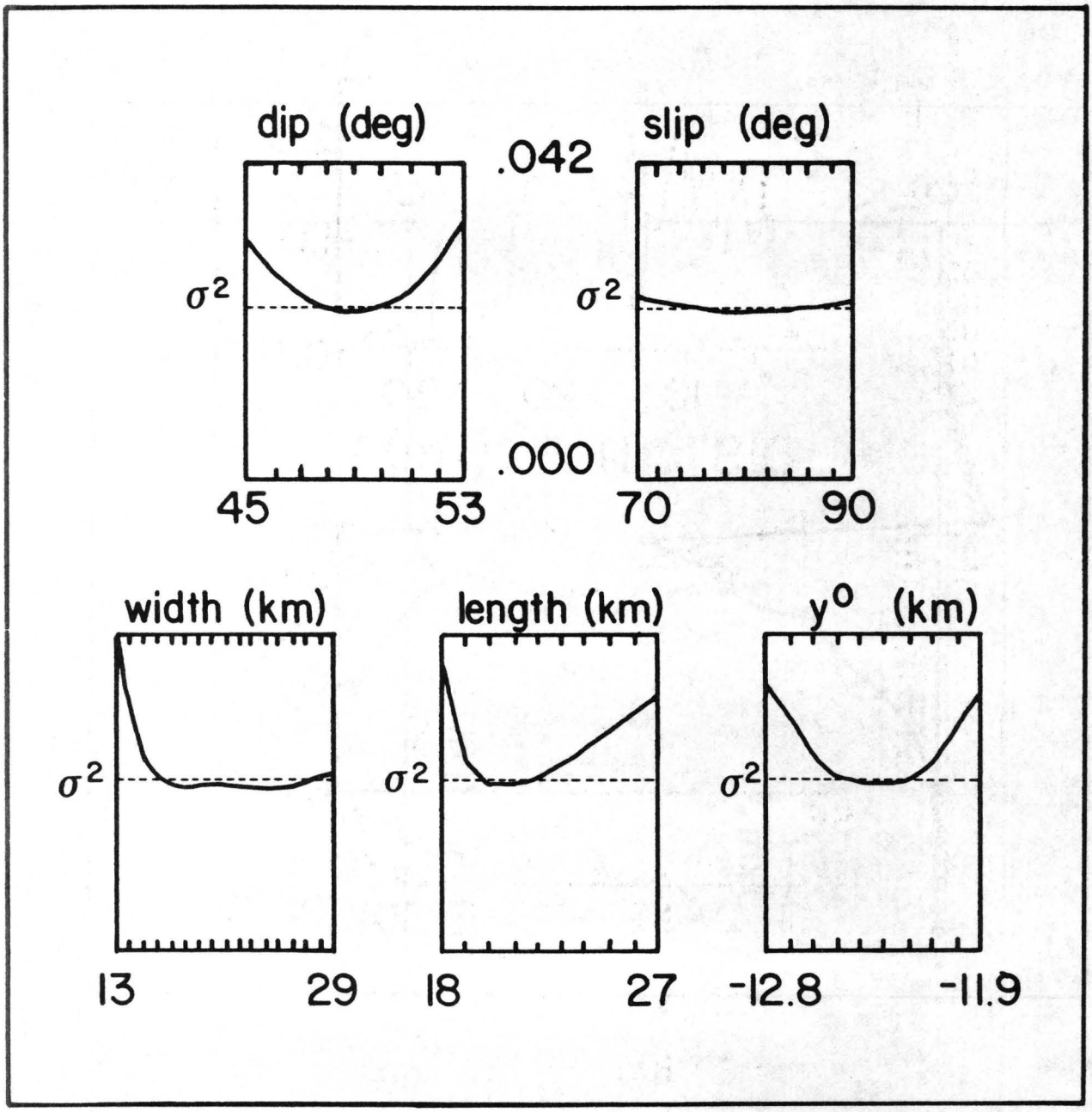

FIG. 8

VARIATION OF SLIP ALONG STRIKE

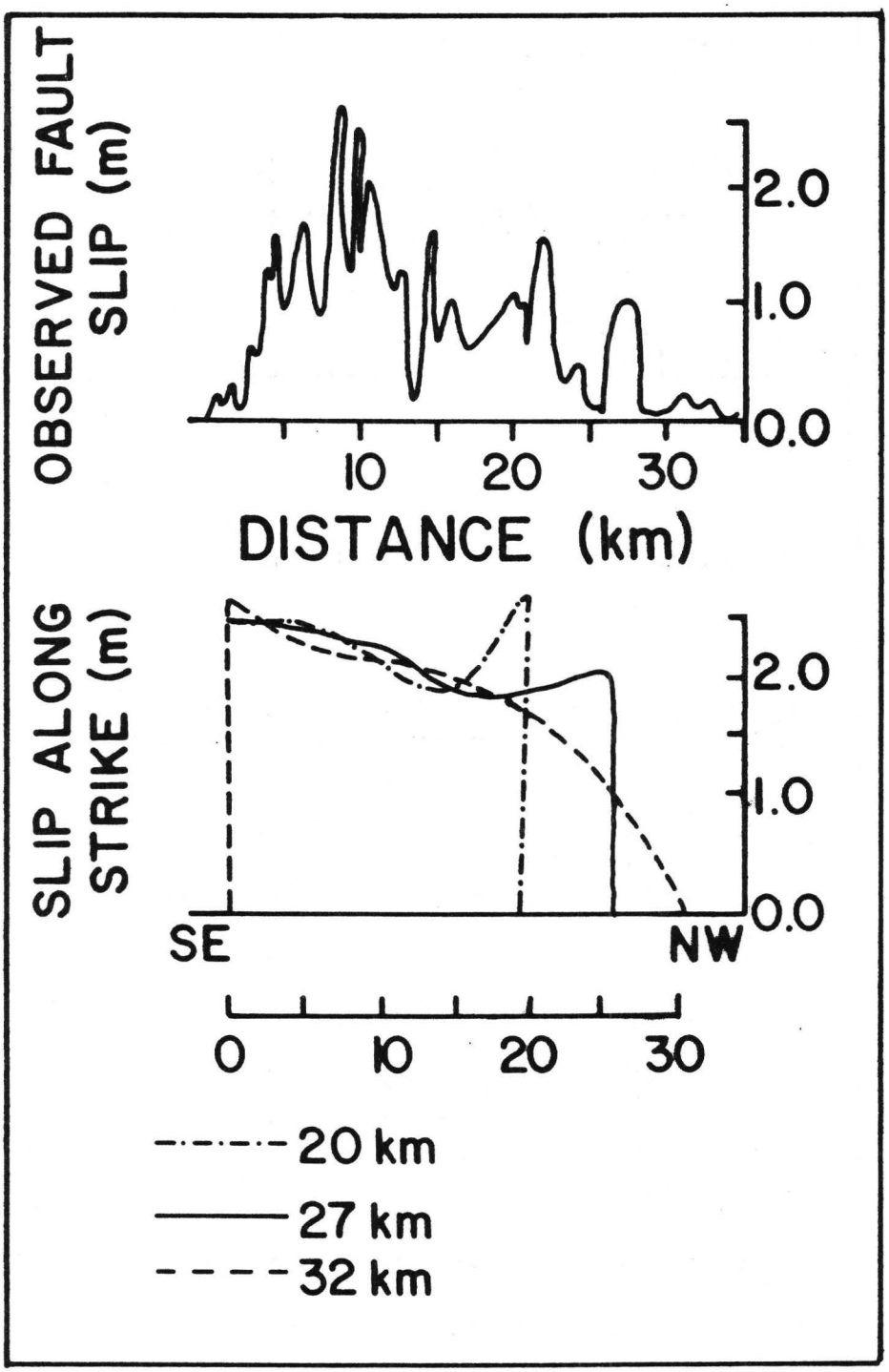

FIG. 9

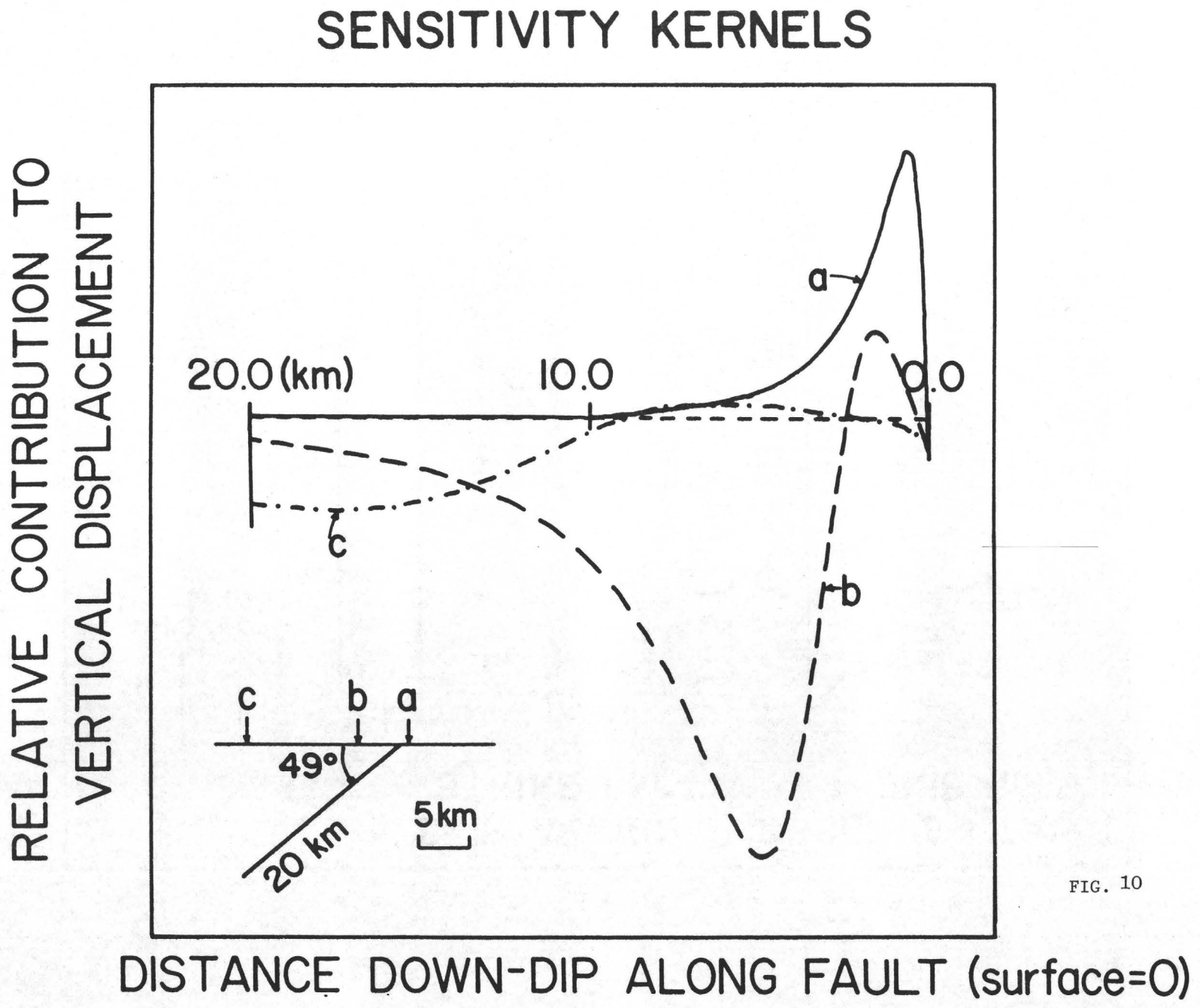
SENSITIVITY KERNELS
RELATIVE CONTRIBUTION TO VERTICAL DISPLACEMENT
20.0 (km)
10.0
0.0
a
b
c
c b a
49°
5km
20 km
DISTANCE DOWN-DIP ALONG FAULT (surface=0)

FIG. 10

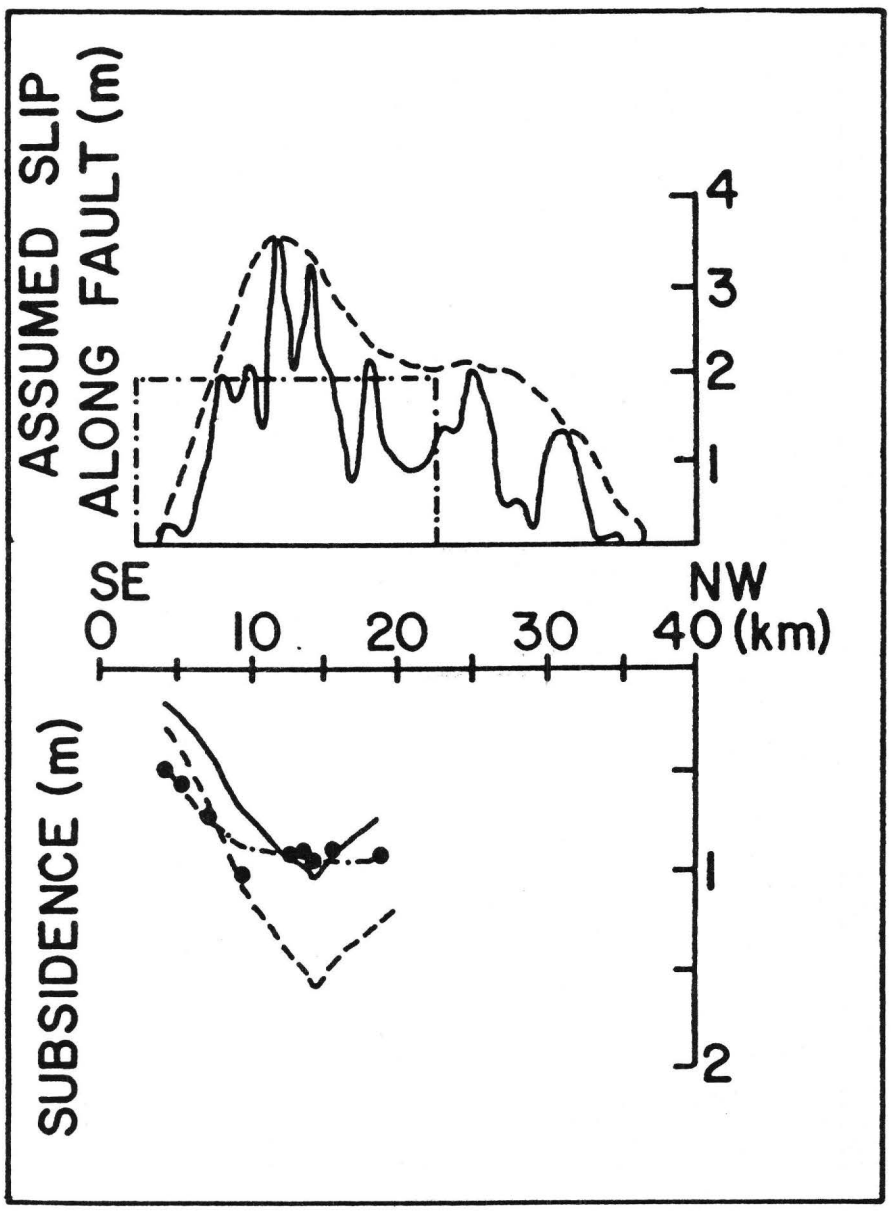
ASSUMED SLIP ALONG FAULT (m)
4
3
2
1
SE
NW
0
10
20
30
40 (km)
SUBSIDENCE (m)
1
2

FIG. 11

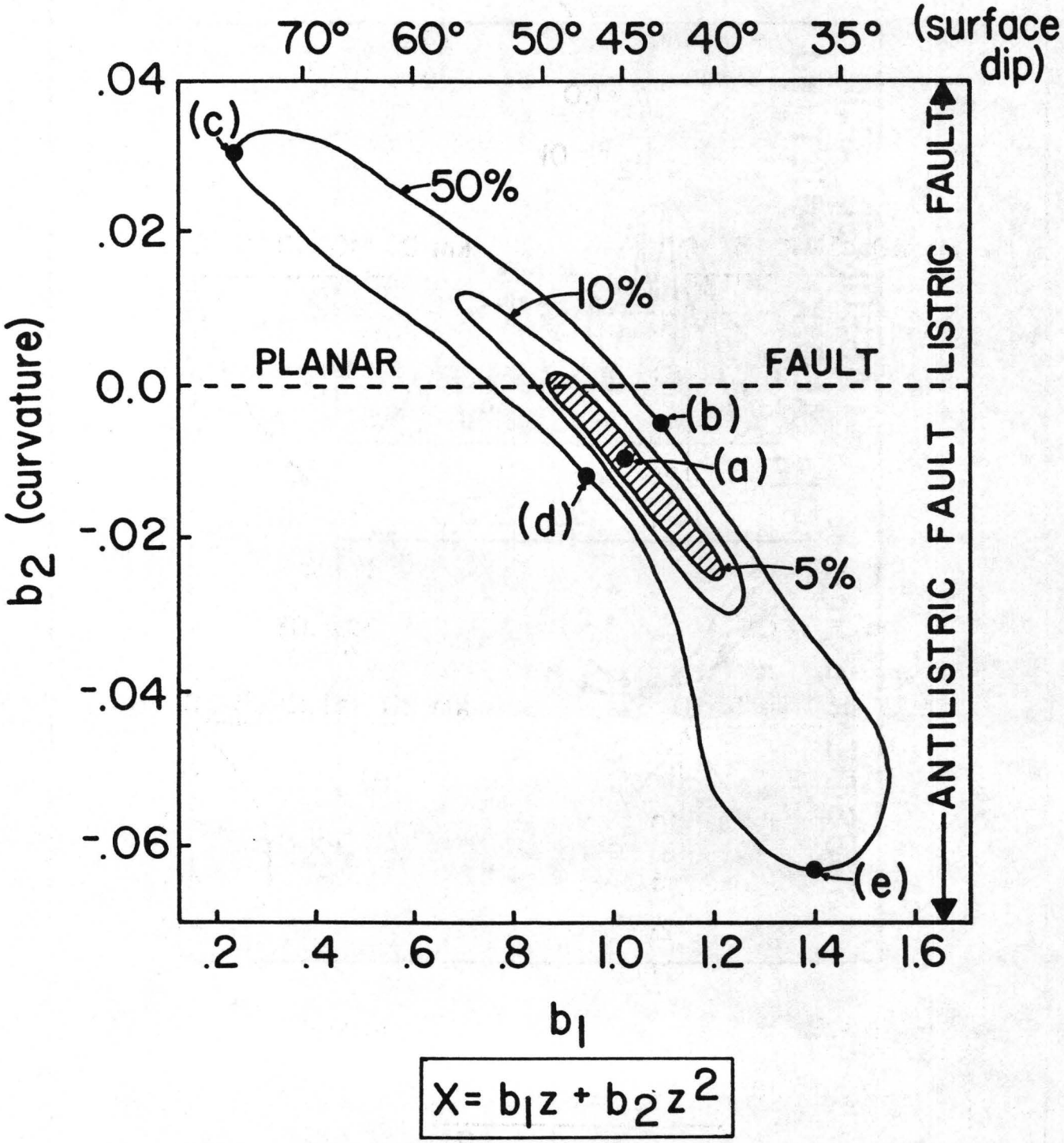
70° 60° 50° 45° 40° 35° (surface dip)
.04
.02
0.0
-.02
-.04
-.06
b2 (curvature)
(c)
50%
10%
PLANAR
FAULT
LISTRIC FAULT
(b)
(a)
(d)
5%
ANTILISTRIC FAULT
(e)
.2 .4 .6 .8 1.0 1.2 1.4 1.6
b1
X= b1z + b2z2

FIG. 12

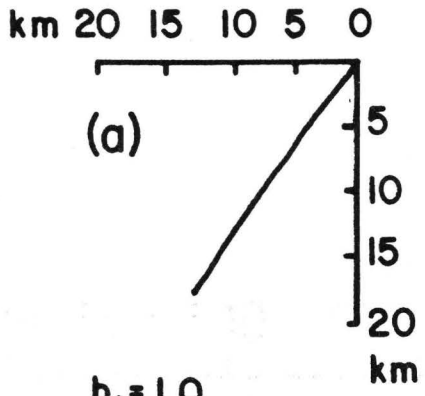

$b_1 = 1.0$

$b_2 = -.01$

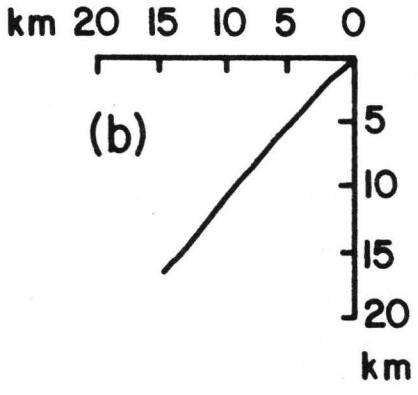

$b_1 = 1.1$

$b_2 = -.005$

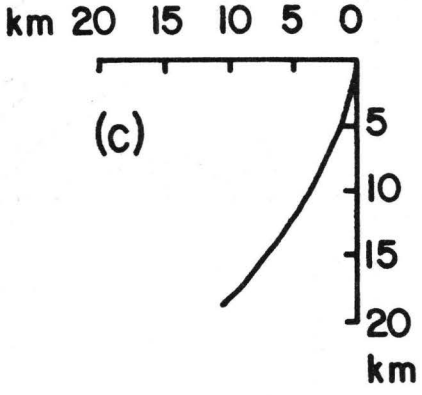

$b_1 = .2$

$b_2 = .03$

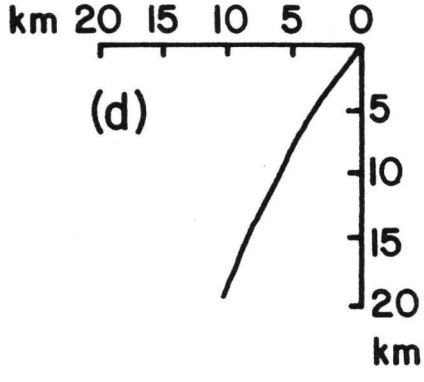

$b_1 = .9$

$b_2 = -.015$

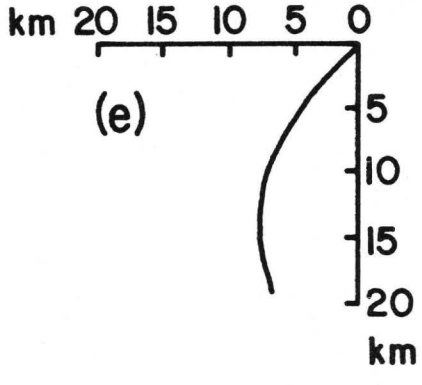

$b_1 = 1.4$

$b_2 = -.06$

$$X = b_1 z + b_2 z^2$$

FIG. 13

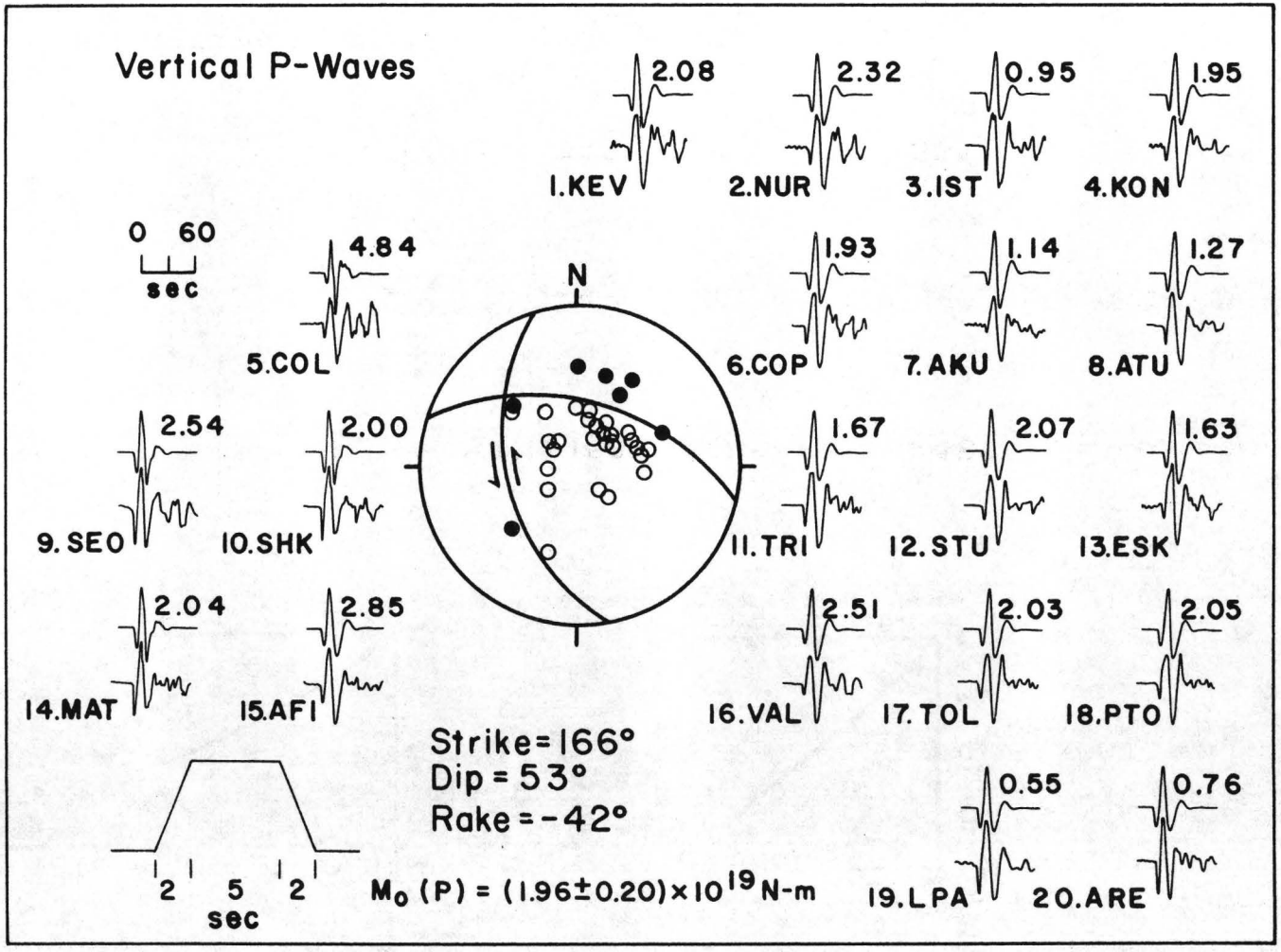
Vertical P-Waves
2.08
2.32
0.95
1.95
1.KEV
2.NUR
3.IST
4.KON
0 60
sec
4.84
1.93
1.14
1.27
5.COL
6.COP
7.AKU
8.ATU
N
2.54
2.00
1.67
2.07
1.63
9.SEO
10.SHK
11.TRI
12.STU
13.ESK
2.04
2.85
2.51
2.03
2.05
14.MAT
15.AFI
16.VAL
17.TOL
18.PTO
Strike=166°
Dip=53°
Rake=-42°
0.55
0.76
2
5
2
sec
M_o (P) = (1.96±0.20)×10^{19} N-m
19.LPA
20.ARE

FIG. 14

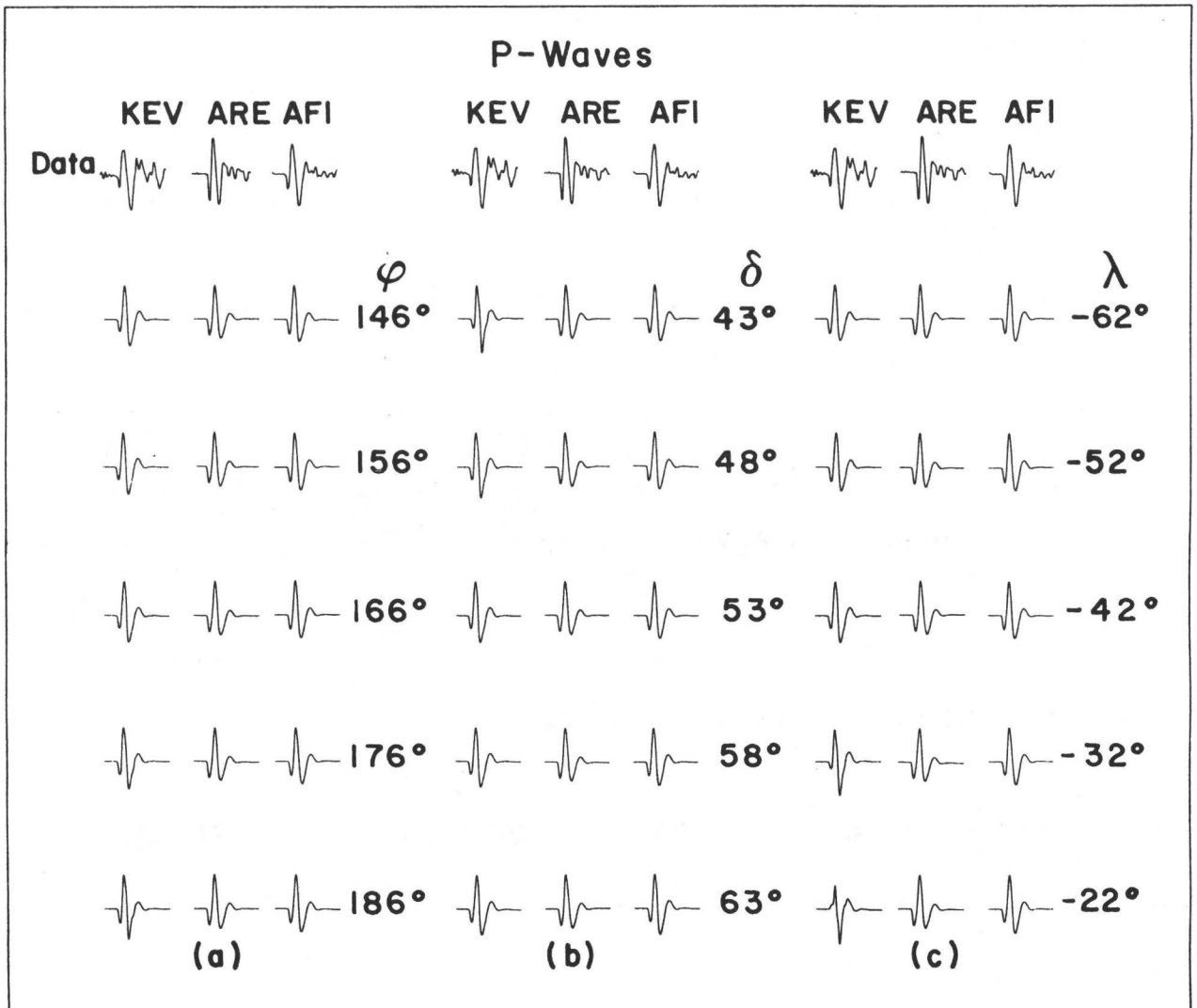
P-Waves
KEV ARE AFI
KEV ARE AFI
KEV ARE AFI
Data
φ
δ
λ
146°
43°
-62°
156°
48°
-52°
166°
53°
-42°
176°
58°
-32°
186°
63°
-22°
(a)
(b)
(c)

FIG. 15

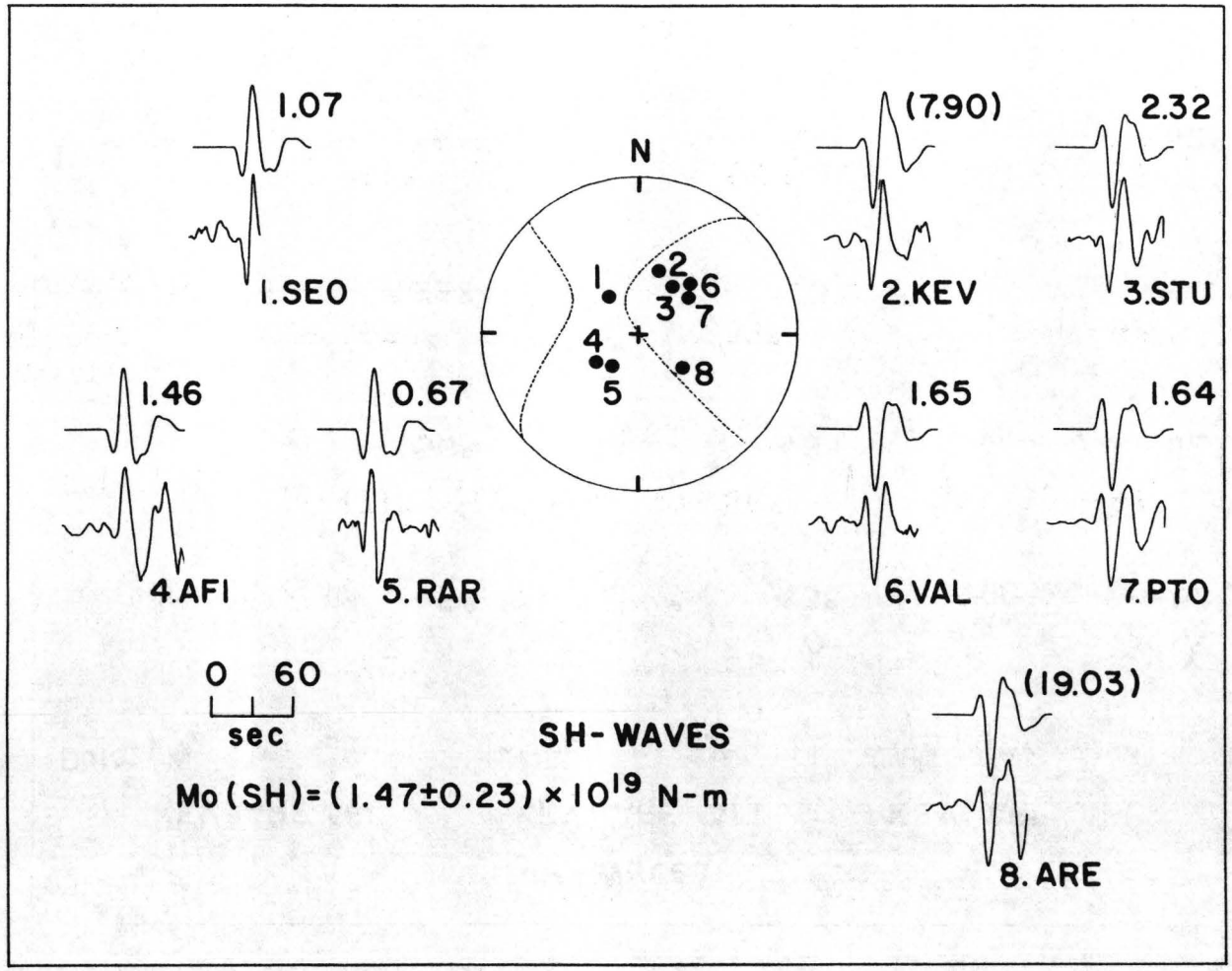
1.07
1.SEO
N
(7.90)
2.KEV
2.32
3.STU
1
2
3
6
7
4
5
8
1.46
4.AFI
0.67
5.RAR
1.65
6.VAL
1.64
7.PTO
0 60
sec
SH-WAVES
Mo(SH)=(1.47±0.23)×10^19 N-m
(19.03)
8.ARE

FIG. 16

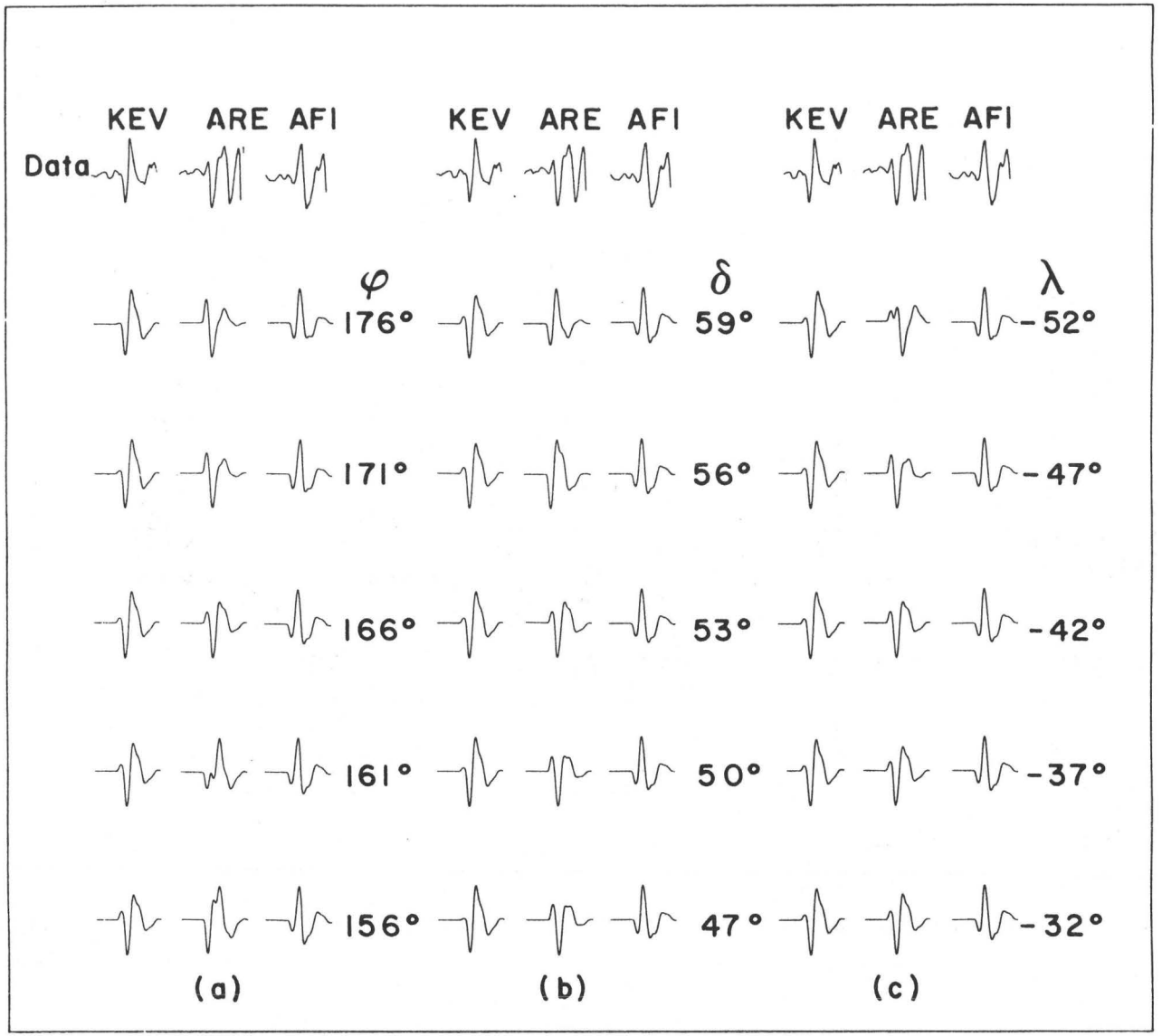
KEV ARE AFI
KEV ARE AFI
KEV ARE AFI
Data
φ
δ
λ
176°
59°
-52°
171°
56°
-47°
166°
53°
-42°
161°
50°
-37°
156°
47°
-32°
(a)
(b)
(c)

FIG.17

Vertical Movements Associated with the 1959, M=7.1 Hebgen Lake Montana Earthquake

Robert Reilinger+
Air Force Geophysics Laboratory
Hanscom Air Force Base, Massachusetts 01731

Abstract

Precise releveling measurements conducted by the National Geodetic Survey in 1983 combined with previous leveling observations in 1923, 1960, 1967, and 1975 provide evidence for continuing uplift of a broad region surrounding the epicentral area of the 1959 Hebgen Lake earthquake. The newly releveled survey route, which passes within 25km of the 1959 epicenter, indicates a maximum uplift during the post-seismic period (1960 to 1983) of about 35cm relative to benchmarks 90km to the south. Post-seismic uplift continued at least through 1967. The spatial pattern of post-seismic deformation along this survey route is very similar, but larger in magnitude, to deformation during the predominantly pre/co-seismic period (1923 to 1960). Maximum uplift during the period 1923 to 1960 reached about 15cm relative to benchmarks 50km to the south. Because the 1960 leveling survey was conducted about one year after the 1959 earthquake, movements during the predominantly pre/co-seismic period (1923 to 1960) may be significantly affected by post-seismic deformation. The doming region appears to be bordered to the south by a zone of relative subsidence which has a wavelength comparable to that of the uplift and about half the amplitude. The peripheral subsidence occurs during both the pre/co-seismic and the post-seismic periods, and is approximately coincident with the Snake River downwarp. The new releveling observations suggest that the area of relative uplift extends 20 to 50km further north than previously reported, giving it a linear extent of about 100km in the region crossed by the leveling route. A number of lines of evidence suggest that the 1959 Hebgen Lake earthquake fault system extends at depth at least 30km east of the mapped surface fault. The 1975, M = 6.0 Yellowstone Park earthquake may have been associated with the eastern segment of the fault responsible for the 1959 Hebgen Lake event. In addition to defining post-seismic doming of the 1959 Hebgen Lake earthquake epicentral area, the new leveling survey indicates that resurgence and associated uplift of the Yellowstone Caldera continued during the period 1975 to 1983.

The structure of the Hebgen Lake region (high regional elevation with superimposed down-faulted basins bounded by normal faults) is consistent with contemporary uplift representing a continuation of

---

+ Now at: Department of Earth, Atmospheric, and Planetary Sciences, Earth Resource Laboratory, E34-342, Massachusetts Institute of Technology, Cambridge, MA 02142

deformational processes which have been active throughout the Late Cenozoic. The high rates of present day movements relative to long term geological rates most likely result from rapid strain changes associated with the 1959 earthquake. Although the fundamental mechanism responsible for contemporary doming of the Hebgen Lake region remains uncertain, viscoelastic response in the asthenosphere to crustal strain induced by the 1959 earthquake may be involved.

Introduction

In 1983, the National Geodetic Survey releveled a 440km long, approximately north-south route extending from Pocatello, Idaho, through West Yellowstone to Livingston, Montana. This route, previously leveled in 1923 and 1960, passes to within about 25km of the reported epicenter of the 1959, M=7.1 Hebgen Lake earthquake (Figure 1). On the basis of the earlier surveys along this route as well as other routes traversing the Hebgen Lake area, together with field observations, Myers and Hamilton (1964) and Savage and Hastie (1966) reported and interpreted co-seismic deformation for the 1959 event. The earthquake was a normal fault event on a northwest-southeast striking, south dipping (dip $\sim 55°$) fault. Co-seismic subsidence reached a maximum of about 6.7 m just south of the major surface break (Hebgen Lake fault). More recently Reilinger et al. (1977) examined elevation changes over a more extensive region and reported a broad doming of the 1959 epicentral area (Figure 2). While the early time behavior of this regional doming was unclear, uplift apparently continued for at least one year following the earthquake. Additional evidence for post-earthquake deformation in the Hebgen Lake area was reported by Prescott et al. (1979) and Savage (1983) on the basis of trilateration surveys during the period 1973 to 1981.

This paper examines the implications of the 1983 releveling for previous interpretations of contemporary deformation in the Hebgen Lake region. These new data confirm the existence of broad doming of the 1959 epicentral area and indicate that deformation continued for at least 16 years following the earthquake. Measurable deformation apparently extends from 50 to 100km from the earthquake epicenter, considerably further than might be expected from the reported co-seismic surface faulting and the distribution of aftershocks.

In addition to their relevance to strain accumulation and release in the Hebgen Lake region, the observations presented here have potential implications for monitoring movements associated with the 1983, M=7.3 Borah Peak earthquake. Broad doming of the epicentral area out to distances of a few fault lengths (i.e. beyond major co-seismic deformation) may be characteristic of normal fault events in elevated regions (marginal evidence for Nevada Seismic Zone; Savage and Church, 1974, Reilinger, 1977). Frequent monitoring of vertical deformation around the site of the Borah Peak earthquake out to distances of 2 to 3 fault lengths could prove useful for testing this possibility and thereby enhance our understanding of the earthquake process in this tectonic setting (e.g. Koseluk and Bischke, 1981).

Leveling Data

The location of the 1983 leveling route is shown in Figures 1 & 2. This route was first surveyed in 1923 (first and second order leveling) and subsequently in 1960 (first order). Sections of the leveling route were surveyed by first order leveling in 1967 and 1975. Profiles of topography and relative elevation change along this route are given in Figures 3, 4, and 5. The movement profiles presented here are derived from observed elevations, uncorrected for possible atmospheric refraction. These profiles have not been connected to any external reference and therefore only relative movements, in effect deformations along the level line, are significant. The movement profile for the period 1923 to 1983 (Figure 3, bottom) has a gap at West Yellowstone making the connection ambigious at this point. This profile was constructed assuming no movement between the two closest benchmarks at West Yellowstone (note that uplift at West Yellowstone relative to points to both the north and south is well defined).

The elevation change profile for the period 1923 to 1960 (pre/co-seismic for 1959 earthquake) indicates the following significant features (Reilinger et al., 1977): 1) relative subsidence of the Snake River Plain - most pronounced above the Pleistocene Island Park caldera, 2) broad uplift centered at West Yellowstone (closest point to Hebgen Lake earthquake) relative to benchmarks to the south, east and north, 3) relative uplift of the Norris-Mammoth Corridor in Yellowstone Park, and 4) steep tilting near the intersection of the Gardiner, Mammoth, and Reese faults. The apparent regional tilt down to the north across the entire profile is probably not significant (this regional tilt is eliminated when the movements on the network of leveling lines shown in Figure 2 are adjusted for internal consistency: Reilinger et al., 1977).

The profile of elevation change for the post-seismic period (1960 to 1983) indicates a continuation of the broad scale movements for the earlier time interval. This includes both continuing relative subsidence of the Snake River Plain and uplift at West Yellowstone relative to benchmarks to the south, east and north. Deformation within Yellowstone National Park (between 280km and 340km) during the post-seismic period has a similar character to the earlier movements (i.e. relative subsidence at 300km and uplift to north), however the later movements have a shorter wavelength and smaller amplitude. Unfortunately there are no benchmarks in common between the 1983 and 1960 surveys in the vicinity of the Gardiner, Mammoth and Reese faults or across the Island Park caldera. The continuing nature of deformation during the post-seismic period is well illustrated by the bottom-most profile in Figure 3 which shows relative movement for the entire time interval, 1923 to 1983, as well as by the short profile segments for the periods 1960 to 1967 and 1960 to 1975 (Figure 4).

It is well known that releveling observations may be affected by systematic errors which can obscure or be mistaken for tectonic deformation (e.g. Reilinger and Brown, 1981). Elevation correlated errors (i.e. rod calibration and atmospheric refraction) which have become a central issue in crustal movement studies in California (e.g. Jackson et al., 1980; Stein, 1981) are believed to be the largest systematic

errors effecting leveling. The regional uplift which reaches a maximum approximately at West Yellowstone shows a gross positive correlation with topography. That is, the high Hebgen Lake - Yellowstone region appears to be uplifting relative to lower areas to the north and south (Figure 3). However, there is strong evidence against systematic errors in these observations. The pattern of relative uplift for the earlier time interval (1923 to 1960) is defined by five independent elevation change profiles (Figure 2) one of which shows a gross negative correlation with topography and one no correlation (Reilinger et al., 1977). In addition, careful examination of the elevation change profiles shows a poor detailed correlation between movements and topography. For example, the steep tilting south of West Yellowstone (195km to 225km) indicated by the 1923 to 1960 and 1960 to 1967 profiles occurs along a segment of the leveling route exhibiting rather low relief (<150 m). Furthermore, the more or less continuous nature of movements through time argues strongly against systematic errors. Thus, while the application of refraction corrections may slightly alter some of the details of the movements shown in Figures 3, 4, and 5, the major deformational features described in this study should not be significantly affected.

Discussion and Interpretation

The new releveling observations clearly indicate that the broad doming of the epicentral region and aftershock zone of the 1959 Hebgen Lake earthquake, previously interpreted as pre/co-seismic (Figure 2), continued at an accelerated rate during the post-seismic period. The average rate of uplift at West Yellowstone relative to benchmarks to the south reached 15mm/yr during the period 1960 to 1983. There are only two common benchmarks between the 1967 and 1983 surveys. These scanty data do however suggest that doming continued after 1967. Continuing deformation of the 1959 Hebgen Lake epicentral area is also supported by repeated trilateration measurements which have been conducted in this area since 1973 (Prescott and Savage, 1979; Savage, 1983). These trilateration measurements indicate uniaxial extension perpendicular to the Hebgen Lake fault at the rate of 0.25μstrain/yr. This strain is comparable in magnitude to those observed along the San Andreas fault and is the largest strain in the conterminous U.S. reported outside of California (Savage, 1983).

The rapid rate of post-seismic uplift of the Hebgen Lake area averaged over a 23-year time period (1960 to 1983) suggests the possibility that doming during the period 1923 to 1960 may be significantly affected by post-seismic movements immediately following the earthquake. The 1960 releveling was conducted about one year following the earthquake, sufficient time for a significant amount of post-seismic uplift to have occurred. In fact, it is quite possible that the entire uplift developed after the earthquake.

The 1975 and 1983 relevelings through Yellowstone National Park provide strong evidence of ongoing magmatic resurgence and associated uplift of the Yellowstone Caldera as well as suggesting some alteration of previous interpretations of deformation in this area presented by Reilinger et al. (1977). Relative subsidence during the period 1960 to 1975 centered near 300 km (Figure 4) has been attributed to co-seismic

deformation of the 1975 Yellowstone earthquake (Pitt et al., 1979). This rather localized relative subsidence is apparently superimposed on the broad doming of the Hebgen Lake region. As mentioned earlier the deformation near the 1975 epicenter (near 300 km on movement profiles) is similar to, although smaller than, deformation in this area during the pre/co-seismic period (1923 to 1960) of the Hebgen Lake event (relative subsidence near 300 km and relative uplift to the north in the Norris-Mammoth corridor: Figure 3). Relative subsidence near 300 km during the period 1923 to 1960 was previously associated with doming of the Hebgen Lake area (i.e., coming down from the maximum uplift near West Yellowstone) while relative uplift of the Norris-Mammoth corridor was attributed to possible magmatic resurgence in this area (Reilinger et al., 1977). Alternatively, it is possible that both relative subsidence near 300 km and uplift to the north during the period 1923 to 1960 result from co-seismic deformation of the 1959 earthquake. The focal mechanism, surface faulting, and co-seismic deformation for the 1959 earthquake indicate normal slip on a south dipping (55°) fault striking about N 80°W (Ryall, 1962; Myers and Hamilton, 1964; Savage and Hastie, 1966). This fault would project to the east just south of the uplift in the Norris Mammoth Corridor. Thus, uplift occurs over the upthrown block and subsidence over the downthrown block during the 1923 to 1960 time period - precisely the movements expected for co-seismic deformation. If the movements between West Yellowstone and Mammoth for the period 1923 to 1960 do represent co-seismic deformation, then doming of the Hebgen Lake region during this period may extend as far north as Mammoth, as appears to be the case for the period 1960 to 1983 (Figure 4 with localized subsidence near 300 km removed.) In addition, the 1959 earthquake fault would have to extend considerably further east than originally believed. The similarity between the deformation associated with the 1975 earthquake (Figure 4) and the possible co-seismic movements of the 1959 earthquake in this same area suggests that the 1975 event resulted from the same stress field as the 1959 earthquake and possibly occurred on an along-strike extension of the eastern segment of the Hebgen Lake fault system. The more or less continuous seismic activity extending from Yellowstone National Park through and northwest of Hebgen Lake (Figure 2; also Trimble and Smith, 1975) and the similar focal mechanisms for the 1959 and 1975 shocks (Pitt et al., 1979; Ryall, 1962) seem consistent with this extension of the Hebgen Lake fault system.

Figure 5 shows elevation changes derived from comparison of a 1975 survey in Yellowstone Park and the corresponding section of the new 1983 survey. Because this profile is rather short and does not extend to West Yellowstone, it is not particularly illuminating in regard to doming of the Hebgen Lake region. However, the profile clearly indicates symmetric relative uplift where the route crosses the Yellowstone Caldera. Pelton and Smith (1979) reported uplift of the caldera from independent leveling surveys for the period 1923 to 1975. They suggested that this uplift was due to inflation of a magma chamber beneath the thermally active Yellowstone area. The leveling profile in Figure 5 indicates that resurgence and associated uplift continued after 1975. The tilt rate indicated by the new elevation change profile is quite similar to that for the earlier time period suggesting that uplift may be occuring at a more or less

uniform rate. Continuing uplift of the Yellowstone caldera is also supported by repeat gravity measurements for the period 1977 to 1983 (Jackson et al., 1984).

Although the detailed mechanism responsible for doming of the 1959 Hebgen Lake epicentral region remains uncertain, the spatial association with the earthquake and the rapid rate of deformation clearly indicate a direct relationship between doming and the 1959 event. In addition, relative subsidence of the Snake River Plain, which occurs immediately south of the uplifted area and is defined by similar tilts, is likely associated with the same underlying mechanism as the adjacent uplift. The long wavelength of the observed deformation indicates a deep seated cause probably involving the entire lithosphere. Furthermore, the volume of crust which subsided during the 1959 earthquake is approximately equal to the volume uplifted since the earthquake (assuming uplift is entirely post-seismic and has the approximate dimensions indicated in Figure 2). The consistency of contemporary movements with the Late Cenozoic structure of the region suggests that present day movements result from processes which have been active intermittently (given high rates at present) throughout the Late Cenozoic. These observations suggest, in a general way, that post-seismic viscoelastic responses to crustal strain accompanying the 1959 earthquake may be responsible for the observed uplift.

More information on the temporal and spatial patterns of deformation in this active area could be obtained by carrying out additional leveling of the routes shown in Figure 2 (most not leveled since 1960). Such information could prove useful for deducing underlying mechanisms and thereby further our understanding of strain accumulation and release in this and similar tectonic areas.

Acknowledgements

I am grateful to the National Geodetic Survey for making available the leveling observations reported here. Diane Doser generously provided me with a preprint of her paper on the Hebgen Lake earthquake. I thank Katharine Kadinsky-Cade and Jim Savage for their reviews and helpful suggestions and comments.

References

Coffman, J. L., and C.A. von Hake, Earthquake history of the United States, Publ. 41-1, pp. 59-88, U.S. Dept. of Commer., Washington, D.C., 1973

Jackson, D. D., W. B. Lee, and C. Liu, Aseismic uplift in southern California: An alternative interpretation, Science, 210, 534-536, 1980.

Jackson, S. M., R. B. Smith, and T. L. Olsen, Recent uplift of the Yellowstone Caldera from precision gravity measurements, EOS, Trans. Am. Geophys. Union, 65, pg. 1118, 1984.

Koseluk, R. A., and R. E. Bischke, An elastic rebound model for normal fault earthquakes, J. Geophys. Res., 86, 1081-1090, 1981.

Myers, W. F., and W. Hamilton, Deformation accompanying the Hebgen Lake earthquake of August 17, 1959, U.S. Geol. Surv. Pap. 435, 55-98, 1964.

Pelton, J. R., and R. B. Smith, Recent crustal uplift in Yellowstone National Park, Science, 206, 1179-1182, 1979.

Pitt, A. M., C. S. Weaver and W. Spence, The Yellowstone Park earthquake of June 30, 1975, Bull. Seismol. Soc. Amer., 69, 187-205, 1979.

Prescott, W. H., J. C. Savage, and W. T. Kinoshita, Strain accumulation in the western United States between 1970 and 1978, J. Geophys. Res., 84, 5423-5435, 1979.

Reilinger, R. E., Vertical crustal movements from repeated leveling data in the Great Basin of Nevada and western Utah, EOS, Trans. Am. Geophys, Union, 58, 1238, 1977.

Reilinger, R. E., G. P. Citron, and L. D. Brown, Recent vertical crustal movements from precise leveling data in southwestern Montana, western Yellowstone National Park, and the Snake River plain, J. Geophys. Res., 82, 5349-5359, 1977.

Reilinger, R. E., and L. Brown, Neotectonic deformation, near-surface movements and systematic errors in U.S. releveling measurements: Implications for earthquake prediction, in Earthquake Prediction, An International Review, edited by D. W. Simpson and P. G. Richards, Maurice Ewing Ser., v. 4, Amer. Geophys. Union, Washington, D.C., p. 422-440, 1981.

Ryall, A., The earthquake of Hebgen Lake, Montana, on August 18, 1959: P waves, Bull. Seismol. Soc. Amer., 52, 235-271, 1962.

Savage, J. C., and L. M. Hastie, Surface deformation associated with dip-slip faulting, J. Geophys. Res., 71, 4897-4904, 1966.

Savage, J. C., and J. P. Church, Evidence for post-earthquake slip in the Fairview Peak, Dixie Valley, and Rainbow Mountain fault areas of Nevada, Bull. Seismol. Soc. Am., 64, 667-698, 1974.

Savage, J. C., Strain accumulation in western United States, Ann. Rev. Earth Planet. Sci., 11, 11-43, 1983.

Stein, R., Discrimination of tectonic displacement from slope-dependent errors in geodetic leveling from southern California, 1953-1979, in Earthquake Prediction, An International Review, edited by D. W. Simpson and P. G. Richards, Maurice Ewing Ser., v. 4, Amer. Geophys. Union, Washington, D.C., p. 441-455, 1981.

Trimble, A. B., and R. B. Smith, Seismicity and contemporary tectonics of the Hebgen Lake - Yellowstone Park region, J. Geophys. Res., 80, 733-741, 1975.

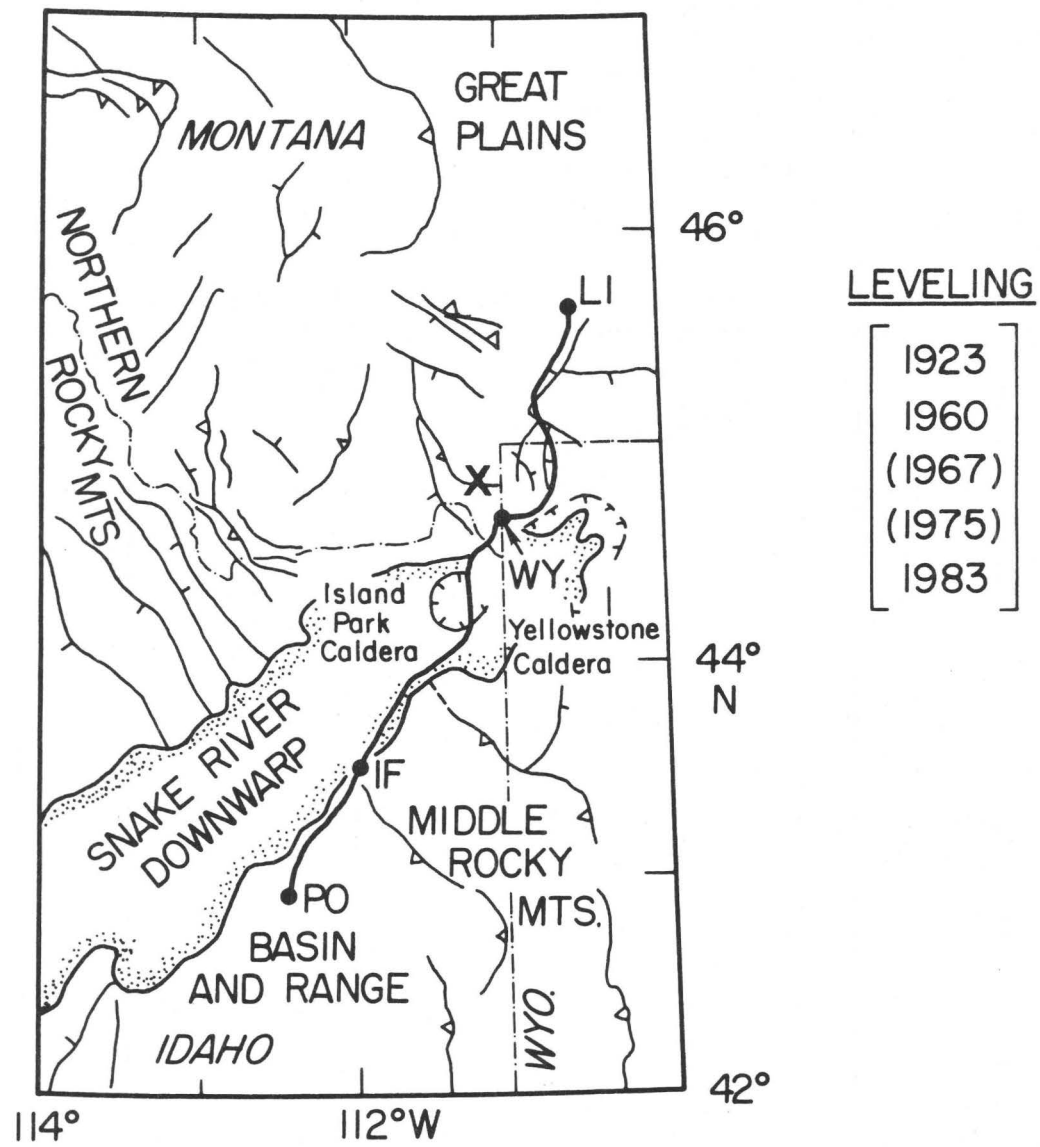

Figure 1: Location of 1983 leveling route. Dates of leveling surveys shown at right (brackets indicate partial coverage). Base map shows physiographic provinces and major faults. Cross shows 1959 Hebgen Lake earthquake epicenter. Abbreviations: PO - Pocatello; IF - Idaho Falls; WY - West Yellowstone; LI Livingston.

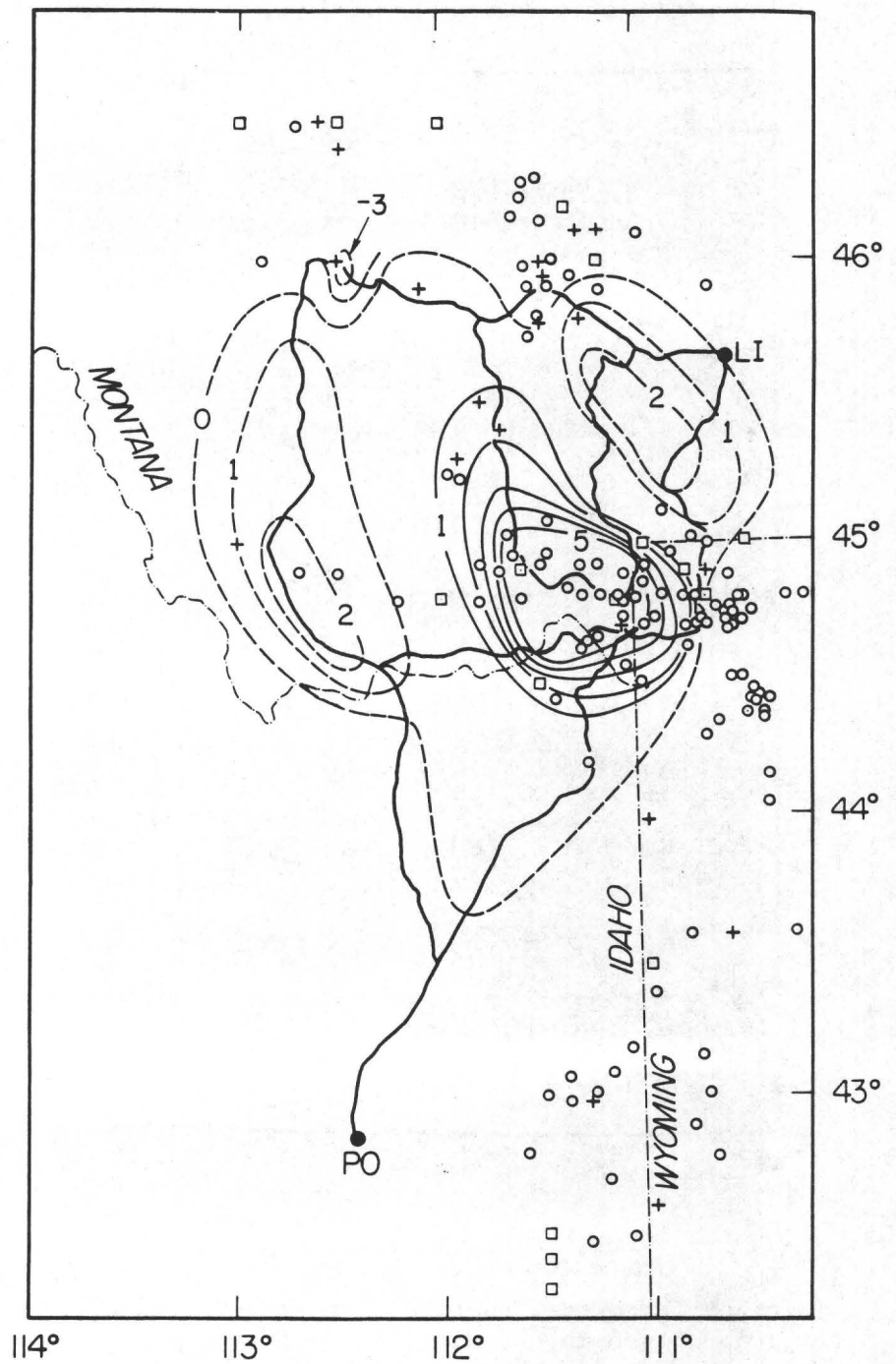

Figure 2: Contours of vertical crustal velocity (mm/yr) derived from repeated leveling along routes shown (heavy lines) for approximate time period 1923 to 1960. Base map shows seismicity in the study area (circles - USGS PDE for earthquakes reported by 10 or more stations for period 1961 - 1975; squares and crosses - instrumentally and non-instrumentally located [felt reports] earthquakes, respectively, for events prior to 1961 from Coffman and von Hoke, 1973). Abbreviations: PO - Pocatello, Idaho; LI - Livingston, Montana. Modified from Reilinger et al. (1977).

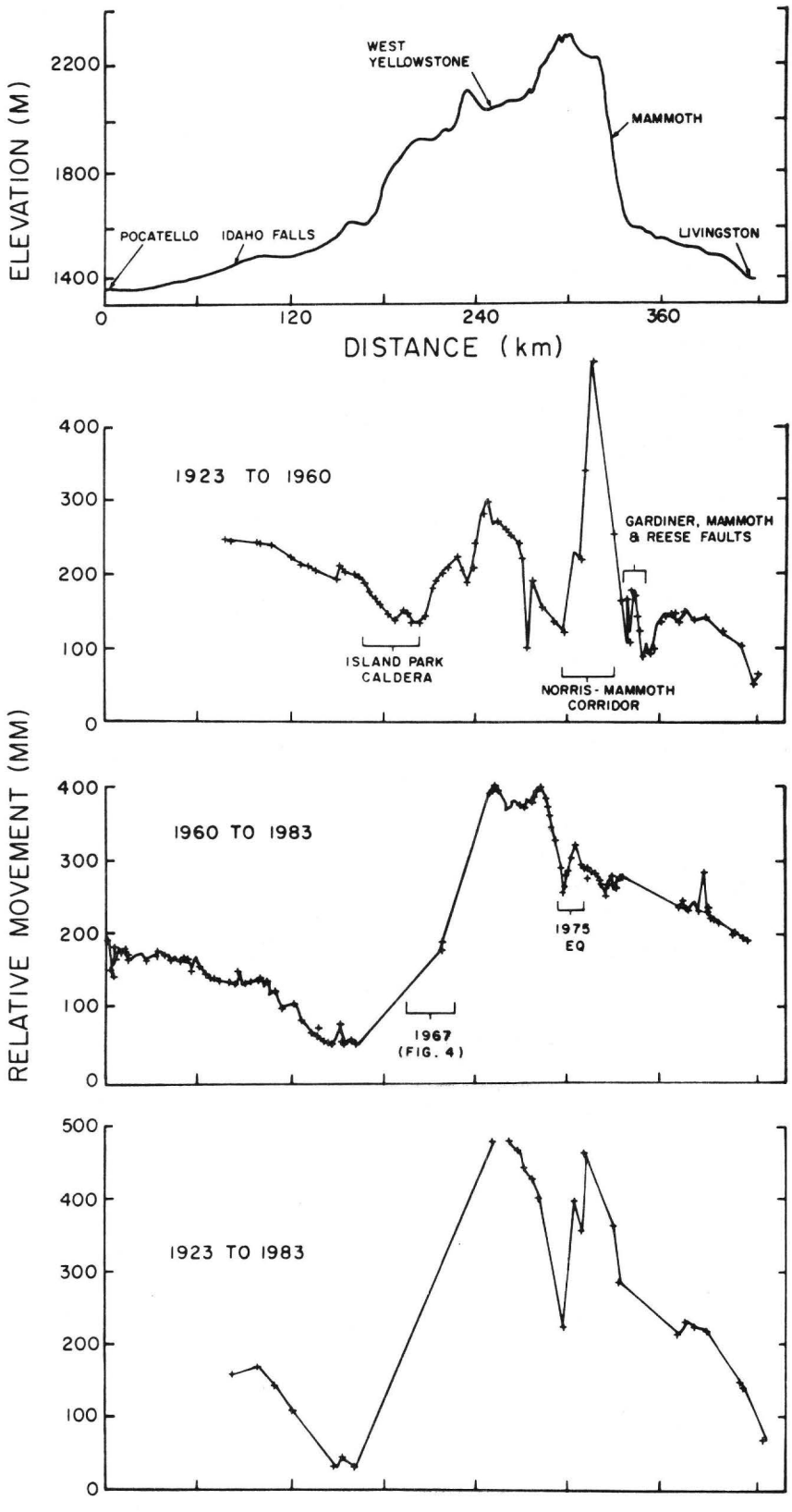

Figure 3: Profiles of topography (top) and relative elevation changes along route shown in Figure 1.

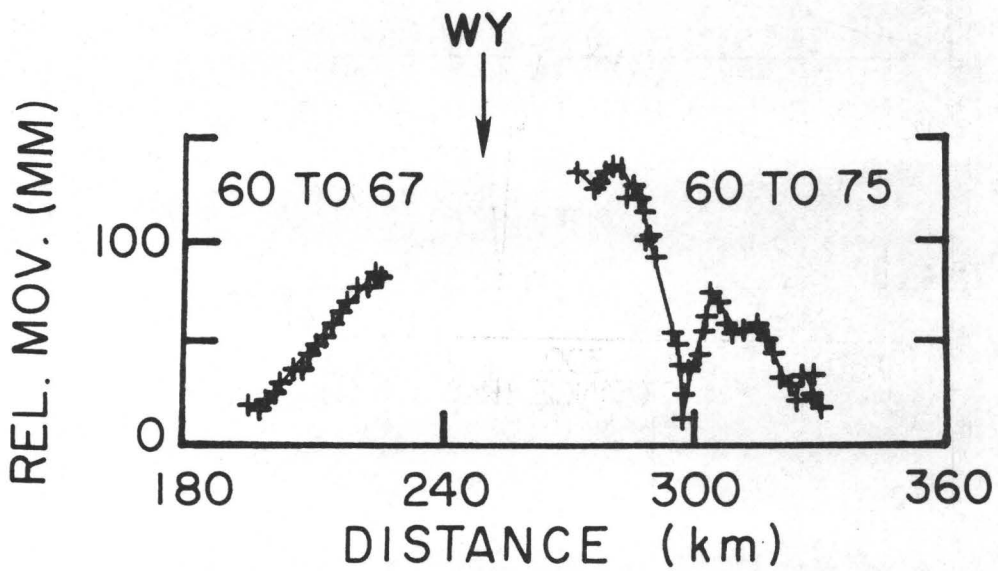

Figure 4: Profiles of relative elevation change along short sections of route shown in Figure 1. Distances correspond to those in Figure 3. (WY: West Yellowstone)

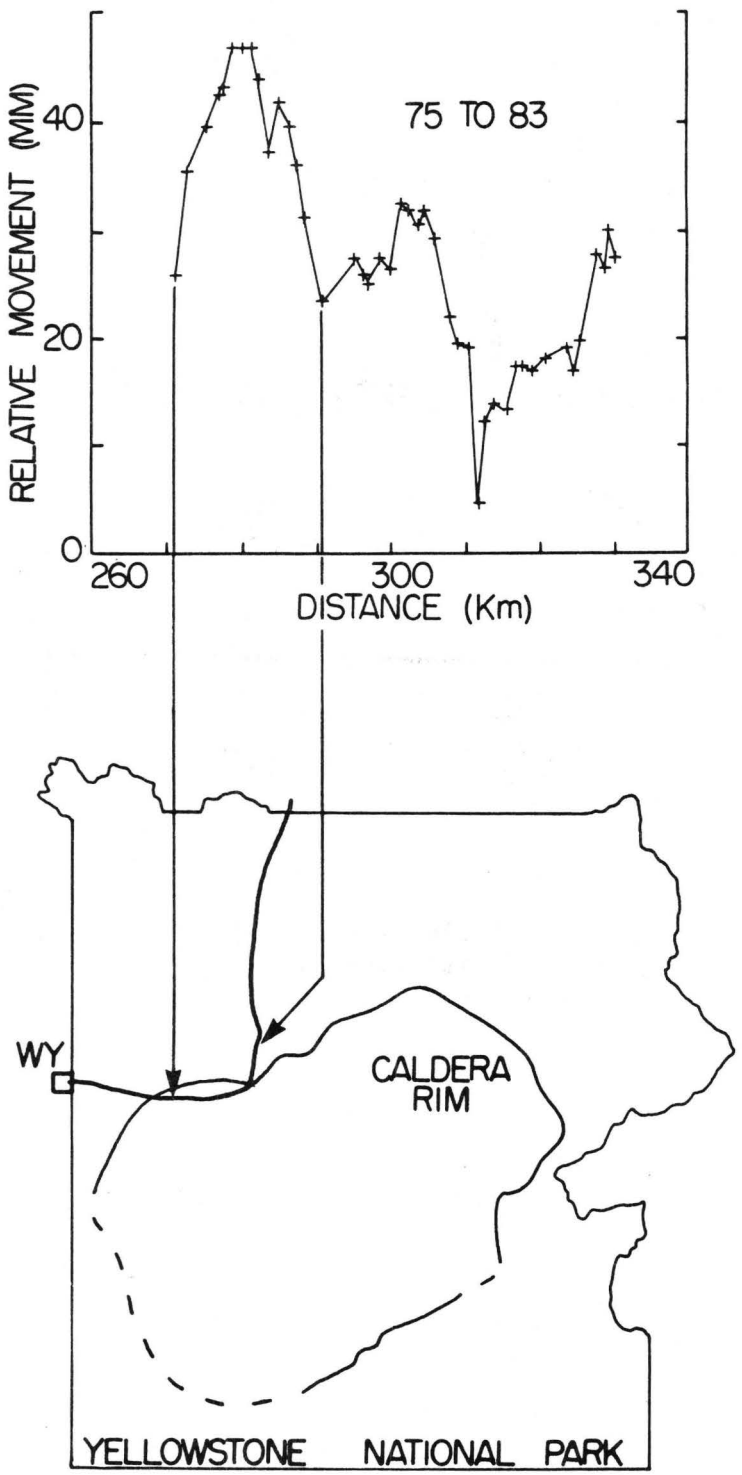

Figure 5: (TOP) Profile of relative elevation change for the period 1975 to 1983 in Yellowstone National Park. Distances correspond to those in Figure 3. (BOTTOM) Map of Yellowstone National Park showing leveling route and caldera boundary. Note relative uplift of caldera.

Dislocation Models for the 1954 Earthquake Sequence in Nevada

Richard A. Snay
Michael W. Cline
Edward L. Timmerman

National Geodetic Survey, Charting and Geodetic Services,
National Ocean Service, NOAA, Rockville, Maryland 20852

Abstract

Horizontal geodetic data are analyzed to estimate fault parameters associated with four major earthquakes that shook central Nevada in 1954. These fault parameters constitute dislocation models for the Fairview Peak earthquake (Dec. 16, M 7.1), the Dixie Valley earthquake (Dec. 16, M 6.9), and two earthquakes that activated the Rainbow Mountain fault (Jul. 6, M 6.6, and Aug. 23, M 6.8). The models explain observed deformations satisfactorily except in the vicinity of the Rainbow Mountain fault. Near the Fairview fault, the models support the existence of a buried fault that is oriented 15° to 25° counterclockwise from the trend of the surface fault that was offset in 1954. Seismic data also support the existence of this buried fault.

Introduction

Four closely spaced earthquakes, each of magnitude 6.6 or larger, jolted central Nevada in 1954. Indeed, no two of their epicenters are separated by more than 60 km. The Rainbow Mountain fault was activated during two of these events, the first on July 6 (M 6.6) and the second on August 23 (M 6.8). The other two earthquakes occurred on December 16, one on the Fairview fault (M 7.1) and the other on the Dixie Valley fault (M 6.9). The M 7.1 mainshock, known as the Fairview Peak earthquake, preceded the Dixie Valley mainshock by only 4 minutes, 20 seconds. The National Geodetic Survey (NGS) is reinvestigating these four events to develop a numerical model descriptive of the observed horizontal movements. With this model NGS will estimate current horizontal coordinates for those geodetic markers positioned prior to 1954.

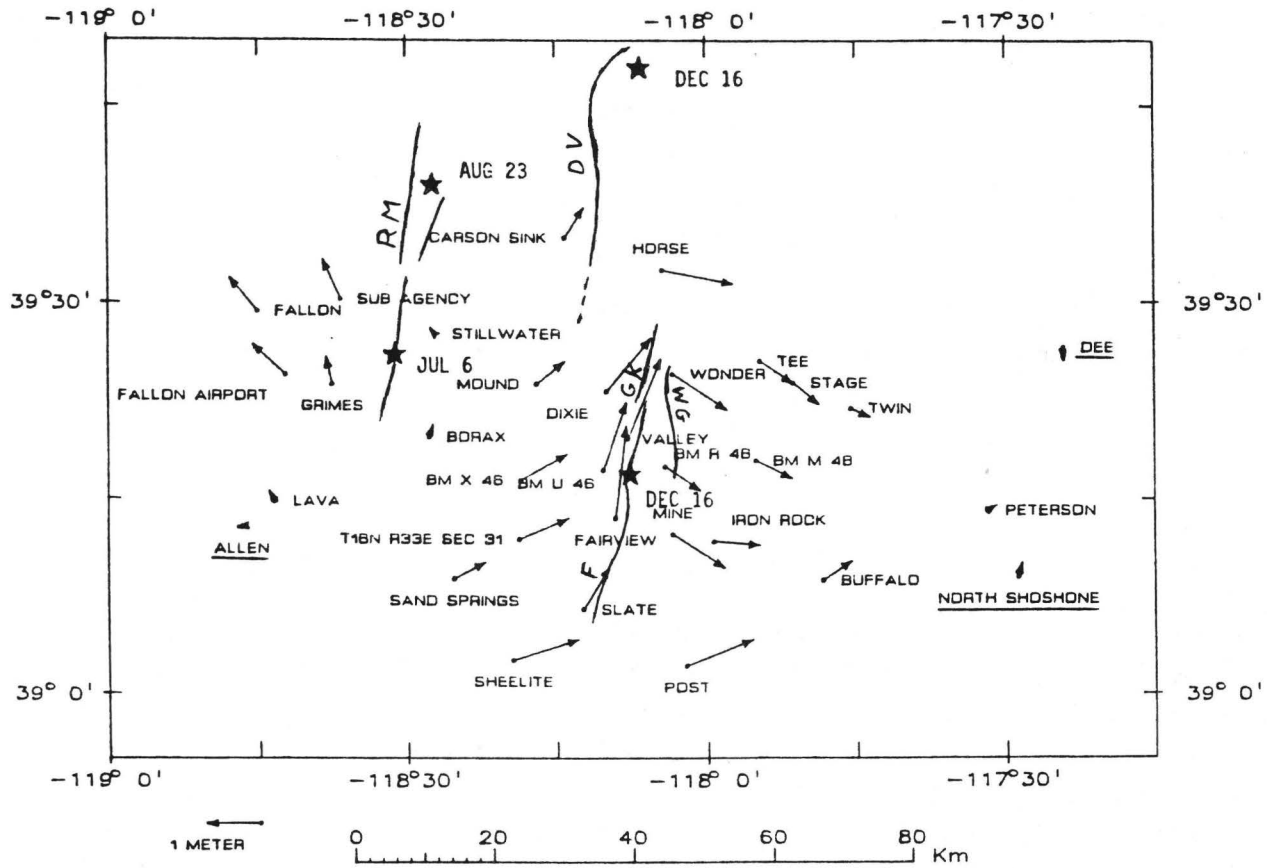

Figure 1. Displacement vectors indicate the horizontal movements associated with four 1954 earthquakes. Stars locate epicenters. The displacements at underlined stations were minimized to estimate the translation, rotation, and scale change used in transforming derived coordinate differences into the vectors displayed here. The July 6 and August 23 earthquakes produced surface offsets on the Rainbow Mountain (RM) fault [Tocher, 1956]. The December 16 events produced surface offsets on the Fairview (F), Gold King (GK), West Gate (WG), and Dixie Valley (DV) faults [Slemmons, 1957].

Pertinent geodetic data for these events were first studied by Whitten [1957]. He determined horizontal displacement vectors for several marks occupied in 1953-1954, before the August 23 event, and then reoccupied in 1955. After selecting a set of triangular areas defined by triads of the geodetic marks, Meister et al. [1968] translated Whitten's displacement vectors into strain components for the individual triangles. Whitten's displacement vectors were also used by Savage and Hastie [1966, 1969] to derive a dislocation model for the Fairview Peak earthquake, alone. Miller [1967] derived a different set of coseismic displacement vectors using the same data studied by Whitten together with 1958 survey data. In his analysis, Miller relaxed several extraneous constraints that Whitten had introduced. These constraints had enforced Whitten's assumption that certain marks on the edge of the geodetic network did not move during the four earthquakes. Miller also derived postseismic displacement vectors from horizontal geodetic data observed in 1955, 1958, and 1966.

In our study we attempt to find a dislocation model for all four 1954 events. Consequently, we discard some of the previously studied data observed between the earthquakes of July 6 and August 23, 1954, and we supplement the remaining data set with several observations from a 1935 horizontal survey. Coseismic displacement vectors are produced, and, like Meister et al. [1968], we translate these vectors into strain components for individual triangles. These strains then serve as paraobservations for estimating fault-plane parameters that constitute various dislocation models. Our models explain the observed deformation adequately near the Fairview fault and to its east. For the deformation to the west, however, our models require either excessive slip on the Rainbow Mountain fault or unsubstantiated slip on a hypothetical fault. This result suggests that we search for an alternative to the fault-slip mechanism for modeling the deformation west of the Fairview fault.

This study also sheds new light on what seems to be a discrepancy between the geologically and seismically derived orientations of the fault that ruptured during the 1954 Fairview Peak earthquake. The offset features documented by Slemmons [1957] for this event occurred along a surface fault striking about N9°E. On the other hand, the P-wave nodal plane of the earthquake strikes N11°W [Romney, 1957]. Our models indicate that significant coseismic slip was not confined to a single planar surface. Indeed, the models suggest that over a meter of slip occurred on both a shallow planar surface and a deeper planar surface with the deeper surface rotated about 15° to 25° counterclockwise relative to the shallow one.

Displacement Vectors and Strain

To compute the coseismic displacements for the four events, we first determined preseismic (x^-,y^-) and postseismic (x^+,y^+) coordinates for geodetic marks using a planar reference system having its positive x-axis oriented east and its positive y-axis north. The preseismic coordinates were estimated via a least squares procedure using horizontal geodetic data (triangulation) from three separate surveys. The first preseismic survey was observed between December 7, 1953 and January 8, 1954. The second survey spanned the interval from July 8, 1954 to August 23, 1954. Because this second survey postdates the July 6 earthquake (M 6.6) on the Rainbow Mountain fault, we excluded all data from that survey west of the 118.25°W meridian. The third preseismic survey, observed in 1935, supplied the necessary geometric strength to compute preseismic positions for several geodetic marks near the Rainbow Mountain fault. In excluding some 1954 data and in including parts of a 1935 survey, we differ from Whitten [1957] and Miller [1967] who each used all data from the first and second surveys for their respective studies. The postseismic coordinates were computed from horizontal geodetic data observed between April 27 and June 6, 1955. Miller [1967] augmented these 1955 observations with those from a 1958 survey. Because postseismic strain rates are expected to be large [Thatcher, 1983], we chose not to include the 1958 data so that our estimated movements would not include the 1955-1958 deformation.

Because triangulation observations supply no information about absolute network position, scale, or orientation; we had to introduce artificial constraints to obtain both the pre- and postseismic coordinates. Consequently, given any translation $(\Delta x,\Delta y)$, rotation ω, and scale factor ρ, a transformation of the preseismic coordinates in the form

$$\begin{bmatrix} x^* \\ y^* \end{bmatrix} = \begin{bmatrix} \Delta x \\ \Delta y \end{bmatrix} + \begin{bmatrix} \rho & \omega \\ -\omega & \rho \end{bmatrix} \begin{bmatrix} x^- \\ y^- \end{bmatrix} \qquad (1)$$

provides an equally valid representation of the preseismic data. After such a transformation, the equation

$$\begin{bmatrix} u \\ v \end{bmatrix} = \begin{bmatrix} x^+ - x^* \\ y^+ - y^* \end{bmatrix} \qquad (2)$$

yields a displacement vector (u,v) as consistent with the observed triangulation as displacements calculated with the $(\bar{x},\bar{y})$-coordinates. For our solution we determined values for the four transformation parameters so as to minimize the rms displacements of three marks (see Figure 1); that is, the quantity

$$S = \sum_{i=1}^{3} (u_i^2 + v_i^2) \qquad (3)$$

was minimized where the index i ranges over the three preselected marks. Thus, our vectors (Figure 1 and Table 1) differ from those of Whitten [1957] and Miller [1967], not only because of the data differences described previously, but also due to the way in which we constrained the solution. Whitten had overconstrained his solution by requiring six marks to have absolutely no displacement--the three marks whose displacements we minimized plus FALLON, CARSON SINK, and a mark, SOUTHBRANCH, that is lost to our study because of our exclusion of some 1954 data. Miller's solution, on the other hand, is a minimally constrained solution like ours, though with a different choice of minimal constraints. Had we used the same data set as Miller, we would have been able to reproduce his solution by appropriately selecting values for the transformation parameters of equation 1.

Table 1. Coseismic displacement vectors

Station	east (m)	north (m)	Station	east (m)	north (m)
ALLEN	-.069	-.011	MINE	.954	-.613
BM M 46	.681	-.328	MOUND	.526	.416
BM R 46	.652	-.442	NORTH SHOSHONE	.063	.250
BM U 46	.434	1.240	PETERSON	.170	.094
BM X 46	.875	.478	POST	1.232	.492
BORAX	.064	.220	SAND SPRINGS	.599	.309
BUFFALO	.542	.359	SHEELITE	1.232	.393
CARSON SINK	.363	.559	SLATE	.483	.774
DEE	.006	-.238	STAGE	.478	-.395
DIXIE	.837	.994	STILLWATER	-.095	.111
FAIRVIEW	.206	1.693	SUB AGENCY	-.331	.730
FALLON AIRPORT	-.610	.549	TEE	.621	-.404
FALLON	-.515	.609	TWIN	.364	-.163
GRIMES	-.113	.500	T16N R33E SEC 31	.916	.388
HORSE	1.327	-.265	VALLEY	.618	1.482
IRON ROCK	.858	-.070	WONDER	1.010	-.666
LAVA	-.125	.198			

We next translated our displacement vectors into strain elements. Here we follow the method described by Meister et al. [1968]. In particular, we computed strain for individual triangles belonging to a preselected triangulation scheme that involved the marks positioned both before and after the four earthquakes. Unlike displacement vectors, the derived shear strains are independent of the choice of artificial constraints in our minimally constrained solution. Said differently, any transformation of the preseismic coordinates using equation 1 would not change our derived shear strains:

$$\gamma_1 = \varepsilon_{EE} - \varepsilon_{NN}$$

$$\gamma_2 = 2\,\varepsilon_{EN} \,. \qquad (4)$$

Here ε_{EE}, ε_{NN}, and ε_{EN} denote the components of the two-dimensional horizontal strain tensor for a coordinate system whose positive axes are oriented east (E) and north (N). Positive strain corresponds to extension. Our estimates for γ_1 and γ_2 (Figure 2, Table 2) have a formal standard error of about 7 μrad.

Dislocation Models

We applied the theory for Volterra dislocations [Mansinha and Smylie, 1971] to describe the coseismic movements. The earth was considered to be an isotropic homogeneous elastic halfspace. Rectangular planes of finite dimensions were embedded in the halfspace to represent geologic faults. The coseismic movements correspond to the displacements that the elastic halfspace undergoes in response to slip along these embedded rectangles. Figure 3 identifies a set of seven parameters that specify the size, location, and orientation of a rectangle. The displacements depend upon these parameters, the Poisson ratio for the halfspace, and the slip vectors. A constant slip vector over each rectangle is required by the mathematical formulation we employ. The Poisson ratio was set at 0.24.

We experimented with several different dislocation models each containing either five or six rectangles. Using a computer program, several parameters for these rectangles were varied systematically until the particular model generated theoretical strains that compared favorably with the observed strains in Table 2. This procedure requires specifying

initial values for the fault parameters together with increments for varying those parameters. After calculating shear strains, γ_1 and γ_2, that correspond to the dislocation model with the specified initial values, the software computes the rms of the differences between these model-generated shears and the observed shears. The software then tests the first adjustable parameter to see if changing its current value by plus or minus one increment decreases the rms. The value is changed, if necessary, to reflect the best fit, and then each of the other adjustable parameters, one-by-one, is tested in the same fashion. After testing the last adjustable parameter, the procedure is iterated, returning to the first adjustable parameter, but first the increments of those adjustable parameters that failed to change during the preceding pass are decreased by a factor of four. We considered the solution to have converged when the change in the rms between iterations became less than a prespecified tolerance, usually 0.001 μrad. If convergence was not attained after 20 iterations, then we customarily stopped the solution to check on the plausibility of the latest parameter values relative to existing geologic and seismic information. Many sets of initial values were tested because the solution is somewhat dependent on the choice of these values. This dependency results from the existence of discontinuties and local minima for the rms as a function of the model parameters; for example, the rms will experience a discontinuity as a function of strike when the surface trace of the fault sweeps across a geodetic mark. For each model, certain parameters, ill-resolved by the geodetic data, were held fixed at values that are seemingly consistent with geologic and seismic information. Once a particular model had converged, we calculated parameter uncertainties that represent the amount that the respective parameter can vary from its converged value before causing a 10% increase in the rms fit. Table 3 presents parameter estimates with their uncertainties for two different models, one containing five rectangles and the other containing six.

Five-Rectangle Model

In each of the models four of the rectangles correspond to surface faults that ruptured in 1954: (1) the Fairview fault, (2) the West Gate-Gold King faults, combined, (3) the Dixie Valley fault, and (4) the Rainbow Mountain fault [Tocher, 1956; Slemmons, 1957]. The fifth rectangle was initially included to correspond to a down-dip extension of the Fairview fault. In experiments without this fifth rectangle, we found that the lower-depth or bottom of the Fairview rectangle converged to

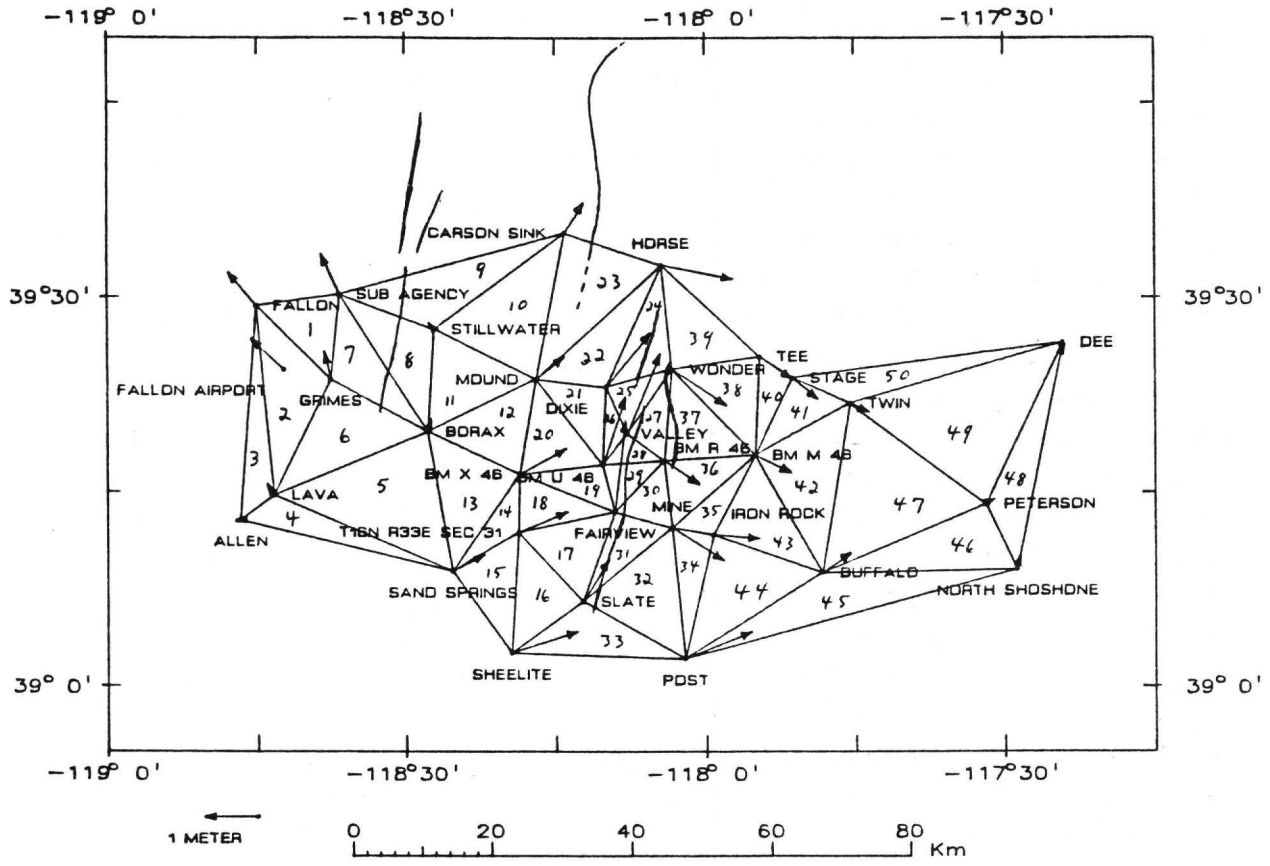

Figure 2. The coseismic shear strains given in Table 2 correspond to the triangles displayed here.

Table 2. Observed versus modeled shear strains (units = μrad)

	GAMMA1			GAMMA2			
GROUP*	OBSVD	MODEL	RESID	OBSVD	MODEL	RESID	RMS**
1	-.1	-34.7	34.6	-12.5	7.5	-20.0	28.3
2	10.0	-36.7	46.7	-7.3	4.8	-12.2	34.2
3	-18.5	-24.0	5.5	14.5	4.3	10.2	8.2
4	-19.5	-13.2	-6.3	-16.1	-32.0	15.9	12.1
5	21.9	4.7	17.2	-21.1	-41.0	19.9	18.6
6	-12.1	-22.8	10.7	-12.6	-34.1	21.5	17.0
7	-17.2	-6.8	-10.4	-27.7	-26.4	-1.3	7.4
8	17.4	-.9	18.3	-58.5	-33.8	-24.7	21.8
9	-43.5	-42.9	-.6	-15.7	-16.0	.3	.5
10	32.8	25.9	7.0	7.2	-6.8	14.0	11.0
11	44.6	33.8	10.9	3.4	17.1	-13.6	12.3
12	53.6	44.9	8.7	-17.9	-2.2	-15.7	12.7
13	54.9	41.3	13.6	1.5	.2	1.3	9.6
14	26.1	26.3	-.3	-3.9	3.6	-7.4	5.3
15	46.7	25.5	21.2	-12.5	-5.2	-7.3	15.9
16	-60.0	-39.0	-21.1	24.4	30.6	-6.1	15.5
17	-91.0	-68.6	-22.4	82.2	56.8	25.4	23.9
18	-58.8	-39.0	-19.8	88.7	69.8	18.9	19.4
19	9.2	17.8	-8.6	93.0	85.6	7.4	8.0
20	-18.4	-9.3	-9.1	46.3	49.6	-3.2	6.8
21	59.7	42.3	17.4	89.7	94.0	-4.3	12.7
22	127.3	114.2	13.1	60.6	52.5	8.1	10.9
23	45.2	52.8	-7.6	-74.0	-55.3	-18.6	14.2
24	2.2	11.7	-9.5	-154.9	-171.4	16.5	13.5
25	145.0	141.4	3.6	-101.2	-96.0	-5.2	4.5
26	33.8	25.9	7.9	136.5	139.2	-2.7	5.9
27	12.6	17.7	-5.1	-326.5	-326.2	-.3	3.6
28	-195.3	-192.9	-2.4	-179.3	-183.6	4.2	3.4
29	135.2	141.5	-6.4	-142.2	-135.6	-6.6	6.5
30	98.4	93.8	4.6	-304.6	-296.7	-7.8	6.4
31	-79.9	-63.4	-16.5	-284.9	-300.3	15.4	16.0
32	109.3	93.1	16.2	-65.2	-89.0	23.8	20.4
33	-47.7	-70.8	23.1	-92.7	-79.3	-13.4	18.9
34	31.6	55.7	-24.1	66.7	58.1	8.6	18.1
35	47.3	39.0	8.3	74.8	64.3	10.5	9.5
36	-14.5	-3.4	-11.2	-23.4	1.7	-25.2	19.5
37	18.3	32.8	-14.5	37.2	47.4	-10.3	12.6
38	-24.2	2.3	-26.5	19.1	35.4	-16.3	22.0
39	-62.4	-30.7	-31.7	35.1	27.8	7.3	23.0
40	-26.5	1.5	-28.0	-4.3	14.3	-18.6	23.8
41	-1.6	-4.0	2.4	11.1	11.0	.2	1.7
42	4.7	5.8	-1.1	22.0	14.2	7.8	5.6
43	9.4	-.4	9.7	12.3	24.1	-11.8	10.8
44	9.7	26.8	-17.1	-.4	6.8	-7.2	13.1
45	-11.7	-2.5	-9.2	-33.8	1.1	-34.8	25.5
46	1.1	-5.9	7.1	-.3	3.0	-3.2	5.5
47	7.4	-3.9	11.3	-7.4	.9	-8.3	9.9
48	-4.0	-4.8	.8	4.4	1.0	3.4	2.5
49	4.0	-1.9	5.9	.1	1.9	-1.8	4.4
50	29.7	10.3	19.4	12.2	-3.4	15.6	17.6
						TOTAL RMS =	15.0

* Numbers correspond to triangle numbering of Figure 2.

** RMS = $\{[\ \text{RESID}(\gamma_1)^2 + \text{RESID}(\gamma_2)^2\ ]/2\}^{1/2}$

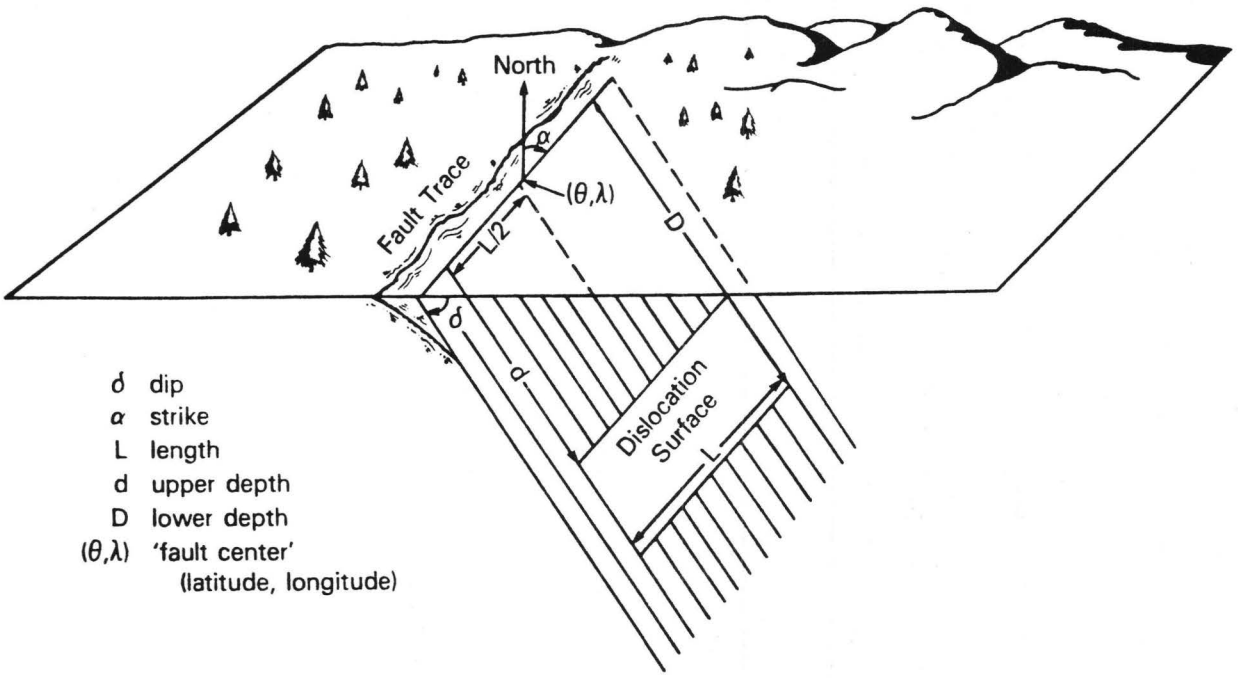

Figure 3. Given a rectangle embedded in an isotropic homogeneous elastic halfspace, dislocation theory describes how each point of the halfspace moves in response to relative slip between the opposing rectangular faces. It is assumed that the upper and lower edges of the rectangle are parallel to the earth's surface and that the slip is pure translation in the plane of the rectangle, in particular, no rotation. The figure identifies seven parameters that define the size, location, and orientation of the rectangle. The motion depends on these parameters, the Poisson ratio of the halfspace, and the slip vector.

Table 3. Fault-parameter estimates derived from observed shear strains.

Fault	Fault Center		Fault Orientation		Fault Size			Slip	
	Latitude deg(N)	Longitude deg(W)	Strike deg	Dip deg	U. Depth km	L. Depth km	Length km	Strike# m	Dip## m
five-rectangle model									
Fairview(surface)	39.221(.020)	118.137(.010)	N12E(3)	63E(10)	0.0*	5.2(1.5)	33.6(4)	3.6(0.4)	2.3(0.5)
Fairview(buried)	39.309(.035)	118.144(.015)	N13W(7)	59E(17)	2.2(2.0)	20.0**	58.3(40)	0.8(0.4)	1.6(0.7)
West Gate-Gold King	39.391(.010)	118.083(.010)	N07W(3)	70W(23)	0.0*	5.0*	23.3(16)	1.3(0.5)	0.5(1.0)
Dixie Valley	39.633(.125)	118.213(.080)	N06E(17)	60E*	0.0*	15.0*	42.0*	-0.3(1.1)	2.4(1.6)
Rainbow Mountain	39.278(.130)	118.483(.025)	N07E(7)	68E(5)	0.0*	6.7(3.0)	112.4**	0.6(0.6)	5.5(3.0)
six-rectangle model									
Fairview(surface)	39.207(.005)	118.147(.010)	N14E(3)	47E(5)	0.0*	5.0(1.0)	26.9(1)	4.0(0.6)	3.5(0.5)
Fairview(buried)	39.312(.040)	118.137(.010)	N01W(5)	84E(10)	3.9(1.5)	20.0(50.)	50.0(9)	1.4(0.6)	2.8(0.7)
West Gate-Gold King	39.392(.005)	118.091(.005)	N11W(4)	80W(13)	0.0*	5.0*	21.9(1)	2.4(0.6)	1.5(0.8)
Dixie Valley	39.596(.090)	118.166(.035)	N02E(16)	54E*	0.0*	5.4(4.5)	33.6*	-1.3(1.7)	4.2(1.9)
Rainbow Mountain	39.478(.125)	118.447(.150)	N13E(30)	35E(50)	0.0*	20.0**	34.8(28)	0.6(0.4)	0.4(0.5)
hypothetical	39.453(.050)	118.313(.065)	N05E(8)	42W(16)	0.0*	20.0**	63.5(12)	-0.1(0.4)	1.8(0.5)

\# Right-lateral strike slip is positive.
\## Normal dip slip is positive.
* Parameter constrained to this value.
** Parameter constrained to this value. Value would have been larger if not constrained.

shallow values, namely, 6 to 8 km. Similarly, Savage and Hastie [1969] obtained 8 ± 2 km for the fault's lower-depth in their one-rectangle dislocation model of the 1954 Fairview Peak earthquake. The seismically determined hypocenter for this event, however, is 15 km deep [Romney, 1957]. Also microseismic data observed in 1966 indicate faulting to the 15-km depth [Stauder and Ryall, 1967]. Consequently, we elected to add the fifth rectangle.

We initiated our estimation process for the five-rectangle model with the two Fairview rectangles in a single plane, the shallower rectangle extending from 0 to 6 km in depth and the deeper rectangle from 6 to 15 km. In the estimation process, however, the deep Fairview rectangle rotated counterclockwise relative to the shallow Fairview rectangle. (Also the upper- and lower-depths of the two rectangles converged to different values.) Our best five-rectangle model generated a strike of N13°W ± 7° for this deep Fairview rectangle and N12°E ± 2° for the shallow Fairview rectangle (Figure 4 and Table 3). This result implies that the fault at depth is not a planar extension of the surface Fairview fault that was visibly offset in 1954. Seismic data support our geodetic evidence for the skewness of this buried structure relative to the surface fault. The seismically inferred nodal plane for the 1954 Fairview Peak earthquake has been assigned strikes of N11°W by Romney [1957] and by Stauder and Ryall [1967] and N4°W by Wickens and Hodgson [1967]. Ryall and Malone [1971], furthermore, report that local seismicity during the 1969-1970 interval trends N12°W in the vicinity of the Fairview Peak epicenter.

A separate example of a deep elongated stucture that is not obvious in the gross surficial pattern of faulting has recently been reported by Wallace [1984]. Near Pleasant Valley, Nevada, which is located less than 150 km north of the Fairview Peak epicenter, a 1915 earthquake (M 7.6) formed four echelon faults contained in a belt 6 km wide by 60 km long. The 1915 earthquake also reactivated several existing range-bounding faults, and although some of these range-bounding faults extend far beyond the 6-km belt width, only those segments contained within the belt were reactivated.

We are not without some misgivings regarding our best five-rectangle model. Residuals between modeled and observed shear strains (see Table 2) have an rms of 15.0 μrad, over twice the 7 μrad random error level. Also

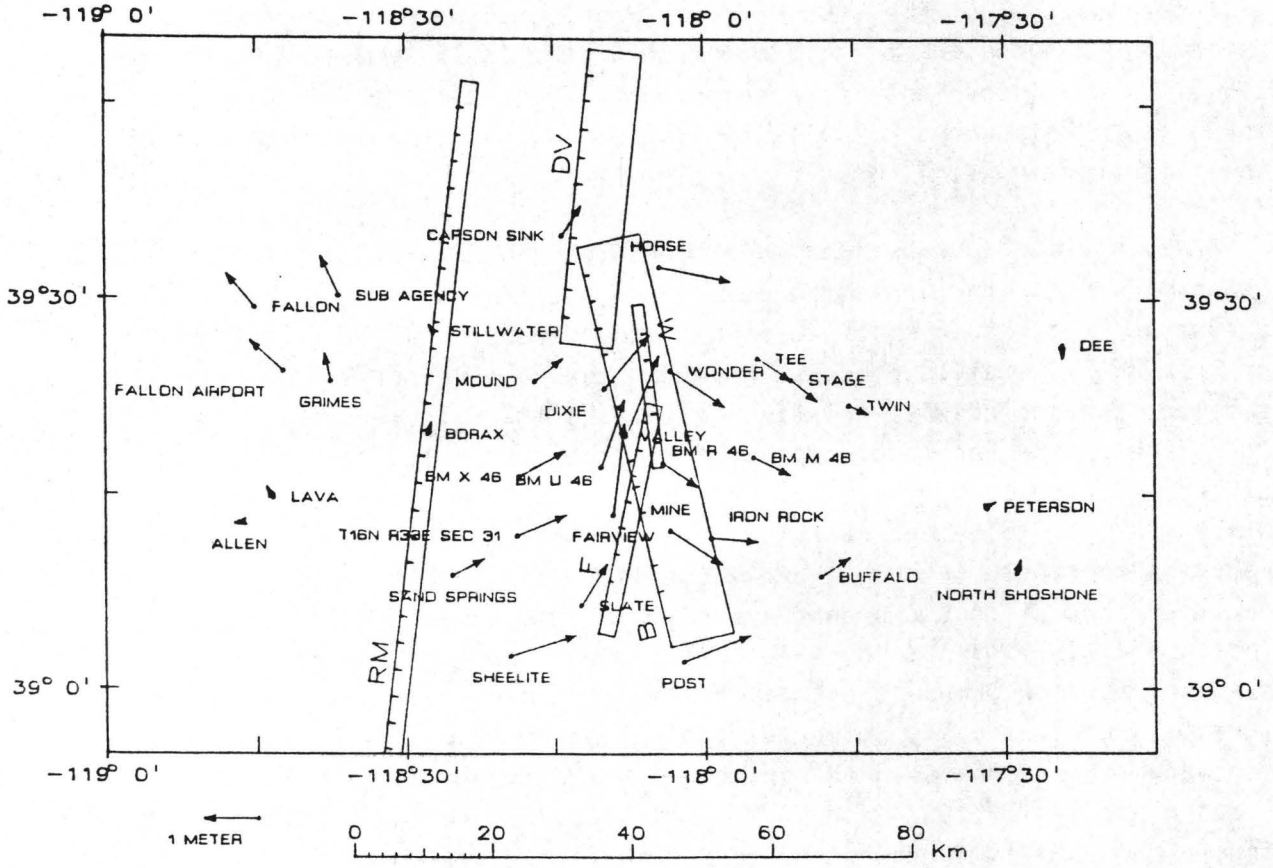

Figure 4. Vertical projection of rectangles onto the earth's surface for five-rectangle dislocation model. Rectangles correspond to the surface Fairview fault (F), a buried Fairview fault (B), the West Gate-Gold King faults (W), the Dixie Valley fault (DV), and the Rainbow Mountain fault (RM). Hatchures identify the upper edges of the various rectangles. Displacement vectors repeated from Figure 1.

the dip slip (5.5 ± 3.0 m) and the fault length (112.4 km) obtained for the Rainbow Mountain rectangle seem excessive. This latter point can be demonstrated by computing the seismic moment M_o for this dislocation model and comparing it with typical moments for earthquakes of the same magnitudes as the four 1954 events. We expect that the different moments should agree within a factor of two, an expectation which may be slightly optimistic (see Hanks et al. [1975]).

The seismic moment for the dislocation model was obtained using the formula

$$M_o = \mu \sum_i (s_i L_i W_i) \qquad (5)$$

μ rigidity modulus
s_i total slip on i-th rectangle
L_i length of i-th rectangle
W_i width of i-th rectangle

In our calculations, μ was set equal to 3.5×10^{11} dyne/cm^2 based on the results of Koseluk and Bischke [1981]. For our best five-rectangle model, M_o is 293×10^{25} dyne-cm of which 145×10^{25} dyne-cm is attributed to the Rainbow Mountain rectangle by itself. An independent estimate for the seismic moment of an earthquake of generic magnitude M can be obtained using Hanks and Kanamori's [1979] empirical relation

$$M_o = 10^{**}[1.5(M + 10.7)] \qquad (6)$$

From this equation the combined seismic moment for the four 1954 earthquakes is 102×10^{25} dyne-cm, less than half the moment of our dislocation model.

Six-Rectangle Models

The five-rectangle model fit the observed shear strains least well in the vicinity of the Rainbow Mountain fault (Table 2). We therefore elected to include a sixth rectangle located somewhere in the western half of the geodetic network. In our first attempt, the additional rectangle corresponded to a down-dip extension of the Rainbow Mountain fault. In this model the shallow Rainbow Mountain rectangle had upper- and lower-depths of 0 and 10 km, respectively, and the deeper Rainbow Mountain

rectangle extended between the depths of 10 and 19 km. The other four rectangles corresponded to the same faults as the previous model, namely, two rectangles for the Fairview fault, one for the West Gate-Gold King faults, combined, and one for the Dixie Valley fault. This new model provided a better fit to the observed shear strains as the rms for the residuals dropped to 10.0 μrad as compared to the 15.0 μrad rms for the previous model. This new model, however, required the deeper Rainbow Mountain rectangle to have 8.5 m of dip slip and a fault length of 100 km. Moreover the model's seismic moment was 443×10^{25}, over four times the moment obtained from the empirical moment-magnitude relation of equation 6. Hence we rejected this particular six-rectangle model.

Our next experiment was to include a sixth rectangle striking approximately north-south and representing a hypothetical fault located between the Fairview and Rainbow Mountain faults (Figure 5). In this model a single rectangle represents the Rainbow Mountain fault, and the other four rectangles correspond to the same faults as in previous models. The hypothetical fault was included basically to account for the large displacements of geodetic marks, MOUND and BM X 46, relative to BORAX and STILLWATER (Figure 5). This new model fits the observed shear strains well with an rms of 10.2 μrad. Also the model's seismic moment, 256×10^{25} dyne-cm, is lower than that of previous models. This moment, however, is still relatively large. Most of the estimated parameters (Table 3) seem reasonable, but the derived dip slip of 1.8 ± 0.5 m on the hypothetical fault seems large. Leveling--observed in 1934 and repeated in 1955--along an east-west route that traverses the hypothetical fault provides strong evidence against this amount of dip slip (see Figure 5 of Savage and Church [1974]).

Estimates for corresponding parameters between this model and our five-rectangle model differ in some respects (Table 3 and Figures 4 and 5). Parameters for the Rainbow Mountain rectangle show the greatest differences between models. A change to these parameters was expected because the additional rectangle was included to better fit observed strains in the western half of the geodetic network. In particular the dip slip on the Rainbow Mountain rectangle decreased from 5.5 ± 3.0 m for the five-rectangle model to 0.4 ± 0.5 m for the six-rectangle model. Also this rectangle's fault length decreased from 112.4 to 34.8 km. Parameter differences for other rectangles were not so drastic. With the six-rectangle model, the slips for each of the other four rectangles,

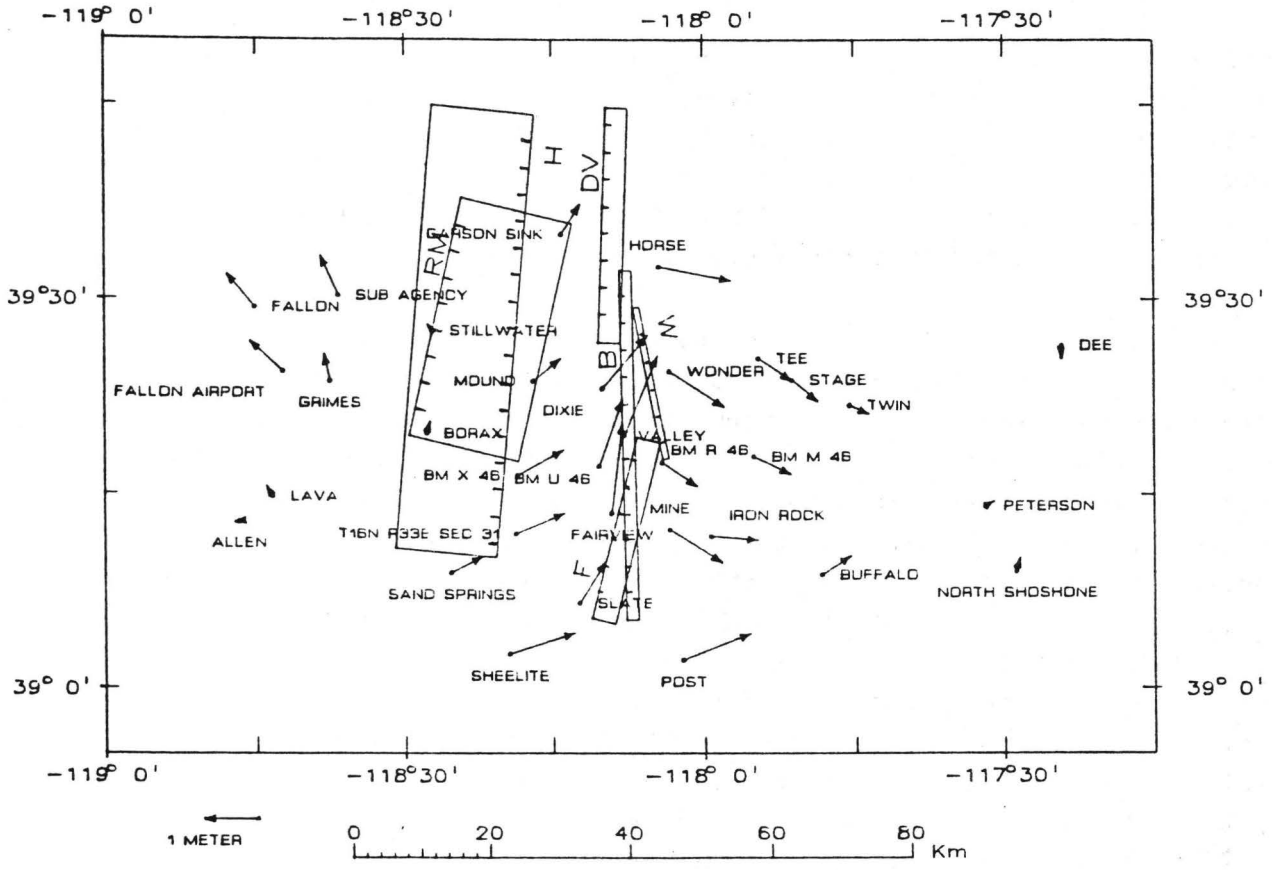

Figure 5. Vertical projection of rectangles onto the earth's surface for six-rectangle dislocation model. The fault-rectangle correspondence is as given in Figure 4 with the additional rectangle corresponding to a hypothetical fault (H). Hatchures identify the upper edges of the various rectangles. Displacement vectors repeated from Figure 1.

common to both models, increased slightly relative to corresponding slips in the five-rectangle model. These increased slips seemingly compensated for the large slip decrease on the Rainbow Mountain fault. The orientation of the deep Fairview fault also differs between the models. The fault's strike in the six-rectangle model is N1°W ± 5° compared to the N13°W ± 7° for the five-rectangle model. This orientation change between models is probably related to the extremely deep lower boundary of the hypothetical fault (20 km) with its 1.8 m of slip. In fact, the lower boundaries for both the hypothetical and the Rainbow Mountain faults would have even exceeded the depth of 20 km in the six-rectangle model, had we not constrained them to this value. In comparison, the lower Fairview rectangle is the only structure deeper than 15 km in the five-rectangle model.

The shortcomings of our various models suggest that a fault-slip mechanism may be inadequate for explaining the observed deformations of this study. Our five-rectangle model requires excessive slip on the Rainbow Mountain fault, and the six-rectangle model requires several 20-km deep structures and unsubstantiated slip on a hypothetical fault. Magma movement within the crust provides an alternative mechanism that we have yet to test at the time of this writing. Indeed the inclusion of a north-south trending dike may prove effective for explaining the apparent east-west speading that occurs near the surface trace of our hypothetical fault (Figure 5). We note that midcrustal magma flow is postulated to be associated with recent California seismicity near Mammoth Lakes which, like the 1954 Nevada seismicity, is characterized by an unusual temporal-spatial clustering of several M 6+ earthquakes [Savage and Lisowski, 1984]. Also Vetter and Ryall [1983] suggest that a combination of magmatic activity and faulting may be related to the systematic change in focal mechanism with depth that is observed throughout the western Basin and Range province, including the Mammoth Lakes and the Fairview Peak areas.

Conclusions

Horizontal geodetic data observed before and after the 1954 Nevada earthquake sequence suggest the existence of a fault at depth beneath the Fairview fault. In different models this fault is rotated about 15° to 25° counterclockwise relative to the surface fault that was visibly offset during the 1954 Fairview Peak earthquake. Seismic data support the

existence of such a buried fault. The geodetic data further indicate that significant deformation occurred near the Rainbow Mountain fault. Dislocation models are able to produce a strain field similar to that which was observed, but these models either require excessive slip on the Rainbow Mountain fault or unsubstantiated slip on a hypothetical fault. An alternative to the fault-slip mechanism may better explain the deformation in the western half of the geodetic network. The fault-slip mechanism, however, seems adequate for explaining deformation near the Fairview fault and to its east.

Acknowledgments

Stephen J. Frakes of the National Geodetic Survey organized the geodetic data employed in this study. The presentation of this work was improved as a result of suggestions by D. C. McAdoo, R. S. Stein, W. E. Strange, G. A. Thompson, and R. E. Wallace.

References

Hanks, T. C. and H. Kanamori, A moment magnitude scale, J. Geophys. Res., 84, 2348-2350, 1979.

Hanks, T. C., J. A. Hileman, and W. Thatcher, Seismic moments of the larger earthquakes of the southern California region, Bull. Geol. Soc. Am., 86, 1131-1139, 1975.

Koseluk, R. A. and R. E. Bischke, An elastic rebound model for normal fault earthquakes, J. Geophys. Res., 86, 1081-1090, 1981.

Mansinha, L., and D. E. Smylie, The displacement fields of inclined faults, Bull. Seismol. Soc. Am., 61, 1433-1440, 1971.

Meister, L. J., R. O. Burford, G. A. Thompson, and R. L. Kovach, Surface strain changes and strain energy release in the Dixie Valley - Fairview Peak area, Nevada, J. Geophys. Res., 73, 5981-5994, 1968.

Miller, R. W., Vicinity of Fallon, Nevada, earthquake movement study, (unpublished report), U.S. Coast and Geodetic Survey, Rockville, Md., 1967.

Romney, C., The Dixie Valley-Fairview Peak, Nevada, earthquakes of December 16, 1954: Seismic waves, Bull. Seismol. Soc. Am., 47, 301-320, 1957.

Ryall, A. and S. D. Malone, Earthquake distibution and mechanism of faulting in the Rainbow Mountain-Dixie Valley-Fairview Peak Area, Central Nevada, J. Geophys. Res., 76, 7241-7248, 1971.

Savage, J. C. and J. P. Church, Evidence for postseismic slip in the Fairview Peak, Dixie Valley, and Rainbow Mountain fault areas of Nevada, Bull. Seismol. Soc. Am., 64, 687-698, 1974.

Savage, J. C. and L. M. Hastie, Surface deformation associated with dip-slip faulting, J. Geophys. Res., 71, 4897-4904, 1966.

Savage, J. C., and L. M. Hastie, A dislocation model for the Fairview Peak, Nevada, earthquake, Bull. Seismol. Soc. Am., 59, 1937-1948, 1969.

Savage, J. C. and M. Lisowski, Deformation in the White Mountain seismic gap, California-Nevada, 1972-1882, J. Geophys. Res., 89, 7671-7687, 1984.

Slemmons, D. B., The Dixie Valley-Fairview Peak, Nevada, earthquakes of December 16, 1954: geological effects, Bull. Seismol. Soc. Am., 47, 353-376, 1957.

Stauder, W. and A. Ryall, Spatial distribution and source mechanism of microearthquakes in central Nevada, Bull. Seismol. Soc. Am., 57, 1317-1345, 1967.

Thatcher, W., Nonlinear strain buildup and the earthquake cycle on the San Andreas fault, J. Geophys. Res., 88, 5893-5902, 1983.

Tocher, D., Movement on the Rainbow Mountain fault, Bull. Seismol. Soc. Am., 46, 10-14, 1956.

Vetter, U. R., and A. S. Ryall, Systematic change of focal mechanism with depth in the western Great Basin, J. Geophys. Res., 88, 8237-8250, 1983.

Wallace, R. E., Fault scarps formed during the earthquakes of October 2, 1915, in Pleasant Valley, Nevada, and some tectonic implications, U. S. Geol. Survey Prof. Paper 1274-A, p. A1-32, 1984.

Whitten, C. A., The Dixie Valley-Fairview Peak, Nevada, earthquakes of December 16, 1954: geodetic measurements, Bull. Seismol. Soc. Am., 47, 321-326, 1957.

Wickens, A. J., and J. H. Hodgson, Computer re-evaluation of earthquake mechanism solutions 1922-1962, Pub. Dom. Obs., Ottawa, 33, 1-560, 1967.

Figure Captions

Figure 1. Displacement vectors indicate the horizontal movements associated with four 1954 earthquakes. Stars locate epicenters. The displacements at underlined stations were minimized to estimate the translation, rotation, and scale change used in transforming derived coordinate differences into the vectors displayed here. The July 6 and August 23 earthquakes produced surface offsets on the Rainbow Mountain (RM) fault [Tocher, 1956]. The December 16 events produced surface offsets on the Fairview (F), Gold King (GK), West Gate (WG), and Dixie Valley (DV) faults [Slemmons, 1957].

Figure 2. The coseismic shear strains given in Table 2 correspond to the triangles displayed here.

Figure 3. Given a rectangle embedded in an isotropic homogeneous elastic halfspace, dislocation theory describes how each point of the halfspace moves in response to relative slip between the opposing rectangular faces. It is assumed that the upper and lower edges of the rectangle are parallel to the earth's surface and that the slip is pure translation in the plane of the rectangle, in particular, no rotation. The figure identifies seven parameters that define the size, location, and orientation of the rectangle. The motion depends on these parameters, the Poisson ratio of the halfspace, and the slip vector.

Figure 4. Vertical projection of rectangles onto the earth's surface for five-rectangle dislocation model. Rectangles correspond to the surface Fairview fault (F), a buried Fairview fault (B), the West Gate-Gold King faults (W), the Dixie Valley fault (DV), and the Rainbow Mountain fault (RM). Hatchures identify the upper edges of the various rectangles. Displacement vectors repeated from Figure 1.

Figure 5. Vertical projection of rectangles onto the earth's surface for six-rectangle dislocation model. The fault-rectangle correspondence is as given in Figure 4 with the additional rectangle corresponding to a hypothetical fault (H). Hatchures identify the upper edges of the various rectangles. Displacement vectors repeated from Figure 1.

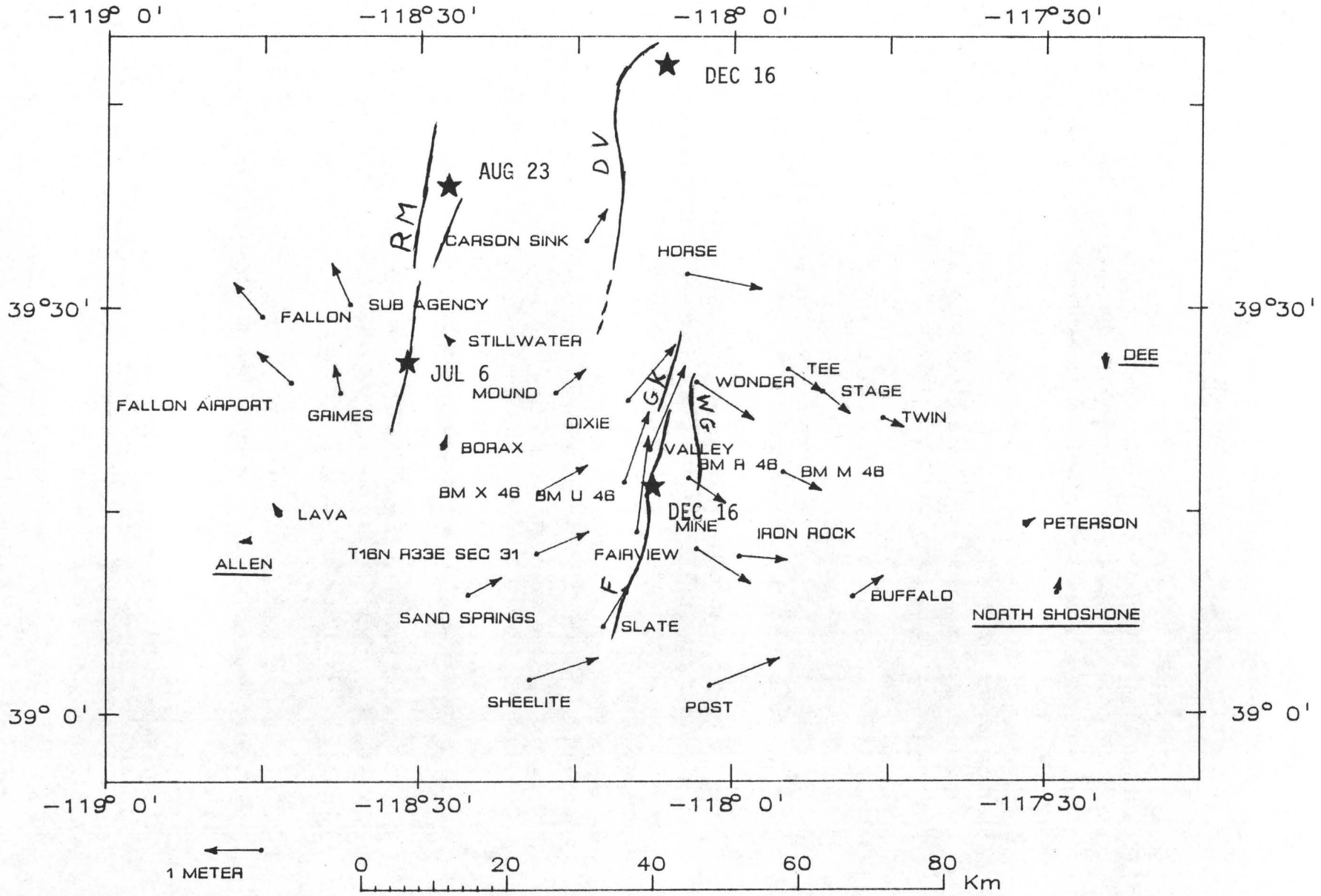
−119° 0'
−118°30'
−118° 0'
−117°30'
39°30'
39° 0'
DEC 16
AUG 23
JUL 6
DEC 16
RM
DV
GK
GW
F
CARSON SINK
HORSE
FALLON
SUB AGENCY
STILLWATER
FALLON AIRPORT
GRIMES
MOUND
DIXIE
BORAX
VALLEY
WONDER
TEE
STAGE
TWIN
DEE
BM R 48
BM M 48
BM X 48
BM U 48
LAVA
MINE
IRON ROCK
PETERSON
ALLEN
T16N R33E SEC 31
FAIRVIEW
BUFFALO
SAND SPRINGS
SLATE
NORTH SHOSHONE
SHEELITE
POST
1 METER
0
20
40
60
80
Km

FIGURE 1

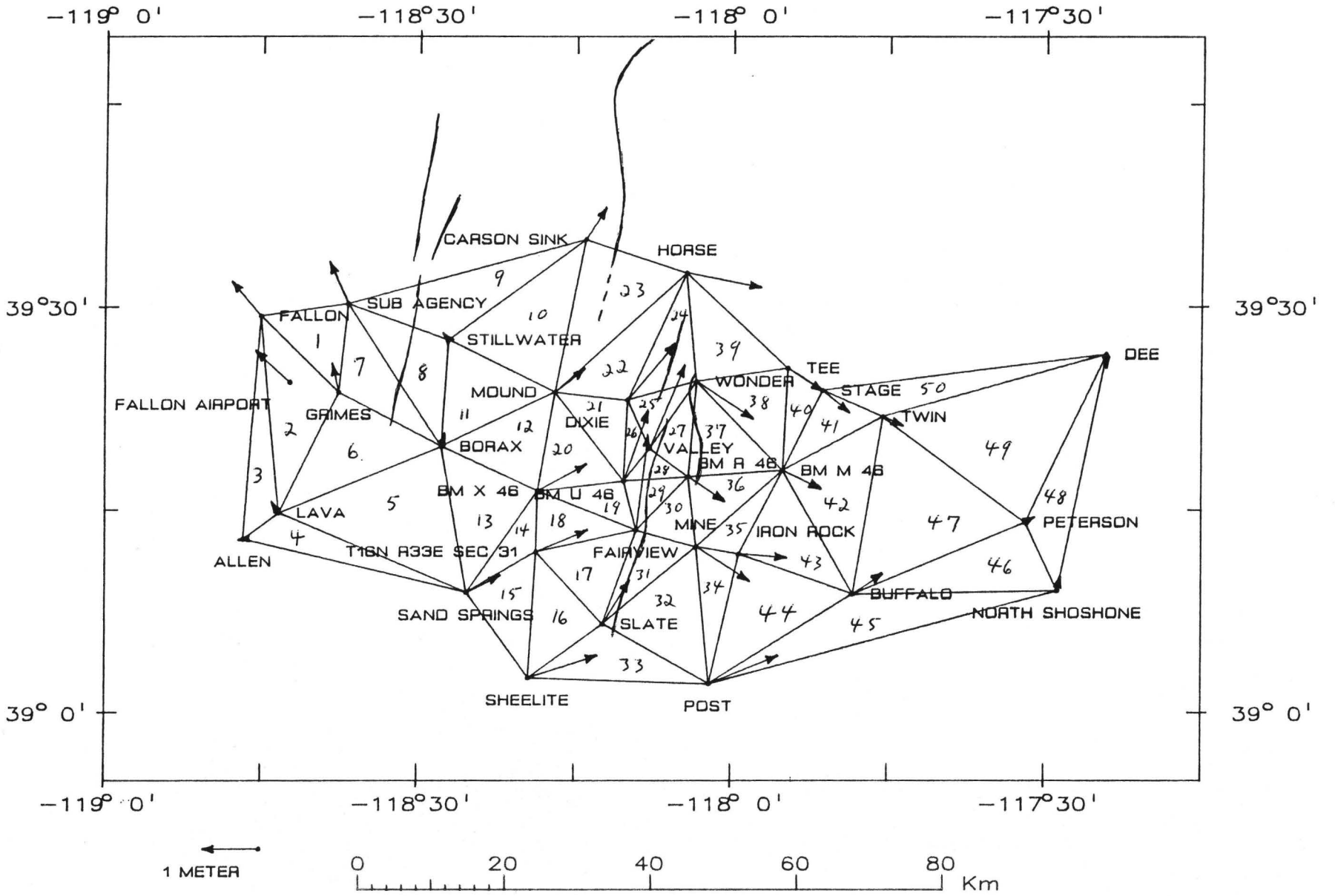
−119° 0'
−118°30'
−118° 0'
−117°30'
39°30'
39° 0'
CARSON SINK
HORSE
SUB AGENCY
FALLON
STILLWATER
FALLON AIRPORT
GRIMES
MOUND
DIXIE
BORAX
WONDER
TEE
STAGE
TWIN
DEE
VALLEY
BM R 48
BM M 48
BM X 46
BM U 48
LAVA
MINE
IRON ROCK
PETERSON
ALLEN
T16N R33E SEC 31
FAIRVIEW
BUFFALO
NORTH SHOSHONE
SAND SPRINGS
SLATE
SHEELITE
POST
1 METER
0
20
40
60
80
Km

FIGURE 2

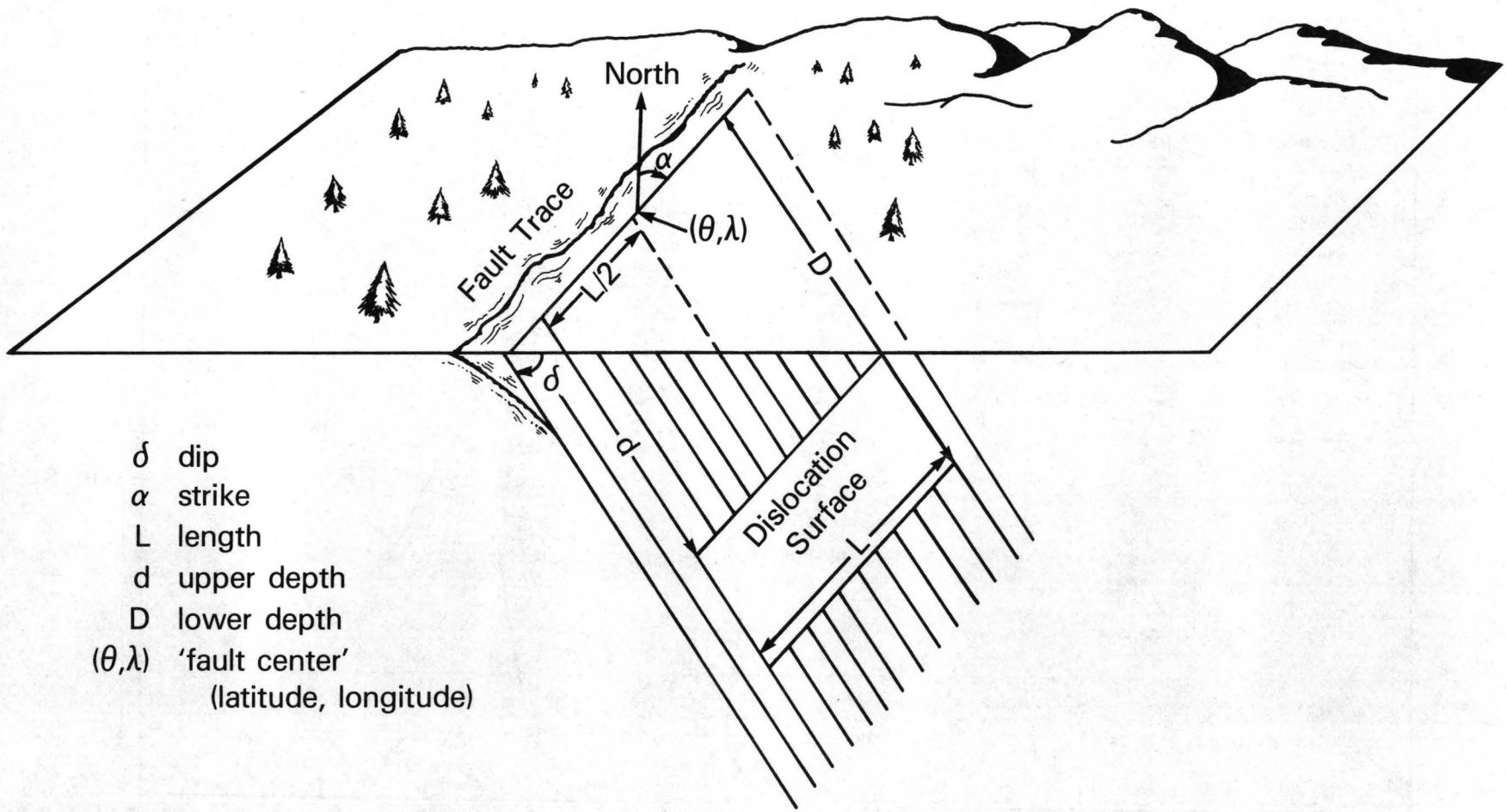

δ dip
α strike
L length
d upper depth
D lower depth
(θ,λ) 'fault center'
(latitude, longitude)

FIGURE 3

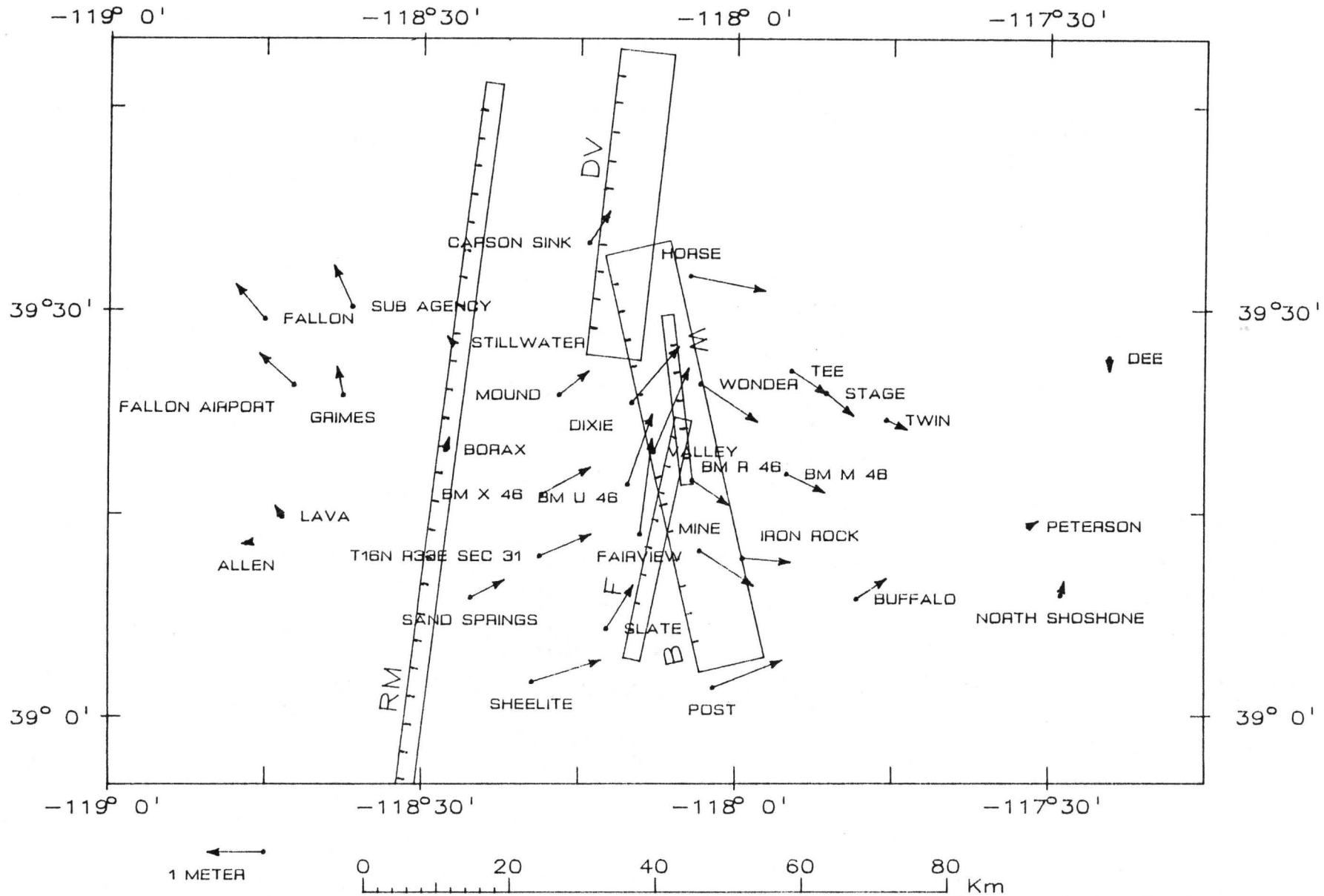
-119° 0'
-118°30'
-118° 0'
-117°30'
39°30'
39° 0'
DV
RM
CARSON SINK
HORSE
FALLON
SUB AGENCY
STILLWATER
MOUND
DIXIE
WONDER
TEE
STAGE
TWIN
DEE
FALLON AIRPORT
GRIMES
BORAX
VALLEY
BM R 46
BM M 48
BM X 46
BM U 46
LAVA
ALLEN
MINE
IRON ROCK
PETERSON
T16N R33E SEC 31
FAIRVIEW
BUFFALO
SAND SPRINGS
SLATE
NORTH SHOSHONE
SHEELITE
POST
1 METER
0
20
40
60
80
Km

FIGURE 4

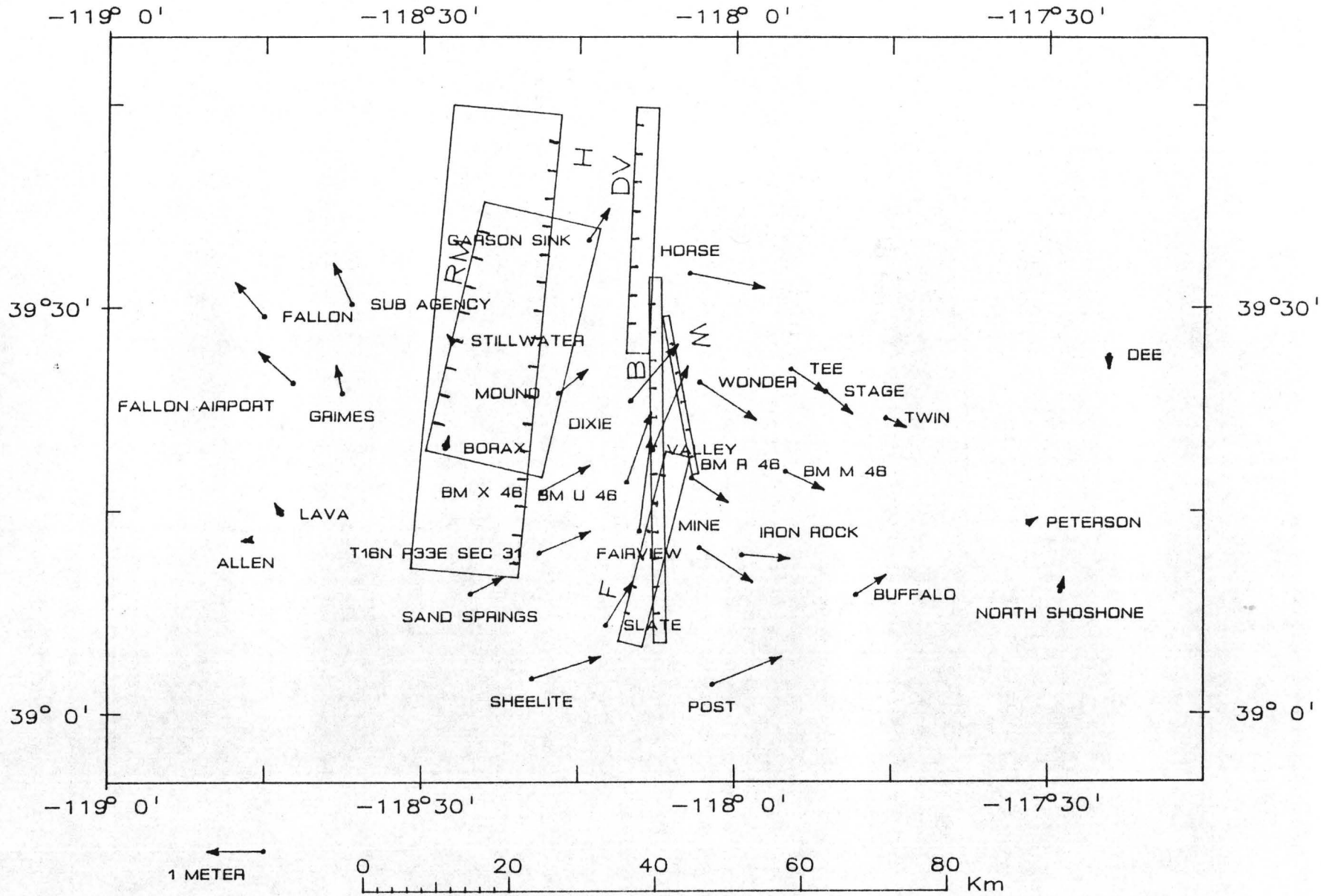
−119° 0'
−118°30'
−118° 0'
−117°30'
39°30'
39° 0'
GARSON SINK
HORSE
FALLON
SUB AGENCY
STILLWATER
FALLON AIRPORT
GRIMES
MOUND
DIXIE
BORAX
BM X 46
BM U 46
LAVA
ALLEN
T16N R33E SEC 31
SAND SPRINGS
SHEELITE
POST
SLATE
FAIRVIEW
MINE
IRON ROCK
VALLEY
BM R 46
BM M 48
WONDER
TEE
STAGE
TWIN
DEE
PETERSON
BUFFALO
NORTH SHOSHONE
RM
H
DV
B
W
F
1 METER
0
20
40
60
80
Km

FIGURE 5

HYDROLOGIC CHANGES FOLLOWING THE IDAHO BORAH PEAK EARTHQUAKE [1]

R. L. Whitehead

U.S. Geological Survey
Water Resources Division

ABSTRACT

Significant hydrologic changes were observed after the Borah Peak earthquake (magnitude 7.3 on the Richter scale) on October 28, 1983, in central Idaho. Ground-water levels rose as much as 4 meters in a well near the epicenter, then declined rapidly for several months before leveling off at about 1½ meters above pre-earthquake levels. Elsewhere on the valley floor, some wells flowed briefly. Discharge in many springs increased and some new springs developed. Near Challis, flow in one warm spring ceased, resumed several days later, and peaked 46 days later at about 9 times its original discharge of 170 liters per second. At Chilly Buttes north of the epicenter and another butte nearer the epicenter, ground water erupted from fissures in the northeast sides of the buttes 35 meters above the valley floor and formed sand boils or craters in the adjacent valley floor. Discharge in many streams increased more than 100 percent after the earthquake and remained high for about 2 weeks before declining to near, but still above, original flows. Analyses of both cold- and thermal-water samples indicated no significant changes in water chemistry.

INTRODUCTION

The Idaho Borah Peak earthquake (magnitude 7.3 on the Richter scale) caused significant changes in the hydrologic system (fig. 1). This article presents preliminary data on post-earthquake hydrologic changes in wells, springs, streams, and other surface-water bodies in central and southern Idaho, and reported changes in Montana.

HYDROLOGIC MONITORING

The U.S. Geological Survey's statewide hydrologic monitoring network provided the basis for post-earthquake monitoring activities (fig. 2). However, coverage was expanded in certain areas by inventorying a few new wells and by reactivating sites with historic data so that changes could be detected. Studies by Crosthwaite and others (1970), Young and Harenberg (1973), and Clebsch and others (1974) provided additional data for detecting hydrologic changes following the earthquake.

Discharge was measured at 25 streams and 4 springs in the Big Lost River basin and at 23 streams and 6 springs in basins north and east of the Big Lost River basin. Areas to the west and south were adequately monitored by the existing network.

---

[1] Reprinted with permission of Birkhauser Boston, Inc.

Water levels were measured in 69 wells, which included 41 wells added to the existing network for this study. Some sites were dropped after the initial post-earthquake measurements; others are being continued (August 1984).

Water samples were collected from 40 sites for chemical analyses and from 15 sites for suspended-sediment concentrations. Sampling for water-quality analyses was repeated in March 1984 at five of the above sites.

HYDROLOGIC CHANGES

The most prominent changes in the hydrologic system occurred near the epicenter. Some changes were noted in wells in other parts of Idaho, as well as in Montana as far away as 700 kilometers (fig. 3). Table 1 summarizes hydrologic changes compiled from gaging-station records for wells, streams, and springs; observations; and unconfirmed reports. Locations of these changes are cross-referenced, by number, to figure 3.

Ground Water

Water levels in wells near the epicenter generally rose rapidly after the earthquake; some temporarily overtopped their casings. Water issuing from many of these wells was muddy and clogged some pumps.

Changes in water levels during the earthquake were noted in numerous wells throughout southern Idaho (fig. 4); however, most returned to pre-earthquake levels. Water levels in some wells north of the epicenter in Montana were reported to have declined after the earthquake. The declines were accompanied by muddy water and, occasionally, an odor of hydrogen sulfide gas (J. A. Moreland, U.S. Geological Survey, written commun., 1984).

The greatest water-level change was recorded in an observation well near Chilly (fig. 5). The recorder malfunctioned on September 15, 1983, and when it was restarted on November 4, the water level in the well had risen nearly 4 meters. Subsequently, it declined steadily until January, then leveled off about 1.5 meters above its pre-earthquake stage. The water level in an observation well 210 kilometers southwest of the epicenter also rose (fig. 6). The well is 409 meters deep in a confined system and flowed prior to ground-water development in the area. Withdrawals of ground water for irrigation near the well lowered the potentiometric head. A flowing well southwest of the epicenter near Twin Falls (fig. 3, no. 40) reacted to the earthquake in a similar manner (fig. 4, nos. 37 and 40).

The Clayton Silver Mine near Challis, Idaho (fig. 1), which routinely pumped about 62 liters per second from the lower level of one of the workings to keep water from the mining operations, had to pump about 126 liters per second after the earthquake to maintain the pre-earthquake water level (Roland Rovetto, Clayton Silver Mine, oral commun., 1984). As of August 1984, pumping of 96 liters per second was adequate to maintain the working level. A similar increase in flow was observed in the mine following the 1959 Hebgen Lake earthquake in Montana (Roland Rovetto, Clayton Silver Mine, oral commun., 1984; Swensen, 1964, p. 162). The flow returned to its pre-earthquake volume after about 8 months.

Ground water gushed from fissures opened in the Chilly Buttes area and in the vicinity of another butte about 8 kilometers to the south, nearer the epicenter, for several hours after the earthquake and caused local flooding. Rising ground-water levels saturated the valley alluvium, which compounded the flooding and formed a temporary lake near Chilly Buttes.

Increased discharge from many springs was reported. The most significant increase was at Warm Springs south of Challis (fig. 7). Pre-earthquake discharge from these springs was 170 liters per second. The springs ceased flowing after the earthquake, began flowing again on November 4, then increased steadily and peaked at 1,640 liters per second on December 20 (S. H. Wood, Boise State University, written commun., 1984). Discharge remained reasonably steady during January and February, ranging from 1,470 to 1,560 liters per second. Discharge increased to 1,750 liters per second by March 8, 1984, then decreased to 1,630 and 1,300 liters per second on April 5 and May 9, 1984. The August 1984 measurement was 1,500 liters per second.

Surface Water

Most streams in the epicenter area and surrounding basins were at or above maximum average discharge prior to the earthquake. Following the earthquake, significant increases were measured at several U.S. Geological Survey gaging stations (table 1 and figs. 2 and 8).

Streamflow increased more than 100 percent in North Fork Big Lost River, about 23 kilometers southwest of the epicenter, and in Big Lost River, about 14 kilometers southwest of the epicenter. Flow in the North Fork increased from 1,420 liters per second prior to the earthquake to 3,400 liters per second. Flow in the Big Lost River increased from 4,960 liters per second prior to the earthquake to 11,300 liters per second. By December, flow in this river had declined slightly to 9,200 liters per second. According to National Weather Service data, there was no major precipitation in the area during October to have caused the increased discharge. Rainstorms before and after the earthquake are labeled in figure 8.

Two lakes formed as a direct result of the earthquake. One at Chilly Buttes, previously mentioned, drained within 2 weeks after the earthquake. The other is in a remote area in the Pahsimeroi River basin drainage (fig. 1). It was reported to have drained by summer of 1984 (Roland Lieby, U.S. Forest Service, oral commun., 1984).

Mackay Reservoir, about 16 kilometers southeast of the epicenter, has a storage capacity of 54.7 cubic hectometers and was about 90 percent full at the time of the earthquake. Safety of the residents of Mackay, about 6 kilometers downstream from the reservoir, was of great concern. The dam did not fail, but a considerable amount of rock from adjacent cliffs fell into the spillway channel. The earthquake shock was reflected in the reservoir by relatively minor wave action. A vertical motion through about a 0.03-meter range that lasted about 30 minutes was recorded.

Water Quality and Sediment

Comparison of pre-earthquake water-quality analyses with the few post-earthquake analyses presently (March 1984) available showed no significant changes. Sediment samples are currently being analyzed.

ACKNOWLEDGMENTS

The author is grateful to residents in the study area for their assistance and valuable information. The assistance of the U.S. Geological Survey's staff at the Idaho National Engineering Laboratory is gratefully acknowledged. Special thanks are given to Dr. Spencer H. Wood, Department of Geology and Geophysics, Boise State University; Roland Rovetto, Clayton Silver Mine; and Roland Lieby, U.S. Forest Service, Challis.

REFERENCES

Clebsch, Alfred Jr., Waite, H. A., and Decker, S. O., 1974, The availability of water in the Little Lost River basin, Idaho: Idaho Department of Water Resources, Water Information Bulletin no. 37, 60 p.

Crosthwaite, E. G., Thomas, C. A., and Dyer, K. L., 1970, Water resources of the Big Lost River basin, south-central Idaho: U.S.G.S. Open-File Report, 109 p.

Swensen, F. A., 1964, Ground-water phenomena associated with the Hebgen Lake earthquake, in The Hebgen Lake, Montana, earthquake of August 17, 1959: U.S.G.S. Professional Paper 435, p. 159-165.

Young, H. W., and Harenberg, W. A., 1973, A reconnaissance of the water resources in the Pahsimeroi River basin, Idaho: Idaho Department of Water Administration, Water Information Bulletin no. 31, 57 p.

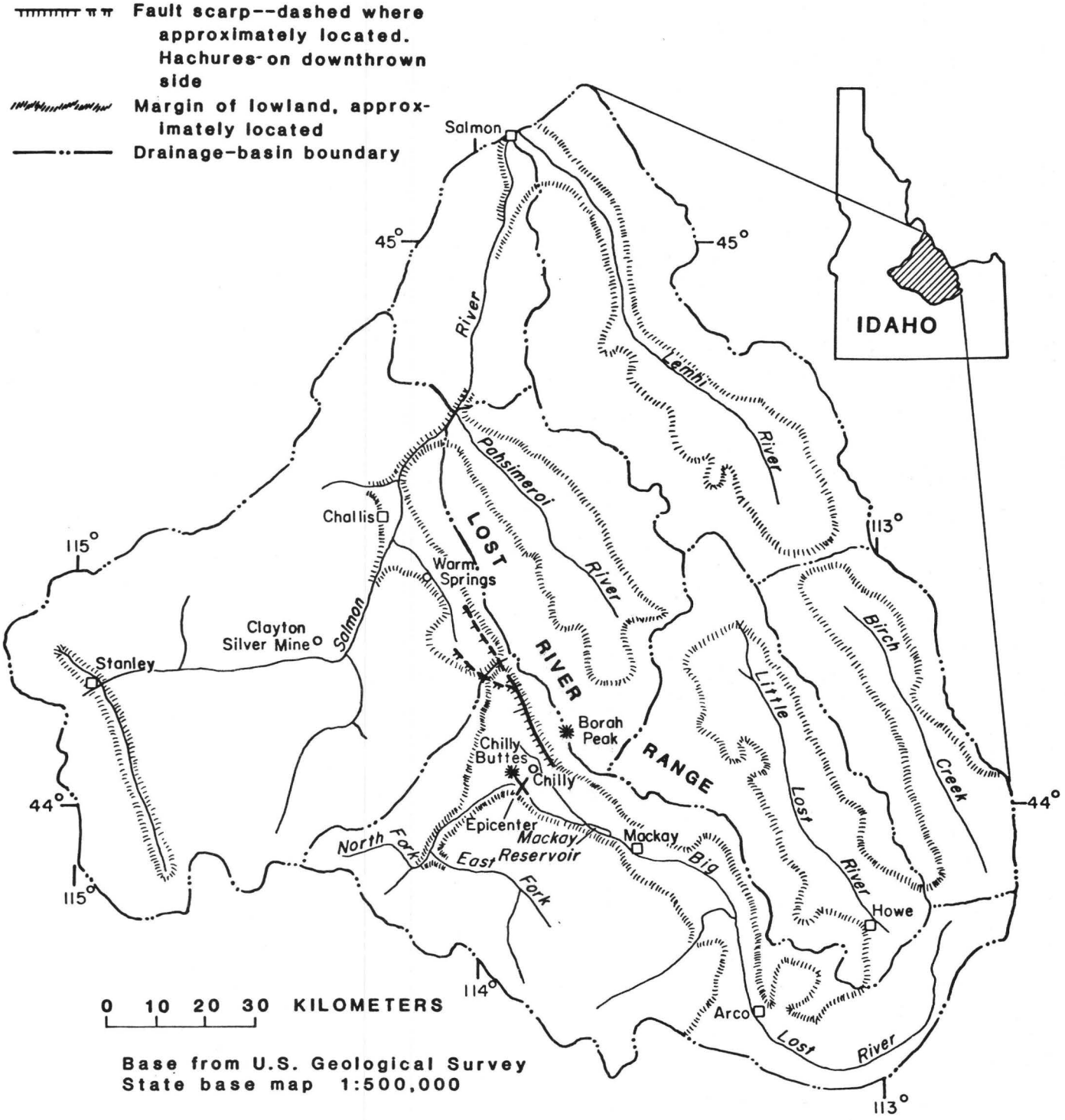

Figure 1.--Geographic features in vicinity of the earthquake epicenter.

Figure 2.--Post-earthquake hydrologic monitoring sites in southern Idaho.

Figure 3.--Locations of observed and reported hydrologic changes in Idaho and Montana following the earthquake.

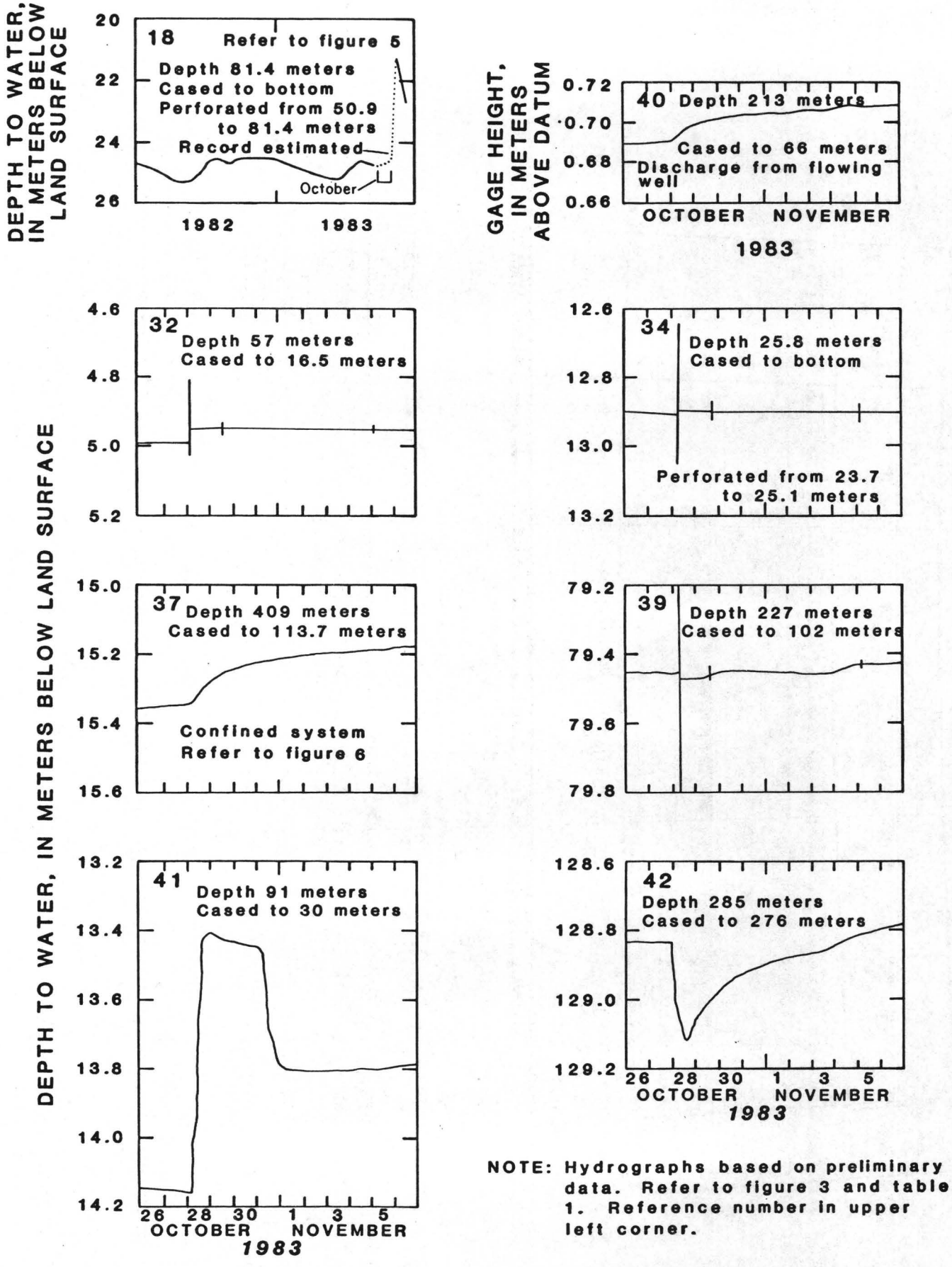

NOTE: Hydrographs based on preliminary data. Refer to figure 3 and table 1. Reference number in upper left corner.

Figure 4.--Hydrographs of selected wells showing water-level changes following the earthquake.

Figure 5.--Hydrographs of observation well near Chilly eight kilometers north of the epicenter showing short- and long-term water-level changes.

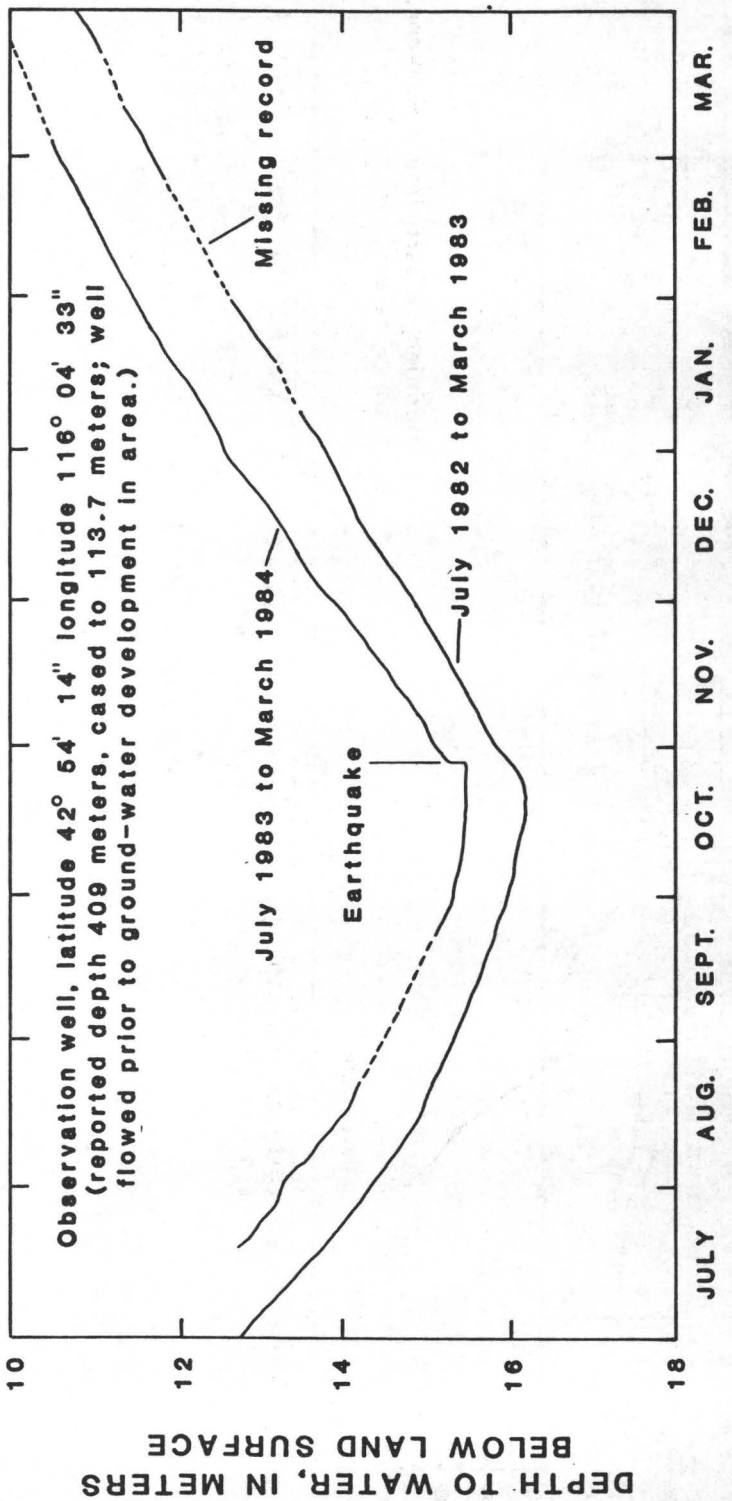

Figure 6.--Hydrographs of observation well 210 kilometers southwest of the epicenter showing comparison of water-level changes following the earthquake with previous year's record.

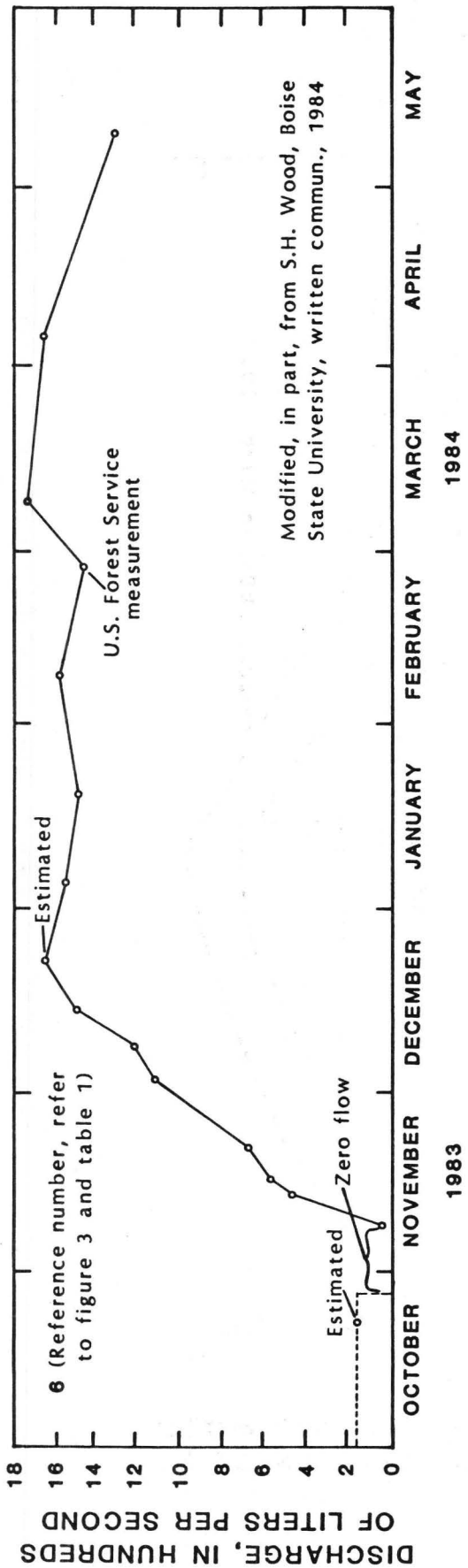

Figure 7.--Hydrograph of Warm Springs south of Challis showing changes in discharge following the earthquake.

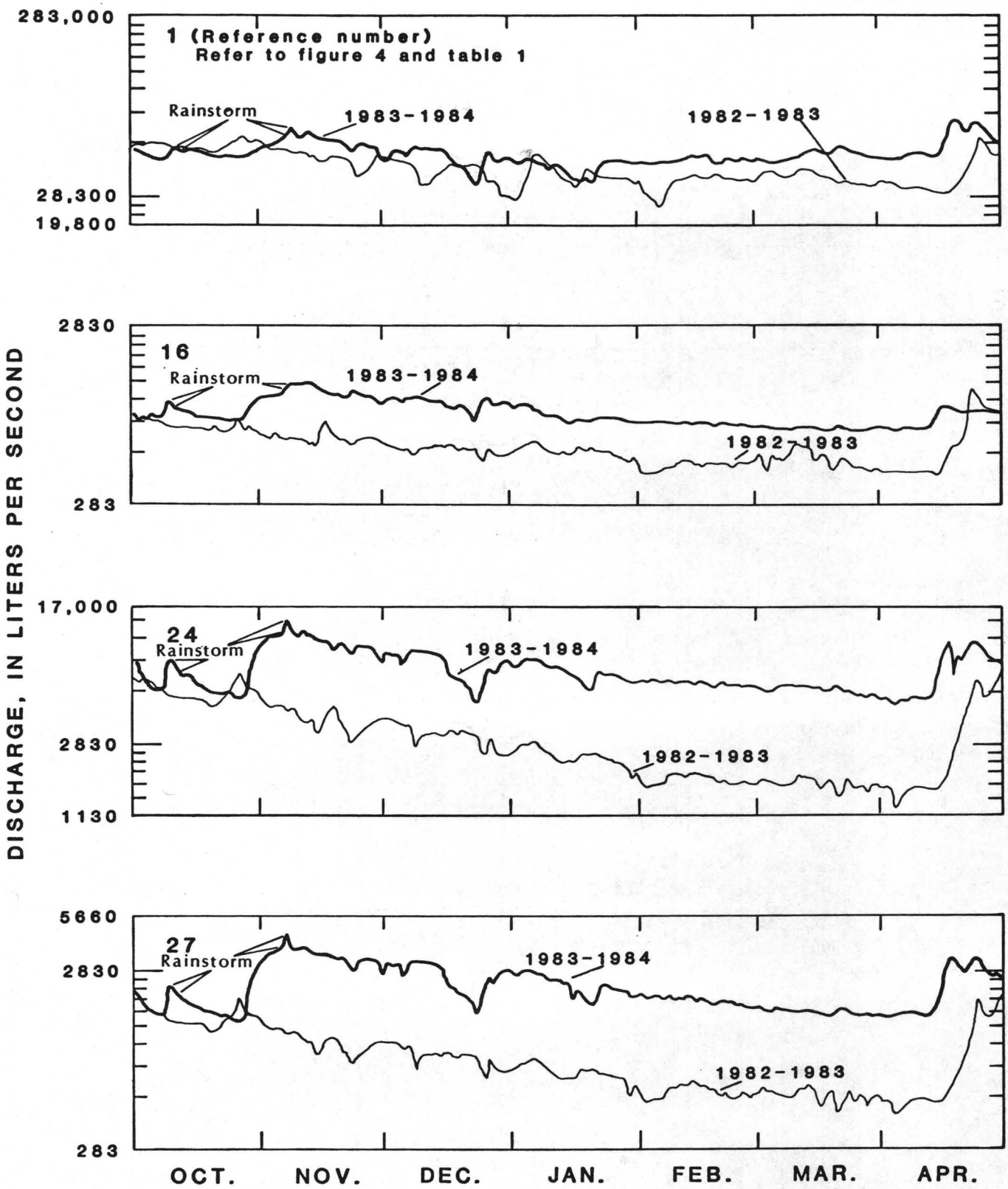

Figure 8.--Hydrographs of selected streams for October 1982 to April 1983 and October 1983 to April 1984 showing comparison of changes following the earthquake with previous year's record.

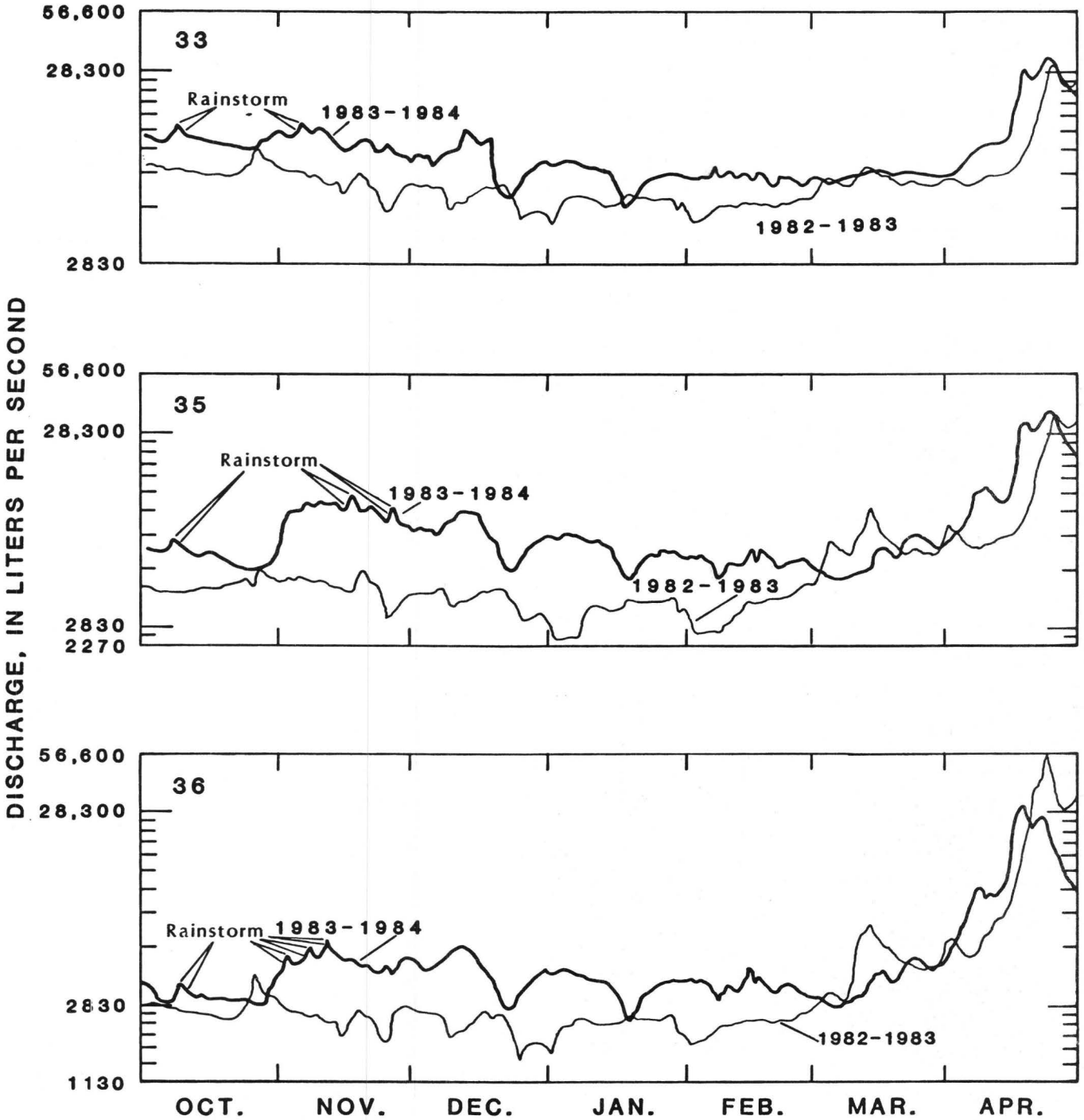

Figure 8.--Hydrographs of selected streams for October 1982 to April 1983 and October 1983 to April 1984 showing comparison of changes following the earthquake with previous year's record--Continued.

Table 1.--Summary of post-earthquake hydrologic changes

[Modified from S. H. Wood, Boise State University, written commun., 1984]

Reference number (refer to figure 3)	Site	Change
	IDAHO SITES[1/]	
1	U.S. Geological Survey gaging station, Salmon River at Salmon	Increased discharge (refer to fig. 8).
2	Lawson Creek	Increased discharge reported. Measured 845 liters per second.
3	Sulphur Creek	Increased discharge reported. Measured 440 liters per second at springs in 1971. Measured 753 liters per second after earthquake.
4	Hole in the Rock Creek	Increased discharge reported.
5	Lime Creek	Do.
6	Warm Springs south of Challis	Spring discharge of 170 liters per second ceased but began again November 4 (refer to fig. 7).
7	Devils Canyon	Increased discharge reported.
8	Grouse Creek drainage	Formed new 8,000 square-meter lake about 3 meters deep, reported by U.S. Forest Service.
9	Clayton Silver Mine	Increased discharge. Pumping rate of 62 liters per second doubled to maintain pre-earthquake water level.
10	Spring near Clayton Silver Mine	Discharge diminished, then increased, reported.
11	Unnamed spring	Increased discharge reported.
12	Tub Spring area	Do.
13	Unnamed spring	New spring reported.
14	Road Creek	Increased discharge reported.
15	Bear Creek	Do.
16	U.S. Geological Survey gaging station, Herd Creek below Trail Creek Gulch near Clayton	Increased discharge (refer to fig. 8).
17	Pine Creek	Increased discharge reported.
18	U.S. Geological Survey observation well	Higher water level (refer to figs. 4 and 5).
19	Whiskey Spring	Discharge diminished, then recovered, reported.
20	Chilly Buttes	Water under high hydraulic head gushed out of fissures on side of butte (head estimated at about 35 meters), discharge exceeded 2,800 liters per second. Sand and water issued from craters in valley floor. A temporary lake formed but drained within 2 weeks.

Table 1.--Summary of post-earthquake hydrologic changes--Continued

Reference number (refer to figure 3)	Site	Change
	IDAHO SITES--Continued	
21	Birch Springs	Springs along fault saturated hillside and caused landslide. Discharge estimated to equal pre-earthquake discharge.
22	Elkhorn Creek Canyon	New springs reported to discharge about 60 liters per second.
23	Bartlett Creek	Increased discharge reported.
24	U.S. Geological Survey gaging station, Big Lost River at Howell Ranch near Chilly	Increased discharge (refer to fig. 8).
25	Hamilton Spring	Surge of water (about 2,800 liters per second). Discharge doubled pre-earthquake discharge of 850 liters per second.
26	Mackay State Fish Hatchery	Surge of water (about 2,000 liters per second). Discharge increased from 620 to 850 liters per second.
27	U.S. Geological Survey gaging station, North Fork Big Lost River at Wildhorse near Chilly	Increased discharge (refer to fig. 8).
28	Mackay Reservoir	Stage fluctuated about 0.03 meter.
29	Mackay City Spring	Increased discharge reported.
30	Easley Warm Spring	Do.
31	Cherry Creek area	New springs and landslide reported.
32	U.S. Geological Survey observation well	Higher water level after earthquake (refer to fig. 4).
33	U.S. Geological Survey gaging station, Big Wood River at Hailey	Increased discharge (refer to fig. 8).
34	U.S. Geological Survey observation well	Higher water level after earthquake (refer to fig. 4).
35	U.S. Geological Survey gaging station, Big Wood River near Bellevue	Increased discharge (refer to fig. 8).
36	U.S. Geological Survey gaging station, Little Wood River above High Five Creek near Carey	Do.
37	U.S. Geological Survey observation well	Higher water level after earthquake (refer to fig. 4).
38	U.S. National Fish Hatchery spring	Large spring fluctuated about 85 liters per second above and below normal discharge of about 740 liters per second for several days.
39	U.S. Geological Survey observation well	Lower water level, then returned to normal following large aftershock (refer to fig. 4).
40	do.	Increased discharge from artesian well (refer to fig. 4).
41	do.	Higher water level, then decline (refer to fig. 4).
42	do.	Lower water level, then return to normal (refer to fig. 4).

Table 1.--Summary of post-earthquake hydrologic changes--Continued

Reference number (refer to figure 3)	Site	Change
	IDAHO SITES--Continued	
43	U.S. Geological Survey gaging station, Lemhi River near Lemhi	Increased discharge (based on estimates).
44	U.S. Geological Survey gaging station, Little Lost River below Wet Creek near Howe	Increased discharge.
45	U.S. Geological Survey gaging station, South Fork Boise River near Featherville	Do.
46	U.S. Geological Survey gaging station, Salmon River below Yankee Fork near Clayton	Do.
47	U.S. Geological Survey gaging station, Thompson Creek near Clayton	Do.
48	U.S. Geological Survey gaging station, Squaw Creek below Bruno Creek near Clayton	Do.
49	U.S. Geological Survey gaging station, East Fork Salmon River above Big Boulder Creek near Clayton	Do.
	MONTANA SITES[2/]	
50	Well in Browning area	Well went dry after earthquake, was good producer previously.
51	Well in Kalispell area	Well yielded brown water 3 hours after earthquake.
52	Spring in Kalispell area	Spring went dry after earthquake; as of December 14, 1983, still dry.
53	Well in Thompson Falls area	Pump set 1.2 meters above bottom pumped dry quickly after earthquake.
54	Well in Superior area	Well yielded muddy, iron-stained water for several hours.
55	Well in Geraldene area	Well developed odor and iron problems after earthquake.
56	Well in Glendive area	Well yielded muddy water.
57	Several wells in Florence area	Wells yielded iron-enriched water after earthquake, stains badly.
58	Springs in Victor area	Discharge increased after earthquake.
59	Well in Corvallis area	Water developed "musty" taste.
60	Wells in Hamilton area	One well yielded red water after earthquake. Seven other wells went dry.

Table 1.--Summary of post-earthquake hydrologic changes--Continued

Reference number (refer to figure 3)	Site	Change
	MONTANA SITES[2]--Continued	
61	Well in Darby area	Well always yielded iron-enriched water, but much worse after earthquake; changed a filter every 2-3 months before earthquake; changed daily after earthquake.
62	Well in Bozeman area	Well now loses prime; was a good producer since 1930.
63	do.	Well yielded iron-enriched water after earthquake.
64	Well in Joliet area	Well went dry within 2 days after the earthquake.
65	do.	Well developed hydrogen sulfide odor. No apparent changes in quality, quantity, temperature, or appearance.

[1] Additional changes probably occurred which have not yet been reported.
[2] J. A. Moreland, U.S. Geological Survey, written commun., 1984.

REGIONAL INCREASE IN GROUNDWATER DISCHARGE AFTER THE 1983 IDAHO EARTHQUAKE: COSEISMIC STRAIN RELEASE, TECTONIC AND NATURAL HYDRAULIC FRACTURING

Spencer H. Wood

Department of Geology and Geophysics,
Boise State University, Boise, Idaho 83725

Abstract

The October 28, 1983 Idaho earthquake (Ms = 7.3) greatly increased the groundwater discharge from springs over a region extending at least 90 km beyond the 34-km long zone of surface rupture at the west base of the Lost River Range. Many warm springs systems nearly doubled in flow, and one major spring increased 10 times its original flow. Numerous seeps became flowing springs. Major rivers draining an area of 18,000 km^2 significantly increased in flow for a period of several months following the earthquake, and at the time of writing (9/84) are still running high. In the 1160-km^2 upper Big Lost river drainage the increased flow for 6 months following the earthquake is equivalent to an 8 cm runoff event over the basin. At the time of writing some spring flows have declined, but many are running well above their pre-earthquake flow. The region is underlain by volcanic, clastic and carbonate sedimentary rock, and granitic rocks.

The mechanism by which spring flows increase following an earthquake has not been clearly identified; however similar groundwater discharges followed the 1952 Kern County, California earthquake (M = 7.7). It follows from Darcy's law that increased discharge must be attributed to either an increase in aquifer pressure or an increase in permeability along the flow path. Coseismic strain release should produce a contraction of volume in the rocks of the hanging-wall block of fault and consequently an increase in pore pressure. By this same process, the footwall rocks should slightly dilate and slightly decrease pore pressure in the mountain side of the fault. Increase in pore pressure might also be caused by compaction of aquifer rocks by seismic shaking or regional tectonic tilting of aquifers. Local increase in permeability could be caused by tectonic fracturing along the main fault zone. Increase in permeability along previous spring conduits could be produced over a wider region by the flushing and cleaning of conduits by surging flows caused by seismic shaking. It is also possible that pore pressure pulses produced by the passage of seismic waves could produce natural hydraulic fracturing.

INTRODUCTION

The October 28, 1983 Idaho earthquake (Ms = 7.3) significantly altered the natural groundwater discharge system in the zone of tectonic deformation and normal faulting and at points up to 90 km from the zone of surface faulting (Fig.1). Flows from springs generally increased shortly after the main shock. The most significant and convincing measure of the great amount of groundwater

produced by the earthquake is in the hydrographs of major rivers of the region reported by Whitehead (1984). Many large rivers nearly doubled in flow following the earthquake and are still running high in the autumn of 1984. Some of the hydrologic effects could have been hazardous in an urban area, and part of the initially assessed damage in Custer and Butte County was caused by flows of water, or loss of water supplies. Hydrologic effects of earthquakes have not been well documented in the past and it is the purpose of this report to document hydrologic observations and offer preliminary explanations for events following the earthquake.

In the epicentral area, a surge in artesian pressure of at least 35 m ft caused spectacular bursts of muddy water from carbonate-rock hills and fissure eruptions and boils of sand from the surrounding alluvium in the Chilly Buttes area (Waag, 1985). Flow from the Chilly Buttes area caused minor flooding and created a temporary lake in Thousand Springs Valley (Figures 2 and 3). Similar large flows of water occurred at spring areas on the west side of the Lost River Valley at Dick Smith's Fish Hatchery (Fig. 2), and damaged much of that hatchery operation. Along the zone of surface breakage several new springs issue from the surface fractures. At points 5 to 60 kms from the zone of surface faulting several warm springs systems have increased in flow. Perhaps the most interesting changes in warm-spring flows have occurred at Ingram's Warm Springs Creek south of Challis. The original flow of about 6 cfs virtually ceased and the springs dried up following the earthquake (Figures 4 and 5)). Eight days later the springs recommenced flowing at an ever increasing rate and at the time of writing (September, 1984) the springs are flowing 51 cfs, about 9 times their original flow (Figures 4 and 6). Major rivers draining the area of the earthquake underwent large increases in discharge within a day after the main shock (Fig. 7) Significant are the flows in the Big Wood River, Little Wood River, Big Lost River, and the Pahsimeroi River. Flows nearly doubled in these rivers. The drainage areas of these rivers is shown in Figure 7. R. Whitehead (1985) has noted that a great many other rivers more distant from the earthquake area also show small increases in flow coincident with the few days following the earthquake.

At the underground Clayton Silver Mine, water levels had been sustained by pumping 980 gpm at 1150 ft below the valley bottom elevation of 5890 ft in order to mine stopes between the 950 and the 1100-ft level (Fig.9). Three hours after the main shock water began to rise at a rate of 5 feet per hour in the shaft from which the water was being pumped. By November 7 it has risen 185 feet to the 965-ft level and continued rise was arrested by installing 2000 gpm pumps that pumped the water level back to the 1100-ft level about January 1, 1984. These effects and a description of the mine area are discussed by Ralston (1985).

A large complex mudflow involving an estimated 200,000 cubic meters of material occurred in the high mountain valley of Lupine Creek about 30 km southeast of the epicenter (Keefer and others, 1985). Most remarkable is the documentation that the mudflow did not occur until two days after the earthquake. The explanation by Keefer and others (1985) is that increased spring flow caused saturation of the colluvium and valley fill, which led to its instability and failure.

Hydrologic effects were particularly noted by residents of south-central Idaho because water supplies from spring flows are vital to many cattle

ranching, farming, and fish hatchery operations in the area. The high mountainous terrain surrounding the Big Lost River and the Salmon River Valleys have large winter-snow accumulations which supply water to the complicated subsurface aquifer systems of folded and faulted Paleozoic sedimentary rocks and the Eocene Challis volcanic rocks and valley alluvium. Snowmelt runoff begins in mid-April and ends in late August. Snowmelt flood flow in the Big Lost River typically peaks in mid-June between 1000 and 2000 cfs. Flow of the Big Lost River at Howell Ranch is typically less than 100 cfs in the period from September to April. During this period of low flow much of the reach between an area known as the "Chilly Sinks" (just below Howell Ranch) and above the Mackay Narrows and Reservoir is dry, because the water percolates into the alluvium and the carbonate aquifer system in the vicinity of the "Chilly Sinks" (Crosthwaite and others, 1970). This "lost" flow reappears in the reach above the Mackay Narrows. Flow from Thousand Springs Creek is derived mostly from the springs in the valley and from runoff from the Lost River Range in Willow Creek, Rock Creek, Cedar Creek, and Elkhorn Creek. Flow of the Big Lost River at Howell Ranch was 150 cfs just prior to the earthquake. Flow from Thousand Springs Creek is estimated to have been also about 150 cfs prior to the earthquake. Both flows were somewhat larger than normal because of higher than normal snowpack in the 1982/83 winter.

Major changes in spring and stream flows are documented with hydrographs in order to quantify the nature of the transient flows and the amounts of water released from the groundwater system because of the earthquake. Measurements were made by standard methods with a current meter and by constructing weirs and stage recorders on some streams. Changes have doubtlessly occurred on many of the smaller springs which we did not have a chance to examine before the area was snow covered.

A number of water wells underwent changes in water level throughout the southern Idaho area (Whitehead, 1985). Fluctuations and permanent shifts in water levels in wells at distant points have been well documented in other earthquakes; however, the permanent shifts have never been well explained. Data from the network of observation wells and stream gaging stations throughout Idaho and monitored by the U.S. Geological Survey, Water Resources Division have been compiled and discussed in a report by Whitehead (1985).

POSSIBLE MECHANISMS PRODUCING INCREASES IN SPRING FLOWS

Changes in spring flows are noted in many large earthquakes, and this effect is listed as a characteristic of earthquake shaking above intensity VII in the 1931 Modified Mercalli Intensity Scale. These effects were well documented in the 1952 Kern County California earthquake by Briggs and Troxell (1955). In that earthquake the major effect was increased flow, although a few springs and wells diminished in flow or went dry. Those authors and Richter (1958) attributed the increased spring flows in that earthquake to disturbance of the alluvial valley fill; however some of the spring flows were also warm springs, and discharged from granitic rocks (Fig. 10). Therefore it is more likely that the mechanism that increases spring flows is a process within the bedrock of the region affected by the earthquake.

It follows from Darcy's equation that an increased discharge of ground water must be attributed to either an increase in aquifer pressure gradient or an increase in permeability along the flow path. The several postulated mechanisms can be classified in this manner:

INCREASE IN AQUIFER PRESSURE GRADIENT	1. Coseismic strain release may increase pore pressure in confined aquifer systems.
	2. Compaction of aquifer rocks by seismic shaking.
	3. Tilting of aquifer layers by coseismic vertical tectonic movement.
PEARMEABILITY INCREASE ALONG FLOW PATH	1. Flushing of spring conduits by surging flows induced by seismic shaking.
	2. Tectonic fracturing along fault zones.
	3. Hydraulic fracturing by pore-pressure pulses accompanying the passage of seismic waves.

The major documented increased groundwater discharges after the Idaho earthquake are from warm springs systems. This would suggest that the water is from relatively deep confined aquifer systems. Temperatures of 16 to 30°C and the regional geothermal gradients suggest depths of the aquifers are 0.5 to 2 km. Geology and water chemistry of most of the spring systems indicate that most are in carbonate rocks. Significant increases in spring flows occurred 90 or more km from the zone of surface rupture. Increased flows have continued for almost one year since the earthquake, although there has been a decline from the original surge and high flow in the first few months following the earthquake. The possible mechanisms proposed above have been discussed by Wood and others (1984). Two of these mechanisms are elaborated in more detail in this paper. The coseismic release of elastic strain could produce increased fluid pressure, particularly in the hanging wall, west of the fault zone. The dynamic strain during the passage of seismic waves could cause hydraulic fracturing under favorable circumstances.

Effect of strain release on groundwater

According to elastic rebound theory of earthquake generation, elastic strain and stress accumulate in the elastic, but brittle rock of the earth's upper crust. Strain accumulates in the brittle rocks because of continuing large scale movements involving the somewhat more ductile rocks of the lower crust and upper mantle. The time interval of strain accumulation before breakage may be several centuries to several millenia depending on the rates of tectonic movement. Over this time interval, rigid blocks beyond the fault zone undergo translation, while weaker, and apparently more elastic rocks along the fault zone undergo elastic strain. When the strength of the outer crust is exceeded, the crust ruptures in shear along a plane or surface of weak shear strength which we call the fault zone. During the earthquake, the "rigid blocks" do not necessarily move, for they have already moved during the interval of strain accumulation. Most of the tectonic movement accompanying the earthquake is

simply the release of elastic strain about the fault zone.

Important to effect of strain release on groundwater is the sense of the strain. The sense of strain can be understood in a qualitative way from the nature of geodetically measured vertical and horizontal displacements from large earthquakes, but details of the strained volume at depth are not well understood. If the rocks dilate upon strain release, it is expected that aquifer pressure and spring flows will diminish. If the rocks contract in volume, then the aquifer pressure and spring flows should increase. The sense of strain for various fault geometries is illustrated in cartoon form in Figure 11. Strain from strike-slip should be of a different sense in each of four quadrants about the fault. In a thrust-fault earthquake, the foot wall should contract and the hanging wall should expand. In a normal-fault earthquake, the foot wall should expand, and the hanging wall should contract.

Geodetic relevelings across dip-slip faults after an earthquake convincingly show that the region of strain release extends many kilometers from the fault. On inclined dip-slip faults (normal and thrust faults) the strain release is greatest in the hanging wall block, indicating that the greatest pre-earthquake strain accumulation was also the greatest in the hanging-wall block (Wood, 1984). Figure 12 illustrates the situation for a normal fault similar to that envisioned for the Borah Peak earthquake. Releveling shows that release of elastic strain resulted in a broad downward bending of the hanging wall and a much smaller upward deflection of the mountainous footwall. The amount of downward deflection of the hanging wall is 2 to 2.5 m (Stein and Barrientos, 1985). If this is distributed as a coseismic compressional strain in the hanging wall over an 8-km thickness of the upper crust, then that strain near the fault must be about 2.5 m / 8 km = 2.5×10^{-4}. The decrease in strain with respect to distance suggests that at 15 km, the strain must be about 2×10^{-5}. This magnitude of permanent coseismic strain adjustment in the shallow crust must effect the pressure in the confined aquifer systems several tens of kilometers distant from the fault rupture. In the hanging wall block it must lead to significant increases in aquifer pressure. In the footwall block, the crust must actually expand, although the magnitude of the strain is an order of magnitude smaller for a dipping fault plane. The region in which rivers underwent large increases in flow following the Borah Peak earthquake is mostly southwest of the fault trace in the hanging-wall block. The region in which significant increases in spring flow occurred (Fig.1) are mostly off the two ends of the zone of surface breakage of the Lost River Fault, and mostly in the footwall block. The only exceptions are springs to the north of Challis, and springs in the Pahsimeroi River drainage which are beyond the zone of surface breakage, but in the footwall block of the Lost River Fault. The hydrographs of springs in the epicentral area (Fig. 2) are also of a form expected from a sudden increase in aquifer pressure. The elevation on Chilly Buttes from which water erupted gives a minimum estimate of the initial fluid-pressure increase in that aquifer system of 35 m of water or about 0.35 MPa. Using a compressibility for water of 4.5×10^{-5} $(MPa)^{-1}$, the volumetric contractual strain necessary to produce this pressure in the aquifer is about 10^{-5}, which is only about an order of magnitude less than that estimated from the geodetic data.

Stein and Barrientos (1985) have computed the pattern of elastic-strain release using a model of a uniform displacement on a rectangular fault surface

embedded in an elastic half-space of uniform elastic modulii. Their result indicates a volume contraction in the hanging wall with strains of 2.5×10^{-5} that lies over the assumed rectangular fault plane. This value is in agreement with our the simplistic calculation discussed above. About 20 km to the west is a nodal region, beyond which strains of much smaller magnitude are dilational. Their model also shows zones of relatively large dilation to the NW and SE beyond the trace of the plane of breakage, and about the region where significant spring flow increases are noted on Figure 1. It is not known whether these zones of volume expansion really exist or whether they are an artifact of the model geometry. Zones of dilation, according to the thesis presented here, should be areas where spring flows decrease, rather than the increases which are actually documented. It is clear that displacement on the fault is not uniform over a rectangular plane as modelled, but tapers to zero at the NW and SE ends and also splays at the NW end into two faults (Crone and Machette, 1984). While certain aspects of the calculation give useful insight, the lack of correspondance of modelled zones of coseismic compression with some of the zones of increased spring flows may indicate the model geometry is not applicable to the field situation especially in the region off the ends of the fault displacement.

Hydraulic Fracturing by Seismic Waves?

Permeability of rocks along existing spring conduits may be increased if existing tight fractures (joints) are parted, opened , or extended and then slip or are otherwise permanently propped open. Pulses in pore water pressure during passage of seismic waves might cause natural hydraulic fracturing in favorable situations. The process of hydraulic fracturing was analyzed by Hubbert and Willis (1957) who showed that fracturing by increased pore pressure is favored in pressurized aquifer or reservoir rocks in the regions of the crust that are under extensional tectonic stresses (normal faulting). They also emphasize that the tensile strength of natural flawed rocks is quite low and essentially zero across a joint so that the pore pressure increase necessary to open and extend a fracture need only be that necessary to overcome the normal stress that holds the rock together across a joint (Fig. 13). During the passing of seismic waves from a large earthquake, rocks of the earth's crust are alternately compressed and dilated through many cycles of strain. For 2-to-3-second-period waves, traveling at 6 km/s, the wavelengths are 12 to 18 km. A part of the earth's crust, perhaps 1/4 of a wavelength, 3 or 4 km wide, may be under compressional strain for 0.5 seconds, or a greater distance and longer time for longer period waves.

The magnitude of dynamic strain can be estimated from strainmeter recordings of nuclear explosions recorded at Round Mountain, Nevada at an epicentral distance of 200 km. The m_b = 6.5 HANDLEY event produced a peak dynamic strain of 1.5×10^{-5} and extrapolation of a curve relating peak dynamic strain at 200 km to magnitude for smaller events (Boucher and others, 1971, fig. 1) gives an estimate of 5×10^{-5} for a m_b = 7.5 event. If such dynamic strains scale at 1/r, where r is the epicentral distance, then at a distance of 30 km, the dynamic strain is of the order of 10^{-4} (Fig.14). Semi-confined water in fractures and pores in the rock will also suffer similar pulses of dynamic

strain. During a compression cycle, the increase in pore pressure can be calculated from the compressibility of water:

$$p = \frac{1}{\beta}\frac{\Delta V}{V}$$

$$p = \left[\frac{1}{4.5 \times 10^{-5}\ (MPa)^{-1}}\right]\left[\frac{\Delta V}{V}\right]$$

$$p = 2.3\ \text{MPa} \quad (333\ \text{psi})$$

where $\frac{\Delta V}{V}$ = volumetric strain

β = compressibility of water

This estimate seems high, and is probably a maximum possible value of dynamic pore pressure for an earthquake of this size. A more certain value can be derived from the elevation of conduits of water eruptions from the sides of Chilly Buttes as described by Waag (1985). Water burst out from a ridge about 35 meters above the surrounding valley floor. The head of 35 meters of water is 0.32 MPa. Can this range of magnitude of increase in pore pressure exceed the minimum horizontal stress, $S_{H(min)}$ in the shallow crust, for it is this horizontal stress ($S_{H_{min}}$) that presumably "holds rock faces together" in jointed rocks, when joints are approximately perpendicular to $S_{H(min)}$?

The value of $S_{H(min)}$ commonly found in extensional tectonic areas is about 12 MPa/km (McGarr, 1982, Fig. 3; Zoback, 1985, Fig. 5)

$$S_{H(min)} = \tfrac{1}{2}\ \rho\ g\ z\ /\ z = 12\ \text{MPa}\ /\ \text{km}$$

McGarr and Gay (1978) indicate that the minimum horizontal stress gradient in the upper 2.3 km of many U.S. sedimentary basins is about 15 MPa/km. Below 2.3 km, their data indicates that the gradient may be somewhat higher in sedimentary basins, or about 18 MPa/kma. Sediments of the Mississippi embayment along the Gulf Coast are known to be essentially in a state of incipient failure and gradients as low as 11.3 MPa/km are measured in the uppermost 2.3 km. In some crystalline basement rocks of sedimentary basins of the west-central U.S, they show values as low as 10 MPa/km. In other shield areas of crystalline rocks the values are much larger, about 25 MPa/km. Figure 15 shows the increase in the vertically oriented maximum principal stress from the weight of overburden rock of density 2.3 g/cm^3 at 23 MPa/km, the gradient of the minimum horizontally directed stress in various geologic situations, and the gradient of hydrostatic stress from a connected column of water at 9.8 MPa/km. For hydraulic fracturing to occur the pore pressure (p) needs to exceed $S_{H(min)}$. If the estimated 2.3 MPa dynamic-pore-pressure increase actually occurs, than the typical minimum horizontal stresses in sedimentary basins is exceeded in rocks shallower than one km. In a variety of instances abnormally high formation pore pressures are encountered in sedimentary rocks, and hydraulic fracturing can occur in those instances at even greater depth (Gretener, 1979; Exploration Logging, Inc., 1981). If $S_{H(min)}$ is exceeded by the pore pressure, fractures approximately perpendicular to $S_{H(min)}$ should be parted, and then extended by the process of hydraulic fracturing. Figure 15 shows that fracturing is more favorable at shallow depths, and could be accomplished with far less than 2.3 MPa increase in pore pressure.

On the passing of the compression pulse, the rocks presumably dilate at the onset of a dilatational wavefront. The fractures would now close, but if any slippage had occurred on the fracture, it is likely that the fractures would

remain propped open by irregularities on the fracture surface. This effect would increase the permeability of such rocks. Such a self-propping mechanism for hydraulic fracturing has been demonstrated in the Fenton Hill Hot Dry Rock project, at the Los Alamos National Laboratory in New Mexico (Murphy and others, 1977).

The distance that a fracture might extend in the short duration of a compressional pulse is not analyzed here. Also not considered here is the effect of the transient seismic stress wave on the value of $S_{H(min)}$ in the rock. It could be that the stress waves increase and decrease the horizontal stresses on the rock, but that the surges in pore pressure are out of phase with the stress wave. Certainly the orientation of the dynamic stress system on the solid rock is important in the processes discussed above.

CONCLUSION

The Idaho earthquake produced an impressive amount of water. Because river flow increases occurred abrubtly after the earthquake, during the autumn period of base flow, one can be certain that the increased water was groundwater discharge. Within the 6 months following the earthquake, the 1160 km^2 drainage area of the North Fork of the Big Lost River produced about 0.1 cubic kilometer of water. Major rivers over an area of 18,000 km^2 increased in flow, and the total amount of water may exceed one cubic kilometer. Two mechanisms are proposed to explain the increase in groundwater discharge. The effects of coseismic strain release should increase spring flows in regions of contractional strain. There is agreement that the hanging wall of a normal fault should undergo contractional strain, and indeed documented increases in spring flow are generally in the hanging wall, but there are a number of exceptions, particularly in the region NW of the zone surface faulting. The flow decline curves of springs in the epicentral area have a shape consistant with decay of an instantaneous fluid pressure increase that could have been produced by coseismic strain release. Tectonic fracturing can explain the behavior of springs near the surface faulting. It is also suggested that hydraulic fracturing may occur in some situations where dynamic pore pressures are produced by the passage of seismic waves. In regions of extensional tectonics, only a small increase in pore pressure is needed to overcome the minumum principal stress and cause fracture surfaces to part and extend. Therefore natural hydraulic fracturing may also be a process in increasing permeability of spring conduits, and increasing the flows from some springs.

ACKNOWLEDGMENTS

We thank Richard Whitehead and Robert Harper of the U.S. Geological Survey, and Roland Rovetto of the Clayton Silver Mine for providing us with their data. Helpful comments from colleagues at the Sun Valley conference are much appreciated. The author wishes to thank Art McGarr, Mike Sorey, Walt Snyder, Jack Pelton, and Charles Waag, all of whom offerred very helpful ideas, comments, and criticisms at various stages of the manuscript. Discussion with John Bredehoeft prompted the sketching of Figure 11. Be it right or wrong, it did provide the author with an idea of what is going on down there. This study is supported by National Science Foundation Grant CEE-840-3585 to S.H. Wood and C.J. Waag.

REFERENCES

Boucher, G., Malone, S.D., and Homuth, E.F., 1971, Strain effects of nuclear explosions in Nevada: Bulletin of the Seismological Society of America, v. 61, p. 55-64.

Briggs, R.C., and Troxell, H.C., 1952, Effects of the Arvin-Tehachipi earthquake on spring and stream flows, in Oakeshott, G.B., editor, Earthquakes in Kern County, California, during 1952: California Division of Mines and Geology Bulletin 171, p. 81-97.

Crosthwaite, E. G., Thomas, C.A., and Dyer, K.L., 1970, Water resources in the Big Lost River Basin, south-central Idaho: U. S. Geological Survey open-file report, 108 p.

Exploration Logging, Inc., 1981, Theory and evaluation of formation pressures: the pressure log reference manual: Exploration Logging Inc., Sacramento, California, 224 pages.

Gretener, P.E., 1979, Pore pressure fundamentals, general ramifications, and implications for structural geology (revised edition): American Association of Petroleum Geologists Education Course Note, Series #4. 131 p.

Gutenberg, B., 1955, The first motion in longitudinal and transverse waves of the main shock and the direction of slip: in Earthquakes of Kern County, California during 1952, California Division of Mines and Geology Bulletin 171, p. 165-170.

Hubbert, M.K., and Willis, D.G., 1957, Mechanics of hydraulic fracturing: AIME, Petroleum Transactions, v. 210 (Journal of Petroleum Technology, v. 9), p. 153-168.

McGarr, A., and Gay, N.C., 1978, State of stress in the earth's crust: Annual Reviews of Earth and Planetary Science, v.6, p. 405,-435.

McGarr, A., 1982, Analysis of states of stress between provinces of constant stress: Journal of Geophysical Research, v.87, p. 9279-9288.

Murphy, H.D., Lawton, R.G., Tester, J. W., Potter, R.M., Brown, D.W., and Aamodt, R.L., 1977, Preliminary assessment of a geothermal energy reservoir formed by hydraulic fracturing: Society of Petroleum Engineers Journal (August, 1977) p. 330-326.

Ralston, D.R., 1985, Hydrologic responses to the 1983 Borah Peak earthquake in the vicinity of the Clayton Silver Mine, Idaho: (this volume).

Richter, C.F., 1958, Elementary Seismology: W.H. Freeman and Co., San Francisco, California, 768 p.

Shaleen, M. and Totorica, D., 1984, Preliminary studies at Little Antelope Flats, earthquake effects on warm springs: unpublished manuscript sent upon request, Department of Geology and Geophysics, Boise State University, 6 p.

Stein, R.S. and Barrientos, S.E., 1985, The 1983 Borah Peak, Idaho earthquake: Geodetic evidence for deep rupture on a planar fault.

Swensen, F.A., 1964, Groundwater phenomena associated with the Hebgen Lake earthquake, : in The Hebgen Lake, Montana earthquake of August 17, 1959: U.S. Geological Survey Professional Paper 435, p. 159-165.

Waag, C.J., 1985, Groundwater eruptions and sediment boil formation in the Chilly Buttes area: (this volume).

Whitehead, R. L., 1985, Hydrologic changes following the Idaho Borah Peak earthquake: (this volume).

Wood, S.H., Wurts,C.N., Lane, T., Ballenger,N., Shalleen, M., Totorica, D.,1985, Hydrologic effects of the October 28, 1983 Idaho earthquake: in Earthquake Engineering Research Institute Recconnaissance Report on the Borah Peak Earthquake (in press) 16 p.

Wood, S.H., 1985, Contemporary vertical tectonics along the Wasatch Fault Zone measured by repeated geodetic leveling: in U.S. Geological Survey open-file report -- Proceedings from workshop on evaluation of regional and urban earthquake hazards and risk in Utah (in press) 22 p.

Young, H.W. and Lewis, R.E., 1982, Thermal springs in the Salmon River Basin, central Idaho: U. S. Geological Survey open-file report 82-104. 27 p.

Zoback, M.L., 1985, Constraints on the in-situ stress field along the Wasatch Front in U.S. Geological Survey open-file report -- Proceedings from workshop on evaluation of regional and urban earthquake hazards and risk in Utah (in press). 18 p.

FIGURE CAPTIONS

Fig. 1. Location map of hydrologic records discussed in this report. Black dots are reported increased spring flows. Drainage area of the Howell Ranch gage on the Big Lost River and the drainage area above the gaging station on the Pahsimeroi River are outlined with a stippled pattern. Trace of surface faulting and location of the epicenter of the Oct. 28, 1983 earthquake are preliminary.

Figure 2. Hydrographs of spring flows in the epicentral area. Peak flows are estimates from eyewitness accounts, high water marks, and photographs. Other flows are from current meter measurements by the USGS Water Resources Division, Boise office, and Boise State University. Flows at the State Hatchery are measured by the Idaho Department of Fish and Game.

Figure 3. Photograph of flooding in Thousand Springs Valley taken from Elkhorn Creek Canyon at 6:30 p.m. on October 29. View is to the northwest. Widest flooded area is about 0.8 km wide at Whiskey Springs. Distant tributary from the left (south) side of photo is the flow from Chilly Buttes area. Outlet of Thousand Springs Creek is to the left (south). Photograph by S. H. Wood.

Fig. 4. Hydrograph of Ingram's Warm Springs compiled from measurements by Boise State University , the U. S. Geological Survey, and observations by W. Ingram, D. Totorica, and M. Shaleen.

Figure 5. Photograph looking south up the channel of Ingram's Warm Springs Creek. Spring system had completely dried up following the earthquake. Dead fish were an introduced species for a hatchery operation. Photgraph by Sue Villard and published with permission from the Challis Messenger.

Figure 6. Photograph looking south up the channel of Warm Springs Creek on November 15, 1983 when the spring had recommenced flowing at a rate of 16.5 cfs. Photograph by Richard Whitehead, U. S. Geological Survey, Boise office.

Figure 7. Hydrographs of major rivers that showed significant increases in flow following the earthquake. Drainage area of rivers is shown on map of the State of Idaho. Data from Whitehead (1985).

Figure 8. Plot showing the rapid rise of water level in the Clayton Silver Mine following the October 28 earthquake, and the decline of water levels as the no. 2 shaft was pumped at 2000 gallons per minute. Water had been maintained at the 1145-ft level prior to the earthquake by continuous pumping of 980 gallons per minute. Water began to rise 3 hours after the earthquake at a rate of 6 ft/hr. The workings at the 1100-ft level were flooded by 1040 P.M on the 28th. By November 7 the water had risen 245 feet to the 963-ft level. At that point the rise ceased and the levels started to decline slightly by pumping 930 gallons per minute. By November 15 a 2000 gallon per minute pump was installed, and the water levels began to decline at a greater rate. By December 17 the water was down to the 1080-ft level. Irregularities in the drawdown curve are caused when the pumps are at reduced capacity or are off for repairs. During the early part of the decline curve, water would rise at a rate of 0.7 ft per hour when pumps were off. During the later part of the decline curve, water would rise at 2.7 ft per hour when the pumps were off. Mine level is referred to a datum elevation of about 5890 ft at the office at the creek level below no. 1 shaft. Information courtesy of Mr. Roland Rovetto, Clayton Silver Mine.

Figure 9. Map showing locations of springs and streams that increased in flow after the July 21, 1952 Kern County, California earthquake (M = 7.7) after Briggs and Troxell (1955). Black dots are location of increased flow. Heavy line indicates the line of surface rupture along the White Wolf Fault. First motion seismographic data indicate a reverse fault with 60° to 66° NW dip, and an oblique left-lateral slip, with a vertical component 1.4 times the horizontal component (Gutenberg, 1955). The pattern of increased flow shows that it is mostly in the hanging wall block, about 15 km south of the surface breakage, and not as predicted in Figure 10 of this report.

Figure 10. Cartoon showing the sense of coseismic strain that is thought to accompany earthquake faulting in the three different kinds of earthquake surface faulting, and the expected sense of change of groundwater flow.

Figure 11. Diagramatic sketch showing the strained region of the elastic crust prior to an earthquake on a normal fault. Also shown is the typical form of vertical surface deformation that accompanies strain release in an earthquake.

Figure 12. Stress element in the subsurface showing the preferred plane of fracture (after Hubbert and Willis, 1957)

Figure 13. Estimate of the variation of peak dynamic strain from seismic waves with distance from the epicenter based on strain measurements of events with $m_b < 6.5$ at epicentral distances of 200 km. Data has been extrapolated to $m_b = 7.5$ and scaled to shorter distances nearer the epicenter using 1/r dependence of strain.

Figure 14. Increase of pore pressure (p) and the horizontal minimum principal stress with depth (after Gretener, 1981; McGarr and Gay, 1978, and Zoback, 1985) showing a possible lower limit to hydraulic fracturing by seismic-stress-wave-induced dynamic pore pressure.

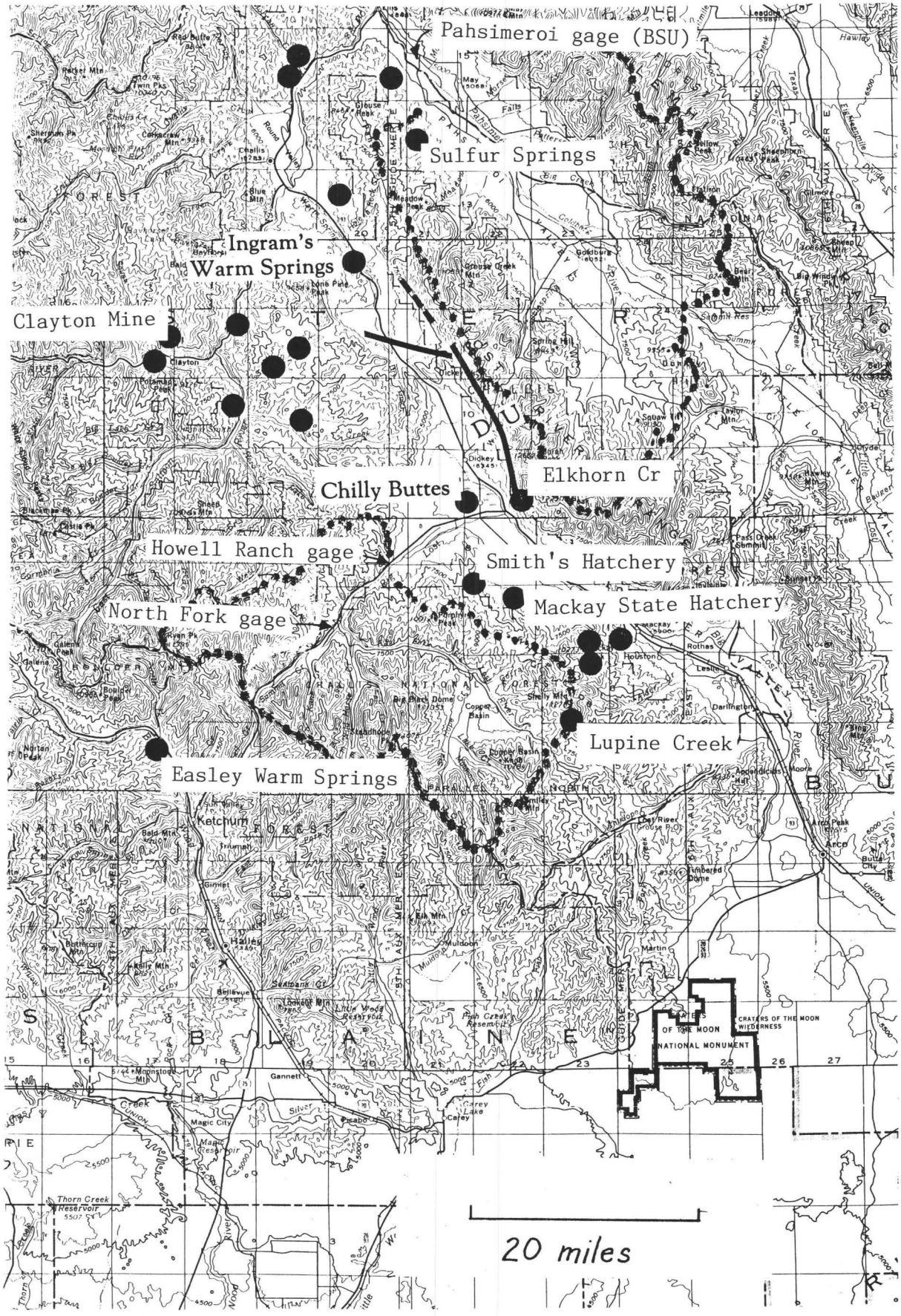
Pahsimeroi gage (BSU)
Sulfur Springs
Ingram's Warm Springs
Clayton Mine
Chilly Buttes
Elkhorn Cr
Howell Ranch gage
Smith's Hatchery
North Fork gage
Mackay State Hatchery
Lupine Creek
Easley Warm Springs
20 miles

Fig. 1

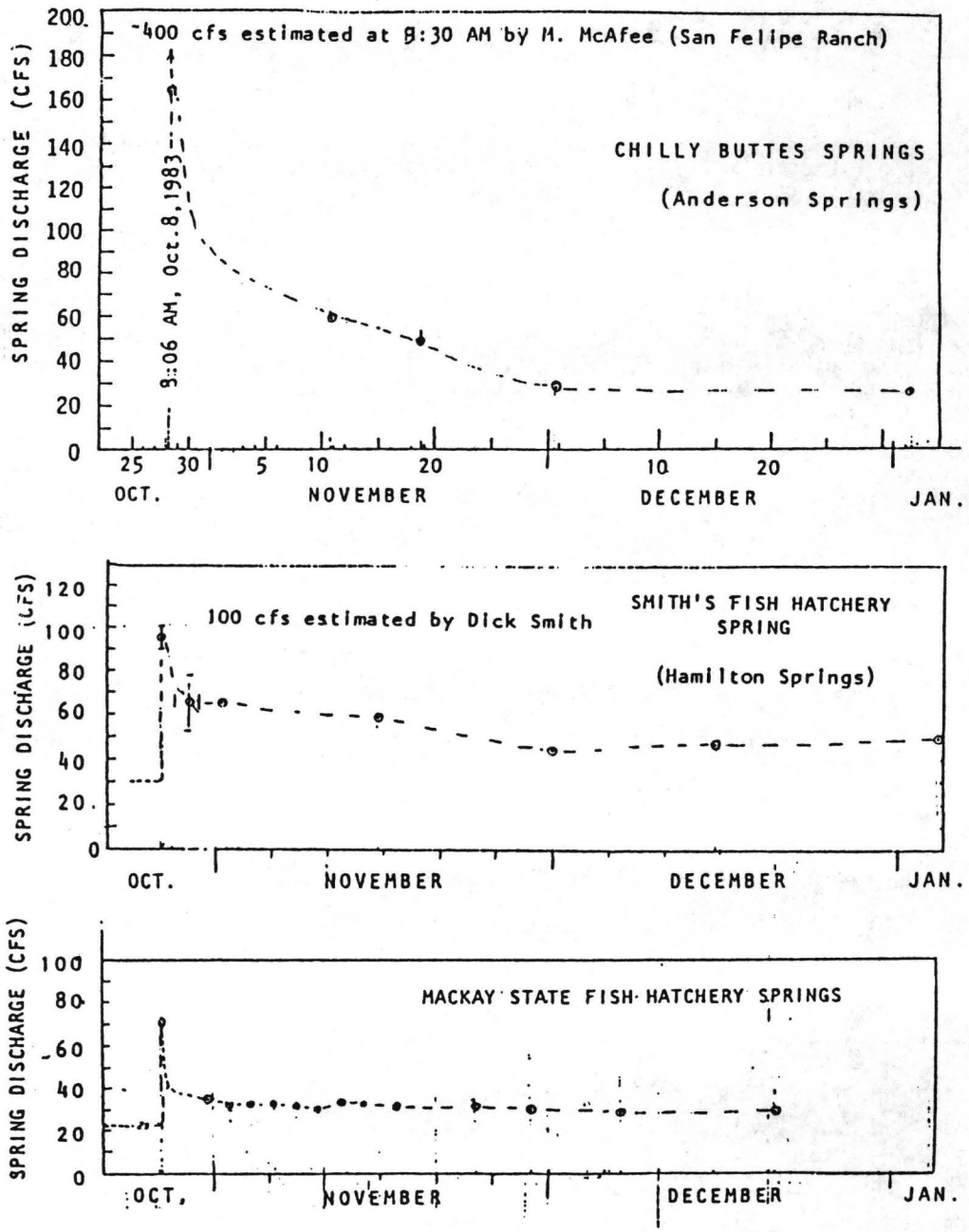
400 cfs estimated at 8:30 AM by M. McAfee (San Felipe Ranch)
9:06 AM, Oct.8,1983
CHILLY BUTTES SPRINGS
(Anderson Springs)
SPRING DISCHARGE (CFS)
200
180
160
140
120
100
80
60
40
20
0
25
30
5
10
20
10
20
OCT.
NOVEMBER
DECEMBER
JAN.
100 cfs estimated by Dick Smith
SMITH'S FISH HATCHERY SPRING
(Hamilton Springs)
SPRING DISCHARGE (CFS)
120
100
80
60
40
20
0
OCT.
NOVEMBER
DECEMBER
JAN.
MACKAY STATE FISH HATCHERY SPRINGS
SPRING DISCHARGE (CFS)
100
80
60
40
20
0
OCT.
NOVEMBER
DECEMBER
JAN.

Fig. 2

Fig. 3

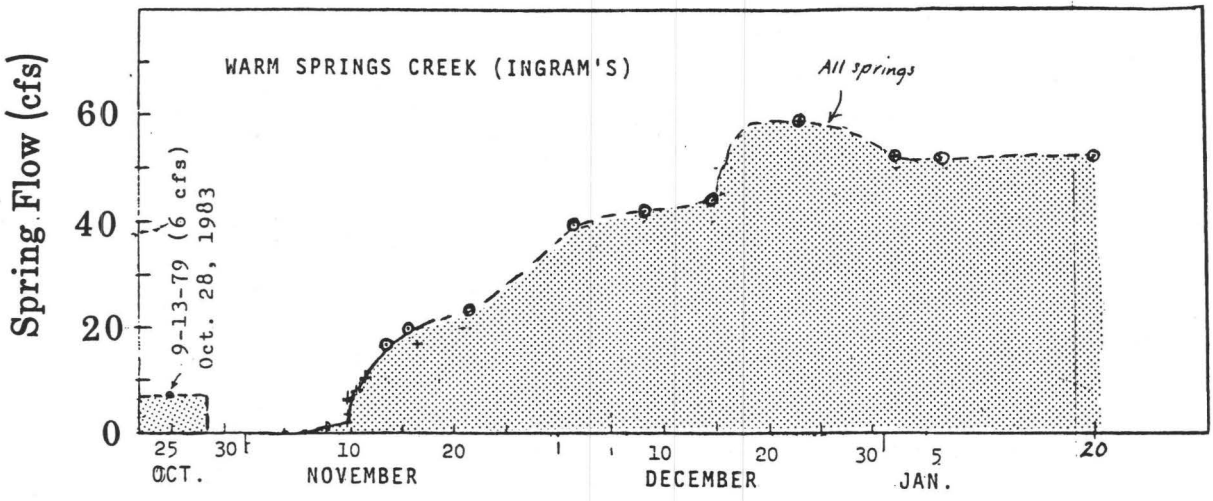
WARM SPRINGS CREEK (INGRAM'S)
All springs
Spring Flow (cfs)
60
40
20
0
9-13-79 (6 cfs)
Oct. 28, 1983
25
30
10
20
1
10
20
30
5
20
OCT.
NOVEMBER
DECEMBER
JAN.

Fig. 4

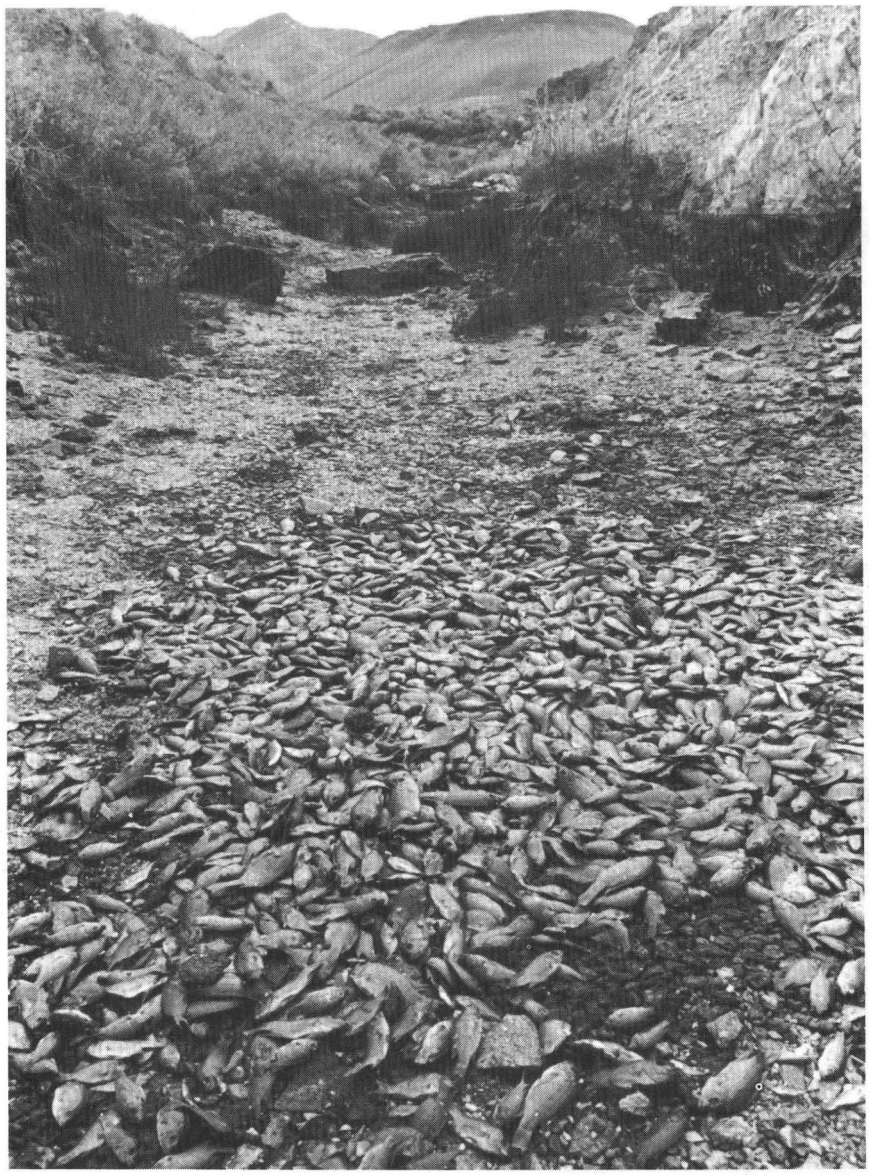

Fig. 5

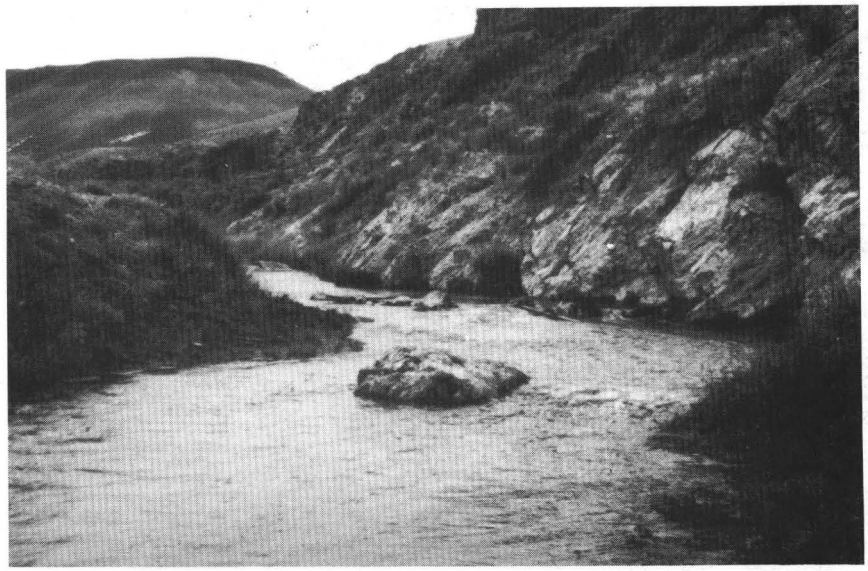

Fig. 6

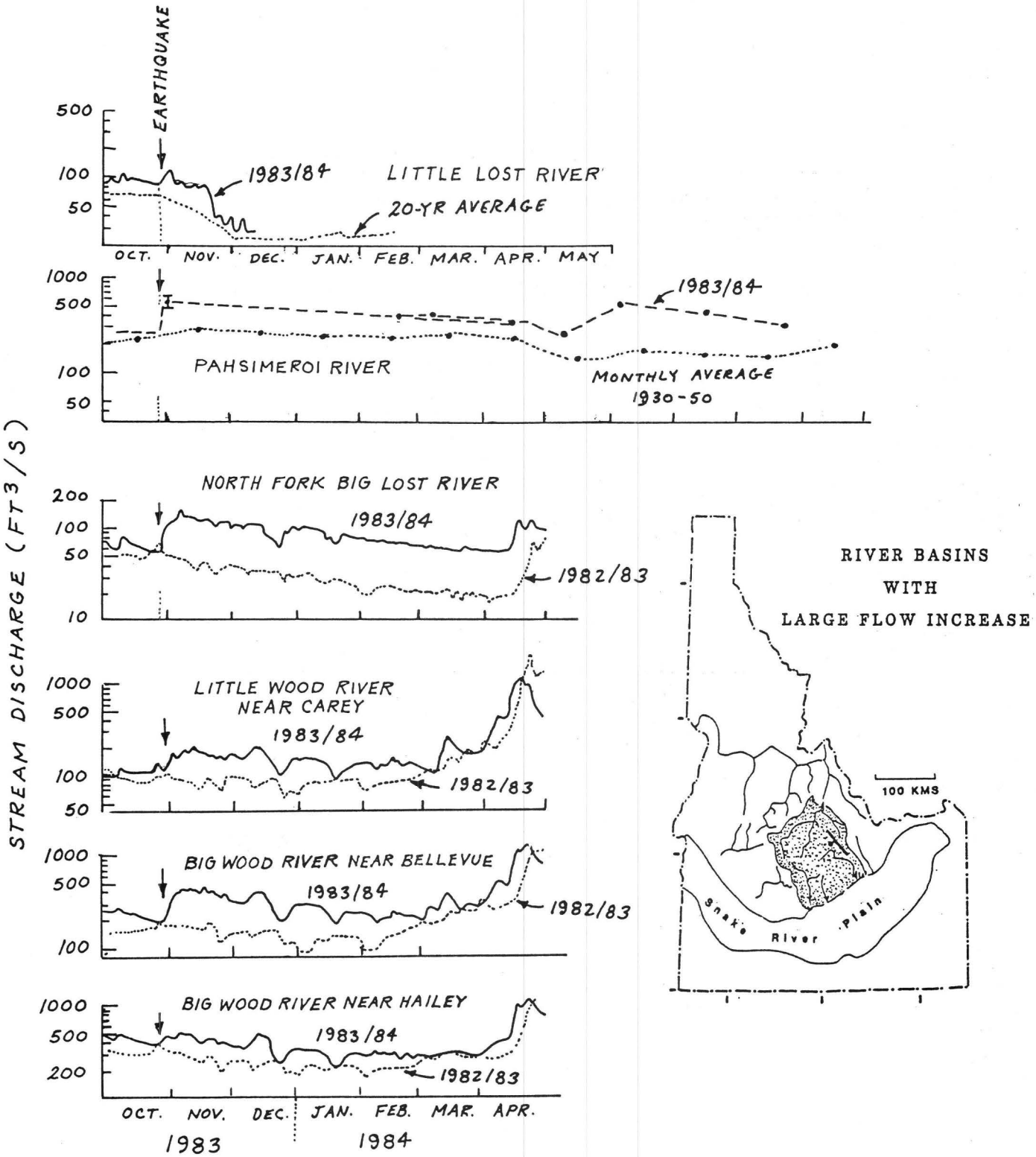
EARTHQUAKE
500
100
50
1983/84
LITTLE LOST RIVER
20-YR AVERAGE
OCT.
NOV.
DEC.
JAN.
FEB.
MAR.
APR.
MAY
1000
500
100
50
1983/84
PAHSIMEROI RIVER
MONTHLY AVERAGE
1930-50
STREAM DISCHARGE (FT3/S)
NORTH FORK BIG LOST RIVER
200
100
50
10
1983/84
1982/83
1000
500
100
50
LITTLE WOOD RIVER
NEAR CAREY
1983/84
1982/83
1000
500
100
BIG WOOD RIVER NEAR BELLEVUE
1983/84
1982/83
1000
500
200
BIG WOOD RIVER NEAR HAILEY
1983/84
1982/83
OCT.
NOV.
DEC.
JAN.
FEB.
MAR.
APR.
1983
1984
RIVER BASINS
WITH
LARGE FLOW INCREASE
100 KMS
Snake River Plain

Fig. 7

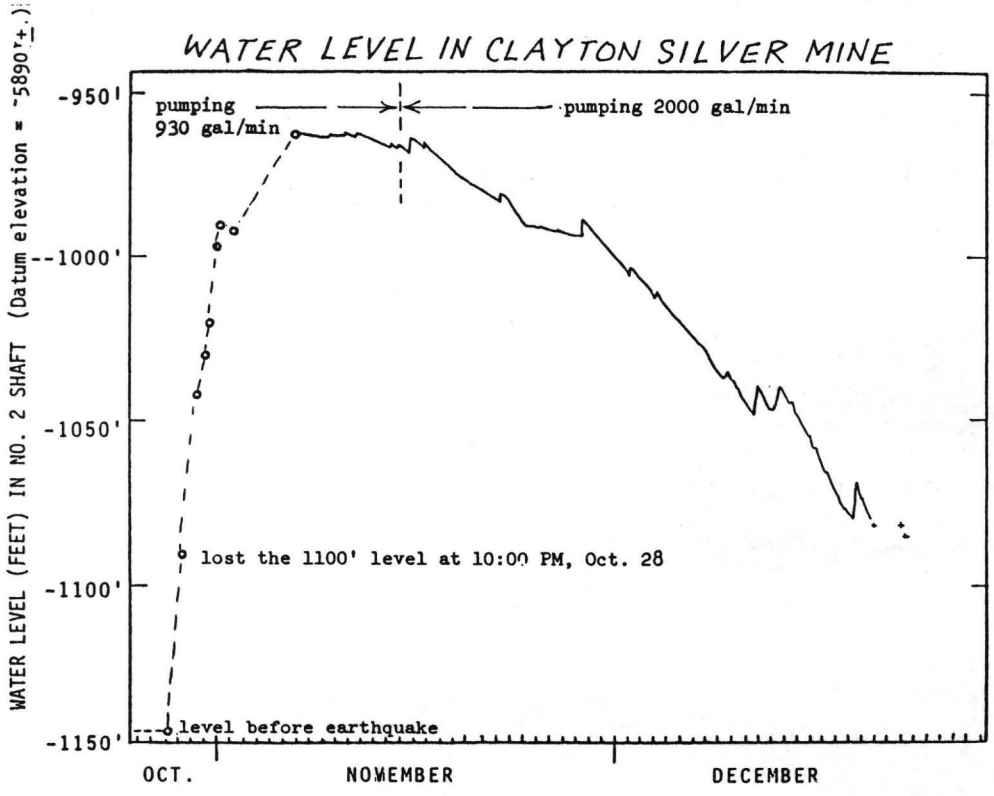
WATER LEVEL IN CLAYTON SILVER MINE
WATER LEVEL (FEET) IN NO. 2 SHAFT (Datum elevation = "5890'±.)
-950'
--1000'
-1050'
-1100'
-1150'
pumping
930 gal/min
pumping 2000 gal/min
lost the 1100' level at 10:00 PM, Oct. 28
level before earthquake
OCT.
NOVEMBER
DECEMBER

Fig. 8

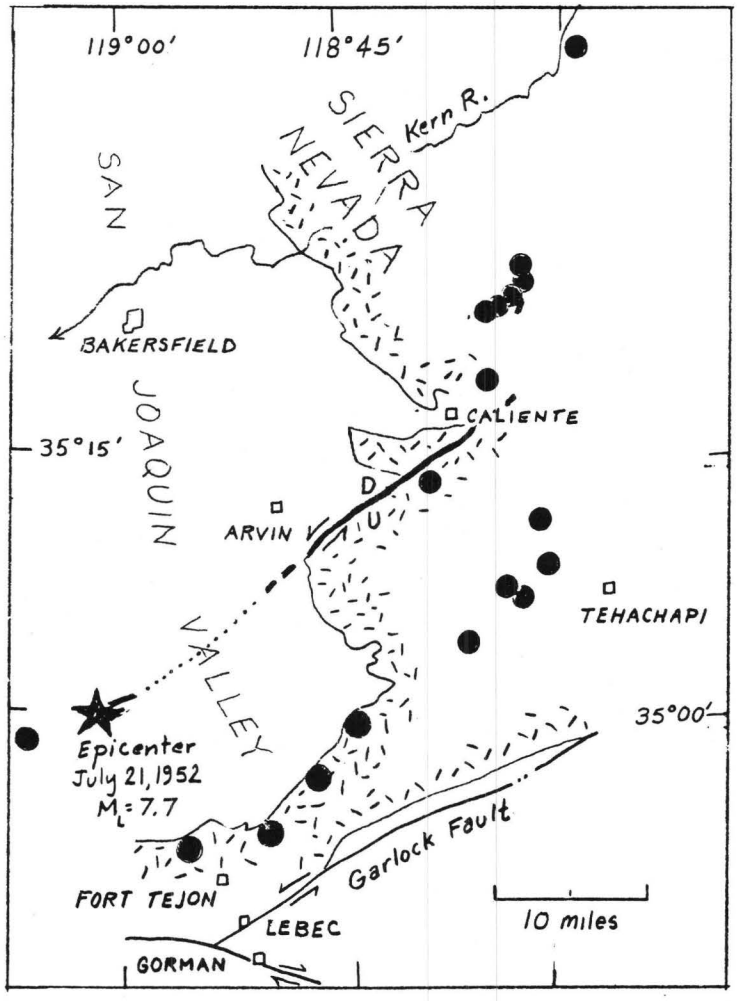

Fig. 9

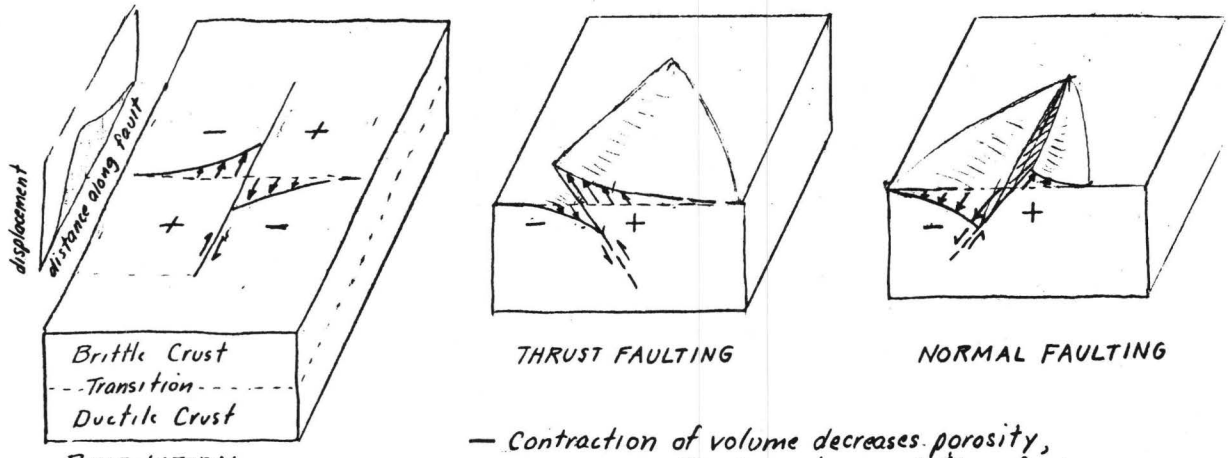

— Contraction of volume decreases porosity, increases fluid pressure and flows from springs

+ Expansion of volume increases porosity, decreases fluid pressure and flows from springs

Fig. 10

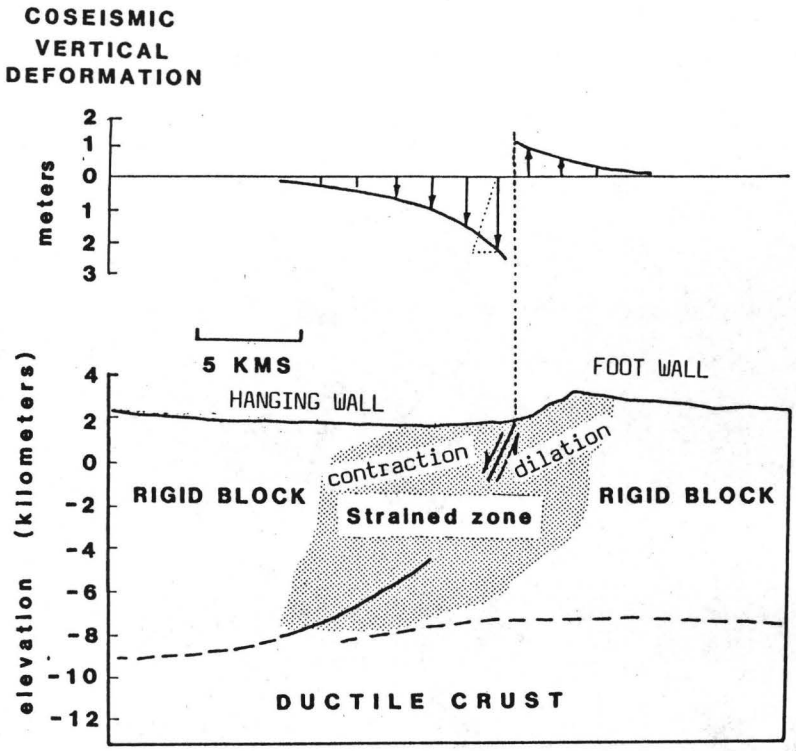

Fig. 11

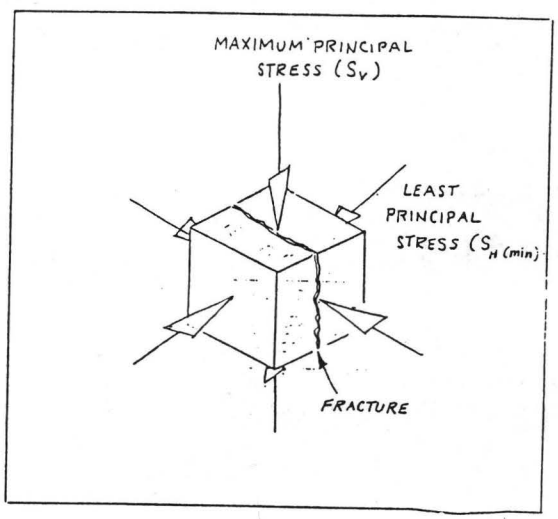

Fig. 12

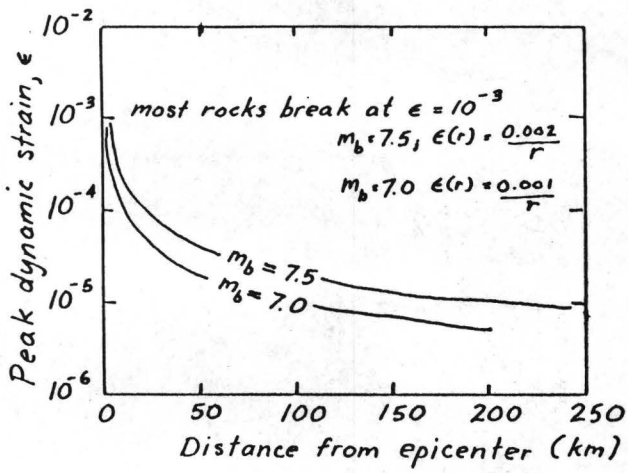

Fig. 13

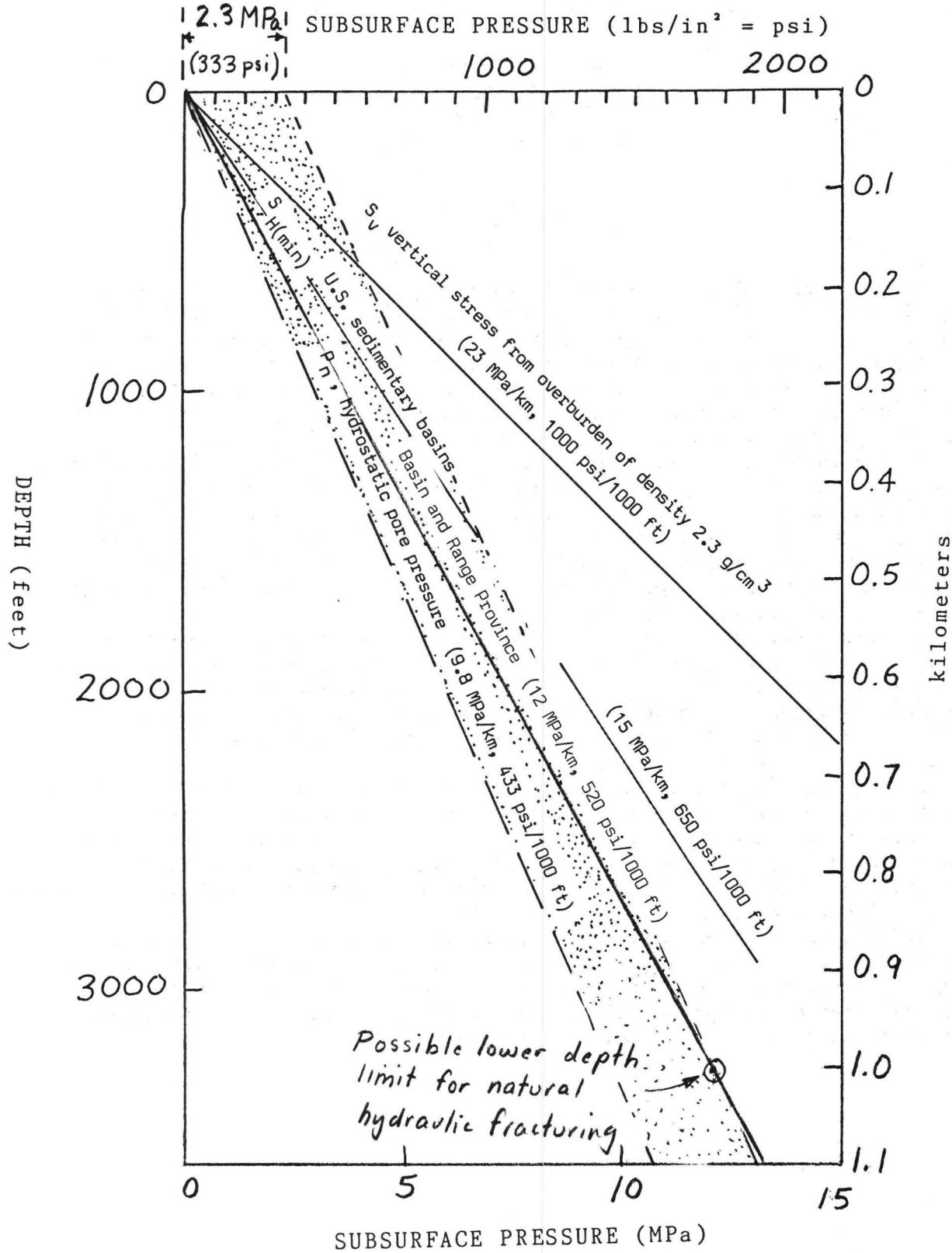
2.3 MPa
(333 psi)
SUBSURFACE PRESSURE (lbs/in² = psi)
0
1000
2000
0
0.1
0.2
0.3
0.4
0.5
0.6
0.7
0.8
0.9
1.0
1.1
kilometers
DEPTH (feet)
1000
2000
3000
Sv vertical stress from overburden of density 2.3 g/cm 3
(23 MPa/km, 1000 psi/1000 ft)
S H(min)
U.S. sedimentary basins
Basin and Range Province (12 MPa/km, 520 psi/1000 ft)
(15 MPa/km, 650 psi/1000 ft)
Pn, hydrostatic pore pressure (9.8 MPa/km, 433 psi/1000 ft)
Possible lower depth limit for natural hydraulic fracturing
0
5
10
15
SUBSURFACE PRESSURE (MPa)

Fig. 14

GROUNDWATER ERUPTIONS AND SEDIMENT BOIL FORMATION IN THE CHILLY BUTTES AREA, MT. BORAH, IDAHO EARTHQUAKE

Charles J. Waag
Department of Geology and Geophysics
Boise State University
Boise, Idaho 83725

Abstract

The Oct. 28, 1983, Mt. Borah, Idaho earthquake (M_s=7.3) produced more than 40 sediment boils, and "sinkholes" near Chilly Buttes in the Big Lost River Valley. The buttes, approximately 3.7km from the epicenter, are within the downthrown, valley, block and are probably exposures of a bedrock high of late Paleozoic carbonates which underlie the Tertiary and Quaternary alluvium. As a result of the seismic shaking, groundwater was erupted (1) as geysers directly from the fractures in the bedrock on north Chilly Butte, (2) into a veneer of alluvium overlying the limestone on the north slope of north Chilly Butte where the flow piped tunnels in the alluvium, and (3) up through the valley alluvium north and east of north Chilly Butte where sediment boils formed pits and large sediment aprons. All of the eruptions were strongly controlled by well developed solution widened fractures in the carbonate, some of which have been imprinted on the overlying alluvium. The dominant fracture set is oriented N15°-20°W.

A shallow seismic refraction survey in the valley east of the base of north Chilly Butte suggests that the depth to carbonate bedrock in the area of those sediment boils is somewhere between 30m and 60m and slopes gently eastward. Holocene movements on the N15°-20°W and other fracture directions within the carbonate have imprinted those structural directions on the relatively thin alluvial cover.

During the 1983 quake, the fractures and shear zones in the alluvium served as important conduits for the discharge of groundwater from the similarly oriented fractures in the underlying carbonate. Water and air expulsed from the underlying carbonate entered the alluvium under high pressure and entrained and fluidized the alluvium forming sediment eruptions along those strongly controlled patterns inherited from the carbonate aquifer.

Hydrologically, the carbonate aquifer is confined by the overlying alluvium. The surge of pressure which caused the groundwater eruptions is thought to have resulted from a pore water pressure increase caused by negative dilation (compression) of the carbonate in the valley or hanging wall block as it dropped downward along the fault.

GROUNDWATER ERUPTIONS AND SEDIMENT BOIL FORMATION IN THE CHILLY BUTTES AREA, MT. BORAH, IDAHO EARTHQUAKE

Charles J. Waag
Department of Geology and Geophysics
Boise State University
Boise, Idaho 83725

INTRODUCTION

The Oct. 28, 1983, Mt. Borah, Idaho earthquake (M_s=7.3) produced more than 40 sediment boils, and sinkholes near Chilly Buttes in the Big Lost River Valley, Figure 1. The buttes, approximately 3.7km from the epicenter, are within the downthrown, valley, block and are probably exposures of a bedrock high of late Paleozoic carbonates which underlie the Tertiary and Quaternary alluvium. The bedrock within the buttes reported to be White Knob Limestone is mainly limestone having thinly interbedded shale and sandstone (Skip, 1985; this volume).

As a result of the seismic shaking, groundwater was erupted (1) as geysers directly from the fractures in the bedrock on north Chilly Butte, (2) into a veneer of alluvium overlying the limestone on the north slope of north Chilly Butte where the flow piped tunnels in the alluvium, and (3) up through the valley alluvium north and east of north Chilly Butte where sediment boils formed pits and large sediment aprons. Locations of these various phenomena are shown on Figure 1 at A, B, C and D respectively.

STRUCTURES WITHIN THE BEDROCK

In the vicinity of the groundwater eruptions, the carbonate bedrock is folded into an open, slightly asymmetrical antiform trending approximately N15°W (Fig. 1). The fold is intensely fractured especially in the hinge where the dominant fracture set strikes N15°-20°W parallel to the fold trend. This fracture set is generally continuous, open, and has been widened considerably by solutioning (Fig. 2). Other fracture directions also exist in the bedrock (Fig. 3). One common set is centered about N45°E and another about N40°W; however, neither of these sets are continuous nor as open as the N15°-20°W set. They are more commonly tightly closed and/or filled with secondary calcite.

GROUNDWATER ERUPTIONS ON NORTH CHILLY BUTTE

The eruptions emitted directly from the bedrock occurred mainly along the base of the butte in the north (Fig. 4) and east (Fig. 5). Geysering, however, occurred at elevations on the butte as high as 30m above the valley. Eruptions at the higher elevations were largely confined to the fractured trace of the antiform, and were strongly controlled by the N15°-20°W fracture set. On the butte, elutriation of all but the largest clasts of coarsest slope colluvium from the fissures and washouts indicates that the geysering occurred in relatively large volumes, and at high velocities and pressures.

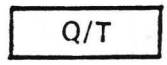

VALLEY ALLUVIUM

SEDIMENT BOILS AND COLLAPSE PITS IN VALLEY ALLUVIUM

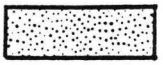

SAND, SILT, GRANULES, GRAVEL AND COBBLES DEPOSITED BY SEDIMENT BOILS

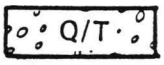

COLLUVIUM AND ALLUVIUM OF BUTTE

SHEAR AND/OR FRACTURE ZONE

COLLAPSE FEATURES ALONG SHEAR ZONE IN COLLUVIUM AND ALLUVIUM ON BUTTE

NEW SPRINGS AND WASHES FORMED BY TRANSIENT WATER ERUPTIONS

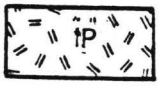

BEDROCK, LIMESTONE, MINOR INTER BEDDED SHALE AND SANDSTONE

STRIKE AND DIP OF BEDDING

TRACE OF AXIAL SURFACE OF FOLD

STRIKE & DIP OF JOINT

STRIKE & DIP OF CLEAVAGE

ROAD

STREAM OR CANAL

LAKE

CONTOUR

EXPLANATION OF FIGURE 1

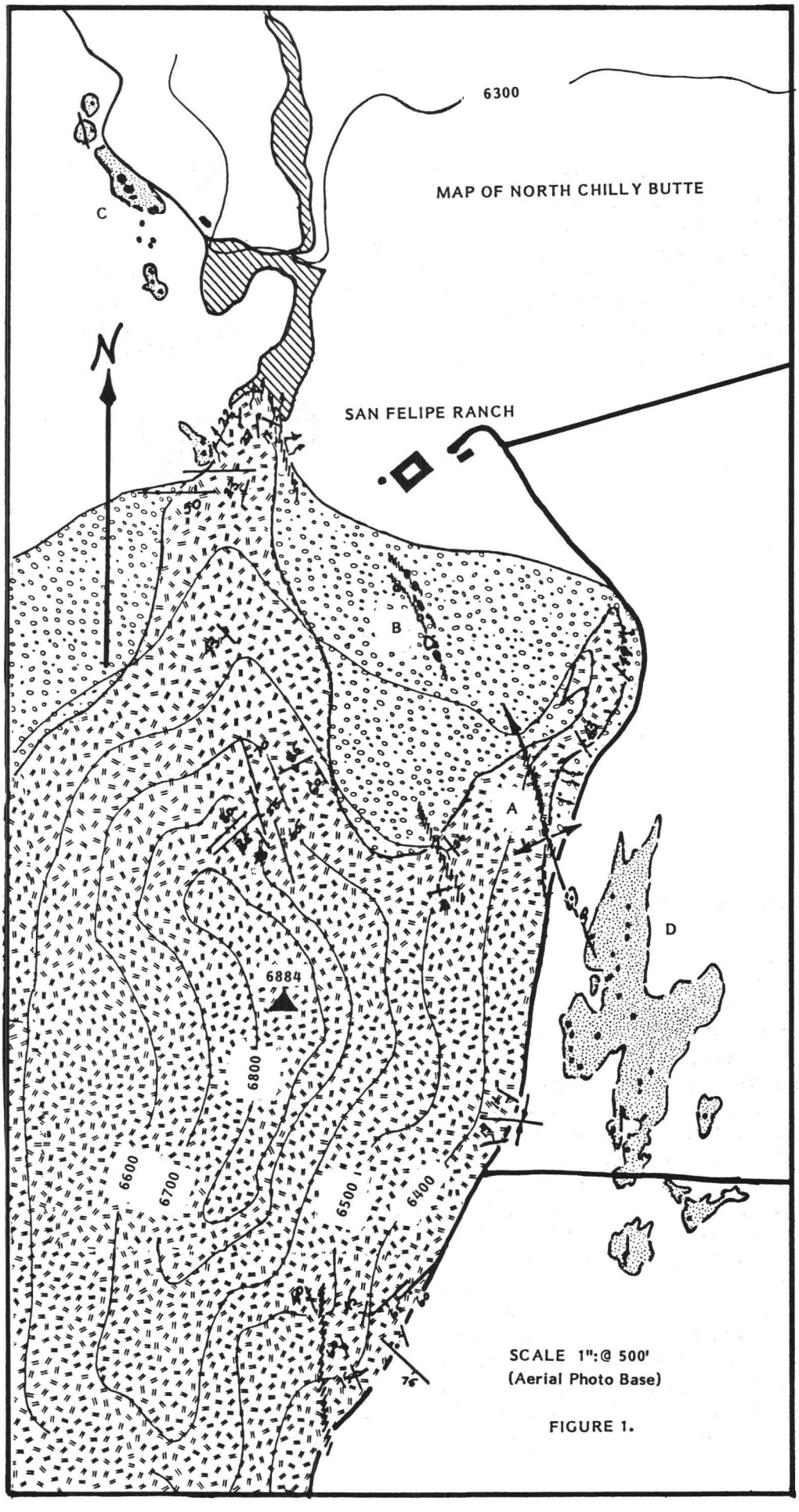
6300
MAP OF NORTH CHILLY BUTTE
C
N
SAN FELIPE RANCH
B
A
D
6884
6800
6600
6700
6500
6400
SCALE 1":@ 500'
(Aerial Photo Base)

FIGURE 1.

Figure 2. East flank of north Chilly Butte. Eruption cavern in colluvium immediately over bedrock fracture zone in hinge of antiform. Looking along N15°W fracture. Clipboard for scale. (Location A on Fig. 1) Photo by C.J. Waag.

GROUNDWATER ERUPTIONS THROUGH ALLUVIUM ON NORTH CHILLY BUTTE

On the north slope of the butte where a veneer of alluvium overlies the carbonate (B, Fig. 1), the water piped a number of tunnels in the alluvium. The tunnels trend N15°W, parallel the fracture set in the carbonate, and are locally collapsed forming interconnected callapse holes or tunnel skylights. In the wall of one collapse hole, the alluvium has an obvious N15°W; 80°W sheared fabric that can be traced along the tunnel (Fig. 6). A subtle linear depression is developed above the sheared zone. In the depression, the sagebrush are larger and more abundant. In the sheared alluvium exposed in the roof of the tunnel a relatively dense mat of sagebrush roots are exposed in preferred alignment.

Compaction of the alluvium into the underlying carbonate solution channels and, perhaps, jigging, creep, and piping during earlier quakes probably caused the planar fabric and topographic lows to form. Whatever their origin, the weak zones and their planar fabric clearly predate the Oct. 28th quake. Several of the tunnels can be traced to topographically lower areas where piped alluvium and water burst to the surface causing washouts. Flow from the tunnel shown in Figure 7 caused a large washout (Fig. 8) which exposed a fault in the carbonate and colluvium (Figs. 9, 10). Regrading of the area has filled in the washout and covered the fault exposure. Evidently this surge of water was directed through the carbon-

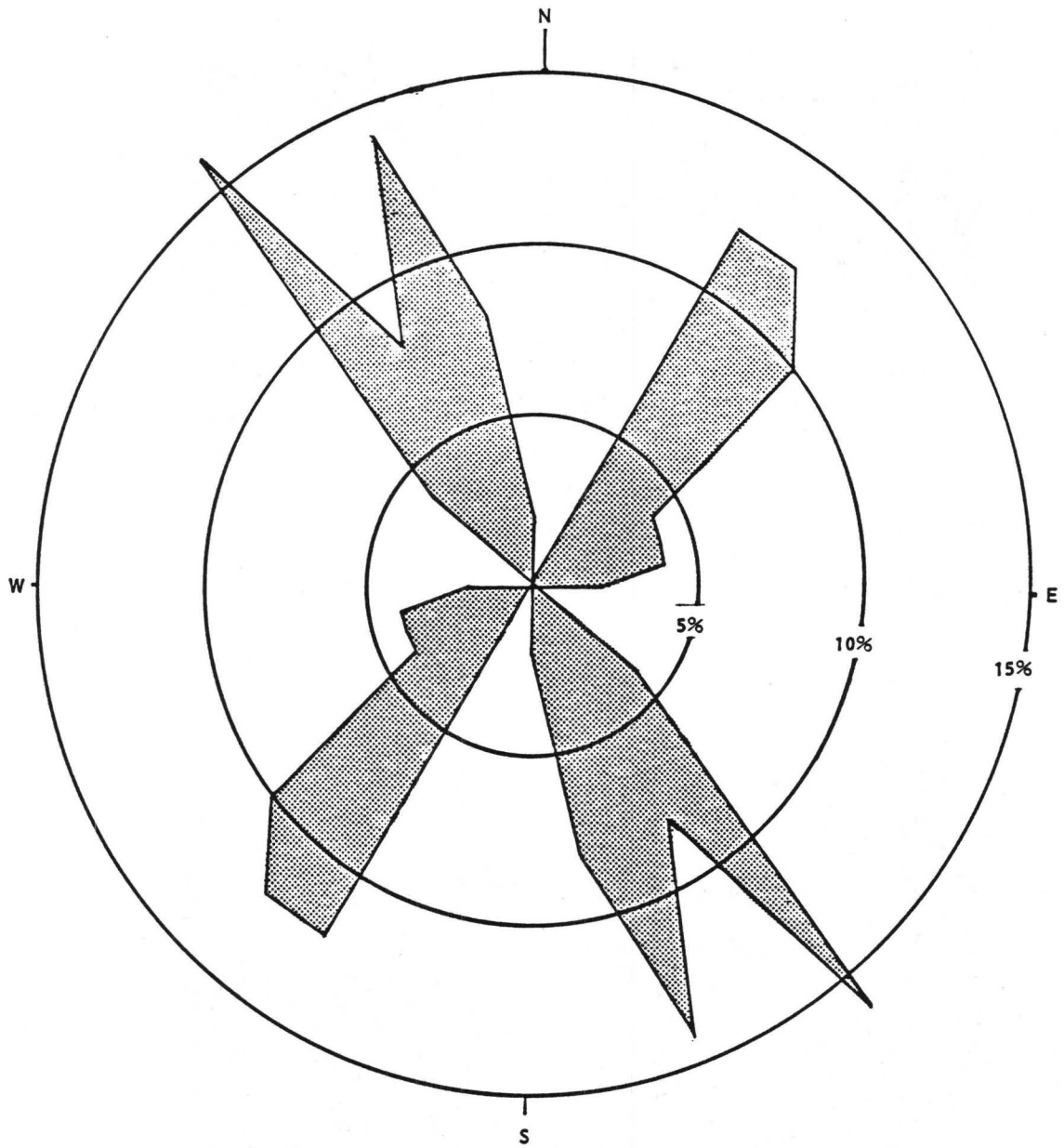

ROSE DIAGRAM OF FRACTURES IN BEDROCK
VICINITY OF GROUNDWATER ERUPTIONS
NORTH CHILLY BUTTE
100 ORIENTATIONS

FIGURE 3

Figure 4. Eruptions of large volume springs flowing muddy water and causing washouts on the north end of North Chilly Butte. Looking east across Thousand Springs Valley. Photo by A. Rafkind.

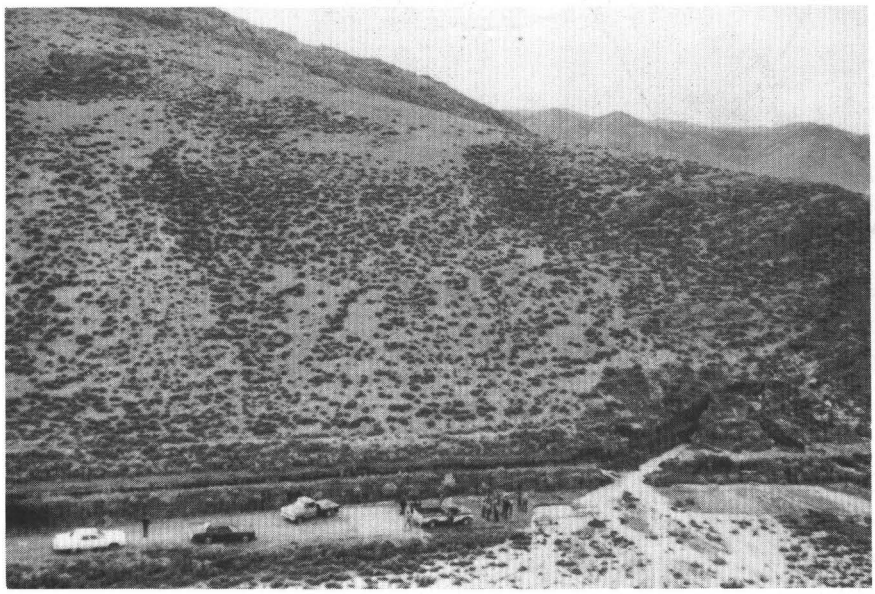

Figure 5. East flank of north Chilly Butte. Muddy water eruptions and washouts along N15° W trending fracture zone in hinge of antiform in large Paleozoic carbonates. Washout can be traced for 175m up slope to a height about 30m above valley floor. (Location A on Fig. 1) Photo by J. Pelton.

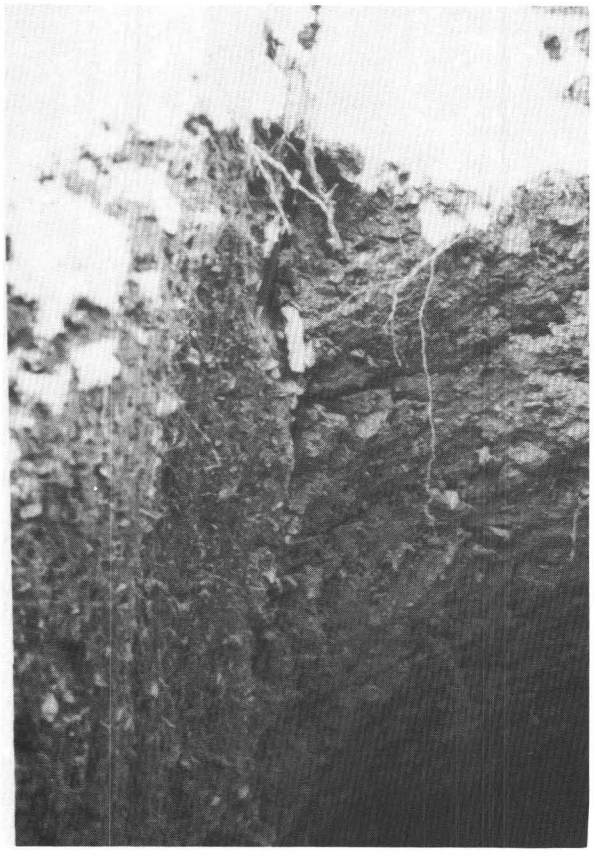

Figure 6. (Left) Collapse hole or skylight exposing shear zone (left), and tunnel (right) piped in alluvium high on north slope of north Chilly Butte. Note: Roots in shear zone. Pencil for scale. Photo by C.J. Waag.

Figure 7. (Below) Piped tunnel exit in colluvium (left) and alluvium (back of tunnel). Tunnel extends about 75m to southeast (left) following colluvium-alluvium contact. Height of tunnel exit about 1.5m. Photo by C.J. Waag.

Figure 8. (Above) Low on north slope of north Chilly Butte. Washout caused by eruption of piped alluvium and water from tunnel shown in Figures 6 and 7. Looking north. Photo by C.J. Waag.

Figure 9. (Left) Exposed fracture zone. Carbonate bedrock (left) against colluvium (right) in north end of washout. Note openness of fracture zone and parallel shearing in bedrock. (Scale: base of wash to top of photo about 3.5m.) Photo by C.J. Waag.

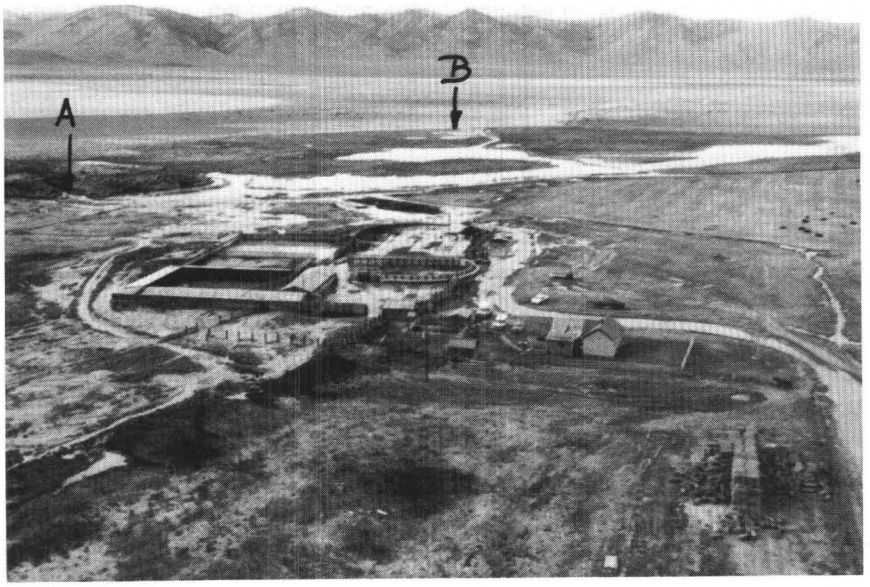

Figure 10. San Felipe Ranch. Washouts and flooding caused by eruption of volume muddy water springs along fault zone (A) and sand boils (B). Looking northwest. Photo by A. Rafkind.

ate solution channels along the fault and up into the sheared alluvium where it piped a 25m long tunnel. Apparently the groundwater surge encountered higher permeabilities within the shear zones, and the pressure was partially dissipated through piping laterally rather than erupting directly to the surface.

GROUNDWATER ERUPTIONS IN THE VALLEY

In the valley, about 300m north of north Chilly Butte, 5 large and many small sand boils erupted onto the surface of the valley floor (Fig. 11) and beneath the water surface of a shallow lake (Fig. 1 and background Fig. 10). The larger of these boils formed at the sites of lakes shown on the Chilly Buttes Quadrangle. The fracture porosity and permeability systems that feed those lakes undoubtedly acted as the conduits for the 1983 groundwater eruptions which formed sediment aprons around the lakes.

The large boils are aligned approximately N40°-45°W parallel to one of the fracture sets shown in Figure 3. This rather strong alignment seems to indicate that the N40°-45°W fracture direction is well developed in carbonate rocks underlying the valley alluvium as well as those exposed in the butte.

The smaller boils are also aligned; however, their orientation is along the N15°-20°W direction. The two alignments seem to intersect near the center of the row of large boils. The largest sinks are about 16m-18m in diameter and slightly eliptical having their long axes in the alignment direction.

A coalescing apron of sand about 30m wide links the larger sinks. At the inner edge of the sinks the sand has an average thickness of .5m thinning to about 15cm at its distal edge. Sieve analyses of three samples of the sediment erupted from these boils are about 90 percent sand ranging

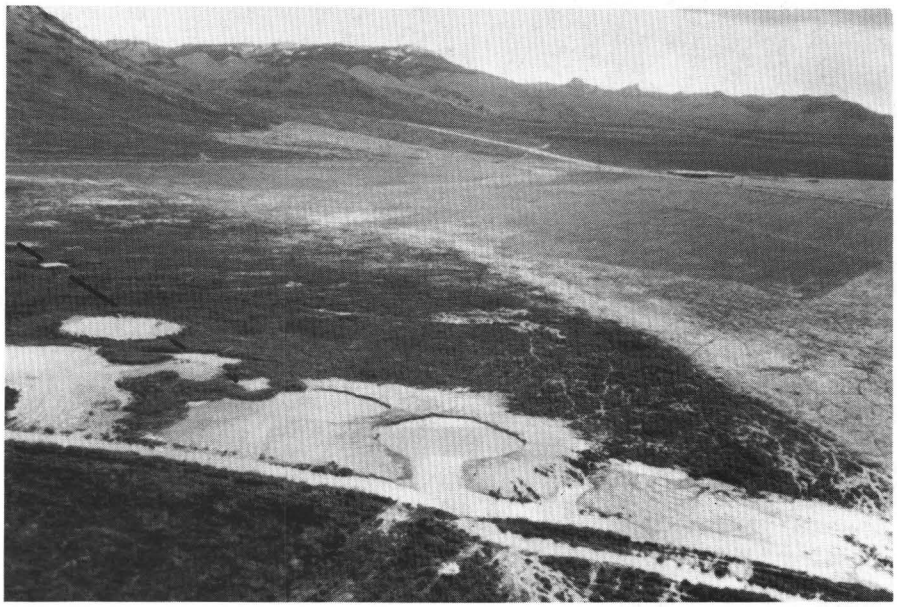

Figure 11. Large sand boils which erupted through beds of lakes. Lakes lie at intersection of 2 alignments, one N40°W parallel to canal, the other, N15°W parallel to line on photo. Photo by A. Rafkind.

from 1mm to .0625 mm, and have a mean diameter of .38mm. Silt, very coarse sand, granules, and a few pebbles comprise the remaining 10 percent. The sediment is also very well sorted having sorting coefficients ranging from 1.46 to 1.43 and averaging 1.44.

Concentric fractures in the sediment aprons near the lake shores were evident after the flux of groundwater from the lakes decreased. The fractures showed down-to-the-lake movement indicating post eruption subsidence. The origin of the lakes, however, is still open to interpretation. They may fill pits that have been left by past eruptions and attendant post eruption subsidence or collapse. Alternatively, the lakes may fill karst sinkholes which have been the sites of eruptions of sediment and water during this and previous quakes in the area. However, the profusion of circular and elliptical features in the vicinity of the lakes leaves little doubt that the area has been similarly active in the past.

In the valley adjacent to the east side of north Chilly Butte approximately 25 large sediment boils and several sediment fissures erupted (Fig. 12). Here again the fissure eruptions and sediment boils show a strong structural control and are aligned along the N15°W direction (Fig. 13). Several of the boils are also elliptical having their long axis aligned parallel to and continuous with fissure eruptions (Fig. 14). Apparently five of the boils erupted through "sinkholes" that were present prior to the quake. According to unsubstantiated information from local residents, 3 of the "sinkholes" developed about the same time as the 1956 Hebgen Lake Montana earthquake. The other two "sinkholes" reportedly formed 10-11 years ago. If sediment

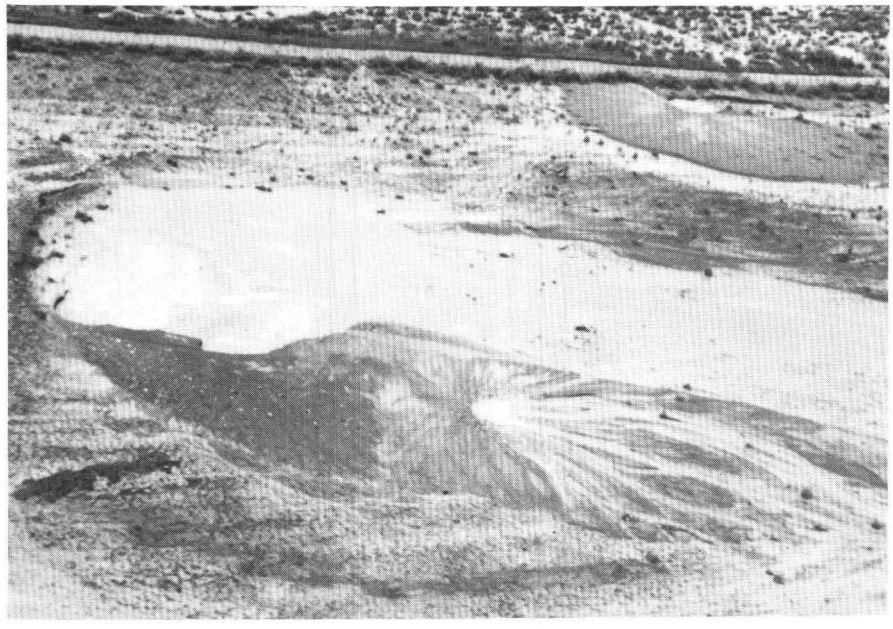

Figure 12. Sediment boils along the E. flank of north Chilly Butte. Photo taken about 4 hours after quake during a period when boils were flowing muddy water. Photo A. Rafkind.

Figure 13. October 30, 1983, 2 days after earthquake. Boise State University Field Geology students viewing sediment boil pit in southern most portion of sediment boil field (see Fig. 1). In pit wall approximately 60cm of erupted sediment (light colored) overlies old soil profile (dark colored). Foreground: crevasse formed by fissure eruptions along the N15°W fracture set.

Figure 14. Collapsed sediment boil in field east of Chilly Butte. Note fissure eruption in foreground which extends through boil and is exposed in opposite wall. Looking NW along N15°W trending fissure. Photo by N. Ballenger.

was erupted in response to the Hebgen Lake earthquake the deposits were not evident at the time of the 1983 earthquake investigations. However, it is evident that at least one "sinkhole" existed in the field prior to the Oct. 28 eruptions, and was being used as a refuse dump. During the Oct. 28 eruptions the earth gave back the refuse depositing it in a series of concentric rings about the crater.

CONCLUSIONS

In contrast to the sediment boil deposits north of the buttes, those east of the buttes contain a wide spectrum of grain sizes ranging from clay to small cobbles (10.2cm) and the stratigraphy seems to reflect more variable depositional conditions. In all of these 1983 boil deposits, multiple sedimentary units can be recognized. Gradational, and distinct or abrupt contacts between the units are common. The bases of many of the sedimentary units are marked by scour and fill structures and other diastems. Although the individual depositional units are quite variable, a general similarity of depositional sequences within most of the deposits seems to be present. Commonly, the basal sedimentary units are well sorted, fine-grained, and non-laminated to poorly laminated. The middle and upper units are poorly sorted, coarser-grained and contain cross-bedding and graded beds. The uppermost or final depositional units are very well sorted, finest-grained, and contain

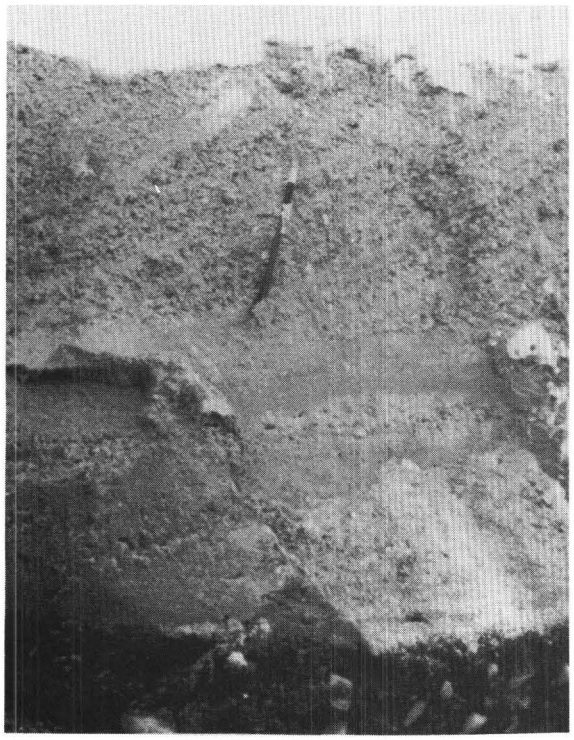

Figure 15. Exposed wall of a collapsed sediment boil in field east of Chilly Buttes. Note fine-grained, poorly-laminated sand at the base, coarse granule layer in middle, and interbedded granule and sand cross-bedded sediment at top. Photo by C.J. Waag.

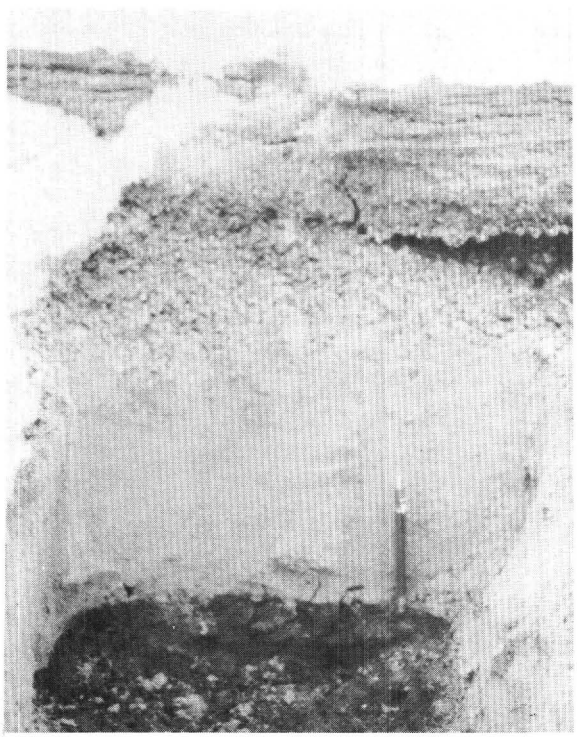

Figure 16. Exposed wall of a collapsed sediment boil in field southeast of Chilly Buttes. Note fine-grained, poorly-laminated sand at base grading upward into poorly-stratified gravels and granules. Uppermost exposed unit is laminated medium- to coarse-grained sand. Photo by C.J. Waag.

ripple-marks and mudcracks. The sedimentary characteristics of the boils seem to indicate that deposition was by surging flow, and that the surge increased in intensity until the final phases at which time the intensity of the flow waned rather abruptly.

The well-sorted, fine-grained, basal unit is especially interesting when considered in conjunction with an eyewitness account of the sediment-boil activity. Mr. Del Clark, manager of the San Felipe Ranch, arrived at the sediment boil field east of the buttes just a few minutes after the quake occurred. He observed that muddy water was spouting from new springs around the base of the buttes and had already flooded the road; however, in the field the boils were blowing sand and no water was present. According to Mr. Clark, the water did not erupt through the boils until after they blew sand and air. Then the mixture of water and sediment erupted. He estimated that the various geysers reached heights ranging from 4 to 6m. According to Mr. Clark's estimates, the duration of sediment-water geysering was about 3-4 minutes. After that, the boils flowed muddy water.

Figure 17 shows plots of sieve analyses of sediment taken from the wall of the boil deposit in Figure 16. Curves A, B, and C are taken from the basal 6cm of the deposit. Curve A is from the lowermost 2cm, curve B from 2-4cm and curve C from 4-6cm of the deposit. Greater than 95% of the sediment in the lowest 6cm of the deposit ranges from fine sand (.25mm) to coarse silt (.03mm) and has an average median diameter of .1mm, or very fine sand. The sediment is very well sorted having an average sorting coefficient of 1.5.

Judging from the lack of lamination in the basal deposit, from these grain-size and sorting data, and from Mr. Clark's observations, it seems probable that at least the basal 6cm are air deposited. It seems likely that negative dilation or compression of the carbonate and alluvial aquifer systems would cause expulsion of air both as a direct consequence of the dilation, and indirectly as a result of the groundwater pressure wave migrating through the aquifer. Thus, perhaps, the intial surge of air caused expansion or inflation of the alluvium. Once inflated, the surge of air through the porous media may have fluidized the sediment elutriating the fine-fraction and depositing the basal unit in a manner similar to that described by Reynolds in her description of fluidization as a geologic process (Reynolds, D.L., 1954). It follows then that the diastem, present in places, at the top of the basal non- or poorly stratified, fine-grained basal unit not only represents a break in the sedimentation, but also a change in the medium of deposition. The overlying units being considerably coarser grained, reflect the increased surge of groundwater expulsed from the aquifer systems, principally the carbonate, by the near field seismic waves. The water surge apparently caused the alluvium to be entrained and piped, enlarging the orifice and depositing the middle and upper units.

Curve D is a plot of sieve analysis data of a sample taken from the middle depositional unit in Figure 15. Ninety-seven percent of the sediment ranges from coarse sand (1mm) to very fine sand (.072mm) having a median diameter of .61mm, coarse sand. Interestingly, although the range of grain sizes is rather large, the sediment is extremely well sorted having a sorting coefficient of 1.24.

Curve E is a plot of the sieve analyses of sediment of a sample of the cross-bedded unit in Figure 15. The sediment spans a wide range of grain sizes from pebbles (8mm) to fine sand (.15mm). The median diameter is .41mm (granules) and the sorting coefficient is 2.16. The sediment clast size

increase and poorer sorting indicated by curves D and E clearly reflect an increase in the flow surge. The waning phase deposits of fine-sand, silt and clay sized sediment are buried beneath the snow in the top of Figure 15.

In the walls of several of the collapsed boils clastic dikes are exposed. Grain sizes within the dikes are variable ranging from sand to gravels. The dikes cut both the old valley fill and newly erupted material, are vertical to nearly vertical, and are commonly deposited in the N15°-20°W fracture set. Large well established sagebrush roots present in the fracturs with the clastic dikes again indicate that the fractures were present prior to the quake (Fig. 18).

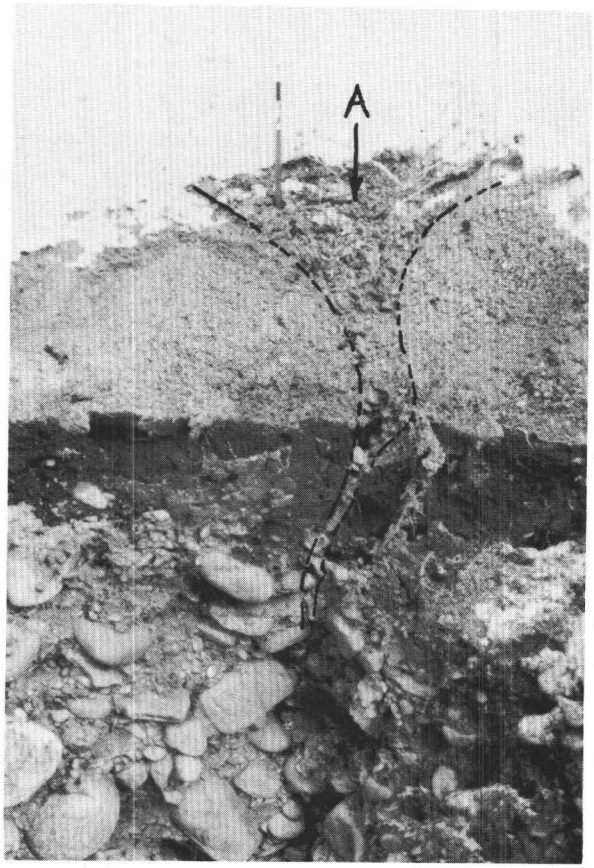

Figure 18. Exposed wall of collapsed sediment boil and intersecting fissure eruption in field east of Chilly Buttes. Funnel shaped clastic dike of erupted sand, granules and gravel filling fissure (A). Dike and fissure cuts coarse valley alluvium (bottom) and finer sediment of earlier sediment boil deposit (top). Photo by C.J. Waag.

A shallow seismic refraction survey in the valley east of the base of north Chilly Butte suggests that the depth to carbonate bedrock in the area of those sediment boils is probably somewhere between 30m and 60m and slopes gently eastward (Pelton, J.R., and others; this volume). This indication that the valley fill is relatively shallow, and the strong similarity of orientations of fractures within the carbonate and the alluvium suggests that the fractures in the alluvium have propagated upward from the carbonate. Holocene movements on the N15°-20°W and other fracture directions within

Figure 17

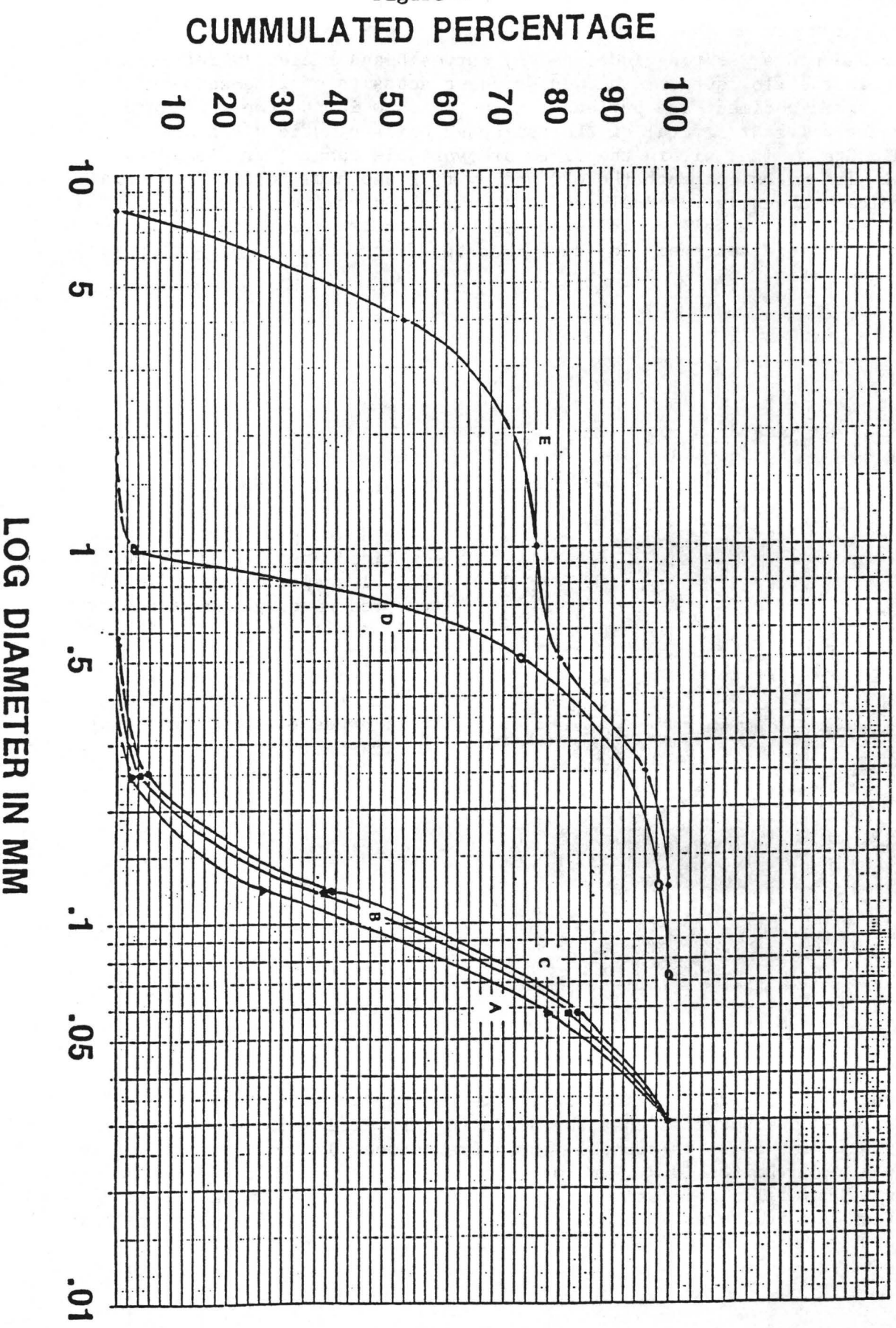
CUMMULATED PERCENTAGE
10
20
30
40
50
60
70
80
90
100
LOG DIAMETER IN MM
10
5
1
.5
.1
.05
.01
A
B
C
D
E

the carbonate have imprinted those structural directions on the alluvium. The imprinting is manifested as sheared fabric in the alluvium (Fig. 6) as-well-as the fractures in the valley alluvium which controlled the sediment eruptions during the 1983 event (Figs. 13, 14). Some of those fractures now host clastic dikes (Fig. 18). Higher permeabilities within the imprinted zones in the alluvium allowed a greater flux of subsurface water and encouraged greater plant and root growth. During the 1983 quake, the fractures and shear zones in the alluvium served as important conduits for the discharge of groundwater from the similarly oriented fractures in the underlying carbonate. Water and air expulsed from the underlying carbonate entered the alluvium under high pressure and entrained and fluidized the alluvium forming sediment eruptions along those strongly controlled patterns inherited from the carbonate aquifer.

Hydrologically, the carbonate aquifer is confined by the overlying alluvium. The surge of pressure which caused the groundwater eruptions is thought to have resulted from a pore water pressure increase caused by negative dilation of the carbonate in the valley or hanging wall block as it dropped downward. During faulting the down-dropped block is thought to have undergone compression (see Stein and Barrientos; this volume) effecting an abrupt increase in pore water pressure and causing a surge of groundwater through the highly permeable limestone aquifer.

On north Chilly Butte where the highly permeable solution widened fracture zones extended to near the surface, the pressure surge resulted in water spouting directly from the limestone outcrops. However, on the butte where a relatively thin veneer of alluvium covered the highly permeable fracture zones, the pressure surge dampened by the alluvium and by the elevation was largely laterally directed along the weakened shear zones in the alluvium. In the valley where the alluvium is thicker but the elevation lower, the most obvious manifestation of the surge was the sediment eruptions at the surface. It is quite likely however that considerable lateral piping has occurred in the valley as well.

Several observations support this interpretation. One, most of the pits enlarged by collapse as flow decreased and as the groundwater level in the area subsided in the post-quake period. Two, many of the pits enlarged along a fracture or fissure eruption intersecting the pit (Fig. 14). Three, at least 1 pit and possibly 2 formed by collapse in late November well after the eruptions. This latter observation lends support to the local information cited earlier that 2 collapse holes formed in the field east of the butte about eleven years before the '83 quake. Apparently, however, their formation was not directly associated with sediment boils or a recorded seismic event. More likely, they resulted from collapse of the alluvium over piped tunnels formed by some earlier Holocene event.

ACKNOWLEDGEMENTS

I wish to thank Boise State University students T.G. Lane and D.A. Prouty, and my colleagues S.H. Wood and J.R. Pelton for their involvement in gathering and interpreting data from the Chilly Buttes area. I also wish to acknowledge the National Science Foundation for partial funding received under grant CEE-840-3585.

REFERENCES

1985, Pelton, J.R., Meissner, C.W., Waag, C.J., Wood, S.H., Shallow seismic refraction studies across the Willow Creek fault rupture zone and the Chilly Buttes sand boils: this volume.

1954, Reynolds, D.L., Fluidization as a geological process and its bearings on the problem of intrusive granites: American Journal of Science, v. 252, pp 517-614.

1985, Stein, R.S. and Barrientos, S.E., The 1983 Borah Peak, Idaho Earthquake: geodetic evidence for deep rupture on a planar fault: this volume.

1984, Waag, C.J., and Lane, T.G., Groundwater eruptions and sediment boil formation in the Chilly Buttes area, a response to the Oct. 28, 1983 Mt. Borah, Idaho earthquake: in Earthquake Engineering Research Institute Reconnaissance Report on Borah Peak earthquake, EERI, Berkeley, CA 11 p (in press).

HYDROTHERMAL CHANGES IN THE UPPER GEYSER BASIN, YELLOWSTONE NATIONAL PARK, AFTER THE 1983 BORAH PEAK, IDAHO, EARTHQUAKE

RODERICK A. HUTCHINSON
NATIONAL PARK SERVICE

Abstract

Hydrothermal features in Yellowstone have long been known to be sensitive to circulatory changes of hot fluids and gases following local seismic swarms or strong regional events. Just as the August 17, 1959, Hebgen Lake, Montana, earthquake (M_S 7.5), the June 30, 1975, Central Plateau - Norris earthquake (M_S 6.1), and the 1978-79 tremors near Mud Volcano all caused major changes in Yellowstone's thermal basins, the October 28, 1983, Borah Peak, Idaho, seismicity is believed to have initiated profound behavioral changes in the Upper Geyser Basin 240 kilometers east of the reported epicenter. A total of 37 features including Old Faithful Geyser are now known to have experienced changes in eruptive activity, temperature, and/or discharge. Evaluation of other possible causes for the thermal changes was made including self-sealing, hydrothermal alteration, weather, earth tidal forces, widespread thermal basin disturbances, and local seismicity. Changes of Old Faithful Geyser's interval and duration patterns were analyzed and found to be similar to those following other strong regional earthquakes. However, many unanswered questions remain on the local hydrologic controls of the response of Yellowstone's thermal springs and geysers to major seismicity.

Immediate Effects

On October 28, 1983, the main shock of the Borah Peak earthquake was felt over much of the western half of Yellowstone National Park. No damage to buildings, roads, or utilities, or ground cracks were reported anywhere in the park. Maximum intensities determined from Sieberg's Mercalli-Cancani modified scale in the Yellowstone area were V at West Yellowstone and Madison Junction, decreasing to IV at Mammoth Hot Springs and Gardiner, Montana (North Entrance), III at Old Faithful and South Entrance, and II at Lake-Fishing Bridge. Only two individuals in the park area reported feeling the 13:52 MDT aftershock; both were indoors near the West Entrance.

With the felt reports, radio broadcasts of the magnitude, and location of the main shock known, a prompt survey of Norris, Upper, Midway, and Lower Geyser Basins was initiated on the same afternoon. The rapid survey suggested that only Daisy Geyser, 1.5 kilometers northwest of Old Faithful, may have been temporarily affected by the seismic waves. This was evident at least until the following day. Prior to the earthquake, Daisy's average interval for the year had been very regular at around 85 minutes. During the afternoon of October 28, 1983, however, its recorded intervals averaged 78 minutes. Such an immediate decrease in time between eruptions of Daisy after seismic activity was witnessed in 1959 and 1975. The effect of the Hebgen Lake earthquake, for example, on this and most of the other near-regular or well-known geysers such as Castle, Riverside, Oblong, Great Fountain, etc., was to shorten their intervals (U.S. Geol. Survey, 1964; Marler, 1973).

A great majority of changes in hot springs have come simultaneously or immediately following the initial ground shaking. The 1959 and 1975 tremors,

and other local seismic swarm activity, have seemed to act as a trigger to start or rejuvenate eruptions. Published accounts by Fischer (1960), Marler (1974), Marler and White (1975), and Pitt and Hutchinson (1982) have described the changes in geyser and hot spring behavior from these and similar events. Hundreds of springs were induced into activity by the 1959 Hebgen Lake earthquake; nearly half erupted for the first time in their known histories. Thus we were somewhat surprised to see no other obvious increased activity, local turbidity, or fluctuations in water levels anywhere else besides Daisy in Yellowstone's thermal basins on October 28, 1983. Old Faithful Geyser remained seemingly stable on the day of the Borah Peak quake and for the last three days of the month while limited observations of 30 intervals were recorded by a seasonal interpretative Park Technician. (The visitor center closed for the season on October 31, 1983, and was not staffed again until December 16.) Old Faithful's daily averages during those last four days of October remained within 2.3 percent of its monthly average.

Although intensive observations were not conducted, no apparent significant changes were detected in other major geysers or the smaller features on Geyser Hill. Furthermore, Giantess seemed to be continuing its record high frequency of eruptions with its forty-first display of the year on November 10, 1983, as indicated by the U.S. Geological Survey helicorder in the visitor center. By November 1, 1983, preliminary evaluation suggested that no significant changes in ground water flow or eruptive activity had occurred. At that time it was recognized that: 1. the epicenter was approximately 240 kilometers from Old Faithful, which was almost 5 times further than that of the 1959 Hebgen Lake earthquake; 2. the preliminary magnitude of the Borah Peak main shock was reported to be 6.9, which was less than the strength of the 1959 tremor; and 3. except for Daisy, obvious changes in thermal activity had not been observed anywhere in the park. No additional investigation was possible until January 1984.

Subsequent Events

In January, one of the winter seasonal interpretative staff reported that a few changes had been noted on Geyser Hill and that Old Faithful was having longer intervals. A number of snowmobile trips were made to the Upper Geyser Basin shortly thereafter to investigate those changes. All other major thermal basins accessible in the winter, including Midway, Lower, Norris, Mud Volcano, West Thumb, and Shoshone Geyser Basins, were also checked, but were found to exhibit no apparent changes in appearance or behavior. The changes were apparently restricted to Geyser Hill in the Upper Geyser Basin and are presented in Table 1. Geyser Hill is the most concentrated collection of erupting springs in the world. If Old Faithful is accepted as an extension, fully a third of Yellowstone's most powerful, frequently-active geysers capable of erupting more than 15 meters high are included. A total of 37 features exhibited abnormal changes in eruptive activity, temperature, and/or discharge since the Borah Peak quake. These include variations much greater than the fluctuations observed over the preceding 12 months, and those variations which produced obvious physical alterations of the vents, sinter basins, or runoff channels. In 15 cases the physical changes of vent enlargement, rupturing of the siliceous sinter sheet, or extensive wash may be long-term or permanent.

Table 1. Summary of thermal changes observed after the 1983 Borah Peak quake. The map coordinates are derived from unpublished U.S. Geological Survey thermal basin maps (Marler, 1973).

Thermal Feature	Map Coordinates	Zone	Comments
Anemone Geyser	J12 240E, 755S	3	Eruptions more powerful; water ejected on boardwalk.
Aurum Geyser	J12 115E, 100S	1	Durations increased from 10 seconds to near 2 minutes; maximum height up, with water reaching boardwalk laterally 7.6 m.
Beehive Geyser	J11 985E, 815S	4	New regularity established after prior erratic eruption pattern; now predictable with 15 hour average interval; duration of Indicator slightly longer.
Bench Geyser	J12 120E, 640S	3	60 cm diameter and 50 cm deep funnel formed in Giantess Geyser's. loose sinter alluvium. Prior to quake, vent had been totally buried.
Bronze Spring	J12 390E, 805S	3	Discharge reduced to a mere seep by January 1984; ebbed 5 cm more by July. Significant color change due to temperature drop to 59°C.
Cascade Geyser	J12 240E, 880S	4	One major eruption at unknown date late fall or early winter; width of wash - 14.38 m.
Depression Geyser	J11 815E, 675S	3	Average interval decreased from more than 6 hours to 2-3 hours.
Dome Geyser	J12 555E, 475S	2	Exchange of function now seen with Vault Geyser instead of Giantess.
Dragon Spring	J12 050E, 570S	3	Discharge decreased, shown by about half of algae mat in runoff channels drying up and dying.
Unnamed geyser SE of Dragon Spring	J12 125E, 585S	3	Rejuvenated into frequent, 1-2 m, performing geyser. Location - 23.2 m from Dragon Spring, 47.9 m from Plume Geyser, and 36.0 m from Surge Geyser.
Ear Spring	J11 890E, 125S	1	Discharge increased from small point outlet on east to frequent overflow in all directions. Sinter wash to west suggests heavy boil or

			small eruption in November or December.
Unnamed spring NW of Ear Spring	I11 805E, 960S	1	Height of "spouting" activity noticeably greater for 5 months.
Giantess Geyser	J12 240E, 485S	2	Became dormant on November 10, 1983, ending the series of 112 eruptions which began February 19, 1980. In contrast only 108 eruptions were recorded during the 50-year period of 1927-1976.
Heart Spring	J11 825E, 385S	3	Increased gas discharge and temperature.
Infant Geyser	J12 400E, 415S	2	Water level ebbed more than 40 cm.
Inverted Geyser	J11 855E, 515S	3	Sinter sheet ruptured over an area approximately 2.7 m in diameter, causing geyser to be destroyed. Location: 44.2 m from Depression Geyser, 26.8 m from Arrowhead Spring and 22.6 m from unnamed white halo vent.
Lion Geyser	J11 730E, 290S	2	Dormant from time of quake for about 15 months. The only prior time Lion Geyser has been known to be dormant was for a two and one-half month period following the 1959 Hebgen Lake quake.
Little Squirt Geyser	J12 325E, 800S	3	Rejuvenated from rare eruptions to long periods of play almost daily.
Pendant Geyser	J11 940E, 035S	1	Rejuvenated from long-dormant, quiet spring to almost continuous spouter, 0.1 to 1.9 m high by early December, but nearly dormant again by 7/31/84.
Plate Geyser	J12 015E, 455S	3	Eruptive activity increased from very rare in 1983 to around 3-4 hour intervals. Geyser crater enlarged to 3.96 x 3.63 m.
Unnamed blowouts E of Plate Geyser	J12 030E, 470S	3	Fresh, unweathered sinter chips torn out and vegetation killed around each of these vents. Distance from Plate Geyser, 6.78 m; dimensions - 1.32 x 1.22 m.
" " "	J12 040E, 470S	3	9.63 m from Plate; dimensions - 0.76 x 0.56 m.

" " "	J12 045E, 470S	3	10.87 m from Plate; dimensions - 1.04 x 0.81 m.
" " "	J12 050E, 475S	3	12.34 m from Plate; dimensions - 0.86 x 0.79 m.
" " "	J12 060E, 475S	3	15.32 m from Plate; dimensions - 1.02 x 0.97 m.
" " "	J12 065E, 480S	3	17.58 m from Plate; dimensions - 0.66 x 0.36 m.
Plume Geyser	J12 145E, 775S	3	Before quake in 1983, Plume would initiate eruption with water level 7-10 cm below lower rim; behavior has changed since then in that it overflows heavily for 15 or more minutes before erupting. Average intervals have decreased from near 40 minutes to 30 minutes, and are strongly influenced by eruptive series of Vault Geyser in place of Giantess.
Unnamed vent near Plume Geyser	J12 155E, 740S	3	Continuous boiling and heavy overflow since the Borah Peak event until July 1984, when pool level dropped 40 cm. Area of vent increased by factor of 9 from vigorous surging.
Pump Geyser	J12 110E, 385S	2	Discharge apparently diminished as suggested by virtual disappearance of the active algae mat.
Roof Geyser	J11 960E, 550S	3	Eruptions more powerful after the quake as shown by new wash; changes in intervals or durations, if any, are unknown.
Scissors Springs	J11 895E, 715S	4	Eruptive activity and runoff from West Scissors ceased; water level down 10-20 cm in both vents.
Sponge Geyser	J12 025E, 420S	3	Water level in vent rose more than 2 m; eruptive activity similar to that before the 1959 earthquake has returned.
Surge Geyser	J12 170E, 690S	3	Frequent eruptive activity rejuvenated after 10/28/83 until late winter. Fresh siliceous sinter eroded from pool and vent.

Vault Geyser	J12 245E, 420S	1	Serial-type eruptions very similar to those between 1947 and 1959 resumed; more powerful than the displays associated with Giantess eruptions of at least the last 10 years.
Unnamed white halo blowout vent	J11 900E, 570S	3	Fresh unweathered white siliceous sinter ejecta rim deposited around vent. Dimensions - 1.78 x 1.70 m.
Unnamed vent E of Arrowhead Spring	J11 845E, 560S	3	New enlargement of vent and heavy wash 2.24 m to the south. Dimensions, 3.45 x 1.52 m.

Discussion

Obviously, there are other possible causes for change in thermal activity than the Borah Peak seismicity. More than 14 years of work in Yellowstone's geyser basins by this author, and close cooperation with other individuals long involved with geyser research such as D.E. White, R.O. Fournier, S.W. Kieffer, and J.S. Rinehart have revealed many instances of changes and hypotheses for their causes. These include self-sealing by sinter deposition; opening of new ground water circulation patterns due to hydrothermal alteration; variations in precipitation, barometric pressure, and earth tidal forces; widespread annual thermal basin disturbances; intense local micro-seismic swarms; and strong, damaging (M 6 or greater) earthquakes (Marler and White, 1975; Pitt and Hutchinson, 1982; and Rinehart, 1972).

Self-sealing, however, has been found to be slow enough outside of the Norris Geyser Basin that change is usually gradual over many months or years for a group of features rather than acting in a few weeks time as was the case on Geyser Hill in 1983. The same is true of hydrothermal alteration opening or eroding new routes through volcanics or surficial deposits. Such a process is much less likely in the Upper Geyser Basin with its silica rich, high chloride, near-neutral thermal fluids as opposed to an acid sulfate area such as portions of the back basin at Norris. Only certain local sensitive geysers and hot springs, such as Splendid and Morning Geysers, have been shown to respond to variations in earth tidal forces or weather. Many in the affected area, including Old Faithful Geyser and several of the smaller springs, in fact have to date given little evidence of sensitivity to these factors. Widespread annual thermal disturbances are only known to occur in the Norris Geyser Basin and have never been recognized in any of the more extensively monitored Firehole River Geyser Basins.

Local seismic swarms have caused significant changes in many thermal features in the Upper Geyser Basin and just about every other thermal area in the park at one time or another. However, Old Faithful Visitor Center helicorder records show such a cause is unlikely to be responsible for the profound circulation shifts in Geyser Hill. Local seismic activity was notably quiet near the Upper Geyser Basin; no major micro-seismic swarms were noted and no felt tremors were reported in the area during the end of 1983. Thus, the most likely cause for the thermal changes at Old Faithful and Geyser Hill was

shifts in hot water circulation induced by strong ground motion from the magnitude 7.3 earthquake of October 28, 1983, near Borah Peak, Idaho.

Two types of evidence support this conclusion. First, the 37 named and unnamed thermal features which experienced significant changes had their manner of modification structurally controlled in four essentially parallel zones (Figure 1). Each zone (numbered 1-4 from north to south) exhibited characteristics of alternately more or less thermal energy than was observed and documented prior to October 28, 1983. Zones of less thermal energy are in a narrow band (Zone No. 2) between Lion and Giantess Geysers (both now dormant!) and south of Scissors Springs to Bronze Spring, including Old Faithful Geyser (Zone No. 4).

Eruptive activity of Old Faithful Geyser also reflects its sensitivity to strong seismic events. A plot of its average annual intervals over each of the last 35 years (Figure 2) shows increases following each of the last 3 major earthquakes.

Monthly values of average intervals are plotted in Figure 3 for 1983 and the first half of 1984. They rarely vary more than 2 minutes between consecutive months. Such a pattern has been maintained during most of the geyser's known history. Due to lack of observers at Old Faithful, no data were collected during the entire month of November or the first half of December while the intervals were beginning their dramatic rise. Since then, more than half of Old Faithful's measured intervals have been 80 minutes or greater, and at least 10 intervals of 100 minutes or more have been observed during the first 8 months of 1984. A possible cause for the longer periods between eruptions may be a diminished rate of water entering its reservoir, since more of its supply has been shifted over to the northern and broad central portions (zones 1 and 3) of Geyser Hill. In addition, debris from persistent vandalism is obstructing Old Faithful's natural flow. Longer intervals are also correlated with a higher frequency of long durations from eruptions which precede them.

The changes in distribution of Old Faithful's normal range of durations of play which are timed from first continuous water ejected to last visible water are shown in Figures 4 and 5 for October 1983, and May 1984, respectively. Note that there is no extension in the range of Old Faithful's durations following the earthquake, only an increase in the percentage of long, 3-to 5-minute durations, from 64 to 80 percent of all those accurately timed each month.

Questions for Evaluation

A critical set of questions, which unfortunately do not have satisfactory answers, involves timing and magnitude of the thermal changes induced by the Borah Peak earthquake: When did the behavioral changes from ground water circulation shifts reach the surface and become visible? Were these changes simultaneous or sequential, transgressing from one margin of Geyser Hill to the other; or, alternatively, did the changes first emerge in the major high-discharge thermal features having more direct connections to the deep aquifer and then spread to the small, more shallow rooted springs? What was the full or greatest magnitude of the fluctuations in pool temperatures, spring discharges, eruption durations, intervals, and heights? Likewise, how long did the most intense activity last for the thermal features: single,

once-only eruptions? over in minutes for some? hours, days, or weeks for others? An effort is now beginning in Yellowstone to more thoroughly investigate thermal behavior of major geysers with instrumented monitoring. Perhaps similar seismic-induced changes in the future will provide a few of the answers and, in turn, offer means of better understanding local hydrologic controls, eruptive behavior of selected geysers, or even provide a little insight on possible hydrothermal explosion or volcanic hazards in Yellowstone National Park.

Acknowledgements

This investigation was aided by a cadre of long-term volunteer thermal observers who helped document hot spring and geyser activity prior to the changes. Their unselfish interest and concern is greatly appreciated.

References Cited

Fischer, W. C., (1960), Earthquake! Yellowstone's living geology: Yellowstone Library & Museum Assn., 62 p.

Marler, G. D., (1973), Inventory of thermal features of the Firehole River Geyser Basins and other selected areas of Yellowstone National Park: Natl. Tech. Info. Service Rept. PB-221 289, 648p.

Marler, G. D., (1974), The story of Old Faithful: Yellowstone Library & Museum Assn., 49 p.

Marler, G. D. and White, D. E., (1975), Seismic Geyser and its bearing on the origin and evolution of geysers and hot springs of Yellowstone National Park: Geol. Soc. Amer. Bull., v. 86, p. 749-759.

Muffler, L. J. P., White, D. E., Beeson, M. H., and Truesdell, A. H., (1982), Geologic map of the Upper Geyser Basin, Yellowstone National Park, Wyoming: U.S. Geol. Survey Misc. Geol. Inv. Map I-1371.

Pitt, A. M. and Hutchinson, R. A., (1982), Hydrothermal changes related to earthquake activity at Mud Volcano, Yellowstone National Park, Wyoming: Jour. Geophys. Research, v. 87, p. 2762-2766.

Rinehart, J. S., (1972), Fluctuations in geyser activity caused by variations in earth tidal forces, barometric pressure, and tectonic stresses: Jour. Geophys. Research, v.77, p. 342-350; Comments by Marler, G. D. and White, D. E., v. 77, p. 5825-5829, and Reply: v. 77, p.5830-5831.

U.S. Geological Survey, (1964), The Hebgen Lake, Montana, earthquake of August 17, 1959: U.S. Geol. Survey Prof. Paper 435, 242 p.

Figure 1

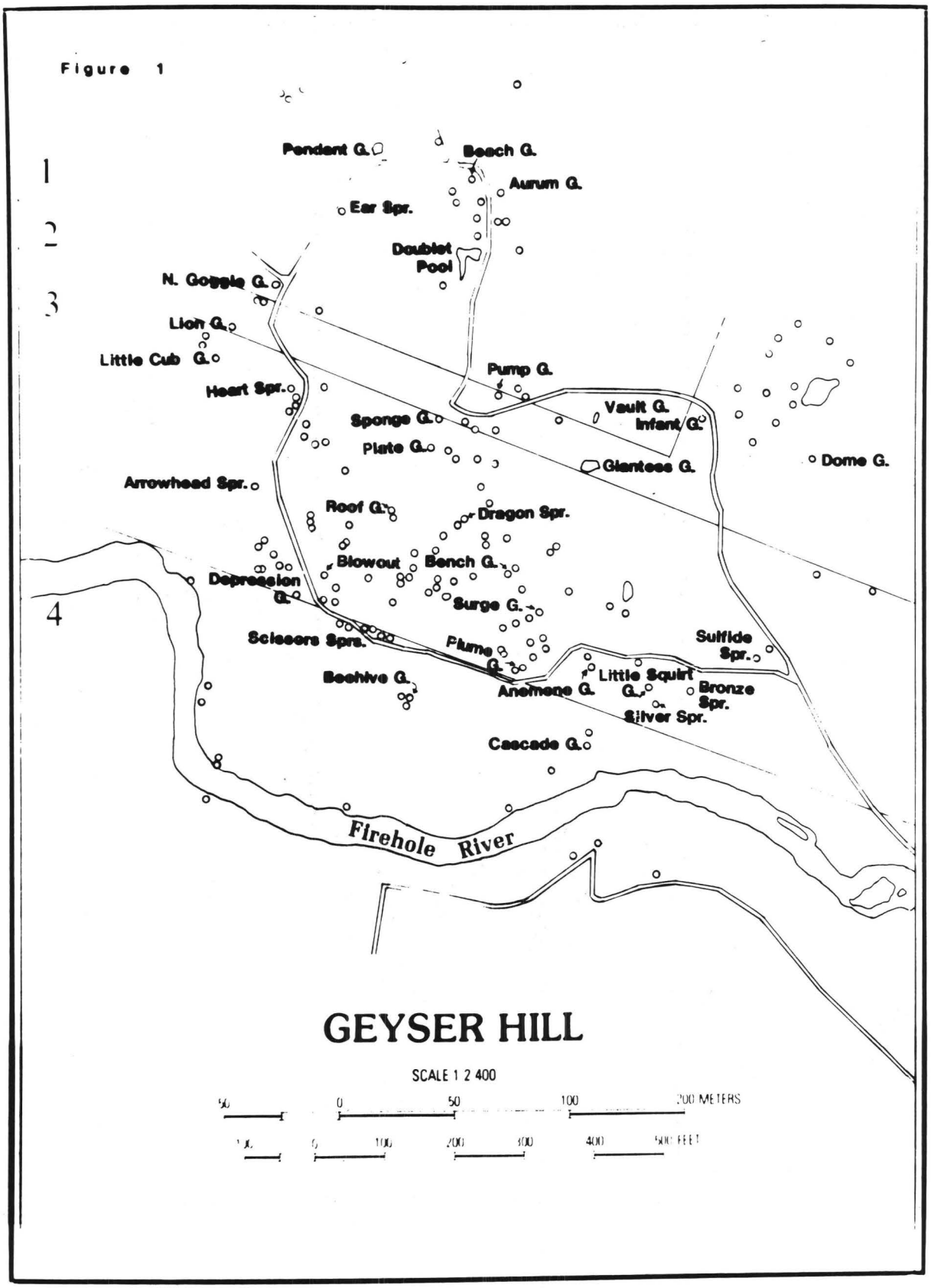

GEYSER HILL

SCALE 1 2 400

50 0 50 100 200 METERS

100 0 100 200 300 400 500 FEET

Figure 2: ANNUAL AVERAGE INTERVALS OF OLD FAITHFUL GEYSER

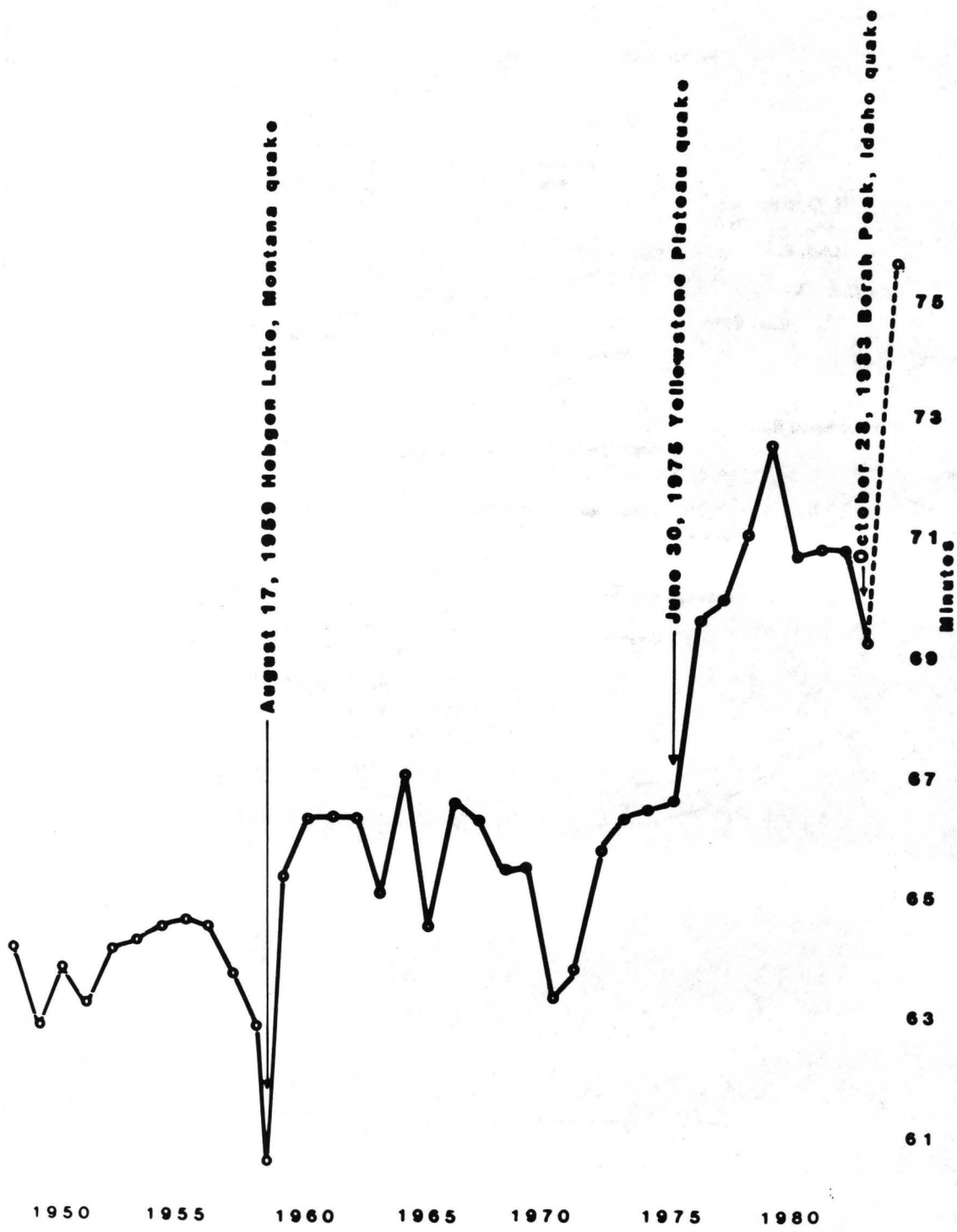

Figure 1 MONTHLY AVERAGE INTERVALS OF OLD FAITHFUL GEYSER, JANUARY 1983 - JULY 1984

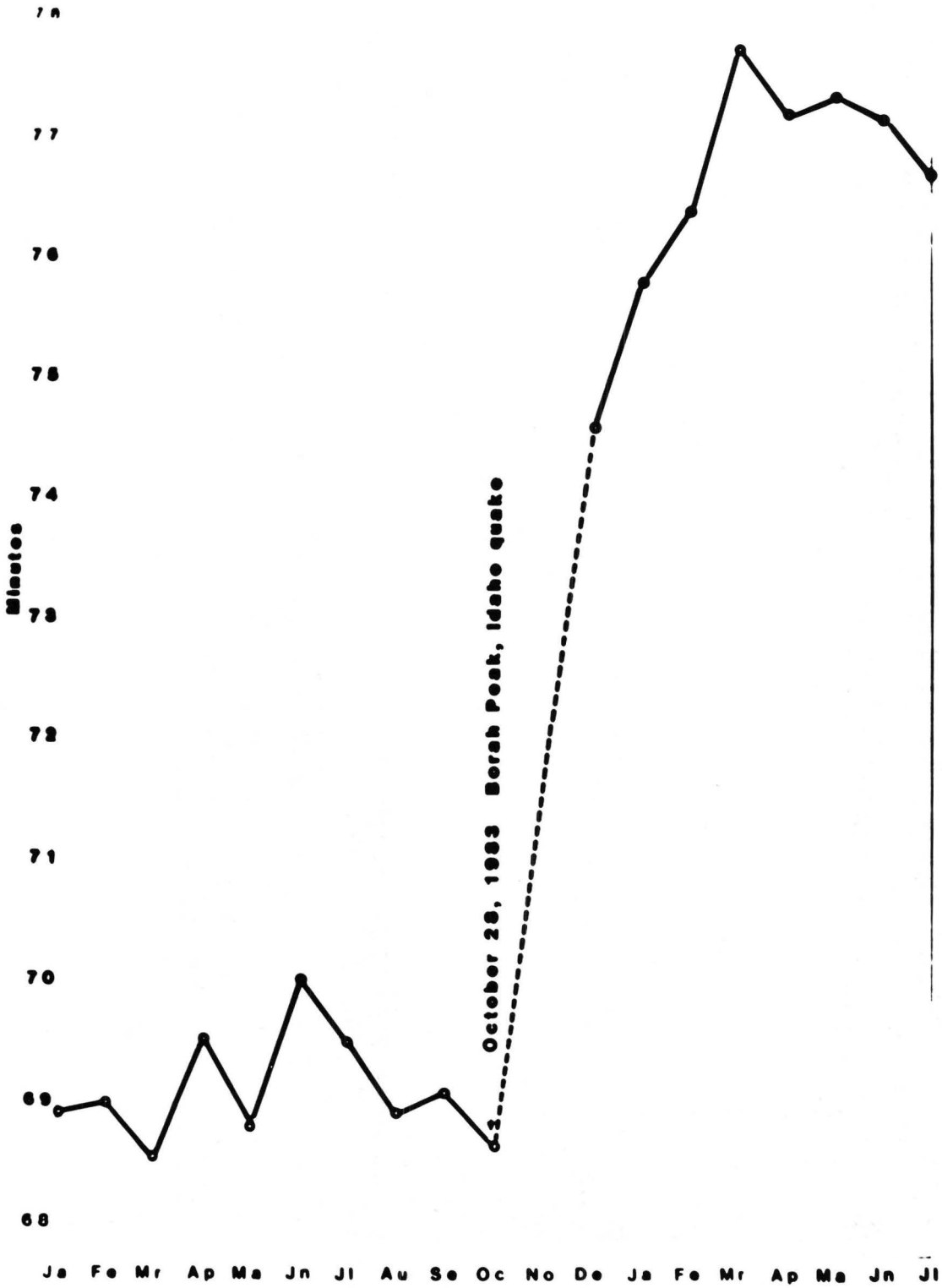

Figure 4: OLD FAITHFUL DURATION FREQUENCY: OCTOBER 1983

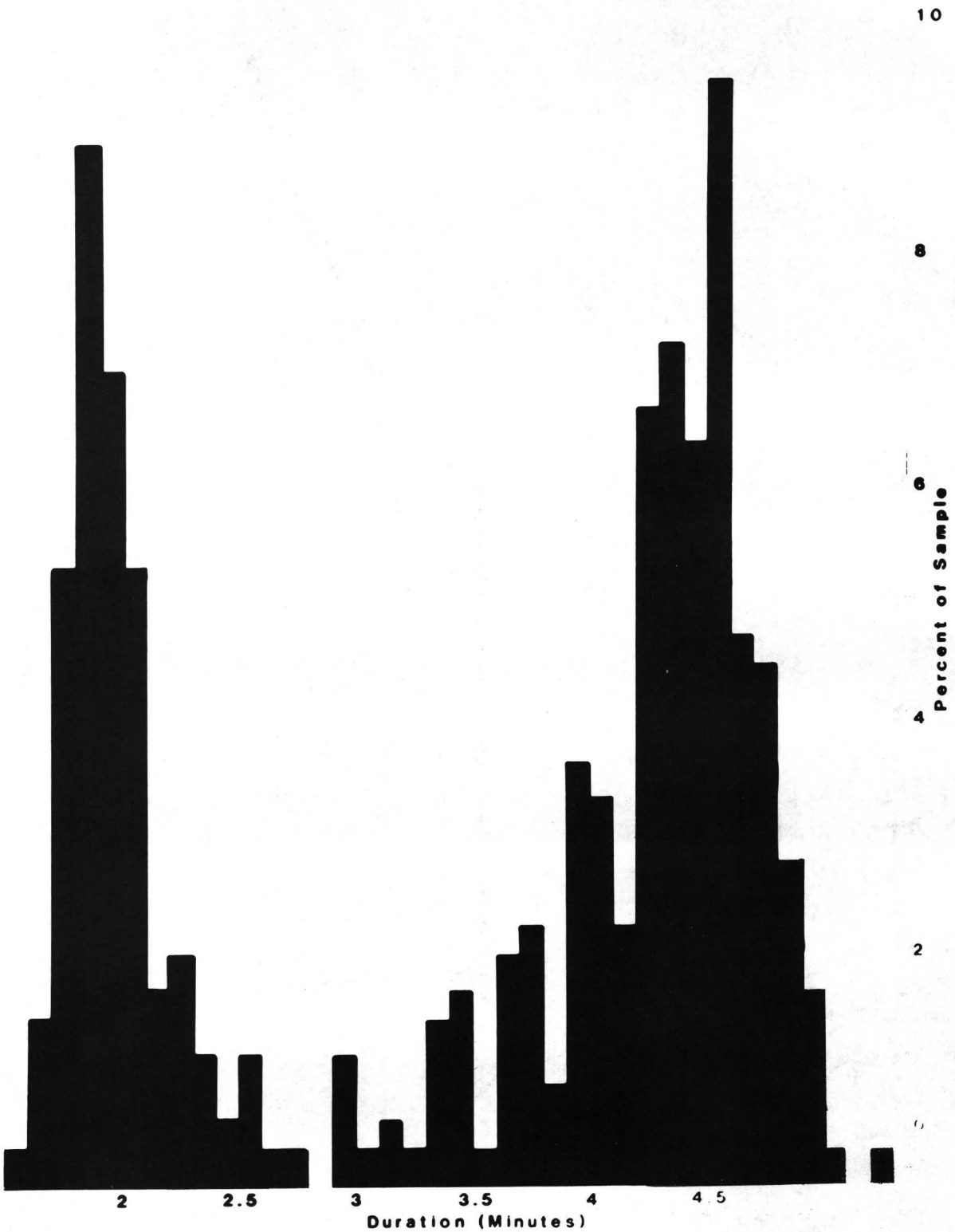

Figure 5: OLD FAITHFUL DURATION FREQUENCY: MAY 1984

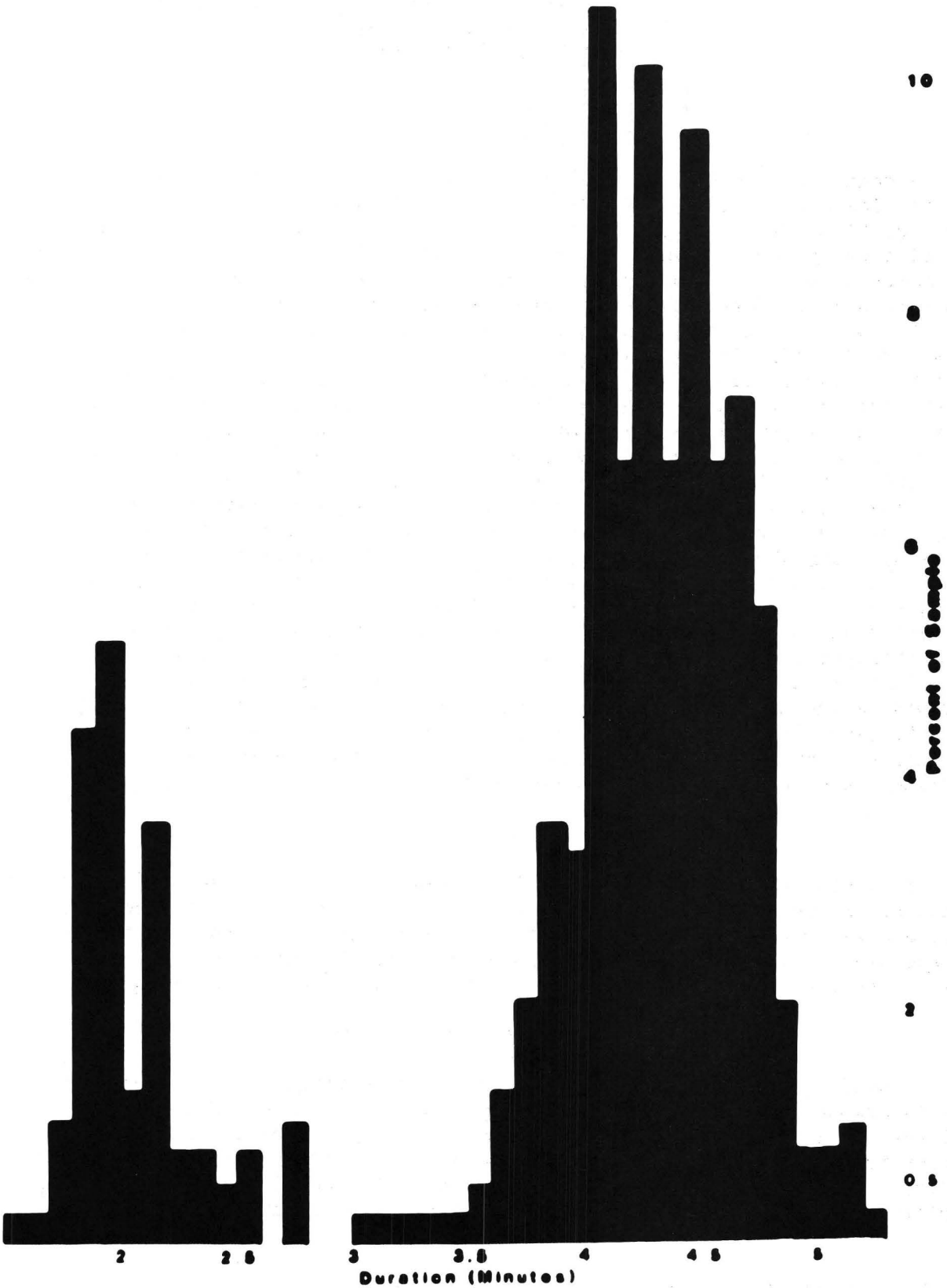

LIQUEFACTION GENERATED BY THE 1983 BORAH PEAK, IDAHO, EARTHQUAKE

T. L. Youd*, E. L. Harp, D. K. Keefer, and R. C. Wilson
U.S. Geological Survey
Menlo Park, California

Abstract

A magnitude 7.3 (M_s) earthquake struck the Borah Peak area of south-central Idaho on October 28, 1983, creating a 23-mi-long surface rupture along the Lost River fault and generating ground motions strong enough to cause building damage and ground failure over about a 3500 square mile area. The shock caused parts of buildings to collapse in several communities, landslides and rockfalls to desend from some steep slopes, and numerous liquefaction effects to form including sand boils, fissures, and lateral spreads. Failures caused by liquefaction disrupted roadways, pastures, and two buildings. In search of liquefaction effects, we examined all localities of reported damage in the epicentral area, drove upon nearly all of the major roads within 40 mi of the fault rupture, and made low-altitude reconnaissance flights over the area. The most abundant and most severe liquefaction effects developed in the Thousand Springs Valley near the southern terminus of the fault rupture. In that area, lateral spreads under cut and pulled apart foundations for a house and a barn, generated a 1.5-mi-long zone of fissures in Pleistocene fan deposits along the east side of the valley, and displaced a highway by several feet. Sand boils erupted in several parts of the valley and a buried pump house buoyantly rose a few inches through a liquefied sand deposit. Large and violent sand boils erupted near Chilly Buttes, but these eruptions were caused by a disruption within a deep aquifer rather than by shallow liquefaction. Beyond the Thousand Springs Valley, relatively small sand boils erupted in a few places and minor fissures and ground settlement scarred some roadways. Liquefaction effects did not occur as far away from the fault rupture as would be expected for a shock of this magnitude. Liquefaction was, however, most abundant in Holocene sediment as expected.

Introduction

Following the October 28, 1983 Borah Peak, Idaho, earthquake (M_s=7.3), we conducted a reconnaissance investigation to locate and describe secondary ground effects caused by liquefaction. We also determined the origin and age of sediment that liquefied and examined the distribution of the effects with respect to the surface fault rupture. These results are reported herein.

Geologic and Hydrologic Setting

Liquefaction effects generated by the 1983 earthquake developed only in the intermountain valleys surrounding the Lost River Range (Fig. 1). These valleys are filled with Quaternary alluvial, fluvial, and glacial sediment (McIntyre and Hobbs, 1978; Nelson and Ross, 1969; Rember and Bennett, 1979a, 1979b). The youngest sediment in the valleys is channel and flood plain deposits of late Holocene age. Alluvial fan, glacial, and fluvial deposits of

* Now at Brigham Young University, Provo, Utah.

earlier Holocene and late Pleistocene age flank the young fluvial deposits and cover the lower slopes of the valleys. Most liquefaction effects developed in the late Holocene deposits, but a few effects also developed in the older sediment.

Permanent artesian conditions beneath the valleys generate numerous springs and seeps and lead to high-ground-water conditions beneath many lowland areas. Nearly all of the liquefaction effects occurred in these areas of high water table. Some lateral spreads, however, extended into areas where unconfined ground water is tens of feet deep.

Big Lost River and Thousand Springs Valleys

We checked the Big Lost River valley for liquefaction effects beginning at Arco and driving northwestward (Fig. 1). About 1 mi southeast of Leslie, fissures as much as 2 in wide disrupted the pavement of Highway 93 over a distance of 500 ft. The fissures were parallel to the road and affected only the outer 5 ft of both sides of the pavement and adjacent shoulder. A railway embankment parallel to the highway contained similar but smaller fissures. The highway and railroad at this locality cross a marsh on 3- to 5-ft-high embankments. No fissures were found in the natural ground on either side of the highway and railroad. Apparently the weight of the fill along with weakening of the underlying soil caused spreading and settlement of the fill and the brittleness of the pavement and shoulder materials led to the development of the fissures. These fissures were 23.5 mi from the fault rupture, and were the liquefaction effect farthest from the rupture. For comparison, the toppling of an exterior brick-veneer wall of a church about 0.5 mi southeast of the damaged highway was the collapsed building component farthest from the fault rupture. This locality also marked the outer bound of the Modified Mercalli intensity VII zone in that area (Carl Stover, oral commun. Jan. 10, 1984).

Fissures similar to those southeast of Leslie developed in most roadways passing over marshy areas in the Big Lost River valley north of Leslie. In the vicinity of Mackay, we noted three zones of fissures on Highway 93 and several other zones of fissures on county roads (Fig. 1). In general, the fissures were wider and more disruptive the nearer they were to the surface rupture on the Lost River fault. For example, the fissures in Highway 93 about 3 mi northwest of Mackay and 12 mi from the fault rupture were as wide as 4 in and disrupted the roadway sufficiently to impede traffic. Near this same area, sand boils with deposits as wide as 2 ft in diameter erupted in the flood plain of the Big Lost River; these were the only sand boils we saw south of Mackay Reservoir.

Along a 2-mile stretch of the Big Lost River upstream from Mackay Reservoir, sandbars in the channel liquefied; this created ground fissures as much as 1 ft wide and sand boils with deposits as much as 6 ft in diameter. A man who happened to be fishing at this locality at the time of the earthquake gave the following account to Frank Baldwin of the National Earthquake Information Service:

> "I was standing on a gravel sandbar when the quake struck. Cracks appeared in the bar and began to gurgle water. Then three or four water spouts with 3 to 4 inch holes opened up and water shot up to 3 feet in

the air. The gravel bar shook like a marshmallow and it was very difficult to stand. Some of the water spouts spewed black water; others spewed clear water."

When the man waded out to the bar, he reported that the water was about calf high. After the shaking ceased, he waded back to the bank and reported the water to be waist high. He estimated the water had risen nearly 10 inches. Upon reaching higher ground, although still in a marshy area, he saw numerous nearby water spouts still spewing water.

The above account indicates that the sand boils must have continued to flow for some time after the shaking ceased because the man waded back to the river bank and saw numerous water spouts still flowing. The account also indicates that the river rose rapidly, presumably from a large influx of water flowing out of sand boils. The fact that some sand boils spewed black water while others spewed clear water indicates differences in the sediment content of the effluents, with some containing very little sediment.

About 3 mi northwest of Mackay Reservoir and 6 mi southeast of the southern terminus of the fault rupture, a lateral spread developed on a low terrace near the Big Lost River (site 1 on Fig. 1). A curved zone of fissures and sand boils marked the head of the spread that passed beneath a house, barn, and adjacent ranch yards (Fig. 2). The fissures were as wide as 1 ft with scarps as high as 1 ft. Sand-boil deposits, as wide as 8 ft, were composed of gravelly sand with pebbles as much as 1 in across (curves 1 and 2, Fig. 3).

The foundation of the damaged house was constructed of small spread footings with wood pillars beneath the interior of the structure and a perimeter footing with concrete-block walls around the exterior. The foundation under the back part of the house was fractured and split apart several inches by the horizontal displacement. Fig. 2B shows the back of the house where about 5 in of horizontal slip occurred between blocks in the foundation. The wood-frame superstructure remained intact and essentially undamaged, although it was slightly distorted due to differential settlement of a few inches. Nearly all of the horizontal displacement was absorbed by the slippage that occurred in the perimeter foundation; the spread footings and wood pillars were only slightly distorted by the horizontal displacement and differential settlement. The floor slab in the garage, which is attached to the house, also was fractured and pulled apart a few inches, and the garage walls were distorted by the displacement.

Eastward from the house, the fissures passed beneath a steel-frame barn with a dirt floor. The fissures gave the floor the appearance of having been plowed (Fig. 2C). Horizontal displacement widened the doorway by about 1 ft at the base and distorted the frame. The fissures continued eastward from the barn, disrupting farm roadways and passing through a hay yard. A wire fence enclosing that yard was pulled apart by 30 in.

About 50 ft behind the house, a water tank and pump were housed in two separate but adjacent concrete boxes that extended from about 2 ft above to about 4 ft below ground surface. Liquefaction during the earthquake caused the box containing the pump to buoyantly rise 3 in while the more heavily loaded box, containing the filled water tank, remained in place (Fig. 4).

Additional sand boils erupted and fissures formed in the general area surrounding the lateral spread noted above. North of the spread, the pavement of Parsons Creek Road was disrupted by fissures and ground settlement over a distance of about 1 m. Emergency repairs to the roadway obliterated most of these fissures before our visit. Sand boils with deposits as much as 3 ft in diameter erupted at a few localities along the shoulder of that road. Southwest of the spread for a distance of about 0.5 mi, sand boils with deposits as much as 6 ft in diameter erupted at sporadic locations in the fields. Sand boils also erupted in the corrals and yards of a ranch about 0.5 mi southwest of the lateral spread, but there was no damage to buildings and other structures at that locality. All of the sand-boil deposits in these areas were composed of gravelly sands. The lateral spread at site 1 and all of the effects in the surrounding area are situated within sec. 30, T. 8 N., R. 23 E.

Highway 93 settled and cracked over a distance of about 200 ft where the roadway crosses a section of marsh 1 mi southeast of the intersection of Trail Creek Road (about 1.5 mi southeast of the fault rupture). About 6 in of differential settlement occurred at the margins of the affected zone and fissures as much as 3 in wide fractured the pavement at several places within the zone. We saw no fissures or other ground effects in the natural ground on either side of the highway.

A nearly continuous zone of ground fissures extended 1.5 mi northward from near Trail Creek Road nearly to Whisky Springs (Fig. 5) The fissures paralleled the alluvial fan fronts on the east side of Thousand Springs Valley and were caused by lateral spreading of distal ends of the fans toward the valley bottom. The zone of fissures was as wide as 250 ft and was about 1 mi west of the southern segment of fault rupture (Fig. 1). Most fissures developed in subparallel sets with individual cracks approximately parallel to the fan front (Fig. 6). Individual fissures were as long as 1,000 ft and were open to depths as great as 10 ft. Extension across the fissures was as great as 2 ft, but openings were as wide as 4 ft because of collapse of material into the fissures. At some localities along the fan-marsh interface, which forms the downslope bound of the fissured zone, segments of marsh sod were thrust outward over the marsh by the spreading movement. The thrusting generated buckles and scarps in the marsh sod as high as 4 ft (Fig. 7). Some pre-earthquake humps in the sod near buckles produced by this event cause us to speculate that they may have been caused by lateral spreading during a previous earthquake. Sand boils erupted at several localities along the fan-marsh interface and at a few localities on the fissured surface. Sand boils were more common at mouths of draws where the ground slope is more gentle than along steeper fan fronts. Small, permanent springs also flow out of distal margins of the fans in several places.

The cause of lateral spreading was liquefaction of a subsurface sediment layer. The eruption of sand boils at several places along the toe and on the spread are evidence of this phenomenon. The sediment deposited by sand boils in this area was fine sand and silt (e.g., curves 6 and 7, Fig. 3), indicating that the layer that liquefied is composed of similarly fine grained material, a material that is finer grained and better sorted than fan materials exposed in fissures. The fan material is poorly sorted and contains clay, silt, sand, gravel, and cobble size particles.

From 1.2 mi northwest of the Trail Creek Road to Whiskey Springs, a 2,000-ft-long segment of Highway 93 traverses the zone of lateral spreading (site 2, Fig. 1; Fig. 8). Fissures as much as 4 ft wide and 10 ft deep marked the head of the lateral spread (about 100 ft upslope from the road), and overturned folds as much as 4 ft high (Fig. 7) marked the toe (about 100 ft downslope from the road). The fissures at the head splayed out, diminished in size, and curved back toward the highway on both ends of the 2,000-ft-long zone. The road pavement across the fissured zone was disrupted in numerous places by fissures, scarps, and offsets with displacements as large as 5 in; fissures in the shoulders and barrow pits along the road, however, were as wide as 16 in. Roughened pavement caused by these fissures and scarps created hazardous driving conditions but did not render the roadway impassable. The roadway and underlying ground were also displaced at least 4 ft downslope across the midpart of the segment of fissured zone crossed by the highway. This displacement created a gentle concave curve in the road (Fig. 9). Sand boils erupted along cracks in the barrow pit on the up-hill side of the road, on the alluvial fan surface between the road and the marsh, and along the toe of the spread.

Northwest of Whiskey Springs on the east side of Thousand Springs Valley, only a few fissures opened along the alluvial fan fronts, however, hundreds of sand boils erupted in parts of this area (site 3). At one locality, we observed more than a hundred sand boils with deposits ranging from 0.5 ft to 8 ft in diameter in a 1,500-ft-long zone. That zone extended 300 ft upslope from the marsh and eastward from Chilly Road toward Whiskey Springs along the north edge of sec. 20, T. 9 N., R. 22 E. Spacings between sand boils were generally greater than 100 ft; the sand-boil deposits were composed of silty sands (curves 4 and 5, Fig. 3). Only a few scattered small fissures developed in this area.

We saw no sand-boil deposits on marsh grass in the Thousand Springs Valley other than those near fan fronts. Many of those sand boils erupted through cracks in the sod at the toes of lateral spreads. Considering the high water table and generally thick section of late Holocene sediment in the grassy areas, liquefiable material should be abundant. Two possible reasons for the absence of sand boils are: (1) The sediment may be too fine grained to liquefy, or (2) the thick mat of roots and dead vegetation beneath the grass may have acted as a filter preventing sediment transported by sand boils from reaching ground surface. The latter explanation seems more likely to us. We also saw very few cracks in areas covered by marsh grass. One reason for this absence is the ductility of the upper soil and grass layer which readily stretches rather than cracks.

We drove a 5-mi-long segment of the Big Lost River southeastward from near the intersection of the Trail Creek and Parsons Creek Roads. We observed parts of the flood plain and river channel as we drove; in addition, we walked across the flood plain at several localities. We did not see any sand boils or ground cracks and conclude from these observations that no significant liquefaction effects occurred along this segment of the river which lies between 2 and 4 mi from the southern terminus of the fault rupture. The flood plain material in this section is mostly gravel and cobbles. Thin veneers of sand and silt overbank deposits cover the surface away from the channel, and thin sandbar deposits sporadically lie near the channel. The probable reason for the absence of effects in this area is that the sediment may be too coarse

and well drained to liquefy or to create surficial liquefaction effects. We also checked the flood plain of the Big Lost River at several localities along Trail Creek Road in the Thousand Springs Valley and in the White Knob Mountains to the southwest, and found no evidence of liquefaction.

Chilly Buttes Area

Some of the most spectacular effects of the earthquake were the violent eruptions of huge sand boils and springs in a 1-mi-long northwest-trending zone that cuts across the eastern tip of Chilly Buttes (Figs. 1 and 11). The sand boils on the valley floor spewed water and sediment 15 to 20 ft into the air for several minutes following the earthquake and quieter flow continued for several hours. This action flooded part of the Thousand Springs Valley, spread hundreds of cubic yards of sediment across the ground surface in the vicinity of the outbursts, and pocked the surface with craters (Fig. 10). Where the zone cuts across the tip of Chilly Buttes, water gushed from transient springs on the hillside as high as 100 ft above the valley floor (Waag, 1985; Wood and others, 1985). These springs washed sediment from the hillside, cut gullies, and blocked a ranch road and irrigation ditch. Two authors (Keefer and Wilson) mapped the cratered area east of Chilly Buttes noting widths and depths of craters and delineating the areas covered by sediment (Fig. 11). They counted 47 craters larger than 2 ft in diameter and measured 19 with diameters greater than 20 ft and depths greater than 5 ft. The largest crater had a diameter of 75 ft and the deepest was 16 ft. At least one and possibly five craters existed before the earthquake and were reactivated by the outburst of water during this event. A local rancher reported that those craters were created by a similar eruption of water during the 1959 Hebgen Lake, Montana, earthquake.

The quantity of water expelled and the fact that eruptions developed high on the hillside of Chilly Butte indicate that some perturbation of a deep aquifer caused the upward flow of water rather than compaction of shallow sediment layers, the usual cause of liquefaction and sand boils. Hence, although the soil in the vicinity of the eruptions certainly liquefied, the usual techniques applied by geotechnical engineers to evaluate liquefaction susceptibility do not apply in this case. More information on the outbursts near Chilley Buttes and increases in spring flow in other parts of the Thousand Springs Valley is given in the papers on hydrological effects (Wood and others, 1985) and groundwater eruptions (Waag, 1985).

Warm Springs, Salmon, and Pahsimeroi Valleys

We drove Highway 93 to Challis, viewing the flood plain of Warm Springs Creek, which is unwooded and clearly visible along most of this route. In addition, we walked the flood plain at several localities where surficial conditions appeared favorable for liquefaction to occur. We found no liquefaction effects in that area.

We checked the flood plain of the Salmon River at several localities between Challis and the Pahsimeroi Valley to look for liquefaction effects. We saw several areas where surficial conditions appeared favorable for liquefaction to occur, but we saw no evidence of liquefaction. Most exposures of

the flood plain, however, are covered with gravel and cobbles, indicating that the materials may be too coarse and well drained to develop surficial liquefaction effects. We also interviewed two residents who live near the river; neither had seen nor heard of any ground effects caused by the earthquake.

We checked the flood plain of the Pahsimeroi River near its confluence with the Salmon River and saw no ground effects caused by the earthquake. We then drove southeastward through the Pahsimeroi Valley, crossing the valley on each public road. These roads, not all of which are marked on Fig. 1, are 3 to 5 mi apart, and thus provide only limited access to areas where liquefaction would most likely occur. The areas we observed and the interviews we had with local residents, however, provide enough information to give the types and general distribution of earthquake effects that occurred and indicate that we probably did not miss any damaging or extra-large liquefaction effects.

A few hundred sand boils erupted in a 2,000-ft-long and 500-ft-wide zone that extends eastward from Hooper Lane across a flat terrace a few hundred feet north of the Pahsimeroi River (site 5, Fig. 1). The zone is 16.5 mi north of the fault rupture. The only house on the east side of Hooper Lane lies within this zone and was undamaged even though several boils erupted within a hundred feet of the structure. The largest sand-boil deposits were about 6 ft wide; most deposits, however, were about 2 ft wide (Fig. 12), and the smallest were only a few inches wide (Fig. 12). All of the deposits were composed of well-sorted medium-grained white sand (curve 3, Fig. 3). In many instances the sand boils erupted along small fissures that were as wide as 4 in. These fissures formed an arcuate pattern, concave to the south, that seemingly outlined a lateral spread with incipient southward movement. A 4-ft-lower terrace lies immediately south of the zone of sand boils; most of this lower terrace is covered by marsh grass. We did not see any sand-boil deposits on the grassy surface, although several deposits lay on bare ground near the north margin of the terrace and a few had erupted within a small stream that quietly flows across the terrace. This observation is consistent with the behavior noted in the Thousand Springs Valley and further suggests that thick marsh grass inhibits the eruption of at least small- to moderate-size sand boils.

The owner of a ranch south of the Pahsimeroi River and about 0.5 mi east of Hooper Lane reported that a number of sand boils, perhaps as many as 100, erupted in his fields. He described their size as small, each containing "two or three buckets full of sand." These sand boils were about 15 mi north of the north terminus of the fault rupture. The rancher had not observed any increases in the flow of springs on his ranch but noted that turbid water flowed from his well for a few days following the shock.

We did not see nor were told about any ground effects attributable to liquefaction in the Pahsimeroi Valley southeastward from the ranch noted above. Our reconnaissance included field checks of several likely sites as well as observations from the public roads and interviews with local ranchers. One rancher whose property is near Goldberg Creek reported that springs in his area had increased their flow, including the one near his home from which the ranch takes its culinary water.

Big and Little Lost River Sinks

Because of high rates of sedimentation and high ground-water levels in the Big and Little Lost River Sinks, conditions commonly associated with high liquefaction susceptibility, a search was made for liquefaction effects in those areas (Fig. 1). The sinks are areas where waters from the two Lost Rivers deposit sediment as they seep into the valley floor. We did not see any liquefaction effects at the localities we visited within the sinks nor learn of any effects from several residents that we interviewed. The sinks lie 50 to 60 mi southeast of the southeast terminus of the fault rupture.

Distribution of Liquefaction Effects

Most liquefaction effects developed in flood-plain alluvium of late Holocene age. This sediment fills the bottoms of valleys that surround the Lost River Range. These valley bottoms are also generally characterized by high ground-water levels. The development of liquefaction in saturated late Holocene sediment of fluvial origin is consistent with behavior of similar materials in other parts of the world. Sediment of this type and age is one of the materials most susceptible to liquefaction (Youd and Perkins, 1978).

During the earthquake, liquefaction also developed in one area of late Pleistocene sediment beneath the distal margins of fans along the east edge of the Thousand Spring Valley. These fans are composed primarily of late Pleistocene materials, although some Holocene deposition has occurred near the larger streams that flow across the fan surfaces (McIntyre and Hobbs, 1978; Nelson and Ross, 1969; Pierce and Scott, 1984; Rember and Bennett, 1979a, 1979b). The parts of alluvial fans affected by liquefaction are remote from the larger channels and thus appear to be late Pleistocene age. The layer that liquefied beneath the fans must be equally as old or slightly older than the overlying fan deposit and hence also of late Pleistocene age. No other liquefaction effects were observed or reported in the extensive area of Pleistocene fan deposition in the epicentral region. This restriction of liquefaction to a very limited part of the Pleistocene materials is also consistent with behavior in other parts of the world. Sediment of that age generally has a low susceptibility to liquefaction (Youd and Perkins, 1978).

We found that the distance from the fault rupture to the farthest localities where liquefaction occurred is much smaller for this earthquake than is predicted from worldwide correlations (Fig. 13). The fissures in Highway 93 near Leslie, 23.5 mi from the fault rupture, are the most distant effects attributable to liquefaction. For a magnitude 7.3 event, that distance is less than half of the 53-mi limit given by Youd and Perkins (1978) and about one fourth of the 93-mi limit given by Keefer (1984). This shorter than expected distance to the limit of liquefaction effects is consistent with Modified Mercalli Intensity and with peak ground motions measured during aftershocks, both of which were smaller at Leslie than would normally be expected. Preliminary plots of zones of Modified Mercalli Intensity place the outer bound of the intensity VII zone just east of Mackay near Leslie (Carl Stover, oral commun., Jan. 10, 1984). The distance from the source to that bound is much shorter than would generally be expected for an earthquake with the magnitude and length of fault rupture produced by the 1983 event (J. F. Evernden, oral commun., Jan. 10, 1984); the absence of liquefaction effects beyond the zone of intensity VII, however, is consistent with past behavior

(Keefer, 1984). Peak ground motions measured at a station near Leslie were much smaller for magnitude 4 and 5 aftershocks than were expected (based on measurements from other earthquakes). For example, peak motions measured following the 1975 Oroville, Calif., earthquake (also generated by normal faulting) were approximately twice as large as those at Leslie for similar-sized aftershocks at similar distances from the recording instruments. By inference, the peak motions at Leslie during the main shock of the 1983 event also were smaller than generally expected for an event of that size (Jack Boatright, oral commun., Jan. 5, 1984). In summary, the reason liquefaction effects did not occur farther from the seismic energy source for the 1983 Borah Peak event is that intensity of ground motion was less than normal at these distances for an event of its magnitude.

Acknowledgements

We appreciate the helpful comments and suggestions of Michael Bennett and Robert Wallace who reviewed this manuscript.

References

Keefer, D. K., 1984, Landslide caused by earthquakes: Geological Society of America Bulletin, in press.

McIntyre, D. H., and Hobbs, S. W., 1978, Geologic map of the Challis quadrangle, Custer County, Idaho: U.S. Geological Survey Open-File Report 78-1059.

Nelson, W. B., and Ross, C. P., 1969, Geologic map of the Mackay quadrangle, south-central Idaho: U.S. Geological Survey Miscellaneous Geologic Investigations Map I-580.

Pierce, K. L., and Scott, W. E., 1984, Pleistocene episodes of alluvial-gravel deposition, southeastern Idaho, in Bonnichsen, Gill, and Breckenridge, R. M., eds., Cenozoic Geology of Idaho: Idaho Bureau of Mines and Geology Bulletin 26, in press.

Rember, W. C., and Bennett, E. H., 1979a, Geologic map of the Dubois quadrangle, Idaho: Idaho Bureau of Mines and Geology, Geologic Map Series, 2 Degree Quadrangle.

Remmber, W. C., and Bennett, E. H., 1979b, Geologic map of the Idaho Falls quadrangle, Idaho: Idaho Bureau of Mines and Geology, Geologic Map Series, 2 Degree Quadrangle.

Waag, C. J., 1985, Groundwater eruptions and sediment boil formation in the Chilly Buttes area, in Workshop XXVIII on the Borah Peak Earthquake: U.S.G.S. Open-File Report, in press.

Wood, S. H., Wurts, Caroline, Lane, Ted, Ballenger, Nick, Shaleen, Mary, and Totorica, Delores, 1985, Hydrologic effects of the October 28, 1983 Idaho earthquake: in workshop XXVIII on the Borah Peak Earthquake: U.S.G.S. Open-File Report, in press.

Youd, T. L., and Perkins, D. M., 1978, Mapping liquefaction-induced ground failure potential: American Society of Civil Engineers Proceedings, Journal of the Geotechnical Engineering Division, v. 104, no. GT4, p. 433-466.

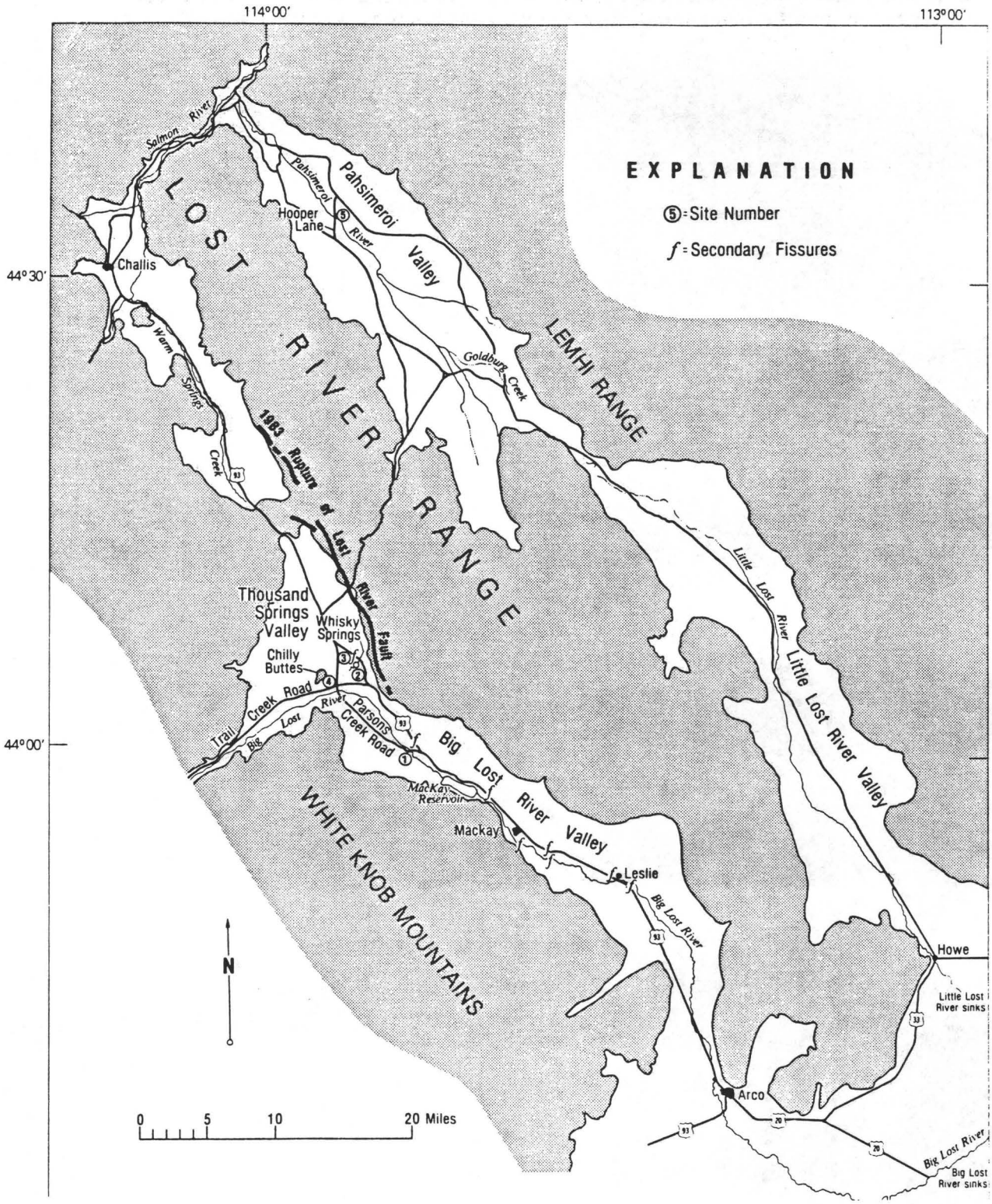

Figure 1. Region investigated showing geographic features, approximate trace of fault rupture (M. G. Bonilla and J. J. Lienkaemper, oral commun., Jan. 5, 1984), and locations of effects associated with liquefaction.

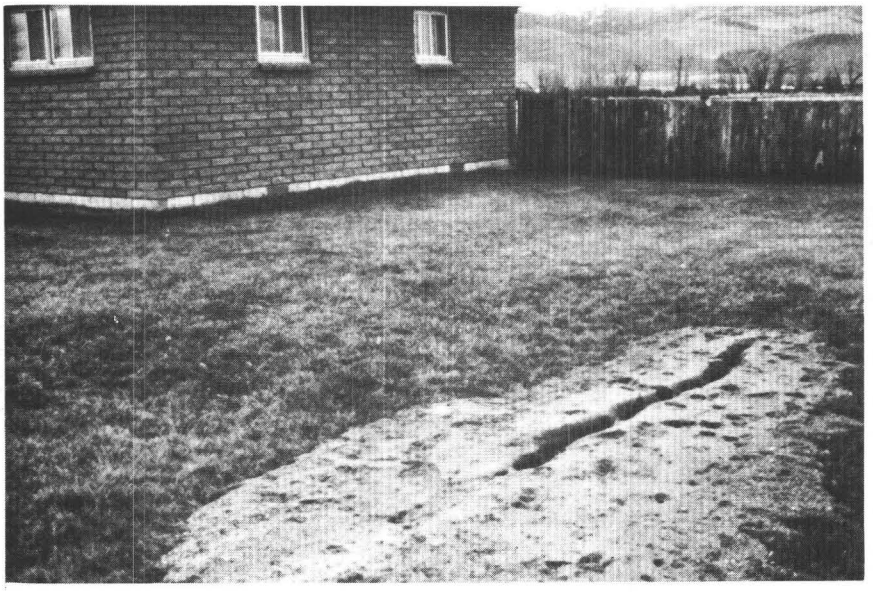

Figure 2A. Sand boil deposit near damaged house.

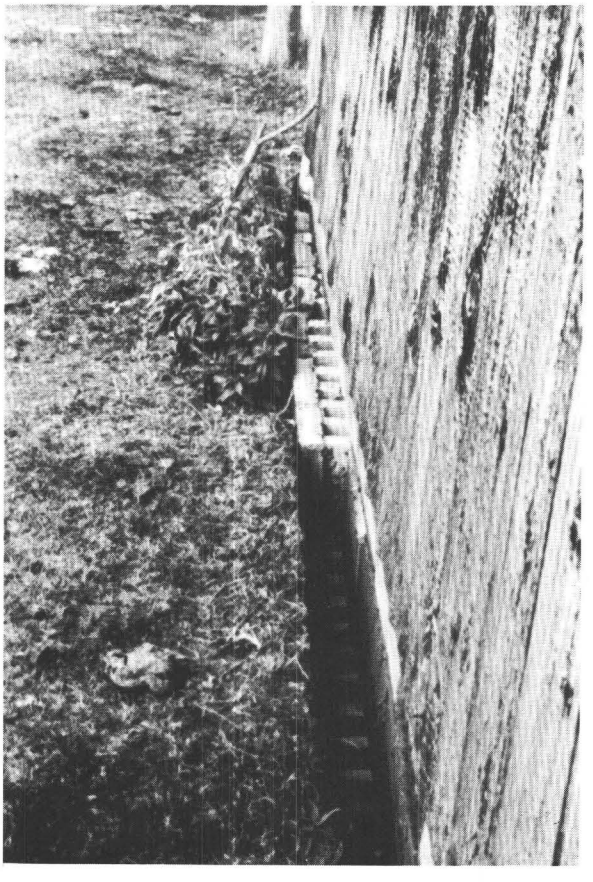

Figure 2B. Damaged perimeter foundation at back of house.

2C

Figure 2. Structures at site 1 damaged by lateral spreading: (A) damaged house with sand-boil deposit on front lawn; (B) foundation at back of house where slippage of 5 in between blocks accommodated lateral displacement that occurred beneath structure; (C) Steel-framed barn that was astride fissured zone and pulled apart at the base by about 1 ft.

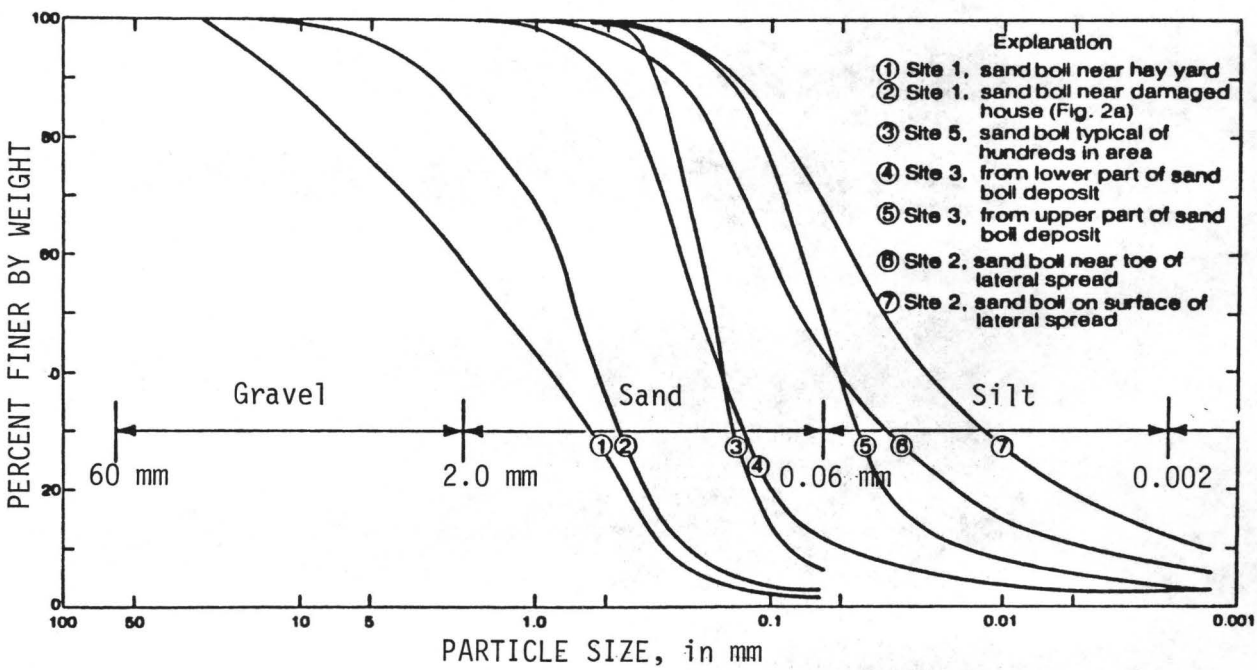

Figure 3. Grain-size distribution curves for samples taken from various sand-boil deposits.

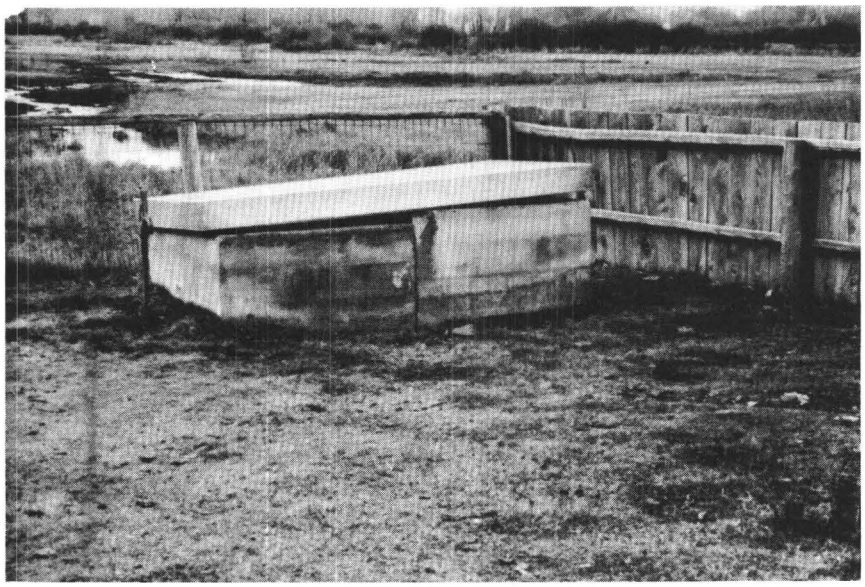

Figure 4. Concrete boxes housing well pump and water tank at site 1; the lighter box containing the pump buoyantly rose 3 in. due to liquefaction of surrounding soil. The heavier box stayed in place.

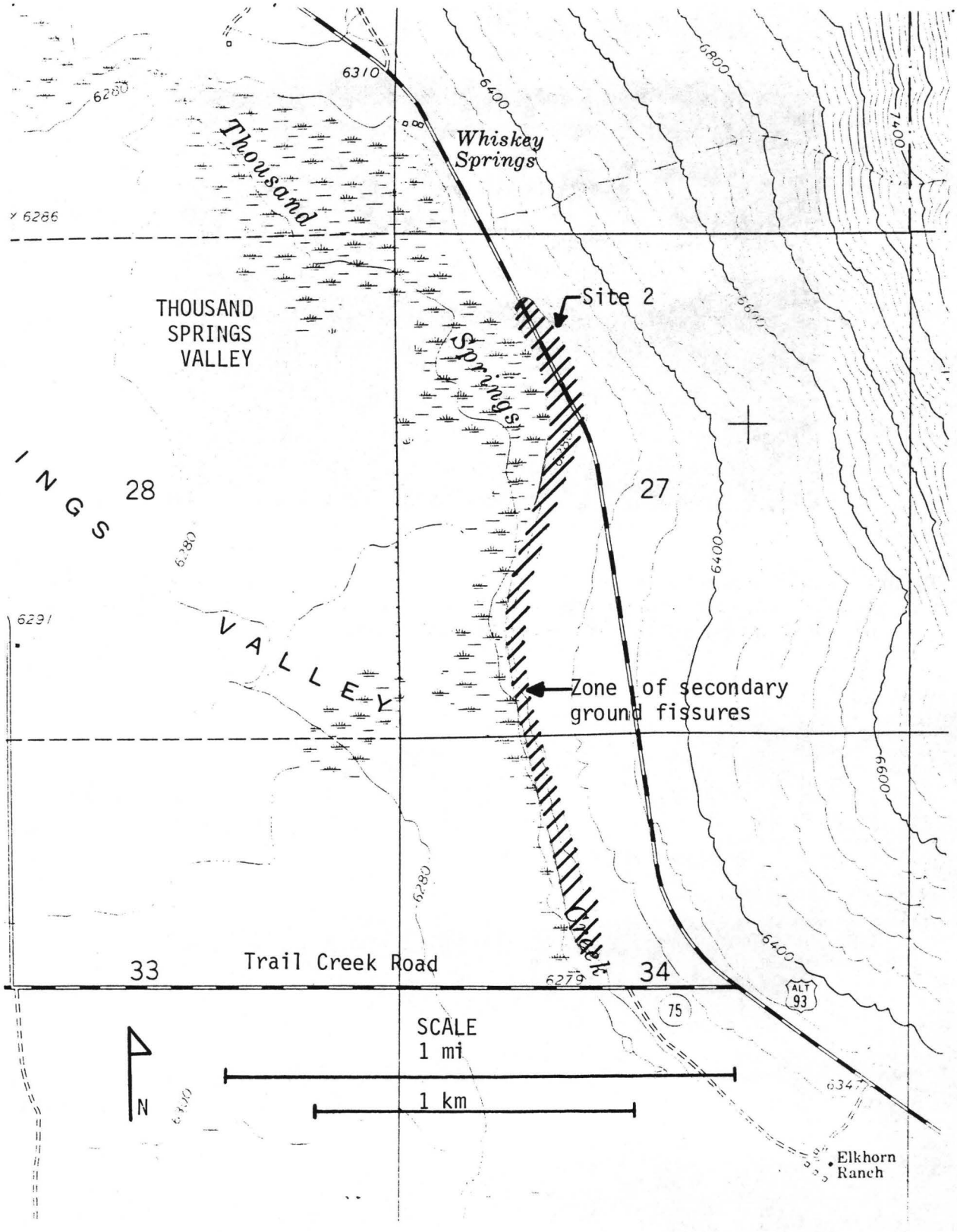

Figure 5. Zone of fissures generated by lateral spreading of distal ends of alluvial fans in the Thousand Springs Valley.

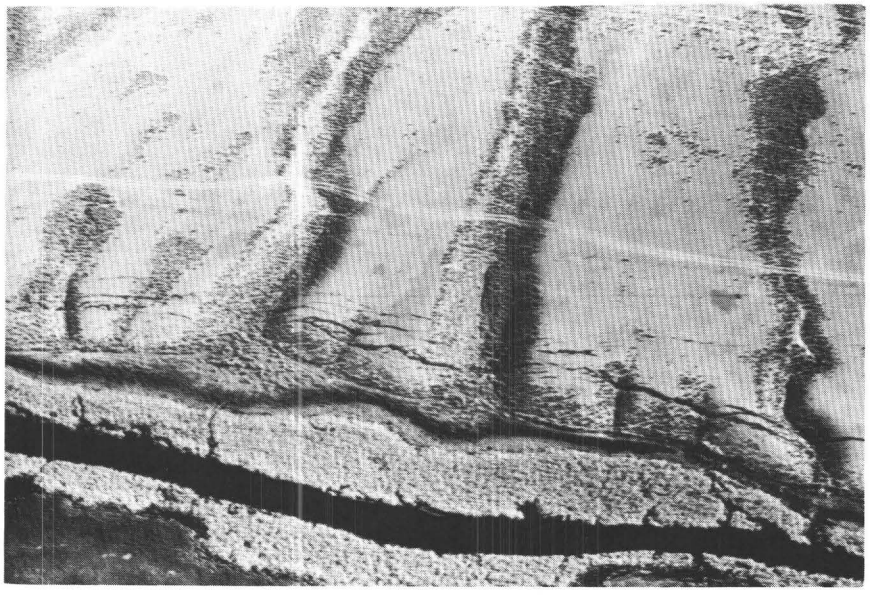

Figure 6. Oblique aerial photo of fissures along alluvial-fan fronts noted on Fig. 5. Car tracks across center of photo are about 5 ft. apart.

Figure 7. Buckled and overturned sod at the toe of lateral spread mapped on Fig. 5. This disruption occurred below damaged section of Highway 93 where fissures above highway and lateral displacement of highway was greatest (site 2).

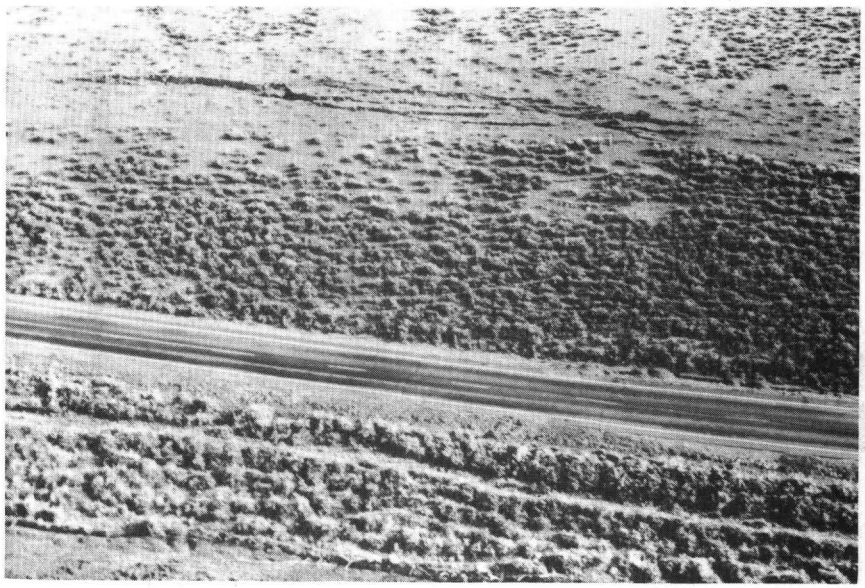

Figure 8. Aerial view of lateral spread south of Whiskey Springs that damaged Highway 93 and produced the buckling shown in Fig. 7.

Figure 9. Displacement of Highway 93 south of Whiskey Springs due to lateral spreading (site 2). Highway slabs nearest the camera moved downslope to the left. View looking north.

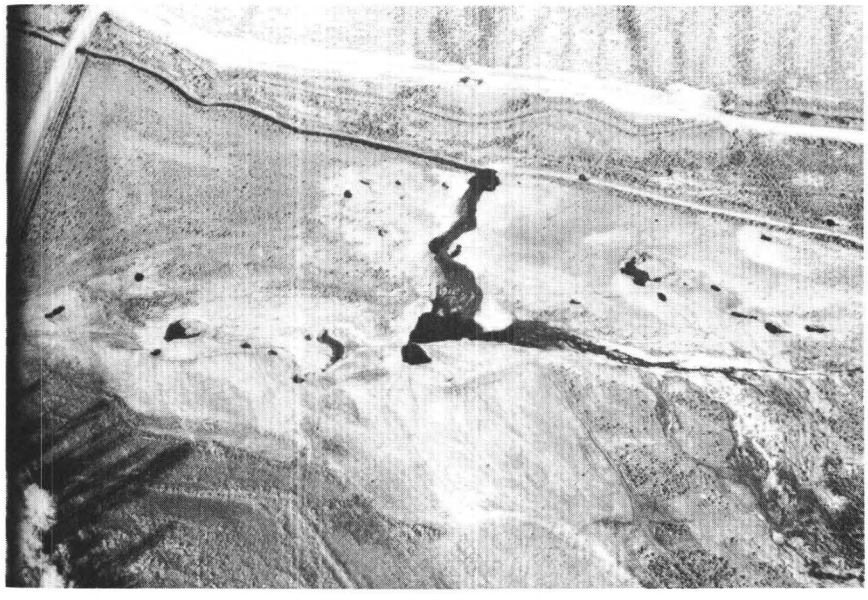

10A.

10B.

Figure 10. Craters near Chilly Buttes which were caused by violent expulsion of water from a deep aquifer and which spewed water and sediment 15 to 20 ft. into the air while eroding the craters. (A) Aerial view looking south. (B) Ground view of a typical crater showing eroded cavity and blanket of deposited sediment surrounding the crater.

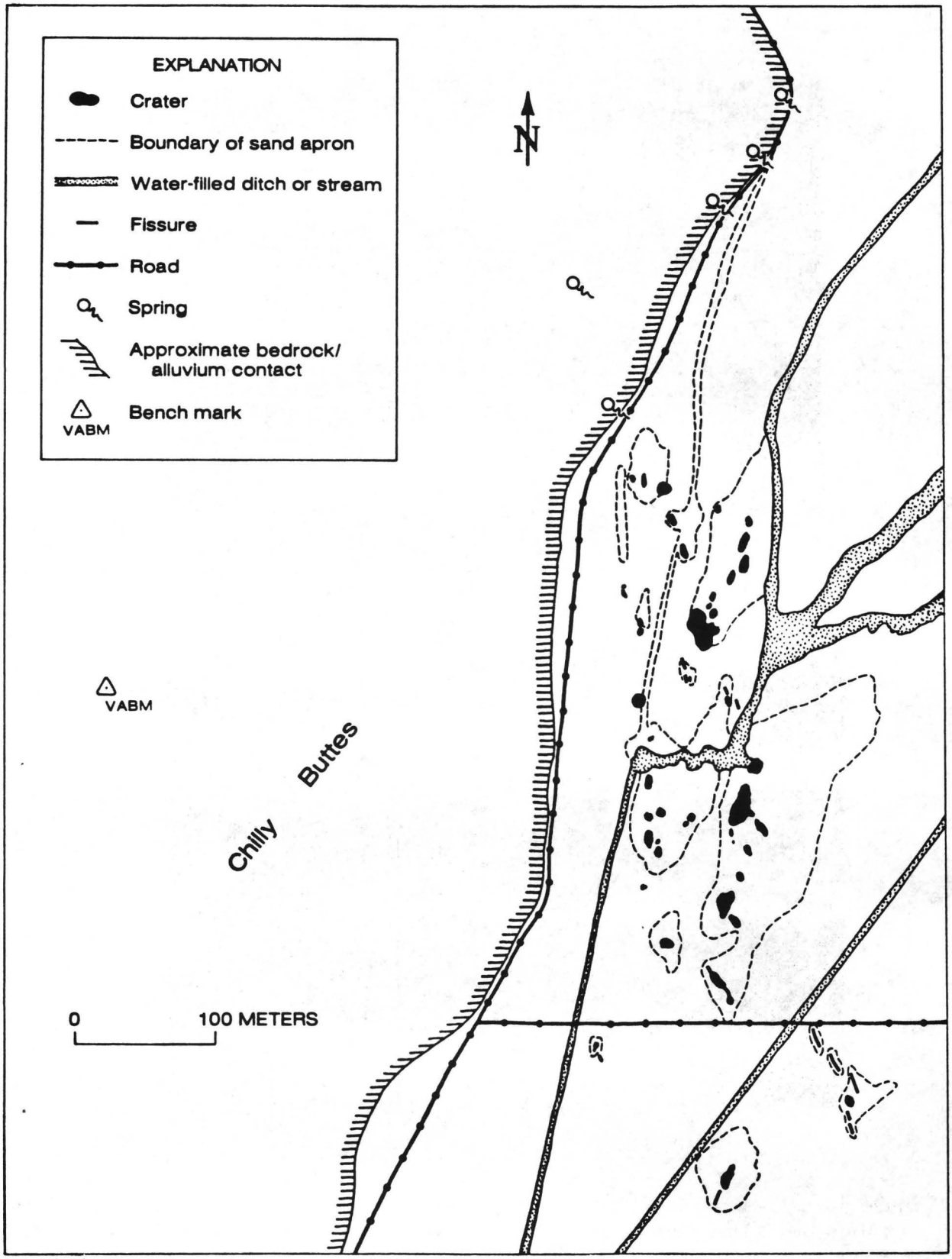

Figure 11. Chilly Buttes area showing craters and areas covered by ejected sediment.

Figure 12. Sand-boil deposit typical of hundreds that occurred in a 2,000-ft-long zone in the Pahsimeroi Valley. Sand-boil deposit is about 2 ft. wide.

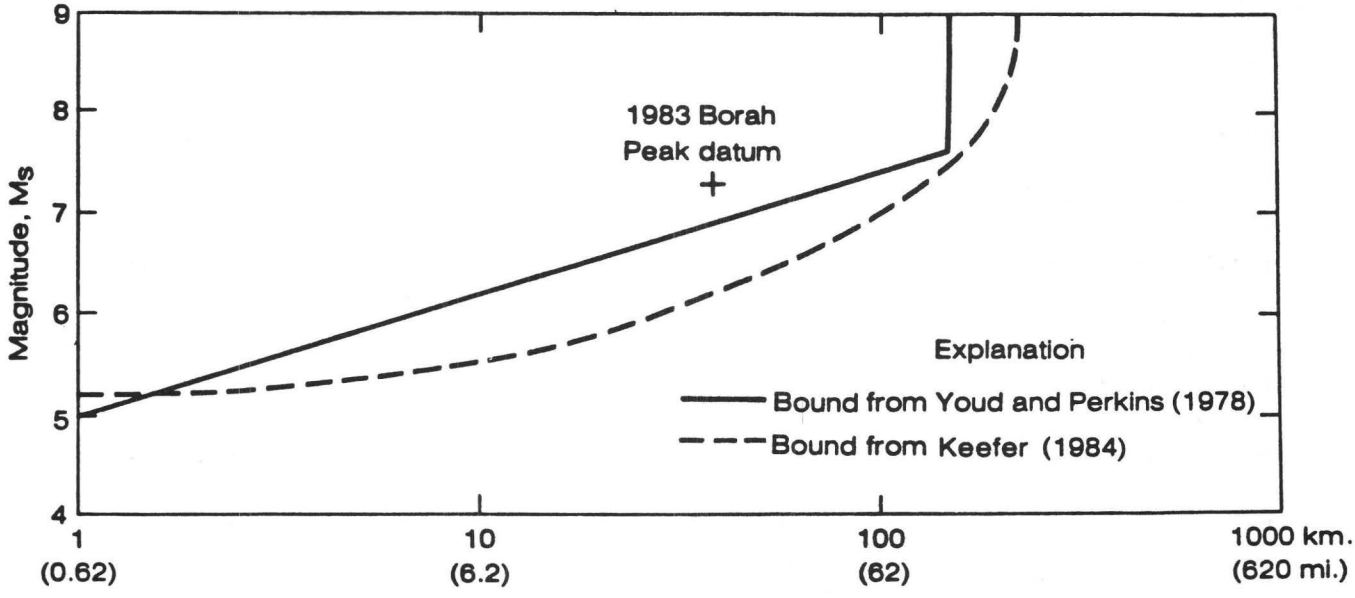

Figure 13. Distance of farthest significant liquefaction effect versus earthquake magnitude for past earthquakes. Datum from 1983 Borah Peak event is plotted for comparison.

Magnetic and Soil Gas Measurements along the Surface Rupture of the Borah Peak Earthquake of October 28, 1983

F. Scherbaum*, C. Roecken, R. H. Ware, and M. Wyss

Cooperative Institute for Research in Environmental Sciences,
University of Colorado/NOAA, Boulder, CO 80309

Abstract

In a search for magnetic signals associated with aftershocks following the Borah Peak (M_s=7.3) earthquake, we deployed two proton magnetometers near the center of the 35-km mainshock surface rupture and 10 km east of it. We observed magnetic differences on October 29, 1983, during which the two largest (m_b = 5.4 and 5.5) aftershocks occurred at a distance of less than 25 km from the magnetometers. No coseismic change in the magnetic difference between these sites was observed, with a detection threshold of 0.5 nTesla. We later found that magnetic rocks which might have generated a piezomagnetic signal are not known to exist in surface geological expressions in the Borah Peak area. However, our observation can be used to place very weak limits on any magnetic signal components that were parallel to the direction of the local geomagnetic field. Mechanisms for such signals are either the electrokinetic effect or stress changes occurring in unmapped magnetic rocks at depth. In a separate experiment we looked for hydrogen released from the surface rupture of the Lost River Range Fault. This attempt was motivated by reports of hydrogen release from active faults in Japan and the western United States. We collected soil gas samples from two localities along the mainshock surface rupture for four days following the event. Analysis by gas chromotography revealed hydrogen concentrations equal to the 0.5 ppm found in ambient air for the 13 samples collected. This result suggests that the activity on this fault, during its occurrence and for several days that followed, did not release a significant amount of hydrogen.

* permanent address: Institut fuer Geophysik, Richard-Wagner-Str. 44, D-7000 Stuttgart 1, FRG.

Introduction

Laboratory measurements and field experiments indicate that observable changes in the local magnetic field occur due to stress changes in magnetic rocks. (Hasbrouck and Allen, 1972; Martin and Wyss, 1975; Smith and Johnston, 1976; Martin et al., 1978; Rikitake et al., 1980; Shapiro and Abdullabekov, 1982; Davis and Johnston, 1983). In addition, magnetic signals can be induced by the flow of ground water through porous rocks as a consequence of stress changes associated with earthquakes (Mizutani et al., 1975, 1976; Fitterman, 1978, 1979, 1981). The streaming potential of flowing ground water that contains dissolved electrolytes creates the electrical current that in turn creates the magnetic signals, also known as the electrokinetic effect.

Because of the rather sparse spatial and temporal distribution of earthquakes and the relatively local and short-term nature of magnetic changes expected from most earthquakes, it is difficult to place magnetometers at the right place and time to observe seismomagnetic events. However, since aftershocks are expected near the epicenters and following the occurrence of large earthquakes, it is reasonable to attempt the observation of seismomagnetic events associated with aftershocks. Following this reasoning, we deployed two magnetometers near the center of the Borah Peak surface rupture one day after it occurred, with the intention of observing magnetic differences during any aftershocks. Differences were taken in order to improve the detection threshold by reducing ionospheric and magnetospheric noise (Johnston et al., 1984).

In a separate measurement, the concentration of hydrogen was determined for soil gas samples collected near the fault. The motivation for this comes from reports of high concentrations of hydrogen in soil gases associated with active faults in Japan (Wakita et al., 1980; Sugisaki et al., 1982) and in western North America (Sato et al., 1983; Ware et al., 1985). Wakita (1980) reported concentrations up to 3% in soil gases collected near the Yamasaki Fault in Japan and concentrations near the 0.5 ppm typically found in ambient air in soil gases collected several hundred meters away from the fault. Time variations of hydrogen levels over a wide range were also reported from various faults in Japan, but the highest levels were found on faults that have been active in the last 1500 years (Sugisaki et al., 1982).

In the western United States, fuel cell sensors were recently installed at a number of sites on major faults for the continuous measurement of hydrogen (Sato and McGee, 1982; Sato et al., 1983). All of these sites showed diurnal variations ranging up to 10 ppm and occasional outgassing events ranging up to 100 ppm. The outgassing events appear to precede earthquakes within about 25 km of the monitoring sites (Sato et al., 1983). It was suggested by McGee et al. (1983) that hydrogen can be generated by the reaction of water with ferrous oxide in magmas and rocks, and that pent-up hydrogen may be released during the fracturing of rocks at depth as a result of magmatic or tectonic activity. It was also suggested by Ware et al. (1985) that ferrous hydroxide may react with water to produce hydrogen.

Hydrogen is also present as an occluded gas that can be released when igneous, metamorphic, or sedimentary rocks are fractured (Giardini et al., 1976; Jiang and Li, 1981). This led Giardini et al. (1976) to suggest that hydrogen could serve as an indicator of stress changes on faults.

Another possible source of hydrogen release, suggested by Kita et al. (1983), is surface reactions between water and freshly crushed rocks. They crushed quartz and granite under various moisture conditions and as a function of temperature. They found that hydrogen is produced and that its production increases with temperature. Kita et al. (1980) also measured the isotopic ratios in hydrogen collected on the Yamasaki Fault and calculated the temperature of dissociation required to produce such ratios. Assuming a geothermal gradient of 2 or 3 degrees C per 100 m, they determined the depths of reactions corresponding to the observed ratios and concluded that they are in agreement with the depths of local microearthquakes. On the basis of this agreement, they suggested that the isotopic ratios of hydrogen in fault gases depend on the depth at which reactions occur between groundwater and surfaces freshly exposed by seismic activity.

Gold and Soter (1980) suggested abiogenic methane, generated at deep levels in the Earth, as a possible source of hydrogen. Conceivably, faults might channel this methane, and hydrogen that dissociates from it, to the surface.

In consideration of the reported observations of hydrogen release from active faults, and

taking the proposed sources of such release into account, it was reasonable to undertake the collection and subsequent analysis of soil gases associated with the Borah Peak earthquake as soon as possible following the event.

Magnetic Observations

Two magnetometers were deployed on October 29, 1983, 45 min before the two strongest aftershocks occurred at 23:29:12.0 (m_b = 5.4) and 23:39:05.7 (m_b = 5.5) Universal Time. Two Geometrics 856 proton precession magnetometers, each having 0.1 nTesla least count and a high accuracy reference oscillator, were used. In order to remove large scale magnetic variations by differencing, one of the magnetometers (B) was installed close to the visible fault scarp, the second one (A) at about ten km distance (Fig. 1).

Figure 2 shows the observed difference field. Due to technical problems, the power supply failed at about 23:45, thus yielding only a short period of data. Unfortunately, just before the first aftershock occurred, an automobile which remained near the site during the installation of the gas samplers was removed, yielding the negative spike of about 4 nTesla in Figure 2 and the following offset of about 1 nTesla. It can be seen that no coseismic changes in the magnetic field difference occurred during either aftershock, with a detection sensitivity of 0.5 nTesla. An additional 16 hrs of data were recorded during several intervals from October 29 to November 4, 1983, however, no strong aftershocks occurred during these intervals.

Hydrogen Detection

We collected gas samples at two different sites along the fresh fault scarp to look for hydrogen release associated with the Borah Peak earthquake. The gas samplers were poly vinyl chloride sewer pipes 30-cm in length and 10-cm in diameter with a cap on one end. To collect samples we dug holes in the ground and placed the samplers in them vertically with the caps on top. Soil gas was allowed to diffuse into the samplers for over 12 hours. After this time gases were withdrawn from the samplers using valved gas syringes inserted through neoprene septa. Gas samples were transported in the syringes to a gas chromatograph in the laboratory for

analysis. Details of this sampling and analysis procedure are discussed by Ware et al. (1985).

Six samples were taken at site G1 (Fig.1) from six parallel cracks in the Quaternary alluvium. The cracks ran parallel to the main scarp for a few hundred meters and had a depth of 0.5 to 1.5 m and a width of 0.2 to 1 m. The cracked area extended 30 m west from the scarp. Samplers were placed at the bottoms of the cracks, along a line perpendicular to the fault. In some of the cracks water had accumulated but no vegetation was present in any of the sampling holes. Seven samples were collected at site G2, within 15 m of the main fault scarp, at a location where the fault cuts a small creek. Samplers were placed in sands without any vegetation 2 m or more from the water, and in black basalt sands located 100 m from the creek. Paleozoic sedimentary bedrock was cropping out near the sampling sites. Standard air samples were also collected near sites G1 and G2.

The soil gas and standard air samples, which were analyzed using a gas chromatograph, showed no significant indications of elevated hydrogen concentrations, compared to the 0.5 ppm present in ambient air. Methane concentrations were in general several times above the ambient level of 2 ppm. In one sample from site G1 we detected a very high methane concentration of 2%. The sampling location did not differ in any obvious way from other nearby sampling holes. In order to determine whether the methane was of organic origin, we attempted an isotopic analysis of the G1 sample using a mass spectrometer, but it was not successful because the analysis required a larger volume than we had collected.

Discussion and Conclusions

The stratigraphic section in the Borah Peak area contains mainly Paleozoic limestones, dolomites, and quartzites, covered by alluvial fan and stream deposits (Ross, 1947). Because magnetic rocks that can act as stress transducers are not known to be present in the fault zone, the absence of coseismic magnetic field changes resulting from piezomagnetic effects is not surprising. However, we cannot rule out piezomagnetic signals generated by stress changes in unmapped magnetic rocks, or electrokinetic signals generated by stress induced flow of ground water in porous rocks.

The aftershocks occurred at a distance and in an orientation that were not optimal for detecting small coseismic magnetic field changes. Our magnetometers were located at distances greater than 20 km (Fig. 1). This is equivalent to 7 source radii of the aftershocks, considering that the source radius of an $m_b = 5.5$ event is expected to be less than about 3 km. Assuming an inverse cube decay of any electrokinetic signals with distance, and a source radius of 3 km, a signal as large as several hundred nTesla would not have been detected. In addition, the orientation was such that the magnetometer sites were nearly equidistant from the respective epicenters. For such an orientation, any radially symmetric signals would cancel in the magnetic difference. Further, the proton magnetometers are total field instruments that are only able to detect changes in the magnetic field component which are parallel to the direction of the local geomagnetic field. Any signals that were orthogonal to that direction would not have been detected. Therefore, our measurements place only a very weak limit, of less than several hundred nTesla, on any coseismic magnetic signals that may have occurred in the aftershock source radii. Of course, coseismic piezomagnetic or electrokinetic effects could very well result from stress changes outside of the source radii and at some distance from the aftershock epicenters. The very weak limits do not apply in such cases.

Considering the hydrogen release measurements, soil gas samples taken from the Lost River Range Fault for four days after the mainshock did not show elevated H_2 levels. Therefore any mechanical release of hydrogen from fractured alluvium and sedimentary bedrock, as well as any production of hydrogen from chemical surface reactions between water and freshly exposed quartzite, ferrous oxide or ferrous hydroxide rock surfaces were insignificant. Hydrogen originating at greater depths may not have been vented immediately to the surface by the earthquake and such gases might not appear until later.

The single high methane value is difficult to explain as a general release of gas from the fault because the methane concentrations in samplers located only a few meters away were several orders of magnitude lower. It is more reasonable to assume that methane was released from organic matter below the sampler.

It is known from Japanese studies as well as from studies in the western United States that the release of H_2 varies strongly with time and may or may not occur, depending on the particular geological setting of the fault. Although hydrogen was not found for several days following the earthquake, if elevated levels of hydrogen are found in future fault gas samples, it will be possible to estimate the time scale for hydrogen accumulation following seismic activity on this fault. We conclude that the release of (1) occluded hydrogen from the near surface limestones, dolomites, and quartzites, (2) hydrogen from immediate geochemical reactions involving quartz, ferrous oxides or hydroxides, and (3) immediate venting of hydrogen from deep sources, were insignificant for the several days following major seismic activity on the Lost River Range Fault.

Acknowledgements

Fran Boler helped during the first experiment, R. E. Sievers and R. M. Barkley gave assistance in gas chromatography. Financial support was provided by CIRES, the Department of Geological Sciences at the University of Colorado, by USGS grant 14-08-000121264, by NSF grant EAR-8212533, and by the Max Kade Foundation (F. Scherbaum).

References

Crone, A. J., and M. N. Machette, Surface faulting accompanying the Borah Peak earthquake, Central Idaho, *submitted to Geology*, 1984.

Davis, P. M., and M. S. Johnston, Localized geomagnetic field changes near active faults in California 1974-1980, *J. Geophys. Res. 82, 9452-9460*, 1983.

Fitterman, D. V., Electrokinetic and magnetic anomalies associated with dilatant regions in a layered earth, *J. Geophys. Res. 83, 5923-5928*, 1978.

Fitterman, D. V., Theory of electrokinetic-magnetic anomalies in a faulted half-space, *J. Geophys. Res. 84, 6031-6040*, 1979.

Fitterman, D. V., Correction to 'Theory of electrokinetic-magnetic anomalies in a faulted half-space', *J. Geophys. Res. 86, 9585-9588*, 1981.

Giardini, A. A., G. V. Subbarayudu and C. E. Melton, The emission of occluded gas from rocks as a function of stress: its possible use as a tool for earthquake prediction, *Geophys. Res. Lett., 3, 355-358*, 1976.

Gold, T., and Soter, S., The deep earth gas hypothesis, *Sci. Am. 242, 154*, 1980.

Hasbrouck, W. P., and J. H. Allen, Quasi-static magnetic field changes associated with the Cannikin nuclear explosion, *Bull. Seismol. Soc. Am. 62, 1479-1487*, 1972.

Jiang, F. L. and G. R. Li, Experimental studies of the mechanisms of seismogeochemical precursors, *Geophys. Res. Lett., 8, 473*, 1981.

Johnston, M. J. S., R. J. Mueller, R. H. Ware and P. M. Davis, Precision of geomagnetic field measurements in a tectonically active region, *J. Geomag. Geoelectr. 36, 83-85*, 1984.

Kita, I., S. Matsuo, and H. Wakita, H_2 generation by reaction between H_2O and crushed rock - An experimental study on H_2 degassing from the active fault zone, *subm. to J. Geochem*, 1983.

Kita, I., S. Matsuo, H. Wakita, and Y. Nakamura, D/H ratios of hydrogen in soil gases as an indicator of fault movements, *Geochem. J. 14, 317*, 1980.

Martin, R. J. III, and M. Wyss, Magnetism of rocks and volumetric strain in uniaxial failure test, *Pageoph 113, 51-61*, 1975.

Martin, R. J. III, R. E. Habermann, and M. Wyss, The effect of stress cycling and inelastic strain on remanent magnetization, *J. Geophys. Res. 83, 3485-3496,*, 1978.

McGee, K. A., A. J. Sutton, M. Sato, and T. J. Casadevall, Correlation of hydrogen gas emissions and seismic activity at Long Valley Caldera, California, *EOS 45, 891*, 1983.

Mizutani, H., T. Ishido, T. Yokokura, and S. Ohnishi, Elektrokinetic phenomena associated with earthquakes, *Geophys. Res. Lett., 3, 365-368*, 1975.

Mizutani, H., and T. Ishido, A new interpretation of magnetic field variation associated with the Matsushiro earthquakes, *J. Geomag. Geoelectr., 28, 179-188*, 1976.

Ross, C. P., Geology of the Borah Peak quadrangle, Idaho, *Geol. Soc. Amer. Bull., 58, 1085-1160*, 1947.

Rikitake, T., Y. Hondura, H. Tanaka, N. Ohsiman, Y. Sasai, Y. Ishikawa, S. Koyama, M. Kawamura, and K. Ohchi, Changes in the geomagnetic field associated with earthquakes in the Izu Peninsula, Japan, *J. Geomag. Geoelectr., 32, 721-740*, 1980.

Sato, M., and K. A. McGee, Continuous monitoring of hydrogen at the south flank of Mt. St. Helens, *USGS Prof. Paper 1250*, 1982.

Sato, M., K. A. McGee, A. J. Sutton, and T. J. Casadevall, Continuous hydrogen monitoring for predicting earthquakes, *EOS, 45, 758*, 1983.

Shapiro, V. A., and K. N. Abdullabekov, Anomalous variations of the geomagnetic field in east Fergana- magnetic precursors of the Alay earthquake with M = 7.0 (1978 November 2), *Geophys. J. R. Astr. Soc. 68, 1-5*, 1982.

Smith, B. E., and M. J. S. Johnston, A tectonomagnetic effect observed before a magnitude 5.2 earthquake near Hollister, California, *J. Geophys. Res. 81, 3556-3560*, 1976.

Sugisaki, R., M. Ido, H. Takeda, Y. Isobe, Y. Hayashi, N. Nakamura, H. Satobe and Y. Mizutani, Origin of hydrogen and carbon dioxide in fault gases and its relation to fault activity,

Chem. Geol., 36, 217, 1982.

Wakita, H., Y. Nakamura, I. Kita, N. Fuji, and K. Notsu, Hydrogen release: new indicator on fault activity, *Science, 210, 188*, 1980.

Ware, R. H., Roecken, C., and M. Wyss, The detection and interpretation of hydrogen fault gases, *Pageoph*, in press, 1985.

Figure Captions

Fig. 1 Map of the Mt. Borah epicentral region with the magnetometer stations (solid squares A, B) and the sites of the gas samplers (open squares G1, G2). The fault scarp was drawn from Crone and Machette (1984). The epicenter of the main shock is indicated by the crossed circle, the two strongest aftershocks are given by the solid circles.

Fig. 2 Magnetic difference field between the magnetometers at sites A and B during a time period that includes the occurrence of the two strongest aftershocks (indicated by the arrows). An automobile caused the negative spike at 22:28 as well as the following offset, as explained in the text.

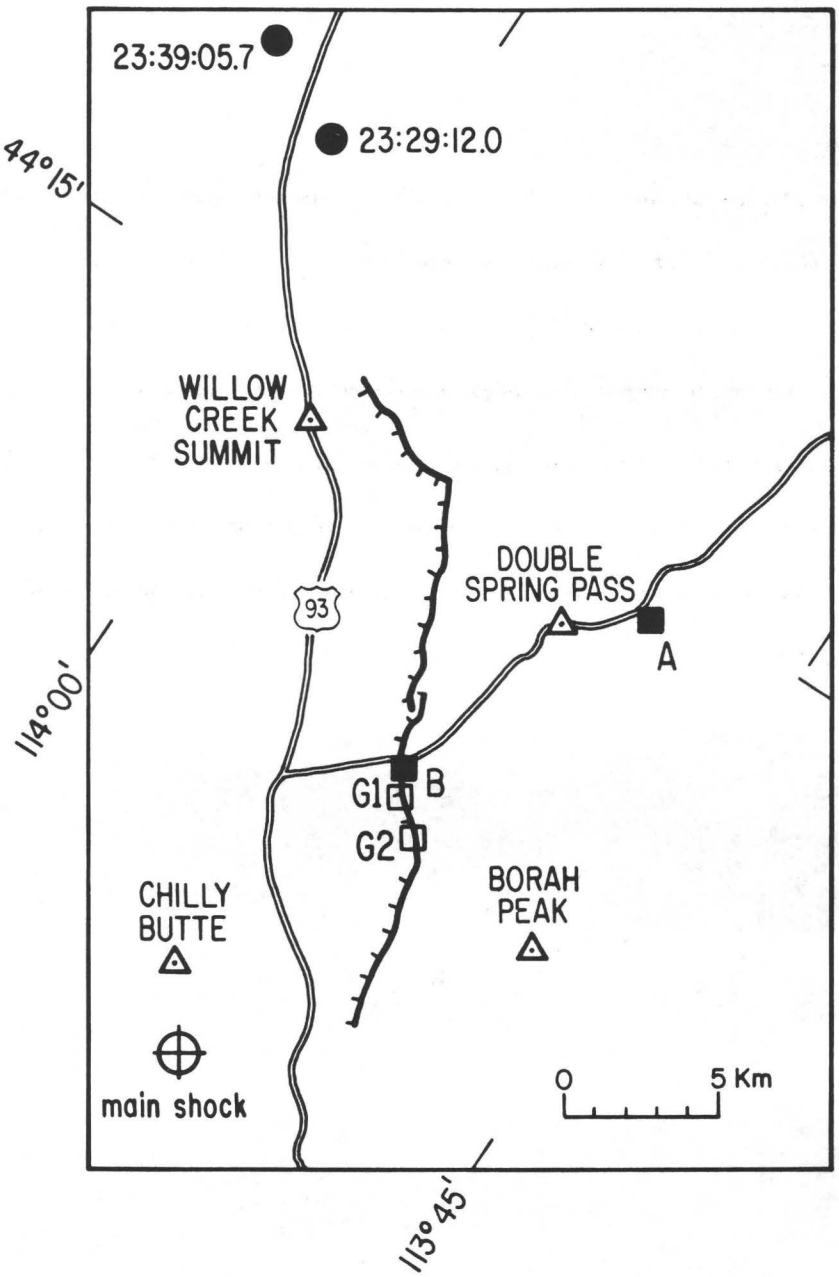
23:39:05.7
23:29:12.0
44°15'
WILLOW
CREEK
SUMMIT
93
DOUBLE
SPRING PASS
A
114°00'
G1
B
G2
CHILLY
BUTTE
BORAH
PEAK
main shock
0
5 Km
113°45'

FIGURE 1

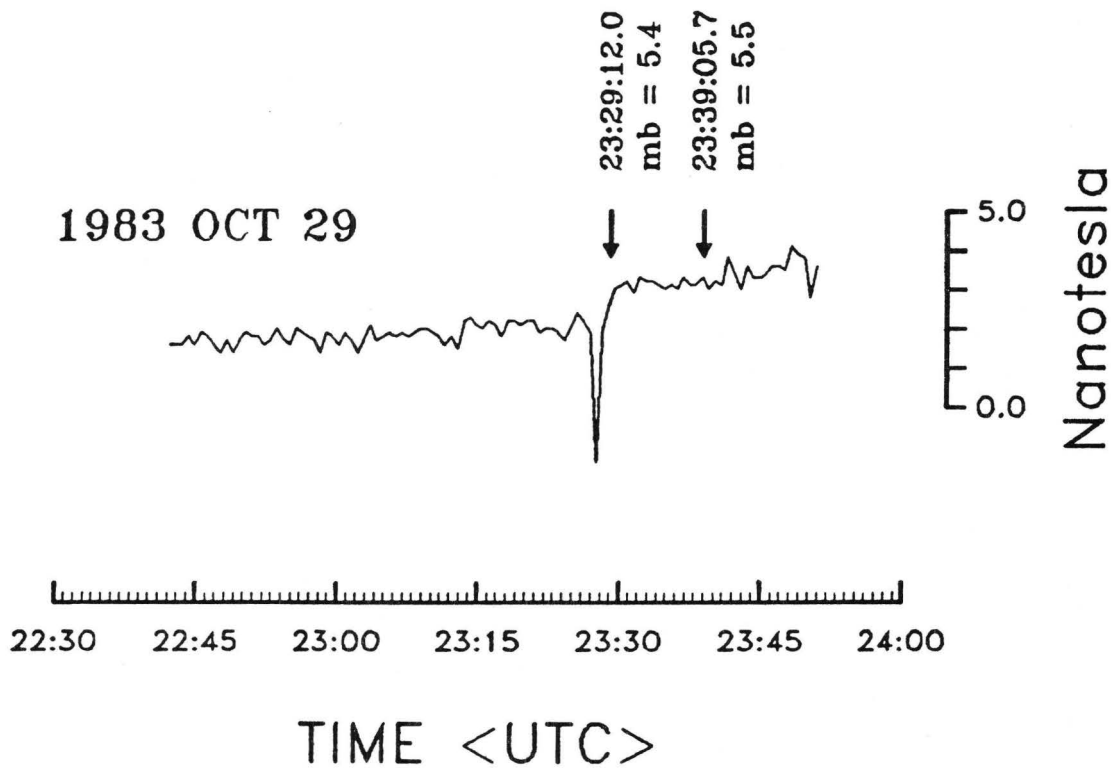
1983 OCT 29
23:29:12.0
mb = 5.4
23:39:05.7
mb = 5.5
5.0
0.0
Nanotesla
22:30
22:45
23:00
23:15
23:30
23:45
24:00
TIME <UTC>

FIGURE 2

Preliminary report on geology of Borah Peak area, Idaho, including interpretation of seismic and gravity data

by

Betty Skipp and Samuel T. Harding
U.S. Geological Survey, Box 25046, DFC, Denver, Colorado, 80225

ABSTRACT

The area of the 1983 Borah Peak earthquake is part of both the Mesozoic Cordilleran thrust belt and the Neogene basin-range structural provinces. In addition, northeast-trending faults of probable Eocene age bound the Borah Peak horst in the Lost River Range.

Paleozoic and Proterozoic(?) rocks of three thrust plates, the Copper Basin, the White Knob, and the Lost River in descending structural order, are present in the area of the earthquake. Segments of the Copper Basin and White Knob thrusts are exposed west of Thousand Springs Valley.

Northeast-trending normal faults of probable Eocene age bound the Borah Peak horst within the Lost River thrust plate in the Lost River Range. A 1974 regional gravity survey by Mabey and others indicates that a western projection of the horst extends into the southern part of the Thousand Springs Valley under thin cover, and connects the Lost River Range in the subsurface with the northern part of the White Knob Mountains. This largely buried ridge (horst) is represented at the surface by several bedrock buttes, including Chilly Buttes. Gravity data north of Chilly Buttes suggests 600 to 1000 m of fill in deeper parts of the Thousand Springs Valley.

Neogene basin-range faults, including the Lost River fault, offset both the thrust plates and the Eocene fault blocks. The part of the Lost River fault that ruptured in 1983 is adjacent to deeper parts of the northern Thousand Springs Valley. The fault did not rupture where bedrock of the Willow Creek summit area juxtaposes the Lost River Range, and to the south, the fault terminates in the area of the Borah Peak horst.

A reflection seismic survey across the Lost River fault at Doublesprings Pass Road shows the fault to be a wide and diffuse zone with a steep dip to the southwest. Both the thick valley fill of the hanging wall and bedrock of the footwall are cut by numerous synthetic and antithetic faults. In addition, reflectors in the valley fill, possibly cemented gravels, have a reverse dip toward the fault plane, and the fill thickens in the same direction, giving older beds steeper dips than younger. These geometries are common for flattening (listric) normal faults.

INTRODUCTION

The area in east-central Idaho that was affected by the Borah Peak earthquake of October 28, 1983, is a part of both the Cordilleran thrust belt and the Basin and Range structural provinces. Thrust plates in the region were emplaced from west to east during Mesozoic, possibly mid-Jurassic to Cretaceous time. Northeast-trending normal faults of probable Eocene age offset rocks of the thrust plates, and, in the Borah Peak area, the Eocene faults are cut by younger basin-range extension faults that have been active since middle Miocene time.

Published large-scale geologic maps of a part of the area affected by the 1983 earthquake (fig. 1) include the Borah Peak 30-minute quadrangle (Ross, 1947), the Doublespring 15-minute quadrangle (Mapel and others, 1965), the Mackay 30-minute quadrangle (Nelson and Ross, 1969), and the Lone Pine Peak 15-minute quadrangle (Hays and others, 1978). Most of the fault system which bounds the Lost River Range on the west, and that ruptured again in the 1983 earthquake, was not included on Ross' 1947 map of the Borah Peak area. The only segment of the fault that was mapped was on the east side of the Willow Creek summit area and it was shown as a thrust fault. This range front fault was identified as a normal basin-range fault by Baldwin (1943) in his unpublished dissertation, and the fault was named the Lost River fault in a later regional study (Baldwin, 1951). The northern part of the Lost River fault was included on the geologic map of the Doublespring quadrangle (Mapel and others, 1965). The epicentral area of the 1983 earthquake is covered by a reconnaissance geologic map of the Mackay 30-minute quadrangle (Nelson and Ross, 1969).

MESOZOIC THRUST PLATES

Parts of two major thrust faults and three thrust plates make up the area surrounding Thousand Springs Valley (fig. 2). From structurally highest to lowest the thrust faults and plates are: (1) the Copper Basin thrust fault, which is the lower boundary thrust of the Copper Basin thrust plate (Skipp and Hait, 1977; Dover, 1981), (2) the White Knob thrust fault, which is the lower boundary thrust of the White Knob thrust plate (Skipp and Hait, 1977; unpublished mapping by Skipp), and (3) western parts of the Lost River plate (fig. 2), a northward extension of the Lost River-Arco Hills allochthon (Skipp and Hait, 1977). The lower boundary thrust of the Lost River thrust plate lies east of the area of figure 1. The interpreted distribution of the rocks of these three thrust plates beneath the fill of Thousand Springs Valley is shown on figure 3.

Rocks of the Copper Basin thrust plate which are exposed at the surface (fig. 2), were involved only in secondary slumps, rockfalls, and mudslides that resulted from seismic shaking during the Borah Peak earthquake, and subsequent hydrologic changes. These rocks are not discussed further.

Rocks of the White Knob and Lost River thrust plates were involved in the faulting that accompanied the earthquake (figs. 2, 3). The White Knob thrust plate which includes Chilly Buttes near the epicenter of the earthquake and much of the western and southern sides of Thousand Springs Valley, consists of a sequence of 2500 m of Lower Mississippian to Lower Pennsylvanian sedimentary rocks. These rocks include mudstone, siltstone, and limestone of the McGowan Creek Formation, limestone, minor conglomerate, sandstone and mudstone of the thick White Knob Formation, sandstone of the Bluebird Mountain Formation, and sandy and argillaceous limestone of the lower part of the Snaky Canyon Formation. A description of some of these formations on the west side of Thousand Springs Valley is included on the preliminary geologic map of the Challis 1° x 2° quadrangle (Fisher and others, 1983).

Rocks of the Lost River plate make up the Lost River Range, the Willow Creek summit area, and part of the mountains on the northwest side of Thousand Springs Valley. They were offset by 1983 ruptures along parts of the Lost River fault, and by fault scarps in the Arentson Gulch area. Rocks of the plate are more than 5000 m thick and range in age from Proterozoic(?) to Early Pennsylvanian. The Proterozoic(?) and Lower Paleozoic rocks have been described by Mapel and others, (1965), Hays and others, (1978), Hays and others, (1980), and Ingwell, (1980); and the Upper Paleozoic rocks have been described by Mapel and others, (1965), Huh, (1967), Sandberg, (1975), and Mamet and others, (1971). Mississippian rocks of the Lost River plate include the McGowan Creek Formation and an overlying carbonate bank sequence equivalent in age to the White Knob Limestone in the adjacent White Knob plate. The carbonate bank sequence includes, in ascending order, the Middle Canyon, Scott Peak, South Creek, Surrett Canyon and Arco Hills Formations (Skipp and others, 1979).

Compressional structures in the thrust plates include open to overturned, generally east-verging concentric folds with north-northwest-trending axes, zones of shearing and brecciation, and prominent axial-plane cleavages. Some of these features are shown on published geologic maps by Ross, (1947), Mapel and others, (1965), Hays and others, (1978), and Fisher and others, (1983).

EOCENE NORMAL FAULTS

The Rock Creek-Mahogany Creek, the Elkhorn Creek, and the Leatherman Pass faults are all northeast-trending faults in the Lost River Range that offset rocks of the Lost River thrust plate, and are truncated by the younger Lost River normal fault (fig. 3). The Rock Creek-Mahogany Creek and the Leatherman Pass faults, named by Baldwin (1951), define the Borah Peak fault block (horst) (figs. 1, 3) in which complexly folded and faulted rocks of Paleozoic and Proterozoic(?) ages are raised as much as 3000 m against younger Paleozoic rocks (Baldwin, 1951; fig. 1).

South of the Borah Peak horst, and immediately southwest of the town of Mackay (fig. 1), there is a similar structure, here named the White Knob horst. This horst is cored by an exposed middle Eocene pluton (Nelson and Ross, 1968), and is bounded by a fault that cuts Eocene Challis Volcanics on the southeast, and a fault that is buried by the same volcanics on the northwest (fig. 1). Both faults probably are related to uplift of the core pluton, and are, therefore, inferred to be largely of Eocene age (Nelson and Ross, 1968). The proximity of the White Knob horst to the Borah Peak horst, and the similarity in trends, suggests the Borah Peak horst also may be cored by an Eocene pluton, and the three northeast trending faults of the Borah Peak horst also probably are mostly Eocene, because they reportedly do not offset Challis Volcanics (Baldwin, 1951).

A regional gravity survey of southern Idaho that includes the area of the 1983 earthquake (Mabey and others, 1974) suggests the presence of an extensive, northeast-trending bedrock ridge in the shallow subsurface of the southern part of the Thousand Springs Valley (fig. 4), that may be a downdropped western projection of the Borah Peak horst. The ridge is expressed on the surface by Chilly and Swensen Buttes, and Bartlett Point (fig. 2). A cross section located between the small butte northeast of Bartlett Point and Challis Volcanics to the southeast (fig. 2), that is based on seismic reflection data, shows just 60 m of valley fill over this bedrock ridge (Crosthwaite and others, 1970), whereas gravity data over deeper parts of the Thousand Springs Valley and the Barton Flats area (fig. 2) indicate

EXPLANATION

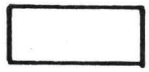

Quaternary-Tertiary deposits undivided

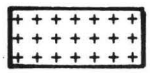

Challis Volcanics (largely Eocene)

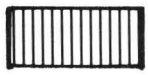

Eocene intrusive rocks

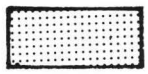

Mississippian and minor Pennsylvanian sedimentary rocks undivided

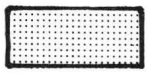

Lower Paleozoic sedimentary rocks undivided

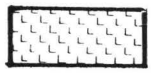

Proterozoic (?) sedimentary rocks undivided

FAULTS: *dotted where concealed*

Normal fault; bar and ball on downthrown side

Thrust fault, teeth on upper plate

Figure 1. Simplified geologic map and index map of the Borah Peak area, south-central Idaho, modified from Bond (1978), showing Lost River fault and epicenter of the October 28, 1983, earthquake. Heavy solid line indicates area of figures 2, 3, and 4. Short-dashed line indicates location of southern part of geologic map of Doublespring 15-minute quadrangle (Mapel and others, 1965). Area north of latitude 44° and east of longitude 114° is part of geologic map of Borah Peak 30-minute quadrangle (Baldwin, 1943; Ross, 1947). Area south of latitude 44° and east of longitude 114° is part of geologic map of Mackay 30-minute quadrangle (Nelson and Ross, 1969). Area west of the Doublespring 15-minute quadrangle is part of the geologic map of the Lone Pine Peak 15-minute quadrangle (Hays and others, 1978)

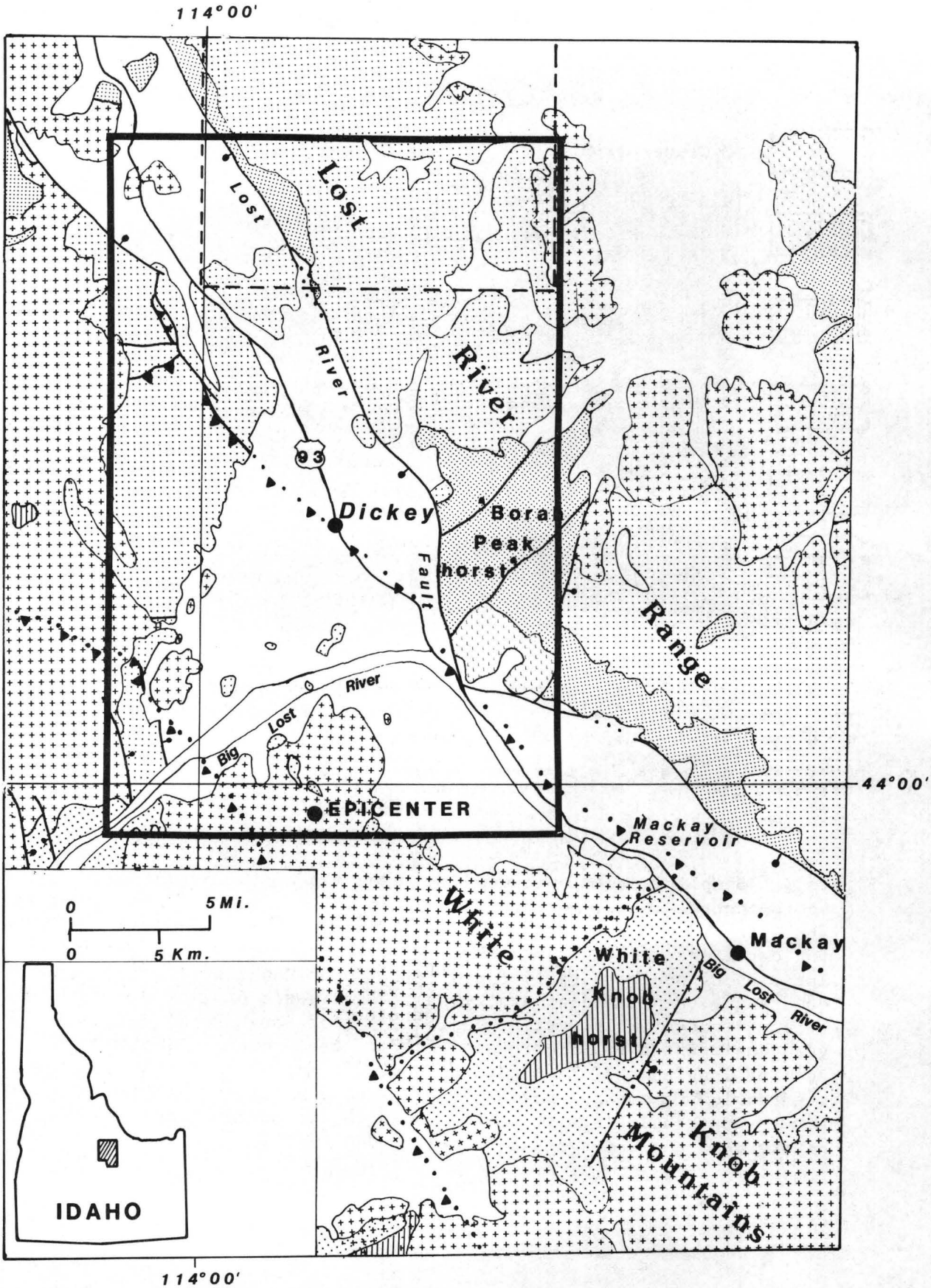
114°00'
Lost River
Lost River
93
Dickey
Borah Peak horst
Fault
Range
Big Lost River
EPICENTER
44°00'
Mackay Reservoir
0 5 Mi.
0 5 Km.
IDAHO
White Knob horst
White Knob Mountains
Mackay
Big Lost River
114°00'

EXPLANATION

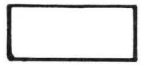

Quaternary-Tertiary deposits undivided

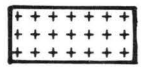

Challis Volcanics (largely Eocene)

Mississippian McGowan Creek, Scott Peak, South Creek and Surrett Canyon Formations of Lost River thrust plate (includes minor Pennsylvanian rocks)

Mississippian McGowan Creek and White Knob Formations of White Knob thrust plate(includes minor Pennsylvanian rocks)

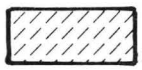

Mississippian Copper Basin Formation of Copper Basin thrust plate

Lower Paleozoic and Proterozoic(?) sedimentary rocks undivided of Lost River thrust plate

FAULTS: *dotted where consealed*

Normal fault; bar and ball on downthrown side

Thrust fault; teeth on upper plate

Segment of Lost River normal fault that ruptured in 1983

Figure 2. Geologic map of Borah Peak area based on Ross (1947), Baldwin (1943), Nelson and Ross (1969), and Mapel and others, (1965), and unpublished mapping by Betty Skipp, that shows epicenter of Borah Peak earthquake, generalized trace (hachured lines) of new ground ruptures on the Lost River fault (see Crone and others, 1985, for details), other major faults, and geographic features referred to in text. Hamilton Springs fault from Crosthwaite and others (1970).

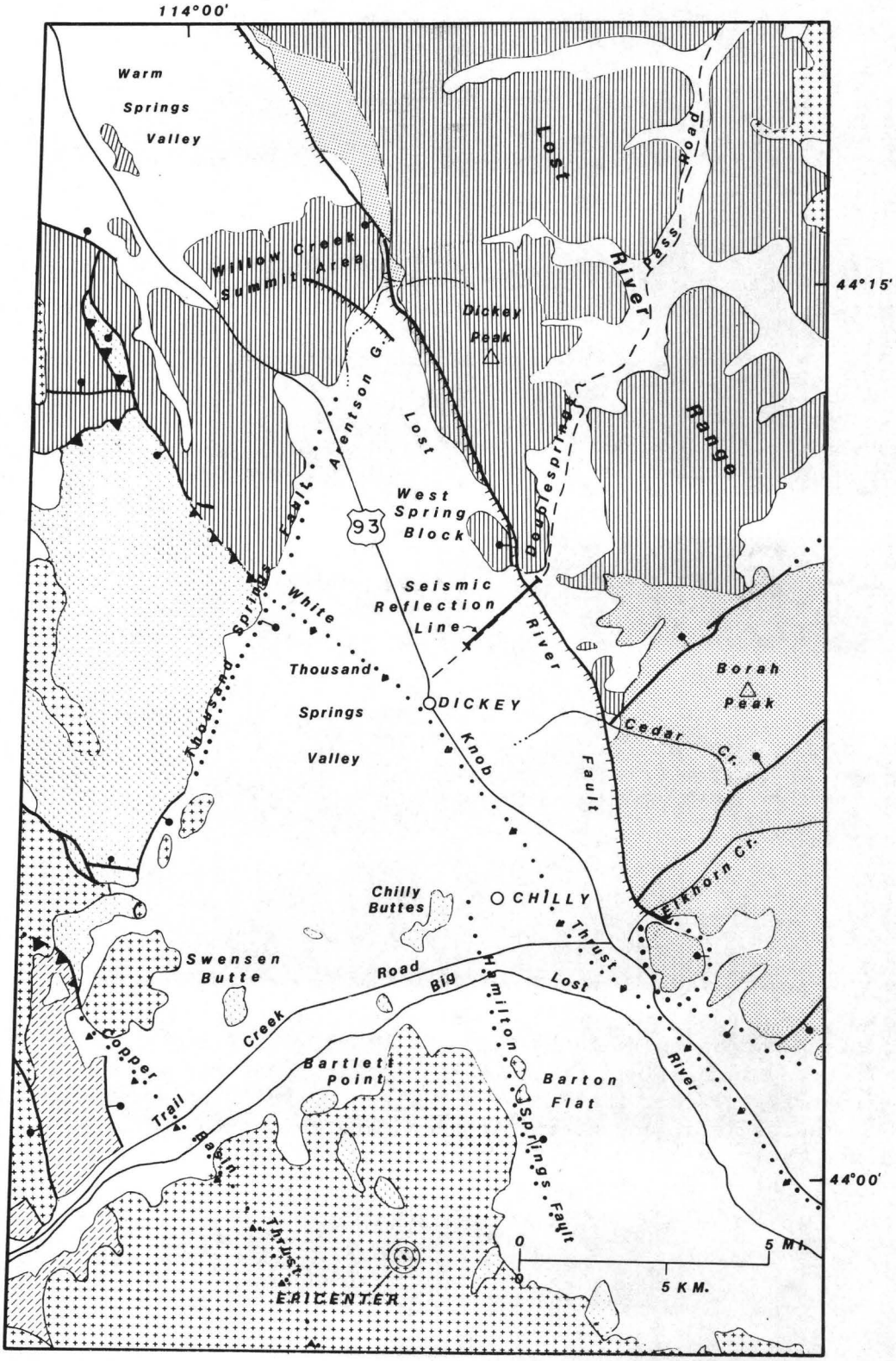
114°00'
Warm
Springs
Valley
Willow Creek
Summit Area
Dickey
Peak
Lost
River
Pass
Lost
River
Range
44°15'
Lost
River
Fault
Aventson G.
West
Spring
Block
93
Seismic
Reflection
Line
White
Thousand
Springs
Valley
Thousand Springs Fault
DICKEY
Knob
Fault
Borah
Peak
Cedar Cr.
Elkhorn Cr.
Chilly
Buttes
CHILLY
Thrust
Swensen
Butte
Road
Big
Lost
Hamilton
Creek
Bartlett
Point
Barton
Flat
River
Springs Fault
Copper
Trail
Basin
Thrust
EPICENTER
44°00'
0
5 Mi.
5 KM.

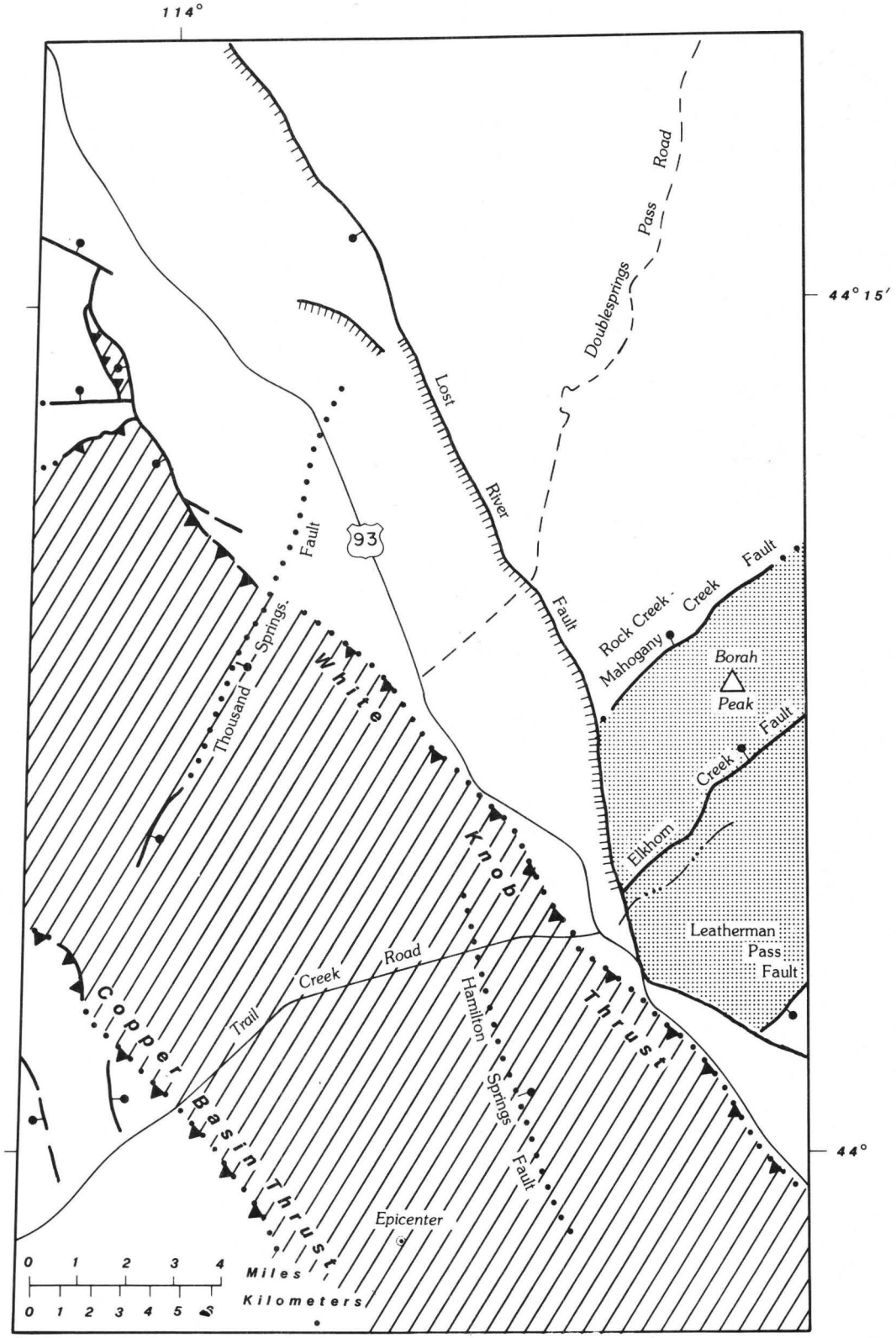

Figure 3. Generalized tectonic map of Borah Peak area showing inferred distribution of thrust faults and thrust plates beneath valley fill, and position of Borah Peak horst (stippled pattern) and bounding faults. Rocks of White Knob thrust plate indicated by diagonal line pattern. Rocks of Copper Basin thrust plate present in unpatterned area southwest of the White Knob plate, and rocks of the Lost River thrust plate are the unpatterned area to the northeast.

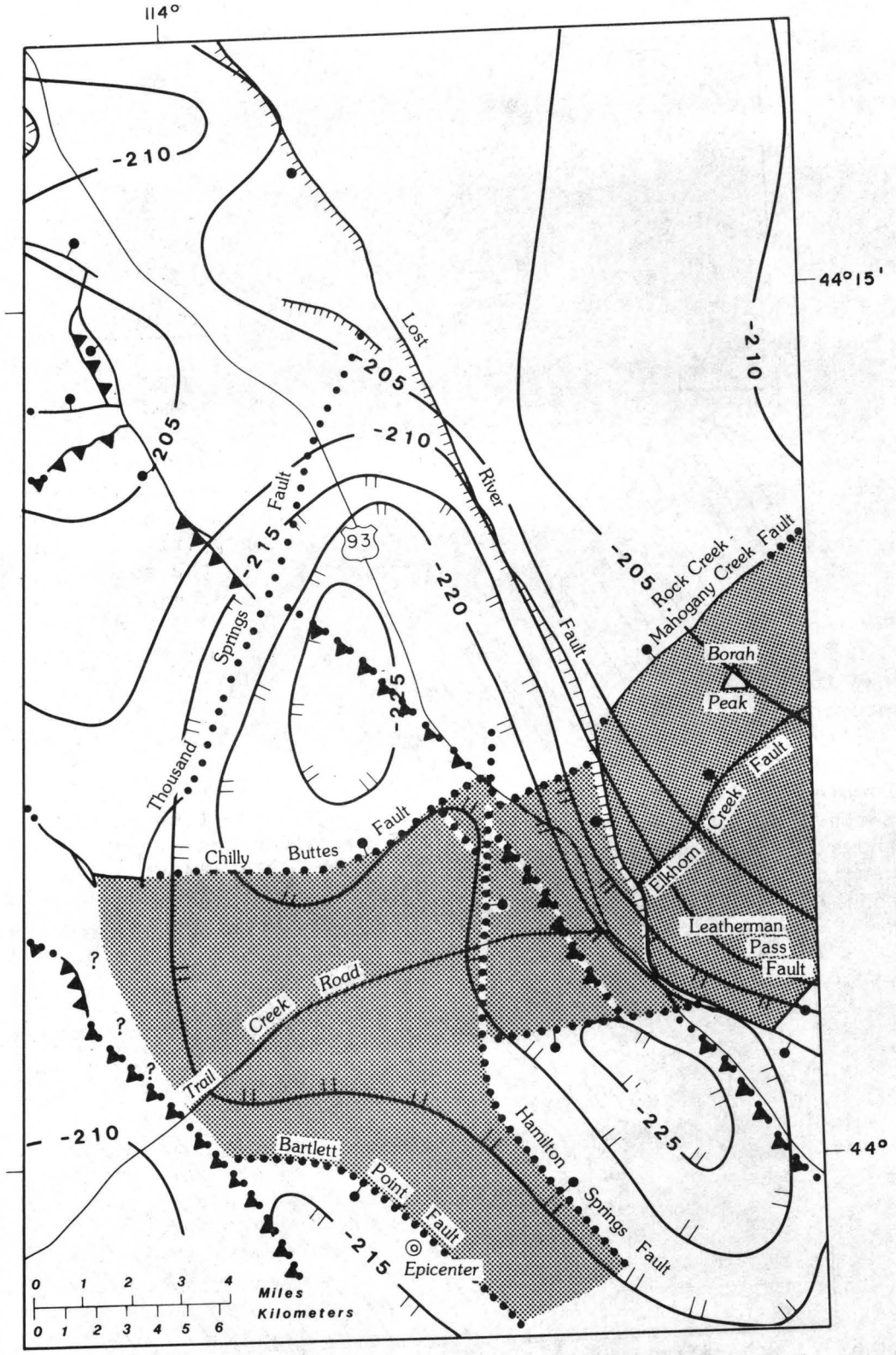

Figure 4. Complete Bouguer gravity anomaly map of the Borah Peak area with a 5 milligal contour interval, slightly modified from Mabey and others (1974). Locations of inferred shallowly buried bedrock ridges (stippled pattern), and associated buried normal faults are shown in southern part of Thousand Springs Valley. Generalized trace of new ruptures on Lost River fault shown by hachures.

about 600 to 1000 m of valley fill (Crosthwaite and others, 1970). The interpretation of the positions of major buried faults and bedrock ridges in the southern part of the Thousand Springs Valley based on gravity data (fig. 4) shows the Chilly Buttes fault on the northern margin of the largely buried ridge, and suggests that the ridge is offset by young basin-range faults with north and northwest trends, such as the Hamilton Springs fault of Crosthwaite and others (1970), and the Bartlett Point fault of this paper.

NEOGENE AND YOUNGER BASIN-RANGE FAULTS

Basin-range faults of middle Miocene to Quaternary age locally disrupt thrust plates in the area and offset the Eocene normal faults. A 36 km-long part of the Lost River fault, the major basin-range fault in the area, was reactivated during the 1983 earthquake (fig. 1; Crone and Machette, 1984; Crone and others, 1985). Net slip on the fault was mainly normal with a small sinistral component and averaged 0.8 m (Crone and Machette, 1984). The hypocenter of the main shock was about 16 km deep (fig. 2) and had a preferred nodal plane that strikes N 22° W and dips 59° to the southwest (Crone and Machette, 1984; Smith and others, 1984). The southeast part of the zone of aftershocks is near the southern termination of 1983 surface breakage, and defines "a single plane dipping 45°SW that intersects the surface near the [Lost River] fault scarp" (Smith and others, 1984). Minimal displacement on the Lost River fault is estimated to be at least 2500 m, the sum of the present topographic relief and the thickness of fill in Thousand Springs Valley (Crone and Machette, 1984).

A high resolution seismic reflection survey conducted along the Doublesprings Pass Road across the Lost River fault shortly after the earthquake (figs. 2, 5) substantiates the steep western dip of the fault, and shows the fault zone to be about 560 m wide. In addition, rocks of both the hanging wall and footwall are cut by several antithetic faults similar to those observed at the surface (Crone and Machette, 1984), and those indicated by shallow reflectors (Miller and Steeples, 1985). A prominent reflector west of the fault (labelled A on fig. 5) at about 156 m depth, possibly a zone of cemented gravel, dips about 1 1/2° t° 4° into the fault zone. A deeper band of reflectors (labelled B on fig. 5), at about 500 m depth, also dips toward the fault zone at an angle of about 4°, and strata between these two reflectors thicken toward the fault, giving the older strata steeper dips than the younger. These characteristics, inclination and thickening of strata toward a fault zone, are considered indicative of curving listric normal faults that flatten with depth (Bally and others, 1966; Dahlstrom, 1970). A curving geometry appears to be at odds with a planar fault suggested by other investigators (Smith and others, 1984; Stein and Barrientos, 1985), but this may indicate a more complex system of faults than has been considered. A similar northeast dip for valley fill is reported from a deep industrial reflection seismic line in the southern part of Thousand Springs Valley (unpublished data cited in Smith and others, 1985). If reflector C east of the fault zone (fig. 5), correlates with reflector B west of the fault zone, a throw of about 180 m is indicated on the fault since the deposition of the offset late Cenozoic strata.

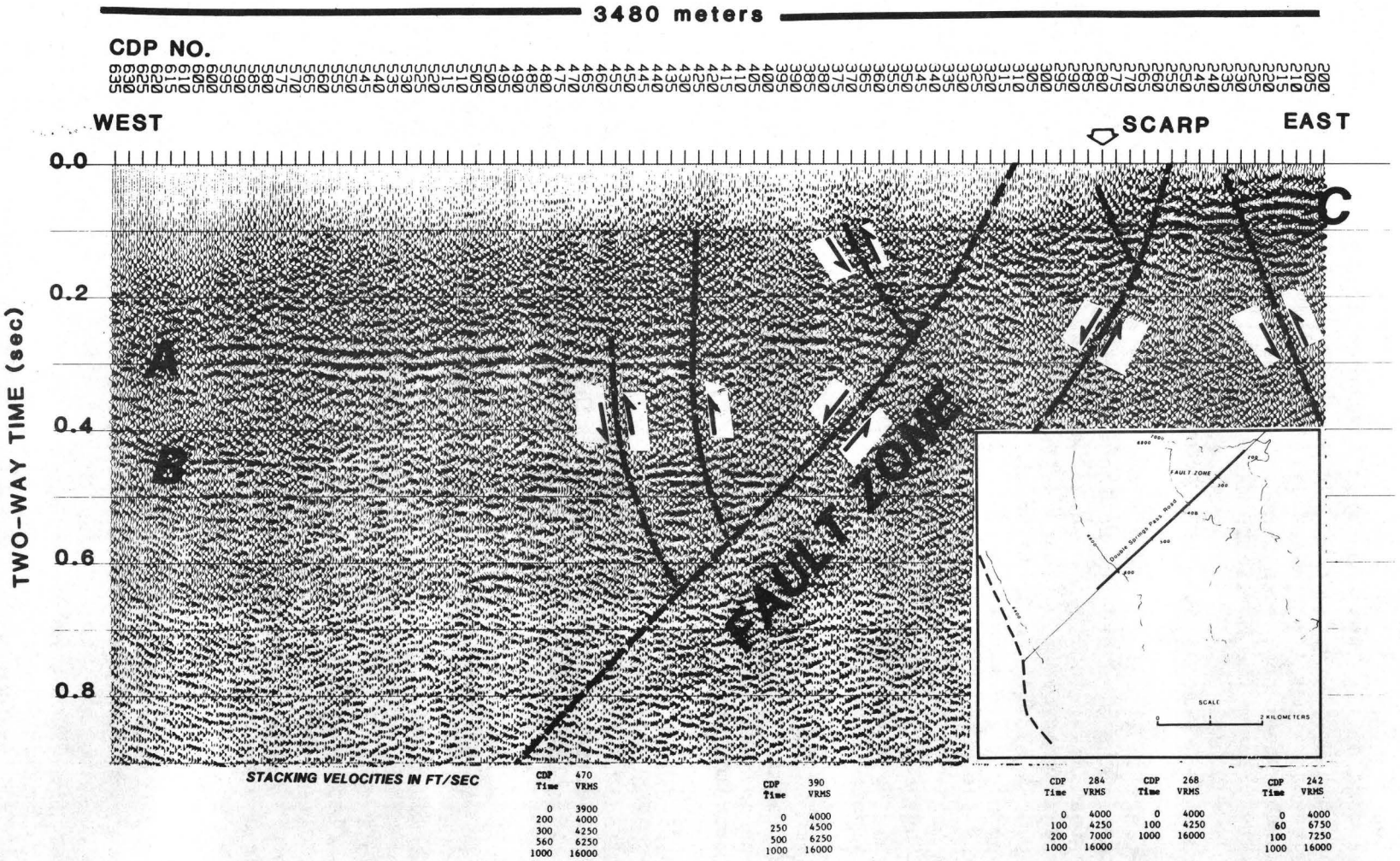

Figure 5. Migrated high resolution seismic reflection line along Double-springs Pass Road (fig. 2), showing interpreted faults (dashed lines). Reflectors labelled A, B, and C discussed in text. No coherent energy return was obtained from below about 0.6 seconds, or about 740 m.

Surface ruptures along the main Lost River fault associated with the Borah Peak earthquake formed two strands separated by a 4.8 km gap east of the Arentson Gulch area (fig. 2). The gap coincides with the position of the northeast trending bedrock ridge, the Willow Creek Summit area, that joins the Lost River Range with mountains to the west. Similarly, the southern segment of the surface fault dies out just south of the projection of the Chilly Buttes fault, which forms the northern margin of another bedrock ridge that joins the Lost River Range with the northern part of the White Knob Mountains. These two northeast-trending ridges seem to have influenced the propagation and extent of recent ruptures along the fault.

DISCUSSION

Little is known, in detail, about the bedrock geology in the epicentral area of the Borah Peak earthquake. Results of Skipp's preliminary post-earthquake mapping of the West Spring block, the Willow Creek Summit block, the Chilly Buttes area, and the Elkhorn Creek area, are reported below (fig. 2).

The West Spring block (fig. 2) contains folded, fractured, and sheared limestones of the Upper Mississippian Scott Peak Formation. These rocks have been dropped down at least 200 m to the west into the Thousand Springs Valley along the Lost River fault zone against folded and sheared beds of the upper part of the Lower Mississippian McGowan Creek Formation. The West Spring block may be either a slide block resting in part on valley fill, or a downdropped tectonic sliver caught in a broad zone of range-front faults. Small synthetic and antithetic fault scarps that formed within the block, during the 1983 earthquake, are numerous, and most are along older bedrock faults. The West Spring block appears to be a part of the Lost River thrust plate, not a structurally higher plate such as the White Knob, and, in this respect, does not resemble slide blocks on the west sides of the Lemhi Range and Beaverhead Mountains (Beutner, 1972; Skipp and Hait, 1977) that are downdropped fragments of structurally higher thrust sheets. The West Spring block lies about 1/2 km north of the reflection seismic line of figure 5, which shows the Lost River fault to be a diffuse zone of disruption. The McGowan Creek Formation, the bedrock of the footwall of the Lost River fault east of the West Spring block, is also the bedrock of the footwall in the position of the seismic line.

The Willow Creek Summit block north of the West Spring block (fig. 1) also is dropped down to the west along the Lost River fault as illustrated by maps of Baldwin (1943, 1951) and Mapel, Read, and Smith (1965). Skipp's mapping of fold axes in this block between the Lost River Range and the mountains west of Thousand Springs Valley shows that they trend northwest rather than north-northwest, the common trend of fold axes in the adjacent Lost River Range (Mapel and others, 1965). The northwest trends suggest the block may have been rotated in a counter-clockwise direction during movement along the Lost River fault, a sense of rotation consistent with the component of sinistral strike slip reported for the surface trace of the Lost River fault and the focal plane mechanism of the earthquake (Crone and Machette, 1984). The part of the Lost River fault on the east side of the block which did not rupture in 1983 was mapped as a thrust fault by Ross (1947), but a stratigraphic omission of slightly more than 1200 m makes that interpretation unlikely. The 1200 m represents the combined thickness of the McGowan Creek Formation and the lower part of the Middle Canyon Formation that is missing between Devonian rocks of the Lost River Range and the upper part of the Upper

Mississippian Middle Canyon Formation in the Willow Creek Summit block (Mapel and others, 1965; Skipp, unpublished mapping). The block also is disrupted by several scarps that resulted from the Borah Peak earthquake. The major northwest-trending scarp in the vicinity of Arentson Gulch (fig. 2) has a history of older movement (Crone and others, 1985), but no major stratigraphic offset was found. No ground breakage took place along the Lost River fault directly east of the Willow Creek Summit block during the Borah Peak earthquake even though there are upper Pleistocene fault scarps in the area (Crone and Machette, 1984).

The approximate location of the epicenter of the 1983 earthquake is south of Chilly Buttes (fig. 2). The buttes are made up of folded and faulted rocks of the White Knob and Bluebird Mountain Formations, and the lower part of the Snaky Canyon Formation (unpublished mapping by M. H. Hait, Jr., and Betty Skipp). These formations are part of the White Knob thrust plate that structurally overlies the Lost River thrust plate. Recent mapping by Skipp also has identified rocks of the White Knob plate in the mountains west of Thousand Springs Valley (fig. 2; Fisher and others, 1983), and south of the valley where earlier maps show Wood River Formation (Ross, 1947), or Copper Basin Formation (Nelson and Ross, 1969). The distribution of rocks of the White Knob thrust plate shown in fig. 3 is based largely on this unpublished mapping.

Lower Paleozoic and Proterozoic(?) rocks, presumably near the boundary thrust of the Lost River thrust plate, are exposed in the Elkhorn Creek area on the east side of Thousand Springs Valley about 6.5 km (4 mi) east of the Chilly Buttes. Here the Lost River fault juxtaposes rocks of the upper part of the White Knob plate, as exposed in the Chilly Buttes area, against rocks of the lower part of the Lost River thrust plate exposed in the Borah Peak horst. The apparent structural offset along the Lost River fault in this area is more than 5000 m, the minimum thickness of the Lost River thrust plate. The 5000 m, however, is the sum of pre-basin-range offset on the faults bounding the Borah Peak horst and basin-range offset on the Lost River fault. Most likely, there is about 3000 m of Neogene offset on the Lost River fault in this area.

REFERENCES CITED

Baldwin, E. M., 1943, Structure and stratigraphy of the north half of the Lost River Range, Idaho: Ithaca, New York, Cornell University, unpublished Ph. D. thesis.

_____1951, Faulting in the Lost River Range area of Idaho: American Journal of Science, v. 249, p. 884-902.

Bally, A. W., Gordy, P. L., and Stewart, G. A., 1966, Structure, seismic data, and orogenic evolution of southern Canadian Rocky Mountains: Bulletin of Canadian Petroleum Geologists, v. 14, p. 337-381.

Beutner, E. C., 1972, Reverse gravitative movement on earlier overthrusts, Lemhi Range, Idaho: Geological Society of America Bulletin, v. 83, p. 839-846.

Bond, J. G., 1978, Geologic map of Idaho: Idaho Department of Lands, Bureau of Mines and Geology, with contributions from U.S. Geological Survey, scale 1:500,000.

Crone, A. J., and Machette, M. N., 1984, Surface faulting accompanying the Borah Peak earthquake, central Idaho: Geology, v. 12, no. 11, p. 664-667.

Crone, A. J., Machette, M. N., Bonilla, M. G., Lienkaemper, J. J., Bucknam, R. C., Pierce, K. L., and Scott, W. E., 1985, Characteristics of surface faulting accompanying the Borah Peak earthquake, central Idaho, in R. S. Stein and R. C. Bucknam, eds., Proceedings of Workshop XXVIII, The Borah Peak Earthquake: U.S. Geological Survey Open-File Report, this volume.

Crosthwaite, E. G., Thomas, C. A., and Dyer, K. L., 1970, Water resources in the Big Lost River basin, south-central Idaho: U.S. Geological Survey Open-File Report, 109 p.

Dahlstrom, C. D. A., 1970, Structural geology in the eastern margin of the Canadian Rocky Mountains: Bulletin of Canadian Petroleum Geology, v. 18, no. 3, p. 332-406.

Dover, J. H., 1981, Geology of the Boulder-Pioneer wilderness study area, Blaine and Custer Counties, Idaho: U.S. Geological Survey Bulletin 1497-A, p. 21-75, 1 Plate, scale 1:62,500.

Fisher, F. S., McIntyre, D. H., and Johnson, K. M., 1983, Geologic map of the Challis 1° x 2° quadrangle, Idaho: U.S. Geological Survey Open-File Report 83-523, scale 1:250,000.

Hays, W. H., McIntyre, D. H., and Hobbs, S. W., 1978, Geologic map of the Lone Pine Peak 15-minute quadrangle, Custer County, Idaho: U.S. Geological Survey Open-File Report 78-1060, scale 1:62,500.

Hays, W. H., Harris, A. G., Dutro, J. T., Jr., and Ross, R. J., Jr., 1980, Stratigraphic Sections of Middle Paleozoic Rocks in the Vicinity of Spar Canyon, Custer County, Idaho: U.S. Geological Survey Open-File Report 80-1097, 82 p.

Huh, O, K., 1967, The Mississippian System across the Wasatch line, east-central Idaho, extreme southwestern Montana, in Guidebook of Centennial basin in southwest Montana: Montana Geological Society 18th Annual Field Conference, p. 31-62.

Ingwell, T. H., 1980, Stratigraphy and Structural Geology of the Merriam Lake Area, Lost River Range, Idaho: Los Angeles, University of California unpublished M.S. thesis, 173 p., scale 1:10,000.

Mabey, D. R., Peterson, D. L., and Wilson, C. W., 1974, Preliminary gravity map of southern Idaho: U.S. Geological Survey Open-File Report 74-78, scale 1:500,000.

Mamet, B. L., Skipp, Betty, Sando, W. J., and Mapel, W. J., 1971, Biostratigraphy of Upper Mississippian and associated Carboniferous rocks in south-central Idaho: American Association of Petroleum Geologists Bulletin, v. 55, no. 1, p. 20-33.

Mapel, W. J., Read, W. H., and Smith, R. K., 1965, Geologic map and sections of the Doublespring 15-minute quadrangle, Custer and Lemhi Counties, Idaho: U.S. Geological Survey Geologic Quadrangle Map GQ-464, scale 1:62,500.

Miller, R. D., and Steeples, D. W., 1985, Seismic reflections within the upper 100 feet near the fault, in R. S. Stein and R. C. Bucknam, eds., Proceedings of Workshop XXVIII, The Borah Peak Earthquake: U.S. Geological Survey Open-File Report, this volume.

Nelson, W. H., and Ross, C. P., 1968, Geology of part of the Alder Creek Mining District, Custer County, Idaho: U.S. Geological Survey Bulletin 1252-A, p. A1-A30, scale 1:24,000.

Nelson, W. H., and Ross, C. P., 1969, Geologic map of the Mackay 30-minute quadrangle, south-central Idaho: U.S. Geological Survey Miscellaneous Geologic Investigations Map I-580, scale 1:125,000.

Ross, C. P., 1947, Geology of the Borah Peak quadrangle, Idaho: Geological Society of America Bulletin, v. 58, no. 12, pt 1, p. 1085-1160.

Sandberg, C. A., 1975, McGowan Creek Formation, new name for Lower Mississippian flysch sequence in east-central Idaho: U.S. Geological Survey Bulletin 1405-E, 11 p.

Skipp, Betty, and Hait, M. H., Jr., 1977, Allochthons along the northeast margin of the Snake River Plain, Idaho: Guidebook of Wyoming Geological Association, 29th Annual Field Conference, p. 499-515.

Skipp, Betty, Sando, W. J., and Hall, W. E., 1979, The Mississippian and Pennsylvanian (Carboniferous) Systems in the United States--Idaho: U.S. Geological Survey Professional Paper 1110-AA, p. AA1-AA42.

Smith, R. B., Richins, W. D., Doser, D. I., Eddington, P. K., Leu, L. L., and Chen, G., 1985, The Borah Peak earthquake--seismicity, faulting, kinematics, and tectonic mechanism, in R. S. Stein and R. C. Bucknam, eds., Proceedings of Workshop XXVIII, The Borah Peak Earthquake: U.S. Geological Survey Open-File Report, this volume.

Smith, R. B., Richins, W. D., Doser, D. I., Pechmann, J. C., and Langer, C., 1984, The 1983 M_s 7.3 Borah Peak, Idaho, earthquake--A model for active crustal extension: Geological Society of America Abstracts with Programs, v. 16, no. 6, p. 661.

Stein, R. S., and Barrientos, S. G., 1985, The 1983 Borah Peak, Idaho, Earthquake--Geodetic evidence for deep rupture on a planar fault, in R. S. Stein and R. C. Bucknam, eds., Proceedings of Workshop XXVIII, The Borah Peak Earthquake: U.S. Geological Survey Open-File Report, this volume.

P-WAVE TRAVEL TIMES AND CRUSTAL STRUCTURE OF SW MONTANA FROM AFTERSHOCKS OF THE OCTOBER 28, 1983 BORAH PEAK, IDAHO, EARTHQUAKE

Michael C. Stickney
Montana Bureau of Mines and Geology
Montana Tech
Butte, Montana 59701

Abstract

The Earthquake Studies Office of the Montana Bureau of Mines and Geology recorded aftershocks of the October 28, 1983 Borah Peak, Idaho earthquake at 20 sites in southwestern Montana. Seventeen portable short-period vertical seismograph stations were operated along a 220 km line segment trending N45^{o}E from the Montana-Idaho border to the southern Big Belt Mountains. Data from three permanent seismograph stations located near the line were also used. The average station spacing along the line was 12 km. P-wave travel-time curves show two distinct line segments of first-arriving P-waves. At distances between 85 and 140 km, the Pg phase arrives first with an apparent velocity of 6.14 km/sec. and beyond 140 km, the Pn phase arrives first with an apparent velocity of 7.96 km/sec. Interpretation of the travel-time curves using standard refraction methods, after correcting for hypocenter depths and assuming horizontal interfaces, suggests the following crustal velocity structure: a single-layer crust 25 km thick with a P-wave velocity of 6.14 km/sec. overlying the upper mantle with a P-wave velocity of 7.78 km/sec. The results of this unreversed refraction profile show similarities with a reversed refraction profile in the region reported by Sheriff and Stickney (1984). The crustal thickness determined from the Borah Peak aftershock refraction profile very likely underestimates the true crustal thickness because a lower crustal layer which probably exists in the region did not produce a first arrival on the travel time-curves.

Data Collection

The Earthquake Studies Office of the Montana Bureau of Mines and Geology installed a portable seismograph along the Montana-Idaho border approximately 90 km northeast of the epicenter of the October 28, 1983 Borah Peak main shock, 27 hours after the earthquake occurred. Over the next 10 days, three portable seismographs were operated at 17 sites along a line extending N45^{o}E from the Montana-Idaho border to the southern Big Belt Mountains in central-southwestern Montana (Figure 1). The initial portable seismograph was operated for 96 hours; all others were operated for time periods ranging between 20 and 48 hours. In addition to data from the portable seismographs, data from three permanent seismograph stations operated by the Earthquake Studies Office, which lie near the line, were included in the data set. The average station spacing along the 220-km line was approximately 12 km.

The signals of short-period, vertical seismometers were recorded on smoked-paper records at the rate of 120 mm/min. for all but the three most distant stations and the initial station on the Montana-Idaho border, which were recorded at 60 mm/min. Timing was provided by internal seismograph clocks which were calibrated against WWV radio signals at the beginning and end of each record. The overall timing accuracy of impulsive P-wave arrivals is estimated to be +/-0.1 seconds.

The University of Utah Seismology Lab provided the origin times and hypocenter locations of the principal aftershocks (Table 1) for the first 21 days of the aftershock sequence (W. D. Richins, written communication, 1984). Eleven aftershocks recorded by the Montana instruments were selected because of clearly recorded P-wave arrivals at one or more stations. All selected aftershocks had well-constrained focal depths between 5 and 10 km and magnitudes ranging between approximately 2.5 and 3.8. P-wave travel times were calculated by subtracting the origin times from the corrected arrival times at each station. A spherical trigonometry relation was used to find the distances between the coordinates of each epicenter and recording station. The P-wave travel times are plotted in Figure 2.

TABLE 1 - Origin times and hypocentral parameters of aftershocks used in the travel time study. Data provided by the University of Utah (W. D. Richins, written communication, 1984).

Date	Origin Time	Lat. N.		Long. W.		Depth	Mag.	No.	Gap	Dmin.	RMS
Yr Mo Dy	UTC	Deg.	Min.	Deg.	Min.						
83/10/30	2302 34.56	44	1.93	113	48.17	7.6	2.7	25	61	4	.14
83/10/31	1515 16.21	44	12.87	113	57.55	6.6	2.5	25	75	1	.15
83/11/02	1241 13.51	44	15.60	114	3.72	4.5	3.5	15	206	3	.17
83/11/03	0150 20.17	44	15.16	114	5.88	7.9	3.8	20	222	6	.16
83/11/04	1730 44.18	44	15.35	114	0.86	5.9	3.2	25	102	4	.15
83/11/04	2329 49.26	44	15.49	114	5.62	8.5	2.9	26	96	3	.16
83/11/06	0326 08.83	44	16.90	114	7.20	8.1	-	14	234	8	.13
83/11/06	0644 15.96	44	9.98	113	58.40	9.9	2.6	32	76	2	.13
83/11/07	1405 46.55	44	16.49	114	6.24	8.1	-	24	82	1	.10
83/11/08	0646 34.02	44	12.78	114	2.21	8.9	3.2	28	69	3	.13
83/11/08	2332 43.03	44	14.00	114	3.24	6.9	3.3	29	72	3	.14

Note: Mag. is earthquake magnitude either estimated from coda length or calculated from a Wood-Anderson seismograph. No. is the number of readings used in the hypocenter solution. Gap is the largest azimuthal separation between seismograph stations. Dmin. is the distance from the epicenter to the nearest seismograph station. RMS is the root mean square of the travel time residuals.

Interpretation and Discussion

The travel-time curves (Figure 2) constructed from the aftershock data shows two distinct line segments of first-arriving P-waves. At distances between 85 and 140 km, first arrivals fall along a line segment with an

apparent velocity of 6.14 km/sec. that is interpreted as Pg. Beyond 140 km, first arrivals fall on a line segment with an apparent velocity of 7.96 km/sec. that is interpreted as Pn.

At distances greater than 190 km, an intermediate phase was sometimes observed between Pn and Pg which never exibited a first arrival on the travel-time curves. This intermediate phase may be a head wave refracted from a lower crustal layer, however, it may also result from another process such as S-to-P conversions, wide-angle reflections, or multiple sources at the earthquake hypocenters. The intermediate phase arriving between Pn and Pg was not consistently observed for all aftershocks recorded at epicentral distances between 190 and 300 km. Also, an intermediate phase was not observed on a nearby reversed refraction profile utilizing explosive sources at the surface (Stickney and Sheriff, 1983; Sheriff and Stickney, 1984). Because the intermediate phase does not exist as a first arrival on the travel-time curves and the origin of the phase can not definitely be attributed to a head wave, it will not be used here for interpreting crustal structure.

Because the focal depths of the aftershock hypocenters lie 5 to 10 km below the surface, corrections must be applied to obtain a realistic estimate of crustal thickness. This was accomplished by applying elevation corrections to the aftershock hypocenters and the recording stations using the method of Dobrin (1960). The aftershock hypocenters and the recording stations were placed on a hypothetical datum 10 km below the land surface (8 km below sea level). Travel times for the portions of the ray paths above the datum were subtracted from the total travel times of the refracted P-waves. The elevation corrections determined in this manner ranged from 2.3 to 2.9 seconds. The apparent velocity of the Pn phase changed from 7.96 km/sec. to 7.78 km/sec. after the elevation corrections were applied. Elevation corrections were insignificant for the direct, Pg phase because the hypocentral depths are small compared to the epicentral distances.

The apparent velocities and time intercepts measured from the corrected travel-time curves were used in conjunction with equations given by Mooney (1980) to determine crustal velocity structure. Because the refraction profile is unreversed, one must assume that the refractors are horizontal. This assumption seems justified because Sheriff and Stickney (1984) reported the Mohorovicic discontinuity (Moho) dips less than one degree northeastward along a reversed refraction profile between the Thompson Creek Mine and the Berkeley Pit (Figure 1).

The crustal velocity structure determined from the corrected travel-time curves indicates a 15.1 km-thick layer below the datum. The total calculated crustal thickness from the ground surface to the Moho is 25.1 km. This crustal thickness is 8 km less than the crustal thickness of 33 km reported by Sheriff and Stickney (1984).

The uncorrected apparent Pn velocity of 7.96 km/sec. observed from the Borah Peak aftershocks is very similar to the apparent velocity of 7.97 km/sec. observed by Sheriff and Stickney (1984) on the southwest-to-northeast

leg of the reversed profile. However, after applying elevation corrections to the Borah Peak Pn data, the apparent velocity dropped to 7.78 km/sec. The 6.14 km/sec. apparent velocity observed on the unreversed profile agrees very well with the upper crustal velocity of 6.16 km/sec. reported by Richins and others (1985) for the upper crustal layer between the depths of 6.5 and 18 km. Sheriff and Stickney (1984) found a Pg velocity of 5.85 km/sec.

The 25 km crustal thickness calculated from these travel-time curves is considerably less than 33 to 60 km crustal thicknesses determined from other refraction studies in the region (Meyer and others, 1961; Ballard, 1980; Sparlin and others, 1982; Sheriff and Stickney, 1984; and Richins and others, 1985). The most likely explanation for the anomalously low value for the crustal thickness is the presence of a hidden layer. The hidden layer problem is inherent to the refraction method which utilizes only travel times of head waves. A hidden layer results from insufficient thickness or velocity contrast of a layer at depth (Won and Bevis, 1984). Failing to recognize a hidden layer may result in an under-estimation of crustal thickness by as much as 40 percent.

Won and Bevis (1984) present a nomogram for determining whether a given crustal velocity configuration will precipitate a hidden layer problem. With the apparent velocities measured from the Borah Peak aftershock travel time curves, it is possible for a 15 km-thick layer with a P-wave velocity of 6.8 km/sec. to exist in the lower crust but go undetected by the refraction method used in this study. The hidden layer problem is also the most likely explanation for the relatively thin crust reported by Sheriff and Stickney (1984).

Travel-time residuals at regional seismograph stations also suggest a crustal thickness greater than 25 km. Richins and others (1985) calculated travel-time residuals from six well-located aftershock hypocenters to approximately 20 regional (epicentral distances less than 650 km) seismograph stations using two different crustal models; one 32 km thick, the other 40 km thick. The travel-time residuals were significantly smaller when the 40-km-thick model was used, indicating better agreement between the thicker crustal model and the observed travel times.

The crustal structure of the extended, seismically active portions of southwestern Montana and central eastern Idaho clearly need additional research to better define crustal structure. The hidden layer problem associated with refraction studies using only head wave travel times suggests that refraction methods using waveform analysis or wide-angle reflection methods may prove more useful for probing lower crustal-upper mantle structure in this region.

References Cited

Ballard, J.H., 1980, Gravity and Seismic Investigation of the Crust and Upper Mantle in Southwestern Montana [M.S. Thesis]: University of Montana, p. 98.

Dobrin, M.B., 1960, Introduction to Geophysical Prospecting: McGraw-Hill Book Company, 446 p.

Meyer, R.P., Steinhart, J.S. and Bonini, W.E., 1961, Montana, 1959; Explosion Studies of Continental Structure: Carnegie Institution of Washington, Publication 622, Washington, D.C., p. 305-343.

Mooney, H.M., 1980, Handbook of Engineering Geophysics, v.1: Bison Instruments Inc., Minneapolis, Minnesota, 165 p.

Richins, W. D., Smith, R. B., Langer, C. J., Zollweg, J. E., King, J. J. and Pechmann, J. C., 1985, The 1983 Borah Peak, Idaho, Earthquake: Relationship of Aftershocks to the Main Shock, Surface Faulting, and Regional Tectonics, in Workshop XXVIII on the Borah Peak Earthquake: U.S.G.S. Open-File Report, in press.

Sheriff, S.D. and Stickney M.C., 1984, Crustal Structure of Southwestern Montana and East-central Idaho: Results of a Reversed Seismic Refraction Line: Geophysical Research Letters, v. 11, no. 4, p. 299-302.

Sparlin, M.A., Braile, L.W. and Smith, R.B., 1982, Crustal Structure of the Eastern Snake River Plain Determined From Ray Trace Modeling of Seismic Refraction Data: Journal of Geophysical Research, v. 87, no. B4, p. 2619-2633.

Stickney, M.C. and Sheriff, S.D., 1983, A Southwestern Montana-Central-Eastern Idaho Reversed Refraction profile: Abstracts with Programs, Rocky Mountain and Cordilleran Section, Geologic Society of America, v. 15, no. 5, p. 317.

Won, I.J. and Bevis, M., 1984, The Hidden-Layer Problem Revisited: Geophysics, v. 49, no. 11, p. 2053-2056.

Figure Captions

Figure 1. Location map showing positions of temporary and permanent seismograph stations used to collect aftershock travel-time data. The position of an earlier reversed refraction profile is shown for reference.

Figure 2. Travel-time curves of Borah Peak aftershocks recorded in southwestern Montana.

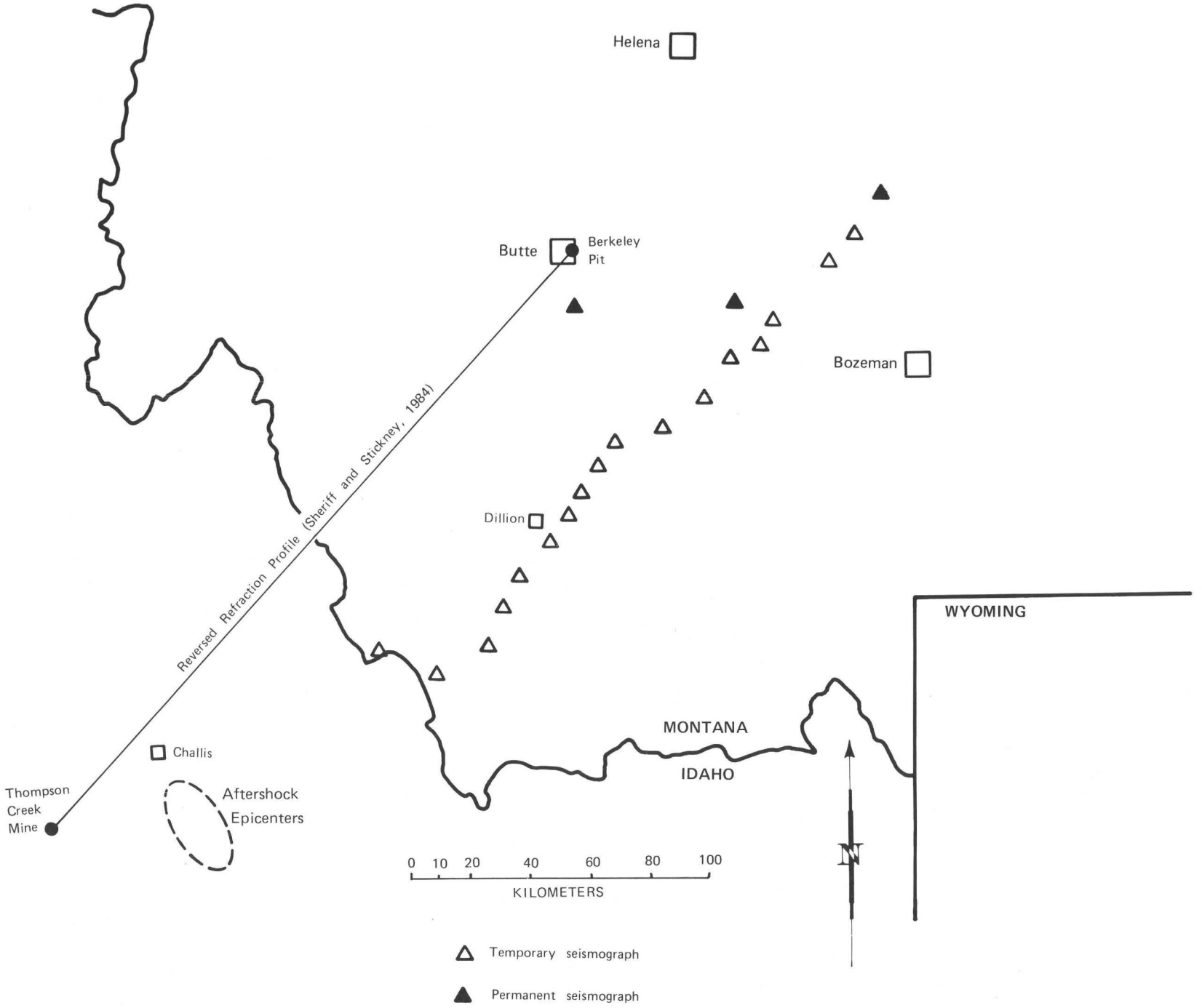
Helena
Butte
Berkeley
Pit
Bozeman
Dillion
Reversed Refraction Profile (Sheriff and Stickney, 1984)
WYOMING
MONTANA
IDAHO
Challis
Thompson
Creek
Mine
Aftershock
Epicenters
0 10 20 40 60 80 100
KILOMETERS
N
Temporary seismograph
Permanent seismograph

FIGURE 1

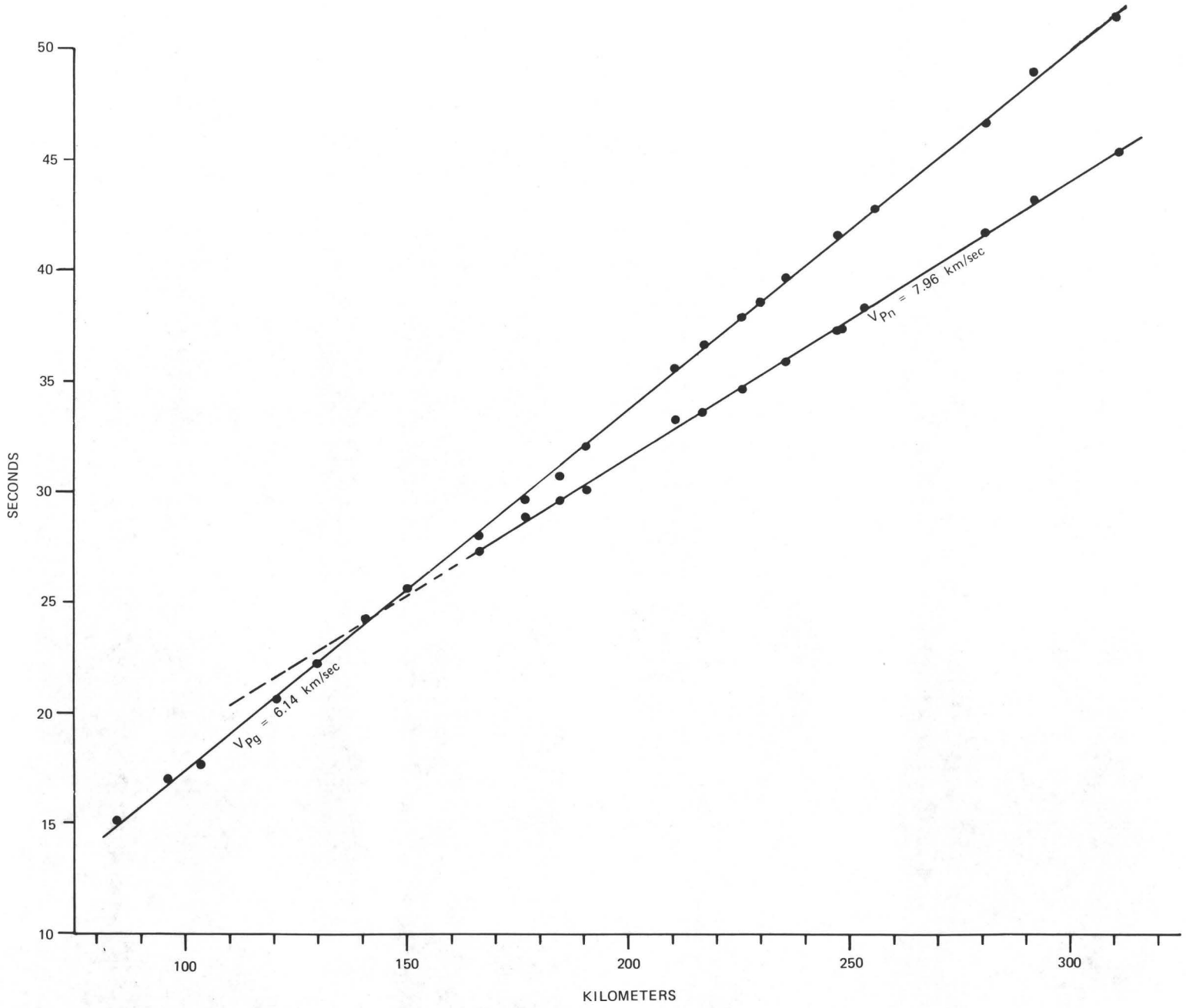
50
45
40
35
30
25
20
15
10
SECONDS
100
150
200
250
300
KILOMETERS
V_{Pg} = 6.14 km/sec
V_{Pn} = 7.96 km/sec

FIGURE 2

Regional Gravity and Magnetic Anomalies in the Borah Peak Region of Idaho

by
Don R. Mabey

Utah Geological and Mineral Survey

ABSTRACT

The regional Bouguer gravity anomaly values in east central Idaho have an inverse correlation with regional elevation with the lowest values over the high regional topography west of the Borah Peak area. A regional average free air anomaly high about 50 km northwest of Borah Peak is coincident with the Bayhorse anticline and may indicate that the anticline is underlain by a basement high. The gravity and magnetic data define two prominent northeast trending lineaments parallel to the eastern Snake River Plain. These lineaments appear to bound the region of current siesmic activity.

INTRODUCTION

Gravity and magnetic data from several surveys have been merged to produce regional gravity and magnetic maps of the region of the Borah Peak earthquake. The gravity data are from surveys of the intermontane valleys by the U.S. Geological Survey (USGS) supplemented by more regional data in the mountainous areas obtained by the USGS and the Department of Defense. The data from these surveys were adjusted to a common datum and merged into a single data set. The data were reduced to the complete Bouguer anomaly using a density of 2.67 g/cc and computer calculated terrain corrections to a distance of 167 km from each station. The Bouguer anomaly values for nearly all stations are believed accurate to within one milligal. In addition, free-air anomalies and average free-air anomalies (Faye anomalies) have been computed. Gravity maps presented here were prepared by Michael W. Webring.

Magnetic data are from airborne surveys flown by or for the USGS. Most of the surveys used in the regional compilation have flight lines 2700 to 3700 m above sea level and 1.6 or 3.2 km apart. Aeromagnetic data are also available from surveys flown for the Department of Energy at about 120 m above the land surface and 4.8 or 9.6 km apart but these data have not been used in this study. Regional magnetic maps have been prepared by removing a common reference field from each survey and mosaicing the resulting contour maps together. The magnetic map presented here is from Mabey and others (1978). For part of the region the individual magnetic surveys have been digitized and adjusted to a common datum and analytically continued to an elevation of 3700 m above sea level with a reference field removed.

In east central Idaho regional gravity and magnetic anomalies reflect a wide variety of geology; a large Cretaceous batholith, Tertiary igneous intrusive rocks in a variety of sizes and shapes, Tertiary volcanic fields including large caldera complexes, Precambrian sedimentary and metamorphic rocks, Paleozoic sedimentary rocks juxtaposed by major overthrusts and basin and range structures.

PHYSICAL PROPERTIES

Most of the rocks in this region fall into six density and magnetization groups. The most dense rocks are of Precambrian age, averaging about 2.7 g/cc. Paleozoic sedimentary rocks have a little lower average density - about 2.6 g/cc. The density of the typical granodiorite and two-mica granites that make up the main mass of the Cretaceous Idaho batholith is 2.58 g/cc. This density is lower than most Cretaceous batholiths in the western United States. Tonalites and related rocks in the western margin of the Idaho batholith are more dense averaging about 2.67 g/cc. The larger Tertiary intrusive bodies are of two density groups. The granites of the Sawtooth batholith and the Casto pluton average about 2.56 g/cc. The Tertiary diorites are more dense - about 2.7 g/cc. The Tertiary volcanic rocks and the Cenozoic sediments are the least dense rocks with the volcanic rocks covering a considerable density range. The magnetic properties are more erratic. The Cenozoic and pre-Cretaceous rocks are generally weakly magnetized with an important exception being the magnetite rich zones in the Precambrian quartzites, which are very strongly magnetized. Most of the rocks of the Idaho batholith are weakly to moderately magnetized. The Tertiary plutons are more strongly magnetized than the Idaho batholith. Some of the Tertiary volcanic rocks are very strongly magnetized with remanent magnetization, both normal and reverse, usually larger than induced magnetization.

GRAVITY AND MAGNETIC MAPS

Although Borah Peak is the highest point in Idaho, the highest average elevations lie to the west in the area of the Sawtooth Range and the White Cloud Peaks. Coincindent with this broad regional topographic high is a broad regional Bouguer gravity low (fig. 1). If the low Bouguer anomaly values in a local gravity low reflecting the very thick basin fill in Lemhi Valley east of Borah Peak are excluded, the Bouguer anomaly values over the regional topographic high are the lowest in the northwestern United States. This broad gravity low reflects the approximate isostatic balance of the region with a negative mass anomaly underlying and bouying up the high topography. Part of this regional negative mass anomaly is likely a thickened crust under central Idaho. Superimposed on this broad regional low are more local anomalies that reflect mass anomalies in the upper crust.

The local anomalies and departures from isostatic equilibrium can be best illustrated if the broad regional is removed, which can be done in several ways. One way is to correct the free-air anomaly value for each station for the gravity effect of a layer of rock with a thickness equal to the difference between the elevation of the station and the average elevation over an area around the station. The corrected value is approximately equal to the free-air anomaly that would be measured at a station at the average elevation and does not have the strong dependence on the elevation of the individual stations. The resulting anomaly values are a form of isostatic anomaly called the average free-air anomaly or Faye anomaly. On the Faye or average free-air anomaly map of the region (fig. 2) the values in eastern Idaho are generally more positive than those to the west. This anomaly is part of an extensive regional isostatic high that extends over a large area of Montana and Wyoming. Over the area of this anomaly the average elevation is significantly higher than can be attributed to isostatic forces. The average free-air

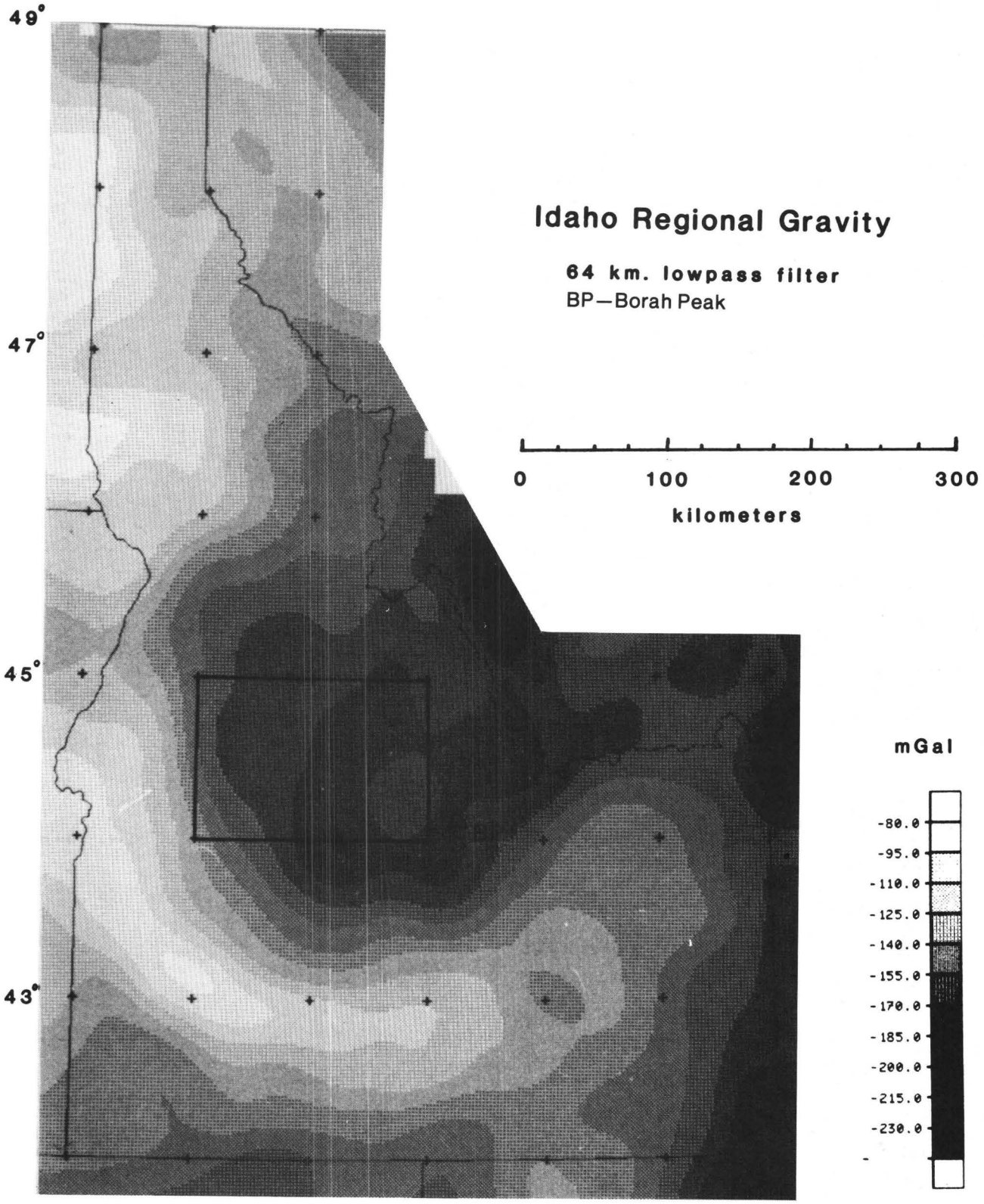

Figure 1. Filtered complete Bouguer gravity anomaly map from Mabey and Webring (in press)

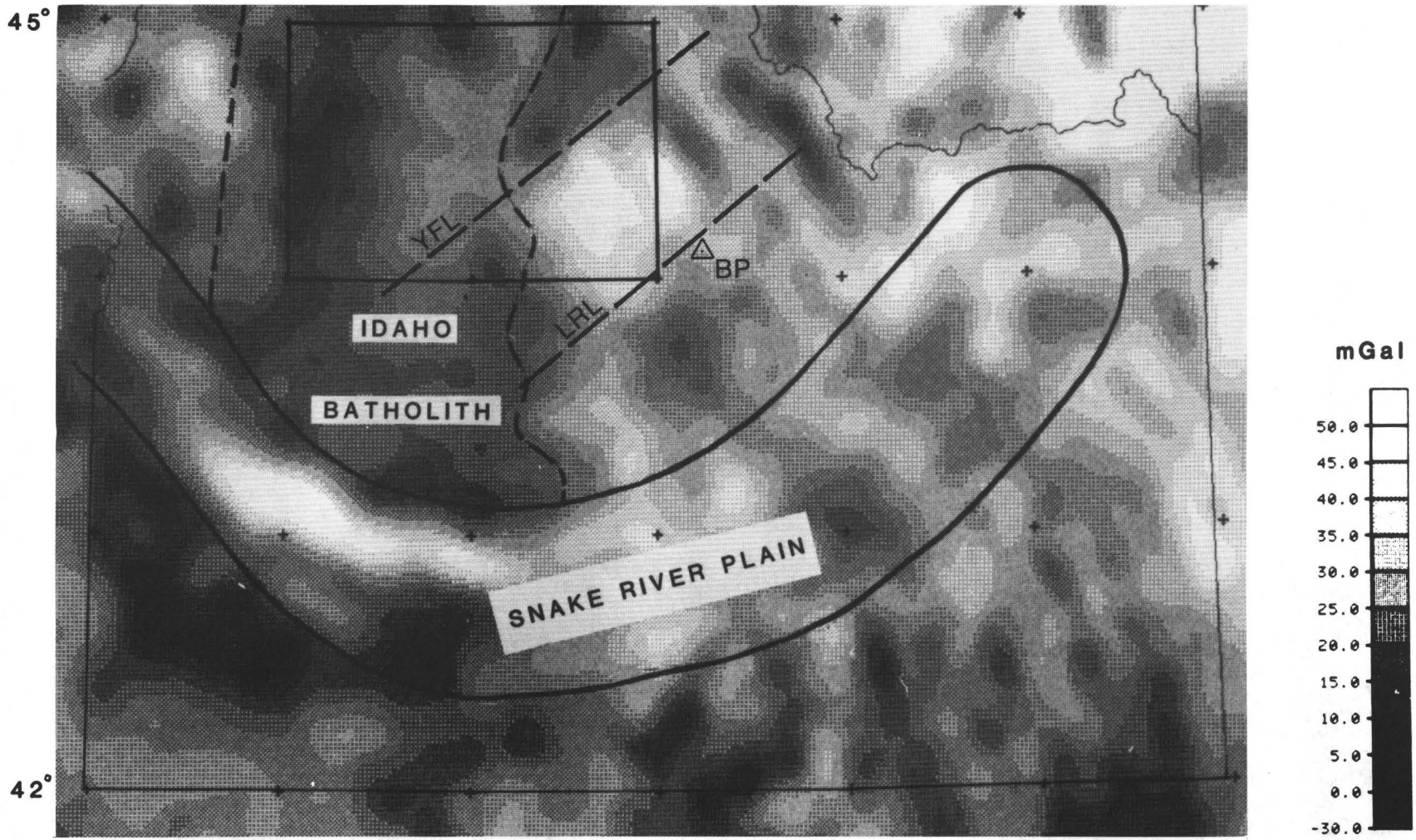

YFL—Yankee Fork Lineament, LRL—Lost River Lineament, BP—Borah Peak

fig. 2 **Faye gravity anomaly map of southern Idaho** radius 64 km

anomaly is generally lower over the Idaho batholith than the area to the east. With values near zero, the area of the Idaho batholith appears to be more nearly in isostatic equilibrium than the area to the east. The major gravity high 50 km northwest of Borah Peak is a prominent regional feature. The crest of this large north-trending gravity high is approximately coincident with the Bayhorse anticline in Paleozoic sedimentary rocks.

The residual magnetic field over central Idaho (fig. 3) shows a broad low over the Idaho batholith. Most of the local highs within this low reflect Tertiary plutons. In the west the border phases of the batholith are marked by an increase in magnetic intensity. The major Tertiary plutons produce large magnetic highs. Several areas of Tertiary volcanic rock produce high amplitude positive or negative anomalies depending on the direction of remanent magnetization. An extensive magnetic high occurs in the same areas as the gravity high 50 km northwest of Borah Peak. A magnetic high north of Borah Peak is part of a 70-mile long high trending northwest across Precambrian quartzites and phyllites. Over much of its length the anomaly is produced by magnetite rich zones in these Precambrian rocks.

Several linear or near linear features are apparent on detailed versions of the gravity and magnetic maps. Two of particular interest in the Borah Peak area are here called the Yankee Fork lineament and The Big Lost River lineament (fig. 2 and 3). These are two of a series of northeast-trending lineaments in eastern Idaho; the most prominent is the eastern Snake River Plain. The Yankee Fork lineament forms the northern limit of abundant Paleozoic rock and the southeast limit of the Van Horn Peak caldera complex. These lineaments appear to outline blocks of crust with contrasting physical properties that have responded differently to the regional stress effecting the region. The current seismic activity is largely confined between the Yankee Fork and Big Lost River lineaments.

The gravity and magnetic highs 50 km northwest of Borah Peak are in the area of the Bayhorse anticline. The gravity high is offset slightly to the west and the magnetic high to the east of the anticline. The axis of the gravity high faithfully follows the axis of the anticline, but the magnetic high does not. The gravity high suggests that the Bayhorse anticline is underlain by a basement high. The magnetic high likely reflects the lithology of the crystalline basement.

A segmented gravity low extends along the west side of the Lost River Range from near Challis southeast to the Snake River Plain. The largest local anomalies reach residual amplitudes of about -20 mgals and generally indicate an east tilted fault block underlying the valley areas. A local gravity low of about 20 mgals in the Thousand Springs Valley is bounded on the east by a steep gravity gradient that reflects the fault that produced the surface rupture in the Borah Peak earthquake. The gravity anomaly could be produced by 1500 m of material with a density contrast of -0.4 g/cc underlying the valley. Assuming a single density contrast model a dip of about 45 degrees is indicated for the fault on the east side of the valley. No major fault is indicated by the gravity data on the west side of the valley. A magnetic high over the valley suggests that volcanic rocks are part of the low density mass underlying the valley. The valley on the west side of the Lost River Range is the western most of three parallel valleys extending north from the eastern

Figure 3. Residual aeromagnetic map of Idaho and western Montana from Mabey and others (1978). YFL - Yankee Fork Lineament, LRL - Lost River Lineament, BP - Borah Peak